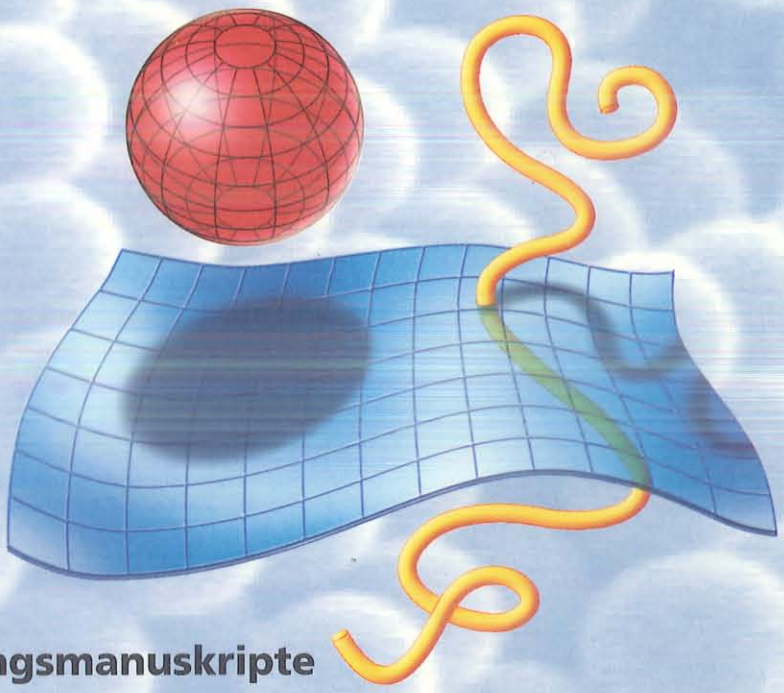
Forschungszentrum Jülich

33. IFF-Ferienkurs 2002
Institut für Festkörperforschung

Soft Matter

Complex Materials on Mesoscopic Scales



Vorlesungsmanuskripte

Materie und Material
Matter and Materials

33. IFF-Ferienkurs 2002
Soft Matter
Complex Materials on Mesoscopic Scales
Materie und Material
Matter and Materials

10

Schriften des Forschungszentrums Jülich
Reihe Materie und Material/Matter and Materials Volume 10

Forschungszentrum Jülich GmbH
Institut für Festkörperforschung

Lecture manuscripts of the
33th IFF winter school

Jan K. G. Dhont, Gerhard Gompper, Dieter Richter (Eds.)

Soft matter:
complex materials on mesoscopic scale

This winter school was organized on March 04 – 15, 2002
in the Forschungszentrum Jülich
by the Institut für Festkörperforschung
in collaboration with
universities, research institutes, and industry.

Schriften des Forschungszentrums Jülich
Reihe Materie und Material/Matter and Materials Volume 10

ISSN 1433-5506 ISBN 3-89336-297-5

Die Deutsche Bibliothek - CIP-Einheitsaufnahme

Soft matter: complex materials on mesoscopic scales : from 4 to 15 March 2002 in the Forschungszentrum Jülich / organized by the Institut für Festkörperforschung in collaboration with universities, research institutes and industry. Ed.: Jan K. G. Dhont ... - Jülich : Forschungszentrum, Zentralbibliothek, 2002
(Lecture manuscripts of... IFF winter school... : 33)
(Schriften des Forschungszentrums Jülich. Reihe Materie und Material ; Volume 10)
ISBN 3-89336-297-5

Publisher:	Forschungszentrum Jülich GmbH Institut für Festkörperforschung 52425 Jülich Phone: (0 24 61) 61-60 48 · Fax: (0 24 61) 61-24 10
Compilation:	Roland G. Winkler
Coverdesign:	Grafische Betriebe, Forschungszentrum Jülich GmbH
Production:	Druckerei Gehler, Düren-Birkesdorf
Copyright:	Forschungszentrum Jülich 2002
Distributor:	Forschungszentrum Jülich GmbH Zentralbibliothek 52425 Jülich Phone: (0 24 61) 61-53 68 · Fax: (0 24 61) 61-61 03 e-mail: zb-publikation@fz-juelich.de Internet: http://www.fz-juelich.de/zb

Schriften des Forschungszentrums Jülich
Reihe Materie und Material/Matter and Materials, Volume 10

ISSN 1433-5506
ISBN 3-89336-297-5

Neither this book nor any part may be reproduced or transmitted in any form or by any means, electronic or mechanical, including photocopying, microfilming, and recording, or by any information storage and retrieval system, without permission in writing from the publisher.

Contents

Preface

I Introduction

I1 Introduction: Soft Matter
J. K. G. Dhont, G. Gompper, D. Richter

A Techniques, Methods, and Synthesis

A1 Scattering
T. Brückel

A2 NMR
G. Meier

A3 Dielectric Spectroscopy
S. Kahle

A4 Polymer Synthesis
J. Allgaier

A5 Colloid Synthesis
J. Buitenhuis

A6 Microemulsion Templating
W. F. C. Sager

A7 Computer Simulations in Soft Matter Science
K. Kremer

B Structure and Phase Behavior

B1 Statistical Mechanics
K. Sturm

B2 Conformations of Polymer Chains
S. Hoffmann

B3 Scaling Laws of Polymers
A. Baumgärtner

B4 Polymer Mixtures
A. Baumgärtner

B5 Polyelectrolytes
R. G. Winkler

B6 Investigations of Polymers by Small Angle Neutron Scattering
D. Schwahn

B7 Capillary Waves on Polymer Thin Films
O. H. Seeck
B8 Self-assembling Amphiphilic Systems
M. Gradzielski
B9 Statistical Mechanics of Membranes
G. Gompper
B10 Polymers Near Surfaces
E. Eisenriegler
B11 Fluid Interfaces and Amphiphiles at Surfaces
P. Lang
B12 Single Membranes and Vesicles
H.-G. Döbereiner
B13 Biopolymers: The Macromolecules of Life
G. Zaccai
B14 Some Aspects of Biomembranes
R. Merkel
B15 Biological Nanomachines
G. Büldt, J. Heberle
B16 Ornstein-Zernike Theories of Fluid Microstructures
G. Nägele
B17 Coarse-Graining Colloids and Polymers
H. Löwen

C Equilibrium and Non-Equilibrium Dynamics

C1 Random Motion in Equilibrium
G. M. Schütz
C2 Polymer Dynamics
D. Richter
C3 Glassy Polymers
U. Buchenau
C4 Rotational Brownian Motion of Colloidal Rods
J. K. G. Dhont
C5 Colloidal Glasses
R. Zorn
C6 Membrane and Microemulsion Dynamics
M. Monkenbusch
C7 Phase Separation Kinetics
M. P. Lettinga

C8 Rheology – Hydrodynamics of Complex Fluids
W. Zimmermann
C9 Practical Rheology
S. Rathgeber

D Industrial Applications

D1 Birth and Fate of Nanoparticles in Water
J. Rieger
D2 Dynamic Light Scattering by Nonergodic Media
J. G. H. Joosten
D3 Colloidal Stability of Casein Micelles in Milk
C. G. de Kruif, R. Tuinier
D4 From the Fundamentals to Balanced Properties of Polymer Products by Means of Structure-Property-Relationships
P. Krüger, K. Sommer

E Index

Preface

In the last years, the traditional research areas of polymers, biological macromolecules, colloids, amphiphilic systems and membranes, as well as liquid crystals have merged into a new research field — *Soft Matter*. This field combines all materials, which are characterized by structures on typical length scales between nanometers and micrometers. Due to the large structural length scale, the number density of their translational degrees of freedom is many orders of magnitude smaller than for an ordinary, molecular material. This and the weak interactions between the structural units, which is typically on the order of the thermal energy k_BT, implies that these materials are easily deformable by external forces — they are soft. As a few examples we want to mention here ink, milk, blood, detergents, plastics, and glue.

The growing together of the different, previously disjoint areas of *Soft Matter* arises on one hand from the recognition of the same underlying mechanisms in the structure and the properties of these systems, and on the other hand from the combination of many of these components in a single material. Examples are polymer-colloid mixtures such as ink, or the cell membranes of biological cells, in which a large number of different, cooperative components are involved.

Essential aspects of *Soft Matter* are the self-assembly of the elementary units to larger, complex aggregates, the cooperative interplay of a large number of degrees of freedom, and the important role of thermal fluctuations. Due to the large range of relevant length-, time- and energy scales, and the large number of cooperating degrees of freedom, the experimental and theoretical investigations to gain an understanding of the properties of these materials are very challenging.

Research in the field of *Soft Matter* is an interdisciplinary enterprise. This includes chemistry, which with the synthesis of increasingly complex molecules provides the building blocks for new materials. Physics provides the methods to investigate the properties of soft materials, and aims at reaching a detailed understanding of the connection between the molecular units and their interaction, and the observed macroscopic properties. Some of the investigated questions are derived from, or have implications, for example, for pharmacology or cell and molecular biology. As far as applications are concerned, material science is interested in finding materials with properties, which can be custom-tailored and tuned over a wide range.

As in previous years, the IFF winter school has been organized in collaboration with several universities in Nordrhein-Westfalen. We are very grateful to our colleagues

Prof. G. Büldt	Institut für Biologische Informationsverarbeitung
Dr. J. Heberle	Institut für Biologische Informationsverarbeitung
Prof. R. Merkel	Institut für Schichten und Grenzflächen

from other Institutes of the Forschungszentrum Jülich, which are doing research in the field of Soft Matter and Biological Physics, for their willingness to participate in this winter school.

We are very glad that several colleagues from universities, research institutes and industry labs have agreed to contribute to the program of the school:

Dr. H.-G. Döbereiner	MPI für Kolloid- und Grenzflächenforschung, Golm
Dr. M. Gradzielski	Universität Bayreuth
Dr. S. Hoffmann	Dutch Polymer Institute, ESRF Grenoble, France
Dr. J. H. G. Joosten	DSM Research, Geleen, The Netherlands
Prof. K. Kremer	MPI für Polymerforschung, Mainz
Dr. P. Krüger	Bayer AG, Zentrale Forschung Physik, Leverkusen
Dr. C. G. de Kruif	NIZO, Ede, The Netherlands
Prof. H. N. W. Lekkerkerker	University of Utrecht, The Netherlands
Prof. H. Löwen	Universität Düsseldorf
Dr. J. Rieger	BASF AG, Polymerforschung, Ludwigshafen
Dr. K. Sommer	Bayer AG, Zentrale Forschung Physik, Leverkusen
Dr. G. Zaccai	Institut de Biologie Structurale, Grenoble, France
Prof. W. Zimmermann	Universität des Saarlandes, Saarbrücken

Without the participation of all these colleagues, the program would not be as interesting, versatile and attractive. We would like to express our thanks to all of them for the effort and enthusiasm which they have put into the preparation and presentation of their contributions.

We are very grateful to the board of directors of the Forschungszentrum Jülich for the organizatonial and financial support, which we have received — as in previous years — for the realization of the IFF winter school and the production of this book of manuscripts. We also thank all the many people in the IFF who have contributed to this school. Our special thanks go to Dipl.-Ing. R. Hölzle for the general management, and to Prof. U. Buchenau, M.-L. Schüsseler and Prof. R. Winkler for their determined help with the preparation of the talks and manuscripts.

J. K. G. Dhont, G. Gompper, D. Richter February 2002

I 1 Introduction: Soft Matter

J. K. G. Dhont, G. Gompper, and D. Richter
Institut für Festkörperforschung
Forschungszentrum Jülich GmbH

Contents

1 What is Soft Matter 2

2 The Classical Systems 4
2.1 Dispersion Colloids 4
2.2 Membranes and Microemulsions 7
2.3 Polymers 10

3 Why "Soft Matter" 12

4 A Short History of Soft Matter Research 16

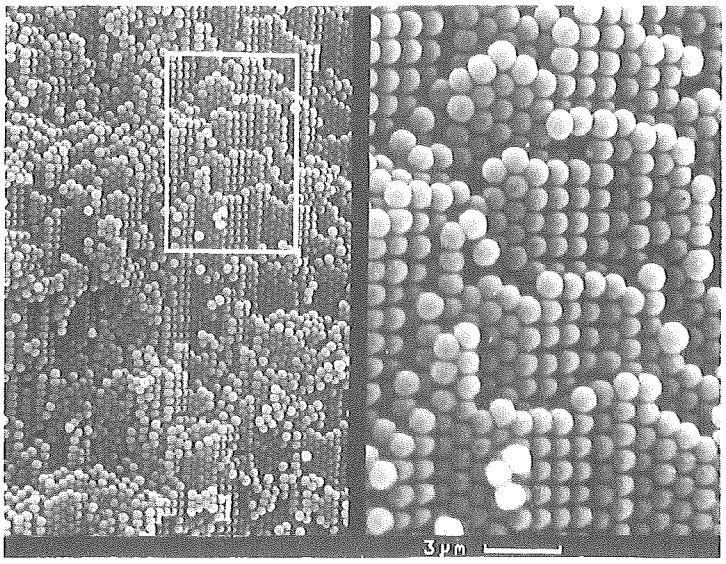


Fig. 1: *Transmission electron microscopy (TEM) picture of a colloidal crystal of spherical particles. The right figure is an enlargement of the part indicated by the white square in the left figure. Clearly visible is the ordered arrangement of the colloidal particles.*

1 What is Soft Matter

When a liquid like water or a crystal of sodium chloride — "kitchen salt" — or silicon are studied under a microscope with a resolution of one Angstrom or less, the atomic or molecular building blocks become visible. Therefore, liquids and crystals made from atoms or small molecules are obviously inhomogeneous, with a structure on the Angstrom scale. With a microscope of 10 Angstrom resolution, this structure can no longer be resolved, the material now looks completely homogeneous. The situation is quite different for a liquid like a suspension of latex particles, or a mixture of oil, water and surfactant molecules. Even at a resolution of 100 or even 1000 Angstrom, the inhomogeneous structure of these materials is still visible. Only on a scale on the order of several microns do these liquids look homogeneous. These systems are therefore often called "complex fluids" or "colloidal systems".

What makes these colloidal systems interesting is that their properties are quite different from liquids or crystals of small molecules. Fig. 1 shows a transmission electron microscopy (TEM) picture of such a colloidal crystal. In particular, materials which consist of extremely large molecules are usually easily deformable. They are therefore also commonly referred to as "*Soft Matter*", a name which has largely replaced the earlier name of "complex fluids". The reason for the softness of such "macromolecular" materials is as follows. Let us compare the energy that is needed to deform the surface of a common molecular crystal (like sodium chloride) and of a crystal of giant spherical "molecules" with a size of, say, 1 micron. The giant spherical "molecules" themselves are rigid aggregates of many millions of ordinary molecules, and are examples of "colloidal particles".

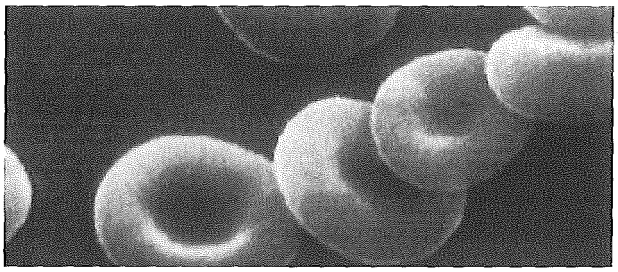


Fig. 2: *Red blood cells (erythrocytes) have a characteristic, discocyte shape.*

The size of ordinary molecules is typically one Angstrom (see above), which is a factor of 10^4 smaller than the colloidal spheres. The shear modulus μ of a crystal of linear size L is defined by the relation

$$\frac{F}{L^2} = \mu \frac{\Delta L}{L} \tag{1}$$

where F is a shearing force, and ΔL is the crystal deformation. Thus, the shear modulus has the dimension energy/(length)^3. The energy scale is here the typical interaction energy of neighboring molecules, which is on the order of the thermal energy $k_B T = (1/40)eV$ for not too low temperatures. The length scale must be proportional to the lattice constant, since this is the only characteristic length scale in a crystal. This simple estimate indicates that the shear modulus of a colloidal crystal is about 12 (!) orders of magnitude smaller than that of a usual crystal. This result indeed reproduces experimentally observed values quite well. Therefore, colloidal crystals are extremely soft and can be destroyed by mechanical means very easily, and the experimental study of colloidal crystallization kinetics requires careful sample manipulation.

There are various other kinds of very large "molecules". Colloids and (bio-) polymers are the most common building blocks of *Soft Matter*. More about colloids and (bio-) polymers will be said in the next section.

For the same reason as sketched above for crystals, membranes consisting of (bio-) polymers are quite easily deformable. A typical example of a such a biological membrane is the "skin" of a red blood-cell, see Fig. 2, the size of which is in the micrometer range. Due to the flexibility of the membrane, a red blood cell can penetrate through openings with a size 10 times smaller than its own size. Without this piece of *Soft Matter*, life in its present form could not exist. Biological membranes have a very complicated structure. Fundamental insight in properties of membranes must be obtained through the study of much simpler structured membranes.

Several books, which cover different areas of *Soft Matter* have been published in recent years. A (necessarily incomplete) list is: Flory (1969) [1], de Gennes (1979) [2], Ferry (1980) [3], Doi & Edwards (1986) [4], de Cloizeaux & Jannink (1987) [5], Meunier, Langevin & Boccara (1987) [6], Russel (1987,1989) [7, 8], van de Ven (1989) [9], Hunter (1989) [10], Nelson, Piran & Weinberg (1989) [11], Elias (1990) [12], Israelachvili (1992) [13], Evans & Wennerström (1994) [14], Gelbart, Ben-Shaul & Roux (1994) [15], Gompper & Schick (1994) [16], Safran (1994) [17], Lipowsky & Sackmann (1995) [18], Chaikin & Lubensky (1995) [19], Dhont (1996) [20], and Kumar & Mittal (1999) [21].

2 The Classical Systems

The "classical" *Soft Matter* systems, which have already been studied since the beginning of the 19th century — see Sec. 4 for more details — are dispersion colloids, amphiphilic systems, and polymers. We want to briefly introduce these systems here.

2.1 Dispersion Colloids

According to what has been said above, colloidal systems can be regarded as solutions of very large, thermally active molecules. Such solutions are commonly referred to as *dispersions* or *suspensions*.

Colloidal particles have a size in the approximate range 1 nm to 10 μ. They most commonly are dissolved in a fluid : without this solvent the colloidal system behaves as a powder. The colloidal particles are small enough to exhibit thermal motion, and therefore behave as "large molecules". The thermal motion of colloidal particles is commonly referred to as "Brownian motion" (named after the English botanist R. Brown, who observed thermal motion of colloidal-like particles through a microscope in 1827). Being just very large thermal molecules in a solvent, colloidal particles exhibit many of the physical phenomena that are found in ordinary molecular systems. Phenomena where quantum effects play a role are of course not observed in colloidal systems, since the colloidal particles are simply too big. Phase transitions (like crystallization, gas-liquid phase separation and formation of nematics and smectics) and critical phenomena (like critical slowing down of diffusion and critical opalescence) are amongst the phenomena that colloidal systems have in common with molecular systems. Colloids can thus be used to study fundamental questions which are also relevant for molecular systems. Due to their large size and slow dynamics, the experimental study of colloids is usually much simpler than for molecular systems (for example, instead of X-ray or neutron scattering, light scattering can be used in many cases, and times that are involved are in the seconds range, instead of the microseconds or even picoseconds range). As will be discussed later in this section, there are many phenomena specific to colloids, which are not found for molecular systems. The lower limit of approximately 1 nm on the size of a colloidal particle assures that the fluid in which the colloidal particles are embedded can be treated as a structureless continuum. Since the typical size of a solvent molecule is 1 Angstrom, the colloidal particle can be regarded as a macroscopic object on the solvent length scale (an exception on this would be a solvent that itself is close to a critical point). Interactions between colloidal particles and solvent molecules can thus be treated on the basis of the Navier-Stokes equation for the solvent. Moreover, relaxation times of degrees of freedom of the solvent molecules are much smaller than those for the colloidal particles. Dynamics and non-equilibrium phenomena can thus be described by equations of motion in which the degrees of freedom of the solvent molecules are integrated out. Both for the structure and dynamics, a colloidal system of identical colloidal particles can thus be regarded as an effective one-component system. The solvent just acts as a "thermal motor" that drives the motion of the colloidal particles.

The interest in colloidal systems goes well beyond the above mentioned possibility to gain insight in fundamental questions that also apply to molecular systems. Colloidal systems have their own specific properties that have no counterpart in molecular systems. There are two reasons why colloids exhibit specific phenomena not found in molecular systems :

(i) the various kinds of interaction potentials that can exist between the colloidal particles which do not exist for molecules, and (ii) the slow dynamics of the colloidal particles, giving rise to non-equilibrium phenomena that are not found in molecular systems. Let us have a closer look at both of these specific properties of colloids.

The interaction potential between molecules is set by their electronic structure. The interaction potential between colloidal particles, however, can almost be chosen at will, ranging from purely long ranged repulsive to very short ranged attractive. The potential can be tuned in a number of ways. First of all, the surface of a colloidal particle can be covered by short or long polymer chains or charged groups. When the solvent is a good solvent for the polymers attached to the surface, and the polymer chains are very short in comparison to the size of the core of the particle, the interaction potential is effectively a so-called hard-core potential: the interaction potential is infinite when the inter-particle separation is smaller than the size of the core and zero otherwise. When, on the other hand the solvent is a bad solvent for the polymer, the interaction potential has a very short ranged attractive part, on top of the hard core repulsion The phase diagram of such a system is shown in Fig. 3. A gel line, below which the colloid particles "freeze" into a long-lived, non-equilibrium state, seems to intersect the gas-liquid critical state. The existence of a gel-state is an example of a state which is not found for the usual molecular systems.

In the good solvent case, one could experimentally study nucleation and crystal growth kinetics for a model hard-core system (which is interesting from the theoretical point of view), while for the poor solvent case one could study gas-liquid phase separation kinetics and gel formation. Secondly, one can change the potential by external means. For example, the quality of the solvent for the polymer attached onto the surface of a colloidal particle can be changed by changing temperature: the depth of the attractive part of the potential is then changed. One could also change the refractive index of the solvent, thereby changing the strength of the always present van der Waals attractions between the cores of the colloidal particles. When the surface of the colloidal particles is charged, one can change the range of the repulsion by adding or removing salt from the solvent. Another possible way to manipulate both the range and strength of a predominantly attractive potential is to add free polymer to the solvent. So-called "depletion attractions" between the colloidal particles are now induced. The range of attraction is set by the size of the polymers while the interaction strength is set by the number concentration of polymers. In this way one can chose an interaction potential depending on the kind of phenomena one wishes to study, or find new kinds of phenomena on changing the potential. The above not only holds for spherical colloidal particles, but also (albeit to a lesser extent until now) for non-spherical particles. Non-spherical colloidal particles that are commonly used are bio-polymers (like fd-virus — see Fig. 4 —, tobacco mosaic virus (TMV) and DNA fragments) or inorganic particles.

The very slow dynamics of colloids also gives rise to phenomena that are not found in molecular systems. The microstructural arrangement of colloidal particles relaxes typically in a time range of seconds. This results in a non-linear response of colloidal systems to, for example, a shear-field. For molecular systems such non-linear response would occur at unrealistically high shear-rates and frequencies. A practical application of this kind of non-linear behavior of colloids is paint. At high shear rates the viscosity of paints should be small, so that one can easily bring paint onto the wall. After that, the paint should stay on the wall and not simply move under gravity to lower parts of the wall. Hence,

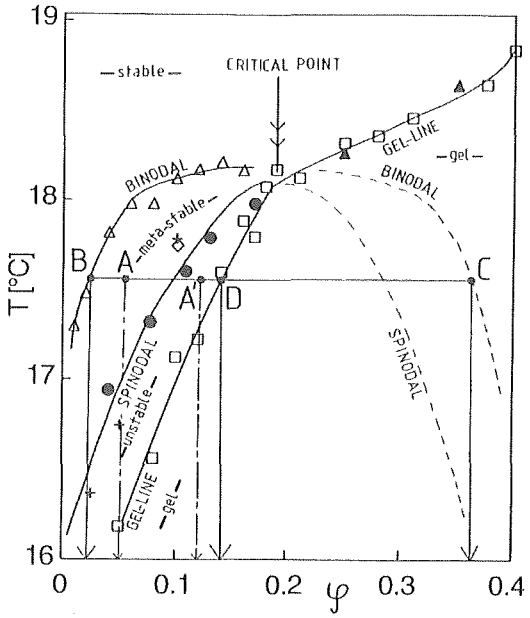


Fig. 3: *Phase diagram of colloidal silica particles covered with very short polymer chains (stearyl alcohol), dissolved in benzene. The quality of the solvent decreases on lowering the temperature. Here, φ is the concentration in terms of the volume fraction of colloidal material. The points relate to various experimental techniques that were used to determine the phase transition lines. Starting from a homogeneous system with a concentration corresponding to point A or A', the system would demix in two coexisting bulk phases with concentrations B and C, in the absence of the gel line. For A the demixing scenario is nucleation and growth, for A' spinodal decomposition. Due to the gel line, in reality, the system will "freeze" in a non-equilibrium state, where patches of gel with concentration D "coexists" with colloidal fluid of concentration B.*

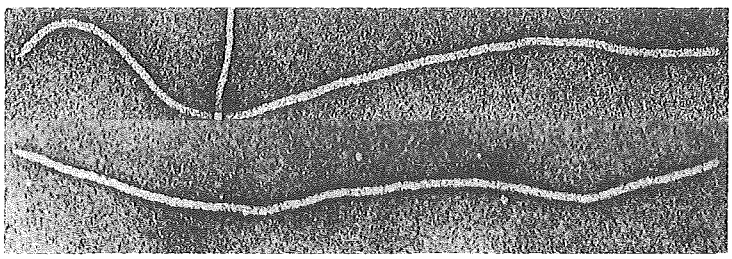


Fig. 4: *A fd-virus has the shape of a long, semi-flexible rod. It has a diameter of about 6 nm, a length of 880 nm, and persistence length of about 2.2 μm.*

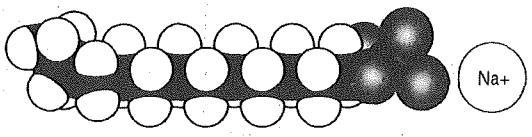


Fig. 5: *Sodium dodecyl sulfonate (SDS) is an typical example of an ionic amphiphile. The dissociable headgroup (right) is linked to one hydrocarbon chain (left).*

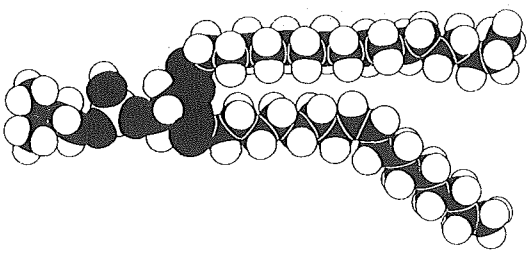


Fig. 6: *Phosphatidyl-choline (PC) is a typical example of a membrane lipid. The polar head (left) is connected to two hydrocarbon tails (right).*

at low shear rates the viscosity of paint should be large. The colloidal particles that are contained in paint not only assure such viscous behavior but in many cases also carry the pigment which gives the paint its color.

2.2 Membranes and Microemulsions

Amphiphilic molecules consist of a hydrophilic , "water-loving" part and a hydrophobic "water-hating" part, see Fig. 5. The hydrophobic part typically consists of one or two hydrocarbon chains. The hydrophilic part is a polar group in the case of non-ionic amphiphiles, and a ionizable group, which dissociates in water, in the case of ionic amphiphiles — such as the molecule shown in Fig. 5. Amphiphilic molecules therefore prefer to sit at the interface between hydrophilic and hydrophobic solvents. Their name derives from the Greek word "amphiphile", which means "loving both". These molecules are also often called "surfactants", for *surf*ace *act*ive substance, since they assemble at surfaces and reduce the surface tension.

As an example, we mention the experiment of Gorter and Grendel (1925). They first extracted lipid molecules (see Fig. 6) from the plasma membrane of red blood cells (compare Fig. 2). By pouring these lipid onto a water surface, and comparing the area of the resulting patch with the surface area of the original cell surfaces, they concluded that the cell membrane consists of a lipid bilayer. Later it turned out that their arguments contained several errors — they had for example underestimated the size of the original

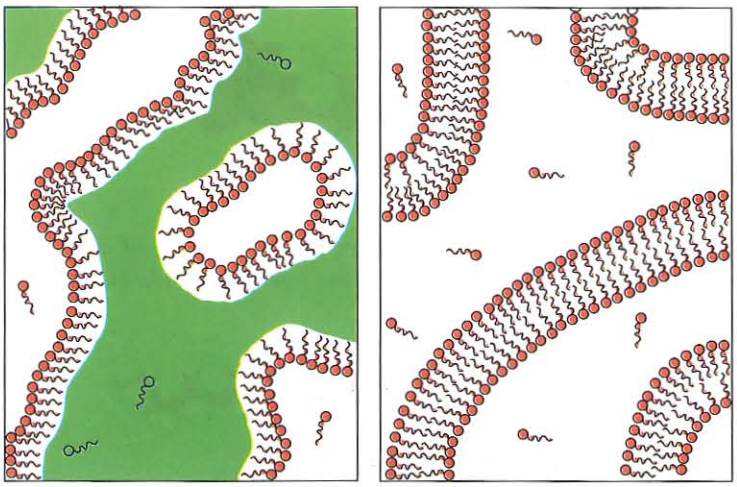


Fig. 7: *Amphiphilic molecules self-assemble into complex aggregates due to the hydrophobic effect. In mixtures with oil and water, they form monolayers at the water-oil interface. In mixtures with water, they form bilayers.*

cell surface. However, these errors cancelled out each other to a large extend, so that their conclusion was indeed correct. Nowadays, it is well established that the major component of the cell membrane consists of a lipid bilayer.

Structure formation in amphiphilic systems occurs by supramolecular aggregation — as in the formation of lipid bilayers discussed above. The dominant driving force is here the *hydrophobic effect*, which makes mixtures of polar and apolar molecules highly unfavorable. The underlying physical mechanism is not very well understood, but is most likely due to the perturbation of the network of hydrogen bonds in polar solvents like water by a apolar solute particle. This effect is responsible for oil and water not to be miscible at ambient temperatures. Amphiphilic molecules preferentially adsorb at the oil-water interface, because in this way both parts of the molecule can be in their favorable environments. The adsorption of surfactants reduces the tension of the oil-water interface, because at the location of the amphiphilic molecule, the unfavorable direct contact between oil and water can be avoided. The interfacial tension decreases with increasing surfactant concentration, until a state is reached in which the amphiphilic molecules are so densely packed that no space is available for more molecules to squeeze in, compare Fig. 7. This state has been called by Schulman a *saturated monolayer*. The interfacial tension is extremely low in this case, or vanishes completely, so that new phases become possible, in which oil and water are mixed on a mesoscopic length scale, typically 1-100 nm. Such phases are called *lyotropic phases* or *microemulsions*. A schematic phase diagram, which contains sketches of the many possible mesophases, is shown in Fig. 8.

In binary mixtures of water and amphiphile, no oil-water interface exists for the surfactants to assemble. Therefore, they form spherical aggregates in this case, called *micelles*, or bilayer (compare Fig. 7). Thus the amphiphilic molecules try in this case to form a favorable environment themselves, by sticking their hydrocarbon tails together and ex-

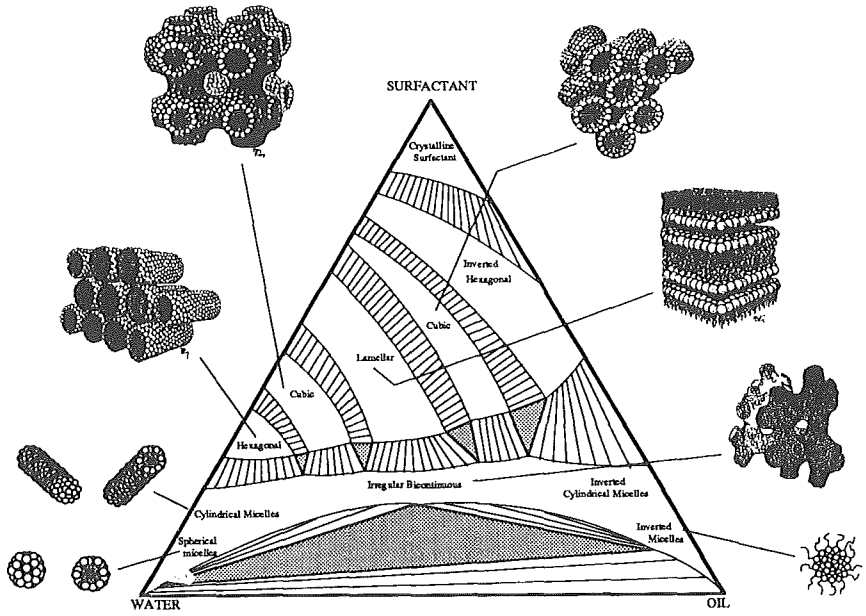


Fig. 8: *Schematic phase diagram of ternary amphiphilic systems. From Ref. [22].*

posing only the polar headgroups to the water. It has already been mentioned above that amphiphilic bilayers are the basic building block of all biological membranes.
Surfactants play of course an essential role in all kinds of cleaning processes. Whether you wash your hand or do your laundry, surfactant molecules — in this context also called soap or detergent — do the work. They reduce the interfacial tension between the oily or fatty dirt by a sufficient amount so that this dirt can be removed from the skin or from fabric fibers and carried away as small droplets by the excess water.
It is interesting to see that surfactants are actually only a minor component in standard detergents, which are composed of [23]

surfactants	10-15%
builder (zeolites etc.)	30-40%
bleaching agents	20-30%
bleaching activators	1.5-4%
lather (froth) regulators	3-5%

The consumption of surfactants in West-Germany in the year 1984 was

anionic	149200 t
non-ionic	136900 t
cationic	32000 t
other	4000 t

Of this consumption, 2/3 of the ionic and 1/2 of the non-ionic surfactants is used in detergents. Finally, it is worth mentioning that in the European Community, 80% of the commercially used surfactants had to be biodegradable in 1987.

2.3 Polymers

In the simplest case, polymers are long, linear chain molecules, which are built from a repeat unit, called a monomer. Such polymers are *linear homopolymers.* Many properties of polymers can be custom tailored by the use of different monomers in the polymerisation process, or by a variation of the polymer architecture — which can be linear, star-shaped, H-shaped, like a bottle-brush, etc.
The individual monomers or building blocks are bound together by covalent bonds. This usually does not restrict rotations around the bond axis, so that such rotations are still possible. Therefore, long chains have a very large number of internal degrees of freedom, which lead to an enormous number of spatial conformations of all the monomers. The entropy of such a chain is directly related to the vast number of conformations, and is therefore also large. The free energy of a chain molecule is therefore not only determined by the internal interaction potentials, but to the same extent by the chain entropy. On distances, which are large compared to the size of a monomer, the chemical structure of the building block plays only a minor role, and the properties of the chain are mainly determined by the statistical mechanics of the chain, i.e. essentially by the chain entropy.

The *central limit theorem*, also called the law of large numbers, states that the most probable spatial conformation of a large number of monomers is governed by Gaussian statistics. An equivalent statement is that the path along the chain from the first to the last monomer follows a random walk — as would be traced out by a diffusing particle, which hops from point to point with a step length given by the monomer size. When external forces act on such a chain, it is stretched out and thereby looses part of its entropy, which thus favors a return to the most probable, coiled-chain conformation. This is equivalent to an entropic force, which is responsible for rubber elasticity.
Many properties of polymers are a direct consequence of the law of large numbers and the laws of statistics, and are therefore *universal valid.* For a polymer chain, which is in a coil conformation (compare Fig. 9), the radius of gyration R_g or the average end-to-end distance R_e depend, for example, on the number N of monomers in the form of a power law,

$$R_e \sim N^{\nu} \ . \tag{2}$$

For a random walk, the exponent is $\nu = 1/2$. The entropic nature of rubber elasticity implies that the restoring force is inversely proportional to the mesh size of the polymer network. As a consequence of the chain topology, the viscosity of a polymer melt of linear chains again depends on the chain length in the form of a power law. There are many other examples of this universality, which we cannot mention here.
In addition, properties which derive from the specific chemical structure of the monomers of course also play a role. The microstructure of a polymer, which can be regular or random, determines for example whether the polymer crystallizes or not. The miscibility of polymer systems is extremely sensitive to the chemical structure of the chain. Also, transport properties like diffusion are determined by a friction coefficient, which is specific for a given material. This interplay between universal and specific properties is one of

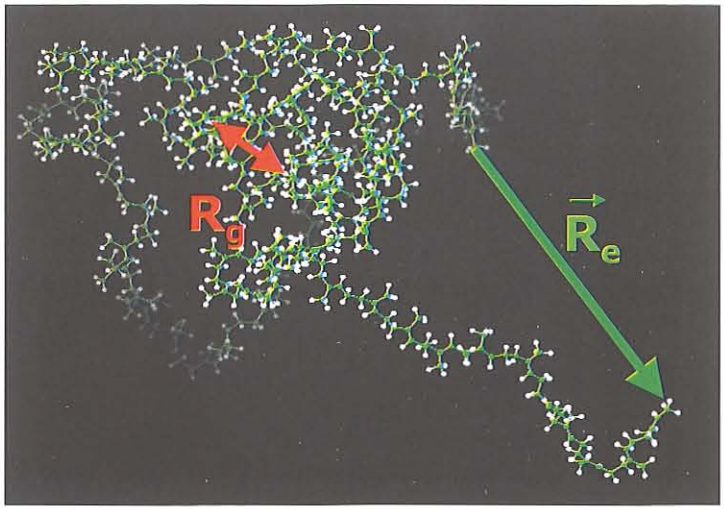


Fig. 9: *The typical conformations of long, flexible polymers — such as polyisoprene shown here — are random coils. These conformations can be characterized by a end-to-end distance R_e and a radius of gyration R_g.*

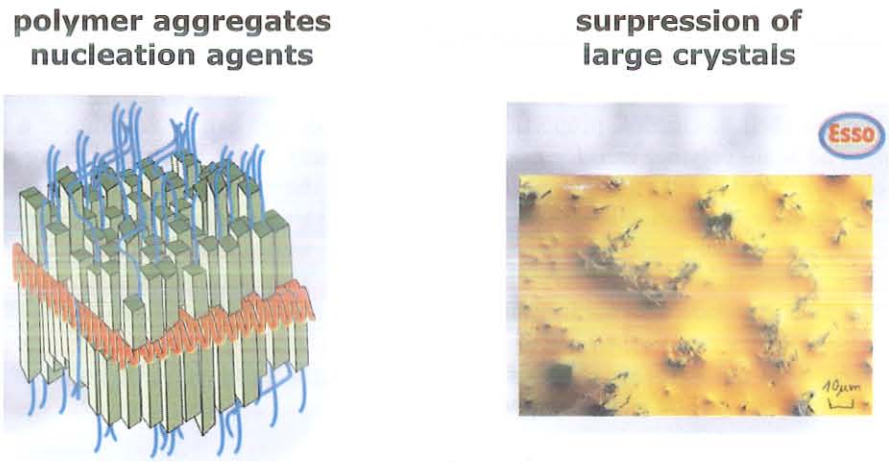


Fig. 10: *Diblock copolymers, with a crystallizable and a non-crystallizable block, can be used to suppress the formation of large wax crystals in diesel fuel at low temperatures. The mechanism is shown on the left. The crystallizable part of the diblock copolymers acts as nucleation centers for wax crystals, so that a large number of small crystals are formed; the non-crystallizable block keeps these aggregates in solution. The right picture shows that this mechanism works very well in practice.*

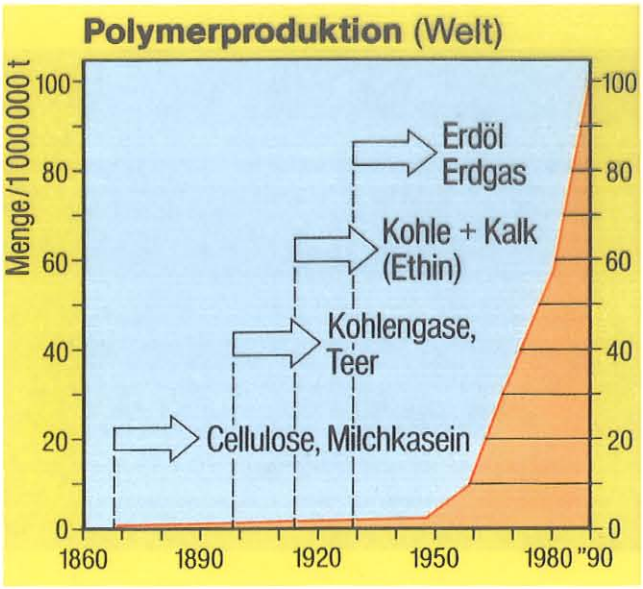


Fig. 11: *Industrial polymer production per year over the last 130 years.*

the major challenges of polymer science. The goal is to employ both of these aspects to construct polymer materials which just the desired properties.

Plastics and polymers play a very important role in our daily lives. Polymer materials are used everywhere, because they are durable, simple to produce and easy to process, and because their mechanical properties are very versatile and can be varied over a wide range. The same polymer can, for example, flow viscously, react like a rubber, or show a pronounced brittleness. Polymeric fibers can have the strength of steel, polymeric electrolytes have an enormous absorption strength — which is employed for example in baby diapers —, polymeric additives make diesel fuel winter hard (compare Fig. 10), polymers are used as viscosity modifiers in motor oil, polymers serve as construction material for a large variety of applications, and polymers are suitable as template materials in nano-technology due to their self-assembling properties.

Therefore, it is not surprising, that the yearly industrial production of polymers has exploded over the last 50 year, as shown in Fig. 11.

3 Why "Soft Matter"

In the last 10-20 years, the previously largely independent research fields of colloids, membranes, microemulsions and polymers have been integrated in the new research field *Soft Matter*. This is not just old wine in new bottles; rather it has been realized that many phenomena in these systems have the same underlying physical mechanisms, so that similar effects do not have to be discovered and understood anew in each subfield. Moreover, combinations of, for example, polymers and colloids, exhibit new properties,

which are not found in both systems separately.

Three aspects are particularly important:

Universality — Many phenomena of *Soft Matter* are *independent* of the chemical structure of the molecular building blocks. A simple example are polymers. As discussed in Sec. 2.3, when the chains are long enough, the average end-to-end distance as well as other polymer properties are found to depend on the monomer number by a power law, with an the exponent ν, which has the same value for *all* polymers of the same topology and the same class of interactions, independent of the chemical architecture of the monomers. Similar relations can be found for membranes and colloids, where also many effects are independent of the chemistry of surfactants or colloid particles.
The reason for the universality is again the large characteristic length scale of *Soft Matter* systems, which implies that a very large number of atoms or atom clusters have to cooperate to make things happen. In the simple case of a linear polymer chain without self-avoidance, the *law of large numbers* implies $\nu = 1/2$. When self-avoidance is taken into account, cooperativity effects get even stronger, and the exponent increases to $\nu = 0.6$. Therefore, from a theoretical point of view, *Soft Matter* physics is the domain of *Statistical Mechanics*, which provides the framework in which cooperative phenomena can be understood.
As already mentioned above, there is also a universality among the different classes of materials. As an example, consider a mixture of two homopolymers A and B (i.e. polymers made of a single type of monomer) with a so-called A-B diblock copolymer, in which two different homopolymers are linked together chemically to form a single, correspondingly longer chain. If the two A- and B-polymers are immiscible, which is often the case, then a mixture can be achieved by addition of small amounts of diblock copolymers. Thus, block copolymers play a very similar role in this case as amphiphilic molecules do in mixtures with oil and water. A second example is the viscosity of dilute polymer solutions. The dependence of the viscosity on the polymer concentration is exactly the same as in a dilute colloidal suspension. Thus, in the dilute regime, polymers behave like hard spheres. Finally, we want to mention rod-like micelles, which can be so long that they exceed their persistence length many times and then behave as "living polymers", i.e. in many respects they behave as polymers, but they have the additional dynamical property of fission of long micelles into shorter ones, and vice versa the fusion of short micelles into longer ones.

Blurred Classifications — For many systems is it very difficult to classify them into one of the classical categories. As rod-like colloids get longer and longer, their flexibility becomes increasingly important. As soon as their length exceeds the persistence length, they behave as a semi-flexible polymer, and even longer ones as flexible polymers. As an example, consider the fd-virus of Fig. 4. Is it more appropriate to call it a colloidal particle or a semi-flexible polymer? Similarly, amphiphilic properties can be varied gradually. Amphiphilic molecules can be short, such as the classical surfactants, or very long, such as amphiphilic block copolymers. This situation is shown schematically in the "magic triangle" of *Soft Matter* in Fig. 12.

Complexity — In the last years, the boundaries between the classical areas of *Soft Matter* has also become more and more diffuse, because increasingly systems have been investigated, which contain several components of the different classes of materials, like

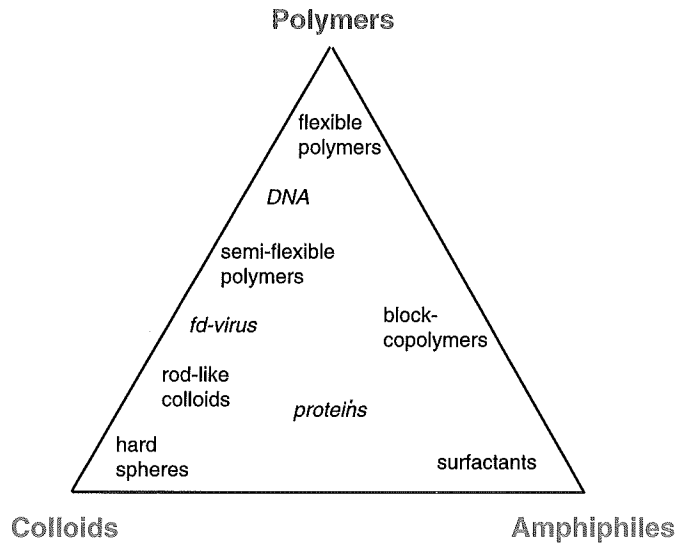


Fig. 12: *The "magic triangle" of Soft Matter, which shows that the classical fields of colloids, polymers and amphiphilic systems have merged into one. The aspect ratio (length/width) increases in the vertical direction, the amphiphilicity in the horizontal direction.*

mixtures of colloids and polymers, polymers at membranes, colloids in microemulsions, etc. These mixed systems have of course a much higher degree of complexity than the classical systems. In order to understand their behavior, knowledge from the various subfields of Soft Matter has to be brought together.

A very nice example for the complexity which can arise in *Soft Matter* systems is a recently investigated mixture of rod-like colloids and polymers [24]. In the regime of very small colloid concentrations, the colloid particles are found to form a thermally fluctuating membrane. The interaction, which keeps the colloids together is the depletion interaction, which has been discussed briefly in Sec. 2.1 above. The colloidal rods in this experiment are the fd-viruses shown in Fig. 4. Thus, these are not stiff rods, but semi-flexible objects, which therefore show themselves polymer-like behavior. Note that the thickness of this membrane is now given by the length of the fd-virus, i.e. about one micron; this is about three orders of magnitude larger than the thickness of the usual lipid bilayer membranes. Finally, the structure of the fd-virus itself is a DNA molecule — again a polymer — which is enclosed by a self-assembled layer of amphiphilic proteins. Thus, this system behaves as a colloidal, a amphiphilic and a polymeric system on several different levels.

An important part of this complexity are the *effective interactions* between the macromolecules. In a complex system, the interaction between macromolecules is not limited to the standard Coulomb and quantum-mechanical interactions. Instead, the interactions between macromolecules depends on the many degrees of freedom of the solvent, and is itself already the result of a thermodynamic average. Therefore, effective interactions can and usually are temperature dependent. Furthermore, they can be controlled an tuned

by additives to the solvent. A good example is the control of the interactions between colloidal particles by polymers in the solvent. If the colloidal particles have an repulsive interaction without polymer, the effective interaction becomes increasingly attractive with increasing polymer concentration, until finally a phase separation into a colloid-rich and a polymer-rich phase occurs. The polymer-mediated interaction is called *depletion interaction* in this case.

In fact, with the enormous complexity of biological membranes, biological cells and biological systems in general, nature points the way towards the investigation of complex *Soft Matter*. Biological membranes, for example, are composed of a many-component mixture of lipids. They also contain a large number of *membrane proteins*, which control the exchange of nutrients and information signals between neighboring cells, and which are therefore essential for the functioning of the cell.

4 A Short History of Soft Matter Research

The classical fields of *Soft Matter* research have a very long and interesting history. We give here a short summary, which is necessarily biased and incomplete, in particular concerning the more recent history.

1827: *R. Brown*, an English botanist, observes through a microscope the thermal motion of pollen grains in water; these grains happen to have the typical micron size of colloid particles.

1835: *H. F. Scherk* finds the first mathematical examples of periodic minimal surfaces, i.e. of surfaces where the mean curvature vanishes everywhere.

1861: *T. Graham* first distinguished between solutions, in which the dissolved species is able to diffuse through a semi-permeable membrane, and solutions, where no diffusion through a semi-permeable membrane is observed. He named the latter kind of solution "colloids" (from the Greek word "kolla" for glue).

1866: *Berthelot* first synthesizes a synthetic polymer — polystyrene – without knowledge of the chemical architecture.

1867: *Schwarz* finds the first triply periodic minimal surface (TPMS), the P-surface. Later, he and his students discover four additional TPMS.

1873: *J. D. van der Waals* derives his equation of state that describes, on a phenomenological basis, the gas-liquid phase transition.

1873: *J. A. F. Plateau* performs detailed experiments on soap bubbles; the results are published in the book *Statique Expérimentale et Théorétique des Liquides Soumis aus Seules Forces Moléculaires.*

1887: *J. H. van 't Hoff* find the law which determines the osmotic pressure dependence on the molecular weight.

1888: *J. H. Gladstone et al.* use osmotic pressure measurements to first determine the high molecular weights of macromolecules such as natural rubber (polyisoprene), starch, and cellulose.

1903: *A. Müller* first identifies high-molecular substances by chemical precipitation.

1905: *A. Einstein* offers an interpretation of Brownian motion and translational diffusion on the basis of a kinetic theory, and shows how this interpretation can be used to determine Avogadro's number. Einstein supplements this work by a more general approach based on the theory of fluctuations in thermal equilibrium, which can also be applied to rotational diffusion.

1906: *M. von Smoluchowski*, a Polish physicist, publishes his kinetic theory approach to Brownian motion, in which he considers the frequent small changes in the direction of motion of a Brownian particle due to collision with solvent molecules.

1908: *P. Langevin*, a French physicist, gives "une démonstration infinitment plus simple" of Einstein's theory by formulating a stochastic differential equation for a Brownian particle.

1910: *J. Perrin* provides definite proof for the existence of molecules by experiments on colloidal systems.

1910: *G. Gouy* (1910), *D. L. Chapman* (1913) and *P. Debye and E. Hueckel* (1923) formulate an approximate theory for the electrical double layer.

1914: *L. S. Ornstein and P. Zernike* formulate a method to include multi-particle interactions in the calculation of structural properties. The Ornstein-Zernike equation is one of the most successful formulations to obtain the static structure factor for liquids from a given pair-interaction potential.

1915: *Wo. Ostwald* publishes the book *Die Welt der vernachässigten Dimensionen* (The World of Neglected Dimensions), which was the the world of colloid phenomena.

1915: *M. von Smoluchowski* formulates the diffusion equation for the probability density of a Brownian particle in position space in the presence of external forces.

1917: *M. Planck* derives the Fokker-Planck equation in abstract configuration space, and discusses the concept of a probability current and the principles of detailed balance. This work was motivated by a paper on electric dipoles rotating in a radiation field by the Dutch physicist *A. D. Fokker* (1914).

1920: *H. Staudinger* shows that polymers are not micellar aggregates, but real *macromolecules*, in which the monomers are held together by covalent bonds.

1925: *Gorter and Grendel* investigate experimentally the area of red-blood-cell lipids on a water surface, and arrive at the hypothesis that the plasma membrane of biological cells is made of lipid bilayers.

1931: *W. H. Carothers* produces the first nylon polymers.

1931: *L. Onsager* derives the fundamental symmetry relations for the transport coefficients, which play an important role in irreversible processes.

1934: *W. Kuhn*, a Swiss chemist and physicist, develops the random coil model for polymers in dilute solution, and derives the probability distribution for the average size and shape of a random coil.

1935: *Danielli and Davson* suggest the first complete model for biological membranes. In this model the membrane consists of a lipid bilayer, which is covered on both sides with a layer of adsorbed proteins.

1941: *B. V. Derjaguin and L. Landau* (1941), and *E. J. W. Verwey and J. Th. G. Overbeek* (1948) independently formulate the interactions between charged colloids. This combines both the repulsive interaction between diffuse, charged ionic clouds around the colloids and the attractive van der Waals forces.

1944: *L. Onsager* gives the first exact solution of the two-dimensional Ising model, and thereby demonstrates the existence of singularities in thermodynamic quantities at phase transitions.

1944: *H. A. Kramers*, a Dutch physicist, develops a kinetic theory for dilute polymer solutions under potential flow. He considered very general polymer models involving constraints, including freely jointed bead-rod chains, rings, and branched molecules.

1948: *P. A. Winsor* classifies the phase equilibria in ternary oil-water-surfactant mixtures.

1953: *P. J. Flory* introduces the rotational isomeric state model for the description of polymer conformations, and calculates the size of self-avoiding polymer coils.

1953: *P. E. Rouse Jr.* formulates the freely-draining bead-spring chain model for polymer chains and calculates dynamic properties of polymer solutions in the linear viscoelastic regime.

1953: *H. Staudinger* receives the Nobel prize in chemistry for his discoveries in the field of macromolecular chemistry.

1953: *K. Ziegler and G. Natta* discover catalyser systems, which polymerize polyethylene at room temperature and ambient pressure. This opens the way for the industrial production of commodity polymers.

1954: *S. Asakura and F. Osawa* describe the effective attractions between colloidal particles due to the presence of free, non-absorbing polymer chains. *A. Vrij* reformulates independently these "depletion attractions" in 1976.

1956: *B. H. Zimm* formulates and solves the bead-spring model for polymers with equilibrium-averaged hydrodynamic interactions.

1958: *J. G. Kirkwood* discusses a diffusion equation for flexible polymer chains that includes interactions.

1961: *J. H. Schulman* introduces the concept of the *saturated interface*, in which the disjoining pressure induced by the repulsion of neighboring amphiphilic molecules leads to a interface of vanishing interfacial tension.

1962: *F. H. C. Crick and J. D. Watson* receive the Nobel prize in medicine for their discoveries concerning the molecular structure of nuclear acids and its significance for information transfer in living material.

1963: *K. Ziegler and G. Natta* receive the Nobel prize in chemistry for their discoveries in the field of the chemistry and technology of high polymers.

1967: *V. Luzatti* and coworkers find the first examples of liquid crystalline phases in lecithin-water and lipid-water mixtures, which are well described by triply-periodic minimal surfaces.

1968: *L. Onsager* receives the Nobel prize in Chemistry for the discovery of the reciprocal relations bearing his name, which are fundamental for the thermodynamics of irreversible processes.

1969: *D. Tabor, R. H. S. Winterton and J. N. Israelachvili* develop the Surface Forces Apparatus. Later improved versions of this apparatus enable the study of interactions on the Angstrom scale with a 10^{-8} N resolution for the force. The first such kinds of direct measurements are due to *B. V. Derjaguin and I. I. Abrikossova (1954).*

1970: *R. M. Mazo, J. M. Deutsch and I. J. Oppenheim* and *T. J. Murphy and J. L. Aguirre* derive the diffusion equation (similar to that discussed by Kirkwood in 1958), which includes both hydrodynamic and direct interactions between the colloidal particles, starting from the Liouville equation for the binary mixture of solvent molecules and the Brownian particles. This equation is nowadays referred to as the Smoluchowski equation.

1970: *A. H. Schoen* discovers 13 new triply periodic minimal surfaces, among them the gyroid phase, which is now the minimal surface observed most frequently in amphiphilic systems.

1970: *P. B. Canham* introduces the concept of curvature elasticity to model the shape of lipid bilayers and calculates the discocyte shape of red blood cells.

1971: *P.-G. de Gennes* introduces *reptation*, i.e. sliding of a polymer chain along its contour, to explain the dynamics of dense polymer melts.

1971: *Singer* proposes the "fluid-mosaic" model for the structure of biological membranes, which is nowadays widely accepted. In this model, the membrane proteins are embedded in the lipid bilayer.

1972: *G. K. Batchelor* describes in a number of papers the calculation of transport properties of dilute colloidal systems where interactions are taken into account. This is the extension of Einstein's formulation of diffusion, viscosity and sedimentation to interacting colloidal systems. His calculations are based on the Smoluchowski equation as derived by Deutsch and others in 1970.

1973: *W. Helfrich* independently proposes a theory of elasticity of lipid bilayers, and introduces the spontaneous curvature into the curvature-elasticity model.

1974: *P. J. Flory* receives the Nobel prize in chemistry, for his fundamental achievements, both theoretical and experimental, in the physical chemistry of the macromolecules.

1974: *J. Schelten* demonstrates the coil conformations of polymers in a melt by small angle neutron scattering.

1976: *L. E. Scriven* proposes a cubic minimal surface structure of the amphiphile film in bicontinuous microemulsions.

1977: *B. U. Felderhof* develops the theory to calculate hydrodynamic interaction functions (the principle of which is due to J. M. Burgers (1940) and H. Brenner (1964), and is nowadays referred to as the "method of reflections").

1978: *W. Helfrich* shows that the large swelling of the lamellar phase can be explained by the entropic repulsion between neighboring membranes due to undulation fluctuations.

1978: *M. Doi and S. Edwards* formulate a theory of viscoelasticity based on the reptation model.

1978: *M. Fixman* develops and applies the mathematical background for performing Brownian dynamics simulations of polymers in flow.

1979: *P.-G. de Gennes* published the book *Scaling Concepts in Polymer Physics*, which makes polymers a fashionable research topic in the physics community.

1980: *L. Leibler* proposes a theory of microphase separation in block copolymers, and uses it to calculate the structure factor in the disordered phase.

1981: *E. Evans* and coworkers develop the technique of micropipette aspiration of cells and vesicles, and use this technique to determine the bending rigidity and the rupture strength of membranes.

1982: *K.-G. Wilson* receives the Nobel prize in physics for his work on the renormalization group, which provides a theoretical framework to understand the cooperative phenomena in connection with second-order phase transitions.

1982: *P.-G. de Gennes and C. Taupin* suggest a description of microemulsions by an ensemble of fluctuating membranes, and calculate the persistence length of membranes.

1985: *L. Peliti and S. Leibler* predict the logarithmic renormalization of the bending rigidity due to thermal membrane undulations.

1986: *J.-P. Hansen and I. R. McDonald* publish the book *Theory of Simple Liquids*, which describes the state of the art of liquid-state theory.

1986: *M. Doi and S. Edwards* publish the book *The Theory of Polymer Dynamics*, which becomes one of the standard references in this field.

1986: *R. Lipowsky and S. Leibler* study theoretically the unbinding transition of interacting membranes.

1986: *C. Safinya, D. Roux* and their coworkers demonstrate experimentally the steric repulsion between membranes by careful X-ray scattering experiments.

1986: *S. Safran, D. Roux, M. E. Cates and D. Andelman* propose an explanation of the origin of middle-phase on the basis of a cell model for oil-water-surfactant mixtures, in which the dominant energy is the curvature of the surfactant membrane.

1987: *Y. Kantor and D. R. Nelson* investigate the thermal crumpling transition of polymerized membranes.

1987: *D. R. Nelson and L. Peliti* study fluctuations in membranes with hexatic order.

1989: *D. Richter et al.* demonstrate the microscopic existence of the entanglement length in polymer melts by careful neutron spin echo experiments.

1990: *H. N. W. Lekkerkerker* calculates phase diagrams for colloid-polymer mixtures which are governed by depletion interactions.

1991: *P.-G. de Gennes* receives the Nobel prize in physics for discovering that methods developed for studying order phenomena in simple systems can be generalized to more complex forms of matter, in particular to liquid crystals and polymers.

1997: *S. Chu* receives the Nobel prize in physics for development of methods to cool and trap atoms with laser light. This method provides the basis for the construction of optical tweezers, which are employed, inter alia, for the controlled stretching of single DNA molecules.

References

[1] P. J. Flory, *Statistical Mechanics of Chain Molecules* (Interscience Publishers, New York, 1969).

[2] P.-G. de Gennes, *Scaling Concepts in Polymer Physics* (Cornell University Press, Ithaca, 1979).

[3] J. D. Ferry, *Viscoelastic Properties of Polymers* (Wiley, New York, 1980).

[4] M. Doi and S. F. Edwards, *The Theory of Polymer Dynamics* (Clarendon Press, Oxford, 1986).

[5] J. de Cloizeaux and G. Jannink, *Les Polymères en Solution: leur Modélisation et leur Structure* (Les Éditions de Physique, Les Ulis, France, 1987).

[6] *Physics of Amphiphilic Layers*, edited by J. Meunier, D. Langevin, and N. Boccara (Springer-Verlag, Berlin, 1987).

[7] W. B. Russel, *The Dynamics of Colloidal Systems* (University of Wisconsin Press, London, 1987).

[8] W. B. Russel, D. A. Saville, and W. R. Schowalter, *Colloidal Dispersions* (Cambridge University Press, Cambridge, 1989).

[9] T. G. M. van de Ven, *Colloidal Hydrodynamics* (Academic Press, London, 1989).

[10] R. J. Hunter, *Foundations of Colloid Science* (Clarendon Press, Oxford, 1989).

[11] *Statistical Mechanics of Membranes and Surfaces*, edited by D. Nelson, T. Piran, and S. Weinberg (World Scientific, Singapore, 1989).

[12] H.-G. Elias, *Makromoleküle* (Hüthig & Wepf, Basel, 1990).

[13] J. N. Israelachvili, *Intermolecular and Surface Forces* (Academic Press, London, 1992).

[14] D. F. Evans and H. Wennerström, *The Colloidal Domain, where Physics, Chemistry, Biology and Technology Meet* (VCH Publishers, New York, 1994).

[15] *Micelles, Membranes, Microemulsions, and Monolayers*, edited by W. M. Gelbart, A. Ben-Shaul, and D. Roux (Springer-Verlag, Berlin, 1994).

[16] G. Gompper and M. Schick, *Self-Assembling Amphiphilic Systems*, in *Phase Transitions and Critical Phenomena*, edited by C. Domb and J. Lebowitz (Academic Press, London, 1994), Vol. 16, pp. 1–176.

[17] S. A. Safran, *Statistical Thermodynamics of Surfaces, Interfaces, and Membranes* (Addison-Wesley, Reading, MA, 1994).

[18] *Structure and dynamics of membranes - from cells to vesicles*, Vol. 1 of *Handbook of biological physics*, edited by R. Lipowsky and E. Sackmann (Elsevier, Amsterdam, 1995).

[19] P. M. Chaikin and T. C. Lubensky, *Principles of Condensed Matter Physics* (Cambridge University Press, Cambridge, 1995).

[20] J. K. G. Dhont, *An Introduction to Dynamics of Colloids* (Elsevier, Amsterdam, 1996).

[21] P. Kumar and K. L. Mittal, *Handbook of Microemulsion Science and Technology* (Marcel Dekker, New York, 1999).

[22] H. T. Davis, J. F. Bodet, L. E. Scriven, and W. G. Miller, in *Physics of Amphiphilic Layers*, edited by J. Meunier, D. Langevin, and N. Boccara (Springer-Verlag, Berlin, 1987), pp. 310–327. See Ref. [6].

[23] K. Siekmann and M. J. Schwuger, Physik in unserer Zeit **18**, 178 (1987).

[24] Z. Dogic and S. Fraden, Phil. Trans. R. Soc. Lond. A **359**, 997 (2001).

TECHNIQUES, METHODS, AND SYNTHESIS



A 1 Scattering

Th. Brückel
Institut für Festkörperforschung
Forschungszentrum Jülich GmbH

Contents

1 Introduction 2

2 Elementary Scattering Theory: Elastic Scattering 3

2.1 Scattering geometry and scattering cross section 3

2.2 The Patterson or pair correlation function 6

2.3 Form-factor 7

2.4 Scattering from a periodic lattice in three dimensions 8

3 Probes for Scattering Experiments in Condensed Matter Science 10

3.1 Suitable types of radiation 10

3.2 X-rays: Thomson scattering 11

3.3 Light scattering 12

3.4 Neutron scattering 13

3.5 Comparison of probes 17

3.6 Radiation sources 19

4 Fluctuations 20

4.1 Van Hove theory 21

4.2 Inelastic light scattering 25

4.3 Inelastic neutron scattering 25

4.4 Dynamic light scattering 29

5 Summary 31

A Autocorrelation Functions 34

1 Introduction

Our present understanding of the properties and phenomena of condensed matter science is based on atomic theories. The first question we pose when studying any condensed matter system is the question concerning the internal structure: what are the building blocks (atoms, colloidal particles, ...) and how are they arranged? The second question concerns the microscopic dynamics: how do these building blocks move and what are their internal degrees of freedom? Once these fundamental questions are answered, the macroscopic properties are in principle determined by quantum theory and statistical physics. The macroscopic response and transport properties such as thermal conductivity, elasticity, viscosity, susceptibility etc. are the quantities of interest for applications. A deeper understanding of these properties has to be based on a microscopic picture.

For the development of modern condensed matter research, the availability of probes to study the structure and dynamics on a microscopic level is therefore essential. Modern scattering techniques can provide all the required information. Radiation, which has rather weak interaction with a sample under investigation provides a non-invasive, non-destructive probe for the microscopic structure and dynamics. This has been shown for the first time by W. Friedrich, P. Knipping and M. von Laue in 1912, when interference of x-ray radiation from a single crystal was observed. Max von Laue received the Nobel price for the interpretation of these observations. One cannot overestimate this discovery: it was the first proof that atoms are the elementary building blocks of condensed matter and that they are arranged in a periodic manner within a single crystal. The overwhelming part of our present-day knowledge of the atomic structure of condensed matter is based on x-ray structure investigations. Of course the method has developed rapidly since 1912. With the advent of modern synchrotron x-ray sources, the source brilliance has since then increased by 18 orders of magnitude. Currently x-ray Free Electron Lasers, e. g. the TESLA project (tesla.desy.de), are proposed which will increase this brilliance by another 10 orders of magnitude. Nowadays the structure of highly complex biological macromolecules can be determined with atomic resolution such as the crystal structure of the ribosome. Extremely weak phenomena such as magnetic x-ray scattering can be exploited successfully at modern synchrotron radiation sources. Besides x-ray scattering, light scattering is an important tool in soft condensed matter research. Light scattering is of particular interest for investigations on larger lengths scales, such as of colloidal particles in solution. Finally, intense neutron beams have properties, which make them an excellent probe for soft condensed matter investigations. In particular, contrast variation techniques are possible by selective deuteration of molecules or molecular subunits. Neutrons give access to practically all lengths scales relevant in soft condensed matter investigations from the atomic level up to about 1000 nm and are particularly well suited for the investigations of the movement of atoms and molecules. As with x-rays the experimental techniques are in rapid evolution and the proposed new spallation sources such as the European Spallation Source ESS (www.ess-europe.de) will increase the capabilities of neutron investigations in condensed matter science drastically in the years to come.

In the following we give an elementary introduction into scattering theory in general and show some applications in soft condensed matter investigations. More details can be found in [1-5].

This lecture is organised as follows: first we give a very basic introduction into elementary scattering theory for elastic scattering. Then we will discuss which probes are relevant for condensed matter investigations (light, x-rays, neutrons), list the properties of the various types of radiation and mention the modern radiation sources. Then we will drop the restriction of a static arrangement of scatterers assumed in the chapter on elastic scattering and discuss time fluctuations and how scattering processes can give information on internal dynamics. Examples will be given for high resolution neutron and light scattering experiments.

I have to emphasise that a lecture on scattering for all the different probes and for the static and dynamic cases is a subject for a full semester university course. With the limited space available it is impossible to deduce the results cited in a strict manner. I will use simple hand waving arguments to motivate the form of the equations presented and refer to the literature [1-5] for the detailed derivation.

We will frequently make use of the particle-wave dualism of quantum mechanics, which tells us that the radiation used in the scattering process can be described in a wave picture, whenever we are interested in interference phenomena and in a particle picture, e. g. for the detection process.

2 Elementary Scattering Theory: Elastic Scattering

2.1 Scattering geometry and scattering cross section

In this chapter we assume that the building blocks within our sample are rigidly fixed on equilibrium positions in space. Therefore we only look at those processes, in which the recoil is being transferred to the sample as a whole so that the energy change for the radiation is negligible and the scattering process appears to be elastic. In chapter 4, we will drop this restriction and discuss so-called inelastic scattering processes due to internal fluctuations in the sample which give rise to an energy change of the radiation during the scattering process.

A sketch of the scattering experiment is shown in figure 1.

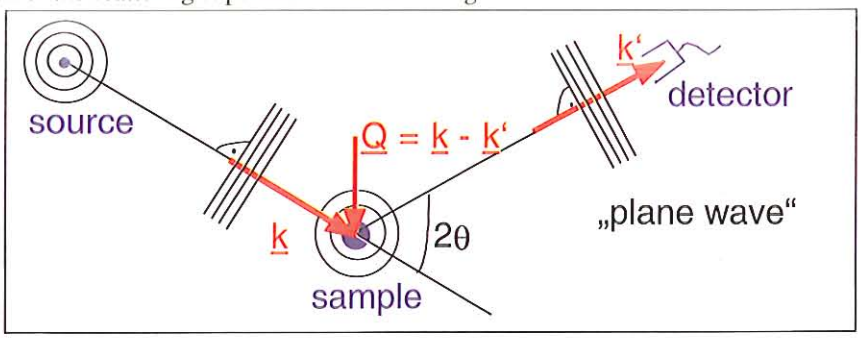


Fig. 1: *A sketch of the scattering process in the Fraunhofer approximation in which it is assumed that plain waves are incident on sample and detector due to the fact that the distance source-sample and sample-detector, respectively, is significantly larger than the size of the sample.*

Here we assume the so-called *Fraunhofer approximation*, where the size of the sample has to be much smaller than the distance between sample and source and the distance between sample and detector, respectively. This assumption holds in all cases discussed in this lecture. In addition we assume that the source emits radiation of one given energy, i. e. so-called *monochromatic* radiation. Then the wave field incident on the sample can be described as a plane wave, which is completely described by a wave vector $\underline{k}$. The same holds for the wave incident on the detector, which can be described by a vector $\underline{k}'$. In the case of elastic scattering (diffraction) we have

$$k = |\underline{k}| = |\underline{k}'| = k' = \frac{2\pi}{\lambda} \tag{1}$$

Let us define the so-called *scattering vector* by

$$\underline{Q} = \underline{k} - \underline{k}'. \tag{2}$$

The magnitude of the scattering vector can be calculated from wavelength λ and scattering angle 2θ as follows

$$Q = |\underline{Q}| = \sqrt{k^2 + k'^2 - 2kk'\cos 2\theta} \Rightarrow Q = \frac{4\pi}{\lambda}\sin\theta. \tag{3}$$

A scattering experiment comprises the measurement of the intensity distribution as a function of the scattering vector. The scattered intensity is proportional to the so-called *cross section*, where the proportionality factors arise from the detailed geometry of the experiment. For a definition of the scattering cross section, we refer to figure 2.

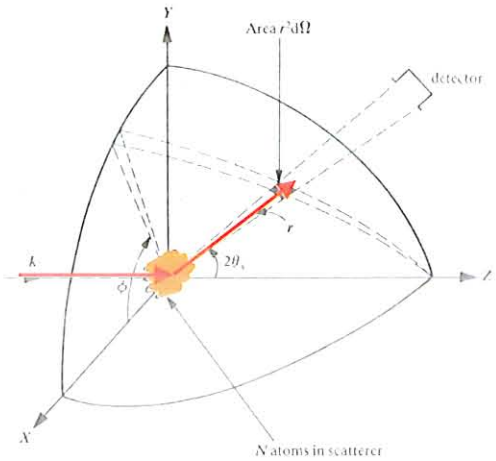


Fig. 2: *Geometry used for the definition of the scattering cross section.*

If n' particles are scattered per second into the solid angle $d\Omega$ seen by the detector under the scattering angle 2θ and into the energy interval between E' and E' + dE', then we can define the so-called *double differential cross section* by:

$$\frac{d^2\sigma}{d\Omega dE'} = \frac{n'}{j d\Omega dE'}. \tag{4}$$

Here j refers to the incident beam flux in terms of particles per area and time. If we are not interested in the change of the energy of our radiation during the scattering process or if our detector is not able to resolve this energy change, then we will describe the angular dependence by the so-called *differential cross section:*

$$\frac{d\sigma}{d\Omega} = \int_0^\infty \frac{d^2\sigma}{d\Omega dE'} dE' . \tag{5}$$

Finally the so-called *total scattering cross section* gives us a measure for the total scattering probability independent of changes in energy and scattering angle:

$$\sigma = \int_0^{4\pi} \frac{d\sigma}{d\Omega} d\Omega . \tag{6}$$

Our task therefore is to determine the arrangement of the atoms in the sample from the knowledge of the scattering cross section $d\sigma/d\Omega$. The relationship between scattered intensity and the structure of the sample is particularly simple in the so-called *Born approximation*, which is often also referred to as *kinematic scattering approximation*. In this case, refraction of the beam entering and leaving the sample, multiple scattering events and the extinction of the primary beam due to scattering within the sample are being neglected. Following figure 3 the phase difference between a wave scattered at the origin of the coordinate system and at position $\underline{r}$ is given by

$$\Delta\Phi = 2\pi \cdot \frac{(\overline{AB} - \overline{CD})}{\lambda} = \underline{k}'\underline{r} - \underline{k} \cdot \underline{r} = \underline{Q} \cdot \underline{r} . \tag{7}$$

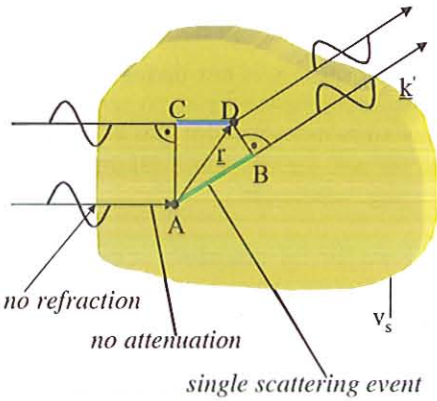


Fig. 3: *A sketch illustrating the phase difference between a beam scattered at the origin of the coordinate system and a beam scattered at the position $\underline{r}$.*

The scattered amplitude at the position $\underline{r}$ is proportional to what I will refer to as the scattering power density $\rho_s(\underline{r})$. ρ_s depends on the type of radiation used. Its meaning will be given in chapter 3. Assuming a laterally coherent beam, the total scattering amplitude is given by a coherent superposition of the scattering from all points within the sample, i. e. by the integral

$$A = A_0 \cdot \int_{V_s} \rho_s(\underline{r}) \cdot e^{i\underline{Q}\cdot\underline{r}} d^3r . \tag{8}$$

Here A_0 denotes the amplitude of the incident wave field. (8) demonstrates that the scattered amplitude is connected with the scattering power density $\rho_s(\underline{r})$ by a simple Fourier transform. A knowledge of the scattering amplitude for all scattering vectors $\underline{Q}$ allows us to determine via a Fourier transform the scattering power density uniquely. This is the complete information on the sample, which can be obtained by the scattering experiment. Unfortunately nature is not so simple. On one hand, there is the more technical problem that one is unable to determine the scattering cross section for <u>all</u> values of $\underline{Q}$. The more fundamental problem,

however, is given by the fact that normally the amplitude of the scattered wave is not measurable. Instead only the scattered intensity

$$I \sim |A|^2 \tag{9}$$

can be determined. Therefore the phase information is lost and the simple reconstruction of the scattering power density via a Fourier transform is no longer possible. This is the so-called *phase problem* of scattering.

Before we address the question, which information we can obtain from a scattering experiment, let us ask ourselves, which wavelength we have to choose to obtain the required real space resolution. For information on a length scale L, a phase difference of about $Q \cdot L \approx 2\pi$ has to be achieved. Otherwise according to (7) $\underline{k}'$ and $\underline{k}$ will not differ significantly. According to (3) $Q \approx 2\pi/\lambda$ for typical scattering angles ($2\theta \sim 60°$). Combining these two estimates, we end up with the requirement that the wavelength λ has to be in the order of the real space length scale L under investigation. To give an example: with the wavelength in the order of 0.1 nm, atomic resolution can be achieved in a scattering experiment.

2.2 The Patterson or pair correlation function

From (9) we see that the phase information is lost during the measurement of the intensity. For this reason the Fourier transform of the scattering power density is not directly accessible in most scattering experiments (note however that phase information can be obtained in certain cases). In this section, we will discuss which information can be obtained from the intensity distribution of a scattering experiment.

Substituting (8) into (9), we obtain for the magnitude square of the scattering amplitude, a quantity directly accessible in a scattering experiment:

$$\begin{aligned} I \sim \left|A(\underline{Q})\right|^2 &\sim \int d^3r' \rho_S(\underline{r}') e^{i\underline{Q}\cdot\underline{r}'} \int d^3r \rho_S^*(\underline{r}) e^{-i\underline{Q}\cdot\underline{r}} \\ &= \iint d^3r' d^3r \, \rho_S(\underline{r}') \rho_S^*(\underline{r}) e^{i\underline{Q}\cdot(\underline{r}'-\underline{r})} = \iint d^3R d^3r \, \rho_S(\underline{R}+\underline{r}) \rho_S^*(\underline{r}) e^{i\underline{Q}\cdot\underline{R}}. \end{aligned} \tag{10}$$

This shows that the scattered intensity is proportional to the Fourier transform of a function $P(\underline{R})$:

$$I(\underline{Q}) \sim \int d^3R \, P(\underline{R}) e^{i\underline{Q}\cdot\underline{R}} \tag{11}$$

This function denotes the so-called *Patterson function* in crystallography or more general the *static pair correlation function:*

$$P(\underline{R}) = \int d^3r \, \rho_S^*(\underline{r}) \rho_S(\underline{r}+\underline{R}). \tag{12}$$

$P(\underline{R})$ correlates the value of the scattering power density at position $\underline{r}$ with the value at the position $\underline{r}+\underline{R}$, integrated over the entire sample volume. If, averaged over the sample, no correlation exists between the values of the scattering power densities at position $\underline{r}$ and $\underline{r}+\underline{R}$, then the Patterson function $P(\underline{R})$ vanishes. If, however, a periodic arrangement of a pair of atoms exists in the sample with a difference vector $\underline{R}$ between the positions, then the Patterson function will have an extremum for this vector $\underline{R}$. Thus the Patterson function reproduces all the vectors connecting one atom with another atom in a periodic arrangement.

2.3 Form-factor

So far we have not specified the nature of our sample. Now we assume an assembly on N scatterers of finite size, see figure 4.

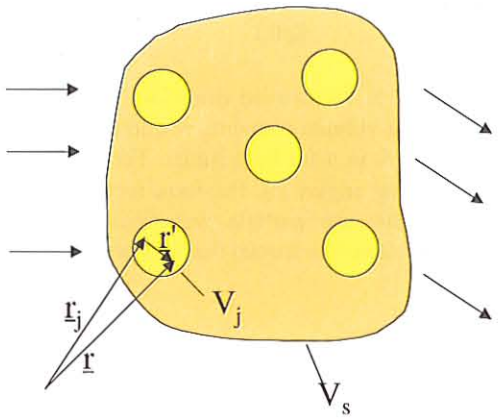


Fig. 4: *Sketch showing the assembly of N scatterers of finite size and defining the quantities needed for the introduction of the form factor.*

These could be atoms in a solid or colloidal particles in a homogeneous solution. In what follows, we will separate the interference effects from the scattering within one such particle from the interference effects arising from scattering from different particles. With the decomposition of the vector $\underline{r}$ into the center-of-gravity-vector $\underline{r}_j$ and a vector $\underline{r}'$ within the particle, the scattering amplitude can be written as:

$$A \propto \int_{V_S} d^3r \rho_S(\underline{r}) e^{i\underline{Q}\cdot\underline{r}} = \sum_{j=1}^{N} \int_{V_j} d^3r \rho_S(\underline{r}) e^{i\underline{Q}\cdot\underline{r}} = \sum_{j=1}^{N} e^{i\underline{Q}\cdot\underline{r}_j} \int_{V_j^0} d^3r' \rho_S(\underline{r}') e^{i\underline{Q}\cdot\underline{r}'}$$

$$\Rightarrow A \sim \sum_{j=1}^{N} A_j(0) \cdot f_j(\underline{Q}) e^{i\underline{Q}\cdot\underline{r}_j} . \qquad (13)$$

The *form-factor* is defined as the normalised amplitude of scattering from within one particle:

$$f(\underline{Q}) \equiv \frac{\int_{V_j^0} d^3r' \varrho_S(\underline{r}') e^{i\underline{Q}\cdot\underline{r}'}}{\int_{V_j^0} d^3r' \varrho_S(\underline{r}')} . \qquad (14)$$

For a homogeneous sphere

$$\rho_S(\underline{r}) = \begin{cases} 0 & |\underline{r}| > R \\ 1 & |\underline{r}| \le R \end{cases}, \tag{15}$$

the form-factor can be calculated by using spherical co-ordinates:

$$\Rightarrow f(Q) = 3 \cdot \frac{\sin QR - QR \cdot \cos QR}{(QR)^3}. \tag{16}$$

The function (16) is plotted in figure 5. In forward direction, there is no phase difference between waves scattered from different volume elements within the sample (note: we assume the Fraunhofer approximation and work in a far field limit). The form-factor takes its maximum value of one. For finite scattering angles 2θ, the form-factor drops due to destructive interference from various parts within one particle and finally for large values of the momentum transfer shows damped oscillations around 0 as a function of QR.

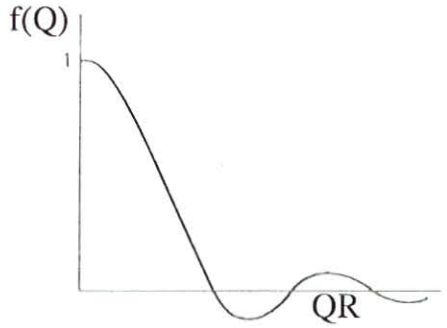


Fig. 5: *Form-factor for a homogeneous sphere according to (16).*

2.4 Scattering from a periodic lattice in three dimensions

As an example for the application of (8) and (9), we will now discuss the scattering from a three dimensional lattice of point-like scatterers. As we will see later, this situation corresponds to the scattering of thermal neutrons from a single crystal. More precisely, we will restrict ourselves to the case of a Bravais lattice with one atom at the origin of the unit cell. To each atom we attribute a scattering power α. The single crystal is finite with N, M and P periods along the basis vectors $\underline{a}$, $\underline{b}$ and $\underline{c}$. The scattering power density, which we have to use in (8) is a sum over δ-functions for all scattering centers:

$$\rho_S(\underline{r}) = \sum_{n=0}^{N-1} \sum_{m=0}^{M-1} \sum_{p=0}^{P-1} \alpha \cdot \delta(\underline{r} - (n \cdot \underline{a} + m \cdot \underline{b} + p \cdot \underline{c})). \tag{17}$$

The scattering amplitude is calculated as a Fourier transform:

$$A(\underline{Q}) \sim \alpha \sum_{n=0}^{N-1} e^{in\underline{Q}\cdot\underline{a}} \sum_{m=0}^{M-1} e^{im\underline{Q}\cdot\underline{b}} \sum_{p=0}^{P-1} e^{ip\underline{Q}\cdot\underline{c}}. \tag{18}$$

Summing up the geometrical series, we obtain for the scattered intensity:

$$I(\underline{Q}) \sim \left| A(\underline{Q}) \right|^2 = |\alpha|^2 \cdot \frac{\sin^2 \frac{1}{2} N\underline{Q} \cdot \underline{a}}{\sin^2 \frac{1}{2} \underline{Q} \cdot \underline{a}} \cdot \frac{\sin^2 \frac{1}{2} M\underline{Q} \cdot \underline{b}}{\sin^2 \frac{1}{2} \underline{Q} \cdot \underline{b}} \cdot \frac{\sin^2 \frac{1}{2} P\underline{Q} \cdot \underline{c}}{\sin^2 \frac{1}{2} \underline{Q} \cdot \underline{c}}. \tag{19}$$

The dependence on the scattering vector $\underline{Q}$ is given by the so-called *Laue function*, which separates according to the three directions in space. One factor along one lattice direction $\underline{a}$ is plotted in figure 6.

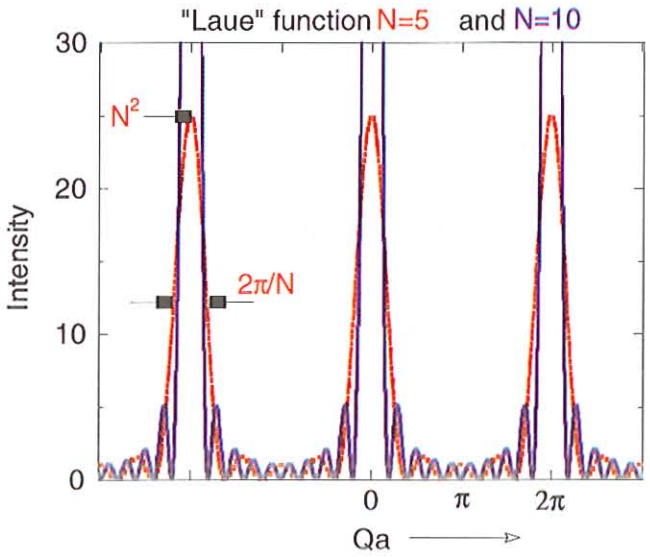


Fig. 6: *Laue function along the lattice direction $\underline{a}$ for a lattice with five and ten periods, respectively.*

The main maxima occur at the positions $Q = n \cdot 2\pi/a$. The maximum intensity scales with the square of the number of periods N^2, the half width is given approximately by $\Delta Q = 2\pi/(N \cdot a)$. The more periods contribute to coherent scattering, the sharper and higher are the main peaks. Between the main peaks, there are N-2 site maxima. With increasing number of periods N, their intensity becomes rapidly negligible compared to the intensity of the main peaks. The main peaks are of course the well known *Bragg reflections*, which we obtain when scattering from a crystal lattice. From the position of these Bragg peaks in momentum space, the metric of the unit cell can be deduced (lattice constants a, b, c and unit cell angles α, β, γ). The width of the Bragg peaks is determined by the size of the coherently scattering volume (parameters N, M, and P) - and some other factors for real experiments (resolution, mosaic distribution, internal strains, ...).

3 Probes for Scattering Experiments in Condensed Matter Science

In this chapter, we will discuss which type of radiation is suitable for condensed matter investigations. For each radiation, we will then discuss the relevant interaction processes with matter separately. Finally, we will mention the radiation sources.

3.1 Suitable types of radiation

A list of requirements for the type of radiation used in condensed matter investigations will look as follows:

1. The achievable spatial resolution should be in the order of the inter-particle distances, which implies (see section 2.1) that the wavelength λ is in the order of the inter-particle distance L.
2. If we want to study volume effects, the scattering has to originate from the bulk of the sample, which implies that the radiation should be at most weakly absorbed within matter.
3. For a simple interpretation of the scattering data within the Born approximation (see chapter 2), multiple scattering effects should be negligible, i. e. the interaction of the radiation with matter should be weak.
4. For the sake of simplicity, the probe should have no inner degrees of freedom, which could be excited during the scattering process (i. e. avoid beams of molecules, which have internal vibrational or rotational degrees of freedom).
5. If, in addition to structural studies, we want to investigate elementary excitations, we would like the energy of the probe to be in the order of the excitation energies, so that the energy change during the scattering process is easily measurable.

This list of requirements leads us to some standard probes in condensed matter research. First of all, electromagnetic radiation governed by the Maxwell equations can be used. Depending on the resolution requirements, we will use x-rays with wavelength λ about 0.1 nm to achieve atomic resolution or visible light ($\lambda \sim 350$ - 700 nm) to investigate e. g. colloidal particles in solution. Besides electromagnetic radiation, particle waves can be used. It turns out that thermal neutrons with a wavelength $\lambda \sim 0.1$ nm are particularly well adapted to the above list of requirements. The neutron beams are governed by the Schrödinger equation of quantum mechanics. An alternative is to use electrons, which for energies of around 100 keV have wavelengths in the order of 0.005 nm. As relativistic particles, they are governed by the Dirac equation of quantum mechanics. The big drawback of electrons as a condensed matter probe is the strong Coulomb interaction with the electrons in the sample. Therefore neither the absorption, nor the multiple scattering effects can be neglected. However the abundance of electrons and the relative ease to produce optical elements predestinates them to imaging purposes (electron microscopy). Scattering experiments with electrons will not be further discussed here.

3.2 X-rays: Thomson scattering

X-rays are electromagnetic waves with wavelengths typically shorter than 1 nm. For electromagnetic waves, the relation between energy and wavelength is given by

$$E = h\nu = \frac{h \cdot c}{\lambda} \tag{20}$$

or in practical units

$$E[\mathrm{keV}] = \frac{1.24}{\lambda[\mathrm{nm}]} \tag{21}$$

i. e. x-rays with a wavelength of 0.1 nm have an energy of 12.4 keV. The corresponding elementary particle - the photon - is massless, has no charge, but spin 1. For a massless particle of spin 1, two polarisation states can be distinguished, corresponding to left or right circular polarised light. According to de Broglie, the relation between momentum p and wavelength λ is given by

$$\underline{p} = \hbar\underline{k};\ p = h/\lambda\,. \tag{22}$$

Electromagnetic radiation has a very complex interaction with matter, as discussed in many quantummechanics, electrodynamics or atomic physics textbooks. Here we consider only the simplest interaction mechanism, which is also the one most relevant for x-ray scattering: the interaction of the electromagnetic wave via the Coulomb force with a free electron without spin. This interaction gives rise to the so-called classical *Thomson scattering*. The process is sketched in figure 7. The incident electromagnetic wave gives rise to an oscillating electric field at the position of the electron. Due to the Coulomb force, the electron will start an oscillatory movement. The accelerated charge gives rise to the re-radiation of electric dipole radiation.

It is straightforward to calculate the scattering cross section, starting from the classical equation of motion

$$-e \cdot E = m \cdot \ddot{x} \tag{23}$$

and inserting the correct time dependence for the electric field vector $\underline{E} = \underline{E}_0 \cdot e^{i(\omega t - \underline{k}\cdot\underline{r})}$. The cross section can be written in the form

$$\frac{d\sigma}{d\Omega} = r_0^{\,2} \cdot P(\theta) \tag{24}$$

where r_0 denotes the classical electron radius, $r_0 = e/m_e c^2 = 2.82\mathrm{fm}$ and $P(\theta)$ is a polarisation dependent factor, corresponding to the typical Hertz dipole characteristic. For an unpolarised x-ray beam $P(\theta) = 1 + \cos^2 2\theta$.

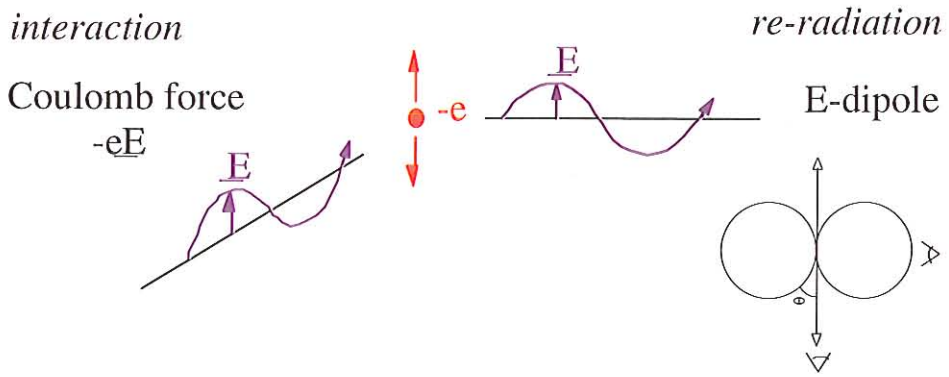


Fig. 7: *Sketch showing the interaction of a free electron without spin with the incident electromagnetic wave via the Coulomb force. The insert explains the origin of the polarisation factor P(θ): an observer which looks precisely into the direction of movement of the electron cannot see the accelerated motion of the electron and does not observe any re-radiation. An observer in a plane perpendicular to the motion of the electron sees the full acceleration and thus observes the maximum intensity of re-radiation.*

3.3 Light scattering

Light is electromagnetic radiation with a wavelength in the range 350 - 750 nm and (20) - (22) hold correspondingly. Quite in contrast to x-rays, the wavelength of light is about three orders of magnitude larger than a typical diameter of an atom. Therefore we can neglect the atomic structure and work in a continuum description. The propagation of light in matter is governed by the Maxwell equations and for a scattering process, we assume that there are no vacuum sources:

$$\begin{aligned} \underline{\nabla} \times \underline{H}(\underline{r},t) &= \frac{\partial}{\partial t}\underline{D}(\underline{r},t) \quad ; \quad \underline{\nabla}\cdot\underline{D} = 0 \\ \underline{\nabla} \times \underline{E}(\underline{r},t) &= \frac{\partial}{\partial t}\underline{B}(\underline{r},t) \quad ; \quad \underline{\nabla}\cdot\underline{B} = 0\,. \end{aligned} \tag{25}$$

In our case of soft matter investigations, we can usually neglect the magnetic response

$$\begin{aligned} \underline{D}(\underline{r},t) &= \underline{\underline{\varepsilon}}(\underline{r})\cdot\underline{E}(\underline{r},t) \\ \underline{B}(\underline{r},t) &= \mu_0\cdot\underline{H}(\underline{r},t) \end{aligned} \tag{26}$$

and thus describe the properties of matter by the tenser of the dielectric constant $\underline{\underline{\varepsilon}}(\underline{r})$. Inhomogeneities are described by the spatial variation of the dielectric constant. Anisotropies lead to the fact, that the dielectric displacement vector $\underline{D}$ may not be parallel to the electric field strength $\underline{E}$. Our task is now to solve the Maxwell equations for the incident plane wave $\underline{E} = \underline{E}_0 \cdot \exp[i(\omega t - \underline{k}\cdot\underline{r})]$. Here we will just quote the solution for the case of light scattering from colloidal particles in a homogeneous solvent. For a detailed derivation we refer to [5]. The scattered amplitude is given by:

$$\underline{E}_s(\underline{r},\underline{Q}) = \frac{k^2}{4\pi}\frac{e^{ikr}}{r}\underline{\underline{P}}(\underline{k}')\cdot\sum_{j=1}^{N}\underline{\underline{B}}_j(\underline{Q})\cdot e^{i\underline{Q}\cdot\underline{r}_j}\cdot\underline{E}_0 . \tag{27}$$

$\underline{E}_0$ is the amplitude of the incident wave. The scattering amplitude of a given particle j is denoted by $\underline{\underline{B}}_j(\underline{Q})$. $e^{i\underline{Q}\cdot\underline{r}_j}$ is the phase factor for particle number j. $\underline{\underline{P}}(\underline{k}')$ is a polarisation factor and e^{ikr}/r corresponds to the decrease of intensity with distance from the sample in the far field spherical wave limit.

If we refer to our simple scattering theory explained in chapter 2, we recognise all the factors appearing in (27). The main difference to our simple scaler scattering theory is the vector nature of the electromagnetic wave giving rise to polarisation effects. The polarisation can be changed during the scattering from each single particle and therefore, the scattering amplitude of the j^{th} particle, as well as the polarisation factor have to be tensors. Their explicit form is given by

$$\underline{\underline{P}}(\underline{k}') = \underline{\underline{1}} - \frac{\underline{k}'\underline{k}'}{k^2} \tag{28}$$

$$\underline{\underline{B}}_j(\underline{Q}) = \int_{V_j^0} d^3r \frac{\underline{\underline{\varepsilon}}(\underline{r}) - \underline{\underline{1}}\varepsilon_f}{\varepsilon_f} e^{i\underline{Q}\cdot\underline{r}} . \tag{29}$$

The quantity that we have called in chapter 2 "scattering strength density" corresponds to the expression $\rho_s(\underline{r}) \sim (\underline{\underline{\varepsilon}}(\underline{r}) - \underline{\underline{1}}\varepsilon_f)/\varepsilon_f$, where ε_f is the dielectric constant of the solvent.

The scattering theory for light under the Born approximation is referred as the *Rayleigh-Gans-Debye-scattering theory* and in what follows, we will refer to the process as *Rayleigh light scattering*. (Note: the factor k^2 gives rise to a dependence of the emitted power on the fourth power of the frequency, which provides the explanation for the blue sky).

3.4 Neutron scattering

We mentioned in the introduction that neutron beams provide a particularly useful probe for condensed matter investigations. The neutron is an elementary particle, a nucleon, consisting of three valance quarks, which are hold together by gluons. It thus has an internal structure, which, however, is irrelevant for condensed matter physics. Keeping in mind the difference in lengths scales (diameter of an atom: about 0.1 nm = 10^{-10} m; diameter of a neutron: about 1 fm = 10^{-15} m), we can safely consider the neutron as point-like particles without internal structure for our purposes. Due to the weak interaction, the neutron is not a stable particle. A free neutron undergoes a β-decay after an average lifetime of about 15 minutes:

$$n \xrightarrow[\text{weak interaction}]{15\,\text{min}} p + e^- + \bar{\nu} \tag{30}$$

This leaves ample time for scattering investigations. In contrast to the massless photon, the neutron has a mass m of about one atomic mass units ~ $1.675 \cdot 10^{-27}$ kg. The finite neutron mass is comparable to the mass of a nucleus and thus an appreciable amount of energy can be transferred during the scattering process. The neutron is a chargeless particle and thus does not show the strong Coulomb interaction with matter which results in large penetration depths. The neutron has a nuclear spin 1/2 giving rise to a magnetic dipolar moment of

$$\mu_n = \gamma\mu_N; \quad \gamma = 1.91; \quad \mu_N = 5.05 \cdot 10^{-27} J/T. \tag{31}$$

Due to this magnetic moment, the neutron can interact with the magnetic field of unpaired electrons in a sample leading to strong magnetic scattering. Thus magnetic structures and excitations can be studied by neutron scattering, a very important application outside of soft condensed matter research. To calculate the interference effects during the scattering process, a neutron has to be described as a matter wave with momentum

$$\underline{p} = m \cdot \underline{v} = \hbar\underline{k} = h/\lambda \tag{32a}$$

and energy

$$E = \frac{1}{2}mv^2 = \frac{\hbar^2 k^2}{2m} = \frac{h^2}{2m\lambda^2} \equiv k_B T_{eq} \tag{32b}$$

where $\underline{v}$ is the velocity of the neutron and T_{eq} defines the temperature equivalent of the kinetic energy of the neutron. In practical units, (32) leads to:

$$\lambda[nm] = \frac{400}{v[m/s]}$$
$$E[meV] = \frac{0.818}{\lambda^2[nm]}. \tag{33}$$

Let us consider the example of so-called *thermal neutrons*, which are defined by $T_{eq} \sim 300$ K. According to (33), their wavelength is 0.18 nm, matching perfectly the distance between atoms. The energy of thermal neutrons is around 25 meV, which matches well the energy of elementary excitations, such as spin waves (magnons) or lattice vibrations (phonons). Together with the usually large penetration depths (charge = 0) and the magnetic interaction, these properties make neutrons so extremely useful for condensed matter investigations.

We will now look at the neutron scattering cross section in some more detail. The dominant interactions of the neutron with matter are the magnetic dipole interaction of the neutron with the magnetic field of unpaired electrons, which we will no longer discuss in this lecture, and the strong interaction of the neutron with the nuclei. To calculate the cross section for neutron scattering, we are looking for a pertubative solution of the Schrödinger equation for the system "sample plus neutron beam". Here we cannot reproduce the full derivation of the form of the cross section and have to refer to [1, 2, 4] or to textbooks of quantum mechanics, e. g. [6]. An elegant way is the expansion into a *Born series*, which separates single, double, triple etc. scattering events. For a sufficient weak interaction, we can neglect all multiple scattering events and write the cross section in the *first Born approximation:*

$$\frac{\partial^2\sigma}{\partial\Omega\partial\omega} = \frac{k'}{k}\left(\frac{m}{2\pi\hbar^2}\right)^2 \sum_a P_a \sum_{a'} \left|\langle \underline{k}', a' | V | \underline{k}, a \rangle\right|^2 \delta\left(\hbar\omega + E_a - E_{a'}\right). \tag{34}$$

The various terms in this cross section can be understood as follows. The δ-function ensures energy conservation: the energy transfer onto the neutron $\hbar\omega$ has to be equal to the energy change within the sample $E_{a'} - E_a$. The term in front of the δ-function can be interpreted in terms of *Fermis' Golden Rule.* It's the magnitude square of the transition matrix element of the interaction potential V (nucleus ↔ neutron) between the initial state of the system (neutron with wave vector $\underline{k}$, sample in the quantum state a) and the final state (neutron with wave vector $\underline{k}'$, sample in the state a'). In general, neither the initial nor the final state of the sample are pure states. Therefore we have to sum over all processes leading to different final states, but also to sum over the initial states with a weight P_a corresponding to the thermodynamical

occupation of state a of the sample. Finally the prefactor k'/k results from the density-of-state consideration in Fermis' Golden Rule.

To evaluate the cross section (34), we have to specify the interaction potential with the nucleus. To derive this interaction potential is one of the fundamental problems of nuclear physics. Fermi has proposed a phenomenological potential based on the argument that the wave length of thermal neutrons is much larger than the nuclear radius. This means that the nuclei are pointlike scatterers and lead to isotropic, Q-independent, (so-called s-wave) scattering. The same argument holds for classical Thomson scattering, where the only angular dependence came from a polarisation factor. We will therefore use the so-called *Fermi-pseudo-potential:*

$$V(\underline{r}) = \frac{2\pi\hbar^2}{m} b\delta(\underline{r} - \underline{R}) \tag{35}$$

to evaluate the cross section (34).

Note, that despite the fact that the strong interaction of high energy physics is responsible for the scattering of the neutron with the nucleus, the scattering probability is small due to the small nuclear radius. Therefore, we can apply the first Born approximation. The quantity b introduced in (35) is a phenomenological quantity describing the strength of the interaction potential and is referred to as the scattering length. The total cross section of a given nucleus is $\sigma = 4\pi|b|^2$, corresponding to the surface area of a sphere with radius b. Since the interaction potential obviously depends on the details of the nuclear structure, b is different for different isotopes of the given element and also for different nuclear spin states. This fact gives rise to the appearance of so-called *coherent* and *incoherent scattering.*

When calculating the scattering cross section, we have to take into account that the different isotopes are distributed randomly over all sides. Also the nuclear spin orientation is random except for very low temperatures in external magnetic fields. Therefore we have to average over the random distribution of the scattering length in the sample:

$$\begin{aligned} \frac{d\sigma}{d\Omega} &= \left\langle \sum_i b_i e^{i\underline{Q}\cdot\underline{r}_i} \sum_j b_j^* e^{-i\underline{Q}\cdot\underline{r}_j} \right\rangle = \sum_i \sum_j \left\langle b_i b_j^* \right\rangle e^{i\underline{Q}\cdot(\underline{r}_i - \underline{r}_j)} \\ &= \langle b \rangle^2 \left| \sum_i e^{i\underline{Q}\cdot\underline{r}_i} \right|^2 + N \left\langle (b - \langle b \rangle)^2 \right\rangle \end{aligned} \tag{36}$$

The scattering cross section is the sum of two terms. Only the first term contains the phase factors $e^{i\underline{Q}\underline{r}}$, which result from the coherent superposition of the scattering from pairs of scatterers. This term takes into account interference effects and is therefore named *coherent scattering*. Only the scattering length averaged over the isotope and nuclear spin distribution enters this term. The second term in (36) does not contain any phase information and is proportional to the number N of atoms (and not to N^2!). This term is not due to the interference of scattering from different atoms. It corresponds to the scattering from single atoms, which subsequently super impose in an incoherent manner (adding intensities, not amplitudes!). For this reason, the intensity is proportional to the number N of atoms. Therefore, the second term is called *incoherent scattering*. This situation is illustrated graphically in figure 8.

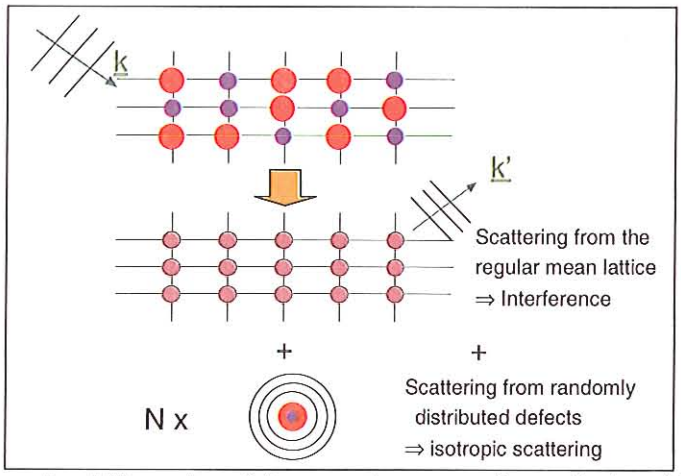


Fig. 8: *Two dimensional illustration of the scattering process from a lattice of N atoms of a given chemical species, for which two isotopes (small blue circle and large red circle) exist. The area of the circle represents the scattering cross section of the single isotope. The incident wave, top part of the figure for a special arrangement of the isotopes, is scattered coherently only from the average lattice. This gives rise to Bragg peaks in certain directions. In the coherent scattering, only the average scattering length is visible. Besides these interference phenomena, an isotropic background is observed, which is proportional to the number N of atoms and to the mean quadratic deviation from the average scattering length. This incoherent part of the scattering is represented by the lower part of the figure.*

In summary for each element we can define a coherent and an incoherent scattering cross section by the following equations:

$$\sigma_{coh} = 4\pi\langle b\rangle^2 \tag{37}$$

$$\sigma_{inc} = 4\pi\left\langle \left(b - \langle b\rangle\right)^2 \right\rangle . \tag{38}$$

The most prominent example for isotope incoherence is elementary nickel. The scattering lengths of the nickel isotopes are listed together with their natural abundance in table 1. The coherent and incoherent scattering cross sections can be calculated according (37) and (38) and are also given in table 1. The large incoherent cross section of nickel is mainly due to isotope incoherence.

Isotope	Natural Abundance	Nuclear Spin	Scattering Length [fm]
^{58}Ni	68.27 %	0	14.4(1)
^{60}Ni	26.10 %	0	2.8(1)
^{61}Ni	1.13 %	$^3/_2$	7.60(6)
^{62}Ni	3.59 %	0	-8.7(2)
^{64}Ni	0.91 %	0	-0.37(7)
Ni			10.3(1)

$\Rightarrow {}_{28}\mathrm{Ni}: \ \sigma_{coh} = 13.3 \text{ barn}; \ \sigma_{inc} = 5.2 \text{ barn}$

Tab. 1: *Scattering lengths for the nickel isotopes and resulting cross sections for natural Ni.*

The most prominent example for nuclear spin incoherent scattering is elementary hydrogen. The nucleus of the hydrogen atom - the proton - has the nuclear spin I = 1/2. The total nuclear spin of the system H + n can therefore adopt to values: J = 0 and J = 1. Each state has its own scattering length: $b_- = -47.5$ fm for the singlet state (J = 0) and $b_+ = 10.85$ fm for the triplet state (J = 1). With the relative weight 1/4 and 3/4 for the singlet and triplet state, respectively, the cross sections can be calculated according to (37) and (38) to be:

$$\Rightarrow {}_1^{}\mathrm{H}: \quad \sigma_{coh} = 1.76 \text{ barn}; \quad \sigma_{inc} = 80.26 \text{ barn}. \tag{39}$$

(39) shows that hydrogen scatters mainly incoherently. As a result, we observe a large background for all samples containing hydrogen.

3.5 Comparison of probes

Figure 9 shows a double logarithmic plot of the dispersion relation "wave length versus energy" for the three probes neutrons, electrons and photons (compare (20) and (32)). The plot demonstrates, how thermal neutrons of energy 25 meV are ideally suited to determine interatomic distances in the order of 0.1 nm, while the energy of x-rays or electrons for this wavelength is much higher. However with modern techniques at a synchrotron radiation source, energy resolutions in the meV-region become accessible even for photons of around 10 keV corresponding to a relative energy resolution $\Delta E/E \approx 10^{-7}$! The graph also shows that colloids with a typical size of 100 nm are well suited for the investigation with light of energy around 2 eV. These length scales can, however, also be reached with thermal neutron scattering in the small angle region. While figure 9 thus demonstrates for which energy-wavelength combination a certain probe is particularly useful, modern experimental techniques extend the range of application by several orders of magnitude.

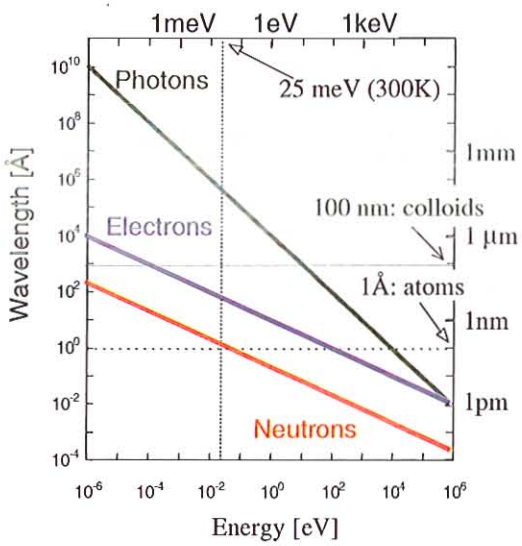


Fig. 9: *Comparison of the three probes - neutrons, electrons and photons - in a double logarithmic energy-wave length diagram.*

It is therefore useful to compare the scattering cross sections as it is done in figure 10 for x-rays and neutrons.

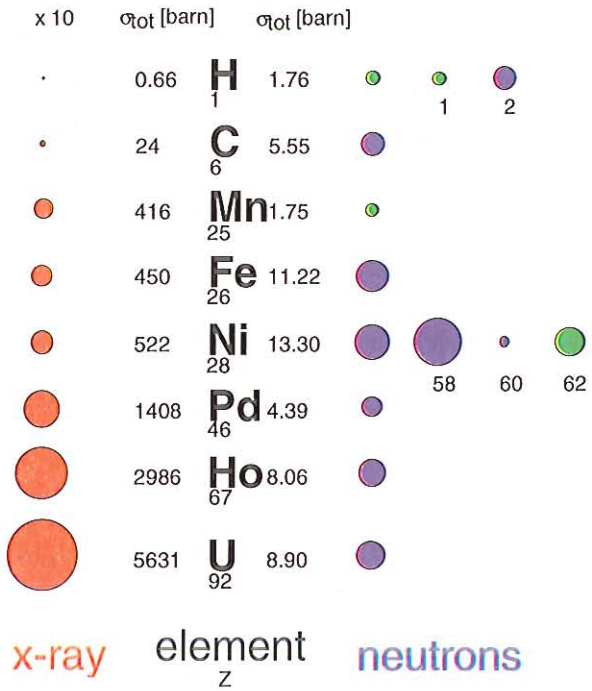


Fig. 10: *Comparison of the scattering crosssections for x-rays and neutrons for a selection of elements throughout the periodic table. The area of the coloured circles represent the scattering cross section, where in the case of x-rays a scale factor 10 has to be applied. For neutrons, the green and blue coloured circles distinguish the cases where the scattering occurs with or without a phase shift of π.*

Note that the x-ray scattering cross sections are in general a factor of 10 larger as compared to the neutron scattering cross sections. This means that the signal for x-ray scattering is stronger for the same incident flux and sample size, but that caution has to be applied that the conditions for kinematical scattering are fulfilled. For x-rays, the cross section depends on the number of electrons and thus varies in a monotonic fashion throughout the periodic table. Clearly it will be difficult to determine hydrogen positions with x-rays in the presence of heavy elements such as metal ions. Moreover, there is a very weak contrast between neighbouring elements as can be seen from the transition metals Mn, Fe and Ni in figure 10. For neutrons the cross sections depend on the details of the nuclear structure and thus varies in a non-systematic fashion throughout the periodic table. As an example, there is a very high contrast between Mn and Fe. The hydrogen atom is clearly visible even in the presence of such heavy elements as uranium. Moreover there is a strong contrast between the two hydrogen isotopes. This fact can be exploited for soft condensed matter investigations by selectively deuterating certain molecules or functional groups and thus varying the contrast within the sample.

3.6 Radiation sources

State of the art scattering studies require very well adapted radiation sources. Just like in a light scattering experiment lasers are used instead of simple light bulbs, modern x-ray scattering experiments are often performed at *high brilliance synchrotron radiation sources* instead of the conventional laboratory x-ray tube. Synchrotron radiation is produced in a circular accelerator. Highly relativistic electrons or positrons, which are stored in a storage ring, are being accelerated radially and as any accelerated charge emit electromagnetic radiation. Due to the Lorentz transformation, this radiation is highly collimated in the direction of the movement of the electron bunches. This leads to a number of excellent properties of synchrotron radiation depicted in figure 11. The synchrotron radiation beams have a broad wave length spectrum and thus allow to tune the wave length to the optimum conditions for the scattering experiment. The beams are highly collimated with divergencies in the order of 0.1 mrad and have a time structure in the 100 ps range. The synchrotron radiation beams are polarised (linearly in the orbital plane, elliptically above and below). Wigglers and undulators are magnet structures that force the electron beam into a sinusoidal movement and since synchrotron radiation is emitted at every magnet pole, the intensity is largely enhanced due to the number of poles.

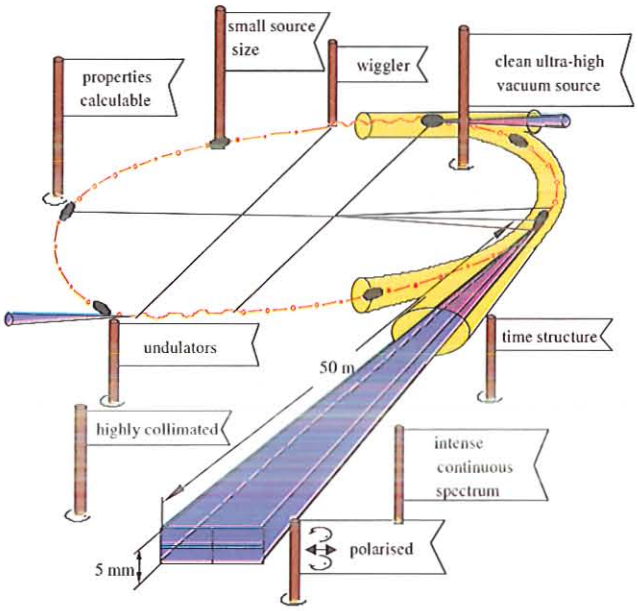


Fig. 11: *Schematic sketch of a synchrotron radiation source.*

Free neutrons are normally produced by fission processes in nuclear reactors. Through beam holes in the biological shieldings, neutrons are guided to the scattering experiments. Taking advantage of external total reflection, neutrons can be guided over long distances in so-called *neutron guides*, thus allowing a very efficient use of a neutron reactor by arranging further instruments in a neutron guide hall. The research center Jülich operates such a research reactor. The layout of the experimental facilities is depicted schematically in figure 12.

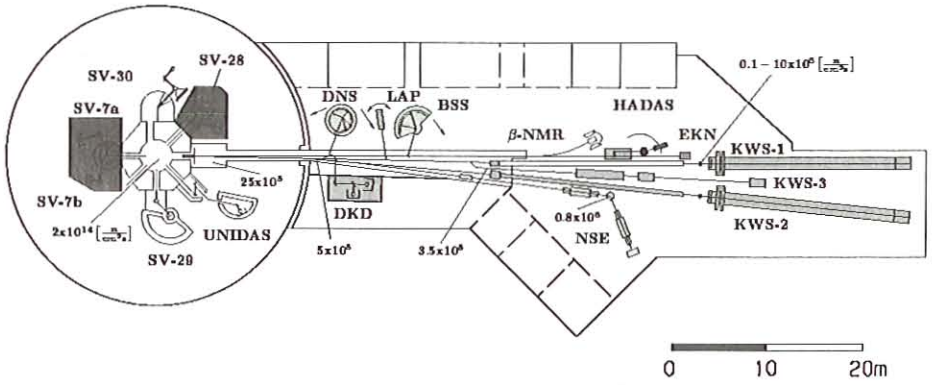


Fig. 12: *Instrument arrangement for the research reactor FRJ-2 DIDO at the research center in Jülich. The neutron flux in the DIDO reactor operating at 20 MW is the order of $2 \cdot 10^{14}$ n/s cm^2. Elastic (red colour) and inelastic (yellow colour) neutron scattering experiments are arranged around the reactor core within the reactor hall. In a so-called cold source, the neutron spectrum is shifted to longer wave lengths and these neutrons are guided into an external guide hall, where they deserve again elastic (green) and inelastic (blue) neutron scattering experiments.*

This facility is open to the use by guest groups from universities, industry and other research centers through a proposal system. Non-neutron-experts are supported by the instrument responsibles during a neutron scattering experiment at such a service facility. Details for the access to neutron beams are described in the internet page "www.neutronscattering.de", where one finds detailed instrument descriptions, a list of instrument responsibles as contact persons, a description of the beamtime application procedure, conditions for travel reimbursement for EU-supported projects and a proposal form to download. The Forschungszentrum Jülich is also participating in an European project for a next generation neutron source, the so-called European Spallation Source (ESS). In such a source, neutrons are not produced in a nuclear chain reaction as fission products, but they are produced by the so-called *spallation process*, where a high energy proton beam hits a heavy metal target. When a proton of energy about 1 GeV is absorbed in a nucleus, the nucleus will evaporate about 10 - 20 neutrons per proton. Peak fluxes can be achieved, which are more than two orders of magnitude higher than at present day reactor sources. More information about the ESS-project can be found on the internet (www.ess-europe.de).

4 Fluctuations

So far, we have assumed a fixed static arrangement of scatterers. This gives rise to elastic scattering, where the intensity or cross section is directly proportional to the spatial pair correlation function or Patterson function of crystallography (compare (11) and (12)). In this chapter, we will generalise these results to the more realistic case, where density fluctuations in time are allowed. One example are colloidal particles in Brownian motion. Not surprisingly, we will have to deal with auto correlation functions in time and a general discussion of their properties is given in appendix A1.

4.1 Van Hove theory

In what follows, we will quote results of the so-called Van Hove theory for correlation functions in the case of neutron scattering. The derivation starts from the general form of the cross section (34). By rewriting the δ-function in an integral representation (Fourier transform) and introducing time-dependent Heisenberg operators, one can show [1, 2, 4] that the cross section for inelastic or quasielastic scattering takes the following form:

$$\frac{\partial^2\sigma}{\partial\Omega\partial\omega} = \frac{k'}{k} N \left\{ \left(\overline{|b|^2} - |\bar{b}|^2 \right) S_{inc}(\underline{Q},\omega) + |\bar{b}|^2 S_{coh}(\underline{Q},\omega) \right\}. \tag{40}$$

As discussed for the case of elastic scattering in section 3.4, the cross section separates into a coherent and incoherent part. In (40), we have introduced the so-called *coherent and incoherent scattering functions* $S_{coh}(\underline{Q},\omega)$ *and* $S_{inc}(\underline{Q},\omega)$. These functions depend solely on the system under investigation and not on the detailed interaction between its constituents and the probe. The strength of this interaction is represented by the coupling constants in front of the scattering functions. The scattering function is given by

$$S_{coh}(\underline{Q},\omega) = \frac{1}{2\pi\hbar} \int_{-\infty}^{+\infty} dt\, e^{-i\omega t} \int d^3r\, e^{i\underline{Q}\cdot\underline{r}} G(\underline{r},t) \tag{41}$$

i. e. is a double Fourier transform of the spatial and temporal pair correlation function:

$$G(\underline{r},t) = \frac{1}{N} \sum_{ij} \int d^3r' \left\langle \delta(\underline{r}' - \underline{r}_j(0)) \cdot \delta(\underline{r}' + \underline{r} - \underline{r}_i(t)) \right\rangle = \frac{1}{N} \int d^3r' \langle \rho(\underline{r}',0) \rho(\underline{r}'+\underline{r},t) \rangle . \tag{42}$$

Here, <...> denotes the thermal average. (42) shows that $G(\underline{r},t)$ can be interpreted as the *correlater of the particle density*. Thus (40) - (42) represent a natural generalisation of the concept of a Patterson function discussed in section 2.2. Besides the scattering functions, which depend on scattering vector and energy transfer, it is often useful to introduce the *intermediate scattering functions*

$$S_{inc}(\underline{Q},t) \equiv \frac{1}{N} \sum_i \left\langle e^{-i\underline{Q}\cdot\underline{r}_i(0)} \cdot e^{i\underline{Q}\cdot\underline{r}_i(t)} \right\rangle ; \; S_{coh}(\underline{Q},t) \equiv \frac{1}{N} \sum_{i,j} \left\langle e^{-i\underline{Q}\cdot\underline{r}_i(0)} \cdot e^{i\underline{Q}\cdot\underline{r}_j(t)} \right\rangle \tag{43}$$

which are related to the scattering function by a Fourier transform:

$$S_{\substack{inc \\ coh}}(\underline{Q},\omega) = \frac{1}{2\pi\hbar} \int_{-\infty}^{+\infty} dt\, e^{-i\omega t} S_{\substack{inc \\ coh}}(\underline{Q},t). \tag{44}$$

The incoherent scattering function is given by a double Fourier transform

$$S_{inc}(\underline{Q},\omega) = \frac{1}{2\pi\hbar} \int dt\, e^{-i\omega t} S_{inc}(\underline{Q},t) = \frac{1}{2\pi\hbar} \int dt\, e^{-i\omega t} \int d^3r\, e^{i\underline{Q}\cdot\underline{r}} G_s(\underline{r},t) \tag{45}$$

of the *self correlation function*

$$G_s(\underline{r},t) = \frac{1}{N} \sum_i \int d^3r' \left\langle \delta(\underline{r}' - \underline{r}_i(0)) \cdot \delta(\underline{r}' + \underline{r} - \underline{r}_i(t)) \right\rangle . \tag{46}$$

In a natural generalisation of the situation for static scattering, the coherent scattering arises from the correlation of a pair of particles, while the incoherent scattering arises from scattering from single particles (see figure 13).

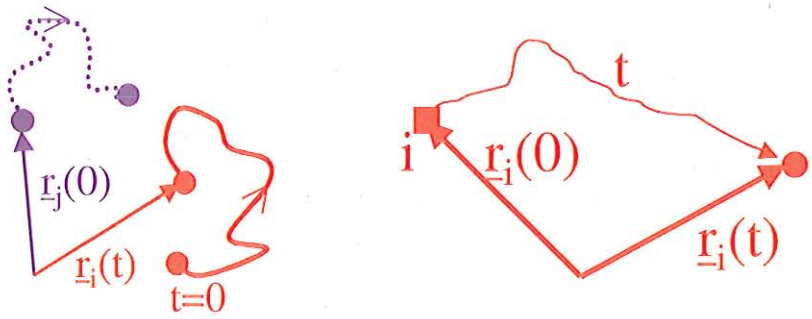


Fig. 13: *Illustration of the correlations responsible for coherent scattering (left) and incoherent scattering (right). In the case of coherent scattering, the position of particle j at time 0 is correlated with the position of particle i at time t, while in incoherent scattering the movements of the individual particles are visible.*

Let us finally discuss the case of so-called *integral scattering*, where the experimental conditions are such that the energy change during the scattering process is not resolved, but instead an integration over all energies is being performed. This scattering function for integral scattering S(Q) is given by (here we drop the distinction between coherent and incoherent scattering for simplicity):

$$S(\underline{Q}) = \int_{-\infty}^{\infty} S(\underline{Q},\omega)d\omega = \frac{1}{2\pi\hbar}\int dt \int d\omega e^{-i\omega t}\int d^3r\, e^{i\underline{Q}\cdot\underline{r}}G(\underline{r},t) = \int d^3r\, e^{i\underline{Q}\cdot\underline{r}}G(\underline{r},0) \qquad (47)$$

(47) shows that with integral scattering, the instantaneous correlations are being measured: a snap shot of the sample at time t = 0 is observed.

Correlation functions are rather abstract concepts and we want to illustrate them for the example of a simple liquid. The constituents of this liquid (atoms, molecules) are assumed to be spherical particles, which have a strong repulsive interaction potential for short distances and an attractive one for larger distances (see figure 14). The minimum in the interaction potential will give rise to a preferred nearest neighbour distance. Due to the hardcore potentials, the spheres cannot penetrate into each other and produce the excluded region in the pair correlation function for small distances r. This naturally explains the shape of the t = 0 correlation function, depicted in figure 14. The scattering function for integral scattering is obtained via a Fourier transform and is also depicted in figure 14.

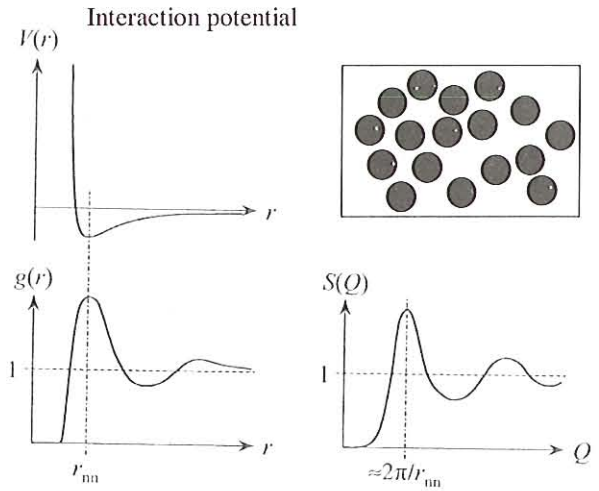


Fig. 14: *Snap shot (top right), pair interaction potential (top left), t = 0 correlation function (bottom left) and the scattering function for integral scattering (bottom right) for a simple liquid.*

Let us now look at the time dependence of the pair correlation and self correlation functions (see figure 15).

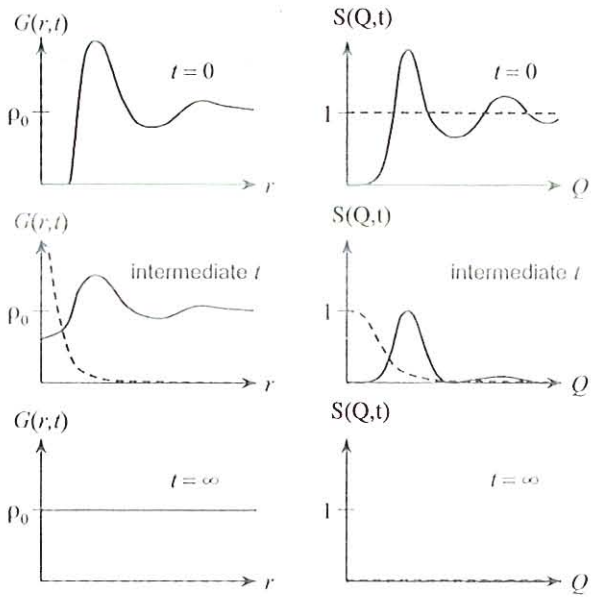


Fig. 15: *Schematic plot of the pair correlation (solid line) and self correlation functions (dotted line) on the left and the resulting intermediate scattering functions on the right for a simple liquid at different times.*

For t = 0 the self correlation function is given by a δ-function at r = 0. The pair correlation function follows the static correlation function. For intermediate times, the self correlation function broadens to a bell-shaped function due to the diffusion process, while the pair correlation function loses its structure. Finally in the long time limit, the self correlation simply vanishes for a liquid while the pair correlation function assumes a constant value. The incoherent intermediate scattering function as the Fourier transform of the self correlation function is Q-independent at t = 0, decays for intermediate t with respect to the t = 0 value, where the decay is faster for higher Q, and finally vanishes in the long time limit. The coherent scattering function is given by the static coherent scattering function for t = 0. It decays for intermediate times with respect to the t = 0 value, but the decay is less pronounced at the structure factor maximum. In the long time limit, the coherent scattering function decays to zero for any Q just as the incoherent scattering function.

Let us return to the case of integral scattering from a simple liquid. We make the simplification that the liquid consists of identical spherical and isotropic particles. Then it is easy to show [1, 4] that the intensity is given by

$$\Rightarrow I_{static} \sim |f(Q)|^2 \cdot \left\{ 1 + \bar{\rho} \int_{V_s} d^3R \; g(\underline{R}) e^{i\underline{Q}\cdot\underline{R}} \right\} \equiv |f(Q)|^2 \cdot S(Q) \qquad (48)$$

i. e. the intensity for static scattering separates into a pre-factor depending on the experimental geometry and the type of radiation, the square of a form factor, which describes scattering from a single particle, and the scattering function (for the static case often referred to as *structure factor*), which contains information on the particle correlation and is independent of the type of radiation used. The structure factor gives an average snap shot picture g(R) of the sample. As an example, figure 16 shows the structure factor of liquid ^{36}Ar at 85 K. The points are deduced from a neutron scattering experiment, the curve is generated by a molecular dynamics calculation using a Lennard-Jones potential. The insert shows the pair correlation function g(R) of liquid Ar calculated by a Fourier transform of the data [7].

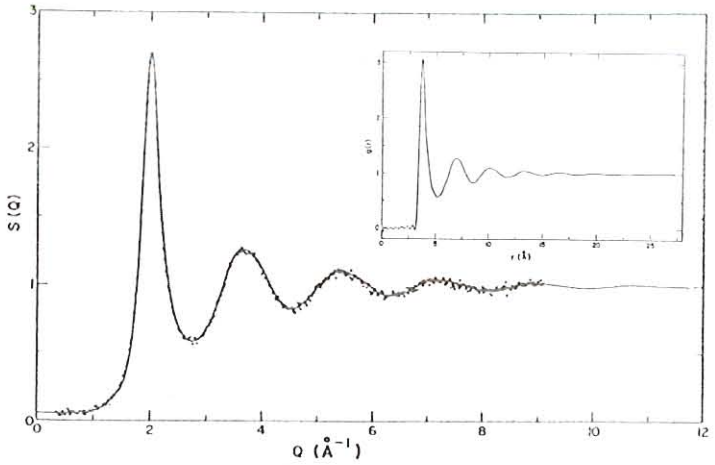


Fig. 16: *Static scattering function for liquid ^{36}Ar at 85 K and resulting pair correlation function (insert) [7].*

4.2 Inelastic light scattering

We have seen in section 4.1 that inelastic or quasielastic scattering is related to density fluctuations. An instructive example is given by a sound wave in a simple liquid. The sound wave will give rise to periodic density modulations travelling through the sample (see figure 17 for a static snap shot). For static density modulations, we expect with a hand waving argument "diffuse Bragg scattering" to occur under an angle giving by $Q = 4\pi/\lambda \cdot \sin\theta = 2\pi/\Lambda_{soundwave}$. The soundwave can be understood as a moving pattern of periodic density modulations. In a wave picture, this will give rise to a Doppler shift of the emitted wave. In a particle picture, the scattered particles will receive the recoil energy from the sound wave particles. We can determine the dispersion relation by considering momentum- and energy conservation for this collective excitation:

$$\begin{aligned} \hbar\underline{k}' &= \hbar\underline{k} - \hbar\underline{Q} \\ \hbar\omega' &= \hbar\omega - \hbar\omega_{CE} \end{aligned} \tag{49}$$

Such elementary excitations can be measured with different probes. Here, we will discuss the case of inelastic light scattering. Visible light has a characteristic frequency of 10^{14} - 10^{15} Hz. The frequency shift in the scattered light can be analysed either by an optical grating monochromator, if the frequency shifts are rather large (> 10^{11} Hz) or a Fabry-Perot-interferometer for rather small frequency shifts (10^{7} - 10^{12} Hz). The technique using optical gratings is referred to as *Raman spectroscopy*, while the technique employing an interferometer is referred to as *Brillouin spectroscopy*. A typical energy spectrum for an elementary excitation such as a sound wave would then for a given momentum transfer consist in a central elastic *Rayleigh line* accompanied by two inelastic lines for energy loss and energy gain, referred to as the *Stokes and Anti-Stokes* line, respectively.

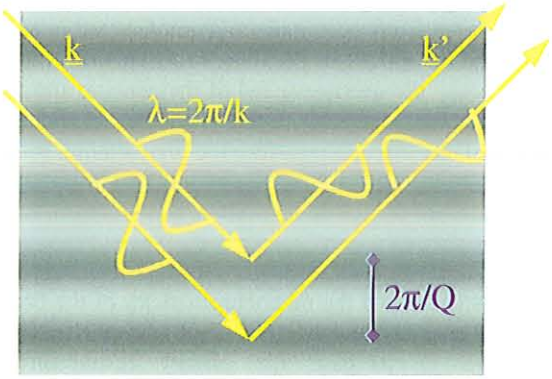


Fig. 17: *The scattering from density fluctuations can be visualised as "diffuse Bragg scattering".*

4.3 Inelastic neutron scattering

There are many techniques, which allow to measure the double differential cross section by means of neutron scattering. For a more detailed discussion, we refer to [1]. Here we just

want to give two examples most relevant for soft condensed matter research: *time-of-flight* (TOF) and *neutron spin echo* (NSE) spectroscopy.

A neutron time-of-flight spectrometer is depicted schematically in figure 18.

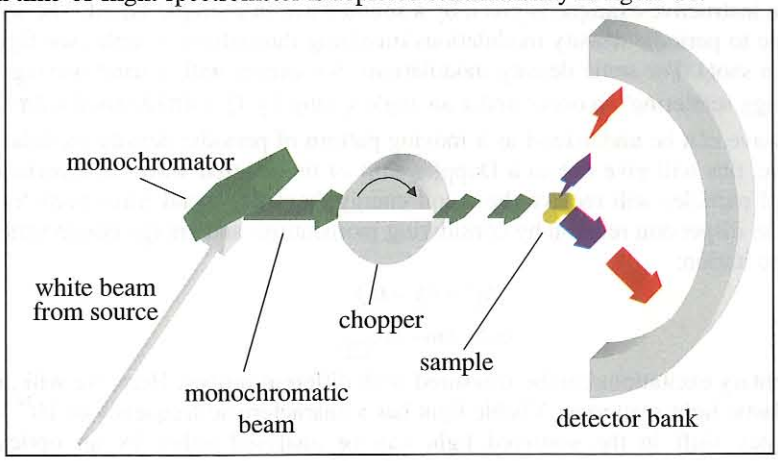


Fig. 18: *A schematic sketch of a neutron time-of-flight spectrometer.*

The white continuous neutron beam from a reactor source is monochromatised by Bragg reflection from a single crystal. By means of a rotating neutron absorbing drum with one slit opening, the beam is chopped into small portions in time. Such a device, which opens the beam pass periodically for a short moment, is called a *neutron chopper*. These neutron pulses travel to the sample, are scattered from the sample and are detected in a detector bank, covering as large solid angle around the sample as possible. From the travelling time of the neutron from the chopper to the detector, the average speed of the neutron and from (32), the energy change of the neutron during the scattering process can be determined. Finally from the positions in the detector and the energy transfer, the momentum transfer for each given neutron can be calculated. The histogram "neutron countrate versus energy and momentum transfer" finally gives us a measure for the double differential neutron scattering cross section.

The limitation of the time-of-flight method arises from the finite energy resolution determined by the uncertainties in the distances and the monochromaticity of the beam. Slow movements of large molecules evidently give rise to relatively small energy transfers. To measure small energy transfers, we have to increase the energy resolution by increasing the monochromaticity and reducing the sample size. Evidently, we will reduce the neutron countrate, which poses a natural limit to the energy resolution of a time-of-flight machine. Typically the energy resolution $\Delta E/E$ of a time-of-flight spectrometer amounts to some 1 %.

How can we improve the energy resolution without reducing the neutron flux? The solution is to use the property that the neutrons carry a magnetic dipole moment and thus undergo a neutron spin precession in a magnetic field. If we can conceive a time-of-flight method, where we use the neutron spin precession as an individual clock for each individual neutron, we can, in principle, use a broad wave length band (about 10 %) and still obtain an energy resolution

up to the neV range. This principle is realised in the so-called *neutron spin echo (NSE) spectrometer*. A sketch of the experimental set up is shown in figure 19.

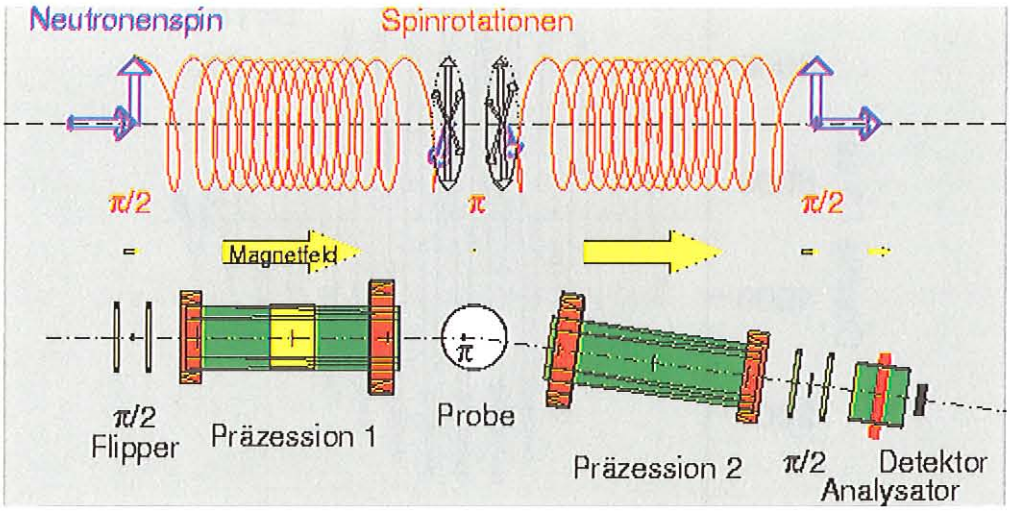


Fig. 19: *Spin rotations and set up of a NSE spectrometer (from Monkenbusch in [2]). In the upper part, the spin precession in the magnetic field shown in the middle part is depicted schematically. The lower part shows a schematic set up of the neutron spin echo spectrometer realised at Forschungszentrum Jülich.*

A "pink" neutron beam with a wavelength spread of $\Delta\lambda/\lambda \approx 10\,\%$ is being polarised, i. e. all the neutron spins point in the same direction, eventually perpendicular to the longitudinal magnetic field. The neutrons traverse a region of homogeneous magnetic field, where they undergo a number of spin precessions (typically 10^4 rotations) in one precession coil of about 3 m length. Neutrons with different velocities spent different times in this field region and thus undergo a different number of spin rotations. Therefore the neutron beam arriving at the sample positions is depolarised. To illustrate the principle, we first assume elastic scattering at the sample. After the scattering events, the spins are flipped by an angle of 180° around a vertical axis by the so-called π flipper. Then they traverse a field region of exactly the same field strength and length as in the primary arm of the spectrometer. The neutrons now undergo the same spin precessions as in the primary arm just in the opposite sense. Therefore all neutrons with different velocities have the same spin orientation after the precession field: the polarisation is fully restored. By means of a polarisation analyser and detector unit, the polarisation of the scattered beam can now be measured. If inelastic scattering occurs at the sample, the polarisation will not be recovered for a completely symmetric arrangement of primary and secondary arm. Only if the field strength in the secondary coil is varied, the resonance condition can be restored. An oscillatory behaviour of the countrate as a function of the current in the secondary coil is observed (see figure 20).

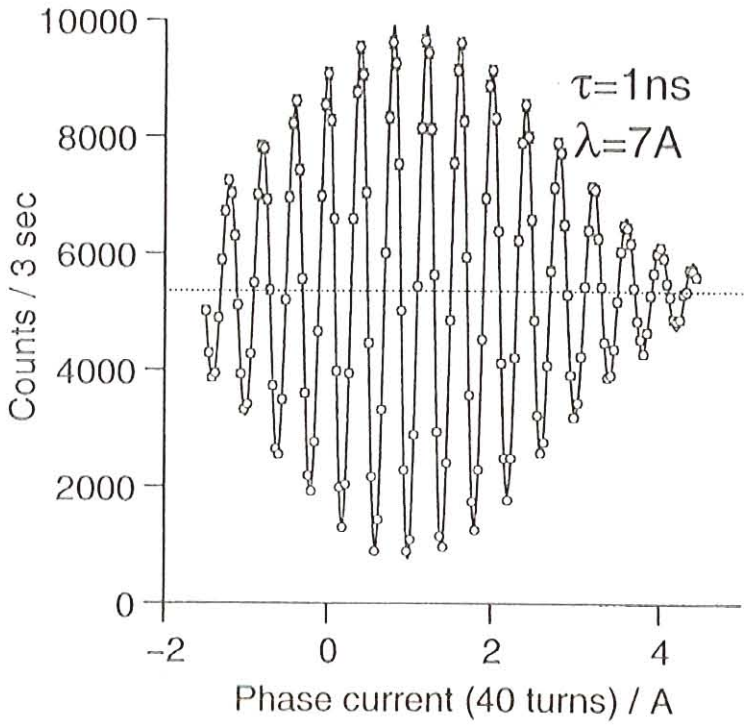


Fig. 20: *Example for a typical echo line shape (Monkenbusch, [2]): countrate as function of the magnetic symmetry proportional to the phase current.*

In fact, a neutron spin echo spectrometer measures the intermediate scattering function with the time being proportional to the field integral

$$\frac{I(Q,t)}{I(Q,0)} = \frac{S(Q,t)}{S(Q)} \quad \text{with} \quad t = \gamma \cdot \int B\,dl \cdot \frac{m_n^2}{2\pi h^2} \cdot \lambda^3 . \tag{50}$$

A typical example of the NSE technique comes from the field of polymer dynamics. In the simplest model for the movement of a polymer chain in a melt, one assumes that the different chains are not hindering each others movements. Entropic forces determine the movement of a single polymer chain. This is the so-called *Rouse model*. However, for longer times, a given chain will feel the restrictions imposed by the other chains encircling it. The motion of a chain in a melt is heavily impeated in directions lateral to its own profile. Therefore the dominant diffusive motion proceeds along the chain profile. The chain will move through the melt like a snake, which gave the name to this *reptation model* of de Gennes. With neutron spin echo techniques, the Rouse dynamic for short times and the cross-over to the reptation model by de Gennes for longer times could be observed (see contribution C2 by D. Richter in this lecture course and figure 21).

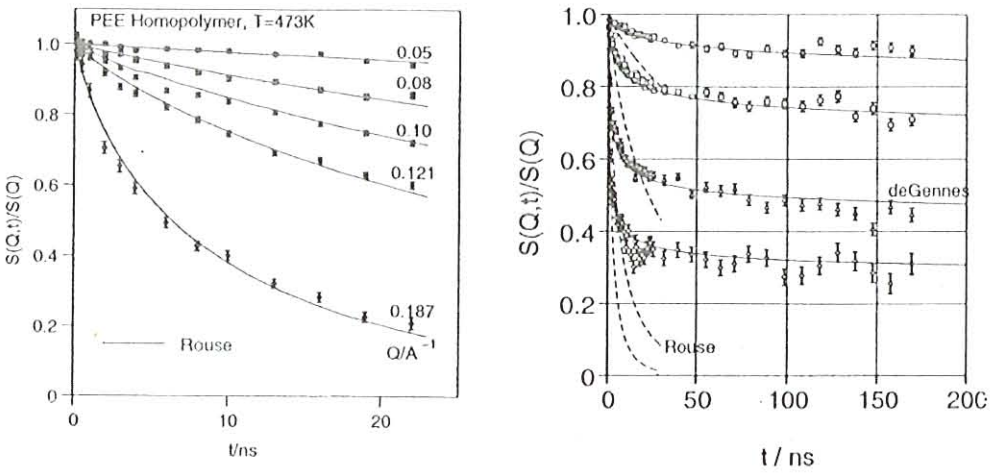


Fig. 21: *NSE observation of Rouse dynamics for short times (left figure; points are experimental, the lines represent the theory for the rouse model) and the cross-over to the reptation model for longer times (right hand side; solid line: reptation model; dashed line: Rouse model).*

4.4 Dynamic light scattering

In section 4.2 we have seen that with inelastic light scattering, where we measure with spectroscopic methods the frequency power spectrum of the auto correlation function, we can observe dynamics from optical frequencies (10^{14} Hz) down to some 10^6 - 10^7 Hz. With neutron spin echo spectroscopy, this frequency range can be extended by about one order of magnitude. In this section we want to ask the question how we can observe even slower dynamics.

The answer is to measure the time evolution of the instantaneous correlation function, i. e. by measuring an integral spectrum at a given time all fast processes have relaxed and we are left with the slow dynamics. In dynamic light scattering, one measures the normalised intensity auto correlation function (IACF):

$$\hat{g}_I(\underline{Q},t) := \langle I(\underline{Q},0)\cdot I(\underline{Q},t)\rangle / I^2 . \qquad (51)$$

In practise the detector is positioned at a given scattering angle corresponding to a momentum transfer Q. The intensity fluctuations in the detector are determined and an auto correlation function is calculated according to appendix A1. This auto correlation function is normalised to the square of the average intensity I in the detector. However, in section 3.3 and 4.1, we have learnt that the quantity of interest is actually the auto correlation function of the electric field (EACF). The normalised EACF is given by

$$\hat{g}_E(\underline{Q},t) := \frac{1}{2}\sqrt{\frac{\varepsilon_F}{\mu_0}}\langle E_S(\underline{Q},0)\cdot E_S^*(\underline{Q},t)\rangle / I . \qquad (52)$$

Since the electric field $E_S^*(\underline{Q},t)$ is related to the scattering power density via the Fourier transform, the EACF is related to the intermediate scattering function. It can be shown that the intensity auto correlation function and the electric field auto correlation function are connected by the so-called *Siegert relation*:

$$\hat{g}_I(\underline{Q},t)=1+\left|\hat{g}_E(\underline{Q},t)\right|. \tag{53}$$

Thus by an experimental determination of the intensity auto correlation function, we get access to the Fourier transform of the density auto correlation function, which is the quantity of interest.

Let us discuss an example for photon correlation spectroscopy. We have chosen the scattering of coherent 8.2 keV x-rays from a synchrotron radiation source by porous silica gel. When the sample is illuminated by the coherent x-ray beam, we observe on the area detector a so-called speckle pattern (figure 22), which is due to the instantaneous density modulations within this sample.

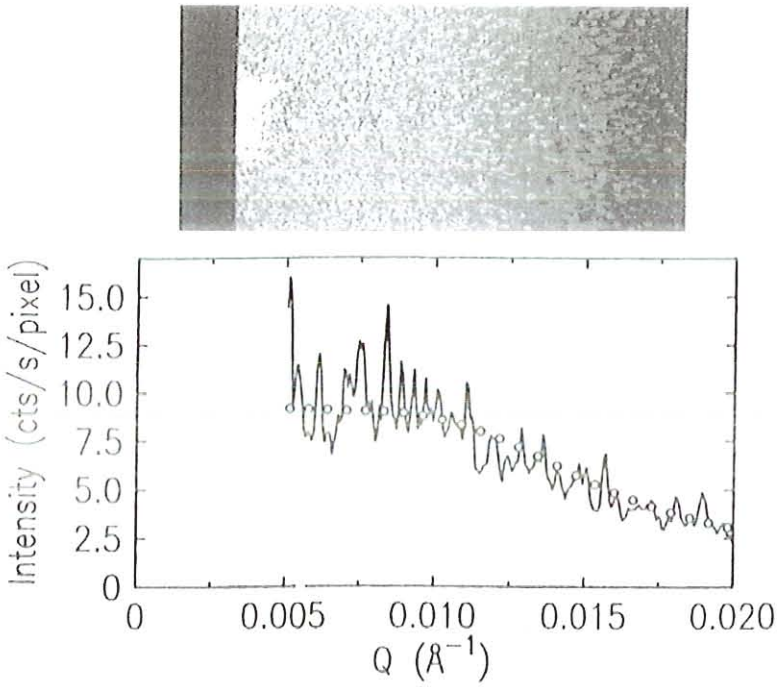


Fig. 22: *Speckle pattern from an aerogel recorded with a CCD detector using coherent x-rays [8]. The speckle structure becomes better visible, if one pixel row in the horizontal direction is plotted (continuums line in the bottom picture).*

For an inhomogeneous sample with a density distribution constant in time, we will observe a static speckle pattern. However for a sample, which has internal slow dynamics, the speckle

pattern will change with time and we can observe the intensity in a given direction with a small pinhole or within one pixel of an area detector. From the Siegert relation, we can deduce the time dependence of the intermediate scattering function. This function is depicted for colloidal silica, suspended in a solvent (water glycerol mixture) in figure 23.

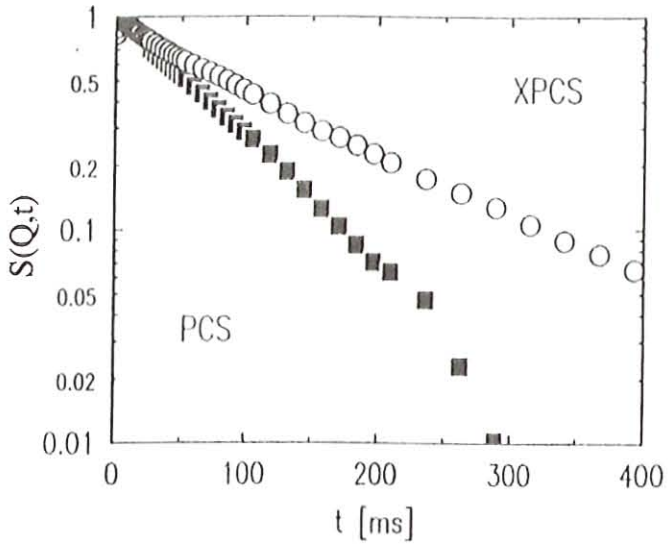


Fig. 23: *Intermediate scattering function measured by x-ray photon correlation spectroscopy XPS (open circles) and optical photon correlation spectroscopy (closed squares) for the same momentum transfer $Q = 9{\cdot}10^{-4}$ Å^{-1} in an optically opaque sample of colloidal silica [8].*

An exponential decay can be fitted to the XPCS measurement and the translational diffusion coefficient can be determined. Figure 22 shows that the PCS intermediate scattering function relaxes faster as compared to the XPCS data. The authors attribute this effect to multiple scattering events, which are present in the optical experiment.

5 Summary

An introduction into the investigation of soft condensed matter systems by scattering methods has been given. We have seen that neutrons, light and x-rays are particularly useful for such studies. However independent of the probe, coherent scattering always measures pair correlation functions and the scattering cross section is proportional to the spatial and temporal Fourier transform of these correlation functions.

Condensed matter investigations face the problem that relevant lengths and time scales cover many orders of magnitude. Figure 24 gives an overview over the characteristic time scales found in condensed matter investigations. These time scales range from the fs regime for fast electronic excitations up to macroscopic time scales for relaxation processes in glasses or spin glasses.

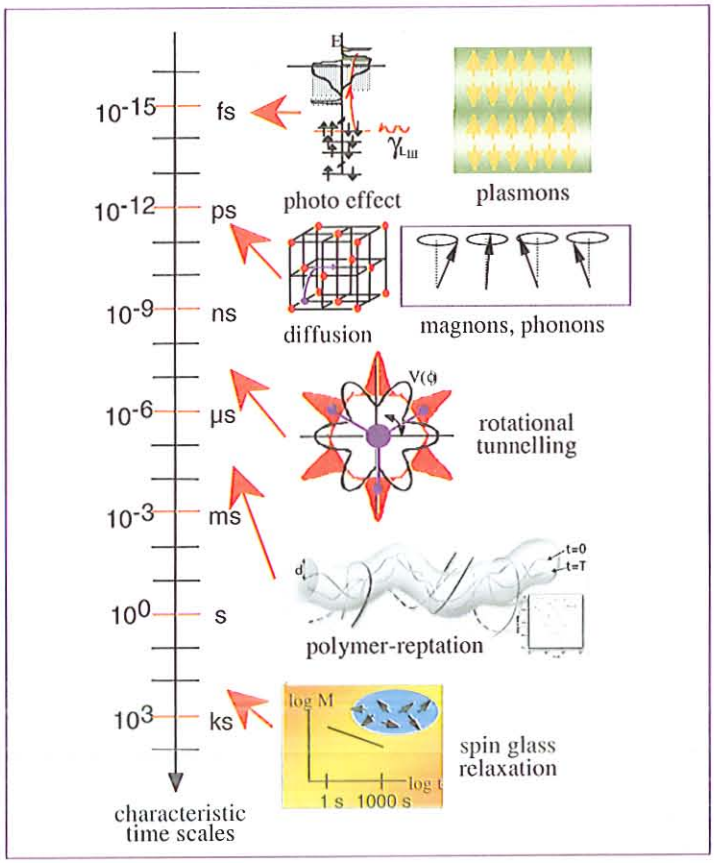


Fig. 24: *Characteristic time scales found in condensed matter research.*

With appropriate scattering methods, all these processes on different time scales can be investigated. Which scattering method is appropriate for which region within the "scattering vector Q - energy E plane" is plotted schematically in figure 25. A scattering vector Q corresponds to a certain length scale, an energy to a certain frequency, so that the characteristic lengths and times scales for the various methods can be directly determined from figure 25.

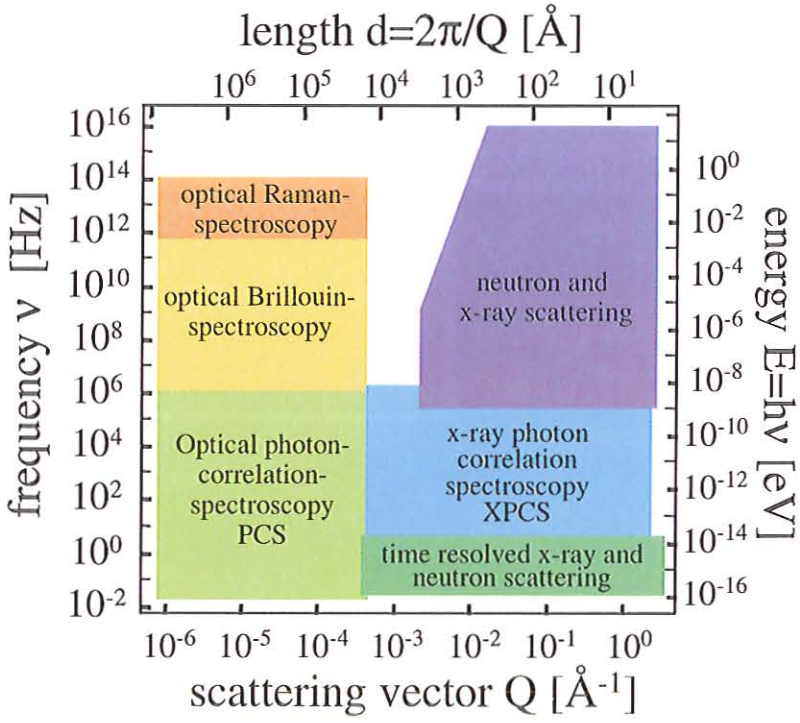


Fig. 25: *Regions in frequency ν and scattering vector Q or energy E and length d plane, which can be covered by various scattering methods.*

Appendices

A Autocorrelation Functions

Let us assume a quantity A that fluctuates in time as depicted in the insert of figure A1.

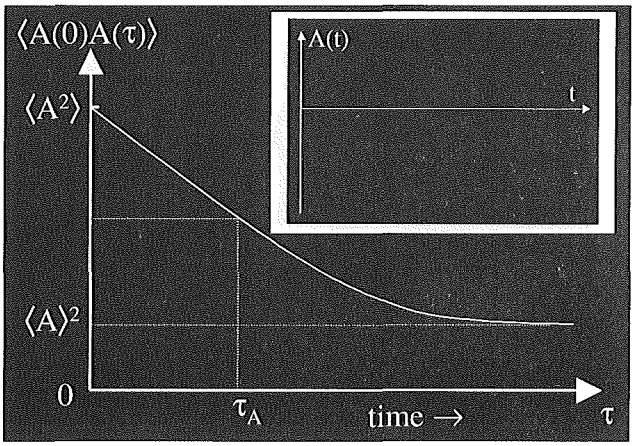


Fig. A1: *The insert gives an example of a quantity A(t) that fluctuates in time. The main figure shows the general behaviour of the autocorrelation function. It has a maximum of $\langle A^2 \rangle$ for $\tau = 0$. From this maximum, it decays with a time constant τ_A towards the asymptotic value of $\langle A \rangle^2$ for infinite times.*

For this quantity, we can define the average value

$$\langle A \rangle = \lim_{T \to \infty} \frac{1}{T} \int_0^T dt A(t). \tag{A1}$$

Around this average value, fluctuations $\delta A(t) = A(t) - \langle A \rangle$ are being observed. If the function A(t) varies monotonically, A(t+τ) approaches the values of A(t) for small values of τ, which means that both are correlated in time. Similar correlations can occur at larger times, e. g. for quasi-periodic fluctuations. As a measure of this correlation, the autocorrelation function is introduced:

$$\left\langle A(0)A(\tau) \right\rangle = \lim_{T \to \infty} \frac{1}{T} \int_0^T dt A(t)A(t+\tau) \Bigg\} \quad \begin{matrix} \tau \to 0: \left\langle A^2 \right\rangle \\ \tau \to \infty: \left\langle A \right\rangle^2 \end{matrix}. \tag{A2}$$

This autocorrelation function has a very general property depicted in figure A1: it decays from a maximum value of $\langle A^2 \rangle$ for $\tau = 0$ to the asymptotic value of $\langle A \rangle^2$ for infinite times with a characteristic time constant of τ_A. Often times, this decay follows a simple exponential law $\exp(-\tau/\tau_A)$.

References

1. "Neutron Scattering",
   Schriften des Forschungszentrums Jülich: Materie und Material; Vol. 9
2. "Femtosekunden und Nano-eV: Dynamik in kondensierter Materie",
   Schriften des Forschungszentrums Jülich: Materie und Material; Band 3
3. John M. Cowley, "Diffraction Physics", North Holland Amsterdam, 1990
4. Steven W. Lovesey, "Theory of neutron scattering from condensed matter", Clarendon Press, Oxford, 1987
5. J. K. G. Dhont, "Light Scattering", chapter 3 in: "An Introduction to Dynamics of Colloids", Elsevier, Amsterdam (1996)
6. A. Messiah, "Quantenmechanik", Band 1 + 2, Walter de Gruyter, Berlin (1976)
7. J. L. Yarnell, M. J. Cats, R. G. Wenzel, S. H. Koenig, Phys. Rev. A 7 (1973), 2130
8. D. O. Riese et al., Phys. Rev. Lett. 85 (2000), 5460

A2 NMR

G. Meier
Institut für Festkörperforschung
Forschungszentrum Jülich GmbH

Contents

1 What is NMR about? 2

2 Quantum Mechanical Foundations 2

3 Longitudinal and Transversal Magnetisation 6

4 Longitudinal and Transversal Relaxation Times 8

5 How is the Basic Experiment Done? 10

6 Measurement of T_1 and T_2 14

7 Relaxations by Fluctuating Fields 17

8 Nature of Interactions 19

1 What is NMR about?

The phenomenon NMR: Nuclear magnetic resonance was discovered in 1945 independently by two groups of physicists Purcell, Torrey and Pound from Havard University and Bloch, Hansen and Packard from Stanford. Purcell and Bloch received the Nobel prize for that discovery in 1952. The nuclear magnetic resonance is today the most powerful spectroscopic method to determine structural relations mostly in liquids where high resolution spectra can be obtained. Here NMR is of uncountable value for chemists. On the other hand it is much less common for solids. The reason is buried in the presence of angular dependent anisotropic interactions leading to spectral resolutions much less than those for liquids. Nevertheless due to several improvements like high speed spinning at the magic angle (where the dipolar interactions ~ $<3\cos^2\theta - 1>$ disappear) or multiple pulse irradiation, high power decoupling and last but not least multi-dimensional NMR techniques (celebrated by the Nobel prize to R. Ernst for this invention) these deficiencies can be overcome. NMR is nowadays the most powerful spectroscopic technique. This small lecture can only try to touch its surface: Either we do it in one hour or in one year, everything in between seems not be possible.

2 Quantum Mechanical Foundations

Many nuclei possess spin angular momentum. A nucleus with spin quantum number **I** (which may be an integer or a half integer) may take 2**I**+1 different orientations relative to an arbitrary axis that are distinguished by the orientational quantum number m_I

$$m_I = \mathbf{I}, \mathbf{I}-1, \ldots\ldots, -\mathbf{I} \qquad (1)$$

A proton as example for a nucleus that has **I** = ½ and can thus take 2 different orientations (other prominent members are ^{13}C, ^{19}F, ^{31}P), ^{2}H has **I** = 1 and takes 3 different orientations and so on. Now, every nucleus with non-zero spin has a magnetic moment μ . The component μ_z of this moment on the z-axis depends on the orientation of the spin, hence

$$\mu_z = \gamma \eta m_I \qquad (2)$$

where γ is the specific gyromagnetic ratio of the respective nucleus.
The value of m_I corresponds to a different orientation of μ_z in an external magnetic field in z-direction (see Fig.1).

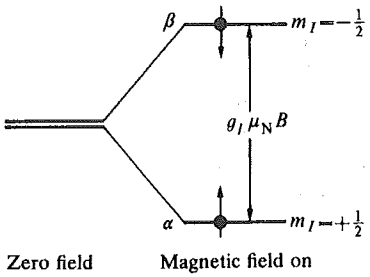


Fig. 1: *The nuclear spin energy levels of a spin 1/2 nucleus in a magnetic field.*

On the left we have no field and thus no splitting on the right the field is on and according to **I** = ½ we observe a splitting into two levels ($m_I = \pm$ ½) α,β which have different energies given by

$$E_{m_I} = -\mu_z B = -\gamma \eta B m_I \tag{3}$$

These energies are expressed in terms of the so called Lamor frequency ω

$$\omega = \gamma B \quad , \quad E_{m_I} = -m_I \eta \omega \tag{4}$$

For a field of 12 Tesla (=120.000 Gauss) the Lamor frequency of ^{1}H is about 500MHz. The energy splitting between the levels α,β of Fig.1 is given by

$$\Delta E = E_\beta - E_\alpha = \frac{1}{2}\gamma \eta B - \left(-\frac{1}{2}\gamma \eta B\right) = \gamma \eta B = g_I \mu_N B \tag{5}$$

Here g_I is the nuclear g-factor (in the order of 1) and μ_N is the nuclear magneton. For most nuclei β lies above α (γ>0) and therefore there are a bit more spins in state α than in β. If the sample is kept in a radio frequency field which corresponds to this ΔE of eq.5 then resonance takes place and spins may perform a transition α → β and we observe absorption.(For protons $\gamma/2\pi$ = 425.8MHz/10Tesla). However, the difference in population between the two states is small. Taking the above values the ΔE is given by

$$\Delta E = 4{,}258 \cdot 10^6 \cdot 6{,}63 \cdot 10^{-34} \cdot 10 = 2{,}8 \cdot 10^{-26} \ J \tag{6}$$

On the other hand kT for room temperature is given by $4{,}1 \cdot 10^{-21}$ J , so we can estimate the population difference N_β to N_α according to a Boltzmann distribution

$$N_\beta / N_\alpha = \exp(-\Delta E / kT) \tag{7}$$

to be $O(10^{-5})$. Since this is a small number the use of high magnetic fields is of advantage.

The sketch shown in Fig.1 corresponds to the classical picture of parallel and antiparallel orientation of the z-component of the magnetic moment μ relative to the external field $\mathbf{B}_0$. First of all a magnetic dipol μ in a field $\mathbf{B}$ experiences a torque $\mathbf{L} = \mu \times \mathbf{B}$, which tries to align it up in field direction. The spin angular momentum of the nucleus, however, causes by that a precession of μ around the z-axis, similar to a gyroscope. The circular frequency of that precession is the Lamor-frequency $\omega_0 = \gamma B_0$ (cf.eq.4). Since ω_0 shows in the negative z-direction we write $\omega_0 = -\gamma B_0$ (for the rotation of μ around the field axis the left hand rule applies: The thumb goes in field direction, then the fingers indicate the direction of rotation ω). This is sketched in Fig.2.

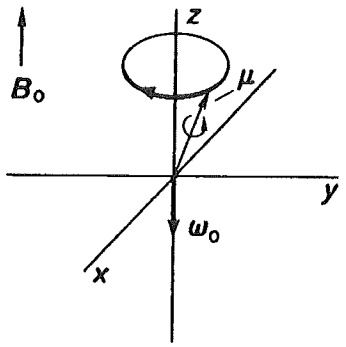


Fig. 2: *Precession of nuclear magnetic moment μ in a fixed coordinate system K(x,y,z).*

For the resonance case it is now important that a magnetic field $\mathbf{B}_1$ which rotates in the x,y-plane, having a circular frequency identical to ω_0, can cause the vector μ to flip into the negative z-direction (see Fig.3).

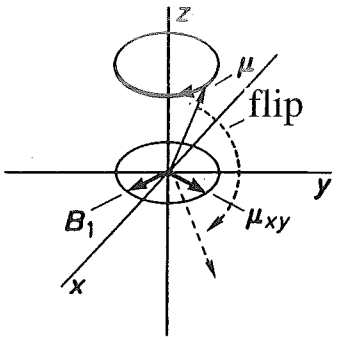


Fig. 3: *A force acting through the rotating vector $\boldsymbol{B}_1$ on the magnetic moment μ.*

In order to make that clear we imagine a fixed coordinate system K(**x**,**y**,z) and a rotating coordinate system (with ω_0 around z) K'(x,y,z). In K' there acts on μ not only the static field $\mathbf{B_0}$ but

$$\mathbf{B'} = \mathbf{B}_0 + \frac{\omega}{\gamma} \tag{8}$$

instead. Here ω/γ is a fictive field $\mathbf{B_f}$, which results from the relative motion between K and K'. For $\omega = 0$, $\mathbf{B_f}$ vanishes, on the other hand for $\omega = -\gamma\mathbf{B_0}$ it follows $\mathbf{B'} = 0$. This corresponds to the fact that μ takes a distinct position in K' if ω is identical to ω_0: Circular frequency and direction of rotation of the rotating system K' match with the precession motion.
Now we switch on $\mathbf{B_1}$ in K' along the x-axis. Then the following effective field emerges:

$$\mathbf{B}_{\text{eff}} = \mathbf{B'} + \mathbf{B}_1 = \mathbf{B}_0 + \frac{\omega}{\gamma} + \mathbf{B}_1 = \mathbf{B}_0\left(1 - \frac{\omega}{\omega_0}\right) + \mathbf{B}_1 \tag{9}$$

The angle θ between $\mathbf{B_{eff}}$ and the z-axis is given by

$$\tan\theta = \frac{B_1}{B_0\left(1 - \dfrac{\omega}{\omega_0}\right)} \tag{10}$$

This is sketched in Fig.4.

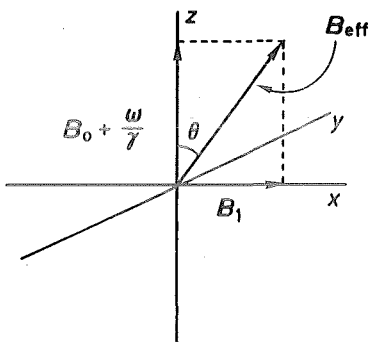


Fig. 4: *The effective magnetic field B_{eff} in the rotating frame.*

We can now discuss two different cases thereby assuming $B_0 >> B_1$ by varying B_0 and thus ω_0

- ω_0 and ω are very different, then $\mathbf{B_{eff}}$ is parallel to z, because of eq.10 for $\omega < \omega_0$ or $\omega > \omega_0$ we find $\tan\theta \approx 0$ and thus $\theta \approx 0°$ or 180°
- $\omega \approx \omega_0$, then $\tan\theta \rightarrow \infty$ and $\theta = 90°$, $\mathbf{B_{eff}} = \mathbf{B_1}$ and μ precesses with ω around $\mathbf{B_1}$,the z-axis and is capable to flip into the negative z direction, see Fig.5.

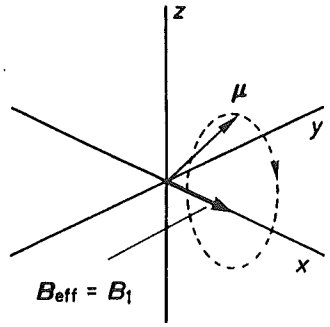


Fig. 5: *The precession of the nuclear moment μ around B_1.*

Since $B_0 >> B_1$, the second case is a classical resonance phenomenon: A small perturbation leads to a large effect. The system is, however, only influenced by $\mathbf{B_1}$ if the Lamor frequency is equal to ω.
In reality the rotating field $\mathbf{B_1}$ is produced by a high frequency transmitter along the x-axis in K. A linear polarized magnetic field in x-direction can be decomposed in two counter rotating fields of which one is the desired one , the other has no influence.

3 Longitudinal and Transversal Magnetisation

The above considerations were valid for isolated nuclei. Now lets consider an ensemble of nuclei. After we have switched on the field $\mathbf{B_0}$ we reach after a certain time an equilibrium population according to the Boltzmann distribution, cf.eq.7. A macroscopic measure of all individual μ's rotating with ω_0 around z is the equilibrium magnetisation **M** ($M=\Sigma\mu_I$). Since all moments μ are out of phase but statistically distributed on a cone (see Fig.6) there is no component of M in the x,y-direction.

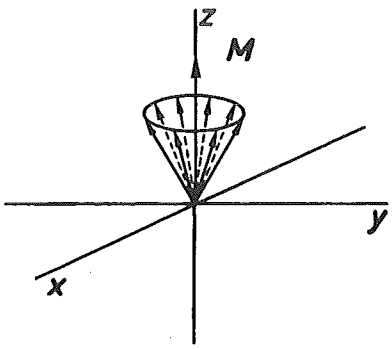


Fig. 6: *The macroscopic magnetisation **M** resulting from all individual nuclear moments μ_i. Shown are only the excess moments in the ground state.*

Along the x-axis we now apply a high frequency field with $\mathbf{B_1}$ constant in time in K'. In case of resonance ($\omega \approx \omega_0$) we observe an interaction between **M** and $\mathbf{B_1}$ which leads the vector **M** to direct a bit into the x-direction. Coarsely the z-magnetisation drops towards M_z and we observe a so called transversal magnetisation M_y. Contrary to an isolated nucleus we find no flip since for small $\mathbf{B_1}$ fields not all spins can take enough energy for that process but the spins perform a precession instead around the z-axis, see Fig.7.

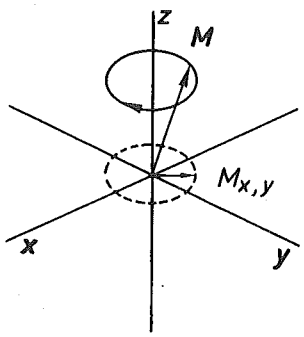


Fig. 7: *Precession of the magnetisation vector **M** in a fixed coordinate system K.*

This transversal magnetisation is varying in time along the x,y-axis in the fixed coordinate system K and can hence be measured as induction signal within a transceiver coil. The magnitude of **M** is proportional to the energy gain from the high frequency field and the signal consequently reflects the interplay between excitation of the nuclei and relaxation. Since in reality not all nuclei have the same Lamor frequency due to the anisotropy of the interactions we can observe an induction signal although $\omega \neq \omega_0$. For a small variation of ω_0, M moves on a circle in K' as shown in Fig.8.

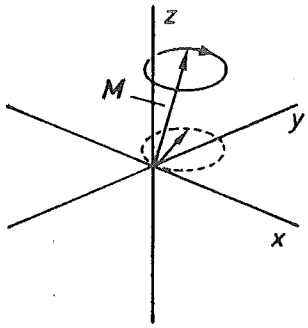


Fig.8: *The motion of **M** in the rotating frame K' while passing through a resonance.*

If we plot M_x and M_y in dependence of $\Delta\omega = \omega_0 - \omega$, we get a dispersion and a absorption curve as shown in Fig.9.

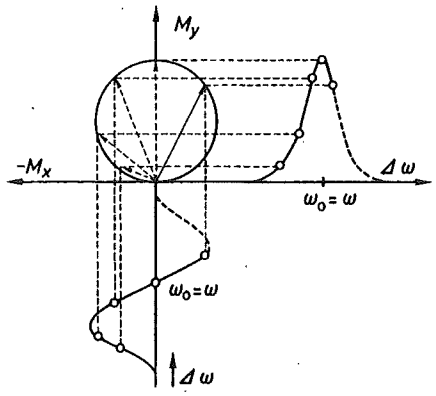


Fig.9: *The transversal magnetisation $M_{x,y}$ in the rotating frame in dependence of the difference $\Delta\omega$ and separation of the vector $M_{x,y}$ in its components M_y and M_x.*

A quantitative description of this resonance phenomenon is given through the Bloch equations. Here we report the expression for M_y (which is the relevant one in our case) for the absorption situation:

$$M_y = \frac{-M_0\gamma}{1+T_2^2(\omega_0-\omega)^2+\gamma^2B_1^2T_1T_2}B_1T_2 \qquad (11)$$

This expression has the form of a Lorentz line if we assume $\gamma^2B_1^2T_1T_2 << 1$. Similar expressions can be derived for M_x and M_z, and also for the respective magnetisations in a fixed coordinate system. The Bloch equations allow us to calculate the components of the transversal magnetisation as a function of M_0, B_1, $\Delta\omega$ and the relevant relaxation times T_1, the longitudinal relaxation time and T_2, the transversal relaxation time. What are these times T_1 and T_2 all about?

4 Longitudinal and Transversal Relaxation Times

The longitudinal relaxation time T_1 (or also called the spin-lattice relaxation time) describes how the magnetisation M_0 reaches its equilibrium value after the field $\mathbf{B_0}$ has been switched on. The z-component of the magnetisation changes with time according to

$$\frac{dM_z}{dt} = \frac{M_0 - M_z}{T_1} \tag{12}$$

T_1 is therefore called spin-lattice relaxation time because the relaxation process takes place such that the spin system transports energy to the surrounding heat bath, the lattice. The mechanism by which energy is transported in liquids is mainly the dipol-dipol interaction (see introduction) .The value of T_1 is most strongly affected by paramagnetic material in a sample due to the strong coupling with the unpaired electron. Other mechanisms might be quadrupolar interaction for nuclei with **I**>1/2 or chemical shift or scalar interactions mostly for heavy nuclei.

An important mechanism for the transversal relaxation time T_2 is based upon energy exchange within a spin system. Any transition of nuclei between their energy levels causes the local environment to vary a bit. This leads to a decrease of lifetime of the involved spin states and thus describes relaxation This process does not change the energy of the system, it is an entropic process wheras T_1 is of enthalpic nature.
In solids T_2 is mainly influenced through dipolar fields and its anisotropy. The dipolar line width is determined by an additional field B_{dip}.

$$B_{dip} = \pm \frac{3\mu_I}{2\mu_0 r_{12}^3}\left(3\cos^2\theta - 1\right) \tag{13}$$

To demonstrate that the ^{1}H spectrum of solid ethanol is shown in Fig.10.

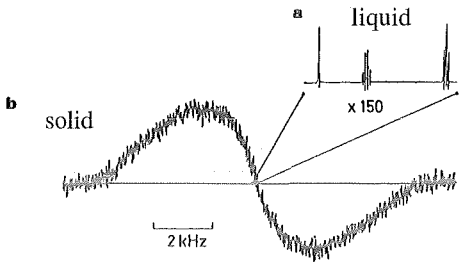


Fig.10: *The ^{1}H spectrum of ethanol a)as neat liquid and b)as solid showing a broad dispersion line due to not averaged out dipol-dipol interactions.*

In liquids , however, $< B_{dip} > = 0$ due to thermal averaging and we are able to observe a high resolution spectrum also shown in Fig.10 (the fine structure will be explained later). Since in liquids the fine structures are important it is necessary to remove any field inhomogeneity to be sure to measure the true line width. According to eq.11 we can write for the intensity

$$I(\omega) = const. \cdot \frac{B_1 T_2}{1 + (\omega_0 - \omega)^2 T_2^2} \tag{14}$$

At resonance ($\omega = \omega_0$) the intensity is then given by

$$I(\omega_0) = const. \cdot B_1 T_2 \tag{15}$$

For half the intensity we can write $I_{1/2} = const. \cdot \frac{T_2}{2}$ or inserted into eq.14

$$\frac{T_2}{2} = \frac{T_2}{1+(\omega_0 - \omega)^2 T_2^2} \tag{16}$$

which leads to $\omega - \omega_{1/2} = \frac{1}{T_2} \Leftrightarrow \Delta = \frac{2}{T_2}$, where Δ is the line width at half height (FWHH) of the Lorentz curve as described by eq.11.

5 How is the Basic Experiment Done?

As we had already seen is the basis of nuclear magnetic resonance the fact that nuclei must have a magnetic moment The interaction between these magnetic moments and an external magnetic field leads to a splitting into various energy levels according to laws of quantum mechanics. In the experiment a high frequency fields is applied which causes transitions between these levels. This is accompanied with absorption of energy and causes a spectral line to occur , a so called resonance signal. This is sketched in Fig.11.

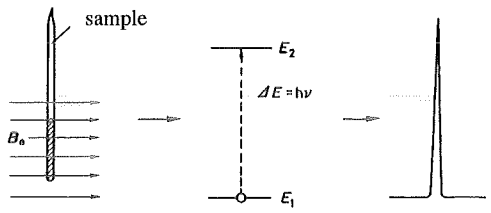


Fig.11: *How a nuclear magnetic resonance signal emerges.*

The most important parts of an NMR spectrometer are the magnet, today it is in most cases a cryomagnet with field strengths up to 14,1 Tesla and a high frequency transmitter and receiver up to 700MHz. This is sketched in Fig.12.

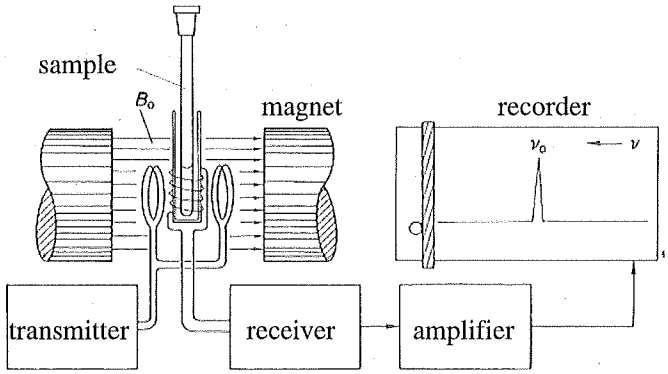


Fig.12: *Schematic of a NMR-spectrometer with separate transmitter – and receiver coils.*

In the sample head the sample is located together with the transmitter coil and the transceiver coil, which are in most cases placed in a crossed configuration. In principle two different kinds of experiments are possible:

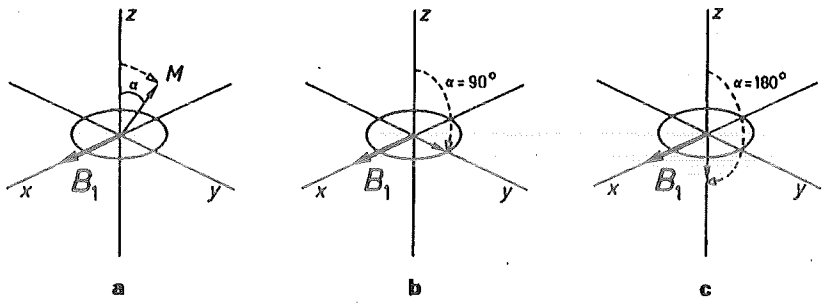


Fig.13: *Various positions of the magnetisation vector* ***M*** *in a rotating frame. Depending on the intensity and the duration of hard pulses the vector* ***M*** *can be turned. Two angles are especially marked: The 90° position, where* ***M*** *is in the x,y-plane (case b) and the 180° position, where* ***M*** *is turned completely into the negative z-direction (case c).*

The CW or the FT-NMR experiment. CW stands for continuous wave spectroscopy and means that the frequency is changed around the Lamor frequency at constant field so to be able to sweep around ω_{Lamor} Most of the explanations given so far in the previous chapters are based upon this description, especially those leading to eq.11 and the phenomenological descriptions of T_1 and T_2. The other above mentioned exp. method is the so called pulse spectroscopy. Thereby very strong but short rectangular B_1 pulses along the x-axis are applied with typical strength of 0,01 - 0,4Tesla and some hundred kW power typically for a few µsec duration. These pulses can completely flip **M** into the x,y-plane (so called 90°-pulse) or even into the negative z-direction, the so called 180°-pulse. This situation is demonstrated in Fig.13.

The situation after a 90°-pulse is of special importance since after such a pulse the magnetisation in the x,y-plane decreases with time and is called the FID, the free induction decay. It's damping constant is proportional to T_2^* which describes the transversal relaxations due to field inhomogeneities ΔB.

$$\frac{1}{T_2^*} = \frac{\gamma \Delta B}{2} + \frac{1}{T_2} \tag{17}$$

A nice example for such an experiment is shown in Fig.14, where the FID signal of ^1H in H_2O is observed after a 90°-pulse shown as tiny rectangle on the left side of the damped wiggle.

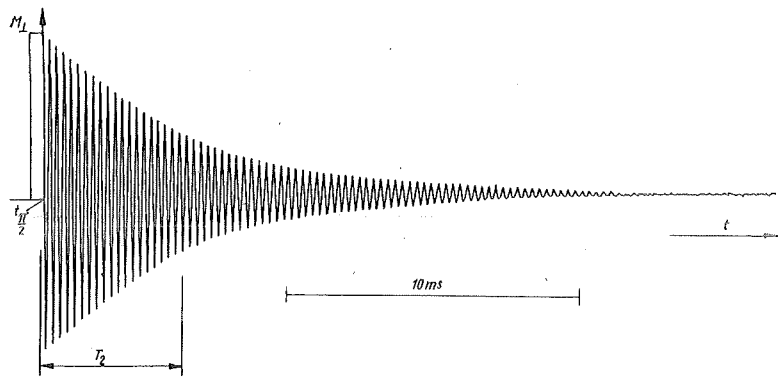


Fig.14: *FID (free induction decay) of ^1H in H_2O with some paramagnetic impurities (to make T_2 short) after a hard 90°-pulse.*

To summarize the above considerations the two cases are shown in Fig.15. The CW method leading to S(ω) (or I(ω)) directly and the pulse method leading to the FID. From Fourier theory it follows, that the spectrum measured in ω-space and the time evolution are Fourier pairs:

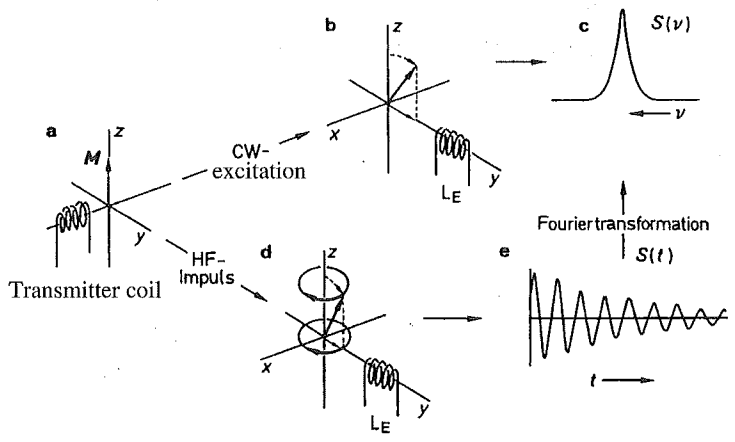


Fig.15: *Schematic how signals are generated in a CW-and in a FT-spectrometer. L_E means transceiver coil. In a) we observe a resulting magnetisation in z-direction which after switching on a continuous HF field along x (CW excitation) will produce a transversal magnetisation b), that is recorded by L_E. In c) the resulting resonance signal is recorded. The FT-spectrometer uses hard pulses which cause **M** to turn into the x,y-plane , see d). The resulting FID in e) yields after Fourier transformation the same signal as in c).*

$$S(\omega) = \frac{1}{\sqrt{2\pi}} \int_{-\infty}^{\infty} f(t) \exp(-i\omega t) dt$$
$$f(t) = \frac{1}{\sqrt{2\pi}} \int_{-\infty}^{\infty} S(\omega) \exp(i\omega t) dt \qquad (18)$$

To demonstrate that we show in Fig.16 the comparison between the CW spectrum of ethylbenzene compared to the FT pulse spectrum obtained from the Fourier transform of the FID. The difference is obvious. Today only pulse spectra are taken.

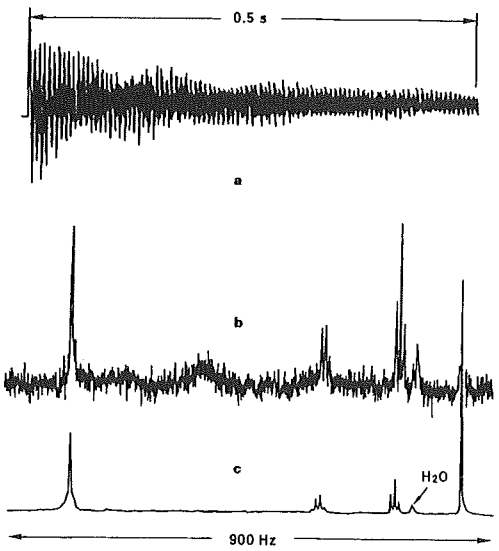


Fig.16: *FT-spectrum of ethylbenzene.a) The FID b)A conventional CW-spectrum, duration 1000s c)The Fourier transform of a) taken 1000times, 1s each.*

6 Measurement of T_1 and T_2

The most used method to measure the longitudinal relaxation time T_1 is the so called inversion recovery experiment. Let's consider a macroscopic magnetisation in z-direction in a rotating coordinate system. A hard 180°-pulse turns M_z completely into the negative z-direction. Due to longitudinal relaxation processes the value of M_z reduces with time, is zero at some time and finally reaches the starting value again. To measure T_1 we apply a 90°-pulse at various different times $\tau_1,\ldots,\tau_i$ which then allow to detect the values of M_z in the x,y-plane. In Fig.17 the two pulses are shown, starting with a 180°-pulse (case b) followed by a

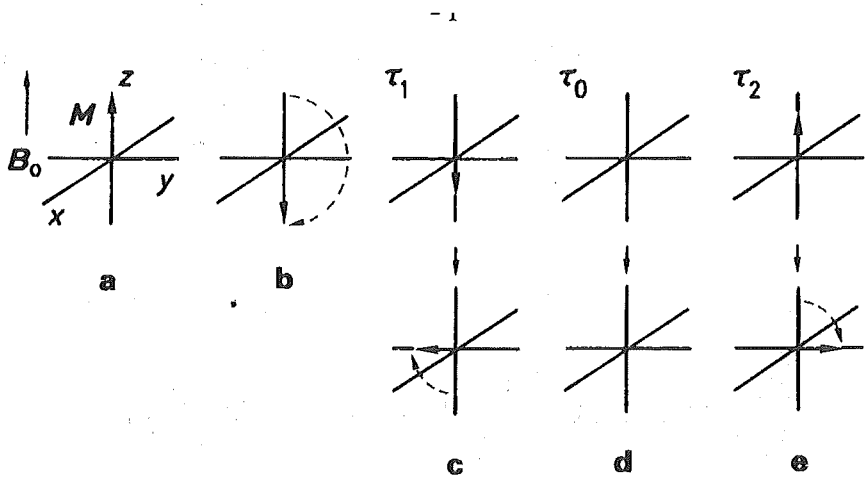


Fig.17: *The inversion recovery experiment to determine T_1. a) shows the starting position with some magnetisation in z-direction. In b)this magnetisation is inverted into the negative z-direction by a 180°-pulse. Then we wait for several different times τ_i and measure the corresponding magnetisation of M_z by a 90°-pulse which will flip M_z into the x,y-plane where it is detected. That is shown in c) -e) in the lower three figures. For τ_0 , M_z is zero(case d)) and T_1 can be estimated.*

waiting time then the 90°-pulse to read M_z out (cases c-e) Clearly the recovery of M_z after long times τ_i can observed (which is usually after $5T_1$ the case). Note that T_1 can be estimated via $\tau_0=\ln 2T_1$. More precisely, however, T_1 is calculated by analysing the time evolution of M_z which is given by eq 12. The integration of that equation yields

$$\ln(M_0 - M_z) = \ln 2M_0 - \frac{\tau}{T_1} \qquad (19)$$

So T_1 can be obtained by plotting $\ln(M_0-M_z)$ vs. τ from the slope.

The measurement of the transversal relaxation time T_2 (or the spin-spin relaxation time) is a bit more complicated because in liquids the value of T_2 depends strongly upon the field inhomogeneities and therefore in some cases not upon interactions between different spins alone. We had seen in Fig.12 how that is the case. In order to overcome this difficulty the spin-echo experiment was developed which is performed in a so called Carr-Purcell pulse sequence. We start again with a magnetisation in z-direction which is flipped into the x,y-plane by a 90°-pulse. Now the transversal relaxation starts and further we observe the spins to fan out due to field inhomogeneities. By that the magnitude of M_y is reduced, as is shown in Fig.18. After some time we apply a 180°-pulse which flips all magnetisation into the negative M_y direction (time τ between 90°-and 180°-pulse).

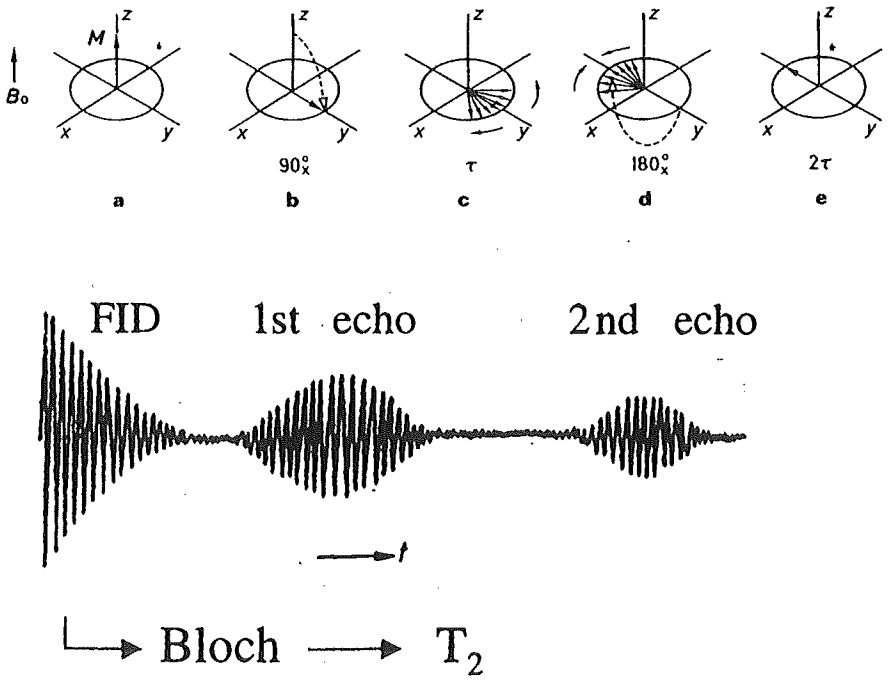


Fig.18: *The spin-echo experiment. We start in a) with some magnetisation **M** in z-direction. This is flipped in the x,y-plane by a 90°-pulse, shown in b). Due to field inhomogeneities the spins fan out , c), and are refocused by a 180°-pulse , d). At time 2τ we have full transversal magnetisation again in the x,y-plane which appears as so called solid echo, e). One can repeat this for times 2τ, 4τ, 6τ... getting echoes as shown in the lower part of the figure. From the decrease of the echo intensities the true transversal relaxation time T_2 is calculated.*

Now , however, the fanning out is reversed leading to a focussing at time 2τ. The restored magnetisation can be detected as spin-echo in the x,y-plane. It can be shown that the amplitude of the spin-echo depends only on T_2. All disturbing effects (field inhomogeneities, spin diffusion etc.) can be overcome by applying a sequence of echoes at times 2τ, 4τ, 6τ,... Then the time evolution of the echo heights is given by

$$I = I_0 \exp(-\frac{\tau}{T_2}) \tag{20}$$

However, spin diffusion can be neglected if τ is sufficiently small.

7 Relaxations by Fluctuating Fields

We briefly had spoken about various interactions leading to relaxation phenomena concerning T_1 and T_2. Generally interactions are described by a Hamiltonian which we split it in a time independent and a time dependent part.

$$H = H_{Zeeman} + \sum_i H_i(t) \tag{21}$$

The time independent part is of course the static Zeeman splitting which we will not consider further (cf. Fig.1).In the Bloch equations relaxations are introduced phenomenologically. The physical reasons for these are interactions of the spins with their surroundings by various mechanisms described below. Due to molecular motions (internal molecular dynamics, rotations, diffusion, lattice vibrations) the local magnetic field fluctuates and so the corresponding term of the spin Hamiltonian. Parts of this spectrum fluctuate at the Lamor frequency and lead thus to resonance and hence to energy transfer between spin and lattice or between spins. The possible time dependent interactions leading to fluctuating local magnetic fields are:

- chemical shift H_s
- spin-spin coupling
- dipolar interactions (**I**=1/2) H_d
- quadrupolar interactions (**I**>1/2) H_q

In order to make contact with our previously introduced relaxation times T_1 and T_2 it is necessary to introduce a correlation function f(t) which is defined as

$$f(t) = < B(0)B(t) > \tag{22}$$

Where <..> is an ensemble average and B(t) denotes the above described fluctuating local magnetic field. Basically if we deal with H_q or with H_s we observe a single particle propagator (^2H resp. ^{13}C are the dominant interactions) in case of H_d we observe for ^1H a many body interacting system due to the lattice sum, see later). We define further a normalized spectral density function J(ω)

$$J(\omega) = \frac{1}{f(t=0)} \mathrm{Re} \int_{-\infty}^{\infty} f(t) \exp(-i\omega t) dt \tag{23}$$

Then it can be shown that T_1 is related to J(ω) via

$$\frac{1}{T_1} = \gamma^2 \left(< B_x^2 > + < B_y^2 > \right) J(\omega) \tag{24}$$

and T_2 is given by

$$\frac{1}{T_2} = \gamma^2 < B_z^2 > J(0) + \frac{1}{2T_1} \tag{25}$$

It is possible to derive similar equations for all kind of interactions as described above, the situation becomes particularly simple for leading single particle interactions. Usually the time decay of f(t) is assumed to be single exponential

$$f(t) =< B^2 > \exp(-\frac{t}{\tau_c}) \tag{26}$$

Then the corresponding spectral density function (see eq.23) is because of the FT a Lorentz line

$$J(\omega) = \frac{\tau_c}{1+\omega^2\tau_c^2} \tag{27}$$

and we have made contact with eq.11.
Within this model $1/T_1$ reaches its maximum for $\omega_0\tau_c=1$, see Fig.19. If the physical process for

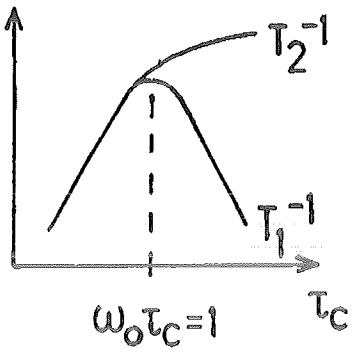


Fig.19: *The relaxation rates $1/T_1$ and $1/T_2$ as function of τ_c.*

example is a thermally activated one we write $\tau_c = \tau_0 \exp(\Delta E/RT)$ and can calculate the activation energy from the temperature dependence of T_1.
We will now discuss more the respective Hamiltonians which we had listed in the beginning of this chapter.

8 Nature of Interactions

The chemical shift, to start with, is of tensoriell character

$$H_s = \gamma \mathbf{I} \underline{\underline{\sigma}} \mathbf{B} \tag{28}$$

and is mediated via the local electronic structure. $\underline{\underline{\sigma}}$ is the chemical shift tensor, a second rank tensor. It fluctuates due to molecular motion of its principal axis relative to $\mathbf{B_0}$. Then eq.28 can be simplified to get the interaction in terms of an additional magnetic field contribution δB. Due to Lenz rule it is opposite to $\mathbf{B_0}$, $\delta B = -\sigma B$. It may also envisaged as a magnetic field which results from the interaction of the magnetic moments with the local magnetic fields. This local field may differ from the applied field because the latter induces electronic orbital momentum which gives rise to the above stated field δB. Then σ is called the shielding constant and we write

$$B_{local} = B_0 + \delta B = (1-\sigma)B \tag{29}$$

or

$$\omega_{Lamor} = \gamma B_{local} = (1-\sigma)\gamma B \tag{30}$$

Please note that the additional field is proportional to B, so the larger the external field the larger the shift. In case of ^{13}C this Hamiltonian is the leading interaction and can reach values of 200ppm which corresponds to $\Delta\omega/2\pi$ (at 7Tesla) of 15kHz. For ^{1}H spectra which form the majority of spectroscopic information especially for chemists, where NMR is a working horse in the organic labs, the information on chemical shifts (here in the range 0-10ppm) is together with the spin-spin coupling the most important issue. Spin-spin coupling, the second item of our list, is an interaction between different spins mediated through the chemical bond between the two interacting nuclei. That has the important consequence that the interaction does not depend on the magnitude of the external field B. The interaction, also called fine structure, is given in terms of the spin-spin coupling constant J[Hz]. In Fig.20 we show some ^{1}H spectra as

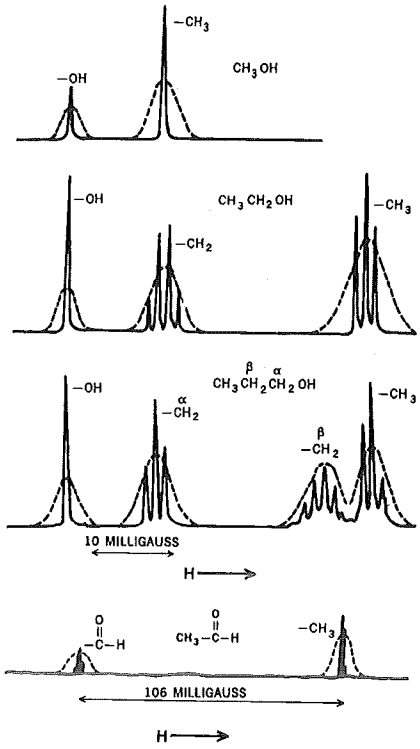


Fig.20: *^1H NMR spectra for some organic materials at B = 14.000 Gauss and 60MHz. Spectra at low resolution (---) and at high resolution (—).*

examples for typical organic materials. Shown are positions of Lamor resonance lines as function of magnetic field (at constant frequency). The field strength increases to the right. What is obvious to see is the shift of lines with a relative separation of at most about 50mG (at 1,4Tesla it corresponds to 10^{-5} shift $\times$ 10^6 gives 0-10ppm rel. shift). Further the magnitude of the spin-spin coupling is in the order of a few Hz. If one measures the spectra as shown in Fig.18 with a bad resolution only broad structureless lines are obtained. Fine structures are only resolved with high resolution spectrometers. In Fig.21 we demonstrate how the fine structure emerges in acetaldehyde. In the upper part we see the spectrum at low resolution.

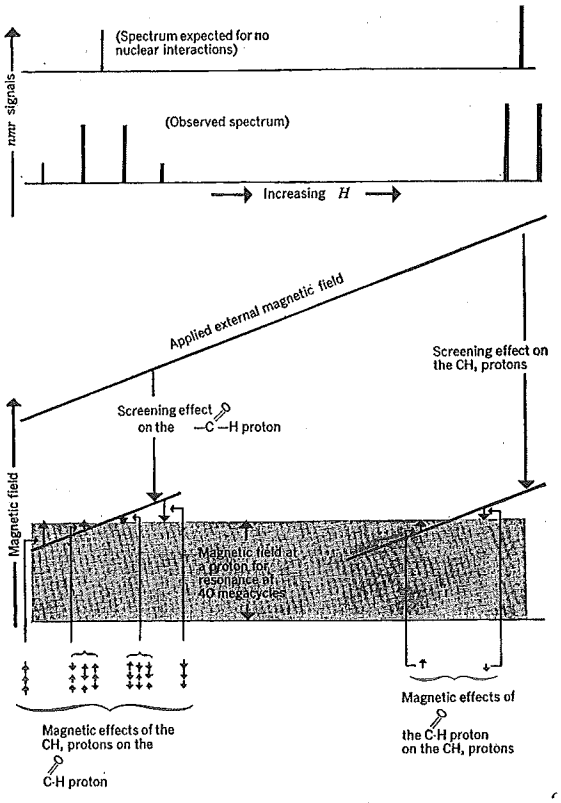


Fig.21: *A schematic representation of the NMR spectrum of acetaldehyde and its interpretation in terms of screening effects and spin-spin interaction.*

showing two resonance lines due to chemical shift. At better resolution this two lines are splitted due to fine structure, the spin-spin coupling. In the lower part this situation is again illustrated. The strength of B_{local} is plotted vs. B. Since $B_{local} \propto B$ we find a line with positive slope. At two particular positions the Lamor condition holds. Magnetically these positions have different shieldings due to different chemical bonds of the ^1H nuclei involved. That are three $-CH_3$ protons and the one aldehyde proton. However, these spins can have different orientations with regard to the external field. Clearly the one aldehyde proton can have only two orientations (with rel. intensities 1:1), the three methyl protons have orientations as indicated in the Fig. and perform a splitting with intensities according to 1:3:3:1. The intensities have a distribution according to Pascal's triangle.

The next Hamiltonian is the dipol-dipol interaction H_d. It reads

$$H_d = \sum_{i<j} \eta\gamma_i\gamma_j r_{ij}^{-3}\left(\mathbf{I}_i\mathbf{I}_j - \frac{3(\mathbf{I}_i\mathbf{r}_i)(\mathbf{I}_j\mathbf{r}_j)}{r_{ij}^5}\right) \tag{31}$$

Here the expression in brackets is also a second rank tensor. The H_d is different from H_s because it is not as the latter a single particle propagator. Instead all many body interactions are present through the lattice sum. The dipolar interaction is the dominating one in solids for ^1H of about 10 - 100kHz width (cf. Fig.10).
The last Hamiltonian is the quadrupolar interaction H_q. It reads

$$H_q = \frac{eQ}{2I(2I-1)} \mathbf{I} \underline{\underline{V}} \mathbf{J} \tag{32}$$

where e is the elementary charge, Q the nuclear quadrupol moment and $\underline{\underline{V}}$ is the electrical field gradient tensor also of second rank. The H_q is the most dominant interaction for ^2H nuclei. There it produces spectra with up to 250kHz width (in solids). For **I** = 1 nuclei (like ^2H) this tensor is in good approximation symmetric and parallel to the principle axis, here in this case the. –C– ^2H axis. A molecular motion leads to reorientation of this axis and thus to a time variation of H_q. So we have seen that all relevant interactions are caused by second rank tensors. Then the observed shift $\delta\omega$ of the observed spectra depend only on the principal values of these tensors that are the coupling constant Δ and the asymmetry η (principal value means that the tensor having in general nine elements can be reduced to only three elements on its trace of which two are alike) Then this $\delta\omega$ depends on Δ,η and the polar coordinates θ and ϕ of the external field $\mathbf{B_0}$ in the principal axis of $\underline{\underline{V}}$ as follows:

$$\delta\omega = \pm\frac{1}{2}\Delta\left(3\cos^2\theta - 1 - \eta\sin^2\theta\cos 2\phi\right) \tag{33}$$

Let's consider as an example the orientation dependent frequency shift of a ^2H –C bond. Here $\eta \approx 0$ and we observe two lines at $\pm\,\delta\omega$ which only depend on θ, the angle between the ^2H –C bond with the external field B. This spectrum, also called Pake spectrum, is shown in Fig.22.

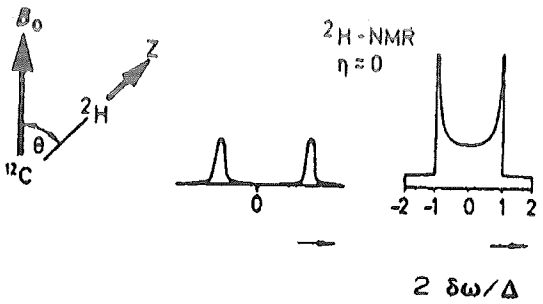


Fig.22: *Orientation dependent frequency shift $\delta\omega$. In case of a ^2H spin with dominating quadrupolar interactions and $\eta \approx 0$ we observe a two line spectrum (shown in the middle) $\pm\delta\omega$ which only depend on θ, the angle between B_0 and the ^2H –C bond (shown on the left).In this case a typical Pake spectrum is obtained, on the right, with the typical two"horns" (rigid Pake).*

Those spectra are in principle very sensitive upon various types of reorientation and hence the value of the respective correlation time of this molecular dynamics. Experimentally it is done in a modified spin-echo experiment which is capable to measure molecular correlation times in a time window between 10^{-6} to 10^{-4} sec. In Fig.23 a calculation for two different motion mechanisms is shown which indicate the sensitivity towards various types of motion and in general the phenomenon of motional narrowing especially in the example for the chain rearrangement.

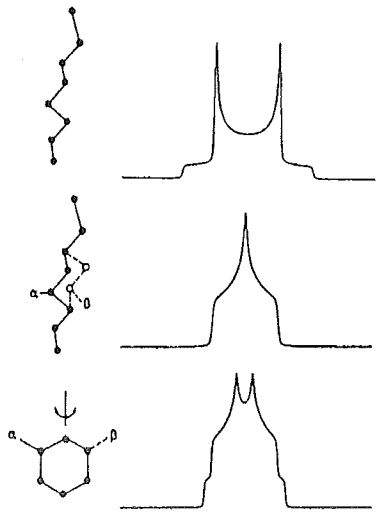


Fig.23: *Calculated ^2H spectra of a selected $-C-^2H$ bond in a rigid chain (top), arising from conformational rearrangement of three carbon atoms in a chain (middle) and from 180° phenyl ring jump (bottom).*

As stated in the introduction there are today so many new developments especially for solid state applications that it is actually impossible to review that, however, we believe that the reader may find some tools in this article to find an easier approach to the advanced literature which is partly listed below.

References

[1] 22.IFF Ferienkurs 1991, lecture 10 by F. Fujara
[2] NMR-Spektroskopie, H. Günther, Thieme Verlag (1992)
[3] Principles of High Resolution NMR in Solids, M. Mehring, Springer Verlag (1983)
[4] Physical Chemistry, G. Barrow, Mc Craw-Hill (1961)
[5] Molekuelphysik, A. Loesche, Akademie-Verlag (1984)
[6] Physical Chemistry, P. Atkins, Oxford University Press (1989)
[7] Multidimensional Solid State NMR and Polymers, K. Schmidt-Rohr and H. W. Spiess, Academic Press (1994)

A 3 Dielectric Spectroscopy

Stefan Kahle
Institut für Festkörperforschung
Forschungszentrum Jülich GmbH

Contents

1 Introduction 2

2 A Historical Trip 3

3 Linear Response Theory 4
- 3.1 General Linear Response 4
- 3.2 Fluctuations, Correlation Function, and Spectral Density 6
- 3.3 Fluctuation Dissipation Theorem 7
- 3.4 Example: Spectral Density and Permittivity of a Rotator in a Plane 9

4 Experimental Techniques of Dielectric Spectroscopy 12
- 4.1 Dielectric Time Spectroscopy ($10^{-6}...10^{3}Hz$) 12
- 4.2 Frequency Response Analyzer ($3 \cdot 10^{-5}...10^{7}Hz$) 13
- 4.3 Coaxial Line Reflector ($10^{6}...2 \cdot 10^{10}Hz$) 13

5 Dielectric Spectroscopy on Liquids and Polymers; Dipole Fluctuations 15

1 Introduction

Dielectric spectroscopy is based on the interaction of electromagnetic field with the electric dipole moment of the material under test. The dielectric parameters of the material are used in various fields of physics, chemistry, and technology. The investigation of the dielectric dispersion spectra of liquids (including polymers) is of importance for the solving of many problems in chemical physics, physical chemistry, and biology. The interpretation of molecular spectra is related to the investigation of molecular dynamics of polar fluids. This connection is explained by the fact that the microscopic dielectric properties are determined by microscopic dynamic processes in polar fluids. The study of dielectric properties of polar fluids over a wide range of frequency, temperature, and pressure gives valuable and unique information about the molecular structure, intermolecular interactions, and characteristic times of molecular motions.

A knowledge of the dielectric properties of gases is necessary for many applications in meteorology, astrophysics, atmosphere optics, etc. Further development of the quantitative and qualitative spectral analysis of a gas composition is a matter of importance in the light of the problems of atmospheric pollution, ozone depletion, global warming, etc.

Monographies about dielectric spectroscopy, dielectric properties, and theory of dielectrics in detail are Refs.[1, 2, 3, 4, 5, 6]. The theory of linear response is presented in very comprehensive manner in Ref.[7]. Today, dielectric spectroscopy covers a frequency range of about eighteen decades in frequency ($10^{-6}...10^{12}Hz$). Of course, for this enormous frequency range different experimental setups are necessary.

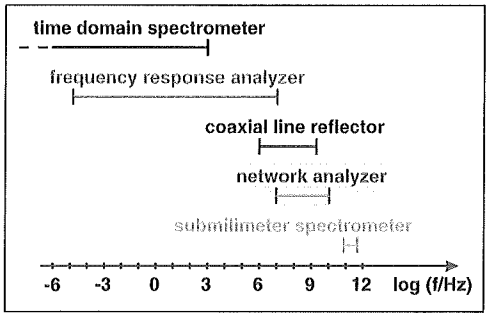


Fig. 1: *Dielectric spectroscopy frequency window (schematic).*

In Figure 1 the frequency range for different setups is schematically shown. Figure 2 shows an example for dielectric spectra which is measured with different experimental setups (from Ref.[8]).

This contribution gives an introduction to the method of dielectric spectroscopy. After a short excursion to the historical development of the theory of dielectric polarization, the general scheme of the linear response theory will be explained. Afterwards, selected experimental dielectric techniques for different ranges in frequency will be shown. At the end, an essentially application, i.e. the investigation of liquids and polymers will be presented.

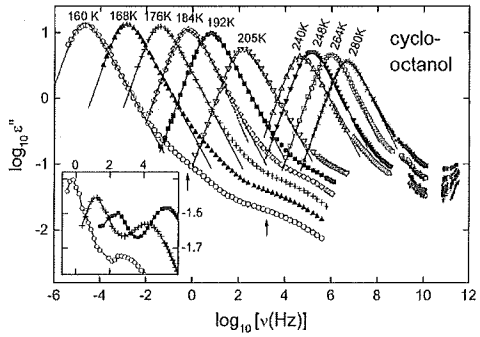


Fig. 2: *Example for frequency and temperature dependence of the imaginary part of the dielectric function (dielectric loss) from Ref.[8]*

2 A Historical Trip

Electric polarization has long been a subject of investigation, different aspects being emphasized in different periods. As a natural phenomenon, electricity was known in ancient times, but the first known experimental studies were undertaken in the eighteenth century. It was discovered **1745** by *Cunaeus* and *Musschenbroek* that large quantities of electric charge could be stored in a condensor, "an apparatus consisting of two conducting plates separated by insulating materials." This condensor became very popular for variety of experimental purposes under the name of Leyden jar.
Relative little attention was paid to the properties of the insulating material. **1837** the first numerical results of measurements on this material was published by *Faraday.* Faradays results indicated that the capacity of a condensor was dependent on the nature of the material separating the conducting surfaces. He called this material the dielectric. *Cavendish* had performed comparable experiments about sixty years earlier, but his results remained unpublished until **1879**. For the ratio between the capacity of condensor filled with a dielectric and the capacity of the same condensor when empty, Faraday introduced the term specific inductive capacity (now generally called the permittivity, or dielectric constant ε).
1847, a formula for the molecular polarizability

$$\alpha_{mol} = \frac{3}{4\pi N}\frac{\varepsilon - 1}{\varepsilon + 2} \tag{1}$$

was derived by *Mossotti*, whereas in **1879** *Clausius* gave a similar derivation independently. Both authors followed Faraday in considering the dielectric to be composed of conducting spheres in a non-conducting medium. In this model the conducting spheres represent the molecules. They did not derive an explicit expression for the internal field, since they used a general potential function. Implicitly, however, their derivation involved the notation of the internal field, which was introduced later, particular in **1879** by *Lorentz.*
In this period, other electric and magnetic phenomena were also investigated intensively. The result were summarized by *Maxwell* in the middle of the **1860**s in his unified theory of electromagnetic phenomena. In this theory the permittivity is conceived to be the ratio

between the electric field and the dielectric displacement. Since light was taken as a form of electromagnetic radiation, it followed that the square of the refractive index n is equal to the permittivity: $\varepsilon = n^2$. This relation is known as the Maxwell relation. After the experimental realization of electromagnetic waves of low frequency by *Hertz* (**1887**), the determination of the refractive index for these frequencies became possible.
In **1912**, *Debye* published a quantitative theory for permanent electric dipoles:

$$\mu^2 = \frac{9kT}{4\pi N}\frac{\varepsilon - 1}{\varepsilon + 2}. \tag{2}$$

Essentially, the concept of molecules with a permanent dipole moment goes back as far as *Berzelius* (**1819**), who assumed molecules to be composed of oppositely charged regions. After *Debye* had introduced the concept of molecular permanent dipole moments into the theory of dielectrics, **1913** he used this concept to explain the anomalous dispersion of the dielectric constant. He pointed out that the process of orientation of the permanent moments, connected with changes in field, requires a definite time interval, since it depends on the rotational movements accomplished by the molecules, i.e. after the removal of an external field the average dipole orientation decays exponentially with time. The characteristic time of this decay is called the relaxation time. In the middle of the 1920s Debye connected the value of the dipole moment with the geometrical arrangements of the atoms in the molecule.
1936, *Onsager* succeeded in constructing a fundamental modification of Debye's approach eq.2:

$$\mu^2 = \frac{9kT}{4\pi N}\frac{(\varepsilon - \varepsilon_\infty)\ (2\varepsilon - \varepsilon_\infty)}{\varepsilon\ (\varepsilon_\infty + 2)^2}. \tag{3}$$

He pointed out that the internal field used by Debye included a part, produced by the permanent moment of the molecules themselves via the moments induced by the dielectric surrounding of these molecules.
Several modifications and extensions of Debye's theory for dielectric relaxation have been proposed generally leading to the replacement of the single relaxation time by a set of different relaxation times in the description of the macroscopic relaxation process. For the description of the experimental results, the introduction of continuous distributions of relaxation times was also proposed in many cases. **1941**, *Cole* and *Cole* introduced an important graphical method, the so-called Cole-Cole plot, to distinguish these cases from that of a single relaxator.
Of course, this collection is not complete. A more complete description for the interested reader can be found in Ref. [3]

3 Linear Response Theory

3.1 General Linear Response

We start from the First-Law fundamental form of thermodynamics:

$$dU = TdS - pdV - V\underline{\underline{\sigma}}d\underline{\underline{\gamma}} + V\vec{E}d\vec{P} \pm ... = \sum f_i dx_i, \tag{4}$$

with f_i the intensive (general 'forces'), and x_i the conjugated extensive (general 'lengths') observable. For small perturbation the response of a subsystem is linear and causal

although the molecular motion inside a subsystem is (highly) non-linear and necessary chaotic. Linear means that the response of two arbitrary perturbation programs are linear superpositions of the individual responses (Boltzmann's superposition principle), and causal means that the current response is only influenced by perturbation programs in the past.

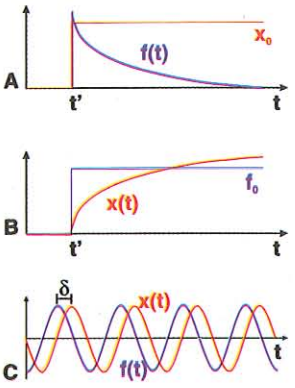


Fig. 3: *Schematic representation of relaxation (A), retardation (B), and periodic experiments (C). x is the extensive and f the energy-conjugated intensive observable, respectively.*

Step Experiments: In the case of step experiments, one distinguishes two different experiments: the relaxation- and the retardation experiment. Figure 3A and B shows schematically the situation for both experiments. The relaxation experiment gives the intensive variable $f_i(t)$ after a step at $t = t'$ in the extensive variable $x_i(t) = x_{i0} \cdot H(t')$, with x_{i0} the step height and $H(t')$ the Heaviside-function. The ratio

$$M(t) \equiv \frac{f_i(t)}{x_{i0}} \tag{5}$$

is called the relaxation modulus. Linearity and causality properties of thermodynamic experiments for arbitrary programs lead to the convolution

$$f_i(t) = \int_0^t M(t-t')\, \dot{x}_i(t')\, dt' \equiv M* \dot{x}_i(t)\,. \tag{6}$$

Conversely, the retardation experiment gives the extensive variable $x_i(t)$ after a step in the intensive variable $f_i(t) = f_{i0} \cdot H(t')$. In this case the ratio

$$\chi(t) \equiv \frac{x_i(t)}{f_{i0}} \tag{7}$$

is called the retardation compliance, and analogous to the relaxation experiment linearity and causality properties lead to the convolution

$$x_i(t) = \int_0^t \chi(t-t')\, \dot{f}_i(t')\, dt' \equiv \chi* \dot{f}_i(t)\,. \tag{8}$$

Periodic Experiments: Complex variable are used for a stationary periodic experiment (cf. Figure 3C):

$$x_i^*(\omega) = x_{i0}\exp(i\omega t), \quad f_i^*(\omega) = f_{i0}\exp(i\omega t + \delta), \tag{9}$$

with x_{i0} and f_{i0} the amplitudes of the extensive and intensive variable, respectively, and δ the phase angle between these two periodic variables. The corresponding susceptibilities

$$M'(\omega) + iM''(\omega) = M^*(\omega) = \frac{f_i^*(\omega)}{x_i^*(\omega)} = \frac{1}{\chi^*(\omega)} = \frac{1}{\chi'(\omega) - i\chi''(\omega)} \tag{10}$$

are called dynamic modulus $M^*(\omega)$ and dynamic compliance $\chi^*(\omega)$. Real- and imaginary part of M^* (and χ^*) are connected via the Kramers-Kronig relation

$$\begin{aligned} M'(\omega) &= \frac{1}{\pi}\oint \frac{M''(\omega)}{\omega^* - \omega}d\omega^*, \qquad M''(\omega) = -\frac{1}{\pi}\oint \frac{M'(\omega)}{\omega^* - \omega}d\omega^*, \\ \chi'(\omega) &= \frac{1}{\pi}\oint \frac{\chi''(\omega)}{\omega^* - \omega}d\omega^*, \qquad \chi''(\omega) = -\frac{1}{\pi}\oint \frac{\chi'(\omega)}{\omega^* - \omega}d\omega^* \end{aligned} \tag{11}$$

This relation states that real and imaginary part contain the same information about the response function of the sample.
Consider again an extensive, x, and intensive, f, observable. The compliance is defined by the convolution eq.8. The dynamic compliance is obtained by a Fourier transformation of $\dot{\chi}(\tau) = d\chi/d\tau(\tau)$,

$$\chi^*(\omega) = \chi_0 + \int \dot{\chi}(\tau)e^{-i\omega\tau}d\tau, \tag{12}$$

with χ_0 the limiting compliance. Again, the relation for the modulus M is analog:

$$M^*(\omega) = M_0 + \int \dot{M}(\tau)e^{-i\omega\tau}d\tau, \tag{13}$$

3.2 Fluctuations, Correlation Function, and Spectral Density

Thermodynamic variables which characterize a thermodynamic system in equilibrium are equal to their median value, the equilibrium average, to a very high precision. Smaller deviations result from the chaotic motions of particles. One says: The thermodynamic variable fluctuates. We consider now the stationary fluctuation of e.g. an extensive variable $x(t)$ in a subsystem, with the additive normalization $\overline{x(t)} = 0$, i.e. the equilibrium average is subtracted. Correlations in time are characterized by the median value of the product $\langle x(t)\cdot x(\tau)\rangle$, with $\tau = t - t'$. The time average of this product

$$\varphi_x(\tau) \equiv \delta x^2(\tau) = \lim_{T' \gg \tau_R'} \frac{1}{T'}\int_{(T')} x(t)\,x(t+\tau)dt \equiv \langle x(t)\,x(t+\tau)\rangle_t$$

is called the correlation function. To cover all correlations the experiment time T' must be larger than the characteristic retardation (or relaxation) time τ_R'. $\varphi(\tau)$ tells us how the observable at time $t \pm \tau$ is correlated to the observable at t; $\varphi = 0$ for $\tau \neq 0$ implies

a statistical independence of $x(t)$ and $x(t+\tau)$. The correlation function of an intensive variable is defined analogously: $\varphi_f(\tau) \equiv \delta f^2(\tau) = \langle f(t)\, f(t+\tau)\rangle_t$.
The Fourier transform of the recorded fluctuations of an observable x, $\delta x(t)$, of finite duration T' is

$$\delta x(\omega, T') = \int_{-T'/2}^{T'/2} \delta x(t)\, e^{i\omega t}\, dt, \tag{15}$$

and its inverse

$$\delta x(t) = \frac{1}{2\pi} \int_{-\infty}^{\infty} \delta x(\omega, T')\, e^{-i\omega t}\, dt. \tag{16}$$

Using $\delta x(\omega, T') = \delta x(-\omega, T')$ and $\langle \delta x(\omega)\, \delta x(\omega')\rangle = 2\pi \cdot \delta x(\omega) \cdot \delta(\omega + \omega')$

$$\delta x^2(t) = \frac{1}{2\pi} \int \delta x^2(\omega)\, e^{-i\omega t}\, dt, \tag{17}$$

and its inverse

$$\delta x^2(\omega) = \int \delta x^2(t)\, e^{i\omega t}\, dt = \lim_{T'\to\infty} \frac{|\delta x(\omega, T')|^2}{T'}.$$

$\delta x^2(\omega)$ is called the spectral density (of the mean square) of fluctuations. Again, for the intensive observable f the relations are similar.

3.3 Fluctuation Dissipation Theorem

Molecular systems have a large number of degrees of freedom. Therefore, it is impossible to get a general formula for $\delta x^2(\omega)$ and $\delta f^2(\omega)$, respectively.
The Fluctuation Dissipation Theorem (FDT, Nyquist 1928 [10]) is one of the important equations in physics since different concepts such as fluctuations and response are considered to be equivalent. For energy-conjugated variables (xdf or fdx in the First Law eq.4) in the classical (non-quantum mechanical) case, the FDT states that

$$\delta x^2(\tau) = -kT\,[\chi(\tau) - \chi_e], \quad \delta f^2(\tau) = kT\,[M(\tau) - M_e]. \tag{19}$$

$$\delta x^2(\omega) = kT\frac{\chi''(\omega)}{\pi\omega}, \quad \delta f^2(\omega) = kT\frac{M''(\omega)}{\pi\omega}, \tag{20}$$

with k the Bolzmann constant, T the temperature, and χ_e and M_e the equilibrium ($\tau \to \infty$) compliance and modulus, respectively. In the linear region, the correlations of fluctuations on the left hand side directly determine the response on the right hand side. The term"dissipation" in the FDT comes from the loss parts of response in eqs.20.
From the FDT we can calculate the mean fluctuations for any retardation (or relaxation) process if we integrate over the retardation (or relaxation) peak:

$$\langle \delta x^2 \rangle = \int_{Peak} \delta x^2(\omega)\, d\omega = \frac{kT}{\pi} \int_{Peak} \frac{\chi''(\omega)}{\omega} d\omega = \frac{kT}{\pi} \Delta\chi, \tag{21}$$

with $\Delta\chi$ the retardation strength of the process (analog for $\langle \delta f^2 \rangle = kT\Delta M/\pi$, ΔM the relaxation strength).

We find different correlation functions (or spectral densities) from the corresponding responses, such as the fluctuations of dielectric polarization μ from the compliance $\varepsilon^*(\omega)$, or the fluctuations of the shear stress σ from the shear modulus G. In Table 1 typical thermodynamic variables according to eq.4 with the corresponding susceptibilities are collected.

Table 1: *Examples for different responses and the corresponding thermodynamic observables*

fluctuation of	program	response	symbol
entropy S	$T(t)$	entropy compliance	$J_S^*(\omega) \equiv C_p^*(\omega)\,;\, J_S^*(\tau)$
temperature T	$S(t)$	temperature modulus	$K_T(\omega)\,;\, K_T(\tau)$
volume V	$p(t)$	bulk compliance	$B^*(\omega)\,;\, B(\tau)$
pressure p	$V(t)$	compression modulus	$K^*(\omega)\,;\, K(\tau)$
shear angle γ	$\sigma(t)$	shear compliance	$J^*(\omega)\,;\, J(\tau)$
shear stress σ	$\gamma(t)$	shear modulus	$G^*(\omega)\,;\, G(\tau)$
polarization μ	$E(t)$	dielectric permittivity	$\varepsilon^*(\omega)\,;\, \varepsilon(\tau)$
electric field E	$\mu(t)$	dielectric modulus	$M^*(\omega)\,;\, M(\tau)$
...			

Now we will consider in detail the linear response of dielectric systems. Figure 4 shows an example of the frequency dependence of the dielectric function (red line). The dielectric function is a trajectory in the $\varepsilon' - \varepsilon'' - \omega-$space. The projections show the real (blue line), and the imaginary part (green line). The Cole-Cole-plot is represented by the black line. This figure ilustrates clearly the connection between real- and imaginary part stated by the Kramers-Kronig relation eq.11.

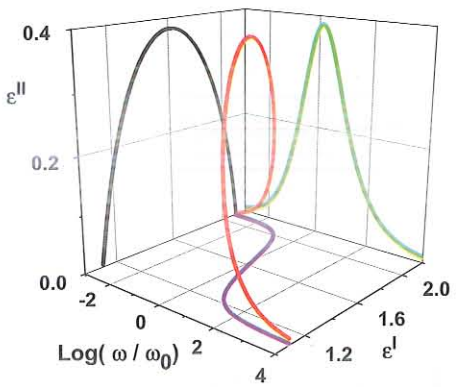


Fig. 4: *3D representation of the dielectric function* $\varepsilon^*(\omega)$.

Any dielectric body consists of a huge number of moving molecules ($N \sim 10^{23}$). This movements (or thermal agitation) results in observable fluctuations in various physical parameters. For example, the volume of a body will undergo very small thermal fluctuations due to continual irregular movements of the constituent molecules. Since all

molecules are built up from collections of positive and negative charges we must expect that their instantaneous dipole (precisely multipole) movements will not necessary vanish but will fluctuate in a random way.

Now we consider the spontaneous fluctuations in the macroscopic polarization of dielectric bodies in thermal equilibrium. The left of Figure 5 shows the temperature dependence of the current noise produced by a glycerol-filled condensor at three selected frequencies (from Ref.[9]). The noise peak is associated with the glass transition. The current noise is proportional to the fluctuations of the polarization, i.e. via the FDT connected with the imaginary part of the dielectric permittivity (dielectric loss). One should regard the extremely tiny absolute values of the current noise (in the order of magnitude of $10^{-27}A^2$!!). The right of Figure 5 shows the comparison between current noise and the noise predicted by FDT, using dielectric measurements at the α relaxation (or glass transition). The agreement of the two different kinds of experiments (fluctuation measurement and susceptibility measurement) is very good.

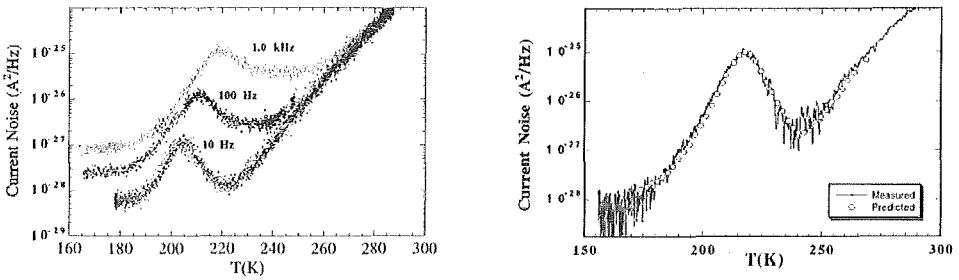


Fig. 5: ***Left:*** *Temperature dependence of the current noise produced by the glycerol-filled condenser is shown for selected frequencies ($\omega/2\pi = 10$, 100, and $1000Hz$).*
Right: *Current noise at $1000Hz$ vs. temperature. Also shown is the noise predicted by FDT using dielectric susceptibility measurements on the same sample (symbols). (both figures from Ref.[9])*

3.4 Example: Spectral Density and Permittivity of a Rotator in a Plane

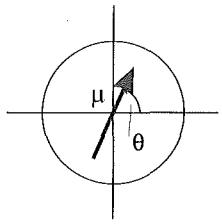


Fig. 6: *Scematic diagram of a plane rotator. The rotator carries a dipole moment, which makes an angle ϑ with a fixed direction in space.*

In this section we calculate the spectral density and the permittivity of a rotating dipol in a plane (see Figure 6).
The motion of a plane rotator is described by the Langevin equation.

$$I\,\ddot{\vartheta} + \xi\,\dot{\vartheta} = \lambda(t), \tag{22}$$

with I the moment of inertia, and $\lambda(t)$ is a random torque, i.e. $\langle\lambda(t)\rangle = 0$.) Fourier transforming the Langevin equation we get for a finite duration time T'

$$-\omega^2 I \cdot \Theta(\omega, T') + i\omega\xi \cdot \Theta(\omega, T') = \Lambda(\omega, T'), \tag{23}$$

so that

$$\Theta(\omega, T') = \frac{\Lambda(\omega, T')}{-\omega^2 I + i\omega\xi}. \tag{24}$$

We use the characteristics of the spectral density eq.3.2 for the angular position $\dot{\vartheta} = \Omega$ and we obtain

$$\delta\Omega^2(\omega) = \lim_{T'\to\infty}\left[\frac{|i\omega\Theta(\omega, T')|^2}{T'}\right] = \frac{1}{|\omega I - i\xi|^2}\lim_{T'\to\infty}\left[\frac{|\Lambda(\omega, T')|^2}{T'}\right].$$

$\lambda(t)$ is a random variable i.e. the correlation function $\varphi_\lambda(\tau) = \langle\lambda(t)\,\lambda(t+\tau)\rangle_t = L\cdot\delta(\tau)$, with $\delta(\tau)$ the Dirac delta function, and therefore in the frequency domain

$$\lim_{T'\to\infty}\left[\frac{|\Lambda(\omega, T')|^2}{T'}\right] \equiv \delta\Lambda^2(\omega) = L.$$

Consequently, for $\delta\Omega^2(\omega)$ we find:

$$\delta\Omega^2(\omega) = \frac{L}{\omega^2 I + \xi^2}. \tag{27}$$

Transformation of $\delta\Omega^2(\omega)$ $\left(\equiv \delta\,\dot{\vartheta}^2(\omega)\right)$ back into the time domain yields:

$$\delta\Omega^2(t) = \frac{L}{2\pi}\int d\omega\,\delta\Omega^2(\omega)\,e^{-i\omega t} = \frac{L}{2\pi}\int d\omega\frac{1}{\omega^2 I + \xi^2}e^{-i\omega t} = \frac{L}{2\xi I}\exp\left(-\frac{\xi}{I}t\right) \tag{28}$$

From the equipartition theorem we get:

$$\delta\Omega^2(t=0) \equiv \langle\Omega^2\rangle = \frac{kT}{I}, \tag{29}$$

and therefore $L = 2\xi kT$. For the autocorrelation function of the change in the angular position we get

$$\delta\Omega^2(t) = \frac{kT}{I}\exp\left(-\frac{\xi}{I}t\right). \tag{30}$$

The autocorrelation function of the dipole moment (see eq.3.2)

$$\begin{aligned}\delta\mu^2(t) &= \lim_{T'\to\infty}\frac{1}{T'}\int_{-T'/2}^{T'/2} dt'\mu(t')\cdot\mu(t'+t) \equiv \langle\mu(t')\cdot\mu(t'+t)\rangle_t \\ &= \mu^2[\langle\cos\vartheta(t)\cos\vartheta(t'+t)\rangle + \langle\sin\vartheta(t)\sin\vartheta(t'+t)\rangle]\end{aligned}$$

With $\Delta\vartheta = \vartheta(t'+t) - \vartheta(t')$ we get

$$\delta\mu^2(t) = \mu^2\langle\cos\Delta\vartheta\rangle_t . \tag{31}$$

Now the time average (identical with the ensemble average) of $\cos\Delta\vartheta$ is to be calculated. After some mathematical evaluations we get

$$\delta\mu^2(t) = \mu^2\exp(-k_\Omega(t)), \tag{32}$$

with

$$\begin{aligned}k_\Omega(t) &= \int_0^t dt'(t-t')\delta\Omega^2(t') = \frac{kT}{I}\int_0^t dt'(t-t')\exp\left(-\frac{\xi}{I}t'\right) \\ &= \frac{kTI}{\xi^2}\left[\exp\left(-\frac{\xi}{I}t\right) - 1 + \frac{\xi}{I}t\right].\end{aligned} \tag{33}$$

Therefore,

$$\delta\mu^2(t) = \mu^2\exp(-k_\Omega(t)) = \mu^2\exp\left\{\frac{kTI}{\xi^2}\left[\exp\left(-\frac{\xi}{I}t\right) - 1 + \frac{\xi}{I}t\right]\right\}. \tag{34}$$

For times $t \gg I/\xi$ the autocorrelation function of a dipole rotating in a plane is

$$\delta\mu^2(t) = \mu^2\exp\left(-\frac{kT}{\xi}t\right), \tag{35}$$

which corresponds to Debye's result for a sphere performing rotational Brownian motions. From FDT eq.19 and Fourier transform we get the complex frequency-dependend polarizability:

$$\begin{aligned}\alpha^*(\omega) &= \alpha_e - \int_0^\infty d/dt\ (\alpha(t))\, e^{-i\omega t}dt \\ &= \alpha_e - \frac{1}{kT}\int_0^\infty d/dt\ (\delta\mu^2(t))\ e^{-i\omega t}dt \\ &= \alpha_e + \frac{\mu^2}{kT}\frac{1}{(1+i\omega\tau_0)},\end{aligned} \tag{36}$$

with $\tau_0 = \xi/kT$. The permittivity is then $V\varepsilon_0(\varepsilon^*(\omega) - 1) = \alpha^*(\omega)$.
From eq.36 we observe that the permittivity of a plane rotator is a Debye process. Figure 7 shows a comparison between the dielectric function at -100^oC and -80^oC of n-Butanol (symbols). The result of the plane rotator (lines) is also shown. The friction coefficient ξ is the only adjustible parameter. From this comparison we can estimate the friction coefficient ξ. Usually, processes by dielectric methods investigated are not Debye-like (see Chapter 5). More complicated models which consider the interactions between neighboring molecules or a distribution of different Debye processes are necessary to discribe dielectric spectra.

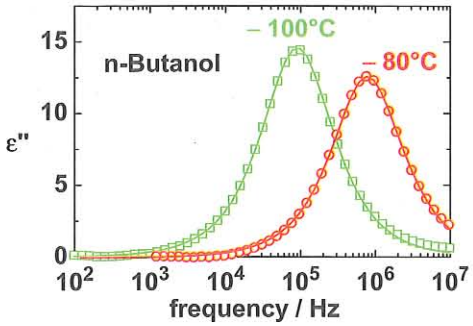


Fig. 7: *Dielectric loss for n-Butanol at $-100°C$ and $-80°C$ (symbols), and the result of the plane rotator (lines). We observe a good agreement.*

4 Experimental Techniques of Dielectric Spectroscopy

It is a feature of the dielectric technique that measurements can be performed nearly continuously over the frequency range 10^{-6} to $10^{12}Hz$. In Figure 1 the essential techniques with the corresponding frequency range are shown. The frequency range should be taken as a guide since the different techniques may be extended to slightly higher or lower frequencies than those indicated, often accompanied by a loss of accuracy in the measurement. In principle dielectric techniques are relatively simple in most of cases, and today this is a standard method. However, experiments at higher frequencies above $10^{10}Hz$ are more elaborate. Within the scope of this lecture three selected techniques will be explained in more detail.

4.1 Dielectric Time Spectroscopy ($10^{-6}...10^{3}Hz$)

In principle the simplest way to measure the dielectric properties of a material is to subject it to an electric field and observe how the polarization develops with time (retardation experiment, compare Section 3.1). The experimental procedure is very simple: A step-voltage is applied to the sample, and the current (conductivity) is recorded as a function of time. A decreasing curve is obtained in this way until a stationary level corresponding to the ohmic conductivity is reached. When the voltage is switched off a similar current response of opposite sign is recorded. A step function represents a wide Fourier spectrum containing components of very low frequency (depending on the duration of the recording) up to high frequencies (depending on the rise time of the step function). This means that the recorded current response contains all the information needed for constructing the dielectric spectrum in a wide frequency range from about 10^{-4} up to $10^{3}Hz$. In order to extract this information from the recorded curve a mathematical transformation should be used: the recorded current response $I(t)$ is subjected to a Fourier-type transformation to get the dielectric permittivity $\varepsilon^*(\omega)$.
According to the general linear response theory (see Section 3.1) the complex permittivity can be expressed in terms of the current-time function $I(t)$ as

$$\frac{\varepsilon^*(\omega) - \varepsilon_\infty}{\Delta\varepsilon} = -\frac{1}{C_S U_0}\int_0^\infty I(t)\, e^{-i\omega t} dt,$$

where $\Delta\varepsilon$ is the step height of the real part of dielectric function (dielectric relaxation strength, strictly speaking retardation strength), ε_∞ the real part of ε^* at higher frequncies (the unrelaxed permittivity), C_S is the capacity of the sample and U_0 the amplitude of the applied step voltage.To arive at lower frequencies the dielectric depolarization spectroscopy is used. For this, a high-voltage stabilized d.c. supply is used for polarizing the sample capacity. Then the depolarization of the sample (a depolarization current) will be measured. With this technique frequencies below $10^{-6}Hz$ can be reached.

4.2 Frequency Response Analyzer $(3 \cdot 10^{-5}...10^{7}Hz)$

In general the techniques to measure direct the dielectric function in the frequency domain are simple: A periodic voltage $U^* = U_0 \exp(i\omega t)$ with a fixed frequency $\omega/2\pi$ is applied to a sample cell which contains the sample material under test. U^* causes a current $I^* = I_0 \exp(i\omega t + \pi/2 + \delta)$ at the same frequency in the sample cell. U_0 and I_0 are the amplitudes of voltage and current, respectively. In addition δ is the from the sample generated phase angle between these two observables. The complex sample capacity results from the relation $C_S^* = I^*/i\omega U^*$. The dielectric permittivity results from $\varepsilon^*(\omega) = \varepsilon'(\omega) - i\varepsilon''(\omega) = C_S^*/C_0$, with $C_0 = \varepsilon_0 A/d$ the empty capacity.

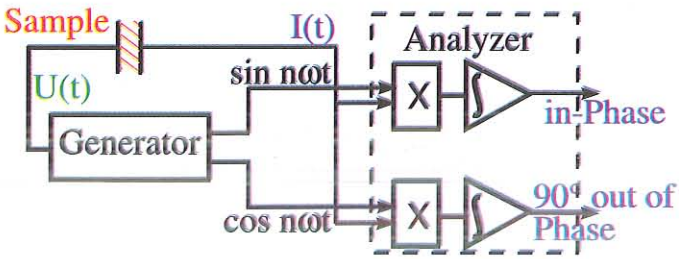


Fig. 8: *Schematic representation of the frequency response analyzer.*

Figure 8 shows schematically the frequency response analyzer. A generated sine voltage U^* applied to the sample causes a current I^* in the sample cell. In a correlator I^* becomes multiplied with the reference signal ($\sin(\omega t)$ and $\cos(\omega t)$, respectively), produced by the generator, and integrated over a few periods. This means that I^* becomes analyzed in the in-phase (0^o) and in the out-of-phase (90^o) components. From this we see that at lower frequencies the dielectric time spectroscopy is more advantageous (faster).

4.3 Coaxial Line Reflector $(10^6...2 \cdot 10^9 Hz)$

At higher frequencies the emitted radiation of non-shielded wires increases strongly. Therefore a coaxial lines is necessary to connect the analyzer with the sample cell. Furthermore, the measuring circuit connecting a test sample to the test port (i.e. the test fixture) actually becomes a part of the sample that the instrument measures. In addition, component electrodes or leads, which should essentially be of negligibly low impedances, also influence the measured sample values because of the presence of certain parasitic impedances. Diverse parasitic impedances existing in the measuring circuit between the test port and the unknown device affect the measurement result. Furthermore, in the

high frequency region, the equivalent electrical length of the measuring circuit, including component leads, rotates the measured impedance vector as a function of the test signal wavelength.
The test fixture is basically composed of two major components, a coaxial coupling terminal and the contact electrodes (terminals), combined in a single unit. Because a correction calculation does not compensate the residual and stray parameters in the contact section, these residual and stray factors in the test fixture contribute to measurement errors.

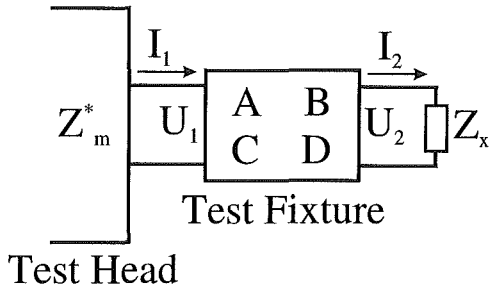


Fig. 9: *Test fixture represented by the F matrix of a two pair network.*

In general, these factors can be represented by F parameters of two terminal-pair as shown in Figure 9. Using this model, the residual and stray factors can be eliminated:

$$\begin{pmatrix} U_1^* \\ I_1^* \end{pmatrix} = \begin{pmatrix} A & B \\ C & D \end{pmatrix} \begin{pmatrix} U_2^* \\ I_2^* \end{pmatrix},$$

with $\begin{pmatrix} A & B \\ C & D \end{pmatrix}$ the compensation matrix.
The actual impedance value Z_x^* of the sample and the measurement value Z_m^* are obtained from the input and output current and voltage as follows:

$$\begin{aligned} Z_m^*(\omega) &= \frac{U_1^*(\omega)}{I_1^*(\omega)} \\ Z_x^*(\omega) &= \frac{U_2^*(\omega)}{I_2^*(\omega)}. \end{aligned}$$

Then, Z_x^* is:

$$Z_x^* = A_{comp} \frac{Z_m^* - B_{comp}}{1 - Z_m^* C_{comp}},$$

with the complex and frequency dependent compensation parameters

$$\begin{aligned} A_{comp} &= D/A \\ B_{comp} &= B/D \\ C_{comp} &= C/A. \end{aligned}$$

There are three unknown parameters to calculate Z_x^* from Z_m^*. Therefore, three standards are needed for perfect compensation: *OPEN*, *SHORT*, and *LOAD*. *OPEN* and *LOAD*

means that the current through the sample cell and the voltage at the sample cell is zero, respectively. *LOAD* means that a 50Ω impedance will be measured.
The permittivity of the sample is again calculated by

$$\varepsilon^*(\omega) = \frac{1}{i\omega C_0 Z_x^*(\omega)}.$$

5 Dielectric Spectroscopy on Liquids and Polymers; Dipole Fluctuations

During the past few decades of dielectric work quite a large body of experimental data on polymers (see e.g. Ref.[1]) and liquids (see e.g. Ref.[11]) has been measured. In the present Chapter examples of dielectric spectra and calculated dipole fluctuations will be shown.

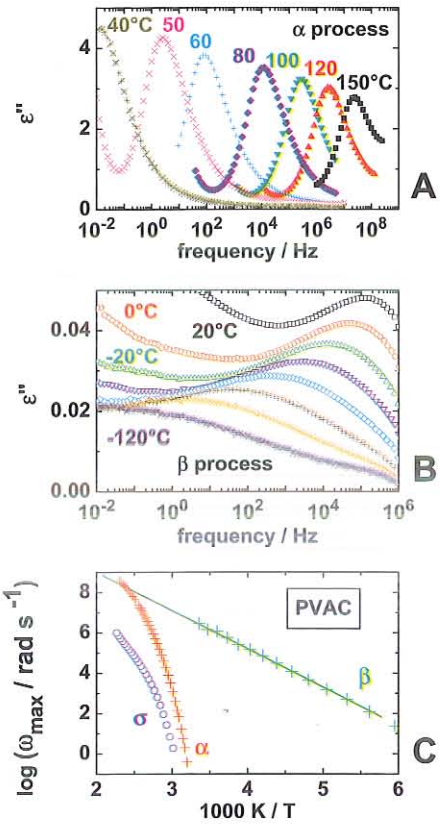


Fig. 10: *Imaginary part of dielectric permittivity as a function of frequency at selected temperatures for the glass transition (A) and the β process (B) of poly vinylacetate. The frequency position of the peak maxima is shown in (C). Also included is the conductivity σ of the sample.*

Figure 10 shows a representative example of the dielectric function of poly vinylacetate over a wide range of temperature and frequency. At higher temperatures the glass transition (α process) is observed (Figure 10A). With decreasing temperatures the peak maximum shifts to lower frequencies. At about 40^oC the process leaves our experimental frequency window. Below the α process dielectric function increase again. This increasing results from results from the transport of ions in the sample. For even lower temperatures the β process becomes visible (Figure 10B). Also, with decreasing temperatures the peak maximum of the β process shifts to lower frequencies. Simultaneously, the width of the β process is drastically increased. At about -120^oC the β process leaves the frequency window. Figure 10C shows the temperature dependence of the peak maxima of both processes, represented in an Arrhenius-diagram. While the β process shows a typical Arrhenius-like behavior, the peak maximum of the α process shows a stronger temperature dependence. At $T \approx 400K$ the traces of both processes intersect. Also included is the temperature dependence of the real part of conductivity at lower frequencies $\sigma^* = \sigma' - i\sigma'' = i\omega\varepsilon_0 (\varepsilon^* - 1)$.

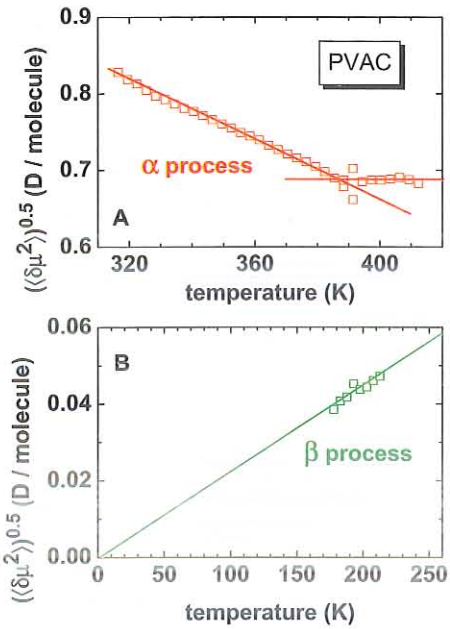


Fig. 11: *Temperature dependence of the mean dipole fluctuations calculated via the FDT eq.21 for the α (A) and β process (B) for poly vinylacetate.*

From the FDT eq.21 we can calculate the mean dipole fluctuations of the $\alpha$and β process, $\langle \delta\mu_\alpha^2 \rangle$, $\langle \delta\mu_\beta^2 \rangle$, respectively. Figure 11 shows the temperature dependence of $\langle \delta\mu_\alpha^2 \rangle$ (A) and $\langle \delta\mu_\beta^2 \rangle$ (B) calculated from the spectra shown in Figure 10A and B. Both processes shows a clearly different temperature dependence: $\langle \delta\mu_\beta^2 \rangle$ is directly proportional to the temperature. This is what we expect for local relaxation processes. However, the fluctuations of the dipole moment of the α process are almost constant at higher temperatures. Below $T \approx 390K$, $\langle \delta\mu_\alpha^2 \rangle$ increases with decreasing temperature. Note that this change is close

to the intersection of α and β process.

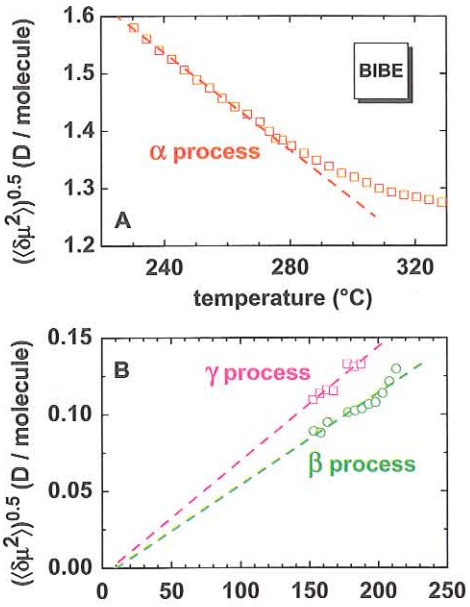


Fig. 12: *Temperature dependence of the mean dipole fluctuations calculated via the FDT eq.21 for the α (A), and β and γ process (B) for benzoin isobutylether.*

Figure 12 shows a second example for the temperature dependence of dipole fluctuations on the basis of benzoin isobutylether (a low molecular weight liquid). We observe qualitatively the same behavior: a linear increase of $\langle \delta\mu^2 \rangle$ for local processes (β and γ) and a decrease of $\langle \delta\mu^2 \rangle$ for the glass transition. This result shows indirectly that the α process results from correlations of many particles.

References

[1] N.G. McCrum, B.E. Read and G. Williams *Anelastic and Dielectric Effects in Polymeric Solids* (Dover, New York, 1967)

[2] B.K.P. Scaife *Principles of Dielectrics* (Clarendon, Oxford, 1989)

[3] C.J.F. Boettcher *Theory of Electric Polarization Vol.1* (Elsevier,Amsterdam, 1973); C.J.F. Boettcher and P. Bordwijk*Theory of Electric Polarization Vol.2* (Elsevier, Amsterdam, 1978);

[4] A.K. Johnscher *Dielectric Relaxation in Solids* (Chelsea Press, London, 1983)

[5] P. Hedwig *Dielectric Spectroscopy of Polymers* (Adam Hilger, Bristol, 1977)

[6] A. Chelkowski *Dielectric Physics* (Elsevier, Amsterdam, 1980)

[7] E. Donth *Relaxation and Thermodynamics in Polymers* (Akademie, Berlin, 1992); E. Donth *The Glass Transition* (AkademieSpringer, Berlin, 2001)

[8] R. Brandl, P. Lunkenheimer and A. Loidl, Phys. Rev. B**56**, 5713 (1995)

[9] N.E. Israelov, Phys. Rev. B**53**, 11913 (1996)

[10] H.Nyquist, Phys. Rev.**32**, 110 (1928)

[11] F.J. Stickel *Untersuchung der Dynamik in niedermolekularen Flüssigkeiten mit Dielektrischer Spektroskopie* (Shaker, Aachen, 1995)

A 4 Polymer Synthesis

J. Allgaier
Institut für Festkörperforschung
Forschungszentrum Jülich GmbH

Contents

1 Introduction 2

2 Synthesis methods 2

2.1 Radical polymerization 2

2.2 Anionic polymerization 3

2.3 Polycondensation 6

2.4 Metallocene catalysed polymerization 8

2.5 Polymers with architecture 9

3 Polymer properties 11

3.1 Molecular weight 11

3.2 Thermal properties 12

3.3 Mechanical properties 14

4 Summary 15

1 Introduction

Polymers are chain-like molecules. They are synthesized by chemically linking together a large number of molecules, the so called monomers. The monomer molecules are of low molecular weight and contain reactive groups. During the polymerization process the monomers are connected via these reactive groups. Polymers are not only known as man-made synthetic materials. They play an important role in nature. Cellulose, proteins and DNA are examples for natural polymers. However, in this chapter we focus uniquely on synthetic materials.

In everyday life synthetic polymers play an important role. They are widely used as construction materials in the building industry or in the automobile industry. Further on, packaging materials and textiles are frequently made of polymers. But also paints, coatings or adhesives contain besides solvents mainly polymers.



Fig. 1: *Polymer applications*

In the following sections some basic concepts for the synthesis of polymers are given. Then fundamental physical properties of polymers are described to show that the chemical design of the polymer strongly influences the physical or material properties.

2 Synthesis methods

Polymers are produced by linking together low molecular weight monomer molecules. In principle there is an endless number of chemical reactions and reactive groups that can be used for polymerization reactions. However, in most cases a few reaction types are used to synthesise polymers. In the following sections some fundamental examples are given to explain the principal features. For a more detailed study see textbooks dealing with polymer science [1][2][3].

2.1 Radical polymerization

This method is the most simple and most common method to obtain polymers [1][3]. Vinyl monomers which contain a reactive carbon double bond are used as monomers. The polymerization process needs radicals. As free radicals are extremely reactive, they cannot be

stored as such and have to be generated during the polymerization. Compounds having week chemical bonds like peroxides are used to generate radicals in the initiation process. If the reaction mixture is heated the O-O bond breaks and produces two radicals (see Fig.2). Each radical is able to start one polymer chain by attacking the C-C double bond of a monomer molecule. In detail, the single electron of the radical reacts with an electron of the double bond, resulting again in the formation of a radical now located at the end of the former monomer unit. This radical attacks in the next step another monomer molecule which is attached to the first unit. The addition of monomers to the growing polymer chain is continued until termination takes place. A typical termination reaction is the combination of two polymer chains containing each a radical at the end. But also freshly generated radicals can be involved in terminations. To minimize such reactions the concentration of radicals has to be low. This is achieved by adjusting the temperature so that during polymerization continuously few radicals are generated. Due to the high reactivity of the radicals the addition of monomers is extremely quick. The growths of a single polymer chain takes millisecond or seconds until termination occurs. As a whole, the polymerization process consists of radical generation, polymer chain growth and termination reactions taking place simultaneously until the monomer and/or initiator is consumed.

The driving force for radical polymerization is the replacement of one carbon double bond by two carbon single bonds. This state is energetically more favorable and leads to the formation of large amounts of heat during the polymerization. The radical polymerization is a simple reaction. The process and the monomers are cheap why it is widely used in industrial polymerizations. On the other hand, the polymers produced by radical methods are undefined. Due to the high reactivity of radicals many side reactions occur and molecular weights or in other words chain lengths are difficult to control because of the random termination event.

2.2 Anionic polymerization

In analogy to radical polymerization the anionic technique uses vinyl monomers. The initiators, however, are of anionic nature [2][3]. In most cases metal-organic compounds as butyl lithium are used. These ionic substances contain negatively charged carbon atoms (carbanions) and metal counter ions. In contrast to free radicals metal organic substances are stable if certain conditions are fulfilled. They can be added to the monomer directly and do not have to be generated in situ. The polymerization itself is similar to the radical technique as shown in Fig.3. The metal-organic compound attacks with its negative charge the vinyl double bond, the negative charge is transferred to the final carbon atom of the monomer unit attached. This molecule attacks another monomer unit etc. As the carbanions are stable the polymerization process continues until all monomer is consumed. Finally, the reaction is terminated by adding alcohol. The negatively charged carbon atom represents a strong base and easily abstracts a proton from the alcoholic OH-group, leading to the formation of an unreactive C-H bond and the lithium salt of the alcohol which itself it no more able to work as initiator. The termination of the active chain ends is necessary because carbanions are highly reactive. Metal organic compounds but also the carbanionic chain ends of the growing

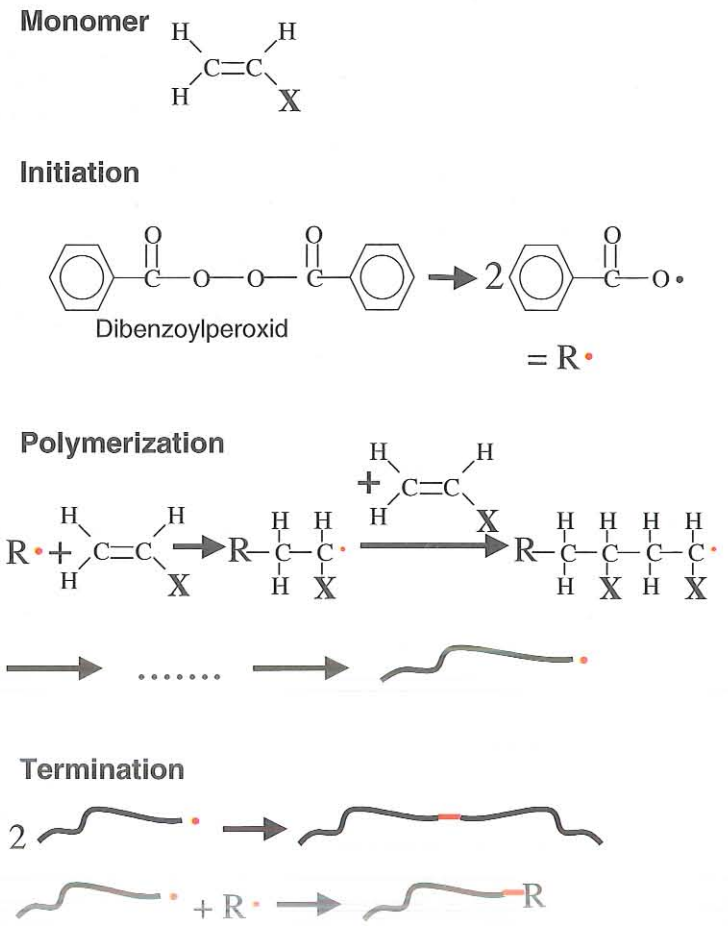


Fig. 2: ***Radical** polymerization*

polymer chain react not only with carbon double bonds but also with a large variety of substances, among them water, oxygen, acids and alcohols which were mentioned already above. Due to the fact that one initiator molecule adds hundreds or thousands of monomer units to form a polymer chain, the amount of initiator in the reaction vessel is extremely small. For this reason highly pure reaction conditions are required. Solvents and monomers have to be purified rigorously and the polymerization has to be carried out under inert gas atmosphere, otherwise remaining impurities would deactivate the initiator and prevent polymerization.

In contrast to the radical process, in anionic polymerization all initiator molecules are active from the beginning and all polymer chains grow simultaneously. Anionic chain ends show a smaller reactivity as the radical chain ends. Therefore, the polymerization process for a single chain and for the whole reaction takes hours or even days in anionic polymerization. As each initiator molecule creates one polymer chain it is possible to predict chain lengths or molecular weights in advance if the molar amounts of initiator and monomer are known for the experiment. In summary, anionic polymerization is useful to produce highly defined polymers, e. g. with respect to molecular weight. Because of the high purity standards this technique is mainly used where defined polymers are needed, for example for the production of research materials.

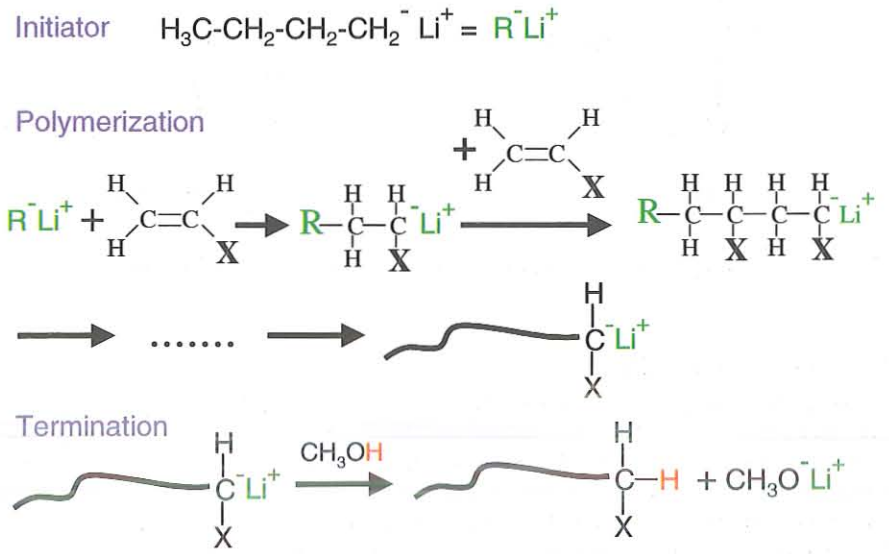


Fig. 3: *Anionic polymerization*

Not all vinyl monomers can be polymerized anionically. Fig.4 shows a list of polymers which are obtained via radical or anionic polymerization. Polyethylene and PVC are not accessible anionically because the corresponding negative chain ends are chemically unstable or the monomer causes deactivation side reactions with the initiator (PVC). Styrene and Methylmethacrylate are useful monomers for the anionic route. In these cases the chain ends are stable and side reactions of initiator and monomer are minimal. Radical polymerization is less demanding with respect to the monomer, all monomers listed in Fig.4 can be polymerized by this technique.

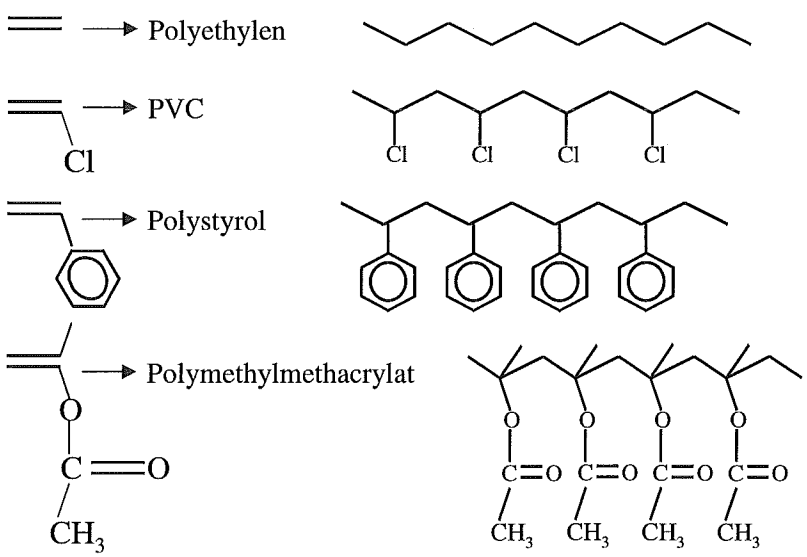


Fig. 4: *Examples for polymers produced by radical or anionic polymerization*

2.3 Polycondensation

The principle of polycondensation is different from radical and anionic polymerization. In the techniques described before the initiator attacks the reactive group of the monomer, in our cases the carbon double bond. The polymerization active species, radical or negative charge, is transferred to the monomer added, so that this unit becomes itself polymerization active and adds another monomer etc. In polycondensation monomers with two reactive groups are used. The monomers are linked together via the reactive groups. Each linking step is an isolated reaction and is finished after the linking process [1][2][3]. An example for polycondensation is the formation of polyesters. The basic reaction step is the ester formation from an alcohol an organic acid under elimination of a water molecule. For polymer formation a difunctional alcohol and a difunctional acid is required to form a linear polymer chain. Fig.5 gives details, it shows also examples for polycondensates. Polyethyleneglycolterephtalate is more known as PET. This polymer is widely used for synthetic fibres and drinking bottles are made from PET. If the difunctional alcohol is replaced by a difunctional amine, polyamides such as nylons are obtained.

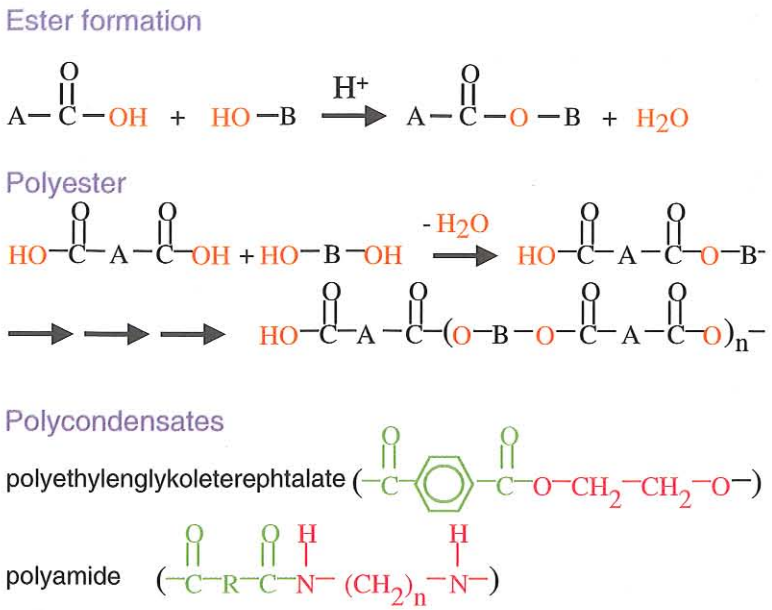
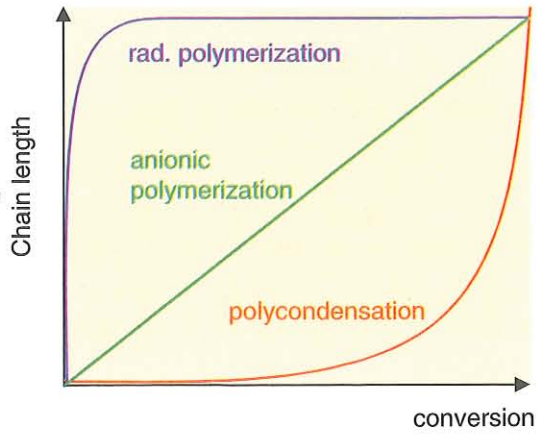


Fig. 5: *Polycondensation*

The ester formation is an extremely simple organic reaction, however, polymer formation is far away from being trivial. The difficult point is to obtain chain lengths which are sufficiently high enough. During polymerization first monomeric alcohol and acid units are linked together, then these units are coupled and form larger and larger chains. But even at a conversion rate of 99 %, which means that 99 % of the alcohol and acid groups have reacted, the average chain length is 100. This length is still small on a polymer scale, on the other hand 99 % of conversion is a very high value for a chemical reaction. High conversion rates require an exact one to one stoichiometry of alcohol and acid groups. If for example there is an excess of alcohol groups, after a short time all acid will be eliminated and the chain ends consist uniquely of alcohol units resulting in short chain lengths. For the same reason monomers of high purity are required. Especially monofunctional monomers lead to non-reactive chain ends and only low chain lengths. In Fig.6 the conversion rate is plotted against the chain length for a polycondensation reaction and for radical as well as anionic polymerization. The curve for polycondensation contains the same details as given in the table aside. Other polymerization techniques show different patterns. For anionic polymerization the chain length depends linearly on the conversion because all chains grow simultaneously and in average at the same rate. The radical process is again different. Here already at very low conversion rates long chains are produced due to the fast polymerization and termination.



Polycondensation

conversion (%)	chain length
50	2
90	10
99	100
99,9	1000

Fig. 6: *Polycondensation vs. Radical and anionic polymerization*

2.4 Metallocene catalysed polymerization

Metallocenes are complexes of transition metals like titanium or zirkonium with organic cyclopentadienyl units and other ligands. Metallocenes can also complex molecules containing a carbon double bond. This property is used for the formation of polymers [2]. As this technique is employed mainly for technical products, cheap monomers as ethylene ($H_2C=CH_2$) or propylene ($H_2C=CH-CH_3$) are used. The polymerization mechanism is shown for polypropylene in Fig.7. The zirconium atom contains besides the circular cyclopentadiene units a methyl group as ligand. If propylene is added it forms a complex with the metallocene molecule. This process weakens the carbon double bond but also the Zr-methyl bond and results in insertion of the propylene unit between the Zr and the methyl group. Then, another propylene molecule can be complexed, inserted etc.; a polymer is formed. There are also termination reactions, mainly on basis of hydride elimination, which will not be discussed here.

One of the important features of metallocene polymerization is the possibility to influence the tacticity of the polymer. Tacticity means the steric orientation of the side groups. In the propylene molecule three H atoms an d one methyl group are attached to the carbon double bond. Consequently, every second carbon atom in the polymer chain contains a methyl group. There are different possibilities for the orientation of these side groups. They can all point into the same direction, this scenario is called isotactic. The orientation of the methyl groups can be also randomly distributed which is the atactic version. Whereas isotactic polypropylene is a material of high symmetrical order, atactic polypropylene shows no order with respect to the side groups. By taking different metallocene catalysts the tacticity can be varied. Different tacticities influences the polymer properties significantly even if the monomer unit is identical. In the next chapter this case will be discussed in more detail.

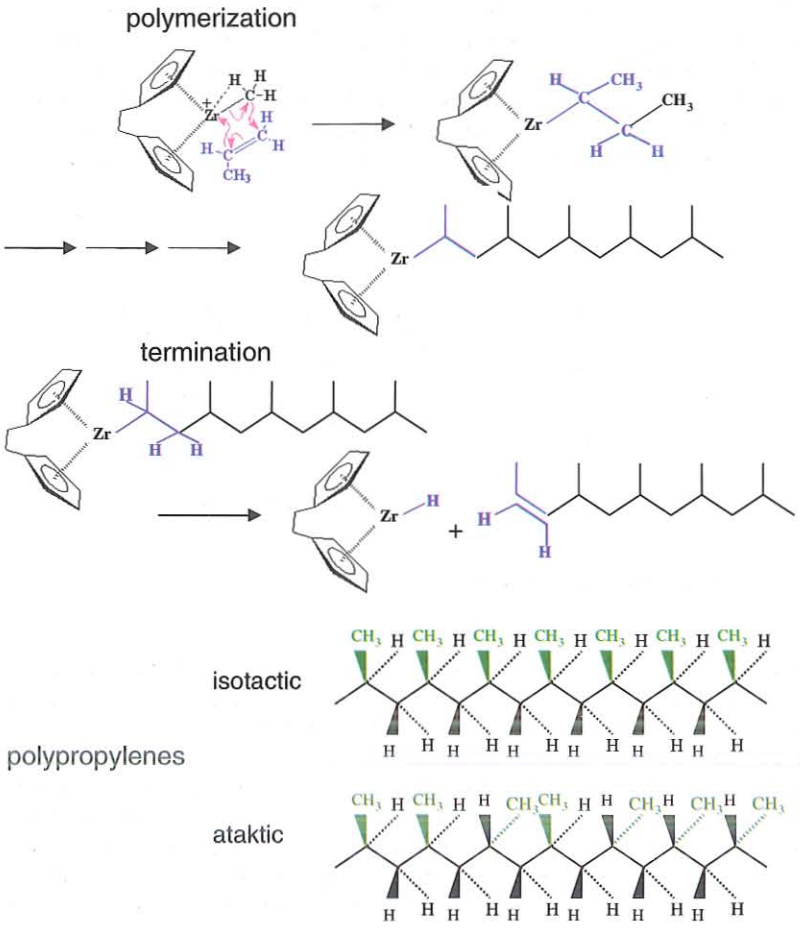


Fig. 7: *Metallocene polymerization*

2.5 Polymers with architecture

The polymers discussed so far are linear chains made from one monomer or in case of the polycondensation of two monomers with different functional groups. In this section now non-linear architectures and copolymers, made from chemically different monomers will be described.

The most simple version of non-linear architectures are branched polymers (see Fig.8). There are different possibilities to synthesize such materials. In radical polymerization for example monomer equipped with two vinyl groups per molecule can be added to the monofunctional monomer. The difunctional molecules are integrated in two polymer chains and work as branching point linking together two different chains. In the case of polycondensation three or four functional monomer is used together with difunctional monomer. Again the higher

functional units work as branching points as they grow in more than two directions. If small amounts of higher functional monomer is added, this leads to isolated branched polymer molecules. If the amount of higher functional monomer is increased branching gets denser and the branched structures are getting larger or even a polymer network is formed. In this case all polymer chains are linked together via covalent bonds. In principal the whole piece of material represents one single molecule. Rubber used in car tires for example is a polymer network.

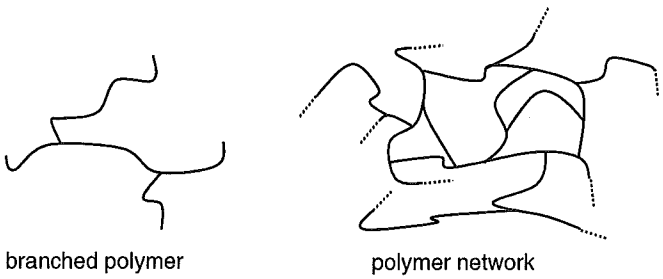


Fig. 8: *Branched polymer and polymer network*

Copolymers consist of two or more different monomers. According to this definition polycondensates are copolymers. Usually they are not classified as copolymers because for their synthesis two differently functional monomers are necessary. Common copolymers are products of two vinyl monomers polymerized by radical or anionic techniques. Styrene-acrylonitrile or styrene-butadiene copolymers are widely used materials. The two monomers can be arranged in different ways in the polymer chain. If they are randomly distributed the product is called statistical copolymer. If they are arranged in segments of only one monomer they are named block copolymer (see Fig.9). Statistical copolymers are produced mainly by radical polymerization, polymerizing simultaneously the two different monomers. The growing polymer chains will add in a more or less random process the one or the other monomer. For the production of block copolymers first the one monomer is added and polymerized. After complete consumption, the other monomer is added and polymerized. Block copolymers cannot be produced by free radical polymerization because of the short life time of the radicals associated with the continuous production of polymer chains. The ideal technique for block copolymer synthesis is anionic polymerization due to the unlimited life time of the active chain end which allows the subsequent addition of monomers. Copolymers are widely used because they combine the properties of the single homopolymers.

In this context it is useful to discuss the aspect of polymer miscibility. Low molecular weight substances are normally miscible if they are chemically not too different. Miscibility is driven by the gain in entropy. Polymers show a different behavior. Apart from rare exceptions they are not miscible. In contrast to low molecular weight substances the molecular weight of a polymer is high. In other words this means that a given amount of polymer is represented by a relatively small number of molecules. As entropy strongly depends on the number of molecules, the gain in entropy too small that miscibility occurs. In block copolymers the segments represent two different polymers. But they cannot separate macroscopically because

the blocks are linked together via a covalent bond. However, the segments can separate on a microscopic level, forming ordered structures which consist of only one polymer (see Fig.9). This phenomenon is called microphase separation and influences the properties of the polymers dramatically as we will see in the next chapter.

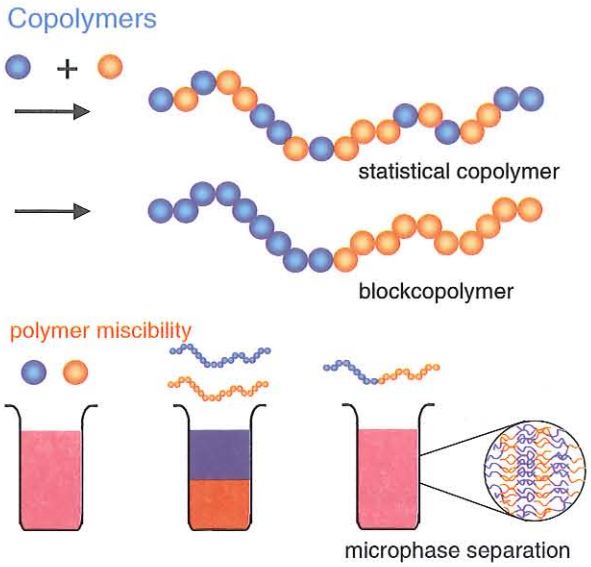


Fig. 9: *Block copolymers and polymer miscibility*

3 Polymer properties

The aim of this chapter is to point out some fundamental physical properties which are unique to polymers and to show how they influence the material properties of polymers used in applications. Further on it will be shown that the synthetic methods for polymer production can be used to modify the properties.

3.1 Molecular weight

Conventional organic or inorganic substances possess a defined molecular weight. Polymers show a different scenario. If we take the radical polymerization as an example, it is understandable that during synthesis long chains are produced together with short chains. Mainly because of the random termination event the life time of an active polymer chain adding monomer units varies and causes chains of different lengths. Polymer molecular weights or chain lengths are for that reason average values. But the average molecular weight

is not the only value necessary to characterize the polymer weight. It is also important to know the weight distribution which is illustrated in Fig.10. Radically synthesized polymers

have a broad distribution, which means that chains of very different lengths exist together. Polymers anionically produced are more defined with respect to the distribution. As all chains grow simultaneously in the absence of termination events they have approximately the same molecular weight and the distribution is small.

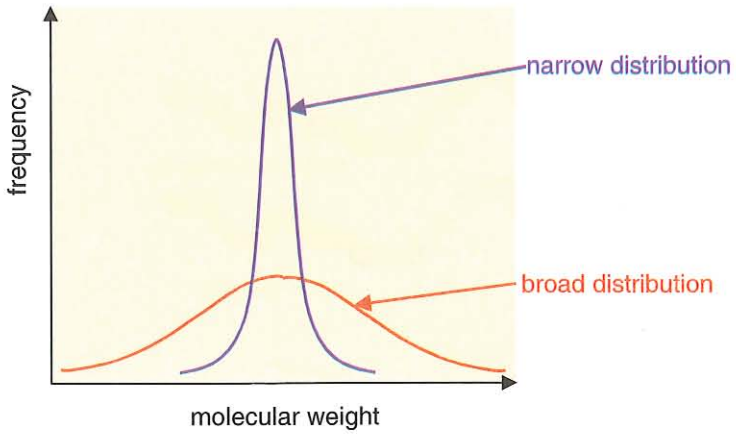


Fig. 10: *Polymer molecular weight distributions*

3.2 Thermal properties

At higher temperatures polymers represent liquids. Due to the increased molecular weight the viscosity usually is orders of magnitudes higher than in conventional liquids of low molecular weight substances. At lower temperatures the liquid solidifies either in a glassy or a crystalline state. Glasses are more frequent. The temperature at which the polymer melt solidifies as glass is called glass transition temperature (Tg). In contrast to a melting temperature (Tm), Tg is less defined and often covers a temperature range of several 10 degrees. Highly symmetrical polymers can crystallise but in most cases they are only partially crystalline. The high viscosity of the melt prevents compete crystallisation during the freezing process, leaving back part of the material trapped in the glassy state.

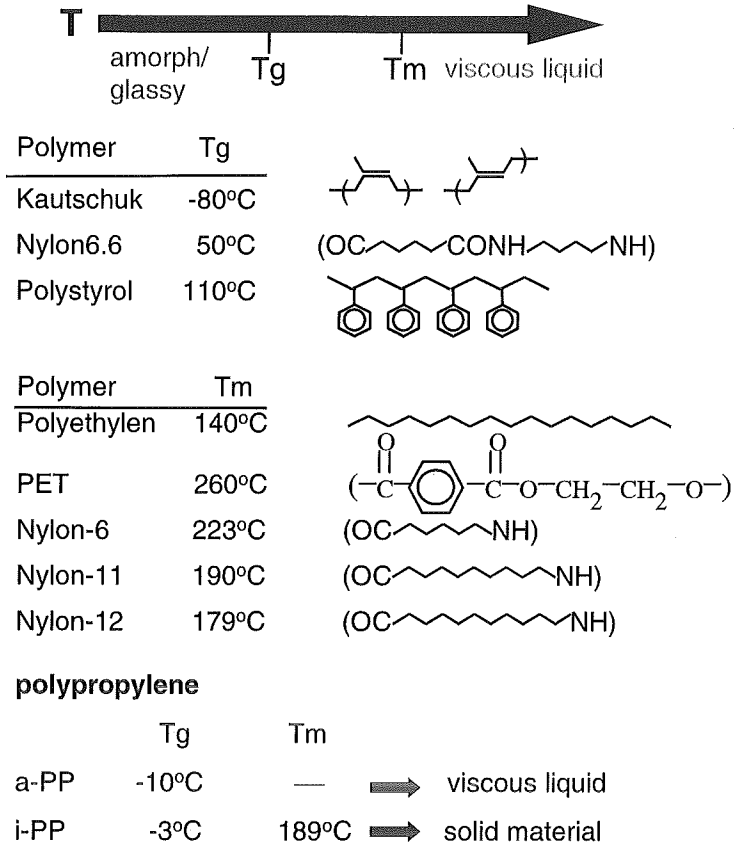


Fig. 11: *Thermal properties*

Typical glass transition temperatures lie between -100°C and more than +200°C. Fig.11 shows a few examples. Nonpolar polymers, having weak intermolecular forces like rubber show low Tg values. If polar groups are present, amide groups in nylons for example, or bulky side groups as in polystyrene, Tg is higher. Melting temperatures show the same scenario. It is extremely high for PET because of the rigid and extended aromatic ester group in the polymer chain. To which extent small changes in the chemical structure can dramatically influence the physical properties, among them the thermal behaviour, is demonstrated with two examples. The first one is polypropylene. In the synthetic chapter it was demonstrated that depending on the polymerization catalyst either atactic polypropylene (a-PP) or isotactic polypropylene (i-PP) can be obtained. In a-PP the methyl side groups are randomly distributed in space, consequently the material is amorphous with Tg = -10°C. At room temperature a-PP is a viscous liquid although Tg is a little below room temperature. It is used as adhesive to some extent. i-PP behaves completely different. The methyl side groups are symmetrically ordered and the polymer is to a high degree crystalline with Tm = 189°C. This polymer is a solid

material with good mechanical properties and used as packaging material and as construction material.

The second example is polystyrene-polybutadiene block copolymer. Both components are amorphous polymers with different Tg values (polystyrene +110°C, polybutadiene -80°C). At room temperature polystyrene is a solid and stiff material, polybutadiene is a viscous liquid. In the block copolymer both polymers exist together as microscopically small domains. Macroscopically the material combines mechanical stability and flexibility, it shows a high impact strength.

3.3 Mechanical properties

The most important feature in this wide field is viscoelasticity. This phenomenon exists for T>Tg. It combines a typical liquid property, viscosity, and a typical solid property, elasticity. Viscosity and elasticity depend on the chain-like structure of polymers and the fact that the polymer molecules do not exist as isolated objects side by side but interpenetrate or entangle (Fig.12). If a mechanical force is applied to a piece of polymer, the flow of the polymer molecules is hindered as the entanglements represent mechanical barriers. The more entanglements per polymer chain exist the stronger these restrictions are. The number of entanglements depends linearly on the molecular weight. For this reason high molecular weight polymers express predominantly elastic behaviour, viscous flow is almost invisible. In contrast to that, polymers with lower molecular weights show only few or no entanglements and consequently, they are mainly fluids with relatively low viscosities.

An exceptional position with respect to viscoelasticity is represented by polymer networks. Networks do not only posses physical entanglements but also covalent chemical bonds linking together the single chains. In this case viscous flow is completely suppressed and the material shows purely elastic behaviour. Examples are rubbers which are widely used in many products.

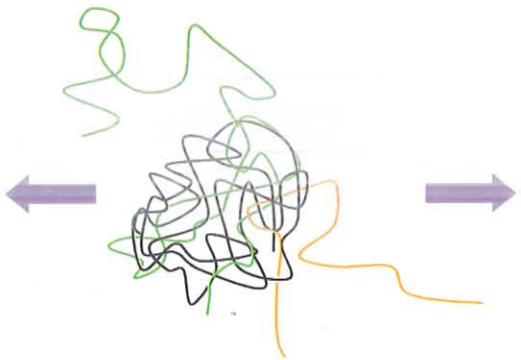


Fig. 12: *Entanglement of polymer chains*

4 Summary

In the preceding chapters it was shown that the different synthetic methods represent tools to produce polymers with a large variation in properties. The choice of different monomers, catalysts and polymerization methods together with the use of multifunctional monomers or copolymerization techniques allows to obtain a large diversity of materials. The synthetic methods enable to tailor the physical properties of a polymer. They permit to specifically change properties as molecular weights, chain flexibility or the symmetry of side groups. This influences the material properties of polymers like thermal and mechanical behaviour, or optical properties and solubility which were not treated in this context. The reason why polymers play such an important role in our everyday life is understandable with this statement. For each application the material used must fulfil very specific conditions which change from case to case. Polymers can be produced tailor made to these conditions.

References

[1]J. W. Nicholson, The Chemistry of Polymers (RCS Paperbacks, 1994)
[2]M. D. Lecher, K. Gehrke, E. H. Nordmeier, Makromolekulare Chemie (Birkhäuser Verlag, 1996)
[3]G. Odian, Principles of Polymerization (John Wiley & Sons, 1991)

A 5 Colloid Synthesis

J. Buitenhuis
Institut für Festkörperforschung
Forschungszentrum Jülich GmbH

Contents

1 Introduction **2**

2 Stability of colloidal particles **3**
2.1 Charge stabilization 3
2.2 Steric stabilization 6

3 Monodisperse particles **7**
3.1 Separation of nucleation and growth 7
3.2 Synthesis of colloidal silica spheres 8
3.3 Non-spherical particles 9

4 Recrystallization and Ostwald ripening **10**

5 Characterization **13**

6 Summary **16**

1 Introduction

In this chapter we describe the general principles of the synthesis of colloidal dispersions. The discussion will be limited to dispersions of solid particles in a liquid, although many of the principles may also be applied to liquid/liquid dispersions (emulsions) and to some extend also to solid/gas(e.g. smoke), liquid/gas(e.g. fog) or gas/liquid (e.g. foam) dispersions. Colloidal particles can be prepared by two methods which involves (1) the breaking of larger particles into smaller ones or (2) the growing of particles from solution or by condensation of even smaller sub-particles[1, 3].

Breaking of larger particles into smaller ones (to disperse) is usually done by mechanical forces. The titanium dioxide used in paints, for example, is processed in a ball mill. A ball mill consists of a vessel filled with the coarse suspension to be ground to which typically ceramic or metal balls are added. After filling, the vessel is rotated so that the balls are moving, breaking the particles down to colloidal size. To prevent reaggregation a dispersing agent stabilizing the small particles may be added. Grinding usually results in very polydisperse particles, i.e. the particles have a very broad size distribution.

By growing colloidal particles from much smaller particles or solution, it is possible to produce very monodisperse particles. This requires however, a precise control of the preparation conditions, as will be discussed later, otherwise a polydisperse product is obtained. Growing of solid particles in a liquid usually involves some sort of precipitation process. For example, by the reduction of the gold chloride complex by hydrogen peroxide

$$Au(Cl)_4^- + H_2O_2 \rightarrow Au(sol) + HCl + 2O_2$$

a gold dispersion (or sol) can be formed and oxidation of hydrogen sulfide with oxygen

$$2H_2S + O_2 \rightarrow 2S(sol) + 2H_2O$$

yields a sulfur sol. A silver iodide sol can be formed by exceeding the solubility limit, for instance by the reaction

$$KI + AgNO_3 \rightarrow AgI(sol) + K^+ + NO_3^- .$$

In the examples shown above chemical reactions form an insoluble solid, however, dispersions can also be formed by a dissolution-reprecipitation process. For example, a fatty acid sol can be prepared by injecting a solution of fatty acid in ethanol into a large amount of water

$$\text{Fatty acid in ethanol} + H_2O \rightarrow \text{fatty acid (sol)} .$$

However, just producing a solid phase by some precipitation process will not always lead to the formation of a stable sol. To obtain a sol one should take care of the colloidal stability of the particles formed (i.e. their stability against coagulation).

2 Stability of colloidal particles

Apart from a few exceptions (microemulsions) colloidal dispersions are thermodynamically unstable. Still colloidal dispersions can be very stable, i.e. they are usually kinetically stabilized. There are two main types of stabilization of colloidal particles[1, 2, 3]:

- charge stabilization and
- steric stabilization.

A combination of both stabilizations is often used too, e.g. with the fat in milk. Furthermore, it is important to note that the nature of the stabilization also determines the interaction potential between the particles and thereby have a major influence on the physical properties of the dispersions.

2.1 Charge stabilization

Colloidal particles can be stabilized by electrical charge simply because equally charged particles will repel each other. Particles can bear an electrical charge by adsorption of amphiphiles or polymers, by covalently bound groups, or by potential determining ions for ionic particles. An example of the origin of the electrical charge will be given for the particles of a silver iodide and bromide sol, which are one of the most studied systems due to the relevance of silver halides in photographic processes.
The solubility product of AgI is 7.5×10^{-17} M^2 at 25 ^oC. If the concentration of silver ions $c(Ag^+)$ is equal to the concentration of iodine ions $c(I^-)$ is 8.7×10^{-9} M, electrophoretic measurements show that the particles are negatively charged. Now, increasing $c(Ag^+)$ to concentrations above 3.0×10^{-6} M results in positively charged particles, at lower concentrations the particles are negatively charged. Exactly at $c(Ag^+) = 3.0 \times 10^{-6}$ M the particles bear no net charge, which is called the iso-electrical point (iep). Electrophoretic measurements show that the potential of AgI particles depends linearly on the logarithm of $c(Ag^+)$ and $c(I^-)$ (at least close to the iep) so the $Ag^+$and I^- ions are potential determining ions.
For AgBr however, the preferential adsorption of the Br^- ions is much less pronounced as for I^- ions, meaning that the iep is close to equal Ag^+ and Br^- concentrations. Now, if AgBr sols are prepared by adding a KBr solution to a $AgNO_3$ solution, to obtain a stable sol an excess of one of the two reacting agents should be used, so that charged particles result. In the same way, the charge on oxides and hydroxides will be determined by the pH.
So far, the origin of the charge has been considered, but not the relation between the charge and the stability of the colloidal particles. The repulsion between the charged particles is usually not coulombic. An electrical double layer of the oppositely charged ions around the particles, the so called counter ions, screen the coulombic interaction, so that, if one considers the particle at a distance a few times the double layer thickness, the particle appears uncharged. A schematic drawing of a negatively charged particle in an ionic solution showing the electrical double layer is given in fig. 1. The counter ions are attracted to the particle but are not directly sticked to its surface, in about the same way as the air of the earth atmosphere is not sticked to the earth surface, but still can not escape its gravity field, yielding a diffuse atmosphere. All this results in an electrostatic

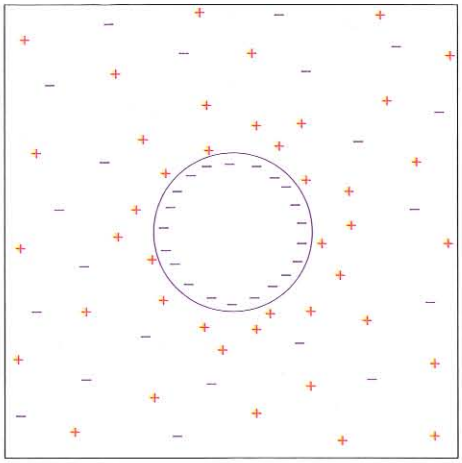


Fig. 1: *Schematic drawing of a negatively charged particle in an ionic solution with a diffuse electrical double layer of positive charges. Single charges are denoted as a red + oder blue - sign.*

repulsion between two charged particles only if the two electrical double layers overlap. A more quantitative description of the electrical double layer can be found in chapter B16 by G. Nägele.

Without repulsion colloidal particles would be unstable, i.e. they would aggregate. This does not only happen if the particles are in direct contact, but the Van der Waals attraction between two colloidal particles becomes long-range. Although the Van der Waals attraction between two molecules is only significant at molecular separations, the attraction between two colloidal particles adds together to a significant magnitude also over colloidal distances and increases especially strong if the separation between the surfaces of two particles h is smaller than the radius of the particles.

Adding the electrostatic repulsion and the Van der Waals attraction together, gives the interaction potential energy between the particles, for which an example is shown in fig. 2. General for these interactions is that the Van der Waals attraction dominates at very low h, a potential energy barrier preventing aggregation at intermediate h ($\approx$1.5 nm in fig. 2) which may be larger or smaller and no interaction or a weak secondary minimum at larger h. For the example in fig. 2, a dispersion of these particles will have a good long term colloidal stability, but a reversible aggregation or phase separation due to the secondary minimum may occur. At high concentration, however, the dispersion will be stable and by dilution with the dispersing solvent but then of lower ionic strength (i.e. lower ionic concentration as in the dispersion) the attraction in the secondary minimum can disappear as demonstrated by repeating the same calculation as in fig. 2 with different ionic concentrations in the dispersing solvent.

As seen in fig. 3 the ionic strength has a very strong influence on the colloidal stability, which originates from the strong ionic strength dependence of the thickness of the electrical double layer shown in fig. 1. The lower the ionic strength, the thicker the double layer (it is increasingly difficult to attract counter ions from the ionic solution to the particle), the more long range the repulsion is. A similar effect is also found for the valency of the ions,

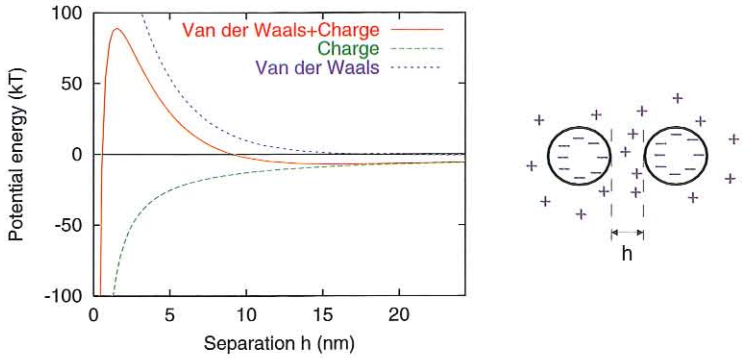


Fig. 2: *Typical potential energy of interaction between two colloidal particles of 100 nm radius, showing the Van der Waals attraction, the electrostatic repulsion (charge) and the sum of these two which gives the total interaction potential.*

as higher charged counter ions are more strongly attracted by the charge on the particle, thus giving rise to thinner double layer and thereby reduced colloidal stability.
To demonstrate the effect of colloidal stability on the preparation of a real colloidal dispersion, fig.4 shows the result for the synthesis of AgBr by the reaction

$$KBr + AgNO_3 \rightarrow AgBr(sol) + K^+ + NO_3^-,$$

using different concentrations for KBr or $AgNO_3$. A red laser beam through the sample tubes shows the light scattering of the samples, where a strong scattering indicates large (i.e. aggregated) particles. If equal and moderate concentrations of KBr and $AgNO_3$ are added together, a non-stable dispersion is obtained, because the sample is to close the the iep of AgBr (fig.4C). Using moderate overall concentrations and an excess of KBr or $AgNO_3$ stable dispersions can be obtained as shown in fig. 4B and D. Repeating the last experiment with higher overall concentrations, however, again results in dispersions with a low stability because of the high ionic strength as shown in fig.4A and E. So, with the

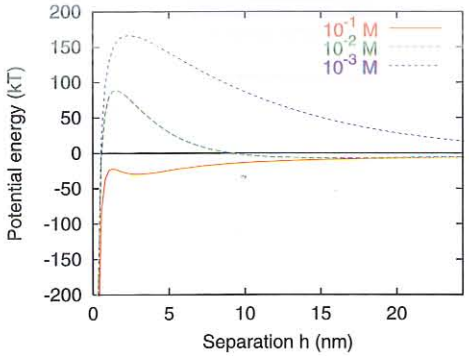


Fig. 3: *The same calculation as in fig. 2 repeated for three concentrations of 1:1 electrolyte in the dispersing solvent.*

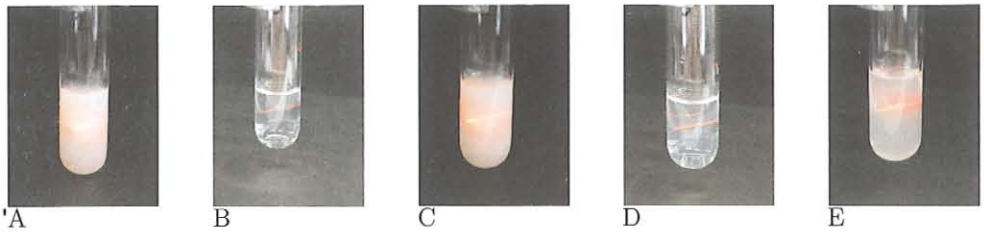


Fig. 4: *Colloidal stability of AgBr, (A) excess KBr, c=0.1 M, (B) excess KBr, c=0.004 M, (C) no excess, iep, c=0.004 M, (D) excess $AgNO_3$, c=0.004 M , (E) excess $AgNO_3$, c=0.1 M*

reaction above one can only prepare dilute dispersions. To obtain higher concentrated dispersions the electrolyte produced by the reaction has to be removed, or an additional stabilizer has to be added be added.

2.2 Steric stabilization

Apart form charge stabilization, colloidal particles can also be sterically stabilized. This is usually done by amphiphiles or polymers that are chemically or physically bound to the surface of the particle. There are two requirements for the stabilizer: (1) the dispersing medium must be a good solvent for the part of the stabilizer that is directed outwards, and (2) the stabilizing layer should be thick enough to overcome the Van der Waals attraction between the particle cores. An example of a chemically bound stabilizer is stearylalcohol bound to silica particles by ether bonds.
The only 2 nm thick coating gives rise to a steep repulsive (hard sphere like) interaction in a good solvent like cyclohexane[4], which is illustrated in fig. 5. By using a dispersing medium for which the solvent quality for the stearyl alcohol coating can be tuned by the temperature, as for benzene, a temperature dependent attraction can be induced between the particles[5] (see fig. 5). Below a critical temperature T_{crit} (in this case approximately room temperature) the particles stick together and the dispersion will form a gel or will

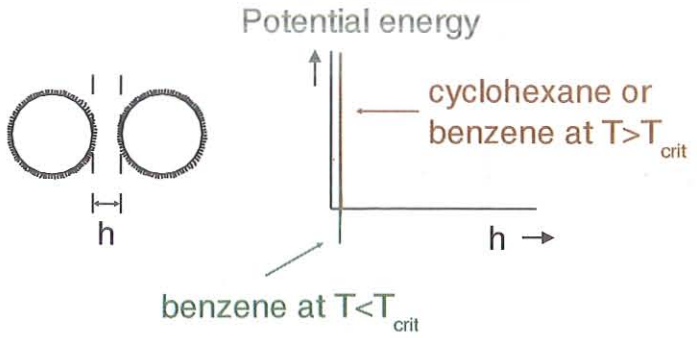


Fig. 5: *Schematic drawing of a thin stearyl coating on silica and the resulting interaction potential energy.*

phase separate. Above T_{crit} the dispersion of these particles will behave similar to the cyclohexane dispersion.
The 2 nm thick stearyl layer is thick enough to stabilize the colloidal silica, which is certainly not a general case. Looking at the Van der Waals attraction of the charged stabilized particle in fig. 2, it is clear that these particles could not be stabilized by a 2 nm thick layer. For silica the stabilization only works because the effective Van der Waals attraction between two silica particles in apolar solvents is very small.

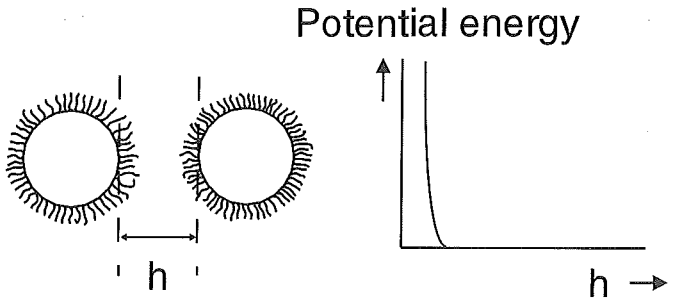


Fig. 6: *Schematic drawing of a relatively thick polymeric stabilizer layer resulting in a soft repulsive interaction potential energy.*

To stabilize particles with a stronger Van der Waals attraction, a thicker polymeric stabilization layer can be used. Of course, such stabilization layer results in a softer interaction potential between the particles, as schematically drawn in fig. 6.

3 Monodisperse particles

3.1 Separation of nucleation and growth

The basic idea to the formation of monodisperse colloidal dispersions is the separation of nucleation and growth, although it is controversial whether this idea holds for all synthesis of monodisperse particles[1, 3]. If the concentration of a substance exceeds its solubility limit, it may be that no solid phase is formed, because usually a considerable supersaturation is needed before the nucleation of a new phase occurs. Of course, for this to succeed it is important to work with clean solutions free of nucleation cores. For the synthesis of colloidal particles one proceeds as schematically drawn in fig. 7. The poorly soluble substance from which the particles are formed, is produced in a slow pre-reaction step, so that it is formed over a longer time during the synthesis. Therefore, at first, the concentration of the poorly soluble substance (from here: concentration) is increasing until the nucleation concentration is reached, then the nucleation starts and the concentration decreases below the nucleation concentration again, after which no new particles are formed, instead the existing particles are growing. The longer the grow time and the shorter the nucleation time, the more monodisperse the particles formed. The grow time can even be prolonged by adding small amounts of reagent, taking care not to induce a new nucleation again, as indicated with the two vertical arrows in fig. 7. If one accidently exceeds the nucleation concentration, then a bimodal distribution of particle

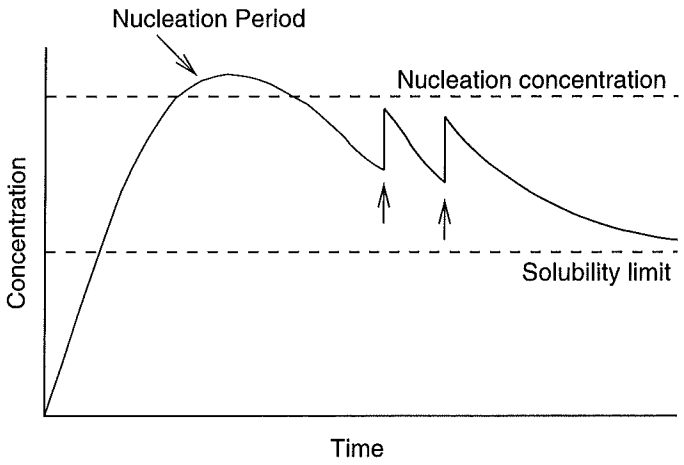


Fig. 7: *Separation of nucleation and growth to produce monodisperse colloidal particles.*

sizes is obtained. An alternative to a slow generation of the poorly soluble substance is to tune the solubility by the temperature, i.e. one starts with a homogeneous solution at high temperature and by decreasing the temperature the solubility decreases giving rise to nucleation followed by growth. The number of nuclei formed during the nucleation period determines the number of particles formed and the length of the growth period determines the size of the particles.

3.2 Synthesis of colloidal silica spheres

An example of the preparation of monodisperse particles by a nucleation and growth mechanism is found in the synthesis of colloidal dispersions of amorphous silica grown from tetraethoxysilane (TES) using ethanol as solvent and ammonia as base catalyst[6, 7]. The synthesis proceeds in two reaction steps, first the TES undergoes hydrolysis

$$Si(OC_2H_5)_4 + 4\ H_2O \rightarrow Si(OH)_4 + 4C_2H_5OH$$

followed by a condensation reaction

$$Si(OH)_4 \rightarrow SiO_2(sol) + 2H_2O$$

in which the colloidal particles are formed. The iso-electrical point of silica is about pH$\approx$2, so the particles are negatively charged in the dilute alkaline ammonia solution. To high concentrations of ammonia, however, decrease the stability of the silica sols, because of the increased ionic strength. The hydrolysis reaction is rate limiting for the synthesis, giving rise to a low intermediate $Si(OH)_4$ concentration. Particles with a radius from 20 upto 1000 nm can be prepared by varying the composition of the reaction mixture.
The reactions shown above are idealized, as it was shown that a significant number of ethoxy groups are included in the final silica particles[8]. Also, the growth is assumed to proceeds through surface condensation of monomers or small oligomers. Although many

studies have been performed on this synthesis and a lot is known, certain observations are not understood completely. For a one step synthesis (i.e. without extra additions of TES) the particle size increases with the water and the ammonia concentration. Explaining this is difficult, as these concentrations determine the reaction kinetics of both the hydrolysis and the condensation reaction, and at the same time they influence the stability of the particles by their influence on the ionic strength as well as the charge on the particles. Then considering the simplifications of the reactions above, it is clear that a complete theoretical description of the synthesis is very difficult.

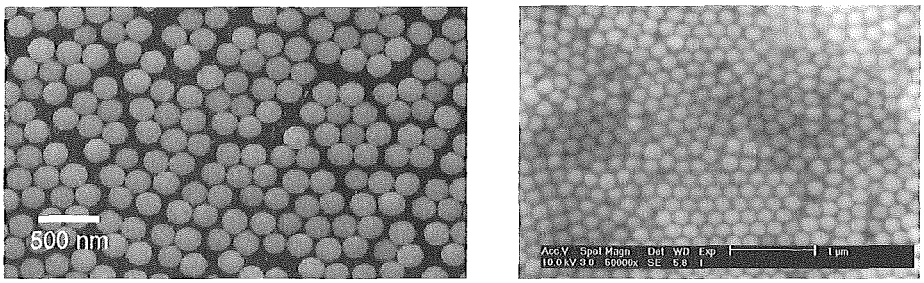


Fig. 8: *Electron microscopy images of silica particles prepared by successive additions of TES.*

Nevertheless, very monodisperse silica particles can be prepared, especially with successive additions of TES. Analyzing the development of the polydispersity of colloidal silica particles grown by repeated additions of TES, demonstrate that the polydispersity, expressed as the standard deviation of the diameter of the particles divided by the mean diameter, is approximately inversely proportional to the mean particle diameter. This implies that the growth of the particles is deposition-controlled growth, although the overall rate is limited by the rate of the hydrolysis. The result of such a synthesis is shown in the electron microscopy images of fig. 8. In the right image the particles are ordered in three dimensions, forming a colloidal crystal similar to the naturally found opal. To obtain a colloidal crystal, however, the polydispersity needs to be below about 6%. So, the polydispersity can have a major influence on the behaviour of colloidal dispersions.

3.3 Non-spherical particles

A synthesis in which nucleation and growth probably are not separated and that results in a polydispersity of about 40% is the preparation of colloidal boehmite rods[9]. The synthesis can be summarize by

$$\text{Al(alkoxide)}_3 + \text{HCl}_{\text{aq}} \rightarrow \text{20 h at } 150^{\text{o}}\text{C} \rightarrow \text{AlOOH(sol)} + \text{alcohol, HCl}_{\text{aq}}, \ldots$$

First, an excess of the aluminum alkoxide is added to the dilute hydrochloride acid solution and stirred for several days. Then, after treating this starting mixture for 20 hours at 150 $^{\text{o}}$C a dispersion of boehmite rods is obtained. The remaining low molecular weight aluminum salts, the alcohols and the hydrochloric acid can be removed by dialysis. Rods with an average length between about 100 and 500 nm can be obtained, depending on

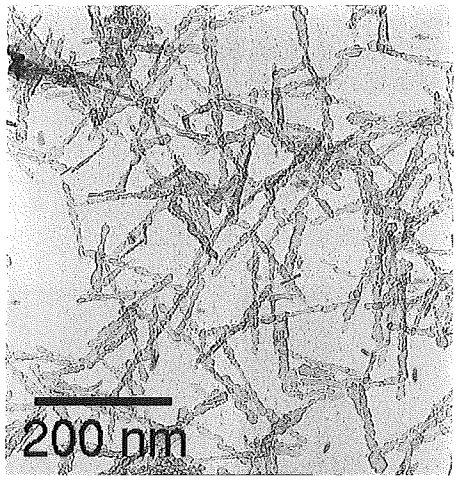


Fig. 9: *Electron microscopy image of rod-like boehmite particles.*

the ratio of alkoxide to HCl in the starting solution. Fig. 9 shows an electron microscopy image of the rod-like boehmite particles.
The mechanism of the particle formation is not well understood. The chemistry is very complex and several intermediate mono- and poly-cation complexes form during particle formation. For instance, aqueous solutions of aluminum chloride are acidic, as the hydrated Al^{3+} ions form protons by the reaction:

$$Al(H_2O)_6^{3+} + H_2O \rightleftharpoons AlOH(H_2O)_5^{2+} + H_3O^+.$$

At pH>3 the equilibrium shifts more to the right and two of those monomers can form a dimer via the condensation reaction:

$$2AlOH(H_2O)_5^{2+} \rightleftharpoons Al_2(OH)_2(H_2O)_8^{4+} + 2H_2O,$$

followed by the formation of other more highly polymerized structures among which $Al_8(OH)_{20}(H_2O)_n^{4+}$ and $Al_{13}O_4(OH)_{24}(H_2O)_{12}^{7+}$ at pH>4. Generally, if the pH is increased the equilibrium shifts to more condensed poly-cations, and eventually at 150^{o}C boehmite is formed. Why the particles are rod-like, is probably connected to the preferential growth of certain crystal planes of the boehmite. The final result is sensitive to the temperature. For instance, repeating the synthesis with exactly the same starting mixture, but then for 72 hours at 85 ^{o}C results in dispersions of gibbsite platelets[10] (see fig. 10).

4 Recrystallization and Ostwald ripening

So far, the stability of colloidal particles against coagulation has been considered. However, if the dispersed solid can occur in an amorphous state, as well as one or more crystalline states, a recrystallization may take place from the amorphous state to a crystalline one, or from a less stable crystalline structure to a more stable one[3]. In this case

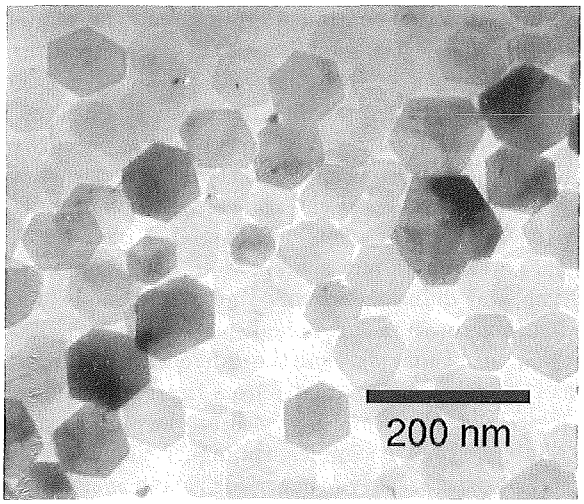


Fig. 10: *Electron microscopy image of gibbsite platelets.*

more stable corresponds to less soluble. For example, amorphous ferric hydroxide has a higher solubility than goethite (α-FeOOH) and akaganeite (β-FeOOH), which have higher solubilities than hematite (α-Fe_2O_3). So, a phase transformation of the particles through the dissolved state can occur, i.e. the solid A of higher solubility will be dissolved and the solid B of lower solubility will grow by deposition of the solute dissolved from solid A, as is schematically drawn in fig. 11. Generally, the concentration of the solute in the dispersing solution is somewhere intermediate between the two solubilities. Depending on the dissolution and growth rates, the concentration may be more close to the solubility concentration of either solid state A or solid state B. If the growth rate constant is much greater than the dissolution rate constant, the concentration of the solute is close to the lower solubility concentration, and the dissolution is rate-determining (dissolution-controlled growth). The other way around, if the dissolution rate constant is much greater than the growth rate constant, the solute concentration is close to the higher solubility concentration, and the growth is rate-determining (deposition-controlled growth). Alternatively, if both the dissolution and the growth are very fast, the diffusion of the solute

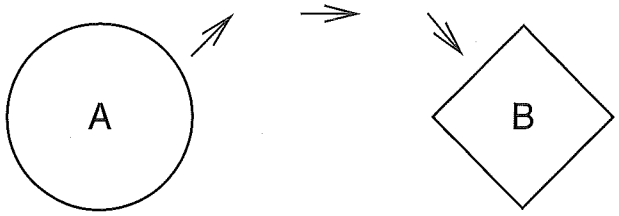


Fig. 11: *Schematic drawing of the recrystallization of a particle of solid state A of higher solubility to a particle of solid state B of lower solubility through the intermediate dissolved state. The arrows indicate net transport of material.*

becomes rate-determining (diffusion-controlled growth) and the solute concentration decays from the particle with the higher solubility to the particle with the lower solubility. Nevertheless, without nuclei of the more stable solid, the solute concentration may be to low for nuclei to form and recrystallization may not occur at all. Even if nuclei of a more stable state exist, recrystallization may still be (very) slow, especially when the solubility of both solid states is (very) low. Practically, these kinds of recrystallizations can be used for the preparation of monodisperse particles using separation of particle nucleation and growth, when solid particles of higher solubility are used as reservoir of the monomers for the growth of the final particles of lower solubility. In doing so, the distinction between dissolution-, deposition- and diffusion-controlled growth is important for adjusting the supersaturation during the growth of the monodisperse particles.
A similar process is Ostwald ripening[3]. Here the difference in solubility does not originate from different states of the solid, but originates from the difference in size of the particles in the dispersion. Especially very small particles are less stable due to the interfacial energy and have a solubility that is significantly higher than the solubility of the bulk material. Lifshitz and Slyozov[12] and Wagner[13] gave a mathematical description of Ostwald ripening, referred to as the LSW theory, in which either diffusion or the reactions at the surfaces of the particles is rate limiting. For diffusion limited growth of a dispersion that reached the steady state form of the size distribution, the rate law is given by[11]

$$\overline{r}^3 - \overline{r_0}^3 = Kt\,,$$

where t is the time, $\overline{r}$ is the mean particle radius and $\overline{r_0}$is the particle radius at t=0. The constant K is given by

$$K = \frac{8\gamma D V_m^2 C_\infty}{9RT}\,,$$

with γ the interfacial energy, D the diffusion coefficient of the solute, V_m the molar volume, C_∞ is the equilibrium concentration at a flat surface, R is the gas coefficient and T the temperature. So, the larger the particles the lower the influence of Ostwald ripening becomes. Also the solubility is an important factor. Generally, materials with a higher solubility are more liable to Ostwald ripening. If the surface reactions (dissolution and deposition) become slower as the diffusion, Ostwald ripening becomes slower too. This also means that Ostwald ripening can be reduced by the adsorption of some species on the surface of the particle, thereby reducing the surface reaction rate of the primary material.

Practically, Ostwald ripening can be used to prepare monodisperse particles in the same way as for recrystallization, by dissolving particles with a higher solubility, here smaller particles, to grow particles of lower solubility, here larger particles. In this case, the supersaturation during particle growth can be kept constant, and an accidental second nucleation can be prevented. In principle, the supersaturation for the larger particles can be tuned by controlling the size of the small dissolving particles. The preparation of silver halide particles, widely used in the photographic industry, is essentially based on the Ostwald ripening process[3]. Very small particles, which are instantly generated by continuous introduction of silver and halide ions, act as a reservoir of silver and halide ions for the growth of the larger stable particles. The method used for such a synthesis is the so called controlled double-jet system, which is shown in fig. 12. The synthesis is performed by introducing silver nitrate and a halide into a gelatine solution at precisely controlled rates. The gelatine acts as an stabilizer, to prevent aggregation at high ionic

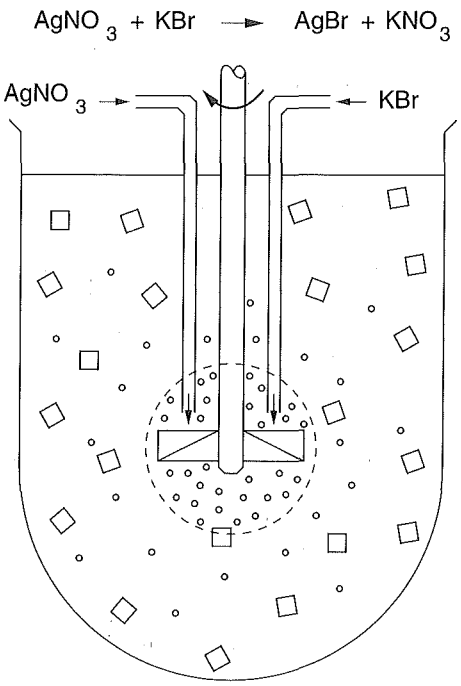


Fig. 12: *Double jet system for the preparation of silver halide particles, showing the nucleation zone and the Ostwald ripening zone.*

strength. Very fine primary particles are produced around the injection points of the reactants. These primary particles are mixed together with the bulk solution, where the relatively large particles grow, resulting in dissolution of the smaller primary particles. Thus, a region in which the small primary particles are produced, coexists with a region in which the larger particles grow at the expense of the small primary particles. At the start of the synthesis, the number of stable nuclei increases because of the increasing supersaturation, but when a sufficient number of stable nuclei has been formed, they are able to absorb all of the solute formed by the dissolution of the small primary nuclei. From this moment, the number of particles remains constant and the primary particles formed in the nucleation zone only act as source of solute for the growing particles in the Ostwald ripening zone. As nucleation and growth are separated in this system, monodisperse silver halide particles can be formed with this method.

5 Characterization

A large number of methods are used to analyse the result of a colloidal synthesis. Here the discussion is restricted to a few common methods that are more or less specific for the characterization of colloidal dispersions. However, one method that is certainly not specific for the analysis of colloidal particles, but should at least be noted here is *electron microscopy*, because it probably is the most important technique with which direct images

of colloidal particle can be obtained. A few examples of images of colloidal particles have been shown already. The most important possibilities of this method are obvious, and more detailed discussions are outside the scope of this chapter.

Scattering methods

Scattering of light, x-rays, and neutrons[1, 3] are methods to obtain information about the size, internal structure and shape of colloidal particles directly in the dispersion. The possibility to measure directly in the dispersion is an important difference compared to electron microscopy. For instance, for two particles touching each other on an electron microscopy image, it may not be clear whether they sticked together already in the dispersion, or whether this is an effect of the sample preparation. Electron microscopy, however, is the first method of choice if the structures in the dispersion become to complicated for a direct interpretation of the scattering results, for instance, for broad size distributions of non-spherical particles. In this case, a combination of both methods can be used, in which the dimensions obtained from electron microscopy images are used as a basis to calculate theoretical scattering curves that are compared to the measured ones. In this way one can still check whether the electron microscopy image indeed reflects the situation in the dispersion.
In a scattering experiment, a monochromatic beam of light, x-rays, or neutrons is directed on the sample and the scattered intensity is measured as a function of the scattering angle θ, which is usually plotted as the magnitude of the scattering scattering vector $\overrightarrow{q}$, given by

$$|\overrightarrow{q}| = \frac{4\pi \sin(\theta/2)}{\lambda},$$

with λ the wavelength of the light, x-rays or neutrons in the sample. X-rays and neutrons used have typical wavelengths of 0.1-1 nm. Therefore, small scattering angles are used, to obtain small enough scattering vectors and are commonly referred to as small angle x-ray scattering (SAXS) and small angle neutron scattering (SANS). An example of a SAXS measurement is shown in fig. 13. For larger particles similar results can be obtained by static light scattering (SLS).
Another type of scattering measurement that has to be noted here is dynamic light scattering (DLS), also called photon correlation spectroscopy. For DLS the correlation between fluctuations of the scattered intensity is analyzed, from which the diffusion coefficient of the particles can be derived. The diffusion coefficient can be related to the size of the particles. More detailed information about scattering methods can be found in several other chapters.

Electrophoresis

With electrophoretic measurements information about the electrical charge on colloidal particles can be obtained[2, 1, 3], which is important in relation to the their colloidal stability as discussed above. In an electrophoretic measurement, an electrical field is applied across the colloidal dispersion and the velocity $\overrightarrow{v}$ of the particles is determined. Note, that the electrical field is directly applied across the dispersion, without the aid of a gel as is commonly used for the analysis of biological materials, where the relative velocity is usually determined by treating the gel with a staining solution afterwards.

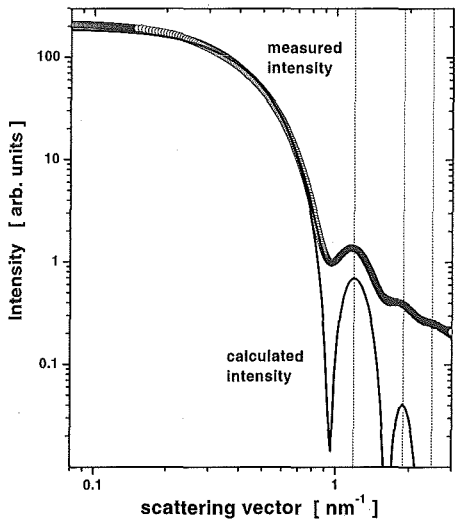


Fig. 13: *SAXS measurement of a dilute sample of small 10 nm spherical particles. The curve denoted as "calculated intensity" is calculated for monodisperse and homogeneous spheres. Including polydispersity and internal structure of the spheres into the calculation, results in a very good agreement between measurement and theoretical calculation.*

Leaving out the gel, however, allows for a more fundamental analysis of the electrophoretic experiment. For particles that are large enough, the velocity can be measured by use of a light microscope. For smaller particles the velocity is measured by Laser Doppler Velocimetry.
The result of an electrophoretic measurement is expressed as the electrophoretic mobility u, defined by

$$u = \frac{\overrightarrow{v}}{\overrightarrow{E}},$$

with $\overrightarrow{E}$ the electrical field strength across the sample. To relate u to the electrical potential or charge of a particle the theory of the electrical double layer around the particles has to be used. Simple approximations only exist when the electrical double layer thickness is much smaller or much larger than the size of the particle. A mathematical treatment of one chapter can be found in ref.[2].

Sedimentation

If a dispersion of larger particles is stored for some time, mostly the particles will settle to form a concentrated sediment at the bottom. For very dilute dispersions of spherical particles, the sedimentation velocity s_0 is given by[2]

$$s_0 = \frac{2r^2 \Delta\rho\, g}{9\eta},$$

with r the radius of the particles, $\Delta\rho$ the density difference between the particles and the surrounding liquid, g the gravitational acceleration and η the viscosity of the liquid. The density of the particles can be determined from the density of a dispersion of known concentration, after which r can be obtained directly from a measurement of s_0. Accurate measurements can be made in a simple test tube, provided that extreme care is taken to prevent temperature fluctuations. For smaller particles the sedimentation process can be accelerated by centrifugation. Accurate measurements, even of samples with a multimodal particle size distribution, can be obtained with the analytical ultracentrifuge, which is equipped with a special optic to measure the complete sedimentation (concentration) profile during the centrifugation process.

6 Summary

A few examples have been given of the synthesis and characterization of colloidal dispersions. It was discussed that it is essential to take care of the colloidal stability of the particles, which can be done by charge and steric stabilization. These stabilizations also determine the interaction potential between the particles and thereby will have a large influence on the properties of the dispersions. Very monodisperse particles can be prepared by the separation of nucleation and growth.
Much more detailed information on colloidal synthesis of monodisperse particles can be found in the book of Sugimoto[3].

Acknowledgment

The author thanks Dr. T.A.J. Lenstra, Dr. S. Rathgeber and Dr. W.F.C. Sager for providing several images for this chapter.

References

[1] D. Fennell Evans and H. Wennerstrm, *The Colloidal Domain : Where physics, chemistry, biology, and technology meet* (VCH, Weinheim, 1994)

[2] W.B. Russel, D.A. Saville and W.R. Schowalter, *Colloidal Dispersions* (Cambridge University Press, 1989)

[3] T. Sugimoto, *Monodispersed Particles* (Elsevier, Tokyo, 2001)

[4] A.K. van Helden, J.W. Jansen and A. Vrij, J. Colloid Interface Sci. **81**, 354 (1981)

[5] J.W. Jansen, C.G. de Kruif and A. Vrij, J. Colloid Interface Sci. **114**, 481 (1986); P.W. Rouw and C.G. de Kruif, Phys. Rev. A **39**, 5399 (1989); A.T.J.M. Woutersen, J. Mellema, C. Blom and C.G. de Kruif, J. Chem. Phys. **101**, 542 (1994)

[6] W. Stber, A. Fink and E. Bohn, J. Colloid Interface Sci. **26**, 62 (1968)

[7] A. van Blaaderen, J. van Geest and A. Vrij, J. Colloid Interface Sci. **154**, 481 (1992)

[8] A. van Blaaderen and A.P.M. Kentgens, J. Non-Cryst. Solids **149**, 161 (1992)

[9] P.A. Buining, C. Pathmamanoharan, J.B.H. Jansen and H.N.W. Lekkerkerker, J. Am. Ceram. Soc. **74**, 1303 (1991)

[10] A.M. Wierenga, T.A.J. Lenstra and A.P. Philipse, Colloids Surfaces A **134**, 359 (1998)

[11] E.M Wong, J.E. Bonevich and P.C. Searson, J. Phys. Chem. B **102**, 7770 (1998)

[12] I.M. Lifshitz and V.V. Slyozov, J. Phys. Chem. Solids **19**, 35 (1961)

[13] C.Z. Wagner, Electrochem. **65**, 581 (1961)

A6 Microemulsion templating

W.F.C. Sager
Institut für Festkörperforschung-Weiche Materie
Forschungszentrum Jülich GmbH

Contents

1 Introduction 2

2 The microemulsion template 4

2.1 Surfactant self-assembly, micelles and microemulsions 6
2.2 Phase behaviour and structural evolution 10
2.3 Statics and dynamics of droplet phases 18
2.4 Comparison between micro- and macroemulsions 20

3 Precipitation of (inorganic) nanoparticles in droplet phases 23

3.1 Spherical nanoparticles 24
3.2 Nanorods and filaments 27

4 (Micro)emulsion polymerisation 28

4.1 Classical emulsion polymerisation 28
4.2 Polymerisation in droplet and bicontinuous microemulsions 30

5 Templating of crystalline phases 32

1 Introduction

Surfactant molecules have for a long time been employed in stabilising finely dispersed matter since they have, due to their amphiphilic character, the tendency to adsorb at hydrophilic/hydrophobic interfaces such as *water/air*, *water/oil* or *water/(hydrophobic) solid* and *oil/(hydrophilic) solid*. In many inorganic or organic (colloidal) particle preparation routes, different types of surfactants have been added to stabilise the formed particles sterically or electrostatically against (irreversible) aggregation (and, if applicable, coalescence) processes. Besides for their stabilising properties, surfactants have progressively gained more attention because they self-assemble under certain conditions in binary and ternary systems of surfactant(s), water and/or oil into *thermodynamically stable nano-heterogeneous systems,* with a variety of different morphologies.

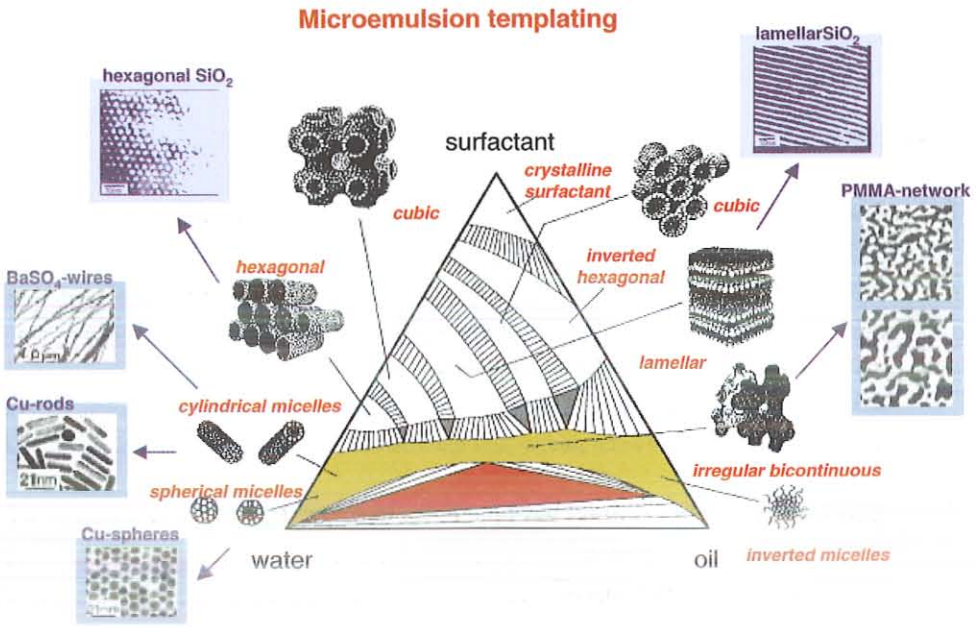


Fig. 1: *Schematic Gibbs triangle (central part) displaying self-assembling structure formation in binary and ternary surfactant systems, stabilised by a strong amphiphile close to its balanced state [4]. The existence regions of the different phases together with all corresponding two- and three-phase equilibria are presented. The compositions of the coexisting phases are indicated by the end points of tie-lines in the two-phase regions, and by the corners of the three-phase triangles. More details about the phase diagram are given in Section 2.2. The outer part shows examples for solid phases of different morphologies that have been prepared from* the indicated *self-assembled surfactant phases and will be described in more detail in Sections 3-5.*

These self-assembled systems can in principal be used as a kind of ***micro-*** or better ***nanoreactor*** to separate and control nucleation and growth processes and as ***template*** to direct growth and to control the morphology of the forming solid phase. Over the last two to three decades the knowledge of *self-assembled surfactant systems* has increased dramatically and a number of these systems have thoroughly been investigated for advanced materials synthesis[1],[2],[3].

Fig.1 shows in the central part a schematic phase diagram that displays (the existence regions of) the variety of morphologically different self-assembled surfactant phases together with their multi-phase equilibria that can principally form in a ternary system of water, oil and a medium- or long-chain surfactant around it's balanced state [4]. The structural polymorphism ranges, at low surfactant concentrations, from spherical and cylindrical micellar surfactant aggregates via swollen micelles and oil-in-water (o/w) droplet microemulsions on the water rich side to water-in-oil (w/o) droplet microemulsions and inverted micelles on the oil rich side, whereby the polar head group of the surfactants is turned inside. At intermediate water/oil ratios bicontinuous microemulsions are stable which consist of an interwoven network of water and oil channels. At higher surfactant concentrations hexagonal or cubic phases are formed, consisting of micellar and reverse micellar aggregates packed into ordered crystalline arrays, as well as lamellar liquid crystalline phases that are built up by a stack of planar surfactant (bilayer)sheets separated by water. The phase diagram and the general phase evolution in binary and ternary self-assembled surfactant systems will be discussed in detail in *Sections 2.2* and *2.3*. The outer part of *Fig.1* shows a selection of solid phases with different morphologies that have been prepared from the indicated self-assembled surfactant systems. Besides thermodynamically stable surfactant self-assemblies, also kinetically stabilised systems such as ordinary emulsions and uni-or multilamellar vesicles have been utilised. As can already be seen from these examples, self-assembled surfactant systems have successfully been employed in the synthesis of differently shaped organic and inorganic *nano*particles and, more recently, of *nano*structured or *nano*porous (composite) materials [5]. Reflecting the changing demands in advanced materials science, emphasis has shifted from first preparing only (monodisperse) spherical particles to controlling the particle morphology and finally to manufacturing well-defined nanostructured materials. Since it has been realised, that new developments in materials science synthesis are possible only if research efforts are not solely concerned with finding novel materials but also with the morphological tailoring of the desired materials, special attention has been paid towards the end of the last century to investigate new techniques for microstructural designing. These efforts include the preparation of well-defined particles of low polydispersity and of increasingly smaller dimensions down to the nanometer scale, ordering of these particles into two- and three-dimensional arrays, directed growth, hierarchical structuring and control from the nano- to the meso-scale. In most of these processes, solid phase preparation and precipitation in surfactant self-assemblies has played a substantial role. In the case of mono-sized nanoparticles, precipitation in micelles or w/o microemulsions has often been the first successful route to prepare such small particles for different inorganic materials and has therefore been employed to study quantum size effects [6]. The preparation of ordered mesoporous materials such as silica by precipitation in crystalline surfactant phases opened a fast developing field in the area of hybrid inorganic-organic mesoporous solids and, especially, zeolites [2],[7].

The basic idea of using the internal (dispersed) phase of the (thermodynamically) stable systems as nanoreactors lies in the possibility of achieving a controlled compartmentalisation and structurisation of the reaction medium. Precipitation and thus formation of the solid phase can then be controlled since it takes place in a more or less isolated and (ultra-)small space as,

e.g., the critical supersaturation of the dissolved (solid phase) precursor is reached. (Direct) templating by precipitation from the continuous medium onto the surface of preformed micellar structures can be obtained if the precursor species of the forming solid phase undergo interactions with the surfactant head groups. This allows (molecular) orientation and directed ordering. The principle of both the defined isolation of space and the structural templating has been adapted from nature. Natural examples are the preparation of magnetic particles in bacteria or the *biomineralisation* processes in algae [8]. Precipitation in self-assembling systems has therefore increasingly been studied for (a better understanding of) *biomimetic approaches* and the development of novel preparation routes which are based on them [1],[8]. But one should keep in mind, that surfactant self-assembled systems are highly dynamic systems and that the precipitation processes taking place in them can be quite complex due to the large number of possible interactions between the mould and the templated structure. Preparation processes might therefore not always be straightforward. To obtain solid phases that are commensurate in size and shape with the self-assembled surfactant system from which they are formed, detailed knowledge on both sides: the templating system as well as the precipitation reaction leading to the desired solid phase formation, is a prerequisite. Generally, the final morphology of the solid phase depends on the reaction kinetics (material exchange and solid phase formation), the reorientation of the surfactant self-assembled system as well the interactions between the surfactant and the precipitating solid. In the latter case surfactants may block oriented growth due to specific adsorption of the surfactant onto certain surfaces (crystal net plains) of a forming crystalline phase or direct ordering and aggregation of nanosized particles into complex inorganic particle-surfactant assemblies that can reach mesoscopic length scales [2],[9],[10]. Since microemulsion templating has developed into a broad field and offers a rich playground for new materials synthesis routes, only a view examples (see *Fig.1*) to explain the main strategies and principles have been selected for this contribution.

The Chapter is organised as follows: In *Section* 2 the microemulsion template will be introduced, whereby special attention is paid to explaining under which conditions the different self-assembled surfactant phases form, allowing for a targeted morphological tailoring of the templating mould. Basic features and trends in the phase evolution and the tuning of the different morphologies will be explained within the concept of the *curvature energy*. Most emphasis is laid on the structural changes and (exchange) kinetics of droplet phases. *Section 3* deals with the preparation of well-defined spherical and rod-like inorganic nanoparticles from single and aggregated w/o droplet phases. In *Section 4*, o/w (micro)emulsion droplet phases and bicontinuous microemulsions are discussed in view of the preparation of latex particles and polymer networks. *Section 5*, finally, introduces basic ideas of employing different crystalline phases to prepare ordered mesoporous solids.

2 The microemulsion template

Surfactant molecules can, due to their amphiphilic nature, stabilise a number of different microscopically heterogeneous systems. In the *binary* water–surfactant and oil–surfactant systems, surfactants self-assemble into *normal* (hydrophobic part inside) and *reverse* (hydrophilic part inside) *micellar aggregates*, respectively, with well-defined aggregation numbers. At high surfactant concentration different liquid crystalline phases form. The morphology of the micellar aggregates depends on the geometry and concentration of the surfactant molecules and (external) variables such as temperature or concentration of added

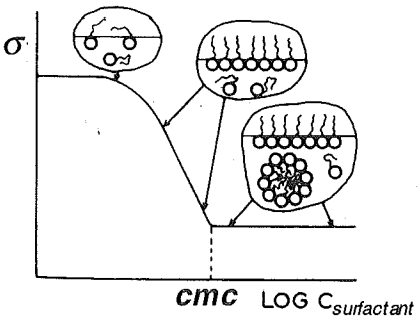
salt. In the *ternary* water–oil–surfactant system, transparent and thermodynamically stable microemulsions can form under certain conditions. These microemulsion phases consist of structurally well-defined nanosized domains of water and oil, separated by a monomolecular surfactant film. The morphology and the characteristic length depend on the water-to-oil ratio and the elastic properties (e.g., spontaneous curvature and rigidity constants) of the surfactant film. Generally, droplet phase microemulsions exist if either oil or water are only present in small amounts, whereas bicontinuous microemulsions are found at comparable amounts of water and oil. The spontaneous or natural curvature of the interfacial surfactant film depends on the geometric properties of the hydrophilic and hydrophobic moieties of the surfactant molecule and these, in turn, on their interactions with water and oil, respectively. If the temperature and/or ionic strength of the aqueous phase is varied, a rich phase behaviour is generally revealed, whereby microemulsion phases can coexist with water and/or oil excess phases as well as liquid crystalline phases forming two- and three-phase equilibria. If two-phase systems, consisting of a microemulsion phase in coexistence with a water or oil excess phase, that generally form at low surfactant concentrations, are mechanically agitated, ordinary or macro-emulsions can be obtained with a milky appearance. In this case the excess phase has mechanically been dispersed into, generally, micrometer-sized droplets, that can, due to the adsorption of surfactants onto the newly formed interface, be kinetically stabilised. The interface is not saturated and the size of the droplets depends on the mechanical energy applied to prepare the emulsion and on the outcome of coalescence and coagulation processes as well as Ostwald ripening that finally lead to phase separation.

In this section self-assembled as well as kinetically stabilised surfactant systems will be introduced in view of their application as precipitation media and as templates. Since microemulsion phases form, so-to-say, at intermediate conditions between the (binary) micellar (nanometer scale) systems and macroemulsions (micrometer scale), they will be treated in this context. *Section 2.1* starts with the binary systems, whereby surface activity, micelle formation and the factors influencing the morphology of the micellar phase formed are discussed. The latter will be performed within the framework of a geometrical model (packing parameter approach). For more details on the different classes of surfactants, micellar systems and a description of the structural evolution within the curvature energy concept, the interested reader is referred to *Chapter **B8*** of this course and more advanced text books such as [11],[12],[13] and [14]. Microemulsions systems will be introduced in the second part of *Section 2.1* and their phase behaviour and structural evolution are described in *Section 2.2*. It has been found that the properties of the microemulsion phases are dominantly determined by those of the interfacial surfactant film, that separates the water and oil domains. Basic features of the microemulsion phases are described within the framework of the curvature free energy. This concept is based on the statistical mechanics of curved interfaces, whereby the main properties are described in terms of spontaneous curvature and the rigidity constants for mean and Gaussian curvature. Since a full theoretical treatment is not in the scope of this Chapter, emphasis is only paid to explain the general trends in (i) the phase behaviour and (ii) the structural evolution of the microemulsion phases and (iii) the macroscopic interfacial tension between microemulsion phases and water and/or oil excess phases in the two- and three-phase equilibria observed. In this context, formulas are only derived for droplet phases. More information on the curvature free energy and its application to more complex (microemulsion) phases, e.g. isotropic and crystalline bicontinuous phases, can be found in *Chapters **B9*** and ***C6*** of this course and [15]. Further knowledge on microemulsions can be obtained from [13],[14] and [16]. To obtain a better understanding of the precipitation reactions performed in droplet phases, *Section 2.3* deals with the stability and

exchange kinetics of microemulsion droplet phases. A comparison with ordinary emulsion droplet systems is finally given in *Section 2.4.*

2.1 Surfactant self-assembly, micelles and microemulsions

Gibbs adsorption isotherm



Packing parameters

	*v/al*<1/3	spherical micelles
	*1/3<v/al*	cylindrical micelles
	*1/2<v/al*<1	vesicles, flexibile bilayers
	*v/al*≈1	lamellae, planar bilayers
	*v/al*>1	inverse cylindrical and spherical micelles

Fig. 2: *Left: Typical adsorption isotherm (schematically) for an aqueous surfactant solution: Surface tension σ plotted against the logarithm of the surfactant concentration c_s [17]. The sketched insets show the state of the surfactant molecules in the water phase (bulk) and at the water/air surface. Right: Surfactant parameter range for different surfactant aggregates [11].*

The binary water–surfactant system: surface activity and micelle formation.
Amphiphiles are surface active molecules. If a surfactant is added to an aqueous solution, it will be distributed between the surface (*water/air* surface) and the bulk water phase. The distribution coefficient depends on the solubility of the surfactant molecules in water. Upon addition of surfactant, the surface tension decreases due to the presence of the surfactant molecules at the water/air surface. The surface pressure Π caused by the spreading of the surfactant molecules is given by $\Pi = \sigma_o - \sigma$. Whereby σ is the surface tension at a given surfactant concentration c_s and σ_o the surface tension of the bare surface without added surfactant. *Fig.2* shows a schematic plot of the *Gibbs adsorption isotherm*, typically observed for surfactants in aqueous solution. The surface excess Γ, excess concentration of surfactant in the interface, is given by

$$\Gamma = -\frac{1}{RT}\left(\frac{d\sigma}{d\ln c_s}\right)_T, \qquad (1)$$

whereby R is the gas constant and T the absolute temperature. At a certain concentration, the so-called ***critical micelle concentration*** cmc, it becomes energetically more favourable for the surfactant molecules to aggregate into micelles. The area of the surfactant in the saturated macroscopic, flat interface can for surfactant concentrations close to the cmc be calculated from the surface excess [18]. Above the cmc the surface tension stays constant, since all additionally added surfactant molecules form micelles in the bulk water phase and the surface excess concentration remains nearly constant. Plateau values for the surface tension ($c_s > c_{cmc}$) lie for conventional surfactants typically in the range of 25-35 mNm^{-1}.

The driving force for *micellisation* is mainly of entropic origin. The contribution to the free energy that favours micelle formation stems from a gain in entropy of the surrounding water molecules (*hydrophobic* or *Tanford effect*) [12],[13]. The presence of the hydrocarbon tail in the molecular dispersed state (below the cmc) induces an increased ordering of the surrounding water molecules (water cluster formation), which is not the case if the hydrocarbon chains form the micellar core and are shielded by the polar head groups from the bulk water phase. Since the operating aggregation forces are opposed by the repulsion between the head groups, finite (self-assembled) micellar aggregates are formed with a well-defined number of surfactant molecules N_p per micelle (N_p~50-80). The size and shape of the micellar aggregates depend on the geometry of the surfactants. This dependence can well be described by a geometric model that is based on the (critical) ***packing parameter*** $v/(al)$, whereby l and v correspond to the length and volume of the aliphatic tail and a corresponds to the effective head group area. N_p can be determined by dividing the total volume of a given micellar aggregate by v or the total surface area by a. For spherical micelles, a packing parameter of $v/(al) \leq 1/3$ is obtained if one assumes that the radius of the micelle $R_{micelle}$ cannot exceed l

$$N_p = \frac{\frac{4}{3}\pi R_{micelle}^3}{v}, N_p = \frac{4\pi R_{micelle}^2}{a} \rightarrow \frac{v}{al} \leq \frac{1}{3}. \quad (2)$$

While for a saturated hydrocarbon chain, v and l can easily be calculated from the van der Waals radii, a depends not only on the size of the head group but also on pH, surfactant and electrolyte concentration for ionic surfactants [13]. Head group areas are usually determined from measured values of the size of the micelle and the number of surfactant molecules per micelle. The head group area is typically in the range of 55-70 Å^2. For ionic surfactants, the effective head group area decreases if the ionic strength of the aqueous phase increases by the addition of salt. Due to screening of the electric charge at higher ionic strength, the repulsion between the head groups of neighbouring surfactant and consequently the effective head group area is smaller. For commonly used nonionic surfactants that are composed of a hydrocarbon chain and a water-soluble ethyleneoxide chain (C_iE_j, whereby the subscripts denote the number of methyl C_i and oxyethylene E_j repeats), the head group area increases with j and decreases for a given j with increasing temperature. Increasing temperature destroys the hydrogen bonds between the ethyleneoxide oxygen atoms and the surrounding water molecules and results in a smaller effective head group area.

The different possible packing geometries of surfactant molecules are listed in the table of *Fig.2* together with the ranges of packing parameters and the structure of the aggregates they form. Generally, surfactants shaped in the way that the effective head group takes more space than the tail region ($v/al<1/3$) form spherical micelles. If v/al approaches 1 first cylindrical micelles and finally (almost) flat films form as they occur in vesicles (bilayers) and lamellar crystals. If $v/al>1$, the surfactants are not anymore soluble in water. Dissolved in an apolar solvent (oil) they will form inverse micelles. In this case the head groups form the interior of the reverse micelle and are shielded by the apolar moiety from the bulk oil. Turning from strongly curved micelles to flat surfactant sheets and even to oppositely curved aggregates (inverse micelles) can generally be achieved by either increasing the bulkiness (volume) of the hydrophobic moiety (e.g. double tailed instead of single tailed surfactants) and/or by decreasing the head group area. The latter can be realised by addition of salt in the case of ionic surfactants, decrease in j and increase in temperature in the case of nonionic surfactants and/or addition of long chain alcohols in multicomponent mixed systems. In the binary water–surfactant system micelles are generally formed at concentrations above the cmc. At

high surfactant concentrations, different liquid crystalline phases may exist, including hexagonal, cubic and lamellar phases (see water–surfactant side of the Gibbs triangle in *Fig.1*). With increasing surfactant concentration in water *v/al* may rise up to values of above 1. For a description of the different morphologies of micellar and crystalline structures in binary systems within the curvature free energy concept, the reader is referred to *Chapter B8* of this course.

The ternary water–oil–surfactant system: microemulsions and (multi)phase equilibria. If small amounts of a third, with water barely miscible, component, such as a medium- or long chain alkane (*oil*), are added to micelles in water (or if water is added to reverse micelles in oil), this third component can be solubilised in the interior of the (reverse) micelles. In the case of normal micelles, first swollen micelles and then *o/w* microemulsions are formed upon the addition of oil, while *w/o* microemulsions form from reverse micelles upon addition of water. If larger amounts of the third component are added, a number of different (coexisting) phases may form and the phase diagram can become rather complex, especially at higher surfactant concentrations.

Microemulsions are structurally well-defined self-organising mixtures of water, oil, and surfactant(s) that can form a wide variety of thermodynamically stable (mainly transparent) phases. These comprise besides droplet phases that consist of more or less spherical nanosized (20-300Å) droplets of oil in water (o/w microemulsions or L_1-phase) and water in oil (w/o microemulsions or L_2-phase), also bicontinuous mono- and bilayer (L_3) phases. The latter two consist of an interwoven network of water and oil channels, separated by a monomolecular surfactant film (see *Fig.3*). If the temperature and/or ionic strength of the aqueous phase is varied, a rich phase behaviour is generally revealed, whereby microemulsion phases can coexist with water and/or oil excess phases as well as liquid crystalline phases forming two- and three-phase equilibria. The different phases and coexistence regions occurring in a three-component water, oil and surfactant system can be represented in a triangular phase diagram (Gibbs triangle). At each point in the diagram, the concentration of each species is determined by drawing a line parallel to the corresponding axis, lying along one edge of the triangle. The central part of *Fig.1* shows a Gibbs triangle displaying a variety of structurally different phases, which can principally form in a ternary system of a strong amphiphile close to its balanced state, together with their two- and three phase coexistence regions. At high surfactant concentrations the different liquid crystalline phases reach from the water–surfactant and oil–surfactant (inverse structures) sides into the triangle. These phases form at intermediate surfactant concentration two and three-phase equilibria with the, at lower surfactant concentrations existing, microemulsion phases (lower 1/3 of the diagram). At the balanced state of a surfactant, the volumes of the hydrophilic and hydrophobic moieties are nearly equal ($v/al \approx 1$) and the interfacial surfactant film is on average not curved. Therefore, bicontinuous microemulsions (and lamellar and bicontinuous crystalline phases at high surfactant concentrations) take in the central part of the Gibbs triangle. Isotropic bicontinuous microemulsions exist only over a small surfactant concentration range at comparable amounts of water and oil. At lower surfactant concentrations, the amount of surfactant present is not high enough to form a bicontinuous structure over the whole sample. In this case the sample splits up into a bicontinuous middle phase and almost pure water and pure oil excess phases. The compositions of the three coexisting phases are given by the corners of the three-phase triangle (marked in red). According to the Gibbs phase rule, a three-component system can separate into a maximum of three coexisting isotropic phases. The general phase behaviour and the structural evolution in microemulsion systems is described in *Section 2.3.*

Microemulsions posses a huge internal interface, since the size of the water and/or oil domains ranges from about 20-500Å. If one considers 10 g of a microemulsion that consists of, e.g., water droplets in oil and contains 1g surfactant and 1g water, the interfacial area formed by the surfactant film amounts to about $500m^2$. Such large internal interfaces can only be formed if the interfacial tension of the macroscopic water/oil interface has become very small. In these cases, the gain in entropy leads to a spontaneous microemulsion formation (*spontaneous emulsification*). Water/oil interfaces that are saturated with a surfactant (plateau values in *Fig.2*) reach values of $\sigma = 10^{-1}$-10^{-3} mNm^{-1}. At these low interfacial tensions curvature effects start to play a (dominant) role. As will be shown in the following subsection (*Section 2.2*), this curvature energy is responsible for the rich phase behaviour displayed.

Historically, the droplet phases are the first and also the most studied microemulsion structures. The reason for this lies probably in the fact that their existence regions are larger and thus easier to find, if, e.g. the temperature or salt concentration is varied. The term "*microemulsion*" was originally coined by Hoar and Schulman [19] in 1943 and was applied to a transparent sample, prepared by emulsifying an oil in an aqueous surfactant solution whereby a fourth component, a so-called cosurfactant (generally an alcohol of intermediate chain length such as hexanol) has consecutively been added. In titrating the emulsion system with the alcohol, they observed a sudden decrease in turbidity and obtained finally a transparent o/w dispersion. They concluded that the size of the droplets must be smaller than the wavelength of visible light and thus microscopically small, not knowing that they are actually in the nanometer range. The type of the dispersion (o/w or w/o) follows in principle the *Bancroft rule*, which had been found earlier for ordinary emulsions [20]: The medium that forms the continuous phase of the dispersion is the one in which the surfactant is better soluble. The bicontinuous structure was first postulated by Scriven in 1976 [21]. A typical micrograph of a bicontinuous structure obtained by freeze fracture transmission electron microscopy is shown in *Fig.3*. Bicontinuous microemulsions can best be evidenced by NMR-self diffusion measurements when samples with differently deuterated compounds are used. For droplet phases, the dispersed phase and the surfactant display the same diffusion coefficient, that depends on the size of the droplets following Stokes's law [13], while the diffusion coefficient for molecules of the continuous phase is much faster. For the bicontinuous structures, the diffusion coefficients for water and oil are of the same order while that of the surfactant is much lower, since it is located in the interface.

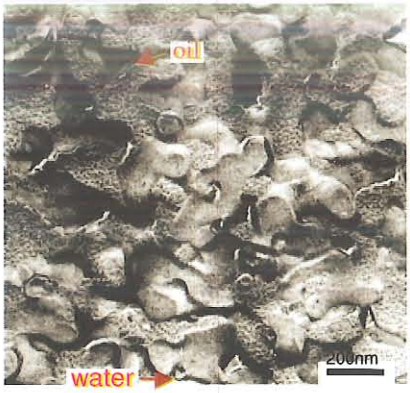


Fig. 3: *Transmission electron micrographs (FF-TEM) of a bicontinuous microemulsion, containing 7wt% $C_{12}E_5$, 37wt% octane and 56wt% water. The sample was prepared by rapid freezing, fracturing and subsequent deposition of a thin tantalum-tungsten coating to obtain a replica. Contrast between the oil and water domains occures because the coating forms a mottled pattern on the oil regions [22].*

2.2 Phase behaviour and structural evolution

Curvature energy model and phase behaviour of microemulsions.

Over the last two decades, it has been realised, that the structure and phase behaviour of microemulsion systems is, apart from the composition, determined by the elastic properties of the surfactant film that separates the water and oil domains. These have successfully been described using a presently well-established approach based on the statistical mechanics of curved interfaces, that was fist introduced by Helfrich in 1973 [23]. The ***Helfrich free energy*** F_H describes the bending energy of an arbitrarily shaped surface in terms of the radius of the spontaneous curvature, H_o, the rigidity constant associated with bending, κ, and the rigidity constant associated with Gaussian curvature, $\bar{\kappa}$,

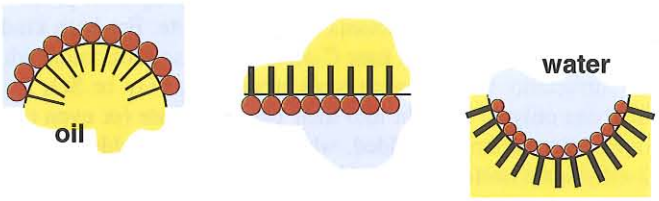
$$F_H = \int dA\left[f_o + 2\kappa(H - H_o)^2 + \bar{\kappa}K\right]. \tag{3}$$

The above form for the free energy is an expansion up to second order in curvature and features an integral over the whole surface area, A, of the mean curvature, $H = 1/2(1/R_1+1/R_2)$, and Gaussian curvature, $K = (1/R_1R_2)$ with R_1 and R_2 the principal radii of curvature at a certain point on the surface A. The sign of the principal radii of curvature is generally taken as positive when the film curves toward oil and negative when it is curved toward water, see *Fig.4*. In terms of R_1 and R_2, F_H can be written as

$$F_H = \int dA\left[\sigma - \frac{2\kappa}{R_o}\left(\frac{1}{R_1}+\frac{1}{R_2}\right)+\frac{\kappa}{2}\left(\frac{1}{R_1}+\frac{1}{R_2}\right)^2+\frac{\bar{\kappa}}{R_1R_2}\right], \tag{4}$$

whereby $R_o = 1/H_o$ is the radius of spontaneous curvature and σ is the surface tension of the planar surface. f_o is defined such that σ comprises all terms that are independent of curvature: $\sigma = f_o + 2\kappa H_o^2$.

The four parameters σ, R_o, κ and $\bar{\kappa}$ can until now not be obtained from a molecular model allowing the direct input of the properties of the surfactant molecules and the interactions of the hydrophilic and hydrophobic moieties with water and oil, respectively. They can experimentally be determined or simulated for (simple) model systems with well defined interaction potentials (e.g. a "surfactant" with Lennard-Jones interactions [24]). A global insight into the general phase behaviour can be gained by minimising the Helfrich free energy for the different phases. Phase boundaries or existence regions can then be obtained in terms of R_o and, e.g. $\bar{\kappa}/\kappa$. It is therefore important to know how they are related to experimentally accessible variables, such as temperature or salt concentration. Since a complete treatment of microemulsion phases within the curvature energy concept is beyond the scope of this chapter, attention is only paid here to its manifestation in the general phase behaviour of microemulsion systems. In this context, formulas will in the following only be derived for microemulsion droplet phases.



spontaneous curvature	$H_o>0$	$H_o\cong 0$	$H_o<0$
interfacial film curved toward	oil	no preferred curvature, balanced state	water
(packing parameter *v/al*	<1	1	>1)
microemulsion type	o/w (L_1-phase)	bicontinuous	w/o (L_2-phase)
multiphase equilibria	Winsor I ($\underline{2}\phi$)	Winsor III (3ϕ)	Winsor II ($\overline{2}\phi$)

Fig. 4: *Curved surfactant monolayers at the water/oil interface, with the corresponding values for the spontaneous curvature H_o and the type of microemulsion formed in the single phase and in multiphase equilibria.*

The *spontaneous curvature*, H_o, is defined as the curvature H a surfactant film will adopt when the film is totally unconstrained. In this case the film is in its lowest free energy state and thus $\partial F_H / \partial H = 0$ for $H = H_o$. H_o corresponds to the energetically most favourable packing configuration of the surfactant molecules in the interface. It can principally be compared with the packing parameters for micelles and depends on the molecular geometry of the surfactant and the solubilisation of the hydrophilic part in the aqueous phase and of the hydrophobic part in the oil. The latter depends in turn on formulation parameters such as temperature, (pressure), salt concentration in the aqueous phase, kind of oil used and type and concentration of cosurfactants (e.g., alcohol). *Fig.4* sketches the possible conformations of surfactant monolayers at a water/oil interface and gives the corresponding values for H_o and the type of microemulsion formed in the single phase and in multiphase equilibria. Positive and negative values for H_o favour the formation of droplets with spherical or cylindrical geometry. When H_o is zero (balanced state), the film will preferably form flat planar bilayers or bicontinuous structures with saddle shaped curvature for which $R_1 = -R_2$.

For a given surfactant, the spontaneous curvature can be tuned and adjusted by the afore mentioned formulation variables. For nonionic surfactants of the C_iE_j type the strongest effect on H_o has temperature. Upon increasing the temperature the hydrogen bonds between the hydrating water molecules and the ether groups of the ethyleneoxide moiety E_j brake, whereby the surfactant becomes increasingly less soluble in the aqueous phase. The interfacial surfactant film turns from curved toward oil ($H_o>0$) via its balanced state ($H_o\cong 0$) to curved toward water ($H_o<0$). The actual transition temperatures depend on the length of the ethylene C_i and ethylene oxide E_j blocks of the surfactants and the oil used. Smaller i, longer j and long chain aliphatic oils favour values of $H_o>0$. For ionic surfactants the strongest influence has the salt concentration of the aqueous phase. If the salt concentration is increased the effective charge of the head group will be screened and the surfactant heads will repel each other less which can lead to a change from $H_o>0 \rightarrow H_o<0$. The temperature dependence of H_o is for an ionic surfactant film with $H_o<0 \rightarrow H_o>0$ opposite to the salt dependence, since the Debye screening length is given by $1/\kappa_D = (\varepsilon RT/2F^2I)^{1/2}$, whereby ε is the permittivity, F the

Farraday constant, and I the ionic strength of the aqueous phase. The temperature dependence for nonionic and ionic surfactants is thus opposite. For both kinds of surfactants, the addition of alcohols with more than four C-atoms stabilises structures which are curved toward water. Ionic surfactants with a strong head group (e.g. SO_3^- or SO_4^-), such as sodium dodecylsulfat (SDS), can only be brought into their balanced state (or even curved toward water) if salt and a long chain alcohol are added, while films of a double tailed ionic surfactant, such sodium di(2-ethylhexyl)sulfosuccinate (AOT), are close to their balanced state.

The *(bending) rigidity constant* or *bending elastic modulus*, κ, is, in principle, a measure of how easily an interfacial surfactant film can be bent and influences both the static and dynamic properties of microemulsions. κ is expressed in units of energy with values typically between 1-20 k_BT, whereby k_B is the Boltzmann constant. Experimentally, κ can be obtained form ellipsometric measurements of fluctuating flat interfaces [25] or from electro-optical birefringence measurements of the form fluctuations of microemulsion droplets [26]. The persistence length of the interfacial film ξ_k describes the length over which the film is locally flat. High values of ξ_k indicate flat surfaces, whereas low values are found with highly curved surfaces. ξ_k is given by

$$\xi_k = l \exp\left(\frac{2\pi\kappa}{k_B T}\right). \tag{5}$$

l is a molecular length that corresponds to the length of the surfactant. If the bending elastic constant κ is of the order of k_BT, ξ_k is microscopic and the interfacial film is flexible. Over a large volume fraction range (see *Figs.1* and *5*), a bicontinuous structure will exist if the spontaneous curvature of the surfactant film is adjusted to be close to zero ($H_o \cong 0$) by, e.g., variation of T, salt and/or alcohol concentration. If κ is much larger than k_BT, ξ_k is macroscopic and the film is rigid. In this case, the droplet structure exists up to very high volume fractions and phase inversion takes place preferably via a lamellar crystalline phase. Flexibility is increased when i) short chain hydrocarbon chains or cosurfactants are added, ii) double chain surfactants with unequal chains are used and iii) short chain oils are employed, that can easily penetrate into the surfactant film, or iv) the salt concentration of the aqueous phase is increased. For the *rigidity constant associated with Gaussian curvature* or *the saddle splay modulus*, $\bar{\kappa}$, only few reliable measurements are available. The integral of the Gaussian curvature depends solely on the topology of the surface (Gauss-Bonnet theorem). Deformations of the film leave the integral over K thus unchanged. This value only changes if the film breaks due to the formation of holes or if two separated domains join. The typical trend is that $\bar{\kappa}$ is negative. The magnitude of it is usually smaller than that of κ for the same system. Experiments have shown, that κ and $\bar{\kappa}$ are approximately constant over the temperature range encountered, but depend for ionic surfactant layers strongly on the salt concentration of the aqueous phase [27]. Generally, the interfacial layer is more stiff when no screening occurs at no or little salt.

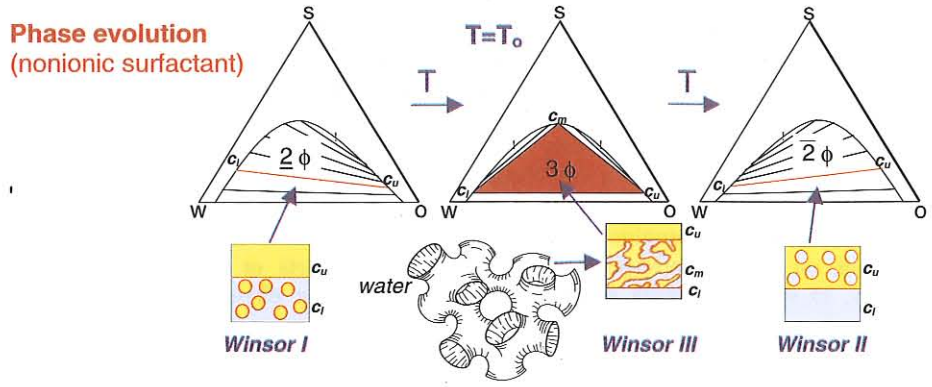


Fig. 5: *Phase evolution resulting in Winsor I-III-II microemulsion equilibria, as observed for microemulsions stabilised by a nonionic surfactant with increasing temperature and for microemulsions stabilised by an ionic surfactant with increasing salt concentration. The compositions c_i of the coexisting phases are indicated by the end points of the tie-lines and the corners of the three phase triangle, whereby the subscripts l, m, or u stand for lower, middle or upper phase, respectively. The bars below and above the 2 in the two-phase systems, indicate whether the microemulsion is formed in the bottom or top phase. It also indicates in which phase the surfactant is preferably soluble. The red lines mark the critical tie-line out of which and into which the three-phase triangle devolops and collapses, respectively. T_o is the temperature at which the three-phase triangle is isosceles.*

Phase and structural evolution in microemulsions.
Fig.5 shows a phase evolution, typically observed for nonionic microemulsion systems with increasing temperature. The same trend can principally be obtained for ionic microemulsion systems with increasing salt concentration in the aqueous phase, but focus will be placed in the following only on the nonionic system. At low temperatures, the surfactant is preferably soluble in the aqueous phase and forms, at concentrations above the cmc, micelles that can take up only small amounts of oil. Within the central miscibility gap at low temperatures an o/w microemulsion is formed which is in equilibrium with an almost pure oil excess phase (all tie-lines decline toward the oil corner), which is classified as *Winsor I* microemulsion system [28]. With increasing temperature, the hydrophilic moiety becomes less soluble in water and the interfacial film becomes less curved toward oil (H_o>0→$H_o \cong 0$). When H_o approaches zero, the lower microemulsion phase of the Winsor I systems separates into a surfactant-rich, bicontinuous middle phase and a water-rich phase (*Winsor III*, which is also depicted in *Fig.1*). The three-phase triangle develops out of a, so-called, critical tie-line, which is indicated in red. At $T = T_o$ the three-phase triangle is isosceles. The concentrations of the three coexisting phases c_i are given by the corners of the triangle, see *Fig.5*. For the samples that are prepared at overall concentrations within the three phase triangle, only the volumina but not the concentrations of the three coexisting phases differ. The degree of freedom, *f*, is given by the *Gibbs phase rule*: $f = C\text{-}P$ at constant temperature and pressure whereby *C* corresponds to the number of components and *P* to the number of phases [13]. For a system consisting of three components and three phases *f* equals 0. Upon further increasing the temperature the surfactant moves via the middle phase into the oil phase. Whereby the

middle phase takes up increasingly larger amounts of oil and the upper, originally almost pure, oil phase more water and surfactant. c_m moves clockwise around the central miscibility gap. While the bottom phase declines in oil and surfactant and c_l moves to the water corner. If the compositions of the both upper phases become identical, they merge ($H_o \cong 0 \rightarrow H_o < 0$) into a two phase system (*Winsor II* system), that is composed of a w/o microemulsion (upper phase) in equilibrium with an almost pure water phase (lower phase). In this case the tie-lines decline toward the water corner. In the Winsor I-III systems the curvature of the surfactant film in the different assemblies/structures formed is related to the spontaneous curvature H_o. At higher surfactant concentrations, enough surfactant is available to solubilise all excess water and/or oil in the corresponding microemulsion droplets or bicontinuous phases, respectively, to span the whole system and as a result single phase microemulsions are formed.

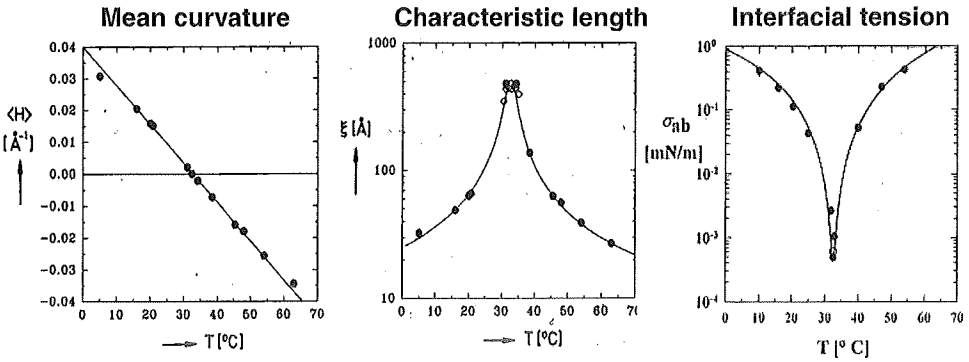


Fig. 6: *Experimentally averaged mean curvature <H> (left) and characteristic length ξ (middle) obtained from SANS and FF-TEM for the system $C_{12}E_5$–water–(n-octane). Around $\overline{T}$ = 32.6°C, <H> changes sign and ξ is maximal. Interfacial tension(right) of the interface between the water-rich and oil-rich phases, indicated by σ_{ab}, in the Winsor I, III and II systems for the same microemulsion system, obtained by spinning drop measurements. The interfacial tension shows a miminum when ξ is maximal [29].*

Fig.6 summarises the main trends found in microemulsions prepared from the H_2O–octane–$C_{12}E_5$ system. The data were collected over a couple of years by Strey and co-workers [29],[30] using small angle neutron scattering (SANS) and FF-TEM to determine the characteristic sizes ξ and main curvatures of the water and oil domains as they evolve with temperature. In addition, spinning drop measurements were performed to determine the interfacial tension σ_{ab} between the water-rich and oil-rich phases of the Winsor I, III, II systems. In the microemulsion region, the mean curvature varies linearly with temperature ($H \sim T\text{-}T_o$), while the characteristic length ξ shows a maximum at $T = T_o$, when the mean curvature passes through zero. Experimentally, it has been found that T_o lies close to the mean temperature $\overline{T}$ of the three-phase temperature interval and can be obtained by $\overline{T} = (T_u+T_l)/2$. T_u and T_l are the temperatures at which the isotropic three-phase triangle appears and vanishes, respectively, in the Gibbs triangle (see *Fig.5*). At high and low temperatures, both H and ξ level off and reach the limiting values of the corresponding (reverse) micellar systems. The interfacial tension σ_{ab} shows a minimum when ξ is maximal. The minimum is the more pronounced the higher the amphiphilicity (amphiphilic strength) of the surfactant.

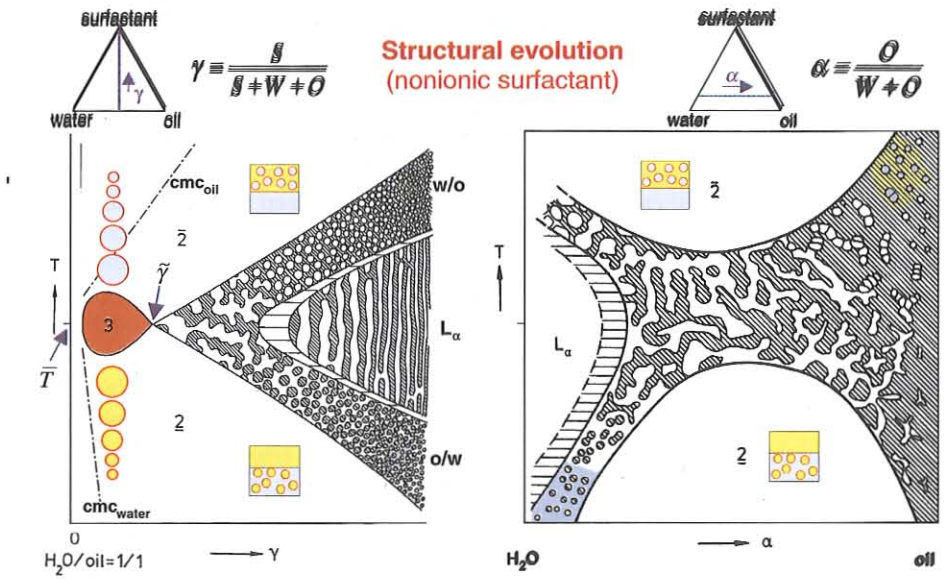


Fig. 7: *Schematic phase diagrams performed at the indicated cuts through the phase prism. Left: fish-cut; right: one-phase-channel. The sketched structures within the the one-phase regions display the stuctural evolution observed by different experiments, including small-angle scattering and FF-TEM [29].*

The determination of all the (co)existence regions and phase boundaries within the Gibbs triangle is quite time consuming. If one is particularly interested in the temperature evolution, it is often sufficient to perform certain cuts through the phase prism constructed from the Gibbs triangle as base and temperature as ordinate. Two of the most instructive phase diagrams obtained in this way are displayed in *Fig.7*. The left one, shows schematically a phase diagram obtainable by measuring the phase boundaries occurring in samples with equal amounts of water and oil as a function of surfactant concentration γ and temperature. This is a cut through the prism that starts in the middle of the water–oil side of the triangle and heads forward to the surfactant corner (see inset in *Fig.7*). In this way it cuts through the central miscibility gap and the three-phase triangle at temperatures between T_l and T_u. At $T<T_l$ Winsor I ($\underline{2}\phi$) phase equilibria are formed within the central miscibility gap, while Winsor II phase ($\overline{2}\,\phi$) equilibria form at $T>T_u$ (see also *Fig.5*). The three-phase region then shows up as a kind of "fish-head", that is surrounded by the two-phase regions. At very low surfactant concentration γ, the surfactant is molecularly dispersed in the water or the oil phase, respectively, depending on, in which medium it is preferably dissolved at a given temperature. At low temperatures ($T<\overline{T}$), the surfactant is soluble in water. If micellar aggregates form at concentrations above the cmc, they contain a certain amount of oil that depends on the spontaneous curvature H_o at that temperature. *Fig.7* shows also the cmc-lines that indicate from which surfactant concentration onwards microemulsion droplets form in the water (cmc_{water}) and oil phases (cmc_{oil}). Both lines decline toward the three-phase region. The two-phase region in front of the "fish-head" corresponds to the two-phase region that surrounds the three-phase triangle in *Fig.5* along the water–oil side of the Gibbs triangle. At T =

$\overline{T}$ (balanced state of the surfactant) the surfactant molecules are most efficient and show the lowest solubility in a water–oil system. Above the three-phase region, the surfactant is preferably dissolved in the oil, and Winsor II microemulsion systems are formed with different droplet sizes, which depend on the temperature and thus H_o. If, at a given temperature more surfactant is added, more microemulsion droplets of the same size can be formed and the microemulsion phase takes up more of the excess phase. Considering, e.g., a Winsor I system at $T<T_l$, more oil becomes solubilised in the o/w microemulsion. If more surfactant is present more oil can be "encapsulated" in order to keep almost the same size. At a certain surfactant concentration all excess phase is taken up and a single o/w microemulsion is formed. When more oil can be solubilised in the o/w microemulsion phase at temperatures closer to $\overline{T}$, more oil is present at low surfactant concentrations and the $2\phi \rightarrow 1\phi$ boundary is shifted to lower surfactant concentrations. The point at which the boundaries of the three-phase region and the one-phase region intersect $\tilde{\gamma}$, corresponds to the corner of the isosceles three-phase triangle that indicates the composition of the middle phase c_m (see *Fig.5*). $\tilde{\gamma}$ marks the lowest surfactant concentration needed to prepare single phase microemulsions. In its balanced state the surfactant film can solubilise the highest amount of water and oil, the domain size is maximal and the surface tension between the excess phases shows a minimum. The sketched structures within the one-phase, "fishtail"-like region in *Fig.7* display the micro-structural evolution that has experimentally been observed. Droplet phases form within the tail at high surfactant concentrations and $T<\overline{T}$ (o/w) or $T>\overline{T}$ (w/o). The transition from one droplet structure to the other can either occur continuously via cylindrical structures and bicontinuous phases or via a 1st order phase transition to the lamellar phase L_α that might intersect with the microemulsion phases at temperatures close to $\overline{T}$ (see *Fig.1*). The phase diagram on the right in *Fig.7* presents a cut through the phase prism at constant surfactant concentration, whereby the concentration is chosen such that at $\overline{T}$ the bicontinuous one-phase microemulsion is just formed. The surfactant concentration is thus chosen to be slightly higher than $\tilde{\gamma}$. In this way, a continuous one-phase microemulsion channel can be obtained that leads from the water to the oil side with a large bicontinuous region at intermediate water/oil ratios. The sketches of the structural evolution within the channel demonstrate nicely that the microemulsion morphology is governed by the composition and the properties of the interfacial surfactant layer. If the temperature is varied the latter is primarily determined by H_o.

In the following, the Helfrich energy is applied to derive expressions for the droplet radius and the interfacial tension in Winsor I and II droplet phases and to determine the $2\phi \rightarrow 1\phi$ boundary, whereby only spherical droplets are considered. For spheres $R_1 = R_2 = R_s$ and volume (V_s) and surface area (A_s) are given by $V_s = (4/3)\pi R_s^3$ and $A_s = 4\pi R_s^2$. For a given sample of a droplet microemulsion phase in equilibrium with an oil ($T<\overline{T}$) or water ($T>\overline{T}$) excess phase, the surfactant concentration and thus the total surface area A can be assumed not to change with temperature, since almost all surfactant is situated in the droplet interfaces of the w/o or o/w microemulsion phases. The radius and the droplet volume increase in the direction of $\overline{T}$. The total interfacial area A is given by $A = N_s 4\pi R_s^2$, with N_s the number of spherical droplets. The Helfrich free energy for a spherical droplet phase, F_s, can be written as

$$F_s = N_s 4\pi R_s^2 \left[\sigma - \frac{4\kappa}{R_o R_s} + \frac{2\kappa + \bar{\kappa}}{R_s^2} \right]. \qquad (6)$$

Minimisation of F_s can then be performed with respect to the droplet radius R_s and the number of droplets N_s under the condition of constant interfacial area and thus surfactant concentration. Minimisation with respect to R_s gives

$$\frac{\partial F_s}{\partial R_s} = 8\pi N_s \sigma R_s - 16\pi N_s \frac{\kappa}{R_o} = 0 \rightarrow \sigma = \frac{2\kappa}{R_o R_s}. \tag{7}$$

The interfacial tension between the droplet and the excess phases is in good approximation proportional to the square of the droplet radius. The expression for σ in eq.7 was first derived by de Gennes [31]. Minimisation with respect to N_s gives

$$\frac{\partial F_s}{\partial N_s} = 4\pi R_s^2 \left[\sigma - \frac{4\kappa}{R_o R_s} + \frac{2\kappa + \bar{\kappa}}{R_s^2} \right] = 0 \rightarrow \sigma = \frac{4\kappa}{R_o R_s} - \frac{2\kappa + \bar{\kappa}}{R_s^2} \tag{8}$$

and thus

$$R_s = \left(1 + \frac{1}{2} \frac{\bar{\kappa}}{\kappa} \right) R_o. \tag{9}$$

Since the bending constant depends in the range considered only weakly on the temperature, the droplet radius is in the Winsor I and II systems proportional to the radius of spontaneous curvature, which is tuned by the temperature. On approaching $\bar{T}$ from high and low temperatures $|R_o|$ increases, leading to an increase in R_s and a decrease in σ.

To obtain the 2ϕ→1ϕ boundary, one has to determine when the droplet radius in the Winsor I and II systems becomes equal to the droplet radius in the neighbouring one-phase regions. The radius of the droplets in the one-phase region is determined by the following argument. If there is no excess phase present, then not only the total surface area A but also the total volume $V_{tot} = N_s(4/3)\ \pi R_s^3$ is determined and consequently $R_s = 3V_{tot}/A = 3\omega$. The phase boundary, which is normally referred to as the *solubilisation limit*, occurs then at

$$R_s = 3\omega = \left(1 + \frac{1}{2} \frac{\bar{\kappa}}{\kappa} \right) R_o \rightarrow \frac{\omega}{R_o} = \frac{1}{6} \left(2 + \frac{\bar{\kappa}}{\kappa} \right) \tag{10}$$

So far, entropic effects have been, neglected. Including translational entropy and a radial polydispersity for the droplets allows to also calculate the droplet polydispersity but shifts the phase boundaries only slightly [32]. To obtain the complete picture not only spherical droplets but also cylindrical domains and interconnected cylinders have to be considered. For more information about the phase behaviour of nonionic and ionic surfactant–water–oil systems the reader is refereed to review articles by the group of M. Kahlweit [33], (nonionic) [34], (ionic) [35].

2.3 Statics and dynamics of droplet phases

One-phase w/o or o/w droplet microemulsions have thoroughly been investigated over the past three to four decades. They have mainly been studied (as model systems) to apply liquid state theories [36], to study (dynamic) percolation phenomena [37] and to investigate their exchange kinetics in view of their employment as reaction media [38]. Recently, the Helfrich energy has been used to describe shape fluctuations [39], droplet aggregation [40] and the

formation of cylinders [32] and interconnected networks [41]. In this section, only results, most relevant for particle preparation, are briefly recalled.

Droplet phase existence regions and droplet aggregation and cylinder formation.

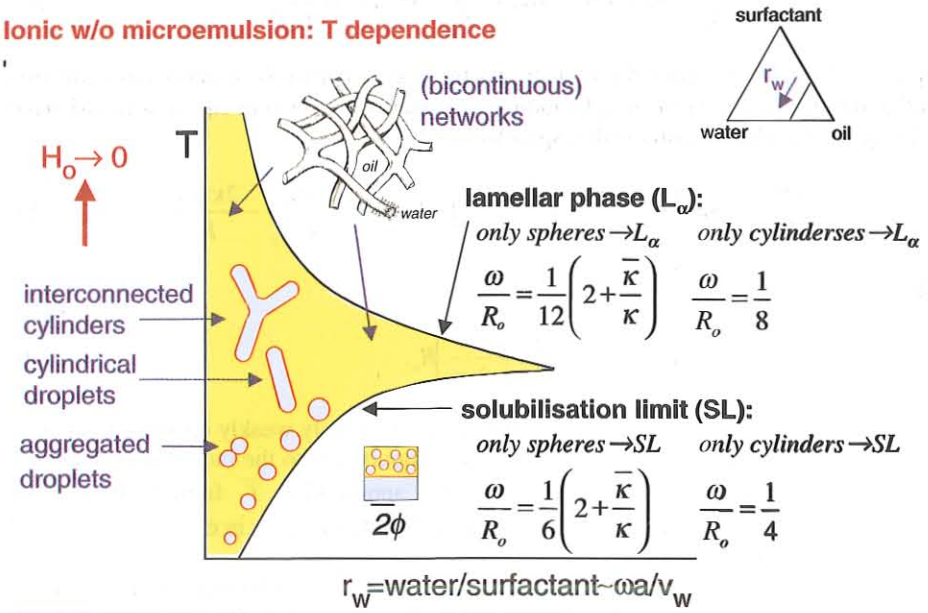


Fig. 8: *Schematic phase diagram showing the existence region of a w/o microemulsion stabilised by an ionic surfactant, such as AOT, as a function of the water/surfactant ratio and temperature. The cut through the phase prism is performed by variing r_w=(water/wt%)/(surfactant/wt%) at constant oil and thus droplet weight fraction.*

Within the one-phase region, total area and total volume are fixed by the concentrations of surfactant and the dispersed phase. This imposes a constraint of area and volume conservation. *Fig.8* shows schematically the existence region of a w/o microemulsion stabilised by an ionic surfactant, such as AOT. The phase diagram can be obtained by a cut through the phase prism as indicated in the inset. The cut is performed by varying the water/surfactant ratio at constant oil and thus droplet weight fraction. Since the temperature dependence of ionic and nonionic surfactants is opposite, the lower phase boundary corresponds to the solubilisation limit boundary (see *Fig.7* for comparison). Close to the solubilisation limit, R_s/R_o equals1 and spherical droplets are formed with a polydispersity of about 20%. Their radius depends linearly on the (molar) water/surfactant ratio, since $V_{tot} \sim v_w N_A[water]$ and $A = aN_A[surfactant]$, with v_w the molar volume of a water molecule, N_A the Avogadro number and the concentrations given in mole/l. The smallest radii reached are those of the inverse micelles and the largest that of the corresponding radius at the solubilisation limit at a given temperature.

If the temperature is increased, $H_o \rightarrow 0$ and the interfacial film tends to be less curved towards the water phase. In the corresponding Winsor II system, the water volume is not fixed and

fewer droplets with larger radii are formed. In the one-phase region, if R_s/R_o«1 the system minimises its free energy by forming a certain amount of aggregated droplets or cylinders. Small angle x-ray or neutron scattering curves, measured for AOT stabilised w/o microemulsions at different temperatures and interpreted in terms of a sticky hard sphere model [42] for the structure factor, have generally shown that the droplets become more attractive with increasing temperature. The degree of attraction depends on the oil used: At constant temperature, w/o emulsions prepared with long chain alkanes, such as decane and dodecane, show more attraction then systems with less hydrophobic oils as continuous phase. Recently, the droplet→cylinder transition has been studied in detail, both experimentally [43] and theoretically [32]. Within the one-phase region spheres and cylinders coexist. When the cylindrical droplets start to form, they have already a certain minimal length that corresponds to a few times of their diameter. If one compares the radius of the spherical droplets at the lowest temperature with that of the cylinders R_c at of the highest temperature measured, the geometrical limit of R_c=0.67R_s is reached. The latter is obtained when all spheres transform into cylinders. At temperatures close to the upper phase boundaries, the cylinders start to interconnect and form (bicontinuous) networks. The existence of these networks can best be evidenced by conductivity measurements. If the temperature is increased the conductivity may show a steep increase over two to three orders of magnitude, reaching values of the same order as that of the aqueous phase [37]. At the upper phase boundary, either two coexisting oil-continous microemulsions (low r_w-values) form or the microemulsion coexists at high r_w-values with a lamellar phase (L_α). The transition from a microemulsion consisting of spherical droplets only to a lamellar phase can easily be determined by setting the contributions stemming from the curvature energy in the Helfrich free energy equal for both phases:

$$F_{s,curv} = -\frac{4\kappa}{R_o R_s} + \frac{2\kappa + \bar{\kappa}}{R_s^2} = F_{L_\alpha,curv} = 0 \rightarrow \frac{\omega}{R_o} = \frac{1}{12}\left(2 + \frac{\bar{\kappa}}{\kappa}\right). \qquad (11)$$

Since the lamellar phase is composed of flat surfactant sheets their contribution to the curvature energy is equal to zero. In *Fig.8* both, the solubilisation limit and the transition to the lamellar phase are also given for phases consisting of infinitely long cylinders, which can be obtained in the same way as described above for spherical droplets using $1/R_1$=$1/R_c$ and $1/R_2$=0. V_{tot} and A are then given by $V_{tot} = N_c\pi R_c^2 L$ and A=$N_c 2\pi R_c L$, with N_c the number and L the length of the cylinders. A full description including the coexistence of spheres and cylinders taking the radial and length polydispersity into account is given in [32].

Exchange kinetics in droplet phases.

Micellar systems and microemulsions are highly dynamic systems. Surfactant molecules that are dissolved in the continuous phase exchange rapidly with those located in the interface of the assembled structures. Fast relaxation measurements have shown that exchange of monomeric surfactants between micelles or microemulsion droplets takes place with relaxation times of τ_1 = 10^{-6}-10^{-3}s. Relaxation times associated with the (much) slower formation or desintegration of entire micelles lie typically in the range of τ_2 = 10^{-3}-1s [44]. In droplet microemulsions, additionally exchange of the dispersed phase occurs. If, for example, two w/o microemulsions are brought together containing the same amounts of surfactant, aqueous phase and oil, but different types of solubilised species in the internal water pools, material exchange sets in instantaneously, leading to a redistribution of the two species over the entire dispersed droplet phase. Solubilisation of two reactants A and B that can undergo a chemical reaction to form C, can then be utilised to measure the exchange kinetics. It is, by

now, generally accepted that material exchange between droplets, necessary for particle formation, takes place via the formation of intermediate dimeric droplet aggregates. Dimers allowing free passage of the solubilised species were for the first time proposed by Fletcher et al. [45]. For AOT w/o microemulsions, exchange of solubilisate between the water pools of the microemulsion droplets occurs with a second order rate constant of $k_{ex} = 10^6$-10^8 dm^3 mol^{-1} s^{-1}, thus two to four orders of magnitude slower than the droplet encounter rate as predicted from simple diffusion theory. This indicates that successful fusion events take place only in 0.01-1% of binary droplet collisions [45],[46]. For microemulsions stabilised by nonionic surfactants of the ethyleneoxide monoalkylether (C_iE_j) type exchange rates of k_{ex} = 10^8-$10^9 dm^3 mol^{-1} s^{-1}$ were measured [47]. Rate constants were found not to depend on the size of the solubilised species but on droplet size, temperature and factors influencing the rigidity of the interfacial surfactant film, such as the kind of surfactants and oil used, presence of cosurfactants (alcohol) and salt concentration of the aqueous phase [45]. How far the interdroplet exchange rate is influenced by the presence of droplet aggregates and cylindrical droplets has so far not been investigated. Generally, it has been observed that the exchange rate is low in droplet phases with rigid interfaces and high if water channels start to form.

2.4 Comparison between micro- and macroemulsions

(Macro)emulsions generally form when water and oil are (vigorously) mixed in the presence of a surface active compound. They are normally of milky appearance and display droplet sizes ranging from 10μm down to 0.1μm. The final size of the emulsion droplets depends on the mechanical energy applied in the preparation process and on their stability. The free energy $\Delta F_{emul.}$ to disperse a liquid of volume V with drops of radius R in another liquid is

$$\Delta F_{emul.} = \sigma \frac{3V}{R}. \qquad (12)$$

If the freshly created droplet interfaces are not stabilised during the emulsification process, coagulation and coalescence processes cause a quick increase in droplet size and lead to rapid macroscopic phase separation. Employing surfactants in the emulsification process enables to lower the surface tension and thus the mechanical energy required and to stabilise the formed droplets electrostatically or sterically. Since macroscopic emulsions are only kinetically stabilised, their preparation, stabilisation and destabilisation resembles those of solid colloidal particles. *Fig.9* shows schematically the destabilisation processes that can principally occur in, e.g., o/w emulsions. Flocculation and coagulation lead to (ir)reversible droplet aggregation, while the density difference between the water and oil phases causes creaming of the oil droplets. Coalescence processes and *Ostwald ripening* cause an increase in droplet size and lead eventually to phase separation. Ostwald ripening occurs only if molecules of the dispersed phase are slightly soluble in the continuous phase. Since the *Laplace pressure* is higher for more curved interfaces, small droplets display a higher tendency to dissolve. Since oil molecules inside the droplets are in equilibrium with those dissolved in the continuous phase, material transport occurs via molecular diffusion from small to large droplets. In this way, the larger droplets increase in size, while the smaller ones disappear.

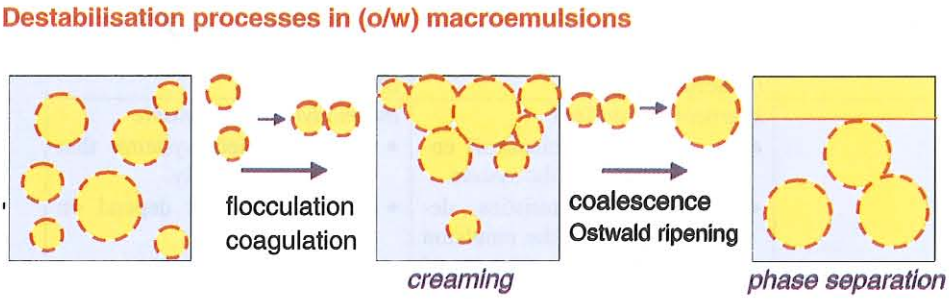


Fig. 9: *Processes that generally lead to a destabilisation of (o/w) emulsions. Creaming occurs normally before phase separation. The broken lines around the droplets indicate that the interfaces are not fully saturated.*

Since emulsions are stabilised by surfactants, they combine the properties associated with colloidal particles and surfactant self-assembled systems. Within a certain water/oil ratio, the type of surfactant used as emulsifier determines the type of emulsion formed. Emulsions displaying long-term stabilities are normally prepared at surfactant concentrations higher than the cmc and formulation conditions adjusted in the way that the surfactant is not in its balanced state ($H_o \neq 0$). At surfactant concentrations above the cmc the macroscopic interfacial tension stays constant (see *Fig.2*) and micelles or microemulsion droplets, formed in the continuous phase, serve as surfactant reservoir to stabilise the newly formed interface. The corresponding, thermodynamic equilibrium phases for o/w and w/o macroemulsions are the Winsor I and II systems. To prepare the emulsions, the water and oil phases do not necessarily have to be in equilibrium but they will finally phase-separate into the Winsor systems. If after the emulsification, micelles or microemulsion droplets are still present in sufficient concentration, they might introduce flocculation by depletion [48]. The attractive *depletion forces* are caused by a difference in osmotic pressure. If two emulsion droplets approach each other by Brownian motion, the distance can become so small that no (swollen) micelles can come in between them. The osmotic pressure of the continuous phase is then (much) lower between the approaching droplets than in the surrounding phase, resulting in an attractive force that can lead to droplet aggregation.

Table 1 *Main characteristics of (macro)emulsions and microemulsions.*

	(Macro)emulsion	Microemulsion
stability	*kinetically stabilised* • form only if (mechanical) energy is applied to the system. • emulsion characteristics depend on the way the emulsion is formed and the amount of mechanical energy applied. • occurrence of *coagulation* and *coalescence* processes as well as Ostwald ripening that lead to an increase in droplet size and finally to macroscopic phase separation.	*thermodynamically stable* • self assembled systems that form spontaneously. • properties do not depend on the preparation. • domain structure and size are thermodynamically controlled; they depend on the composition and the elastic properties of the separating surfactant film and thus on H_o, κ and $\bar{\kappa}$. • domain size does not change with time.
properties of the interfacial film	• stable emulsions are formed if the macroscopic (bulk water/ oil) interfacial tension is reduced by 10-40 mN/m. • the emulsion droplet interface is not fully saturated. • large internal interface.	• Winsor phase equilibria form when the interfacial tension between the water- and oil-rich phase $\sigma = 5\text{-}10^{-3}$ mNm^{-1}. • the interfacial film is formed by a saturated surfactant mono- or bilayer. • huge internal interface of up to 100m^2/g.
emulsion structure and domain size	• interfacial energy is low but still larger than κ. • the structure formed has the minimal surface/volume ratio. • spherical droplets of oil (o/w) or water (w/o) with sizes of 0.1-10μm and high polydispersity are formed • milky appearance.	• the interfacial tension is comparable with κ. • rich phase behaviour: droplet phases form if $H_o \neq 0$. For $H_o \approx 0$ bicontinuous microemulsions form at low κ and L_α phases at high κ. • characteristic length of 2-50 nm and low polydispersity. • transparent.
surfactant (type and concentration)	• water- (o/w) or oil-(w/o) soluble surfactants. • instable emulsions if the surfactant is at its balanced state. • low surfactant concentrations. • stable emulsions form at surfactant concentrations ≥ cmc: at concentrations a few times larger than the cmc flocculation occurs.	• water- (o/w) or oil-(w/o) soluble surfactants; at the balanced state of the surfactants either bicontinuous microemulsions or L_α phases form. • high surfactant concentrations. • surfactant concentration > cmc up to 20-30 wt %.

At the balanced state of the surfactant, the prepared emulsions are not stable and phase separate quickly. $\bar{T}$ then corresponds to the *phase inversion temperature* PIT [49] of

emulsions. Phase separation can thus also be induced by changing a formulation variable after the emulsion has been formed. Changes performed afterwards in temperature, salt or alcohol concentration acting in the way that $H_o \rightarrow 0$ lead to a destabilisation of the emulsion.

For more information concerning the relatively broad field of emulsion preparation, stabilisation and emulsion braking, the reader is referred to [13] and [50]. In order to obtain a better overview of the different emulsions systems employed in particle preparation routes, *Table1* lists important properties and characteristics of microemulsions in comparison to ordinary (macro)emulsions.

3 Precipitation of (inorganic) nanoparticles in droplet phases

Microemulsion droplet phases, e.g. water-in-oil (w/o) microemulsions stabilised by ionic or nonionic surfactants or surfactant mixtures, have extensively been utilised over the past two decades as nano-reactors for the preparation of well-defined small spherical particles of a variety of different inorganic materials. These include metals, semiconductors, metal halides, as well as magnetic, ferroelectric, superconducting and ceramic precursor particles. Because employing microemulsions enabled for some materials the preparation of monodisperse particles of a few nanometres in diameter for the first time, a large number of investigations could focus on studying the optical, electrical and magnetic properties of the particles synthesised and on the study of quantum size effects [1][51][52][53]. The advantages w/o microemulsions offer are directly linked to the easily performable tailoring of the compartmentalised reaction medium in terms of droplet size and concentration and the extremely small size of the aqueous cores. Compared to conventional methods using homogeneous reaction media, an often better control of the size and size distribution of the nanoparticles and an enhancement of the reaction rates have been achieved. In recent years, interest has shifted from making monodisperse nanoparticles of mostly spherical shape of different materials to the control of particle morphology (anisotropic and high-axial-ratio particles), introduction of crystallinity and oriented growth [54][55] as well as the ordering of (spherical) nanoparticles into 2D or 3D structured arrays and superlattices [56][57].

Microemulsions are both highly dispersed and highly dynamic systems, which makes them a good candidate for the precipitation of inorganic nanoparticles. The surfactant-stabilised cavities provide a cage-like effect that can control nucleation, growth and agglomeration. Particle nucleation and growth are governed by the occupation numbers of the reactants (solutes) in the aqueous droplet cores, the kinetics of the chemical reaction(s) leading to particle formation and the rate of solute exchange between the droplets. The final particle morphology is influenced by the properties of the microemulsion system, the chemistry of the precipitation reaction and specific interactions between surfactants and the forming solid phase. The particles prepared can be of amorphous, quasi-crystalline or crystalline nature and the set of independently variable and intrinsic parameters is quite large. Besides the increasing employment of microemulsion systems in preparation routes for nanoparticles, much less systematic work has, however, been performed on what actually controls the size, shape and stability of the particles formed. To prepare (monodisperse) particles of a given size and material, the proper precipitation conditions have to be determined experimentally and the chemical reaction conditions have to be matched with the stabilisation criteria of the microemulsion system. Metal ions can be introduced to the microemulsion via the aqueous core or in the case of anionic surfactants as surfactant counterions. The reactant agent can

then be brought in via the dispersed phase of a second microemulsion of the same composition or added directly to the microemulsion if it is soluble in the continuous phase. In any case, reactants and concentrations should be chosen such that phase separation leading to uncontrolled precipitation conditions is avoided. If the reactions that lead to the formation of the solid phase are much faster than the solute exchange between the droplets, the latter becomes the rate limiting step. The exchange kinetics then dominates nucleation and growth allowing to establish general trends that can be used for the tailoring of spherical nanoparticles. The observed dependence of the size and distribution of spherical nanoparticles on compositional parameters and on the exchange rate will be described in *Section 3.1*. The morphology of the solid phase formed is not in all cases commensurate with that of the microemulsions from which they are formed. If only a few nuclei are formed, particle growth due to solute exchange can lead to particle sizes that are a few times larger than the droplet cores. Furthermore, secondary growth processes, such as (uncontrolled) aggregation or reorganisation and (re)crystallisation might lead to complex inorganic-surfactant assemblies that can reach mesoscopic length scales. Lately, w/o microemulsion systems have also been investigated to prepare non-spherical particles such as nanorods and nanofibres. The underlying idea, is to perform the precipitation in cylindrical aggregates or interconnected cylinder phases. But how far the self-assembled surfactant systems can really serve as mould for high-axial ratio particles has not completely been established yet. Conditions under which rod-like particles and fibres have been obtained are described in Section 3.2.

3.1 Spherical nanoparticles

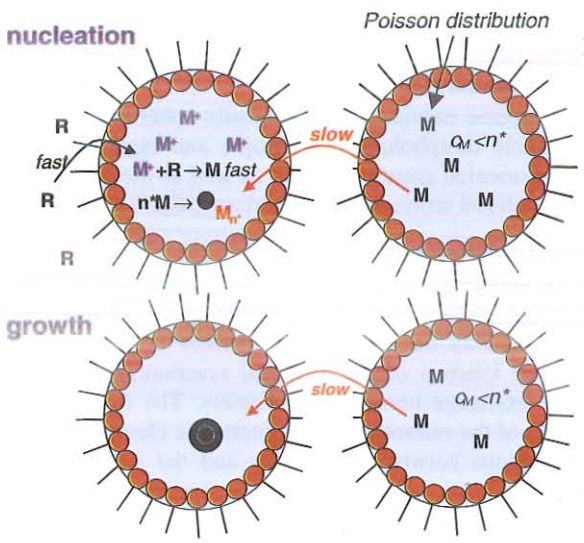


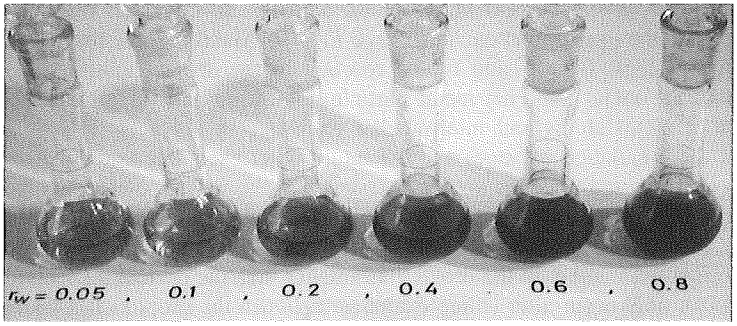
Fig. 10: *Schematic presentation of nucleation and growth processes occuring in the reduction of metal ions in w/o microemulsions. Metal ions M^+ solubilised in the aqueous core become reduced when the reduction agent R enters the droplet interior. If the number of metal atoms is higher than the critical aggregation number n*, a metal cluster nucleus forms that grows due to exchange of metal ions from other droplets.*

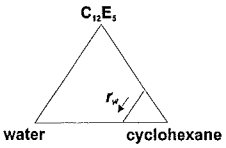
In the following, basic trends observed in the formation of nanoparticles in w/o microemulsions will be described in more detail allowing a better insight into the nucleation and growth processes that are taking place. It has been found that under certain conditions the number density of microemulsion droplets and particles obtained can differ by up to three to four orders of magnitude, indicating the importance of interdroplet solute exchange [6][58].

Let us for the sake of simplicity consider the reduction of a metal ion under the condition that the reduction agent is brought in via the continuous phase and that all chemical reactions involved are fast compared to the interdroplet exchange (see *Fig.10*). Metal particle formation then involves the following steps: i) Diffusion of the reactant to the droplet interface, ii) instantaneous reduction of the metal ions, iii) metal particle nucleation and iv) growth via intramicellar attachment of metal atoms and intermicellar exchange of droplets. The final particle size depends on the population balances and the interdroplet exchange rate constant k_{ex}. Since diffusion into the reversed micelles proceeds faster than the interdroplet exchange process, the initial distribution of the metal ions equals that of the metal atoms. It has been found by fluorescence measurements that the ion distributions generally obey Poisson statistics. If the metal occupation number in the droplets is smaller than the critical nucleation number n^*, nucleation can only occur after solute exchange between the droplets has taken place and n^* has been reached. Nuclei formed grow via interdroplet exchange until all free metal ions are used up. The described situation allows to predict the following trends: Generally, the more nuclei are formed the less free metal ions are left for particle growth. Low metal occupation numbers that can be obtained at low metal salt concentrations and high droplet number densities lead to extended particle growth and low particle number densities. If k_{ex} is high more nuclei can form due to faster exchange kinetics leading to smaller particles and higher particle number densities. The number of droplets N_s depends on the relative amounts of water and surfactant present, whereby $N_s \sim [surfactant]^3/[water]^2$. The fraction of particles having a particular size increases if n^* is higher since more free metal atoms would be available for growth. The polydispersity also becomes larger as n^* *is* increased. This can be explained by the fact that for higher n^* more free metal atoms are available for the formation of nuclei as well as for particle growth. The particles would therefore start gathering over wider ranges and larger sizes. Therefore, for systems in which n^* is high, low and moderate salt concentrations are expected to give highly polydisperse particles.

Fig.11 displays samples with silver particles that have been prepared in a water–$C_{12}E_5$–cyclohexane microemulsion system at different water/surfactant weight ratios r_w [59]. The silver particles were prepared by mixing a Ag^+ ion containing microemulsion with a microemulsion of the same composition that contains $NaBH_4$ as reduction agent. The microemulsions were either prepared with a 0.1 M $AgNO_3$ or a 0.1 M $NaBH_4$ solution. Reduction occurs by exchange of Ag^+ and BH_4^- between the droplets. The total amount and the amount of surfactant plus aqueous phase were kept constant, for the cut through the phase prism, see the inset in *Fig.11*. As can be seen from the particle size distribution, the radius passes a maximum as r_w is increased. In this set the overall concentration of silver ions increases with r_w, whereas the number of microemulsion droplets decreases. Both effects lead to higher occupation numbers, whereby the latter is much stronger than the first. Since nonionic and ionic surfactants show an opposite phase behaviour with respect to temperature, the upper boundary corresponds to the solubilisation limit and aggregation processes occur with decreasing temperature ($H_0 \rightarrow 0$), see *Fig.8* for comparison. In this case the interdroplet exchange rate is expected to increase if the lower phase boundary is approached at high r_w values. Thus the formation of more smaller particles is expected at high r_w. If one estimates the number of droplets N_s present in 3g microemulsion, then this number decreases from $N_s \sim 10^{20}$ at $r_w = 0.05$ to $N_s \sim 10^{17}$ leading to average occupation numbers that are smaller than 10^{-2} at $r_w = 0.05$ and about 25 at $r_w = 0.8$.

Reduction of silver ions in w/o microemulsions

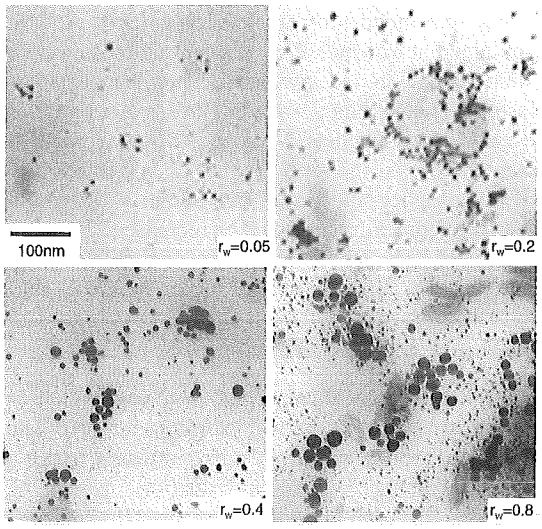


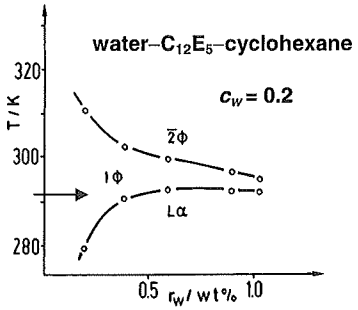


$$r_w = \frac{w}{s} = \frac{water}{C_{12}E_5}$$

$$c_w = \frac{w+s}{w+s+o}$$

Precipitation conditions: 0.1 M $AgNO_3$; 0.1 M $NaBH_4$; T = 23°C





Particle size distribution

r_w	d/nm	σ_d/nm
0.05	3.3	1.8
0.1	4.4	2.2
0.2	8.8	3.4
0.4	8.8	4.7
0.6	6.6	5.3
0.8	4.4	3.0

Fig. 11: *Solutions and TEM-micrographs obtained by reduction of silver ions in w/o emulsions by varying the water/surfactant weight fraction r_w at constant oil weight fraction (c_w = 0.2) performed at 23°C [59]. The colour changes from yellow to red, because both absorption and scattering depends on the size of the particles (Mie-scattering). The phase diagram shown has been performed for the system water–C12E5–cyclohexane along the cut indicated in the Gibbs triangle as a function of r_w and temperature at c_w = 0.2. Since for nonionic surfactant systems, temperature has a much larger effect on the phase behaviour than added salt, the phase boundaries change only slightly for the concentrations of $AgNO_3$ and $NaBH_4$ used for the precipitation. The arrow in the phase diagram marks the temperature at which the precipitation has been performed. In the Table the averaged radius and its standard deviation obtained from the TEM-micrographs are given in nanometers.*

These values indicate that enormous growth takes place for the very small droplets, explaining the observed maximum in the radius if r_w is increased. The polydispersity is increased at high occupation numbers.

3.2 Nanorods and filaments

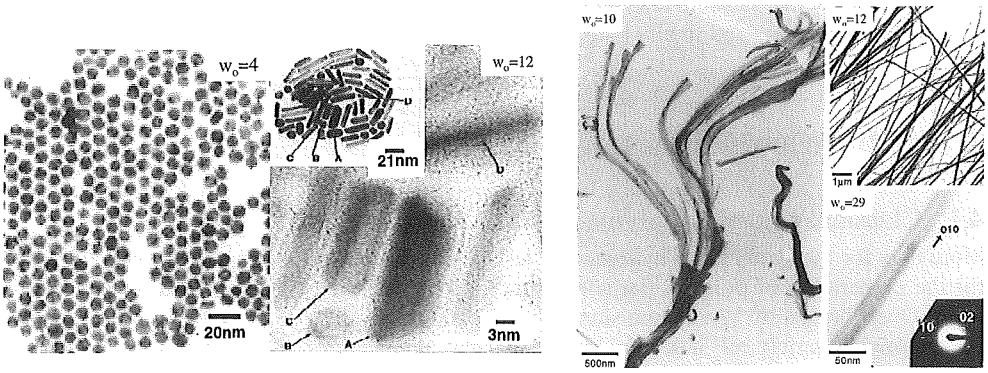


Fig. 12: *Particle of different morphology obtained by reduction of copper [60] in water-Cu(AOT)$_2$-iso-octane microemulsions (left) and mineralisation of BaSO$_4$ [62] in water–Ba$_{0.019}$Na$_{0..962}$AOT–iso-octane microemulsions at different molar water/ surfactant ratios w_o (right).*

Fig.12 shows examples for nanorods and nanofilaments and fibres prepared from AOT w/o microemulsions. Pileni and coworkers have demonstrated in a couple of papers [60][61] that the system water-Cu(AOT)$_2$-iso-octane can be employed to prepare well defined spherical copper nanoparticles and nanorods. Cu(AOT)$_2$ was prepared by exchanging the usual Na^+ counter-ion against Cu^{2+} and the was reduction performed by addition of hydrazine under nitrogen atmosphere at room temperature. If water is added to spherical inversed Cu(AOT)$_2$ micelles at low molar water/Cu(AOT)$_2$ ratio w_o, they first swell and elongate into cylinders that then form interconnected cylindrical networks. Mostly spherical Cu particles were obtained when spherical and cylindrical rods are used as template (w_o = 4), whereby polydispersities below 15% could be reached. In this case the spherical Cu particles self-assembled into hexagonal arrays on the TEM-grid. As soon as the interconnected cylinders form in the mould, mixtures of copper spheres and cylinders with up to 40% cylinders were obtained (w_o = 12). The cylinders were on average 18-25 nm long and 7-8nm thick. Examples for both Cu nanospheres and nanorods are shown on the left side in *Fig.12*. Further elongated cylinders could be obtainned if NaCl or KCl were added. Both salts are known to inhibit growth along the [100] direction and favour that along the [110] direction.

The right side of *Fig.12* shows barite fibers and filaments that are obtained by addition of $NaSO_4$ to a water–Ba$_{0.019}$Na$_{0..962}$AOT–iso-octane microemulsion system at different w$_o$-values. The crystallisation was performed within one week. At w_o = 10, a non-compact fibre, consisting of 2-20 µm long multiple filaments formed. While for $12 \leq w_o \leq 29$ single highly ordered crystalline barrite filaments 1-100µm long and 20-200nm wide were obtained. All filaments formed in this w_o-range were found to be single crystalline and elongated predominately along the [010] crystallographic axis displaying a uniform thickness and aspect ration of 1000. These results indicate that the final morphology is not determined by the microemulsion template. Extended oriented growth took place that might be induced by

secondary growth processes influenced by the presence of surfactants in high concentrations [62][63]. Studies of the time dependence in the formation of $CaSO_4$ obtained form comparable systems showed that in most cases first spherical particles were formed that elongate into cylinders and finally long fibers [64].

4 (Micro)emulsion polymerisation

4.1 Classical emulsion polymerisation

More than for the synthesis of inorganic materials, compartmentalisation has become relevant for the preparation of polymer particles (latexes) by radical polymerisation on an industrial scale. Over the last 50 years, emulsion polymerisation has developed into a broad field with an enormous variety of industrial and academic applications. Contrarily to suspension polymerisation, where the monomer starts to nucleate in a suitable solvent (diluent) in which it is dissolved, classical emulsion polymerisation makes use of the low solubility of most common monomers in water. Monomers that contain (at least) one double bound are dispersed into micrometer-sized droplets in the water phase. The monomer molecules in the droplets are in equilibrium with monomer molecules dissolved in the water phase. When water-soluble initiators start the radical polymerisation, polymer chains grow until they become insoluble in the water-phase and form primary particles. Principally, polymer particles can form under *homogeneous* nucleation conditions and the formation of the critical nuclei can be described by homogeneous nucleation theory. For the nucleation process to be spontaneous, the energy ΔF_s required for creating the polymer–water interface has to be compensated. Energy is in this case gained by the aggregation of the hydrophobic parts of the growing chain, ΔF_c, so that the overall free energy of a growing chain is given by

$$\Delta F = \Delta F_s + \Delta F_c = 4\pi R^2 \sigma_{pw} - \frac{4}{3}\pi R^3 f_v, \tag{13}$$

whereby R is the radius of the incipient particle , σ_{pw} the interfacial tension between polymer and water and f_v the free energy of condensation per unit volume of the primary particle or nucleus. At very small sizes R the first term dominates and prevents the formation of particles. With increasing R, the released condensation energy overcomes the surface energy requirement, and ΔF passes through a maximum. Beyond the maximum, the critical nucleus can further grow. Particle growth then takes place by diffusion of monomer molecules form the emulsion droplets, which serve as a reservoir for monomers. (Ionic) surfactants have been widely used to reduce σ_{pw} and to stabilise the particles formed against aggregation. Employing a micellar phase as continuous medium ensures surfactant concentrations high enough for particle stabilisation and might lead to *heterogeneous* nucleation conditions and thus leads to particle formation which is not restricted by surface energy requirements. The largest application of the water-born latex particles is probably in the paint industry, but they find increasingly more applications in the floor coatings (polishes), printing inks, adhesives, paper overprint varnishes, carpet backing and paper making. Water-based paints consist of a dispersion of (inorganic) pigment and latex particles made of a polymer that posses a sufficiently low glass transition temperature T_g. When the water evaporates from the applied paint, the particles coalesce to form a continuous film paint.

Using emulsion polymerisation submicrometer-sized latex particles made of, e.g., acrylonitrile, butadiene, styrene and polymethacrylate have been attained. Advantages compared to suspension polymerisation are that i) high molecular weight polymers can be prepared at rapid reaction rates due to the fact that the free radicals grow in relative isolation and that ii) heat transfer can easily be controlled during the polymerisation due to the low viscosity of the medium even at high solid contents. In same cases, latexes with an extremely narrow size distribution and a homogeneous charge density could be obtained, that could be employed as ideal model system to study order-disorder phenomena in colloidal suspensions. Since it is not possible within the scope of this chapter to explain the different processes involved in emulsion polymerisation in more detail by discussing the different mechanisms proposed and the kinetic models applied, only a brief description of the different stages observed during emulsion polymerisation in the presence of micelles in the aqueous phase is given next. This allows a better comparison to polymerisation in microemulsion systems. For more information the reader is referred to recent text books or text book contributions on emulsion polymerisation such as [65][66][67].

Emulsion polymerisation in the presence of micelles.
Free radical polymerisation proceeds generally via initiation and propagation followed by termination and chain transfer. The reaction is started by the induced dissociation of an added initiator into two radicals that can attack the monomer and form new radicals with added monomer units. A constant overall concentration of propagating free radiacals can be obtained if the initial radicals are formed under steady state conditions. In this case they are generated at the same rate as they disappear, which is the case when the initiator decomposition is much slower than the subsequent reactions. *Fig.13* sketches three different stages of emulsion polymerisation in the presence of micelles. At the beginning the continuous water phase might contain dissolved monomer, inactive monomer swollen micelles and the initiator. Polymer latex particles are generated by two processes which might occur simultaneously. The first is the entry of the free radicals into the micelles (micellar nucleation). Despite their large size, the monomer droplets are greatly outnumbered by the small micelles which have a much larger total surface area. The radicals enter the micelles rather than large monomer droplets. The second process involves nuclei formation in the continuous phase, whereby oligomeric radicals (homogeneous nucleation) are formed. If they increase in size they might be solubilised in the micellar core or the surfactant might adsorb onto the nucleus when the chain becomes insoluble. In both cases polymer particles are formed surrounded by surfactant. In this first interval grown particles are stabilized by adsorbing surfactants from surroundings micelles. By the end of interval I (at about 2-25% conversion), the micelles have either been nucleated to form new polymer particles or depleted to stabilize those particles. Most of the polymerisation occurs in interval II where the nucleated polymer particles continue to grow due to diffusion of monomer molecules from the monomer droplets through the continuous medium and into the particles. The primary radicals which are formed in interval II enter the polymer particles. In particles which already have a growing polymer radical, termination occurs more or less rapidly depending on particle size. After a short interval, another radical enters the particle, and a new chain starts. Thus, these single latex particles may at the end of the polymerisation contain a large number of polymer chains. It Ishould be noted that termination between two growing polymer radicals, predominant in bulk, does not occur because the chains are isolated from one another in the heterogeneous solution. Finally, interval III is reached when all of the monomer in the monomer droplets is consumed and only the monomer in the still-swollen particles remains to be polymerised.

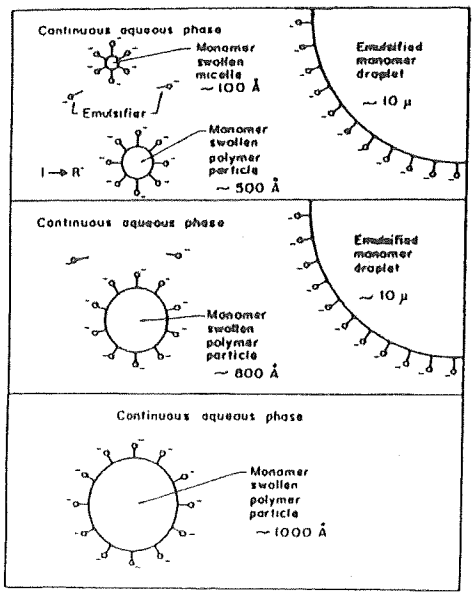


Fig. 13: *Schematic presentation of the different intervals taking place in emulsion polymerisation in the presence of (monomer swollen) micelles.*

4.2 Polymerisation in droplet and bicontinuous microemulsions

From 1980 onwards microemulsions have been investigated to prepare latex particles within the nanosize range (<50nm), starting with o/w droplet phases. In this case, *o/w microemulsions* were prepared with a monomer, such as styrene or methyl methacrylate (MMA) as dispersed phase. Nucleation takes then place inside the droplets by diffusion of water soluble initiators into the droplet interior. The final droplet size is determined by the oil/surfactant ratio and the droplet exchange processes taking place. At too high monomer concentrations phase separation occurred during the polymerisation. Stable latex dispersions were generally obtained at surfactant/monomer ratios ranging form 1-5, which are quite high in comparison to emulsion polymerisation were the surfactant/monomer ratio is usually smaller than 0.03. Additional, *w/o microemulsions* could be employed to polymerise water-soluble monomers, such as acrylic acid and 2-hydroxyethylmethacrylate (HEMA). Generally the monomer had first to be dissolved in water and w/o mircroemulsions formed then from the four components. *Bicontinuous microemulsions* were first studied to improve the interdroplet exchange rates and later to obtain interconnected polymer networks.

In templating the morphology of microemulsions it has often been observed that the solid phase that nucleates in the microemulsion cavities (e.g., droplets or channels) finally grows out of these cavities. The solid structures thus formed are not commensurate in size and even shape with the template, especially in polymerising bicontinuous microemulsions. When the monomeric oil starts to polymerise, surfactant molecules may adsorb on the forming polymer, whereby the surfactant concentration in the remaining microemulsion may change. If the monomer continues to solidify while morphological changes or even phase inversion or separation processes occur, the final structure may even be homogeneous but will certainly differ in size and shape [68]. Bicontinuous microemulsions have only successfully been

solidified, yielding porous polymeric films in the same size range, if the polymerisation reaction was sufficiently fast and the surfactant itself took part in the reaction. In this case the surfactant has to posses the same polymerisable group as the monomer in its hydrophobic moiety. The first brake through in polymerising bicontinuous microemulsions was realised by Gan et al. [69][70]. They obtained nanoporous polymeric materials by water/methylmethacrylate (MMA) microemulsions stabilised by a zwitterionic or a quaternary ammonium salt surfactant, possessing the same polymerisable group. Solidification took place only in a certain range of composition (water and surfactant). The channel width of the remaining water domains increased with decreasing surfactant or increasing water concentration. The resulting pore sizes could furthermore be decreased by the addition of a more water soluble monomer, which will partly polymerise in the water phase and then precipitate onto the pore surfaces. In this way a continuous variation of the channel width from 4-60 nm could be obtained. A higher mechanical strength of the polymeric film was attained if a crosslinker was added. The polymerisation reaction was either initiated using UV light or a redox initiator at 50°C. Meanwhile, also polymerisable nonionic surfactants and microemulsions could be prepared which allow even for a copolymerisation with vinylbenzenesulfonate [71].

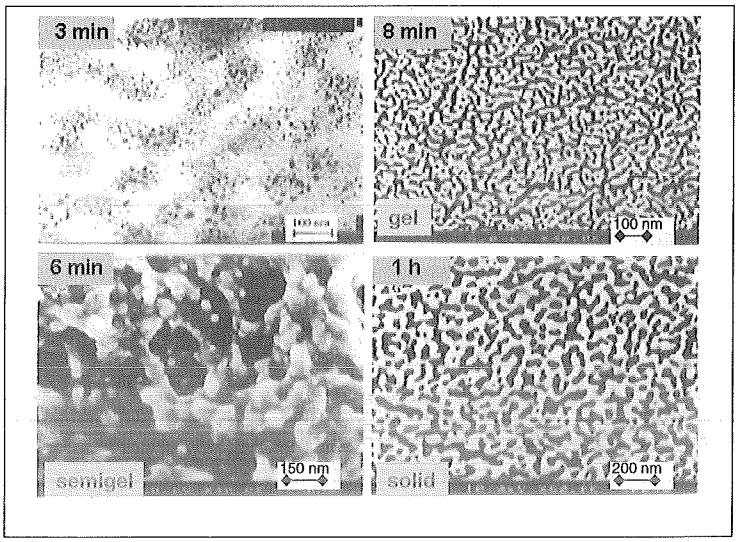


Fig. 14: *TEM micrographs of a sample prepared of 30wt% water, 32wt% MMA, 38wt% (((acryloxyloxy)-undecyl)dimethylammino) acetate (AUDMAA), a polymerisable zwitterionic surfactant, and 2wt% cross-linking agent (ethylene glycol dimethacrylate) during polymerisation. The reaction was photoinitiated at 35°C and samples were taken after 3-8 min and after 1h. The polymeric phase is presented by the light contrast [69].*

Fig.14 shows the network formation as a function of time in a sample prepared of 30wt% water, 32wt% MMA, 38wt% (((acryloyloxy)-undecyl)dimethylammino) acetate (AUDMAA), a polymerisable zwitterionic surfactant, and 2wt% cross-linking agent (ethylene glycol dimethacrylate) [69]. Numerous nanoparticles can be seen from the TEM micrograph after 3 min of polymerisation, when the sample is still very fluid. A semigel formed after 6 min with

polymer particles in the form of interconnected clusters with interdispersed pores and sizes smaller than 250nm. The sample was totally gelled after 8 min. The obtained nanostructured network resembles that of the original bicontinuous microemulsion. The dimensions of the channels were in the range of 50-70nm in width and 100-200nm in length. The structure did not alter much even after polymerisation for 1h when a transparent solid polymer was obtained as final product.

5 Templating of crystalline phases

The synthesis of inorganic mesoporous materials using ionic surfactant templates first reported in 1992 [72][73], lead to the discovery of a novel family of molecular sieves called M41S (see *Fig.16)* and opened up a new field of organised matter chemistry. The synthesis was performed by combining appropriate amounts of a silica (and alumina) source, a alkyltrimethylammonium halide surfactant (e.g. cetyltrimethylammonimum bromide, CTAB), a base and water. The inorganic phase is formed by hydrolyses of an alkoxide (e.g. tetramethylorthosilicate) that reacts with water followed by condensation. The mixture was then aged at elevated temperatures for 24-144h, which resulted in a solid precipitate. The organic-inorganic mesostructured product was, after washing, calcined at about 500°C. With well-defined pore sizes of 15-100Å and a hexagonal symmetry, these first mesoporous (alumino)silicate materials, break past the pore-size constraint (<15 Å) set by microporous zeolites. Surfactant–mediated synthesis has since been intensively investigated and employed to form a variety of mesoporous materials. The extremely high surfaces areas (>1000m^2g^{-1}) and the precise tuning of pore sizes made these materials highly attractive for applications in catalysis, membrane and separation technology, and molecular engineering. The M41S materials also ushered in a new approach in materials synthesis where, instead of the use of single molecules as templating agents, as in the synthesis of zeolites, self-assembled (molecular) surfactant aggregates or supramolecular assemblies are employed as the structure directing agents [74]. Recently, considerable attention is being focussed on tailoring the chemical composition of ordered mesoporous silicas for possible applications. The introduction of inorganic heteroatoms such as Al, Ti, or V into the silica framework, the synthesis of non-silica analogues (oxides of Al, Ti, V, W, Sb, Pb), and attachment of metallocene derivatives via pendent Si-O-H groups (to form Si-θ metal linkages) have been explored as routes to the preparation of catalytically active, ordered mesophases. Furthermore, cocondensation of siloxane and organosiloxane precursors has been investigated to produce inorganic-organic networks. These organically functionalised, uniformly porous, ordered silica materials offer a high potential in applications in organometallic chemistry, catalysis and host-guest systems [75].

There is still some debate on the actual mechanism that leads to the formation of the mesoporous materials. Principally, two different paths are possible, which are depicted in *Fig.15* for mesoporous materials with hexagonally ordered pores. In the original preparation route from 1992, the synthesis was performed at very low surfactant concentrations of about 1wt%. This concentration is above the cmc but much too low to allow the formation of liquid crystalline arrays such as the hexagonal phase H_1 that is built up of hexagonally ordered rodlike micelles. In this case, a sort of cooperative process must be at work requiring specific interactions between the soluble silicate species and the surfactant head group. The processes involved include specific binding of the silica precursor to the interfacial surfactant film, polymerisation of the silica at the interface and a kind of interfacial charge density matching

that leads to the mechanism sketched in *Fig.15*, depicting an ordering of the coadapted micelles into a hexagonal array. Pattern replication then proceeds by further condensation and polymerisation of silica within the interstitial spaces of the coassembled template. Postsynthesis removal of the organic phase affords an ordered mesoporous inorganic material with channel dimensions commensurate with the width of the rodlike surfactant micelles. Besides preparation via cooperative assembling, mesoporous silica has also been prepared by direct templating of a liquid crystalline phase, leading to a monolithic solid material that spans the whole sample.

Liquid crystal templating mechanism

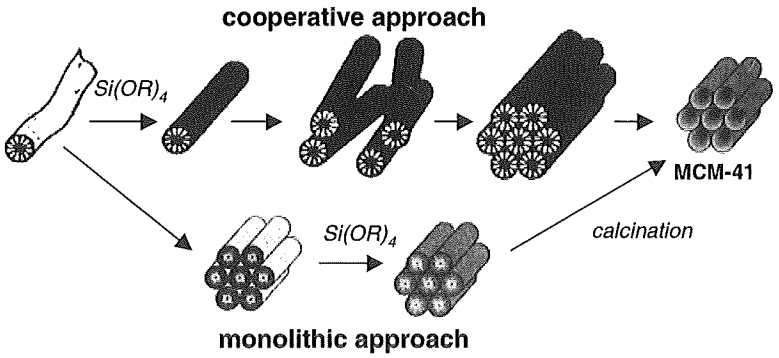


Fig. 15: *Two principally different paths to prepare mesoporous silica (MCM-41). The cooperative approach has been performed by adding a silica precursor to a surfactant solution at low surfactant concentration. Specific interactions between the silicate precursors and the surfactant molecules are necessary to abtain coassembly into a hexagonal array. The monolithic approach has been performed at high surfactant concentrations and employs direct templating of a hexagonal liquid crystal [74].*

Fig. 16 shows mesostructured materials that have been synthesised by direct templating of the corresponding liquid crystalline phases (monolithic approach) [76]. The mesoporous silica with hexagonal symmetry was obtained from the H_1 phase of $C_{12}E_8$. The silica was prepared by adding tetramethylorthosilicate (TMOS) in quantities of 0.25 mole equivalent with respect to water to a H_1 phase of $C_{12}E_5$ with a surfactant/water ratio of 50wt% at pH = 2. Methanol released from the hydrolyses of TMOS had to be removed by a mild vacuum, since it destroys the H_1 phase, before the sample was let at room temperature for 18h to form the monolith. The TEM-micrograph on the left in *Fig.16* shows a hexagonal array of regularly sized holes of 28Å diameter separated by ~12 Å-thick silica walls. X-ray diffraction shows that the value for the lattice parameter decreases only slightly upon solidifying the H_1-phase. The monolithic approach could also be applied in templating cubic and lamellar liquid crystals. The middle part of *Fig.16* shows mesoporous silica with a lamellar structure obtained from the L_α-phase of $C_{16}E_8$. When the same nonionic surfactants used in the monolithic approach were employed in the cooperative approach at much lower concentrations, no mesostructured precipitate was formed, indicating that not specific interactions but rather direct templating was responsible for the formation of the monoliths.

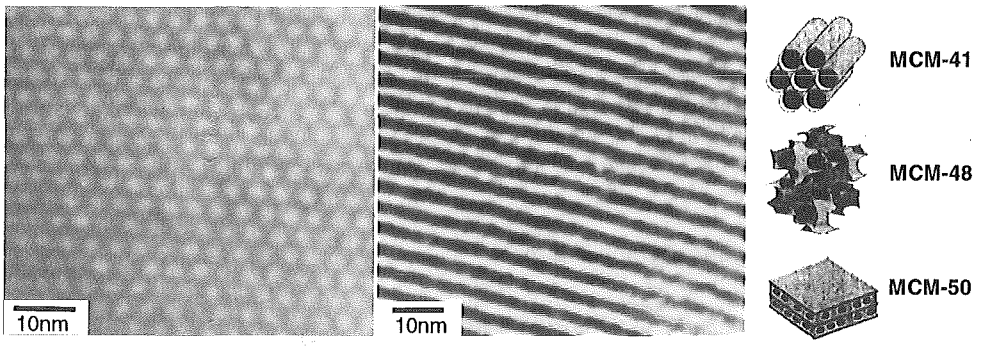


Fig. 16: *Mesoporous M41S silica obtained by direct templating of a H_1 phase of $C_{12}E_8$ (left) and of the L_α-phase of $C_{16}E_8$ (middle) [76] together with schematic illustrations of the mesoporpous M41S materials of hexagonal (MCM-41, space group: p6m), cubic (MCM-48, space group: $Ia\bar{3}d$) and lamellar (MCM-50, space group p2) structure [74]. Silica is presented by the lighter contrast.*

References

[1]J.H. Fendler, Chem. Rev. 87, 877 (1987)
[2]G.A. Ozin, Adv. Mater. 4, 612 (1992)
[3]S. Mann, S.L. Burkett, S.A. Davis, C.E. Fowler, N.H. Mendelson, S.D. Sims, D. Walsh, and N.T. Whilton, Chem. Mat. 9, 2300 (1997)
[4]H.T. Davis, J.F. Bodet, L.E. Scriven, and W.G.. Miller, in: Physics of Amphiphilic Layers, edited by J. Meunier, D. Langevin, and N. Boccara (Springer-Verlag, Berlin, 1987), pp. 310-327
[5]W.F.C. Sager, Curr. Opin. Colloid Interface Sci. 3, 276 (1998)
[6]M.P. Pileni, J. Phys. Chem. 97, 6961 (1993)
[7]J.Y. Ying, C.P. Mehnert, and M.S. Wong, Angew. Chem. Int. Ed. 38, 56 (1999)
[8]K.K.W Wong and S. Mann, Curr. Opin. Colloid Interface Sci. 3, 63 (1998)
[9]A. Stein, B.J. Melde, and R.C. Schroden, Adv. Mater. 12, 1403 (2000)
[10] I. Soten and G.A. Ozin, Curr. Opin. Colloid Interface Sci. 4, 325 (1999)
[11] I.W. Hamley, Introduction to Soft Matter: Polymers, Colloids, Amphiphiles and Liquid Crystals (Wiley, New York, 2000)
[12] J. Israelachvili, Intermolecular & Surface Forces, 2nd Ed. (Academic Press, London, 1992), pp.341-381
[13] D.F. Evans, H. Wennerström, The Colloidal Domain: Where Physics, Chemistry, Biology and Technology Meet, 2nd Ed. (Wiley-VCH, New York, 1999)
[14] Micelles, Membranes, Microemulsions, and Monolayers, edited by W.M. Gelbart, A. Ben-Shaul, and D. Roux (Springer-Verlag, Berlin, 1994)
[15] S.A. Safran, Statistical Thermodynamics of Surfaces, Interfaces, and Membranes (Addison-Wesley, Reading, MA,1994)
[16] Physics of amphiphiles: micelles, vesicles and microemulsions, edited by V. Degiorgio and M. Corti (North Holland, Amsterdam, 1985)
[17] J.Th.G. Overbeek, K. Ned. Akad. Wet. Ser. B 89, 61 (1986)
[18] R.J. Hunter, Introduction to Modern Colloid Science (Oxford University Press, Oxford 1993)
[19] T.P. Hoar and J.H. Schulman, Nature 152, 102 (1943)
[20] W. Bancroft and C. Tucker, J. Phys. Chem. 31, 1680, 1927
[21] L.E. Scriven, Nature 263, 123 (1976)
[22] W. Jahn and R. Strey, J. Phys. Chem. 92, 2294 (1988)
[23] W. Helfrich, Z. Naturforsch. C28, 693 (1973)
[24] R.Goetz, G. Gompper and R. Lipowsky, Phys. Ref. Let. 82, 221 (1999)
[25] H. Kellay, B.P. Binks, Y. Hendrikx, L.T. Lee, and J. Meunier, Adv. Colloid Interface Sci. 49, 85 (1994)
[26] E. van der Linden, D. Bedeaux, and M. Borkovec, Physica A 162, 99 (1989)
[27] D.J. Mitchell and B.W. Ninham, Langmuir 5, 1121 (1989)
[28] P.A. Winsor, Solvent Properties of Amphiphilic Compounds (Butterworths, London, 1954)
[29] R. Strey, Colloid Polym. Sci. 272, 1005 (1994)
[30] R. Strey, Curr. Opin. Colloid Interface Sci. 1, 402 (1996)
[31] P.G. de Gennes and C. Taupin, J. Phys. Chem. 86, 2294 (1982)
[32] E.M. Blokhuis and W.F.C. Sager, J. Chem. Phys. 115, 1073 (2001)
[33] M. Kahlweit, R. Strey, and G. Busse, J. Phys. Chem. 94, 3881 (1990)
[34] M. Kahlweit, R. Strey, P. Firman, D. Haase, J. Jen, and R. Schomäcker, Langmuir 4, 499

(1998)
[35] M. Kahlweit, R. Strey, R. Schomäcker, and D. Haase, Langmuir 5, 305 (1989).
[36] G.J.M. Koper, W.F.C. Sager, J. Smeets, and D. Bedeaux, J. Phys. Chem. 99, 13291 (1995)
[37] M. Kahlweit, R. Strey, D. Haase, H. Kunieda, T. Schmeling, B. Faulhaber, M. Borkovec, H.-F. Eicke, G. Busse, F. Eggers, T. Funck, H. Richmann, L. Magid, O. Söderman, P. Stilbs, J. Winkler, A. Dittrich, and W. Jahn, J. Colloid Interface Sci. 118, 436 (1987)
[38] P.D.I. Fletcher and J.F. Holzwarth, J. Phys. Chem. 95, 2550 (1991)
[39] M. Borkovec, H.-F. Eicke, Chem. Phys. Lett. 147, 195 (1988)
[40] E.M. Blokhuis and W.F.C. Sager, J. Chem. Phys. 111, 7062 (1999)
[41] T. Tlusty and S.A. Safran, J. Phys-Condens. Mat. 12, A253 (2000)
[42] R.J. Baxter, J. Chem. Phys. 49, 2270 (1968)
[43] D.I. Svergun, P.V. Konarev, V.V. Volkov, M.H.J. Koch, W.F.C. Sager, J. Smeets, and E.M. Blokhuis, J. Chem. Phys. 113, 1651 (2000)
[44] R.J. Stokes and D.F. Evans, Fundamentals of Interfacial Engineering, (Wiley-VCH, New York, 1997)
[45] P.D.I. Fletcher, A.M. Howe, B.H. Robinson, J. Chem. Soc. Faraday. Trans. I 83, 985 (1987)
[46] T.K. Jain, G. Casin, J.P. Badiali, M.P. Pileni, Langmuir 12,2408 (1996)
[47] P.D.I. Fletcher and D.I. Horsup, J. Chem. Soc. Faraday Trans. 88, 855 (1992)
[48] B.P. Binks, P.D.I. Fletcher, and D.I. Horsup, Colloids Surfaces 61, 291 (1991)
[49] K. Shinoda, J. Colloid Interface Sci. 24, 4 (1967)
[50] Encyclopedia of Technology, edited by P. Becher, 1st Volume (Marcel Dekker, New York, 1983)
[51] M.J. Hou, D.O. Shah, in: Interfacial Phenomena in Biology and Materials Processing, edited by Y.A. Attia , B.M. Moudgil, S. Chander S. (Elsevier, Amsterdam,1988) pp. 443-458
[52] M.P. Pileni , J. Phys. Chem., 97, 6961 (1993)
[53] Boutonnet M, Kizling J, and Stenius P, Colloids Surfaces, 5, 209 (1982)
[54] D. Walsh and S. Mann S, Nature, 377, 320 (1995)
[55] M. Möller and J.P. Spatz, Curr. Opinion Colloid Interface Sci., 2, 177 (1997)
[56] J.H. Fendler JH, *Curr.* Opinion Solid State Materials Sci., 2, 365 (1997)
[57] M.P. Pileni, L. Motte, F. Billoudet, J. Mahrt, and F. Willig , Mater. Lett., 31, 255 (1997)
[58] U. Natarajan, K. Handique, A. Mehra, J. R. Bellare, and K. Khilar, Langmiur 12, 2670 (1996)
[59] P. Barnickel, A. Wokaun, W. Sager, and H.F. Eicke, J. Colloid Interface Sci. 148, 80 (1992)
[60] J. Tanori, and M.P. Pileni, Langmuir 13, 639 (1997)
[61] M.P. Pileni, Langmuir 17, 7476 (2001)
[62] J.D. Hopwood and S. Mann, Chem. Mat. 9, 1819 (1997)
[63] M. Li and S. Mann, Langmuir 16, 7088 (2000)
[64] G.D. Rees, R. Evans-Gowing, S.J. Hammond, and B.H. Robinson, Langmuir 15, 1993 (1999)
[65] Emulsion Polymerisation and Emulsion Polymers, edited by P.A. Lovell and M.S. El-Aasser (John Wiley, Chichester, 1997)
[66] R.G. Gilbert, Emulsion Polymerisation (Academic Press, London, 1995)
[67] R.M. Fitch, Polymer Colloids: A Comprehensive Introduction (Academic Press, San Diego, 1997)
[68] M. Antonietti, and H.P. Hentze, Colloid Poly. Sci. 274, 696 (1996)

[69] L. M. Gan, T. D. Li, C. H. Chew, W. K. Teo and L. H. Gan, Langmuir 11, 3316 (1995)
[70] L. M. Gan, T. H. Chieng, C. H. Chew and S. C. Ng, Langmuir 10 4022 (1994)
[71] Liu, W. K. Teo, C. H. Chew and L. M. Gan, J.Appl.Polym Sci. 77, 2785 (2000)
[72] C.T. Kresge, M.E. Leonowicz, W.J. Roth, J.C.Vartuli and J.S. Beck, Nature 359, 710 (1992)
[73] J.S. Beck, J.C. Vartuli, W.J. Roth, M.E. Leonowicz, C.T. Kresge, K.D. Schmitt, C.T.W. Chu, D.H. Olson, E.W. Sheppard, S.B. McCullen, J.B. Higgins, and J.L. Schlenker, J. Am. Chem. Soc. 114, 10834 (1992)
[74] J. Y. Ying, C.P. Mehnert, and M.S. Wong, Angew. Chem. Int. Ed. 38, 56 (1999)
[75] S. Mann, S.L. Burkett, S.A. Davis, C.E. Fowler, N.H. Mendelson, S.D. Sims, D. Walsh, and N.T. Whilton, Chem. Mat. 9, 2300 (1997)
[76] G.S. Attard, J.C. Glyde, and C.G. Göltner, Nature 378, 366 (1995)



A 7 Computer Simulations in Soft Matter Science

Kurt Kremer

Max-Planck-Institut für Polymerforschung

55021 Mainz Germany

Contents

1 Introduction **2**

2 Basics of computer simulations **4**
2.1 Molecular dynamics (MD) 4
2.2 Monte Carlo simulations 6

3 Polymer simulations **8**
3.1 General considerations 8
3.2 How to generate conformations 11
3.2.1 Simple sampling techniques 11
3.2.2 Dimerization and Pivot 11
3.2.3 Many-chain methods: generalised reptation algorithms 13
3.3 More complex single polymer problems: two examples 14

4 Dynamics **15**
4.1 MC versus MD for dense systems 21
4.2 Dynamics and flow of melts: reptation 22

5 Network structures **23**

6 Further reading **25**

7 Non Equilibrium Simulations (NEMD) **26**

8 Linking Scales **27**
8.1 Coarse graining 28
8.2 Restoring chemical detail 31

9 An even coarser view on polymers **33**

Note: This contribution is a somewhat shortened and updated review, which appeared in: Soft and Fragile Matter, M. E. Cates, M. R. Evans (eds.) IoP Publishing, London 2000.

1 Introduction

This school covers a huge area of modern chemical physics. For all the questions considered, computer simulation methods are becoming, or are already, important scientific tools. To give an introduction one can choose a number of different approaches ranging from a somewhat complete, but certainly superficial overview to the deep discussion of the few examples. For the present contribution I try to combine both approaches, accepting the necessary shortcomings. After a general introduction on simulation strategy and characteristic length scales, the basics of Monte Carlo and molecular dynamics will be introduced. Lateron, as examples, I will discuss mainly the simulation of polymers as well as first attempts towards a multiscale modelling of polymeric materials. A number of nice reviews and books, some extensive, exist [1–10, 12] Thus, the present paper can also be viewed as a guide to the literature.

There are two basic concepts that are used in computer simulations of those materials. A conceptually direct approach is the molecular dynamics method. One numerically solves Newton's equations of motion for a collection of particles, which interact via a suitable interaction potential. Through the equations of motion, a natural time scale is built in. The simulation classically samples phase space *deterministically.* Though this sounds very simple, there are many technical and conceptual complications, which I will come back to later. The second approach, the Monte Carlo method, samples phase space *stochastically.* Monte Carlo is intrinsically stable but has no inbuilt time scale. There are ways to rectify this (discussed below).

These two very different basic approaches are both used to explore the statistical properties of systems and materials. Nowadays many applications employ hybrid methods, where combinations of both are used. Before going into details we first ask when each kind of model is appropriate. To do this we must discuss the different time and length scales relevant for the question under consideration. Figure 1 illustrates this for the example of polymers.

At a first sight it is tempting to simulate a melt of polymers with all details of the chemical structure of the monomers included. For instance, the chain diffusion constant D could be measured by monitoring the mean square displacement of the monomers of the chains or the centre of gravity of the chains. This, however, is tempting only at the very first glance. Even with the largest computers, one would need an exceedingly large amount of computer time. As is true for many disordered, complex materials, polymers can be characterised by a hierarchy of different length and time scales, spanning an extremely wide range [13].

Figure 1 illustrates that the typical range easily can exceed ten decades in time. On the microscopic level the properties are dominated by the local oscillations of bond angles and lengths. (To study chemical reactions or excited states, one requires quantum chemistry methods that are beyond the scope of the present paper.) Their typical time constant of about 10^{-13} sec requires a simulation time step of 10^{-15}sec. On the semi-macroscopic level the behaviour is dominated by the overall relaxations of conformation of the chains or even

Various regions of time and length scales

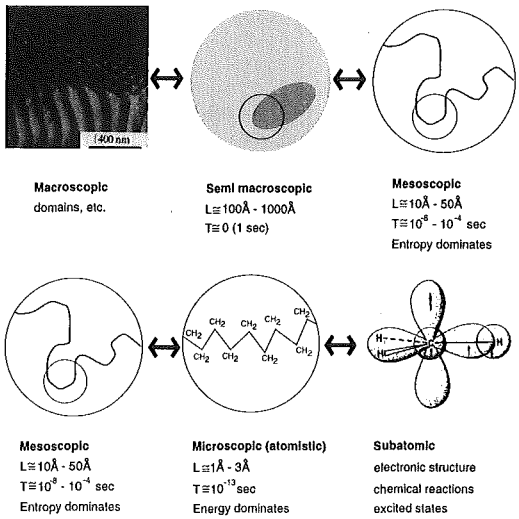


Fig. 1: *The different time and length scales in polymer problems. Starting from the top one first observes domain structures. On this level a continuum description is appropriate and one should not use 'particle based' simulation techniques. Looking more closely one could observe a marked chain in a melt or dense solution of otherwise identical chains as a very pale shadow. The typical extension of the shadow is given by the diameter of the overall coil, as indicated. Looking more closely more of the chain structure is revealed. This is the universal entropy dominated coil regime. Typical experimental time scales are indicated. Only if one again looks much more closely can the chemical details of the polymers be identified. There the behaviour is governed by the local chemical details and is energy dominated. The lower time boundary is given by the highest frequency, which usually is from the C-C bond oscillations. To study reactions, or excited states, details of the electronic structure have to be considered. Here we deal with the three 'middle levels' of the above scheme. Typical coarse-grained simulations are situated somewhere in between the coil and the microscopic regime.*

larger units (domains *etc.*). These times, depending on chain length and temperature, easily reach seconds and, if one approaches the glass transition, even longer times. To cover such a range within a conventional computer simulation is certainly impossible. On the other hand, it is important to relate the chemical structure of a system to its macroscopic properties. Thus, a long standing challenge within the modelling of complex materials is to apply 'multi-scale' methods to cover the range from microscopic to the semi-macroscopic regime [8, 12, 13].

Remark:
This school covers a much broader range of systems and questions than this contribution can deal with. Here, the case of (mostly) linear macromolecules is discussed. Though this is only a subset, the characteristic aspects of soft matter simulations in all cases are rather similar or even simpler, than in the case of polymers.

2 Basics of computer simulations

2.1 Molecular dynamics (MD)

MD simulations date back to the early fifties of last century. (For a rather complete overview see [1].) Consider a cubic box of volume $L^3 = V$ containing N identical particles of mass m. In order to avoid surface effects and (as much as possible) finite size effects, one typically uses periodic boundary conditions; the particle number density is $\rho = N/L^3$. The first simulations employed hard spheres of radius R_o and mass m, which have volume fraction $\rho_v = (4/3)\pi R_o^3 \rho$. The 'excluded volume' interaction potential $U(\mathbf{r}_{ij})$, with $\mathbf{r}_{ij}$ the distance vector between two particles i and j, is given by

$$U(\mathbf{r}_{ij})/k_BT = \begin{cases} 0 & , \mid \mathbf{r}_{ij} \mid \geq 2R_o \\ \infty & , \mid \mathbf{r}_{ij} \mid < 2R_o \,. \end{cases} \tag{1}$$

Since the interactions are athermal (U/k_BT is independent of T) the only relevant variable is the volume fraction ρ_V. The particles are assigned random initial velocities with the condition that their total momentum is zero. Then one performs on the computer a (conceptually) simple collision dynamics. The temperature defines the time scale via the equipartition theorem: $\frac{m}{2}\langle|\dot{\mathbf{r}}|_i^2\rangle = 3k_BT/2$. The simulation progresses the system to the point where two particles meet. At each such collision the necessary momentum and energy exchange is performed, and the run continues. Since the hard sphere potential is the most anharmonic one possible (the "modes" of the system mix very efficiently and the system equilibrates very fast), it is clear that for large systems this dynamics requires very small time steps, as very many collisions occur. Since all the sequential collisions have to be taken care of, such a program cannot easily be parallelised, an important feature for modern large-scale applications. For some time, the hard sphere problem was mainly of historical interest. However, with the development of modern colloid science hard sphere simulations became very important again. On the computer, 'microgravity experiments' are a little easier than in space; however, our systems are still somewhat smaller!
Many of the technical problems discussed above can be avoided if one replaces the hard sphere potential by a soft sphere potential, such as the Lennard Jones potential $U^{LJ}(\mathbf{r}_{ij})$, derived originally for interactions of noble gases. In its simplest form, for two identical

particles

$$U^{LJ}(\mathbf{r}_{ij}) = 4\epsilon\left\{\left(\frac{\sigma}{r_{ij}}\right)^{12} - \left(\frac{\sigma}{r_{ij}}\right)^{6}\right\} \tag{2}$$

Usually, a cutoff r_c is introduced for the range of the interaction. This typically varies between 2.5 σ (a classical LJ interaction with an attractive well) and $2^{1/6}\sigma$ where only the repulsive part of the potential remains.
The unit of energy can be chosen as ϵ, the unit of length σ and of mass m. This defines the 'LJ-units' of temperature $[T] = \epsilon/k_B$, time $[t] = \sqrt{\sigma^2 m/\epsilon}$ and number density $[\rho] = \sigma^{-3}$. In many practical programs σ, m, ϵ are set to one.
The straightforward MD approach is now to integrate Newton's equations of motion:

$$m_i\ddot{\mathbf{r}}_i = -\nabla_i \sum_{j\neq i} U(\mathbf{r}_{ij}) \tag{3}$$

Since energy in such a simulation is conserved, this generates the microcanonical ensemble. Again the average kinetic energy defines the temperature T via $\Sigma_i m_i|\dot{\mathbf{r}}_i|^2/2 = 3Nk_BT/2$. A simple but very efficient and stable integration scheme for Equation 3 is the Verlet algorithm.
With a simulation time step $\delta t \ll 2\pi/\omega_{max}$ where ω_{max} is the highest characteristic frequency of the system (eg. the Einstein frequency of an LJ crystal) we have ($m = 1$, in one dimension)

$$\begin{aligned} r_i(t+\delta t) &= r_i(t) + \delta t\dot{r}_i(t) + \frac{\delta t^2}{2}\ddot{r}_i(t) + \frac{\delta t^3}{6}\dddot{r}_i(t) \\ r_i(t-\delta t) &= r_i(t) - \delta t\dot{r}_i(t) + \frac{\delta t^2}{2}\ddot{r}_i(t) - \frac{\delta t^3}{6}\dddot{r}_i(t) \end{aligned} \tag{4}$$

addition and subtraction of these two equations yields

$$r_i(t+\delta t) = 2r_i(t) - r_i(t-\delta t) + \delta t^2\ddot{r}_i(t) + 0(\delta t^4) \tag{5}$$

$$v_i(t) = \dot{r}_i(t) = \frac{1}{2\delta t}[r_i(t+\delta t) - r_i(t-\delta t)] + 0(\delta t^3) \tag{6}$$

Thus, the position and velocity calculations have an algorithmic error of $0(\delta t^4), 0(\delta t^3)$ respectively. There are many variants of this basic method used throughout the literature. One can follow the realistic time evolution of a system, as long as the forces/potentials are realistic and as long as classical mechanics is sufficent. If the system is ergodic, which is not trivial and requires 'mixing of modes' (there is the famous Fermi-Pasta-Ulam problem, where one asks how anharmonic a potential has to be in order to equilibrate a one dimensional chain of [11]) one can equate ensemble averages to averages over time steps:

$$\langle A\rangle = \frac{1}{M}\sum_{i=1}^{M} A(t_i) \tag{7}$$

for any physical quantity A of interest. This is the basis for simulating a microcanonical ensemble [7], also called the NVE ensemble, where all extensive thermodynamics variables of the system, namely N, V, E are kept constant. Nowadays, most applications employ other ensembles such as the canonical (NVT), the isobaric-isothermal (NPT) or even

the grand canonical (μPT) ensemble. As a general rule, in order to avoid two-phase coexistence and equilibration problems one should choose an ensemble which has as many intensive variables kept constant as possible.
So far only equilibrium MD simulations have been mentioned. In addition there is a huge literature on different nonequilibrium simulations to study the shear viscosity of liquids [14] [15] and or other transport properties like heat conductivity [18].

2.2 Monte Carlo simulations

The classical version of MD simulation, just outlined, is a fully deterministic simulation technique. While there are many variants of the classical MD which add stochastic terms (see below) the other extreme, namely purely stochastic sampling, corresponds to the classical Monte Carlo (MC) approach.
Let's come back to the basic problem of hard spheres. We have seen that the only relevant parameter is the volume fraction in this athermal case (if one is only concerned with structural information). Then one can replace the ballistic motion of spheres by a stochastic one. Starting from a particular configuration, randomly a sphere is selected and displaced by a random jump. If this new configuration does not comply with excluded volume constraints the move is rejected, if it does, it is accepted. Then one starts the whole procedure again. Once every particle had a chance to move once (on average), one Monte Carlo step is complete. This is the most basic Monte Carlo simulation (see eg. [1] [19] [20] [21]). Since for hard spheres there is no energy involved, all states have the very same probability $P_{\rm eq}$. Also if the system is in state x, the probability $W(x \to y)$ of it jumping into y is the same as that from y to x. So the "dynamics" trivially fulfils the detailed balance condition

$$W(x \to y)P_{\rm eq}(x) = W(y \to x)P_{\rm eq}(y). \tag{8}$$

To discuss a few more basic aspects of MC simulation let's go back to the "fruit fly of MC simulations", the 2-d Ising model [1]. Consider a two dimensional square lattice, with spins on each lattice site. Each spin can assume two states $S_i = \pm 1$, corresponding to the 'spin up' and the 'spin down' state. The energy function (Hamiltonian) is

$$H(\{S_i\}) = -J\sum_{\langle i,j\rangle} S_i S_j + h\sum_i S_i$$

where $\langle i,j\rangle$ denotes all nearest neighbour pairs, J is the coupling constant, and h is an applied external field. Any observable A is given on average by

$$\langle A\rangle = \sum_{\{S_i\}} A(\{S_i\})P_{\rm eq}(\{S_i\}) \tag{9}$$

$$P_{\rm eq}(\{S_i\}) = \exp(-H/k_BT)/Z$$

$$Z = \sum_{\{S_i\}} \exp(-H/k_BT) \tag{10}$$

A direct method of calculation would be to sample all possible states. There are however 2^{L^2} states, L being the lattice linear dimension, making this impossible for large systems. (For small systems such enumeration can lead to very good results!) Instead we sample

phase space stochastically. Taking a spin at random, we flip the spin and calculate the energy change. With $P(x)$ the Boltzmann probability of the orginal state and $P(y)$ that of the new state, detailed balance is obeyed if

$$\frac{W(x \to y)}{W(y \to x)} = \exp\{-\left(H(x) - H(y)\right)/k_B T\} \tag{11}$$

This is normally a sufficient condition for a MC simulation to relax into thermal equilibrium, though this may take a very long time. (However, we will see later that in some cases improper choice of 'moves' can lead to a non-ergodic behaviour with equilibrium only attained on a subspace!) Algorithms without detailed balance will not be discussed here.

The *Metropolis criterion* is the one most frequently used to accept or reject a move:

$$W(x \to y) = \Gamma \begin{cases} \exp\{-\left(H(x) - H(y)\right)/k_B T\} & , \ \triangle H > 0 \\ 1 & , \ \triangle H < 0 \end{cases} \tag{12}$$

Since only the ratio of the rates W is relevant, Γ is an arbitrary constant between zero and one. A random number r, equally distributed between 0 and 1, is used to decide upon the acceptance of a move. If $r < W(x \to y)$the move is accepted, otherwise rejected. (Usually $\Gamma = 1$ is chosen so that any move that lowers the energy is accepted.) This is the basic MC procedure, which allows the sampling of phase space, and equilibrium averages to be found from Equation 7.

In many cases, however, one also would like to gain information on the dynamics of a (model) system. How can one use MC simulations, without an intrinsic time scale, to obtain information on the dynamics? The method described before evolves a system from one state to another by a local spin flip. By this local stochastic flips the magnetisation changes with 'time'. This can also be seen as a dynamic MC method based on a stochastic Markov process, where subsequent configurations $x \to x' \to x'' \to ...$ are generated with transition probabilities $W(x \to x'), W(x' \to x'')...$ To a large extent the choice of the move is arbitrary, as long as one can interpret it as a local basic unit of motion. As seen before, the actual choice of W is somewhat arbitrary as well: the prefactor Γ in Equation 12 can vary. Γ actually can be interpreted as fixing an attempt rate, $\Gamma = \tau_o^{-1}$, for the moves and so introduces a timescale. Thus we reinterpret the transition probability $W(x \to y)$ as a transition probability per unit time [3] [19]. To compare the simulated dynamics with an experiment, the basic task is to properly determine τ_o (eg. from the diffusion of chains in a polymer melt). It is obvious, however, that this (overdamped) simulation does *not* include any hydrodynamic effects since there is no momentum involved. (There are very interesting more advanced methods like "dissipative particle dynamics" and "lattice Boltzmann MC" which are currently being developed to repair this. [22] [23] [24])

Using this interpretation, ensemble averages can again be written as time averages:

$$\langle A \rangle = \frac{1}{M - M_o} \sum_{i=M_o+1}^{M} A\left(x(t_i)\right) \cong \frac{1}{t - t_o} \int_{t_o}^{t} dt' A\left(x(t')\right) \tag{13}$$

where we can interpret one attempted move per particle as one time step. Typically, the first configurations in a simulation are not characteristic equilibrium configurations. One first has to 'relax' the system into equilibrium, meaning the data for the first M_o steps

are omitted. (The same of course has to be done for MD simulations as well.) In this interpretation the dynamic Monte Carlo procedure is nothing but a numerical realization of a Markov process described by a master equation

$$\frac{d}{dt}P(x,t) = -\sum_y W(x \to y)P(x,t) + \sum_y (W(y \to x)P(y,t)$$

with $P(x,t)$ the probability of being in microstate x at time t. The condition of detailed balance is sufficient to ensure that $P_{eq}(x) = \exp[-H(x)/k_BT]/Z$ is the unique steady-state solution of the master equation (so long as all states are mutually accessible). Thus $P(x,t)$ must relax towards $P_{eq}(x)$ as $t \to \infty$ irrespective of the starting state. Note however that the choice of a 'good' starting state can save enormous amounts of CPU time (reducing M_o).
So far, the two extreme cases for classical, particle-based computer simulations were discussed: microcanonical MD, and MC. There are many approaches in between. Here I just want to mention them. The techniques range from

- *pure molecular dynamics* where Newton's equations of motion are solved: $m\ddot{x} = -\nabla U$, via
- *MD coupled to a heat bath and a friction* ('Langevin MD', 'Noisy MD'), where one solves $m\ddot{x} = -\nabla U - \zeta\dot{x} + f(t)$ with ζ a friction and f a random force (heat bath), via
- *Brownian Dynamics (BD)* where one solves $\zeta\dot{x} = -\nabla U + f$, via
- *Force biased MC*, where attempted moves are selected from the beginning according to local forces, to
- *plain MC* as described above.

3 Polymer simulations

3.1 General considerations

Now let us turn to some specific questions related to polymers. Compared to simulations of small molecules, polymers (like many other forms of soft matter) require special attention due to the huge number of intra-molecular degrees of freedom. This causes both computational advantages and disadvantages. Polymers are chain molecules built of repeat units called monomers or 'beads'. Typical examples range from the simple, widely used, PE to the technically very important but more complicated BPA-PC, which is used, among other things, for compact discs:

PE	$(CH_2)_N$	polyethylene
PS	$(CH_2(CH(C_6H_5))_N$	polystyrene
PEO	$((CH_2)_2O)_N$	polyethylene oxide
BPA-PC	$(C_6H_4C(CH_3)_2C_6H_4CO_3)_N$	bisphenyl A polycarbonate

While three out of the above examples are only soluble in organic solvents, PEO is also water soluble. Biopolymers easily have more complicated sequences.
The molecular weight of a single polymer molecule can easily reach $\sim 10^5$ Daltons (several thousands of monomers). Full scale MD simulations are not suitable (Figure 1), but in any case, would be restricted to the study of a very few specific systems. Even then it is very difficult to determine proper intra- *and* inter-molecular interaction potentials, and one would also need an effective and computationally convenient parametrization for them. In particular the complicated inter-chain or polymer-solvent interactions are only poorly understood at present.
Despite these seemingly tremendous complications, the situation is not that bad. To what extent do we really need the chemical details? Figure 1 gives a caricature of the various relevant scaling regimes. It also illustrates universality. Properties, which are governed by length scales larger than a few Kuhn lengths, the characteristic length measuring the chain stiffness, are independent of the chemistry. For example in the limit of long chains of N monomers the mean squared end-to-end distance $\langle R^2(N)\rangle = AN^{2\nu}$. The exponent ν is universal, and takes values $0.588 \simeq 6/5$ in a good solvent (for $d = 3$) and 0.5 in the melt or in a Theta solvent. The chemical details are hidden in the prefactor A. This suggests a relatively satisfactory situation, namely for most physics questions one can confine the simulation to the simplest and, for computational purposes, fastest models. In many cases we just need the monomer-monomer excluded volume and the chain connectivity. These models are often called coarse-grained models. Later on, we will face the problem of 'mapping properties back to a given chemical system' in order to determine amplitudes (like A) as well.

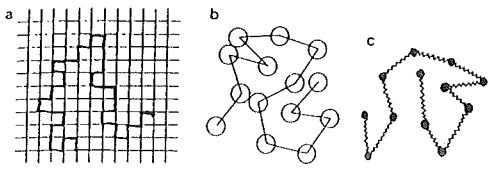


Fig. 2: *Typical models for polymers used in simulations.*

We now apply the previously described techniques to coarse-grained polymer models. Typically, three classes of models are used for computer simulations of polymers, see Figure 2. The first and historically most widely used model of a single chain is the *self-avoiding walk* (SAW) on a lattice [3]. In such a walk, each lattice point can be occupied only once; it is trivial to introduce nearest-neighbour energies and other generalizations. The second model is the direct generalization of this for continuous space, the *pearl necklace model*. The chain consists of hard spheres of diameter σ_0 and a fixed bond length ℓ_0. The third variant is a *bead-spring model*, mainly used in MD simulations: the monomers are particles which interact with, in most cases, a (purely repulsive) Lennard Jones interaction Equation 2. For the bonded nearest-neighbours along the chain, an additional spring potential is added which, together with the repulsion, determines the bond length ℓ.
The purpose of a simulation is to generate statistically independent conformations (equilibrium) or to follow the time evolution of a given global conformation (dynamics). Again, the most natural ansatz would be to simply perform a MD simulation, where Newton's

Table 1: *An illustration of the timescales in polymer simulations.*

	Liquid	Polymer melt
particles	N_{TOT}	N_{TOT}
density	ρ_0	ρ_0
CPU time per timestep	$\propto N_{\mathrm{TOT}}$	$\propto N_{\mathrm{TOT}}$
equilibration distance	$\propto \rho_0^{-1/d} \propto N_{\mathrm{TOT}}^0$	$\propto \langle R^2(N)\rangle^{1/2} \propto N^{1/2}$
physical relaxation time	$\tau \propto N_{\mathrm{TOT}}^0$	$\tau_N \propto N^z,\ 2 \leq z \leq 3.4$ (varies with chain length)
CPU time for relaxation	$T \propto N_{\mathrm{TOT}}$	$T \propto N_{\mathrm{TOT}} \cdot N^z$

equations of motion (Equation 3) for a bead spring model are solved numerically. However, this direct approach cannot be used for an isolated chain. The reason lies in its structural properties: a linear-chain polymer without excluded volume interactions has the structure of a random walk (harmonic chain). Its structure and dynamics can be described by eigenmodes, the Rouse modes which decouple [25]. Thus solving Equation 3 exactly, without excluded volume or external noise, would never equilibrate the chain. (cf. chapters on dynamics)

For a chain with excluded volume, the Rouse modes are no longer eigenmodes. However, the deviations, which affect the large length scales, come mainly from "long range" contacts between monomers which are far apart along the chain but close by in space. For long chains the internal monomer density decays with a power law $N^{1-d\nu}$. (The chains are fractal objects with a fractal dimension $d_f = 1/\nu$). Consequently, these "long range" collisions, which cause the swelling of the chains, are very infrequent: equilibration is not guaranteed. The single SAW is an example of the direct relevance of the aforementioned Fermi-Pasta-Ulam problem, which to date is not yet solved [26].

Thus the natural MD approach can only be used for a chain interacting directly with solvent or other chains, or for chains with long range interaction potentials. To avoid this problem one has to couple the motion of chain beads to a stochastic process, for example a heat bath comprising a friction and a random force. In the overdamped limit this results in Brownian dynamics. The other approach is the dynamic Monte Carlo method, where again the conformation changes come from local stochastic jumps. Both approaches follow realistically the (Langevin) dynamics of the chains. Though this leads to information about chain dynamics as well as statics, this should be avoided if the dynamic information is not needed. To illustrate this, we compare in Table 1 a simple liquid (or a lattice gas) and a polymer melt of the same density and total number of particles.

The comparison in the Table assumes that we are not close to a critical point of the liquid, where critical slowing down occurs. But in fact, the exponent $z = 2 \ldots 3.4$ in the relaxation time $\tau \sim N^z$ of polymers is analagous to that for critical slowing down [25] [27]. (In the language of critical phenomena the inverse chain length corresponds to $(T - T_c)/T_c$.) This N-dependent slowing causes significant problems since N values of interest start at around 50 to 100. As a result there is one important rule for polymer simulation: if possible, avoid algorithms with *realistically slow* physical dynamics. (However, if one wants to study chain dynamics itself, there is no alternative.)

3.2 How to generate conformations

Having demonstrated that the methods which follow the realistic dynamics are not very useful for single isolated chains, we now try to generate the conformations by a purely stochastic process.

3.2.1 Simple sampling techniques

First let us consider SAW's on a lattice. To fulfil the excluded volume requirement each lattice site can only be occupied once; but otherwise each conformation of an N-step walk has the same probability. If we fix the first step, then each new step is taken with probability $1/(q-1)$, where q is the coordination number of the lattice, and we account for the fact that backward steps are ruled out.
This most naive way of generating conformations with equal probability is called simple sampling. Each time an attempted new bond hits a site which is already occupied, one has to start again at the beginning. Otherwise, different SAW conformations will receive different probabilities, generating an (attractive) effective interaction among the monomers. Each sampled conformation is therefore taken randomly out of the $q(q-1)^{N-1}$ possible random walk paths, which do not include direct back-folding, whereas the total number of SAW's on a lattice is given by [3]

$$Z(N) = c_0\, q_{\text{eff}}^N\, N^{\gamma-1} \qquad N \gg 1 \tag{14}$$

with $q_{\text{eff}} < q-1$ and c_0 a number of order unity. The critical exponent γ is dimension- but not lattice-dependent ($\gamma \approx 7/6$ for $d=3$, and $4/3$ for $d=2$). Typical numbers for q_{eff} are 2.6385 (square, $q=4$), 2.879 (diamond, $q=4$) and 4.6835 (simple cubic, $q=6$) [3] . Thus the success rate of the sampling process, $A(N) = A_o(q_{\text{eff}}/(q-1))^N\, N^{\gamma-1}$, decays exponentially with N. A typical best value for A is eg. $A(100) = 0.03$ on the diamond lattice. This illustrates that simple sampling is only useful to get a rough estimate for chain properties like q_{eff} and γ.
The first improvement was suggested as early as 1955 by Rosenbluth and Rosenbluth [28]. Their idea of the *inversely restricted* or *biased sampling* is to look ahead for at least one step in order to overcome the attrition. More modern approaches look several steps ahead or implement this idea within in a dynamical scheme [8] [10] [29]. Here I explain two alternatives, which can mainly be used for isolated chains. Grassberger extended this to the so called "prime enriched Rosenbluth" method, which allowed him to generate walks of up to 10^6 steps. The ansatz in principal combines ideas of different indiviudal approaches discussed in this contribution.

3.2.2 Dimerization and Pivot

The *dimerization* approach [30,31] allows a simultanous determination of both the exponents γ and ν. The idea is to begin by generating many short SAW's of length N_0. These walks can then be combined randomly. For every step the success rate P_{bin} for binary assembly of walks of length N_1, and $N_2 = N - N_1$ is $P_{\text{bin}}(N_1, N_2) = Z(N)/(Z(N_1)Z(N_2))$. Using $Z \propto q^N N^{\gamma-1}$ we get $P_{\text{bin}}(N_1, N_2) = N^{\gamma-1}/(N_1 N_2)^{\gamma-1}$. P_{bin} is optimal for $N_1 = N_2 = N/2$. The original procedure, where short walks were generated and then stored, is computationally not very efficient. It is more direct to generate each sub-walks

by simple sampling, as follows [3,32]. After a SAW of N_1 monomers is generated we continue. If the next N_1 steps violate the excluded volume condition *within the second piece*, we start at N_1 again. Only an overlap with the first N_1 monomers makes it necessary to start at the very beginning. This defines a very efficient hierarchical procedure. j t can directly be extended to the study of branched polymers. In particular, the dependence of γ on the number f of arms of a star polymer is interesting and very difficult to estimate analytically. Using this method we were able to give precise results for $\gamma(f)$ and also size statistics such as the mean radius of gyration, and the mean hydrodynamic radius $\langle R_H \rangle = N^{-2} \sum_i \sum_{i \neq j} \langle 1/r_{ij} \rangle$. For R_H, very strong corrections to scaling are observed, which explain deviations of experiments such as light scattering from the asymptotic power law behaviour.

The pivot algorithm [33, 34], as illustrated in Figure 3, is a "dynamic" version of the dimerization idea. A point on the chain is chosen randomly and one part of the chain

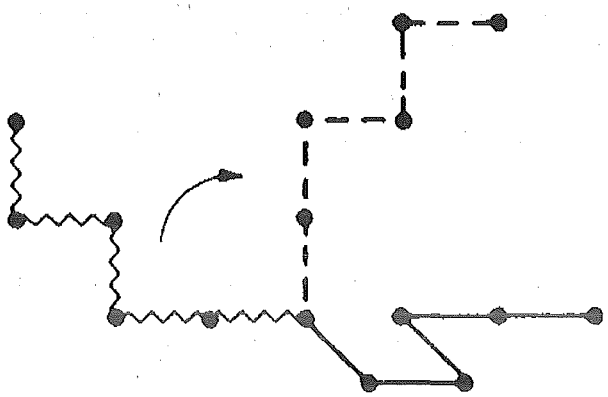


Fig. 3: *Illustration of the pivot algorithm.*

is rotated at random. As with dimerization, this can easily be done for both lattice and off-lattice systems. Given a chain of length N and a pivot point at position N_1, then the acceptance rate p is given by the probability that the new conformation has no overlaps. On a lattice this needs a simple $\mathcal{O}(N)$ check, while in continuous space this is more difficult. On lattices, especially for $d = 2$, one has to take care that the choice of moves does not contain hidden conservation rules. The approach is then ergodic as shown by Madras and Sokal [33] who claim an $N^{0.2}$ power law for the 'relaxation time' of the mean-square end-to-end distance. This method was used to obtain very precise estimates of the exponent ν, $\nu = 0.7496 \pm 0.0007$ ($d = 2$: exact value 3/4) and $\nu = 0.592 \pm 0.003$ ($d = 3$), which is about as accurate as the results coming from dimerization. Figure 4 shows results of a precize determination of the corrections to scaling for the hydrodynamics radius. For the single isolated SAW there is probably no better way to generate very quickly many conformations that are globally different.

However there is no 'free lunch'. As soon as the concentration is increased, either due to other chains or monomer-monomer attraction along the same chain, the acceptance rate is dramatically reduced. A more subtle aspect is that this method relaxes large length scales very fast, while short ones need a longer time. For example, nearest-neighbour bond correlations need up to $\mathcal{O}(N^2)$ moves to relax completely. For many problems it is

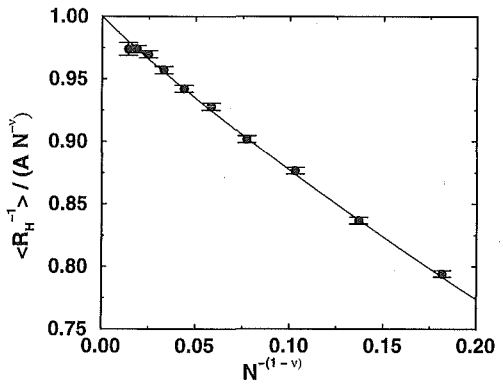


Fig. 4: *Corrections to scaling in the inverse hydrodynamic radius R_H^{-1}: The ratio $\langle R_H^{-1} \rangle / (AN^{-\nu})$ is plotted as a function of $N^{-(1-\nu)}$, where $A = 2.753$ was found from the fit $\langle R_H^{-1} \rangle = AN^{-0.5877} + BN^{-1} + CN^{-1.15}$, which is shown as well ($B = -4.3$, $C = 2.2$). Data are results of a Monte Carlo simulation (dimerization on the fcc lattice, bond length $\sqrt{2}$), where chains of length $N = 64, 128, \ldots, 32768$ were generated. [36]*

essential to cover the equilibration of the short as well as the long distances. This can be overcome in two ways (depending on the model). One is a hybrid method of pivot moves and molecular dynamics simulations (bead spring models) [8] [35]. For fixed bond lengths it is sufficient instead to generalise the pivot approach so that not only tails of the chain, but also internal pieces of arbitrary length, are rotated. The choice of lengths is then adjusted to the density, so that the acceptance rate stays above 10%. This version can be applied to ring polymers as well.

3.2.3 Many-chain methods: generalised reptation algorithms

In semidilute solutions or melts the generalised pivot algorithm will only produce acceptable success rates for moves involving a small number of monomers. Eventually it joins the class of dynamic algorithms, which follow realistically the very slow physical dynamics of the system. This is certainly not what we are looking for in the present context.
The generalised reptation algorithm is an effective way to simulate dense solutions, and also for single chains, in the collapsed regime for $T < \Theta$, the Theta temperature. The method is explained here for a single lattice chain. The original idea of the "slithering snake" goes back to Kron in 1965 and Wall and Mandel 1975 [37]. One randomly takes an end monomer and tries to add it at the other chain-end with a random orientation. If the new chain fulfills the SAW condition, the move is accepted, otherwise rejected. In this way the chain moves (forward and backward) like a snake along its own contour. (The algorithm resembles, but should not be confused with, the *physically realistic* reptation dynamics of polymer melts!) For this method detailed balance is fulfilled trivially, but on a lattice, only a subspace of all conformations is reached. (This subspace excludes conformations where both chain ends are completely surrounded by other monomers.) In continuous space this problem is absent. The extension to many chains as well as interacting chains is trivial. One can also introduce a grand canonical version by allowing

the chain length to fluctuate. The use of pointers allows for very fast and efficient codes. How fast is the relaxation of a chain conformation in CPU time? To estimate this, let us look at the position of the middle monomer of the chain. A measure of the relaxation time T_N^{CPU} is the time until this space point is not occupied by the chain for the first time. For random walks this first passage time follows the same power law as a one-dimensional diffusion along the chains. Since each move only requires a constant N-independent number of operations we get $T_N^{CPU} \propto N^2$ for ideal chains. (To simulate this is a good check on the program.) This method is $\mathcal{O}(N)$ faster than algorithms with "realistic dynamics" such as the Rouse model (see below), whose *real* relaxation time is $T_N \sim N^2$ giving N^3 in CPU time.
Somewhat more complicated is the situation for SAW's. In physical time one expects for the diffusion constant $D \propto N^{-1}$. With $R^2 \propto N^{2\nu}$ and $DT_N \approx R^2$ we expect $T_N^{CPU} \sim NT_N \sim N^{2+2\nu}$. This is, however, not correct. Numerically one finds for the autocorrelation function of $\langle R^2 \rangle$ a relaxation time of $T_N^{CPU} \propto N^{2.15}$ $(d = 2)$ and $N^{2.02}$ $(d = 3)$ instead of $N^{2.5}$ and $N^{2.18}$ respectively. This result, although of advantage for simulations, is not completely understood. The explanation is probably in the difference between diffusion times and first passage times. In addition, it should be kept in mind that because of the SAW condition, SAW's are correlated objects! There are many variants of the aforementioned examples for the study of expecially dense systems. Most notably is here the CBMC method [10] [Configurational Biased Monte Carlo] and a number of elegant variants and extensions, which are widely used in the study of systems with all chemical details included. For an overview see [38]

3.3 More complex single polymer problems: two examples

The above methods are the basis for many applications to more complicated chemical designs or molecular architectures. Branched polymers were already mentioned. There is however a whole zoo of other systems available: H-shaped objects, comb polymers, double stranded polymers *etc.*. Two other interesting classes are copolymers, especially random copolymers, often dicussed in the context of protein folding, and charged polymers. Here I want to discuss two applications on the level of single chains: polyampholytes, and the collapse transition of PEO (polyethylene oxide)in water under pressure.
Many biopolymers are on average neutral, however they contain, from a physicists view, randomly distributed charges, of either sign, along the backbone. The simplest model of such a *polyampholyte* chain [39] treats electrostatics and excluded volume only. A chain with an extensive number of excess charges of one sign, is certainly stretched, while one might expect the opposite from an overall-neutral chain. Analytical theories give contradictory results and are only approximate.
To approach the problem Kantor and coworkers [39] looked at a random copolymer, where the comonomers are either positively or negatively charged. With N monomers, on the average there is an excess charge of $\sqrt{N}$. They found that in the limit of very long chains (and/or low temperatures) those chains with less than $O(\sqrt{N})$ excess charges will collapse, while the others will be expanded. A more closer look shows that the conformations of isolated random polyampholyte chains are determined by a subtle balance between two opposing effects. Fluctuation-induced attraction between oppositely charged monomers and electrostatic repulsion due to an overall net charge. Overall neutral chains collapse to globules. The same holds for chains with net charges up to the root-mean square net

charge $\sqrt{N}$ in an ensemble of randomly charged chains of length N. Beyond this limit the chains adopt pearl-necklace like conformations, an effect which can be understood in analogy to the Rayleigh instability of charged droplets. The figure shows a polyampholyte chain of length $N = 1024$ consisting of 544 positively charged and 480 negatively charged monomers in a random sequence [40].



Fig. 5: *Typical conformation of a huge polyampholyte chain with an asymmetric charge distribution. Note that this picture holds for isolated chains only. At higher concentration, due to the overall neutrality of the whole system, oppositely charged chains and agglomerates will cluster step by step, from [40]*

For standard, uncharged polymers, the chain global conformation changes continuously as a function of temperature and/or solvent quality. But there are contrasting examples as well. PEO is soluble in water under normal atmospheric pressure (as well as in organic solvents), but separates out under high pressure. There is a Flory type theory, which relates this phase separation/collapse transition to the destruction of the hydration shell around the oxygen under pressure [41]. If this hydration shell is destroyed, one is left with the strong hydrophobic interaction of hydrocarbon backbone and the water. Within a simulation this can be taken account of by a simple model [42], where the monomers have an internal degree of freedom. The situation with a hydration shell corresponds to the good solvent case and a fairly large excluded volume. If the hydration shell is destroyed, the excluded volume is smaller and the monomers attract each other, since water is a very poor solvent for the hydrocarbon part of PEO. We now can study the conformations as a function of temperature for a given (pressure dependent) activation barrier for the hydration shell. It turns out that already on the single chain level the collapse transition becomes discontinuous.
Figure 6 illustrates this for the chain form factor $S(q)$. Right at the phase transition point one gets an internal energy distribution function with two maxima. Dividing the configuration space at the minimum yields two coexisting sets of conformations. The figure shows $S(q)$ averaged separately for the two subsets and clearly displays a collapsed and an expanded structure. Most of these runs were performed with the slithering snake algorithm combined with a Metropolis update of the hydration shell. For a general survey of such questions see [43]

4 Dynamics

To obtain information about dynamics, we have to follow the slow, physically realistic, simulation path. There are many tricks to vectorise and parallelise or simplify the algorithms, but these only influence the *prefactors* of the power laws shown in Table 1. Faced with a naturally very slow process, we are forced to employ extremely simple models.

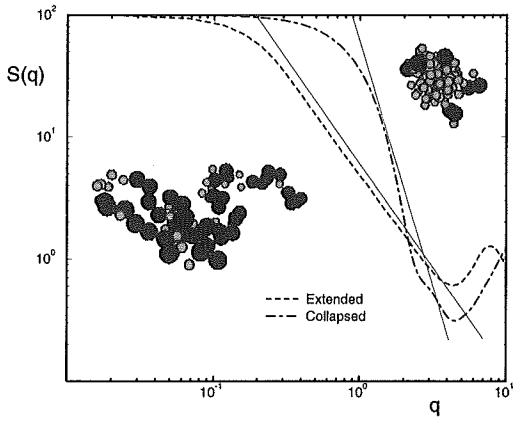


Fig. 6: *Static structure function for $N = 100$ at the collapse transition point for the simple PEO model. The bigger spheres denote the hydrated monomers. For the expanded configurations these are equally distributed all over the chain, while for the collapsed ones only a few surface sites remain available to build up a solvation shell. The asymptotic slopes for the two cases of $q^{-1/0.588}$ and q^{-4} respectively are indicated by straight lines, from [42].*

To test the applicability of any chosen method we need a basic model for dynamics, the Rouse model [25]. This is still the only model on a 'molecular level', which can be solved analytically. The Rouse model treats the dynamics of a gaussian random walk in the overdamped (Brownian) limit. All the complicated inter-chain and intra-chain interactions are summarised in the viscous and random forces from a heat bath. Thus, we totally disregard excluded volume and topological constraints beyond the plain chain connectivity. This model, which represents the dynamics of molten but unentangled (short) chains can readily be solved analytically.
Here we recap the essentials, which will be needed at various lectures in this school. With $\mathbf{r}_i$ the position of the i^{th} monomer, the Rouse equation of motion is

$$\zeta \frac{\mathrm{d}\mathbf{r}_i}{\mathrm{d}t} = -\kappa(2\mathbf{r}_i - \mathbf{r}_{i+1} - \mathbf{r}_{i-1}) + \mathbf{f}_i(t)\,. \tag{15}$$

Here ζ is the monomeric friction constant, κ the bond spring constant and $\mathbf{f}_i(t)$ the random (heat bath) force with $\langle \mathbf{f}_i \rangle = 0$, and (via the fluctuation dissipation theorem) $\langle \mathbf{f}_i(t)\mathbf{f}_j(0)\rangle = 2\zeta T\delta(t)\mathbf{I}\delta_{ij}$. In the discrete version, the Rouse amplitudes $\mathbf{X}_p$ are given by

$$\mathbf{X}_p(t) = \frac{1}{N-1}\left\{\sum_{i=1}^{N-1} \mathbf{r}_i(t)\cos\left(\frac{p\pi(i+1/2)}{N-1}\right)\right\} \tag{16}$$

with relaxation times (for large N)

$$\tau_p = \tau_1/p^2 \quad ; \quad \tau_{Rouse} = \frac{\zeta N\langle R^2\rangle}{3\pi^2 k_B T}\,. \tag{17}$$

Eigenmodes decay exponentially, $\langle \mathbf{X}_p(t)\mathbf{X}_p(0)\rangle / \langle |\mathbf{X}|_p^2 \rangle = \exp(-t/\tau_p)$, resulting in an overall chain diffusion constant $D = k_BT/\zeta N$ and a single chain dynamic structure function $S(q,t)$ scaling as $\ln(\frac{S(q,t)}{S(q,0)}) \propto -q^2\sqrt{t}/6$.
The most natural quantity to measure from a simulation is the mean square displacement of the individual monomers, $g_1(t) = \langle \Delta r^2(t) \rangle = \langle |\mathbf{r}_i(t) - \mathbf{r}_i(0)|^2 \rangle$. One finds

$$g_1(t) \sim \begin{cases} t^{1/2} & t < \tau_1 \ (= \tau_{\text{Rouse}}) \\ t^1 & t \geq \tau_1, \end{cases}$$

while the centre of gravity of the chain always follows $r_{cm}^2(t) \propto t$. There is a simple way to rationalise this. The motion of the single monomer is given by the single monomer diffusion constant k_BT/ζ. For $\langle \Delta r^2(t) \rangle$ each monomer has to carry along as many other monomers n, as there are within the sphere of radius Δr. Thus $\langle \Delta r^2(t) \rangle \propto t k_BT/\zeta \langle \Delta r^2 \rangle$, since the chain is a random walk ($n = \langle \Delta r^2 \rangle$), leading to the above power law. The typical sequence of mean square displacements is shown in Figure 7.

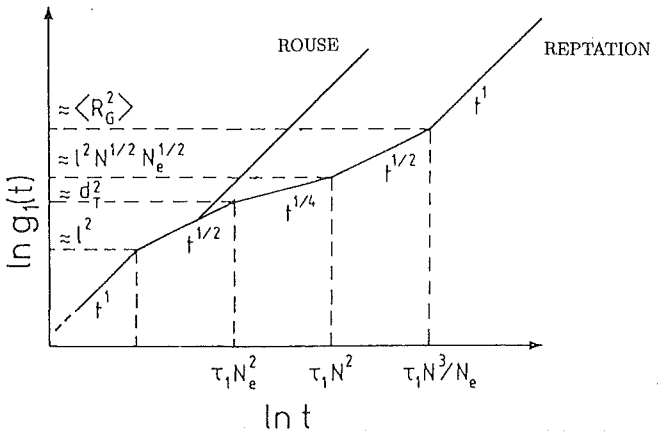


Fig. 7: *A sketch of the monomer mean square displacements for the standard Rouse model and for the reptation model. The time and length scales are indicated for the reptation case.*

This model is a basis for the dynamic interpretation of stochastic algorithms for polymers. Besides the standard requirements for MC procedures (detailed balance *etc.*) we need the following property (for an extensive discussion of details see [3]): to simulate polymer dynamics, any algorithm with stochastic (or other artificial) dynamics must involve only local moves, and must yield Rouse dynamics for gaussian random walks. Below we concentrate on lattice models; however, the generalisation to continuous space is obvious.
The standard procedure is the kink jump method, Figure 8, as follows: (i) select monomer at random; (ii) select trial local move at random; (iii) check the move is topologically permitted; (iv) implement a Metropolis check; (v) decide on acceptance; (vi) start over again.
It is natural to define a MC timestep as one attempted move per monomer of the whole system. This defines, up to a prefactor, the physical time unit τ_0. The prefactor is adjusted in direct comparison to experiment or other simulations. In a simulation we are

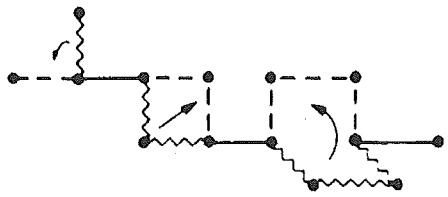


Fig. 8: *Typical kink jump moves for a dynamic Monte Carlo simulation.*

mainly interested in SAW's, but to check the validity of a method for dynamics we need to recover Rouse behaviour for ideal, gaussian chains. To check a given set of local move rules for the SAW, the test for Rouse behaviour is actually performed on non-reversing random walks (NRRW's). NRRW's are walks which do not allow direct back-folding but do not have any long range excluded volume interaction. (Such walks are ideal on large length scales, but have the same local conformations as SAW's and consequently the same set of local moves.)

To achieve Rouse dynamics, the set of local moves must contain moves which create new bond vectors $\{\mathbf{b}_i\}$ inside the chain. In Figure 8, there are 2-bond moves and 3-bond moves. The 2-bond moves only exchange positions of bonds along the chain but do not change the set of bonds vectors. For rings, an algorithm only containing such moves would never equilibrate, while for open chains new bond vectors could only diffuse in from the freely rotating chain ends. This would increase the relaxation time at least by a factor of N. Local rotations, such as the 3-bond move, are needed, so that $\{\mathbf{b}_i\}$ is not conserved and Rouse behaviour recovered. The minimal number of bonds involved in $d = 3$ varies from 2 in continuum or on the fcc lattice to 4 on the diamond lattice. But in $d = 2$, for the 180^o rotation of the 3-bond move we again only exchange of bonds. To circumvent this difficulty, one can use off-lattice models, where both the bond lengths and angles vary. (This would be the MC complement to MD.) For such a model, the excluded volume constraints are usually time consuming to evaluate. Distances have to be calculated at every time step between several monomers. This results in the loss of the main advantage of the MC methods compared with the MD.

A now frequently used alternative approach is the *bond fluctuation* (BF) method. [44], which combines advantages of lattice simulations and continuous space. Figure 9 illustrates the method for $d = 2$ and $d = 3$.

Each monomer consists of 2^d lattice sites. In addition to the excluded volume interaction, the bond length l is restricted to a maximum extension to avoid bond crossing. On the square lattice, one has the constraint that $1 < l < \sqrt{16}$. For $d = 3$, the situation is slightly more complicated. In this case a set of 108 different bonds are allowed [45–47]. Since each monomer occupies 2^d sites, but every jump only requires 2^{d-1} empty sites, the method works effectively at high densities. (It also suffers less from non-ergodicity problems than the standard methods do.)

A first serious application was the study of a 2-d melt of chains [48]. There one would expect the chains to segregate for entropic reasons [27]. In a Monte Carlo study using the bond fluctuation model chains of up to $N = 100$ monomers at a density of up to

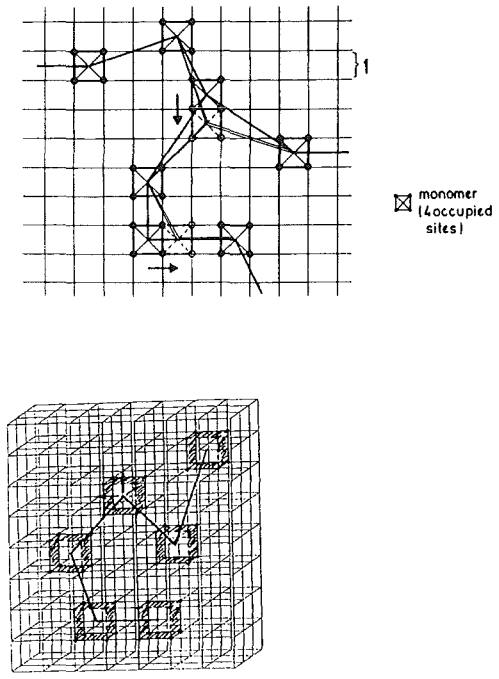


Fig. 9: *An illustration of the bond fluctuation model for a 2-d branched polymer and for a 3-d linear polymer. Typical elementary moves are indicated.*

80% occupied lattice sites were investigated. Figure 10 shows the segregation procedure clearly.

These conformations have recently directly been observed by confocal microscopy on DNA on a membrane support as shown in Figure 11

Even more interesting, however, is the *dynamics* of the $d = 2$ melt. The chains cannot cut through each other; on the other hand, they are compact objects with $\langle R^2(N)\rangle \propto N \propto R^d$. One finds a typical 2-d soft sphere liquid with an average of 6 chains surrounding a given chain. The Rouse model does not take into account any constraints on motion besides the connectivity. Both, the Rouse models and the chain diffusion constant D_0 yield an independent estimate of the monomeric friction constant ζ, which should be consistent, if the Rouse model describes the motion. For $d = 2$, however, one finds that $\zeta_{\text{mode}} > \zeta_D$, and that ζ_{mode} is governed by the conformational relaxation of the chain, while D_0 is controlled by motion of the chain without really reorganizing its internal conformational structure. Recently this picture was impressively supported by experiments on 2-d confined DNA molecules [49], see Figure 11.

More relevant to most actual experiments, of course, is the study of 3-d melts, where one wants to test the concept of chain reptation. Besides standard kink-jump and BF MC, another alternative is to perform a MD simulation. Simulations using the MD method usually employ the bead-spring model [9,50,63], with, in addition, each monomer weakly coupled to a heat bath. (Technically, this is a hybrid method or 'noisy MD'.) Each polymer chain consists of N monomers of mass m connected by an anharmonic spring.

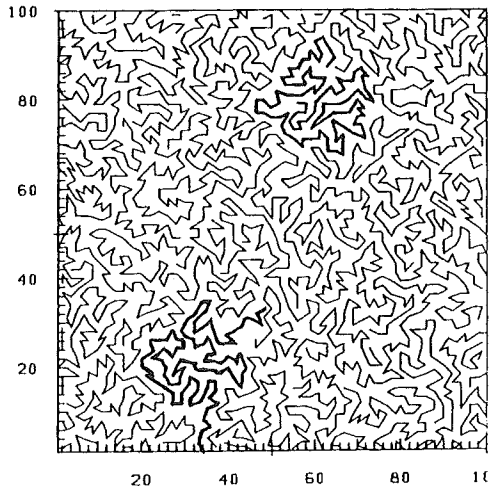


Fig. 10: *A 2-d polymer melt with* $N = 100$ *and* $\Phi = 0.8$ *for an almost completely equilibrated sample [48].*

The monomers interact through a repulsive Lennard-Jones potential given by equation 2 with $r_c = 2^{1/6}\sigma$. For connected monomers we add an attractive interaction

$$U^{\text{bond}}(r) = \begin{cases} -0.5\kappa R_0^2 \ln\left[1 - \left(\frac{r}{R_0}\right)^2\right] & r \leq R_0 \\ \infty & r > R_0 \end{cases} . \tag{18}$$

For melts the parameters $\kappa = 30\epsilon/\sigma^2$ and $R_0 = 1.5\sigma$ usually are chosen, while in solution softer potentials are mostly used [9].
In this algorithm, the equation of motion for monomer i is

$$m_i \ddot{\mathbf{r}}_i = -\nabla_i \sum_{j \neq i} U(\mathbf{r}_{ij}) - \Gamma \frac{\mathrm{d}\mathbf{r}_i}{\mathrm{d}t} + \mathbf{W}_i(t) . \tag{19}$$

Here Γ is the bead friction which acts to couple the monomers to the heat bath, and $\mathbf{W}_i(t)$ describes the random force acting on each bead, with $\langle \mathbf{W}_i(t)\mathbf{W}_j(t')\rangle = \delta_{ij}\delta(t-t')\mathbf{I}2k_BT\Gamma$. Strict MD runs for polymers typically exceed the stability limits of a microcanonical simulation; these small damping and noise terms extend stability and define a canonical ensemble. We have used $\Gamma = 0.5\tau^{-1}$ and $T = 1.0\epsilon$ in most cases and $m = 1$. This value of Γ is large enough to stabilise the run but small enough *not* to produce in itself Rouse-like behaviour on length and time scales of the order of a few bond lengths. Thus Γ and $\mathbf{W}$ are not be confused with ζ and $\mathbf{f}$ in the Rouse equation 15 for a single chain; in this simulation, the Rouse friction is dominated instead by collisions with other chains. The program can be vectorised [52,53] or parallelised [54]. One can use equally distributed random numbers, which have the mean value and the second moment required by Equation 19. The use of a Verlet algorithm then allows for time steps as large as 0.012τ and for up to about 300000 particle timesteps per second for a typical vector processor or more than 100000 particle steps per processor or on a Cray T3E. With this method a huge variety of systems have

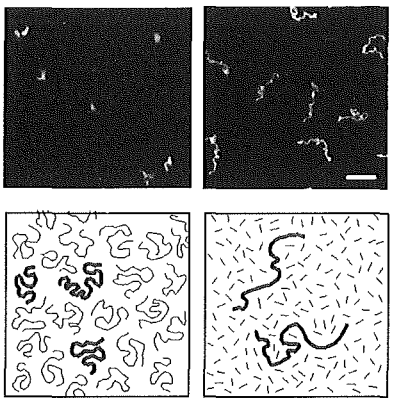


Fig. 11: *Experiment analogous to the simulation in Figure 10. On the left side fluorescent marked DNA in a dense 2-d DNA layer on a membrane are shown. This is the same situation as shown in Figure 10. On the right the same marked DNA are in a 2-d "dilute Solution" on a membrane, illustrating the dramatic chain expansion. The length scale indicated in 10 μ m from [49]*

been studied. Most recently a melt of chains of length N = 10000 was simulated [56]. There are a number of other thermostats in the literature. Especially I would like to mention the DPD (dissipative particle dynamics) thermostat, which conserves momentum and thus hydrodynamics as well [55]

4.1 MC versus MD for dense systems

Which method is best to use for studying the dynamics of dense polymeric systems? I think that the choice should be between the BF Monte Carlo method and MD, or variants of these two approaches. For the athermal case (hard core repulsion only) we can compare the CPU time to reach the crossover time for entanglements τ_e as a measure of the relative speed of the algorithms. By doing this we estimate that BF Monte Carlo is somewhat faster than MD on vector computers. However the inclusion of soft interactions has a much stronger effect on slowing down BF than it does for MD. (The main speed advantage of the MC comes from the simple acceptance test for the moves compared to the more complicated force calculations of MD.) Which method to use therefore depends on the particular question under consideration, whether it is better to work in the continuum (for example, to study shear flow), and whether it is acceptable to have stochastic dynamics on all time scales: using MD, the Rouse behaviour for short chains (or early times) is a consequence of the interactions, while it is built in explicitly in MC. If one is interested in the behaviour of gels or polymer networks under swelling or elongation, or the forces between polymer brushes [57] [58], then a continuum simulation using MD is probably

more appropriate; generally speaking, the MD method is more flexible. Taking modern RISC processors, as found in workstations and most parallel computers, most of the speed advantages of the MC approach are lost anyhow. These processors typically do not take advantage of especially fast integer arithmetic.

4.2 Dynamics and flow of melts: reptation

The dynamics of polymer melts is observed experimentally to change from an apparent Rouse-like behaviour to a dramatically slower dynamics for chains exceeding the characteristic length N_e. (For longer chains, one observes a much slower diffusion, $D \propto N^{-2}$, and an increased viscosity, $\eta \propto N^{3.4}$.) There are several theoretical models which try to explain this behaviour. However, only the reptation concept of Edwards and de Gennes [25] and variants of this approach take the non-crossing of the chains explicitly into account. This approach is the only one which, at least qualitatively, can account for a wide variety of different experimental results, such as neutron spin echo scattering, diffusion and viscosity. While it cannot explain all experimental data it does remarkably well, particularly considering its conceptual simplicity.

The idea of reptation is that the topological constraints imposed by the surrounding on each chain cause a motion along the polymers own coarse-grained contour. The diameter of the tube, to which the chain is constrained to, is the diameter of a subchain of length N_e, namely $d_T \propto N_e^{1/2}$. The chains follow the Rouse relaxation up to the time $\tau_e \propto N_e^2$. For longer times the constraints become dominant and the chain moves along its own contour. To leave the tube, the chain has to diffuse along the tube a distance of the order of its own contour length, $d_T N/N_e$. In order to leave this original tube the chain needs a time $\tau_d \propto N^2(N/N_e)$, giving $D \propto N^{-2}$ and $\eta \propto N^3$. The difference between the predicted and the measured exponent for η is still not completely understood. For the mean square displacements of the monomers, $g_1(t)$, the model predicts the standard Rouse behaviour $g_1(t) \propto t^{1/2}$ for $t \leq \tau_e \propto N_e^2$, the Rouse relaxation along the tube with $g_1(t) \propto t^{1/4}$ for $t \leq \tau_N \propto N^2$, the diffusion along the tube with $g_1(t) \propto t^{1/2}$ for $t \leq \tau_d \propto N^3$ and finally the free diffusion of the chains. These four distinct regimes are a direct consequence of the reptation model. (For a more general discussion of this and the competing but less successful concepts, and a rather complete list of references see [25] [9] [61].) Below we review a few results, which have been obtained recently by both MD and MC simulations. The transition from Rouse to reptation can be identified from the centre-of-mass diffusion constant,

$$D(N) = \frac{k_B T}{N\zeta}, \quad N < N_e \tag{20}$$

$$D(N) \propto N^{-2}, \quad N \gg N_e . \tag{21}$$

Here ζ is the monomeric friction coefficient. Several forms exist in the literature for the prefactor of the second expression and the crossover. To compare results from different simulations and also experiment, a plot of $D(N)/D_{\text{Rouse}}(N)$ versus N/N_e or M/M_e respectively should give one universal curve since N_e is thought to be the only characteristic scale at the crossover. Here $D_{\text{Rouse}} = k_B T/\zeta N$ and M_e is the experimental entanglement mass. This mapping is important for our understanding, since experiment and simulation use different methods to estimate M_e or N_e. Figure 12 shows the results for simulation and experiment [9] [56]. The MD simulations were performed at a density of $\rho = 0.85\sigma^{-3}$ and

the MC simulations [59] at two different volume fractions $\phi = 0.4, 0.5$. The experimental data are NMR measurements of Pearson *et al.* [60]. This gives $M_e = 1350$ or equivalently $N_e = 96$ monomers.

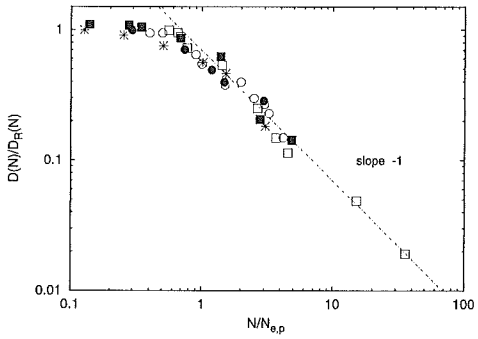


Fig. 12: *Scaled diffusion constant $D(N)/D_R(N)$ vs. scaled chain length $N/N_{e,p}$ for polystyrene (•) ($M_{e,p}$ = 14600, T = 485 K), polyethylene (filled box - symbol) ($M_{e,p}$ = 870, T = 448 K), PEB2 (filled △), ($M_{e,p}$ = 992, T = 448K), our bead spring model (△) ($N_{e,p} = 72$), the bond-fluctuation model for $\Phi = 0.5$ (box) and tangent hard spheres at $\Phi = 0.45$ (○). All data are scaled with $N_{e,p}$ from the plateau modulus or with 2.2 N_e from $g_1(t)$, from Ref. [56].*

Both simulations and the experiment show a clear crossover from the Rouse $D(N) \propto N^{-1}$ behaviour towards the $D(N) \propto N^{-2}$ regime. From these numbers it is clear that the simulations are in a position to analyse the crossover towards the reptation regime in some detail and, increasingly, to reach the fully entangled regime. For more details I refer to recent publications [56] and subsequent lectures of this school.

5 Network structures

There has been extensive research on polymer networks for many years. A major problem is that it is experimentally not feasible to collect the necessary structural information in order to allow an unambiguous test of theoretical predictions. By simulation it is possible to analyse in detail the structural properties. This allows for a more thorough investigation of the effects of the non-crossing of the chains. One expects the consequences of conserved topology to be even stronger in crosslinked systems than in uncrosslinked ones. (This should hold for dilute polymer gels as well as for dense networks; however due to the importance of hydrodynamic effects, gels are even more complicated to simulate.) There have been various simulations on the properties of dense polymer networks. These simulations range from rather rigid model systems, where the crosslinks cannot move, to highly complicated, fully mobile randomly crosslinked polymer melts [57]. The simulation techniques used are both MD and (lattice) MC. More recently also the swelling behaviour of networks have been investigated [62].
Refs. [62–66] performed MD simulations on a variety of different model networks with two different interaction potentials. These different simulations were used to study the influence of the possibility of chains crossing each other, the influence of different kinds

of disorder (strand length, connectivity, topology) as well as the elasticity and relaxation as a function of the strand length.

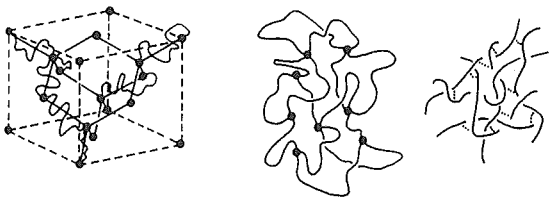


Fig. 13: *Sketches of the typical network topologies considered in simulations.*

Figure 13 illustrates three different classes of networks. The first system, an equilibrated polymer melt with randomly placed crosslinks, certainly resembles most closely many experimental systems such as those produced by radiation crosslinking or vulcanization. These systems have several kinds of disorder. The strands between subsequent crosslinks are extremely polydisperse, with an exponential distribution of strand lengths. Only a few crosslinks per chain are needed to give a gel-fraction which is nearly 100%, though the elastically active part of the network is significantly smaller. In this case there are many dangling chain ends or even some dangling clusters, like little trees which are connected to the network by only one strand. Those dangling pieces are expected to be responsible for the extremely slow decay (in the time-dependent modulus $G(t)$, for example) seen in most experiments. In addition, trapped loops and knots may play an important role in both linear and nonlinear elasticity, while the length of the shortest chemical pathway through the network cluster is expected to be of special relevance in nonlinear elasticity (since extension of a sample beyond this length forces breakage of covalent bonds). Although it is possible to identify the elastically active part of the cluster unambiguously [63] , such disordered systems are extremely difficult to analyze in a systematic manner.
A somewhat more idealised case is an end-crosslinked polymer melt [62] [63] . Such systems have been considered experimentally as well [67] . There one starts with a monodisperse melt. After equilibrating, the chains are kinetically crosslinked at the ends. All strands in the network have the same length. (In a different type of end-linking, each free end binds instead to a randomly selected neighbour bead.) Now there are only two sources of quenched disorder in the system. One involves permanent topologica links, the second, the distribution of chemical pathways through the system, which again is highly polydisperse, either at the level of individual network strands, or that of a percolating chemical pathways across the system.
Finally one can consider highly idealised networks, which certainly are somewhat remote from experiments, where the *only* source of disorder the occurrence of linked loops. These are the interpenetrating lattice networks, in which each subnet is an ordered diamond lattice that interpenetrates other, similar nets [64–66]. They can be analyzed and investigated in a variety of ways in order to shed some light on the role of entanglements and conserved topology. The effects of disorder in networks are especially important under strong elongational stress.
The use of modern parallel computers now allows us to simulate much larger systems, including the dynamics/relaxation of gels and testing current theories on a semi-microscopic view.

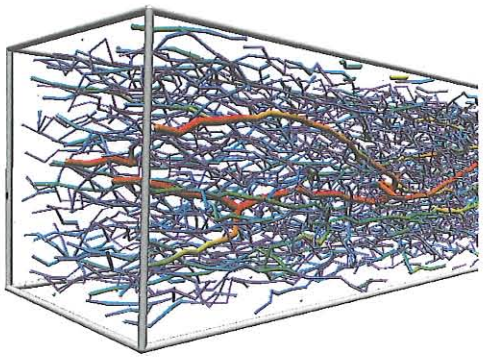


Fig. 14: *Visualization of the stress distribution in a highly extended polymer network [66] from a simulation of randomly interpenetrating polymer networks with diamond topology. The only source of disorder in this particular system are random knots. The 'shortest topological paths' carry most of the stress.*

6 Further reading

There are of many other interesting polymer simulation problems, which were not discussed above. An extensive overview can be found in a recent book edited by K. Binder [68]. For a more microscopic approach the recent book edited by Monnerie and Suter [12] provides an interesting set of papers. Here we summarise these fields briefly.

Polyelectrolytes: The simplest charged polymers are weakly charged polyelectrolytes. The whole field of macromolecules with long range interactions is still not well developed in spite of many years of research [43,69,70]. Simulations start to give some clear answers, which await a better theoretical understanding. Until now one has been able to handle up to about 1000 chain monomers and 1000 counterions. Recent algorithmic improvements allow to study up to 20000 charges for a typical polyelectrolyte or colloid solution. Figure 15 illustrates a typical solution of charged chains, where the counterions are explicitely taken into account. Note that for many biosystems the screening is so strong, that the long range nature (partially) gets lost! [71]. A thorough analysis on algorithms dealing with long range forces can be found in [72] [73].

Tethered chains: There is a huge literature on polymers that stick with either one or both ends to another object. The most common classes, polymer networks and star polymers were mentioned above. For details of simulations on the other classes of tethered chains see [74]. If the polymers are not connected to a center molecule, but stuck to a surface/interface, one speaks of a polymer brush. Such brushes range from amphiphilic monolayers, where the chains are very much stretched (eg. layers of a membrane) to rather soft systems. A class somewhat in between stars and brushes is given by polymer stabilized colloids. There the structure of the surface layer is in between that of a classical brush and that of a multi-arm star polymer.

Phase separation: Polymers in melts and dense solutions interpenetrate each other strongly.However, they are 'poor in translational entropy', so that even a very small

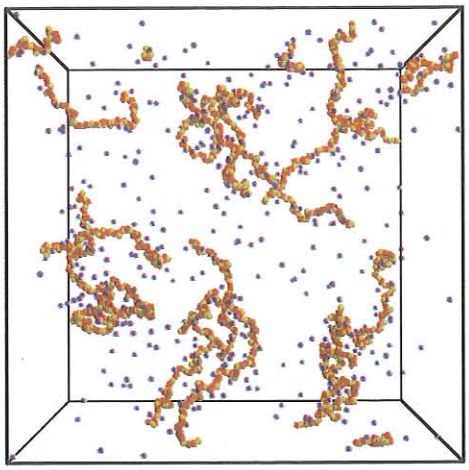


Fig. 15: *Typical solution of a good solvent polyelectrolyte [71]*

repulsion between unlike polymers lead to phase separation. Even deuteration is sufficient to derive phase separation from similar protonated chains. Phase separation has attracted much simulation activity over the years; for a review see [68].

Block co-polymers: A block co-polymer consists of two or more stretches of different polymer linked together in a single chain. As a function of composition they can show lamellar phases, crystalline ordered phases of spheres, bicontinous phases and so on. Most simulations so far were done using a quasi grand canonical approach, derived from blend simulations. Recently, also the dynamics was studied by MD simulation [75]. Figure 16 shows a typical picture of a multidomain lamellar structure.

Membranes: A special case of lamellar systems are membranes. Depending on the nature of the systems, namely tethered or liquid, different methods are used. In the first case, algorithms very close to the ones here (2-d "polymer") have been widely used. In the second case two major directions have been emerged. One in the MD simulation of "real" model amphiphiles, similar to the ones shown in Figure 16, the others are "randomly triangluated surfaces", see [77]. To cover this in more detail would require a review of its own.

7 Non Equilibrium Simulations (NEMD)

With increasing computer power and also significantly improved algorithms, the properties of driven complex fluids slowly become accessible to simulations. There is an extended literature on MD simulations of small particle systems (LJ-Fluids). Many conceptual problems, such as the proper definition of a temperature in a sheared system become less critical, if one can work at e. g. reasonable small shear rates. For complex fluids, such as polymers the typical shear velocities Figure 16 have to be much smaller than the thermal bead motion.

Thus, with optimized algorithms a number of classical problems can be approached nowa-



Fig. 16: *Lamellar system of nearly 10^6 amphiphilic molecules. The whole system is sheared and slowly huge ordered domains are emerging. Note that one finds, just as in experiments on block copolymers, shear bands. [76]*

days. Kröger and co-workers [16] used the MD simulation model to perform NEMD (nonequilibrium MD) simulations where the sample is subject to a steady shear or stress. They were able to fully covers chains of up to N = 100 monomers of equivalently about $3N_e$. While this is too short to study the viscosity or the shear-alignment of highly entangled chains, changes from Rouse to the entangled regime were observed. [16]
In another variant the heat conductivity of both polymers and smaller molecules (but now with more chemical details) as well as the shearing behavior of a lamellar block copolymer system could be studied [17, 18]. While in the first example the strain rate or the stress is imposed via the periodic boundary condition, in the second momentum is exchanged allowing for microcanonical simulations.

8 Linking Scales

A simulation eventually should provide complete information about the properties of the system under investigation. This goes beyond the generic problems discussed so far. Thus we have to link different scales: we want to relate the chemical structure of a system to the overall behaviour of the material [13]. One of the long-standing challenges within the modelling of complex materials is to apply methods which allow coverage of the range from microscopic to semi-macroscopic regime. Recently, methods were developed which map polymers to a mesoscopic level and then reintroduce the atomistic structure [78–81]. Below I first describe a mapping procedure to go from microscopic description of a polymer chain to the mesoscopic description, which allows fairly effective simulation on a

coarse grained level. The study of three modifications of one polymer structure, namely polycarbonates allows a test of the sensitivity.
Thereafter, first steps toward the next level of description are discussed. Starting from the conformations of polymer chains on the coarse-grained level, each chain is mapped onto an extended soft particle with only three internal degrees of freedom. All methods will be within continuous space and not confined to a lattice structure.

8.1 Coarse graining

As an example, a systematic approach to renormalise the intra-chain interactions towards a coarser level for three different polycarbonates is explained. [78]. The three modifications of the basic polycarbonate structure are BPA-PC, BPZ-PC, and TMC-PC (Figure 17). Although the backbone sequence is the same these have remarkably different physical

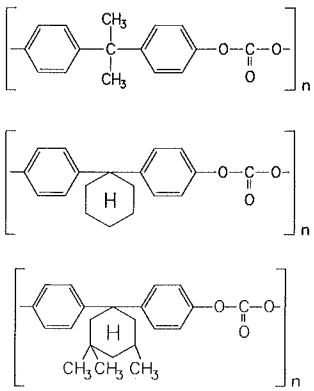


Fig. 17: *Three modifications of BPA repeat units tested for the coarse graining procedures. From top to bottom: BPA-PC, BPZ-PC, TMC-PC.*

properties. For the first two (BPA and BPZ) the glass transition temperature T_G is roughly the same ($T_G \approx 420$K), while the third one has a glass transition temperature which is about 80 to 100 K higher, around 500 K. On the other hand, BPA-PC is ductile while BPZ-PC is brittle; TMC-PC is less ductile than BPA but much less brittle than BPZ. Not only are the glass transition properties different, but also the entanglement chain lengths N_e in the melt are significantly different. For BPA-PC an extremely short entanglement length of $N_e = 7$ monomers is reported. This length increases through $N_e = 9$ monomers (BPZ) to $N_e = 14$ monomers for TMC-PC. In particular, the extremely short entanglement length for BPA-PC is not understood. Considering other well studied-polymers like polyethylene or PDMS (polydimethylsiloxane), one would expect it to be larger by a factor of at least 5 to 10. Whether this is the result of a special local chain structure (banana shaped repeat units joined by almost pivot-like junctions) is beyond the scope of the present paper, but is a matter of current studies.
The coarse graining procedure is explained in some detail here for BPA-PC. The coarse-grained monomers have to be designed to be easily be identified with specific chemical groups of the polymer itself. Considering the chemical structure of the three different

polycarbonates a 2:1 mapping onto spherical beads seems to be a first reasonable choice, as illustrated in Figure 18.

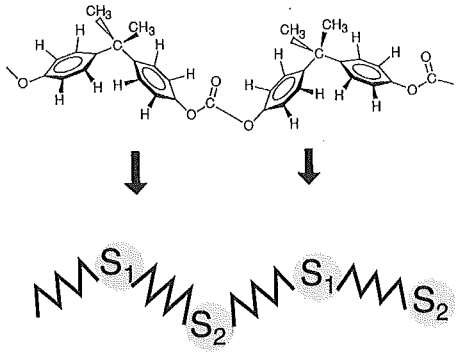


Fig. 18: *Illustration of the mapping procedure fro a 2:1 mapping where the repeat unit of a BPA-PC chain is replaced by two monomers of a generalised bead spring chain. The geometrical centers of the carbonate group and the geometrical centre of the isoprpylidene group respectively are mapped onto the centers of the new spherical bead [78].*

The resulting coarse-grained structure then only has four relevant internal degrees of freedom: the bond length ℓ between carbonate and isopropolydene group, α, the carbonate-isopropolydene-carbonate bond angle, β, the isopropolydene-carbonate-isopropolydene bond angle and ϑ, the torsion angle. Of course there are many other alternatives, and a priori it is not obvious which is the best! Thus, the focus is more on the general idea rather than on specific details.

To arrive at the coarse-grained interactions from the microscopic model one can imagine a number of empirical fitting procedures. Here, we follow a different route. The coarse-grained potentials not only have to include energetic aspects of the microscopic model but also entropic terms from the different possibilities of local conformations. We first use intra-chain distribution functions to construct the bonded potentials in the coarse-grained model. Knowing the potential functions of the detailed chemical system, it is rather straightforward to perform a single chain MC simulation to a very high accuracy at a given temperature of the conformations of individual free random walks. The probability distribution functions of conformations of such a model system are only dependent on temperature and originate from the bonded interactions along the backbone of a chain. The potentials for the microscopic models are derived from *ab initio* quantum chemistry calculations. Using the microscopic model to generate configurations, we sample the probability distribution function $P(\ell, \alpha, \beta, \delta)$ for the coarse-grained model in the limit of single isolated random walks.

The coarse-grained distribution function is temperature dependent via the Boltzmann weights of the different states of the microscopic model. The most crucial assumption now is, that the distribution function of the set of variables factorises into independent distribution functions of the individual variables:

$$P(\ell, \alpha, \beta, \vartheta) = P(\ell)P(\alpha)P(\beta)P(\vartheta) \tag{22}$$

The distribution function P is determined at each temperature separately, and may be written

$$\begin{aligned} P(\ell) &\propto \exp(-U(\ell)) \\ P(\alpha) &\propto \exp(-U(\alpha))\ldots \end{aligned} \tag{23}$$

U is a generalised potential function at that temperature, already expressed in units of k_BT, so that one may in effect keep the simulation temperature at $k_BT = 1$, which is of technical advantage for molecular dynamics simulations. From Equation 23 we get the forces

$$\begin{aligned} F_\ell &= -\frac{d}{d\ell}\ln P(\ell) \\ F_\alpha &= -\frac{d}{d\alpha}\ln P(\alpha)\ldots \end{aligned} \tag{24}$$

as they originate from the conformations of the coarse-grained model. This approach avoids the fitting of a functional form of the coarse-grained potential functions to the microscopic parameters. The only fitting procedure is a smoothing for potentials in order to get rid of the scatter in the sampling and to stabilise the resulting force. There is no need to determine the partition function explicitly, since it only shows up as a constant in the potential and thus does not alter the resulting forces.

Using this model we can now simulate dense polymer systems. The volume of the effective hard-sphere beads of the coarse-grained model is adjusted to give the same Van-der-Waals volumes as in the experimental case (normalised to the simulation density). The simulations are then performed as molecular dynamics simulations at constant volume. The simulation density is adjusted to the experimental mass density in every case; after this, there is no freedom left to adjust parameters.

If this procedure is to reproduce the essential aspects of the different chemical species, then not only should the static structure which comes out of this simulation compare well to the experimental systems, but also the dynamics. MD melt simulations were performed as described before. The excluded volume interactions of the monomers are taken into account through a repulsive Lennard-Jones interaction. For static properties, the mapping between simulation and physical units requires a length, fixed by equating the the mass density in simulation and experiment. Starting from a mass density of $\rho_{pc} = 1.05$ g/cm^3 (BPA-PC at 500 K) and the simulation number density of $\rho_{MD} = 0.85\sigma^{-3}$, we arrive at a length scaling of $\sigma = 5.56$ Å for the present case.

To compare the dynamic properties, a time scale is also required. This if found by using the Rouse model to calculate the melt viscosity in terms of the centre-of-mass diffusion constant of the chains, and equating this to the observed viscosity at some reference temperature. This is possible as we have one case where the highest experimental temperature and the lowest simulation temperature coincide. For the present example one gets $\tau = 2.21 \times 10^{-10}$ sec, where τ is the simulation (Lennard-Jones) time unit. The simulation time step is typically $\delta t = 0.01\tau$. However, the absolute comparison of dynamic quantities should only be taken as indicative since the experimental systems and the simulations systems comprise different chain lengths and also the effect of polydispersity might alter this absolute scale by some prefactor. Compared to other molecular dynamics simulations of microscopic models, the simulation time step is roughly three orders of magnitude larger than there. Taking the simplicity of the potentials and the

short range nature of the interactions into account the resulting speed-up is of order 10^4. The simulated systems typically comprised between 1000 and 10000 model monomers on chains of 20 or 60 model monomers. For our cubic simulation box this means that one can easily simulate systems of up to 125 Å^3. As it turns out, the inter-chain interactions strongly modify the angular distribution functions compared to the isolated chain. For the coarse-grained model we first check the dynamical properties as a function of temperature, especially approaching the glass transition temperature. The properties of many materials when approaching the glass transition temperature are well described by the so called Vogel-Fulcher behaviour

$$D = D_o \exp(-\frac{A_o}{T - T_{VF}}) \tag{25}$$

given here for the tracer diffusion constant D of the chains: A_o is a generalised activation energy and T_{VF}, the so called Vogel-Fulcher temperature, typically is about 80 degrees below the calorimetric glass transition temperature. The prefactor D_o is a hypothetical high temperature diffusion constant. For the present situation D_o is easy to determine, because it simply corresponds to the freely jointed polymer melt with athermal excluded volume, and all the chemistry dependent intra-molecular interactions are set to zero. (Extensive computer simulations are available for that case.)
The results qualitatively match the experimental situation, namely that the Vogel-Fulcher temperature for TMC-PC is about 80–100 degrees above the Vogel-Fulcher temperature of BPZ-PC and BPA-PC while the generalised activation energy, is roughly the same for BPA and TMC while it is different for BPZ-PC. Even quantitatively the results are not that different from the typical experimental value as Table 2 shows, since due to the short chains in the simulation, the values of T_{VF} are expected to be too low by about 50K.

T_{VF}	BPA-PC	TMC-PC	BPZ-PC
Simulation (N=20)	322	407	292
Experiment	387	477	392
A_0	BPA-PC	TMC-PC	BPZ-PC
Simulation (N=20)	1305	1363	1443
Experiment	1012	1073	1534

Table 2: *Activation energies A_o (below) and Vogel-Fulcher temperatures T_{VF} (above) for experiment and simulation. While the error bar for T_{VF} is fairly small, it is significant ($\approx$ 30 %) for the experimental determination of A_o due to the large polydispersity of the typical commercial samples.*

8.2 Restoring chemical detail

There are various ways to check the quality of the resulting structures with respect to experiment. A typical test would be to compare the mean square end-to-end distance $\langle R^2 \rangle$ to results from scattering experiments. However, since the experimental samples are highly polydisperse, the resulting answers from scattering experiments are somewhat questionable. Furthermore, a crucial check is the direct comparison of conformations of

systems. To compare the conformations resulting from the simulations unambigously to experiment, we reintroduce the chemical details into the coarse-grained chain. This is one of the reasons why it was important to device a mapping procedure which stays near to the chemical structure of the objects. We have a one-to-one correspondence of the model monomers to the different parts of the chemical repeat unit of the chains.

We start out with a chemically detailed chain with the correct bond angles and bond lengths, but free torsion angles. Then the chain is placed in the system and rotated via the torsional degree of freedom along the path of the coarse-grained chain. The structure is then optimised by a steepest descent method in energy space. By this approach, all coarse-grained chains are mapped onto their chemically detailed counterparts individually. The deviations of the minimised structure from the starting structure are extremely small: $\langle \Delta r^2 \rangle = 0.01$ Å^2. In a second step, all chains are combined and, to allow for the introduced Van-der-Waals interaction, are locally equilibrated within a short MD run. This local equilibration of course only includes motion on a very small distance.

Since for the resulting local packing structures the polydispersity effects of the experimental melts should not be that important, we now can calculate the structure function of the whole system and compare it directly to neutron scattering. The neutron scattering structure function $S(q)$ is given by

$$S(q) = \langle | \sum_j b_j \exp(i\mathbf{q} \cdot \mathbf{r}_j) |^2 \rangle \tag{26}$$

For this comparison all atoms of the systems are explicitly included with their corresponding scattering length b.

Figure 19 gives a typical example for BPA-PC, where we show the results for a fully protonated system and compare the data to both neutron scattering and a previous (amorphous cell) simulation.

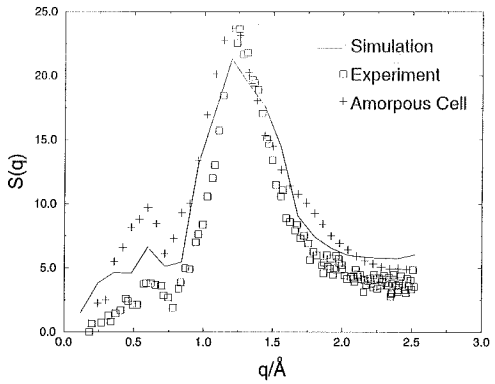


Fig. 19: *Coherent structure function $S(q)$ in absolute units in comparison to amorphous cell simulation and neutron scattering data [78, 80].*

Other structure functions show the same agreement to experiments. For a more general discussion of such problems I refer to [13, 80]

9 An even coarser view on polymers

So far, all models considered allow the correspondence of a bead of a polymer to one or to a few repeat units of a given chemical species. This still means that the number of degrees of freedom that have to be considered is proportional to the number of monomers of a given chain, causing enormous problems if one wants to try to simulate big systems (many chains instead of many monomers, mixtures of colloids and polymers, where the diameter of the colloids is of the order of the coil diameter ...). For this we go back to Figure 1. There, three levels of description were illustrated. I have discussed the microscopic and the mesoscopic regime and, in one case, the link between the two. Now we want to consider another step, namely to try to map the chains from the mesoscopic system up to the semi-macroscopic regime where we replace the chains by soft ellipsoidal particles which can strongly overlap in the melt [13, 82–84]. For such a model each chain is represented by a soft ellipsoid which varies its size and shape.
We separate the free energy of a system into an intra-chain part and an inter-chain part. For the total free energy F we make the ansatz:

$$F = \sum_{i=1}^{M} F_{intra}^{i} + F_{inter} \tag{27}$$

The first sum runs over all M chains of the system. First let us consider the intra-chain part of the free energy. In a melt, the allowed conformations of a polymer chain are the same as a self avoiding walk in 'vacuum'. (The change from self-avoiding to idea random walk statistics in a melt is a result of the inter-chain interactions causing reweighting of configurations, but not of the intra-chain conformational distribution.) Thus, we characterise the intra-chain contribution to the free energy by the number of states which correspond to a specified moment of inertia tensor of the chain. Denoting this $\underline{\underline{R}}$ and its eigenvalues R_1, R_2, R_3 (with $R_1 > R_2 > R_3$), we generate microscopically, in a similar manner to that described in the previous sections, a probability distribution $P(\underline{\underline{R}})$. To each $\underline{\underline{R}}$ belongs an average intra-chain monomer density distribution $\rho(\mathbf{r}, \underline{\underline{R}})$ which is sampled as well. Here $\mathbf{r}$ is the position vector from the centre of mass in the principal frame.
The averaging for ρ is carried out over all conformations with a given $\underline{\underline{R}}$). Taking into account that the set of allowed conformations of individual chains in the melt and for the isolated chain are the very same, the intra-chain contribution to the free energy from chain i is simply given by

$$F_{intra}^{i} = -k_B T \ln P(\underline{\underline{R}}^{i}) \, . \tag{28}$$

Now we assume that the inter-chain interaction is given by the pairwise overlap of the ellipsoids of the different chains. Since each inertia tensor corresponds to a density distribution, we can write for the inter-chain free energy contribution of the pair ij

$$F_{inter}^{(ij)} = \epsilon(N) \int \rho_i(r - r_i^{cm}, \underline{\underline{R}}^{i}) \rho_j(r - r_j^{cm}, \underline{\underline{R}}^{j}) d^3 r \tag{29}$$

Here each of the two density distributions is centered on the centre of mass of the corresponding chain, and $\epsilon(N)$ is an adjustable parameter accounting for the binary excluded volume as well as the overlapping contribution of the probability distributions. For technical details refer to [82].

A typical test system consists of 10000 chains of N = 100 monomers. The simulation procedure is a standard Metropolis Monte Carlo procedure as described in section 3. The ellipsoidal particles are first randomly distributed in the system, with a distribution of shapes corresponding to isolated SAW's. Then MC simulation is performed such that the ellipsoids can move in space (translation) and can change both the length and the orientation of their principal axes (shape deformation).
By doing this one is able to investigate phase separation kinetics and morphology development of huge polymer samples or the phase diagram of polymer colloid mixtures [83]. The next step will be the reintroduction of the explicit chains in order to complete the scheme as indicated in Figure 1.

Acknowledgments

The present chapter contains many results of collaborations with many colleagues through the last years. The work on coarse-grained models especially benefitted from a longstanding collaboration with G. S. Grest, B. Dünweg, K. Binder, R. Everaers, M. Murat and M. Pütz. CPU time was granted by the German Supercomputer Centre, HLRZ Jülich and the Rechenzentrum Garching of the Max-Planck-Society. The multiscale simulations were supported by the BMBF under Grant No. 03N8008E0 and the Bayer Corp..

References

[1] *Monte Carlo and Molecular Dynamics of Condensed Matter Systems, Como Conference Proceeding*, edited by K. Binder and G. Ciccotti (Società Italiana di Fisica, Bologna, 1996).

[2] Baumgärtner and K. Binder, *Applications of the Monte Carlo Method in Statistical Physics* (Springer, Berlin, 1984),

[3] K. Kremer and K. Binder, Comp. Phys. Reports **7**, 259 (1988).

[4] K. Binder, in *Computational Modeling of Polymers*, edited by J. Bicerano (Springer, Berlin, Heidelberg, New York, 1992).

[5] *Computer Simulation of Polymers*, edited by R. J. Roe (Prentice Hall, Englewood Cliffs, NJ, 1991).

[6] *Elastomeric Polymer Networks*, edited by H. E. Mark and B. Erman (Prentice Hall, Englewood Cliffs, 1992),

[7] M. P. Allen and D. J. Tildesley, *Computer Simulations of Liquids*, 2nd ed. (Oxford Univ. Press, London, 1989).

[8] K. Kremer, in *Monte Carlo and Molecular Dynamics of Condensed Matter Systems*, Como Conf. Proceedings 1995, edited by K. Binder and G. Ciccotti (Societa Italiana di Fisica, Bologna, 1996), p. 671.

[9] S. G. Whittington, *Numerical Methods for Polymeric Systems, The IMA Volumes in Mathematics and its Applications* (Springer, New York, 1998),

[10] D. Frenkel and B. Smit, *Understanding Molecular Simulation: From Basic Algorithms to Applications* (Academic Press, San Diego, CA, 1996).

[11] Proc. Int. School of Phys. "Enrico Fermi": Molecular Dynamics simulation in statistical mechanics systems. G. Ciccotti. W. G. Hover (eds.), North Holland (1986), an "old" classic book.

[12] L. Monnerie and U. W. Suter, *Atomistic Modelling of Physical Properties*, Vol. 116 of *Advances in Polymer Science* (Springer, Heidelberg, 1994).

[13] J. Baschnagel *et al.*, in *Bridging the Gap Between Atomistic and Coarse Grained Model of Polymers: Status and Perspectives, Advances in Polymer Science* (Springer, Berlin, in press 1998).

[14] D. J. Evans and G. P. Morris, *Statistical Mechanics of Non-Equilibrium Liquids* (Academic Press, London, 1990)

[15] S. Hess et al., in *Monte Carlo and Molecular Dynamics of Condensed Matter Systems, Como Conference Proceeding*, edited by K. Binder and G. Ciccotti (Società Italiana di Fisica, Bologna, 1996, p. 823

[16] M. Kröger, S. Hess, Phys. Rev. Lett. **85**, 1128 (2000)

[17] F. Müller-Plathe, Phys. Rev. E59, 4894 (1999).

[18] F. Müller-Plathe, J. Chem. Phys. **106**, 6082 (1997)

[19] *Monte Carlo Methods in Statistical Physics* (Springer Verlag, Berlin, Heidelberg, New York, 1979)

[20] *Applications of the Monte Carlo Method in Statistical Physics*, edited by K. Binder (Springer Verlag, Heidelberg, New York, 1984).

[21] *Monte Carlo Methods in Condensed Matter Physics*, edited by K. Binder (Springer Verlag, Berlin, Heidelberg, New York, 1992)

[22] P. Ahlrichs and B. Dünweg, J. Chem. Phys. **in press**, (1999).

[23] P. J. Hoogerbrugge and J. M. V. A. Kroelman, Europhys. Lett. **19**, 155 (1992).

[24] S. Chen and G. D. Doolen, Annu. Rev. Fluid Mech. **30**, 329 (1998).

[25] M. Doi and S. F. Edwards, *The Theory of Polymer Dynamics* (Clarendon Press, Oxford) (1986)

[26] G. Bennetin, in *Proc. of Intern. School of Physics "Enrico Fermi"*, edited by G. Ciccoti and W. W. Hoover (North Holland, Amsterdam, 1986).

[27] P. G. DeGennes, *Scaling Concepts in Polymer Physics* (Cornell Univ. Press, New York, 1979

[28] A. W. Rosenbluth and M. N. Rosenbluth, J. Chem. Phys. **23**, 356 (1955).

[29] P. Grassberger, Phys. Rev. E **56**, 3682 (1997)

[30] Z. Alexandrowicz, J. Chem. Phys. **51**, 561 (1969).

[31] K. Suzuki, Bull. Chem. Soc. Japan **41**, 538 (1968).

[32] J. Batoulis and K. Kremer, Macromol. **22**, 4277 (1989).

[33] N. Madras and A. Sokal, J. Stat. Phys. **50**, 109 (1988).

[34] A. D. Sokal, in *Monte Carlo and Molecular Dynamic Simulations in Polymer Science*, edited by K. Binder (Oxford Univ. Press, New York, 1995).

[35] U. Micka and K. Kremer, Phys. Rev. E **54 (3)**, 2653 (1996).

[36] B. Dünweg, D. Reith, M. Steinhauser, and K. Kremer, Corrections to scaling in the hydrodynamic properties of dilute polymer solutions, preprint, submitted to Journal of Chemical Physics (2002)

[37] F. T. Wall and F. Madel, J. Chem. Phys. **63**, 4562 (1975).

[38] A. Uhlherr, V. G. Mavrantzas, M. Doxastakis, D. N. Theodorou, Macromol. **34**, 8554 (2000)

[39] Y. Kantor, M. Kardar, and H. Li, Phys. Rev. E **49**, 1383 (1994).

[40] Vesselin Yamakov, Andrey Milchev, Hans Jörg Limbach, Burkhard Dünweg and Ralf Everaers, *Phys. Rev. Lett.* **85**, 4305 (2000)

[41] S. Bekiranov, R. Bruinsma, and P. A. Pincus, Europhys. Lett. **24**, 183 (1993).

[42] C. Jeppesen and K. Kremer, Euro Phys Lett **34**, 563 (1996).

[43] Electrostatic Effects in Soft Matter and Biophysics, C. Holm, P. Kekicheff, R. Podgornik (eds.) NATO Science Series II, 46 (2001)

[44] I. Carmesin and K. Kremer, Macromol. **21**, 2819 (1988).

[45] H. P. Wittmann and K. Kremer, Comp. Phys. Comm **61**, 309 (1990).

[46] H. P. Wittmann and K. Kremer, Comp. Phys. Comm **71**, 343 (1992).

[47] H. P. Deutsch and K. Binder, J. Chem. Phys. **94**, 2294 (1990).

[48] I. Carmesin and K. Kremer, J. Phys. (Paris) **51**, 915 (1990).

[49] B. Maier and J. Rädler, Phys. Rev. Lett. **82**, 1911 (1999).

[50] G. S. Grest and K. Kremer, Phys. Rev. **A33**, 3628 (1986).

[51] B. Dünweg, G. S. Grest, and K. Kremer, in *Numerical Methods for Polymeric Systems, Preprint*, edited by S. G. Whittington (Springer Verlag, Berlin, Heidelberg, New York, 1996).

[52] G. S. Grest, B. Dünweg, and K. Kremer, Comp. Phys. Comm. **55**, 269 (1989).

[53] R. Everaers and K. Kremer, Comp. Phys. Comm. **81**, 19 (1994).

[54] M. Pütz and A. Kolb, Comp. Phys. Comm. **113**, 145 (1998).

[55] T. Soddemann, B. Dünweg, K. Kremer, Comp. Phys. Comm., submitted.

[56] M. Pütz, K. Kremer, and G. S. Grest, Europhys. Lett. **49** 735 (2000).

[57] K. Kremer and G. S. Grest, in *Monte Carlo and Molecular Dynamics Simulations in Polymer Science*, edited by K. Binder (Oxford Univ. Press, Oxford 124, 1995).

[58] G. Grest and M. Murat, in *Monte Carlo and Molecular Dynamic Simulations in Polymer Science*, edited by K. Binder (Oxford Univ. Press, New York, 1995).

[59] W. Paul, K. Binder, D. W. Heermann, and K. Kremer, J. Chem. Phys. **95**, 7726 (1991).

[60] D. S. Pearson, G. VerStrate, E. von Meerwall, and F. C. Schilling, Macromol. **20**, 1133 (1987).

[61] K. Kremer and G. S. Grest, J. Chem. Phys. **92**, 5057 (1990).

[62] M. Pütz, R. Everaers, and K. Kremer, Phys. Rev. Lett. **84**, 298 (2000).

[63] E. R. Duering, K. Kremer, and G. S. Grest, Macromol **26**, 3241 (1993).

[64] R. Everaers and K. Kremer, Phys Rev. E **53**, R37 (1996).

[65] R. Everaers and K. Kremer, Macromol. **28**, 7291 (1995).

[66] R. Everaers and K. Kremer, J. Mol. Model. **2**, 293 (1996).

[67] J. Bastide and C. Candau, in *Physical Properties of Gels*, edited by A. Cohen-Addad (J. Wiley, Chichester, 1995).

[68] *Monte Carlo and Molecular Dynamic Simulations in Polymer Science*, edited by K. Binder (Oxford Univ. Press, New York, 1995).

[69] J. L. Barrat and J. F. Joanny, Adv. Chem. Phys. **XCIV**, (1996).

[70] S. Förster and M. Schmidt, Adv. Pol. Sc. **120**, (1995).

[71] U. Micka, C. Holm, and K. Kremer, Langmuir **15**, (1999).

[72] M. Deserno and C. Holm, J. Chem. Phys. **109**, 7678 (1998).

[73] M. Deserno and C. Holm, J. Chem. Phys. **109**, 7694 (1998).

[74] G. Grest, in *Monte Carlo and Molecular Dynamic Simulations in Polymer Science*, edited by K. Binder (Oxford Univ. Press, New York, 1995).

[75] M. Murat, G. S. Grest, and K. Kremer, Macromol. **32**, 595 (1999).

[76] T. Soddemann, PhD Thesis Univ. Mainz 2001, http://www.mpip-mainz.mpg.de/theory.html

[77] G. Gompper, D. M. Kroll, J. Phys. Condens. Matter **12**, A29 (2000).

[78] W. Tschöp *et al.*, Acta Pol. **49**, 61 (1998).

[79] W. Tschöp *et al.*, Acta Pol. **49**, 75 (1998).

[80] J. Eilhard *et al.*, J. Chem. Phys. **110**, 1819 (1999).

[81] K. Kremer, F. Müller-Plathe, MRS Bulletin **26**, 205 (2001).

[82] M. Murat and K. Kremer, J. Chem. Phys. **108**, 4340 (1998).

[83] Bolhuis, P. G., Louis A. A., Hansen, J. P., Phys. Rev. E **6402 (2)** (2001).

[84] Eurich F., Maass P., J. Chem. Phys. **114**, 7655 (2001).

STRUCTURE AND PHASE BEHAVIOR

B

B 1 Statistical Mechanics

K. Sturm
Institut für Festkörperforschung
Forschungszentrum Jülich GmbH

Contents

1 Introduction 2

2 Liouville equation and the BBGKY hierarchy 3
2.1 Microscopic classical mechanics 3
2.2 Phase space probability density and the Liouville equation 3
2.3 Reduced phase space distribution function and the BBGKY hierarchy . . . 4
2.4 Approximations: Vlasov equation and Boltzmann equation 5

3 Time averages in thermodynamic equilibrium 6

4 Ensemble averages in thermodynamic equilibrium 8
4.1 Canonical ensemble 9
4.2 The ideal gas as reference system 11
4.3 Chemical potential and grand canonical ensemble 12

5 Equilibrium particle densities and distribution functions 15
5.1 The role of $g(r)$ in the physics of monatomic fluids 16
5.2 Representation of $\rho_N^{(n)}(\mathbf{r}^n)$ by averages of δ-functions 19
5.3 The YBG hierarchy and the Born-Green equation 20

6 Interaction potentials 22
6.1 Classification of interactions 22
6.2 Interactions between molecules in a medium 24

1 Introduction

The physics of *Soft Matter* is part of the physics of *Condensed Matter*. There the goal is to derive the macroscopic properties from the microscopic structure, i.e. from the mutual dynamical interactions of the microscopic particles that constitute the macroscopic body and from their response to external fields.
In thermal equilibrium there are relationships between the macroscopic parameters that describe the macroscopic properties. These relationships are independent of nature of the systems. (For details see standard textbooks [1, 2].) This is demonstrated in table 1 below, where T, P, V, N_j, μ_j are the temperature, pressure, volume, particle number and chemical potential of the species j, respectively.

Thermodynamic potentials	Independent variables	Differentials
Energy U	$S,\quad V,\quad N_j$	$dU = T\,dS - P\,dV + \sum_j \mu_j\,dN_j$
Entropy S	$U,\quad V,\quad N_j$	$dS = \frac{1}{T}\,dU + \frac{P}{T}\,dV - \sum_j \frac{\mu_j}{T}\,dN_j$
Free energy $A = U - TS$	$T,\quad V,\quad N_j$	$dA = -S\,dT - P\,dV + \sum_j \mu_j\,dN_j$
Enthalpy $H = U + PV$	$S,\quad P,\quad N_j$	$dH = T\,dS + V\,dP + \sum_j \mu_j\,dN_j$
Gibbs free energy $G = U - TS + PV$	$T,\quad P,\quad N_j$	$dG = -S\,dT + V\,dP + \sum_j \mu_j\,dN_j$
Grand potential $\Omega = U - TS + PV$	$T,\quad V,\quad \mu_j$	$d\Omega = -S\,dT - P\,dV - \sum_j N_j\,d\mu_j$

Table 1: *Some thermodynamic functions*

The differentials in the third column tell us that, for example in the first row, the temperature T, pressure P and the chemical potential μ_j are given by partial derivatives of $U = U(S, V, N_j)$, more precisely by

$$T = \left(\frac{\partial U}{\partial S}\right)_{V,N_j}, \quad P = -\left(\frac{\partial U}{\partial V}\right)_{S,N_j}, \quad \mu_j = \left(\frac{\partial U}{\partial N_j}\right)_{V,S}. \tag{1}$$

What is needed is the explicit form of the thermodynamic potential $U = U(S, V, N_j)$. This, of course, depends on the nature of the system in question. Similar relationships hold for the other thermodynamic potentials exhibited in table 1.
From the microscopic point of view every macroscopic piece of material is a many particle system with typical particle numbers $N \sim 10^{23}$ in cm^3. If we restrict ourselves to classical particles, in principle, one has to solve $\sim 10^{23}$ coupled equations of motion subject to some initial conditions. In practice this is impossible.
In *Statistical Mechanics* methods are developed to determine the macroscopic properties of the system in question from the microscopic basic equations by some suitable averaging procedure.
This lecture is devoted to a brief summary of the principles of classical statistical mechanics and their links to thermodynamics [3, 4].

2 Liouville equation and the BBGKY hierarchy

2.1 Microscopic classical mechanics

We consider an isolated, macroscopic system of N identical particles, each of which has three translational degrees of freedom. The dynamical state of the system at a given time is completely specified by $3N$ coordinates $\mathbf{r}^N \equiv \{\mathbf{r}_1, \cdots, \mathbf{r}_N\}$ and $3N$ momenta $\mathbf{r}^N \equiv \{\mathbf{p}_1, \cdots, \mathbf{p}_N\}$ that define a point in a $6N$-dimensional phase space. Then the Hamiltonian $\mathcal{H}_N(\mathbf{r}^N, \mathbf{p}^N)$ of the system is of the form

$$\mathcal{H}_N(\mathbf{r}^N, \mathbf{p}^N) = \frac{1}{2m} \sum_{i=1}^{N} |\mathbf{p_i}|^2 + V_N(\mathbf{r}^N) \tag{2}$$

with the particle mass m and the total potential energy $V_N(\mathbf{r}^N)$. The motion of the point along its trajectory is determined from *Hamilton's equations* :

$$\dot{\mathbf{r}}_i = \frac{\partial \mathcal{H}_N}{\partial \mathbf{p}_i} = \frac{\mathbf{p}_i}{m} \equiv \mathbf{v}_i, \qquad i = 1, \cdots, N \tag{3}$$

$$\dot{\mathbf{p}}_i = -\frac{\partial \mathcal{H}_N}{\partial \mathbf{r}_i} = -\frac{\partial V_N}{\partial \mathbf{r}_i}, \qquad i = 1, \cdots, N. \tag{4}$$

Here $\mathbf{v}_i$ is the velocity of the i-th particle. In principle these $6N$ coupled equations have to be solved subject to $6N$ initial conditions.

2.2 Phase space probability density and the Liouville equation

Following Gibbs, observable (macroscopic) properties of the system are calculated as averages over an ensemble of equivalent systems. These are systems that are characterized by the same macroscopic parameters. For this purpose a phase space probability density function (pdf) $f^{(N)}(\mathbf{r}^N, \mathbf{p}^N; t)$ is introduced.

$$f^{(N)}(\mathbf{r}^N, \mathbf{p}^N; t)\, d\mathbf{r}^N\, d\mathbf{p}^N$$

is the probability that at a time t the system is in a microscopic state represented by a point $\{\mathbf{r}^N, \mathbf{p}^N\}$ lying in the infinitesimal phase space $d\mathbf{r}^N\, d\mathbf{p}^N$. The complete knowledge

of the pdf enables us to determine the average value of any function of the coordinates and the momenta. The time evolution of the phase space probality density is governed by the *Liouville equation* , given by

$$\begin{aligned} 0 &= \frac{\partial f^{(N)}}{\partial t} + \sum_{i=1}^{N} \left[\frac{\partial f^{(N)}}{\partial \mathbf{r}_i} \cdot \frac{\partial \mathcal{H}_N}{\partial \mathbf{p}_i} - \frac{\partial f^{(N)}}{\partial \mathbf{p}_i} \cdot \frac{\partial \mathcal{H}_N}{\partial \mathbf{r}_i} \right] \\ &\equiv \frac{\partial f^{(N)}}{\partial t} - \{\mathcal{H}_N, f^{(N)}\}, \end{aligned} \tag{5}$$

where we introduced the *Poisson* bracket, defined by

$$\{\mathcal{H}_N, f^{(N)}\} = \frac{\partial \mathcal{H}_N}{\partial \mathbf{r}_i} \cdot \frac{\partial f^{(N)}}{\partial \mathbf{p}_i} - \frac{\partial \mathcal{H}_N}{\partial \mathbf{p}_i} \cdot \frac{\partial f^{(N)}}{\partial \mathbf{r}_i}. \tag{6}$$

The Liouville equation is the $6N$-dimensional analog of the equation of continuity of an incompressible fluid; it describes the fact that phase points of the ensemble are neither created nor destroyed as the time evolves. This is illustrated by Fig. 1.

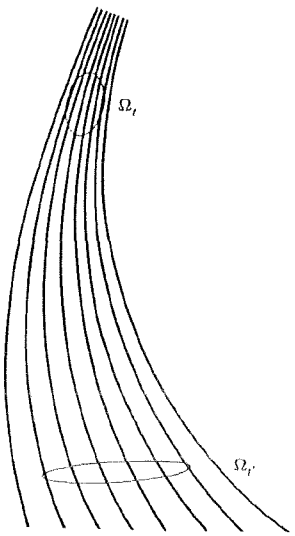


Fig. 1: *Trajectories in two-dimensional* $\mathbf{rp}$ *space. The region* $\Omega_{t'}$ *contains at time* t' *just those points that the motion has carried from region* Ω_t *at time* t*. Liouville's equation asserts that* Ω_t *and* $\Omega_{t'}$ *have the same volume. [From Ref. [5]]*

2.3 Reduced phase space distribution function and the BBGKY hierarchy

In practice, one is interested often only in the behaviour of a subset of particles of size n. The unwanted information is eliminated by integrating $f^{(N)}$ over the coordinates and momenta of the remaining $(N-n)$ particles and we obtain a *reduced phase space distribution function* $f^{(n)}(\mathbf{r}^n, \mathbf{p}^n; t)$, defined by

$$f^{(n)}(\mathbf{r}^n, \mathbf{p}^n; t) = \frac{N!}{(N-n)!} \int\int f^{(N)}(\mathbf{r}^N, \mathbf{p}^N; t)\, d\mathbf{r}^{(N-n)}\, d\mathbf{p}^{(N-n)}, \quad n < N. \tag{7}$$

The combinatorial factor $N!/(N-n)!$ accounts for the number of ways choosing n out of N particles. Using this definition of $f^{(n)}$, from the Liouville equation a hierarchy of equations for the reduced phase space distribution function can be derived. Let us suppose that the total force acting on a particle i is the sum of an external force $\mathbf{F}_i^{ext}$ and of pair forces $\mathbf{F}_{ij}$ representing the interaction with the other particles j (with $\mathbf{F}_{ii}=0$). Then the Liouville equation can be written in the form

$$\frac{\partial f^{(N)}}{\partial t}+\frac{1}{m}\sum_{i=1}^{N}\mathbf{p}_i\cdot\frac{\partial f^{(N)}}{\partial \mathbf{r}_i}+\sum_{i=1}^{N}\mathbf{F}_i^{ext}\cdot\frac{\partial f^{(N)}}{\partial \mathbf{p}_i}=-\sum_{i}^{N}\sum_{j}^{N}\mathbf{F}_{ij}\cdot\frac{\partial f^{(N)}}{\partial \mathbf{p}_i}. \tag{8}$$

We now apply the definition of $f^{(n)}$ and after some algebra obtain a complicated set of integro-differential equations that couple $f^{(n)}$ with $f^{(n+1)}$:

$$\begin{aligned}&\left\{\frac{\partial}{\partial t}+\sum_{i=1}^{n}\left[\frac{1}{m}\mathbf{p}_i\cdot\frac{\partial}{\partial \mathbf{r}_i}+\left(\mathbf{F}_i^{ext}+\sum_{j=1}^{n}\mathbf{F}_{ij}\right)\cdot\frac{\partial}{\partial \mathbf{p}_i}\right]\right\}f^{(n)}(\mathbf{r}^n,\mathbf{p}^n;t)\\&=-\sum_{i=1}^{n}\int\int\mathbf{F}_{i,n+1}\cdot\frac{\partial}{\partial \mathbf{p}_i}f^{(n+1)}(\mathbf{r}^{n+1},\mathbf{p}^{n+1})\,d\mathbf{r}_{n+1}\,d\mathbf{p}_{n+1}\end{aligned} \tag{9}$$

This set of equations for $n=1,\cdots,N-1$ was first derived by Yvon (1935) and is known as the *BBGKY hierarchy* (Kirkwood (1935); Bogolyubov (1946), Born and Green (1949)).

2.4 Approximations: Vlasov equation and Boltzmann equation

As an important application of the BBGKY hierarchy one can construct approximations that close the system of equations at some stage. The most important case in practice is obtained for $n=1$, i.e.

$$\begin{aligned}&\left(\frac{\partial}{\partial t}+\frac{1}{m}\mathbf{p}_1\cdot\frac{\partial}{\partial \mathbf{r}_1}+\mathbf{F}_1^{ext}\cdot\frac{\partial}{\partial \mathbf{p}_1}\right)f^{(1)}(\mathbf{r}_1,\mathbf{p}_1;t)\\&=-\int\int\mathbf{F}_{12}\cdot\frac{\partial}{\partial \mathbf{p}_1}f^{(2)}(\mathbf{r}_1,\mathbf{p}_1,\mathbf{r}_2,\mathbf{p}_2;t)d\mathbf{r}_2\,d\mathbf{p}_2.\end{aligned} \tag{10}$$

To find some solution for $f^{(1)}$ the function $f^{(2)}$ is approximately related to $f^{(1)}$.

Following Vlasov the simplest approximation is to ignore correlations between pairs of particles altogether. This leads to

$$f^{(2)}(\mathbf{r},\mathbf{p},\mathbf{r}',\mathbf{p}';t)=f^{(1)}(\mathbf{r},\mathbf{p};t)f^{(1)}(\mathbf{r}',\mathbf{p}';t) \tag{11}$$

with the result that $f^{(1)}$ can now be determined from the *Vlasov equation*

$$\left(\frac{\partial}{\partial t}+\frac{1}{m}\mathbf{p}\cdot\frac{\partial}{\partial \mathbf{r}}+[\mathbf{F}^{ext}(\mathbf{r},t)+\bar{\mathbf{F}}(\mathbf{r},t)]\cdot\frac{\partial}{\partial \mathbf{p}}\right)f^{(1)}(\mathbf{r},\mathbf{p};t)=0, \tag{12}$$

where the average force is given by

$$\bar{\mathbf{F}}(\mathbf{r},t)=\int\int\mathbf{F}(\mathbf{r},\mathbf{r}')\,f^{(1)}(\mathbf{r}',\mathbf{p}',;t)\,d\mathbf{r}'\,d\mathbf{p}'. \tag{13}$$

The two equations have to be solved selfconsistently. The Vlasov equation is widely used in plasma physics since the long range Coulomb interaction provides a justification for such a mean field treatment of the interactions.

For short range interactions and sufficiently low densities the interaction between the particles is treated in terms of binary collisions. With the additional assumption that successive collisions are uncorrelated Boltzmann derived the following equation for $f^{(1)}$

$$\left(\frac{\partial}{\partial t}+\frac{1}{m}\mathbf{p}_1\cdot\frac{\partial}{\partial \mathbf{r}}+\mathbf{F}^{ext}(\mathbf{r},t)\cdot\frac{\partial}{\partial \mathbf{p}_1}\right) f^{(1)}(\mathbf{r},\mathbf{p}_1;t)=\left(\frac{\partial f^{(1)}}{\partial t}\right)_{collisions}. \tag{14}$$

The *collision integral* on the right hand side of Eq. (14) is Boltzmann's approximation to the right hand side of Eq. (10) given by

$$\left(\frac{\partial f^{(1)}}{\partial t}\right)_{collisions}=\frac{1}{m}\int\int\sigma(\Omega,|\mathbf{p}_1-\mathbf{p}_2|)\,|\mathbf{p}_1-\mathbf{p}_2|$$
$$\times[f^{(1)}(\mathbf{r},\mathbf{p'}_1;t)f^{(1)}(\mathbf{r},\mathbf{p'}_2;t)-f^{(1)}(\mathbf{r},\mathbf{p}_1;t)f^{(1)}(\mathbf{r},\mathbf{p}_2;t)]\,d\Omega\,d\mathbf{p}_2. \tag{15}$$

Here the primes denote post-collisional momenta. For a given interparticle potential the scattering cross-section $\sigma(\Omega,|\mathbf{p}_1-\mathbf{p}_2|)$ into a solid angle $d\Omega$ and hence the collision integrals can be evaluated numerically. For the evaluation the conservation laws of momentum and angular momentum are needed.
Boltzmann showed that this form of the collision term is able to account for the observed fact that many-particle systems evolve irreversibly towards an equilibrium state (Boltzmann's H-theorem). Solution of the *Boltzmann equation* Eq. (14) leads to explicit expressions for the hydrodynamic transport coefficients.

3 Time averages in thermodynamic equilibrium

We consider a system of N spherical particles that is isolated from its surroundings. In this case the hamiltonian $\mathcal{H}_N(\mathbf{r}^N,\mathbf{p}^N)$ is a constant of motion. In the state of themodynamic equilibrium averages must be independent of time. Given the initial coordinates and momenta of the particles the positions at any later (or earlier) time can in principle be obtained as the solution to Newton's equation of motion, i.e. a set of $3N$ coupled, second order, differential equations:

$$m\ddot{\mathbf{r}}_i=-\frac{\partial}{\partial \mathbf{r}_i}V_N(\mathbf{r}^N),\qquad i=1,\cdots,N. \tag{16}$$

For any function $\mathcal{F}(\mathbf{r}^N,\mathbf{p}^N)$ its associated thermodynamic property F according to Boltzmann is defined as a *time average* , i.e.

$$F\equiv\langle\mathcal{F}(\mathbf{r}^N,\mathbf{p}^N)\rangle_t=\lim_{\tau\to\infty}\frac{1}{\tau}\int_0^\tau\mathcal{F}(\mathbf{r}^N(t),\mathbf{p}^N(t))\,dt. \tag{17}$$

This definition is, for example, the basis for molecular dynamics simulations.

A simple application is the calculation of the temperature of an isolated system as the time average of the kinetic energy, namely

$$\frac{3}{2}k_BT = \frac{3}{2}k_B\langle\mathcal{T}(\mathbf{p}^N(t))\rangle_t = \frac{1}{N}\lim_{\tau\to\infty}\frac{1}{\tau}\int_0^\tau dt\sum_{i=1}^N\frac{|\mathbf{p}_i|^2}{2m}. \tag{18}$$

With this result we can show that the equation of state of a system is related to the time average of the *Clausius virial function* that is defined by

$$\mathcal{V}(\mathbf{r}^N) = \sum_{i=1}^N \mathbf{r}_i\cdot\mathbf{F}_i. \tag{19}$$

Here $\mathbf{F}_i$ is the total force acting on the i-th particle. Then

$$\begin{aligned}\langle\mathcal{V}\rangle_t &= \lim_{\tau\to\infty}\frac{1}{\tau}\int_0^\tau dt\sum_{i=1}^N\mathbf{r}_i(t)\cdot\mathbf{F}_i(t)\\ &= \lim_{\tau\to\infty}\frac{1}{\tau}\int_0^\tau dt\sum_{i=1}^N\mathbf{r}_i(t)\cdot m\ddot{\mathbf{r}}_i(t)\\ &= -\lim_{\tau\to\infty}\frac{1}{\tau}\int_0^\tau dt\sum_{i=1}^N m|\dot{\mathbf{r}}_i|^2\\ &= -3N\,k_B\,T. \end{aligned}\tag{20}$$

The total virial function can be separated into two parts:

$$\mathcal{V} = \mathcal{V}_{int} + \mathcal{V}_{ext}. \tag{21}$$

$\mathcal{V}_{int}$ arises from the interparticle forces, while the external virial $\mathcal{V}_{ext}$ comes from the forces exerted on the particles by the walls of the system. Their average effect can be related to the pressure. As illustrated in Fig. 2, due to the pressure P the infinitesimal surface df exerts a force $P\,df$ parallel to the inner normal on the particles in the neighborhood of df. If r_n is the outer normal component of $\mathbf{r}$ the contribution from df to the external virial is

$$-P\,r_n\,df.$$

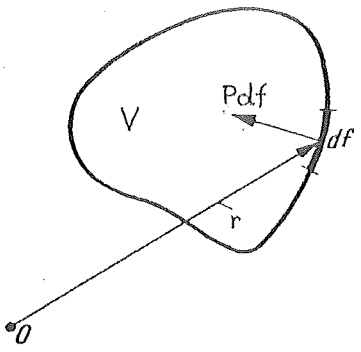


Fig. 2: *For the evaluation of the average external contribution to the virial [From Ref. [1]]*

We integrate over the whole surface of the volume V and obtain

$$\langle \mathcal{V}_{ext} \rangle_t = -P \int\int r_n \, df = -P \int\int\int \nabla \cdot \mathbf{r} \, dV = -3PV, \tag{22}$$

because $\nabla \cdot \mathbf{r} = 3$. Expressing the internal forces as gradients of the interparticle potential $V_N(\mathbf{r}^N)$ we have

$$\langle \mathcal{V}_{int} \rangle_t = -\langle \sum_{i=1}^{N} \mathbf{r}_i(t) \cdot \frac{\partial}{\partial \mathbf{r}_i} V_N(\mathbf{r}^N(t)) \rangle_t \tag{23}$$

and finally arrive at the equation of state or virial equation:

$$P\,V = N\,k_B\,T - \frac{1}{3} \langle \sum_{i=1}^{N} \mathbf{r}_i(t) \cdot \frac{\partial}{\partial \mathbf{r}_i} V_N(\mathbf{r}^N(t)) \rangle_t. \tag{24}$$

4 Ensemble averages in thermodynamic equilibrium

We now come back to the pdf and again consider the important case of thermodynamic equilibrium. In this case

$$\frac{\partial f^{(N)}}{\partial t} = 0 \quad \rightarrow f^{(N)} = f_0^{(N)}(\mathbf{r}^N, \mathbf{p}^N).$$

The index 0 denotes the state of themodynamic equilibrium. The *equilibrium ensemble average* of any function $\mathcal{F}(\mathbf{r}^N, \mathbf{p}^N)$ is defined by

$$\langle \mathcal{F}(\mathbf{r}^N, \mathbf{p}^N) \rangle_e = \int\int \mathcal{F}(\mathbf{r}^N, \mathbf{p}^N)\, f_0^{(N)}(\mathbf{r}^N, \mathbf{p}^N) d\mathbf{r}^N, d\mathbf{p}^N, \tag{25}$$

where $f_0^{(N)}$ is normalized such that

$$\int\int f_0^{(N)}(\mathbf{r}^N, \mathbf{p}^N)\, d\mathbf{r}^N\, d\mathbf{p}^N = 1. \tag{26}$$

Various versions of the Monte Carlo method provide efficient computational schemes to determine ensemble averages.
The explicit form of $f_0^{(N)}(\mathbf{r}^N, \mathbf{p}^N)$ depends on the macroscopic parameters that characterize the ensemble. For example, the systems of a *microcanonical ensemble* are characterized by the same number of particles, the same volume and the same total energy E_0. These are isolated systems that cannot exchange heat or particles with their surroundings. The equilibrium pdf is

$$f_0^{(N)}(\mathbf{r}^N, \mathbf{p}^N) = C\,\delta(\mathcal{H}_N(\mathbf{r}^N, \mathbf{p}^N) - E_0), \tag{27}$$

where C is a constant chosen to satisfy the normalization condition. The thermodynamic internal energy $U = E_0$ as follows from

$$\begin{aligned} U &= \langle \mathcal{H}_N \rangle_e \\ &= \int\int \mathcal{H}_N(\mathbf{r}^N, \mathbf{p}^N)\, f_0^{(N)}(\mathbf{r}^N, \mathbf{p}^N)\, d\mathbf{r}^N\, d\mathbf{p}^N \\ &= \int\int \mathcal{H}_N(\mathbf{r}^N, \mathbf{p}^N)\, C\,\delta(\mathcal{H}_N(\mathbf{r}^N, \mathbf{p}^N) - E_0)\, d\mathbf{r}^N\, d\mathbf{p}^N \\ &= E_0 \int\int C\,\delta(\mathcal{H}_N(\mathbf{r}^N, \mathbf{p}^N) - E_0)\, d\mathbf{r}^N\, d\mathbf{p}^N \\ &= E_0. \end{aligned} \tag{28}$$

This is exactly the situation we encountered when we considered time averages in a isolated system. Indeed, time everages and ensemble averages are identical if the system is *ergodic*.

4.1 Canonical ensemble

The *canonical ensemble* is a collection of systems characterized by the same values of N, V and T. In this case the systems are in contact with a heat bath of temperature T. Then the equilibrium pdf is given by

$$f_0^{(N)}(\mathbf{r}^N, \mathbf{p}^N) = \frac{!}{N!\,h^{3N}} \frac{\exp[-\beta \mathcal{H}_N(\mathbf{r}^N, \mathbf{p}^N)]}{Q_N(V,T)}, \tag{29}$$

where $\beta = 1/k_B T$ (k_B: Boltzmann's constant) and h is Planck's constant. The factor $N!$ takes care of the indistinguishability of the particles and the *canonical partition function* $Q_N(V,T)$ guarantees the correct normalization, defined by

$$Q_N(V,T) = \frac{!}{N!\,h^{3N}} \int\int \exp[-\beta \mathcal{H}_N(\mathbf{r}^N, \mathbf{p}^N)]\, d\mathbf{r}^N\, d\mathbf{p}^N. \tag{30}$$

The inclusion of the factor h^{-3N} ensures that both $f_0^{(N)}(\mathbf{r}^N, \mathbf{p}^N)\, d\mathbf{r}^N\, d\mathbf{p}^N$ and $Q_N(V,T)$ are dimensionless.
The link between statistical mechanics and thermodynamics is established via the relation

$$A = -k_B T \ln Q_N(V,T). \tag{31}$$

The Helmholtz free energy A is the thermodynamic potential as a function of N, V and T. If A is a known function of the independent variables V and T, all other thermodynamic state functions can be obtained by differentiation. From

$$dA = -S\, dT - P\, dV$$

follows

$$P = -\left(\frac{\partial A}{\partial V}\right)_T = k_B T \left(\frac{\partial \ln Q_N(V,T)}{\partial V}\right)_T \tag{32}$$

and because of

$$A = U - T S$$

$$\begin{aligned} U &= \langle \mathcal{H}_N \rangle \\ &= \frac{1}{N!} \frac{1}{h^{3N} Q_N(V,T)} \int\int \mathcal{H}_N(\mathbf{r}^N, \mathbf{p}^N) \exp[-\beta \mathcal{H}_N(\mathbf{r}^N, \mathbf{p}^N)]\, d\mathbf{r}^N\, d\mathbf{p}^N \\ &= \left(\frac{\partial \beta A}{\partial \beta}\right)_V \\ &= -\left(\frac{\partial \ln Q_N(V,T)}{\partial \beta}\right)_V \end{aligned} \tag{33}$$

For the specific heat at constant volume defined by

$$C_V = \left(\frac{\partial U}{\partial T}\right)_V . \tag{34}$$

one finds

$$C_V = \frac{1}{k_B T^2}[\langle \mathcal{H}_N^2 \rangle - \langle \mathcal{H}_N \rangle^2], \tag{35}$$

where we made use of

$$\frac{1}{k_B}\frac{\partial U}{\partial T} = -\beta^2 \frac{\partial U}{\partial \beta} \quad \& \quad \frac{1}{Q_N}\frac{\partial Q_N}{\partial \beta} = \frac{\partial \ln Q_N}{\partial \beta}.$$

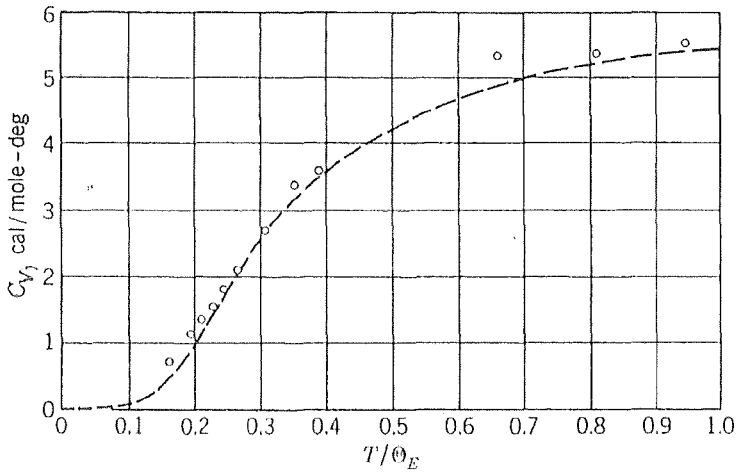


Fig. 3: *Comparison of experimental results of the specific heat of diamond with values calculated on the Einstein model using the characteristic temperature* $\Theta_E = \hbar\omega_E/k_B = 1320K$ *(After A. Einstein, Ann. Physics* **22**, *180 (1907)) [From Ref [6]]*

As a simple example we consider the *Einstein model* of a lattice [6, 5]. It consists of oscillators with the same resonance frequency ω_E. If N is the number of oscillators the internal energy is found to be

$$U = N\frac{\hbar\omega_E}{e^{\beta\hbar\omega_E} - 1} \tag{36}$$

Then the specific heat is

$$C_V = N\, k_B\, (\beta\hbar\omega_E)^2 \frac{e^{\beta\hbar\omega_E}}{(e^{\beta\hbar\omega_E} - 1)^2}, \tag{37}$$

which is plotted in Fig. 3.

4.2 The ideal gas as reference system

Working with the canonical ensemble we observe that all thermodynamic quantities can be related to the canonical partition function or its derivatives. Because of the rather simple form of the kinetic energy term in the hamiltonian Eq. (2) the integrations over momenta can be performed. For every degree of freedom we obtain a factor

$$(2\pi\, m\, k_B\, T)^{1/2}.$$

We introduce the so called *de Broglie thermal wavelength* Λ, defined by

$$\Lambda = h/(2\pi\, m\, k_B\, T) \tag{38}$$

and rewrite the canonical partition function as

$$Q_N(V,T) = \frac{\Lambda^{-3N}}{N!}\, Z_N(V,T) \tag{39}$$

with the *configuration integral* defined by

$$Z_N(V,T) = \int d\mathbf{r}^N \exp[-\beta\, V_N(\mathbf{r}^N)]. \tag{40}$$

For an ideal gas $V_N(\mathbf{r}^N) = 0$ and $Z_N(V,T) = V^N$ with the consequence that the partition function of the ideal gas $Q_N^{id}(V,T)$ becomes

$$Q_N^{id}(V,T) = \frac{\Lambda^{-3N}}{N!}\, V^N \tag{41}$$

Then if Stirling's approximation for $\ln N!$ is used the Helmholtz free enegy A^{id} of the ideal gas is

$$\beta\, A^{id}/N = \ln[N/V] + 3\ln\Lambda - 1. \tag{42}$$

When inserted in Eq. (32) the ideal gas equation of state follows, i.e.

$$P\,V = N\, k_B\, T.$$

The results for the ideal gas can be used as reference system when we write

$$Q_N(V,T) = Q_N^{id}(V,T)\, Z_N(V,T)\, V^{-N}. \tag{43}$$

We can now decompose A according to

$$A = A^{id} + A^{ex},$$

where the *excess free energy* , given by

$$A^{ex} = -k_B\, T\, \ln \frac{Z_N(V,T)}{V^N}, \tag{44}$$

accounts for the contributions that arise from the interaction between particles. Similarly for the internal energy $U = U^{id} + U^{ex}$ we obtain from Eq. (33)

$$U^{id} = \frac{3}{2} N\, k_B\, T \tag{45}$$

and

$$\begin{aligned} U^{ex} &= \frac{1}{Z_N(V,T)} \int d\mathbf{r}^N V_N(\mathbf{r}^N)\, \exp[-\beta\, V_N(\mathbf{r}^N)] \\ &= \langle V_N \rangle. \end{aligned} \tag{46}$$

4.3 Chemical potential and grand canonical ensemble

So far the discussion has been restricted to one-component systems with a fixed number of particles. In the more general case, the system may contain several species of particles and the particle numbers may vary. As a result of the variation of particle numbers N_ν the thermodynamic description of such an open system involves the *chemical potentials* μ_ν which are expressible as derivatives of any of the functions U, A or G (See table 1):

$$\mu_\nu = \left(\frac{\partial U}{\partial N_\nu}\right)_{V,S} = \left(\frac{\partial A}{\partial N_\nu}\right)_{V,T} = \left(\frac{\partial G}{\partial N_\nu}\right)_{P,T}. \tag{47}$$

The chemical potentials in a mixture of ideal gases are given by

$$\beta\,\mu_\nu^{id} = \left(\partial A^{id}/\partial N_\nu\right)_{V,T} = \ln(N_\nu/V) + 3\ln\Lambda_\nu. \tag{48}$$

The thermodynamic potential appropriate to a system characterized by fixed values of V, T and a set $\{\mu_\nu\}$ is the *grand potential* Ω, defined as

$$\Omega = A - \sum_\nu N_\nu\,\mu_\nu = G - P\,V - \sum_\nu N_\nu\,\mu_\nu \tag{49}$$

and the change in Ω is

$$d\Omega = -P\,dV - S\,dT - \sum_\nu N_\nu\,d\mu_\nu, \tag{50}$$

which means that

$$P = -\left(\frac{\partial\Omega}{\partial V}\right)_{T,\{\mu_\nu\}}, \quad S = -\left(\frac{\partial\Omega}{\partial T}\right)_{V,\{\mu_\nu\}}, \quad N_\nu = -\left(\frac{\partial\Omega}{\partial\mu_\nu}\right)_{T,V}. \tag{51}$$

One can show that for a homogeneous phase the *Duhem-Gibbs equation* is valid [1], i.e.

$$G = \sum_\nu N_\nu\,\mu_\nu.$$

This leads to

$$\Omega = -P\,V. \tag{52}$$

An ensemble of open, one-component systems that are characterized by fixed values of V, T and the chemical potential μ is called a *grand canonical ensemble.* The constancy of T and μ is ensured by supposing that the systems of the grand canonical ensemble are allowed to come to equilibrium with a reservoir due to exchange of heat and matter. The phase space of the grand canonical ensemble is the union of phase spaces corresponding to all values of N and the pdf is now the probability that the systems contains N particles and that their coordinates and momenta are $\mathbf{r}^N$ and $\mathbf{p}^N$, respectively. We now have to include N in the arguments of the equilibrium pdf that is given by

$$f_0(\mathbf{r}^N, \mathbf{p}^N;\, N) = \frac{1}{N!\,h^{3N}}\,\frac{1}{\Xi(\mu,\,V,\,T)}\exp(N\,\beta\,\mu)\,\exp[-\beta\,\mathcal{H}_N(\mathbf{r}^N, \mathbf{p}^N), \tag{53}$$

where the *grand canonical partition function* Ξ is defined by

$$\begin{aligned}\Xi(\mu, V, T) &= \sum_{N=0}^{\infty} \exp(N\beta\mu)\, Q_N(V, T) \\ &= \sum_{N=0}^{\infty} \frac{z^N}{N!} Z_N(V, T),\end{aligned} \tag{54}$$

with *activity* z defined by

$$z = \Lambda^{-3} \exp(\beta\mu). \tag{55}$$

The link between statistical mechanics and thermodynamics is established through

$$\Xi = \exp[-\beta\Omega(\mu, V, T)] = \exp(\beta PV). \tag{56}$$

The probability $P(N)$ that the system contains precisely N particles, irrespective of the coordinates and the momenta is

$$\begin{aligned}P(N) &= \int\int f_0(\mathbf{r}^N, \mathbf{p}^N, N)\, d\mathbf{r}^N\, d\mathbf{p}^N \\ &= \frac{1}{\Xi} \exp(N\beta\mu)\, Q_N(V, T) \\ &= \frac{1}{\Xi} \frac{z^N}{N!} Z_N(V, T)\end{aligned} \tag{57}$$

and it follows the relationship between the grand canonical and canonical pdf

$$f_0(\mathbf{r}^N, \mathbf{p}^N; N) = P(N)\, f_0^{(N)}(\mathbf{r}^N, \mathbf{p}^N). \tag{58}$$

As an application we express the isothermal compressibility in terms of the mean square deviation ($\langle N^2\rangle - \langle N\rangle)^2$), where

$$\begin{aligned}\langle N\rangle &= \sum_{N=0}^{\infty} N\, P(N) \\ &= \frac{1}{\Xi} \sum_{N=0}^{\infty} N\ \exp(N\beta\mu)\, Q_N(V, T) \\ &= \frac{1}{\Xi} \frac{\partial}{\partial(\beta\mu)} \sum_{N=0}^{\infty} \exp(N\beta\mu)\, Q_N(V, T) \\ &= \frac{1}{\Xi} \frac{\partial}{\partial(\beta\mu)} \Xi \\ &= \frac{\partial}{\partial(\beta\mu)} \ln \Xi\end{aligned} \tag{59}$$

and

$$\begin{aligned}\frac{\partial}{\partial(\beta\mu)} \langle N\rangle &= \frac{\partial^2}{\partial(\beta\mu)^2} \ln \Xi \\ &= \left[\frac{\partial}{\partial(\beta\mu)} \frac{1}{\Xi}\right] \frac{\partial}{\partial(\beta\mu)} \Xi + \frac{1}{\Xi} \frac{\partial^2}{\partial(\beta\mu)^2} \Xi \\ &= -\left(\frac{1}{\Xi}\right)^2 \left(\frac{\partial}{\partial(\beta\mu)} \Xi\right)^2 + \frac{1}{\Xi} \frac{\partial^2}{\partial(\beta\mu)^2} \Xi \\ &= \langle N^2\rangle - \langle N\rangle^2.\end{aligned} \tag{60}$$

On the other hand exploiting the Duhem-Gibbs equation it follows from

$$d\Omega = -P\,dV - V\,dP = -P\,dV - S\,dT - N\,d\mu \tag{61}$$

that for $dT = 0$ (isothermal)

$$V\,dP = N\,d\mu \tag{62}$$

and hence for constant V

$$\begin{aligned} N\left(\frac{\partial\mu}{\partial N}\right)_{V,T} &= V\left(\frac{\partial P}{\partial N}\right)_{V,T} \\ &= \left(\frac{\partial P}{\partial \rho}\right)_{N,T} \\ &= \frac{1}{\rho\,\chi_T}. \end{aligned} \tag{63}$$

where $\rho = N/V$ and in the last step we used the identity

$$\chi_T = -\frac{1}{V}\left(\frac{\partial V}{\partial P}\right)_{N,T} = -\rho\left(\frac{\partial(1/\rho)}{\partial P}\right)_{N,T} = \frac{1}{\rho}\left(\frac{\partial \rho}{\partial P}\right)_{N,T}. \tag{64}$$

In the thermodynamic limit N may be replaced by $\langle N\rangle$ and we obtain

$$\frac{\langle N^2\rangle - \langle N\rangle^2}{\langle N\rangle} = \frac{\langle (N - \langle N\rangle)^2\rangle}{\langle N\rangle} = \rho\,k_B\,T\,\chi_T > 0. \tag{65}$$

Finally we reproduce an interesting equation for the excess chemical potential μ_{ex} for a translationally invariant system that was originally derived by Widom in 1963.

$$\begin{aligned} \mu^{ex} &= \left(\frac{\partial A^{ex}}{\partial N}\right)_{V,T} \\ &= A^{ex}(N+1,\,V,\,T) - A^{ex}(N,\,V,\,T) \\ &= k_B\,T \ln\left(\frac{V\,Z_N(V,T)}{Z_{N+1}(V,T)}\right). \end{aligned} \tag{66}$$

We use the definition of the configuration integral and in addition define

$$V_{N+1}(\mathbf{r}^{N+1}) - V_N(\mathbf{r}^N) = \phi. \tag{67}$$

In a translationally invariant system $\mathbf{r}_{n+1}$ can be taken as the origin. Then the integration over $\mathbf{r}_{n+1}$ yields a factor V and we find

$$\begin{aligned} \frac{Z_{N+1}(V,\,T)}{Z_N(V,\,T)} &= V\,\frac{\int \exp(-\beta\phi)\exp[-\beta V_N(\mathbf{r}^N)]\,d\mathbf{r}^N}{\int \exp[-\beta V_N(\mathbf{r}^N)]\,d\mathbf{r}^N} \\ &\equiv V\,\langle \exp(-\beta\phi)\rangle_{canonical}. \end{aligned} \tag{68}$$

Here the brackets denote a canonical ensemble average for a system containing N particles and we arrive at

$$\mu^{ex} = -k_B\,T\,\ln\langle \exp(-\beta\,\phi)\rangle_{canonical}. \tag{69}$$

5 Equilibrium particle densities and distribution functions

Factorization of the equilibrium phase-space probability functions into kinetic and potential terms leads to a separation of thermodynamic properties into ideal and excess parts. A similar factorization can be applied to the reduced phase-space distribution function defined earlier. In the canonical ensemble integration over all momenta yields the *n-particle density* , defined by

$$\begin{aligned}\rho_N^{(n)}(\mathbf{r}^n) &= \frac{N!}{(N-n)!}\frac{1}{Q_N(V,T)}\int\int \exp[-\beta\mathcal{H}_N(\mathbf{r}^N,\mathbf{p}^N)]\,d\mathbf{r}^{(N-n)}\,d\mathbf{p}^N \\ &= \frac{N!}{(N-n)!}\frac{1}{Z_N(V,T)}\int\int \exp[-\beta V_N(\mathbf{r}^N)]\,d\mathbf{r}^{(N-n)} \end{aligned} \tag{70}$$

with the nomalization:

$$\int \rho_N^{(n)}(\mathbf{r}^n)\,d\mathbf{r}^n = \frac{N!}{(N-n)!}. \tag{71}$$

Specifically for $n = 1$:

$$\int \rho_N^{(1)}(\mathbf{r})\,d\mathbf{r} = N. \tag{72}$$

If the system is homogeneous it follows that

$$\rho_N^{(1)}(\mathbf{r}) = N/V = \rho. \tag{73}$$

For an ideal gas $V_N(\mathbf{r}^N) = 0$ and $Z_N(V,\,T) = V^N$. Then

$$\rho_N^{(n)}(\mathbf{r}^n) = \rho^n\frac{N!}{N^n\,(N-n)!} = \rho^n\left(1+\mathcal{O}\left(\frac{n}{N}\right)\right). \tag{74}$$

For example, the pair density of an ideal gas is

$$\rho_N^{(2)}(\mathbf{r_1},\,\mathbf{r_2}) = \rho^2\left(1-\frac{1}{N}\right). \tag{75}$$

Closely related with the n-particle density $\rho_N^{(n)}(\mathbf{r}^n)$ is the *n-particle distribution function* $g_N^{(n)}(\mathbf{r}^n)$ defined by

$$g_N^{(n)}(\mathbf{r}^n) = \rho_N^{(n)}(\mathbf{r}^n)/\prod_{i=1}^{n}\rho_N^{(1)}(\mathbf{r}_i). \tag{76}$$

In particular for a homogeneous system

$$g_N^{(n)}(\mathbf{r}^n) = \rho_N^{(n)}(\mathbf{r}^n)/\rho^n. \tag{77}$$

For a homogeneous system the particle distribution function measures the deviation from complete randomness.
If the system is isotropic in addition, the pair distribution function $g_N^{(2)}(\mathbf{r}_1,\mathbf{r}_2)$ is a function of $r_{12} = |\mathbf{r}_2 - \mathbf{r}_1|$ and is then called the *radial distribution function* denoted by $g(r)$.
When the separation r_{12} is much larger than the range of the interparticle potential $g_N^{(2)}(\mathbf{r}_1,\mathbf{r}_2)$ approches the ideal gas limit, i.e.

$$\lim_{r_{12}\to\infty} g_N^{(2)}(\mathbf{r}_1,\mathbf{r}_2) = g^{id}(r) = 1-\frac{1}{N}. \tag{78}$$

5.1 The role of $g(r)$ in the physics of monatomic fluids

The radial distribution function $g(r)$ plays a central role in the physics of monatomic fluids. It can be determined from neutron scattering or x-ray scattering experiments. The results of such an experiment on liquid argon are shown in Fig. 4. Provided that the interaction between the atoms can be represented by pair potentials, i.e.

$$V_N(\mathbf{r}^N) = \frac{1}{2}\sum_{i}^{N}\sum_{j\neq i}^{N} v(r_{ij}) \tag{79}$$

thermodynamic properties of the fluid can be written as integrals over $g(r)$.

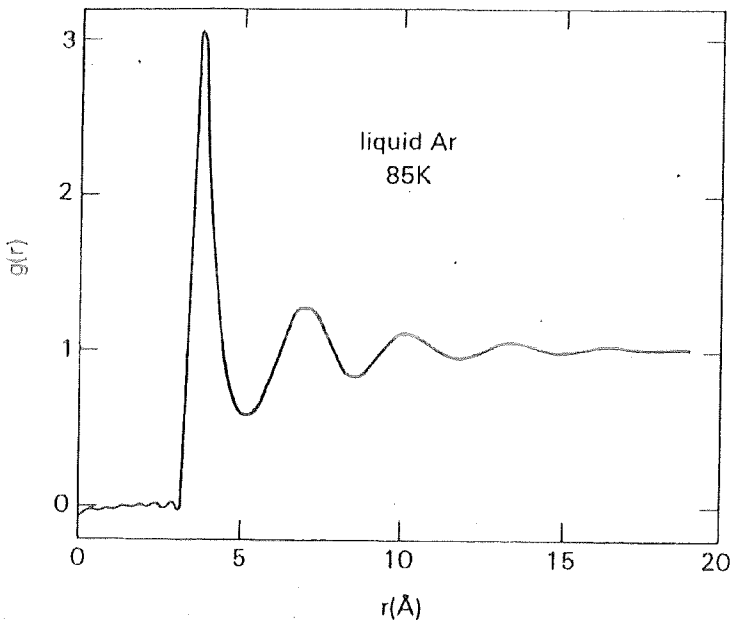


Fig. 4: *Results of neutron scattering experiments for the radial ditribution function of liquid argon. (The riples at small r are artefacts of the data analysis) (After Yarnell et al (1973)) [From Ref [3]]*

For example, if we write $U = U^{id} + U^{ex}$ the excess internal energy U^{ex} is given by

$$\begin{aligned} U^{ex} &= \frac{1}{Z_N(V,T)} \int V_N(\mathbf{r}^N) \exp[-\beta V_N(\mathbf{r}^N)]\, d\mathbf{r}^N \\ &= \frac{1}{2} N(N-1) \int\int v(r_{12})\, d\mathbf{r}_1\, d\mathbf{r}_2 \\ &\quad \times \left(\frac{1}{Z_N(V,T)}\right) \int\int \exp[-\beta V_N(\mathbf{r}^N)] d\mathbf{r}^{(N-2)} \\ &= \frac{N^2}{2V^2} \int\int v(r_{12})\, g(r_{12})\, d\mathbf{r}_1\, d\mathbf{r}_2 \\ &= 2\pi N\rho \int v(r)\, g(r)\, dr. \end{aligned} \tag{80}$$

This result is called the *energy equation.* It is intuitively clear. The mean number of particles in a spherical shell of thickness dr at a distance r is $4\pi r^2\, dr\rho\, g(r)$, the potential energy of a particle at $r = 0$ due to the interaction with the particles in the shell is $v(r)\, 4\pi r^2\, dr\rho\, g(r)$. Integrating from 0 to ∞ and deviding by 2 to avoid double counting leads to the above result.

Another example is the evaluation of the previously derived virial equation or equation of state. With the same assumptions it becomes

$$\begin{aligned} \frac{\beta P}{\rho} &= 1 - \frac{\beta}{3N\, Z_N(V,T)} \int \exp[-\beta V_N(\mathbf{r}^N)] \sum_{i=1}^{N} \mathbf{r}_i \cdot \nabla_i \left(\sum_{j\neq i}^{N} v(r_{ij})\right) d\mathbf{r}^N \\ &= 1 - \frac{1}{6}\beta(N-1) \int d\mathbf{r}_1\, d\mathbf{r}_2\, r_{12}\, v'(r_{12}) \\ &\quad \times \left(\frac{1}{Z_N(V,T)}\right) \int \exp[-\beta V_N(\mathbf{r}^N)] d\mathbf{r}^{(N-2)} \\ &= 1 - \frac{2}{3}\pi\beta\rho \int dr\, r^3\, v'(r)\, g(r), \end{aligned} \tag{81}$$

where

$$v'(r) = \frac{dv(r)}{dr}. \tag{82}$$

This result is called the *pressure equation.* Although this form of the virial equation has a faily simple structure, because it involves only a one-dimensional integral, the difficulty lies in the determination of $g(r)$ from the pair potential via Eq. (70) and Eq. (77).

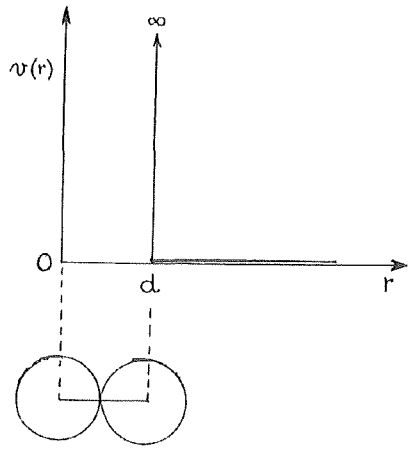


Fig. 5: *Illustration of the hard sphere potential*

The integration can be performed for a hard sphere potential (See Fig. 5):

$$\begin{aligned} v(r) \quad &= \infty \qquad r < d \\ &= 0 \qquad r > d, \end{aligned} \tag{83}$$

where d is the hard-sphere diameter. One hopes that the model of hard spheres will exhibit most of the salient features of a real system. The problem that arises from the derivative of such a discontinuous potential can be resolved by the introduction of the "indirect" correlation function $y(r)$, defined by

$$y(r) = g(r)\, \exp[\beta\, v(r)]. \tag{84}$$

We rewrite the pressure equation and find by partial integration

$$\begin{aligned} \frac{\beta\, P}{\rho} \quad &= 1 - \frac{2}{3}\pi\beta\rho \int dr\, r^3\, v'(r)\, y(r)\, \exp[-\beta\, v(r)] \\ &= 1 + \frac{2}{3}\pi\rho \int dr\, r^3\, y(r)\, \frac{d}{dr} \exp[-\beta\, v(r)] \\ &= 1 + \frac{2}{3}\pi\rho \int dr\, r^3\, y(r)\, \delta(r-d) \\ &= 1 + \frac{2}{3}\pi\rho\, d^3\, g(d), \end{aligned} \tag{85}$$

because for the hard sphere potential

$$\exp[-\beta\, v(r)] = \Theta(r-d)$$

and

$$\frac{d}{dr} \exp[-\beta\, v(r)] = \delta(r-d),$$

where $\Theta(x)$ is the unit step function. An approximate theory that permits the evaluation of $g(r)$ and in particular of $g(d)$ is the Percus-Yevick (PY) theory [3]. There one can obtain

an analytical result for a hard sphere fluid. This result is shown together with "exact" results obtained by Monte Carlo simulation in Fig. 6. Although the overall agreement is good one observes that the PY theory underestimates $g(d)$.

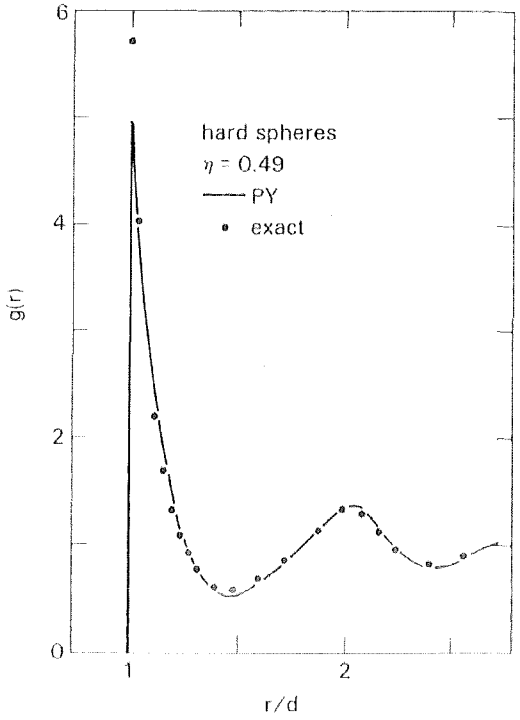


Fig. 6: *Percus-Yevick pair distribution function $g(r)$ for hard sphere potential [From Ref. [3]]*

5.2 Representation of $\rho_N^{(n)}(\mathbf{r}^n)$ by averages of δ-functions

By working in the canonical ensemble, it is possible to obtain useful expressions for the particle densities in terms of delta-functions of position. We note that

$$\begin{aligned}\langle\delta(\mathbf{r}-\mathbf{r}_1)\rangle &= \frac{1}{Z_N(V,T)}\int \delta(\mathbf{r}-\mathbf{r}_1)\exp[-\beta V_N(\mathbf{r}^N)]\,d\mathbf{r}^N \\ &= \frac{1}{Z_N(V,T)}\int\cdots\int \exp[-\beta V_N(\mathbf{r},\mathbf{r_2},\cdots,\mathbf{r_N})]\,d\mathbf{r}_2\cdots d\mathbf{r}_N. \qquad (86)\end{aligned}$$

It then follows from the definition of $\rho_N^{(1)}(\mathbf{r})$ that

$$\rho_N^{(1)}(\mathbf{r}) = \langle\sum_{i=1}^{N}\delta(\mathbf{r}-\mathbf{r}_1)\rangle. \qquad (87)$$

Similarly, the statistical average of a product of delta-functions is

$$\langle \delta(\mathbf{r}-\mathbf{r}_1)\ \ \delta(\mathbf{r}'-\mathbf{r}_2)\rangle = \frac{1}{Z_N(V,T)}\int \delta(\mathbf{r}-\mathbf{r}_1)\,\delta(\mathbf{r}'-\mathbf{r}_2)\exp[-\beta\, V_N(\mathbf{r}^N)]\,d\mathbf{r}^N$$
$$= \frac{1}{Z_N(V,T)}\int\cdots\int \exp[-\beta\, V_N(\mathbf{r},\mathbf{r}',\mathbf{r_3},\cdots,\mathbf{r_N})]\,d\mathbf{r}_3\cdots d\mathbf{r}_N \qquad (88)$$

and hence

$$\rho_N^{(2)}(\mathbf{r},\mathbf{r}') = \langle \sum_i^N \sum_{j\neq i}^N \delta(\mathbf{r}-\mathbf{r}_i)\,\delta(\mathbf{r}'-\mathbf{r}_j)\rangle. \qquad (89)$$

5.3 The YBG hierarchy and the Born-Green equation

It was shown in Section 2.3 that the non-equilibrium reduced probability densities $f^{(n)}(\mathbf{r}^n,\mathbf{p}^n;t)$ are coupled by a set of $(N-1)$ equations called the BBGKY hierarchy. A similar hierarchy exists for the equilibrium particle densities; this is generally known as the Yvon-Born-Green or *YBG hierarchy.* Since in equilibrium

$$\frac{\partial f^{(n)}}{\partial t} = 0,$$

the BBGKY hierarchy reduces to

$$\sum_{i=1}^n \left[\frac{1}{m}\mathbf{p}_i\cdot\frac{\partial}{\partial \mathbf{r}_i} + \left(\mathbf{F}_i^{ext} + \sum_{j=1}^n \mathbf{F}_{ij}\right)\cdot\frac{\partial}{\partial \mathbf{p}_i}\right] f_0^{(n)}(\mathbf{r}^n,\mathbf{p}^n)$$
$$= -\sum_{i=1}^n \int\int \mathbf{F}_{i,n+1}\cdot\frac{\partial}{\partial \mathbf{p}_i} f_0^{(n+1)}(\mathbf{r}^{n+1},\mathbf{p}^{n+1})d\mathbf{r}_{n+1}\,d\mathbf{p}_{n+1}, \qquad (90)$$

where the same restriction to pair forces that was invoked earlier is made and $F_{ii}=0$. The reduced probability density $f_0^{(n)}(\mathbf{r}^n,\mathbf{p}^n)$ can be factorized as

$$f_0^{(n)}(\mathrm{r}^n,\mathrm{p}^n) = \mathcal{P}(\mathrm{p}^n)\,\rho_N^{(n)}(\mathrm{r}^n), \qquad (91)$$

where $\mathcal{P}(\mathbf{p}^n)$ is a product of n independent Maxwell-Boltzmann distributions, i.e.

$$\mathcal{P}(\mathbf{p}^n) = (2\pi\, m\, k_B\, T)^{-3n/2}\ \exp\left(-\beta\sum_{i=1}^n |\mathbf{p}_i|^2/2m\right) \qquad (92)$$

with the properties that

$$\frac{\partial}{\partial \mathbf{p}_i}\mathcal{P}^{(n)}(\mathbf{p}^n) = -\frac{\beta}{m}\mathbf{p}_i\,\mathcal{P}^{(n)}(\mathbf{p}^n) \qquad (93)$$

and

$$\int \mathcal{P}^{(n+1)}(\mathbf{p}^{n+1})\,d\mathbf{p}_{n+1} = \mathcal{P}^{(n)}(\mathbf{p}^n). \qquad (94)$$

With these identities the BBGKY hierarchy reduces to a system of equations that involves only particle densities, namely

$$\sum_{i=1}^{n} \mathbf{p}_i \cdot \left[\nabla_i - \beta \left(\mathbf{F}_i^{ext} + \sum_{j=1}^{n} \mathbf{F}_{ij} \right) \right] \rho_N^{(n)}(\mathbf{r}^n)$$
$$= \beta \sum_{i=1}^{n} \mathbf{p}_i \cdot \int \mathbf{F}_{i,n+1}\, \rho_N^{(n+1)}(\mathbf{r}^{n+1})\, d\mathbf{r}_{n+1}. \tag{95}$$

Because the particles are identical the functions $\rho_N^{(n)}(\mathbf{r}^n)$ must be symmetric in all $\mathbf{r}_i$ for $1 \leq i \leq n$. Since the equation is valid for any choice of the n momenta $\mathbf{p}^n$ it must hold term by term. For $i = 1$ we arrive at the *YBG hierarchy* in an external field $\mathbf{F}^{ext}$, i.e.

$$k_B\, T\, \nabla_1\, \rho_N^{(n)}(\mathbf{r}^n) = \left(\mathbf{F}_1^{ext} + \sum_{j=2}^{n} \mathbf{F}_{1j} \right) \rho_N^{(n)}(\mathbf{r}^n) + \int \mathbf{F}_{1,n+1}\, \rho_N^{(n+1)}(\mathbf{r}^{n+1})\, d\mathbf{r}_{n+1}. \tag{96}$$

Without an external field the system is homogenuous, i.e. $\rightarrow \rho_N^{(n)}(\mathbf{r}^n) = \rho^n\, g_N^{(n)}(\mathbf{r}^n)$ and the YBG hierarchy becomes a system of equations for the particle distribution functions

$$-k_B\, T\, \nabla_1\, g_N^{(n)}(\mathbf{r}^n) = \sum_{j=2}^{n} \nabla_1\, v(r_{1j})\, g_N^{(n)}(\mathbf{r}^n) + \rho \int \nabla_1\, v(r_{1,n+1})\, g_N^{(n+1)}(\mathbf{r}^{n+1})\, d\mathbf{r}_{n+1}. \tag{97}$$

In common with the BBGKY hierarchy, the YBG hierarchy is useful only if a closure relation between $g_N^{(n)}$ and $g_N^{(n+1)}$ is available due to some approximation.
We consider such an approximation for the most important case $n = 2$. This relates the pair and triplet distribution functions by

$$-k_B\, T\, \nabla_1\, g_N^{(2)}(\mathbf{r_1}, \mathbf{r_2}) = \nabla_1\, v(\mathbf{r_1}, \mathbf{r_2}), g_N^{(2)}(\mathbf{r_1}, \mathbf{r_2}) + \rho \int \nabla_1\, v(\mathbf{r_1}, \mathbf{r_3})\, g_N^{(3)}(\mathbf{r_1}, \mathbf{r_2}, \mathbf{r_3})\, d\mathbf{r}_3. \tag{98}$$

We devide by $g_N^{(2)}(\mathbf{r_1}, \mathbf{r_2})$ and note that for an isotropic fluid

$$\int \nabla_1\, v(\mathbf{r_1}, \mathbf{r_3})\, g_N^{(2)}(\mathbf{r_1}, \mathbf{r_3})\, d\mathbf{r}_3 = 0.$$

Then we obtain

$$-k_B\, T\, \nabla_1\, \ln g_N^{(2)}(\mathbf{r_1}, \mathbf{r_2})$$
$$= \nabla_1\, v(\mathbf{r_1}, \mathbf{r_2}) + \rho \int \nabla_1\, v(\mathbf{r_1}, \mathbf{r_3}) \left(\frac{g_N^{(3)}(\mathbf{r_1}, \mathbf{r_2}, \mathbf{r_3})}{g_N^{(2)}(\mathbf{r_1}, \mathbf{r_2})} - g_N^{(2)}(\mathbf{r_1}, \mathbf{r_3}) \right) d\mathbf{r}_3 \tag{99}$$

We now make the *Kirkwood superposition approximation* which presents the triplet distribution function in terms of a product of pair distribution functions, i.e.

$$g_N^{(3)}(\mathbf{r_1}, \mathbf{r_2}, \mathbf{r_3}) = g_N^{(2)}(\mathbf{r_1}, \mathbf{r_2})\, g_N^{(2)}(\mathbf{r_2}, \mathbf{r_3})\, g_N^{(2)}(\mathbf{r_3}, \mathbf{r_1}) \tag{100}$$

and we arrive at the *Born-Green equation* (BG)

$$-\nabla_1 \left[\ln g_N^{(2)}(\mathbf{r_1}, \mathbf{r_2}) + \beta\, v(\mathbf{r_1}, \mathbf{r_2}) \right]$$
$$= \rho \int \left[\nabla_1\, \beta\, v(\mathbf{r_1}, \mathbf{r_3}) \right] g_N^{(2)}(\mathbf{r_1}, \mathbf{r_3}) [g_N^{(2)}(\mathbf{r_2}, \mathbf{r_3}) - 1]\, d\mathbf{r}_3. \tag{101}$$

For a given pair potential the equation can be solved numerically to yield the pair distribution function from which, in turn, all thermodynamic properties of the system may be obtained. In Fig. 7 a numerical solution of the BG equation [7] is compared with the "exact" $g(r)$ of a Monte Carlo (MC) simulation obtained for a Lennard-Jones potential

$$v(r) = 4\,\epsilon[(a/r)^{12} - (a/r)^{6}] \tag{102}$$

Presenting the radial distribution function in the form

$$g(r) = \exp[-\beta\, v(r) + f(r)] \tag{103}$$

the BG equation becomes an integral equation for $f(r)$. In an attempt to improve the agreement with the MC simulation the radius scale of the BG solution is altered. Since for $\lim \rho \to 0$ $f(r) \to 0$

$$g(r) \to \exp[-\beta\, v(r)]$$

in the dilute limit.

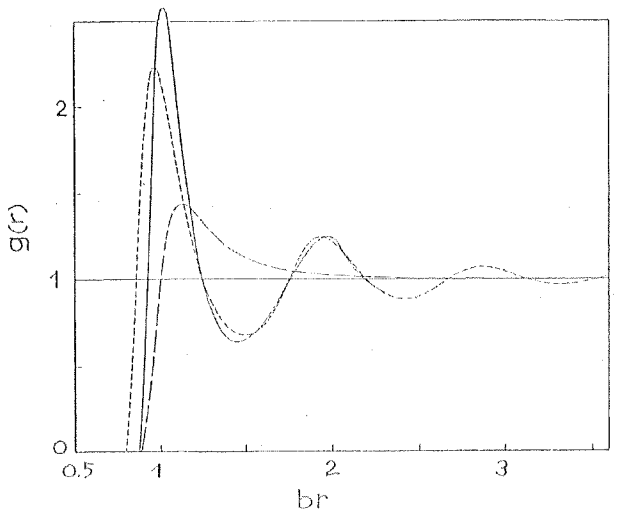


Fig. 7: *The radial distribution function $g(r)$ versus br for $\rho = a^{-3}$ and $\beta\epsilon = (2.74)^{-1}$ from the MC simulation (solid curve) and the BG equation (short dashed). The function $\exp[-\beta\, v(r)]$ (long dashed). The parameter $b = 1/a$ for the MC simulation and for $\exp[-\beta\, v(r)]$ and $b = 0.898/a$ for the Born-Green curve. [From Ref. [7]]*

In practice, the Born-Green equation leads to satisfactory results only at low densities.

6 Interaction potentials

6.1 Classification of interactions

From the preceeding sections it is clear that the interaction potentials between the particles that constitute the system are the most important ingredients when one wishes to compute the macrocopic properties by the methods that statistical mechanics offers.

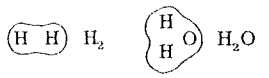
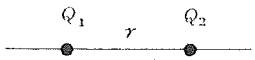
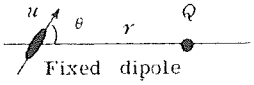
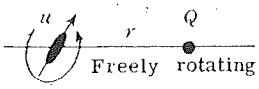
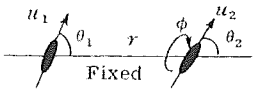
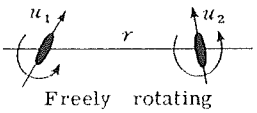
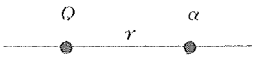
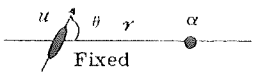
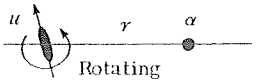
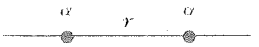
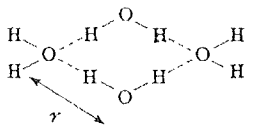
Type of interaction		Interaction energy $\mathcal{U}(r)$
Covalent		Complicated, short range
Charge–charge		$Q_1Q_2/4\pi\varepsilon_0 r$ (Coulomb energy)
Charge–dipole		$-Qu\cos\theta/4\pi\varepsilon_0 r^2$
		$-Q^2u^2/6(4\pi\varepsilon_0)^2kTr^4$
Dipole–dipole		$-u_1u_2[2\cos\theta_1\cos\theta_2 - \sin\theta_1\sin\theta_2\cos\phi]/4\pi\varepsilon_0 r^3$
		$-u_1^2u_2^2/3(4\pi\varepsilon_0)^2kTr^6$ (Keesom energy)
Charge–nonpolar		$-Q^2\alpha/2(4\pi\varepsilon_0)^2r^4$
Dipole–nonpolar		$-u^2\alpha(1+3\cos^2\theta)/2(4\pi\varepsilon_0)^2r^6$
		$-u^2\alpha/(4\pi\varepsilon_0)^2r^6$ (Debye energy)
Two nonpolar molecules		$-\left(\frac{3}{4}\right)\frac{h\nu\alpha^2}{(4\pi\varepsilon_0)^2r^6}$ (London dispersion energy)
Hydrogen bond		Complicated, short range, energy roughly proportional to $-1/r^2$

Fig. 8: *Common types of interactions between atoms, ions and molecules in vacuum. $v(r)$ is the interaction (free) energy (in J); Q, electric charge (C); u, the electric dipole moment (C m); α, electric polarizability ($C^2\,m^2\,J^{-1}$); r, distance between atoms or molecules (m); k, Boltzmann's constant ($1.38 \times 10_{-23}\,J\,K^{-1}$); T, absolute temperature (K); h, Planck's constant ($6.626 \times 10^{-34}\,J\,s$); ν, electronic absorption (ionization) frequency (s^{-1}) ; ε_0, permittivity of free space ($8.854 \times 10^{-12}\,C^2\,J^{-1}\,m^{-1}$). From Ref. [8]]*

The interaction potentials can be loosely classified into three categories[8] . First, there are those potentials that are purely *electrostatic* in origin arising from the Coulomb interaction between charges. The interaction between charges, permanent multipoles such as dipoles, quadropoles, etc, fall also into this category. Second, there are *polarization* interactions between the dipole moments, induced in atoms and molecules, and charges or permanent dipoles. Third, there are interactions that can be understood only quantum mechanically. For example, interactions that lead to covalent binding or exchange interactions.
Falling into the above categories are a number of fairly distinct interaction that are illustrated in Fig. 8.

6.2 Interactions between molecules in a medium

When one considers interactions between molecules, for example, in a liquid, several effects are involved that do not occur when the molecules interact in free space. Some of the effects are illustrated in Fig. 9.

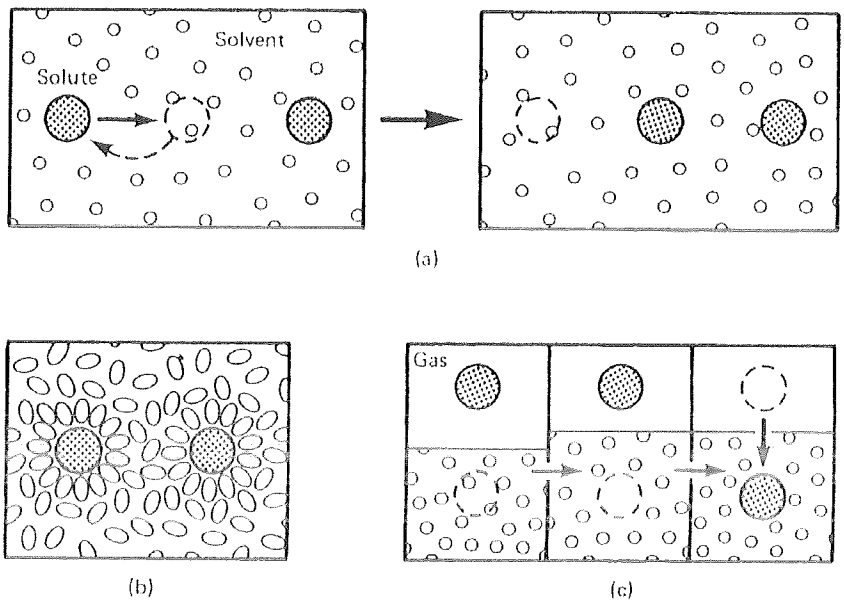


Fig. 9: *Some solvent effects involved in the interaction of dissolved molecules or particles. (a) Displacement of solvent by two approaching molecules. (b) Solvation (reordering) of solvent molecules by solute. (c) Cavity formation by solvent prior to solute insertion. [From Ref. [8]]*

1. For two solute molecules in a solvent, their total pair potential $v(r)$ includes not only the direct solute-solute interaction but also any changes in the solute-solvent and solvent-solvent interaction as the two molecules approach each other. A dissolved solute molecule can approach another only by displacing solvent molecules from its path (Fig. 9a). The net force therefore depends on the attraction between the

solute molecules and the solvent molecules. Thus, while two molecules may attract each other in free space, they may repel each other in the medium, for as the two molecules move towards each other the work that must be done to displace the solvent may exceed that gained by the approaching molecules. In such cases it becomes energetically more favorable for the two molecules to move apart.

2. Solute molecules often disturb the local ordering or structure of the solvent molecules (Fig. 9b). If the (free) energy associated with perturbation depends on the distance between the two dissolved molecules, it produces an additional solvation force between them.

3. Solute-solvent interactions can change the properties of dissolved molecules, such as their diplole moments and charge (degree of ionization). The properties of dissolved molecules may therefore be different in different media.

4. Finally, when an individual molecule is introduced into a condensed medium, there is the cavity energy expended by the medium when it forms the cavity to accomodate the guest molecule (Fig. 9c).

These effects are interrelated and are collectively referred to as solvent effects or medium effects.

References

[1] R. Becker, *Theorie der Wärme* (Springer-Verlag, Berlin, 1964)

[2] L. D. Landau und E. M. Lifschitz, *Lehrbuch der Theoretischen Physik V, Statistische Physik, Teil 1* (Akademie-Verlag, Berlin 1979)

[3] We closely follow Chapter 2 in: J. P. Hansen and J. R. McDonald, *Theory of Simple Liquids* (Academic Press, 2nd Edition, London 1986)

[4] See also J. K. G. Dhont, *An Introduction to Dynamics of Colloids*, (Elsevier, Amsterdam 1996)

[5] N. W. Ashcroft and N. D. Mermin, *Solid State Physics* (Holt, Rinehart and Winston, Philadelphia, 1976)

[6] C. Kittel, *Introduction to Solid State Physics* (John Wiley & Sons, Inc., New York, Third Edition, 1967)

[7] A. A. Broyles, *Radial Distribution Function from the Born-Green Integral Equation*, J. Chem. Phys. **33**, 456 (1960).

[8] J. N. Israelachvili, *Intermolecular and Surface Forces, Chapter 2* (Academic Press, 2nd Edition, London 1991)

B 2 Conformations of Polymer Chains

S. Hoffmann
Dutch Polymer Institute
c/o Dubble CRG, ESRF Grenoble,
B.P. 220, F-38043 Grenoble Cedex, France

Contents

1 Introduction 2

2 Mathematical description of chain molecules 2

3 Characterization of the polymer structure 4

4 The freely rotating chain 6

5 The freely jointed chain 7

6 Further characteristic quantities 9

7 The Gaussian chain 10

8 The form factor of a Gaussian chain 11

9 Statistical mechanics of model chains 14

10 Self-avoiding polymer chains 17

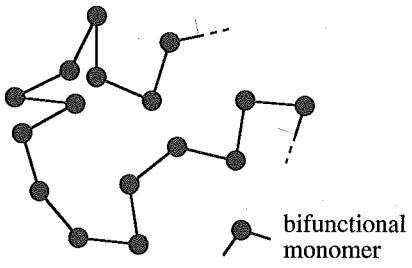


Fig. 1: *Schematic view of a linear polymer.*

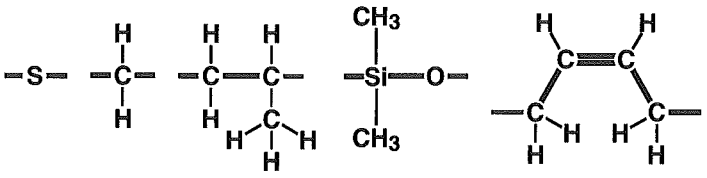


Fig. 2: *Repeating units of some typical linear homopolymers; from left to right: sulfur, polyethylene, polypropylene, poly(dimethyl siloxane), 1,4-polybutadiene.*

1 Introduction

The word polymer is derived from the greek word 'polumeres' which roughly means "consisting of many parts" (from 'polu-' many and 'meros' part). According to this etymology, a polymer means any kind of (macro-)molecule that consists of a large number of (various or identical) elementary building blocks like most synthetics, sugars, cellulose, DNA, and many others. In this course we will treat the case of linear polymers (see Fig. 1). These emerge from polymerization reactions when each monomer develops exactly two bindings as it is built into the macromolecule. In the ideal case, polymers produced in this way have no branching point at all and can attain a considerable high numbers of repeating units. Some examples for synthetic polymers of this kind are displayed in Fig. 2. If only one type of monomers is present in a given polymer it is called a homopolymer. In the following, we will consider more closely what the structural properties of long linear homopolymers are and how they can be characterized. For this, we will assume that the polymer chain is always more or less flexible. Furthermore, we will restrict our considerations to the case of unperturbed polymer chains, i. e. no external potential or preferential orientation should be present.

2 Mathematical description of chain molecules

Conformations of a polymer. The monomers shown in Fig. 2 demonstrate the local structure of typical polymer chains. The chemical composition of the monomers and the

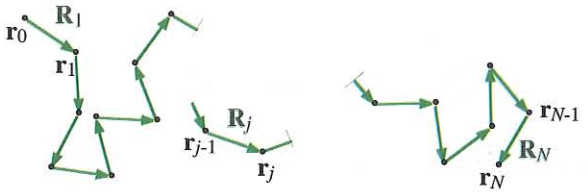


Fig. 3: *Mathematic description of a polymer chain by either $N+1$ location vectors $\{\mathbf{r}_j\}$ pointing at the position of the backbone atoms or equivalently by N bond vectors $\{\mathbf{R}_j\}$.*

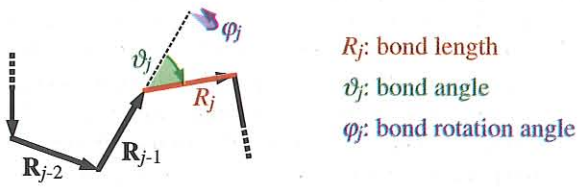


Fig. 4: *Representation of a bond vector $\mathbf{R}_j$ in polar coordinates.*

way how they are integrated into the polymer chain are called the configuration of the polymer segments. On the other hand, by the conformation of a polymer we mean all the possible arrangements of its given chemical structure in space which are accessible due to the flexibility of the molecule.

Bond vectors. In order to build a model for the spatial structure of a polymer, we have to describe it mathematically. For this, we consider only the atoms which are situated on the backbone of the molecule and the bindings which relate them. The chain can now be described either by the $N+1$ location vectors $\{\mathbf{r}_j\}$ of the backbone atoms or, equivalently, by the N bond vectors $\{\mathbf{R}_j\}$ (see Fig. 3) which are defined by

$$\mathbf{R}_j := \mathbf{r}_j - \mathbf{r}_{j-1} \quad \text{with} \quad j = 1, \ldots, N. \tag{1}$$

Polar coordinates. These bond vectors are most usefully expressed in polar coordinates. The system of coordinates for each bond vector $\mathbf{R}_j$ is defined by the orientation of the two preceding bond vectors (See Fig. 4). The polar axis is given by the direction of the preceding vector $\mathbf{R}_{j-1}$. Hence, the polar angle ϑ_j is identical to the angle between the two successive bond vectors $\mathbf{R}_{j-1}$ and $\mathbf{R}_j$ and is therefore called the bond angle. The reference to measure the azimuthal or bond rotation angle φ_j is the bond vector $\mathbf{R}_{j-2}$ (more precisely: its vector component perpendicular to $\mathbf{R}_{j-1}$). The third polar variable is finally the radius R_j which represents the length of the bond vector or shorter: the bond length.

From these definitions we can see that three polar angles for a given chain configuration remain undefined, namely ϑ_1, φ_1, and φ_2. These three angles determine the spatial orientation of the chain and represent together with the coordinates $\mathbf{r}_0$ of the starting point the six global degrees of freedom of the molecule (three for its translation and three

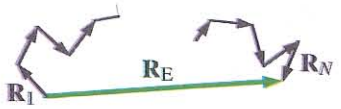


Fig. 5: *End-to-end vector* $\mathbf{R}_\mathrm{E}$ *of a polymer chain.*

for its rotation). All other polar coordinates stand for internal degrees of freedom of the polymer chain.

Physical restrictions. The main restriction on the possible values of these chain coordinates are imposed by the nature of the covalent binding between the chain atoms. The value of R_j is determined by the binding potentials between the atoms. The binding energies are normally considerably larger than the thermal energy $k_\mathrm{B}T$. Hence, the fluctuations of the bond lengths around their average value $l_0 := \langle R_j \rangle$ are very small and can generally be neglected. The bond angles ϑ_j are mainly defined by the electronic configuration of the corresponding atom. In case of a carbon atom with four single bonds, the configuration of the binding electrons is given by a sp^3-hybridization. This leads to a tetrahedral orientation of the four bonds. The bond angle for an ideal tetrahedral configuration would be $\vartheta \approx 70.53$ (corresponding to $\cos\vartheta = \frac{1}{3}$). The rotation around single covalent bonds which is represented by the bond rotation angle φ_j is relatively free as usually only week rotational barriers are involved. This high freedom in the bond rotation angle is in fact the reason for the high flexibility of most polymers. On the other hand, in case of double or triple bindings, rotations around φ_j is prohibited.

3 Characterization of the polymer structure

Chrarcteristic quantities. Several quantities are used in order to characterize the structural properties of a polymer chain and many of them are interchangeable. Some of them will be introduced in the following subsections and others will be presented later, once the results of the basic chain models will have been provided.

End-to-end vector. The end-to-end vector $\mathbf{R}_\mathrm{E}$ of a linear polymer is the vector which relates the starting point $\mathbf{r}_0$ with the end point $\mathbf{r}_N$ of the backbone chain (see Fig. 5),

$$\mathbf{R}_\mathrm{E} := \mathbf{r}_N - \mathbf{r}_0 = \sum_{j=1}^{N} \mathbf{R}_j. \tag{2}$$

Its length and orientation can vary considerably from one individual chain to another and also fluctuate over time for each of the chains. Therefore, one considers thermal averages in order to define useful characteristic quantities which describe the typical structural features of a given chain molecule.

In a completely disordered system without any preferential direction of orientation, the thermal average of $\mathbf{R}_\mathrm{E}$ is obviously the zero vector. The smallest moment of $\mathbf{R}_\mathrm{E}$ which

does not vanish under thermal averaging is the second one. Hence, we define

$$\bar{R}_{\mathrm{E}}^2 := \langle R_{\mathrm{E}}^2 \rangle = \langle \mathbf{R}_{\mathrm{E}} \cdot \mathbf{R}_{\mathrm{E}} \rangle = \sum_{j=1}^{N} \sum_{k=1}^{N} \langle \mathbf{R}_j \cdot \mathbf{R}_k \rangle \tag{3}$$

where $\bar{R}_{\mathrm{E}}$ is the root-mean-square of the end-to-end distance. As $\mathbf{R}_j \cdot \mathbf{R}_k = \mathbf{R}_k \cdot \mathbf{R}_j$, this expression can be further split up into two parts,

$$\bar{R}_{\mathrm{E}}^2 = \sum_{j=1}^{N} \langle R_j^2 \rangle + 2 \sum_{j=1}^{N} \sum_{k=j+1}^{N} \langle \mathbf{R}_j \cdot \mathbf{R}_k \rangle \,. \tag{4}$$

This quantity $\bar{R}_{\mathrm{E}}$ is in fact regularly used in order to represent the spatial extension of a linear polymer chain. The important task of the different existing polymer chain models is now to provide an explicit expression for the term $\langle \mathbf{R}_j \cdot \mathbf{R}_k \rangle$ which represents the pair correlation of distinct bond vectors of the chain.

Radius of gyration. A second quantity which is suited to express the spatial extension of a polymer is the radius of gyration R_{g}. It is defined via the second central moment of the mass distribution of the molecule,

$$R_{\mathrm{g}}^2 := \frac{\sum_{j=0}^{N} m_j \left(\mathbf{r}_j - \mathbf{r}_{\mathrm{cm}}\right)^2}{\sum_{j=0}^{N} m_j} \quad \text{with} \quad \mathbf{r}_{\mathrm{cm}} = \frac{\sum_{j=0}^{N} m_j \mathbf{r}_j}{\sum_{j=0}^{N} m_j} \tag{5}$$

where $\mathbf{r}_{\mathrm{cm}}$ is the location vector of the center of mass and m_j the mass of the j-th chain segment. For the further considerations we will assume that $m_j \equiv m$ for all j so that

$$R_{\mathrm{g}}^2 = \frac{1}{N+1} \sum_{j=0}^{N} (\mathbf{r}_j - \mathbf{r}_{\mathrm{cm}})^2 \quad \text{and} \quad \mathbf{r}_{\mathrm{cm}} = \frac{1}{N+1} \sum_{j=0}^{N} \mathbf{r}_j. \tag{6}$$

Persistence length. The local rigidity of a chain is often expressed in terms of the persistence length l_{p}. To illustrate the concept of the persistence length, we pose the following question: Where will we find, in average, the end of a linear polymer chain when we keep the first bond vector fixed? Let H_N be the projection of the end-to-end vector $\mathbf{R}_{\mathrm{E}}$ on the unity vector $\mathbf{e}_1$ in direction of the first bond of the chain (see Fig. 6). Obviously, H_N is given by

$$H_N = \mathbf{e}_1 \cdot \mathbf{R}_{\mathrm{E}} = \frac{\mathbf{R}_1 \cdot \mathbf{R}_{\mathrm{E}}}{R_1} = \frac{\mathbf{R}_1}{R_1} \cdot \sum_{j=1}^{N} \mathbf{R}_j. \tag{7}$$

The persistence length l_{p} is now defined as the thermal average value of H_N in the limit of an infinitely long chain,

$$l_{\mathrm{p}} := \lim_{N \to \infty} \langle H_N \rangle = \sum_{j=1}^{\infty} \left\langle \frac{\mathbf{R}_1 \cdot \mathbf{R}_j}{R_1} \right\rangle . \tag{8}$$

The stiffer the chain under study, the further apart we will find the average position of its end point from the (virtually fixed) first bond and the larger values we will find for l_{p}. The persistence length l_{p} is therefore a suitable quantity which is often used to express the stiffness of a polymer.

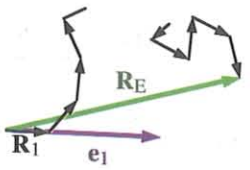


Fig. 6: *Projection of the end-to-end vector onto the unity vector of the first chain bond.*

4 The freely rotating chain

Assumptions. In this section, we will calculate in detail the statistics for a simple model of a homopolymer chain and study the typical results for the structural properties of this model polymer chain. Following the arguments concerning bond lengths and bond angles of a covalently bound polymer which we cited above, we assume that the bond lengths R_j have a constant value of l_0 and that the bond angles ϑ_j have a constant value of γ. Apart from this, we allow a free rotation around the bond vectors so that the bond rotation angles φ_j are equally distributed over the whole range from 0 to 2π.

End-to-end distance. As we want to calculate the end-to-end vector as given by Eq. (4), we have to determine an expression for the thermal averages $\langle \mathbf{R}_j \cdot \mathbf{R}_k \rangle$. Lets consider the average of one bond vector $\mathbf{R}_k$ over all possible orientations of this vector and while all other bond rotation angles are kept fixed. As the rotation around φ_k is free, the average of $\mathbf{R}_k$ must be parallel to the preceding vector. Hence, we find

$$\langle \mathbf{R}_k \rangle_{\mathbf{R}_k} = \langle \mathbf{R}_k \rangle_{\varphi_k} = \mathbf{R}_{k-1} \langle \cos\vartheta \rangle \tag{9}$$

where $\langle \cos\vartheta \rangle = \cos\gamma$. The indices added to the brackets in the equation above indicate the variables over which has been averaged. Multiplying both sides with $\mathbf{R}_j$ and averaging over all remaining chain coordinates (bond rotation angles) leads to

$$\langle \mathbf{R}_k \cdot \mathbf{R}_j \rangle = \langle \mathbf{R}_{k-1} \cdot \mathbf{R}_j \rangle \langle \cos\vartheta \rangle . \tag{10}$$

This a recursive equation for the expression we are looking for. Setting in $\langle \mathbf{R}_j^2 \rangle = l_0^2$ as a starting condition, we obtain the result

$$\langle \mathbf{R}_k \cdot \mathbf{R}_j \rangle = l_0^2 \langle \cos\vartheta \rangle^{|k-j|} . \tag{11}$$

From here, it is straight forward to calculate the mean square of the end-to-end vector to be

$$\bar{R}_\mathrm{E}^2 = \frac{N l_0^2}{1 - \langle \cos\vartheta \rangle} \left[1 + \langle \cos\vartheta \rangle - \frac{2 \langle \cos\vartheta \rangle \left(1 - \langle \cos\vartheta \rangle^N \right)}{N \left(1 - \langle \cos\vartheta \rangle \right)} \right] . \tag{12}$$

Note that this is still a general result for the only condition that all bond lengths are constant and that all bond rotation angles are completely free. We have not yet specified the nature of the bond angle ϑ. To obtain the final result for the freely rotating chain, where $\vartheta_j \equiv \gamma$, we only have to set in that $\langle \cos\vartheta \rangle = \cos\gamma$.

Asymptotic behavior. There are two limiting cases for this equation. The first one is given when the bond angle is zero, $\vartheta \equiv 0$, for all bonds. Then we obtain the trivial result that

$$\bar{R}_{\mathrm{E}}^2 = N^2 l_0^2. \tag{13}$$

In this case the chain is just a long stiff rod where the end-to-end distance is given by the product Nl_0.

The second and more interesting case is the limit for a very large number N of repeating units with $N \gg 1$ and $\langle \cos\vartheta \rangle < 1$. Then, the end-to-end distance approaches

$$\bar{R}_{\mathrm{E}}^2 = N l_0^2 \frac{1 + \langle \cos\vartheta \rangle}{1 - \langle \cos\vartheta \rangle}. \tag{14}$$

Apart from numerical factors we see that $\bar{R}_{\mathrm{E}} \propto \sqrt{N}$. As we will see later, this result is characteristic for all chain models which consider only interactions between neighboring segments and thereby neglecting possible "long range interactions" between segments that are well separated along the contour of the polymer chain. The relation $\bar{R}_{\mathrm{E}} \propto \sqrt{N}$ has its analogy in the brownian motion of a particle. There, the time t which passes between two observations of a diffusing particle corresponds to number of segments N in case of a polymer chain. A freely diffusing particle describes a three-dimensional random walk and its mean square displacement from the starting point is proportional to the elapsed time, $\left\langle [\mathbf{r}(t) - \mathbf{r}(0)]^2 \right\rangle \propto t$ similar to the relation $\left\langle (\mathbf{r}_N - \mathbf{r}_0)^2 \right\rangle \propto N$ which we found for a polymer chain.

Persistence length. The persistence length of a freely rotating chain can be directly calculated from the Eqs. (8) and (11) giving

$$l_{\mathrm{p}} = \frac{l_0}{1 - \langle \cos\vartheta \rangle}. \tag{15}$$

This result shows that as the bond angle of a chain becomes smaller its persistence length will increase, i. e. its local stiffness becomes larger.

5 The freely jointed chain

Assumptions. We can very quickly pass from the results of the freely rotating chain to the corresponding results for the most simple chain model, the freely jointed chain. Here, the chain is assumed to consist of N bonds of a fixed length l_0 while the orientation of all bonds is considered to be completely free.

Characteristic quantities. In this case, the bond rotation angle φ is equally distributed and the bond lengths are invariable so that we can directly refer to Eq. (14) above. Due to the free orientation of the bond vectors, we find for the bond angle ϑ that $\langle \cos\vartheta \rangle = 0$ and with this we get the following expressions for the mean square end-to-end distance,

$$\bar{R}_{\mathrm{E}}^2 = N l_0^2, \tag{16}$$

and the persistence length,

$$l_{\mathrm{p}} = l_0. \tag{17}$$

Note that, here again, we find the proportionality $\bar{R}_{\mathrm{E}} \propto \sqrt{N}$.

The mean square radius of gyration of a freely joint chain with $N+1$ segments can easily be calculated explicitly resulting in the relation

$$\bar{R}_{\mathrm{g}}^2 := \langle R_{\mathrm{g}}^2 \rangle = \frac{N(N+2)}{6(N+1)} l_0^2. \tag{18}$$

From this equation, we find that for large values of N the quantities $\bar{R}_{\mathrm{E}}$ and $\bar{R}_{\mathrm{g}}$ are related by

$$\bar{R}_{\mathrm{g}}^2 = \frac{N l_0^2}{6} = \frac{\bar{R}_{\mathrm{E}}^2}{6}. \tag{19}$$

This results holds in general for all chain models as long as only short range interactions between chain segments and large values of N are considered.

Distribution of chain configurations. We will now use the model of the freely jointed chain to derive the distribution function for the end-to-end vector $\Phi(\mathbf{R}, N)$. To do so, we first have to find the probability function which describes the configuration of the N bond vectors. This task is easy for a freely jointed chain. As all bond vectors are uncorrelated, the probability (or distribution) function for the chain configuration $\Psi(\{\mathbf{R}_j\})$ is just the product of the probability functions $\psi(\mathbf{R}_j)$ for the N single bonds,

$$\Psi(\{\mathbf{R}_j\}) = \prod_{j=1}^{N} \psi(\mathbf{R}_j), \tag{20}$$

where the probability function for a single bonds is given by

$$\psi(\mathbf{R}_j) = \frac{1}{4\pi l_0^2} \delta(R_j - l_0). \tag{21}$$

Distribution of end-to-end distances. Now, the probability that a given vector $\mathbf{R}$ is identical to the end-to-end vector $\mathbf{R}_{\mathrm{E}}$ can be calculated from

$$\Phi(\mathbf{R}, N) = \int \Psi(\{\mathbf{R}_j\})\, \delta(\mathbf{R} - \mathbf{R}_{\mathrm{E}})\, \mathrm{d}^{3N}\{\mathbf{R}_j\}. \tag{22}$$

Replacing the delta function by introducing $\delta(\mathbf{x}) = (2\pi)^{-3} \int \exp(\mathrm{i}\mathbf{k} \cdot \mathbf{x})\, \mathrm{d}^3\mathbf{k}$ and using Eqs. (2) and (20), we get

$$\Phi(\mathbf{R}, N) = \frac{1}{(2\pi)^3} \int \left[\int \psi(\mathbf{R}') \exp(-\mathrm{i}\mathbf{k} \cdot \mathbf{R}')\, \mathrm{d}^3\mathbf{R}' \right]^N \exp(\mathrm{i}\mathbf{k} \cdot \mathbf{R})\, \mathrm{d}^3\mathbf{k} \tag{23}$$

and furthermore, by introducing Eq. (21) and evaluating the inner integral,

$$\Phi(\mathbf{R}, N) = \frac{1}{(2\pi)^3} \int \left(\frac{\sin k l_0}{k l_0} \right)^N \exp(\mathrm{i}\mathbf{k} \cdot \mathbf{R})\, \mathrm{d}^3\mathbf{k}. \tag{24}$$

In order to calculate the last expression analytically, we will do the following approximation: N is assumed to be very large and therefore the term $[(\sin k l_0)/k l_0]^N$ will always

be very small as long as kl_0 itself is not small. Now, if kl_0 is small ($kl_0 \ll 1$) we can approximate the cited term by

$$\left(\frac{\sin kl_0}{kl_0}\right)^N \approx \left(1 - \frac{k^2 l_0^2}{6}\right)^N \approx \exp\left(\frac{Nk^2 l_0^2}{6}\right) \tag{25}$$

and obtain

$$\Phi(\mathbf{R}, N) = \frac{1}{(2\pi)^3} \int \exp\left(\frac{Nk^2 l_0^2}{6}\right) \exp(\mathrm{i}\mathbf{k} \cdot \mathbf{R}) \, \mathrm{d}^3\mathbf{k}. \tag{26}$$

Within this last equation, we can evaluate the integral and obtain as the final result for the distribution of the end-to-end vector of a long polymer chain the relation

$$\Phi(\mathbf{R}, N) = \left(\frac{3}{2\pi N l_0^2}\right)^{\frac{3}{2}} \exp\left(-\frac{3R^2}{2Nl_0^2}\right). \tag{27}$$

We see that the distribution of the end-to-end vector is, to a good approximation, described by a Gaussian distribution which is centered around the average value $\langle \mathbf{R} \rangle = 0$. The width of the Gaussian distribution can be identified from Eq. (27) to be $\sigma = l_0\sqrt{N} = \bar{R}_\mathrm{E}$. Hence, the distribution of end-to-end vectors of polymer chains is very broad. The quantity $\bar{R}_\mathrm{E}$ should therefore better be retained as a characteristic quantity which describes the width of the distribution of end-to-end vectors rather than a typical size of the polymer coil.

6 Further characteristic quantities

Effective bond length. We have stated above that the result $\bar{R}_\mathrm{E}^2 \propto N$ holds for all chains when only local interactions between neighboring segments are considered. It can actually be shown in general that when the distribution function for the chain configuration can be written in the form

$$\Psi(\{\mathbf{R}_j\}) = \prod_{j=1}^{N-j_\mathrm{c}} \psi(\mathbf{R}_j, \mathbf{R}_{j+1}, \mathbf{R}_{j+2}, \ldots, \mathbf{R}_{j+j_\mathrm{c}}) \quad \text{with} \quad j_\mathrm{c} \ll N \tag{28}$$

the result for $\bar{R}_\mathrm{E}$ has always the form

$$\bar{R}_\mathrm{E}^2 = Nl^2 \tag{29}$$

for large values of N ($N \gg j_\mathrm{c}$). The quantity l is called the effective bond length and is yet another quantity which is regularly used to characterize the structure of a polymer chain. The effective bond length ascribed to a given chain is the bond length of a corresponding freely jointed chain which has the same number of segments N and the same value of $\bar{R}_\mathrm{E}$.

Characteristic ratio. The simple result for the freely jointed chain serves as the reference standard in order to define the characteristic ratio c_∞,

$$c_\infty := \lim_{N\to\infty} \frac{\bar{R}_\mathrm{E}^2}{Nl_0^2} = \frac{l^2}{l_0^2}. \tag{30}$$

For example, in case of the freely rotating chain we find from Eq. (14) that

$$c_\infty = \frac{1+\cos\gamma}{1-\cos\gamma}. \tag{31}$$

Kuhn's segment. Another important concept to compare a real chain with the model of the freely jointed chain is Kuhn's concept of the statistical segment length l_K: Analogously to the case of the effective bond length, we describe the structural properties of a polymer by a freely jointed chain. But the two experimental quantities which should be met by the model chain are now the mean square end-to-end distance $\bar{R}_\mathrm{E}^2$ and the largest extension $R_\mathrm{E,max}$ that is theoretically possible for the given polymer structure (The largest possible end-to-end distance $R_\mathrm{E,max}$ is essentially determined by the nature of the covalent bindings involved). These conditions define the appropriate number N_K and length l_K of freely jointed segments. As stated above the ascribed freely joint chain should fulfill the conditions

$$R_\mathrm{E,max} = N_\mathrm{K} l_\mathrm{K} \quad \text{and} \quad \bar{R}_\mathrm{E}^2 = N_\mathrm{K} l_\mathrm{K}^2. \tag{32}$$

Inverting these two relations, we can calculate the number and the size of the Kuhn segments directly from the experimental parameters of the polymer chain,

$$l_\mathrm{K} = \frac{\bar{R}_\mathrm{E}^2}{R_\mathrm{E,max}} \quad \text{and} \quad N_\mathrm{K} = \frac{R_\mathrm{E,max}^2}{\bar{R}_\mathrm{E}^2}. \tag{33}$$

The Kuhn length l_K for a given polymer can be considered as the smallest chain segments which can still be considered to be statistically independent from each other. This justifies that l_K is also called the statistical segment length.

To calculate the corresponding values for the example of the freely rotating chain, we have to find an expression for the maximal end-to-end distance $R_\mathrm{E,max}$ first. If the chain is completely stretched the chain contour will be a zigzag line and all bond vectors will be oriented under the same angle compared to the end-to-end vector. This angle is just the half of the bond angle ϑ so that

$$R_\mathrm{E,max} = N l_0 \cos\frac{\gamma}{2} = N l_0 \sqrt{\frac{1+\cos\gamma}{2}}. \tag{34}$$

From these relations, we find for the Kuhn segments that

$$l_\mathrm{K} = \frac{\sqrt{2(1+\cos\gamma)}}{1-\cos\gamma} l_0 \quad \text{and} \quad N_\mathrm{K} = \frac{1-\cos\gamma}{2} N. \tag{35}$$

Comparing this result for l_K with the corresponding expression for the persistence length l_p of the freely rotating chain, we find that, for small bond angles ϑ, the statistical segment is about twice as large as l_p.

7 The Gaussian chain

Assumptions. We have seen that the local nature of the chain segments plays no role when considering the global structure of a linear polymer (Here, "local" means on length

scales smaller than the statistical segment l_K). It is therefore possible to replace the segments of a model chain by any convenient other kind of segment as long as the global structural properties are conserved. This holds even if the constructed segment has very unrealistic features. In this way, the Gaussian chain is constructed by assuming that the lengths l_j of the chain segments are variable and follow a Gaussian distribution where the standard deviation of the distance between the end points of the segments is identical to the effective bond length l,

$$\psi(\mathbf{R}_j) = \left(\frac{3}{2\pi l^2}\right)^{\frac{3}{2}} \exp\left(-\frac{3R_j^2}{2l^2}\right). \tag{36}$$

Apart from this, the orientations of the bond vectors are considered to be completely free as for the freely jointed chain.

Distribution of chain configurations. The distribution function of the chain configuration $\Psi(\{\mathbf{R}_j\})$ can then again be factorized as given by Eq. (20) so that

$$\begin{aligned}\Psi(\{\mathbf{R}_j\}) &= \prod_{j=1}^{N} \left(\frac{3}{2\pi l^2}\right)^{\frac{3}{2}} \exp\left(-\frac{3R_j^2}{2l^2}\right) \\ &= \left(\frac{3}{2\pi l^2}\right)^{\frac{3}{2}N} \exp\left(-\frac{3}{2l^2}\sum_{j=1}^{N} R_j^2\right).\end{aligned} \tag{37}$$

With this distribution function we can now recalculate the different characteristic quantities for the Gaussian chain. In doing so we can, for example, find $\bar{R}_E^2 = Nl^2$ and also the distribution of the end-to-end vector as given in Eq. (27). In this way we can confirm that the global properties have in fact been maintained when going from the freely connected chain to the Gaussian chain. The mayor argument for the application of the model of the Gaussian chain is that the calculation of characteristic quantities becomes much easier when using independent variables following a Gaussian distribution.

8 The form factor of a Gaussian chain

Scattering in general. The structural properties of polymers are often studied by scattering experiments, typically by using light, x-rays, or neutrons. The scattered intensity from an arbitrary system of $\mathcal{N}$ particles is given by

$$I(\Omega) \propto \sum_{j=1}^{\mathcal{N}} \sum_{k=1}^{\mathcal{N}} a_j a_k^* \exp\left(\mathrm{i}\,\mathbf{Q}\cdot(\mathbf{r}_k - \mathbf{r}_j)\right) \tag{38}$$

with the scattering amplitude a_j of the particle j and the scattering vector $\mathbf{Q} = \mathbf{k}_0 - \mathbf{k}_1$ ($\mathbf{k}_0$: wave vector of the incident radiation, $\mathbf{k}_1$: wave vector of the scattered radiation). For a homogeneous system where all scattering particles have the same scattering amplitude ($a \equiv a_j$) the expression above can be simplified to

$$I(\Omega) \propto |a|^2 \sum_{j=1}^{\mathcal{N}} \sum_{k=1}^{\mathcal{N}} \exp\left(\mathrm{i}\,\mathbf{Q}\cdot(\mathbf{r}_k - \mathbf{r}_j)\right). \tag{39}$$

The double sum in the equation above contains all the structural information which is accessible by a classical scattering experiment. It is used to define the structure factor $g(\mathbf{Q})$ of the sample by the thermal average

$$g(\mathbf{Q}) := \frac{1}{\mathcal{N}} \sum_{j=1}^{\mathcal{N}} \sum_{k=1}^{\mathcal{N}} \langle \exp\left(\mathrm{i}\,\mathbf{Q} \cdot (\mathbf{r}_k - \mathbf{r}_j)\right) \rangle \,. \tag{40}$$

For polymer systems, the two summations run over all segments of all polymer chains which are present. This means that inter- and intramolecular correlations contribute to the structure factor.

Form factor of a single chain. If the concentration of scattering polymer chains is low enough then the interference between different chains can be neglected. In this case, the sums in the structure factor can be limited to the segments of one single molecule. The structure factor of the system is then identical to the form factor of a single chain

$$f(\mathbf{Q}) = \frac{1}{N} \sum_{j=0}^{N} \sum_{k=0}^{N} \langle \exp\left(\mathrm{i}\,\mathbf{Q} \cdot (\mathbf{r}_k - \mathbf{r}_j)\right) \rangle \,. \tag{41}$$

For a Gaussian chain, all vectors $\mathbf{r}_k - \mathbf{r}_j$ are Gaussianly distributed. It can be shown in general that for a Gaussian distribution of variables $\{x_j\}$ the following relation holds (e. g. see Ref. [2]),

$$\left\langle \exp\left(\sum_j \xi_j x_j\right) \right\rangle = \exp\left(\frac{1}{2} \sum_j \sum_k \xi_j \xi_k \langle x_j x_k \rangle\right) . \tag{42}$$

Hence we obtain

$$\begin{aligned} \langle \exp\left(\mathrm{i}\,\mathbf{Q} \cdot (\mathbf{r}_k - \mathbf{r}_j)\right) \rangle &= \left\langle \exp\left(\mathrm{i} \sum_{\alpha=x,y,z} Q_\alpha (r_{k\alpha} - r_{j\alpha})\right) \right\rangle \\ &= \exp\left(-\frac{1}{2} \sum_{\alpha=x,y,z} Q_\alpha^2 \left\langle (r_{k\alpha} - r_{j\alpha})^2 \right\rangle\right) . \end{aligned} \tag{43}$$

The mean square distance between two segments of an unperturbed Gaussian chain is given by $\langle (\mathbf{r}_k - \mathbf{r}_j)^2 \rangle = 3 \langle (r_{k\alpha} - r_{j\alpha})^2 \rangle = |k-j| l^2$ so that

$$\langle \exp\left(\mathrm{i}\mathbf{Q} \cdot (\mathbf{r}_k - \mathbf{r}_j)\right) \rangle = \exp\left(-\frac{Q^2 l^2}{6} |k-j|\right) . \tag{44}$$

With this result, the form factor of the Gaussian chain becomes

$$f(\mathbf{Q}) = \frac{1}{N} \sum_{j=0}^{N} \sum_{k=0}^{N} \exp\left(-\frac{Q^2 l^2}{6} |k-j|\right) . \tag{45}$$

For large N, we can replace the summation $\sum_{j=0}^{N}(\ldots)$ by the integral $\int_0^N (\ldots)\,\mathrm{d}j$ and get

$$f(\mathbf{Q}) = \frac{1}{N} \int_0^N \mathrm{d}j \int_0^N \mathrm{d}k \, \exp\left(-\frac{Q^2 l^2}{6} |k-j|\right) . \tag{46}$$

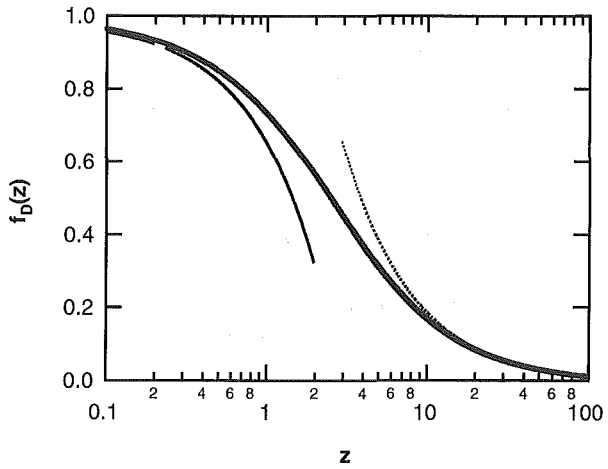


Fig. 7: *Debye function $f_D(z)$ (bold line) and its asymptotic functions for small (dashed line) and large (dotted line) values of z.*

The double integral can be easily evaluated and we finally obtain an analytic expression for the form factor of a single Gaussian chain,

$$f(\mathbf{Q}) = N f_D\left(\frac{Q^2 N l^2}{6}\right) = N f_D(Q^2 \bar{R}_g^2) \tag{47}$$

with the Debye function

$$f_D(z) = \frac{2}{z}\left(z - 1 + e^{-z}\right). \tag{48}$$

The asymptotic behavior of the form factor $f(\mathbf{Q})$ which follows from the Debye function is given by

$$f(\mathbf{Q}) \approx N\left(1 - \frac{Q^2 \bar{R}_g^2}{3}\right) \quad \text{for} \quad Q\bar{R}_g \ll 1 \tag{49}$$

and

$$f(\mathbf{Q}) \approx \frac{2N}{Q^2 \bar{R}_g^2} \quad \text{for} \quad Q\bar{R}_g \gg 1. \tag{50}$$

In Fig. 7, the Debye function and its asyptotic behavior are plotted over a logarithmic z axis. We recognize that $f_D(z)$ and correspondingly the scattering intensity from a single polymer chain are centered around zero and continuously decrease towards larger z and Q values. If we arbitrarily choose the value $z = 1$ to represent the decay of the Debye function then the corresponding decay of the single chain form factor $f(Q)$ can be characterized by a value of $Q = 1/\bar{R}_g$. As the radius of gyration $\bar{R}_g$ attains large values for macromolecules, one has to go to very small Q values in order to characterize the polymer structure by scattering techniques. In case of neutron or x-ray scattering, the wavelength of the incident radiation is typically around 1 Å and small values of the wave vector transfer Q can only be achieved in going to very small scattering angles. Therefore small-angle neutron scattering (SANS) and small-angle x-ray scattering (SAXS) are the

most adequate techniques to study the structural properties of polymers here. In case of light scattering, the typical wavelengths are in the range of 300 nm (visible light) so that the behavior of the single chain form factor can be observed at large angles. This is very convenient and consequently static light scattering is a standard method to characterize polymer structures in many laboratories.

9 Statistical mechanics of model chains

General description of chain configurations. The statistical mechanics allows to obtain the distribution function of the chain configurations directly from the Hamiltonian $H(\{\mathbf{R}_j\})$ which can be attributed to a given system or chain model by

$$\Psi(\{\mathbf{R}_j\}) = \frac{1}{Z} \exp\left(-\frac{H(\{\mathbf{R}_j\})}{k_\mathrm{B}T}\right) \tag{51}$$

with the normalization constant

$$Z = \int \exp\left(-\frac{H(\{\mathbf{R}_j\})}{k_\mathrm{B}T}\right) \mathrm{d}^{3N}\{\mathbf{R}_j\}. \tag{52}$$

Once $\Psi(\{\mathbf{R}_j\})$ is explicitly known, it is possible to calculate the characteristic quantities which describe the structure of the polymer chain.

In this way it is possible to introduce binding potentials into the consideration of chain models. This is for example the basis of the rotational isomeric state (RIS) model where the potentials which govern the bond rotation are calculated as a function of the conformation of a finite number of neighboring bonds (e. g. see Ref. [4]). By this approach it becomes possible to incorporate the fact that the orientation of consecutive chain segments (essentially the bond rotation angles) are highly correlated due to interdepending rotation potentials and, even more important, due to steric effects.

A further application of the statistical mechanics approach is the calculation of chain conformations in the presence of external potentials (walls, electric fields, stress fields, and so on). This is done by adding appropriate terms to the respective Hamiltonian of the considered chain model which represent the bounding conditions imposed to the system.

Pseudo-potential of a Gaussian chain. Here, we want to consider which kind of Hamiltonian $H_\mathrm{G}(\{\mathbf{R}_j\})$ can be attributed to a Gaussian chain. From the comparison of Eqs. (51) and (37), we can directly deduce that

$$H_\mathrm{G}(\{\mathbf{R}_j\}) = \frac{3k_\mathrm{B}T}{2l^2} \sum_{j=1}^{N} R_j^2. \tag{53}$$

From this expression we can see that the lengths of the bonds in a Gaussian chain are governed by a harmonic potential. The beads of the chain appear to be connected by elastic springs with the spring constant $k = \frac{3k_\mathrm{B}T}{l^2}$. Note, anyway, that the elastic forces between the segments do not stem from a change of any internal energy but have a purely entropic origin. The Hamiltonian $H_\mathrm{G}(\{\mathbf{R}_j\})$ for a Gaussian chain is therefore considered

to describe a pseudo-potential rather then a real interaction potential. The reason for the entropic contribution to the Hamiltonian is that the number of accessible conformation states of a chain is decreasing very rapidly when its end points are separated, i. e. when the chain is stretched. Thereby, the entropy of a polymer chain is reduced when the polymer is in a stretched configuration. This decrease in the entropy is such that the "restoring forces" become harmonic. The Hamiltonian $H_{\mathrm{G}}(\{\mathbf{R}_j\})$ is in fact the basis for many extensions of the Gaussian chain model in order to describe more complicated physical situations.

Worm-like chains. Above, we calculated "backwards" which kind of Hamiltonian corresponds to a given model (there, the Gaussian chain). We will now follow the opposite direction and study the properties of a model chain by starting from a given definition of the Hamiltonian. The model we will consider in the following is known a the worm-like chain or the Kratky-Porod model. In literature, worm-like chains are most often described as continuous chains using differential geometry. Here, we will consider the model of worm-like chains in its discrete version where the chain consists of a finite number of segments N with finite length l_0. In this way we will stay conform with the other chain models described so far.

So, for a worm-like chain, we assume (in analogy to the freely jointed chain) that all bond lengths are fixed to l_0 and that the bond rotation angles $\{\varphi_j\}$ are free and independent. Concerning the bond angles $\{\vartheta_j\}$, we want to impose that subsequent segments should possess a certain stiffness agains bending.

Mathematically, the local bending of the polymer chain is described by the curvature of the chain contour. The curvature of a given trajectory is defined by the change in the tangential unity vector of the curve. For the discrete case which we are treating here, we can consider the unity vector $\mathbf{e}_j$ to a given chain bond to be identical to the tangential unity vector of the chain contour in the point $\mathbf{r}_j$. The curvature of the chain in this point is then equal to the difference $|\mathbf{e}_j - \mathbf{e}_{j-1}|$ of subsequent unity vectors. With this curvature given, we can define the bending energy. Here, we make the most simple approach in assuming that the bending energy H_{B} is a purely harmonic potential as a function of the chain curvature. Hence, we have

$$H_{\mathrm{B}} = \frac{\kappa}{2} \sum_{j=2}^{N} (\mathbf{e}_j - \mathbf{e}_{j-1})^2 \tag{54}$$

where κ is the constant representing the strength of the bending potential. From a simple geometric consideration, we find that $|\mathbf{e}_j - \mathbf{e}_{j-1}| = 2 \sin \frac{\vartheta_j}{2}$. Then we have $(\mathbf{e}_j - \mathbf{e}_{j-1})^2 = 2(1 - \cos \vartheta_j)$ and the bending energy becomes

$$H_{\mathrm{B}} = \kappa \sum_{j=2}^{N} (1 - \cos \vartheta_j). \tag{55}$$

We now assume that the bending energy is high so that $\kappa \gg k_{\mathrm{B}}T$. We can then argue that all bond angles ϑ_j will be small and we can approximate the cosine term by $\cos x \approx 1 - \frac{1}{2}x^2$ giving

$$H_{\mathrm{B}} = \frac{\kappa}{2} \sum_{j=2}^{N} \vartheta_j^2. \tag{56}$$

This result for the bending energy can now be introduced into the general expression for the conformational distribution function given by Eq. (51) and we obtain the distribution function for the conformations of a worm-like chain,

$$\Psi(\{\vartheta_j\}) = \left(\frac{E}{2\pi k_\mathrm{B}T}\right)^{\frac{N-1}{2}} \exp\left(-\frac{E}{2k_\mathrm{B}T}\sum_{j=2}^{N}\vartheta_j^2\right). \tag{57}$$

We recognize from this expression that we are dealing again with a Gaussian distribution but this time it is a Gaussian distribution of bond angles ϑ_j instead of bond lengths R_j as in case of the Gaussian chain.

To conclude the model of the worm-like chain, we calculate the characteristic quantities which can be deduced from Eq. (57). First, we note that the bond rotation angles were assumed to be free so that we can apply Eq. (12). It is more appropriate to express the characteristic quantities for the worm-like chain in terms of the persistence length and the contour length $L = Nl_0$ of the chain. For $N \gg 1$, Eq. (12) becomes then

$$\bar{R}_\mathrm{E}^2 = (2l_\mathrm{p} - l_0)L - 2l_\mathrm{p}(l_\mathrm{p} - l_0)\left[1 - \exp\left(-\frac{L}{l_\mathrm{p}}\right)\right]. \tag{58}$$

In order to evaluate l_p from Eq. (15), we need an expression for the average $\langle\cos\vartheta\rangle$. It is obtained from

$$\langle\cos\vartheta_j\rangle = \int \Psi(\{\vartheta_j\})\cos\vartheta_j \,\mathrm{d}^{N-1}\{\vartheta_j\} \tag{59}$$

which, by using Eq. (57), gives the result

$$\langle\cos\vartheta_j\rangle = \exp\left(-\frac{k_\mathrm{B}T}{2\kappa}\right). \tag{60}$$

The discrete worm-like chain is now completely characterized by the three quantities L, l_0, and l_p with

$$l_\mathrm{p} = \frac{l_0}{1 - \langle\cos\vartheta_j\rangle} \approx \frac{2\kappa}{k_\mathrm{B}T}l_0. \tag{61}$$

At this point, we can note the corresponding result for the continuous worm-like chain. It is obtained in the limit that the segmental length l_0 goes to zero while the contour length L and the persistence length l_p are kept constant. We see immediately from Eq. (58) that then we have

$$\bar{R}_\mathrm{E}^2 = 2l_\mathrm{p}^2\left[\exp\left(-\frac{L}{l_\mathrm{p}}\right) + \frac{L}{l_\mathrm{p}} - 1\right]. \tag{62}$$

Application of the worm-like chain model. A beautiful and impressive example for a wormlike chain has been found in recent stretching experiments [5] on DNA, perhaps the most famous biological molecule, with a double-helix structure of relatively large stiffness, leading to a persistence length of 50 nm. This means that the projection of the molecule on a freely jointed chain has Kuhn segments which are 100 nm long. This in turn has the consequence that it is easy to stretch the molecule; the entropic restoring force is inversely proportional to this segment length.

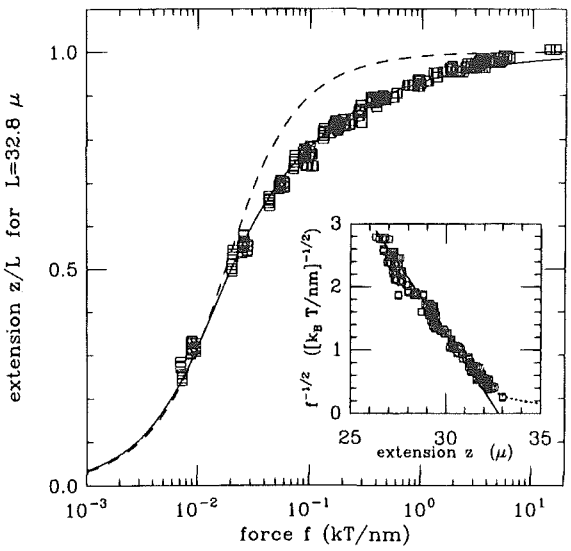


Fig. 8: *Stretching DNA to its full length (after [5]); full line: modelling with worm-like chain, dashed line: freely jointed chain fitted to small extensions.*

However, this holds only in the beginning, when the end-to-end length is small compared to the total length of the polymer. In the case of DNA, thanks to huge technical advances in manipulation of the structure of the double-helix DNA, it has become feasible to measure the force versus extension of single 10-100 μm long DNA molecules up to practically the full length. In Fig. 8, one notes that towards the end the data do not follow the behaviour of the freely jointed chain fitted to the beginning. The worm-like chain provides a much better fit.

10 Self-avoiding polymer chains

Excluded volume interaction. And the end of this course we consider an important limitation of the chain models which have been discussed above. Up to now, we have always assumed that "long range interactions" between segments which are well separated along the chain contour can be neglected. But, due to the flexibility of most polymer chains, such segments have the possibility to come very close together in space despite their large separation on the chain contour (see Fig. 9) and to interact with each other in this way. One interaction which will always be present in this case is the steric effect. It represents the fact that a segment can not penetrate the volume which is occupied by yet another segment of the chain. Due to this effect, the chain swells and the extension of its coil will be larger than that of an ideal chain without this kind of long range interaction. Even in the chase that attractive forces between the segments are present, the chain will swell as long as the repulsive steric interaction dominates. This effect is called the

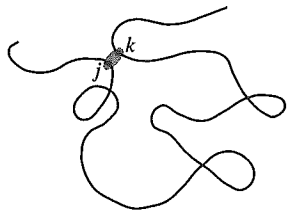


Fig. 9: *Illustration of the excluded volume interaction.*

excluded volume effect.

Screened excluded volume interaction. In some cases, the excluded volume interaction can be "screened" so that it vanishes (at least in a first order). This is the case for homopolymer melts were each chain segment is surrounded by many other segments of the same kind. Practically all of these surrounding segments belong to other molecules as the self concentration of a polymer, i. e. the concentration of segments which belong to the same chain as a given segment, is very low. The interaction with neighboring molecules is then identical to the long range interactions of each chain and by consequence the excluded volume effect disappears. The same argument holds for certain polymer solutions when the excluded volume interaction of the polymer chains and the interactions between the chain segments and the solvent molecules are exactly balanced. This is usually only the case at one precise temperature, the so called θ point, in function of the polymer type and the solvent. A solvent fulfilling this condition is called a θ solvent. In both cases, melts and θ solutions, where no effective excluded volume effect is present, the polymer structure can be well described by the simple chain models which we have treated so far. When excluded volume interactions are present the swollen chain structure will strongly deviate from this behavior and $\bar{R}_{\mathrm{E}}^2$ depends on a higher power of N,

$$\bar{R}_{\mathrm{E}}^2 \propto N^{2\nu}, \tag{63}$$

with an exponent ν of about $\frac{3}{5}$.

Gaussian chain with excluded volume. When we are interested in the structural features only on larger length scales we can consider the excluded volume interactions between segments as a very local interaction. Although it might be quite complicated, the concrete nature of these interactions will be unimportant for the large scale structure of the molecule and we can describe the excluded volume interaction between any pair of polymer segments j and k by a short range potential of the form

$$k_{\mathrm{B}}T\tilde{v}(\mathbf{r}_k - \mathbf{r}_j) \tag{64}$$

which can normally even be replaced by a delta function giving

$$vk_{\mathrm{B}}T\delta(\mathbf{r}_k - \mathbf{r}_j) \tag{65}$$

where v represents the excluded volume. The total interaction energy of one chain can now be written as

$$U_1(\{\mathbf{r}_j\}) = \frac{1}{2}vk_{\mathrm{B}}T\sum_{j=0}^{n}\sum_{k=0}^{n}\delta(\mathbf{r}_k - \mathbf{r}_j). \tag{66}$$

Adding this to the effective Hamiltonian of a Gaussian chain, we can immediately write down the distribution function for the model of the excluded volume chain,

$$\Psi(\{\mathbf{r}_j\}) = \frac{1}{Z}\exp\left(-\frac{H_G(\{\mathbf{r}_j\}) - U_1(\{\mathbf{r}_j\})}{k_B T}\right)$$

$$\propto \exp\left(-\frac{3}{2l^2}\sum_{j=1}^{N}(\mathbf{r}_j - \mathbf{r}_{j-1})^2 - \frac{v}{2}\sum_{j=0}^{n}\sum_{k=0}^{n}\delta(\mathbf{r}_k - \mathbf{r}_j)\right). \tag{67}$$

We recognize that this model includes only two parameters: the effective bond length l which represents the short range interactions between successive chain segments and the excluded volume v which represents the long range interactions. Although the assumption that the interactions can be separated into distinct long and short range contributions can be questioned, Eq. (67) is generally considered to be a correct starting point for the analysis of the excluded volume problem. But, as soon as excluded volume interactions are introduced, it is impossible to calculate the characteristic quantities of the chain model explicitly. Anyway, there exists a variety of approximative calculations based on different theoretical techniques, beginning with the famous mean-field-like treatment given by Flory.

The Flory theory. Flory argues that the restoring force for a given length R_E of the end-to-end vector of a Gaussian chain is given by the free energy

$$F(R_E) = k_B T\frac{R_E^2}{\bar{R}_E^2} = \frac{k_B T}{Nl^2}R_E^2 \tag{68}$$

and uses the crude estimate $\bar{c} = N/R_E^3$ for the average concentration of monomers inside the polymer coil interacting with each other. He further assumes that a given monomer feels the presence of another one only within its monomer cell of volume l^3. Setting the interaction energy for an intersegmental contact equal to vk_BT, the full interaction energy for one polymer chain is

$$E = vk_B T N\bar{c}l^3 = vk_B T\frac{N^2 l^3}{R_E^3}. \tag{69}$$

Minimizing the sum of the two terms, Eq. (68) and Eq. (69), with respect to R_E, one finds

$$\frac{R_E}{Nl^2} = 3v\frac{N^2 l^3}{R_E^4}, \tag{70}$$

which implies $R_E \propto N^{3/5}$ and hence the value $\frac{3}{5}$ is found for the exponent ν. One can extend this result to a general d-dimensional space. The restoring force does not change exponents, but the interaction energy becomes proportional to R_E^{-d}. This supplies the general result for d dimensions

$$R_E \propto N^{\nu} \quad \text{with} \quad \nu = \frac{3}{d+2}. \tag{71}$$

Results from other theories. In three dimensions, the mean field theory provides an exponent of $\nu = \frac{3}{5} = 0.6$ which is already a good approximation for the result of more exact calculations. The drawback of the mean field theory is that it does not consider that

collisions between segments of a polymer are closely correlated due to the connectivity of the chains. These effects can be accounted for by applying the renormalization group theory to the problem which leads to an improved numerical value for ν. The most exact value of $\nu = 0.588$ can be extracted from a perturbation calculation or equally from an ϵ-expansion approach. However, the calculations behind these theoretical approaches are quite sophisticated. An introductory description of the basics of these calculations can be found in Ref. [2].

References

[1] P. J. Flory, *Statistical Mechanics of Chain Molecules* (Interscience Publishers, New York, 1969).

[2] M. Doi and S. F. Edwards, *The Theory of Polymer Dynamics* (Claredon Press, Oxford, 1988).

[3] M. Rawiso in *Diffusion de Neutrons aux Petits Angles*, J. Phys. IV France **9**, Pr1-147 (1999).

[4] K. Sturm in *22. IFF-Ferienkurs, Physik der Polymere* (Forschungszentrum Jülich GmbH, Jülich, 1991).

[5] J. F. Marko and E. D. Siggia, Macromolecules **28**, 8759 (1995).

B 3 Scaling Laws of Polymers

Artur Baumgaertner
Institut für Festkörperforschung
Forschungszentrum Jülich GmbH

Contents

1 A Single Chain under Constrained Conditions **2**
1.1 Ideal Chain under Traction 2
1.2 Ideal Chain in a Tube 3
1.3 Adsorption of an Ideal Chain 4
1.4 Real Chain under Traction 5
1.5 Real Chain in a Tube 6
1.6 Adsorption of a Real Chain 7

2 Scaling Laws for Polymer Solutions **8**
2.1 Correlation length ξ 9
2.2 End-to-End Distance 9
2.3 Correlation Functions 10

In general every polymer has a different chemical composition and local geometrical structure due to different sequences of atoms. However, if we do not look at a scale of a few Angstroem, but rather at a broader scale, say, in the range of 100 to 300 Å, the polymer exhibit features "universal ", i.e., independent of the details of the monomer structure. It is these features which we want to emphasis here. It should be noted that this situation is somewhat similar to what is found in the physics of phase transitions. Similar as in the latter case, it had turned out that the universal scaling laws can be established, which provide functional relationships between observables (in many cases experimental quantities) and characteristic parameters (chain length, correlation lengths, temperature, pressure, etc.). In present lecture some universal properties of polymer chains are addressed from a theoretical point of view.

The first preliminary steps towards a universal understanding of polymers had been made by several great scientist in the forties, as Debye, Kuhn, Kramers, Flory and others. The basic ideas are summerized in Flory's book [1]. In the late sixties and early seventies the next major step towards a more complete understanding of polymers from a theoretical point of view had been made by Edwards, de Gennes, des Cloiseaux and others. The related methods and results are reviewed among others in the books of de Gennes [2] and des Cloiseaux and Jannink [3].

1 A Single Chain under Constrained Conditions

1.1 Ideal Chain under Traction

If a force of strength f is applied in, say, x directions at both ends, it is of interest to calculate the elongation of the chain. Since the force can derived from the free energy F of the chain

$$\mathrm{f} = \partial F / \partial \mathrm{r} \tag{1}$$

and since no energy is involved, the force can be obtained from the entropy

$$S_N(\mathbf{r}) = \ln C_N(\mathbf{r}) \tag{2}$$

where the total number of chain conformations are given by

$$p_N(\mathrm{r}) = C_N(\mathrm{r}) / \sum_{\mathrm{r}} C_N(\mathrm{r}) \sim N^{-3/2} exp(-3r^2/2R_0^2) \tag{3}$$

where $R_0 = a\sqrt{N}$ is the average end-to-end distance. Hence we have

$$S_N(\mathbf{r}) = S_N(0) - 3r^2/2R_0^2 \tag{4}$$

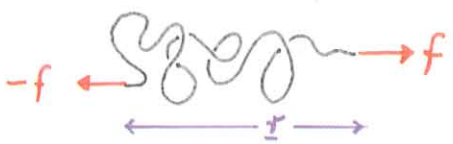


Fig. 1: *Ideal chain under traction.*

From the free energy $F = E - TS$ we obtain

$$< r >_f = f\frac{R_0^2}{3kT}. \tag{5}$$

This relation holds whenever $< r >$ is much smaller than Na, or, $af << kT$.

1.2 Ideal Chain in a Tube

Now we consider an ideal chain which is trapped in a narrow tube of diameter $D << R_0$. Since we are not interested in effects from chemical details of the polymer, we have to assume that the diameter is much larger than the size of a monomer, $D >> a$. Also the walls of the tube are assumed to be purely repulsive. The questions we address are the average lateral and perpendicular sizes of the chain, $R_\parallel$ and $R_\perp$, respectively. It turns out that the parallel size is $R_\parallel = R_0 \sim \sqrt{N}$ and hence not affected by the perpendicular constraint. It is just a consequence of the multiplicative properties of the Gaussian distribution $p(\mathbf{r})$ as given above.
On the other hand, the perpendicular extension of the chain $R_\perp \approx D$ must have an influence on the free energy, i.e. the entropy, of the chain. If we try to estimate the reduction ΔS of the chain entropy of the chain due to the confinement, we can make two plausible assumption :
-) The leading term in ΔS should be a linear function of N.
-) ΔS is dimensionless and should depend only on the length ratio R_0/D.
This leads to

$$\Delta S = -(R_0/D)^x \sim N^{x/2}, \tag{6}$$

which leads to x=2, and hence the free energy

$$\Delta F/kT = \Delta S = \frac{R_0^2}{D^2}. \tag{7}$$

This relation is valid for other confinements, as slits or spheres, as well.
However, it should be noted that this simple picture is not valid if a Gaussian chain is trapped in an irregular environment, for example in a porous media. In this case the randomness of the environment causes the chain to shrink in such a dramatic way that the end-to-end distance becomes almost independent of the chain length N. The corresponding scaling relation is [4, 5]

$$R^2 = a^2 N\ \phi[(1-p)\sqrt{N}], \tag{8}$$

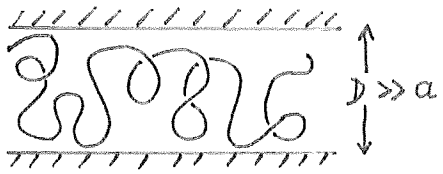


Fig. 2: *Ideal chain in a tube.*

where $1-p$ is the percentage of solid material, p is the porosity. The scaling function has the limiting behaviors, $\phi(x) \approx 1$ for $x \to 0$, in the case of small amounts of solid materials, and for low porosities. For large amount of material, we have

$$\phi(x) \approx x^{-2}, \qquad for \;\; x >> 1, \tag{9}$$

and hence in the latter limit $R^2 \sim (1-p)^{-2}$, which is a collapse of the chain. The scaling function can be understood by simple arguments. As in a solution of many polymer chains, the only characteristic concentration relevant to the chain is the overlap concentration c^* (see also subsection 2, eq.27) of the chain unperturbed by the porous media. For Gaussian chains, it is $c^* \sim N^{-1/2}$. Writing the concentration $c = 1-p$ of the solid particles in units of c^* , the dimensionless variable therefore becomes $x \equiv c/c^* \sim (1-p)N^{1/2}$.

1.3 Adsorption of an Ideal Chain

We consider, as depicted in fig.3, the situation where the chain is weakly adsorbed to an impenetrable wall. Large loops of the chain are protruding into the space. This kind of brush has an average thickness of D. Exact calculations on this system has been performed by several authors and are listed in reference [6]. However, de Gennes [2] has presented simple scaling arguments which we present below. First we consider the free energy in the Flory approximation

$$\Delta F/kT \approx \frac{R_0^2}{D^2} - \varepsilon f_b N, \tag{10}$$

where the first term is the confinement energy 7 as derived for the above case of a chain inside the tube. the second term describes the contact interactions of strength ε with the surface, and f_b is the fraction of adsorbed monomers. This equation represents the balance between the attraction and the induced loss of conformational entropy. Assuming that the monomer density is continuously spread over the slab of thickness D (no special density profile is assumed near the wall !), then we must expect

$$f_b \approx a/D. \tag{11}$$

Inserting this into eq. 10 and minimizing the free energy with respect to D, an equilibrium thickness is obtained of

$$D \approx a/\varepsilon \qquad (for \;\; D << R_0, \;\; and \;\; \varepsilon << 1), \tag{12}$$

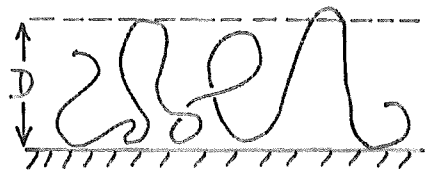


Fig. 3: *Adsorption of an ideal chain.*

and the free energy of binding

$$\Delta F/kT \approx -N\varepsilon^2. \tag{13}$$

Of course, the present situation of a single chain adsorbed is almost never achieved in experiments, however this example provides a very useful starting point for other polymer adsorption problems [6].

1.4 Real Chain under Traction

So far the lecture was concerned with a single ideal chain which has no interaction among its monomers except the successive bonding between monomers forming a chain. This situation is in general not representative for real chains in solvents. We will see that the non-bonded monomer-monomer interactions, e.g., van der Waals forces or Coulomb forces, has profound effects on the universal properties of the conformational characteristics. We will illustrate this by considering again the same three situations of polymer chains under certain constraints.

At first we consider again a chain under the traction of a force of strength f, Fig. 4. Similar as in the case of the ideal chain (see above) we could start with the free energy derived from the partition function

$$Z = \int d\mathbf{r} p_N(\mathbf{r}) \exp(\mathbf{fr}/kT). \tag{14}$$

Using (3) we could compute all averages. However, a much simpler approach is due to Pinus [7] based on simple scaling arguments. The characteristic strategy to apply scaling arguments is in many cases to find a few characteristic length scales. In the present case :

(*i*) The Flory radius characterizing the average end-to-end distance, $R_F \approx aN^\nu$, where the universal exponent $\nu = 3/(2+d)$ depends only on the space dimensionality of the model system, i.e., in d=3 and d=2 are $\nu = 3/5$ and $\nu = 3/4$, respectively. For more details and exact results and approaches see for example the books of des Cloiseaux-Jannink [3] and Schäfer [8].

(*ii*) A characteristic length scale $\xi_p = kT/f$ whose physical signifance will turn out later. First we consider the limit of large chain extensions, which is illustrated in Fig. 4. What happens in this case is a disentanglement of the coiled chain where at small scales the chain is still coiled, only weakly affected by the applied force. We assume that the strechted chains is made up of a serie of small coils. We assume that such a small coil, coined by de Gennes as a "blob", has a size of ξ_p. Therefore at scales $r > \xi$ we have a string of

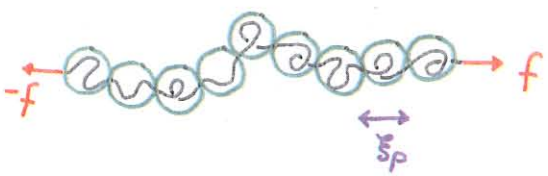


Fig. 4: *Real chain under traction.*

independent blobs, whereas at small scales each blob retains the local correlations of a Flory chain. If the number of monomers per blob is g_p, then we can use the Flory relation between the number of monomers and the average size, i.e.,

$$\xi_p \approx a g_p^{3/5}, \tag{15}$$

or,

$$g_p = (kT/af)^{5/3}, \tag{16}$$

using the definition of ξ as above. Since the total number of blobs is N/g_p, the chain elongation is

$$< \mathbf{r} > \approx \xi_p \frac{N}{g_p} \approx Na(fa/kT)^{2/3}. \tag{17}$$

Second, we consider the case of small chain extensions $x = R_F/\xi_p << 1$. In this case it is reasonable to assume a functional dependence of

$$< \mathbf{r} >= R_F \phi(x) \tag{18}$$

where $\phi(x)$ is a dimensionless function. For samll f, and hence small x, we expect $< \mathbf{r} >$ to be linear in x, and thus $\phi(x) \approx x$, and therefore

$$< \mathbf{r} >= f\frac{R_F^2}{kT} = f\frac{aN^{6/5}}{kT} \qquad (fR_F < kT). \tag{19}$$

It should be noted that the extension is *not* linear in N at small f, which means, as has been pointed out by de Gennes [2], that the tension f is not only transmitted through the backbone, as in the ideal case (eq.5) where $< \mathbf{r} > \sim N$, but also through repulsive contacts between pairs of monomers.
In summary, we see that a real chain has an elastic response which is significantly more *nonlinear* than in the case of an ideal chain.

1.5 Real Chain in a Tube

The significant effect of excluded volume is most clearly seen in systems where the effective space dimensionality is one. Therefore we consider again a chain trapped in a thin cylindrical tube of diameter $D << R_F$ (fig.5), but the tube diameter is still much larger than the size of a monomer, $D >> a$. We will address two questions : what is the size $R_\parallel$, and the confinement energy ? The longitudinal extension $R_\parallel$ must have the scaling

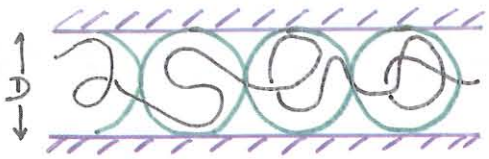


Fig. 5: *Real chain in a tube.*

form

$$R_{\|} = R_F \Phi(R_F/D) \tag{20}$$

where $\Phi(x) \to 1$ for $x \to 0$ when the tube becomes very wide. In the limit of a very thin tube we expect a power-law dependence $\Phi(x) \to x^m$ for $x \to \infty$. If the monomers are uniformly distributed along the cylindrical axis, then the longitudinal extension must be expected (see Fig. 5) to be $R_{\|} \sim N$. Since the unperturbed Flory radius is $R_F \sim N^{3/5}$, we obtain consequently from Eq.20 the resulting relation $N \sim N^{3/5+3m/5}$, which leads to $m = 2/3$. Thus eq.20 becomes

$$R_{\|} \approx aN(a/D)^{2/3}. \tag{21}$$

Of course, $R_{\|}$ is larger than R_F because of the squeezing effect, but it is interesting to note that this behavior is very different from an ideal chain where $R_{\|} \sim \sqrt{N}$.
A second derivation of the result given by eq.21 has been given by de Gennes based on the concept of "blobs". Similar as in the above example of a real chain under traction, the chain behaves inside the tube as a string of blobs of diameter D. Inside each blob the effect of the boundary is weak and thus each blob behave similar as self-avoiding coil of size D with g monomers inside, and hence the Flory relation holds $D = ag^{3/5}$. Successive blobs act as impenetrable spheres and are packed into a chain of pearls. Thus, $R_{\|} = DN/g$ in agreement with eq.21.
Now we want to compare the confinement free energies of ideal and real chains. According to fig.5 the energy must be linear in the number of blobs, and hence linear in N. For the functional form of the free energy, we can use the arguments and use the same ansatz as for $R_{\|}$ (eq.20),

$$F/kT = \Phi_f(R_F/D) \tag{22}$$

where similarly $\Phi_f(x) \to x^n$ for $x \to \infty$. Thus R_F^n must be linear in N, and therefore $n = 5/3$, and

$$F/kT \approx N(a/D)^{5/3}. \tag{23}$$

It is interesting to note the difference of the free energy of confinement between ideal chains (eq.7) and real chains (eq.23). The energy is, as intuitively expected, for real chains larger than for ideal one.

1.6 Adsorption of a Real Chain

Similar as in the above case for ideal chains, we consider the adsorption of a single chain in the weak adsorption limit, but now taking into account the excluded volume effect between monomers of the chain(fig.6). In order determine the width of the adsorption layer D, we consider the modified form of the free energy (10),

$$\Delta F/kT \approx N\left(\frac{a}{D}\right)^{5/3} - \varepsilon f_b N, \tag{24}$$

where the first term is the confinement energy as given by eq.22 which is also valid for a chain confined to a slab of width D. Then, minimizing with respected to D leads to

$$D \approx a/\varepsilon^{3/2} \qquad (for D << R_F, and \quad \varepsilon << 1), \tag{25}$$

and the free energy of binding

$$\Delta F/kT \approx -N\varepsilon^{5/2}. \tag{26}$$

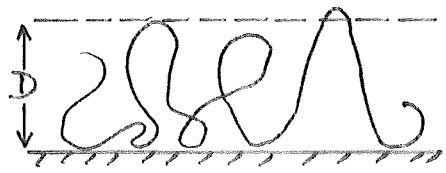


Fig. 6: *Adsorption of a real chain.*

This a first simple approach to the adsorption of a self-avoiding chain. However, the actual situation is in general more complex. Due to the competition between wall-chain repulsion and short range attraction (van der Waals forces), there exists a depletion of monomers near the wall and an accompanying density profile. In the case of many polymers competing for the adsorption sites at the wall, the results are more complex. More details and more references can be found in the book of Eisenriegler [6].

2 Scaling Laws for Polymer Solutions

From the last section we know some of the characteristic properties of dilute (non-overlapping) polymer coils in a good solvent under some geometric contraints. In the section below we will consider the situations where the coils starts to overlap and do interact very strongly a high concentrations. For a long time the only method to explore this state was a mean field theory of Flory and Huggins [1]. However, as realized by these authors the mean field concept do not adequately describe the situation at low and intermediate concentrations. Fortunately, this situations has been clarified subsequently using modern concepts of scaling and renormalization group methods (see e.g. references [2, 3]).
The situations of polymer coils at various concentrations are depicted in fig.7. From left to right the various regimes are termed : dilute, onset of overlap, and semi-dilute regimes. The characteristic concentration at which the coils start to overlap can be obtained by the fact that at this point

$$c^* \approx N/R_F^3 = a^{-3}N^{1-3\nu} = a^{-3}N^{-4/5} \tag{27}$$

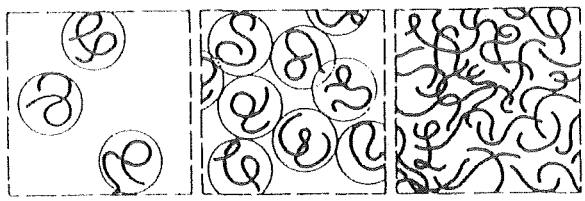


Fig. 7: *Polymers in solution.*

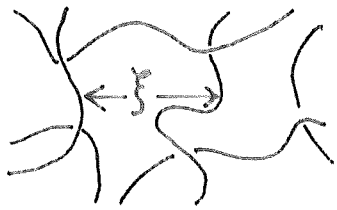


Fig. 8: *Correlation length* ξ.

where we assume the exponent for three dimensions $\nu = 3/5$. Sometimes it is useful to use instead the dimensionless "polymer fraction" $\Phi = ca^3$. In this case we have $\Phi^* = N^{-4/5}$, where a is the effective volume of a monomer.

2.1 Correlation length ξ

A reasonable picture of the properties of a semi-dilute solution can be obtained by investigating the spatial properties, e.g. as depicted in fig.8. At a certain scale the solution looks like an entangled mesh with a certain average size ξ. In the following we want to find the scaling form of the correlation length ξ. This can be achieved by two requirements :
(i) At higher concentrations $\Phi > \Phi^*$, it is reasonable to assume that the correlation length depends only on the polymer fraction Φ, because in this case the end-to-end distance R is expected to be much larger than ξ, and hence ξ independent of R and therefore independent of the chain length N.
(ii) Just at the threshold $\Phi \approx \Phi^*$, the two characteristic length scales in our problems are comparable, $R \approx \xi$.
These two requirements lead to a functional form

$$\xi(\Phi) = R_F \left(\frac{\Phi^*}{\Phi} \right)^y . \tag{28}$$

Obviously, the requirement (ii) is fulfilled. Using requirement (i) we can calculated the exponent y : in this case the N-dependencies in eq.28 of $R_F \sim N^{3/5}$ and $\Phi^* = N^{-4/5}$ must cancel in order to satisfy requirement (i). From this we obtain $y = 3/4$, and hence

$$\xi(\Phi) = a\Phi^{-3/4}. \tag{29}$$

This result is reasonable, since the mesh size must be expected to decrease with increasing concentration.

2.2 End-to-End Distance

In the following paragraph we will investigate how strongly the end-to-end distance R of a chain depends on the polymer fraction Φ. It has been demonstrated by de Gennes [2] that the concept of "blobs" provides a simple, but powerful method in order to set up scaling laws for polymers not only for dilute, but for semi-dilute solutions as well.

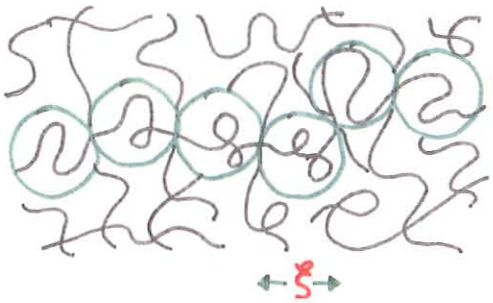


Fig. 9: *End-to-end distance in the blob picture.*

Considering a particular chain embedded in many others, as depicted in fig.9, one may imagine that the whole system can be described by an almost closed packed configuration of spherical blobs, each of size ξ. According to the previous paragraph on the mesh size ξ, each blob must consist of a certain number (g) of monomers (of the same chain) which do not interact with monomers of other chains but only among themselves, by definition. Thus, the size of the blob is related to the number g by the usual Flory scaling

$$\xi \approx a g^{3/5}. \tag{30}$$

Using eq.29 one obtains

$$g = \left(\frac{\xi}{a}\right)^{5/3} = \Phi^{-5/4}. \tag{31}$$

Of course, this solution is consistent with the above made assumption of a closed packed system of blobs, since

$$c = g/\xi^3. \tag{32}$$

At this point, we have to introduce the so-called "Flory theorem" which says : *Chains in concentrated solutions and melts behave ideal on large length scales, and hence their end-to-end distance is* $R \sim \sqrt{N}$. This was first understood by Flory [9, 1], but took a long time to be accepted and finally be proven by other methods, as self-consistent field methods and screening concepts [10].
The derivation of the Flory theorem is out of the scope of the present lecture and we just take this result to give the formula of the end-to-end distance in solutions. This can be estimated [11] from the ideal chain formula for N/g blobs of size ξ,

$$R^2(\Phi) = \xi^2 \frac{N}{g} = a^2 N \Phi^{-1/4} \qquad (\Phi^* << \Phi << 1). \tag{33}$$

This has been verified by experiments [11] and is depicted in fig.10.

2.3 Correlation Functions

Correlations functions can be measured by neutron scattering, which has been pointed out during other lectures of this spring school. The usual relation between structure factor

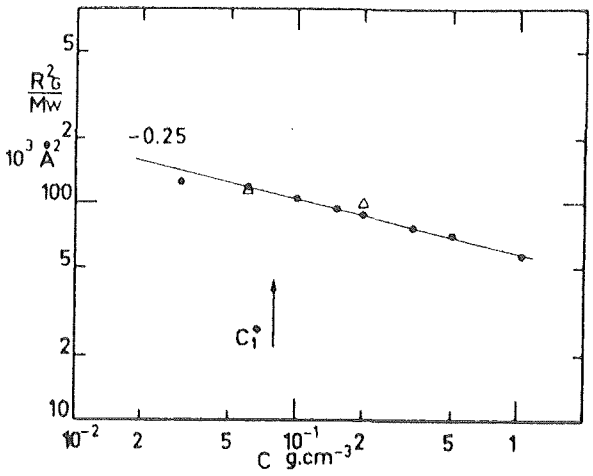


Fig. 10: *Experiments [11] verifing scaling relation (33).*

and density correlation function is

$$S(\mathbf{q}) = \int d^3\mathbf{r} < \delta\rho(0)\delta\rho(\mathbf{r}) > e^{i\mathbf{qr}} \tag{34}$$

where the density fluctuation is defined as

$$\delta\rho(\mathbf{r}) = \rho(\mathbf{r}) - < \rho > \tag{35}$$

and accordingly the correlation function

$$< \delta\rho(0)\delta\rho(\mathbf{r}) > = < \rho(0)\rho(\mathbf{r}) > - < \rho >^2 . \tag{36}$$

It can be shown that the correlation function can be separated in the self-correlation of a single (labeled) chain and the correlations with other chains, according to

$$< \rho(0)\rho(\mathbf{r}) > = g_1(\mathbf{r}) + g_a(\mathbf{r}). \tag{37}$$

Within a blob, the pair correlation function obey simple scaling rules :

$$g_1(\mathbf{r}) = N\tilde{g}(r/R_F) \tag{38}$$

where $\tilde{g}(x)$ is a universal function, whose scaling form can be found by simple arguments in the limit $r < \xi << R_F$. In a sphere of radius r we have a certain number of monomers n related by the Flory relation $r \approx an^\nu$. Since

$$\int g_1(\mathbf{r}) d^3\mathbf{r} = N, \tag{39}$$

the correlation function scales as the density of monomers, $g_1(\mathbf{r}) \sim n/r^3$. Therefore we obatain for an ideal chain

$$g_1(\mathbf{r}) \approx \frac{1}{a^2 r} \tag{40}$$

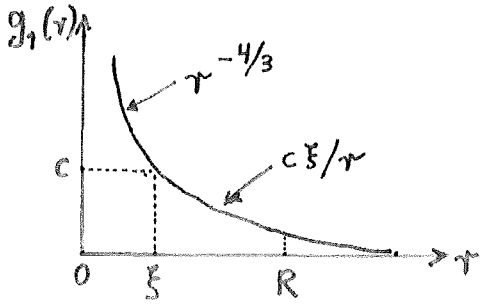


Fig. 11: *Crossover of correlation function between ideal and excluded volume behavior.*

and for a self-avoiding chain

$$g_1(\mathbf{r}) \approx \frac{1}{a^{5/3}r^4/3}. \tag{41}$$

The corresponding Fourier transforms are

$$g_1(\mathbf{q}) \approx \frac{1}{(aq)^{1/\nu}}, \tag{42}$$

where $\nu = 1/2$ and $\nu = 3/5$, for ideal and self-avoiding chains, respectively. These scaling forms for ideal and self-avoiding chains have been derived long time ago by Debye [12] and by Edwards [13].
In the range $\xi < r < R_F$, the chain starts to feel the effect of the surrounding chains and the conformation of the chain under consideration becomes ideal. Thus

$$g_1(\mathbf{q}) \approx c\frac{\xi}{r}. \tag{43}$$

Just at $r = \xi$ the two laws, eqs.41 and 43 cross over smoothly, since the number of blobs $N_{blob} = c\xi^3$. This is depicted in fig.11.
The characteristic scattering data are presented in fig.12 for polystyrol in cabonsulfid at various dilutions (given by the numbers at each curve). The arrows indicate the cross over from excluded volume behavior at large q to "blob" behavior.

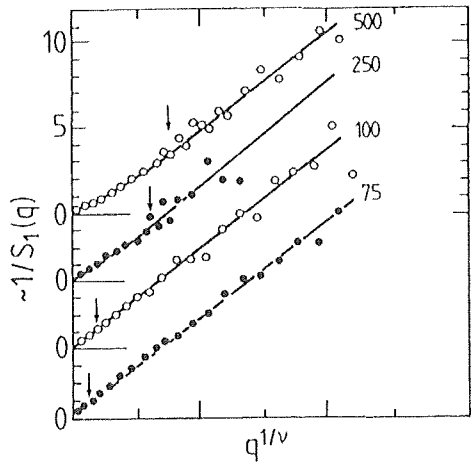


Fig. 12: *Neutron scattering experiment.*

References

[1] P.J. Flory, *Principles of Polymer Chemistry*, (Cornell University Press, Ithaca, 1971).

[2] P.G. de Gennes, *Scaling Concepts in Polymer Physics*, (Cornell University Press, Ithaca, 1979).

[3] J. des Cloiseaux, and G. Jannink, *Polymers in solution: their modelling and structure*, (Oxford : Clarendon Press, 1990)

[4] A. Baumgaertner, and M.Muthukumar, J.Chem.Phys. **87**, 3082 (1987); Adv.Chem.Phys. **94**, 625 (1996).

[5] S.F. Edwards, and M.Muthukumar, J.Chem.Phys. **89**, 2435 (1988).

[6] E.Eisenriegler, *Polymers near Surfaces*, (World Scientific, Simgapore, 1991).

[7] P. Pincus, Macromolecules **9**, 386 (1977).

[8] L. Schäfer, *Excluded volume effects in polymer solutions : as explained by the renormalization group*, (Berlin, Springer, 1999)

[9] P.J. Flory, J.Chem.Phys. **17**, 303 (1949).

[10] S.F. Edwards, Proc.Roy.Soc (London) **88**, 265 (1966).

[11] M. Daoud, *et al.*, Macromolecules **8**, 804 (1975).

[12] P. Debye, J.Phys.Colloid Chem. **51**, 18 (1947).

[13] S.F. Edwards, Proc.Roy.Soc (London) **85**, 605 (1965).

B 4 Polymer Mixtures

Artur Baumgaertner
Institut für Festkörperforschung
Forschungszentrum Jülich GmbH

Contents

1 Flory-Huggins Theory **2**
1.1 Entropy od Mixing 2
1.2 Enthalpy of Mixing 4
1.3 Phase Separation 5

2 The Structure Factor in the Random Phase Approximation **9**
2.1 Linear Response 9
2.2 Random Phase Approximation 11
2.3 Polymer Mixture 12

In the present lecture we discuss a mean-field theory suitable in general for concentrated polymer solutions, polymer melts and polymer mixtures. Here, in particular, we focus on polymer mixtures. The theory is derived from a lattice model, similar as commonly used for gases and liquids. The advantage of lattice models are their simplicity for deriving the entropy and enthalphy. The lecture follows to a large extent the approach as described in the books of Flory [1] and de Gennes [2].

1 Flory-Huggins Theory

1.1 Entropy od Mixing

Before we are going to consider polymer mixtures, we consider for simplicity the case of binary alloys, where each atom is represented either by filled or open circles, fig.1. The lattice consists of n cells occupied by either one or the other type of atom. The numbers n_1 and n_2 are the corresponding particle numbers, and $n_1 + n_2 = n$. There is no interaction between atoms, except that double occupancy of a cell is forbidden (excluded volume condition). The number of possible configurations of distribution of particles is given by

$$\Omega = \frac{n!}{n_1! n_2!}. \tag{1}$$

This expression is also the partition function of an "athermal" mixture where local interactions are neglected. The entropy is obtain as usual by $S = k_B \ln \Omega$, where k_B is the Boltzmann constant. Using the Stirling formula valid for large n,

$$\ln(n!) = n \ln n - n + ..., \tag{2}$$

one obtains

$$S = k_B[n \ln n - n_1 \ln n_1 - n_2 \ln n_2]. \tag{3}$$

Using the definition for the volume fraction

$$\phi_1 = \frac{n_1}{n_1 + n_2}, \quad and \qquad \phi_2 = \frac{n_2}{n_1 + n_2}, \tag{4}$$

we finally have

$$S = n k_B[\phi_1 \ln \phi_1 + \phi_2 \ln \phi_2]. \tag{5}$$

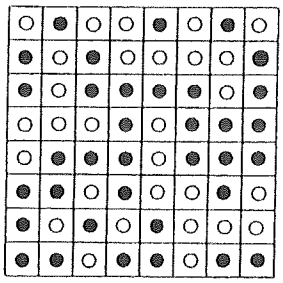


Fig. 1: *Lattice model.*

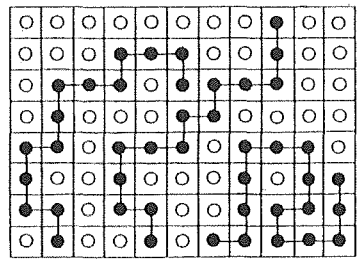


Fig. 2: *Lattice model of polymer solution.*

The entropy is proportional to the number of lattice cells n. Now we turn to the case of a polymer solution. We redefine n_1 as the number of solvent molecules and n_2 is the number of polymers. The chain length, which is the number of monomers of each chain, is denoted by N. In a first step, we assume only the excluded volume condition, no other interaction. In order to evaluate the partition function for this system, we are faced with the problem to calculate the number of possible conformations of the polymers embedded on the lattice. This is not a trivial task, since the connectivity prohibits a simple calculation as in the case of single unconnected atoms. This problem has been solved approximately by Flory [1] using the following arguments.
Assuming that i polymers are successfully embedded on the lattice, then by generating the next chain $i+1$ on the lattice, its number possible conformations ν_{i+1} is approximately given by

$$\nu_{i+1} \approx (n - iN)(1 - f_i)^{N-1} z(z-1)^{N-2}, \tag{6}$$

The first factor accounts for the number of available lattice sites at the start of generating the new chain. The factor $(1 - f_i)$ represents the availabilty of free sites during the embedding process. The number f_i is given approximately by

$$f_i \approx \frac{iN}{n}. \tag{7}$$

The number of possibilities to add a new monomer to the growing chain is given by the coordination number z of the lattice, and $(z-1)$ is the number to add a subsequent atom without hitting the previous one. It is clear that self-crossing of the chain, and hence self-avoiding effects cannot be taken into account by this procedure. But since the conformation of a chain at high concentrations is according to the Flory theorem a random walk (and not a self-avoiding walk), the Flory approximation for calculating the partition function is reasonable.
Using eq.6 we can estimate the number of conformations as

$$\nu_{i+1} \approx (n - iN)^N \left(\frac{z-1}{n}\right)^{N-1}. \tag{8}$$

The total number of configurations of n_2 polymers is accordingly

$$\Omega = \frac{1}{n_2!} \prod_{i=1}^{n_2} \nu_i, \tag{9}$$

where division by $n_2!$ takes in to account for the number of permutations of identical polymers. The calculation of $S = k_B \ln \Omega$ using eq.9 is a bit lenghty, and does not provide new physical insight, and therefore is omitted here. We refer to books as this of Flory [1]. The result for the entropy is

$$S = -k_B \left[n_1 \ln \frac{n_1}{n_1 + N n_2} + n_2 \ln \frac{n_2}{n_1 + N n_2} - n_2 (N-1) \ln \frac{z-1}{e} \right]. \tag{10}$$

Since we are primarily interested in the contribution of mixing the polymers with the solvent molecules, we have to subtract from eq.10 the contribution S_{dis} due to the conformational disorder of the polymers. This part is obtained if there are no solvent molecules present, $n_1 = 0$, and thus

$$S_{dis} = S(n_1 = 0) = n_2 k_B \left[\ln N + (N-1) \ln \frac{z-1}{e} \right]. \tag{11}$$

Therefore the "entropy of mixing" is given by

$$\Delta S_m = S - S_{dis} = -k_B \left[n_1 \ln \frac{n_1}{n_1 + N n_2} + n_2 \ln \frac{N n_2}{n_1 + N n_2} \right]. \tag{12}$$

Using the volume fractions

$$\phi_1 = \frac{n_1}{n_1 + N n_2}, \quad \textit{and} \qquad \phi_2 = \frac{N n_2}{n_1 + n_2} = 1 - \phi_1 \tag{13}$$

we obtain

$$\Delta S_m = -k_B [\phi_1 \ln \phi_1 + \frac{\phi_2}{N} \ln \phi_2]. \tag{14}$$

It should be emphasized that comparing eqs.5 and 14, the mixing entropy of polymer is significantly reduced by the reduction $1/N$ as compared to small molecules. According to eq.14 the entropy of mixing of two types of polymers in the absence of solvent is

$$\Delta S_m = -k_B [\frac{\phi_1}{N_1} \ln \phi_1 + \frac{\phi_2}{N_2} \ln \phi_2]. \tag{15}$$

1.2 Enthalpy of Mixing

In order to obtain the complete free energy of mixing we have to fomulate the enthalpy of mixing. In this case we have to introduce a selective interaction between the two types of monomers 1 and 2. For simplicity we assume that the range of interaction is restricted to nearest neighbors on the lattice. In general, the energy must contain three terms, each proportional to product of the corresponding volume fractions ϕ and $1 - \phi$,

$$\Delta E / k_B T \sim \frac{1}{2} w_{11} \phi^2 + \frac{1}{2} w_{22} (1-\phi)^2 + w_{12} \phi (1-\phi), \tag{16}$$

where w_{ij} is the interaction constant between monomers of type 1 or 2. However, we do not need three constants. Therefore, we introduce

$$\phi = \frac{1+\sigma}{2}, \qquad 1 - \phi = \frac{1-\sigma}{2}. \tag{17}$$

Inserting this into eq.16, then transforming back using $\sigma = 2\phi - 1$, we can separate linear and constant terms from nonlinear one,

$$\Delta E/k_BT \sim w\phi(1-\phi) + \alpha(w_{11} - w_{22})\phi + \beta w, \tag{18}$$

where α and β are some numbers, and

$$w = w_{12} - \frac{1}{2}(w_{11} + w_{22}). \tag{19}$$

The interesting feature of $\Delta E(\phi)$ is the curvature. Therefore, retaining only nonlinear terms in ϕ we can write,

$$\Delta E/k_BT = \chi\phi(1-\phi), \tag{20}$$

where

$$\chi = w/k_BT \tag{21}$$

is the dimensionless Flory interaction parameter. In summary, the change of the free enthalpy ("Gibbs free energy") per lattice site is given in the mean-field Flory approximation by

$$\Delta G/k_BT = \Delta E/k_BT - \Delta S_m/k_B = \frac{\phi_1}{N_1}\ln\phi_1 + \frac{\phi_2}{N_2}\ln\phi_2 + \chi\phi_1\phi_2. \tag{22}$$

1.3 Phase Separation

The Flory-Huggins theory provides a possibility for a discussion of phase separation in polymer blends where $\phi_1 = \phi$ and $\phi_2 = 1 - \phi$. First we discuss in short some general features of phase separation. The essential properties of the free energy ΔF is discussed in fig.3. When do we expected phase separation where a single homogeneous phase of volume fraction $\bar{\phi}$ decomposes in two separate phases of fractions ϕ_α and ϕ_β with their relative weights α and β,

$$\phi = \alpha\phi_\alpha + \beta\phi_\beta, \qquad \alpha + \beta = 1. \tag{23}$$

In this case we have to consider the corresponding free energy $\Delta\bar{G}$

$$\Delta\bar{G} = \alpha\Delta G(\phi_\alpha) + \beta\Delta G(\phi_\beta). \tag{24}$$

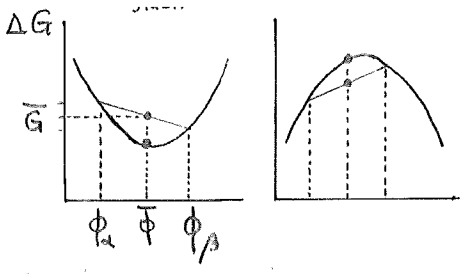


Fig. 3: *Local free energy profiles.*

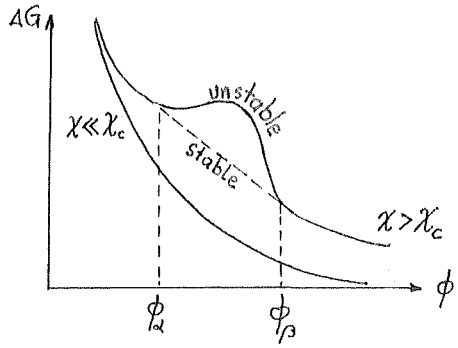


Fig. 4: *Examples of the Flory-Huggins free energy.*

In general, ΔG may have locally a convex or concave form, left and right part of fig.3, respectively. In the convex case $\Delta G < \Delta\bar{G}$, the free energy of the homogeneous mixture is lower as compared to that of the separated phase, and hence the homogeneous phase is stable. In the concave case $\Delta G > \Delta\bar{G}$, phase separation takes place. This argument is known as the "Gibbs' criterion of stability".

In general, there may be more complicated situations and a typical curve is depicted in fig.4. Above and below a critical value of the Flory-Huggins parameter χ_c, defined below, the free energy curves have different profiles. At $\chi < \chi_c$ the curve is convex, the entropy term dominates and thus mixing of the two components is favored. However, at $\chi > \chi_c$ the free energy curve has at the left and right side, $\phi < \phi_\alpha, \phi_\beta$ and $\phi > \phi_\alpha, \phi_\beta$ regimes of a stable homogeneous phase. In the intermadiate regime, $\phi_\alpha < \phi < \phi_\beta$, the homogeneous phase is unstable. This situation is explained in more details in fig.5 for the symmetric case where both types of polymers have the same chain length $N_1 = N_2 = N$. At the left and the right side of the concentration regime the system is stable, whereas in the central regime unstable. The two regimes at the left and right sides, between one of the minima and the neigboring inflection point, are called the *metastable* regimes. The curve separating unstable and metastable regimes is called the *spinodal*. In order to determine the various regimes of the free energy as a function of ϕ, we dicuss the various derivatives of ΔG with respect to ϕ. The *coexistence* curve is obtained from the free energy (here, for the symmetric case) :

$$\Delta G/k_BT = \frac{\phi}{N}\ln\phi + \frac{(1-\phi)}{N}\ln(1-\phi) + \chi\phi(1-\phi), \tag{25}$$

$$\frac{\partial G}{\partial \phi} = 0 = \frac{1}{N}\ln\frac{\phi}{1-\phi} + \chi(1-2\phi). \tag{26}$$

Phase separation takes place only if the Flory-Huggins parameter χ is larger than a certain critical value

$$\chi_c = \frac{1}{N}\frac{-1}{1-2\phi}\ln\frac{\phi}{1-\phi}. \tag{27}$$

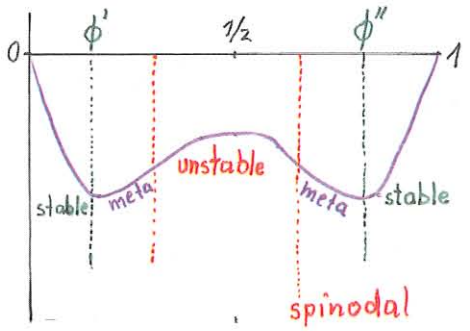


Fig. 5: *Free energy for the symmetric case.*

For the symmetric case the maximum is located at $\phi_c = 1/2$, and hence

$$\chi_c = \frac{2}{N}. \tag{28}$$

Since usually $N >> 1$, the critical value is very small which explains the strong incompatibility for many types of polymer mixtures.
The curvature of ΔG at a certain ϕ decides between the convex and the concave cases, and thus whether an instability occurs or not. In the asymmetric case we obtain

$$\frac{\partial^2 G}{\partial \phi^2} = 0 = \frac{1}{N_1(1-\phi)} + \frac{1}{N_2 \phi} - 2\chi. \tag{29}$$

This determines the spinodal line which is depicted in fig.6 by the broken line. In the asymmetric case, the critical point ϕ_c, which is the minimum value of χ on the spinodal, is determined by the third derivative

$$\frac{\partial^3 G}{\partial \phi^3} = 0 = \frac{1}{N_1(1-\phi)^2} - \frac{1}{N_2 \phi^2}, \tag{30}$$

which leads to

$$\phi_c = \frac{1}{\sqrt{N_2/N_1} + 1}, \tag{31}$$

and hence the corresponding critical value

$$\chi_c = \frac{1}{2N_2}(1 + \sqrt{N_2/N_1}). \tag{32}$$

A typical experimentally established phase diagram is shown in fig.7. This has to compared to fig.6 where according to (21) temperature and Flory parameter are related by $\chi \sim 1/T$.

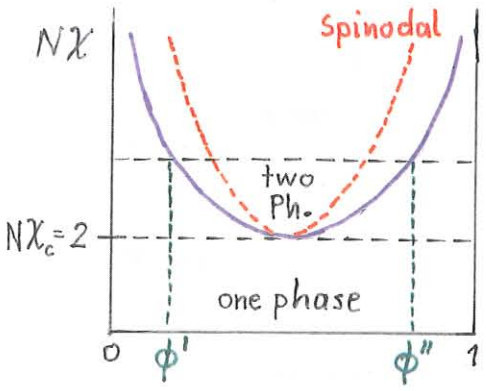


Fig. 6: *Coexistence curve and spinodal.*

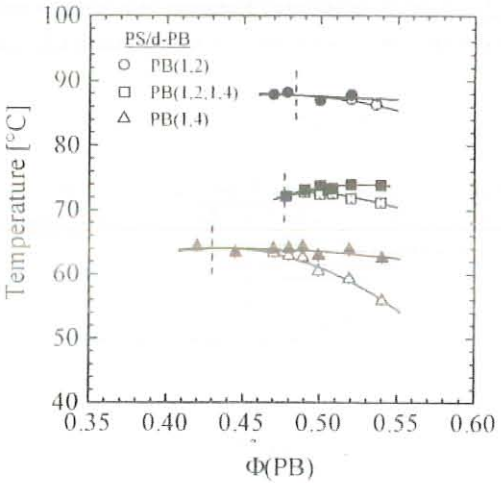


Fig. 7: *Phase diagram of three d-PB/PS polymer blends. The filled and open symbols correspond to the coexistence and spinodal curve, respectively. The dashes line locates the critical point [3].*

2 The Structure Factor in the Random Phase Approximation

In order to make correct interpretations of the structure factor, we have to discuss its relation to the density correlation function and to show how the latter function can be related to the Flory-Huggins free energy.
Mean field thoeries, as the Flory-Huggins theory, generally neglect fluctuations. However, using self-consistent field methods the fluctuation, in particular density fluctuations, can be calculated. The approach, as presented below, has been developed in various areas of physics. It is known by various names, e.g., Debye-Hückel theory for electrolytes, Ornstein-Zernicke correlation function, self-consistent field method. The name "random phase approximation" had been introduced in the context of the theory of the dielectricity constant of an electron gas. The random phase approximation had been introduced and applied to polymer physics by Jannink and de Gennes [4]. The ideas of a self-consistent field approach to polymers has been introduced in pioneering works by S.F.Edwards [5, 6]. We will follow here the outlines given in refs.[2, 7].

2.1 Linear Response

We consider a single chain embedded on a regular lattice. At each lattice point occupied by the polymer, a potential $U(\mathbf{r})$ acts on each monomer. A chain of $N-1$ steps has a statistical weight of

$$\sim \exp[-\beta \sum_{i=1}^{N} U(\mathbf{r}_i]. \tag{33}$$

The sum of all statistical weights of all possible polymer conformations with fixed endpoints $\mathbf{r}_1 = \mathbf{r}'$ and $\mathbf{r}_N = \mathbf{r}$ is defined by

$$z^N G_N(\mathbf{r}', \mathbf{r}), \tag{34}$$

where z is the lattice coordination number, and the prefactor z^N is the total number of unperturbed conformations (random walks). In order to find a recursion relation for G_N, we ask for the change of G_N by adding one more monomer to the chain,

$$G_{N+1}(\mathbf{r}', \mathbf{r}) = \frac{1}{z} \sum_{<\mathbf{r}'', \mathbf{r}>} G_N(\mathbf{r}', \mathbf{r}'') e^{-\beta U(\mathbf{r})}, \tag{35}$$

where the sum is over all nearest neighbors of $\mathbf{r}$. Similarly, we have the relation

$$G_N(\mathbf{r}', \mathbf{r}) = \sum_{\mathbf{r}''} G_{N'}(\mathbf{r}', \mathbf{r}'') G_{N-N'}(\mathbf{r}'', \mathbf{r}), \qquad 0 < N' < N. \tag{36}$$

This relation says, that the total weight is just the product of partial weights. This means that the corresponding random walk is a "Markov process". Of course, excluded volume effects are neglected. The total weight of all polymer conformations is therefore given by

$$Z(\{U\}) = \sum_{\mathbf{r}'', \mathbf{r}'} G_N(\mathbf{r}'', \mathbf{r}') \tag{37}$$

and depends on the distribution of the local potentials $U(\mathbf{r})$. The concentration of monomers at site $\mathbf{r}$ is given by

$$\langle\phi(\mathbf{r})\rangle = \frac{1}{Z(U)} \sum_{\mathbf{r}'',\mathbf{r}'} \sum_{N'=0}^{N} G_{N'}(\mathbf{r}'',\mathbf{r}) G_{N-N'}(\mathbf{r},\mathbf{r}'). \tag{38}$$

The interpretation of this relation is, that it contains the weighted sum of all chains which have a monomer N' at site $\mathbf{r}$. The factor $Z(U)$ is used for normalization.
It should be noted that the volume fraction $\langle\phi(\mathbf{r})\rangle$ is assumed to be a slowly varying quantity in space ("hydrodynamic limit") in order to obtain a resonable averaging. Its value varies between zero and one. It is obtained from the actual concentration by $c(\mathbf{r}) = \phi(\mathbf{r})/a^3$, where a^3 is the volume of a lattice cell. Using eq.36, one obtains

$$\sum_{\mathbf{r}} \langle\phi(\mathbf{r})\rangle = N+1\ ; \qquad 0 \le \phi(\mathbf{r}) \le 1, \tag{39}$$

which means that for $U(\mathbf{r}) = 0$ the average is $\langle\phi(\mathbf{r})\rangle = 1$. Other normalizations are possible as well.
The concentration of monomers can also be expressed as the derivative of the partition function $Z(U)$. Consider the contribution to G_N at a given site $\mathbf{r}$

$$G'_N(\mathbf{r}'',\mathbf{r}') = \sum_{N'=0}^{N} G_{N'}(\mathbf{r}'',\mathbf{r}) G_{N-N'}(\mathbf{r},\mathbf{r}'). \tag{40}$$

According to eq.35 we obtain at small changes of $U(\mathbf{r})$ in a linear approximation

$$\exp[-\beta(U+\delta U)] - \exp[-\beta U] \approx -\beta\delta U \exp[-\beta U] \tag{41}$$

and therefore

$$\delta G_N(\mathbf{r}'',\mathbf{r}') = -\beta \sum_{N'=0}^{N} G_{N'}(\mathbf{r}'',\mathbf{r}) G_{N-N'}(\mathbf{r},\mathbf{r}') \delta U(\mathbf{r}). \tag{42}$$

Changing $U(\mathbf{r})$ by $\delta U(\mathbf{r})$ in $Z(U)$, we obtain

$$\langle\phi(\mathbf{r})\rangle \delta U(\mathbf{r}) = -\frac{1}{\beta}\frac{\delta Z(U)}{Z(U)} = -\frac{1}{\beta}\delta \ln Z(U) \tag{43}$$

which can be rewritten as

$$\langle\phi(\mathbf{r})\rangle = -\frac{1}{\beta}\frac{\delta \ln Z(U)}{\delta U(\mathbf{r})}. \tag{44}$$

Considering the change of $\langle\phi(\mathbf{r})\rangle$, if $U(\mathbf{r}')$ is changed by $\delta U(\mathbf{r}')$, the same procedure can be applied to eq.38. The calculation can be found appendix A. The result is

$$\delta\langle\phi(\mathbf{r})\rangle = -\beta[\langle\phi(\mathbf{r})\phi(\mathbf{r}')\rangle - \langle\phi(\mathbf{r})\rangle\langle\phi(\mathbf{r}')\rangle]\delta U(\mathbf{r}') = -\beta\langle\delta\phi(\mathbf{r})\ \delta\phi(\mathbf{r}')\rangle\delta U(\mathbf{r}') \tag{45}$$

where

$$\delta\phi(\mathbf{r}) \equiv \phi(\mathbf{r}) - \langle\phi(\mathbf{r})\rangle. \tag{46}$$

Equation (45) represents the linear reponse of $\langle\phi(\mathbf{r})\rangle$ to the change of $U(\mathbf{r}')$. The correlation function of the monomer density can be formally rewritten as

$$\langle\delta\phi(\mathbf{r})\ \delta\phi(\mathbf{r}')\rangle = \frac{1}{\beta^2}\frac{\delta^2 \ln Z(U)}{\delta U(\mathbf{r})\delta U(\mathbf{r}')}. \tag{47}$$

The correlation function is closely related to the structure factor which describes the intensity of scattering experiments. According to van Hove, the intensity can be calculated from the correlation function according to

$$S(\mathbf{q}) = \sum_{\mathbf{r}} e^{i\mathbf{q}\mathbf{r}}\langle\delta\phi(\mathbf{r})\ \delta\phi(0)\rangle \tag{48}$$

which is the structure factor in the case of translational invariant systems. If we consider the case of non-interacting polymer chains, then $S(\mathbf{q})$ is identical with the Debye function [8] of one non-self-interacting chain

$$S_0(\mathbf{q}) = \frac{2N}{x^2}[e^{-x} - 1 + x], \qquad x = Na^2q^2/6. \tag{49}$$

On a lattice the monomer size a is the same as the lattice constant.

2.2 Random Phase Approximation

The starting point is the relation between the local change of the monomer density and the change of the local potential energy, eq.45, which can be rewritten to

$$\langle\delta\phi(\mathbf{r})\rangle = -\beta\sum_{\mathbf{r}'} S_0(\mathbf{r},\mathbf{r}')\delta U_{ext}(\mathbf{r}'). \tag{50}$$

The potential has been marked as external. The density correlation function has been renamed to $S_0(\mathbf{r},\mathbf{r}')$ because of equation (48) and because we consider here the non-interacting case. If we assume that there are additional internal interactions among the monomers (see below, polymer mixtures), then we can generalize

$$\langle\delta\phi(\mathbf{r})\rangle = -\beta\sum_{\mathbf{r}'} S_0(\mathbf{r},\mathbf{r}')\ [\delta U_{ext}(\mathbf{r}') + \delta U_{int}(\mathbf{r}')]. \tag{51}$$

This equation represents a *linear* relation between the deviation of the local monomer density from its average and the fluctuations of the local potentials. The average of U_{int} is of less importance, and the average of ϕ is given by external conditions. It can be expected that the linear relation (51) is correct in the hydrodynamic limit, i.e., for long-range fluctuations, whereas for shorter scales, say, on molecular distances, the relation becomes a poor approximation.
A second, more important approximation, is the assumption that the internal potentials at $\mathbf{r}'$ are determined by the fluctuations of the monomer density at the same place, i.e.,

$$\delta U_{int}(\mathbf{r}') \sim \langle\delta\phi(\mathbf{r})\rangle. \tag{52}$$

It can be shown that the proportionality factor in the mean-field approximation of Flory-Huggins is given by $-2k_BT\chi$. Inserting (52) into (51), we obtain

$$\langle\delta\phi(\mathbf{r})\rangle = -\beta\sum_{\mathbf{r}'} S_0(\mathbf{r},\mathbf{r}')\ [\delta U_{ext}(\mathbf{r}') - 2k_BT\chi\langle\delta\phi(\mathbf{r}')\rangle]. \tag{53}$$

The corresponding fourier transform is

$$\langle \delta\phi(\mathbf{q}) \rangle = -\beta S_0(\mathbf{q})[U(\mathbf{q}) - 2\beta^{-1}\chi\langle \delta\phi(\mathbf{q})\rangle], \tag{54}$$

which can solved to

$$\langle \delta\phi(\mathbf{q}) \rangle = -\beta \frac{S_0(\mathbf{q})}{1 - 2\chi S_0(\mathbf{q})} U_{ext}(\mathbf{q}), \tag{55}$$

which can formally be written as

$$\langle \delta\phi(\mathbf{q}) \rangle = -\beta S(\mathbf{q}) U_{ext}(\mathbf{q}), \tag{56}$$

which gives by comparison the structure factor in the random phase approxiamtion

$$S^{-1}(\mathbf{q}) = S_0^{-1}(\mathbf{q}) - 2\chi, \tag{57}$$

and $S_0(\mathbf{q})$ is the Debye function (49).

2.3 Polymer Mixture

In the following we discuss the structure factor of polymer mixtures of two different types of polymers where the monomers have different scattering properties. More theoretical details and corresponding computer simulations my be found in the works of Binder and collaborators [9, 10, 11].
Here we consider the special case of neutron scattering where the two types monomers are characterized by scattering lengths a and b. The scattering intensity is

$$I(q) \sim a^2 S^{(11)}(q) + 2ab S^{(12)}(q) + b^2 S^{(22)}(q), \tag{58}$$

where

$$S^{(\alpha\beta)}(\mathbf{q}) = \sum_{\mathbf{r}} e^{i\mathbf{q}\mathbf{r}} \langle \delta\phi_\alpha(\mathbf{r})\ \delta\phi_\beta(0)\rangle. \tag{59}$$

Using the requirement that at each lattice site is occupied only by one of the two types of monomers, which means

$$\phi_1(\mathbf{r}) + \phi_2(\mathbf{r}) = 1, \qquad \text{(incompressibility condition)} \tag{60}$$

yields the following simplified form of eq.59

$$I(\mathbf{q}) \sim (b-a)^2 S^{(22)}(\mathbf{q}), \quad |\mathbf{q}| > 0. \tag{61}$$

At $\mathbf{q} = 0$, constant terms has to be taken into account during the fourier transform, which gives rise to "Bragg reflection" at the points of the reciprocal lattice.
The calculation of $S^{(22)}(\mathbf{q})$ under condition (60), which is shown in Appendix B, leads to

$$S^{-1}(\mathbf{q}) = [(1-\phi_2) S_0^{(11)}(\mathbf{q})]^{-1} + [\phi_2 S_0^{(22)}(\mathbf{q})]^{-1} - 2\chi \tag{62}$$

where S_0 is the Debye function (49) and ϕ is the volume fraction of component 2.
In fig.8 a typical result for the structure factor from neutron scattering is presented.
In the limit $\mathbf{q} \to 0$ the structure factor reduces to the sum of the density correaltion function over $\mathbf{r}$,

$$\lim_{\mathbf{q}\to 0} S(\mathbf{q}) = \sum_{\mathbf{r}} \langle \phi(\mathbf{r})\phi(0)\rangle. \tag{63}$$

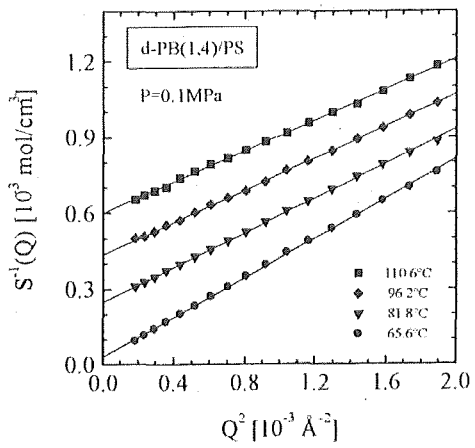


Fig. 8: *Structure factor for a polymer blend at constant pressure and various temperatures [3].*

In the Appendix B it is shown the structure factor can be related to the free energy,

$$\lim_{\mathbf{q}\to 0} S^{-1}(\mathbf{q}) = \frac{\partial^2}{\partial \phi^2}\left(\frac{G}{k_B T}\right). \tag{64}$$

In the continuum representation this free energy can be replaced e.g. by the Flory-Huggins expression, where the second derivative is given by eq.29. Since

$$\lim_{\mathbf{q}\to 0} S_0^{(\alpha)}(\mathbf{q}) = N_\alpha \tag{65}$$

we obtain

$$\lim_{q\to 0} S^{-1}(\mathrm{q}) = [(1-\phi_2)N_1]^{-1} + [\phi_2 N_2]^{-1} - 2\chi \tag{66}$$

in agreement again with (29).

Appendix A : Linear Response function of Monomer Concentration.

We start at eq.38 which has the explicit form

$$\langle\phi(\mathbf{r})\rangle = \frac{\sum_{\mathbf{r}'',\mathbf{r}'}\sum_{N'=0}^{N} G_{N'}(\mathbf{r}'',\mathbf{r})G_{N-N'}(\mathbf{r},\mathbf{r}')}{\sum_{\mathbf{r}'',\mathbf{r}'} G_N(\mathbf{r}'',\mathbf{r}')}. \tag{67}$$

Changing $U(\mathbf{r}')$ by $\delta U(\mathbf{r}')$, the function G changes also, where all paths passing $\mathbf{r}'$ have to be included. These changes has to taken into account in the nominator and the denominator.

$$\begin{aligned}\delta\langle\phi(\mathbf{r})\rangle/\beta = & - \frac{\sum_{\mathbf{r}''',\mathbf{r}''}\sum_{N'}\sum_{N''} G_{N''}(\mathbf{r}'',\mathbf{r}')G_{N'-N''}(\mathbf{r}',\mathbf{r})G_{N-N'}(\mathbf{r},\mathbf{r}'')}{\sum_{\mathbf{r}''',\mathbf{r}''} G_N(\mathbf{r}''',\mathbf{r}'')} \\ & + \frac{\sum_{\mathbf{r}''',\mathbf{r}''}\sum_{N'} G_{N'}(\mathbf{r}''',\mathbf{r})G_{N-N'}(\mathbf{r},\mathbf{r}'')}{\sum_{\mathbf{r}''',\mathbf{r}''} G_N(\mathbf{r}''',\mathbf{r}'')} \\ & \times \frac{\sum_{\mathbf{r}''',\mathbf{r}''}\sum_{N'} G_{N'}(\mathbf{r}''',\mathbf{r}')G_{N-N'}(\mathbf{r}',\mathbf{r}'')}{\sum_{\mathbf{r}''',\mathbf{r}''} G_N(\mathbf{r}''',\mathbf{r}'')}\end{aligned} \tag{68}$$

The first term on the right hand side corresponds to $-\beta\langle\phi(\mathbf{r}')\phi(\mathbf{r})\rangle$. The second term is the product of two monomer concentrations, $\beta\langle\phi(\mathbf{r}')\rangle\langle\phi(\mathbf{r})\rangle$, which completes to eq.45.

Appendix B : Calculation of $S(\mathbf{q})$ for Polymer Mixtures in the Random Phase Approximation.

The following calculations can be found similarly in the paper by Binder [10]. An alternative can be found in the book of Doi and Edwards [12]. The partition function $Z(\{U\})$ is a functional of the potential $U(\mathbf{r})$. Similarly as the usual relation between free energy and partition function we define the thermodynamic potential $Y(\{U\})$ and the corresponding average of $\phi(\mathbf{r})$

$$Y(\{U\}) = -\frac{1}{\beta}\ln Z(\{U\}). \tag{69}$$

$$\langle\phi(\mathbf{r})\rangle = \frac{\delta Y}{\delta U(\mathbf{r})}. \tag{70}$$

In the following we omit the brackets $\langle ... \rangle$. By Legendre transformation we obtain the free energy

$$F = Y - \sum_{\mathbf{r}} \phi(\mathbf{r})U(\mathbf{r}). \tag{71}$$

and hence the functional derivative

$$\frac{\delta F}{\delta\phi(\mathbf{r})} = -U(\mathbf{r}). \tag{72}$$

This free energy is a functional of $\phi(\mathbf{r})$ and a generalization of the free energy $F(T,\phi)$, as discussed in the first section on the Flory-Huggins theory, to space-dependent volume

fraction $\phi(\mathbf{r})$. It should be noted that $\phi(\mathbf{r})$ is a defined a coarse-grained variable averaged over a few lattice sites.
The density-density correlation function $S_0(\mathbf{r},\mathbf{r}')$ is the second derivative of Y, (compare eq.45 and Appendix A),

$$S_0(\mathbf{r},\mathbf{r}') = -\frac{1}{\beta}\frac{\delta\phi(\mathbf{r})}{\delta U(\mathbf{r}')} = -\frac{1}{\beta}\frac{\delta^2 Y}{\delta U(\mathbf{r})\delta U(\mathbf{r}')}. \tag{73}$$

This can be reformulated to the inverse derivative of F

$$S_0(\mathbf{r},\mathbf{r}') = -\frac{1}{\beta}\left[\frac{\delta U(\mathbf{r}')}{\delta\phi(\mathbf{r})}\right]^{-1} = \frac{1}{\beta}\left[\frac{\delta^2 F}{\delta\phi(\mathbf{r})\delta\phi(\mathbf{r}')}\right]^{-1} \tag{74}$$

In the case of a polymer mixture, we consider two types of monomers and hence to types of potentials $U_1(\mathbf{r})$ and $U_2(\mathbf{r})$ which act only on their corresponding type of monomer. The corresponding partition function $Z(\{U_1,U_2\})$ leads to a thermodynamic potential

$$Y(\{U_1,U_2\}) = -\frac{1}{\beta}\ln Z(\{U_1,U_2\}). \tag{75}$$

Considering still the case where the two monomer types do not interact specifically, we obtain the density-density correlation function of ideal polymer chains of type 1,

$$\phi_1 S_0^{(11)}(\mathbf{r},\mathbf{r}') = -\frac{1}{\beta}\frac{\delta^2 Y}{\delta U_1(\mathbf{r})\delta U_1(\mathbf{r}')}\Big|_{U_2=const} \tag{76}$$

Similarly for type 2 polymers. The free energy is obtained again by Legendre transformation

$$F = Y - \sum_{\mathbf{r}}[\phi_1(\mathbf{r})U_1(\mathbf{r}) + \phi_2(\mathbf{r})U_2(\mathbf{r})]. \tag{77}$$

The derivatives are

$$\frac{\delta F}{\delta\phi_1(\mathbf{r})} = -U_1(\mathbf{r}), \qquad \frac{\delta F}{\delta\phi_2(\mathbf{r})} = -U_2(\mathbf{r}). \tag{78}$$

Elimination of one of the two components by the inkompressibility condition $\phi_1(\mathbf{r}) + \phi_2(\mathbf{r}) = 1$, one obtains a new functional

$$\frac{\delta\hat{F}}{\delta\phi_2(\mathbf{r})} = U_1(\mathbf{r}) - U_2(\mathbf{r}). \tag{79}$$

The density-density correlation function is given accordingly by

$$\langle\phi_2(\mathbf{r})\phi_2(\mathbf{r}')\rangle = -\frac{1}{\beta}\frac{\delta^2 Y}{\delta(U_1(\mathbf{r}) - U_1(\mathbf{r}))\delta(U_2(\mathbf{r}) - U_2(\mathbf{r}))} = \frac{1}{\beta}\left[\frac{\delta^2\hat{F}}{\delta\phi_2(\mathbf{r})\delta\phi_2(\mathbf{r}')}\right]^{-1} \tag{80}$$

$$\begin{aligned}\frac{\delta^2\hat{F}}{\delta\phi_2(\mathbf{r})\delta\phi_2(\mathbf{r}')} &= \frac{\delta^2 F}{\delta\phi_1(\mathbf{r})\delta\phi_1(\mathbf{r}')} + \frac{\delta^2 F}{\delta\phi_2(\mathbf{r})\delta\phi_2(\mathbf{r}')} \\ &= \beta[\phi_1 S_0^{(1)}(\mathbf{r},\mathbf{r}')]^{-1} + \beta[\phi_2 S_0^{(2)}(\mathbf{r},\mathbf{r}')]^{-1}\end{aligned} \tag{81}$$

and hence we obtain after Fourier transformation the structure factor (62) for noninteractiong chains ($\chi = 0$)

$$S^{-1}(\mathbf{q}) = [\phi_1 S_0^{(11)}(\mathbf{q})]^{-1} + [\phi_2 S_0^{(22)}(\mathbf{q})]^{-1} \tag{82}$$

where $S_0^{(\alpha\alpha)}$ is the Debye function (49).

References

[1] P.J. Flory, *Principles of Polymer Chemistry*, (Cornell University Press, Ithaca, 1971).

[2] P.G. de Gennes, *Scaling Concepts in Polymer Physics*, (Cornell University Press, Ithaca, 1979).

[3] H. Frielinghaus, D. Schwahn, L. Willmer, Macromolecules **34**, 1751 (2001).

[4] G. Jannink, and P.G. de Gennes, J.Chem.Phys. **48**, 2260 (1968).

[5] S.F. Edwards, Proc.Roy.Soc (London) **85**, 613 (1965).

[6] S.F. Edwards, Proc.Roy.Soc (London) **88**, 265 (1966).

[7] J. des Cloiseaux, and G. Jannink, *Polymers in solution: their modelling and structure*, (Oxford : Clarendon Press, 1990)

[8] P. Debye, J.Phys.Colloid Chem. **51**, 18 (1947).

[9] K. Binder, Phys.Rev.A **29**, 341 (1984).

[10] K. Binder, J.Chem.Phys. **79**, 6387 (1983).

[11] K. Binder, Adv.Polym.Sci. **112**, 181 (1994).

[12] M. Doi, and S.F. Edwrards, *The Thoery of Polymer Dynamics*, (Clarendon Press, Oxford, 1986).

B 5 Polyelectrolytes

R. G. Winkler
Institut für Festkörperforschung
Forschungszentrum Jülich GmbH

Contents

1 Introduction 2

2 Poisson-Boltzmann Equation – Debye-Hückel Potential 3

3 Conformational Properties of Polyelectrolytes in Solution 5
3.1 Polyelectrolyte at infinite dilution 5
3.2 Polyelectrolyte at finite dilution 5

4 Structure of Polyelectrolyte Solutions 10
4.1 PRISM and model 11
4.2 Results for rodlike polyelectrolytes 13

5 Counterion Condensation 18

6 Polyelectrolyte in Poor Solvent 23

A Solution of Linearized Poisson-Boltzmann Equation 26

B Thermal Averages of Edwards-Singh Approach 27

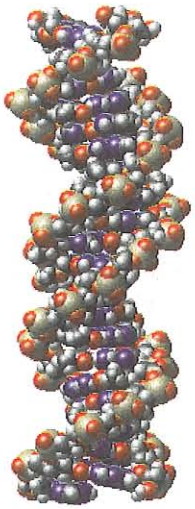
C Electrostatic Persistence Length in the Rod Limit 28

1 Introduction

Polyelectrolytes are macromolecules build of monomers with ionizable groups. When the molecules are dissolved in a polar solvent such as water, the ion pairs dissociate. The electrostatic charges of one sign remain localized on the chain whereas the large number of oppositely charged counterions are scattered in the solution. The long range Coulomb interaction among the various charges is the origin of a rich variety of properties of such solutions which are not found in neutral polymers. Hence, polyelectrolyte systems are of considerable interest from a basic scientific point of view. On the other hand, polyelectrolytes play a fundamental role in our everyday live. Most biopolymers, including DNA and many proteins, are polyelectrolytes. Technologically they are used in a wide-range of applications such as dewatering agents, drug reduction agents, as additives in detergents and cosmetics, in gels, in superabsorbants etc. [1–3]. Despite more than 50 years of continuing interest, the unique properties of charged polymers are poorly understood compared to those of their neutral counterparts [4–6]. Experiments on polyelectrolyte solutions using different methods often lead to controversial results. Furthermore, experimental results on single polyelectrolyte chains are still lacking due to the immense problems caused by trace impurities and very low scattering intensities when measuring dilute solutions [7]. Thus, scattering experiments and measurements of the radius of gyration are almost always performed in the semidilute regime [8]. From a theoretical point of view the problem is the long range Coulomb interaction. Renormalization group theories and scaling ideas, which have proved to be very successful for neutral polymer solutions [9], are now difficult to apply. The long range Coulomb interaction, together with screening effects caused by counterions, introduces more than one new length scale in the problem, which means that short range and medium to long range interactions are simultaneously present. This coupling of different length scales leads to a severe influence of local chain properties on the properties of the whole system.

Valuable insight into the properties of polyelectrolyte solutions is obtained by computer simulations [10–12] and liquid state theory [13, 14]. The latter is based upon the Ornstein-Zernike integral equation and uses the *Polymer Reference Interaction Site Model* (PRISM) [15].

In the present contribution I will discuss various fundamental properties of polyelectrolyte solutions. In a first step we will consider a (neutral) atomic system with positive and negative charges to derive an effective interaction potential between two of the charges based on the Poisson-Boltzmann approach. In the next section we will address the conformational properties of polyelectrolyte chains. Here the influence of counterions is taken into account by the Debye-Hückel potential, which follows from the linearized Poisson-Boltzmann equation. In the following section we will discuss the structural properties of a polymer solution taking into account counterions explicitly. The study will be based on the PRSIM approach for molecular systems. In addition, the phenomenon of counterion condensation is outlined. For illustrative purposes, results of computer simulations will also be presented. Finally, the conformational properties of a weakly charged polyelectrolyte in a poor solvent (hydrophobic polymer backbone) will be discussed.



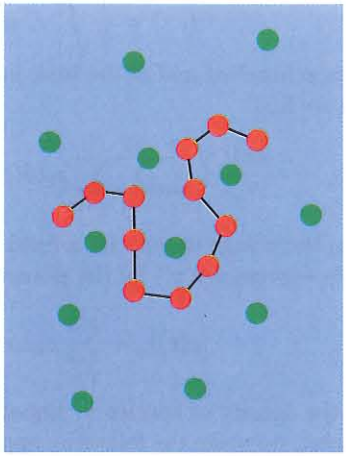


Fig. 1: *DNA molecule as an example of a polyelectrolyte (left). Model of a polyelectrolyte (green) with its counterions (red) (right). The solvent is considered a continuous background with dielectric constant ϵ.*

2 Poisson-Boltzmann Equation – Debye-Hückel Potential

To gain insight into the effective interaction between two charged particles of a solution of similar particles, we neglect chain connectivity for a moment, i.e., we consider a solution of charged point particles, N_+ of positive charge and N_- of negative charge. The total electrostatic energy can then be written as

$$\beta V = \frac{1}{2}\sum_{\alpha=1}^{2}\sum_{i=1}^{N_\alpha} z_\alpha \phi(\mathbf{r}_i^\alpha)\,, \tag{1}$$

$$\phi(\mathbf{r}) = \sum_{\gamma=1}^{2}\sum_{j=1}^{N_\gamma} \frac{z_\gamma l_B}{|\mathbf{r}-\mathbf{r}_j^\gamma|}\,. \tag{2}$$

The indizes α, γ indicate the two different species of particles[1]. ϕ is the electrostatic potential, $l_B = e^2/(\epsilon k_B T)$ the Bjerrum length[2], where k_B denotes the Boltzmann factor, T the temperature, and e the elementary charge, and z_α is the valency of the particle. The solvent is considered a continuous background with dielectric constant ϵ. Next, we consider the canonical average of ϕ when we fix a particle of kind α at $\mathbf{r}'$. Using the properties of δ-functions, we obtain

$$\langle \phi(\mathbf{r},\mathbf{r}')\rangle_\alpha = \frac{V}{N_\alpha}\left\langle \sum_{i=1}^{N_\alpha} \phi(\mathbf{r})\delta(\mathbf{r}'-\mathbf{r}_i^\alpha)\right\rangle\,, \tag{3}$$

[1]For $\alpha=\gamma$ the term with $i=j$ is left out from the summation

[2]For water at room temperature: $\epsilon \approx 78.5$ and $l_B \approx 7.14$Å.

where

$$\langle \ldots \rangle = \frac{1}{Z} \int \ldots \exp\left(-\beta V\right)\, d^{3N}x\,. \tag{4}$$

(Z is the partition function and N the total number of particles.) By taking the Laplacian (Δ) of Eq. (3) we find

$$\Delta \left\langle \phi(\mathbf{r},\mathbf{r}') \right\rangle_\alpha = -\frac{4\pi V}{N_\alpha \epsilon} \left\langle \sum_{\gamma=1}^{2} \sum_{i=1}^{N_\alpha} \sum_{j=1}^{N_\gamma} z_\gamma e \delta(\mathbf{r}-\mathbf{r}_j^\gamma)\delta(\mathbf{r}'-\mathbf{r}_i^\alpha) \right\rangle = -\frac{4\pi}{\epsilon} \left\langle \rho(\mathbf{r},\mathbf{r}') \right\rangle_\alpha\,, \tag{5}$$

where $\rho(\mathbf{r},\mathbf{r}')$ is the charge density for a fixed point. Considering a homogeneous system[3], we can formally express $\rho(\mathbf{r},\mathbf{r}')$ by the potential of mean force $w_{\alpha\gamma}(\mathbf{r})$ via

$$\left\langle \rho(\mathbf{r}) \right\rangle_\alpha = \sum_{\gamma=1}^{2} \rho_\gamma z_\gamma e \exp\left(-\beta w_{\alpha\gamma}(\mathbf{r})\right)\,. \tag{6}$$

$\rho_\gamma = N_\gamma/V$ is the density of species γ. Equations (5) and (6) are exact so far. Following Debye and Hückel, we make the following approximations to obtain an analytical solution of equation (5) [17]:

- The potential of mean force is replaced by

$$w_{\alpha\gamma}(\mathbf{r}) \approx z_\gamma e \left\langle \phi(\mathbf{r}) \right\rangle_\alpha := z_\gamma e \bar{\phi}_\alpha(\mathbf{r})\,. \tag{7}$$

  We then arrive at the **Poisson-Boltzmann** equation

$$\Delta\bar{\phi}_\alpha(\mathbf{r}) = -\frac{4\pi}{\epsilon} \sum_{\gamma=1}^{2} \rho_\gamma z_\gamma e \exp\left(-\beta z_\gamma e \bar{\phi}_\alpha(\mathbf{r})\right)\,. \tag{8}$$

- The right-hand side of Eq. (8) is linearized:

$$\sum_\gamma \rho_\gamma z_\gamma e \exp\left(-\beta z_\gamma e \bar{\phi}_\alpha(\mathbf{r})\right) \approx \sum_{\gamma=1}^{2} \rho_\gamma z_\gamma e - \beta \sum_{\gamma=1}^{2} \rho_\gamma (z_\gamma e)^2 \bar{\phi}_\alpha(\mathbf{r})\,.$$

  Since the total system is neutral, the first term on the right-hand side vanishes and the linearized Poisson-Boltzmann equation is obtained

$$\Delta\bar{\phi}_\alpha(\mathbf{r}) = \kappa^2 \bar{\phi}_\alpha(\mathbf{r})\,, \tag{9}$$

  where κ^{-1} is the Debye screening length

$$\kappa^2 = 4\pi l_B \sum_{\gamma=1}^{2} z_\gamma^2 \rho_\gamma\,. \tag{10}$$

With the appropriate boundary conditions for a sphere of diameter σ in infinite space the solution of equation (9) is given by (see Appendix A)

$$\bar{\phi}_\alpha(r) = k_B T z_\alpha l_B \frac{e^{-\kappa(r-\sigma)}}{r(1+\kappa\sigma)}\,; \quad r > \sigma\,, \tag{11}$$

i.e., the presence of the various ions leads to a screened Coulomb interaction between two charges (**Debye-Hückel** potential). For point particles, i.e., $\sigma = 0$, the potential reduces to $\bar{\phi}_\alpha(r) = k_B T z_\alpha l_B e^{-\kappa r}/r$. In section 3 we will use the Debye-Hückel potential to gain insight into the conformational properties of polyelectrolyte chains.

[3]For a homogeneous system, $\rho(\mathbf{r},\mathbf{r}')$ is a function of the difference $\mathbf{r}-\mathbf{r}'$ only.

3 Conformational Properties of Polyelectrolytes in Solution

The conformational properties of polyelectrolytes in solution depend on the polymer concentration, the interaction strength, and chain length. The long range Coulomb interaction prevents a straightforward calculation of the partition function even for very simple chain models. The coupling of different length scales in charged systems, however, will lead to phenomena which are not present for uncharged chains. Thus, it is important to elucidate the dependence of the characteristic chain dimensions on the above quantities, even if we have to resort to (severe) approximations.

3.1 Polyelectrolyte at infinite dilution

The effect of the long range nature of the Coulomb interaction is most pronounced for an isolated chain. Such a situation is reached at infinite dilution.

The effect of the repulsive interaction between the like-charged monomers on the chain conformation can by understood by a Flory-type calculation [5]. It relies on simplifying assumptions but provides a simple physical picture. In a mean-filed approach, the Flory-type free energy is given by

$$F = k_B T \frac{R^2}{Nl^2} + k_B T l_B \frac{N^2}{R} \,. \tag{12}$$

The first term is the contribution from a Gaussian chain with mean squared end-to-end distance $\langle \mathbf{r}_e^2 \rangle = Nl^2$. The second term is the electrostatic energy of the N charges. R is a typical length scale of the system. Minimization with respect to R yields

$$R \sim N(l_B l^2)^{1/3} \,. \tag{13}$$

Thus, the size of a chain increases linearly with the chain length. This is quit different form the behavior of a Gaussian chain ($R = \sqrt{N}l$) or a chain in good solvent (self avoiding walk; $R \sim lN^{\nu}$, with $\nu \approx 0.6$). The long range Coulomb interaction leads to an increase of typical chain dimensions proportional to the chain length. This however, does not imply that the chain is fully extended. A local flexibility may still be present but R nevertheless scales with N.

From the calculations of section 2, we expect a screening of the Coulomb interaction among the monomers by the counterions at finite dilution. The characteristic chain dimension will then depend on the screening length.

3.2 Polyelectrolyte at finite dilution

To study the conformational properties of a chain at finite dilution, we consider a single chain whose monomers interact via the Debye-Hückel potential. The influence of counterions and density is captured by the screening parameter κ.

Polyelectrolytes can possess very complex structures as is obvious from the DNA molecule shown in Fig. 1. For a theoretical description a much simpler model is used. The simplest

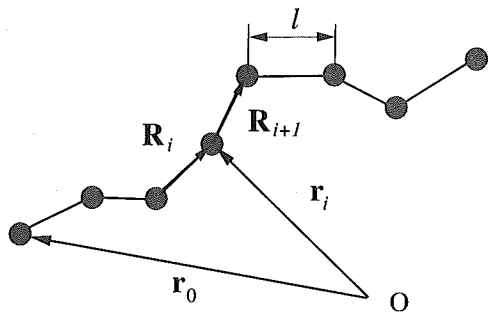


Fig. 2: *Model of a polymer chain.*

model is a linear chain of connected beads (Figs. 1, 2). The positions of the mass points, which might represent several monomers, are denoted by $\mathbf{r}_i$ $(i = 0, \ldots, N)$. The (average) length of a bond is l (cf. Fig. 2). The interaction potential between two particles is given by $V_{ij} = v_{ij}^{EV} + v_{ij}^{DH}$, where v_{ij}^{EV} is the excluded volume interaction taking into account the fact that two points cannot be locate at the same point in space

$$v_{ij}^{EV} = v_e \delta\left(\mathbf{r}_i - \mathbf{r}_j\right) \tag{14}$$

(v_e is the strength of the excluded volume interaction) and v_{ij}^{DH} is the Debye-Hückel potential (11)

$$v_{ij}^{DH} = k_B T l_B \frac{e^{-\kappa|\mathbf{r}_i - \mathbf{r}_j|}}{|\mathbf{r}_i - \mathbf{r}_j|} \,. \tag{15}$$

The chain character of a linear molecule is well captured by a (discrete) semiflexible chain model [18]. The partition function of an uncharged chain without excluded volume interaction is

$$Z = \int \exp\left(-\lambda \sum_{i=2}^{N-1} \mathbf{R}_i^2 - \lambda_0 \left(\mathbf{R}_1^2 + \mathbf{R}_N^2\right) - \frac{\mu}{2} \sum_{i=1}^{N-1} \left(\mathbf{R}_i^2 - \mathbf{R}_{i+1}^2\right)^2 \right) d^{3N}x \,, \tag{16}$$

where $\mathbf{R}_i = \mathbf{r}_i - \mathbf{r}_{i-1}$ denotes the bond vector, $\lambda = 3(1-t)/(2l^2(1+t))$, $\lambda_0 = 3/(2l^2(1+t))$, $\mu = 3t/(l^2(1-t^2))$, and $t = \langle \mathbf{R}_i \mathbf{R}_{i+1} \rangle / l^2$, i.e., t is the average cosine of the angle between two successive bond vectors. The terms with λ and λ_0 take into account the inextensibility constraint $\langle \mathbf{R}_i^2 \rangle = l^2$ and represent the entropy penalty for chain stretching. The last term is the energy penalty for bending the polymer chain. Taking into account the excluded volume interaction and the Debye-Hückel potential, the partition function is given by

$$Z = \int \exp\left(-\lambda \sum_{i=2}^{N-1} \mathbf{R}_i^2 - \lambda_0 \left(\mathbf{R}_1^2 + \mathbf{R}_N^2\right) - \frac{\mu}{2} \sum_{i=1}^{N-1} \left(\mathbf{R}_i^2 - \mathbf{R}_{i+1}^2\right)^2 - \frac{\beta}{2} \sum_{i=0}^{N} \sum_{j=0}^{N} (v_{ij}^{EV} + v_{ij}^{DH}) \right) d^{3N}x \,. \tag{17}$$

Unfortunately, this partition function cannot directly be evaluated. Consequently, we have to resort to an approximate calculation. Two approximation schemes are widely used:

- The variation of the free energy (F) using the Gibbs-Bogoliubov approximation [13]

$$F \leqq F_T + \langle H - H_T \rangle_T \ , \tag{18}$$

- The perturbation approach according to Edwards and Singh [19].

For both methods a trial Hamiltonian (H_T) is introduced with undetermined parameters. In the variational ansatz, these parameters are determined by minimizing the free energy expression. The Edwards-Singh approach is a perturbation calculation and assumes that the conformational properties of the trial chain are close to those of the charged chain. Since the latter approach seems to produce more adequate results, the essential steps of the Edwards-Singh method will be presented here.

Various trial Hamiltonians have been suggested in the literature. We will use the semi-flexible chain of equation (16) as reference system.

The mean square end-to-end distance of the charged system is given by

$$\langle \mathbf{r}_e^2 \rangle = \frac{\left\langle e^{-\beta(H-H_T)} (\mathbf{r}_N - \mathbf{r}_0)^2 \right\rangle_T}{\left\langle e^{-\beta(H-H_T)} \right\rangle_T} \ . \tag{19}$$

The averages are performed with the trial distribution function. Assuming small deviations between the actual and trial system we can write

$$\langle \mathbf{r}_e^2 \rangle = \langle \mathbf{r}_e^2 \rangle_T + \beta \langle \mathbf{r}_e^2 \rangle_T \langle H - H_T \rangle_T - \beta \left\langle \mathbf{r}_e^2 (H - H_T) \right\rangle_T + \mathcal{O}\left((\langle H - H_T \rangle_T)^2 \right) \ . \tag{20}$$

(H_T is the Hamiltonian of the partition function (16) with t replaced by t_T and H is the Hamiltonian of Eq. (17).) Since the reference polymer should exhibit configurational and structural properties of the original polymer chain, we require that

$$\langle \mathbf{r}_e^2 \rangle = \langle \mathbf{r}_e^2 \rangle_T \tag{21}$$

and neglect the higher order terms ($\mathcal{O}\left((\langle H - H_T \rangle_T)^2 \right) \approx 0$). From the remaining equation

$$\langle \mathbf{r}_e^2 \rangle_T \langle H - H_T \rangle_T - \left\langle \mathbf{r}_e^2 (H - H_T) \right\rangle_T = 0 \tag{22}$$

the parameter t_T is determined, which in turn yields λ_T, λ_{0T}, and μ_T. Due to the Gaussian nature of our ansatz for the trial Hamiltonian, all averages can be calculated analytically. The results are summarized in Appendix B. The solution of Eq. (22) allows us to calculate all characteristic quantities of the reference system, because these quantities depend on the parameter t_T only. In particular, the mean square end-to-end distance is

$$\langle \mathbf{r}_e^2 \rangle_T = Nl^2 \left(\frac{1 + t_T}{1 - t_T} + \frac{2t_T}{N} \frac{t_T^N - 1}{(t_T - 1)^2} \right) \ . \tag{23}$$

For flexible chains, i.e., for $t_T \ll 1$ and $N \gg 1$, this expression reduces to

$$\langle \mathbf{r}_e^2 \rangle_T = Nl^2 \frac{1 + t_T}{1 - t_T} = 2Nll_p = Nll_s \ . \tag{24}$$

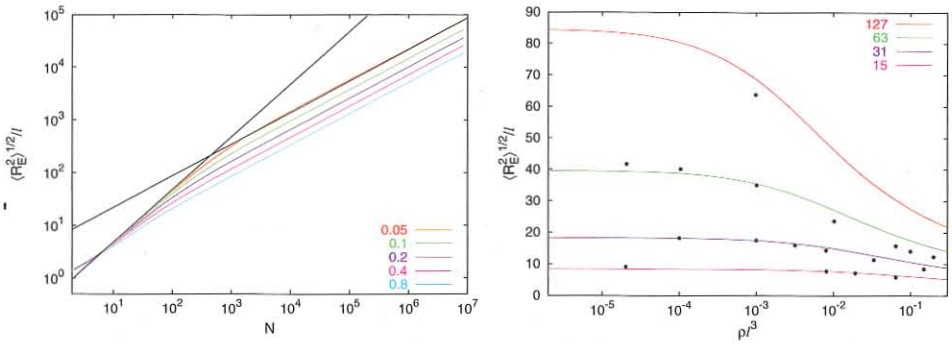


Fig. 3: *Root mean square end-to-end distance of flexible polyelectrolyte chains as a function of chain length for $l_B/l = 0.5$ (right). The Debye screening length decreases from top to bottom ($\kappa = 0.05$, 0.1, 0.2, 0.4, 0.8). The scaling regimes are given by $\sqrt{\langle R^2 \rangle} \sim N^\nu$, with $\nu = 1$ (straight line for small N) and $\nu \approx 0.6$ (straight line for large N). Density dependence of the root mean square end-to-end distance for the chain lengths $N = 127$, 63, 31, 15 (top to bottom) and $l_B/l = 0.833$ (left). Dots mark results form computer simulations of Ref. [11].*

Here we introduced the persistence length l_p

$$l_p = \frac{l}{2} \frac{1+t_T}{1-t_T} \tag{25}$$

and the Kuhn-segment length $l_s = 2l_p$. It is the persistence length, which is usually used to describe the conformational properties of a polyelectrolyte chain. For the semiflexible chain t_T determines all structural properties in a unique way. Aside from the mean square end-to-end distance t_T follows also from the orientational correlation function C_k among two bond vectors separated by k bonds along the chain

$$C_k = \langle \mathbf{R}_i \mathbf{R}_{i+k} \rangle / l^2 = t_T^k = e^{k \ln t_T} . \tag{26}$$

Thus, t_T can be determined in various ways using either global chain properties (mean square end-to-end distance) or local properties (correlation). This may no longer be true, if such quantities are calculate for a polyelectrolyte chain. Indeed, computer simulations demonstrate that C_k depends on the length (k) of the considered part in a non-exponential way. As a consequence we conclude, that the approximation scheme should not be over emphasized. The trial system is not able to capture all structural details of a polyelectrolyte chain. From the chosen ansatz, we may expect to obtain properties on the length scale of the radius of gyration or the root mean square end-to-end distance. In general, we should keep in mind that results obtained by variational methods or the Edwards-Singh method are only as good as the trial Hamiltonian.

In section 3.1, it is demonstrated that the typical dimension of a polyelectrolyte at infinite dilution increases linearly with the chain length. Using the perturbation approach, scaling relations at finite dilution are obtained. Figure 3 displays the dependencies of the root mean square end-to-end distance on chain length (left) and density (right). In

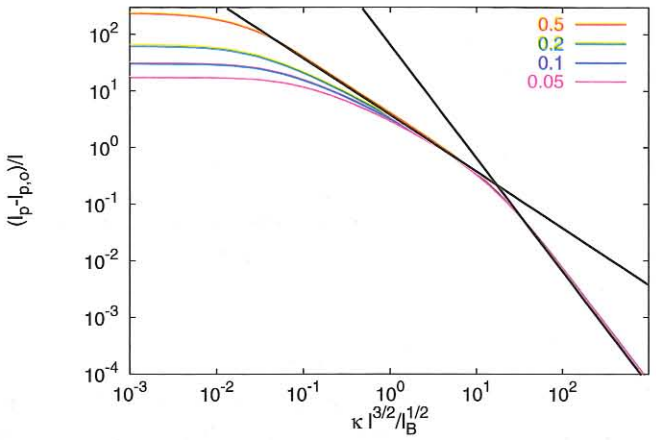


Fig. 4: *Electrostatic persistence length of a flexible polyelectrolyte chain as function of* $\kappa/\sqrt{l_B}$ *for the Bjerrum lengths* $l_B/l = 0.05, 0.1, 0.2, 0.5$ *(bottom to top). The chain length is* $N = 1000$ *and* $l_0/l = 1/2$. *The slopes of the straight lines are* -1 *and* -2, *respectively.*

the left plot the Debye screening length is varied keeping density constant. Two different scaling regimes are observed: For small N the mean square end-to-end distance increases proportional to N^2, corresponding to rodlike behavior. This is similar to the behavior for the unscreened Coulomb interaction of section 3.1. The rodlike regime is most pronounced for small κ. For large N the mean square end-to-end distance increases approximately like $N^{1.2}$, typical for a short range excluded volume interaction. With increasing N the chain length exceeds the screening length and the interaction becomes short ranged (Debye-Hückel potential). Thus, we obtain the universal $N^{1.2}$ dependence of short range interactions. With increasing κ the Coulomb interaction is more and more screened and the transition to short range behavior is found at smaller chain lengths. As depicted in the right part of Fig. 3, chains are expanded at low concentrations, and they contract with increasing concentration. The latter is a consequence of an increased screening by the more close by counterions at higher densities. The results of our perturbation theory are in excellent agreement with computer simulations [11, 20] as shown in Fig. 3. (Note, the simulations take explicitly into account the intermolecular excluded volume interaction, whereas the analytical approach considers the Debye-Hückel potential only. Thus we observe small deviations between the two results. Taking into account an effective fluid interaction, a much better agreement is achieved.)

Aside from the dependence of characteristic chain dimensions on the Bjerrum and screening length an intensively discussed issue is the characterization of a polyelectrolyte chain by a quantity like a persistence length. As mentioned in the introduction, the long range nature of the Coulomb interaction couples all length scales. Hence, it is a priory not obvious that a single quantity describes the conformational properties of a polyelectrolyte chain on all length scales like it is true, e.g., for semiflexible chains [18]. Computer simula-

tions indeed yield a correlation function C_k (cf. Eq. 26) which exhibits a non-exponential decay [21,22]. Nevertheless, in Ref. [22] it is demonstrated that various definitions of an effective persistence length provide an appropriate and definition independent characterization of a polyelectrolyte chain.

Already more than 20 years ago Odijk [23] and Skolnick & Fixman [24] calculated the contribution l_e of the Coulomb interaction to the persistence length of a rodlike semiflexible chain. Assuming only small deviations from a rodlike conformation and taking into account the Coulomb interaction by the Debye-Hückel potential they showed that the total persistence length can be written as $l_p = l_0 + l_e$. Here l_0 is the persistence length of the uncharged system[4] and l_e is given by

$$l_{\mathrm{OSF}} = \frac{1}{4}\frac{l_B}{\kappa^2 l^2} \tag{27}$$

in the OSF theory (the relation is explicitly derived in Appendix C). Experimentally this result has been confirmed for intrinsically very stiff polyelectrolytes like DNA [25]. Flexible polymers, however, exhibit a different dependence on the Debye screening length. Experimental findings generally point towards a linear relationship, i.e., $l_e \sim \kappa^{-1}$, for such chains [22,26]. The results of the outlined perturbation theory for a flexible chain ($l_0/l = 1/2$) are presented in Fig. 4. The Bjerrum length varies from $l_B/l = 0.05$ to 0.5 and the chain length is $N = 1000$. Within a certain range of screening parameters we find the experimentally observed dependence of the electrostatic persistence length $l_e \sim \kappa^{-1}$. For larger κ values a transition to a $l_e \sim \kappa^{-2}$ behavior is found. Previous calculations [27–30] yield the following approximate dependencies

$$l_e \sim \begin{cases} \frac{l_B}{\kappa^2 l^2}\,; & l_0 \gg l_{\mathrm{OSF}} \\ \sqrt{\frac{l_B}{l}}\frac{1}{\kappa}\,; & l_0 < l_{\mathrm{OSF}} \end{cases} \tag{28}$$

for $l_0 l_B/l^2 \sim \mathcal{O}(1)$, in agreement with the numerical results. In the limit $l_0 l_B \ll l^2$ another behavior is predicted theoretically [29,31–33]. Very long ($Nl\kappa \gg 1$) polyelectrolyte chains exhibit Gaussian (or self avoiding walk) properties on small length scales. On an intermediate length scale the chains are linearly stretched and can be considered as a sequences of Gaussian blobs (persistent regime). Finally, at large lengths the chains are isotropically swollen, because of a short range type interaction among the blobs. The persistence length in the persistent regime is of OSF type, i.e., $l_e \sim \kappa^{-2}$, because the blobs align in a rodlike manner.

4 Structure of Polyelectrolyte Solutions

Aside from the conformational properties of a polyelectrolyte chain, the structure of a polyelectrolyte solution is accessible by scattering experiments [4] . From the theoretical side computer simulations and liquid state theory provide valuable structural information [11,34,36]. In addition, the Poisson-Boltzmann equation is sometimes used, combined with a cell geometry for a rodlike polymer [37].

[4] In analogy to Eq. (25) l_0 is defined as $l_0 = l(1+t)/(2(1-t))$.

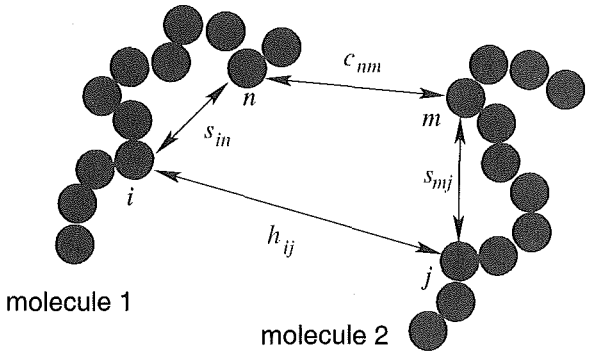


Fig. 5: *Contribution of the direct correlation function c and intramolecular distribution function s to the total correlation function h in a molecular system.*

Of particular interest is the distribution of counterions with respect to a polyelectrolyte chain. The distribution depends significantly on the interaction strength among the charged units. Considering the Bjerrum length $l_B = e^2/(k_B T\epsilon)$, the interaction strength is varied by changing the temperature and/or the solvent (dielectric constant). In addition, counterions can be replaced by counterions of a larger or smaller valency. For sufficiently large interaction strengths – we will later on provide a more quantitative criterion – the counterions start to condense on the polymer chain (**counterion condensation**). Hence, the charges of the macroion are partially neutralized and the conformations may change severely. Ultimately a collapse of a flexible chain is observed experimentally and confirmed by computer simulations [11, 12] and theory.

4.1 PRISM and model

To qualitatively and quantitatively understand the structure of a solution we will provide a few results of a liquid state theory approach and also experimental results.

For the theoretical description, we adopt the *Polymer Reference Interaction Site Model* (PRISM) [16], which is based on the Ornstein-Zernike integral equation theory[5] [13] for molecular systems and relates the total correlation function $h(r) = g(r) - 1$, where $g(r)$ is the pair correlation function, with the direct correlation function $c(r)$ and the intramolecular correlation function ω_{ij} of two sites (i, j) of a molecule. In the atomic case the total correlation function between two particles is the sum of all possible paths of direct correlations that propagate via all possible intermediate particles. In a molecular system there are in addition intramolecular correlations. The intramolecular correlations originate from various sources like for example two, three, or even higher order many body interactions. Hence, they cannot simply be described by pair potentials. Nevertheless, a expression for the total correlation function between two sites of two molecules can be derived similar to

[5]For more details on the Ornstein-Zernike equation see chapter B16 by G. Nägele.

the total correlation function between two sites of an atomic system by introducing the intramolecular correlation function ω_{ij} of a site i and j of the same molecule [13]:

$$\omega_{ij}(\mathbf{r}_i, \mathbf{r}_j) = \delta_{ij}\delta(\mathbf{r}_i - \mathbf{r}_j) + s_{ij}(\mathbf{r}_i, \mathbf{r}_j) \,. \tag{29}$$

The total correlation function between site i of a molecule 1 and site j of a molecule 2 is then

$$\begin{aligned} h_{ij}(\mathbf{r}_{1i}, \mathbf{r}_{2j}) &= \sum_{nm} \int \omega_{in}(\mathbf{r}_{1i}, \mathbf{r}_{1n}) c_{nm}(\mathbf{r}_{1n}, \mathbf{r}_{2m}) \omega_{mj}(\mathbf{r}_{2m}, \mathbf{r}_{2j}) \, d^3x_{1n} d^3x_{2m} \\ &+ \rho \sum_{nm} \int c_{in}(\mathbf{r}_{1i}, \mathbf{r}_{3n}) \omega_{nm}(\mathbf{r}_{3n}, \mathbf{r}_{3m}) h_{mj}(\mathbf{r}_{3m}, \mathbf{r}_{2j}) \, d^3x_{3n} d^3x_{3m} \,. \end{aligned} \tag{30}$$

ρ is the density of monomers. The first term on the right-hand side is illustrated in Fig. 5. The second term comprises contributions from more and more molecules. Equation (30) may be considered as definition equation for the direct and intramolecular correlation function. To solve the integral equation additional equations have to be provided. The direct correlation function is usually determined via a so called closure relation (see below). For the evaluation of the intramolecular correlation function additional approximations are applied and s_{ij} is replaced by the intramolecular distribution function for the two sites. Given these relations, the direct correlation function can by determined in principle. However, Eq. (30) constitutes a set of equations including every pair of monomers between two molecules. For long chains the number of equations is quite large and the calculation of the total correlation functions very time consuming. To reduce the numerical effort the following assumptions are incorporated:

- all sites of a chain are equal
- chain end effects are neglected
- the correlation between two sites depends on their separation only and not on their absolute positions on a polymer.

As a result, identical equations for all the monomer pairs are obtained and the original set of equations reduces to a single equation.

Since a polyelectrolyte solution contains macroions and counterions, i.e., it is a multicomponent system, the equation for the total correlation function for the monomers has to be complimented by equations including counterions. For the considered primitive model (see Fig. 1) of a binary system three different correlation functions are relevant: the monomer-monomer (g_{mm}), the counterion-counterion (g_{cc}), and the monomer-counterion (g_{mc}) correlation function. Within the above approximations the following set of equations is then obtained in Fourier space:

$$h_{mm}(k) = \omega(k) c_{mm}(k) \omega(k) + \rho\omega(k) \left[c_{mm}(k) h_{mm}(k) + c_{mc}(k) h_{mc}(k) \right] \,, \tag{31}$$

$$h_{mc}(k) = \omega(k) c_{mc}(k) + \rho\omega(k) \left[c_{mm}(k) h_{mc}(k) + c_{mc}(k) h_{cc}(k) \right] \,, \tag{32}$$

$$h_{cc}(k) = c_{cc}(k) + \rho \left[c_{mc}(k) h_{mc}(k) + c_{cc}(k) h_{cc}(k) \right] \,. \tag{33}$$

Since we restrict ourselves to a homogeneous system only the magnitude (k) of the wave vector appears. ρ is the number density of counterions (or, equivalently, the sites on the

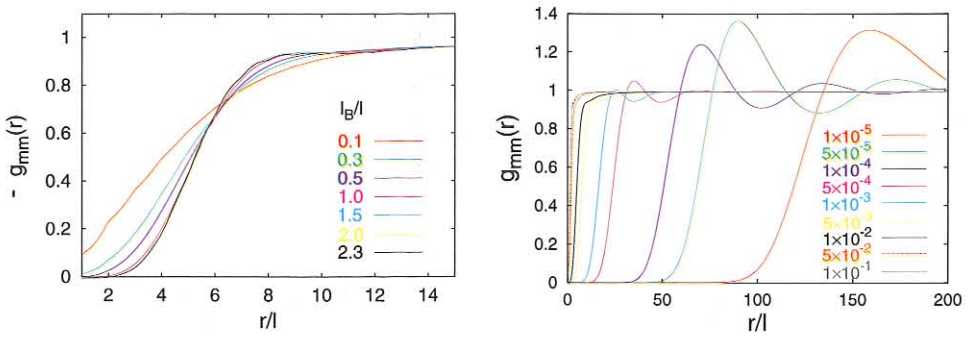


Fig. 6: *Monomer-monomer pair correlation function $g_{mm}(r)$ for various Bjerrum lengths (left) and densities (right). Other parameters are: Chain length $N = 80$, density $\eta = 10^{-2}$ (right), and Bjerrum length $l_B/l = 0.6$ (left).*

chains), and $\omega(k)$ is the structure factor of a molecule. To solve the PRISM equations closure relations are required. A variety of closures have been proposed in the literature but most of them turn out to be inadequate for polyelectrolyte systems. As has been shown, the *Reference-Laria-Wu-Chandler Closure* (RLWC) [14, 35]

$$\omega_\alpha(r) * c_{\alpha\gamma}(r) * \omega_\gamma(r) = \omega_\alpha(r) * c_{0,\alpha\gamma}(r) * \omega_\gamma(r)$$
$$-\omega_\alpha(r) * \beta v(r) * \omega_\gamma(r) + h_{\alpha\gamma}(r) - h_{0,\alpha\gamma}(r) - \ln\left(\frac{g_{\alpha\gamma}(r)}{g_{0,\alpha\gamma}(r)}\right) \; ; \quad \alpha, \gamma \in \{m, c\} \quad (34)$$

provides an excellent description of polyelectrolyte systems [36]. The index 0 denotes reference functions obtained for pure hard core systems of the same densities with the Percus-Yevick (PY) closure [13] and the asterisk denotes convolution integrals. It should be noted that in our notation $\omega_m(k) = \omega(k)$ and $\omega_c(k) = 1$. The set of coupled integral equations together with the appropriate closures is solved iteratively by a Picard iteration scheme [13].

4.2 Results for rodlike polyelectrolytes

As an example a few results are presented for rodlike polyelectrolytes in solution. The macroions are modelled as a sequence of N touching charged hard spheres of diameter l (see Fig. 8). The counterions, which are taken into account explicitly, are also considered hard spheres of the same diameter. Since the overall system is neutral, the density of monomers ρ_m and counterions ρ_c are equal for the considered monovalent counterions and single charged monomers. Hence, I will use $\rho = \rho_m = \rho_c$ in the following. The solvent is treated in a mean-field manner and described as a homogeneous dielectric continuum with the dielectric constant ϵ. The pair interaction potential for all ionic species is given by the hard core potential $v_{ij}^{HC}(r)$ and the Coulomb potential, hence

$$\beta v_{ij}(r) = \beta v_{ij}^{HC}(r) - \frac{l_B}{r} \; ; \quad i, j \in \{m, c\} \, . \quad (35)$$

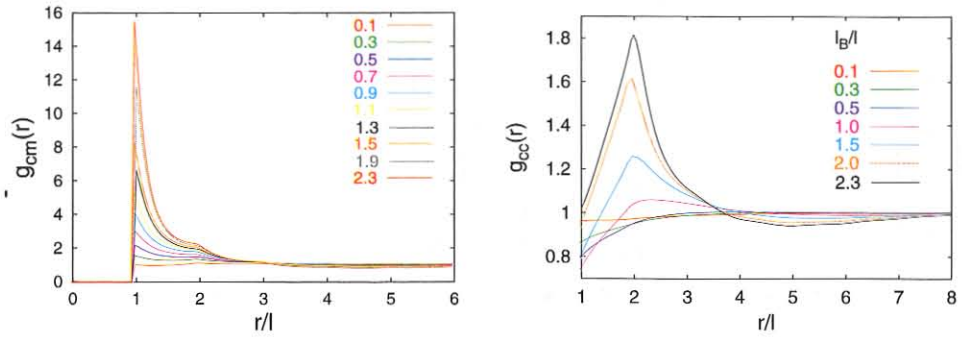


Fig. 7: *Monomer-counterion (left) and counterion-counterion (right) pair correlation function for various Bjerrum lengths. The chain length is* $N = 80$ *and the density is* $\eta = 10^{-2}$.

The advantage of rodlike polyelectrolytes is that the structure factor is known:

$$\omega(k) = 1 + \frac{2}{N} \sum_{j=1}^{N-1} (N-j) \frac{\sin(jkl)}{jkl} \,. \tag{36}$$

For semiflexible chains, the structure factor has to be determined selfconsistently because the conformations of such chains depend upon the the interaction strength and density.

Polyelectrolyte solutions exhibit liquid-like order in dilute solutions which diminishes as the concentration increases. This is reflected in Fig. 6 (right). At infinite dilution $g_{mm}(r)$ has a value close to zero at small separations and monotonically increases to its asymptotic value of one at larger separations. At low concentrations a peak appears on the length scale of the order of the size of the molecules. As the concentration is increased further the liquid-like order first becomes more pronounced and then disappears at sufficiently high concentrations. At even higher concentrations liquid-like order appears on the length scale of the order of the size of the beads. For a fixed density, the ordering increases with increasing interaction strength (cf. Fig. 6 (left)). At very low interaction strengths the liquid-like structure is mainly determined by the hard core interaction. With increasing l_B/l the equally charged monomers repel each other and g_{mm} decreases at small distances. At the same time the structure becomes more pronounced. The characteristic peak, however, remains approximately at the same position. Thus, the characteristic length scales of the structures are mainly determined by the density. The emerging picture is similar to the behavior of simple hard sphere liquids at moderate densities.

The distribution of counterions adjacent to a monomer is captured in the monomer-counterion distribution function g_{cm} (cf. Fig. 7 (left)). For small interaction strengths ($l_B/l \ll 1$) g_{cm} is almost constant with a value of about one for all r. Hence, the local counterion density matches the bulk density almost everywhere, i.e., the counterions are distributed homogeneously over the whole system. With increasing Bjerrum length an increasing peak appears at $r = l$ and a much smaller peak at $r = 2l$. Thus, the counterions are no longer homogeneously distributed, but found more likely in the vicinity of a chain.

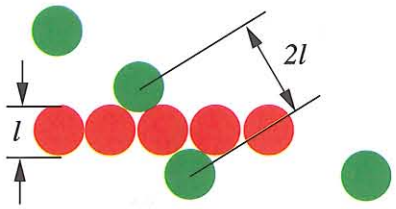


Fig. 8: *Location of the counterions condensed at the polyelectrolyte rod which yield the peak at $r/l = 2$ of the counterion-counterion pair correlation function.*

The strong increase of the counterion density next to a macroion reflects counterion condensation.

The counterion-counterion correlation function provides deeper insight into the issue of counterion condensation. As is obvious from Fig. 7 (right), g_{cc} indicates a homogeneous distribution of the counterions for small interaction strengths. With increasing l_B/l the equally charged ions repel each other and g_{cc} decreases at small distances ($r \lesssim 3l$). Beyond a certain interaction strength the trend reverts and a peak appears at $r = 2l$. The height of the peak increases with increasing l_B. This is the manifestation of counterion condensation. For l_B below the critical Bjerrum length for counterion condensation, an increase of l_B results in a stronger repulsion of the counterions. When the Bjerrum length crosses the critical value for Manning condensation, the counterions are attracted by the polyion and start to condensate on the chain, which is accompanied by a decrease of the mean separation between ions. Hence, despite the repulsive Coulomb interaction the counterions are, for sufficiently strong interactions, subject to an effective attractive potential next to a polymer chain. The position of the peak at $r = 2l$ is quite simple to explain if we consider the configuration with lowest energy. The electrostatic interaction forces the condensed ions to be as close to a monomer as possible but at the same time as far apart as possible from each other. This is achieved, if the counterions are located at opposite sides of the chain monomers (see Fig. 8).

Further insight into the consequences of counterion condensation is gained by an effective monomer-monomer and counterion-counterion potential. The idea is to reduce the multicomponent system (macromolecules + counterions) to effective one-component systems (macromolecules or counterions, respectively). We define the simplified model in such a way that the effective potential between the counterions or monomers, respectively, of the new system yields exactly the same correlation function (g_{cc}, g_{mm}) as found in the multicomponent case at the same density. Starting from the correlation function g_{cc} – respectively g_{mm} – of the multicomponent model we calculate an effective direct correlation function c_{eff} via the one-component Ornstein-Zernike equation. An effective potential is then obtained from the RLWC closures of the one- and multicomponent models [34]. For low and moderate densities the effective potential is well approximated by

$$\beta v_{\alpha\alpha,\text{eff}}(r) = \beta v_{\alpha\alpha}(r) + (c_{\alpha\alpha}(r) - c_{\alpha\alpha,\text{eff}}(r)) \ , \tag{37}$$

where $\alpha \in \{m, c\}$. Hence, the effective potential is equal to the bare potential plus a

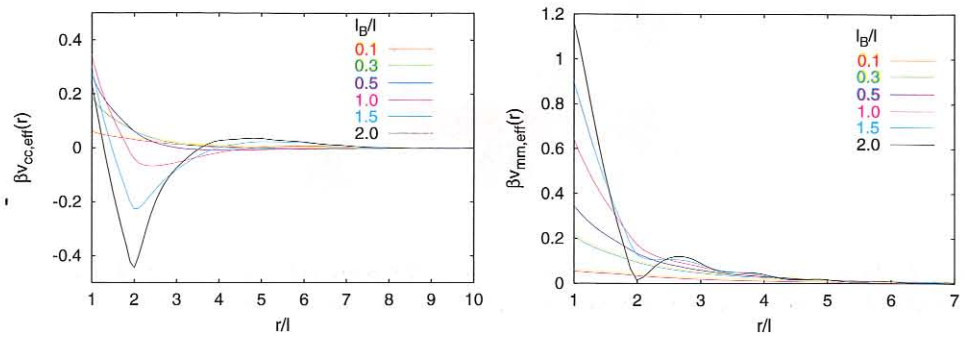


Fig. 9: *Effective potential between two counterions (left) and two monomers (right), respectively for various Bjerrum lengths l_B. The chain length is $N = 80$ and the density $\eta = 10^{-2}$.*

modification given by the correlation functions of the multicomponent and one-component model[6]. Figure 9 depicts the effective counterion (left) and monomer (right) potential, respectively. The effective counterion potential is purely repulsive for low values of l_B and can very well be approximated by the bare Coulomb potential. With increasing Bjerrum length the potential becomes negative for distances larger than a certain critical distance leading to an attractive force between two counterions. For even larger values of l_B, the effective potential exhibits a distinct minimum at a distance of about $r = 2l$ in agreement with the position of the peak in g_{cc}. Similar to the counterion-counterion potential, we observe a minimum in the effective monomer-monomer potential (Fig. 9 (right)) at $r \approx 2l$ for Bjerrum lengths $l_B \gtrsim 1.5l$. Hence, the monomers attract each other at large interaction strengths and small distances. The distance of $r \approx 2l$ indicates that the attraction is counterion mediated and that precisely one counterion is located between two monomers. Moreover, the effective potential is a monotonous decreasing function for $r > 2l$ in agreement with the Debye-Hückel approximation. For $r < 2l$ we find deviations from the Debye-Hückel potential due to the depletion interaction. At high Bjerrum lengths ($l_B > l$) the effective potential still decays in the average as predicted by the Debye-Hückel model. The quantitative comparison between our calculations and the Debye-Hückel potential exhibits excellent agreement for the screening length dependence as well as the dependence on the interaction strength. The deviations from the Debye-Hückel representation of the interaction among the monomers is not surprising. The condensation of the counterions leads to a screening of the Coulomb interaction which is not captured by the Debye-Hückel approximation.

Given the total correlation functions other quantities like the partial structure factors or thermodynamic quantities like the pressure can be calculated. To demonstrate the usefulness of the PRISM approach, I will compare the monomer-monomer structure factor (S_{mm}) with scattering measurements on tobacco mosaic virus (TMV) solutions [40]. The

[6]The effective potential is different from the potential of mean force [13]. The potential of mean force $\bar{V}$ is directly related with the pair correlation function $g(r) = \exp(-\beta\bar{V})$, whereas the effective potential is determined by the closure relation.

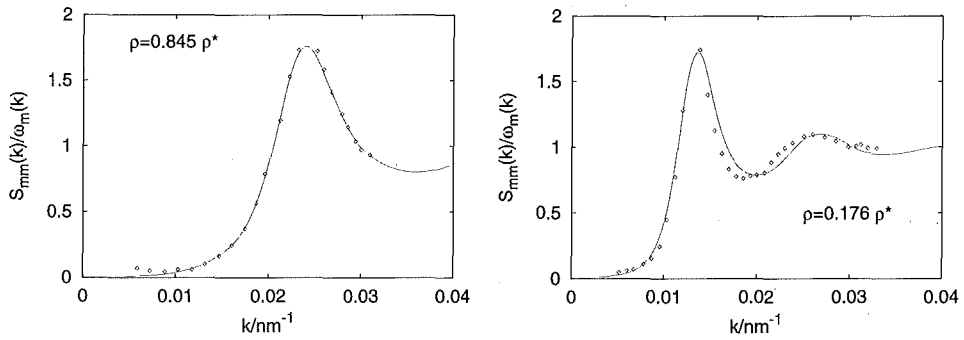


Fig. 10: *Comparison of theoretical predictions for the S_{mm}/ω_m to experimental data of TMV solutions [14, 40] for various concentrations. The fitted charges of the TMV molecules are $Q = 125e$ (left) and $Q = 195e$ (right).*

structure factor S_{mm} follows from the relation $S_{mm} = \omega(k) + \rho_m h_{mm}(k)$. The length and diameter of the rodlike TWV particles are 300 nm and 18 nm, respectively. Figure 10 compares theoretical predictions to experimental data for various concentrations. The solid lines are theoretical results for $N = 200$ and $l = 18$ nm. Since the total charge of a TMV particle is not known, it has been determined by matching the height of the first peak of the theoretical predictions with the experimental data. As is obvious from the figure, the theory describes the experimental data qualitatively and quantitatively very well. Moreover, the position of the first peak in S_{mm}/ω depends on density. There are two characteristic scaling regimes. In the dilute regime, if one assumes that the charged particles uniformly occupy space due to their repulsion, the mean particle distance is $\Delta r \approx \rho^{-1/3}$. Since the peak in S_{mm}/ω is related to the mean separation of the molecules, the relation $k_{\max} \sim \rho^{1/3}$ is obtained. At the critical density[7] $\rho^* = N/V^* \sim N^{-2}$ the correlation length among the rods is $\xi = N$. Using scaling ideas [41], the correlation length in the semidilute regime depends on density according to $\xi = N\,(\rho/\rho^*)^{\nu}$. Due to chain overlap, the correlation length is independent of chain length. Hence $k_{\max} \sim 1/\xi \sim \rho^{1/2}$. These arguments suggest that a power law is obtained for the position of the maximum of the peak of the structure factor as a function of density ($k_{\max} \sim \rho^{\nu}$) with the exponents $\nu = 1/3$ and $1/2$ in the dilute and semidilute regime, respectively. This is consistent with experimental results and is also found by the presented PRISM approach [14].

Sofar I discussed systems of charged macromolecules and counterions. In addition, other kind of charges can be present. Typical in, e.g., biological systems, is the presence of salt like NaCl. The additional charges lead to a screening of the bare Coulomb interaction. Hence, the structure observed in salt-free solution will be decreased considerably. The influence of salt is well captured within the Debye-Hückel approximation by the screening length κ^{-1} (Eq. (10)). The charge density of the salt components have simply to be added, which will result in a smaller screening length as compared to the salt-free case.

[7] Rodlike molecules overlap, when the spheres with diameter of their length touch each other.

5 Counterion Condensation

In the last section I introduced the phenomenon of counterion condensation. This issue will now be addressed in more detail.

The terminology *counterion condensation* was already introduced in the 60s of the last century [42, 43] and refers to drastic changes in the behavior of counterions when the interaction strength exceeds a critical value.

For illustrative purposes we will consider an infinite long and infinitely thin charged rod, i.e., an infinite line charge (cf. Fig. 11). The charge density of the rod is $\rho_l = e/l$. The potential of the line charge is obtained from the Poisson equation with the charge density $\rho_R = \rho_l \delta(x)\delta(y)$, if we consider the rod located in the origin of the reference system and pointing along the z-axis. Because of the translational symmetry along the z-axis, it is sufficient to solve the two-dimensional Poisson equation, which yields the result

$$\phi_R(r) = -\frac{2e}{l\epsilon} \ln r \,, \tag{38}$$

where $r = \sqrt{x^2 + y^2}$. The partition function of a single charge in front of the line charge is given by

$$Z_R \sim \int_0^{\rho_0} \exp\left(-(l_B/l) \ln r\right) 2\pi r \, dr = \int_0^{\rho_0} r^{1-2l_b/l} \, dr \,. \tag{39}$$

(The distance ρ_0 is chosen in such a way that other counterions are exclude, i.e., a very dilute system is considered and interactions among the counterions are neglected.) The integral of Eq. (39) diverges at the lower limit for $1 - 2l_B/l \leq 1$ or

$$l_B \geq l \,. \tag{40}$$

The physical interpretation of the divergence is that systems characterized by such values are unstable. Sufficiently many counterions will condense on the line charge to reduce the interaction strength $l_B/l > 1$ to a value just less than one [43]. This is called counterion condensation. The critical value $l_B = l$ is obtained for an infinitely thin line charge at any concentration. For a rod of finite thickness Eq. (40) is valid only in the limit of zero concentration [43].

Considering the results of section 4, we indeed find qualitative changes in the behavior of the counterions for interaction strengths $l_B/l \gtrsim 1$. To determine a critical interaction strength l_B/l for a system at finite density and flexible chains is difficult. The major problem is to separate condensed from non-condensed ions. Various criteria have been applied. Based upon the counterion-counterion correlation function we considered all counterions within a certain distance from each other as condensed [34]. In Ref. [37] the counterion distribution of an infinite rod has been investigated within the cell model by the Poisson-Boltzmann theory and computer simulations. The authors suggest to use the inflection point of the probability distribution of counterions transverse to the rod axis to separate condensed form non-condensed ions. The idea is intriguing but the criterion is difficult to apply in an three-dimensional system.



Fig. 11: *Counterion in front of a line charge (left). Counterion arrangement in the low temperature limit on two charged rods (right).*

Valuable insight into the phenomenon of counterion condensation is obtained by computer simulations (molecular dynamics simulations, Monte Carlo simulations). By solving the Langevin equation

$$m\ddot{\mathbf{r}} = \mathbf{F} - m\gamma\dot{\mathbf{r}} + \mathbf{\Gamma} \tag{41}$$

we studied the conformational properties and the counterion distribution of individual flexible polyelectrolyte chains [12]. The force $\mathbf{F}$ comprises contributions from the bond length potential (harmonic potential), intramolecular as well as inter-particle excluded volume potentials (Lennard-Jones potential), and the Coulomb interaction. The stochastic force $\mathbf{\Gamma}$ is assumed to be stationary, random, and Gaussian (white noise)

$$\langle \mathbf{\Gamma}(t) \rangle = 0\,, \tag{42}$$

$$\langle \mathbf{\Gamma}(t)\mathbf{\Gamma}(t') \rangle = 6k_B T m\gamma\delta(t-t')\,, \tag{43}$$

with T the temperature of the system and γ the damping constant [38]. This type of equation keeps the temperature fixed rather than the energy and produces canonical time averages. The system is placed in a cubic box and periodic boundary conditions are applied. The long range Coulomb interaction in the infinite periodic system is taken into account by the Ewald sum [39]. The size of the periodic system is readjusted to yield the same density for any considered chain length.

Figure 12 displays the radius of gyration as a function of the interaction strength and for various chain lengths. For zero charges, the conformations of a chain in good solvent are found. Here only the short range excluded volume interaction is relevant. For non-zero charges the chains elongate with increasing interaction strength. The maximum extension is reached close to the interaction strength where Manning condensation occurs. For the simulated systems the critical Bjerrum length is in the vicinity of $l_B/l \approx 1.2$. For larger l_B the ions condense on the chain resulting in a decrease of chain dimension by screening of the bare Coulomb interaction. For very large interaction strengths $l_B/l \gtrsim 10$ ion pairs are formed, which leads to an attractive intramolecular interaction and a collapse of the whole structure into a dense globular state (see Fig. 13). For the considered system, the radius of gyration in the collapsed state is even smaller than for a neutral chain in

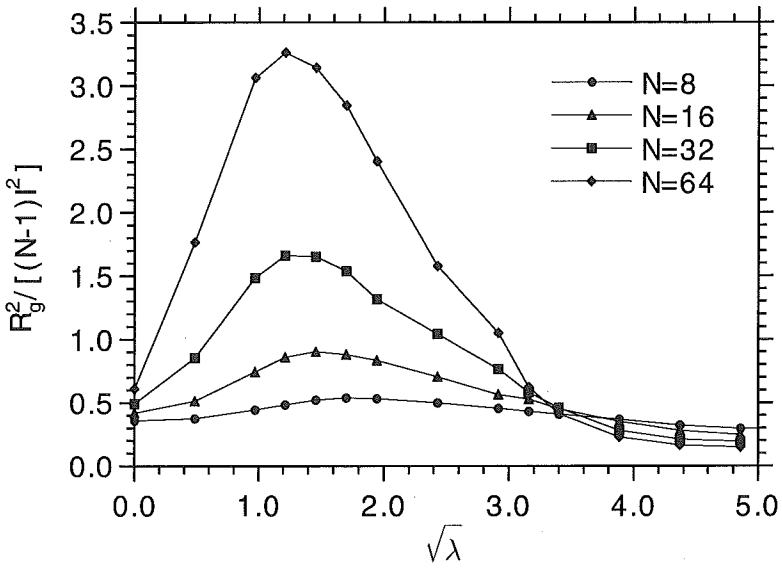


Fig. 12: *Squared radius of gyration divided by the number of bonds as a function of the square root of the interaction strength* $\lambda = 1.2l_B/l$ *for various chain lengths* N.

good solvent. As simulations with other counterion-monomer radii ratios show, this does not hold for all ratios. Instead, we find flexible ring-like structures for counterions much smaller than a monomer.

Figure 13 depicts snapshots of chain conformations at various interaction strengths. For zero charges, the conformations of a chain in good solvent are found (top left snapshot of Fig. 13). The top right snapshot corresponds to a chain close to its maximum extension. In the bottom left snapshot almost all counterions are condensed on the chain leading to flexible chain behavior. Finally, at large interaction strengths compact globular structures are obtained. The condensation of counterions leads to ion-pair formation. The resulting dipole moments of the various pairs are the origin of an intramolecular attraction and the formation of compact structures.

As a consequence of counterion condensation, rodlike macroions attract each other in solutions as we found by the PRISM approach. Computer simulations of two charged rods yield similar results [44]. Considering two parallel uniformly charged rods the authors find a short range attractive mean force for multivalent ions and a sufficiently large charge density of a rod. Form the simulation the distribution of the condensed counterions is inferred. At low temperatures (ground state) the origin of the attraction is the formation of two interlocking structures, resembling Wigner crystals, arranged around the two cylinders (see Fig. 11). In the low temperature limit, electrostatic attraction is always encountered, independent of the valency of the counterions. This simply reflects a general feature of the electrostatics of charged particles. With increasing temperature, the two Wigner crystals lose long range positional order, but short range order survives

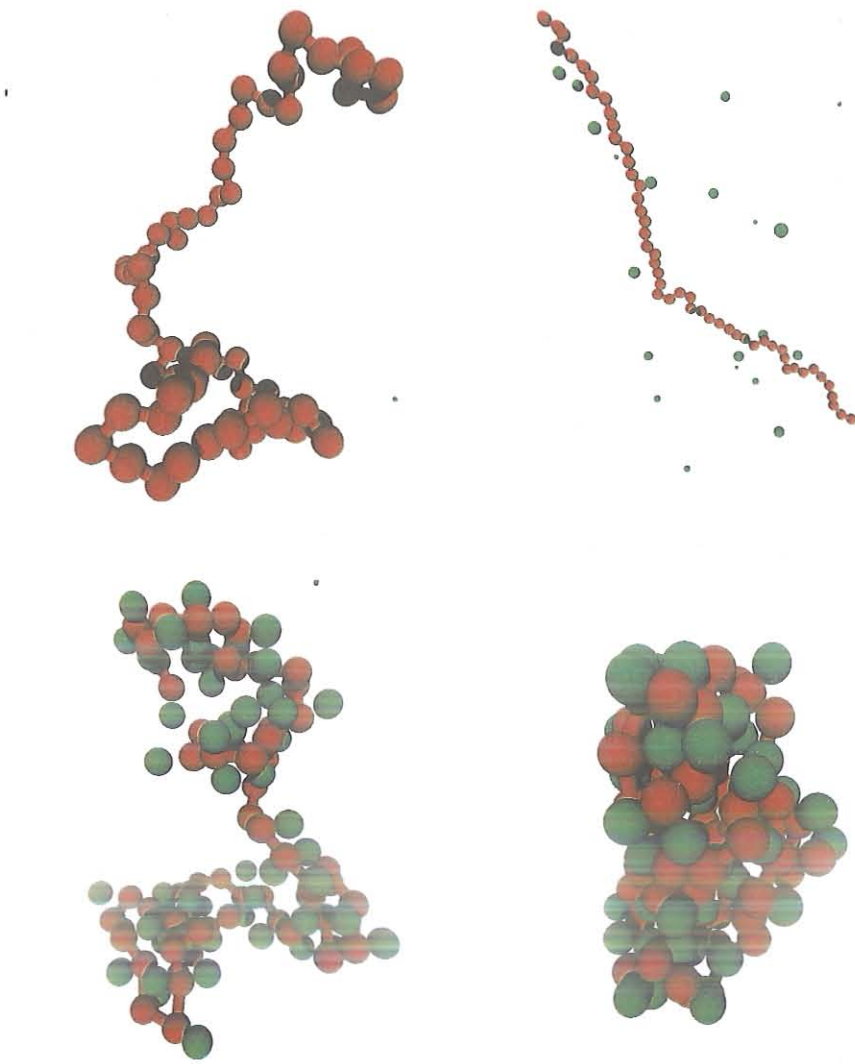


Fig. 13: *Snapshots of polyelectrolyte macromolecules for the interaction strengths* $l_B/l = 0$ *(top left),* $l_B/l = 1.3$ *(top right),* $l_B/l = 9.7$ *(bottom left), and* $l_B/l = 19.7$ *(bottom right). Counterions are colored green.*

up to high temperatures. The attraction at finite temperature may be attributed to this residual positional order, which is correlated for small rod diameters [44]. The general observations of the simulations agree with the results of the PRISM approach. However, in the considered isotropic and homogeneous solutions rods are not parallel in general. Although there are correlations among the counterions in the solution, I do not expect even short range order. In contrast, the presence of attractive force in solutions suggests that already liquid-like order is sufficient for attraction.

Another aspect of charged systems is the possibility of overcharging. Colloids, macromolecules, and charged surfaces are able to carry more charges than necessary to compensate the electrostatic charge. The amount of extra charge depends on various parameters like size ratio between colloid and counterions or the total charge of a colloid. Overcharging spherical or rodlike colloids by, e.g., counterions is possible due to correlations among the adsorbed particles (not included in the Poisson-Boltzmann theory). In the ground state (zero temperature) the smaller ions arrange themselves in the energetically most favorable state. As far as the number of adsorbed particles allows it, a Wigner crystal like state is assumed [50]. Adsorption of a polymer chain can lead to an even stronger overcharging. Depending on the interaction strength (e.g. on temperature) and chain length other interesting phenomena can be observed for polymers next to spherical colloids. For example, a polymer chain is adsorbed if its length exceeds a certain value and pushed apart form the surface if its length exceeds a second value. The latter is caused by the repulsive intramolecular Coulomb interaction. There are other aspects of charged colloid-polymer mixtures which have not been discovered yet and may proof useful in technical applications.

6 Polyelectrolyte in Poor Solvent

Usually polyelectrolytes are dissolved in water. However, water is a poor solvent for many polymers. Thus the monomers try to avoid water contacts in favor of monomer-monomer contacts and collapse into spherical globules (cf. Fig. 14). The monomer density ρ inside this globule is determined by the balance of the two-body attraction ($-\tau l^3 N\rho$), where $\tau = (T_\theta - T)/T_\theta$ (T_θ: θ-temperature), and the three-body repulsion ($l^3 N\rho^2$). Hence, the size R of the globule with density ρ is equal to $R \approx (N/\rho)^{1/3} \approx l(N/\tau)^{1/3}$. Polyelectrolytes are solvable in water due to their charges. If only a fraction of the monomers of a polyelectrolyte are charged, there is a competition between the intramolecular Coulomb repulsion and the hydrophobicity of a chain. The question is then what kind of structures are assumed in a poor solvent.

The problem of the shape of a charged globule is similar to the classical problem of the instability of a charge droplet, considered by Rayleigh [45]. He showed that a spherical droplet with radius R and charge $Q > e(\gamma R^3/(k_B T l_B))^{1/2}$ (where γ is the surface tension) is locally unstable and will spontaneously deform. The equilibrium state of this system is a set of smaller droplets with the charge on each of them lower than the critical one and placed at an infinite distance from each other. This final state is impossible for the charged polymer because of the existing chemical bonds. In this case the system can reduce its energy by splitting into a set of smaller charged globules connected by narrow strings the so called necklace globule [46–48].

Consider a chain with charge fraction f, i.e., fN monomers of the chain are charged. The globular state of the chain can by considered as assembly of thermal blobs each of size ξ_T, the size of density fluctuations (see Fig. 14). The surface tension γ of the globule is of order $k_B T$ per thermal blob at the globular surface, hence $\gamma \approx k_B T \xi_T^{-2}$. If the Coulomb energy $F_C \approx e^2 f^2 N^2/(\epsilon R)$, which is repulsive, becomes comparable to the surface energy $F_S \approx k_B T R^2/\xi_T^{-2}$, the total energy of the globule can be lowered either by elongating it into a cylinder or by splitting it into an assembly of smaller globules connected by narrow strings. The deformation occurs when $F_C \gtrsim F_S$, or when fN becomes larger than $(N\tau l/l_B)^{1/2}$, which is identical to the above Rayleigh criterium.

The size of the cylinder can be found by optimizing the sum of the surface energy $F_{SC} \approx k_B T L_{\rm cyl} D/\xi_T^2$ and Coulomb energy $F_{CC} \approx k_B T l_B (fN)^2/L_{\rm cyl}$ at a fixed volume $L_{\rm cyl} D^2 \approx R^3$. The minimization of the cylinder free energy $F_{\rm cyl} = F_{SC} + F_{CC}$ yields the cylinder length and cylinder diameter [49]

$$L_{\rm cyl} \approx \frac{lN}{\tau}\left(\frac{l_B f^2}{l}\right)^{2/3}, \tag{44}$$

$$D \approx l\left(\frac{l}{l_B f^2}\right)^{1/3}. \tag{45}$$

Thus, the deformation sensitive part of the free energy of the cylindrical globule is

$$\frac{F_{\rm cyl}}{k_B T} \approx \frac{l_B f^2 N^2}{L_{\rm cyl}} \approx \tau N\left(\frac{l_B f^2}{l}\right)^{1/3}. \tag{46}$$

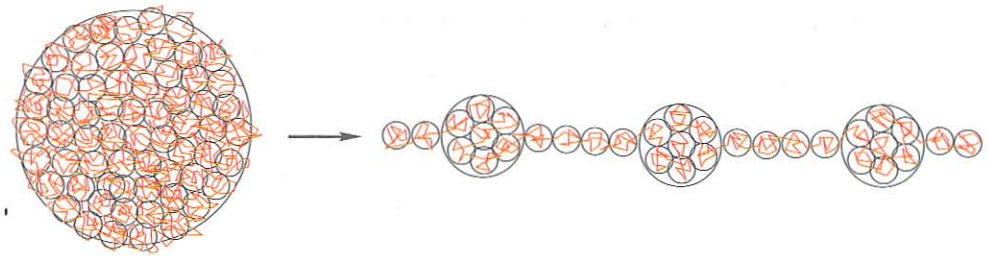


Fig. 14: *Spherical globule (left) and a necklace globule (right).*

This equations holds as long as the thermal blob size ξ_T is smaller than the width of the cylinder D (for $\tau > (l_B f^2/l)^{1/3}$).

To calculate the free energy of a necklace globule, the model of Fig.14 (right) is considered. For a necklace of $N_{\rm bead}$ beads of $m_{\rm bead}$ monomers in each ($d_{\rm bead} \approx l\tau^{-1/3} m_{\rm bead}^{1/3}$) joined by $N_{\rm bead}-1$ cylindrical strings (of blobs) of length $l_{\rm str}$ and blob diameter $d_{\rm str}$ containing $m_{\rm str}$ monomers each ($m_{\rm str} \approx \rho l_{\rm str} d_{\rm str}^2 \approx \tau l_{\rm str} d_{\rm str}^2/l^3$) the free energy $F_{\rm nec}$ is approximately given by

$$\frac{F_{\rm nec}}{k_BT} \approx N_{\rm bead}\left[\frac{l_B f^2 m_{\rm bead}^2}{d_{\rm bead}} + \frac{d_{\rm bead}^2}{\xi_T^2}\right] + (N_{\rm bead}-1)\left[\frac{l_B f^2 m_{\rm str}^2}{l_{\rm str}} + \frac{l_{\rm str} d_{\rm str}}{\xi_T^2}\right] + \frac{l_B f^2 N^2}{L_{\rm nec}}\,, \quad (47)$$

where $L_{\rm nec} = (N_{\rm bead}-1)l_{\rm str} + N_{\rm bead} d_{\rm bead}$ is the total length of the necklace. The first two terms in brackets are the electrostatic self-energy and surface energy of the beads. The second two terms in brackets are the electrostatic self-energy and surface energy of the strings. The last term is the electrostatic repulsion between different beads and strings. The electrostatic self-energy of a string is by a factor of $(d_{\rm str}/D)^3$ smaller than its surface energy. Since necklaces with narrow strings are considered, this contribution to the free energy can be neglected. The total number of monomers in all beads and strings has to be equal to the degree of polymerization N of the chain. Thus, the constraint

$$N_{\rm bead} m_{\rm bead} + (N_{\rm bead}-1) m_{\rm str} = N_{\rm bead} m_{\rm bead} + M_{\rm str} = N \quad (48)$$

has to be taken into account, where the parameter $M_{\rm str} = (N_{\rm bead}-1)m_{\rm str}$ is introduce. The free energy of the necklace in the limit of a string much longer than a bead ($l_{\rm str} \gg d_{\rm bead}$) is

$$\frac{F_{\rm nec}}{k_BT} \approx \frac{l_B f^2 \tau^{1/3}(N-M_{\rm str})^{5/3}}{l N_{\rm bead}^{2/3}} + \tau^{4/3} N_{\rm bead}^{1/3}(N-M_{\rm str})^{2/3} + \frac{\tau l M_{\rm str}}{d_{\rm str}} + \frac{l_B f^2 \tau N^2 d_{\rm str}^2}{l^3 M_{\rm str}}\,. \quad (49)$$

The optimal values of the parameters $N_{\rm bead}$, $M_{\rm str}$, and $d_{\rm str}$ correspond to the minimum of the free energy. Minimization yields the free energy

$$\frac{F_{\rm nec}}{k_BT} \approx N f \left(\frac{\tau l_B}{l}\right)^{1/2}\,, \quad (50)$$

where $d_{\rm str} \approx \xi_T$ has been used. This free energy is lower than the free energy of the above polyelectrolyte cylinder: $F_{\rm nec}/F_{\rm cyl} \approx (\xi_T/D)^{1/2}$ as long as it is in the poor solvent regime

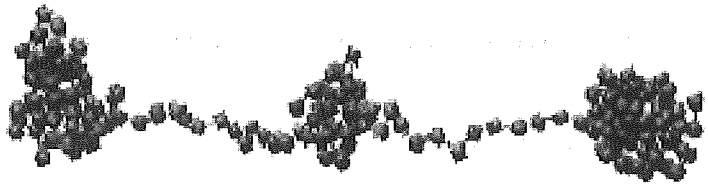


Fig. 15: *Configuration of a freely jointed uniformly charged chain with $N = 200$ monomers interacting via Coulomb and Lennard-Jones potentials ($f = 0.15$). The Configuration is a result of a Monte Carlo simulation [47].*

$\xi_T < D$. Hence, the equilibrium state is the necklace globule. Upon changing the valence f or the solvent quality, the globule undergoes a cascade of transitions between states of different integer numbers of beads of the necklace. These results of the scaling theory have been confirmed by computer simulations [47] (cf. Fig 15).

There is an analogy between the necklace shape of the polyelectrolyte in a poor solvent and the necklace configuration of a polyampholyte [46] (a chain containing both positive and negative charges). In the polyampholyte case, both the attractive and repulsive forces are related to electrostatic interactions. The long range repulsion is due to the overall charge of the chain. The attraction results form spatial charge density fluctuations of Debye-Hückel type. An important difference between the systems is that the polyelectrolyte is a homogeneous homopolymer. Quenched randomness in the position of positive and negative charges along the chain is intrinsic to random polyampholytes. The attraction in random polyampholytes is due to statistical fluctuations. Randomness on the placement of the charges of a polyelectrolyte chain is not essential for the existence of the necklace cascade of transitions.

Appendices

A Solution of Linearized Poisson-Boltzmann Equation

The linearized Poisson-Boltzmann equation for spherical particles of diameter σ is given by

$$\Delta\bar{\phi}_\alpha(\mathbf{r}) = \begin{cases} \kappa^2\bar{\phi}_\alpha(\mathbf{r}) & r > \sigma \\ 0 & 0 < r < \sigma \end{cases} , \tag{51}$$

where $r = |\mathbf{r}|$. The boundary conditions are that $\bar{\phi}_\alpha(r)$ must vanish at infinity, that $\bar{\phi}_\alpha(r)$ be continuous across the surface specified by $r = \sigma$, and that ϵ times the normal derivative of $\bar{\phi}_\alpha(r)$ be continuous across the surface $r = \sigma$. The last condition comes from the fact that the normal component of the displacement vector $\mathbf{D}$ is continuous across any charged free surface. Fixing particle α at the origin of the reference system and introducing spherical coordinates gives

$$\frac{1}{r^2}\frac{d}{dr}\left(r^2\frac{d\bar{\phi}_\alpha(r)}{dr}\right) = \begin{cases} \kappa^2\bar{\phi}_\alpha(r) & r > \sigma \\ 0 & 0 < r < \sigma \end{cases} . \tag{52}$$

To solve the equation for $r > \sigma$ the function $\chi(r) = r\bar{\phi}_\alpha(r)$ is introduced, which yields the linear differential equation

$$\frac{d^2\chi}{dr^2} - \kappa^2\chi = 0\,; \quad r > \sigma\,.$$

The solution of this equation is easily found. Applying the boundary condition $\bar{\phi}_\alpha(r \to \infty) = 0$, the solution for $\bar{\phi}_\alpha$ is

$$\bar{\phi}_\alpha(r) = \frac{A}{r}e^{-\kappa r}\,; \quad r > \sigma\,. \tag{53}$$

The solution for $0 < r < \sigma$ follows directly from Eq. (52) and is given by

$$\bar{\phi}_\alpha(r) = \frac{B}{r} + C\,; \quad 0 < r < \sigma\,. \tag{54}$$

To evaluate the constant B Gauss' law is applied. Since the charge density within the sphere with radius $r < \sigma$ is $\rho = z_\alpha e\delta(\mathbf{r})$, integration of the Maxwell equation $\nabla\mathbf{D} = 4\pi\rho$ gives $B = z_\alpha e/\epsilon$ and hence

$$\bar{\phi}_\alpha(r) = \frac{z_\alpha e}{\epsilon r} + C\,; \quad 0 < r < \sigma\,. \tag{55}$$

The condition that $\bar{\phi}_\alpha(r)$ and $\epsilon d\bar{\phi}_\alpha(r)/dr$ have to be continuous at $r = \sigma$ yields the remaining constants A and C:

$$\begin{aligned} A &= \frac{z_\alpha e e^{\kappa\sigma}}{\epsilon(1+\kappa\sigma)}\,, \\ C &= -\frac{z_\alpha e\kappa}{\epsilon(1+\kappa\sigma)}\,. \end{aligned}$$

Thus, the total solution is

$$\bar{\phi}_\alpha(r) = \begin{cases} \dfrac{z_\alpha e e^{-\kappa(r-\sigma)}}{\epsilon r(1+\kappa\sigma)} & r > \sigma \\ \dfrac{z_\alpha e}{\epsilon r} - \dfrac{z_\alpha e \kappa}{\epsilon(1+\kappa\sigma)} & 0 < r < \sigma \end{cases} . \tag{56}$$

(57)

B Thermal Averages of Edwards-Singh Approach

The Hamiltonian of a semiflexible chain with the intramolecular potential V is given by

$$\beta H = \lambda \sum_{i=2}^{N-1} \mathbf{R}_i^2 + \lambda_0 \left(\mathbf{R}_1^2 + \mathbf{R}_N^2\right) + \frac{\mu}{2} \sum_{i=1}^{N-1} (\mathbf{R}_i - \mathbf{R}_{i-1})^2 + \beta V = \beta H_0 + \beta V . \tag{58}$$

The Hamiltonian of the reference system is

$$\beta H_T = \lambda_T \sum_{i=2}^{N-1} \mathbf{R}_i^2 + \lambda_{0T} \left(\mathbf{R}_1^2 + \mathbf{R}_N^2\right) + \frac{\mu_T}{2} \sum_{i=1}^{N-1} (\mathbf{R}_i - \mathbf{R}_{i-1})^2 , \tag{59}$$

with

$$\lambda_T = \frac{3}{2l^2} \frac{1-t_T}{1+t_T} , \quad \lambda_{0T} = \frac{3}{2l^2} \frac{1}{1+t_T} , \quad \mu_T = \frac{3}{2l^2} \frac{2t_T}{1-t_T^2} . \tag{60}$$

Perturbation theory up to first order yields for a quantity A according to Edwards and Singh [19]

$$\langle A \rangle \approx \langle A \rangle_T + \beta \left(\langle A \rangle_T \langle H_0 - H_T \rangle_T - \langle A(H_0 - H_T) \rangle_T \right) + \beta \left(\langle A \rangle_T \langle V \rangle_T - \langle AV \rangle_T \right) . \tag{61}$$

Using $\langle A \rangle = \langle \mathbf{r}_e^2 \rangle = \langle \mathbf{r}_e^2 \rangle_T$ the following equation is obtained to determine t_T of the reference system

$$\begin{aligned} 0 &= \left\langle (\mathbf{r}_N - \mathbf{r}_0)^2 \right\rangle_T \langle H_0 - H_T \rangle_T - \left\langle (\mathbf{r}_N - \mathbf{r}_0)^2 (H_0 - H_T) \right\rangle_T \\ &\quad + \left\langle (\mathbf{r}_N - \mathbf{r}_0)^2 \right\rangle_T \langle V \rangle_T - \left\langle (\mathbf{r}_N - \mathbf{r}_0)^2 V \right\rangle_T . \end{aligned} \tag{62}$$

The individual averages can been calculated and we find

$$0 = (\lambda - \lambda_T) l^2 A + (\lambda_0 - \lambda_{0T}) l^2 B + \frac{1}{2} (\mu - \mu_T) l^2 C + D , \tag{63}$$

with

$$\begin{aligned} A &= \frac{1}{l^4} \left(\left\langle (\mathbf{r}_N - \mathbf{r}_0)^2 \right\rangle_T \left\langle \sum_{n=2}^{N-1} \mathbf{R}_n^2 \right\rangle_T - \left\langle (\mathbf{r}_N - \mathbf{r}_0)^2 \sum_{n=2}^{N-1} \mathbf{R}_n^2 \right\rangle_T \right) \qquad (64) \\ &= \frac{2}{3(1-t_T)^2} \left(-N[(1+t_T)^2 + 2t_T t_T^N] + 2(1-t_T^N) \frac{(1-t_T^N) + 2t_T(1+t_T+t_T^2)}{1-t_T^2} \right) \\ B &= \frac{1}{l^4} \left(\left\langle (\mathbf{r}_N - \mathbf{r}_0)^2 \right\rangle_T \left\langle \mathbf{R}_1^2 + \mathbf{R}_N^2 \right\rangle_T - \left\langle (\mathbf{r}_N - \mathbf{r}_0)^2 (\mathbf{R}_1^2 + \mathbf{R}_N^2) \right\rangle_T \right) \qquad (65) \\ &= -\frac{4}{3} \left(\frac{t_T^N - 1}{t_T - 1} \right)^2 \end{aligned}$$

$$C = \frac{1}{l^4}\left(\left\langle(\mathbf{r}_N-\mathbf{r}_0)^2\right\rangle_T\left\langle\sum_{i=1}^{N-1}(\mathbf{R}_i-\mathbf{R}_{i-1})^2\right\rangle_T - \left\langle(\mathbf{r}_N-\mathbf{r}_0)^2\sum_{i=1}^{N-1}(\mathbf{R}_i-\mathbf{R}_{i-1})^2\right\rangle_T\right)$$

$$= \frac{4}{3(1-t_T^2)}\left((N-1)(1-t_T^2)t_T^N + (t_T^{2N}-t_T^2)\right) \tag{66}$$

$$D = \frac{1}{l^2}\left(\left\langle(\mathbf{r}_N-\mathbf{r}_0)^2\right\rangle_T\langle\beta V\rangle_T - \left\langle(\mathbf{r}_N-\mathbf{r}_0)^2\beta V\right\rangle_T\right) \tag{67}$$

$$= \frac{l^2}{18\pi^2}\int_0^\infty dq\, q^4\tilde{v}(q)\sum_{n=1}^{N}\exp\left(-\frac{q^2}{6}nl^2\left(\frac{1+t_T}{1-t_T}+\frac{2t_T}{n}\frac{t_T^n-1}{(t_T-1)^2}\right)\right)$$

$$\times\left\{n^2(N-n+1)\left(\frac{1+t_T}{1-t_T}\right)^2+\frac{2(t_T^n-1)t_T^2}{(t_T-1)^4}\Big[(N-n)t_T^{N-n}(t_T^n-1)\right.$$

$$\left.-\frac{(t_T^n-1)(t_T^{N-n+2}-1)(t_T^{N-n}+1)}{1-t_T^2}-2n\frac{1+t_T}{t_T}(t_T^{N-n+1}-1)\Big]\right\}$$

The potential $\tilde{v}(q)$ is the Fourier transformed intramolecular potential. For the excluded volume interaction and the Debye-Hückel potential (cf. Eqs. (14), (15)) V reads[8]

$$\beta V = \frac{\beta}{2}\sum_{i=0}^{N}\sum_{j=0}^{N}\left(v_{ij}^{EV}+v_{ij}^{DH}\right) = \frac{\beta}{2}\sum_{i=0}^{N}\sum_{j=0}^{N}\left(v_e\delta(\mathbf{r}_i-\mathbf{r}_j)+k_BTl_B\frac{e^{-\kappa|\mathbf{r}_i-\mathbf{r}_j|}}{|\mathbf{r}_i-\mathbf{r}_j|}\right). \tag{68}$$

$\tilde{v}(q)$ is then given by

$$\tilde{v}(q) = \beta\int\left(v_{ij}^{EV}+v_{ij}^{DH}\right)e^{-i\mathbf{k}\mathbf{r}_{ij}}\,d^3x_{ij} = \frac{v_e}{k_BT}+\frac{4\pi l_B}{k^2+\kappa^2}, \tag{69}$$

where $\mathbf{r}_{ij}=\mathbf{r}_i-\mathbf{r}_j$.

C Electrostatic Persistence Length in the Rod Limit

To calculate the electrostatic persistence length in the rod limit, we describe the polymer as an infinite space curve $\mathbf{r}(s)$, i.e., we consider here a continuous inextensible chain and no longer, as in section 3, a Gaussian semiflexible chain [18]. The inextensibility implies for the tangent vector $\mathbf{u}(s)=\partial\mathbf{r}(s)/\partial s$ of the space curve: $\mathbf{u}^2=1$. The bending energy is then given by

$$\frac{\mu}{2}\sum_{i=1}^{N-1}\left(\mathbf{R}_i^2-\mathbf{R}_{i+1}^2\right)^2 \to \frac{l_0}{2}\int_0^\infty\left(\frac{\partial\mathbf{u}}{\partial s}\right)^2 ds, \tag{70}$$

where l_0 is the persistence length of the uncharged chain. The intramolecular Coulomb interaction of the continuous charge distribution is taken into account via the Debye-Hückel potential

$$\beta V^{DH} = \frac{l_B}{l^2}\int_0^\infty\int_{s'}^\infty\frac{e^{-\kappa|\mathbf{r}(s)-\mathbf{r}(s')|}}{|\mathbf{r}(s)-\mathbf{r}(s')|}\,dsds'. \tag{71}$$

[8] In the Debye-Hückel potential the term with $i=j$ is excluded.

No rearrangement or fluctuations of the charges are allowed. With the tangent vector the difference of the coordinates is expressed by

$$\mathbf{r}(s) - \mathbf{r}(s') = \int_{s'}^{s} \mathbf{u}(s'')\, ds'' \,. \tag{72}$$

If a weakly bending rod is assumed, $\mathbf{u}$ is well approximated by the following Taylor expansion

$$\mathbf{u}(s'') \approx \mathbf{u}(s') + \frac{\partial \mathbf{u}}{\partial s'}(s'' - s') + \frac{1}{2}\frac{\partial^2 \mathbf{u}}{\partial s'^2}(s'' - s')^2 \,. \tag{73}$$

Substitution of Eq. (73) into Eq. (72) yields

$$\mathbf{r}(s) - \mathbf{r}(s') \approx \mathbf{u}(s')(s - s') + \frac{1}{2}\frac{\partial \mathbf{u}}{\partial s'}(s - s')^2 + \frac{1}{6}\frac{\partial^2 \mathbf{u}}{\partial s'^2}(s - s')^3 \,, \tag{74}$$

and

$$\frac{e^{-\kappa|\mathbf{r}(s)-\mathbf{r}(s')|}}{|\mathbf{r}(s) - \mathbf{r}(s')|} \approx \frac{e^{-\kappa|s-s'|}}{|s - s'|} + \frac{1}{24}\left(\frac{\partial \mathbf{u}}{\partial s'}\right)^2 e^{-\kappa|s-s'|}\left[|s - s'| + \kappa(s - s')^2\right] \,. \tag{75}$$

The constraint of a unit tangent vector implies $\mathbf{u}\partial\mathbf{u}/\partial s = 0$ and $(\partial\mathbf{u}/\partial s)^2 = -\mathbf{u}\partial^2\mathbf{u}/\partial s^2$, which has been taken into account to derive Eq. (75). The first term on the right-hand side of Eq. (75) accounts for the Debye-Hückel energy of a straight rod. It is independent from any particular conformation of the chain. Hence, the term yields a constant contribution to the partition function and vanishes in any calculation of thermal averages. Thus, we will neglect this term in the following. Substitution of the rest of Eq. (75) into Eq. (71) and evaluation of one of the integrals yields

$$\beta V^{DH} = \frac{l_B}{8\kappa^2 l^2}\int_0^\infty \left(\frac{\partial \mathbf{u}}{\partial s}\right)^2 ds \,. \tag{76}$$

Collecting the various energy terms we find

$$\begin{aligned} &\frac{l_0}{2}\int_0^\infty \left(\frac{\partial \mathbf{u}}{\partial s}\right)^2 ds + \frac{l_B}{l^2}\int_0^\infty \int_{s'}^\infty \left(\frac{e^{-\kappa|\mathbf{r}(s)-\mathbf{r}(s')|}}{|\mathbf{r}(s) - \mathbf{r}(s')|} - \frac{e^{-\kappa|s-s'|}}{|s - s'|}\right) ds ds' \\ &\qquad \approx \frac{l_0}{2}\int_0^\infty \left(\frac{\partial \mathbf{u}}{\partial s}\right)^2 ds + \frac{l_B}{8\kappa^2 l^2}\int_0^\infty \left(\frac{\partial \mathbf{u}}{\partial s}\right)^2 ds = \frac{l_p}{2}\int_0^\infty \left(\frac{\partial \mathbf{u}}{\partial s}\right)^2 ds \,. \end{aligned} \tag{77}$$

As is obvious form the above calculations, the (screened) Coulomb interaction yields a contribution to the bending stiffness of the rodlike molecule. The effective persistence length l_p is given by

$$l_p = l_0 + \frac{1}{4}\frac{l_B}{\kappa^2 l^2} \,, \tag{78}$$

which is the expression derived by Odijk [23] and Skolnik & Fixman [24] (cf. Eq. (27)).

References

[1] C. Tanford, *Physical Chemistry of Macromolecules* (Wiley, New York, 1961)

[2] M. Mandel, *Polyelectrolytes* (Ridel, Dordrecht, 1988)

[3] M. Hara Ed., *Polyelectrolytes: Science and Technology* (Marcel Dekker, New York, 1993)

[4] S. Förster and M. Schmid, Adv. Polym. Sci. **120**, 51 (1995)

[5] J.-L. Barrat and J.-F. Joanny, Adv. Chem. Phys. **XCIV**, 1 (1996)

[6] *Macro-ion Characterization: From Dilute Solutions to Complex Fluids*, edited by K. Schmitz (American Chemical Soceity, Washington, DC, 1994)

[7] C. F. Foster and M. Schmid, Adv. Polym. Sci. **120**, 50 (1995)

[8] M. Sedlak and E. Amis, J. Chem. Phys. **96**, 817 (1992)

[9] P. G. de Gennes, *Scaling Concepts in Polymer Physics* (Cornell Univerity Press, Ithaca, NY, 1979)

[10] J. L. Barrat and D. Boyer, J. Phys. II **3**, 343 (1993)

[11] M. Stevens and K. Kremer, J. Chem. Phys. **103**, 1669 (1995)

[12] R. G. Winkler, M. Gold, and P. Reineker, Phys. Rev. Lett. **80**, 3731 (1998)

[13] J.-P. Hansen and I. R. McDonald, *Theory of Simple Liquids* (Academic Press, London, 1986)

[14] C.-Y. Shew and A. Yethiraj, J. Chem. Phys. **106**, 5706 (1997)

[15] K. S. Schweizer and J. G. Curro, Adv. Polym. Sci. **116**, 319 (1995)

[16] K. S. Schweizer and J. G. Curro, J. Chem. Phys. 87, 1842 (1987)

[17] D. A. McQuarrie, *Statistical Mechanics* (Harper and Row, New York, 1979)

[18] R. G. Winkler, P. Reineker, and L. Harnau, J. Chem. Phys. **101**, 8119 (1994)

[19] S. F. Edwards and P. Singh, J. Chem. Soc., Faraday Trans. 2 **75**, 1001 (1979)

[20] C.-Y. Shew and A. Yethiraj, J. Chem. Phys. **113**, 8841 (2000)

[21] U. Micka and K. Kremer, Phys. Rev. E **54**, 2653 (1996)

[22] M. Ullner, B. Jönsson, C. Peterson, O. Sommelius, and B. Söderberg, J. Chem. Phys. **107**, 1279 (1997)

[23] T. Odijk, J. Polym. Sci., Polym. Phys. Ed. **15**, 477 (1977)

[24] J. Skolnick and M. Fixman, Macromolecules **10**, 944 (1977)

[25] G. Maret and G. Weill, Biopolymers **22**, 2727 (1983)

[26] V. Degiorgio, F. Mantegazza, and R. Piazza, Europhys. Lett. **15**, 75 (1991)

[27] J. L. Barrat and J. F. Joanny, Europhys. Lett. **24**, 333 (1993)

[28] J. P. Donley, J. Rudnick, and A. J. Liu, Macromolecules **30**, 1188 (1997)

[29] B.-Y. Ha and D. Thirumalai, J. Chem. Phys. **110**, 7533 (1999)

[30] M. Muthukumar, J. Chem. Phys. **86**, 7230 (1987)

[31] A. R. Khokhlov and K. A. Katchaturian, Polymer **23**, 1742 (1982)

[32] H. Li and T. Witten, Macromolecules **28**, 5921 (1995)

[33] R. R. Netz and H. Orland, Eur. Phys. J. B **8**, 81 (1999)

[34] T. Hofmann, R. G. Winkler, and P. Reineker, J. Chem. Phys. **114**, 10181 (2001)

[35] D. Laria, D. Wu, and D. Chandler, J. Chem. Phys. **95**, 4444 (1991)

[36] C.-Y. Shew and A. Yethiraj, J. Chem. Phys. **110**, 5437 (1999)

[37] M. Deserno, C. Holm, and S. May, Macromolecues **33**, 199 (2000)

[38] H. Risken, *The Fokker-Planck Equation* (Springer, Berlin, 1984)

[39] M. P. Allen and D. J. Tildesley, *Computer Simulation of Liquids* (Clarendon Press, Oxford, 1987)

[40] E. E. Maier, S. F. Schulz, and R. Weber, Macromolecules **21**, 1544 (1988)

[41] P. G. De Gennes, P. Pincus, R. M. Velasco, and F. Brochard, J. Phys. (Paris) **37**, 1461 (1976)

[42] T. Onishi, N. Imai, and F. Oosawa, J. Phys. Soc. Japan **15**, 896 (1960)

[43] G. S. Manning, J. Chem. Phys. **51**, 924 (1969)

[44] N. Grønbech-Jensen, R. J. Mashl, R. F. Bruinsma, and W. M. Gelbert, Phys. Rev. Lett. **78**, 2477 (1997)

[45] Lord Rayleigh, Philos. Mag. **14**, 184 (1882)

[46] Y. Kantor and M. Kardar, Phys. Rev. E **51**, 1299 (1995)

[47] A. V. Dobrynin, M. Rubinstein, and S. P. Obukhov, Macromolecules **29**, 2974 (1996)

[48] A. V. Lyulin, B. Dünweg, O. V. Borisov, and A. A. Darinskii, Macromolecules **32**, 3264 (1999)

[49] A. R. Khokhlov, J. Phys. A **13**, 979 (1980)

[50] R. Messina, C. Holm, and K. Kremer, Phys. Rev. E **64**, 021405 (2001)

B 6 Investigations of Polymers by Small Angle Neutron Scattering

D. Schwahn
Institut für Festkörperforschung
Forschungszentrum Jülich GmbH

Contents

1 Introduction 2

2 Small Angle Neutron Scattering Technique 2

3 Single Polymer in Solution and Melt 3

3.1 Single Chain on a "Flory" Lattice 3
3.2 Single Chain in a good Solvent 6
3.3 Single Chain in a Melt – Ideal Mixture of Polymers 7
3.4 Contrast Variation 8

4 Binary Polymer Mixture 10

4.1 Structure Factor in Random Phase Approximation 11
4.2 Phase Diagram of dPB/PS Blends: Spinodal and Binodal 12
4.3 Deviations from Random Phase Approximation 13

5 Diblock Copolymers 14

5.1 Structure Factor of a Symmetric Diblock Copolymer 14
5.2 Phase Diagram of Diblock Copolymers 15

6 Summary 16

1 Introduction

Scattering techniques with neutrons play an important role in the investigation of polymers, especially, to explore their structure, dynamic, and thermodynamic properties. One very important advantage of neutron scattering are the relatively easy and effective possibilities of contrast variation by the exchange of proton (H) and deuterium (D) atoms. So, one can adjust the scattering contrast in order to become sensitive to selected properties of the sample, as local fluctuations of polymer composition and density, or even the structural conformation of single polymers in melt and solution. Such experimental possibilities quite naturally lead to detailed insight into sometimes very complicated structures.

In this lecture we deal with the method of elastically scattered neutrons into small angles and thereby with structural polymer properties in their equilibrium state. We, furthermore, limit our discussions to linear polymers consisting of one and two types of monomers, namely, homopolymers and symmetric diblock copolymers. The content of this lecture can be found in textbooks and review articles given in the references [1]-[9].

2 Small Angle Neutron Scattering Technique

A schematic lay-out of a small angle neutron scattering (SANS) experiment is given in Fig. 1 [10]. Neutrons coming from a reactor after being moderated in a cold source first pass the

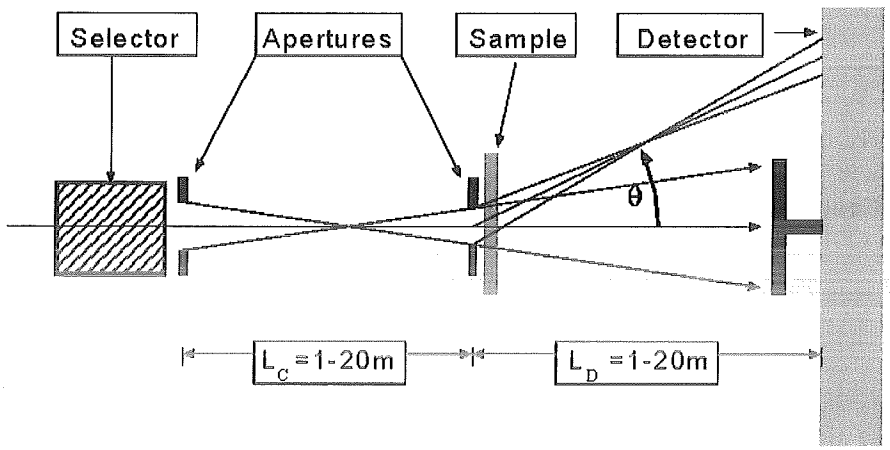


Fig. 1: *Schematic design of a pinhole SANS instrument.*

selector, then enter the collimator system with the two apertures, pass through the sample, and then are detected in a position sensitive detector if scattered into a given angular interval. Selector and collimator, respectively, determine the wavelength and divergence of the neutrons. Only part of the neutrons (intensity I_0) passing through the sample will be scattered whereas the non-scattered neutrons (intensity I_0^*) are absorbed in a beam stopper in front of the detector. The distances of detector and sample as well as of the two apertures are variable typically from 1 to 20m allowing to measure angles from roughly 0.1° to 20° and to adjust an

optimal relationship between maximum intensity and sufficiently good resolution. The scattered intensity is usually given as a function of the momentum transfer Q

$$|\underline{Q}| = 4\pi / \lambda \sin \Theta \qquad (1)$$

being inversely proportional to the neutron wave length λ and proportional to sinΘ. Typical values for λ are between 5 and 10 Å and, therefore, a measurement range of $10^{-3} < Q[Å^{-1}] < 0.3$ is available. This Q range can be extended to smaller Q range by using SANS instruments different from that in Fig.1 by using a focussing optics or perfect Silicon single crystals as monochromator and analysator. In order to measure at larger Q other diffractometer techniques have to be used allowing energy analysis. The detected neutron intensity $I_D(Q)$ is described in eq 2, it is proportional to the primary intensity I_0, the sample thickness D, the

$$I_D(\underline{Q}) = I_0 \cdot D \cdot T \cdot \frac{d\Sigma}{d\Omega}(\underline{Q}) \cdot \Delta\Omega_D \qquad (2)$$

sample transmission $T=I_0^*/I_0$ giving the weakening of the non-scattered neutrons, and the space angle $\Delta\Omega_D$ of a detector element. The macroscopic cross section $d\Sigma/d\Omega$ is the number to be determined, it is given in units of cm^{-1}.

3 Single Polymer in Solution and Melt

In this section we will discuss scattering from single homopolymers in solution and melt.

3.1 Single Chain on a "Flory" Lattice

To formulate the scattering law of a single coil in a solvent we consider a chain on a "Flory" lattice as depicted in Fig.2. Each lattice point is occupied by a monomer of the chain (red points) or by solvent molecules (open points). We consider V_S as the volume of the sample, n as the number of lattice points, and N as the number of monomers. For such a problem the

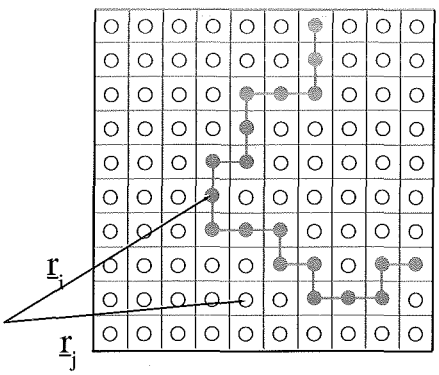


Fig. 2: *Single Chain on a "Flory" lattice*

scattering law is generally given as

$$\frac{d\Sigma}{d\Omega}(\underline{Q}) = \frac{1}{V_S}\left|\sum_{i=1}^{n} \bar{b}_i \exp(i\underline{Q}\underline{r}_i)\right|^2 \tag{3}$$

with the coherent scattering length of the lattice point i given as $\bar{b}_i$ and the corresponding phase factor $\exp(i\underline{Q}\underline{r}_i)$ [9]. To proceed, we define in eq.4 an occupation number σ_i with the following meaning

$$\begin{aligned} \sigma_i = 1 &\rightarrow \bar{b}_i = \bar{b}_P \\ \sigma_i = 0 &\rightarrow \bar{b}_i = \bar{b}_S \end{aligned} \tag{4}$$

The value σ_i is one, if the lattice point i is occupied by a monomer of the polymer and zero if occupied by a solvent molecule. The coherent scattering length of the lattice point i is then given as $\bar{b}_i = \sigma_i \bar{b}_P + (1-\sigma_i)\bar{b}_S = \sigma_i \Delta\bar{b} + \bar{b}_S$ with $\Delta\bar{b} = (\bar{b}_P - \bar{b}_S)$ and leads to

$$\frac{d\Sigma}{d\Omega}(\underline{Q}) = \frac{\Delta\bar{b}^2}{V_S}\left|\sum_{i=1}^{n} \sigma_i \exp(i\underline{Q}\underline{r}_i)\right|^2 \tag{5}$$

and finally

$$\frac{d\Sigma}{d\Omega}(\underline{Q}) = \frac{\Delta\bar{b}^2 N^2}{V_S} P(Q) = K\,\Phi\,V_P\,P(Q) = K\,S(Q) \tag{6}$$

with the structure factor S(Q), the polymer form factor P(Q), and the contrast factor $K=\Delta\rho^2/N_A$. The structure factor S(Q) describes fluctuations of the monomers as represented by the lattice points in Fig.2. The form factor of the monomers is assumed being equal one ($P_M(Q)=1$) which is reasonable as the internal structure of monomers only becomes visible at about $Q>1\text{Å}^{-1}$ and which is outside the "SANS" Q range. The polymer form factor P(Q) is obtained after averaging over all configurations of the polymer according to

$$P(Q) = \frac{1}{N^2}\left\langle\left|\sum_{i=1}^{n} \sigma_i \exp(i\underline{Q}\underline{r}_i)\right|^2\right\rangle \tag{7}$$

The symbols in the equations have the following meaning: • $\rho_i = \sum b_j/\Omega_j$ coherent scattering length of a monomer; • $K=(\rho_P - \rho_S)^2/N_A = \Delta\rho^2/N_A$ scattering contrast; • Φ volume fraction of the polymer; • $V_P = N\Omega_P N_A$ molar volume of the polymer in units [cm^3/mol].

An approximate expression of P(Q) in eq 7 has been derived for a freely jointed chain by Debye according to

$$P_{Debye}(Q) = \frac{2}{x^2}[x - 1 + \exp(-x)] \tag{8}$$

with $x = R_g^2 Q^2$ and which is depicted in Fig.3 [see also lecture: S. Hoffmann], [9]. The intensity has a maximum at Q=0 and decreases at larger Q depending on the radius of gyration R_g. In experimental praxis one often prefers to use approximate forms of eq 8. So, for $Q < 1/R_g$ one gets the Zimm approximation

$$P_{Debye}^{-1} \cong 1 + \frac{1}{3} R_g^2 Q^2 \tag{9}$$

and for $Q>1/R_g$ one gets with

$$P_{Debye} \propto 1/(Q \cdot R_g)^2 \tag{10}$$

a scaling law with a fractal dimension D=2. Both approximate equations are depicted in Fig.4 as dashed blue lines, the left part shows the Zimm approximation and the right part the Q^{-2} part in the so-called Kratky representation. The exact limits can be read from the figures.

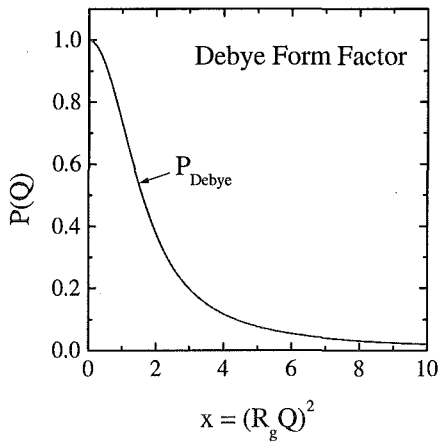


Fig. 3: *Debye form factor of a linear homopolymer*

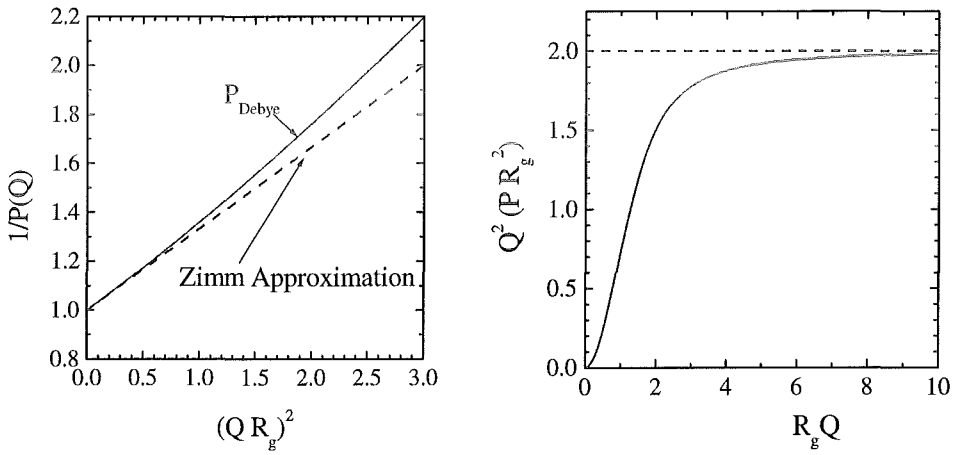


Fig. 4: *Approximations of Debye form factor at $Q<1/R_g$ (left) and $Q>1/R_g$ (right) shown by blue line.*

3.2 Single Chain in a good Solvent

The model of a freely jointed chain assumes several idealizations which are usually not fulfilled in nature. Real chains cannot cross or, equivalently, two monomers cannot occupy the same point on a Flory lattice and which leads to a smaller number of configurations. Consequently, one observes chains with a larger radius of gyration following a scaling law with the Flory exponent $\nu=3/5$ ($R_g^2 \propto N^{2\nu} \propto N^{1.2}$) instead of $\nu=1/2$ ($R_g^2 \propto N^1$) for a freely jointed chain [1]-[3].

The interaction of polymers in solution is also determined by the solvent molecules and, therefore, it is a function of temperature, polymer concentration, and chemistry of the solvent molecules. At the Θ condition the interaction between the polymer segments becomes zero; the polymer behaves as a freely jointed chain with the Flory exponent $\nu=1/2$. The interaction between the polymer enters into the structure factor S(Q) (eq 6). Within the random phase approximation (RPA) formulated by deGennes [1], [Lecture: A. Baumgärtner] one gets in the limit of small Q ($Q<1/R_g$)

$$\Phi / S(Q) = \Phi / S(0) + R_g^2 /(3V_P)\, Q^2 \tag{11}$$

with the inverse structure factor at Q=0 according to

$$S^{-1}(0) = (1/\Phi V_P + 1/(1-\Phi)\Omega - 2\chi) \underset{\Phi<<1}{=} (1/V_P + 2A_2\Phi)/\Phi\,. \tag{12}$$

S(0) is a susceptibility and related to the second virial coefficient A_2 and the Flory-Huggins (FH) parameter χ describing the polymer interaction. The second virial coefficient and the Flory-Huggins parameter are equivalent according to $2A_2 = 1/\Omega - 2\chi$. A positive, zero, and negative A_2 means, respectively, a good, Θ, and bad solvent system. A scaling behavior similarly to a freely jointed chain (see eq.10), however, with a larger exponent $\nu=3/5$ according to $S(Q) \propto Q^{-1/\nu}$ is observed in good solvent condition at $Q>1/R_g$.

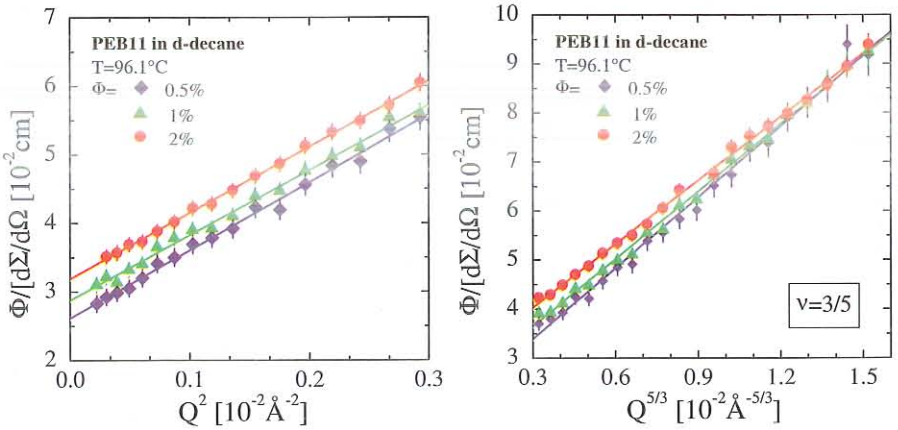


Fig. 5: *Dilute polymer solution at constant temperature and three concentrations. Left part show small Q behavior (eq 11) the right part the scaling behavior at large Q according to* $S^{-1}(Q) \propto Q^{1/\nu}$.

Fig.5 shows an experimental example of a dilute solvent of a PEB11 polymer in decane solution [11]. This polymer is a random copolymer of poly(ethylene-butene) with 11 ethyl side branches per 100 backbone carbons. Both figures show the solution at 96.1°C and at three concentrations. The left figure depictss the behavior at small Q in Zimm representation; according to eq 11 the slope is determined by the ratio of $R_g^2/(3V_P)$ while the extrapolated $\Phi/S(0)$ gives A_2 and the FH-parameter (eq 12). In the right part a plot of $S^{-1}(Q) \propto Q^{1/\nu}$ with $\nu=3/5$ confirm the Flory exponent for good solvent systems.

3.3 Single Chain in a Melt – Ideal Mixture of Polymers

Blending two polymers with zero energy of mixing ($\chi=0$) leads to an ideal mixture. Such ideal mixtures are realized within good approximation by isotopic mixtures which consist of protonated and deuterated polymers of the same species. In order to determine the structure

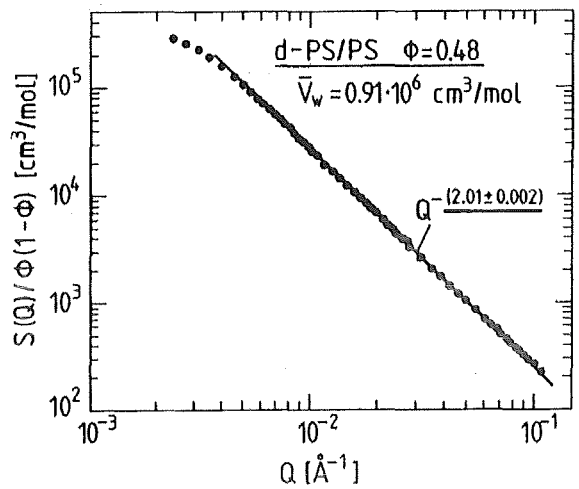


Fig. 6: *Double logarithmic presentation of an isotopic mixture shows the –2 power law at large Q according to a freely jointed chain conformation with $\nu=1/2$.*

factor S(Q) of such a melt we again consider the chains on a "Flory" lattice and define an occupation number σ_i with the following meaning

$$\sigma_i = \begin{cases} 1 & \bar{b}_i = \bar{b}_D \\ 0 & \bar{b}_i = \bar{b}_H \end{cases} \tag{13}$$

and the coherent scattering length of the deuterated or protonated monomer at position i. The scattering length is then given as $\bar{b}_i = \sigma_i(\bar{b}_D - \bar{b}_H) + \bar{b}_H = \sigma_i \cdot \Delta\bar{b} + \bar{b}_H$ and the cross section becomes

$$\frac{d\Sigma}{d\Omega}(Q) = \frac{\Delta\bar{b}^2}{V_s} \sum_{ij}^{N} < \sigma_i \sigma_j \exp(i\underline{Q}\underline{r}_{ij}) > = \frac{\Delta\bar{b}^2}{V_s} S_{DD}(Q) \tag{14}$$

The partial structure factor S_{DD} is determined by intra- und inter molecular interferences between the deuterated monomers. A separation of $S_{DD}(Q)$ into intra- {P(Q)} and inter molecular {W(Q)} interferences gives ([9])

$$S_{DD}(Q) = \Phi V_P[P(Q)+\Phi n_D W(Q)] \tag{15}$$

The equation for S_{DD} can be further simplified

$$\frac{d\Sigma}{d\Omega}(Q)=K\Phi(1-\Phi)V_P P(Q) \tag{16}$$

e.g. the structure factor is determined by the polymer form factor alone. The step from eq 15 to 16 can be understood from the following argument. In case Φ=1 one has a melt of only the deuterated component which in the incompressible limit does not scatter, e.g. $S_{DD}(Q)$ =0 in eq 15 and therefore P(Q) = -n_D W(Q) [9].

A further simplification is obtained from the fact that the excluded volume interaction is screened out in polymer melts by the other chains. This has consequences for the conformation becoming that of a freely jointed chain and the polymer form factor being described by $P_{Debye}(Q)$ of eq 8 [1]. So, the structure factor $S(Q)\equiv S_{DD}(Q)$ reads

$$S(Q)=\Phi(1-\Phi)V_P P_{Debye}(Q) \tag{17}$$

An experimental example of a 50% isotopic mixture of protonated and deuterated polystyrene is depicted in Fig. 6 [12]. The double logarithmic plot shows over a large Q interval a –2 power law which corresponds to the expected exponent ν=1/2 of the freely jointed chain.
Two comments have to be given here:

1.) As for polymers in solution (eq. 4) we neglect here the monomer structure ($P_m(Q)$=1) and the occurrence of free volume as no empty lattice points were considered and which is equivalent with an incompressible melt.
2.) In the definition of $d\Sigma/d\Omega$ in eqs 3 and 14 there was always a constant term over all lattice points $\bar{b}_i=\bar{b}_S(\bar{b}_H)$ whose integration would give a $\delta(Q)$ like contribution to the scattering. For a macroscopic large sample of the order of cm a contribution would be visible for Q of the order of 10^{-8} Å^{-1}. The smallest Q observed with the double crystal diffractometer is of the order of 10^{-5} Å^{-1}. This means that this contribution can safely be ignored.

3.4 Contrast Variation

The contrast factor $K=(\rho_P-\rho_S)^2/N_A = \Delta\rho^2/N_A$ (eq 6) describes the interaction of neutrons and the atoms of the samples. The contrast factor plays an essential role as it must be sufficiently large for a strong scattering signal. The coherent scattering lengths are different for isotopes of the same element as we are mainly concerned with neutron scattering through the interaction with the nucleus of the atoms. These numbers were determined experimentally and can be found in several publications e.g. in [13]. In polymer research the very different scattering lengths of deuterium and hydrogen is of special importance being b_H=-3.739 and b_D=6.671 in units of 10^{-13}cm. The solvent contrast of water and toluene is shown in Fig. 7; the contrast can be changed over a large range by mixing different concentrations of deuterated and protonated molecules. In this way a polymer can be measured with a large contrast or

even can be made invisible by matching the scattering length density of polymer and solvent molecules.

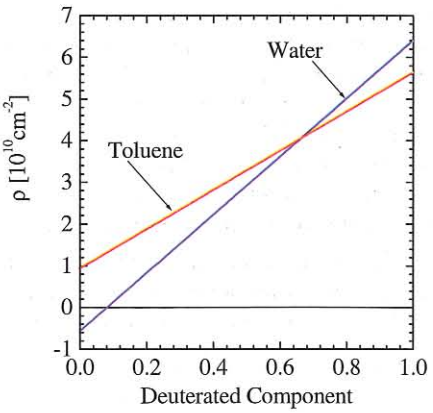


Fig. 7: *Coherent scattering length density of mixtures of deuterated and protonated toluene and water.*

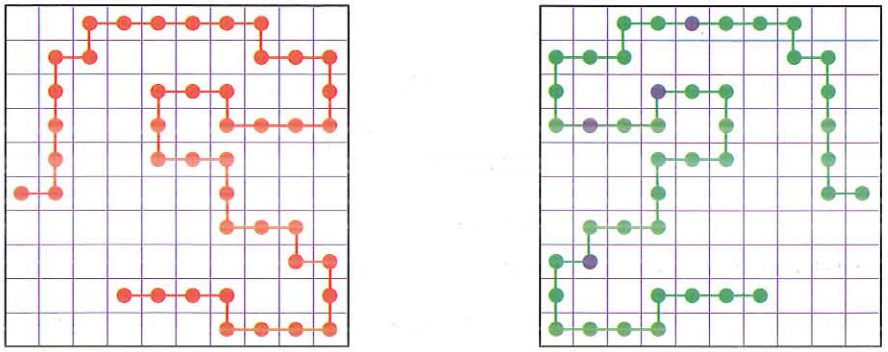


Fig. 8: *Single chains of dPS (left) and $PB_x - dPB_{(1-x)}$ (right) on a "Flory" lattice.*

Another example is shown in Fig. 8. Usually, if mixing two polymers one would like to have maximum scattering contrast; a mixture of deuterated and protonated components leads to good scattering contrast. In some special cases, however, one would like to have two chemically different polymers indistinguishable in order to study f.i. the behavior of a third component. So, two polymers as polystyrene PS and polybutadiene PB are not distinguishable in neutron scattering if a fully deuterated PS is mixed with a partially deuterated PB consisting statistically of 4.4% protonated and 95.6% deuterated monomers. The two polymers on a Flory lattice should demonstrate the last example. The right figure shows the statistically PB copolymer with four protonated monomers. Its average coherent scattering length should be the same as for the deuterated PS homopolymer. In this way one could f.i. explore the individual properties of a third polymer in a three component mixture.

4 Binary Polymer Mixture

An ideal mixture of two different polymers is an idealization which is not fulfilled in reality [1],[6]. Even mixtures of deuterated and protonated polymers of same species as discussed in the last chapter are an idealization as there always exists a very small finite energy of mixing. There are also chemically identical polymers which may exist in different microstructures as the (1,4) and (1,2) monomers of polybutadiene (PB) also showing a small FH-parameter [14]. These very small values for the energy of mixing (FH-parameter) can become important and lead to phase decomposition in case of a comparably small entropy of mixing. It is a characteristic property of polymer blends that the entropy of mixing can be made very small as it is inversely proportional to the degree of polymerization or molar volume.

In Fig. 9 a schematic phase diagram (temperature versus composition) of a symmetric binary mixture is shown. Symmetric blend means a polymer mixture with same molar volume and, therefore, the critical point at 50% composition. At high temperatures above the binodal

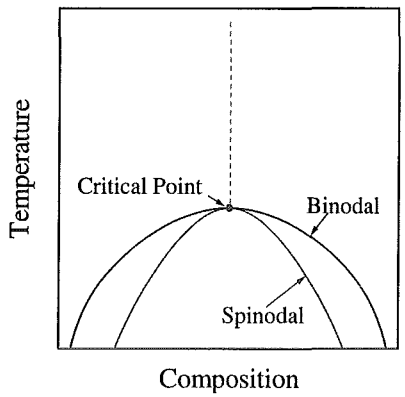


Fig. 9: *Schematic phase diagram of a binary blend*

line a macroscopically homogeneous phase is found. Cooling the mixture below the binodal line decomposition occurs in two macroscopically large phases with the equilibrium composition determined by the binodal at the phase transition temperature; both phases are rich in one of the two components. The two-phase region is separated by the spinodal; the homogeneous phase is unstable below the spinodal and metastable between binodal and spinodal. A metastable phase decomposes by a nucleation and growth process after overcoming a threshold energy. In an unstable state long wave length fluctuation modes are unstable while the shorter ones are stabilized by the surface energy expressed by a gradient energy in the Ginzburg-Landau Hamiltonian [6]. At the critical point stable and unstable regions contact each other. At this point fluctuation modes with infinite wave length or correspondingly Q=0 become unstable showing an infinite susceptibility S(0). The spinodal is only realized within the mean field approximation and appears as a line with the property of $S(Q=0) \rightarrow \infty$ similarly to the critical point [6].

4.1 Structure Factor in Random Phase Approximation

The structure factor of two polymers with a finite energy of mixing has been derived by deGennes within the random phase approximation (RPA) according to ([1],[6],[Lecture: A. Baumgärtner])

$$S^{-1}(Q)=\frac{1}{\Phi V_D P^D_{Debye}(Q)}+\frac{1}{(1-\Phi)V_H P^H_{Debye}(Q)}-2\chi \tag{18}$$

The RPA is a mean field approximation neglecting thermal fluctuations. The first two terms are described by the form factor of both components in accordance with eq 17, the third term represents the Flory-Huggins parameter which according to $\chi=\chi_h/T-\chi_\sigma$ is a free energy of mixing with an enthalpic and entropic term χ_h and χ_σ, respectively. The inverse structure factor at Q=0 is a susceptibility and related to the Gibbs free energy of mixing ΔG according to [1],[6]

$$S^{-1}(0)=\partial^2_\Phi(\Delta G/RT) \tag{19}$$

The expression of ΔG for polymer blends within the Flory-Huggins model leads as the RPA in eq 18 to

$$S^{-1}(0)=2[\chi_S-\chi]=(2\chi_h/T_S)\frac{(1/T_S-1/T)}{1/T_S}=C_{MF}\tau \tag{20}$$

with the critical amplitude $C_{MF}=2\chi_h/T_S$, the reduced temperature $\tau=[1/T_S-1/T]/1/T_S$, and the FH-parameter at the spinodal,

$$2\chi_S=(\frac{1}{\Phi V_A}+\frac{1}{(1-\Phi)V_B}) \tag{21}$$

which at the critical point becomes $\chi_C=2/V$ for $V=V_A=V_B$ and $\Phi_C=0.5$. For small Q ($<1/R_g$) the structure factor can be expanded in *Zimm approximation* similarly to eq 11

$$S^{-1}(Q)=S^{-1}(0)+AQ^2 \tag{22}$$

with

$$A=[R^2_{g,A}/\Phi V_A+R^2_{g,B}/(1-\Phi)V_B]/3 \tag{23}$$

An experimental example is shown in Fig.10, namely a blend of deuterated polybutadiene and protonated polystyrene of about 2000 g/mol molar volume and of critical composition [15]. The left side shows the structure factor in Zimm representation at four temperatures. The scattering curves follow straight lines in accordance with eq 22. Decreasing the temperature from about 110 to 65°C leads to stronger scattering as the thermal composition fluctuations increase. In the right side of Fig. 10 the inverse susceptibility is depicted versus inverse temperature. According to mean field approximation in eq 24

$$S^{-1}(0)=2\chi_h[1/T_S-1/T] \tag{24}$$

the experimental points should follow a straight line. The enthalpic term of the FH-parameter is evaluated from the slope of this line while the entropic term from $\chi_\sigma = \chi_h / T_S - \chi_S$. The RPA is based on assuming mean field approximation and the conformation of freely jointed chains. The test of both assumptions is still subject of present research.

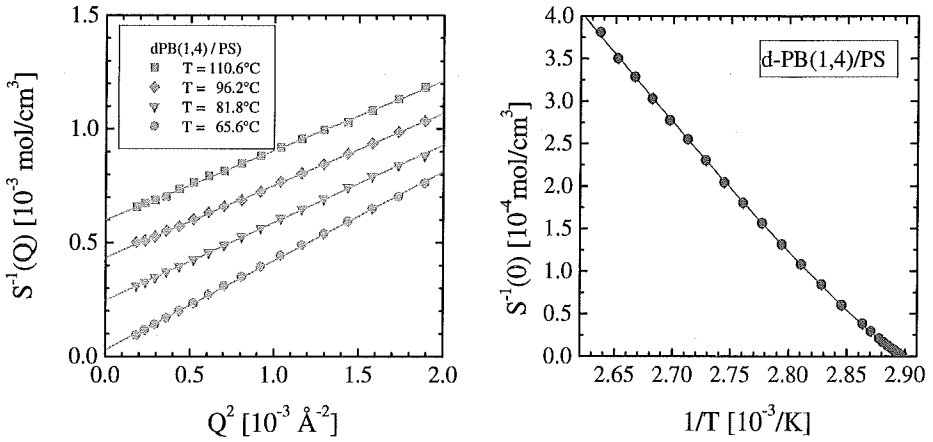


Fig. 10: *Structure factor in Zimm representation(left) and inverse susceptibility versus 1/T (right)*

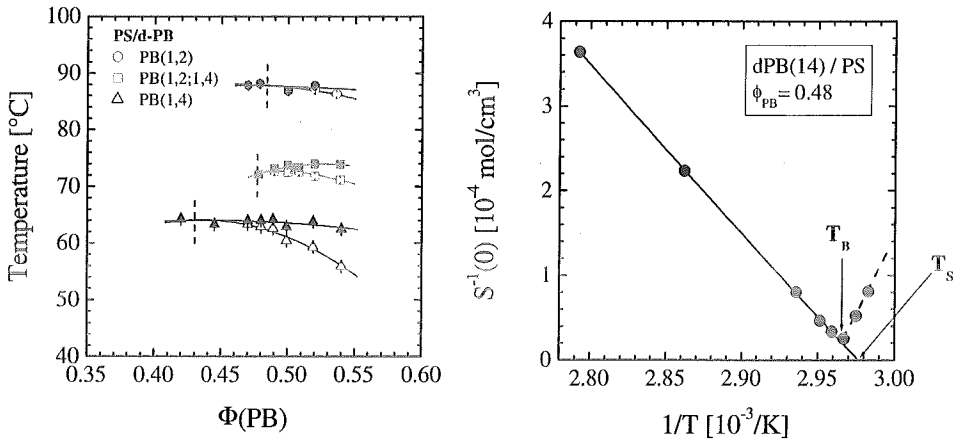


Fig. 11: *Phase boundaries of three polybutadiene polystyrene blends (left) and susceptibility of an off critical mixture to determine spinodal and binodal(right)*

4.2 Phase Diagram of dPB/PS Blends: Spinodal and Binodal

In Fig. 11 the binodal and spinodal phase boundaries of polybutadiene and polystyrene are shown [15]. The PB components nearly have the same molar volume but differ in their microstructure. The PB with 1,4 microstructure has the largest compatibility while the 1,2 (vinyl content) the lowest one. The right side of Fig.11 shows the characteristics of scattering from which binodal and spinodal are determined. Cooling the sample below the binodal leads

to a sharp decrease of S(0) which is related to thermal composition fluctuations within the domains. These fluctuations become smaller with decreasing temperature as one removes from the spinodal temperature. On the other hand, the spinodal temperature is determined from the linearly extrapolated (eq 24) $S^{-1}(0) = 0$.

4.3 Deviations from Random Phase Approximation

As already mentioned several times the RPA is a mean field theory neglecting the effect of thermal composition fluctuations. The susceptibility is described by a scaling law according to eq 20 with the critical exponent $\gamma=1$. Thermal fluctuations are always present; they are weak far from the critical temperature and can then be described within the Gaussian approximation leading in most cases to the same critical exponents as in the mean field approximation. Approaching the critical point thermal fluctuations become strong and lead to non-linear effects. Experimentally one observes a crossover to the scaling behavior of the 3D-Ising model, namely

$$S^{-1}(0) = C_{MF}\,\tau \;\rightarrow\; S^{-1}(0) = C\,\tau^{\gamma} \qquad (25)$$

with $\gamma=1.24$ and the critical amplitude C [7],[16]-[18]. The observation of such a crossover behavior is shown in Fig 12 for the PB/PS blend [15]. Near the critical temperature the inverse susceptibility shows deviations from a straight line (green line) while the data are described by $\tau^{1.24}$ only over a narrow range above T_C (red line). The solid blue lines represent

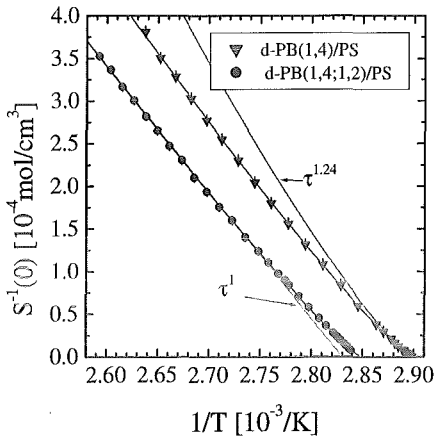


Fig. 12: *Crossover behavior of two PB/PS blends of critical composition [15].*

fits of a crossover function: $S^{-1}(0) = F(T_C, T_X, C_{MF})$ being a function of the mean field critical amplitude, a crossover temperature (Ginzburg number), and the critical temperature [18]. From these parameters the Flory-Huggins parameter can be determined [7][17].

5 Diblock Copolymers

Another class of polymers are diblock copolymers which has been schematically depicted in Fig. 13. The two blocks of polymers A and B are covalently connectet to a linear chain. The behavior of thermal fluctuations and phase behavior of these polymers have been widely investigated over the last years [5], [8], [19].

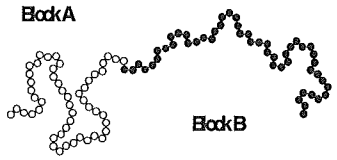


Fig. 13: *Schematic sketch of a diblock copolymer*

5.1 Structure Factor of a Symmetric Diblock Copolymer

We limit the discussions to symmetric diblock copolymer when both blocks are of same length. The structure factor of such a chain is given in eq 26. It is determined by the

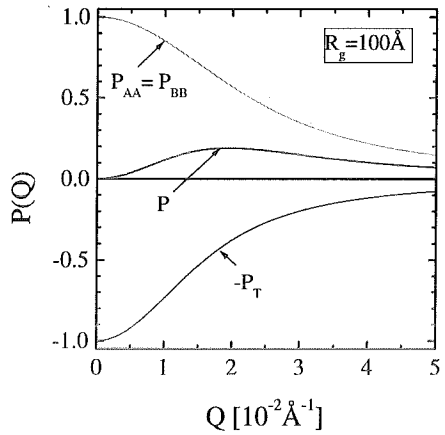


Fig. 14: *Form factor P(Q) of a symmetric diblock copolymer. The form factors of a single block and the total polymer are depicted; both determine P(Q) (eq 26).*

difference of the form factor from a single block ($P_{AA}=P_{BB}$) and the total polymer (P_T) as [9].

$$S(Q)=\frac{V}{4}[P_{AA}(Q)-P_T(Q)] \qquad (26)$$

Both form factors are depicted in Fig. 14 for a chain with R_g=100Å. The resulting form factor P is zero at Q=0, shows a maximum at Q^* and decays with Q^{-2} at large Q. The maximum at Q^* can be understood from the fact that P(Q) from the whole chain decreases faster with Q than P(Q) from a single block. Another more physical argument is that composition fluctuations

can only occur on the length scale of the polymer leading to the peak position which is related to the size of the chain according to $Q^* \cdot R_g = 1.9$.

5.2 Phase Diagram of Diblock Copolymers

Diblock copolymers show a rather complex phase behavior as depicted in both phase diagrams of Fig.15. Structures of lamellar, hexagonal, bcc, gyroid order are predicted and observed [5][6][8][18]. The reason of the ordering is that the two blocks of a chain can only separate on the length scale of the polymer. This ordering process needs a driving force $\chi N > 10.5$ in mean field approximation (see Fig. 15) which is much larger than in blends; phase separation in blends is observed at the critical point for χ larger than $\chi > 2/N$. In Fig.15 (χN) is plotted versus the composition f of the diblock copolymer [5][19].

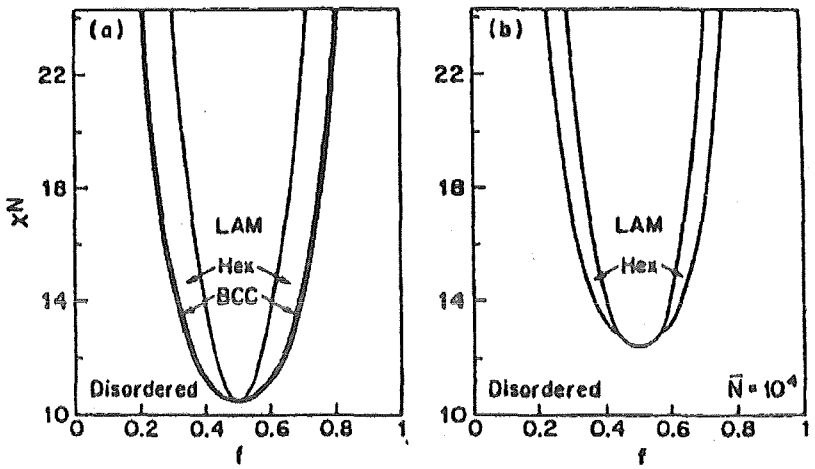


Fig. 15: *Schematic phase diagram of a diblock copolymer based on mean field(left) and non mean field evaluations (right).*

Experimental results from a symmetric diblock copolymer measured at different temperatures and pressures are shown in Fig.16 [20]. The left figure shows the structure factor which increases when lowering the temperature. The peak position of S(Q) is a susceptibility which has been plotted (right figure) versus the inverse temperature for three pressure fields. If one compares these data with corresponding experimental results from a polymer blend (Fig. 12) two characteristic differences are observed:

1.) In the disordered regime at high temperatures the experimental points follow a much more "curved" line indicating a much stronger influence of thermal composition fluctuations. Indeed, diblock copolymers obey a different universality class than the 3D-Ising model. The reason is that fluctuations become singular at a finite Q which leads to larger corrections of the renormalization procedure. A mean field theory for diblock copolymers was first formulated by Leibler [21] while the effect of thermal fluctuations were first discussed by Fredrickson and Helfand [22].

2.) The observation of a weakly first order transition at the so called order-disorder temperature T_{ODT}. In mean field approximation a second order transition is predicted

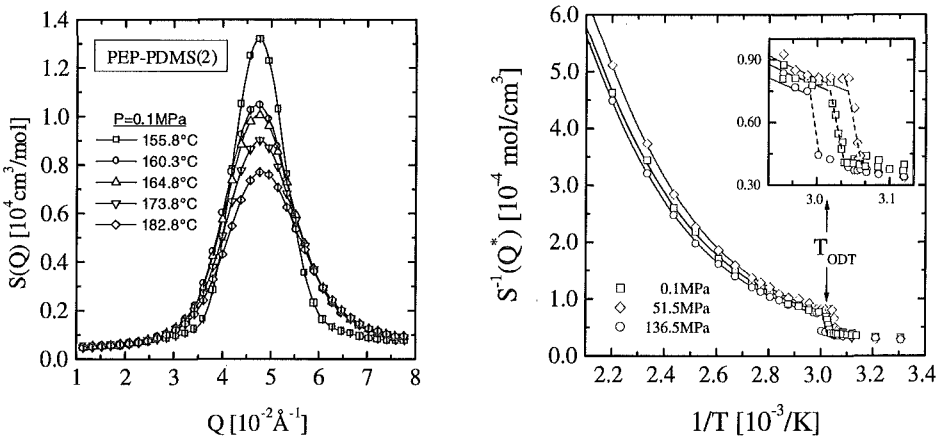


Fig. 16: *SANS data from a symmetric diblock copolymer as a function of temperature and external pressure. The structure factor shows the peak representing a susceptibility plotted in the right figure versus 1/T for three pressure fields. At high temperatures in the disordered phase the data follow a curve line according to deviations from mean field approximation. The fitted solid lines represent the theoretical approach by Fredrickson and Helfand [22]. The ordering transition is a weak fluctuation induced first order transition as observed by the step wise change of the data.*

for symmetric diblock copolymers similarly to polymer blends. The effect of fluctuations, however, leads to a weakly first order phase transition. Such a first order transition is seen in Fig.16 by the stepwise change of the susceptibility at the ordering transition.

6 Summary

We discussed single chain behavior in good solvents and in melts and cooperative phenomena in binary homopolymer blends and diblock copolymers. Depending on whether two homopolymers are separated or covalently connected one observes very different phase diagrams as well as different universality classes for thermal composition fluctuations near the transition temperatures. These observations may give an impression about the complexity and richness of soft matter research.

References

[1] P.G. deGennes, *Scaling Concepts in Polymer Physics* (Cornell University Press,1979)
[2] M. Doi, S.F. Edwards, *The Theory of Polymer Dynamics* (Oxford Science Publications, 1989)
[3] A.Y. Grosberg, A.R. Khokhlov, *Statistical Physics of Macromolecules* (AIP Press, 1994)
[4]G. Strobl, *The Physics of Polymers* (Springer, 1996)
[5]I.W. Hamley, The Physics of Block Copolymers; (Oxford Science Publications, Oxford,1998)
[6] K. Binder, *Advances in Polymer Science* 112, 181 (1994)
[7] D. Schwahn, K. Mortensen, *Thermal Composition Fluctuations in Polymer Blends studied with Small Angle Neutron Scattering* in „ Scattering in Polymeric and Colloidal Systems", eds. W. Brown and K. Mortensen, (Gordon & Breach Publishers, 2000)
[8]K. Mortensen, *Block Copolymers Studied with Small Angle Neutron Scattering* in „Scattering in Polymeric andColloidal Systems", eds. W. Brown and K. Mortensen, (Gordon & Breach Publishers, 2000)
[9]J.S. Higgins, H. Benoit, *Polymers and Neutron Scattering*; (Clarendon Press, 1994)
[10] *Neutron Scattering Experiments at the FRJ-2 in Jülich* (www.neutronscattering.de)
[11] D. Schwahn , D. Richter, P. J. Wright, Ch. Symon, L. J. Fetters, M. Lin, Macromolecules (in press)
[12] D. Schwahn, K. Hahn, J.Streib, T. Springer, J.Chem. Phys. 93, 8383 (1990)
[13] Neutron News 3 (No.3), 30 (1992)
[14] D. Schwahn, L. Willner, Macromolecules 35, 239 (2002)
[15] H. Frielinghaus, D. Schwahn, L. Willner, Macromolecules 34, 1751 (2001)
[16] J.van Sengers in *Supercritical fluids: Fundamentals for application*, edited by E.Kiran and J.M.H. Levelt Sengers; (Kluwer Academic Publishers: Dordrecht, 1994)
[17] D. Schwahn, G. Meier, K. Mortensen, S. Janssen, J. Phys.II (France) 4, 837 (1994)
[18] M.Y. Belyakov, S.B. Kiselev, Physica A190, 75 (1992)
[19] F.S. Bates and G.H. Fredrickson, Ann.Rev.Phys.Chem. 41, 525 (1990)
[20] D. Schwahn, H. Frielinghaus, K.Mortensen, K. Almdal, Macromolecules 34, 1694 (2001)
[21] L. Leibler, Macromolecules 13, 1602 (1980)
[22] G.H. Fredrickson, E.J. Helfand, J.Chem.Phys. 87, 697 (1987)

B 7 Capillary Waves on Polymer Thin Films

O. H. Seeck

Institut für Festkörperforschung

Forschungszentrum Jülich GmbH

Contents

1 Introduction **2**

2 Theory of Capillary Waves **4**
2.1 General Concept 4
2.2 Dispersion Relation and Power Spectral Density 6
2.3 The Static Case 9

3 Examples **10**
3.1 Introduction in Scattering Methods 10
3.2 Coherent X–ray Photon Correlation Spectroscopy 12
3.3 Capillary Waves on Partially Dewetted Polymer Films 13

Present address: Hasylab am Desy, Notkestraße 85, 22603 Hamburg, Germany
E–mail : ohseeck@mail.desy.de

1 Introduction

In daily life everybody gets involved with surfaces of soft matter materials or liquids. There are obvious examples such as surfaces of water which are usually quite wavy if they are excited (see Figure 1). This is different for more viscous liquids such as oil or honey where excited surface modes damp out quickly so that very smooth surfaces are experienced. Less obvious is that many surfaces of supposedly hard matter are just frozen states of the material after it was molten. Examples are glasses or polymers which surfaces can almost be compared with a 'snapshot' of a liquid surface.

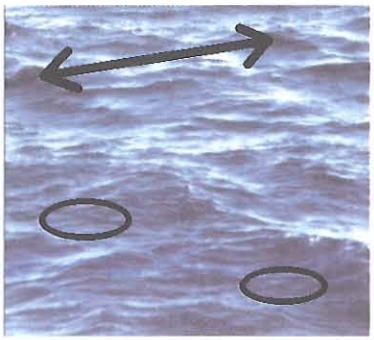


Fig. 1: *Picture of a water surface excited by an external force field (wind). A detailed analysis shows that extremely long ranged surface modes (arrow, meter scale) are present as well as modes with microscopic dimensions (circles, micrometer scale and less).*

The static and dynamic surface properties of liquids or soft matter materials are determined by parameters such as surface tension, viscoelasticity, gravitation, temperature and externally applied fields. The latter case will not be considered further on (though it is an extremely interesting topic). Therefore, in this article it is sufficient to use the simple concepts of thermodynamics and hydrodynamics for the theoretical description of soft matter surfaces. Qualitatively, it turns out that a balance of the ordering enthalpy determined by the interaction in the liquid and entropic terms which favor disorder lead to nanometer scaled rough surfaces (see Figure 2) (e.g. [1]).

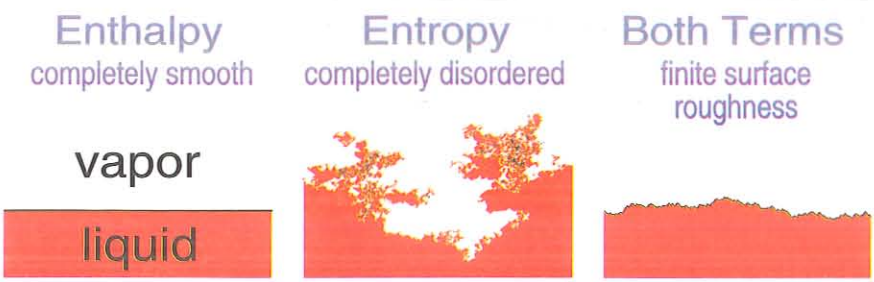


Fig. 2: *Schematic sketches of liquid surfaces which have been developed after some time starting from completely smooth. Left: Molecular interactions exceed the entropic terms by many orders of magnitude. Center: Entropy dominates completely. Right: Real liquid with both terms comparable. A fluctuating surfaces with finite roughness results.*

Roughness is defined as a statistical deviation of the local surface from the mean surface. Therefore, parameters and functions such as the root mean square deviation from the mean surface (the rms–roughness), correlation lengths, correlations functions or power spectral densities can be introduced. For fluctuating surfaces they do not only depend on space but also on time. In this article it will be shown how surfaces of viscous liquids are connected with these functions and values.
Polymers are not simple liquids. They consist out of long organic chain molecules which can easily and in many ways interact with each other. A strong dependence of the polymer surface structure on the chemical composition, molecular weight, glass temperature, cross–linking or nesting features is expected (see Figure 3). However, surprisingly in many cases even surfaces of quite complicate polymers behave like simple liquid surfaces. Thus, the role of the above mentioned special properties of the polymers will not be discussed in this article in detail.

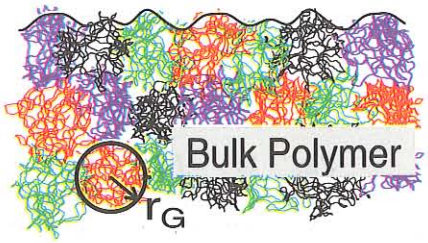


Fig. 3: *Sketch of a bulk polymer at the surface (top line). For the different molecules with radius of gyration r_G different colors are used. The special properties of the polymer determines the surface structure.*

Of eminent interest nowadays is the microscopic and mesoscopic surface structure of extremely thin soft matter films which are used e.g. as coatings, lubricants or very recently as flexible display screens. The surface properties of thin films are strongly influenced by the substrate material and can be totally different from those of the bulk material (see Figure 4). Keywords are cut–off lengths in the surfaces correlation functions or partially dewetting. Even if no substrate is present finite size effects can dramatically effect the surface (cross–correlated surfaces during film rupture) [2].

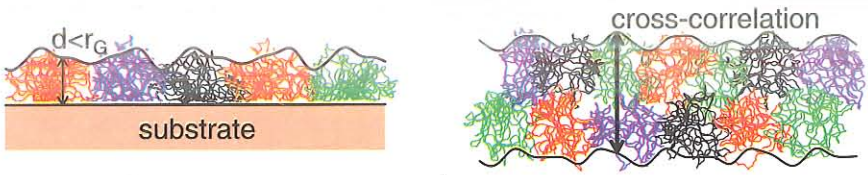


Fig. 4: *Two examples of thin film polymers. Left: The thickness of the polymer film prepared on a substrate is comparable or smaller to radius of gyration r_G. In this case simple hydrodynamics fails to explain the polymer surface. Right: The two surfaces of extremely thin free standing polymer films may by correlated with each other especially during rupture.*

Because of their eminent importance the surface structure of soft matter thin films will be

explained in more detail in this article, especially the influence of the substrate potential on the surface correlation function.
Finally, some examples of experiments on polymer surfaces are addressed. It will be shown how x–ray scattering methods and atomic force microscopy can be used to investigate the static and dynamic surface properties. For this, a very brief introduction in x–ray scattering methods is given.

2 Theory of Capillary Waves

As mentioned in the previous chapter liquid surfaces are not atomically flat but microscopicly rough due to a balance between entropic and enthalpic terms. Also, the local surface is not static but fluctuates. These fluctuating surfaces can be associated with a sum of propagating plane waves with different amplitudes A_j, wave numbers k_j and phases φ_j where j is the running index (see Figure 5). If these waves are excited thermodynamically (and not by external forces) on liquid surfaces they are called capillary waves [3].

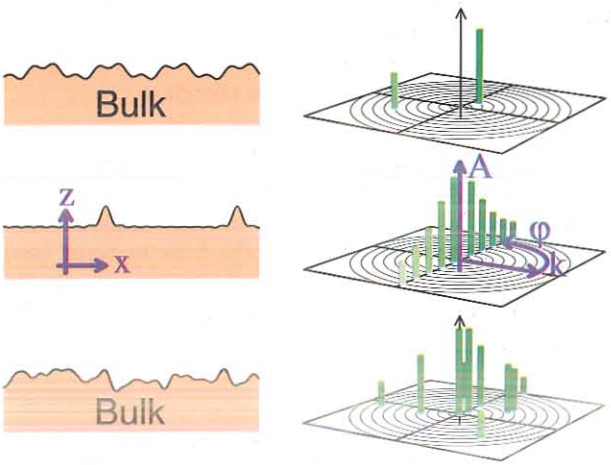


Fig. 5: *Interfaces with* $z = \sum A_j(k_j)sin(k_j x + \varphi_j)$. *The amplitudes* A_j *of the Fourier components (FC) scale Lorentzian–like* $A_j \sim 1/(1+k_j^2)$. *Top: Surface with two FCs. Both waves are distinguishable. Middle: Sum of 10 FCs with* $k_j \sim j$ *and* $\varphi_j = j\pi$. *A highly periodic surface structure results. Bottom: Random* k_j *and* φ_j. *The sum of the 10 FCs gives an unperiodically looking surface.*

2.1 General Concept

In this article, for the theoretical treatment of capillary waves using hydrodynamics the liquid is considered as a continuous medium [4–6]. It can be described by

mass density:	$\rho(\boldsymbol{r},t)$	velocity field:	$\boldsymbol{v}(\boldsymbol{r},t)$
momentum density:	$\boldsymbol{\pi}(\boldsymbol{r},t)$	pressure field:	$p(\boldsymbol{r},t)$
energy density:	$\epsilon(\boldsymbol{r},t)$	temperature field:	$T(\boldsymbol{r},t)$

with the position vector $\boldsymbol{r}$ and the time t. In the equilibrium state the sum of all forces has to be zero. In a simple approach only the forces acting on volume elements $\rho \cdot \partial \boldsymbol{v}/\partial t$,

resulting from pressure gradients ∇p and friction $-\eta\Delta\boldsymbol{v}$ (with the viscosity η) are taken into account. From this follows

$$\rho\frac{\partial}{\partial t}\boldsymbol{v} = -\nabla p + \eta\Delta\boldsymbol{v} \tag{1}$$

which is a simplified form of the Navier–Stokes equations. To solve Eq. 1 for capillary waves the fact is used that small deviations of the local surface from the mean surfaces can always be approximated by a sum of plane waves (see again Figure 5). Introducing the ansatz for plane waves

$$\boldsymbol{v} = \begin{pmatrix} v_x(z) \\ 0 \\ v_z(z) \end{pmatrix} \exp(i[kx - \omega t]) \qquad , \qquad p = p_0(z)\exp(i[kx - \omega t]) \tag{2}$$

with the wave number k and the frequency ω the Navier–Stokes equation modifies to

$$\begin{aligned} -i\omega\rho v_x &= -ikp_0 + \eta\left(\frac{\partial^2}{\partial z^2} + k^2\right)v_x \\ -i\omega\rho v_z &= -k\frac{\partial}{\partial z}p_0 + \eta\left(\frac{\partial^2}{\partial z^2} + k^2\right)v_z \end{aligned}$$

where the pressure $p_0(z)$ can easily be eliminated yielding

$$\left(\frac{\partial^2}{\partial z^2} - k^2\right)w = \frac{-i\omega\rho}{\eta}w \tag{3}$$

with

$$w(z) = \frac{\partial}{\partial z}v_x(z) - ikv_z(z) \tag{4}$$

and the solution

$$w = A\cosh\left(z\sqrt{k^2 - i\omega\rho/\eta}\right) + B\sinh\left(z\sqrt{k^2 - i\omega\rho/\eta}\right).$$

For incompressible and source free liquids the additional condition $\nabla\cdot\boldsymbol{v} = 0$ applies. Using the ansatz 2 this condition can be rewritten as

$$ikv_x + \frac{\partial}{\partial z}v_z = 0. \tag{5}$$

With Eqs. 3, 4 and 5 the whole problem can be decoupled in $v_x(z)$ and $v_z(z)$. To actually solve the equations and to determine the motion of the liquid at the surface one has to use the proper boundary conditions. One is simply given by $\boldsymbol{v} = 0$ deep in bulk liquid or at a solid liquid interface. At the surface the situation is more complicate and the stress tensor $\bar{\boldsymbol{\sigma}}$ has to be included in the calculation. For plane wave one gets

$$\sigma_{xz} = \eta\left(\frac{\partial}{\partial z}v_x + \frac{\partial}{\partial x}v_z\right) = 0$$

and

$$\sigma_{zz} = \gamma\frac{\partial^2}{\partial^2 x}u_z + g\rho u_z + P_z$$

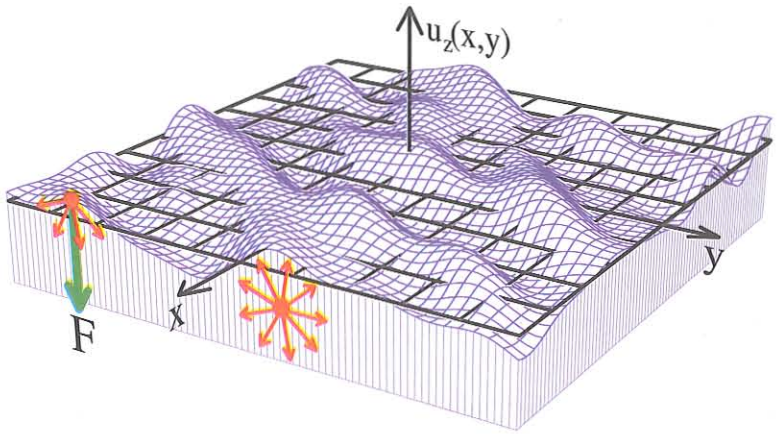


Fig. 6: *A liquid surface. The close meshed grid is the real surface the wide the averaged mean surface. The local distance in z–direction between both surfaces is the vertical surface displacement $u_z(x, y)$. Additionally shown is the concept of surface tension: A volume element in the bulk is homogeneously surrounded by the liquid. All forces compensate each other. At the surface the symmetry is broken and a resulting force points into the bulk.*

with the surface tension γ, the gravitational constant g and the vertical surface displacement $u_z(x, y)$ (see Fig. 6).
Following the article from J. Jäckle [7] with these boundary conditions the dynamic susceptibility of the surface waves $\chi_{zz}(k, \omega) = u_z/p_z$ can be derived (note that the pressure is defined as an external force per surface area, therefore χ_{zz} is the response of the surface on external forces). The longish calculations are skipped. Only the results which are important for this article are presented in the next section.
For very thin films of thickness d finite size effects can occur. The interaction of the polymer with the substrate material has additionally to be taken into account at the surface. Assuming van der Waals interaction the so–called effective Hamaker constant A_{eff} is of importance. Depending on d this interaction can dramatically influence the capillary wave spectrum as will be shown in the next section.

2.2 Dispersion Relation and Power Spectral Density

After presenting the general physical concepts of capillary waves in the previous chapter two quantities will be introduced which can directly be used to describe liquid surfaces. The first one is the dispersion relation of surface waves $\omega_s(k)$ which connects the speed of the surface waves c_s with their wavelength λ_s via $\omega_s = c_s k = 2\pi c_s/\lambda_s$.
The dispersion relation for thin films can be derived as [8]

$$\omega_s^2(k) = \left[\left(g + \frac{A_{\text{eff}}}{2\pi\rho d^4}\right) k + \frac{\gamma}{\rho} k^3\right] \tanh(kd) \tag{6}$$

which for bulk liquids ($d \to \infty$) simplifies to the well known behavior $\omega_s^2(k) = gk + \gamma k^3/\rho$.

Figure 7 visualizes Eq. 6 and shows the effects of finite film thickness and interaction with the substrate material. For bulk liquids a transition can be seen at a wavelength of around some centimeters (or $k \approx 600\mathrm{m}^{-1}$, respectively): The propagation of surface modes with larger wavelengths is dominated by gravitation and a relation $c_s^2 \sim \lambda_s$ (or $\omega_s^2 \sim k$, respectively) is found. On the other hand, waves on microscopic scale are mostly affected by the surface tension and the density of the liquid. An anomalous dispersion relation $c_s^2 \sim \lambda_s^{-1}$ (or $\omega_s^2 \sim k^3$, respectively) is observed.

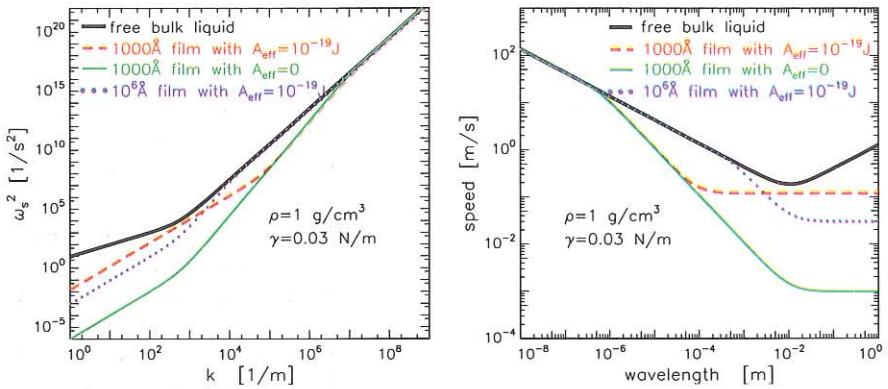


Fig. 7: *Dispersion relations for liquid surfaces. The left figure displays Eq. 6, the right figure is the equivalent representation of the speed of the waves depending on the wavelength. The chosen parameters are typical for organic liquids on silicon substrates.*

In the case of thin films only capillary waves with very small wavelengths remain unchanged. But for λ_s larger than a particular value (typically $[10^{-7}...10^{-4}]\mathrm{m}^{-1}$) which depends on the film thickness d and the interaction parameter A_{eff} with the substrate the dispersion relation is completely different than observed at the bulk. Qualitatively, this additional transition occurs at wavelengths comparable to the film thickness. This is in good agreement with the expectations from simple hydrodynamics where the penetration depth of surface waves into the bulk scales with the wavelength: All modes with $\lambda_s > d$ touch the substrate interface and are hindered in their propagation.

A complete statistical picture of the surface structure in space and time can be derived from the dynamical power spectral density (PSD) $\tilde{C}(k,\omega)$ which is a measure of the time changing number of surfaces modes in a particular k–range. The PSD can simply by calculated by

$$\tilde{C}(k,\omega) = 2k_B T \frac{\Im\{\chi_{zz}(k,\omega)\}}{\omega} \tag{7}$$

where $\chi_z z = u_z/p_z$ is the susceptibility introduced in the previous chapter, T is the temperature and k_B the Boltzmann constant. The operator $\Im\{\}$ selects the imaginary part of the function on which it was applied to.

Following Jäckle [7] the susceptibility of a semi–infinite liquid ($d \to \infty$) has the form

$$\chi_{zz}(k,\omega) = \frac{k/\rho}{\omega_s(k)^2 - \omega^2 - i\omega D_{\eta\rho}(k,\omega)} \tag{8}$$

with a complex damping function $D_{\eta\rho}(k,\omega)$, whereas in the limit $d \to 0$ one gets

$$\chi_{zz}(k,\omega) = \frac{k/\rho \cdot kd}{\omega_s(k)^2 - \omega^2 \cdot [6/5] - i\omega \cdot [3\eta/(d^2\rho)]} \tag{9}$$

with the dispersion relation ω_s given by Eq. 6. From these results a phase diagram of surface modes of viscous liquids, such as liquid polymers or polymer solutions, can be extracted (see Fig. 8).

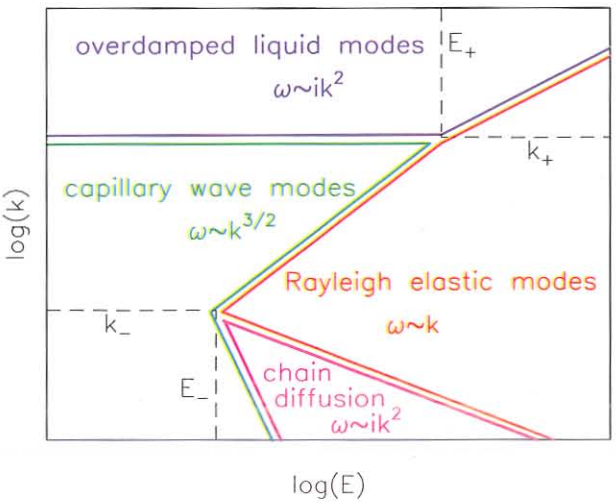


Fig. 8: *Phase diagram of the surface modes of viscous polymer solutions. The abscissa is given by the logarithm of the shear modulus E which is introduced by the frequency dependent viscosity $\eta(\omega) = \eta + E/(i\omega)$. The ordinate is defined by the logarithm of the wave number with the value of k_+ given by $k_+ = \rho\gamma/\eta^2$. The figure is taken from Harden et. al [9].*

From the phase diagram a separation of capillary wave modes with the usual behavior $\omega^2 \sim k^3$ from so called overdamped liquid modes with $\omega \sim ik^2$ can be seen [9]. The separation line is given by $k_+ \approx \rho\gamma/\eta^2$. For a typical polymer such as polystyrene with a molecular weight of 120k at a temperature of about 180°C values of $\rho \approx 1000\text{kg/m}^3$, $\gamma \approx 0.01\text{N/m}$ and $\eta \approx 10^4\text{kg/(ms)}$ are found. This means $k_+ \approx 10^{-6}\text{m}^{-1}$. Therefore, capillary waves on polymer surfaces with wavelengths smaller than some meters are strongly overdamped and a wave number dependent relaxation time

$$\tau(k) \approx \frac{2\eta}{\gamma k} \cdot \frac{\cosh^2(dk) + d^2k^2}{\sinh(dk)\cosh(dk) - dk} \begin{array}{l} \xrightarrow{d\to\infty} \quad \frac{2\eta}{\gamma k} \\ \xrightarrow{dk\ll 1} \quad \frac{3\eta}{\gamma d^3 k^4} \end{array} \tag{10}$$

can be introduced [10]. With the values of polystyrene given above relaxation times in the order of milliseconds to seconds are expected for modes with wave numbers $k \approx 10^7\text{m}^{-1}$ (or with about 1μm wavelength, respectively). Most importantly, τ decreases with increasing k (or decreasing wavelength, respectively) which means that short capillary waves decay more quickly than long waves. This behavior can also be verified experimentally as will be shown in the experimental section 3.2.

2.3 The Static Case

Many polymers are solid at room temperature or are extremely viscous liquids or glasses. Others are liquid with low viscosity even at room temperature. In the first case the relaxation times become almost infinite and frozen capillary waves are expected if the samples are prepared from the melt. In the latter case relaxation times τ are less than microseconds and an averaged surface is observed if the sampling time of the experiment is on the order of seconds.
Both cases can be accounted as static surfaces. For solid polymers this is obvious. For liquids this is only true if the system is ergodic and all τ are much smaller than the sampling time. In this case the time averaged surface is quasi–static even though it is fluctuating on short time scale. The time averaged quasi–static PSD $\tilde{C}(k)$ is deduced by integrating the dynamical PSD $\tilde{C}(k,\omega)$ over all ω:

$$\tilde{C}(k) = \int_{-\infty}^{+\infty} \tilde{C}(k,\omega)\frac{\mathrm{d}\omega}{2\pi} = k_B T \chi_{zz}(k,0).$$

Using the results 8 and 9 one gets

$$\tilde{C}(k) = \frac{k_B T}{4\pi^2\gamma} \cdot \left[k^2 + \left(\frac{g\rho}{\gamma} + \frac{A_{\mathrm{eff}}}{2\pi\gamma d^4}\right)\right]^{-1} = \frac{k_B T}{4\pi^2\gamma} \cdot \frac{1}{k^2 + k_s^2} \tag{11}$$

which is a Lorentzian–like form with a wave number cut–off given by k_s. Due to the integration, the viscosity completely dropped out of the PSD. Figure 9 displays time averaged quasi–static PSDs for liquids and liquid films.

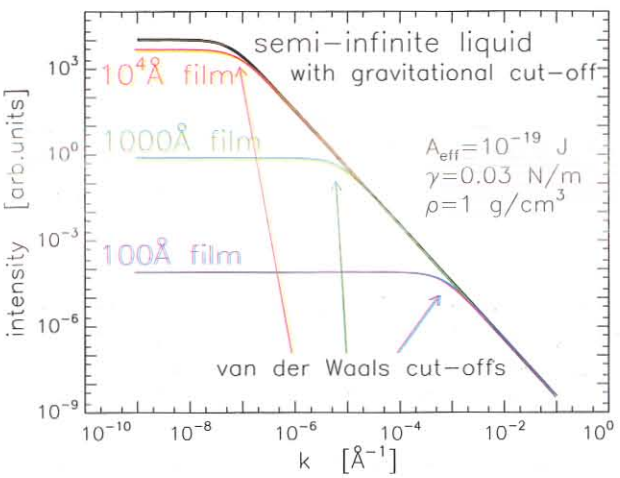


Fig. 9: *Log–log representation of static PSDs of liquid surfaces. A typical kink can be seen due to the cut–off k_s. For films thinner than 10^4Å this cut–off is dominated by the van der Waals interaction with the substrate. Thicker films behave like bulk liquids with a dominating gravitational term.*

Generally, it can be seen that the number of modes is increasing with a power law for decreasing wave number (or growing wavelength) until the cut–off k_s is reached. For semi–infinite liquids this cut–off is simply given by $k_s = g\rho/\gamma$ and is of gravitational origin. Typical liquid polymers yield $k_s \approx 10^{-7}\text{Å}^{-1} = 10^3\text{m}^{-1}$ which corresponds to wavelengths

of some millimeters (compare also Fig. 7). Thin film polymers ($d < 1\mu$m) exhibit another cut–off $k_s = A_{\text{eff}}/(2\pi\gamma d^4)$ according to the van der Waals interaction with the substrate. The position of this cut–off strongly depends on the film thickness d. In Section 3.3 an example will be shown, how time averaged quasi–static PSDs can be measured and analyzed.

3 Examples

In the following sections some examples are presented how to measure dynamic and static PSDs of polymer or polymer–like surfaces and how to interpret the data. Most data have been taken by x–ray scattering methods. Therefore, a very brief introduction in the scattering methods is given first.

3.1 Introduction in Scattering Methods

To investigate surfaces and buried interfaces scattering methods can most sufficiently be used if statistical parameters such as correlation lengths or relaxation times should be determined. To get an image of the real surface microscopic methods are preferred.
For the scattering experiment, the surface of the sample is illuminated with light, x–rays or neutrons under an incident angle α_i (see Fig. 10). The scattered beam is detected under an exit angle α_f. The beams are treated as plane waves, therefore, the wave vectors $\boldsymbol{k}_i$ and $\boldsymbol{k}_f$ can be introduced which point in the direction of propagation. For elastic scattering the absolute values of $\boldsymbol{k}_i$ and $\boldsymbol{k}_f$ are $2\pi/\lambda$ with the wavelength of the light λ.

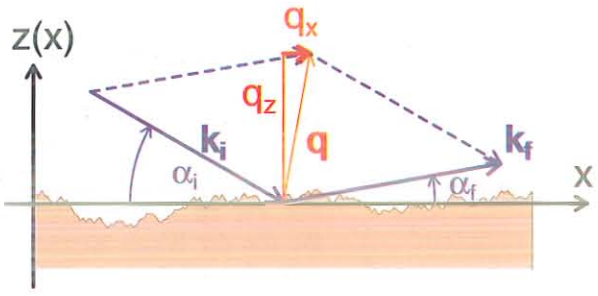


Fig. 10: *Sketch of a scattering experiment at a rough surface. The symbols are explained in the text.*

The properties of the interfaces which can be determined by the scattering experiment are given by the wave vector transfer $\boldsymbol{q} = \boldsymbol{k}_f - \boldsymbol{k}_i$. E.g. if $\alpha_i = \alpha_f$ there is no component q_x and this kind of experiment is not sensitive to in–plane information of the interfaces. On the other hand, if $\alpha_i \neq \alpha_f$ the surface properties with wave numbers $k = q_x$ can be sampled.
This is shown in Fig. 11. Simple optical considerations yield that a completely smooth surface only reflects intensity at $\alpha_i = \alpha_f$. This is different, if a periodic structure modifies the surface. Each surface mode with wavelength λ_s causes an intensity spike at a position $q_x = \pm k_s = \pm 2\pi/\lambda_s$. Therefore, the sum of all these spikes which are called speckles represent the dynamical PSD $\tilde{C}(k,\omega)$ of the surface. Usually, a liquid surface has an enormous number of speckles which are located extremely close to each other and which

are fluctuating in intensity due to the dynamics of the surface modes. The challenge for a scattering experiment is to resolve the speckles in reciprocal space and in time to get the full dynamical and spatial surface information. Otherwise, by averaging the speckle pattern smears and only the time averaged quasi–static PSD can be observed.

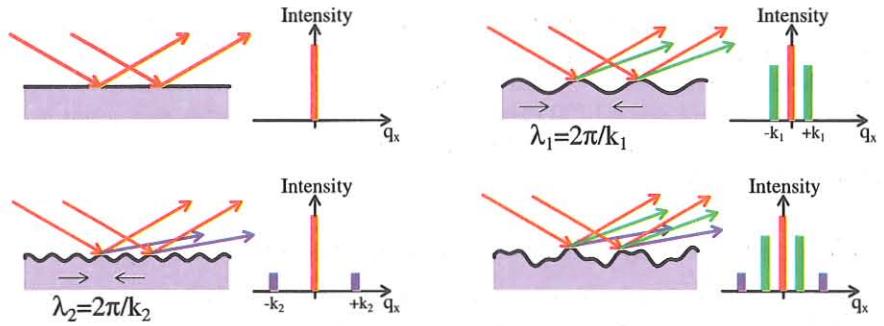


Fig. 11: *Speckle scattering for different surfaces. The averaged surface gives a speckle at $q_x = 0$. Each mode on the surface with wavelength λ_s results in two speckles at the q_x–position $q_x = \pm k_s = \pm 2\pi/\lambda_s$. The sum of all speckles represent the PSD of the surface.*

An example for a scattering experiment at a glycerol surface is displayed in Fig. 12. Glycerol is a glassy material with a glass transition temperature of $T_g = -87°C$. Below and around T_g all relaxation times are almost infinite, for higher temperatures (with dropping viscosity) the τ–values are finite and become smaller for increasing T.

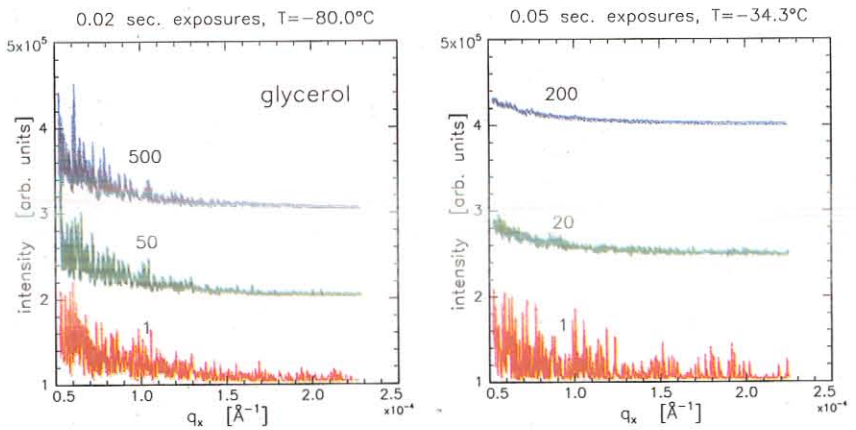


Fig. 12: *Scattering experiments at glassy glycerol. The data are shifted in intensity for clarity. The small numbers beside the data curves denote the number of exposures which are used to integrate the data. So 500 in the left graph means 10 seconds integration time as well as the number 200 in the right graph.*

To record the data a CCD–camera was used which can perform a whole q_x–scan in one shot with a minimum sampling time of some milliseconds. A coherent x–ray synchrotron

radiation source was used to create the primary beam. The left part of Fig. 12 shows the data taken at $T = -80°C$ which is a bit above T_g. In this case the relaxation times $\tau(k) = \tau(q_x)$ are almost infinite due to the high viscosity (see Eq. 10) and an almost static surface is expected. At a first sight, even after integrating 500 exposures which means a sampling time of 10 seconds the speckles remain visible. However, a closer look at high q_x shows that the speckles start to smear with increasing sampling time. Thus, according to Eq. 10 the relaxation times are on the order of 1..100 seconds in the taken k–range. The data taken at $T = -34.3°C$ exhibit speckles only for very short exposures. After integrating over 1 second (20 exposures) the spikes are almost gone even at small q_x. After 10 seconds the time averaged static picture is gained. This means time scales of some 10 milliseconds for τ.

3.2 Coherent X–ray Photon Correlation Spectroscopy

In this section an example is given how to extract the dynamic behavior of $\tilde{C}(k, \omega)$ for polymer thin films from scattering experiments. The purpose was to verify Eq. 10 especially concerning the dependence of the relaxation times on the film thickness. The results are displayed in Fig. 13.

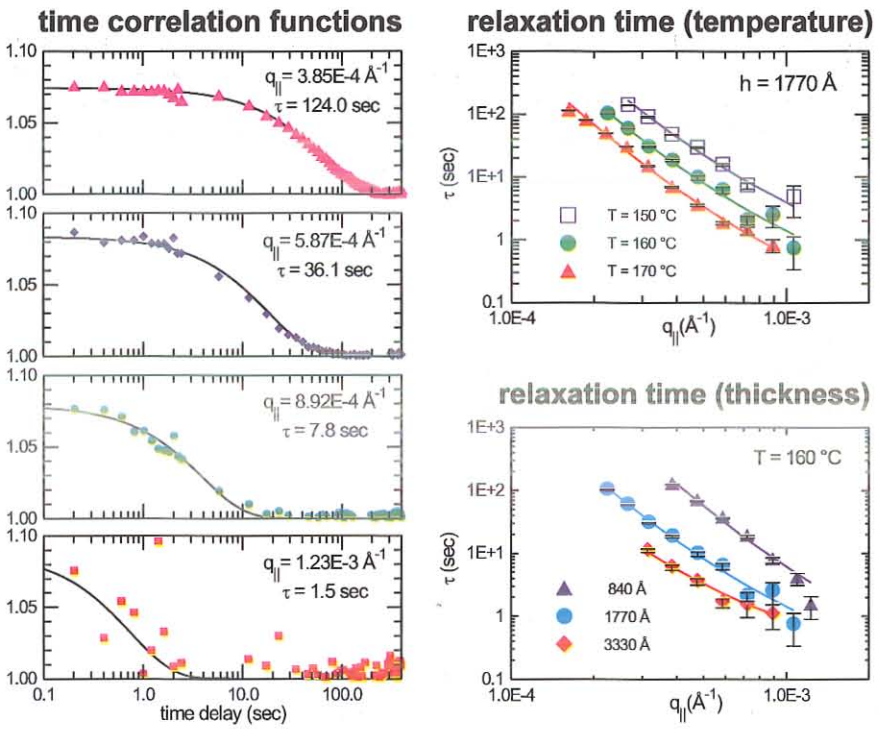


Fig. 13: *Time correlation functions and relaxation times of thin polystyrene films. The symbols are the data, the lines are the calculations. The ordinate of the left figures is the intensity of the autocorrelation functions. They are taken from the 840Å film at* $T = 160° C$.

The samples were prepared by spin coating thin polystyrene (PS) films on silicon wafers with thicknesses of $d_1 = 840$Å, $d_2 = 1770$Å and $d_3 = 3330$Å. The molecular weight was $M_W = 123$k which means a glass transition temperature of $T_g = 110$°C. The surface tension is about $\gamma = 0.03$N/m. Literature values for the viscosity are: $\eta_{150°C} = 5.0 \cdot 10^5$kg/(ms), $\eta_{160°C} = 1.3 \cdot 10^5$kg/(ms) and $\eta_{170°C} = 3.3 \cdot 10^4$kg/(ms). The scattering experiments have been performed by Hyungjung Kim at the beamline 8–ID at the synchrotron radiation source APS (Chicago, USA) using a coherent x–ray beam with a wavelength of $\lambda = 1.62$Å. In principle, she analyzed pictures similar to Fig. 12. By calculating the time dependent intensity autocorrelation function from the CCD camera data

$$C(q_x, t) = \frac{< I(q_x, t')I(q_x, t' + t) >}{< I(q_x, t') >^2}$$

one gets graphs such as displayed on the left hand of Fig. 13. They can be fitted with an exponential decay function $1 + A\exp(-2t/\tau)$ where τ is the relaxation time of the mode with wave number $k = q_x$.
In this way one gets temperature, thickness and wave number depending relaxation times such as shown on the right hand side of Fig. 13. The theory presented in chapter 2.2 matches the measurements extremely well: The solid lines are refinements with the only free parameter η/γ which turns out to be very close to the literature values for bulk PS.

3.3 Capillary Waves on Partially Dewetted Polymer Films

The measurement of speckle patters requires an extremely coherent incident beam and high resolution instruments, especially when x–rays are used. Both are available only since short time. Prior, time averaged quasi–static PSDs could be observed by measuring the intensity which is diffusely scattered from the surfaces. These data contain only spatial information. However, they are useful to determine e.g. the van der Waals interaction parameters by analyzing the van der Waals cut–off k_s introduced in Eq. 11. In the example presented in this section the diffusely scattered intensity is used to learn if capillary waves can form on partially dewetted polymer films.
For this polyethylenpropylen (PEP) films have been prepared on silicon substrates [11]. Atomic force microscopy (AFM) shows that the polymer surfaces exhibit an island structure with island sizes depending on the film thickness (see Fig. 14). However, the AFM cannot resolve capillary waves with typical amplitudes of some angstroms.

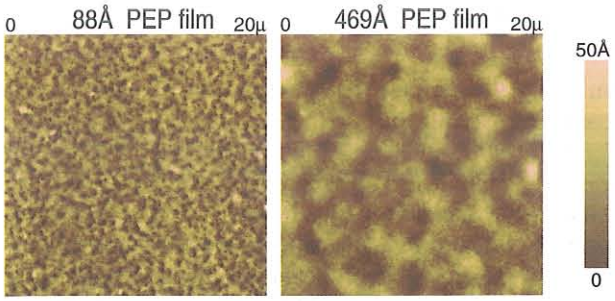


Fig. 14: *Atomic force microscopy pictures of thin PEP–films on silicon substrates. The island structure can clearly be seen. The island size depends on the film thickness. Capillary waves cannot be resolved with this method.*

As PEP has a glass transition temperature of $T_G = -62$°C the system is in a completely liquid state at room temperature and quasi–static measurements are performed. Speckles

cannot be seen. In good approximation the diffusely scattered intensity is given by

$$I_{\text{diff}}(q_x, q_z) \propto \frac{\exp(-q_z^2\sigma^2/2)}{q_z^2} \int \left(\exp[q_z^2 C(x)] - 1\right) \cos(q_x x)\mathrm{d}x \qquad (12)$$

with the surface roughness σ and the correlation function $C(x) \approx -k_B T/(2\pi\gamma)[\ln(k_s x/2)+ 0.5772]$ which is the Fourierbacktransformation of the quasi–static PSD $\tilde{C}(k)$ given by Eq. 11. Putting this logarithm form of the correlation function in Eq. 12 yields a typical power law behavior for the diffusely scattered intensity [12] where the exponent $\kappa = k_B T q_z^2/(2\pi\gamma)$ depends on q_z and on the surface tension γ. Typical measurements of the diffusely scattered intensity of the PEP–films are displayed in Fig. 15

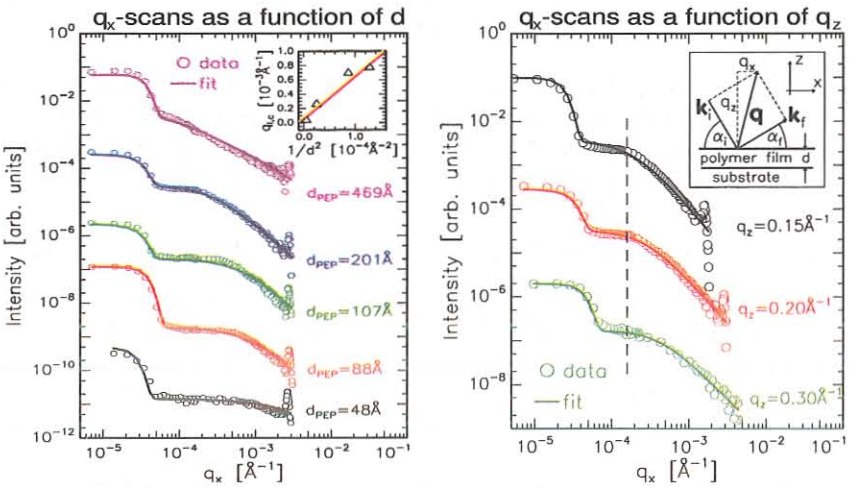


Fig. 15: *Diffusely scattered intensity from thin PEP–films. The left graphs are taken as a function of the film thickness d the right as a function of q_z (see the inset for the scattering geometry). The curves are shifted in intensity for clarity. The vertical dashed line marks the van der Waals cut–off. The maxima at $q_x < 10^{-4}\text{Å}^{-1}$ are due to specular scattering and contain no information about the in–plane structure of the films. The value $q_{l,c}$ in the left inset is identical to the cut–off k_s.*

The data resemble the graphs shown in Fig. 9 except for very small q_x where a peak can be found in the data. This is due to specular scattering and is not discussed in more detail at this place. The diffuse scattering for $q_x > 10^{-4}\text{Å}^{-1}$ shows all features which are expected for capillary waves of thin liquid films: 1) A film thickness dependent van der Waals cut–off $k_s = A_{\text{eff}}/(2\pi\gamma d^4)$, visible as a kink in the scattering (see left graphs of Fig. 15). 2) A q_z–dependent slope of the intensity for $q_x > k_s$ in the log–log representation according to the exponent κ introduced above. A careful analysis of the data using Eq. 12 in fact yield that the features of the diffuse scattering cannot be explained by only assuming an island structure on the surface as seen by the AFM–picture. Additionally, capillary waves exist on each island but with a maximum wavelength comparable to the island size.

References

[1] *Physics of Polymer Surfaces and Interfaces*, edited by I.C. Sanchez (Butterworth–Heinemann, Boston, 1992).

[2] K. Shin, Y. Pu, M.H. Rafailovich, J. Sokolov, O.H. Seeck, S.K. Sinha, M. Tolan, and R. Kolb, Macromolecules **34**, 5620 (2001).

[3] F.P. Buff, R.A. Lovett, and F.H. Stillinger, Phys. Rev. Lett. **15**, 621 (1965).

[4] H. Lamb, *Hydrodynamics* 6th edition (University Press, Cambridge, 1992).

[5] *Light Scattering by Liquid Surfaces and Complementary Techniques*, edited by D. Langevin (Marchel Dekker Inc., New York, 1992).

[6] L.D. Landau, and E.M. Lifshitz, *Fluid Mechanics* (Pergamon Press, New York, 1959).

[7] J. Jäckle, J. Phys.: Condens. Matter **10**, 7121 (1998).

[8] D. Beaglehole, Physica A **200**, 696 (1990).

[9] J.L. Harden, H. Pleiner, and P.A. Pincus, J. Chem. Phys. **94**, 5208 (1991).

[10] D. Foster, *Hydrodynamic Fluctuations, Broken Symmetry, and Correlation Functions* (W.A. Benjamin, Reading, MA, 1974).

[11] M. Tolan, O.H. Seeck, J.–P. Schlomka, W. Press, J. Wang, S.K. Sinha, Z. Li, M.H. Rafailovich, and J. Sokolov, Phys. Rev. Lett. **81**, 2731 (1998).

[12] M. Tolan, *X-ray Scattering from Soft Matter Thin Films* (Springer, Berlin, 1999).

B 8 Self-assembling Amphiphilic Systems

M. Gradzielski
Lehrstuhl für Physikalische Chemie I
Universität Bayreuth

Contents

1 Types of Amphiphiles 2
2 Properties of Amphiphiles - cmc - Micelle Formation 3
3 Driving Force for Self-aggregation - Hydrophobic Effect 5
4 Factors Affecting the cmc 5
5 Thermodynamic Description of Micelles 8
6 Dynamics of Micelle Formation and Dissolution 10
7 Krafft Point and Cloud Point 11
8 Shape and Size of Aggregates 12
9 Liquid Crystals - Phase Behaviour 13
10 The Packing Parameter 15
11 Bending Elasticity 17
12 Solubilisation - Microemulsions 20
13 Surfactant Mixtures - Mixed Micelles 21
14 Further Aspects 22

1 Types of Amphiphiles

Amphiphilic molecules are composed of two parts, one **hydrophilic** (solvophilic) part and one **hydrophobic** (solvophobic) part (for simplicity we want to regard water as solvent if not otherwise stated) that are linked together chemically. Such molecules have a natural tendency to be surface active, i.e. they are enriched at the surface and thereby lower the surface tension. Therefore they are commonly called **surfactants**. In the simplest case one may have water as a solvent and the hydrophobic part can simply be a **hydrocarbon chain**. The **hydrophilic (polar) head group** can be of various type and the surfactants are classified accordingly:

- **nonionic** head group: e.g. alkyl polyglycol monoethers (e.g. $C_{12}H_{25}$-O-$(C_2H_4O)_5H$ ($C_{12}E_5$)), (niosomes), phosphine oxides, alkyl polyglycosides (nonionic surfactants)
- **amphoteric** (**zwitterionic**) head group: e.g. betaines, amine oxides, lipids (zwitterionic surfactants)
- **cationic** head group: alkyl trimethylammonium halides (e.g. $C_{14}H_{29}$-$N(CH_3)_3^+$ Br^- (TTAB)), alkyl pyridinium halides (cationic surfactants)
- **anionic** head group: alkyl sulfates (e.g. $C_{12}H_{25}$-OSO_3^- Na^+ (Sodium dodecyl sulfate, SDS), alkyl sulfonates (e.g. $C_{12}H_{25}$-SO_3^- Na^+ (Sodium dodecyl sulfonate)), alkyl carboxylates, alkyl sarcosides (R-CO-$N(CH_3)$-CH_2-COO^-) (anionic surfactants)

One way to distinguish the different surfactant molecules is given by the number of their hydrocarbon chains. Therefore one can have single chain, double chain, triple chain, etc. surfactants.
It is also possible to have several polar head groups covalently bound together as it is the case in the so-called gemini surfactants (Fig.1) [1]:

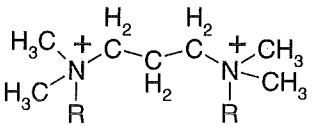


Fig. 1: *A bis-(dimethyl, alkyl)ammonium gemini surfactant with a propylene spacer*

Another way to subdivide various surfactants is by the nature of the hydrophobic part. As stated, normally this is a hydrocarbon chain (hydrocarbon surfactant, "normal" surfactant). Other frequently encountered hydrophobic parts are perfluoro alkyl chains (**perfluoro surfactants**; used for galvano techniques, hydrophobisation of surfaces, repellents for leather, paper, textiles, soil retardants, polymerisation of fluoro monomers, etc.) [2] or silicon chains (**silicon surfactants**; used as foam stabilizers, anti-statics, hydrophobisation and glossiness of surfaces, treatment of textiles, solubilisation of silicon oils, lubrification, etc.) [3].
Surfactants are of vast commercial importance with a production of $\approx 7 \cdot 10^6$ tons per year world-wide. They are employed as follows:

- 50%: washing, cleaning
- 17%: textiles, fibres
- 7%: cosmetics, pharmacy (shampoos, cremes, emulgators, etc.)

- 7%: mining, flotation (separation of minerals)
- 5%: food products (emulgators for food, baking, etc.)
- 2%: crop protection
- metallurgy, lubrification, corrosion inhibition

2 Properties of Amphiphiles - cmc - Micelle Formation

As already discussed amphiphilic molecules are composed of two parts, a hydrophilic (solvophilic) part and a hydrophobic (solvophobic) part. Therefore the basic ingredient of amphiphilic behaviour is the inherent tendency of both parts of the molecule to separate from each other but this is not possible due to the fact that both parts are chemically linked. Nonetheless, for the case of an aqueous solution the hydrophobic part wants to avoid or at least to minimise the contact with water. One way to do so for the amphiphiles is to concentrate at the air-liquid interface.

The concentration of the amphiphiles at the surface results in a change of the surface tension of the liquid, i.e. in a reduction of the surface tension. The surface tension decreases with increasing surfactant concentration until at a certain point it becomes constant (see Fig.2). Beyond this point not only the surface tension remains constant but evidently also the chemical potential of the surfactant molecules in solution. Before this point there is a linear region of the surface tension as a function of the logarithm of the concentration. In this range the air-liquid surface is already saturated with surfactant molecules and the surface tension is reduced according to the **Gibbs isotherm**:

$$d\sigma = -\Gamma \cdot k \cdot T \cdot d \ln a \qquad (1)$$

where a is the activity of the surfactant species, k the Boltzmann constant, T the temperature, and Γ the surface concentration of the surfactant species (in dimensions of molecules per area). Accordingly from the slope of the surface tension curve just before the bending point one can directly evaluate the area at the surface required per surfactant molecule - the **head group area** $\mathbf{a_s} = 1/\Gamma$.

Beyond the bending point formation of aggegates of the surfactant molecules - so called micelles - has set in. This point of micelle formation is called **critical micelle concentration (cmc)**. It can be discerned from the measurement of a variety of physical quantities of the corresponding surfactant solutions as a function of concentration, such as electric conductivity, self diffusion, turbidity, partial molar volume of the surfactant, etc. (see Fig.2). When more surfactant is added it will be present in the form of micelles while one commonly assumes that beyond the cmc the monomer concentration remains constant and has the value of the cmc. This point is not always easily verified but an indication for a constant monomer concentration is given by the constant surface tension which indicates that the chemical potential of the surfactant species should be constant as well.

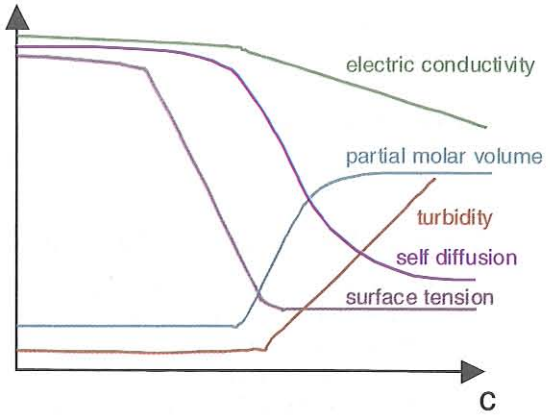


Fig. 2: *The change of some typical physical quantities that are sensitive to micelle formation*

Looking at Fig.2 it is already apparent that the cmc is not really an easily defined quantity. In practice values found in the literature may easily vary by a factor of more than 2 for the same surfactant under identical conditions. The reason for such relatively large discrepancies is in principle two-fold. First the cmc can be strongly influenced by amphiphilic impurities. Even more important is the fact that different techniques are in different ways susceptible to the formation of micellar aggregates in solution and one has to define a criterion for the cmc. A commonly applicable definition for the cmc is given by:

$$\left(\frac{d^3y}{dc_s^{\,3}}\right)_{c_s=\mathrm{cmc}} = 0 \qquad (2)$$

where y can be any one of the physical properties such as indicated in Fig.2 and c_s is the concentration of the surfactant [4]. But even with a rigorous application of this criterion to the various experimental data one will still end up with a range of cmc values which is simply due to the fact that the formation of micellar aggregates is not a simple first-order phase transition but thermodynamically a much more complex process (and therefore much less well-defined), i.e. one never has a point of micelle formation but one always has a relatively broad range in which formation of aggregates takes place.

Experimental evidence, for instance from NMR (nuclear magnetic resonance) [5], ESR (electron spin resonance), fluorescence depolarisation, or x-ray scattering shows that the alkyl chains in these aggregates (micelles) are liquid like. For instance NMR experiments on micellar solution typically yield sharp lines.

3 Driving Force for Self-aggregation – Hydrophobic Effect

So far we have simply accepted the formation of micellar aggregates as a matter of fact - but what is the driving force of their formation? This question has been subject of intensive research for a substantial time and by now it is agreed upon that the thermodynamic driving force is mainly due to the water structure. If a hydrophobic molecule (e.g. a hydrocarbon molecule) is present in an aqueous environment the water molecules surrounding the hydrophobic molecule will become more highly ordered. This corresponds to a **loss of entropy**. Accordingly formation of micellar aggregates, which reduce the contact between water molecules and hydrophobic chains, is favoured entropically.

In general one observes that during micelle formation enthalpic changes are close to zero while the entropic contribution due to the ordering process of the water molecules is responsible for the segregation of hydrophobic and hydrophilic regions in aqueous amphiphilic systems. This is the thermodynamic explanation of the inmiscibility of hydrocarbon and water. It is called the **hydrophobic effect** and it is responsible for a variety of important physicochemical effects, such as self-aggregation, surface activity, folding of biomolecules to superstructures, etc..

So far we have only considered water as a solvent but, of course, there exists a large variety of other polar solvents (e.g. ethanol, methanol, formamide, glycerol, glycol, diethylene glycol, dimethyl sulfoxide (DMSO), aceton, etc.). In principle the same considerations apply to these solvents. However, the solvophobic effect may be less pronounced here and empirically one finds that it is proportional to the surface tension of the given solvent. The lower the surface tension the smaller the driving force for aggregation. Typically it is observed that no micelle formation takes place in solvents that have a surface tension below 50 mN/m (compared to waters 72.8 mN/m). Some values for the surface tension of solvents are given in Table 1

Solvent	water	glycerol	glycol	formamide	DMSO	hydrazine	ethyl acetate
σ in mN/m	72.8	63.4	47.7	58.2	48.0	91.5	23.9

Table 1: *Surface tension σ for various polar solvents.*

One may also observe **self-aggregation in apolar solvents**, such as oils. In this case **reverse micelles** are formed where the hydrophobic chain points to the solvent and the hydrophilic head groups form a core. However, in almost all cases investigated so far the presence of small amounts of water is a necessary prerequisite for the formation of reverse micelles (in particular for ionic surfactant that need some solvent for the hydration of the ionic groups).

4 Factors Affecting the cmc

Of course, it is of much interest to identify how the molecular constitution of a given surfactant molecule affects its cmc. In general one can expect that the monomeric solubility of an amphiphilic molecule is determined by 2 factors:

- the free energy for the transfer of the hydrophobic part of the molecule from the aqueous environment into the micellar interior
- the solvation energy of the hydrophilic head group

Experimentally a straightforward relation is found between the length of the aliphatic hydrocarbon chain of a surfactant and its cmc. In Fig.3 cmc values are plotted as a function of the number n of C-atoms of the corresponding aliphatic chain. One finds an exponential relation between n and the cmc, according to:

$$\log(\text{cmc}) = A - B \cdot n \tag{3}$$

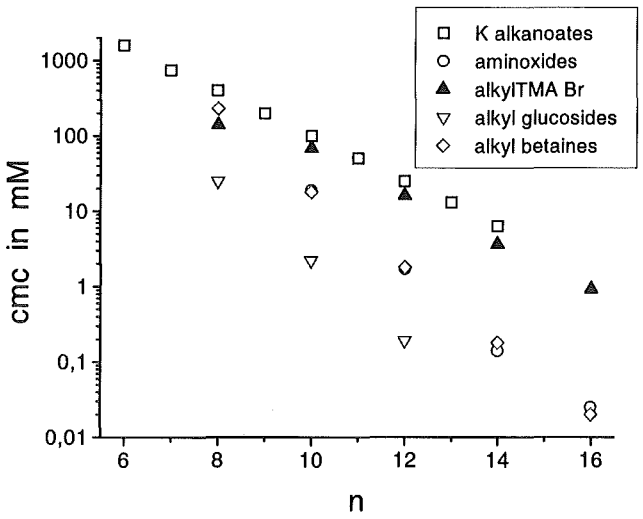


Fig. 3: *cmc values for alkyl surfactants with various head groups as a function of the number of C-atoms of the alkyl chain*

For the different types of surfactants (here differing by their head groups) it is observed that the slope is about the same for all uncharged head groups. For ionic surfactants the slope is significantly lower which is a result of the electrostatic interaction between the charged head groups. If the electrostatic interactions become screened by a high ionic strength of the solution (i.e. addition of relatively large amounts of salt) the same slope as for the nonionic surfactants is recovered. Then the surfactant types are distinguished only by the absolute values, i.e. the lines are shifted with respect to each other.

From the slope one can deduce that the gain of free energy for the transfer of one CH_2 group from the aqueous environment into the micellar interior is about 2.8 - 3.3 kJ/mol (1.2 - 1.4 kT).
Accordingly lengthening the alkyl chain by one CH_2 group reduces the cmc by a factor ≈ 3. It might be noted here that the presence of an aromatic ring in the aliphatic chain corresponds

only to the equivalent of 3.5 CH_2 groups - an indication for the fact that the aromatic ring is much more polar and therefore less hydrophobic than a simple alkyl chain. Such molecules that form micelles are called surfactants.

It should be noted that not all amphiphilic molecules will exhibit a cmc and form micelles. Typical representatives of this type of amphiphile are medium chain alcohols. They are surface-active and will lead to a substantial reduction of the surface tension. However, before they reach the bend in the surface tension curve, that is typical for micelle formation, they exceed their solubility in water. Instead of forming a micellar solution they become biphasic where additional alcohol goes into an excess phase. Nonetheless such molecules are very important for amphiphilic systems. They are called **cosurfactants** as in combination with surfactants they form mixed amphiphilic aggregates and they may strongly influence the properties of amphiphilic systems.

For ionic surfactants one observes that an increase of ionic strength leads to a decrease of the cmc. In general, it can be stated that the cmc is the higher the stronger the electrostatic interaction of the head groups. Accordingly one also observes a strong dependence of the cmc on the type of **counterion** for ionic surfactants (for same ionic amphiphile type). In general the solubility of the surfactant (and therefore the cmc) is the higher, the less strongly the counterion is bound at the amphiphilic interface. For instance one finds for dodecylsulfate that the cmc decreases in the following order for the various counterions:

$$Li^+ > Na^+ > K^+ > Cs^+ > N(CH_3)_4{}^+ > N(C_2H_5)_4{}^+ > Ca^{2+}, Mg^{2+}$$

The addition of **salt** to ionic surfactants, i.e. the increase of the ionic strength of the solution leads also to a decrease of the cmc, as it reduces the electrostatic repulsion between the charged head groups. Here one observes typically a dependence of the type:

$$\log(\text{cmc}) = -a \cdot c_{ion} + b \qquad (4)$$

where c_{ion} is the total counterion concentration, and a and b are constants for a given ionic head group and at a particular temperature.

In practice, one frequently encounters amphiphilic mixtures that contain in addition to a surfactant a so-called **cosurfactant** (e.g. a medium chain alcohol or amine) in order to modify the amphiphilic properties of the corresponding systems in a desired way. With such a cosurfactant mixed micellar aggregates are formed, where the presence of the cosurfactant molecules reduces the electrostatic repulsion between the charged head groups. Accordingly the cmc is reduced where approximately a linear relationship between the cmc and the concentration of the present alcohol present is observed.

More complex is the situation for the cmc of **surfactant mixtures**. Here the cmc of the mixture depends strongly on the detailed interactions between the different types of surfactants (see Ch. 13).

The addition of purely hydrophobic compounds (oils) has only a minor influence on the cmc and typically one observes a slight reduction of the cmc.

Finally the influence of the **temperature** on the cmc is relatively complex. As a general pattern it is found that the values of the cmc first decrease with temperature to a minimum and then increase again with further increase of temperature. The reason for this is that a temperature increase leads to decreased hydration of the polar head group, which favours micellisation. However, at the same time increasing temperature disrupts the water structure progressively and thereby reduces the magnitude of the hydrophobic effect, which disfavours micellisation. These counteracting effects explain the occurrence of a minimum but how exactly the cmc changes as a function of temperature depends on the detailed structure of the amphiphilic molecules.

5 Thermodynamic Description of Micelles

In the simplest description the formation of micelles of a given aggregation number n is just described by one equilibrium reaction (closed association model):

$$n \cdot M \rightleftharpoons M_n$$

The micellisation constant is then simply given by:

$$K = \frac{a(M_n)}{a(M)^n} = \exp\left(-\frac{n \cdot \Delta G_{mic}}{R \cdot T}\right) \tag{5}$$

In a more complete way one has to describe micellisation as a cooperative association process that takes into account the various association steps:

$$M + M_{n-1} \rightleftharpoons M_n$$

where one has a **multiple equilibrium** condition that takes into account each association step. For a comprehensive thermodynamic analysis of the phenomenon of micellisation we have to consider the chemical potential of the surfactant molecules in the monomeric state (μ_1) and in the aggregated state ($\mu_{mic,n}$):

$$\mu_1 = \mu_1^0 + R \cdot T \cdot \ln(a_1) \tag{6}$$

$$\mu_{mic,n} = \mu_{mic,n}^0 + \frac{R \cdot T}{n} \ln\left(\frac{a_n}{n}\right) \tag{7}$$

where a_1 is the activity of the monomerically dissolved surfactant and a_n the activity of a surfactant molecule in an aggregate of aggregation number n.
From the equilibrium condition one has:

$$\mu_{mic,n}^0 - \mu_1^0 = R \cdot T \cdot \ln(f_1 \cdot x_1) - \frac{R \cdot T}{n} \ln\left(\frac{f_n \cdot x_n}{n}\right) \tag{8}$$

where f is the activity coefficient and x the mol fraction. This equation yields directly the micellar size distribution function (Fig.4) - provided that the standard chemical potentials are known. Now we introduce the following notation:

$$x_1 = x_0 - x_{mic} \qquad \sigma = x_{mic}/x_0$$

where x_0 is the total mol fraction of surfactant. With this one obtains:

$$\left(\mu_{mic,n}{}^0 - \mu_1{}^0\right)/R \cdot T = \ln(f_1 \cdot x_1) - \frac{1}{\bar{n}}\ln(f_{mic} \cdot x_{mic}) + \frac{1}{n}\ln(\bar{n}) \qquad (9)$$

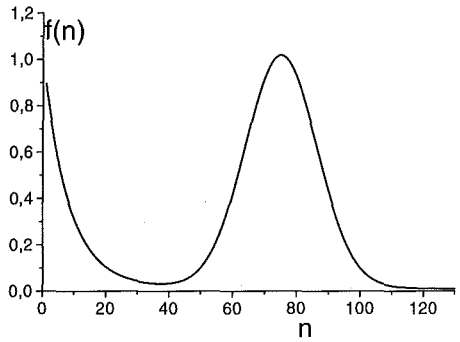


Fig. 4: *Typical size distribution for the aggregation number of micelles*

where we have assumed that only micelles of a mean aggregation number $\bar{n}$ have been formed (that contain a mol fraction x_{mic}). After some algebraic manipulation we obtain (f_n has been assumed to be 1 since we are here mainly interested in the cmc and typically at the cmc the concencentration of micelles is so low that $f_{mic} = 1$):

$$\left(\mu_{mic,n}{}^0 - \mu_1{}^0\right)/R \cdot T = \ln f_1 + \ln(x_0 - x_{mic}) - \frac{1}{\bar{n}}\ln(x_0) + \frac{1}{n}\ln(\bar{n}/\sigma) \qquad (10)$$

$$\left(\mu_{mic,n}{}^0 - \mu_1{}^0\right)/R \cdot T = \ln f_1 + \ln(1-\sigma) + \frac{\bar{n}-1}{\bar{n}}\ln(x_0) + \frac{1}{n}\ln(\bar{n}/\sigma) \qquad (11)$$

If one now considers the case of a relatively large aggregation number ($\bar{n} >> 1$), the onset of micelle formation ($\sigma << 1$), and low concentration of the surfactant ($f_1 = 1$) one can simplify this to the following relation:

$$\mu_{mic,n}{}^0 - \mu_1{}^0 = \Delta G_{mic} = R \cdot T \cdot \ln(x_0) \approx R \cdot T \cdot \ln(cmc/(55.5\,mol/l)) \qquad (12)$$

With that formula one can directly relate the measured cmc values to the free energy of micellisation ΔG_{mic} (and with this method the increment values given in Ch. 4 for the transfer of CH_2 into the micelle were deduced).

6 Dynamics of Micelle Formation and Dissolution

Micelles are not static objects but are highly dynamic objects. In general one observes that dynamic processes of micelles are relatively complex and take place over an extended range of time - from less than 1 μs to many seconds, i.e. the lifetime of a micelle is typically shorter than a second.

Experimentally the dynamics of micelle formation has been studied by means of fast kinetic methods, such as the stopped-flow method and in particular by means of relaxation methods. For largely different surfactants always **two different relaxation times** (τ_1, τ_2) have been observed, where the short time is in the μs-range and the long time in the ms- or s-range [6]. The two different time scales arise from two different processes. The fast process is due to the **exchange of monomers** between micelle and solution. The second process is associated with a **complete dissolution of a micelle** or the formation of a new micelle [7].

When starting from a given micellar distribution in order to achieve a new equilibrium in micellar systems one first observes a fast equilibration process that takes place via monomer diffusion. However, in this process the number of aggregates has to remain unchanged and only the size distribution is altered. In order to change the number of micelles it is necessary to completely dissolve micelles or form new ones starting from monomers. For that process to take place as an intermediate step it is necessary to have aggregates present of low aggregation number which according to the micellar size distribution (cf. Fig.4) are only very unlikely to be formed, and the concentration of such oligomers is by several orders of magnitude lower than that of the monomers or that of the average micelles. The micellar oligomer with lowest concentration can be considered as a nucleating species for this reaction. This acts like a bottle-neck for the micellar reorganisation. Therefore this process is by several orders of magnitude slower than the monomer exchange process.

Aniansson and Wall deduced the following relations for the concentration dependence of the two relaxation times:

$$1/\tau_1 = \frac{k^-}{\sigma^2} + k^- \cdot \frac{c_0 - cmc}{n \cdot cmc} \tag{13}$$

$$1/\tau_2 = \frac{k^- \cdot c_i \cdot \left(cmc + n^2 \cdot c_m\right)}{c_m \cdot \left(cmc + \sigma^2 \cdot c_m\right)} \tag{14}$$

Here k^- is the rate constant for the monomer to leave a micelle, k^+ the rate constant of a monomer to enter a micelle (with $k^+ = k^-/cmc$), n the mean aggregation number, σ the variance of the distribution function, c_i the concentration of the nucleating particle of aggregation number i, c_0 the total concentration and c_m the concentration of micelles ($c_m \approx (c_0 - cmc)/n$).

Experimentally one finds that k^+ is in the range of diffusion-controlled reactions, i.e. the incorporation of monomers into a micelle requires almost no activation energy. However, k^-

decreases strongly with increasing length of the alkyl chain of the surfactant. The change can be described by the following formula:

$$k^{-}/n = \frac{D}{l_C{}^2} \cdot \exp\left(-\frac{\varepsilon}{k \cdot T}\right) \qquad (15)$$

where D is the diffusion coefficient, l_C is close to 1.1 Å (the projection of a C-C bond on the surfactant chain axis), and ε the free energy change for the dissociation of a surfactant monomer from a micelle. According to Ch. 4 ε should vary linearly with the length of the alkyl chain of the surfactant which explains the large changes observed in homologous series of surfactants. The average residence time of a monomer in a micelle is given by N/k^{-}. Typically this time is in the μs-range but it depends exponentially on the length of the surfactant. Therefore this time can vary over a large range.

7 Krafft Point and Cloud Point

The solubility of ionic surfactants normally increases with rising temperature. For longer chain surfactants one often observes that they are almost insoluble at low temperatures, but that there exists a certain temperature above which the solubility increases suddenly significantly. The reason for this is that beyond this temperature the solubility reaches the cmc, and therefore further added surfactant does not have to become dissolved in form of monomers but is dissolved in form of micelles. Therefore the solubility of the surfactant increases jump-wise at this point, which is called **Krafft temperature** or Krafft point.

Of course, the Krafft temperature is also related to the tendency of the corresponding surfactant micelles to form stable crystals. This tendency can be reduced by having branched alkyl chains or double bonds present in the aliphatic chain. Also mixing with other amphiphilic compounds suppresses the tendency for crystallization and accordingly all these modifications of an amphiphilic system lead to an increase of the Krafft temperature.

For nonionic surfactants - especially ones with ethylene oxide (EO) head groups - one may observe the opposite behaviour as a function of temperature. Upon increasing the temperature one will reach a point where the surfactant solution becomes turbid and separates into a surfactant-rich and a water-rich phase. This point where the solution becomes turbid is called **cloud point**. The reason for this behaviour is that the hydration of EO is reduced progressively with increasing temperature. Its solubility decreases and therefore a nonionic surfactant with an EO head group becomes less hydrophilic with increasing temperature. With rising temperature the micelle start to grow and also the **attractive interactions** between them become so strong that they start to aggregate and form a so-called coacervate phase. Beyond a critical temperature the solubility then becomes so low that **phase separation** takes place.
All modifications of the surfactant system that increase the repulsive interaction between the surfactant aggregates will lead to an increase of the cloud temperature. Correspondingly already the addition of small amounts of ionic surfactants to a nonionic surfactant typically leads to a significant increase of the cloud point. In contrast addition of medium chain alcohol typically leads to a lowering of the cloud point temperature.

8 Shape and Size of Aggregates

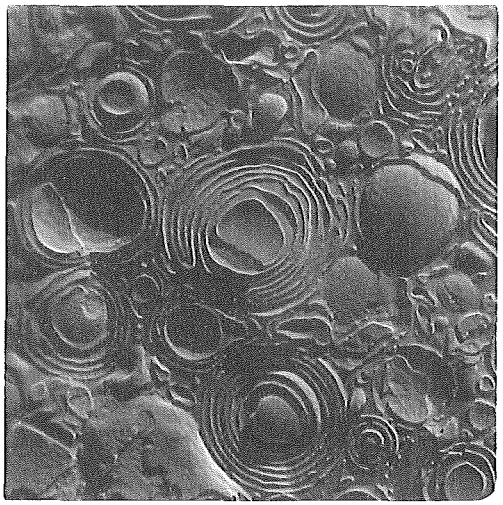
So far we have given no indication regarding the shape of formed aggregates. It is generally assumed that micelles at the cmc have a spherical shape but for higher concentrations they can assume various different shapes.

As stated the simplest case is that of **spherical micelles** but they can also possess ellipsoidal structures, which may be **prolate or oblate**. It is also possible to have one-dimensional growth of the micelles which leads to the formation of **rod-like micelles**, which typically are very polydisperse with respect to their length. Commonly one finds that the length of rod-like micelles increases with increasing surfactant concentration.

Solutions of rod-like micelles are more viscous than their spherical counterparts. Once the rods are sufficiently long and concentrated that they start to overlap in solution the viscosity increases steeply. For still higher concentrations a network of entangled micelles is formed that exhibits highly **viscoelastic properties** [8][9].

Another possibility is a 2-dimensional growth of the aggregates. Here bilayers of surfactant are formed. Such **bilayers** can lead to a variety of different structures. The simplest is that of stacked planar bilayers (**lamellae**), i.e. the formation of a lamellar phase.

However, the bilayers may also close and form vesicles. Vesicles occur in a large variety of sizes ranging from **small unilamellar vesicles (SUV)** of 50Å radius to **large unilamellar vesicles (LUV)** of radii of several μm. Such isotropic vesicle solutions are often denoted as L_4 phase. There exists also the possibility of the formation of **multi-lamellar vesicles (MLV)** (Fig.5) that are also called "onions" due to their structural similarity [10][11]. Classically vesicles are formed by ultra-sonification, microfluidisation or shearing. However, there exist also a variety of cases where vesicles form spontaneously, such as is observed for mixtures of cationic and anionic surfactants, or mixtures of surfactants with cosurfactants [12][13][14].
Finally bilayers may also form an isotropic interconnected array of sheets that resembles a sponge (Fig.6). This phase is called **sponge phase** or **L_3-phase**. It is strongly scattering - typically somewhat bluish - but despite the fact of the high connectivity this phase is of very low viscosity.



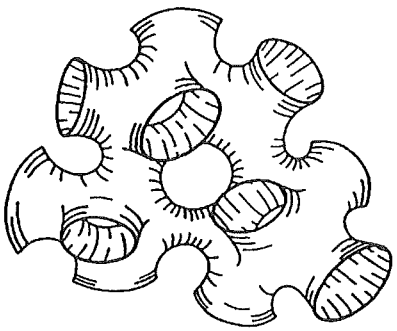


Fig. 5: *Freeze-fracture electronmicrograph of a multilamellar vesicle solution*
Fig. 6: *Sketch of the structure of the L_3(sponge)-phase*

9 Liquid Crystals - Phase Behaviour

Once surfactant systems are sufficiently concentrated (commonly above 20-30 wt% and then up to the pure surfactant) they have a tendency to form liquid crystalline (LC) phases.

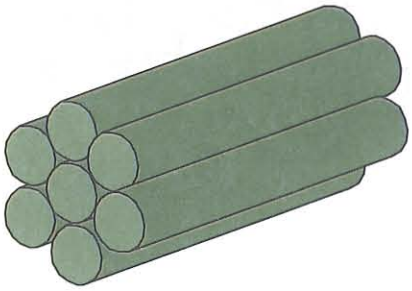
The most commonly encountered liquid crystalline surfactant phases are the **hexagonal phase** ("middle phase") and the **lamellar phase** ("neat phase"), which are made up from regularly packed rod-like micelles (on a hexagonal lattice) (Fig.7) or stacked lamellae (Fig.8), respectively. Both are birefringent and can be distinguished by means of polarisation microscopy. Normally lamellar phases are viscous but they still flow under their own weight, whereas hexagonal phases typically are highly viscous and have a "gel-like" appearance. The spacing in lamellar phases can become so large that it is in the range of visible light. Such lamellar phases are coloured and they are called iridescent phases (Fig.9).

Less frequently observed is the formation of **nematic phases** and typically their extension in the phase diagram of surfactant is systems is relatively small. There are 2 types of nematic phase, those that are composed of rod-like micelles and those that are composed of disc-like micelles [15][16]. In a nematic phase the aggregates possess only an orientational ordering but no positional ordering, which distinguishes the nematic phase from hexagonal and smectic (lamellar) phases. The general phase sequence of a surfactant with increasing concentration is given by:

micellar solution (L_1) ↔ hexagonal phase (H_1) ↔ lamellar phase (L_α) ↔ reverse hexagonal phase (H_2) ↔ reverse micelles (L_2)

All these phases are separated by a first-order phase transition. In the **reverse phases** the hydrophilic parts of the surfactants are in the micellar interior (i.e. the structure has been

reversed from that of a continuous phase of aqueous solvent to one where one may have an oil as continuous solvent phase). It should be noted that this is just a general scheme. For a particular surfactant system some of these phases may not occur.



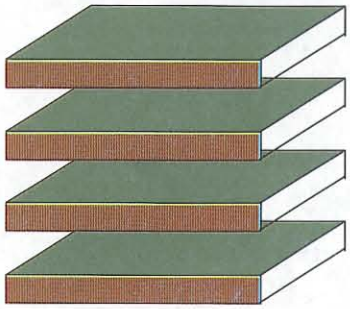


Fig. 7: *Schematic drawing of a hexagonal phase*
Fig. 8: *Schematic drawing of a lamellar phase*

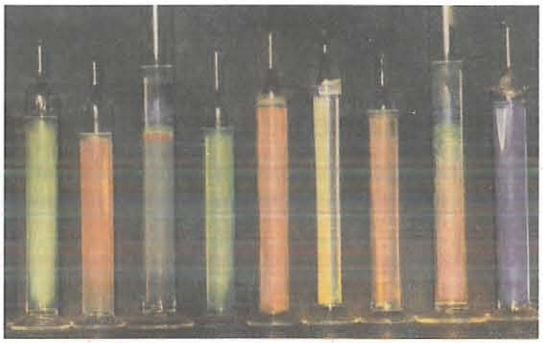


Fig. 9: *Various iridescent lamellar phases*

Even spherical micelles can exhibit LC phases by forming **cubic phases** in which the micelles are ordered like the metal atoms in a solid metal. This is one type of cubic phases that is composed of individual aggregates but cubic phases can also have a bicontinuous structure [17][18]. Cubic phases are isotropic, transparent and very stiff. Often they possess pronounced elastic properties and may exhibit an acoustic resonance phenomenon ("ringing gel").

Cubic phases may be observed in the phase diagram at the transition points of the general phase sequence, e.g. between micellar phase and hexagonal phase, between hexagonal and lamellar phase, and so on. Therefore already in a binary system cubic phases with 4 principally different locations in the phase diagram can be observed, and all of the four different types have been observed experimentally. Typically their structure depends strongly on the location in the phase diagram. Cubic phases located between micelles (L_1, L_2) and hexagonal phase (H_1, H_2) are typically composed of individual micellar aggregates. Cubic phases located between hexagonal phase (H_1, H_2) and lamellar phase are typically of

bicontinuous structure. It should be stressed they can be observed but whether and where in the phase diagram one finds a cubic phase depends completely on the surfactant under study. It might be added that also intermediate phases between hexagonal and lamellar phases have been reported, in particular for the case of nonionic surfactants [19].

10 The Packing Parameter

A simple geometric explanation for the various shapes of micellar aggregates can be given when one considers the molecular build-up of an amphiphilic molecule. In a first-order approximation we may simplify it to a geometrical object that is characterised by a volume v_s, a head group area a_s, and length L - as sketched in Fig.10. Looking at Fig.10 it is obvious that the relative ratio of these factors determines what **curvature** the surfactant molecules wants to attain at the amphiphilic interface. For a cut pyramid as in Fig.10 one obtains for the natural curvature c_0 (inverse of the natural radius R_0):

$$c_0 \,(=1/R_0) = \frac{1.5 - \sqrt{\frac{3 \cdot v_s}{a_s \cdot L}} - 0.75}{L} \qquad (16)$$

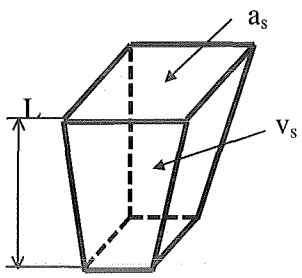


Fig. 10: *A surfactant molecule modelled as a cut pyramid*

Accordingly the parameter $v_s/a_s \cdot L$ - the **packing parameter p** - determines the **spontaneous curvature** of the surfactant film, e.g. whether this film wants to be convex or concave. The larger the packing parameter p the more the film wants to assume a concave shape.

For a surfactant molecule v_s is simply the molecular volume, a_s the head group area (as it may for instance be determined from surface tension measurements; in general the surface area of an amphiphilic film can be assumed to be incompressible, i.e. the head group area is a constant that is characteristic for a given amphiphilic molecule), and the length L which can be approximated by the length of the stretched surfactant molecule.

If we consider now as a simple example a spherical micelle of radius R and aggregation number n the following equations for volume and surface apply:

$$V = \frac{4\pi}{3} R^3 = n \cdot v_s \qquad A = 4\pi \cdot R^2 = n \cdot a_s \tag{17}$$

Equating both relations yields the following condition: $v_s/a_s = R/3$.

The maximum radius R is given by the length L of the stretched surfactant molecule and with that one obtains as a condition for the formation of spherical micelles: $p < 1/3$. In analogy one can distinguish ranges of p where different aggregate shapes are stable (Fig.11) [20]:

$1/3 < p < 1/2$:	cylindrical micelles
$1/2 < p < 1$:	planar lamellae, bilayers, vesicles
$1 < p$:	reverse structures

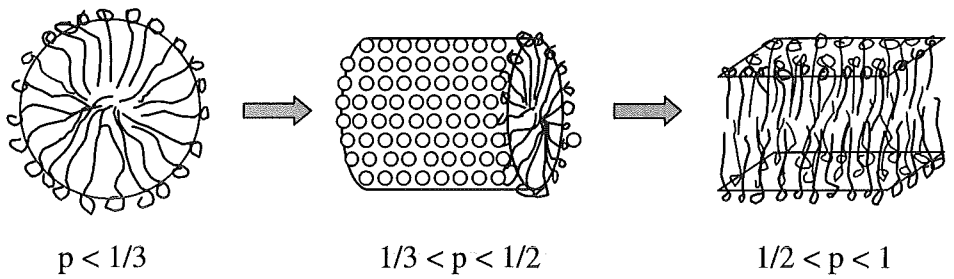


Fig. 11: *The influence of the packing parameter on the aggregate structure*

One commonly encountered structural sequence is that for increasing addition of a cosurfactant (typically a medium chain alcohol) to a surfactant solution one observes that originally spherical micelles are transformed into rodlike micelles that grow in size with increasing cosurfactant concentration. Further addition of cosurfactant then transforms the rods to lamellar structures (or vesicles).

We may employ the concept of the packing parameter now to rationalise the structural behaviour observed in amphiphilic systems. For hydrocarbon surfactants the following simple relations for volume v_s and length L of a surfactant have been given by Tanford [21]:

$$v_s/\text{Å}^3 = 27.4 + 26.9 \cdot n_C$$
$$L/\text{Å} = 1.5 + 1.265 \cdot n_C$$

where n_c is the number of carbon atoms in the alkyl chain. Of course this is still a very crude geometrical model, and one may improve on it by taking into account more precisely the detailed nature of the head group, that has been neglected completely so far. The head group may increase the effective length of the surfactant and there may also be parts that contribute

to the hydrophobic volume v_s (whereas all the hydrophilic parts, for instance ethylene oxide groups etc., must not be counted to the volume v_s).

We may now consider as an example the surfactant tetradecyl dimethyl amine oxide (TMDAO) and the cosurfactant 1-hexanol. For these 2 molecules one finds accordingly the geometric parameters given in table 2 (the packing parameter of hexanol is hypothetical since hexanol does not aggregate itself).

system	L/Å	a_s/Å^2	v_s/Å^3	p
TDMAO	19.2	51	404	0.411
1-hexanol	9.1	10	161.9	"1.78"

Table 2: *Length, head group area, molecular volume and packing parameter.*

The packing parameter for pure TDMAO is somewhat above the limit given for spherical micelles and that is in agreement with the experimental fact that here one finds short rod-like micelles. What happens now upon admixing 1-hexanol to an aqueous TDMAO solution? Of course, it should lead to an increase of the packing parameter p.

For a 1:1 molar ratio one would calculate a packing parameter of 0.483, which means that a preference for a less curved interface as present in rods should be favoured. Experimentally one observes a pronounced growth of the rods and a viscoelastic solution is formed - just as predicted by the packing parameter.

If we consider a molar ratio of 2:1 for TDMAO:1-hexanol p increases further to a value of 0.526. Here now planar bilayers should become stable and that is exactly what is observed experimentally. In this range first multilamellar vesicles are formed which upon further addition of hexanol transform into planar bilayers.

11 Bending Elasticity

Another concept that allows to rationalise the behaviour of amphiphilic systems is that of the **bending energy** of amphiphilic films that arises from deforming an amphiphilic film away from its preferred curvature [22]. For systems of low interfacial tension the bending energy should be the leading term in the free energy of the system and therefore determine its properties [23]. The basis for this description is given by the Helfrich formula for the free energy F of a film [24]:

$$F_b = \int \left\{ \tfrac{\kappa}{2} \cdot (c_1 + c_2 - 2 \cdot c_0)^2 + \bar{\kappa} \cdot c_1 \cdot c_2 \right\} \cdot dA \qquad (18)$$

where κ is the mean bending modulus, $\bar{\kappa}$ the Gaussian (or saddle-splay) modulus, c_0 the spontaneous curvature, and c_1 and c_2 the 2 principal curvatures of the surface. The meaning of the two different bending moduli can directly be visualized as in Fig.12 by considering in which ways one may principally deform a planar surface.

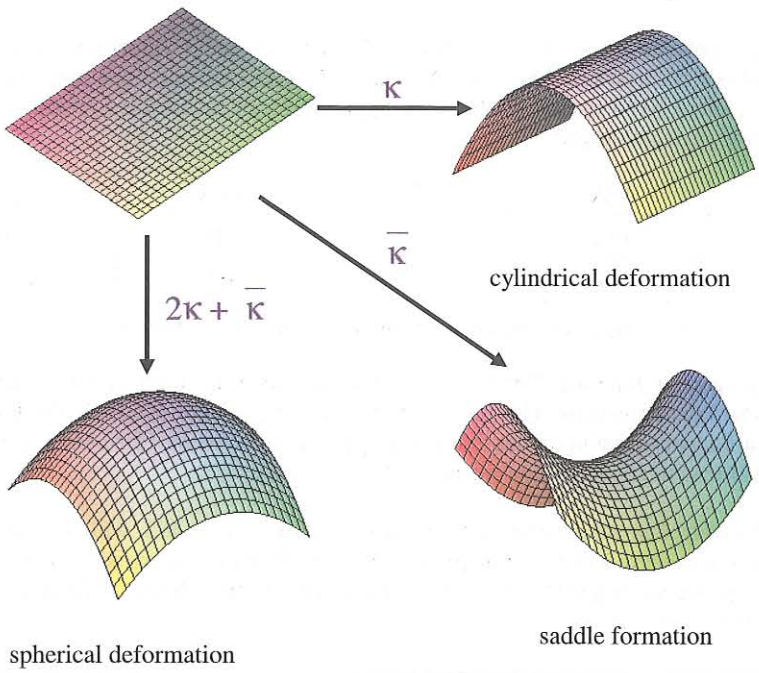


Fig. 12: *Fundamental ways to deform a surface and their relation to the bending moduli*

Some information about the bending moduli can directly be deduced from eq. 18. κ is necessarily **positive** because otherwise there would not be an attractive potential for the spontaneous curvature. It is instructive to rewrite eq. 18 in the form:

$$F_b = \int \left\{ \frac{2\kappa + \bar{\kappa}}{2} \cdot \left(c_1 + c_2 - \frac{4\kappa}{2\kappa + \bar{\kappa}} \cdot c_0 \right)^2 + \frac{\bar{\kappa}}{4} \cdot c_1 \cdot c_2 - \frac{2 \cdot \kappa \cdot \bar{\kappa}}{2\kappa + \bar{\kappa}} \cdot c_0^2 \right\} \cdot dA \qquad (19)$$

It becomes evident that for the formation of stable structures the condition: $-2\kappa < \bar{\kappa} < 0$ has to be met in order to have an attractive potential for c_0. For positive $\bar{\kappa}$ the formation of saddle structures (as in L_3-phases) is favoured and according to eq. 19 this would mean that c_1 (c_2) would tend to + (-) ∞. However, so far we have not considered entropy terms and especially terms of higher order (in the curvatures) of the bending energy that are not yet contained in the quadratic approximation given by eq. 18. Therefore positive values for $\bar{\kappa}$ are possible but $\bar{\kappa}$ cannot attain too large positive values.

Amphiphilic films are not rigid objects but perform deformations (undulations) driven by the thermal energy. Of course, the extent of these deformations, i.e. whether a surfactant film is more rigid or more flexible, is determined by its bending elasticity. The characteristic quantity in that context is the **persistence length l_p** of the amphiphilic film (which can be a surfactant mono- or bilayer) that is controlled by the mean bending modulus κ:

$$l_p = a \cdot \exp(4 \cdot \pi \cdot \kappa / \alpha \cdot k \cdot T) \qquad (20)$$

a is a molecular length (e.g. v_s/a_s) and α a numerical value between 2 or 3. According to eq. 20 one can expect that for $\kappa > kT$ relatively stiff surfactant films are formed, which for instance support the formation of lamellar phases. In contrast for $\kappa \approx kT$ the formation of less highly ordered phases (e.g. microemulsions) is favoured, and for still lower values for κ finally only molecular mixtures are formed.

With the help of the bending elasticity it is possible to rationalise the phase behaviour of surfactant systems. One example are systems of surfactant bilayers which can occur in the form of lamellar phases, vesicles, or L_3-phases. In the simplest approximation one can directly take eq. 18 and for a symmetric bilayer (as it has to be present for one component bilayer) the spontaneous curvature has to be zero ($c_{0,b} = 0$). Neglecting entropy effects the free energy per unit area, F/A, for the 3 different structural cases is given by (the index b stands for bilayer):

- planar lamellar phase ($c_1 = c_2 = 0$): $F/A = 0$
- vesicle with curvature $c_v = c_1 = c_2 \neq 0$: $F/A = (2 \cdot \kappa_b + \bar{\kappa}_b) \cdot c_v^2$
- L_3-Phase ($c_1 = -c_2 \neq 0$): $F/A = -\bar{\kappa}_b \cdot c_1^2$

From a comparison of these energetic terms one obtains directly the phase diagram given in Fig.13. For positive $\bar{\kappa}_b$ the L_3-Phase is stable and for the case of negative $2\kappa_b + \bar{\kappa}_b$ the vesicle phase is stable. In between is the existence range of the lamellar L_α-Phase composed of planar lamellae. Of course, for a more detailed description one has to consider entropy terms but Fig.13 reflects the basic properties of the phase behaviour. Accordingly the bending moduli determine directly the phase diagram of amphiphilic systems.

The bending modulus of a bilayer can become related to the bending moduli of the corresponding monolayers of this bilayer. For instance for the Gaussian modulus one obtains:

$$\bar{\kappa}_b = 2 \cdot \bar{\kappa} - 8 \cdot \kappa \cdot \varepsilon \cdot c_0 \qquad (21)$$

where c_0 is now the spontaneous curvature of the monolayer. This relation allows to understand the commonly observed phase sequence: **vesicle phase -> lamellar L_α-phase -> L_3-phase** that is found upon the addition of medium chain alcohol to a surfactant solution. The addition of cosurfactant leads to a reduction of the spontaneous curvature c_0 by an increase of the packing parameter (as detailed in 10.). However, according to eq. 21 a reduction of c_0 corresponds to an increase of $\bar{\kappa}_b$ (while κ_b is only little affected). Looking at Fig.13 this change of $\bar{\kappa}_b$ explains straightforwardly the experimentally observed phase progression.

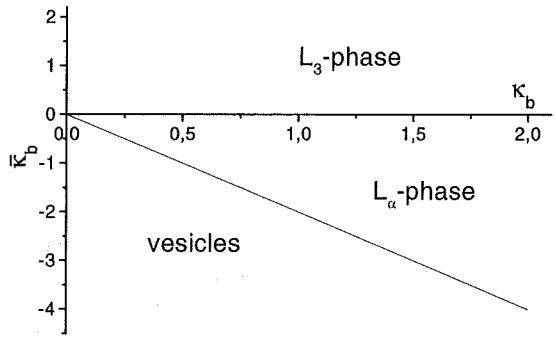


Fig. 13: *Schematic phase diagram of bilayer structures as a function of the bending moduli* κ_b *an* $\bar{\kappa}_b$

12 Solubilisation - Microemulsions

One of the most important properties of amphiphilic systems is their ability to solubilise other molecules that otherwise would not be soluble in this solvent, e.g. oil, dye molecules, triglycerides, etc.. This property is the basis of all cleaning applications of surfactants but also for the formation of complex membranes as they are instrumental for the functioning of cellular membranes.

The solubilised hydrophobic molecules become incorporated into the hydrophobic micellar core which explains the solubility. For instance, under many circumstances one observes that significant amounts of oil, e.g. hydrocarbon, can be dissolved in micellar systems. Here it is often possible to solubilise amounts of oil that are larger than the amount of surfactant present. Such **thermodynamically** stable mixtures are called **microemulsions**. They are fundamentally different from emulsions where oil droplets are stabilized kinetically by the presence of a surfactant coverage. However, emulsions are thermodynamically metastable. Therefore with passing time they will always decompose into a two-phase system.

As described so far microemulsions are small droplets (with a size range of 30-250Å radius) in which an oily core is surrounded by the surfactant. Such microemulsions are called oil-in-water (O/W) microemulsions. It is also possible to have water-in-oil (W/O) or so-called reverse microemulsions, and it is even possible to have bicontinuous microemulsions where equal amounts of oil and water are dispersed and form a structure similar to that of the L_3-phase (cf. Fig.6).

An important quantity for the understanding of the formation of microemulsions is the interfacial tension. The **interfacial tension** γ is the free energy necessary to create an interface A between the oil to be solubilised and the surfactant solution:

$$\gamma = \left(\frac{\partial G}{\partial A}\right)_T \tag{22}$$

It has been observed that the amount of oil that can be solubilised is inversely proportional to the interfacial tension, i.e. the lower the interfacial tension γ the more pronounced the tendency for formation of microemulsions. For the radius R_m of the formed microemulsion droplets that are saturated with the oil, i.e. at the solubilisation limit (or emulsification failure), one finds:

$$R_m{}^2 = \frac{k \cdot T}{8\pi \cdot p^2 \cdot \gamma} \tag{23}$$

where p is the polydispersity index of the droplets. This relation can be deduced from an analysis in terms of the bending energy and has also been confirmed experimentally [25].

13 Surfactant Mixtures - Mixed Micelles

In many practical situation one works with mixtures of different surfactants, as they exhibit frequently synergistic effects that render such mixtures more effective for applications. Surfactants commonly mix easily and form mixed micelles. In the simplest case they **mix ideally** and then the cmc of the mixed system is given by:

$$\frac{1}{cmc} = \sum_i \frac{\alpha_i}{cmc_i} \tag{24}$$

where α_i is the total mole fraction of surfactant component i and cmc_i its cmc for the pure component. However, the case of ideal mixing is rarely observed and in reality one finds that different surfactant molecules interact with each other.

In the simplest approximation such interactions are treated by Rubingh's theory for **non-ideal mixtures of surfactants** [26]. Here the non-ideality is accounted for by introducing a parameter β that is defined in analogy to the Flory-Huggins theory for polymer mixtures by the interaction energy between the different surfactant molecules:

$$\beta = \frac{E_{11} + E_{22} - 2 \cdot E_{12}}{k \cdot T} \tag{25}$$

From this interaction parameter β parameter activity coefficients f_i are deduced and one obtains for a two-component system:

$$f_1 = \exp(\beta \cdot (1 - x_1)^2) \qquad f_2 = \exp(\beta \cdot x_1{}^2) \tag{26}$$

where x_1 is the mol fraction of component 1 in the micellar aggregates, which will differ from the total mol fraction.

Accordingly one obtains for the cmc of such more complex mixtures:

$$\frac{1}{cmc} = \sum_i \frac{\alpha_i}{f_i \cdot cmc_i} \tag{27}$$

In Fig.14 the cmc as a function of the mixing ratio is plotted for various values of β. One observes that attractive interactions (β < 0) lead to a minimum of the cmc while repulsive interactions (β > 0) lead to a maximum in the cmc curves. It should also be noted that the interaction parameter β can not be larger than 2 as in this case phase separation would take place, which for surfactant mixtures would mean that in the solution not mixed micelles are present but two different sorts of micelles formed by the two different surfactants. However, such cases have so far only been reported for some mixtures of hydrogenated and perfluorinated surfactants [27].

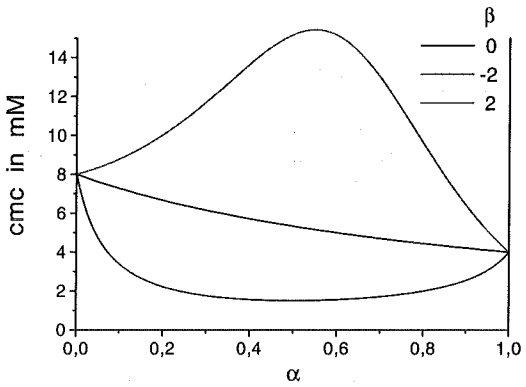


Fig. 14: *cmc as a function of the total mol fraction α of component 2 for various values of the interaction parameter β.*

14 Further Aspects

Of course, this lecture is not able to cover comprehensively the physical chemistry of self-aggregating systems. Due to the large chemical variety of amphiphilic molecules and the complex ways of self-assembly only some of the most important properties have been discussed here.

Further interesting aspects of self-assembling systems (some of which are subject of other lectures) are for instance:

- self-assembly at interfaces
- foams and foam stability
- interactions of amphiphiles with polymers
- interactions of amphiphiles with biomolecules and in biomembranes
- reactions in micelles (micellar catalysis)
- use of self-assembled aggregates as templates in chemical reaction

In general self-assembly in the presence of other colloidal material is a very active field of current research since it allows the formation of **complex materials** by processes governed by **self-organisation**. Such processes are often key points in the synthesis and for the understanding of **nanostructured materials**, as they are currently of high interest in a variety of fields.

References

[1]F.M. Menger, J.S. Keiper, Angew. Chem. Int. Edit. 39, 1907 (2000)
[2]E. Kissa, Fluorinated Surfactants and Repellents, Surfactant Science Series Vol. 97, (Marcel Dekker, New York, 2001)
[3]Silicone Surfactants, R.M. Hill (Ed.), Surfactant Science Series Vol. 86, (Marcel Dekker, New York, 1999)
[4]J.N. Phillips, Trans. Faraday Soc. 51, 561 (1955)
[5]Y. Chevalier, C. Chachaty, J. Phys. Chem. 89, 875 (1985)
[6]E.A.G. Aniansson, M. Almgren, S.N. Wall, H. Hoffmann, I. Kielmann, W. Ulbricht, R. Zana, J. Lang, C. Tondre, J. Phys. Chem. 80, 905 (1976)
[7]E.A.G. Aniansson, S.N. Wall, J. Phys. Chem. 79, 857 (1975)
[8]H. Rehage, H. Hoffmann, Mol. Phys. 74, 933 (1991)
[9]A. Khatory, F. Lequeux, F. Kern, S.J. Candau, Langmuir 9, 1456 (1993)
[10] O. Diat, D. Roux, F. Nallet, J. Phys. II 3, 1427 (1993)
[11] P. Panizza, D. Roux, V. Vuillaume, C.Y.D. Lu, M.E. Cates, Langmuir 12, 248 (1996)
[12] E.W. Kaler, A.K. Murthy, B.E. Rodriguez, J.A.N. Zasadzinski, Science 245, 1371 (1989)
[13] Y. Talmon, D.F. Evans, B.W. Ninham, Science 221, 1047 (1983)
[14] U. Munkert, H. Hoffmann, C. Thunig, H.W. Meyer, W. Richter, Progr. Coll. Polym. Sci. 93, 137 (1993)
[15] G. Bartusch, H.D. Dörfler, H. Hoffmann, Progr. Coll. Polym. Sci. 89, 307 (1992)
[16] M. Boidart, A. Hochapfel, M. Laurent, Mol. Cryst. Liq. Cryst. 154, 61 (1988)
[17] K. Fontell, Coll. Polym. Sci. 268, 264 (1990)
[18] V. Luzzatti, P. Mariani, T. Gulik-Krzywicki, Springer Proc. Phys. 21, 131 (1987)
[19] C.E. Fairhurst, M.C. Holmes, M.S. Leaver, Langmuir 13, 4964 (1997)
[20] J.N. Israelachvili, D.J. Mitchell, B.W. Ninham, J. Chem. Soc. Faraday Trans. II 72, 1525 (1976)
[21] C. Tanford, The Hydrophobic Effect: Formation of Micelles and Biological Membranes, 2nd Ed., (Wiley, New York, 1980)
[22] S.A. Safran, Statistical Thermodynamics of Surfaces, Interfaces, and Membranes, (Addison-Wesley, Reading, MA, 1994)
[23] P.G. de Gennes, C. Taupin, J. Phys. Chem. 86, 2294 (1982)
[24] W. Helfrich, Z. Naturforsch. 28, 693 (1973)
[25] M. Gradzielski, D. Langevin, B. Farago, Phys. Rev. E 53, 3900 (1996)
[26] D.N. Rubingh, in Solution Chemistry of Surfactants, Vol. 1, p. 337, K.L. Mittal (Ed.), (Plenum Press, New York, 1979)
[27] P. Mukerjee, A.Y.S. Yang, J. Phys. Chem. 80, 1388 (1976)

B 9 Statistical Mechanics of Membranes

G. Gompper
Institut für Festkörperforschung
Forschungszentrum Jülich GmbH

Contents

1 Introduction 2

2 Shapes and Fluctuations of Membranes 4
2.1 Short Introduction to Differential Geometry of Surfaces 4
2.2 Curvature Energy 6
2.3 Gauss-Bonnet Theorem 8

3 Minimal Surfaces 9

4 Almost Planar Membranes 11
4.1 Differential Geometry and Curvature Energy 11
4.2 Persistence Length 14

5 Fluctuating Topology: Sponge Phases and Microemulsions 15
5.1 Oil-Water-Surfactant Mixtures 15
5.2 Membrane Ensembles and Phase Behavior 19
5.3 Gaussian Random Fields 22
5.4 Variational Approach 26
5.5 Comparison of Theoretical Approaches 28
5.6 Monte Carlo Simulations of Dynamically Triangulated Surfaces 28
5.7 Experimental Evidence 33

6 Amphiphilic Block Copolymers in Ternary Mixtures 35

7 Summary and Conclusions 41

A Curvature Tensor of Almost Planar Membranes 42

B Joint Distribution of Gaussian Random Fields 42

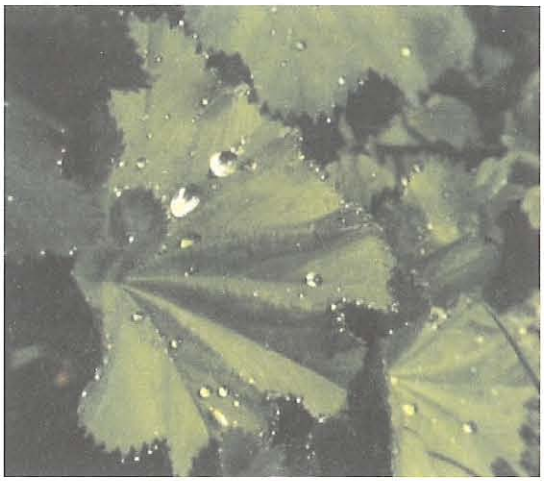


Fig. 1: *Water droplets form on the surface of a plant leave. This process is controlled by the surface tensions of the water-air, the water-leave, and the leave-air interfaces. In the case shown here, water does not wet the leave surface.*

1 Introduction

The existence of surfaces and interfaces on many different scales — from nanometers to many thousands of kilometers — makes life possible and interesting. When we look around, most of what we see are surfaces and interfaces. The basic building block of our body is the cell, a small fluid compartment enclosed by the plasma membrane, which separates the interior of the cell from the environment, but which is also responsible for the controlled exchange of material between inside and outside. Our body is covered by the skin, which plays a similar role for the whole organism as the plasma membrane for the cell. When we clean our hands with soap and water, the soap molecules form a monolayer around small droplets of oil, which is thereby removed from the skin. And, as a final example, this text is written on the surface of a thin sheet of paper.

Several types of interfaces can be distinguished:

- Interfaces between a crystalline solid and a liquid or between a solid and a vapor: The properties of these interfaces are determined by the *anisotropic surface energy* of the crystal. This surface energy controls the crystal shapes in thermal equilibrium, but also the structures which occur in homo- or hetero-epitaxy (crystal growth on a substrate of the same or a different material, respectively).

- Interfaces between two liquids, between a liquid and an amorphous solid, or between a liquid and a vapor:
  The shapes and fluctuations of such interfaces are dominated by the *(isotropic) surface tension.* The surface tension controls the wetting properties of a liquid on a solid substrate (see Fig. 1), the shape of liquid droplets, and the capillary waves on liquid-liquid and liquid-vapor interfaces.

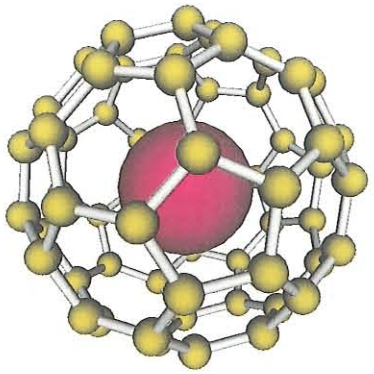


Fig. 2: *A C-60 fullerene molecule has the structure of a spherical cage, in which other atoms or molecules can be enclosed.*

- Two-dimensional, incompressible sheets and films:
  In the previous cases, the interface is defined by the boundary of two different bulk phases. The main difference between such interfaces and two-dimensional films is that the film is formed by its own material, so that the phases on both sides on the film can very well be the same. The shapes and fluctuations of thin films are dominated by their *curvature and shear elasticity.* A few examples are fullerenes (see Fig. 2), cell membranes made of a lipid bilayer and embedded or attached membrane proteins (see Fig. 3), and sheets of paper.

The topic of this lecture is the statistical mechanics of two-dimensional, incompressible films, which will be called *membranes* in the following. It is important to emphasize that the membranes are not planar, but are *embedded in three-dimensional space*, and can therefore fluctuate out of plane.
Membranes can be classified according to their internal properties. Membranes can be

- polymerized – with fixed connectivity;
  examples: graphite sheets, fullerene molecules, polymer network attached to plasma membrane of red blood cells

- crystalline – with a density of lattice defects determined by the defect free energy;
  examples: gel phase of lipid bilayers, membrane proteins crystallized in a fluid lipid bilayer

- fluid, with fixed topology;
  examples: lipid bilayer vesicles (closed bilayers of spherical topology)

- fluid, with fluctuating topology;
  examples: microemulsion and sponge phases (mesoscopically structured phases in mixtures of water, oil and amphiphilic molecules — compare Chaps. A6 and B8), endo- and exocytosis of transport vesicles.

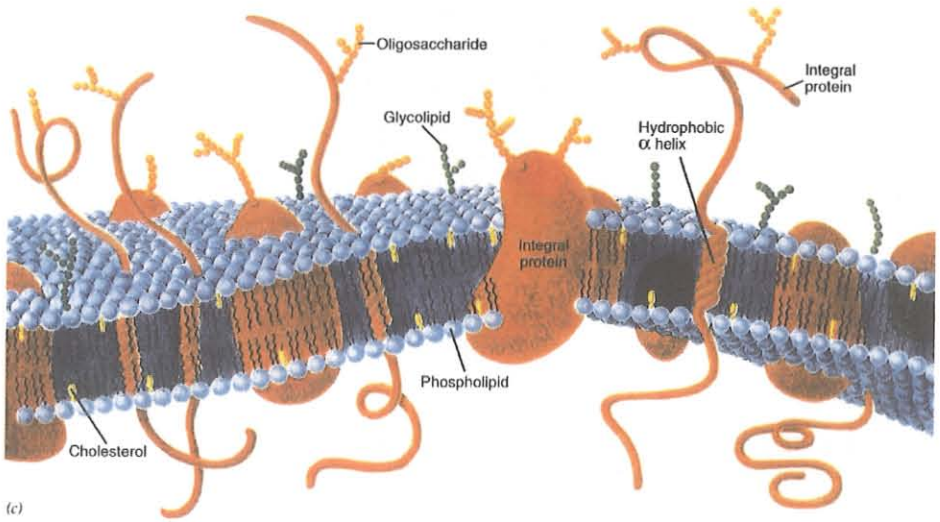


Fig. 3: *The basic structural element of the plasma membrane of eucaryotic cells is a lipid bilayer. This bilayer contains embedded and attached membrane proteins. From Ref. [1].*

Fluid membranes are characterized by free diffusion of the molecules within the membrane. This lecture gives an overview about the thermal properties and phase behavior of an ensemble of fluid membranes.
The statistical mechanics of membranes and related subjects have been discussed in recent years in a number of books and reviews by Nelson et al. (1989) [2], Porte (1992) [3], Gompper and Schick (1994) [4], Gelbart et al. (1994) [5], Safran (1994) [6], Lipowsky and Sackmann [7], David et al. (1996) [8], Seifert (1997) [9], and Gompper and Kroll (1997) [10].

2 Shapes and Fluctuations of Membranes

2.1 Short Introduction to Differential Geometry of Surfaces

A surface is defined mathematically by a vector field $\mathbf{R}(\underline{\sigma}) \in \mathbb{R}^3$, which maps a two-dimensional coordinate system $\underline{\sigma}$ onto a smooth two-dimensional object in the three-dimensional embedding space, see Fig. 4. A basis for the tangent plane to the surface at some point P is given by the two *tangent vectors*

$$\mathbf{t}_i = \partial_i \mathbf{R}(\underline{\sigma}) \equiv \frac{\partial \mathbf{R}}{\partial \sigma^i}, \quad i = 1, 2 \tag{1}$$

With the tangent vectors, the *metric tensor*

$$g_{ij}(\underline{\sigma}) = \partial_i \mathbf{R} \cdot \partial_j \mathbf{R} = \mathbf{t}_i \cdot \mathbf{t}_j \tag{2}$$

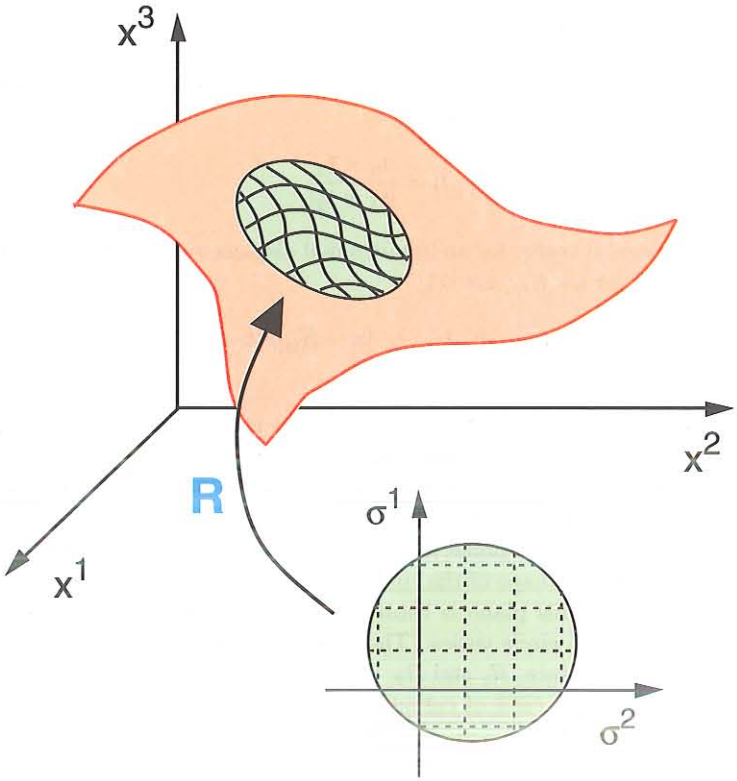


Fig. 4: *A surface is described mathematically by a map* $\mathbf{R}(\underline{\sigma})$ *of a two-dimensional coordinate system* $\underline{\sigma}$ *onto a smooth, two-dimensional object in the three-dimensional embedding space.*

can be defined. The metric tensor determines the infinitesimal Euclidean distance ds between two points on the surface, which is given by [11]

$$\begin{aligned} ds^2 &\equiv [\mathbf{R}(\underline{\sigma}+d\underline{\sigma})-\mathbf{R}(\underline{\sigma})]^2 = \partial_i\mathbf{R}(\underline{\sigma})\cdot\partial_j\mathbf{R}(\underline{\sigma})\; d\sigma^i d\sigma^j \\ &= g_{ij}(\underline{\sigma})\; d\sigma^i d\sigma^j \end{aligned} \tag{3}$$

Similarly, the infinitesimal area element is found to be

$$\begin{aligned} dS &\equiv |\mathbf{t}_1 d\sigma^1 \times \mathbf{t}_2 d\sigma^2| = \sqrt{(\mathbf{t}_1)^2(\mathbf{t}_2)^2-(\mathbf{t}_1\cdot\mathbf{t}_2)^2}\; d\sigma^1 d\sigma^2 \\ &= \sqrt{\det g(\underline{\sigma})}\; d\sigma^1 d\sigma^2 \end{aligned} \tag{4}$$

The unit *normal vector* $\mathbf{n}(\underline{\sigma})$ at some point P on the surface is perpendicular to the tangent plane, so that it can be written as

$$\mathbf{n} = \frac{\mathbf{t}_1\times\mathbf{t}_2}{|\mathbf{t}_1\times\mathbf{t}_2|} \tag{5}$$

The change of the normal vector for an infinitesimal displacement along the surface finally defines the *curvature tensor* K_{ij}, via [11]

$$\partial_i\mathbf{n} = -K_{ij}\mathbf{t}^j \qquad [= -K_{ij}g^{jl}\mathbf{t}_l = -K_i^j\mathbf{t}_j] \tag{6}$$

where $g^{jl} = (g^{-1}_{mn})_{jl}$.
The curvature tensor K_i^j can be diagonalized. The eigenvalues are the two *principal curvatures*, $c_1 = 1/R_1$ and $c_2 = 1/R_2$. Since the curvature tensor is symmetric, the two eigenvectors are perpendicular to each other. These results can be interpreted as follows [11]. Consider a plane, which intersects the surface at the point P and which is perpendicular to the tangent plane at P. A circle can be drawn in this plane, which optimally approximates the shape of the curve of intersection of the plane with the surface in the vicinity of P. As this plane is rotated around the normal vector, the radius of curvature of the "optimal" circle varies. The minimum and maximum of these radii are the principal radii of curvature, R_1 and R_2; their corresponding planes are perpendicular to each other. The principal radii of curvature are illustrated in Fig. 5.
The local geometry of a surface can now be classified by the signs of c_1 and c_2. The corresponding geometries are shown in Fig. 6.

2.2 Curvature Energy

The energy functional of a *fluid membrane* must satisfy the following conditions

- Motion invariance:
  The energy must be invariant under translations and rotations of the whole membrane

- Reparametrization invariance:
  Since the molecules can diffuse freely within the membrane, no preferred coordinate system can exist — which would correspond physically to a labelling of distinct constitutive elements of the membrane. Therefore, the energy must be invariant under a change of the coordinate system.

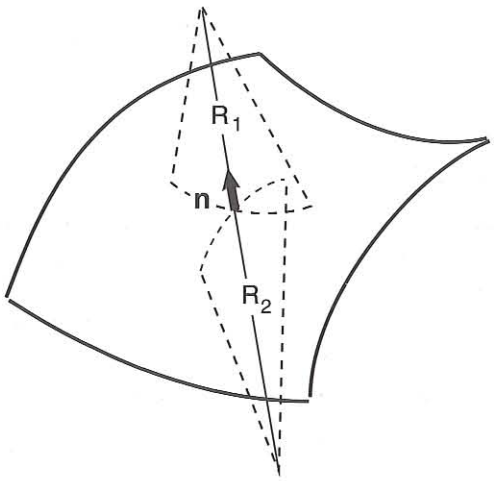


Fig. 5: *The two principal radii of curvature, R_1 and R_2, of a point on the surface.*

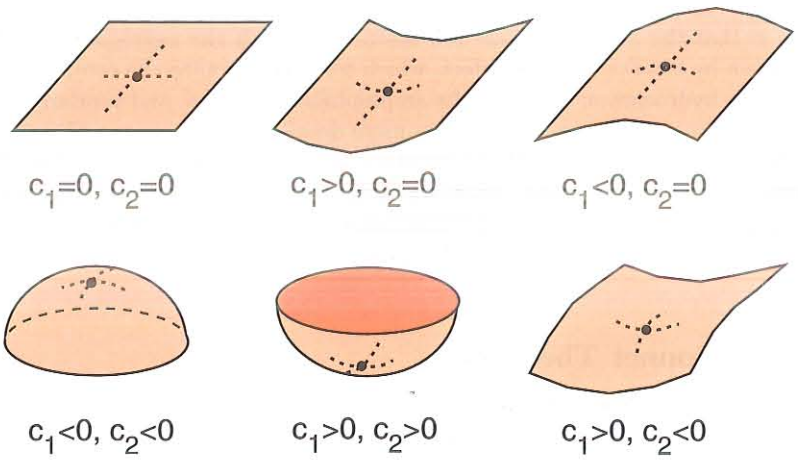


Fig. 6: *The six possible cases of local curvatures of a surface: Plane, concave cylinder, convex cylinder, convex spherical cap, concave spherical cap, and saddle.*

These conditions imply that in an expansion in powers of the inverse radii of curvature, the curvature energy to leading order is given by [12, 13]

$$\mathcal{H}_{curv} = \int d^2\sigma \sqrt{\det g}\,\left[\gamma + 2\kappa(H - c_0)^2 + \bar{\kappa}K + ...\right] \tag{7}$$

where

$$2H = Tr(K_i^j) \equiv g^{ij}K_{ij} = K_i^i = c_1 + c_2 \tag{8}$$

$$K = \det(K_i^j) \equiv \left[K_1^1 K_2^2 - K_1^2 K_2^1\right] = c_1 c_2 \tag{9}$$

are the mean and Gaussian curvatures, respectively. The parameters γ, κ, $\bar{\kappa}$ and c_0 are the elastic constants of the membrane, which depend on the structure and interactions of the constitutive molecules.
It can easily be seen that all the terms in Eq. (7) satisfy the conditions of motion invariance and of reparametrization invariance since

- only derivatives of the position vector $\mathbf{R}$ appear in the form of scalars
- it is well known that the trace and the determinant of a tensor are invariant under similarity transformations.

The different terms in the elastic energy (7) have simple physical interpretations. The first term is proportional to the area of the membrane. Its elastic constant γ is therefore just the surface tension. The second term measures the deviation of the mean curvature H from a preferred or "spontaneous" curvature c_0; the elastic constant κ is the bending rigidity. The last term is a bit more difficult to interpret. It will be shown in Sec. 2.3 below that the surface integral over the Gaussian curvature K is related to the topology of the membrane; the elastic constant $\bar{\kappa}$ is called the saddle-splay modulus.
For amphiphilic membranes, the surface tension γ is very small or vanishes completely. The reason is that the membranes are self-assembling, with the aggregation of the amphiphiles driven by the hydrophobic effect, which tries to minimize the contact of a polar solvent with the hydrocarbon chains of the amphiphilic molecules, and similarly of a apolar solvent with the polar headgroups. For a more detailed discussion see Chaps. A6 and B8. Therefore, it costs free energy for an amphiphilic mono- or bilayer to increase its area per molecule. On the other hand, when the amphiphilic molecules are tightly packed, squeezing them together even more also costs energy. The result of these competing interactions is an optimal area per molecule, which corresponds to a state of zero surface tension.

2.3 Gauss-Bonnet Theorem

The Gauss-Bonnet theorem states that for a *closed* membrane, the surface integral over the Gaussian curvature K is a topological invariant,

$$\int dS\, K = 2\pi\chi_E \tag{10}$$

which for fixed topology has always the same value, independent of its shape. The topological constant χ_E is the Euler characteristic. It can be obtained very easily from the expression

$$\chi_E = 2 \times (\text{No. of objects} - \text{No. of handles}) \tag{11}$$

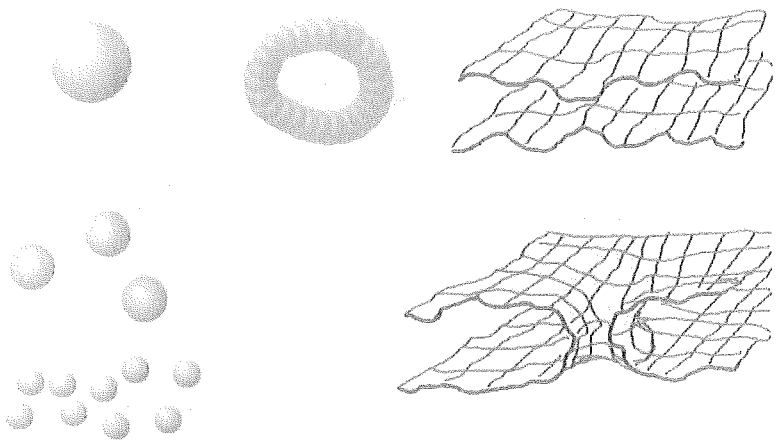


Fig. 7: *The Euler characteristic χ_E of a membrane ensemble is twice the number of objects minus twice the number of handles. Left: for the collections of spheres, $\chi_E = 2$, 6 and 18, from top to bottom. Middle: A torus has $\chi_E = 0$. Right: Two parallel membranes have $\chi_E = 0$ as long as they are disconnected, but $\chi_E = -2$ if they are connected by a passage.*

For a surface, which is composed of polygons, there is also the famous Euler formula, which states that

$$\chi_E = N_{plaquettes} - N_{edges} + N_{vertices} \tag{12}$$

where $N_{plaquettes}$, N_{edges} and $N_{vertices}$ denote the numbers of polygons, edges and vertices, respectively.
Some examples are shown in Fig. 7. For a sphere, Eqs. (10) and (11) give $\chi_E = 2$, while for a topologically equivalent cube, Eq. (12) gives — consistently — $\chi_E = 6 - 12 + 8 = 2$. For a torus, which has one handle, Eq. (11) gives $\chi_E = 0$, while for a torus formed by 8 connected cubes, Eq. (12) gives — again consistently — $\chi_E = 32 - 64 + 32 = 0$. For a plane, Eq. (10) gives $\chi_E = 0$. Two planes with a connecting passage, as shown in the lower right of Fig. 7, according to Eq. (11) then have $\chi_E = -2$.
With the Gauss-Bonnet theorem and Eq. (11), the interpretation of the last term in the curvature energy (7) is now straightforward.

3 Minimal Surfaces

For membranes with spontaneous curvature $c_0 = 0$ and saddle-splay modulus $\bar{\kappa} = 0$, the curvature energy is minimized by shapes which have $H = (c_1 + c_2)/2 \equiv 0$ at all points of the surface. Such surfaces are called *minimal surfaces*. It has been proven mathematically that an infinite number of minimal surfaces exists. However, many of these are self-intersecting, and therefore not interesting for physical systems.
Some examples for minimal surfaces, which are relevant for amphiphilic systems, are listed below.

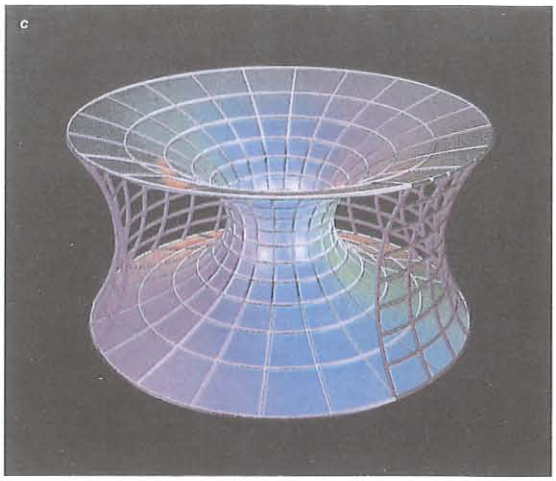


Fig. 8: *The catenoid is a minimal surface of revolution. From Ref. [14].*

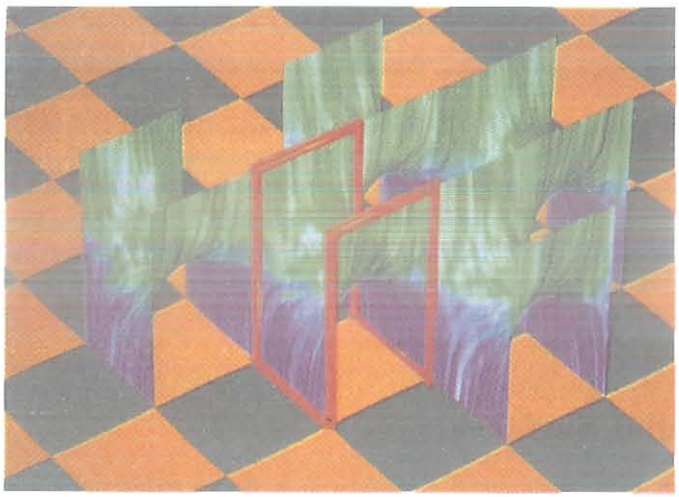


Fig. 9: *Scherk's surface is a doubly-periodic minimal surface. The surface can be build up by repeating the unit cell (red frame) periodically. From Ref. [14].*

- Plane:
  $c_1 = c_2 = 0$ at each point of the surface, so that $K \equiv 0$.

- Catenoid:
  Its shape — see Fig. 8 — is given by the implicit equation $\cosh^2(z) = x^2 + y^2$. In this case, the Gaussian curvature $K < 0$, and varies over the surface, as explained in more detail in Appendix A. The catenoid can be used to describe a passage between two neighboring membranes in a lamellar phase.

- Doubly-periodic surfaces:
  Minimal surfaces which form a two-dimensional Bravais lattice are called doubly periodic. An example is Scherk's minimal surface, which is shown in Fig. 9. Such surfaces describe the tilt grain boundary between two domains of a lamellar phase.

- Triply-periodic minimal surfaces (TPMS):
  Minimal surfaces which form a three-dimensional Bravais lattice are called triply periodic. The three most important TPMS have a cubic unit cell, and are shown in Fig. 10. All of these TPMS have been observed experimentally in the mixture of 2:1 lauric acid / dilauroyl phophatidylcholine and water [15].

4 Almost Planar Membranes

4.1 Differential Geometry and Curvature Energy

Despite of its deceptive simplicity, the general form (7) of the curvature energy cannot be used directly for analytical calculations. Therefore, we consider now a membrane, which deviates not too strongly from a planar reference state. As long as there are no overhangs, the membrane configuration can then be described by a single-valued function $z = h(x_1, x_2)$, see Fig. 11. This is called the *Monge representation*. The position vector $\mathbf{R}(\underline{\sigma})$ of Sec. 2.1 then takes the form

$$\mathbf{R}(\underline{\sigma}) = (\sigma^1, \sigma^2, h(\sigma^1, \sigma^2)) \tag{13}$$

The calculation of the tangent vectors, and of the metric and curvature tensors is now straightforward. The tangent vectors are

$$\mathbf{t}_1(\underline{\sigma}) = \partial_1 \mathbf{R} = (1, 0, \partial_1 h(\sigma^1, \sigma^2)) \tag{14}$$

$$\mathbf{t}_2(\underline{\sigma}) = \partial_2 \mathbf{R} = (0, 1, \partial_2 h(\sigma^1, \sigma^2)) \tag{15}$$

which gives the normal vector

$$\mathbf{n} = \frac{\mathbf{t}_1 \times \mathbf{t}_2}{|\mathbf{t}_1 \times \mathbf{t}_2|} = \frac{(-\partial_1 h, -\partial_2 h, 1)}{\sqrt{1 + (\nabla h)^2}} \tag{16}$$

The expressions for the tangent vectors show that the mean curvature can be obtained very easily from the relation

$$\partial_1 n_x + \partial_2 n_y = K_1^1 + K_2^2 = 2H \tag{17}$$

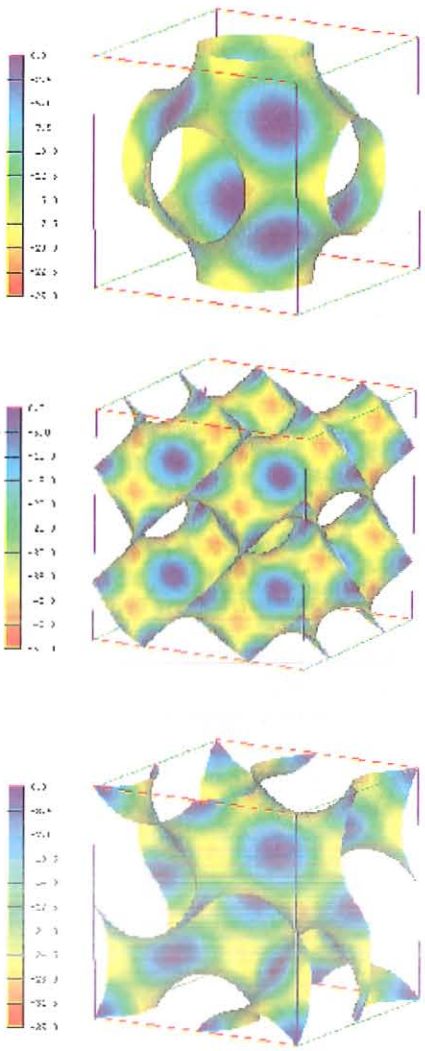


Fig. 10: *The three most important triply periodic minimal surfaces (TPMS) of cubic symmetry: Schwarz P-surface (top), Schwarz D-surface (middle), and Schoen's gyroid surface (bottom) [16]. The color code indicates the distribution of the Gaussian curvature K on the surface, with blue colors for small $|K|$ and red colors for large $|K|$.*

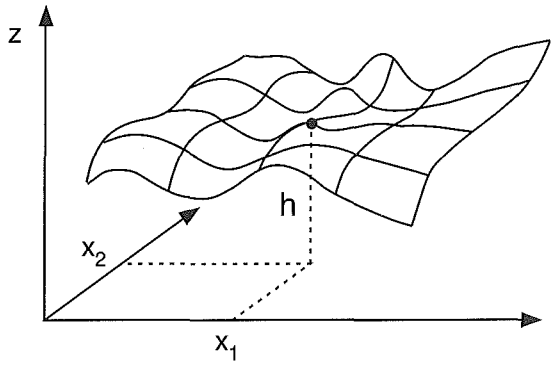


Fig. 11: *In the Monge representation, the surface is described by a single-valued function* $z = h(x_1, x_2)$.

Therefore, the mean curvature is found to be

$$2H = \nabla \cdot \frac{\nabla h}{\sqrt{1 + (\nabla h)^2}} \tag{18}$$

A more detailed derivation is given in Appendix A, where also the result

$$K = \frac{\partial_1^2 h \partial_2^2 h - (\partial_1 \partial_2 h)^2}{[1 + (\nabla h)^2]^2} \tag{19}$$

for the Gaussian curvature is obtained.
With these results, an explicit form of the curvature energy (7) is now available. It is important to notice that in the derivation of Eqs. (18) and (19) no approximations have been made. Thus, these expressions are still exact in the Monge representation. In order to proceed with the calculation of membrane *fluctuations*, we now assume that the deviations from the planar reference state are small enough that an expansion in powers of $|\nabla h|$ is justified. To leading order in this expansion, the curvature energy then becomes

$$E_b \simeq \frac{\kappa}{2} \int d^2x \ \left(\nabla^2 h(\mathbf{x})\right)^2 \tag{20}$$

Note that the Gaussian curvature term does not appear in this equation. This can be seen in general from the Gauss-Bonnet theorem and $\chi_E = 0$ for planar membranes, or explicitly in this case from Eq. (19), which for $|\nabla h| \ll 1$ can be written as a perfect derivative

$$2K \simeq -\epsilon_{im}\epsilon_{jn}\partial_m\partial_n[(\partial_i h)(\partial_j h)] \tag{21}$$

where ϵ_{ij} is the totally anti-symmetric matrix. With the help of Stokes integral theorem, the surface integral over K can then be written as a boundary integral, which can be neglected in the thermodynamic limit.
In Fourier space, with

$$h(\mathbf{x}) = \int \frac{d^2q}{(2\pi)^2} h(\mathbf{q}) e^{i\mathbf{q}\cdot\mathbf{x}} \tag{22}$$

the expression (20) simplifies to

$$\begin{aligned}\int d^2x\ \left(\nabla^2 h(\mathbf{x})\right)^2 &= \\ &= \int \frac{d^2q}{(2\pi)^2} \int \frac{d^2q'}{(2\pi)^2} (-q^2)(-q'^2) h(\mathbf{q}) h(\mathbf{q}') \underbrace{\int d^2x\ e^{i(\mathbf{q}+\mathbf{q}')\cdot\mathbf{x}}}_{(2\pi)^2\delta(\mathbf{q}+\mathbf{q}')} \\ &= \int \frac{d^2q}{(2\pi)^2}\ q^4 |h(\mathbf{q})|^2\end{aligned} \tag{23}$$

where

$$h(-\mathbf{q}) = h^*(\mathbf{q}) \tag{24}$$

since $h(\mathbf{r}) \in \mathbb{R}$. Therefore we finally obtain

$$E_b = \frac{\kappa}{2} \int \frac{d^2q}{(2\pi)^2}\ q^4 |h(\mathbf{q})|^2 \tag{25}$$

This is an important result, since it shows that the fluctuation modes, which are called *undulation modes* for membranes, *decouple* in Fourier space. The calculation of the fluctuation spectra then becomes very simply, since the *equipartition theorem* — which states that the energy of each independent mode is $k_BT/2$ on average — then implies

$$\langle |h(\mathbf{q})|^2 \rangle = \frac{k_BT}{\kappa q^4} \tag{26}$$

This behavior has indeed been verified in neutron scattering experiments on ternary microemulsions, as described in detail in Chap. C6 of this school.

4.2 Persistence Length

We now want to calculate the fluctuations of the angle θ of the normal vector $\mathbf{n}$ with the z-axis,

$$n_z \equiv \mathbf{n} \cdot \mathbf{e}_z = \cos\theta \simeq 1 - \frac{1}{2}\theta^2 \tag{27}$$

for a membrane of *linear size* L with periodic boundary conditions. In the Monge representation, we have found (see Eq. (16))

$$n_z = 1/\sqrt{1 + (\nabla h)^2} \simeq 1 - \frac{1}{2}(\nabla h)^2 \tag{28}$$

so that with the equipartition theorem (26)

$$\langle \theta^2 \rangle = \langle (\nabla h)^2 \rangle = \int \frac{d^2q}{(2\pi)^2}\ q^2\ \frac{k_BT}{\kappa q^4} = \frac{k_BT}{2\pi\kappa} \ln(L/a) \tag{29}$$

where a is a molecular length. The fluctuations of the angle θ thus increase *logarithmically* with increasing membrane size L. Clearly, this is not possible without violating the condition $|\nabla h| \ll 1$, which was used in the derivation of the expression (20) of the curvature energy. The length where this happens, the *persistence length* ξ_p, can be defined

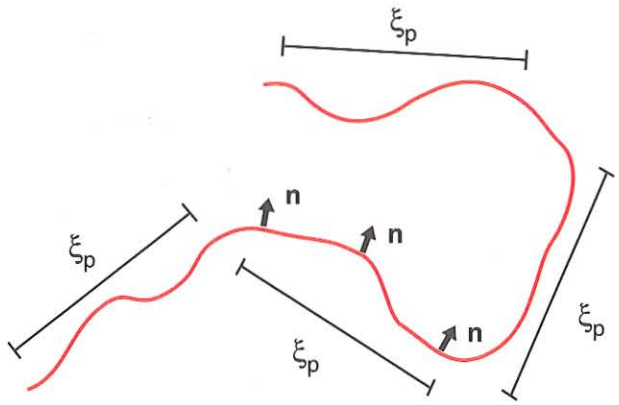


Fig. 12: *On length scales short compared to the persistence length ξ_p, normal vectors point roughly into the same direction, while on larger scales, normal vectors are uncorrelated.*

— somewhat arbitrarily — by $\langle\theta^2\rangle = 1$ (de Gennes & Taupin 1982) [17]. The inversion of Eq. (29) gives immediately

$$\xi_p = a \exp(2\pi\kappa/k_B T) \tag{30}$$

with molecular length a. The interpretation of the persistence length is explained in Fig. 12. For a membrane patch, which is much smaller than the persistence length, the fluctuations of the normal vector around the average orientation are small — the membrane is almost planar on this scale. On the other hand, membrane patches, which are much larger than the persistence length, have a wildly fluctuating normal vector, which means that no preferred orientation exists. This is the situation sketched in Fig. 12.
It is instructive to consider two examples:

- Lipids: $a = 1nm$, $\kappa = 10 k_B T \rightarrow \xi_p = 10^{24} km$. The persistence length is *astronomical*, certainly much larger than the size of a typical cell.
- Surfactants: $a = 1nm$, $\kappa = 0.5 k_B T \rightarrow \xi_p = 25nm$. The persistence length is *mesoscopic*.

5 Fluctuating Topology: Sponge Phases and Microemulsions

5.1 Oil-Water-Surfactant Mixtures

Phase Behavior of Water-Surfactant Mixtures — The experimental phase diagram of the binary mixture of the non-ionic surfactant $C_{12}E_5$ and water is shown in Fig. 13. The phase diagram is dominated by the two-phase coexistence between a dilute micellar phase L_1' and a more concentrated micellar phase L_1'' at low temperatures (see Chap. B8 for a detailed discussion of micelles). At high surfactant concentration, a lamellar phase L_α —

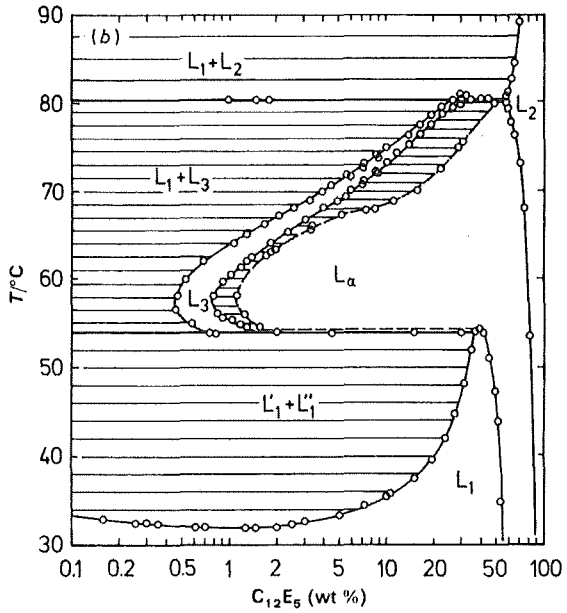


Fig. 13: *Experimental phase diagram of the binary mixture of $C_{12}E_5$ and water (Strey, Schomäcker, Roux, Nallet, Olsson 1990) [18]. The phase diagram is dominated by the two-phase coexistence between a dilute (L_1') and a more concentrated (L_1'') micellar phase at low temperatures. At higher temperatures, the lamellar phase (L_α) becomes stable already at high dilution of only a few percent surfactant. Simultaneously, a sponge (L_3) phase appears at even lower surfactant concentration. Note the logarithmic scale of the abscissa.*

a one-dimensional stack of surfactant bilayers separated by thin water films — is stable in this temperature range. At higher temperatures, the lamellar phase suddenly becomes stable already at very high dilution of only a few percent surfactant. Simultaneously, a sponge phase L_3 appears at even lower surfactant concentration.

Both the lamellar phase and the sponge phase are made of surfactant *bilayers*. Since the two leavlets of the bilayers are equivalent, these membranes cannot have a spontaneous curvature by symmetry, so that $c_0 \equiv 0$ in Eq. (7) in this case.

Lamellar Phase L_α — The stability of the lamellar phase at these strikingly low surfactant concentrations has caught the imagination of physicists in the late seventies of the last century. It was proposed by Helfrich (1978) [19] that this swelling behavior of the lamellar phase under the addition of water can be understood by the repulsive force generated by the suppression of long wave-length undulation modes of an individual membrane by its neighbors in the stack. This leads to a reduction of its entropy, and therefore to an increase of the free energy Δf per unit area, which was predicted to have the form

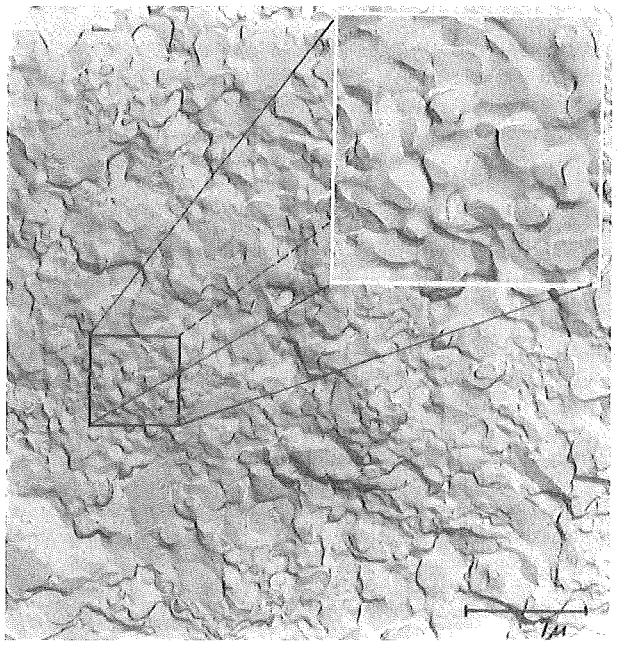


Fig. 14: *Freeze-fracture-microscopy picture of a sponge phase in the system water/NaCl and AOT (Strey, Jahn, Skouri, Porte, Marignan, Olsson 1992) [23]. Note the local saddle-shape structure of the membrane, which can be seen most clearly in the inset.*

[19]

$$\Delta f = c_\infty \frac{(k_B T)^2}{\kappa} d^{-2} \tag{31}$$

where d is the repeat distance of the lamellar phase. This behavior has since been investigated and verified experimentally [20, 21]. Monte Carlo simulations [22] give a value

$$c_\infty = 0.106 \tag{32}$$

for the value of the universal coefficient in Eq. (31).

Sponge Phase L_3 — Freeze-fracture microscopy reveals the mesoscopic structure of the sponge phase, as shown in Fig. 14. The fluid is frozen very rapidly to preserve its mesoscopic structure during the freezing process, then fractured into pieces. Fortunately, the fracture surface follows preferentially the midplane of the bilayer. Therefore, the three-dimensional structure of the membrane is revealed by this technique. Fig. 14 demonstrates impressively that the sponge phase is a complicated network of water channels, which are separated by membranes with a locally *saddle-shaped* structure.
The "sponge phase" has gotten it's name because its structure resembles the structure of a *sea-water* sponge (compare Fig. 15). The pore space of the sea-water sponge has to be connected in order for the water to be able to penetrate the sponge; its solid component has also to be connected to keep the sponge together. Thus, both objects are "bicontinuous" (see below). However, the length scales are very different.

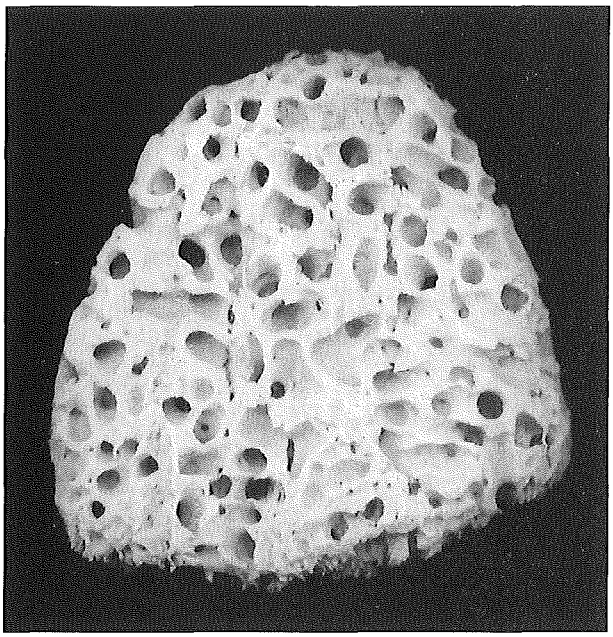


Fig. 15: *A sea-water sponge.*

Microemulsions — When oil is added as a third component to a mixture of water and surfactant, the phase diagram obviously gets considerable more complicated [4]. A detailed discussion of the phase behavior of ternary amphiphilic systems can be found in Chap. A6 of this school. The spontaneous curvature of the monolayer membrane is in general non-zero in these systems. However, for most non-ionic surfactants, where the spontaneous curvature depends sensitively on temperature (compare Sec. 5.7), it vanishes for one particular temperature, the hydrophobic-hydrophilic-balance temperature $\bar{T}$. In a temperature interval around $\bar{T}$, a phase is stable, which is macroscopically homogeneous and isotropic, and which contains equal amounts of oil and water. This phase is called a *microemulsion* . It has a very similar mesoscopic structure as the sponge phase:

- The membrane in the sponge is a bilayer, in the microemulsion it is a monolayer.
- The microemulsion consists of network of oil- and water-channels, which are separated by a surfactant monolayer. The sponge phase consists of (at least) two distinct networks of water-channels, which are separated by a bilayer.

A microemulsion is called *bicontinuous*, because both the oil- and the water-networks span the whole system. Since the sponge phase has an equivalent mesoscopic structure with two networks of water channels, it is also called bicontinuous.

5.2 Membrane Ensembles and Phase Behavior

We want to try to understand the structure and phase behavior of binary mixtures of water and surfactant on the basis of a model, in which the surfactant film is described by a surface, whose shapes and fluctuations are controlled by the curvature energy (7). First attempts for such a description go back to Scriven (1976) [24], de Gennes and Taupin (1982) [17], and Safran et al. (1986) [25].
From a statistical mechanics point of view, this is a formidable problem. It amounts to calculating the partition function

$$Z = \sum_{topologies} \int' \mathcal{D}\mathbf{R}(\underline{\sigma}) \exp\{\mathcal{H}[\mathbf{R}(\underline{\sigma})]/k_B T\} \tag{33}$$

where $\int' \mathcal{D}\mathbf{R}(\underline{\sigma})$ denotes an integration over all possible shapes with parametrization $\mathbf{R}(\underline{\sigma})$ of the surface at fixed topology, where $\underline{\sigma}$ is a two-dimensional coordinate system on the surface, as explained in Sec. 2.1. However, this integral cannot be just over all possible parametrizations $\mathbf{R}(\underline{\sigma})$ of a surface of fixed topology, but has to be restricted to those parametrizations, which lead to physically different shapes in the embedding space; this is indicated by the prime. Finally, the contributions off all different topologies have to be summed over. It is clear that this problem is sufficiently complex that no exact solution will be found anytime soon. Therefore, approximations have to be made in order to get some insight into the behavior of these phases.

Energy considerations — Let us first take a closer look at the curvature *energy* itself, and consider the effect of fluctuations in a second step. It is easily seen that for $c_0 = 0$ the curvature Hamiltonian (7) can be rewritten in the form

$$E = \int dS \left[\frac{1}{2}\kappa_+ \left(\frac{1}{R_1} + \frac{1}{R_2} \right)^2 + \frac{1}{2}\kappa_- \left(\frac{1}{R_1} - \frac{1}{R_2} \right)^2 \right] \tag{34}$$

with

$$\kappa_+ = \kappa + \frac{1}{2}\bar{\kappa} \quad , \quad \kappa_- = -\frac{1}{2}\bar{\kappa} \tag{35}$$

This form is convenient to show that the stability of lamellar phase requires

$$\kappa_+ > 0 \quad , \quad \kappa_- > 0 \tag{36}$$

since otherwise the energy of the system could be lowered without bounds by making the term with negative amplitude very large in magnitude. With Eq. (35), the stability conditions (36) are equivalent to

$$-2\kappa < \bar{\kappa} < 0 \tag{37}$$

Instabilities occur as κ_+ or κ_- approach zero:

- For $\kappa_+ \to 0$, it costs no energy to make $|c_1 + c_2|$ large, as long as $|c_1 - c_2|$ remains small. Thus, in this limit it costs no energy to form small spherical objects with $c_1 \simeq c_2$, which in the case of amphiphilic bilayers are called *vesicles*.

- For $\kappa_- \to 0$, it costs no energy to make $|c_1 - c_2|$ large, as long as $|c_1 + c_2|$ remains small. Thus, in this limit it costs no energy to form minimal surfaces with $c_1 \simeq$

$-c_2$ and small lattice constant, such as the cubic triply periodic minimal surfaces discussed in Sec. 3. These phases are also often called *plumber's nightmare phases*, because this multiply connected system of tubes would be almost impossible for a plumber to prevent such a structure from leaking.

Scaling Considerations — Let us consider an arbitrarily shaped piece of membrane with fixed geometry. Let the local curvatures be denoted by c_i, and the curvature energy of this patch be E_b. When this membrane piece is rescaled uniformly by a scale factor λ — i.e. the "shape" remains the same but the size changes — then the new local curvatures become $c_i' = \lambda^{-1} c_i$, and the curvature energy changes to

$$\begin{aligned} E_b' &= \int dS' \left\{ 2\kappa H'^2 + \bar{\kappa} K' \right\} \\ &= \int dS \lambda^2 \left\{ 2\kappa \lambda^{-2} H^2 + \bar{\kappa} \lambda^{-2} K \right\} \equiv E_b \end{aligned} \tag{38}$$

Thus, the curvature energy remains invariant under uniform scale transformations. This results implies immediately that the energy *density*, which is the energy *per unit volume*, depends on the surface-to-volume ratio, S/V, which is proportional to the amphiphile concentration, as [26]

$$E_b/V \sim (S/V)^3 \tag{39}$$

Eq. (39) shows that the curvature energies of all membrane structures scale in exactly the same way (although with different prefactors), so that an intersection of the energy curves for different structures as a function of S/V cannot occur. This result allows an important conclusion. On the basis of the curvature energy alone, without thermal fluctuations, we will not be able to understand transitions between different mesophases as the amphiphile concentration is varied, such as the lamellar-to-sponge transition in Fig. 13 at fixed temperature. It must be the *entropy* which is responsible for these transitions.

Membrane Fluctuations — The thermal fluctuations on small scales — i.e. small compared to the typical domain size of a sponge phase, or small compared to the average separation of membranes in a lamellar phase — modify the curvature elasticity on larger scales. This effect can be easily demonstrated with a sheet of paper for *polymerized* membranes (with fixed connectivity of neighboring molecules): A corrugated sheet has a higher bending rigidity on scales larger than the characteristic ripples than a smooth sheet. Thus, "fluctuations" increase the rigidity in this case. In *fluid* membranes, fluctuations have the opposite effect of softening the rigidity on larger scales. There is no macroscopic example to demonstrate this effect. It follows from renormalization group calculations [27, 28], which show that thermal fluctuations lead to renormalized, *scale-dependent* rigidities κ^R, $\bar{\kappa}^R$ of the form

$$\kappa_R(\xi) = \kappa - \alpha \frac{k_B T}{4\pi} \ln(\xi/a) \tag{40}$$

$$\bar{\kappa}_R(\xi) = \bar{\kappa} - \bar{\alpha} \frac{k_B T}{4\pi} \ln(\xi/a) \tag{41}$$

with $\alpha = 3$ and $\bar{\alpha} = -10/3$ (Peliti & Leibler 1985, David 1989) [27, 29]. This implies immediately that the elastic moduli of Eq. (34) are also renormalized, and are given by

$$\kappa_\pm^R(\xi) = \kappa_\pm - \alpha_\pm \frac{k_B T}{4\pi} \ln(\xi/a) \tag{42}$$

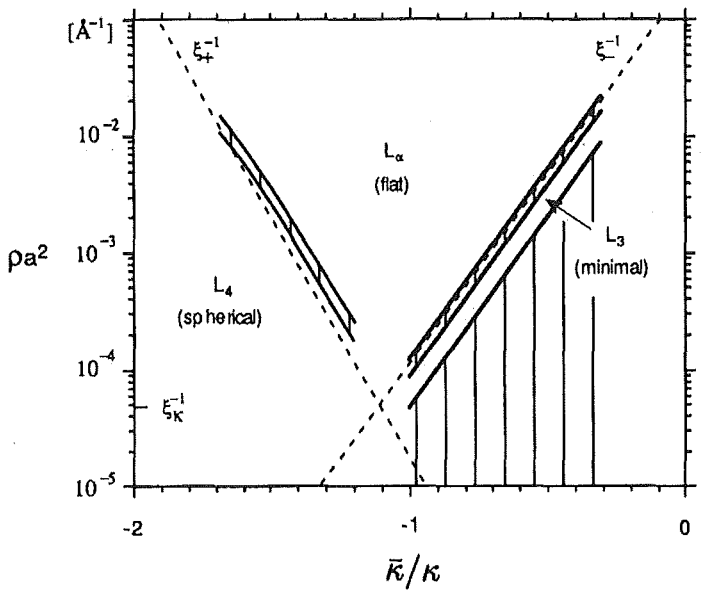


Fig. 16: *Phase diagram of binary or balanced ternary amphiphile mixtures, as predicted on the basis of the renormalization of the bending rigidity κ and the saddle-splay modulus $\bar{\kappa}$, for fixed $\kappa/k_BT = 2$ (Morse 1994) [30]. The phase behavior is shown as a function of the membrane volume fraction Ψ (denoted here ρa^2) and the bare saddle-splay modulus $\bar{\kappa}$. L_3 denotes the sponge phase, L_4 a vesicle phase. The two dashed lines are the stability boundaries (45).*

with

$$\alpha_+ = \alpha + \frac{1}{2}\bar{\alpha} = \frac{4}{3} \quad , \quad \alpha_- = -\frac{1}{2}\bar{\alpha} = \frac{5}{3} \tag{43}$$

Phase Behavior — When the fluctuation on short scales are taken into account, the instabilities of the lamellar phase discussed above now occur where the *renormalized* rigidities vanish, i.e. at $\kappa_\pm^R(\xi) = 0$. The length scale ξ, where the renormalization is cut off, is determined by the average separation of neighboring membranes, which is given by the membrane volume fraction

$$\Psi \equiv \frac{aS}{V} = a/\xi \tag{44}$$

where a is again a molecular scale, here the length of the amphiphiles. This finally implies (Morse 1994) [30]

$$\ln(\Psi) = -\frac{4\pi}{\alpha_\pm}\frac{\kappa_\pm}{k_BT} \tag{45}$$

The phase diagram, which is predicted on the basis of this calculation, is shown in Fig. 16. This phase diagram does not only contain the instability lines (45), but also results of a somewhat more detailed calculation, in which estimates of the free energies of the sponge phase (based on an approximation by minimal surfaces, so that the free energy is taken

to be $\bar{\kappa}_R(\xi) \int dS\ K$) and of the lamellar phase (based on the steric repulsion expression (31)) are compared. Fig. 16 shows that the two results are in good agreement.
The phase diagram is dominated by a V-shaped region, where the lamellar phase is stable. With decreasing amphiphile concentration, a phase transition to the sponge phase occurs for $0 > \bar{\kappa}/\kappa > -10/9$, while a transition to a vesicle phase occurs for $-10/9 > \bar{\kappa}/\kappa > -2$. The sponge phase exists only in a narrow strip parallel to the instability line. When the amphiphile concentration is decreased further, *emulsification failure* occurs, i.e. the sponge phase cannot take up any more water, and therefore coexists with an (almost pure) water phase at these low membrane volume fractions.

5.3 Gaussian Random Fields

An alternative description of sponge phases is to employ *level surfaces* of a scalar field $\Phi(\mathbf{r})$, with $\mathbf{r} \in \mathbb{R}^3$, which are defined by

$$\Phi(\mathbf{r}) = \alpha \tag{46}$$

This implicitly defines a surface in three-dimensional space. An illustration of this concept is shown in Fig. 17, where the level "surfaces" are shown for a scalar field in two dimensions. Thermal fluctuations of the scalar field $\Phi(\mathbf{r})$ — according to a Boltzmann weight $\exp(-\mathcal{H}_0)$ — then imply fluctuations of the level surfaces. The properties of the membranes are therefore induced by the statistical mechanics of the scalar field Φ.
A particularly useful case are *Gaussian random fields* (GRF) , where the fluctuations of Φ are controlled by a Boltzmann weight with a *quadratic* Hamiltonian

$$\mathcal{H}_0 = \frac{1}{2} \int d^3r \Phi(\mathbf{r}) \nu^{-1}(|\mathbf{r} - \mathbf{r}'|) \Phi(\mathbf{r}') \tag{47}$$

with *spectral density* $\nu(\mathbf{r} - \mathbf{r}')$. Requirements on $\nu^{-1}(|\mathbf{r} - \mathbf{r}'|)$ are that it decays sufficiently fast for large $|\mathbf{r} - \mathbf{r}'|$ so that the integral and the second and fourth moments are finite. The normalization

$$\langle \Phi(\mathbf{r}) \rangle = 0 \quad , \quad \langle \Phi(\mathbf{r})^2 \rangle = 1 \tag{48}$$

is usually employed, where the first identity follows immediately from the $\Phi \to -\Phi$ symmetry of the Hamiltonian, while the second identity implies the normalization $\int d^3k\ \nu(k) = (2\pi)^3$. The advantage of the Gaussian random field model is that all averages can be calculated exactly.
In particular, the *average geometry* of the level surfaces can be calculated for Gaussian random fields (GRF), with the analytical results (Teubner 1991) [31]:

$$S/V = \frac{2}{\pi} \exp[-\alpha^2/2] \sqrt{\frac{1}{3}\langle q^2 \rangle_\nu} \tag{49}$$

$$\langle K \rangle = -\frac{1}{6} \langle q^2 \rangle_\nu (1 - \alpha^2) \ , \tag{50}$$

$$\langle H \rangle = \frac{1}{2} \alpha \sqrt{\frac{\pi}{6} \langle q^2 \rangle_\nu} \ , \tag{51}$$

$$\langle H^2 \rangle = \langle K \rangle + \frac{1}{5} \frac{\langle q^4 \rangle_\nu}{\langle q^2 \rangle_\nu} \tag{52}$$

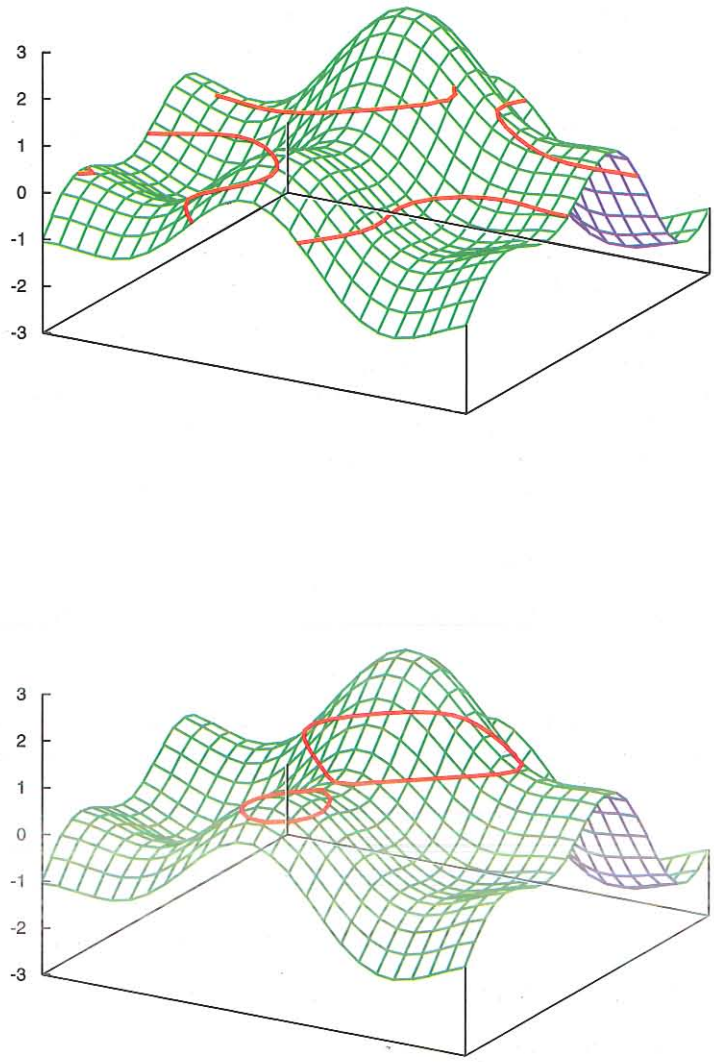


Fig. 17: *Level "surfaces" of a scalar field* $\Phi(\mathbf{r})$*, with* $\langle\Phi(\mathbf{r})\rangle = 0$*. For illustration purposes,* $\mathbf{r} \in \mathbb{R}^2$*, so that the level "surfaces" are in fact lines in this case. Top: Level surface (red lines) for* $\alpha = 0$*, so that the surface has no preferred curvature,* $\langle H\rangle = 0$*, and a sponge-like structure can be envisaged. Bottom: Level surface (red lines) for* $\alpha = 1$*, so that the level surface bends preferentially to one side, and droplet-like structures can be seen.*

where

$$\langle q^n \rangle_\nu \equiv \int \frac{d^3q}{(2\pi)^3} q^n \nu(q) \tag{53}$$

These results imply some interesting conclusions for the symmetric case $\alpha = 0$:

- Eq. (51) shows that mean curvature vanishes, $\langle H \rangle \equiv 0$, so that $\alpha = 0$ corresponds to a balanced system, such as in sponge phases or balanced microemulsions. Compare Fig. 17.
- From Eq. (50), we find $\langle K \rangle = -\frac{1}{6}\langle q^2 \rangle_\nu < 0$; this implies that the average geometry of level surfaces in Gaussian random fields is *saddle-shaped.* Eqs. (50) and (49) can be combined to give the dimensionless quantity $\langle K \rangle (S/V)^{-2} = -\pi^2/8 = -1.234$, which characterizes the topology of a characteristic "unit cell" of the sponge phase. It is important to note that this number is *universal* in the Gaussian random field model, since it is completely independent of the spectral density ν.

As an example how the average geometry of the level surfaces can be calculated for Gaussian random fields, the calculation of the *surface density* S/V is sketched briefly here. It is clear that the surface density must be related to the average of $\delta(\Phi(\mathbf{r}) - \alpha)$. However, note that in contrast to the particle density of molecules or colloidal particles, which is given by $\rho(\mathbf{r}) = \sum_i \delta(\mathbf{r} - \mathbf{r}_i)$, the δ-function for the level surfaces acts on the Φ-variable, rather than the space variable $\mathbf{r}$ is in the usual case. Therefore, we need the mathematical identity

$$\delta(\Phi(\mathbf{r}) - \alpha) = \frac{1}{|\nabla\Phi(\mathbf{r})|} \delta(\mathbf{r} - \mathbf{r}_0) \tag{54}$$

where $\mathbf{r}_0$ is the location of the level surface. The surface density is therefore given by

$$S/V = \langle |\nabla\Phi(\mathbf{r})| \; \delta(\Phi(\mathbf{r}) - \alpha) \rangle \tag{55}$$

There is another, more intuitive way to arrive at the same conclusion. Let us consider a smeared-out δ-function of width ϵ, as shown in Fig. 18 (upper part). The contribution to the average of the function δ_ϵ now clearly depends on the gradient of Φ; if the gradient is small (large), the contribution is large (small), as shown in Fig. 18 (lower part). Since for the calculation of S/V the contribution of all parts of the surface must be the same — independent of the local gradient of Φ — this effect has to be divided out, which gives again Eq. (55).
In order to calculate the average (55), we need the joint probability distribution function

$$P[\Phi(\mathbf{r}) = \alpha, \nabla\Phi(\mathbf{r}) = \mathbf{v}] = \langle \delta(\Phi(\mathbf{r}) - \alpha) \; \delta(\nabla\Phi(\mathbf{r}) - \mathbf{v}) \rangle \tag{56}$$

It is shown in detail in Appendix B that

$$P[\alpha, \mathbf{v}] = P_0 \exp\left[-\frac{\alpha^2}{2} - \frac{v^2}{2\sigma_v^2} \right] \tag{57}$$

with

$$\sigma_v = \frac{1}{3} \int \frac{d^3q}{(2\pi)^3} \; q^2 \nu(q) \equiv \frac{1}{3} \langle q^2 \rangle_\nu \tag{58}$$

and normalization

$$P_0 = (2\pi)^{-2} \sigma_v^{-3} \tag{59}$$

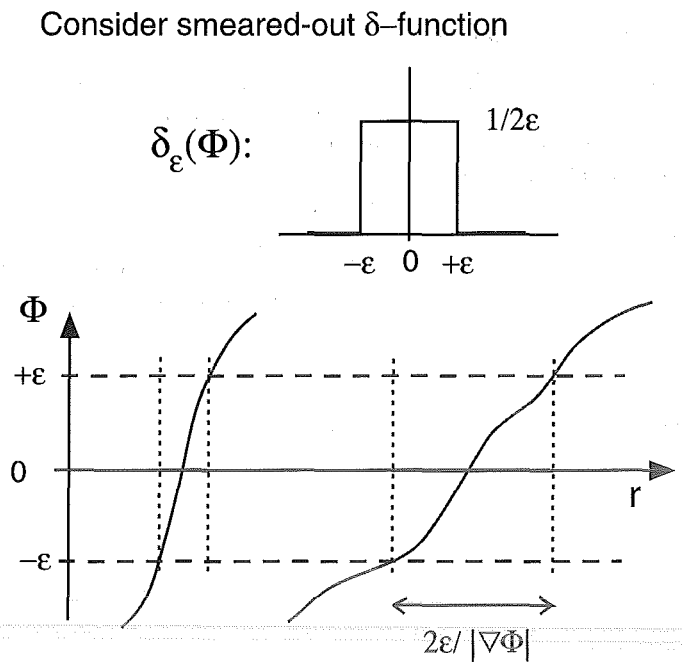


Fig. 18: *In order to calculate the surface area of level surfaces of Gaussian random fields, the δ-function in Φ has to be corrected for the different local gradients of the order-parameter field. For details see text.*

This implies

$$\begin{aligned} S/V &= \int d^3v|v|P(\alpha,\mathbf{v}) \\ &= 4\pi P_0 \int_0^\infty dv v^3 \exp[-\alpha^2/2 - v^2/(2\sigma_v^2)] \\ &= \frac{2}{\pi}\exp[-\alpha^2/2]\sqrt{\frac{1}{3}\langle q^2\rangle_\nu} \end{aligned} \tag{60}$$

This is just the result (49).

5.4 Variational Approach

In Sec. 5.3, the spectral density ν has never been specified. The application of the Gaussian random field model to sponge phases therefore remains qualitative on this level [32, 33, 31]. What is missing is a relation of the spectral density ν to the Hamiltonian which describes the system under consideration. For a membrane ensemble controlled by the curvature energy, considerable progress can be made by employing the Gaussian random field model in a variational approach (Pieruschka & Safran 1993) [34].
The variational approach is based on the Gibbs-Bogoliubov-Feynman inequality [35, 36]. It relates the energies and free energies of the system under consideration (in our case the membrane ensemble with curvature energy) to a reference system, which can be treated more easily (in our case the Gaussian random field model).
Let the full system be described by a Hamiltonian $\mathcal{H}$ and have free energy F, and the reference system be described by Hamiltonian $\mathcal{H}_0$ and have free energy F_0. The Gibbs-Bogoliubov-Feynman inequality is based on the inequality $\langle\exp(f)\rangle \geq \exp\langle f\rangle$ for any function $f \in \mathbb{R}$ [36]. This implies

$$F \leq F_0 + \langle\mathcal{H} - \mathcal{H}_0\rangle_0 \tag{61}$$

The main idea of the variational approach is then to choose a reference system with free parameters, which can be used to find an optimal (i.e. lowest) upper bound for the free energy of the full system.
The application of this approach to membrane ensembles requires the calculation of $\langle\mathcal{H}\rangle_0$ and F_0. The average curvature energy is

$$\langle\mathcal{H}_{curv}\rangle_0 = S\left(2\kappa\langle H^2\rangle_0 + \bar{\kappa}\langle K\rangle_0\right) \tag{62}$$

which can be easily expressed as a functional of the spectral density with Eqs. (49)-(52). The calculation of the free energy of a Gaussian model is a standard problem of statistical field theory, as described for example in detail in Ref. [36], and has the result

$$F_0 = -\frac{1}{2}\int \frac{d^3k}{(2\pi)^3}\ln(\nu(k)) \tag{63}$$

Functional differentiation of Eq. (61) with Eqs. (62) and (63) then gives the *optimal spectral density* (Pieruschka & Safran 1995) [38]

$$\nu(q) = \frac{a}{q^4 - bq^2 + c} \tag{64}$$

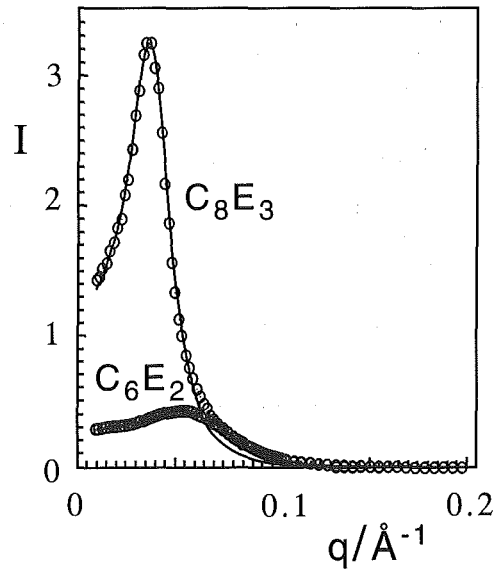


Fig. 19: *The scattering intensity $I(q)$ of a balanced microemulsion in bulk contrast for two different surfactants. The data are very well fitted by the functional form of Eq. (64) (Teubner & Strey 1987) [37].*

where a, b, and c are now functions of κ and S/V.
The spectral density (64) can be identified with the scattering intensity $I(q)$ in bulk contrast of ternary microemulsions, i.e. with scattering contrast between oil and water. It was shown already more than 10 years ago (Teubner & Strey, 1987) [37] that the functional form of Eq. (64) indeed fits experimental scattering data very well, compare Fig. 19.
The correlation function in real space is obtained from the scattering intensity by Fourier transformation, as explained in detail in Chaps. A1 and B1. Fortunately, the form of Eq. (64) is simple enough that this Fourier transformation can be done analytically, so that [37]

$$G(r) = \int \frac{d^2q}{(2\pi)^2} I(q) e^{-i\mathbf{q}\cdot\mathbf{r}} \sim \frac{1}{r} e^{-r/\xi} \sin k_0 r \tag{65}$$

with *characteristic wave vector* k_0 and *correlation length* ξ, where

$$k_0 = \frac{1}{2}\sqrt{2\sqrt{c} - b} \quad , \quad \xi^{-1} = \frac{1}{2}\sqrt{2\sqrt{c} + b} \tag{66}$$

The results of the variational approach then imply (large κ/k_BT):

$$k_0 \sim S/V \quad , \quad \xi \sim \kappa (S/V)^{-1} \quad , \quad k_0 \xi \sim \kappa \tag{67}$$

Thus, the characteristic wave vector increases linearly with the amphiphile concentration, while the correlation length decreases. The dimensionless ratio of the two length scales, which characterize a microemulsion or sponge phase — the domain size $2\pi/k_0$ and the

correlation length ξ, however, is predicted to be independent of the amphiphile concentration, and only to depend on the bending rigidity. These are very specific predictions, which can be tested experimentally.

5.5 Comparison of Theoretical Approaches

We have now predictions by two different theoretical models, which we abbreviate by the names 'Fluctuating Membranes" and "Gaussian Random Fields". It is instructive to summarize the main points discussed above:

- "Fluctuating Membranes" and "Gaussian Random Fields" are *complementary models*
- The variational approach provides a link between these models
- A direct comparison is possible for the *free energy*:
  Fluctuating Membranes —

$$\begin{aligned} f = F/V &\sim [\kappa_R(\Psi) + \bar{\kappa}_R(\Psi)]\Psi^3 \\ &= [A + B\ln(\Psi)]\Psi^3 \end{aligned} \tag{68}$$

  as shown in Refs. [39, 40, 26, 3].
  Gaussian Random Fields —

$$f = F/V = A'\Psi^3 + B'\ln(\Psi) \tag{69}$$

  as derived in Ref. [38]. It is obvious from the comparison of these two equations that although the results look similar they do *not* agree!

5.6 Monte Carlo Simulations of Dynamically Triangulated Surfaces

As in all entropically dominated, strongly fluctuating systems, simulation methods provide a very important tool to obtain information about the system properties, which are not easily accessible by purely analytical approaches. For sufficiently small systems, thermal averages can be calculated by simulation techniques with very high precision. The extrapolation to large system sizes is sometimes difficult, but often possible with good reliability.

Motivation — What are the particular reasons to apply simulations to membrane ensembles:

- Clarify the discrepancy between functional forms of the free energies of the "Fluctuating Membranes" and the "Gaussian Random Field" approaches, Eqs. (68) and (69).
- Different results have been obtained for the universal values of the prefactors α and $\bar{\alpha}$ of the logarithmic renormalization of κ and $\bar{\kappa}$ — compare Eqs. (40) and (41), respectively:
  $\alpha = +3$, $\bar{\alpha} = 10/3$ (Peliti & Leibler 1985; Cai *et al.* 1994) [27, 28];

$\alpha = +1$, $\bar{\alpha} = 0$ (Helfrich 1985) [41]
$\alpha = -1$, $\bar{\alpha} = 0$ (Helfrich 1998) [42]
The phase diagram of Fig. 16 has been calculated for $\alpha = +3$, $\bar{\alpha} = 10/3$. It looks very different for the other values given above.

- The instability argument for the position of the phase transitions, as well as the other calculations which lead to the phase diagram of Fig. 16 apply for $\kappa \gg k_B T$. However, microemulsions and sponge phases typically occur in systems with small bending rigidities of $\kappa \simeq k_B T$.

- Sponge phases with random geometry and bicontinuous *cubic* phases with minimal surface structure cannot be distinguished in the "Fluctuating Membranes" approach. Therefore, few predictions are available from this approach for the structure of the bicontinuous phases.

Simulation method — The simulation of highly dilute sponge phases, with characteristic domain sizes on the order of 10-100nm is impossible on the basis of a molecular model, since it would require an enormous number of "solvent molecules". Therefore, the most appropriate model is again the random surface model discussed above. In order to make this model suitable for simulations, the continuous surface has to be approximated by a network of vertices and bonds, see Fig. 20. A triangular network is usually used because it provides the most homogeneous and isotropic discretization of the surface. A Monte Carlo step then consists of a random displacement of a randomly selected vertex. This step is accepted with the probability determined by the Boltzmann weight, as long as the vertices remain within the maximum bond lengths with their neighbors. The energy, which appears in the Boltzmann weight is the curvature energy, which can be discretized in the form [43, 44]

$$E_b = \lambda_b \sum_{<ij>} (1 - \mathbf{n}_i \cdot \mathbf{n}_j) \tag{70}$$

where $\mathbf{n}_i$ and $\mathbf{n}_j$ are the normal vectors of neighboring triangles, and the sum runs over all pairs of neighboring triangles. The coupling constant λ_b in Eq. (70) is related to the bending rigidity and saddle-splay modulus by $\kappa = \sqrt{3}\lambda_b/2$ and $\bar{\kappa} = -\kappa$ [45]. The discretization (70) of the curvature energy is not without problems; better discretizations are discussed in Ref. [46].
Such a model has first been suggested and simulated for *polymerized membranes* by Kantor and Nelson (1987) [43, 44]. When hard spheres of diameter σ_0 are placed on the vertices, and the bond lengths ℓ are restricted to be $\ell \leq \sqrt{3}\sigma_0$, the surface is *self-avoiding*, since an arbitrary sphere does *not* fit through the holes of the network, so that no interpenetration of different parts of the network is possible.
For a study of fluid membranes, the connectivity of the membrane cannot remain fixed during the simulation, because otherwise a diffusion of vertices within the membrane is not possible. Therefore, dynamically triangulated surfaces [10] have to be used in this case. The essential step of the dynamic triangulation procedure is shown at the bottom of Fig. 20. Among the four vertices of two neighboring triangles, the "diagonal" bond is switched from one of the two possible positions to the other. This bond-switching is only allowed if the vertices remain connected to at least three neighbors after the switch. Also, the distance between the newly connected vertices has to be smaller than the maximum bond length. This Monte Carlo step has the advantages that

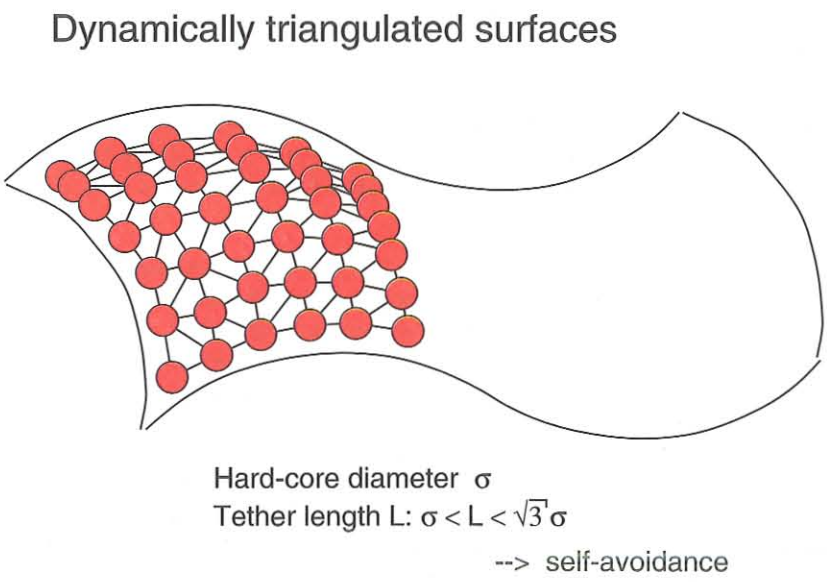


Fig. 20: *A triangulated network model of a fluctuating surface. Top: Hard spheres connected by bonds of maximum extension ℓ are used to describe self-avoiding membranes. Bottom: The Monte Carlo step, which makes the triangulation dynamic, is required to model fluid membranes.*

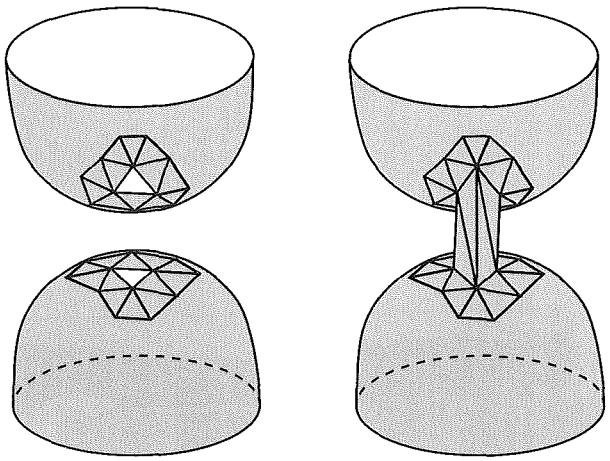


Fig. 21: *Schematic representation of the Monte Carlo step, which is used to change the topology of a randomly triangulated surface. For details see text.*

- is is local, i.e. only the vertices of two neighboring triangles are involved, and
- it guarantees that the network retains its two-dimensional connectivity during the whole simulation run.

Finally, in order to study membrane ensembles with fluctuating topology, a Monte Carlo step is required which changes the topology. Such a step is shown schematically in Fig. 21. It consists of removing two triangles from the network, which are located sufficiently closely in the embedding space that a prism of six new triangles can be inserted without exceeding the maximum bond lengths to form a passage-like connection between the previously disjoint membrane patches [47]. Obviously, the inverse step is also possible, where a passage is removed and two triangles are inserted to close the holes in the network.

Simulation Results — A typical conformation of the membrane in the region of the parameter space, where the sponge phase is stable, is shown in Fig. 22. This configuration shows all the characteristic features of a sponge phase, which have been discussed above, such as the bicontinuous structure and the local saddle-like shape of the membrane.
A more quantitative analysis is possible by calculating thermal averages for many different values of the parameters, and then constructing a phase diagram, as shown in Fig. 23. The Monte Carlo data [47] for the phase boundaries are found to follow the logarithmic dependence expected from Eq. (45). Furthermore, the slopes of these phase boundaries in a semi-logarithmic plot are quite consistent with the $\bar{\alpha} = 10/3$, while $\bar{\alpha} = 0$ can clearly be ruled out. Thus, the Monte Carlo results strongly support the "Fluctuating Membranes" predictions, with the value of $\bar{\alpha}$ predicted in Refs. [27, 28].
Another quantity, which can be obtained from the simulations and compared directly with the analytical predictions is the osmotic pressure p . In the analytical approaches,

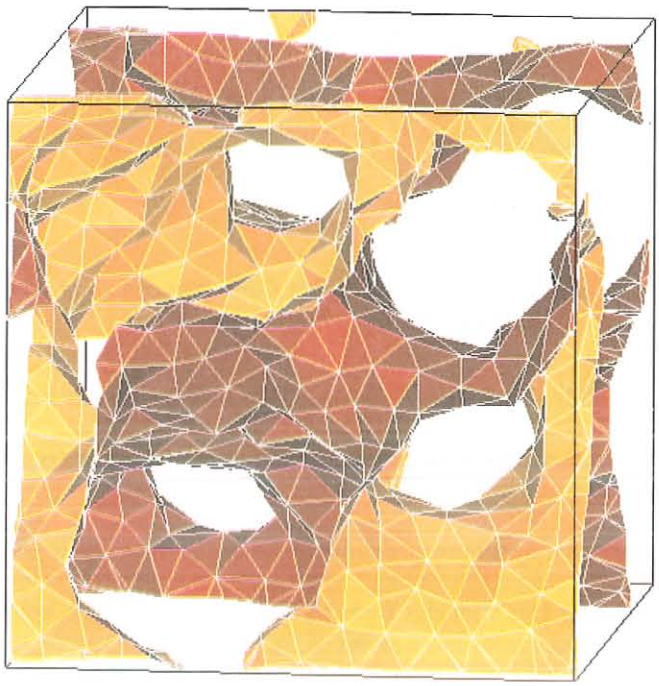


Fig. 22: *A typical conformation of the membrane in a sponge phase, as obtained from Monte Carlo simulations of randomly triangulated surfaces (Gompper & Kroll 1998) [47]. The two sides of the membrane are colored differently to emphasize the bicontinuous structure.*

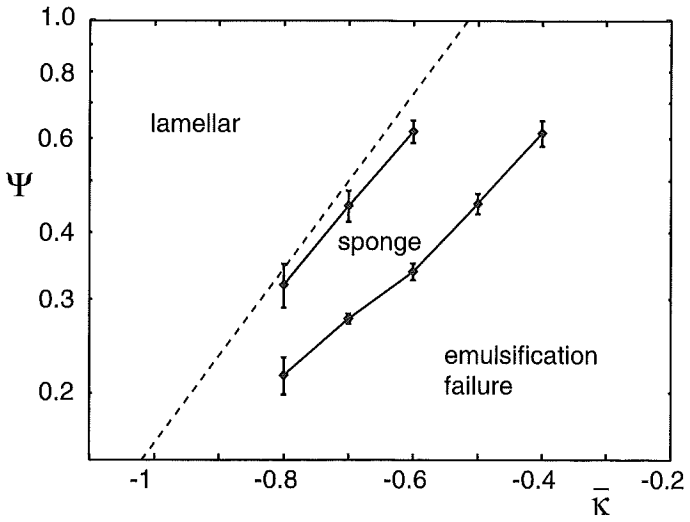


Fig. 23: *Phase diagram of random surfaces controlled by curvature elasticity, as obtained from Monte Carlo simulations of randomly triangulated surfaces with $\kappa \simeq 1.7 k_B T$ (Gompper & Kroll 1998) [47]. The dashed line shows the theoretical prediction (45), with $\bar{\alpha} = 10/3$.*

it is obtained from the free-energy density f by differentiation,

$$\begin{aligned} \frac{p}{k_B T} &= \Psi \frac{\partial f}{\partial \Psi} - f \\ &= [A'' + B'' \ln(\Psi)]\Psi^3 \qquad \text{(fluctuating membranes)} \end{aligned} \tag{71}$$

and in the case of the free-energy density (68) has the same functional form as f itself. The simulation results (Gompper & Kroll 1998) are compared with this prediction in Fig. 24. Again, the simulation results are in very good agreement with the "Fluctuating Membranes" prediction.

5.7 Experimental Evidence

Phase behavior of binary systems — The elastic properties of an amphiphilic bilayer can be rather easily related to the elastic properties of the two monolayers of which the bilayer is composed (Petrov et al. 1978, Porte 1989) [48, 49]. This is done by writing the bilayer energy of a spherical cap as

$$\begin{aligned} E_b = \int dS \quad & \left\{ \left[2\kappa \left(\frac{1}{R+\epsilon} + c_0 \right)^2 + \bar{\kappa} \frac{1}{(R+\epsilon)^2} \right] \frac{(R+\epsilon)^2}{R^2} \right. \\ & \left. + \left[2\kappa \left(\frac{1}{R-\epsilon} - c_0 \right)^2 + \bar{\kappa} \frac{1}{(R-\epsilon)^2} \right] \frac{(R-\epsilon)^2}{R^2} \right\} \end{aligned} \tag{72}$$

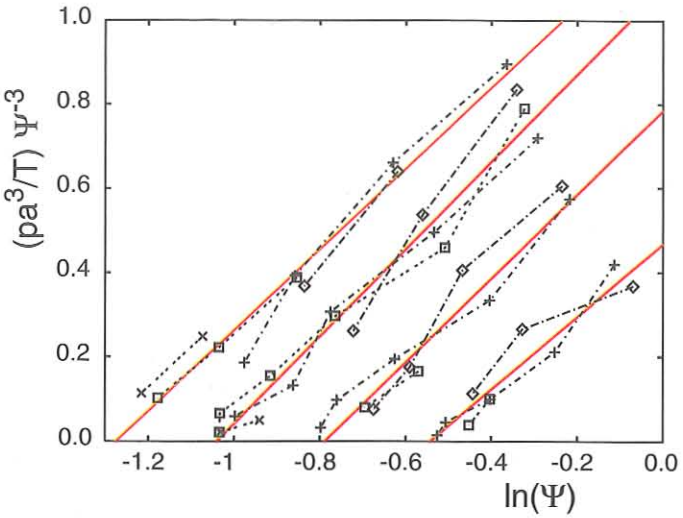


Fig. 24: *Scaled osmotic pressure $(pa^3/k_BT)\Psi^{-3}$ of random surfaces controlled by curvature elasticity, as obtained from Monte Carlo simulations of randomly triangulated surfaces for $\kappa \simeq 1.0k_BT$ (Gompper & Kroll 1998) [47]. Here, a is the membrane thickness. Data sets from right to left correspond to $\bar{\kappa} = -0.4k_BT$, $\bar{\kappa} = -0.5k_BT$, $\bar{\kappa} = -0.6k_BT$ and $\bar{\kappa} = -0.7k_BT$. The solid red lines indicate the theoretical prediction (68).*

where R is the radius of curvature of the bilayer midsurface, ϵ is the thickness of a monolayer, and the integral extends over the surface of the midplane. The expansion of this expression in powers of $1/R$, together with a similar expansion of the energy of a cylindrical or saddle-shaped surface, gives again the form of the curvature energy, but now with

$$c_0^{(bi)} = 0 \quad , \quad \kappa^{(bi)} = 2\kappa \quad , \quad \bar{\kappa}^{(bi)} = 2\bar{\kappa} + 8\kappa c_0 \epsilon \tag{73}$$

Thus, the spontaneous curvature of a bilayer vanishes due to symmetry, but its saddle-splay modulus is related to the spontaneous curvature of the monolayers.
Now, the spontaneous curvature of monolayer has been shown experimentally (Strey 1994) [50] in ternary microemulsions to follow a linear temperature dependence

$$c_0^{(mono)} \sim (T - \bar{T}) \tag{74}$$

over a wide range of temperatures, where $\bar{T}$ is the hydrophobic-hydrophilic-balance temperature, which corresponds to balanced microemulsions. Therefore, $\bar{\kappa}^{(bi)} \sim (T - T^*)$, where T^* is a constant, and we expect the lamellar-to-sponge and the emulsification failure phase transitions to follow the relation

$$\ln(\Psi) \sim (T - T^*) \tag{75}$$

which corresponds to a straight line in a semi-logarithmic representation of the phase diagram. The experimental phase diagram is indeed consistent with such a behavior, as

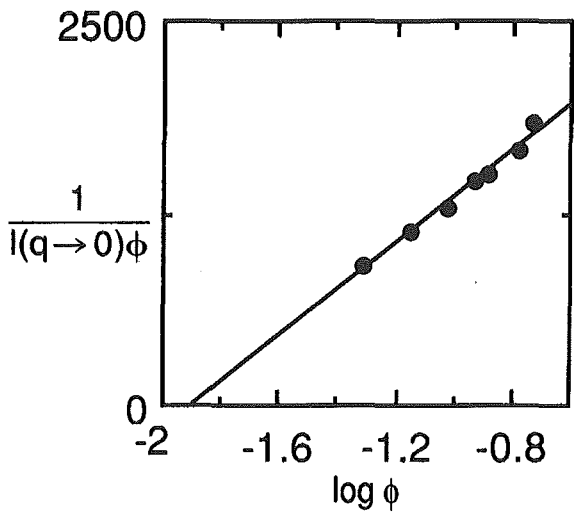


Fig. 25: *Experimental results for the film scattering intensity $I(q)$ in the limit of zero wave vector* **q** *in the system AOT–water–NaCl (Skouri, Marignan, Appell, Porte 1991) [51].*

can be seen from Fig. 13.

Small-Angle Scattering — In the limit of very small wave vectors q, the scattering intensity in *film contrast* is determined by the osmotic compressibility (compare Chap. B1), so that [26]

$$\begin{aligned} I(q \to 0) &= \Psi \left(\frac{\partial p}{\partial \Psi} \right)^{-1} \\ &\sim \Psi^{-1} [A''' + B''' \ln(\Psi)]^{-1} \quad \text{(fluctuating membranes)} \end{aligned} \tag{76}$$

This expression is compared to experimental data [26, 51] for the system *AOT*–water–*NaCl* in Fig. 25. The data nicely agree with the behavior predicted behavior for "Fluctuating Membranes".

6 Amphiphilic Block Copolymers in Ternary Mixtures

It has been found very recently that the addition of small amounts of amphiphilic block copolymers to balanced microemulsions has a dramatic effect on the phase behavior (Jakobs, Sottmann, Strey, Allgaier, Willner, Richter 1999) [52]. As shown in Fig. 26, the ability of a short-chain surfactant to solubilize oil and water into a macroscopically homogeneous and isotropic microemulsion phase increases dramatically when a small percentage of the total surfactant weight is added as amphiphilic block copolymer. The block

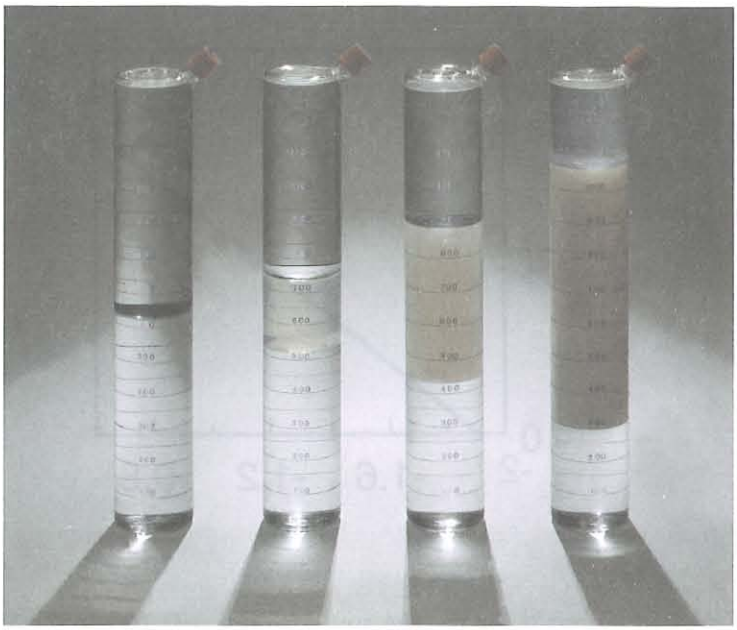


Fig. 26: *Effect of small amounts of amphiphilic block copolymer PEP-PEO (compare Fig. 28 below) on the phase behavior of balanced microemulsions. Far left: oil-water coexistence. Left: 7 weight % surfactant $C_{10}E_4$ produce a three-phase coexistence with a microemulsion phase in the center. Right: 0.5 weight % of PEP5-PEO5 increase the microemulsion volume two-fold. For right: 1.0 weight % of PEP5-PEO5 increases the microemulsion volume three-fold (preparation and photo: J. Allgaier).*

copolymer used in this study is polyethyleneoxide–polyethylenepropylene PEOx-PEPy, where x and y denote the molecular weights of each block in kg/mol. The chemical structure of the polymers mimics the structure of the non-ionic C_iE_j surfactant, and PEP10-PEO10 corresponds roughly to $C_{715}E_{230}$. Note that while the microemulsion is completely transparent without block copolymer, it becomes more and more opaque with increasing block-copolymer concentration. This indicates that the scale of the oil- and water domains is increasing with increasing block-copolymer concentration, and it approaches the wavelength of light at the highest polymer concentrations in Fig. 26.

A schematic view of the structure of a microemulsion phase containing amphiphilic block copolymers is shown on a mesoscopic scale in Fig. 27. The block copolymers are incorporated into the surfactant-monolayer membrane, such that the hydrophilic block is located in the water domains, while the hydrophobic block is in the oil domains.

The dramatic effect of amphiphilic block copolymers on the microemulsion can be understood on the basis of the membrane-curvature model [54, 53, 55]. As explained in detail in Chap. B10, polymer chains anchored to a membrane modify the curvature elasticity

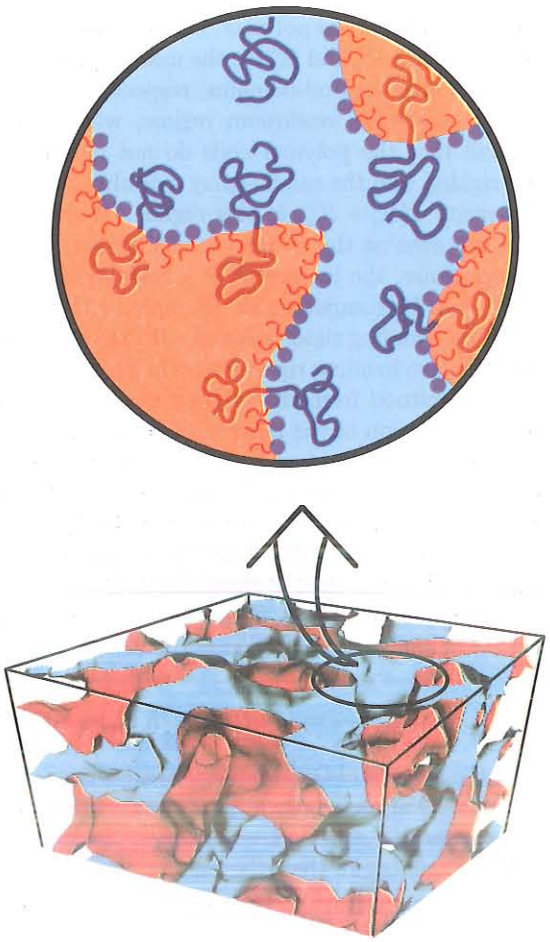


Fig. 27: *Schematic view of the structure of an oil-water-surfactant microemulsion, which contains in addition a small amount of amphiphilic block copolymer (Endo et al. 2001) [53]. For details see text.*

such that (Hiergeist & Lipowsky 1996, Eisenriegler et al., 1996) [56, 57]

$$\kappa_{eff} = \kappa + \frac{k_BT}{12}\left(1+\frac{\pi}{2}\right)\sigma(R_w^2+R_o^2) \quad (77)$$

$$\bar{\kappa}_{eff} = \bar{\kappa} - \frac{k_BT}{6}\sigma(R_w^2+R_o^2) \quad (78)$$

where σ is the grafting density of the polymer, i.e. the number of polymer anchoring points per unit membrane area, and R_w^2 and R_o^2 are the mean-squared end-to-end distances of the polymer blocks in the water- and oil-domains, respectively (compare Fig. 28). Eqs. (77) and (78) apply in the so-called mushroom regime, where the polymer density on the membrane is so small that the polymer coils do not interact directly with each other. Thus, the bending rigidity and the saddle-splay modulus increase *linearly* with the scaled polymer grafting density $\sigma(R_o^2+R_w^2)$ in this regime. It should be noticed that this is a very *small effect*, since even at the overlap concentration, where $\sigma(R_o^2+R_w^2)=2$ for a symmetric block copolymer, the increment of κ and $|\bar{\kappa}|$ is only a fraction of k_BT. The results (77) and (78) can be compared, for example, with the elastic properties of solid elastic sheets, where the bending rigidity scales with the sheet thickness ℓ_0 as $\kappa \sim \ell_0^3$ [58]. The increase of the effective bending rigidity κ_{eff} in Eq. (77) and of the magnitude of $\bar{\kappa}_{eff}$ in Eq. (78) can be understood from the entropy loss of each polymer coil in a confined geometry due to the restriction of the number of accessible configurations. This entropic repulsion suppresses membrane fluctuations *and* disfavors saddle-like conformations near the anchoring points. A simple, heuristic argument for the suppression of saddle-like conformations has been given by Milner and Witten (1988) [59] for polymers in the brush regime, where there is a strong overlap between neighboring chains on the membrane. Consider the volume V of a thin shell of thickness ℓ_0 above a surface of area A bent with local curvatures c_1 and c_2. The ratio $V/(A\ell_0)$ is the ratio of volume available for chains in a layer of thickness ℓ_0 and grafting area A in the bent and unbent geometries, and may be expanded as

$$\frac{V}{A\ell_0} = 1 + H\ell_0 + \frac{1}{3}K\ell_0^2 + ... \quad (79)$$

where H and K are the mean and Gaussian curvatures, respectively. This relation can be checked easily for a spherical and a cylindrical surface. Then for a saddle surface, $H=0$ and $K=-1/R^2$, so that $V/(A\ell_0) \simeq 1-\frac{1}{3}(\ell_0/R)^2$; the bent thin shells have therefore *less space* available for monomers than the unbent shells, and the polymer chains must stretch upon bending, which costs free energy. The same argument should also apply to the mushroom regime.

Thus, from the combination of Eqs. (45) and (78), the prediction

$$\ln(\Psi/\Psi^*) = -\frac{4\pi}{\alpha_-}\frac{1}{12}\left(1+\frac{\pi}{2}\right)\sigma(R_w^2+R_o^2) = -\frac{\pi}{5}\sigma(R_w^2+R_o^2) \quad (80)$$

for the dependence of the emulsification boundary on the scaled polymer density is obtained. This result is compared with experimental data for a number of different block-copolymer lengths in Fig. 29. The exponential dependence of the membrane volume fraction Ψ at three-phase coexistence is very nicely confirmed. In fact, this *exponential* dependence is responsible that the small increment in the magnitude of the saddle-splay

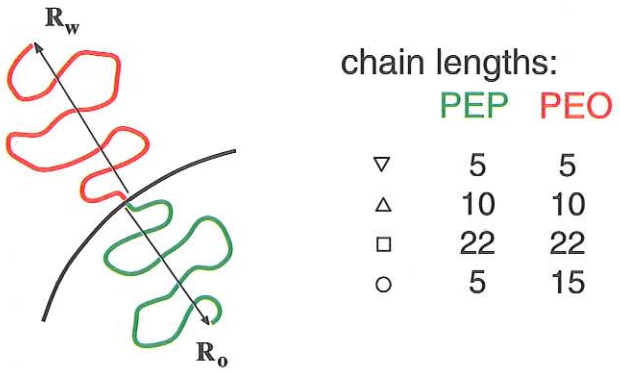


Fig. 28: *Average end-to-end distances of the two blocks in the water and oil subphase are denoted by R_w and R_o, respectively. The molecular weights (in kg/mol) of the four different PEP-PEO polymers shown in Fig. 29.*

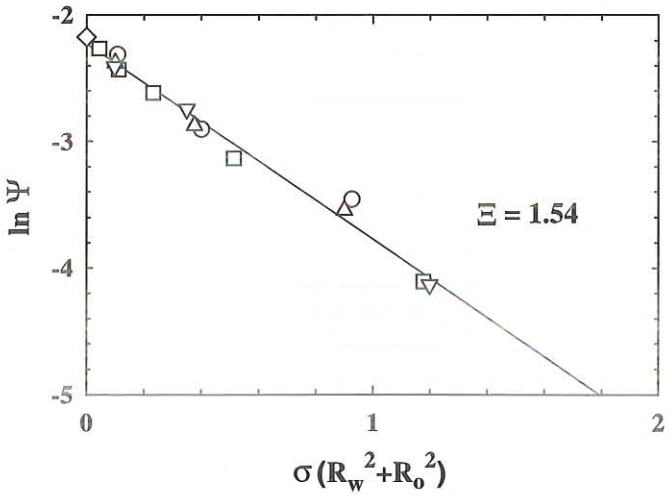


Fig. 29: *Phase diagram of a microemulsion of water–decane–$C_{10}E_4$ with amphiphilic block copolymer. The membrane volume fraction Ψ of the microemulsion at three-phase coexistence is shown as a function of the scaled polymer grafting density on the membrane (Endo, Allgaier, Gompper, Jakobs, Monkenbusch, Richter, Sottmann, Strey 2000) [54]. The different symbols correspond to different lengths of the polymer blocks, as explained in Fig. 28.*

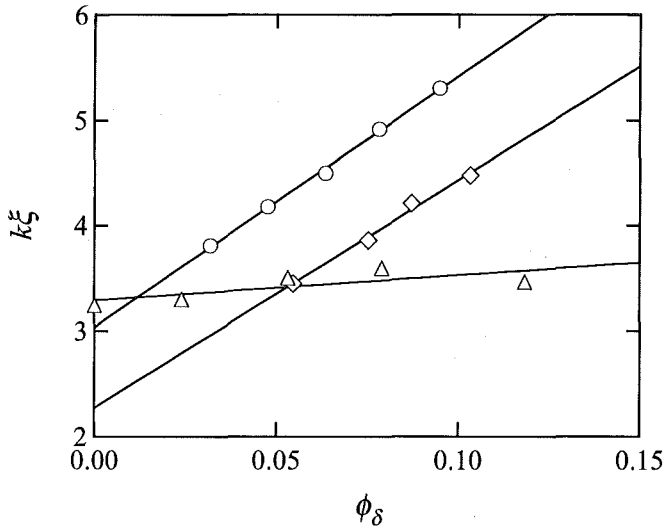


Fig. 30: *Dimensionless ratio $k_0\xi$ of the two characteristic length scales of a microemulsion, as a function of the polymer content, ϕ_δ, in the mixture of both amphiphiles, which is proportional to the polymer grafting density on the membrane (Gompper, Endo, Mihailescu, Allgaier, Monkenbusch, Richter, Jakobs, Sottmann, Strey 2001) [60]. The two data sets marked by circles (○) and diamonds (◇) were obtained for PEP5-PEO5 at fixed membrane volume fractions of $\Psi = 0.12$ and $\Psi = 0.08$, respectively. The data set marked by triangles (△) were taken for PEP10-PEO10 along three-phase coexistence.*

modulus has the dramatic effects on the phase behavior shown in Fig. 26. Also, the data for different polymer lengths scale exactly as predicted by Eq. (80). A fit of the experimental data in Fig. 29 to the functional form of Eq. (80) yields a prefactor $\Xi = 1.54$, which is a bit more than a factor two larger than the theoretical result $\pi/5 \simeq 0.628$. A possible reason for this discrepancy is the theoretical result (77) has been obtained for ideal chains, while the polymer chains are self-avoiding in the real system. This is one of the few examples, where a *quantitative* comparison of experimental data and theoretical results has been achieved for these complex, disordered, and mesoscopically structured fluid phases.

It is possible to go one step further and also investigate the scattering behavior [60]. In this case, the Gaussian random field (GRF) model predicts (compare Eq. (67)),

$$k_0\xi \sim \kappa \sim \sigma(R_o^2 + R_w^2) \qquad (GRF) \tag{81}$$

where the later relation follows from Eq. (77). The experimental data for this characteristic number are shown in Fig. 30. The data for fixed surfactant concentration, i.e. for fixed membrane area, follow precisely the behavior of Eq. (81). It is important to notice, however, that although the lines have equal slope, as expected from Eq. (81), they are shifted relative to each other. The data along the coexistence line still depend linearly on the polymer content ϕ_δ in the mixture of both amphiphiles, but even the slope is different, in *contrast* to Eq. (81).

Thus, although the Gaussian random field model obviously captures part of the physics of the domain correlations by Eq. (81), an important part is still missing. We propose that this is the logarithmic renormalization of the bending rigidity. Indeed, if κ is replaced by $\kappa_R(\Psi)$ in Eqs. (67) and (81), all the data of Fig. 30 are found to be entirely consistent [60].

7 Summary and Conclusions

Research in the field of Soft Matter systems is an interdisciplinary endeavor. The work on random surfaces and fluctuating membranes brings together mathematicians (minimal surfaces), theoretical physicists (statistical physics, field theory), experimental physicists (neutron scattering, microscopy), chemists (synthesis, phase behavior), biologists (cell membranes), and material scientists (nanoscale materials).

Over the last twenty years, the joint effort of researches from these different disciplines has lead to significant progress in our understanding of amphiphilic systems. For the "simple" system of an ensemble of membranes without internal structure, the qualitative behavior is reasonably well understood. On the quantitative level, there remains still a lot of work to be done. As the discussion of the previous sections has demonstrated, the results of different approximate approaches do not always agree. Also, experiments are often done in rather complex systems, where several different physical mechanisms are at work simultaneously, which make the interpretation of the results difficult. Therefore, even the "simple" system will require much more work before a satisfactory level of understanding has been reached.

The comparison of the theoretical models, the computer simulations and the experimental data indicates that the "fluctuating interfaces" approach works surprisingly well. The effect of the logarithmic renormalization of the elastic curvature moduli now seems to be well established. On the other hand, this approach is limited in its applicability, so that for example scattering intensities in the microemulsion or sponge phase cannot be predicted. This is where the "Gaussian random fields" show their advantage. The combination of the two approaches indeed seems to be able to make quantitative predictions of the scattering functions.

In the recent past, and undoubtedly in the future, the trend will go towards more complex systems. With the increasing number of components, the system will become more flexible, with properties which can be controlled and manipulated externally. Here, the contact with biology will certainly intensify. For Statistical Physics, it will be a very interesting task to predict the properties of such complex systems quantitatively.

Appendices

A Curvature Tensor of Almost Planar Membranes

For almost planar membranes, the full curvature tensor can be calculated explicitly. Eq. (6) implies

$$\mathbf{t}_l \cdot \partial_i \mathbf{n} = -K_{ij}\mathbf{t}^j \cdot \mathbf{t}_l = -K_{il} \tag{82}$$

Differentiation of the orthogonality relation $\mathbf{t}_j \cdot \mathbf{n} = 0$ gives

$$K_{ij} = -\mathbf{t}_j \cdot \partial_i \mathbf{n} = \mathbf{n} \cdot \partial_i \mathbf{t}_j = \mathbf{n} \cdot \partial_i \partial_j \mathbf{R} \tag{83}$$

This relation demonstrates that the curvature tensor is symmetric. It can now easily be evaluated with Eqs. (14), (15) and (16), with the result

$$K_{ij} = \frac{\partial_i \partial_j h}{\sqrt{1+(\nabla h)^2}} \tag{84}$$

This implies

$$2H = Tr(K_i^j) = \nabla \cdot \frac{\nabla h}{\sqrt{1+(\nabla h)^2}} \tag{85}$$

$$\begin{aligned} K &= \det(K_i^j) = \det(K_{il}) \det(g^{lj}) = \det(K_{il})/\det(g_{lj}) \\ &= \frac{\partial_1^2 h \partial_2^2 h - (\partial_1 \partial_2 h)^2}{[1+(\nabla h)^2]^2} \end{aligned} \tag{86}$$

As an *example* for the calculation of the mean and Gaussian curvature, let us consider the catenoid of Fig. 8. The shape equation for the catenoid can be written in the form of a Monge representation, $h(x_1, x_2) = \pm \mathrm{arcosh}\sqrt{x_1^2 + x_2^2}$. The application of the expressions (85) and (86) then shows that $H \equiv 0$ — which proves that the catenoid is indeed a minimal surface — and

$$K = -(x_1^2 + x_2^2)^{-2} \tag{87}$$

The Gaussian curvature of the catenoid is negative, as expected; its magnitude is largest near the center, at $x_1^2 + x_2^2 = 1$, and approaches zero for $x_1^2 + x_2^2 \to \infty$.

B Joint Distribution of Gaussian Random Fields

First, the probability distribution

$$P[\Phi(\mathbf{r}) = \alpha, \nabla\Phi(\mathbf{r}) = \mathbf{v}] = \langle \delta(\Phi(\mathbf{r}) - \alpha)\ \delta(\nabla\Phi(\mathbf{r}) - \mathbf{v}) \rangle \tag{88}$$

has to be calculated [31, 6]. Since this probability distribution only contains a single spatial variable, and the system is homogeneous on average, $\mathbf{r} = 0$ can be chosen without loss of generality. The representation

$$\delta(x) = \int_{-\infty}^{\infty} \frac{dk}{2\pi} \exp(ikx) \tag{89}$$

can now be used to obtain

$$P[\alpha, \mathbf{v}] = \int \frac{d\omega}{2\pi} \int \frac{d^3k}{(2\pi)^3} \left\langle e^{i\omega(\Phi(\mathbf{r})-\alpha)} e^{i\mathbf{k}\cdot(\nabla\Phi(\mathbf{r})-\mathbf{v})} \right\rangle \tag{90}$$

With the Fourier-representation

$$\Phi(\mathbf{r}) = \int \frac{d^3k}{(2\pi)^3} \Phi(\mathbf{q}) e^{i\mathbf{q}\cdot\mathbf{r}} \tag{91}$$

this becomes

$$P[\alpha, \mathbf{v}] = \int \frac{d\omega}{2\pi} \int \frac{d^3k}{(2\pi)^3} e^{-i\omega\alpha - i\mathbf{k}\cdot\mathbf{v}} \left\langle \exp \int \frac{d^3q}{(2\pi)^3} [i\omega\Phi(\mathbf{q}) - \mathbf{k}\cdot\mathbf{q}\Phi(\mathbf{q})] \right\rangle \tag{92}$$

at $\mathbf{r} = 0$. The average in Eq. (92) has to be evaluated with the Boltzmann weight

$$\exp[-\mathcal{H}_0] = \exp\left\{ -\frac{1}{2} \int \frac{d^3q}{(2\pi)^3} \nu(q)^{-1} |\Phi(\mathbf{q})|^2 \right\} \tag{93}$$

which implies in particular

$$\langle \Phi(\mathbf{q})\Phi(\mathbf{q}') \rangle = \nu(q)(2\pi)^3 \delta(\mathbf{q} + \mathbf{q}') \tag{94}$$

For a Gaussian-distributed variable $x \in \mathbb{C}$, the relation

$$\langle e^{ikx} \rangle = \exp(-\frac{1}{2} k^2 \langle x^2 \rangle) \tag{95}$$

holds exactly. Therefore,

$$\begin{aligned} &\left\langle \exp \int \frac{d^3q}{(2\pi)^3} [i\omega - \mathbf{k}\cdot\mathbf{q}] \Phi(\mathbf{q}) \right\rangle \\ &= \exp\left[\frac{1}{2} \int \frac{d^3q}{(2\pi)^3} \int \frac{d^3q'}{(2\pi)^3} (i\omega - \mathbf{k}\cdot\mathbf{q})(i\omega - \mathbf{k}\cdot\mathbf{q}') \langle \Phi(\mathbf{q})\Phi(\mathbf{q}') \rangle \right] \\ &= \exp\left[-\frac{1}{2} \int \frac{d^3q}{(2\pi)^3} (\omega^2 + (\mathbf{k}\cdot\mathbf{q})^2) \nu(q) \right] \end{aligned} \tag{96}$$

so that

$$P[\alpha, \mathbf{v}] = \int \frac{d\omega}{2\pi} \int \frac{d^3k}{(2\pi)^3} e^{-i\omega\alpha - i\mathbf{k}\cdot\mathbf{v}} \exp \int \frac{d^3q}{(2\pi)^3} \left[-\frac{1}{2}\omega^2 - \frac{1}{2}(\mathbf{k}\cdot\mathbf{q})^2 \right] \nu(q) \tag{97}$$

The remaining integrals are now straightforward. In particular,

$$\int \frac{d^3q}{(2\pi)^3} (\mathbf{k}\cdot\mathbf{q})^2 \, \nu(q) = \frac{1}{3} k^2 \langle q^2 \rangle_\nu \equiv k^2 \sigma_v^2 \tag{98}$$

with $\langle ... \rangle_\nu$ defined in Eq. (53), and

$$\int \frac{d^3k}{(2\pi)^3} e^{-i\mathbf{k}\cdot\mathbf{v}} \, e^{-\frac{1}{6}k^2\langle q^2 \rangle} = (2\pi)^{-3/2} \sigma_v^{-3} \exp\left[-\frac{1}{2} \frac{v^2}{\sigma_v^2} \right] \tag{99}$$

References

[1] D. Voet and J. G. Voet, *Biochemistry*, 2nd ed. (Wiley, New York, 1995).

[2] *Statistical Mechanics of Membranes and Surfaces*, edited by D. Nelson, T. Piran, and S. Weinberg (World Scientific, Singapore, 1989).

[3] G. Porte, J. Phys.: Condens. Matter **4**, 8649 (1992).

[4] G. Gompper and M. Schick, in *Phase Transitions and Critical Phenomena*, edited by C. Domb and J. Lebowitz (Academic Press, London, 1994), Vol. 16, pp. 1–176.

[5] *Micelles, Membranes, Microemulsions, and Monolayers*, edited by W. M. Gelbart, A. Ben-Shaul, and D. Roux (Springer-Verlag, Berlin, 1994).

[6] S. A. Safran, *Statistical Thermodynamics of Surfaces, Interfaces, and Membranes* (Addison-Wesley, Reading, MA, 1994).

[7] *Structure and dynamics of membranes - from cells to vesicles*, Vol. 1 of *Handbook of biological physics*, edited by R. Lipowsky and E. Sackmann (Elsevier, Amsterdam, 1995).

[8] *Fluctuating geometries in statistical mechanics and field theory*, edited by F. David, P. Ginsparg, and J. Zinn-Justin (Elsevier, Amsterdam, 1996).

[9] U. Seifert, Adv. Phys. **46**, 13 (1997).

[10] G. Gompper and D. M. Kroll, J. Phys. Condens. Matter **9**, 8795 (1997).

[11] E. Kreyszig, *Differential Geometry* (Dover Publications, New York, 1991).

[12] P. B. Canham, J. Theor. Biol. **26**, 61 (1970).

[13] W. Helfrich, Z. Naturforsch. **28c**, 693 (1973).

[14] H. Karcher and K. Poltier, Spektrum der Wissenschaft **Oktober**, 96 (1990).

[15] R. H. Templer *et al.*, J. Phys. Chem. B **102**, 7251 (1998).

[16] U. S. Schwarz and G. Gompper, Phys. Rev. E **59**, 5528 (1999).

[17] P.-G. de Gennes and C. Taupin, J. Phys. Chem. **86**, 2294 (1982).

[18] R. Strey *et al.*, J. Chem. Soc. Faraday Trans. **86**, 2253 (1990).

[19] W. Helfrich, Z. Naturforsch. **33a**, 305 (1978).

[20] C. R. Safinya *et al.*, Phys. Rev. Lett. **57**, 2718 (1986).

[21] C. R. Safinya, E. B. Sirota, D. Roux, and G. S. Smith, Phys. Rev. Lett. **62**, 1134 (1989).

[22] G. Gompper and D. M. Kroll, Europhys. Lett. **9**, 59 (1989).

[23] R. Strey *et al.*, in *Structure and Dynamics of Strongly Interacting Colloids and Supramolecular Aggregates in Solution*, edited by S.-H. Chen, J. S. Huang, and P. Tartaglia (Kluwer, Dordrecht, 1992), pp. 351–363.

[24] L. E. Scriven, Nature **263**, 123 (1976).

[25] S. A. Safran, D. Roux, M. E. Cates, and D. Andelman, Phys. Rev. Lett. **57**, 491 (1986).

[26] G. Porte *et al.*, J. Phys. II France **1**, 1101 (1991).

[27] L. Peliti and S. Leibler, Phys. Rev. Lett. **54**, 1690 (1985).

[28] W. Cai, T. C. Lubensky, P. Nelson, and T. Powers, J. Phys. II France **4**, 931 (1994).

[29] F. David, in *Statistical Mechanics of Membranes and Surfaces*, edited by D. Nelson, T. Piran, and S. Weinberg (World Scientific, Singapore, 1989), pp. 157–223.

[30] D. C. Morse, Phys. Rev. E **50**, R2423 (1994).

[31] M. Teubner, Europhys. Lett. **14**, 403 (1991).

[32] N. F. Berk, Phys. Rev. Lett. **58**, 2718 (1987).

[33] N. F. Berk, Phys. Rev. A **44**, 5069 (1991).

[34] P. Pieruschka and S. A. Safran, Europhys. Lett. **22**, 625 (1993).

[35] R. P. Feynman, *Statistical Mechanics* (Addison-Wesley, Reading, MA, 1972).

[36] J. J. Binney, N. J. Dowrick, A. J. Fisher, and M. E. J. Newman, *The Theory of Critical Phenomena* (Clarendon Press, Oxford, 1992).

[37] M. Teubner and R. Strey, J. Chem. Phys. **87**, 3195 (1987).

[38] P. Pieruschka and S. A. Safran, Europhys. Lett. **31**, 207 (1995).

[39] D. Roux *et al.*, Europhys. Lett. **11**, 229 (1990).

[40] D. Roux, C. Coulon, and M. E. Cates, J. Phys. Chem. **96**, 4174 (1992).

[41] W. Helfrich, J. Phys. France **46**, 1263 (1985).

[42] W. Helfrich, Eur. Phys. J. B **1**, 481 (1998).

[43] Y. Kantor and D. R. Nelson, Phys. Rev. Lett. **58**, 2774 (1987).

[44] Y. Kantor and D. R. Nelson, Phys. Rev. A **36**, 4020 (1987).

[45] H. S. Seung and D. R. Nelson, Phys. Rev. A **38**, 1005 (1988).

[46] G. Gompper and D. M. Kroll, J. Phys. I France **6**, 1305 (1996).

[47] G. Gompper and D. M. Kroll, Phys. Rev. Lett. **81**, 2284 (1998).

[48] A. G. Petrov, M. D. Mitov, and A. Derzhanski, Phys. Lett. A **65**, 374 (1978).

[49] G. Porte, J. Appell, P. Bassereau, and J. Marignan, J. Phys. France **50**, 1335 (1989).

[50] R. Strey, Colloid and Polymer Sci. **272**, 1005 (1994).

[51] M. Skouri, J. Marignan, J. Appell, and G. Porte, J. Phys. II France **1**, 1121 (1991).

[52] B. Jakobs *et al.*, Langmuir **15**, 6707 (1999).

[53] H. Endo *et al.*, J. Chem. Phys. **115**, 580 (2001).

[54] H. Endo *et al.*, Phys. Rev. Lett. **85**, 102 (2000).

[55] G. Gompper, D. Richter, and R. Strey, J. Phys. Condens. Matter **13**, 9055 (2001).

[56] C. Hiergeist and R. Lipowsky, J. Phys. II France **6**, 1465 (1996).

[57] E. Eisenriegler, A. Hanke, and S. Dietrich, Phys. Rev. E **54**, 1134 (1996).

[58] L. D. Landau and E. M. Lifshitz, *Theory of Elasticity* (Addison-Wesley, Reading, MA, 1959).

[59] S. T. Milner and T. A. Witten, J. Phys. France **49**, 1951 (1988).

[60] G. Gompper *et al.*, Europhys. Lett. **56**, 683 (2001).

B 10 Polymers near Surfaces

E. Eisenriegler
Institut für Festkörperforschung
Forschungszentrum Jülich GmbH

Contents

1 Introduction 2

2 How to obtain the polymer partition function 2

3 Polymer in the half space 5

4 Polymer near a spherical particle 5
4.1 Chain end-grafted to the surface 6
4.2 Immersing a sphere into a solution of free nonadsorbing polymer chains . . 7

5 Polymer-induced bending rigidities 9

6 Surfactant membrane decorated with copolymers 10

7 Bending rigidities induced by free polymers 12

8 Monomer density profiles and the density-pressure relation 13

A An ideal chain in an external potential 14

B Density-pressure relation for ideal chains 15

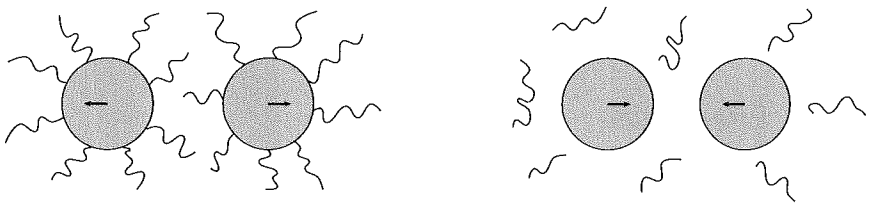


Fig. 1: *Colloids with surface-grafted polymer chains (left) and polymers in a solution of free nonadsorbing polymer chains (right).*

1 Introduction

Polymers near surfaces of colloidal particles lead to diverse remarkable effects. The left part of Fig. 1 shows two particles with nonadsorbing polymers which are *end-grafted* to the surface. If the particles approach each other the number of possible polymer configurations is reduced leading to an entropic *repulsion* between the particles. This mechanism is operative for ink and paints. For polymer size much larger than the particle size the colloids in the left part of Fig. 1 degenerate to star polymers which have also a repulsive interaction. In the case of drug transport by so-called stealth liposomes grafted polymers prevent attacks from the resistance system of the body.
A quite different effective interaction is provided by *free* nonadsorbing polymers. As shown in the right part of Fig. 1 free polymers by entropic reasons do not enter the narrow space between two close particles and the unbalanced polymer pressure from outside pushes the two particles towards each other. Note that this effective *attraction* between particles is due to interactions which are purely repulsive! This mechanism leads to gas-liquid and liquid-solid phase transitions in a mixture of hard sphere colloids and nonadsorbing free polymers, and it can be used , e.g., for the separation of viruses.
In this lecture we shall consider the interaction of a single polymer chain with a planar wall and with single particles of spherical or cylindrical shapes. This allows to discuss a particle in a dilute solution of free chains or a particle with surface-grafted chains in the mushroom regime where chains do not overlap. The results for small particle-curvature can be written in terms of a Helfrich expansion and allow to evaluate the polymer-induced contribution to the bending rigidities and the coefficient of spontaneous curvature in the case of membranes. We shall apply this expansion to surfactant membranes which are decorated with copolymers. Throughout the lecture we shall consider purely repulsive surfaces (i.e. disregard polymer adsorption) and single chain situations (disregarding semidilute solutions or polymer brushes). Actually the gross features are already displayed by ideal chains and we shall confine the discussion to this case.

2 How to obtain the polymer partition function

First consider an ideal polymer chain in free space. Fig. 2 shows a chain with N links. Its partition function with the two ends fixed

$$Z(\mathbf{r},\mathbf{r}') = \int d^3r_1 ... \int d^3r_{N-1}\, P(\mathbf{r}-\mathbf{r}_1)...P(\mathbf{r}_{N-1}-\mathbf{r}') \qquad (1)$$

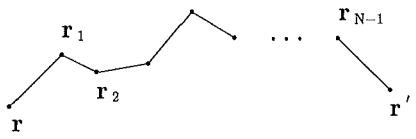


Fig. 2: *A polymer chain with N links.*

contains a factor

$$P(\mathbf{x}) = (4\pi l^2)^{-3/2}\, e^{-x^2/(4l^2)} \tag{2}$$

from each link which is a normalized Gaussian. Here one invokes the central limit theorem by assuming that each of our links is mesoscopic and is composed of the sum of many identical microscopic links. In the following l will be addressed as the monomer size. It follows from Eqs. (1) and (2) that

$$Z(\mathbf{r},\mathbf{r}') = (4\pi L)^{-3/2}\, e^{-|\mathbf{r}-\mathbf{r}'|^2/(4L)}\ ,\ L = Nl^2 \tag{3}$$

is also a normalized Gaussian with a width that is N times larger than the width of (2). The meaning of L derives from the mean square end-to end distance

$$\mathcal{R}_{ee}^2 \equiv \mathcal{R}^2 = \int d^3r'\, |\mathbf{r}-\mathbf{r}'|^2\, Z(\mathbf{r},\mathbf{r}') \Big/ \int d^3r' Z(\mathbf{r},\mathbf{r}') = 6L \tag{4}$$

which also implies that the mean square radius of gyration $\mathcal{R}_g^2 = \mathcal{R}^2/6$ equals L. One expects that the partition function (1) of our random-walk like ideal chain is related to diffusion. Actually Z satisfies the equation

$$\left(\frac{\partial}{\partial L} - \Delta_{\mathbf{r}}\right) Z(\mathbf{r},\mathbf{r}') = 0 \quad , \quad Z(\mathbf{r},\mathbf{r}')|_{L=0} = \delta(\mathbf{r}-\mathbf{r}') \tag{5}$$

of a diffusion pole in which L plays the role of the time in the diffusion equation. Eqs. (4) and (5) follow most easily from the Fourier transform

$$\int d^3r\, e^{i\mathbf{p}\mathbf{r}}\, P(\mathbf{r}) = e^{-p^2l^2} \tag{6}$$

of P.

Next we consider an ideal polymer chain subjected to an external monomer-potential l^2W in units of k_BT. In this case each link contributes apart from P in (2) a Boltzmann weight

$$Q(\mathbf{y}) = e^{-l^2W(\mathbf{y})} \tag{7}$$

to the partition sum

$$Z(\mathbf{r},\mathbf{r}') = \int d^3r_1 ... \int d^3r_{N-1}\, P(\mathbf{r}-\mathbf{r}_1)\, Q\left(\frac{\mathbf{r}+\mathbf{r}_1}{2}\right) ... P(\mathbf{r}_{N-1}-\mathbf{r}')\, Q\left(\frac{\mathbf{r}_{N-1}+\mathbf{r}'}{2}\right). \tag{8}$$

Note that Z is symmetric

$$Z(\mathbf{r},\mathbf{r}') = Z(\mathbf{r}',\mathbf{r})\,. \tag{9}$$

It is shown in Appendix A that in the continuum limit

$$l \to 0\ ,\ L = Nl^2 \text{ fixed} \tag{10}$$

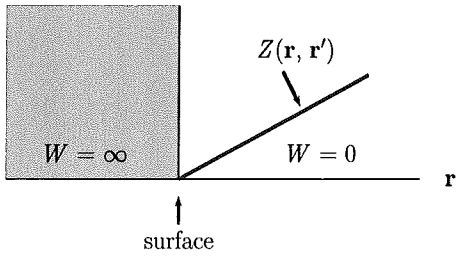


Fig. 3: *Dirichlet boundary condition at a hard surface.*

Z satisfies a modified diffusion equation [1]

$$\left(\frac{\partial}{\partial L} - \Delta_{\mathbf{r}} + W(\mathbf{r})\right) Z(\mathbf{r}, \mathbf{r}') = 0 \tag{11}$$

with the 'initial condition'

$$Z(\mathbf{r}, \mathbf{r}')|_{L=0} = \delta(\mathbf{r} - \mathbf{r}') \tag{12}$$

as in Eq. (5).
These results are very closely related to the quantum mechanical motion of a point particle with mass m in a potential $\mathcal{V} = (\hbar^2/(2m))W$. Here the polymer path integral (8) corresponds to Feynman's path integral of the quantum mechanical propagator and the 'diffusion equation' (11) to the time-dependent Schrödinger equation. In particular, the mean square radius of gyration L corresponds to the quantum mechanical expression $i\hbar t/(2m)$ where t is the time.
In the following we shall consider hard impenetrable surfaces. This corresponds to $W = 0$ in the space available to the polymer and $W = \infty$ in the forbidden space. It implies that $Z(\mathbf{r}, \mathbf{r}')$ satisfies (5) in the available space and the Dirichlet boundary condition

$$Z(\mathbf{r}, \mathbf{r}') \to 0 \qquad \text{for } \mathbf{r} \text{ or } \mathbf{r}' \to \text{hard surface}\,, \tag{13}$$

compare Fig. 3.
Besides $Z(\mathbf{r}, \mathbf{r}')$ we shall also consider the partition function

$$\mathcal{E}(\mathbf{r}) = \int d^3r'\, Z(\mathbf{r}, \mathbf{r}') \tag{14}$$

of the chain with only one end fixed while the free end $\mathbf{r}'$ is integrated over the available space. This is proportional to the density profile of endpoints in a dilute solution of chains in the available space bounded by the surface. It also satisfies the diffusion equation in (5) and the Dirichlet boundary condition in (13), the 'initial condition' in (5) is, however, changed to

$$\mathcal{E}(\mathbf{r})|_{L=0} = 1\,. \tag{15}$$

For $\mathbf{r}$ far away from any surface one expects from (3) that

$$\mathcal{E}(\mathbf{r} \to \text{bulk}) = 1\,,\ L \text{ arbitrary}\,. \tag{16}$$



Fig. 4: *A polymer configuration in the half space (left); end-density in the half space (right).*

3 Polymer in the half space

The left part of Fig. 4 shows a conformation of a polymer with two fixed ends in the half space $z > 0$. In order to satisfy the hard wall condition (13) at the boundary $z = 0$ one can use the method of images. Subtracting from the diffusion pole (3) which 'starts' from $\mathbf{r}' = (x', y', z')$ a pole which starts from the image point $\mathbf{r}'_I = (x', y', -z')$ one finds

$$Z(\mathbf{r}, \mathbf{r}') = (4\pi L)^{-1} e^{-[(x-x')^2+(y-y')^2]/(4L)} (4\pi L)^{-1/2} \{e^{-(z-z')^2/(4L)} - e^{-(z+z')^2/(4L)}\} . \quad (17)$$

This satisfies the diffusion equation and initial condition (5) in the half space as well as the boundary condition (13) at $z = 0$.
For the partition function with only one end fixed

$$\mathcal{E}(\mathbf{r}) = \mathcal{E}_{\rm hs}(z) \equiv \int_{(z'>0)} d^3r' \, Z(\mathbf{r}, \mathbf{r}') \quad (18)$$

one finds from Eq. (17)

$$\mathcal{E}(\mathbf{r}) = \operatorname{erf} \frac{z}{\sqrt{4L}} \quad (19)$$

where

$$\operatorname{erf} y = \frac{2}{\sqrt{\pi}} \int_0^y d\zeta \, e^{-\zeta^2} \quad (20)$$

is the error function. The right part of Fig. 4 shows that the width of the depletion zone of $\mathcal{E}_{\rm hs}$ near the wall is of the order of the root mean square end-to-end distance.

4 Polymer near a spherical particle

For the bulk-normalized end density near a spherical particle of radius R and centered at the origin one finds [2]

$$\mathcal{E}(\mathbf{r}) = \int_{(r'>R)} d^3r' \, Z(\mathbf{r}, \mathbf{r}') = 1 - \frac{R}{r} \operatorname{erfc} \frac{r - R}{\sqrt{4L}} \quad (21)$$

with

$$\operatorname{erfc} x = 1 - \operatorname{erf} x \quad (22)$$

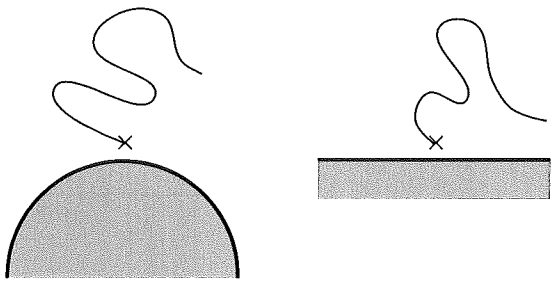


Fig. 5: *A polymer chain end-grafted to the surface of a sphere (left) and to a planar surface (right)*

the complementary error function. This expression satisfies the diffusion equation in (5), the initial condition (15) and the Dirichlet boundary condition (13) at the particle surface $r = R$.

Let us compare two limits of this expression. For $R \to \infty$ with the distance from the surface $r - R \equiv z$ fixed Eq. (21) reduces to the half space result of Eq. (19). For R, r fixed and $L = \mathcal{R}_g \to \infty$

$$\mathcal{E}(\mathbf{r}) \to 1 - \frac{R}{r} \,. \tag{23}$$

Note that this profile displays a width of the depletion zone of the order of R while the width is of order $\mathcal{R}_g$ for a large particle or a planar wall. This illustrates the crucial role played by the particle to polymer size ratio $R/\mathcal{R}_g$.

4.1 Chain end-grafted to the surface

For $r \searrow R$ the expression in Eq. (21) reduces to

$$\mathcal{E}(\mathbf{r}) \to \mathcal{E}^{\rm egs} = (r - R)\left[\frac{1}{\sqrt{\pi L}} + \frac{1}{R}\right] \tag{24}$$

where the superscript egs denotes 'end-grafted to the surface'. Comparison with a *planar* wall leads to a ratio of partition functions

$$\frac{\mathcal{E}^{\rm egs}}{\mathcal{E}^{\rm egs}_{\rm planar}} = 1 + \frac{\sqrt{\pi L}}{R} \tag{25}$$

and to a difference in free energies

$$\frac{F^{\rm egs} - F^{\rm egs}_{\rm planar}}{k_B T} = -\ln \frac{\mathcal{E}^{\rm egs}}{\mathcal{E}^{\rm egs}_{\rm planar}} = -\frac{\sqrt{\pi L}}{R} + \mathcal{O}\left(\frac{L}{R^2}\right) . \tag{26}$$

Thus the partition function $\mathcal{E}$ is larger and the free energy F is smaller for a spherical particle than for the case of a planar wall. This is obvious since outside a sphere there is more space for the grafted chain to coil than for the case of a planar wall, compare Fig. 5.

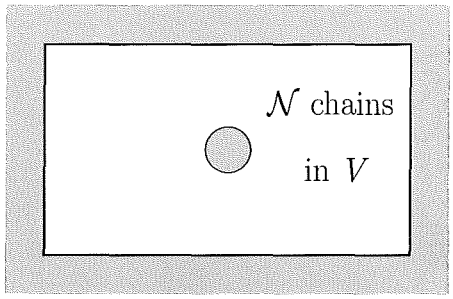


Fig. 6: *Colloid and free chains in a normalization volume V*

4.2 Immersing a sphere into a solution of free nonadsorbing polymer chains

On immersing a spherical particle in a dilute solution of $\mathcal{N}$ polymer chains in a big normalization volume V (see Fig. 6) the polymer free energy changes by

$$\frac{F - F_{\text{bulk}}}{k_B T} = -\mathcal{N} \ln \frac{\int_{V\backslash S} d^3r\, \mathcal{E}(\mathbf{r})}{\int_V d^3r\, \mathcal{E}_{\text{bulk}}(\mathbf{r})} = -\mathcal{N} \ln \left[1 - \frac{\int_V d^3r\, (\mathcal{E}_{\text{bulk}}(\mathbf{r}) - \mathcal{E}(\mathbf{r}))}{\int_V d^3r\, \mathcal{E}_{\text{bulk}}(\mathbf{r})} \right] . \tag{27}$$

Here $V\backslash S$ denotes the outer space of the sphere and $\mathcal{E}_{\text{bulk}}(\mathbf{r})$ is the partition function in absence of the sphere which in our normalization is equal to one. Expanding the logarithm in (27) and using that $\mathcal{E}(\mathbf{r})$ vanishes for $\mathbf{r}$ inside the sphere we find

$$\frac{F - F_{\text{bulk}}}{k_B T} = \frac{\mathcal{N}}{V} \left\{ \frac{4\pi}{3} + 4\pi \int_R^\infty dr\, r^2 [1 - \mathcal{E}(\mathbf{r})] \right\} . \tag{28}$$

Using the ideal chain result (21) and introducing the integration variable $x = (r-R)/\sqrt{4L}$ the integral in (28) becomes

$$4\pi \int_R^\infty = 4\pi R \cdot 4L \int_0^\infty dx \left(x + \frac{R}{\sqrt{4L}} \right) \text{erfc} x = 4\pi RL + 8\sqrt{\pi} R^2 \sqrt{L} \tag{29}$$

and [3,4]

$$F - F_{\text{bulk}} = p\, 4\pi R^3 \left[\frac{1}{3} + \frac{2}{\sqrt{\pi}} \frac{\sqrt{L}}{R} + \frac{L}{R^2} \right] \tag{30}$$

where

$$p = k_B T \mathcal{N}/V \tag{31}$$

is the ideal gas pressure of the polymer solution. Eq. (30) applies to arbitrary particle to polymer size ratio $R/\sqrt{L} = R/\mathcal{R}_g$. It leads to a small curvature expansion

$$F - F_{\text{bulk}} = pV_S + \int dA_S \left\{ p \frac{2}{\sqrt{\pi}} \sqrt{L} + \frac{1}{R} pL \right\} \tag{32}$$

which contains a polymer-induced surface tension and spontaneous curvature term (the last two terms on the right hand side of (32)) but no bending rigidity term. Here V_S is the volume and dA_S a surface element of the sphere. The spontaneous curvature term enters

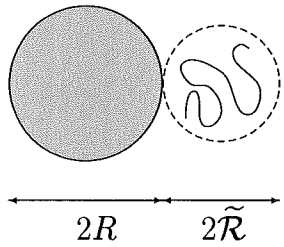


Fig. 7: *Colloidal particle interacting with a rigid polymer sphere.*

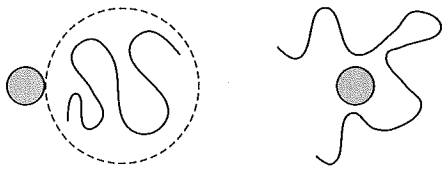


Fig. 8: *Small colloidal particle interacting with a rigid (left) and with a flexible (right) polymer.*

with a positive sign and favors a planar surface rather than a convex sphere. This should be compared with the case of a surface-grafted polymer, Eq. (26), in which a convex sphere rather than a planar wall is favored.
It is interesting to compare Eq. (30) with the free energy cost in the simple model of Asakura and Oosawa [5] in which polymer flexibility is neglected and a free polymer interacts with the colloid like a hard sphere of radius $\tilde{\mathcal{R}}$ which is of the order of $\mathcal{R}_g$, compare Fig. 7. Thus instead of (21) the partition function $\mathcal{E}(\mathbf{r})$ equals 1 for $r > R + \tilde{\mathcal{R}}$ and vanishes for $r < R + \tilde{\mathcal{R}}$ so that the fraction inside the square brackets in (27) becomes

$$\frac{\int_V d^3r\,(\mathcal{E}_{\rm bulk}(\mathbf{r}) - \mathcal{E}(\mathbf{r}))}{\int_V d^3r\,\mathcal{E}_{\rm bulk}(\mathbf{r})} = \frac{\frac{4\pi}{3}(R+\tilde{\mathcal{R}})^3}{V} \tag{33}$$

and the free energy cost is given by

$$F - F_{\rm bulk} = p\,4\pi\left(\frac{R^3}{3} + R^2\tilde{\mathcal{R}} + R\tilde{\mathcal{R}}^2 + \frac{\tilde{\mathcal{R}}^3}{3}\right). \tag{34}$$

On comparing (34) with (30) one finds that for large particle to polymer size ratio $R/\mathcal{R}_g \gg 1$ the leading term is correctly reproduced. Even the leading correction which corresponds to the surface tension is reproduced if we choose an Asakura-Oosawa radius of

$$\tilde{\mathcal{R}} = 2\sqrt{L/\pi} \equiv 2\mathcal{R}_g/\sqrt{\pi}\,. \tag{35}$$

However, for small size ratio $R/\mathcal{R}_g \ll 1$ the Asakura-Oosawa model leads to a free energy cost $\propto \tilde{\mathcal{R}}^3 \propto \mathcal{R}_g^3$ which is much larger than the free energy cost $\propto R\mathcal{R}_g^2$ for flexible chains. This is not surprising since a flexible polymer chain can coil around the small particle and the entropy loss vanishes for $R \to 0$ while in case of a rigid polymer sphere there is a finite entropy loss even in the case of a point particle with $R = 0$, compare Fig. 8.

5 Polymer-induced bending rigidities

In order to evaluate the polymer-induced bending rigidities in a Helfrich expansion for an arbitrary surface with small curvature we need results for the behavior of polymers both for a spherical and a cylindrical surface [4,6]. Closed form expressions are obtained most easily for the Laplace transform

$$\chi(t;\mathbf{r}) = \int_0^\infty dL\, e^{-Lt}\, \mathcal{E}(L;\mathbf{r}) \tag{36}$$

of the partition function $\mathcal{E}(\mathbf{r}) \equiv \mathcal{E}(L;\mathbf{r})$ with only one end fixed or normalized end-density. Multiplying the diffusion equation in (5) for $\mathcal{E}(\mathbf{r})$ with e^{-Lt}, integrating over L and using that

$$\int_0^\infty dL\, e^{-Lt}\, \frac{\partial}{\partial L}\, \mathcal{E}(L;\mathbf{r}) = -\mathcal{E}(0;\mathbf{r}) + t\,\chi(t;\mathbf{r}) \tag{37}$$

together with the initial condition (15) leads to

$$(t - \Delta_{\mathbf{r}})\, \chi(t;\mathbf{r}) = 1\,. \tag{38}$$

The Laplace transform $\chi(t;\mathbf{r})$ also satisfies the Dirichlet condition $\chi \to 0$ for $\mathbf{r}$ approaching the surface.

For the plate centered around the plane $z = 0$, $\mathcal{E}$ and χ only depend on $r_\perp = z$, for the cylinder with axis $x = y = 0$ on $r_\perp = \sqrt{x^2 + y^2}$, and for the sphere with center at $x = y = z = 0$ on $r_\perp = \sqrt{x^2 + y^2 + z^2}$. Using that

$$\Delta_{\mathbf{r}}\chi = \left(\frac{d^2}{dr_\perp^2} + \frac{d-1}{r_\perp}\frac{d}{dr_\perp}\right)\chi \tag{39}$$

with $d = 1$, 2, and 3 for the plate, cylinder, and sphere, one finds that [4]

$$\chi(t;r_\perp) = \frac{1}{t}\left[1 - \left(\frac{R}{r_\perp}\right)^\alpha \frac{K_\alpha(r_\perp\sqrt{t})}{K_\alpha(R\sqrt{t})}\right] \quad , \quad \alpha = \frac{d-2}{2} \tag{40}$$

with K a modified Bessel function. Here R is the radius in case of the sphere or the cylinder and $2R$ is the thickness in case of the plate. Note that for both the planar wall with $\alpha = -1/2$ and the sphere with $\alpha = 1/2$ the expression for χ in (40) can be written in terms of elementary functions while for the cylinder with $\alpha = 0$ one remains with the special function K_0.

Now consider the chain *end-grafted* on the surface of the cylinder or sphere with small curvature so that $R/\mathcal{R}_g \gg 1$. Since this corresponds to $R\sqrt{t} \gg 1$ we may asymptotically expand the Bessel functions in (40) to obtain

$$\left(\frac{d}{dr_\perp}\chi\right)_{r_\perp=R} = \frac{\alpha}{tR} - \frac{1}{\sqrt{t}}\frac{K'_\alpha(R\sqrt{t})}{K_\alpha(R\sqrt{t})} \to \frac{1}{\sqrt{t}} + \frac{d-1}{2}\frac{1}{Rt} + \frac{(d-1)(d-3)}{8R^2t^{3/2}} \tag{41}$$

and inverting [7] the Laplace transform (36) leads to

$$\left(\frac{d}{dr_\perp}\mathcal{E}(L;\mathbf{r})\right)_{r_\perp=R} = \frac{1}{\sqrt{\pi L}} + \frac{d-1}{2}\frac{1}{R} + \frac{(d-1)(d-3)}{4R^2}\sqrt{\frac{L}{\pi}}\,. \tag{42}$$

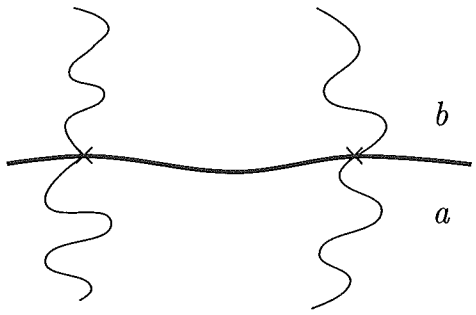


Fig. 9: *A membrane decorated with copolymers.*

This implies for the ratio of partition functions [4, 6]

$$\frac{\mathcal{E}^{\rm egs}}{\mathcal{E}^{\rm egs}_{\rm planar}} = 1 + \frac{d-1}{2}\frac{\sqrt{\pi L}}{R} + \frac{(d-1)(d-3)}{4}\frac{L}{R^2} \tag{43}$$

and the free energy change

$$\frac{F^{\rm egs} - F^{\rm egs}_{\rm planar}}{k_B T} = \frac{d-1}{2}\left\{-\frac{\sqrt{\pi L}}{R} + \frac{L}{R^2}\left[\frac{d-1}{4}\pi + \frac{3-d}{2}\right]\right\}. \tag{44}$$

For $d = 3$ Eqs. (43) and (44) reduce to the expressions (25) and (26) for the sphere. On introducing the mean curvature

$$H = \frac{1}{2}\left(\frac{1}{R_1} + \frac{1}{R_2}\right) \tag{45}$$

and the Gaussian curvature

$$K = \frac{1}{R_1 R_2} \tag{46}$$

with R_1, R_2 the two principal radii of curvature and on using the expression (4) for the mean square end-to-end distance $\mathcal{R}^2$, the result (44) for cylinder and sphere can be written as [6]

$$\frac{F^{\rm egs} - F^{\rm egs}_{\rm planar}}{k_B T} = -\sqrt{\frac{\pi}{6}}\mathcal{R}H + \frac{1}{6}\left(\frac{\pi}{2} + 1\right)(\mathcal{R}H)^2 - \frac{1}{6}\mathcal{R}^2 K\,. \tag{47}$$

6 Surfactant membrane decorated with copolymers

Fig. 9 shows a membrane decorated with copolymers with a surface density σ of anchor points. For non-overlapping copolymers, the contributions (47) of single polymers add up and lead to a small curvature Helfrich expansion for the polymer-induced free energy

$$F^{\rm egs} - F^{\rm egs}_{\rm planar} = k_B T \int dA\, \sigma(\mathcal{R}_a^2 + \mathcal{R}_b^2)\,\frac{1}{2}\left\{\frac{\pi}{24}\left(\frac{1}{R_1} + \frac{1}{R_2}\right)^2 + \frac{1}{12}\left(\frac{1}{R_1} - \frac{1}{R_2}\right)^2\right\}. \tag{48}$$

Here $\mathcal{R}_a^2$ and $\mathcal{R}_b^2$ denote the mean square end-to-end distances of the two polymer blocks, we have assumed symmetric diblock copolymers so that the spontaneous curvature terms cancel, and we have used

$$H^2 - K = \frac{1}{4}\left(\frac{1}{R_1} - \frac{1}{R_2}\right)^2. \tag{49}$$

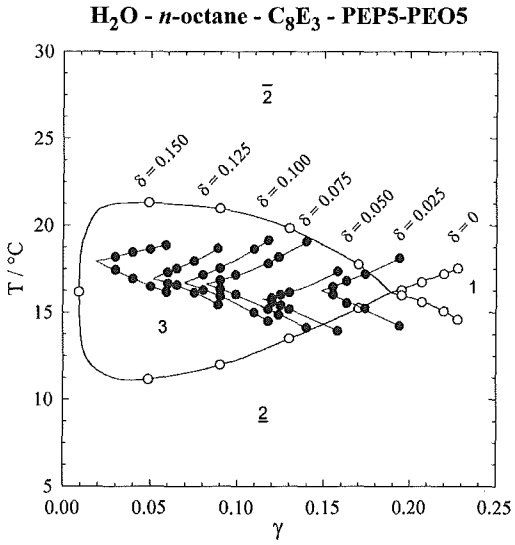


Fig. 10: *Fish-tail point of an oil-water microemulsion for various mass fractions δ of PEP5-PEO5 copolymer [11, 12]. The mass fractions δ and γ of copolymer and surfactant are proportional to the quantities σ and ρ in the text.*

With the usual [8,9] notation $\kappa_\pm$ for the rigidity coefficients in front of the $\int dA\,(1/2)\,((1/R_1)\pm(1/R_2))^2$ terms of the free energy we find that grafted polymers *increase* the rigidities as

$$\begin{aligned} \kappa_+ &= \kappa_{+0} + k_B T \sigma \frac{\pi}{24}(\mathcal{R}_a^2 + \mathcal{R}_b^2) \\ \kappa_- &= \kappa_{-0} + k_B T \sigma \frac{1}{12}(\mathcal{R}_a^2 + \mathcal{R}_b^2)\,. \end{aligned} \tag{50}$$

Here $\kappa_{\pm 0}$ are the membrane rigidities without polymer.
It is shown in the lecture of G. Gompper that upon dilution of the surfactant the lamellar phase of surfactant membranes with lamellar spacing D becomes unstable against the formation of an infinite minimal surface with $1/R_1 = -1/R_2$ if a 'renormalized rigidity' $\kappa_-^{(\mathrm{ren})}(D)$ vanishes while the corresponding rigidity $\kappa_+^{(\mathrm{ren})}(D)$ remains positive. This condition reads

$$\ln(\rho_\mathrm{I}\lambda^3) = -\frac{4\pi}{\alpha_-}\frac{1}{k_B T}\kappa_- \tag{51}$$

where $\rho = \rho_\mathrm{I}$ is the surfactant density at the instability point, λ is a microscopic length, and α_- is a coefficient with the value of 5/3 [10]. On inserting (50) in (51) one finds

$$\ln(\rho_\mathrm{I}\lambda^3) = \ln(\rho_{\mathrm{I}0}\lambda^3) - \frac{\pi}{5}\sigma(\mathcal{R}_a^2 + \mathcal{R}_b^2)\,. \tag{52}$$

Here $\rho_{\mathrm{I}0}$ is the instability density without polymer. Eq. (52) predicts $\rho_\mathrm{I} < \rho_{\mathrm{I}0}$, i.e. the instability is shifted to lower surfactant concentration in the presence of grafted copolymer. The shift of the surfactant concentration $\rho = \rho_\mathrm{FT}$ of the fish-tail point in an oil-water microemulsion which separates the three phase body from the one phase bicontinuous microemulsion (compare the lecture of G. Gompper) follows the same law

$$\ln(\rho_\mathrm{FT}/\rho_{\mathrm{FT}0}) = -\frac{\pi}{5}\sigma(\mathcal{R}_a^2 + \mathcal{R}_b^2)\,. \tag{53}$$

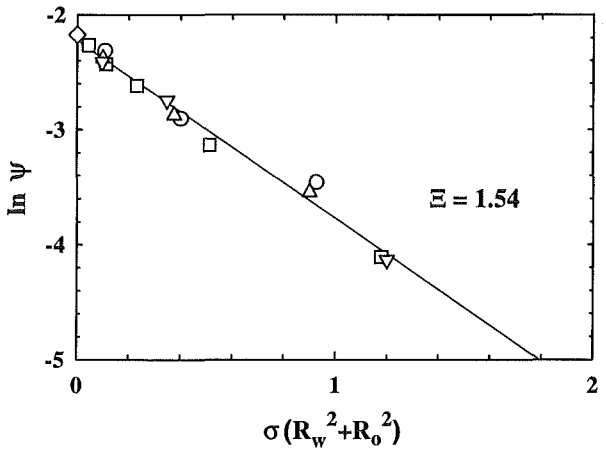


Fig. 11: *Membrane volume fraction Ψ at the fish-tail point against the scaled polymer grafting density $\sigma(\mathrm{R_w^2}+\mathrm{R_o^2})$. Here $\mathrm{R_o^2}\equiv\mathcal{R}_a^2$ and $\mathrm{R_w^2}\equiv\mathcal{R}_b^2$ denote the mean square end-to-end distances of PEP and PEO homopolymers in oil and water which correspond to the two blocks in the PEP-PEO copolymer. Different symbols denote copolymers of different chain lengths [11, 12]. Ψ is proportional to ρ_{FT} in the text.*

The experimental data in Fig. 10 show increasing shifts of the fish-tail point towards lower surfactant concentration for increasing concentration of copolymer [11,12]. Neutron scattering experiments [11, 12] have carefully checked that the copolymers are indeed located at the oil-water interface and behave as isolated chains that are neither attracted to the membrane nor compressed by other polymers. Fig. 11 shows $\ln\rho_{\mathrm{FT}}$ for various concentrations and chain lengths of copolymer. Note that the data nicely collapse onto the scaling curve $\sigma(\mathcal{R}_a^2+\mathcal{R}_b^2)$. However, the slope $\Xi = 1.54$ of the curve is about twice as large as the prediction $\Xi = \pi/5 = 0.63$ of the simple ideal-chain theory.

7 Bending rigidities induced by free polymers

Proceeding as in Section 4.2 the polymer free energy changes for immersing a plate per cross-sectional area ab, a cylinder per unit length a, and a sphere are given by

$$\frac{F-F_{\mathrm{bulk}}}{p\mathcal{V}_{\|}} = \mathcal{V}_{\perp} + \Omega_d \int_R^{\infty} dr_{\perp}\, r_{\perp}^{d-1}\,[1-\mathcal{E}(L,r_{\perp})]\,. \tag{54}$$

Here $(d, \mathcal{V}_{\|}, \mathcal{V}_{\perp}, \Omega_d)$ are given by $(1, ab, 2R, 2)$ for the plate of width $2R$, by $(2, a, \pi R^2, 2\pi)$ for the cylinder, and by $(3, 1, (4\pi/3)R^3, 4\pi)$ for the sphere. Inserting for $\mathcal{E}$ the inverse Laplace transform $\mathcal{L}_{t\to L}\chi$ of χ in (40) the integral in (54) is given by

$$\int_R^{\infty} = R^d \mathcal{L}_{\tau\to L/R^2} \frac{K_{\alpha+1}(\sqrt{\tau})}{\tau^{3/2}K_{\alpha}(\sqrt{\tau})}\,. \tag{55}$$

For the small curvature expansion $L/R^2 \ll 1$, i.e. $\tau \equiv tR^2 \gg 1$. Using the asymptotic expansion of the Bessel functions, performing the inverse Laplace transform in (55), and

inserting $\int_R^\infty$ into (54) yields

$$\frac{F-F_{\rm bulk}}{p\mathcal{V}_\parallel} = \mathcal{V}_\perp + A_\perp\left\{\frac{2}{\sqrt{\pi}}\sqrt{L} + \frac{d-1}{2}\frac{L}{R} + \frac{(d-1)(d-3)}{6\sqrt{\pi}}\frac{L^{3/2}}{R^2}\right\} \tag{56}$$

with $A_\perp = R^{d-1}\Omega_d$. These results are consistent with the small curvature Helfrich expansion

$$\frac{F-F_{\rm bulk}}{p} - \mathcal{V} = \int dA\left\{\sqrt{\frac{2}{3\pi}}\mathcal{R} + \frac{1}{6}\mathcal{R}^2 H - \frac{1}{9\sqrt{6\pi}}\mathcal{R}^3\frac{1}{4}\left(\frac{1}{R_1}-\frac{1}{R_2}\right)^2\right\} \tag{57}$$

of the free energy of immersion $F - F_{\rm bulk}$ of a particle of arbitrary shape [13] with volume $\mathcal{V}$ and surface elements dA. Here $\mathcal{R} = \mathcal{R}_{ee}$ is the root mean square end-to-end distance (4) of a polymer in free space. Thus free ideal polymers favor a bending of the surface towards the polymer solution and lead to a softening of the bending rigidity κ_-. Note that ideal chains do not lead to a change of κ_+. This is different for a dilute solution of chains with excluded volume interaction between monomers. A $d = 4 - \epsilon$ expansion [14] shows that κ_+ is also softened in this case. The excluded volume effects are small, however.

8 Monomer density profiles and the density-pressure relation

For the discrete chain in Sec. 2 the monomer density at $\mathbf{r}$ is the average over chain configurations of $\Sigma_{j=1}^N \delta(\mathbf{r} - \mathbf{r}_j)$. For a solution of free ideal chains and in the continuum limit the bulk-normalized monomer density profile is given by

$$\mathcal{M}(L;\mathbf{r}) = \frac{1}{L}\int_0^L dL'\,\mathcal{E}(L';\mathbf{r})\,\mathcal{E}(L-L';\mathbf{r}) = \frac{1}{L}\mathcal{L}_{t\to L}[\chi(t;\mathbf{r})]^2 \tag{58}$$

with χ the Laplace transform in Eq. (36). For plate, cylinder, and sphere, χ is given in (40). Closed form expressions for $\mathcal{M}$ in terms of exponential and error functions follow for the plate and the sphere in which case $K_\alpha = K_{1/2}$ is an elementary function, see e.g. [4]. Of particular interest is the behavior of the monomer density *near* the surface since it is related to the pressure on the surface. For example consider the case of the sphere in which

$$\chi_{\rm sphere}(t;\mathbf{r}) = \frac{1}{t}\left[1 - \frac{R}{r}e^{-(r-R)\sqrt{t}}\right]. \tag{59}$$

Expanding about $r = R$ and using (58) leads to

$$\mathcal{M}_{\rm sphere} \to \mathcal{M}^{\rm (as)}_{\rm sphere} = \frac{1}{L}(r-R)^2\mathcal{L}_{t\to L}\left[\frac{1}{\sqrt{t}} + \frac{1}{tR}\right]^2 = \frac{1}{L}(r-R)^2\left\{1 + \frac{4}{R}\sqrt{\frac{L}{\pi}} + \frac{L}{R^2}\right\} \tag{60}$$

in the asymptotic scaling region $r \to R$. This is indeed proportional to the pressure

$$p_{\rm sphere} \equiv \frac{1}{4\pi R^2}\frac{dF}{dR} = p\left[1 + \frac{4}{R}\sqrt{\frac{L}{\pi}} + \frac{L}{R^2}\right] \tag{61}$$

which the polymer solution exerts on the sphere surface. Here F is the free energy in (30) and p is the ideal gas pressure in (31).

The factor of proportionality depends, of course, on the distance $r - R$ from the surface but is independent of the surface curvature. It is consistent with the density-pressure relation [15]

$$(\mathcal{R}^2/3)^{1/(2\nu)}\, n\, \mathcal{M}^{(\mathrm{as})}_{\mathrm{sphere}} = B\, \frac{p_{\mathrm{sphere}}}{k_B T}\, (r-R)^{1/\nu} \tag{62}$$

with $\mathcal{R}^2 = \mathcal{R}^2_{ee}$ the mean square end-to-end distance, n the number density of chains, ν the Flory exponent, and B a universal constant, if we use the ideal chain expressions $\mathcal{R}^2 = 6L$ (see (4)), $\nu = 1/2$, and $B = 2$. A derivation of the density-pressure relation for a sphere in a solution of ideal chains is most transparent in the framework of a Ginzburg-Landau theory and is sketched in Appendix B.

Appendices

A An ideal chain in an external potential

Consider the change in the partition function (8) by adding one link to the chain. In the continuum limit (10) this determines

$$Z(L + l^2; \mathbf{r}, \mathbf{r}') - Z(L; \mathbf{r}, \mathbf{r}') = l^2 \frac{\partial}{\partial L} Z(L; \mathbf{r}, \mathbf{r}') \,. \tag{63}$$

The change follows from (8) as

$$\int d^3 r''\, Z(L; \mathbf{r}, \mathbf{r}'')\, P(\mathbf{r}'' - \mathbf{r}')\, Q\left(\frac{\mathbf{r}'' + \mathbf{r}'}{2}\right) - Z(L; \mathbf{r}, \mathbf{r}') \tag{64}$$

and has to be calculated to order l^2. With the new integration variable

$$\mathbf{s} = \frac{\mathbf{r}'' - \mathbf{r}'}{2l} \tag{65}$$

the first term in (64) becomes

$$\int d^3 r'' = \pi^{-3/2} \int d^3 s\, Z(L; \mathbf{r}, \mathbf{r}' + 2l\mathbf{s})\, e^{-s^2}\, e^{-l^2 W(\mathbf{r}' + l\mathbf{s})} \,. \tag{66}$$

Expanding to second order in l

$$Z(L; \mathbf{r}, \mathbf{r}' + 2l\mathbf{s}) = \left[1 + 2l \sum_{\alpha=1}^{3} s_\alpha \frac{\partial}{\partial r'_\alpha} + \frac{1}{2}(2l)^2 \sum_{\alpha,\beta} s_\alpha s_\beta \frac{\partial}{\partial r'_\alpha} \frac{\partial}{\partial r'_\beta}\right] Z(L; \mathbf{r}, \mathbf{r}') \tag{67}$$

and

$$e^{-l^2 W(\mathbf{r}' + l\mathbf{s})} = 1 - l^2 W(\mathbf{r}') \tag{68}$$

and evaluating the integrals

$$\pi^{-3/2} \int d^3 s\, e^{-s^2} \left[1\,,\, s_\alpha\,,\, s_\alpha s_\beta\right] = \left[1\,,\, 0\,,\, \delta_{\alpha\beta}/2\right] , \tag{69}$$

the expression in (64) is up to order l^2 given by

$$l^2 \left[\Delta_{\mathbf{r}'} - W(\mathbf{r}')\right] Z(L; \mathbf{r}, \mathbf{r}') \,. \tag{70}$$

Equating (63) and (70) and using the symmetry (9) of Z leads to the modified diffusion equation (11).

B Density-pressure relation for ideal chains

The pressure $p_{\rm sphere}$ on the sphere surface in (61) is proportional to the R-derivative of F in (28) which is given by

$$\frac{d}{dR}\frac{F}{p} = -\int_{(r>R)} d^3r\,\frac{d}{dR}\mathcal{E}(\mathbf{r}) = -\int_{(r>R)} d^3r \int_{(r'>R)} d^3r'\,\frac{d}{dR}Z(\mathbf{r},\mathbf{r}') \qquad (71)$$

with p the ideal gas pressure in (31). Note that the R-derivative of $(4\pi/3)R^3$ and of the lower boundary of the integral in (28) cancel each other. Likewise the R-derivative of the integration boundary $r' > R$ in $\mathcal{E}(\mathbf{r}) = \int_{(r'>R)} Z(\mathbf{r},\mathbf{r}')$ vanishes due to the Dirichlet boundary condition. We now use that the partition function $Z(\mathbf{r},\mathbf{r}')$ is given by the inverse Laplace transform $\mathcal{L}_{t\to L}$ of the order parameter correlation function $\langle\Phi(\mathbf{r})\Phi(\mathbf{r}')\rangle$ of a Ginzburg-Landau field theory which is Gaussian in the case of ideal chains [1, 15]. This leads to

$$-\frac{d}{dR}Z(\mathbf{r},\mathbf{r}') = -\mathcal{L}_{t\to L}\frac{d}{dR}\langle\Phi(\mathbf{r})\Phi(\mathbf{r}')\rangle = \mathcal{L}_{t\to L}\int dA\,\langle\frac{1}{2}\big(\partial_n\Phi(\mathbf{r}_A)\big)^2\cdot\Phi(\mathbf{r})\Phi(\mathbf{r}')\rangle\,. \quad (72)$$

Here ∂_n is a derivative perpendicular to and $\int dA$ an integral over the sphere surface. The last step in (72) follows since the 'stress tensor component' $(\partial_n\Phi(\mathbf{r}_A))^2$ at the surface generates a shift of the surface towards the center of the sphere. For more details see e.g. Appendix A of Ref. [16]. Inserting Eq. (72) into (71) and taking into account the spherical symmetry leads to

$$\frac{1}{A}\frac{d}{dR}\frac{F}{p} = \mathcal{L}_{t\to L}\langle\frac{1}{2}\big(\partial_n\Phi(\mathbf{r}_A)\big)^2\cdot\int_{(r>R)} d^3r\,\Phi(\mathbf{r})\int_{(r'>R)} d^3r'\,\Phi(\mathbf{r}')\rangle = \mathcal{L}_{t\to L}\,[\partial_n\chi(t;\mathbf{r}_A)]^2 \qquad (73)$$

with $A = 4\pi R^2$ the surface of the sphere and $\mathbf{r}_A$ an arbitrary point in the surface. In the last step we have used Wick's theorem and the fact that the Laplace transform $\chi(\mathbf{r})$ of $\int d^3r' Z(\mathbf{r},\mathbf{r}')$ introduced in Eq. (36) equals the 'susceptibility' $\langle\Phi(\mathbf{r})\int d^3r'\,\Phi(\mathbf{r}')\rangle$ of the Ginzburg-Landau model. Comparing the last expression in (73) with the ideal chain formula (58) for $\mathcal{M}$ shows that

$$\frac{1}{A}\frac{d}{dR}\frac{F}{p} = L\,\frac{\mathcal{M}^{(\rm as)}_{\rm sphere}(r)}{(r-R)^2} \qquad (74)$$

which is consistent with the density-pressure relation Eq. (62).

References

[1] P.G. de Gennes, *Scaling Concepts in Polymer Physics* (Cornell University, Ithaca, 1979).

[2] R. Lipowsky, Europhys. Lett. **30**, 197 (1995).

[3] K.M. Jansons and C.G. Phillips, J. Colloid Interface Sci. **137**, 75 (1990).

[4] E. Eisenriegler, A. Hanke, and S. Dietrich, Phys. Rev. E**54**, 1134 (1996).

[5] S. Asakura and F. Oosawa, J. Chem. Phys. **22**, 155 (1954); J. Polym. Sci. **33**, 183 (1958).

[6] C. Hiergeist and R. Lipowsky, J. Physique (Paris) II **6**,1465 (1996).

[7] See e.g. M. Abramowitz and I. Stegun, *Handbook of Mathematical functions* (Dover, New York, 1972).

[8] D.C. Morse, Phys. Rev. E**50**, R2423 (1994).

[9] G. Gompper and D.M. Kroll, Phys. Rev. Letters **81**, 2284 (1998).

[10] See the discussion near Eqs. (3)-(5) in Ref. [12]

[11] H. Endo *et al.*, Journal of Chem. Physics **115**, 580 (2001).

[12] G. Gompper, D. Richter, and R. Strey, J. Phys.: Condensed Matter **13**, 1 (2001).

[13] For plate, cylinder, and sphere $\mathcal{V} = \mathcal{V}_{\|}\mathcal{V}_{\perp}$ and $\int dA = \mathcal{V}_{\|}A_{\perp}$.

[14] A. Hanke, E. Eisenriegler, and S. Dietrich, Phys. Rev. E**59**, 6853 (1999).

[15] E. Eisenriegler, in: *Field Theoretical Tools in Polymer- and Particle-Physics*, (H. Meyer-Ortmanns, A. Klümper eds.), Lecture Notes in Physics **508** (Springer, Berlin, 1998).

[16] R. Maassen, E. Eisenriegler, and A. Bringer, J. Chem. Phys. **115**, 5292 (2001).

B 11 Fluid Interfaces and Amphiphiles at Surfaces

P. Lang

Institut für Festkörperforschung

Forschungszentrum Jülich GmbH

Contents

1 Introduction 2

2 Surface tension and adsorption 3
- 2.1 Surface thermodynamics and surface tension . . . 3
- 2.2 The dividing surface concept . . . 4
- 2.3 Surface excess quantities and adsorption . . . 4
- 2.4 The Gibbs adsorption equation . . . 5

3 Two simple cases 6
- 3.1 Surface tension of pure liquids . . . 6
- 3.2 Surface tension of ideally dilute solutions . . . 7

4 Two dimensional phase transitions 9

5 Structure determination in surface films 10
- 5.1 Surface sensitive x–ray scattering . . . 10
- 5.2 Grazing incidence x–ray diffraction . . . 11
- 5.3 2D–crystalline monolayers at the surface of pure alkanes . . . 12
- 5.4 2D–crystalline monolayers of amphiphiles adsorbed at the surface . . . 14

6 Conclusions 16

1 Introduction

In this lecture we will discuss the thermodynamic and structural properties of simple fluid surfaces, e. g. interfaces between a liquid and a gas phase at equilibrium. Fluid surface are different from solid surfaces in two important aspects.

- Usually the energetic contribution of interfaces is neglected in thermodynamic considerations. However, daily evidence shows that surface free energy plays an important role in the case of liquids. Consider an isolated system of two droplets of a pure liquid in equilibrium with the corresponding vapor at constant temperature and constant pressure. The droplets will coalesce spontaneously into one larger droplet if brought into contact, while the opposite process will never be observed. According to the thermodynamic definition of spontaneity, this means that the free energy of the systems is higher if two small droplets are present, than in the state where only one larger droplet exists. Since in our thought experiment temperature, pressure and the volume of the liquid are constant, there has to be an additional significant contribution to the free energy. The only parameter, which was changed is the surface area of the liquid. Consequently the free energy has to be considered a function not only of temperature and pressure but also of the surface area σ.

- Unlike the surfaces of solid bodies, fluid interfaces, i. e. gas/liquid or liquid/liquid interfaces do not represent sharp boundaries where the physical properties of one phase change abruptly to the properties of the other phase. On a microscopic level there is rather an inhomogeneous interfacial region where the density of the extensive variables changes continuously. For the planar interface between a liquid and its vapor at which the mass density ρ changes only in the z–direction perpendicular to the surface, already Rayleigh [1] derived an expression for the density variation across the surface. Fisk and Widom [2] extended this fundamental work to the more general case of the interface between two imiscible fluids, which have a critical point of mixing. The density profile turns out to be basically a tanh–function of the z–coordinate, as is sketched in Fig. 1.

The continuous density profile (or composition profile for systems with more than one component) renders the thermodynamic description of the surface to be rather complicated, since in general, the free energy of a multi–component system is also a function of composition. However, the solution of this problem has already been given by Gibbs [3] and there have been only insignificant improvements since then.

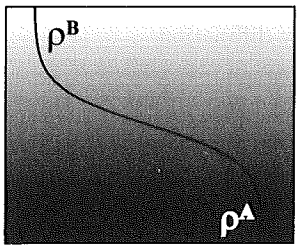


Fig. 1: *Density variation across the surface of a liquid.*

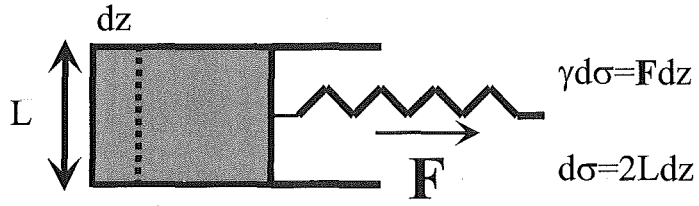


Fig. 2: *Work due to the expansion of a liquid film.*

2 Surface tension and adsorption

2.1 Surface thermodynamics and surface tension

As depicted on an empirical level in the preceding section the free energy of a fluid system contains a significant surface contribution. This shall now be discussed in more detail. Consider a liquid film spread across a rectangular wire frame, which has a movable barrier at it's right side as sketched in Fig. 2. If the frame is moved to the left to expand the area of the film, there will be a force, $\mathbf{F}$, exerted onto the spring. The work done $dw_\sigma = \mathbf{F}dz$ is proportional to the increase of surface area and the proportionality constant is the γ. Thus, to the total differential of the internal energy of the system has to be written as

$$dU = \delta q - pdV + \gamma d\sigma \tag{1}$$

Accordingly, the total differential of the Gibbs free energy becomes

$$dG = -SdT + Vdp + \gamma d\sigma \tag{2}$$

for a one component system. In multi–component systems changes in composition have to be accounted for by adding the chemical potential of each component μ_i weighted by their amount dn_i

$$dG = -SdT + Vdp + \gamma d\sigma + \sum_{i=1}^{c} \mu_i dn_i \tag{3}$$

Here c is the number of components. Integration of eq. 3 with respect to sample volume and surface at constant temperature and constant pressure gives

$$G = \gamma\sigma + \sum_{i=1}^{c} \mu_i n_i \tag{4}$$

which is in turn the definition of the chemical potentials if surface contributions habe to be taken into account. If we now compare the total differential of eq. 4

$$dG = \sigma d\gamma + \gamma d\sigma + \sum_{i=1}^{c} \mu_i dn_i + \sum_{i=1}^{c} n_i d\mu_i \tag{5}$$

with eq. 3 we obtain the well known Gibbs–Duhem equation

$$SdT - Vdp + \sigma d\gamma + \sum_{i=1}^{c} n_i d\mu_i = 0 \tag{6}$$

This allows us to write down the surface energy in dependence of the bulk composition

$$\sigma d\gamma = -SdT + Vdp - \sum_{i=1}^{c} n_i d\mu_i \tag{7}$$

However we do not know the bulk composition exactly, due to the continuous density profile at the surface. To overcome this problem we use the Gibbs dividing surface concept. We define a reference system, which is related to the real system in the way to be discussed in the next section

2.2 The dividing surface concept

To allow the complete thermodynamic description of a fluid system with a continuous surface density profile, we define a reference system as sketched in Fig. 3, in which all physical properties of the phases A and B are constant up to the infinitely sharp between them. The reference system shall have the same volume as the real system and the amount of each component n_i shall be the same in the reference system and in the real system. In the following, properties assigned to the reference system will be marked with an asterisk. Let us first consider the general case of two partially miscible fluid phases A and B with a common interface. The majority component of phase A is 1 and the majority component of phase B is 2. We may safely assume, that in any small (however large enough to be treated thermodynamically) volume element ΔV far from the interface, all density variables have the same values as in the reference system, e. g. the number density of all components in each phase,

$$\frac{\Delta n_i^A}{\Delta V} = \frac{n_i^{A^*}}{V^{A^*}} \quad \text{and} \quad \frac{\Delta n_i^B}{\Delta V} = \frac{n_i^{B^*}}{V^{B^*}}. \tag{8}$$

With these conventions the system is thermodynamically completely defined, and it is thus of no importance where the dividing surface between the two phases A and B is exactly located in the real system. We may therefore chose it's location in the way, which is most convenient for our purposes, as will be done in the next section.

2.3 Surface excess quantities and adsorption

At the interface of the real system the density variables are generally different from the bulk values, and therefore we define

$$\frac{Y^\sigma}{\sigma} = \frac{Y}{\sigma} - \frac{Y^A}{\sigma} - \frac{Y^B}{\sigma} \equiv y^\sigma \tag{9}$$

where Y may be any extensive variable of the system. The excess quantity y^σ is the value of Y per unit area, which is due to the continuous variation of y across the interface. In the reference system all y^σ are zero.
The excess quantity of the component amount n_i is of particular interest in this context. According to the definition 9 it is

$$\frac{n_i^\sigma}{\sigma} = \frac{n_i}{\sigma} - \frac{n_i^A}{\sigma} - \frac{n_i^B}{\sigma} \equiv \Gamma_i^\sigma \tag{10}$$

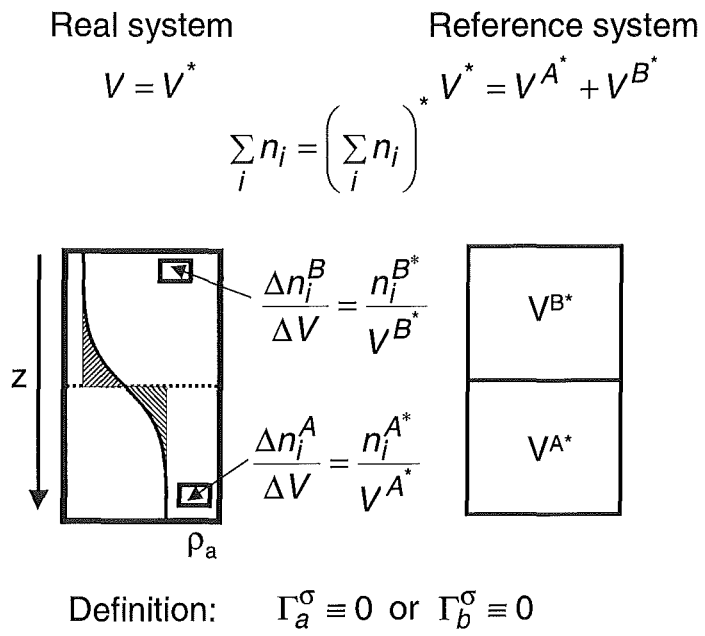


Fig. 3: *Sketch of the dividing interface concept. Left: Real system with a continuous change of the physical properties from phase A to phase B. Right: Reference system with an infinitely sharp interface separating phase A from phase B.*

Γ_i^σ is called the of component i at the interface, which may be positive as well as negative. Components with high adsorption values are called surface active.
We finally use the definition of Γ to eventually chose the location of the dividing interface of the real system. We define that it shall be located where the adsorption of either of the majority components is zero, e. g. for a liquid solution in equilibrium with its vapor it is convenient to chose the dividing surface such that the adsorption of the solvent is zero, $\Gamma_1^\sigma = 0$.

2.4 The Gibbs adsorption equation

With the above definitions we may now further explore eqs. 6 and 7. Dividing the Gibbs–Duhem equation by the surface area gives

$$s dT + d\gamma + \sum_{i=1}^{c} \frac{n_i}{\sigma} d\mu_i = 0 \tag{11}$$

if we consider isobaric conditions. Here s is the entropy per unit area of the entire system. Far away from the dividing surface the Gibbs–Duhem equation will hold also in the two phases separately. Since we do not have to account for surface effects in this case we may write

$$s^A dT + \sum_{i=1}^{c} \frac{n_i^A}{\sigma} d\mu_i = 0 \tag{12}$$

and

$$s^B dT + \sum_{i=1}^{c} \frac{n_i^B}{\sigma} d\mu_i = 0. \tag{13}$$

Subtracting eqs. 12 and 13 from eq. 11 following to the definition of the surface excess quantities (eq. 9) yields

$$d\gamma + \left(s - s^A - s^B\right) dT + \sum_{i=1}^{c} \left(\frac{n_i - n_i^A - n_i^B}{\sigma} \right) d\mu_i = 0, \tag{14}$$

which according to the definition of the adsorption may be rewritten as

$$d\gamma = -s^\sigma dT - \sum_{i=1}^{c} \Gamma_i^\sigma d\mu_i. \tag{15}$$

This is the famous .

3 Two simple cases

In its general formulation eq. 15 is still not an easy to handle tool to relate thermodynamic properties of the surface to measurable quantities. The main problem is to find appropriate expressions for the chemical potentials μ_i involved in the Gibbs adsorption equation. However, this problem may be overcome if we consider systems with less than three components at constant pressure. We will discuss these cases in more detail in the following sections.

3.1 Surface tension of pure liquids

For a single component liquid in equilibrium with its vapor at constant pressure eq. 15 reduces to

$$\frac{d\gamma}{dT} = -s^\sigma, \tag{16}$$

since the adsorption is zero by definition, $\Gamma_1 \equiv 0$.
Thus, the surface excess entropy can be easily obtained by the measurement of the temperature gradient of the surface tension. Since the entropy is always a positive quantity, one expects the surface tension of a liquid to decrease linearly with increasing temperature. This can be understood on a qualitative level by the fact that with increasing temperature the boiling point of the liquid is approached, where the surface and hence the surface tension ceases to exist. As an important example we have plotted the surface tension of pure water against temperature in Fig. 4 where the slope of the γ vs. T plot yields a surface excess entropy of $s^\sigma = 0.17$ mJm^{-2}K^{-1}. The amount of excess entropy per square meter of a flat water surface is thus about equivalent to the entropy gain by the evaporation of a water droplet of about 25 μL at ambient temperature.

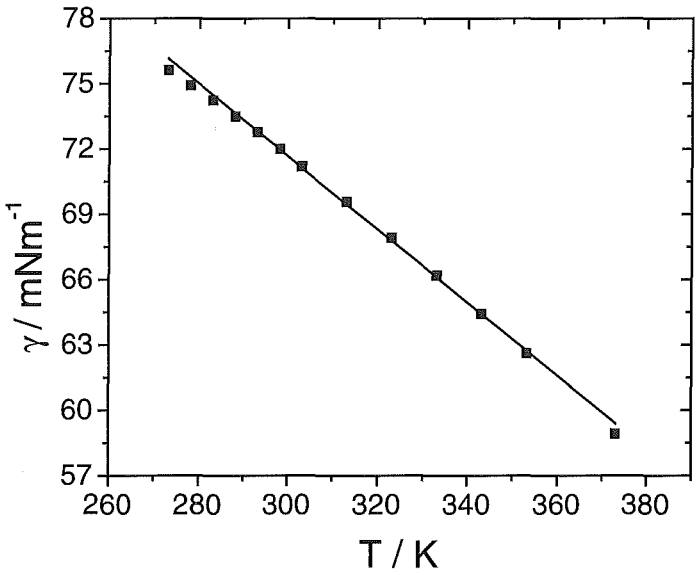


Fig. 4: *Temperature dependence of the surface tension of pure water. The symbols are experimental data and the full line represents a linear regression with a slope of* $\frac{d\gamma}{dT} = -0.17$ $mNm^{-1}K^{-1}$. *Data taken from reference [4].*

3.2 Surface tension of ideally dilute solutions

The next system to be discussed shall consist of two components, i. e. a solvent and a solute in equilibrium with the vapor phase. Even this appearingly simple system can be treated only applying certain approximations:

- The solution shall be ideally diluted. In this case, the chemical potential of the solute may be expressed in terms of Henry's law

$$\mu_2 = \mu_2^{\ominus} + RT \ln x_2^A \tag{17}$$

  where $\mu_2^{\ominus}$ is the standard value of the solute chemical potential and x_2^A is it's molar fraction. R is the gas constant.

- The solute shall be contained only in the liquid phase such that the value of x_2^A is always equal to the experimentally preset value.

With these approximations the adsorption equation for a two component system can be rewritten as

$$d\gamma = -s^{\sigma} dT - \Gamma_2^{\sigma} d\left(\mu_2^{\ominus} + RT \ln x_2^A\right), \tag{18}$$

which allows the determination of the surface excess entropy and the adsorption of the solute.
At constant temperature the variation of the surface tension with composition is given as

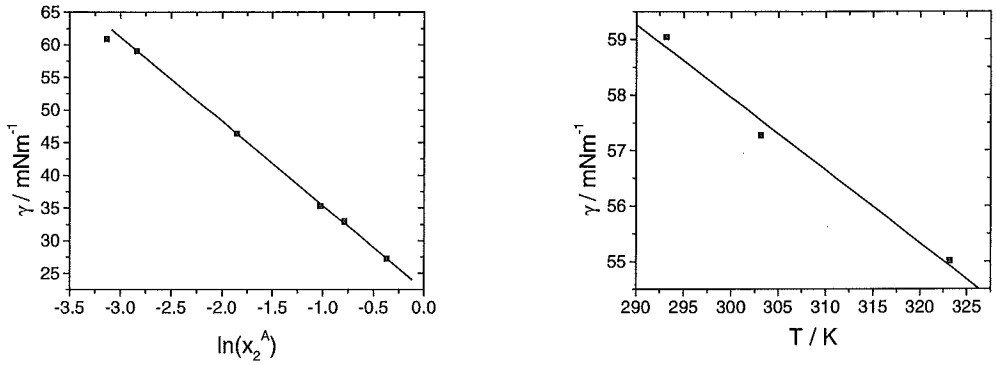


Fig. 5: *Surface tension data from solutions of Methanol in water. Left: Surface tension as a function of the solute molar fraction. The symbols are experimental data and the full line represents a linear regression with a slope of* $\frac{d\gamma}{d\ln x_2^A} = -12.43\ mNm^{-1}$. *Right: Temperature dependence of the surface tension. The symbols are experimental data and the full line represents a linear regression with a slope of* $\frac{d\gamma}{dT} = -0.1313\ mJm^{-2}K^{-1}$. *Data taken from reference [4].*

$$\left(\frac{\partial\gamma}{\partial x_2^A}\right)_T = -\Gamma_2^\sigma RT \left(\frac{\partial \ln x_2^A}{\partial x_2^A}\right)_T \tag{19}$$

Accordingly the surface tension is expected to decrease linearly with increasing $\ln x_2^A$ at constant temperature, and the adsorption of the solute may be calculated from the slope by

$$\Gamma_2^\sigma = -\left(\frac{\partial\gamma}{\partial \ln x_2^A}\right)_T (RT)^{-1}. \tag{20}$$

In left part of Fig. 5 the surface tension of a solution of methanol in water is displayed as an example. The surface excess amount of methanol at 25 C°is $\Gamma_{MeOH}^\sigma \approx 5 \cdot 10^{-6}$ mol/m^2, which corresponds to an average area per molecule of $A_{MeOH} \approx 33$ Å^2.
On the other hand the temperature gradient of the surface tension at constant solution composition is given by

$$\left(\frac{\partial\gamma}{\partial T}\right)_{x_2^A} = -s^\sigma - \Gamma_2^\sigma R \ln x_2^A \tag{21}$$

As shown in the right part of Fig. 5 the surface tension of an aqueous methanol solution depends linearly on temperature with a slope of $\frac{d\gamma}{dT} \approx -0.13$ mJm^{-2}K^{-1}. The second term in eq. 21 may be interpreted as an entropy loss due to adsorption. However, if we calculate this term introducing the value for the adsorption of methanol, it turns out to be much smaller than the total value of $\left(\frac{\partial\gamma}{\partial T}\right)_{x_2^A}$ even for very small molar fractions of the solute. Thus, also in the case of two component solutions the temperature gradient of the surface tension may be used as a good approximation for the surface excess entropy.

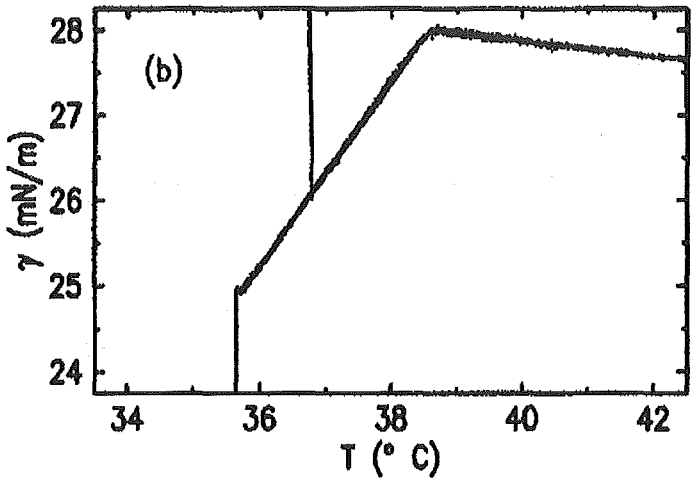


Fig. 6: *Temperature dependence of the surface tension of eicosan. Note the change of sign of the slope about two K above the freezing point of the melt. In this temperature range the surface excess entropy is negative (reproduced from reference [5].*

4 Two dimensional phase transitions

We have seen in section 3.1 that the surface tension of a simple liquid is expected to decrease linearly with increasing temperature. However, as displayed in Fig. 6 it may occur that the temperature gradient of the surface tension becomes positive upon cooling close to the freezing point of the liquid [5]. In a single component system at constant pressure the temperature gradient of the surface tension is equivalent to the temperature gradient of the surface excess free energy g^σ.

$$\frac{\partial \gamma}{\partial T} = \frac{\partial g^\sigma}{\partial T} \tag{22}$$

However, a discontinuous change of the temperature gradient of the free energy is a clear sign for a first order phase transition.

The change of surface excess entropy assigned with this phase transition is $\Delta s^\sigma = 1.16$ $\mathrm{mJK^{-1}m^{-2}}$, if we go from the low temperature phase to the high temperature phase, which is typical for an order $\rightarrow$ disorder transition. Since the system is still liquid in the bulk, it shall be assumed for the moment that the transition takes place only in a molecular monolayer at the surface. Taking into account the effective area of an chain, which is $A_{C20} \approx 18$ Å^2, we may than calculate the molar entropy change of the transition $\Delta s^\sigma_{molar} = \Delta s^\sigma A_{C20} N_A = 126$ $\mathrm{Jmol^{-1}K^{-1}}$. This value corresponds roughly to the molar entropy change assigned with the melting of the eicosan rotator phase, $\Delta S_{molar} = 139$ $\mathrm{Jmol^{-1}K^{-1}}$ [6]. This correspondence is a qualitative confirmation of the working hypothesis that the phase transition should take place only in a molecular monolayer at the surface. However a sound proof has to be obtained by methods, which are structure sensitive on a molecular level. This will be discussed in the next section.

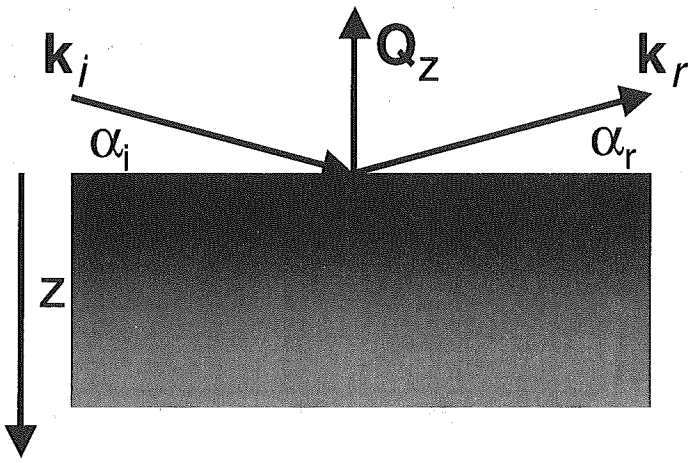


Fig. 7: *Scattering geometry for specular reflectivity measurements.*

5 Structure determination in surface films

5.1 Surface sensitive x–ray scattering

As discussed in the preceding section the surface of a liquid may undergo an disorder/order transition leading to a two dimensionaly ordered film, while the sample bulk remains in a disordered liquid state. Powerful tools for the structural investigation of such 2D–films on a molecular level are surface sensitive scattering methods, namely x–ray (XR) and (GIXD) experiments [7]. In an XR-experiment an x–ray beam of wavelength λ and intensity I_0 hits the surface under a small angle α_i, which is typically varied from about zero to less than 3°. Below a critical angle α_c the x–ray beam will be totally reflected, while for $\alpha_i \geq \alpha_c$ the incident beam is partially refracted into the sample volume and partially it is reflected. The intensity reflected under specular conditions ($\alpha_i = \alpha_r$), I_{spec}, is recorded in dependence of the angle of incidence and normalized to the incident intensity to yield the specular reflectivity $I_{spec}/I_0 \equiv R(Q_z)$ as a function of the wave vector transfer perpendicular to the surface $Q_z \equiv \mid \mathbf{k}_r - \mathbf{k}_i \mid = 4\pi \sin\alpha/\lambda$. Here $\mathbf{k}_i$ and $\mathbf{k}_r$ are the wave vectors of the incident and the reflected beam as depicted in Fig. 7. Since in this particular geometry only scattering vectors normal to the surface are probed, $R(Q_z)$ is the Fourier–transform of the electron density profile perpendicular to the surface $\rho_e(z)$. In the case of ordered surface layers this profile can be interpreted in terms of thickness and lateral electron density of the film.
The effect of various electron density profiles $\rho_e(z)$ on the specular reflectivity is displayed in Fig. 8. For a simple step–like profile, where the electron density jumps from zero to the bulk value $\rho_{e\infty}$ the reflectivity decays monotonically following

$$R_F(Q_z) = \mid \frac{Q_z - \sqrt{Q_z^2 - Q_c^2}}{Q_z - \sqrt{Q_z^2 - Q_c^2}} \mid^2 \qquad (23)$$

where Q_c is the scattering vector corresponding to α_c. A layer with enhanced electron density of thickness d on top of the sample will cause undulations in the reflectivity curve.

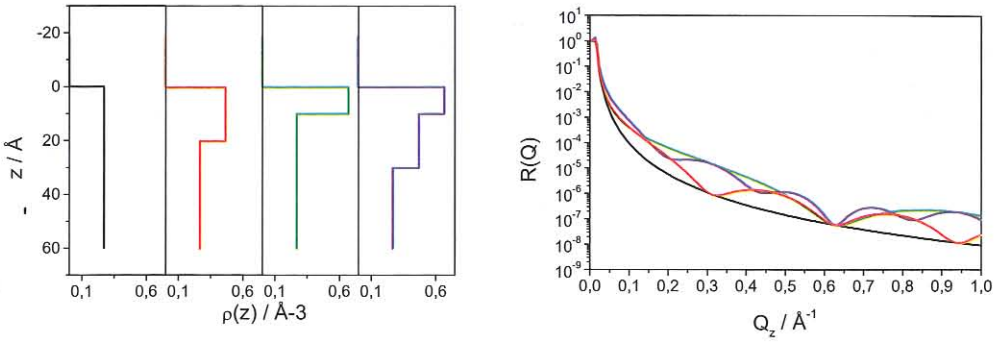


Fig. 8: *Left: Model profiles of the electron density. Right: Resulting reflectivity curves.*

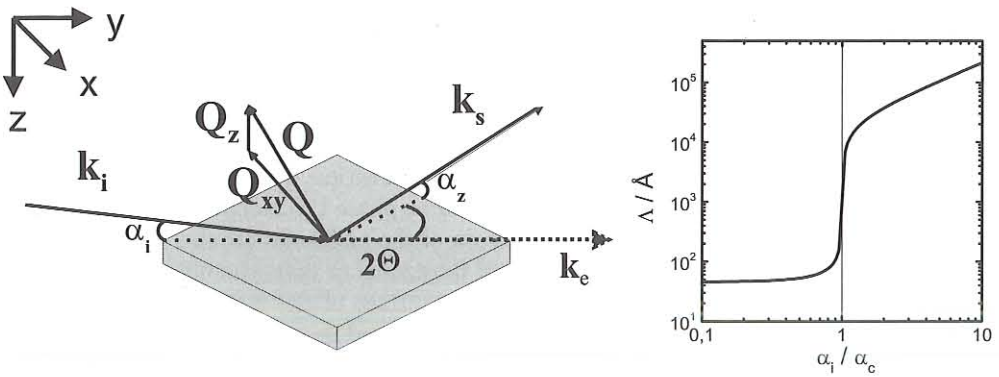


Fig. 9: *Left: General scattering geometry of a GIXD–experiment. Right: Penetration depth of x–rays into water as a function of the angle of incidence.*

While the amplitude of these undulations is related to the the difference $\rho_e - \rho_{e\infty}$, the distance between two adjacent minima is roughly given by $\Delta Q_z \approx 2\pi/d$.

5.2 Grazing incidence x–ray diffraction

If the primary beam impinges on the surface with an angle of incidence smaller than a critical angle α_c, occurs, because the refractive index of condensed matter is smaller than unity for x–rays. Under this condition the transmitted beam degenerates to an evanescent wave, which propagates paralell to the surface in the direction of the projection of the incident beam onto the surface. The intensity of the is damped exponentially in the direction of the surface normal. As to be seen from Fig. 9 the $1/e$ Λ is in the range of 50 to 100 Å for water. Thus, a scattering experiment, which uses the evanescent wave as the incident beam, will be sensitive only to structures within a thin layer close to the sample surface. This effect is exploited in GIXD experiments, which allow to study regular two dimensional structures on a surface by Bragg–diffraction. The scattering geometry of a GIXD–experiment is sketched in Fig. 9

The scattering vector is then $\mathbf{Q} \equiv \mathbf{k}_s - \mathbf{k}_e$, where $\mathbf{k}_e$ is the wave vector of the evanescent wave. $\mathbf{Q}$ is usually separated into a part perpendicular to the surface $\mathbf{Q}_z$ and a part

parallel to the surface $\mathbf{Q}_{xy}$. In a GIXD-experiment the scattered intensity is mapped in these two dimensions. In most cases data can be analyzed to a fair level of accuracy using the routines, which have been developed in the field of GIXD–experiments from Langmuir–monolayers [7, 8]. There the molecules making up the film are regarded as cylindrical bodies, the centers of mass of which are arranged in a two dimensional array with hexagonal or centered rectangular unit cells. These structures cause scattering patterns with sharp peaks in the xy–direction, which have a comparatively broad distribution of scattered intensity in the z–direction along so called as is shown in Fig. 11. The Bragg–spacing, d, of the two dimensional lattice can be calculated from the Q_{xy}–positions of the maximum scattered intensity using the familiar Bragg–condition $Q_{xy} = 2\pi/d$. Further, the Q_z–positions of the maxima allow the determination of and directions of the cylindrical units. However, this topic will not be addressed in the present lecture.

5.3 2D–crystalline monolayers at the surface of pure alkanes

As discussed in section 4 the melt of eicosan (and other long chain hydrocarbons [5]) shows a two dimensional order/disorder transition at the surface at a temperature T_s some K above the bulk freezing point T_f of the alkane. Surface tension measurements indicate that this phase transition is structurally related to the transition from the so–called rotator phase of alkanes to the isotropic melt. In this rotator phase the mobility of the molecular segments is high enough to allow for the rotation of the molecules around their long axis, while their centers of mass are still fixed on an hexagonal or orthorhombic lattice. If this rotator phase is formed upon cooling first at the surface of the melt, one might expect a molecular to form, in which the molecules are arranged as cylindrical bodies in a two dimensional solid–like lattice. This leads to an enhancement of the electron density in the monolayer with respect to the bulk value, which can be detected by x–ray reflectivity. In Fig. 10 two reflectivity curves from an eicosan surface are shown. The first was recorded at a temperature above T_s and shows a monotonic decay, while the second, which was recorded between T_s and T_f shows the undulations, that are typical for a layer of enhanced electron density.

According to the electron density profile displayed in the inset the thickness of the layer is about 25 Å, which is comparable to the length of a fully extended eicosan chain, $l_e \approx 28$ Å. The electron density in the layer of $\rho_e = 0.31$ Å^{-3} is also in very good agreement with the data from crystalline hydrocarbons. Hence, the reflectivity data imply that eicosan molecules in the monolayer are standing upright on the surface and are arranged in a closed packed quasi crystalline array, which has than to have hexagonal symmetry.

This implication is confirmed by the two–dimensional GIXD–pattern from such a monolayer, which is shown in Fig. 11. There is only one first order Bragg–rod observed, which has it's maximum intensity at $Q_z = 0$, which is a clear proof for the structure described above. (For details on the data evaluation of GIXD–pattern the reader is referred to reference [8].) The Bragg–spacing in the xy–plane is $d = 2\pi/Q_{xy} = 4.16$ Å,which results an effective area per molecule of $A_{C20} = d^2 2/\sqrt{3} = 19.76$ Å^2. The working hypothesis originally implied by surface tension experiments, that eicosan forms a mono molecular layer at the surface in the temperature interval $T_f < T < T_s$, which is structurally related to the bulk rotator phase, was thus confirmed. In the next section we will discuss the application of surface sensitive x–ray scattering to the investigation of adsorbed layers of a surface active component at the surface of a solution.

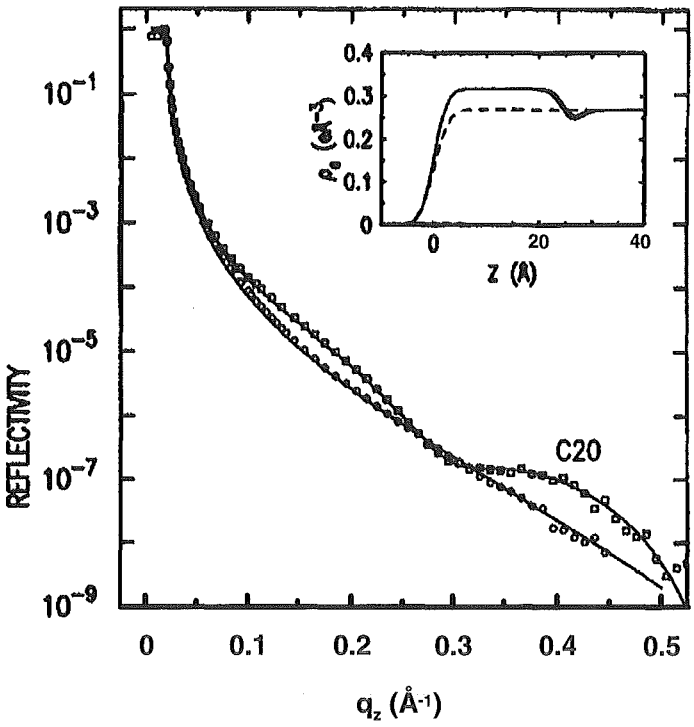


Fig. 10: *X–ray reflectivity from the surface of eicosan (reproduced from reference [5]). Symbols are experimental data, $T > T_S$ (○), $T_f < T < T_s$ (□), and the lines are theoretical curves calculated from the electron density profiles shown in the inset (high T dashed, low T full).*

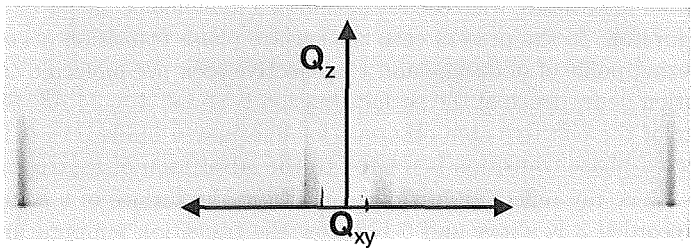


Fig. 11: *Two dimensional diffraction pattern from a monomolecular surface layer of 2D–crystalline eicosan on top of bulk liquid eicosan. (The intensity monitored at small Q_{xy} are remnants of the specularly reflected beam)*

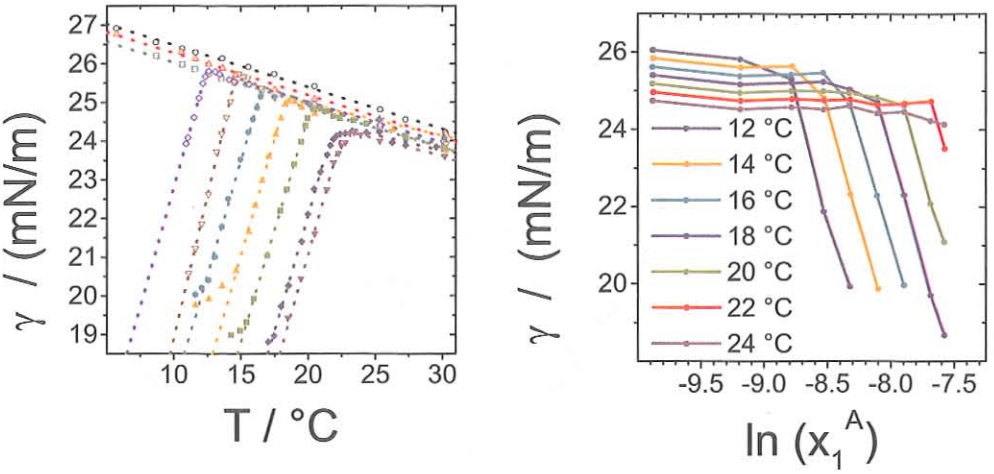


Fig. 12: *Left: Temperature dependence of the surface tension of $F_{12}H_{18}$ solutions in dodecane with various concentrations of the amphiphile. Right: Concentration dependence of the surface tension at different temperatures.*

5.4 2D–crystalline monolayers of amphiphiles adsorbed at the surface

After having discussed deviations from common the surface behavior of pure liquids in the last section, we will now proceed to two component systems by adding to alkanes. These components further denoted as F_mH_n consist of a hydrocarbon chain with n carbon atoms, which is covalently linked to a fully fluorinated carbon chain with m carbon atoms. Due to the mutual imiscibility of the two moieties the perflouroalkylalkanes act as nonpolar amphiphiles. Fig. 12 shows surface tension data of a solution of $F_{12}H_{18}$ in dodecane [9, 10]. These data can be analyzed according to the procedure described in sections 3.2 and 4. Like in the case of pure eicosan the γ vs. T–curves are indicative of a first order surface phase transition. And the entropy change $\Delta s^\sigma \approx 1.1$ mJm^{-2}K^{-1} assigned with the transition is in the range of the value observed for eicosan. One might therefore speculate that we are dealing with the formation of a monomolecular layer of dodecane at the surface. However, in the present case the surface phase transition occurs about 20 K above the freezing point of dodecane and the effective area per molecule calculated from the concentration dependence of the surface tension is about $A \approx 34$ Å^2. Since this value is in the range of the effective area observed for fluorinated lipids [11], it is rather likely that the observed phase transition is related to the adsorption of $F_{12}H_{18}$ at the surface.
Fig. 13 shows the x–ray reflectivity experiments from the surface of a solution of $F_{12}H_{18}$ in dodecane recorded 3 K above and 3 K below the transition temperature. To amplify the differences between the curves they were normalized to the Fresnels–reflectivity from an ideal dodecane surface. In the inset the corresponding electron density profiles $\rho(z)$ are plotted. At high temperature the transition from the electron density of the vapor phase ($\rho_e \approx 0$ Å^{-3}) to the value of the bulk phase ($\rho_e \approx 0.27$ Å^{-3}) is almost step–like. Below T_f however, the profile exhibits a very pronounced maximum, the width of which is approximately 50 Å, which is larger than the length of a fully extended $F_{12}H_{18}$ molecule,

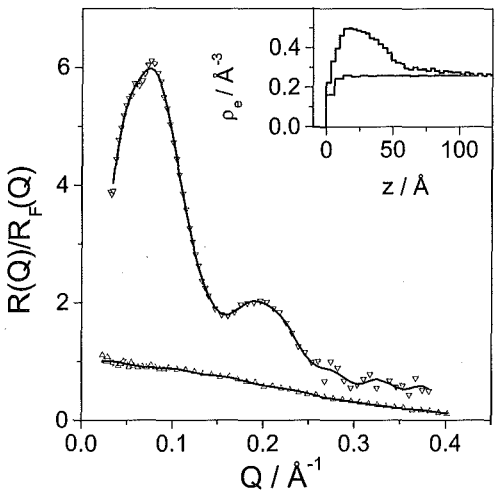


Fig. 13: *Normalized reflectivity from the surface of a solution of $F_{12}H_{18}$ in dodecane recorded at 3 K above C (△) and 3 K below (▽) the transition temperature (reproduced from reference [9]). The inset shows the corresponding electron density profiles.*

$l_e \approx 40$ Å. The maximum height of the profile is $\rho_{max} \approx 0.5$ Å^{-3}, which is intermediate between the value for a close packed hydrocarbon layer $\rho_H = 0.31$ Å^{-3} and the value expected for close packed fluorocarbon chains, $\rho_F = 0.67$ Å^{-3}. On the other hand the integral electron density is in very good agreement with the value for a model monolayer of $F_{12}H_{18}$. This suggests that the surface is completely covered by the amphiphile, but the molecules are only weakly ordered in their longitudinal direction. This will also perturb the ordering in the lateral direction, since the fluorinated part has a much larger effective area than the hydrocarbon part, which can be tested by GIXD. Fig. 14 shows the corresponding GIXD–data.

In the right part the scattered intensity at constant in–plane scattering vector Q_{xy} integrated for $0 \leq Q_z \leq 0.1$ Å^{-1} is plotted versus Q_{xy}. Above the phase transition temperature, the intensity falls monotonously with increasing scattering vector except for a broad halo at $Q_{xy} \approx 1.37$ Å^{-1}, which is typical for fluid n-alkanes[12]. At $T < T_s$ a distinct diffraction peak appears at $Q_{xy} = 1.266$ Å^{-1}. Since only a single peak occurs, the scattering centers have to be arranged in a two dimensional array with hexagonal symmetry. Concerning the results of the reflectivity experiments it is obvious that the uppermost part of the surface layer consists of fluorinated chains. It is therefore quite likely that the F_{12}–units are standing perpendicular on the surface and are hexagonally packed in the direction parallel to the surface with a lattice spacing of $d = 4.96$ Å, which is only about two percent larger than the corresponding value in the bulk state of $F_{12}H_{18}$ [13]. Accordingly, the area of the two dimensional unit cell is$A_{F_{12}H_{18}} = 28.4$ Å^2, which appears to be in contradiction to the results of surface tension measurements where significantly higher molecular areas have been deduced. However, as indicated by the reflectivity experiments the system is probably only weakly ordered. This assumption may be verified analyzing the width of the diffraction signal,which may be regarded as a measure for the positional correlation length ξ, which is given by $\xi = 0.9\lambda/(\text{fwhm}\cos\theta) = 22$ Å [14]. Thus the layer

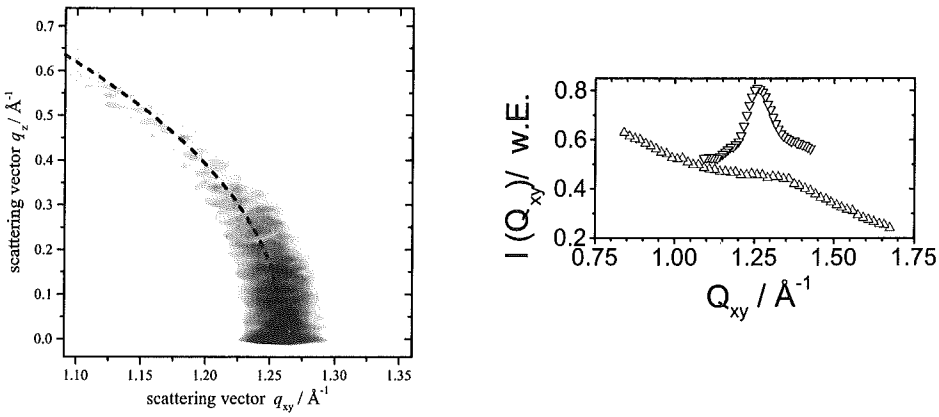


Fig. 14: *Left: Two dimensional contour plot of the GIXD–intensity from the surface of a solution of $F_{12}H_{18}$ in dodecane recorded at 3 K below the surface phase transition temperature. Right: Intensities integrated over $0 \leq Q_z \leq 0.1$ Å^{-1} at constant Q_{xy} 3 K above C ($\triangle$) and 3 K below ($\triangledown$) the transition temperature. (reproduced from reference [9])*

is indeed only very weakly ordered, the reason for which may be understood considering the left part of Fig. 14. There the scattered intensity is mapped in a two dimensional contour plot. The intensity is scattered into a circle like band around the coordinates origin, the radius of which is $\sqrt{Q_{xy}^2 + Q_z^2} = 1.266$ Å^{-1}. The reason for this radial distribution of scattered intensity is the fact that the alkyl parts of the PFAA have to be tilted with respect to the surface normal (see Fig. 15) in order to accomodate the difference of cross sections of the two parts the molecule consists of. Further it is very likely that there is no exact tilt angle but rather a distribution of tilt angles and azimuth angles [9, 10].
Thus, the scattering experiments show, that the perflouroalkylalkaneforms a molecular monolayer at the surface of the solution, which is densely packed at a short length scale. At larger scale a large amount of defects occur, which lead to the discrepancy between the molecular area detected by surface tension and scattering experiments respectively.

6 Conclusions

In the present lecture we have discussed the thermodynamics of fluid surface. We have seen that surfaces are characterized by excess quantities. From surface tension measurements surface excess entropy and adsorption may be determined, which contain information about two dimensional phase transitions and the two dimensional structure of surface layers. However, these information have to be confirmed and refined by structure sensitive measurements, namely surface sensitive scattering techniques

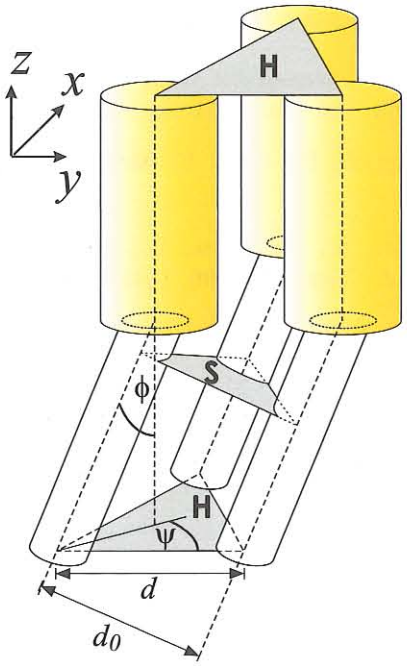


Fig. 15: *Model sketch for the arrangement of $F_{12}H_{18}$ in the 2D–crystalline layer at the surface of a dodecane solution (reproduced from reference [9]). Yellow cylinders represent the fluorinated parts of the amphiphile.*

References

[1] For an overview see Rowlinson, J. S.; Widom, B. *Molecular Theory of Capillarity*, Clarendon Press, Oxford 1992.

[2] Fisk, S.; Widom, B. *J. Chem. Phys.* **50**, 3219 (1969).

[3] Gibbs, J. W. *Trans. Conneticut Acad.* **3**, 108 (1875).

[4] *Handbook of Chemistry and Physics*, Vol. 53 CRC-Press, Cleveland 1973.

[5] Ocko, B. M.; Wu, X. Z.; Sirota, E. B.; Sinha, S. K.; Gang, O.; Deutsch, M. *Phys. Rev. E* **3164**, 55 (1997).

[6] Timmermans. J. *Physico-Chemical Constants of Pure Organic Compounds* American Elsevier, New York, 1965; Poser, C. I.; Sanchez, I. C. *J. Coll. Interf. Sci.* **69**, 539 (1979).

[7] for a review see Als-Nielsen, J.; Jacquemain, D.; Kjær, K.; Leveiller, F.; Lahav, M.; Leiserowitz, L. *Physics Reports* **246**, 251 (1994). or Lang, P *Amphiphiles at Interfaces Studied by Surface Sensitive X–Ray Scattering* in *Modern Characterization Methods of Surfactant Systems; Surfactant Science Series Vol. 83*, Binks, B. P. (Ed.) Marcel Dekker Inc., New York 1999.

[8] for a brief introduction see Kjær, C. *Physica B* **198**, 100 (1994).

[9] Marczuk, P. *Struktur und Amphiphilie von Perfluoalkylalkanen*, Dissertation Technische Universität Berlin, Der Andere Verlag, Osnabrück,2000.

[10] Marczuk, P.; Findenegg, G. H.; Lang, P., Metha, S. Manuscript submitted to *J. Phys.Chem. B*

[11] Barton, S. W.; Goudor, A.; Bouloussa, O.;, Rondelez, F.; Lin, B.; Novak, F.; Acero, A.; Rice, S. A. *J. Chem. Phys.* **96**, 1343 (1992).

[12] Wu, X. Z.; Sirota, E. B.; Sinha, S. K.; Ocko, B. M., Deutsch, M. *Phys. Rev. Lett.* **70**, 958 (1993).

[13] Marczuk, P.; Lang, P. *Macromolecules* **31**, 9013 (1998).

[14] Warren, B. E. *Dover Publications*, New York, 1990.

B 12 Single Membranes and Vesicles

H.-G. Döbereiner
Max-Planck-Institut für Kolloid- und Grenzflächenforschung
Am Mühlenberg, 14476 Golm, Germany

Contents

1 Introduction 2
1.1 Amphiphiles and Vesicles . . . 2
1.2 Thermodynamic Considerations . . . 3
1.3 Vesicle Classification . . . 4

2 Material Properties 4
2.1 The Fluid-Gel Transition . . . 4
2.2 Thermo-Mechanical Parameters . . . 6
2.3 Transport Behavior . . . 8

3 Phase Contrast Microscopy of Fluctuating Vesicles 9

4 Bending Elasticity and Vesicle Shapes 13
4.1 The Area-Difference-Elasticity (ADE) Model . . . 13
4.2 The ADE Phase Diagram . . . 15

5 Membrane Interactions 24
5.1 Physical Chemistry of Membrane Curvature . . . 24
5.2 A Photochemical Morphology Switch . . . 27
5.3 Shape Transitions of Complex Membranes . . . 30

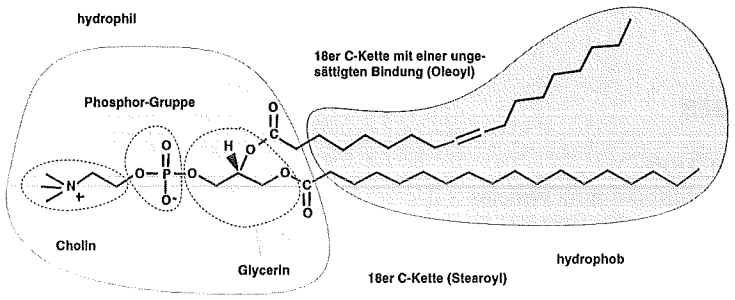
6 From Lipid- to Polymermembranes 34
6.1 Ultraviscous Membranes . . . 34
6.2 Non-Spherical Topologies . . . 36

1 Introduction

In this lecture, I will talk about some aspects of giant vesicles research. Rather than attempting to give an overview of this fascinating field [1, 2], which would necessarily be somewhat superficial due to the limited space and time available, let us concentrate on a few general concepts and specific examples. After introducing basic membrane properties, we cover bending elasticity and membrane morphology. Based on this material, the morphological response of fluid membranes to environmental changes can then be characterized and discussed in some depth. At the end, recent advances in polymer membrane physics will be presented.

1.1 Amphiphiles and Vesicles

Membranes are composed of amphiphilic molecules. One of the best studied classes are the phospholipids. These molecules are the main components of cellular membranes. A paradigmatic example, the lecithin Stearoyl-Oleoyl-Phosphatidyl-Cholin (SOPC) is shown in Fig. 1a.



a)

b) $H\,[-O-CH_2-CH_2]_{25}-[-CH(CH=CH_2)-CH_2-]_{30}\,H$

Fig. 1: *Structures of membrane forming molecules: (a) The phospholipid stearoyl-oleoyl-phosphatidyl-cholin and (b) the diblock-copolymer polybutadiene-b-polyethylenoxide.*

In phospholipid molecules, one or two of the hydroxyl groups of a glycerol backbone are linked to fatty acid chains, while the third hydroxyl is linked to phosphoric acid. The phosphate carries one of a variety of polar groups; in the example in Fig. 1a, it is a positively charged choline, which makes SOPC a zwitterionic molecule.
At ambient temperatures and in aqueous solution, phospholipids self-assemble into bilayer membranes, see Fig 2a. [3, 4] Usually, these double layer sheets are closed onto themselves to form vesicles in order to avoid large edge energies due to restructuring of phospholipid molecules shielding their non-polar hydrocarbon chains from water. In Fig 2b, a typical

picture of such a vesicle obtained with a phase-contrast microscope is shown. An important feature of these objects is the large ratio of their typical size to the thickness of the membrane. This large length ratio (10^6) endows giant vesicles with unusually soft elastic properties.
Another very interesting group of molecules forming membranes are amphiphilic diblock copolymers with suitable chain length and hydrophilic-to-hydrophobic component ratio. An example, polybutadiene(32)-b-polyethylenoxide(20) (PB-PEO), is shown in Fig. 1b, where the hydrophilic polyethylenoxide orients towards the water. Vesicles made from these molecules are - in analogy to liposomes - denoted polymersomes [5].

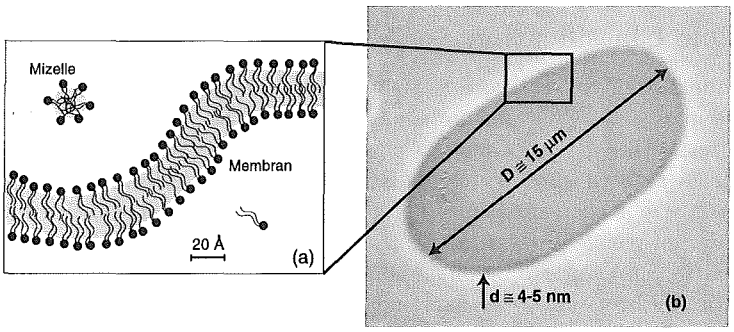


Fig. 2: *Cartoon of a bilayer membrane (a) and phase-contrast image of a giant vesicle (b). Double chain phospholipids like SOPC usually self-assemble into bilayer sheets and are generally very insoluble in water. For short chain lengths or single-chain lipids, formation of micelles is preferred. Due to the small thickness of the membrane, giant vesicles on the micro-meter length scale can be described as quasi-2-dimensional elastic surfaces.*

1.2 Thermodynamic Considerations

Giant vesicles composed of double chain phospholipids or specific diblock-copolymers are typically not in thermodynamic equilibrium with respect to the exchange of molecules with the bulk on experimentally relevant time scales. The reason for this is the low water solubility of these species. This is different from the equilibrium vesicle formation observed with single (short) chain surfactants [8]. These amphiphilic systems *are* in thermodynamic equilibrium and may form a bulk vesicle phase.
Most experiments and all theoretical models to be discussed are restricted to *Closed Vesicle Systems*, i.e., we consider single, isolated vesicles in thermodynamic equilibrium with respect to their mechanical degrees of freedom. In closed vesicle systems, the number of lipids in the membrane is taken to be constant. Conceptually, one should keep in mind that a vesicle is a finite object. In contrast, vesicles in full thermodynamic equilibrium with the bulk constitute an *Open Vesicle System.* [1] In this case, the bending elastic constants will depend on the bulk concentration of amphiphiles which determines the surface concentration [8].

[1] We note that the meaning of the term "Open System" is not uniquely defined in the literature. We adopt the nomenclature of [6] for equilibrium systems, whereas in [7], this term is used to denote a driven system out of equilibrium.

Open vesicle systems form a bulk vesicle phase, which may coexist with another amphiphilic phase of different morphology. These vesicles have an equilibrium size distribution and should not be considered as single objects on time scales longer than the exchange time of amphiphiles with the bulk and between the vesicles themselves. In mixed lipid vesicles, there is also the possibility that only one of the components is insoluble in water. Then, one can have a single isolated vesicle where the surface concentration of one or more components is set by the bulk concentration via the partition coefficient of the respective amphiphile. For example, double chain phospholipid vesicle with grafted hydrophilic polymers linked to a modestly hydrophobic membrane anchor belong to this class.

1.3 Vesicle Classification

Vesicles are roughly classified according to their size into small ($20 - 50$ nm), large ($50 - 500$ nm), and giant ($0.5 - 100$ μm) unilamellar vesicles. They are named SUV's, LUV's, and GUV's, respectively. Obviously, this classification is not very precise and it depends somewhat on the taste of the experimentalist where the boundaries are set. However, this classification in size is connected to the preparation method used, which allows a better characterization of vesicle properties.
Small vesicles may be prepared by ultrasonification of an aqueous suspension of lipid and water. Membrane sheets are torn apart and refuse during sonification. For double chain phospholipids, which are essentially unsoluble in water, this treatment leads to spherical vesicles with highly stressed membranes. Thus, specific properties of sonicated vesicles should not be generalized to more relaxed membrane systems at larger length scales.
The common preparation method for large vesicles is extrusion by high pressure through narrow pores with a defined diameter, which roughly sets the vesicle size. [9] The precise formation mechanism is, in fact, not well understood. Interestingly, vesicles obtained with this procedure are not spherical in general, but have flaccid shapes. The morphology of these systems has been taken into account only recently in the interpretation of light scattering data obtained with extruded vesicles [10]. Both SUV's and LUV's have more or less well-defined average bulk properties.
Finally, giant vesicles are prepared by gentle swelling of prehydrated membrane stacks [11] or via electroformation [12]. Whereas, the latter method produces quasi-spherical vesicles which are often connected to each other via thin lipid tethers, swelling of vesicles results in flaccid shapes with various morphologies. One advantage of electroformation is that one can produce huge vesicles within a few hours, whereas swelling leads to medium sized giant vesicle and is usually done over night. Due to the heterogeneity of giant vesicle preparations, GUV's should be considered as single objects. A general method, which would produce giant vesicles with a given shape and/or a narrow size distribution in large numbers, unfortunately, does not exist. Nevertheless, taken as an isolated object, a single giant vesicle may be very well characterized and studied, as we will see in the following.

2 Material Properties

2.1 The Fluid-Gel Transition

The hydrocarbon chain length and the number of double bonds along the chain determine whether phospholipids assembled in a membrane form a 2-dimensional fluid or a gel

[13]. The transition between these two states is called the main transition. Short chains and kinks induced by double bonds favour a low melting temperature T_M. Below this temperature, the oily chains adopt a more ordered configuration than above, see Fig. 3 [14]. The freezing of chain configurational degrees of freedom is usually coupled to a strong decrease in lateral mobility. [2] Cholesterol (CHOL) decouples these two processes in binary mixtures with lipids. One may have an ordered fluid phase, where the chains are frozen but maintain high lateral mobility [].

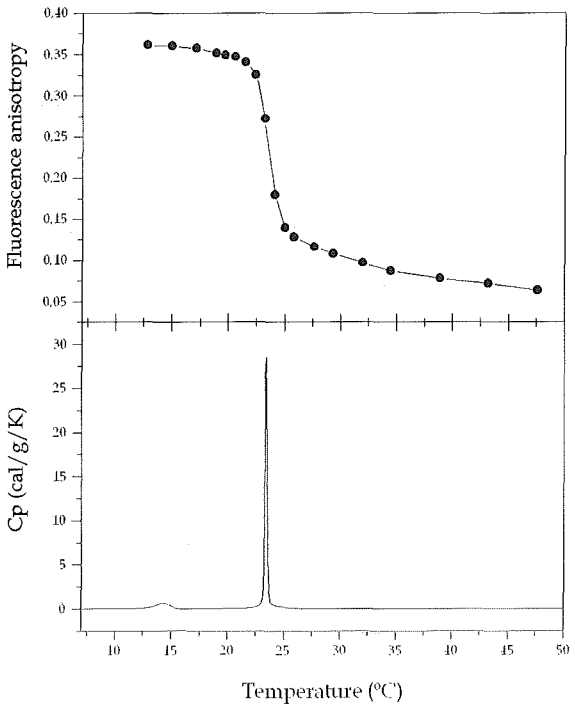


Fig. 3: *Fluorescence anisotropy* $A = (I_\parallel - I_\perp)/(I_\parallel + I_\perp)$ *(measured with* 0.5 *mol 1,6-diphenyl-1,3,5-hexatryene) and heat capacity* C_p *of 1 mM dimyristoyl phosphatidylcholine (DMPC) vortexed in 10 mM Hepes buffer at pH 7.4. Note the correlation of the melting peak in* C_p *with a gain in chain configurational mobility signaled by the decreasing anisotropy.*

Membranes formed by PB-PEO do not to show a fluid-gel transition in liquid water. The bilayer appears to be fluid down to 0° Celsius. At ambient temperatures, one stays favorably above the glass transition of polybutadien.

[2]Due to the quasi 2-dimensional membrane, the molecules do not form a regular crystal.

2.2 Thermo-Mechanical Parameters

We define now some relevant material parameters for fluid bilayer membranes and give their typical magnitudes.

Stretching Elasticity

Let us first consider stretching or compression of a membrane sheet from an equilibrium area A to a new area $A \pm \Delta A$. The stretching elastic modulus K is then defined by writing down the elastic energy density E_A in quadratic approximation

$$E_A = \frac{1}{2} K \left(\frac{\Delta A}{A}\right)^2 . \quad (1)$$

The numerical values for K are on the order of $10^2 - 10^3$ dyn/cm [13]. For SOPC, one finds $K = 200$ dyn/cm [11]; for PB-PEO we get $K = 470$ dyn/cm [15] from micropipette stretching experiments. Lipid membranes can be expanded only by about 3% to 5% percent [11] before they show material failure at a critical lysis tension $\tau_{lysis} = K(\Delta A/A)_{crit}$. Membranes typically lyse by opening up hydrophilic pores in the membrane [16]. The lysis tension for SOPC is found to be $\tau_{lysis} = 9$ dyn/cm. In contrast, polymer membranes can be stretched a few 10% percent before failure. They are considerably tougher with a higher lysis tension [5].

Bending Elasticity

We now turn to membrane bending. For a cylindrical deformation of a flat membrane, we can measure the curvature $c = 1/R$ by the radius$R$ of the deformed membrane cylinder. We assume full solution and monolayer symmetry across the membrane. Accordingly, we set the spontaneous curvature to zero, which makes the flat membrane the equilibrium configuration. The quadratic elastic energy density is then given by

$$E_B = \frac{1}{2} \kappa c^2 , \quad (2)$$

which defines the bending modulus κ. Its numerical value is found to be $\kappa = 0.9 \pm 0.06 \times 10^{-12}$ dyn cm for SOPC [17], which, in units of thermal energy, is the same as $\kappa = 22\ kT$ at $T = 298\ K$. The bending elastic modulus is generally on the order of 10 kT for all membranes. [13, 18] In deed, for PB-PEO we obtain $\kappa = 42\ kT$. Due to their small bending moduli, amphiphilic membranes show thermally induced fluctuations around their mechanical stable morphological configurations.

One may obtain an estimate of the bending modulus κ from the stretching modulus K by considering the relative stretching and compression of the two monolayers with the respect to the neutral surface of the membrane. [19, 20] For symmetric stretching moduli $K_m = K/2$ of the monolayers, the neutral surface of the membrane corresponds to the *bilayer* midplane. We measure the area of a *monolayer* at its respective midplane located at a distance $D/4$ from the bilayer center. The relative area change of a monolayer is then given by $\Delta A^m/A = \pm D/(4R)$. The total bending elastic energy of the bilayer E_B is obtained by summing up the stretching/compression contributions E_A^m, Eq. (1), from the

two monolayers as follows

$$E_B = 2\,E_A^m = \frac{1}{2}\,(2K_m)\left(\frac{\Delta A^m}{A}\right)^2 = \frac{1}{2}\left(\frac{KD^2}{16}\right)\frac{1}{R^2}\,. \tag{3}$$

We can thus define an effective bending modulus of the bilayer.

$$\kappa_e \equiv \frac{KD^2}{16}\,. \tag{4}$$

The essential physics is that the bending modulus κ_e is proportional to the stretching modulus K and scales with the square of the bilayer thickness D. The numerical coefficient depends on the location of the monolayer neutral surfaces, which we have taken to be a distance $D/2$ apart. In a more general calculation, one would allow for a stress distribution across the membrane instead of locating the forces at the monolayer midplane. Further, we have neglected the bending energy of the monolayers coming from the splay of the lipid molecules. This will actually contribute *equally* to the total elastic energy. In fact, both contributions, bending and relative stretching/compression of the monolayers, are incorporated in the area-differential-elasticity (ADE) model to be introduced in Sec. 4.1. Nevertheless, let us employ Eq. (4) to obtain an estimate of κ for SOPC. With $K = 200$ dyn/cm from above and a bilayer thickness of $D = 4\ nm$, we find $\kappa_e = 2\ \times 10^{-12}$ dyn cm, which agrees within a factor of two with the measured value, $\kappa = 0.9\ \times 10^{-12}$ dyn cm, for SOPC. For PB-PEO, which has a bilayer thickness of $D = 8\ nm$, the naive model gives less convincing results. Nevertheless, we see that the reason for the quite small bending modulus is the molecular scale thickness of the bilayer membrane. We note that generally, the modulus of an open vesicle systems is *smaller* then the corresponding closed system which has the additional constraint of fixed surface density of amphiphile.

Shear Elasticity

Above their gel-fluid transition, lipid membranes show no static resistance to shear. Below the gel-fluid transition, their shear modulus becomes finite.

Thermal Expansivity

The total membrane area A depends on the equilibrium molecular area a of the molecules in the membrane. This molecular area a is temperature dependent which leads to the definition of the thermal expansion coefficient of a membrane,

$$\beta_A \equiv \frac{1}{A_0}\frac{d\,A}{d\,T} = \frac{1}{a_0}\frac{d\,a}{d\,T}\,. \tag{5}$$

From pipette experiments [21], one gets a value $\beta_A = 3.3 \pm 0.7 \times 10^{-3/K}$ for SOPC. This value is consistent with measurements following the thermal expansion of a freely floating prolate vesicle. One finds $\beta_A = 2.7 \pm 0.1 \times 10^{-3}/K$ with a somewhat smaller experimental error. For PB-PEO, one obtains $\beta_A = 1 \pm 0.5 \times 10^{-3}/K$ with the latter technique.

Volume and Area Constraints

From the above considerations, it becomes clear that a giant vesicle in an aqueous medium has a fixed enclosed volume V and a constant membrane area A, at a given concentration of external solution and temperature T, independent of its shape.

In principle, there is a small amount of osmolarity difference which can be maintained across a curved membrane. It depends on the curvature scale and, thus, on the vesicle shape. This difference can be estimated by equating the change in bending energy E_B with volume V to the osmotic pressure [22], $\frac{\partial E_B}{\partial V} \simeq \frac{8\pi\kappa}{V} = RT\,\Delta n$, where R is the gas constant; T, the temperature; and Δn, the molarity difference. With $\kappa = 10^{-19}J$ and $V = \frac{4\pi}{3}(10\mu m)^3$, one finds at room temperature the extremely small number $\Delta n \simeq 10^{-10}$ mol/l. Thus, the volume is, in fact, constant during a change in shape, induced, e.g., by a variation in spontaneous curvature or membrane area.

The membrane area is a function of temperature, as explained above. The membrane area expansion coefficient, $\beta_A(SOPC) = 2.7 \pm 0.1 \times 10^{-3}/K$, is about an order of magnitude larger than the corresponding thermal volume expansion of water. One has $\beta_V(H_2O) \approx 3 \times 10^{-4}/K$. Thus, one may neglect the expansion of the enclosed water inside a vesicle compared to its membrane area expansion during an increase in temperature.

In summary, one can control vesicle volume by the concentration of the external solution, and membrane area by temperature.

2.3 Transport Behavior

Diffusion and Surface Viscosity

The diffusion constant D_f of lipid molecules in a fluid membrane is on the order of $1\ \mu m^2/s$. [13] Thus, for giant vesicles with a typical radius of $R = 10\ \mu m$, it takes about $t \sim R^2/D_f = 100\ s$ for one molecule to diffuse all over the vesicle surface. This shows that a fluid giant vesicle will exhibit, in fact, a *dynamic* shear viscosity, when deformed by the application of force on a time scale of a few seconds. However, the relevant dissipative mechanism is due to hydrodynamic friction. The situation is different for PB-PEO membranes, which exhibit a 500 times higher shear viscosity than those found in common phospholipids [15]. Here, the dissipation essentially occurs within the membrane.

Permeability

We close our brief compendium of membrane material parameters by noting the permeability coefficient of fluid membranes to water. One finds $P_{H_2O} \approx 1\ \mu m/s$ for lecithin bilayer vesicles. [23] Thus, these membranes are well permeable to water molecules. However, for charged ions or larger molecules, like simple sugars, the permeability drops by several orders of magnitude. [23, 24] Therefore, concentration asymmetry of a specific molecular species across the vesicle membrane can be maintained on experimentally relevant time scales. The total concentration in the vesicle interior, comprising all desolved molecules, adjusts by osmotically driven water flow to the concentration of the exterior solution. Depending on giant vesicle size, concentration equilibrium after osmotic shock is reached on a typical time scale on the order of a few seconds to minutes.

3 Phase Contrast Microscopy of Fluctuating Vesicles

Vesicles are thermally fluctuating objects. Thus, single snapshots of a vesicle shape do not allow to deduce specific properties of the vesicle under investigation. Instead, one has to perform a careful statistical analysis of a full shape ensemble.[3] In this respect, experimental conditions have to be stabilized and maintained over a time course of several hours. Experimental mean shapes and mean-square fluctuations can then be compared to theory in order to deduce the elastic parameters of the vesicle membrane.
Quantitative image analysis in real time using video phase contrast microscopy can be performed with a setup as shown in Fig. 4. Here, the external vesicle solution can be exchanged during observation of a single vesicle. Precise environmental control and real time data analysis were only achieved in recent years. The ability to do quantitative online analysis of the curvature response of a membrane to changing transmembrane asymmetry made it possible to follow new avenues and allowed to explore qualitative effects which would have been missed otherwise. In the following, we discuss the principle components of such experiments. More detailed descriptions may be found elsewhere [25, 26, 27].

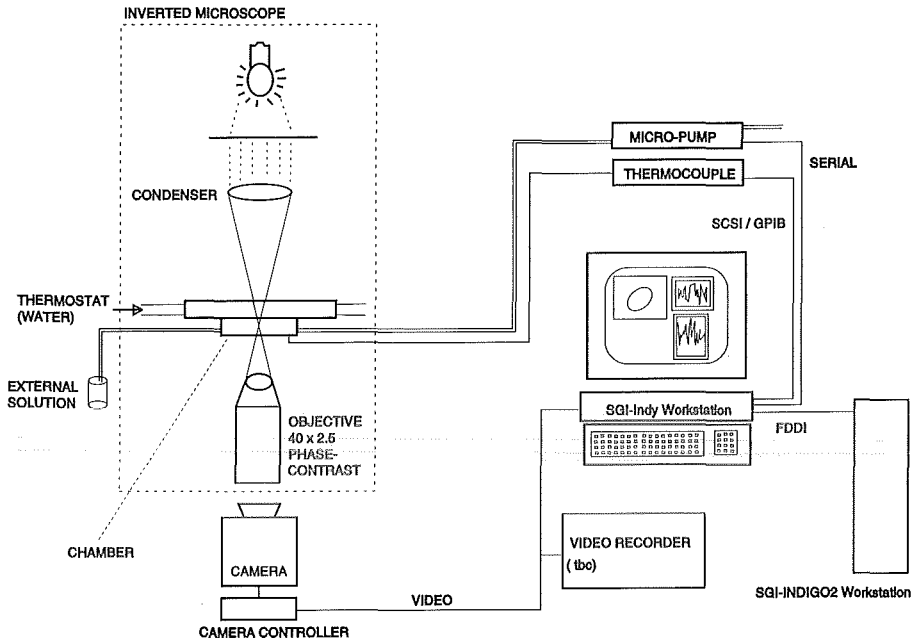


Fig. 4: *Experimental setup for Video Microscopy. Giant vesicles are observed in a thermostated micro-chamber using an inverted microscope equipped with phase-contrast optics. Image analysis and subsequent shape analysis is done in real-time on two SGI workstations.*

Our aim is to quantify the morphological response of a single vesicle under controlled changes in the external (or internal) solution and/or other system parameters, e.g., tem-

[3] We note that ensemble refers here to all the thermally accessible configurations of a *single* vesicle.

perature. In this respect, vesicle shapes are characterized by their maximal cross sections in the focal plane of a phase-contrast microscope. Vesicles are stabilized using gravity at the bottom of an observation chamber in order to record long time sequences of fluctuating shapes.

A micro-chamber where the outer solution can be exchanged *during* observation of a vesicle, is shown in Fig. 5). This chamber basically consists of a Teflon spacer sealed by a sapphire window on top and a common cover-slide on the bottom. Sapphire is used for the top window because of its high thermal conductivity, guaranteeing optimal thermal contact to a thermostat water cushion. Solution exchange is realized via two tubing ports connecting the chamber to a micro-liter pump and a liquid reservoir. Porous walls in the inlet path homogenize the flow. Pumping with typical rates of about 1 $\mu l/sec$ results in an almost homogeneous shear flow at the vesicle position with a shear rate on the order of 1 sec^{-1}. One observes that a) shear flow lifts the vesicles from the chamber bottom where they have accumulated due to gravity and b) even minute shear flow has considerable influence on the vesicle shapes. Stationary non-equilibrium shapes are generally quite different from the corresponding equilibrium shapes. Indeed, one sees oblate vesicles being deformed into prolates under shear flow. The first finding points to an effective hydrodynamic repulsion of the vesicles from the wall. As it is clear from the above remarks, equilibrium shape analysis should be done only *after* the solution has been exchanged and fluid flow has come to a complete stop. The described chamber-thermostat combination is mounted on the object table of an inverted microscope equipped with a CCD camera which directly passes the phase-contrast images of the vesicles to the video-board of a Unix workstation, see Fig. 4.

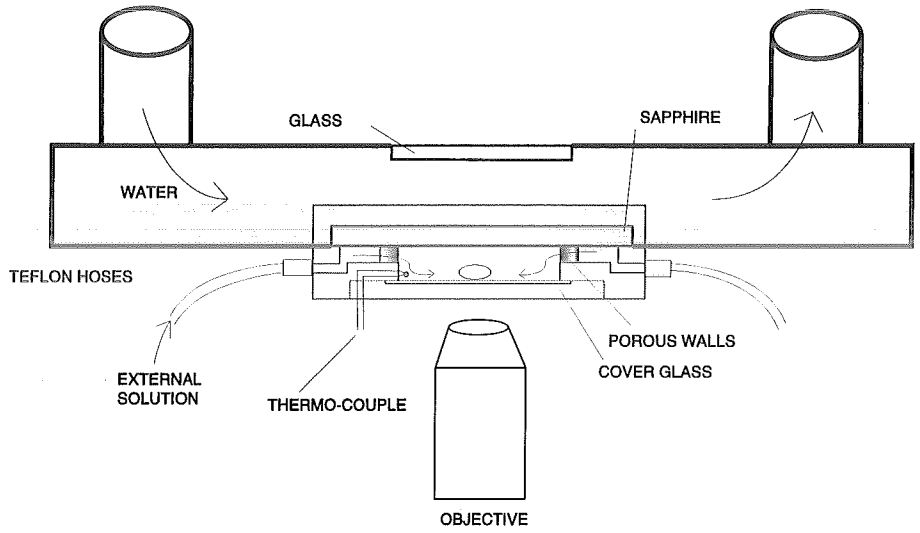


Fig. 5: *Environmental control chamber: Temperature* and *external vesicle solution can be changed according to the desired experimental protocol.*

Vesicle contours can be obtained from the video signal with a relative spatial resolution of a few ten nanometers. We note that it is the membrane position *not* its structure which

can be obtained with such a high precision; i.e., one monitors a shift of the diffraction pattern not the fine details of the pattern itself [25]. For the optical point resolution, the usual limits given by the wavelength of light and numerical aperture apply. In Fig. 6, the extraction of the position of a vesicle membrane along one video line is exemplified. All the membrane positions along the contour of a single vesicle snapshot at some moment in time constitute a closed 2-dimensional loop representing the basic data unit.

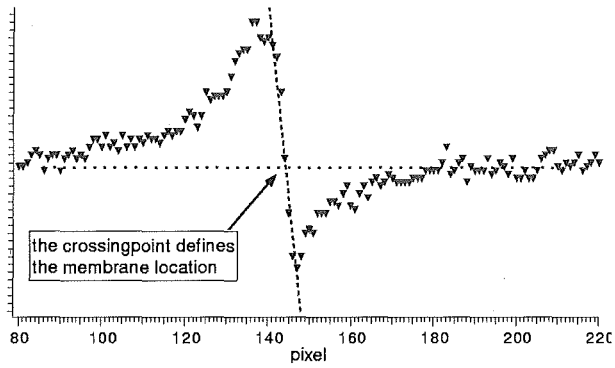


Fig. 6: *Greyvalues along a video line across the vesicle membrane showing a typical contour profile. The nominal membrane position is found by the crossing point of the steepest gradient with the local background value.*

Real Time Image Analysis

Experimental vesicle shapes are analyzed online with video frequency (25 frames/second). Online analysis includes the actual image analysis and subsequent Fourier transformation of the vesicle contours. The availability of these data during experiment allows to adjust the specific experimental protocol in order to optimize measurement of a particular feature.

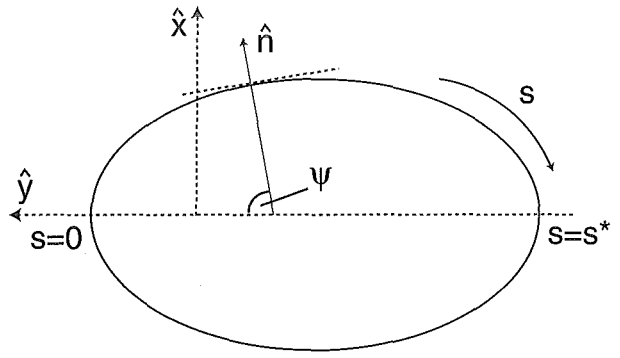


Fig. 7: *Illustration of the shape representation defined in Eq. (6).*

In order to perform Fourier transformation of the data, on has to choose a particular shape representation. Depending on vesicle geometry, several choices are possible. For nearly spherical vesicle, one usually employes polar coordinates with respect to the center of gravity of the vesicle contour. For strongly non-spherical vesicles, a polar representation leads to problems due to overhangs in the contour. In this case, one may find the long axis of the vesicle shape, which divides the contour in two segments. Then, a half-contour can be written in terms of its arclength s which starts at the north pole ($s = 0$) and ends at the south pole ($s = s^*$). A representation which will be convenient for our purposes is

$$\psi(s) = \pi\frac{s}{s^*} + \sum_{n=1}^{\infty} a_n \sin(n\pi\frac{s}{s^*}) \ , \tag{6}$$

where $\psi(s)$ is the angle between the polar axis and the outward-pointing normal to the curve, see Fig 7. For prolate vesicles, the amplitude a_2 is a measure of ellipticity, whereas a_3 describes a pear-shape like symmetry breaking. The spontaneous curvature of the vesicles is essentially encoded in the mean value of the amplitude a_4 [25], and as well in the mean-square fluctuations of the amplitudes a_2 and a_3. More generally, the bending modulus and the spontaneous curvature of the membrane may be obtained from the fluctuation spectrum of a prolate vesicle. In Fig. 8, an experimental example of the probability distribution of the amplitudes (a_2, a_4) is shown. A typical time series of the first two independent amplitudes (a_2, a_3) is documented in Fig. 9.

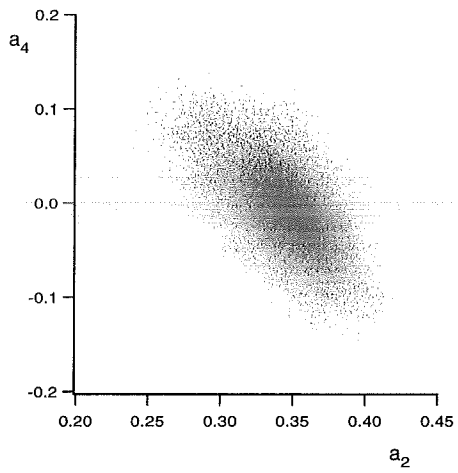


Fig. 8: *Experimental distribution of the contour amplitudes* (a_2, a_4). *Their mean values uniquely fix the theoretical shape parameters* $(v, \bar{c}_0)$. *The plot contains over* 53.000 *points corresponding to more than* 35 *minutes of real time data recorded at a rate of* 25 *video frames per second.*

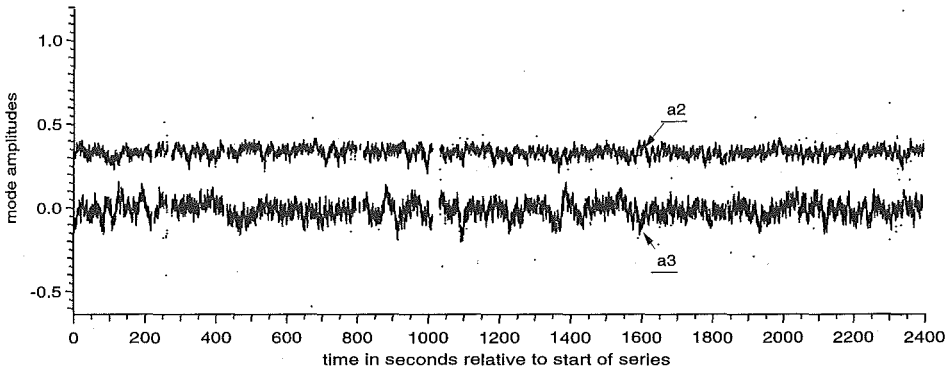


Fig. 9: *Typical experimental time series of the shape amplitudes a_2 (elliptical mode) and a_3 (pear mode) of a prolate vesicle as a function of time. The a_2 amplitude shows a finite mean value corresponding to the deviation from the spherical shape. The a_3 amplitude fluctuates around zero corresponding to a mirror symmetric mean shape with occasional larger pear fluctuations to either side.*

4 Bending Elasticity and Vesicle Shapes

4.1 The Area-Difference-Elasticity (ADE) Model

As we have seen, fluid bilayers respond elastically to mechanical deformations which include bending, and stretching or compression of the membrane [28, 29, 30]. There is no resistance to shear. The bilayer may be idealized as a quasi two-dimensional sheet consisting of two monolayers with separately fixed number of molecules. [4] As discussed in Sec. 2.2, it is much harder to stretch a membrane than to bend it. In building a theory for the morphology of membranes [19, 22, 31, 32, 33, 34], one can thus assume to a good approximation that the overall surface area of the membrane is fixed. However, the energetic contributions of the relative stretching and compression of the two monolayers, which arise when the membrane is bent, are of the same order of magnitude as the pure bending energy, which originates from splaying the molecules in the two monolayers (compare the discussion in Sec. 2.2). Therefore, there are two contributions to the bending energy of a closed bilayer: The bending of the two monolayers at fixed bilayer area A, and the relative stretching and compression of the monolayers. This implies a fixed mean area $A = (A^{out} + A^{in})/2$, but allows for changes in the differential area $\Delta A = A^{out} - A^{in}$. Thus, we have identified the geometrical quantities needed to formulate the expression for the bending energy: i) Local membrane curvature $C_i(r)$ along the two principal directions and ii) global area difference between the monolayers ΔA. It follows from differential geometry that the latter quantity is, to a good approximation, proportional to the integrated mean curvature of the vesicle

[4] We remind the reader that this implies we consider only membranes prepared from molecules which exhibit no flip-flop between the monolayers and are insoluble in water; compare the discussion in Sec. 1.2.

$$\Delta A = D \int dA(C_1 + C_2), \tag{7}$$

where D is the bilayer thickness. [5] This equation makes the connection between shape and differential area explicit. One finds for the total energy [19]

$$E_B = \frac{\kappa}{2} \int dA(C_1 + C_2 - C_0)^2 + \frac{\bar{\kappa}}{2} \frac{\pi}{AD^2} (\Delta A - \Delta A_0)^2, \tag{8}$$

where C_0 is the spontaneous curvature of the membrane, which accounts for a possible non-flat relaxed state of the bilayer, $\Delta A_0 = A_0^{out} - A_0^{in}$ is the difference of the unstressed monolayer areas, and κ and $\bar{\kappa}$ are the local and non-local bending moduli of the membrane. In the first term, one simply integrates the local deviations in mean curvature from the relaxed state over the whole vesicle area. The second term accounts for the difference between the actual geometrical area difference and the relaxed one, which would be preferred by the monolayers. This preferred differential area is proportional to the difference in the number of molecules: $\Delta A_0 = a_{lipid}^{out} N^{out} - a_{lipid}^{in} N^{in} \simeq \bar{a}_{lipid} \Delta N$. Both terms are quadratic and correspond to a generalization of Hooke's law for the spring to bending and differential area elasticity. The relative importance of the two contributions to the bending energy is measured by the ratio of the elastic moduli $\alpha = \bar{\kappa}/\kappa$. For $\alpha = 0$, there is no resistance to bending from differential area elasticity and one recovers the spontaneous curvature model [30]. For $\alpha \to \infty$, the geometrical area difference ΔA does not deviate from the preferred area difference ΔA_0 of the monolayers. The latter statement is the essence of the bilayer-couple hypothesis [35] which was formulated independently in the context of elasticity theory [28, 29, 36]. However, one estimates α to be on the order of one for all phospholipids [19]. This estimate is corroborated by measurements of this quantity [37]. Both terms are therefore important. Indeed, experiments on shapes and shape transitions of giant vesicles have shown that the general model is required to account quantitatively for the observations [25].

The relevant geometrical parameters controlled in experiment [25, 38, 39, 40, 41, 42] are the area and volume of the vesicles. Given a mean area per molecule, the membrane area can be considered fixed at constant temperature and constant number of molecules. The volume is controlled by the osmolarities of the inner and outer solutions due to the high water permeability of the membrane. Any osmolarity differences would lead to large osmotic forces inducing water flow through the membrane. It is thus the *permeability* of the membrane to water which keeps the enclosed water volume constant at given external osmolarity.

For a vesicle of radius $R_A = (A/4\pi)^{\frac{1}{2}}$, the area available for shape changes is measured by the dimensionless volume-to-area ratio

$$v = \frac{V}{(4\pi/3)R_A^3} \,. \tag{9}$$

This reduced volume v is scaled so that a sphere is characterized by unity, the maximal possible volume-to-area ratio for a geometrical object. Deflated vesicles have values

[5] The reader is invited to verify Eq. (7) for the simple case of a thin spherical shell.

smaller than one, and zero would correspond to an empty membrane bag without any aqueous content. The reduced volume v represents a convenient measure of the enclosed volume of a vesicle independent of size. Apart from this purely geometrical quantity one needs a parameter which describes the overall tendency of the membrane to curve. It is given by a dimensionless combination of the preferred area difference and the spontaneous curvature.

$$\overline{\Delta a_0} = \Delta a_0 + \frac{1}{2\pi\alpha} c_0, \tag{10}$$

where $\Delta a_0 = \Delta A_0/(8\pi D R_A)$ and $c_0 = C_0 R_A$ are scaled quantities. Again this scaling singles out the sphere. A spherical vesicle with radius R_A, a scaled spontaneous curvature $c_0 = 1$, and a scaled area difference $\Delta a_0 = 1$, is in a totally relaxed state with energy zero. It would have no differential area stresses and no bending stresses in its membrane. It is clear that this is a rather special situation. In general, a vesicle will be in a stressed state, it's morphology being determined by the most relaxed shape consistent with constraints imposed. The effective differential area $\overline{\Delta a_0}$ is reflecting the different sources of membrane curvature. Besides the ratio of the elastic moduli α, and the reduced volume v, it is the third relevant quantity for the classification of shapes. Vesicle shapes are obtained by minimizing Eq. (8) under the constraints of fixed area A and volume V [19]. In analogy to thermodynamics, minimal energy shapes can be placed in a two-dimensional phase diagram which is described in detail below.
The ratio of the elastic moduli α is given by the lipid system studied and is essentially fixed for each set of experiments. Although α is important for the topology of the phase-diagram, existing shapes and shape classes, in fact, do not depend on it. Thus, it is convenient to define the effective spontaneous curvature [25, 19]

$$\bar{c}_0 = c_0 \; + \; 2\pi\alpha \; (\Delta a_0 - \Delta a) \; . \tag{11}$$

This parameter fully characterizes the shape of a vesicle with reduced volume v. We note that Eq. (11) captures the physics of the two sources of preferred membrane curvature. Whereas c_0 is only a property of the vesicle membrane, the result of changing Δa_0 depends also on the reference shape via its integrated mean curvature which is proportional to Δa. A large preferred differential area Δa_0 greater than Δa tends to curve the membrane further outward, whereas a smaller value would lead to more invaginated shapes.

4.2 The ADE Phase Diagram

Overview

The shape of an individual fluid bilayer vesicle is obtained by minimizing the bending energy (8) given the geometrical parameters area A and volume V, as well as the material parameters, spontaneous curvature C_0, and preferred differential area ΔA_0. When these parameters are tuned externally, the shape changes. Different regions of the parameter space correspond to different classes of shapes. In Fig. 10, experimental examples of a stomatocyte and a discocyte vesicle are shown. Theoretically, these classes result from the existence of multiple solutions to the shape equations, derived by variational calculus from Eq. 8. At the boundary between those regions, shape transitions occur, which are manifested, for instance, in a change of symmetry or another shape attribute. The

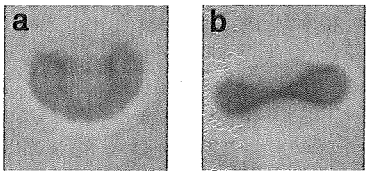


Fig. 10: *Example of a stomatocyte (a) and discocyte (b) vesicle. The discocyte was obtained from the stomatocyte by raising the effective spontaneous curvature via grafting of an amphiphilic polymer onto the outer monolayer from solution [43].*

bending modulus κ sets the overall energy scale. Its ratio α with the non-local bending modulus influences the relative energies between different shape classes, and, thus, the exact location and quality of the shape boundaries. However, the shapes themselves do not depend on α. In Fig. 11, the ADE phase diagram [19, 44, 45, 46] is shown for the typical value $\alpha = 1.4$. On the horizontal axis, the reduced volume v is plotted. The vertical axis shows the effective differential area $\overline{\Delta a_0}$. For medium values of $\overline{\Delta a_0}$, and not too small v, the stable shapes are prolate vesicles. The prolate phase extends into the upper left of the phase diagram in the form of long tubular vesicles, see Fig. 12. For large effective differential area, vesicles show generally an outward curved morphology, e.g., the budded shapes consisting of two-spheres, whereas for small values of the effective differential area, shapes are predominantly curved inward, e.g., the discocytic or stomatocytic vesicles. Lowest-energy shapes are illustrated for each region. As indicated for the prolate, all rotational symmetry axes are along the vertical $\overline{\Delta a_0}$-axis, except for the starfish-like vesicles which have a non-axisymmetric shape. This region intervenes between the prolate and oblate phase. Note that for medium to small reduced volume, the oblate vesicles resemble the biconcave form of the red blood cell. First-order boundaries (D), i.e., those where shapes change discontinuously, are indicated by solid lines; second-order boundaries (C,) where a particular shape symmetry is broken continuously, by dashed lines. Further, the pear and stomatocyte regions are bounded by limiting lines (L) which consist of two spheres connected by a neck with an infinitesimal radius. Beyond these lines and for small reduced volume, there is *terra incognita* which has not been studied in detail. Vesicle shapes may touch themselves along special self-adhesion lines (A) where membrane-membrane interactions have to be taken into account in addition to bending energy [47].
All the shapes and shape classes shown in the diagram have by now been seen in experiment [25, 39, 40, 45, 48]. However, only the prolate phase and its boundaries were studied systematically. In Fig. 13, a close-up view of the prolate region of the phase diagram is shown. In addition to the location of the phase transitions discussed above, the spinodals (M) [6] of the prolate phase are given and denoted by dotted lines. Prolate shapes are locally stable between the upper spinodal line M^{pro}_{odd} and the lower spinodal line M^{pro}_{even}. The lines $D^{pro/pear}$, $C^{pro/pear}$, $D^{pro/obl}$, and $D^{pro/nas}$ bound the region where prolates are the lowest-energy shapes. In the region immediately above $D^{pro/pear}$ lowest-energy shapes

[6] Spinodal lines delimit the regions of metastable shapes. At its respective spinodal, a particular shape becomes unstable to small perturbations and decays into the globally stable configuration. Due to thermal fluctuations, a spinodal line becomes somewhat fuzzy at finite temperatures, and vesicles decay already within a finite distance to the spinodal whenever the activation energy to overcome the elastic barrier is on the order of kT.

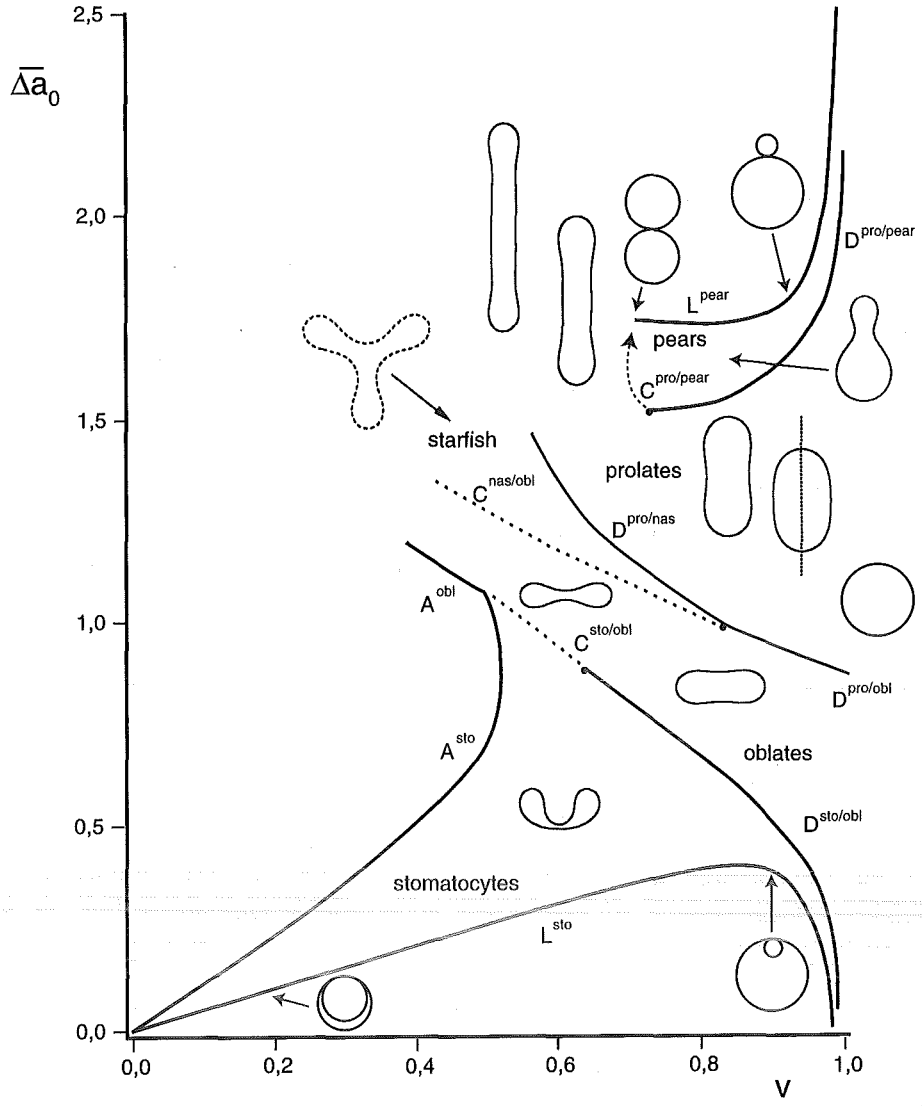


Fig. 11: *Phase diagram of the ADE model at $\alpha = 1.4$. For each region, lowest-energy shapes are indicated with their centers of gravity located at the corresponding position in the phase diagram. The horizontal axis gives a measure of the volume-to-area ratio expressed by the reduced volume v, whereas the vertical axis shows the effective differential area $\overline{\Delta a}_0$, i.e., the preferred curvature of the vesicles. For a full description, see Sect. 4.2.*

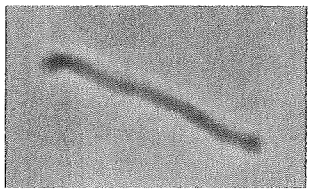


Fig. 12: *Example of a fluctuating tubular vesicle which belongs to the prolate phase.*

are pear-like. In the region immediately below the prolates, oblate and non-axisymmetric (nas) shapes have lowest energy. The endpoint E of the limiting line L^{pear} represents two spheres of equal radii connected by a infinitesimal neck. The point T on the prolate/pear phase boundary is a tricritical point. [7] CEP labels a special kind of a critical end point. [8] In the following, we will describe the expected theoretical features of the transitions out of the prolate phase and their experimental signatures.

The Budding Transition

Budding, where a small satellite is expelled from a larger vesicle, is a paradigmatic example of a morphological transition. During the last decade, it has attracted a lot of interest [25, 19, 38, 39, 42, 49]. The theoretical and experimental efforts to describe and characterize this transition have considerably improved our understanding of vesicle shapes and the theory of bending elasticity in general. Starting from a prolate vesicle, budding can be induced by raising temperature [25, 39] or by increasing spontaneous curvature directly via appropriate exchange of the external solution [50]. The transition is first-order on the right of the tricritical point T and second-order on the left. Indeed, for budding at small reduced volume, one observes a continuous symmetry breaking [38, 51]. Prolate vesicles loose their equatorial mirror-symmetry during budding and become gradually more pear-shaped. In contrast, for large reduced volume, prolate shapes become instable at the spinodal line M_{odd}^{pro} and spontaneously expel a small bud, see Fig. 17 [25, 49]. The approach to this instability is characterized by a strong increase in the pear-like fluctuations of the vesicles [42]. These spinodal fluctuations have long relaxation times and can easily be mistaken as stable pear shapes [38, 39]. In Fig. 14 and Fig. 15, a fluctuating prolate vesicle is shown at two different points in the phase diagram approaching the spinodal line of the budding transition, see Fig. 13.
The first sequence of fluctuating shapes (Fig. 14) is located within the stable prolate regime ($v = 0.937, \overline{\Delta a}_0 = 1.21$) [25]. At this point, the vesicle fluctuates around a prolate shape; subsequent frames are not visibly correlated. This situation changes near the budding instability, see Fig. 15. The shape parameters ($v = 0.907, \overline{\Delta a}_0 = 1.78$) [25] now place the vesicle within the meta-stable prolate region. The vesicle has crossed the first-

[7] In analogy to thermodynamics, this tricritical point separates a line of first ($D^{pro/pear}$) and second-order ($C^{pro/pear}$) phase transitions . At the first-order transition, there is a jump is the slope of the elastic bending energy as a function of the control parameter, e.g., $\overline{\Delta a}_0$. This corresponds to a discontinuous shape change. In contrast, at the second-order phase transition, there is a continuous change in slope, and the vesicles change their shape smoothly.

[8] At this critical end point, the first-order transition $D^{pro/obl}$ disappears, revealing a pair of transitions, one first-order ($D^{pro/nas}$) and one second-order ($C^{nas/obl}$), previously hidden beneath it.

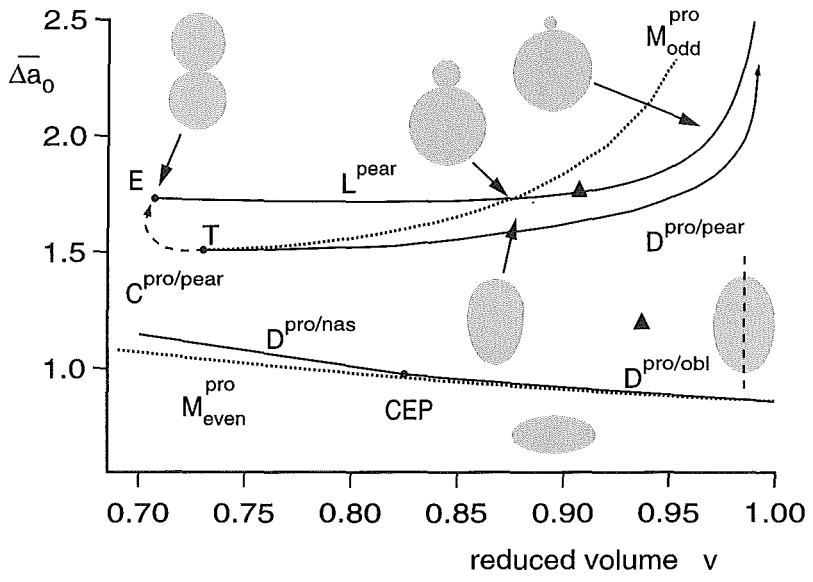


Fig. 13: *Prolate region of the ADE phase diagram for $\alpha = 1.4$. Dotted lines correspond to the upper and lower stability boundary of prolate shapes. The two triangles mark the positions of the vesicle depicted in Figs. 14 and 15, where the one with the smaller effective differential area $\overline{\Delta a_0}$ corresponds to Fig. 14.*

order line, but keeps the prolate shape due to a finite activation energy of the budding transition in this region of the phase diagram. The approach to the spinodal line, where the prolate shapes become unstable, is characterized by the development of a soft mode. There are clearly strong pear-shape fluctuations visible with a long relaxation time, see Fig. 16. These spinodal fluctuations have been quantitatively characterized [42]. Both the mean-square amplitudes and the relaxation times of this soft pear-like mode scale with the inverse distance in reduced volume to the spinodal line.

The final budding is caused by a particular strong thermal fluctuation which overcomes the residual energy barrier near the spinodal. An example of such an event can be seen in Fig. 17. Note the quasi-stable appearance of the pear-like shape as it diffuses over the saddle point of the bending energy landscape.

Due to the crossing of the spinodal line M^{pro}_{odd} with the limiting line L^{pear}, budding at large reduced volume misses the pear phase completely. Vesicles assume a double-spherical shape after the budding instability. With single component membranes, the bud stays connected to the parental vesicle. However, in a multi-component sphingomyelin system, fission has been found to occur after the budding event [49]. Separation of the vesicles can also be observed in polymer-induced budding. Here, water-soluble polymers are grafted from the external side to the membrane via hydrophobic anchors, see Section 5.3. In this case, the two vesicles stay connected by an umbilical cord [43]. In both systems, there is likely lateral inhomogeneity in the molecular components within the membrane.

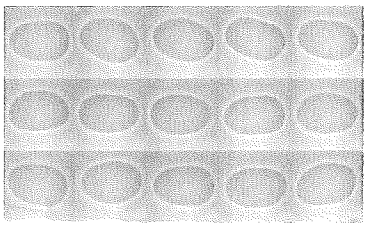


Fig. 14: *Prolate vesicle fluctuations at* ($v = 0.937, \overline{\Delta a_0} = 1.21$). *The elapsed time between snapshots is* $\Delta t = 6.3$ *s. [25]*

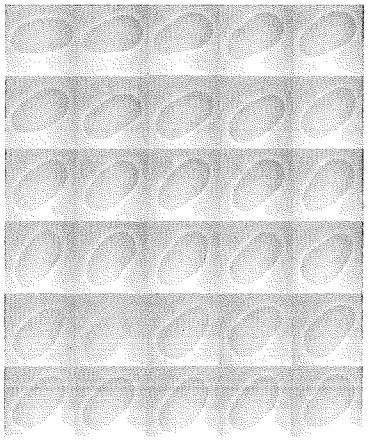


Fig. 15: *Pear fluctuations of a prolate vesicle near the spinodal line of the budding transition. The same vesicle as in Fig. 14 is shown, but now with parameter values* ($v = 0.907, \overline{\Delta a_0} = 1.78$) *which are much closer to the budding instability. The snapshots are taken at equal time intervals of* $\Delta t = 6.3$ *s* .

In this respect, one has to distinguish thermodynamically driven phase separation from molecular segregation due to the coupling of molecular density to membrane curvature. In the first case, the vesicles exhibit domain-induced budding [52], whereas in the second case, it is the budding transition itself which allows for segregation into region of high curvature [53]. The latter scenario is only effective for sufficiently small vesicles due to the entropy of mixing.

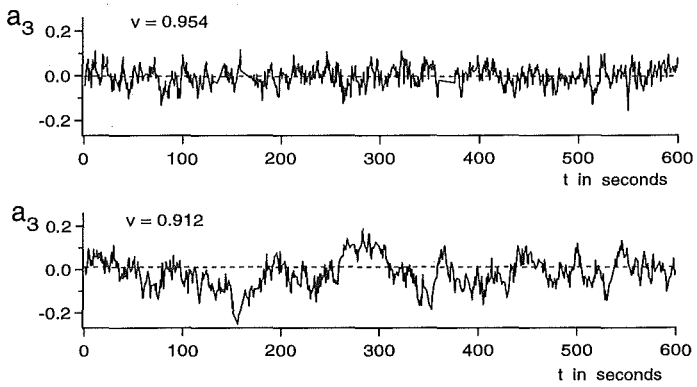


Fig. 16: *Time sequence of pear fluctuations. The amplitude a_3 of the soft mode of the budding transition is plotted as a function of time for two reduced volumes. At $v = 0.954$, the vesicle is far away from the budding instability. It fluctuates around a stable prolate vesicle. Close to the instability, at $v = 0.921$, the shape exhibits pronounced pear fluctuations with long relaxation times.*

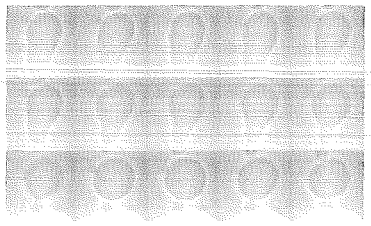


Fig. 17: *Time sequence of the final budding instability at constant control parameters $(v, \overline{\Delta a_0})$ very close to the spinodal line [25]. The initial pear-like shape results from a giant thermal fluctuation of a meta-stable prolate vesicle onto the saddle point of the bending energy landscape. The elapsed time between snapshots is $\Delta t = 1.2$ s. First, one observes a slow diffusion over the saddle point region corresponding to the pear-like shapes until, finally, the vesicle relaxes towards the budded configuration by quickly closing down the neck between the two quasi-spherical parts of the shape.*

The Prolate-Oblate Transition

In the last section, we have seen that thermal fluctuations play a major role in morphological transitions of vesicles. At the lower phase boundary of the prolate shapes, thermal fluctuations become even the dominant feature. The prolate-oblate transition, to the right of the critical end point (CEP), is weakly first-order [44, 46]. Thus, the energy barriers between the meta-stable shape and the shape of lowest energy can be crossed thermally in both directions. Indeed, prolate-oblate fluctuations have been observed experimentally [48]. In Fig. 18, a time sequence of a vesicle near the prolate-oblate transition is shown.

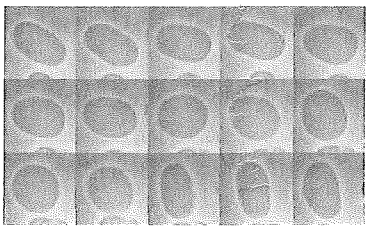


Fig. 18: *Prolate-oblate fluctuations of a vesicle [48]. The long-axis of the prolate vesicle is located within the focal plane. The oblate vesicle appears quasi-spherical since its rotational-symmetry axis is normal to the focal plane. The elapsed time between snapshots is* $\Delta t = 6.3$ *s. One observes a bistable behavior where time sequences of fluctuating prolate and oblate shapes are separated by comparatively short-lived transitional shapes. Such a scenario confirms the theoretical expectations of a weakly-first order transition between prolate and oblate shapes. A statistical analysis of the shape distribution allows to identify the prolate configuration as the meta-stable shape in this example.*

The vesicle is seen to alternate between prolate and oblate shapes. The latter shape appears as a quasi-spherical vesicle in the focal plane due to observation from below. The bistability is quantitatively expressed in the elliptical mode a_2 which clearly shows fluctuations around two distinct levels, see Fig. 19. A statistical analysis of the bistable shape distribution allowed to extract an effective potential for the transition. Further, mean-escape times out of the prolate and oblate shapes, respectively, have been measured [48]. This dynamic quantity depends on the energy dissipation mechanism. In future experiments, it may be possible to distinguish between bulk and surface hydrodynamic drag and inter-monolayer viscous coupling. The latter friction effect depends on the degree of molecular interdigitation and could be used for a characterization.
To the left of the point CEP (see Fig. 11), the upper spinodal of the oblate phase turns into a real second-order transition from oblates to non-axisymmetric shapes [46]. These shapes resemble starfish at small reduced volume and connect the prolate and oblate vesicle phases. They will be described in the next section.

Starfish Vesicles

A fascinating class of non-axisymmetric shapes exist for medium values of the effective differential area. In Fig. 20, a comparison of experimental and theoretical shapes is shown [45]. Starfish vesicles are found in several subclasses including n-armed stars, H-formed shapes, and shapes with even lower symmetry, as depicted in Fig. 21.

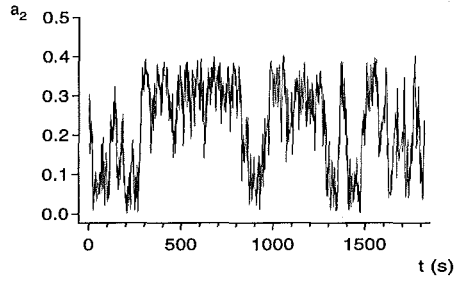


Fig. 19: *Time sequence of prolate-oblate fluctuations. Two distinct mean levels corresponding to the prolate and the oblate shape are visible. Note that the amplitude a_2 is always larger than zero. This reflects the fact that the circular equatorial contour of the oblate shape is distorted into an ellipse due to fluctuations and never shows the rotational symmetry of the minimal energy shape calculated for $T = 0$.*

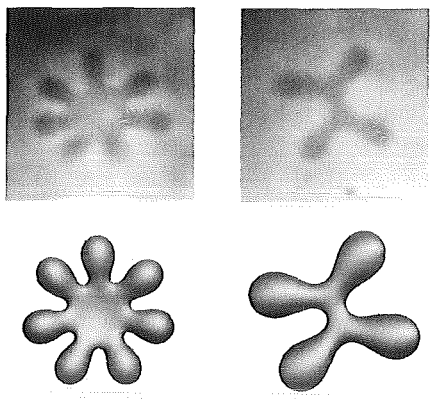


Fig. 20: *Comparison of theoretical and experimental non-axisymmetric starfish vesicles [45]. A 7-armed star and an H-formed shape are shown. These vesicles are swollen from the single phospholipid SOPC. Thus, highly branched shapes can be formed by homogeneous membranes.*

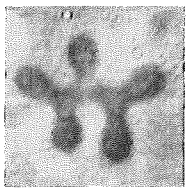


Fig. 21: *Complex starfish vesicle with minimal symmetry [27]. The mean shape is mirror symmetric to the focal plane of the microscope and a plane orthogonal to it through the center of gravity of the vesicle.*

These figures reveal the general building principle of this particular shape class. Whenever possible, the morphology is locally axisymmetric and consists of tubular sections which are connected via non-axisymmetric joints. Increasing spontaneous curvature drives budding of the tubular arms [43]. We note that starfish vesicles can be formed by homogeneous membranes. There is no segregation of lipids into region of lower and higher curvature necessary. Indeed, starfish have been found in single component membranes [45]. The branched tubular structure can be understood from the requirement to accommodate a large area-to-volume ratio at medium values of differential area. Theoretical shapes have been obtained via direct minimization of the energy with a finite element method [45]. The vesicle shape shown in Fig. 21 exhibits diffusion-like relative rotations of the arms with respect to each other. Thus, one concludes that the energy difference of the various configurations is well below one kT. As a consequence, the shape exhibiting two mirror planes depicted in Fig. 21 is repeatedly visible in the microscope only for a small fraction of time.

5 Membrane Interactions

5.1 Physical Chemistry of Membrane Curvature

In this Section, we want to discuss the various mechanisms leading to the curvature of an amphiphilic interface. First, we give an overview of possible effects and experimental systems. Then, we introduce the concept of effective elastic layers.

Transversal Membrane Asymmetry

We have discussed in Sec. 4.1 that there are two different elastic parameters which control the curvature of a vesicle membrane. These parameters, the spontaneous curvature c_0 and the preferred differential area Δa_0, depend on the properties of the membrane molecules and the surrounding aqueous medium. Any asymmetry across the membrane will lead to a curved vesicle bilayer characterized by an effective spontaneous curvature $\bar{c}_0 = c_0 + 2\pi\alpha\,(\Delta a_0 - \Delta a)$. In Fig. 22, a cartoon of several situations leading to membrane curvature is shown. In the following, we will give a brief discussion of these mechanisms
One factor is the effective molecular shape [54]. Molecules may be cone- or wedge-shaped, thereby inducing bending of the monolayer they form. [9] Thus, different molecular monolayer densities on both sites of the membrane result in a spontaneous curvature of the bilayer. Similarly, an asymmetric change in the number of molecules or mean molecular area on the two sides of the membrane will lead to a change in the differential area. The mean molecular area depends, e.g., on temperature and surface charge. The difference in the number of molecules may vary by free [55, 56] or driven flip-flop [41, 57]. Further, surface charge and the equilibrium distribution of molecules across the membrane depend on the electrolyte strength and pH of solution [58]. However, even for symmetric surface charge, a gradient in electrolyte concentration across the membrane leads to an electrostatic spontaneous curvature [59, 60, 61, 62, 63]. Interestingly, even a pH gradient across zwitterionic membranes induces curvature of the interface [51]. We note again that the

[9] The concept of a molecular shape should be taken with some caution. In fact, molecular configurations are a function of the local environment and, strictly speaking, cannot be viewed as an independent property of a molecule.

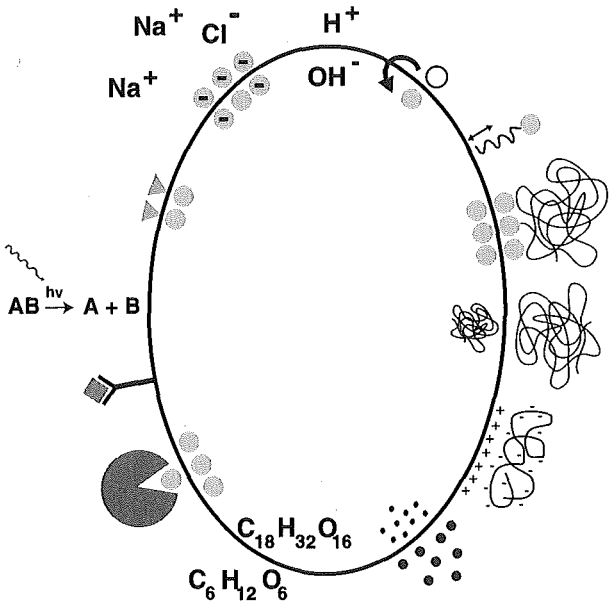


Fig. 22: *Schematic illustration of several mechanisms for membrane asymmetry discussed in the text. Generally, any type of asymmetry across the bilayer induces curvature of the membrane. Asymmetry may be created by surface fields, as well as boundary values of bulk fields at the interface.*

differential area is not an intrinsic quantity of the system, but depends on the particular (preparation) history of the vesicle studied. The distribution of molecules between the inner and outer monolayer is fixed at the time of membrane closure and, generally, varies widely from vesicle to vesicle. This explains why one usually observes a great variety of different vesicle shapes within one sample. However, taking into account these individual offsets, relative changes of the effective spontaneous curvature are well defined and can be measured quantitatively as we will see in the next Section.

A particular interesting class of effects can be observed by monitoring the interactions of polymers [43, 64, 65, 66, 67] or colloids [68, 69, 70, 71] with membranes. The molecules or particles may be adsorbed or depleted from the interface. In either case, the membrane reacts by adjusting its curvature. Water-soluble polymers can be grafted to one or both sides of the membrane with hydrophobic anchors. This leads to an increase of the differential area due to the insertion of the anchor-molecule. In addition, the grafted mushroom-shaped polymer induces spontaneous curvature by balancing its gain in configurational entropy in the curved state against the bending elastic energy of the bare membrane [71]. For polymers which are not associated with the membrane, there is a depletion layer with a thickness on the order of the radius of gyration. In this situation, the membrane bends towards the side with the larger molecule with a corresponding gain in translational entropy. This depletion effect is not restricted to polymers but can also be observed for colloidal particles [71] and even for small molecules such as simple sugars

[43].
In polyelectrolyte systems, the interplay of configurational entropy and electrostatic energies leads to quite a number of phenomena. Especially interesting are DNA and cationic-lipid interactions [72]. Particular complexes formed by these molecules, which are relevant for gene therapy [73], have been characterized [74]. DNA induced membrane curvature may be important in the initial process of formation of these complexes. Endocytosis of single or multiple DNA strands into cells [75] can be understood as a morphological transition which is triggered by a change in the effective spontaneous curvature as the DNA associates with the plasma membrane.
Another important mechanism for membrane curvature are chemical reactions at or near the interface. During the course of the reaction, the chemical environment changes. The increase, respectively, decrease of products and educts in the bulk alters the various interactions of the membrane with the aqueous medium. The amphiphilic molecules building the membrane itself may also be modified. This can happen via reactions involving small molecules or molecular machines. Enzymatic cleavage of lipids by, e.g., phospholipase molecules are biological relevant examples [76].
Any asymmetric change in molecular properties in the interface and/or the bulk will induce membrane curvature by the effects discussed above or via another specific mechanism. In biomembranes, the resulting change in the stress profile within the membrane may, in turn, alter the functional state of membrane spanning protein machinery, like channels and pumps [77, 78].

Effective Elastic Layers

Before giving examples of experimental asymmetric systems, we want to formulate in this Section the general concept for an induced spontaneous curvature of an elastic interface. Let us consider for the moment the interaction of an elastic surface with the half-space above it. (Below, we will identify this surface with one side of a membrane. What we have in mind are entropic and/or electrostatic interactions of the (charged) membrane with neutral and/or charged solute molecules.) We take the intrinsic bending modulus of the surface to be κ, and set the intrinsic spontaneous curvature to zero. Thus, in the absence of any interaction, the surface will be flat. In general, any additional free energy of interaction will curve the interface. (We note that we ignore any changes in the intrinsic bending modulus due to the presence of an additional interaction.) We consider cylindrical deformations. One may expand the interfacial free energy into a power series in the mean curvature C. The coefficients of the linear and quadratic term define the spontaneous curvature C_0^i and the bending modulus κ^i of an additional, effective elastic layer. We have for the total free energy density

$$F_{\text{eff}} = \frac{\kappa}{2}C^2 + \frac{\kappa^i}{2}(C - C_0^i)^2 \tag{12}$$

We can find the effective spontaneous curvature C_0^{eff} of the surface via simple minimization with respect to the curvature C. One gets

$$C_0^{\text{eff}} = \frac{\kappa^i}{\kappa + \kappa^i}\, C_0^i\,, \tag{13}$$

i.e., the effect of an interfacial interaction, which induces spontaneous curvature, is always scaled by the ratio of the effective interfacial modulus κ^i to the total modulus $\kappa+\kappa^i$. This is a somewhat obvious, but important conclusion.
For strong interactions ($\kappa^i \gg \kappa$), the induced spontaneous curvature equals the effective interfacial spontaneous curvature; i.e., one observes directly the characteristic length scale $(C_0^i)^{-1}$. In contrast, for weak interactions ($\kappa^i \ll \kappa$), the induced spontaneous curvature is reduced by a factor κ^i/κ.
When the two half-spaces on both sides of the membrane are decoupled, the total effective spontaneous curvature of the membrane is simply given by the sum of the two effective spontaneous curvatures of the interfacial interactions. Note that this quantity vanishes for a symmetric membrane due to the different orientations of the two interfaces.

5.2 A Photochemical Morphology Switch

We turn now to the interesting effect of a bulk chemical reaction on phosphocholine membranes. The shape of bilayer lipid membranes can be sensitively tuned by coupling their curvature to photo chemistry [79]. More generally, we show how light can be used to control the morphology of supramolecular aggregates.

Interaction of Iron-Cyanide Complexes with Membranes

Under illumination in aqueous solution, the iron complex $Fe(CN)_6^{3-}$ undergoes photoaquation [80]:

$$Fe(CN)_6^{3-} + H_2O \overset{h\nu}{\rightleftharpoons} Fe(CN)_5H_2O^{2-} + CN^- \tag{14}$$

This photochemical process is reversible upon switching off the light. It is accompanied by a rise in pH because of the protonation of the released cyanide ion [81]. As a result the preferred curvature of a pure PC bilayer membrane changes when the reaction (14) takes place predominantly on one side of the membrane. In turn, this induces pronounced changes in the shapes of giant SOPC vesicles. Typical examples are presented in Fig. 23 and 24. Depending on whether the light sensitive ion, $Fe(CN)_6^{3-}$, is present in the outside solution (Fig. 23) or is trapped in the interior of the vesicle (Fig. 24) in varying concentrations, one can control the sign as well as the magnitude of the photo-morphological response.
In Fig. 23a-e, the response of a vesicle to illumination with high intensity light (0.03 mW/mm^2) in an external ferricyanide solution is shown. One always observes shape transitions towards a more outwardly curved morphology for systems where the concentration of the ferricyanide ion outside the vesicle capsule is higher than in the inside. The shape sequence in Fig. 23 also demonstrates that the light-induced shape transitions are reversible. Stopping illumination leads to a relaxation of the vesicle to the original shape (Fig. 23f-h). Whenever the photochemical process is induced in the vesicle interior, one finds transitions toward more inwardly curved morphologies. Fig. 2 illustrates a typical example of this case. In total, the above material shows that zwitterionic membranes curve away from the photo active iron complex under illumination.

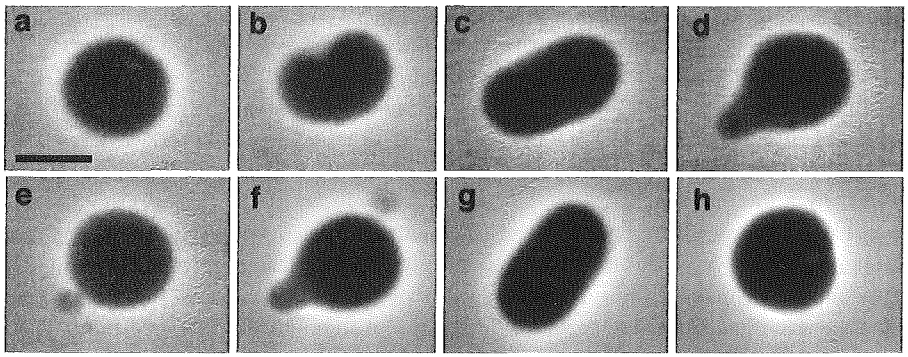


Fig. 23: *Reversible light induced shape transitions of a giant vesicle. Vesicles were swollen in 231 mM sucrose solution. Subsequently, they were incubated in an iso-osmolal solution of potassium ferricyanide (100 μM) and glucose (231 mM). Thus, the light sensitive compound,* $Fe(CN)_6^{3-}$*, was present in the vesicle exterior. At low illumination intensity, the initial vesicular shapes are generally stable as monitored for at least 10 minutes. Snapshot (a) shows a stable closed stomatocyte vesicle which exhibited thermal shape fluctuations. After the reaction (14) is initiated by high intensity white light using epi-illumination, the vesicle undergoes a fast sequence of shape transitions (Fig. 23b-d) within about 20 seconds to assume a final budded shape (Fig. 23e). Switching off the illumination (0.03* mW/mm^2*)results in the opposite transition, as illustrated in the sequence (e) - (h). The bar denotes 5 μm.*

Discussion

Transition sequences between different shapes can be understood as special trajectories in the ADE phase diagram resulting from a *change* in the solution conditions. Inspection of Fig. 11 shows that transitions to more outwardly curved shapes are generally connected with an increase in preferred differential area, whereas a decrease in preferred differential area drives transition to inwardly curved morphologies. Thus, considering the experiments shown, one concludes that illumination with light increases the effective spontaneous curvature of the membranes when ferricyanide is present outside the vesicle, whereas an excess of ferricyanide in the vesicle interior leads to a decrease of this parameter under illumination. Note that only the relative changes in the effective spontaneous curvature not its absolute value (which is set by the preparation history [50]) are related to the action of light. The magnitude of the effect may be quantified by reading off from Fig. 11 the shift in $\overline{\Delta a_0}$ between the limiting vesicle shapes depicted in Fig. 1a and 1e. We find $\overline{\Delta a_0}(\text{on}) - \overline{\Delta a_0}(\text{off}) = 1.43$. For $\alpha = 1.4$, this corresponds to a change in the effective spontaneous curvature of $\Delta \bar{c}_0 = 12.6$. [10]

The magnitude of the curvature response can be decreased by adjusting ferricyanide concentration and light intensity. Indeed, analysis of the thermal fluctuation spectra alows to detect minute changes in preferred membrane curvature, e.g., an external ferricyanide solution with a concentration as low as 50 μM. Exploring a fluctuating prolate vesicle

[10]Since $\bar{c}_0 = c_0 + 2\pi\alpha\ (\Delta a_0 - \Delta a)$ depends (weakly) on the vesicle shape, the latter number is given with respect to a sphere ($\Delta a = 1$).

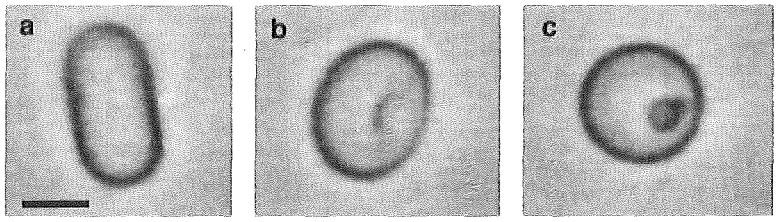


Fig. 24: *Light driven prolate-to-closed-stomatocyte transition. Vesicles were swollen in 1 mM* $K_3Fe(CN)_6$ *and incubated in 4 mM sucrose solution. Thus, the vesicles contained excess ferricyanide in their interior. The initial prolate shape (a) was found to be stable under low intensity illumination. High intensity illumination induced a shape transition to a closed stomatocyte vesicle (c) through an intermediate non-equilibrium shape (b). Note that contrary to the situation presented in Fig. 23, where ferricyanide was present only in the exterior solution, the preferred vesicle curvature now decreases after initiating the photochemical process (14). The bar denotes 5* μm.

with a reduced volume $v = 0.934(1)$, similar to the one shown in Fig. 23c and 23g, one observes a clear shift in the relative strength of the ellipsoidal and pear-like fluctuation modes, as evidenced by their probability densities shown in Fig. 25. This corresponds to an increase of the preferred differential area. In total, we see that morphological effects of solutes with a concentration of a few 10 μM or lower can be very well detected.

We proceed now to a discussion of the possible mechanisms for the observed photo-morphological response. The vesicle shape may be affected by interactions of its bilayer membrane with several molecular species, including $Fe(CN)_6^{3-}$, $Fe(CN)_5H_2O^{2-}$, CN^-, and OH^- which change their relative concentrations during the process (1). As the most probable mechanisms, one expects that illumination results in the association of one or several ions with the membrane.

Control experiments show that raising pH in the vesicles surrounding at iso-osmolar conditions induces budding [51]. This is due to the charging of the external monolayer via the association of the hydroxyl ion with the choline group of SOPC at high pH [51]. Since during illumination the pH in the photochemical system increases as well, the same mechanism is effective. However, when the photochemical process (14) is initiated in the presence of phosphate buffer in order to eliminate the influence of the pH change, shape transitions of the same kind and with the same direction in the phase diagram are found, albeit with a lower magnitude. This suggests that another adsorption process affecting membrane curvature [71] takes place in addition to the association of the hydroxyl ion with the PC head group induced by changes in pH. In fact, there is a surface excess of the complex $Fe(CN)_6^{3-}$ due to the positively charged trimethylammonium groups of the choline heads [82, 83]. The photoaquation of the latter anion to $Fe(CN)_5H_2O^{2-}$ will change headgroup hydration, thereby inducing additional curvature response.

To summarize, we have given an example for a relationship between (photo-) chemical processes and the geometry of supra-molecular structures, a list of which would also include photo-biological systems. Illumination by light provides a morphological switch with a fast and homogeneous response of the amphiphilic aggregates.

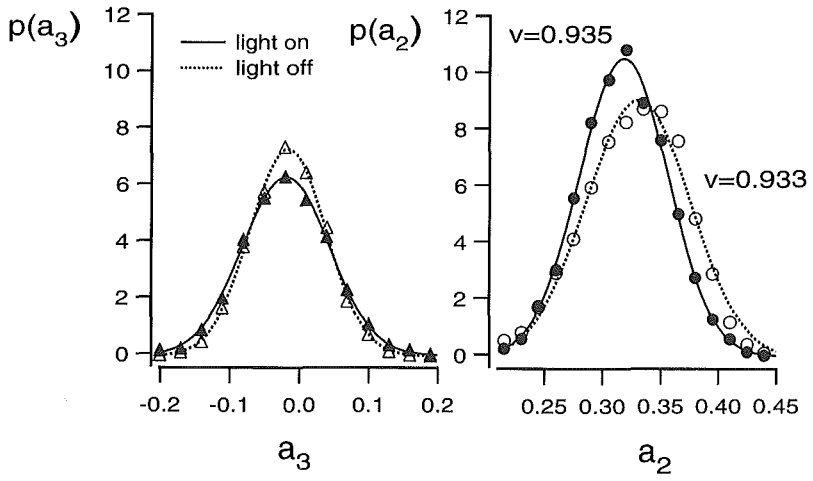


Fig. 25: *Normalized histograms of the ellipsoidal (a_2) and pear (a_3) mode amplitudes of vesicle shape fluctuations. Gaussian fits are shown. Note that the widths σ_n of the histograms are inversely proportional to their heights, i.e., enhancement of fluctuations corresponds to an decrease in peak height and vice versa. For a particular vesicle in 50 μM external ferricyanide solution, one finds that illumination results in enhanced pear ($\sigma_3 = 0.077 \rightarrow \sigma_3 = 0.089$) and depressed ellipsoidal ($\sigma_2 = 0.063 \rightarrow \sigma_2 = 0.054$) fluctuations of the prolate shape signaling an increase in preferred differential area. The volume-to-area ratio of the vesicle before and during illumination can be monitored as well with high precision. One detects only a very small upward shift of* 0.2 *percent in the apparent reduced volume v under illumination.*

5.3 Shape Transitions of Complex Membranes

In this Section, we review the budding of complex membranes. Further, the general role of spontaneous curvature in inducing morphological transitions in biological cells is discussed. First, we consider the effect of grafting amphipilic polymers onto single component membranes [43]. Then, domain-induced budding [52, 84] of a sphingomyelin mixture is explored [49]. Finally, we consider osmotically induced budding of a binary mixture of DMPC with cholesterol. In the last two systems, budding is followed by fission of the vesicle [49]. In contrast, budding of single component membranes, as well as budding induced by polymer grafting, does not lead to fission. In single component membranes, the bud stays closely attached to the parental vesicle (see Fig. 17), whereas in polymer-coated membranes, the bud separates, but stays connected via an umbilical tube.

Budding of Polymer-coated Membranes

Shape transitions of single component vesicles swollen from stearoyl-oleoyl-phosphatidylcholine (SOPC) or dimyristoyl-phosphocholine (DMPC) in sugar solution were induced at iso-osmolal conditions by adding cholesteryl-modified polyethylenoxid to the outer solution [43, 85]. Due to its amphiphilic character, this polymer partitions between the bulk solu-

tion and the outer monolayer. Incorporation into the membrane was verified by labeling the polymer (PEO-Flu-Chol) with Fluorescein [86]. The transition from a stomatocyte vesicle to a discocyte shown in Fig. 26 is driven by addition of polymers to the external solution. Note, that the last two frames (d, e) in Fig. 26 show two orthogonal cuts of the same shape. It is a flat biconcave disk with broken rotational symmetry. The observed shape change is in accord with an increase of the spontaneous curvature [19, 25]. As discussed in Sec. 5.1, the anchoring in the membrane increases both components of the effective spontaneous curvature $\bar{c}_0$. The addition of the cholesteryl-anchor to the outer monolayer increases the outer monolayer area and thereby raises Δa_0. Further, the configurational restriction of the polymer at the membrane can be partially relieved when the membrane curves away from the polymer. The balance between entropy gain of the polymer and bending energy cost of the membrane results in a positive spontaneous curvature [64, 65].

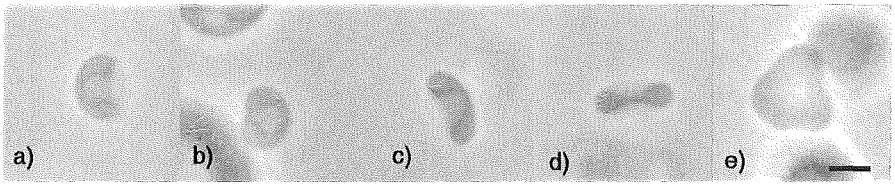


Fig. 26: *Shape change from a stomatocyte to a starfish-like vesicle by adding PEO-Flu-Chol solution (10^{-4} mol/l): a) Pure SOPC-vesicle without polymer. b) After polymer solution is added. Note that $\bar{c}_0$ is first decreasing and than increasing; c) 4 min from b); d) 6 min from b; e) 10 min from b). The bar denotes 5 μm.*

As we have seen repeatedly by now, a sufficiently large increase of the spontaneous curvature of a prolate vesicle leads to a budding transition. Fig. 27 demonstrates this effect with the PEO-polymer. Interestingly, incorporation of polymers leads to a separation of the bud. However, the two vesicles are still connected by an umbilical tube (see Fig. 27). The budded configuration is topologically a sphere. We may speculate, that the polymer grafting density is different in the umbilical tube and the spheres connected by it.

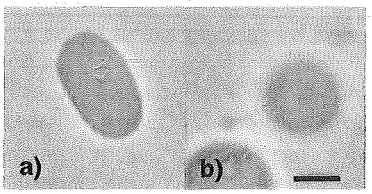


Fig. 27: *PEO induced budding: The bud separates but is still connected by an umbilical tube. The bar denotes 5 μm.*

Fission of Multicomponent Vesicles

Fissioning of the budded vesicle seems to take place in multi-component lipid membranes [49]. In Fig. 28, one observes repeated expulsion of a small vesicle from a large, strongly

fluctuating vesicle as it is heated through the fluid-gel transition of its constituting membrane. The vesicle was prepared from the natural lipid sphingomylein, which has a wide distribution of chain length with a transition temperature of 41 degree Celsius. The fluid-gel coexistence region is broad ranging from 35 till 50 degrees. Note that the repeated budding events, shown in Fig. 28, take place inside the fluid-gel coexistence region. Thus,

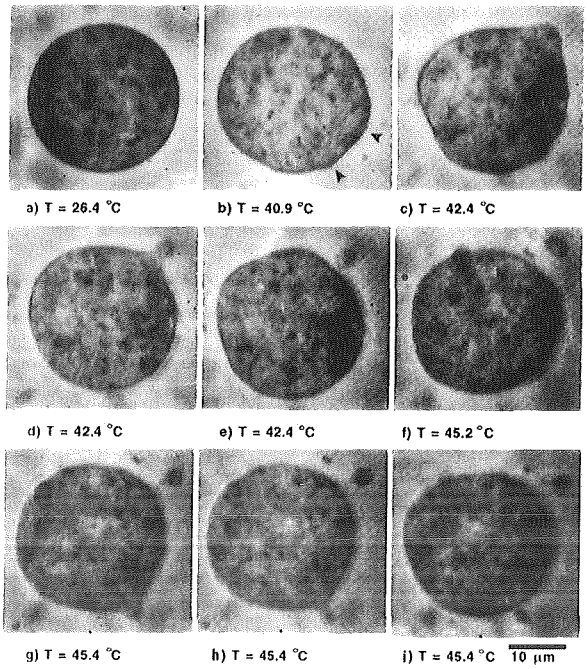


Fig. 28: *Budding and fission of sphingomyelin vesicles at the fluid-gel transition.*

one possible explanation of this shape transition is domain induced budding [52, 84]. Further, an intriguing mechanism for asymmetric domains has been suggested [87]. It is argued that the bilayer might develop a spontaneous curvature by asymmetric melting into laterally ordered monolayers at the fluid-gel transition.
Another fascinating phenomenon, osmotically induced fission [49], is shown in Fig. 29. Sequential shape transitions of a vesicle prepared from an artificial DMPC:CHOL (60:40) mixture are visible. By reducing the enclosed volume osmotically, one finds a remarkable cascade process. The vesicle shown in Fig. 29 repeatedly divides into smaller vesicles at constant temperature. In contrast, attempts to induce fission by thermally creating excess area are not successful in this system.

Cellular Morphology and Signaling

We close this Section, with a few remarks on the role of spontaneous curvature in living cells. We may ask whether bending elasticity plays a role in Biology. [88] Considering the generality of asymmetry induced membrane curvature and the extreme sensitivity to

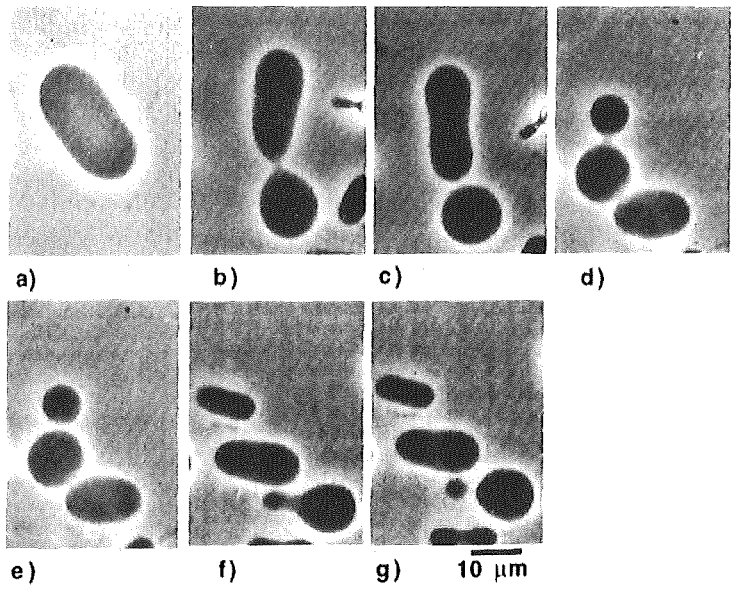


Fig. 29: *Osmotically induced fission of DMPC:Chol vesicle. Mixed lipid vesicles were subject to osmotic deflation by slowly reducing the concentration of the external vesicle solution via natural evaporation from the open observation chamber. The first fission event appeared after a decrease of reduced volume by 30 percent starting from a sphere. [49]*

small concentration differences, the right question seems, in fact, not whether spontaneous curvature is relevant for biological systems, but rather how does the cell avoid uncontrolled budding induced by asymmetry across the various intra-cellular membrane and the plasma membrane? Indeed, it is quite delicate to fine tune the necessary morphological changes for cellular function.

Physiological processes rely on the compartmentalization of the cell interior into various membrane bound organelles and the cytoplasm. [89] These compartments are not static entities but incessantly exchange material via molecular transfer or vesicular transport. The latter process involves budding and fission of protein-coated and non-coated vesicles from internal organelles or the plasma membrane and subsequent fusion of the vesicles with a specific target membrane [89, 90, 91]. Whereas much effort has been focussed on the physics of the fusion process [92], there has been much less attention paid to budding and fission of vesicles in the cell [93]. These vesicular carriers are now well characterized both morphologically and functionally [94, 95, 96] in the biochemical literature, but not much is known about the actual physical mechanisms involved in their creation.

We have seen that budding of membranes can be induced in synthetic single component phospholipid vesicles. The resulting small vesicles remain attached to the parent vesicle by a narrow neck. In the preceding subsection, it has been shown that budding followed by fission of small vesicles can and does occur in lipid mixtures, see Fig. 28 and Fig. 29. The vesicles in this study were protein free, so the observed budding and fission are physical properties of the lipid bilayer alone. Real biomembranes are of course much more complex

systems. However, it is tempting to assume that morphological changes in the cell are controlled by the effective spontaneous curvature of the cellular membranes. In most cases, budding seems to be related to an asymmetric protein coat [96] of the membrane which induces a local spontaneous curvature of the composite system. These protein patches could lead to domain induced budding [52, 84, 49]. The situation is complicated by the fact that, e.g., the clathrin coat of endocytic vesicles forms a tethered network and introduces a shear elastic energy contribution in addition to the bending energy of the biomembrane.[11] Nevertheless, the spontaneous curvature of the composite system remains a key parameter. It is quite likely that a lot of the morphological changes in the cell [88], in particular the budding process, can be explained by the physical concept of bending elasticity of membranes. The elastic parameters of the bilayer, which tune the morphological transition, would be controlled and regulated biochemically.
One may speculate about a cross-coupling of the morphology of a membrane with its signaling function via molecular asymmetry. [98] One example of such a relationship may be the inositol phospholipid pathway or another biochemical cascade involving lipid-derived second messengers [99]. In the former pathway, the phospholipase C cleaves off the head group of inositol phospholipids to produce inositol triphosphate and diacylglycerol. The latter lipid has quite a small head group and, thus, membrane asymmetry clearly changes during this process. The variation in membrane asymmetry could in turn trigger morphological transformations of the bilayer. It may also be used to couple distinct biochemical reactions. An asymmetry-induced change in the mechanical stress profile of the bilayer membrane could alter the activity of enzymes or ion channels which are some distance apart [78]. It remains to be seen whether these effects are in fact widely employed by nature.

6 From Lipid- to Polymermembranes

So far, the material discussed focused primarily on lipid membranes. Let me close the lecture with a few more remarks on diblock copolymer vesicles. These polymersomes are very promising both in terms of basic research as well as applications.

6.1 Ultraviscous Membranes

As already mentioned, polymersomes are not only tough vesicles with a high lysis tension but posses robust rheological properties as well. Their surface viscosity, $\eta_s = 1.5 \times 10^{-3}\ dyns/cm$, is three orders of magnitude higher than for lipids in the fluid phase. This fact has profound consequences on membrane dynamics. In Fig. 30, time series of lipid (SOPC) and polymer (Pb-PEO) shape fluctuations are juxtaposed. Even without doing a quantitative analysis by evaluating static and dynamic correlation functions

$$\langle a_n(0)a_n(\tau)\rangle = \langle a_n(0)a_n(0)\rangle \ \exp(-t/\tau_n) \ , \tag{15}$$

we see qualitatively for the special pear-like mode $n = 3$ (see Fig. 15) that thermal fluctuations have comparable magnitude but rather different relaxation times. The comparable

[11] Recently, a model of endocytosis has been proposed including such a term [97].

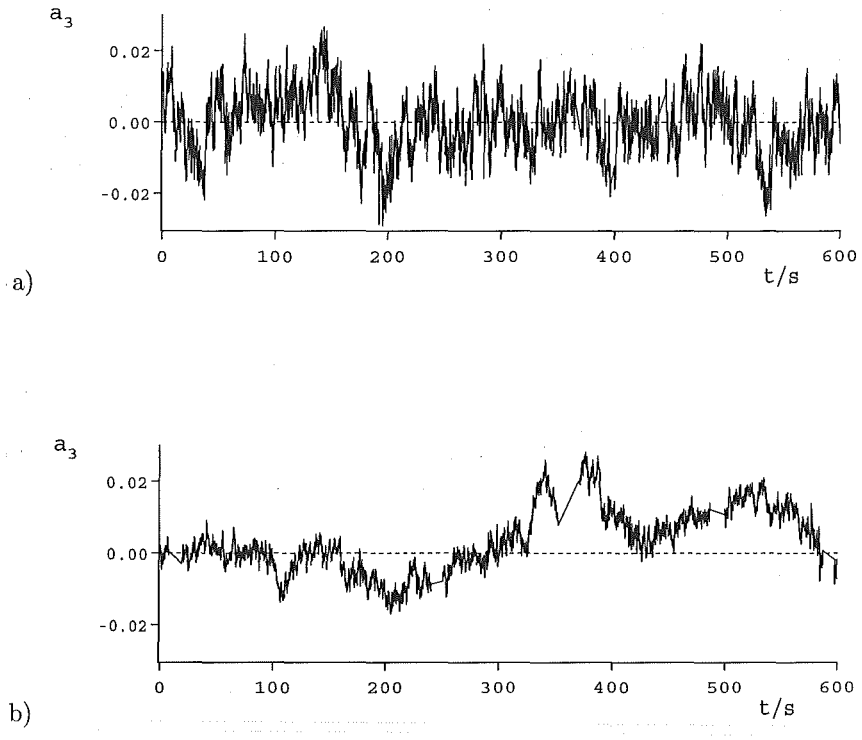


Fig. 30: *Time series of pear-like fluctuations a_3 of a prolate lipid (a) and polymer (b) vesicle.*

magnitude of thermal fluctuations, $\langle (a_3)^2 \rangle \sim kT/\kappa$, reflect the similar bending moduli of the two molecules differing by just a factor two. The large difference in correlation times stems from very large surface viscosity of the polymer membrane, which leads to dissipation within the membrane rather than in bulk water as for lipid membranes. We can get the right order of magnitude of the two effects by simple dimensional analysis. For bulk hydrodynamic dissipation, we have $\tau_B = \eta_B R^3/\kappa$ [18], whereas for membrane dissipation, we find $\tau_s = \eta_S R^2/\kappa$. Using the bulk viscosity of water $\eta_B = 10^{-3} Ns/m$, we get with a typical liposome radius $R = 10\ \mu m$ and $\kappa = 25\ kT$ a relaxation time $\tau_B \sim 10\ s$. For the polymersome, the large surface viscosity $\eta_S = 1.5 \times 10^{-6} Ns/m$ implies indeed a long relaxation time $\tau_s \sim 10^3\ s$.

6.2 Non-Spherical Topologies

Low Genus Shapes and Dynamics

In addition to topological spherical shapes, polymersomes form more complex morphologies with low and high genus g, i.e., number of handles of a single vesicle. For non-fixed topology, there is an additional contribution to the elastic energy of the membrane, the Gaussian bending term

$$E_g = \frac{\tilde{\kappa}}{2} \int dA(C_1 C_2), \tag{16}$$

where $\tilde{\kappa}$ is the Gaussian modulus. However, according to the Gauss-Bonnet theorem, the integral is a topological constant and one may omit the Gaussian bending energy for the analysis of vesicle shapes and shape transformations with constant genus g. Lipid-bilayer vesicles with a small number of handles have been investigated for genus $g = 2$ [100, 101], and $g = 3, 4$ [102, 103], where for $g > 2$ conformal diffusion[12] in vesicle shape space is observed [102, 103]. In Fig. 31, we show genus $g = 2, 4$ polymersomes.

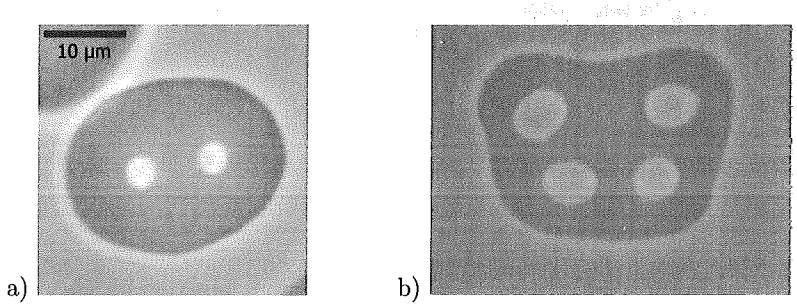


Fig. 31: *Low Genus Vesicles for a) $g = 2$ and b) $g = 4$*

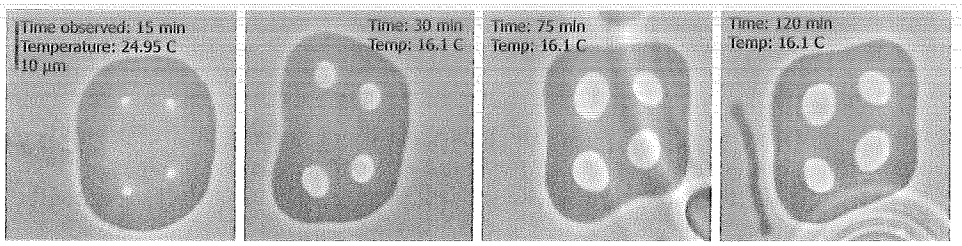


Fig. 32: *Low Genus Button Vesicle: Slow relaxation of a $g = 4$ PB-PEO polymersome after a temperature quench.*

The shape sequence in Fig. 32 illustrates nicely the ultra slow equilibration dynamics of a PB-PEO polymersome after a temperature quench. Decreasing temperature increases

[12] Vesicle exhibiting conformal diffusion show large zero-energy fluctuations of their shape described by conformal deformations.

the spontaneous curvature of the polymer vesicle and the previously stable shape becomes unstable. First, the hole radii adjust. Then, the global shape changes symmetry from a wagon-like configuration to a tilted square. Effectively, these transformations may be parameterized by the average radius and spacing of the holes. In Fig. 33, we show the time dependence of these quantities. Note the overshoot of the hole spacing due to the quicker relaxation of hole radius. Consistent with the equilibrium dynamics of thermal fluctuations, the non-equilibrium dynamics of shape changes is characterized as well by relaxation times on the order of 20 minutes.

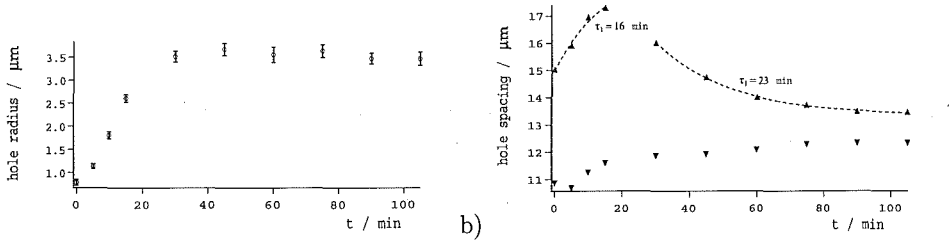


Fig. 33: *Dynamics of Low Genus Button. The hole radius (a) and the largest and smallest hole spacing (b) of the vesicle in Fig. 32 are plotted as a function of time after temperature is quenched by* $\Delta T = 9K$.

High Genus Shapes

Finally, polymersomes exhibit microstructured membranes which form giant vesicles with a double bilayer wall connected by a lattice of passages [104]. In Fig. 34, we show an example of the generic morphology. The bending elastic energy of the polymer membrane provides the underlying mechanism of the observed micro-structure formation.
Indeed, the local membrane shapes can be well reproduced by theoretically modeling a doubly-periodic surface with hexagonal symmetry. One finds several shape classes, small and large passages, budded vertices, tubes, and spindles, which are stable for different values of $v = V/S^{3/2}$ and $c_0 = C_0 S^{1/2}$, where vesicle volume V [13] and membrane area S are calculated for the unit cell of the hexagonal lattice. Transitions between distinct classes can be induced by temperature. Decreasing temperature progressively leads to double membrane structures with higher curvatures, see Fig. 35.
Remarkably diblock-copolymer membranes do exhibit regular superstructures on a micrometer scale. Typical structures of melts [105] and block copolymers aggregates in aqueous solution [106] reported in the literature are in fact on the nanometer length scale. It is promising that the controlled structuring of materials could be extended into the micrometer domain. Further, we found a pronounced morphological response to changes in spontaneous curvature, which allows a precise control of the shape of the pores in the double-bilayer membrane. In addition to temperature, there are other natural control parameters of interfacial shape, like electrolyte concentration and pH as well as the degree of hydrogen bonding, which will be effective via their influence on PEO chain

[13] This is the space between the two membranes of the double bilayer vesicle wall, not the interior of the giant vesicle, which is topologically equivalent to the exterior volume and is not constraint.

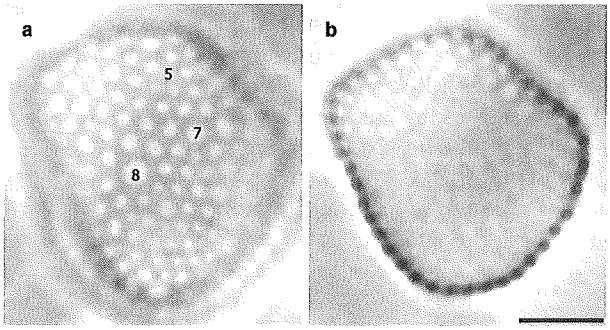


Fig. 34: *High genus polymersome. The top view (a) shows a hexagonal lattice of passages in the double bilayer vesicle surface. Note the two larger holes forming 7- and 8-fold coordination defects together with a 5-fold coordinated hole. The cross section (b) of the same vesicle shows nearly-circular tubes forming the double bilayer surface. The scale bar corresponds to 10 μm.*

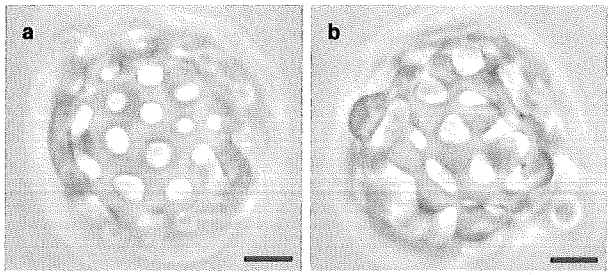


Fig. 35: *Temperature induced transformation from (a) "Large-passages" ($T = 45.7\ °C$)to (b) "budded-vertices" ($T = 41.7\ °C$). The scale bars correspond to 10 μm.*

conformations in solution. Structuring polymeric interfaces on micrometer length scales may prove useful for applications requiring materials with giant pores. In a biomimetic context, we note the striking resemblance of the membrane structure in Fig. 34 to the tests of certain sea urchins, see Fig. 36, which use syncytial membranes to direct growth of their mineral skeleton [107]. Albeit this biological controlled inorganic morphosynthesis [108] is far from being complexly understood, it seems promising to employ superstructures of diblock copolymer membranes in order to cast desired mineral materials into micron-sized geometrical shapes.

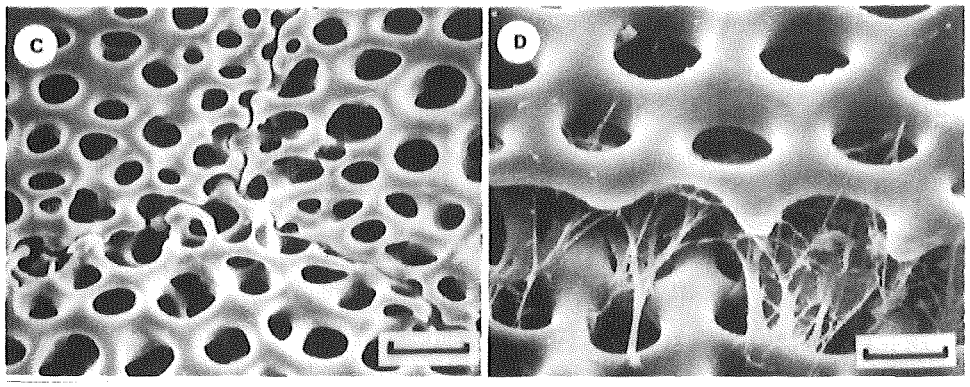


Fig. 36: *Outer mineral skeleton of sea urchins. Note the regular hole pattern, resembling closely the arrangement in Fig. 35 The scale bars correspond to 50 μm. Taken from [107].*

References

[1] *Giant Vesicles, Perspectives in Supramolecular Chemistry* **vol. 6**, Eds., P. Walde & L. Luisi, John Wiley & Sons (2000).

[2] H.-G. Döbereiner, *Properties of Giant Vesicles*, Curr.Op.Coll.Int.Sci. **5**, 256 (2000).

[3] R. Lipowsky, *Nature*, **349**, 475 (1992).

[4] *Physics of Amphiphilic Layers*, (ed. J. Meunier, D. Langevin, and N. Boccara), Springer Proc. Phys. **21** (1987).

[5] B. M. Discher *et al.*, *Science* **284**, 1143 (1999).

[6] L.E. Reichl,*A Modern Course in Statistical Physics*, Arnold 1980.

[7] W. Gebhard, U. Krey, *Phasenübergänge und kritische Phänomene*, Vieweg.

[8] S.A. Safran, *Adv. Phys.* **48**, 395 (1999).

[9] Hope, M.J., M.B. Bally, G. Webb, and P.R. Cullis. *Biochim. Biophys. Acta.* **812**, 55 (1985).

[10] A.J. Jin, D. Huster, K. Gawrisch, R. Nossal, Eur. Biophys. J. **28**, 187 (1999).

[11] D. Needham and E. Evans, Biochem. **27**, 8261 (1988).

[12] D. S. Dimitrov, M. Angelova, Bioelectrochem. Bioenerg **19**, 323 (1988).

[13] D. Marsh, *Handbook of Lipid Bilayers*, CRC Press, Boca Raton, 1990.

[14] K.A. Riske, H.-G. Döbereiner, and M.T. Lamy-Freund, J. Phys. Chem. B, in press.

[15] R. Dimova, U. Seifert, B. Pouligny, S. Förster, and H.-G. Döbereiner, Eur. Phys. J. E, submitted.

[16] D.V. Zhelev, D. Needham and R.M. Hochmuth, Biophys. J., **67**, 720 (1994)

[17] E. Evans and W. Rawicz, *Phys. Rev. Lett.*, **64**, 2094 (1990).

[18] U. Seifert, *Adv. Phys.*, **46**, 13 (1997).

[19] L. Miao, U. Seifert, M. Wortis and H.-G. Döbereiner, *Phys. Rev. E*, **49**, 5389 (1994).

[20] E. A. Evans, R. Skalak, *Mechanics and Thermodynamics of Biomembranes*, CRC Press, 1980.

[21] E. Evans and D. Needham, J. Phys. Chem **91**, 4219 (1987).

[22] U. Seifert, K. Berndl and R. Lipowsky, *Phys. Rev. A*, **44**, 1182 (1991).

[23] R. B. Gennis, *Biomembranes*, Springer, 1989.

[24] B. L.-S. Mui, P. R Cullis, E. A. Evans, and T. D. Madden, Biophys. J., **64**, 443 (1993).

[25] H.-G. Döbereiner, E. Evans, M. Kraus, U. Seifert and M. Wortis, *Phys. Rev. E*, **55**, 4458 (1997).

[26] H.-G. Döbereiner, *The Budding Transition of Phospholipid Vesicles: A Quantitative Study via Phase Contrast Microscopy*, PhD thesis, Simon Fraser University, 1995.

[27] O. Selchow, *Vesikelformen im Schwerfeld*, Diplomarbeit, TU München, 1996.

[28] W. Helfrich, *Z. Naturforsch.*, **29**, 510 (1974).

[29] E. Evans, *Biophys. J.*, **14**, 923 (1974).

[30] W. Helfrich, *Z. Naturforsch.* **28c**, 693 (1973).

[31] S. Svetina, M. Brumen and B. Žekš, *Stud. Biophys.*, **110**, 177 (1985).

[32] H.J. Deuling and W. Helfrich, *Biophys. J.* , **16**, 861 (1976).

[33] S. Svetina and B. Žekš, *Eur. Biophys. J.*, **17**, 101 (1989).

[34] L. Miao, B. Fourcade, M. Rao, M. Wortis and R.K.P. Zia, *Phys. Rev. A*, **43**, 6843 (1991).

[35] Sheetz and Singer, *Proc. Natl Acad. Sci.*, (USA), **71**, 4457 (1974).

[36] E.A. Evans, *Biophys.J.* **30**, 265 (1980).

[37] R.E. Waugh, J. Song, S. Svetina and B. Žekš, *Biophys. J.*, **61**, 974 (1992).

[38] K. Berndl, J. Käs, R. Lipowsky, E. Sackmann and U. Seifert, *Europhys. Lett.*, **13**, 659 (1990).

[39] J. Käs and E. Sackmann, *Biophys. J.*, **60**, 825 (1991).

[40] F. Farge, P. Devaux, *Biophys. J.*, **61**, 347 (1992).

[41] B.L.-S. Mui, H.-G. Döbereiner, T.D. Madden and P.R. Cullis, *Biophys. J.*, **69**, 930 (1995).

[42] H.-G. Döbereiner, E. Evans, U. Seifert and M. Wortis, *Phys. Rev. Lett.* , **75**, 3360 (1995).

[43] H.-G. Döbereiner, A. Lehmann, W. Goedel, O. Selchow and R. Lipowsky, in *Materials Science of the Cell*, (eds. B. Mulder, V. Vogel, and C. Schmidt), *Mat. Res. Soc. Symp. Proc.*, **489**, 101, 1998.

[44] V. Heinrich, S. Svetina and B. Žekš, *Phys. Rev. E* , **48**, 3112 (1993).

[45] W. Wintz, H.-G. Döbereiner and U. Seifert, *Europhys. Lett.*, **33**, 403 (1996).

[46] M. Jarić, U. Seifert, W. Wintz and M. Wortis, *Phys. Rev. E*, **52**, 6623 (1995).

[47] M. Kraus, U. Seifert and R. Lipowsky, *Europhys. Lett.*, **32**, 431 (1995).

[48] H.-G. Döbereiner and U. Seifert, *Europhys. Lett.*, **36**, 325 (1996).

[49] H.-G. Döbereiner, J. Käs, D. Noppel, I. Sprenger and E. Sackmann, *Biophys. J.*, **65**, 1396 (1993).

[50] H.-G. Döbereiner, O. Selchow, and R. Lipowsky, *Eur. Biophys. J.*, **28**, 174 (1999).

[51] J. Lee, P.G. Petrov and H.-G. Döbereiner, Langmuir **15**, 8543 (1999).

[52] R. Lipowsky, *J. Phys. II France*, **2**, 1825 (1992).

[53] U. Seifert, *Phys. Rev. Lett.*, **70**, 1335 (1993).

[54] J. Israelachvili, J. *Intermolecular and Surface Forces*, 2nd edn., Academic Press: London, 1991.

[55] R. Homa and H.J. Pownall, *Biochim. Biophys. Acta*, **938**, 155 (1988).

[56] R.D. Kornberg and H.M. McConnell, *Biochem.*, **10**, 1111 (1971).

[57] M.R. Raphael and R. Waugh, *Biophys. J.*, **71**,1374 (1996).

[58] T.E. Redelmeier, M.J. Hope and P.R. Cullis, *Biochem.*, **29**, 3046 (1990).

[59] M. Winterhalter and H. Helfrich, *J. Phys. Chem.*, **92**, 6865 (1988); ibid. **96**, 327 (1992).

[60] D.J. Mitchell, B.W. Ninham, *Langmuir*, **5**, 1121 (1989).

[61] M. Winterhalter and H. Helfrich *J. Phys. Chem.*, **96**, 327 (1992).

[62] S. May, *J. Chem. Phys.* , **105**, 8314 (1996).

[63] T. Chou, M.V. Jaric and E.D. Siggia, *Biophys. J.*, **72**, 2042, (1998).

[64] R. Lipowsky, *Europhys. Lett.*, **30**, 197, (1995).

[65] C. Hiergeist and R. Lipowsky, *J. Phys. II France*, **6**,1465, (1996).

[66] C. Hiergeist, V. Indrani and R. Lipowsky, *Europhys. Lett.* **36**, 491 (1996).

[67] E. Eisenriegler, A. Hanke, S. Dietrich, *Phys. Rev. E*, **54**, 1134 (1996).

[68] C. Dietrich, M. Angelova and B. Pouligny, *J. Phys II*, **7**, 1651 (1997).

[69] K. Yaman, P. Pincus and C. M. Marques, *Phys. Rev. Lett.*, **78**, 4514 (1997).

[70] A.D. Dinsmore, D.T. Wong, P. Nelson and A.G. Yodh, *Phys. Rev. Lett.*, **80**, 409 (1998).

[71] R. Lipowsky and H.-G. Döbereiner, *Europhys. Lett.*, **42**,219 (1998).

[72] C.R. Safinya, I. Koltover and J. O. Rädler, *Current Opinion in Colloid Interface Science*, **3**, 69 (1998).

[73] M.J. Hope, B. Mui, S. Ansell and Q.F. Ahkong, *Molecular Membrane Biology*, **15**, 1 (1998).

[74] J. O. Rädler, I. Koltover, T. Salditt and C. R. Safinya, *Science*, **275**, 810 (1997).

[75] M. I. Angelova, N. Hristova, and I. Tsoneva, Eur. Biophys. J., **28** 142 (1999).

[76] R. Wick, M.I. Angelova, P. Walde and P.L. Luisi, *Chem. Bio.*, **3**, 105 (1996).

[77] M. Sokabe, F. Sachs and Z.Q. Jing, *Biophys. J.* , **59**, 722 (1991).

[78] S.L. Keller, S.M. Bezrukov, S.M. Gruner, M.W. Tate, I. Vodyanoy, and V.A. Parsegian, *Biophys. J.*, **65**, 23 (1993).

[79] P.G. Petrov, J. Lee, and H.-G. Döbereiner, Europhys. Lett. **48**, 435 (1999).

[80] L. Moggi, F. Bolletta, V. Balzani, & F. Scandola, *J. Inorg. Nucl. Chem.* **28**, 2589 (1966).

[81] Y. Mori, G. Rábai & I. Hanazaki, *J. Phys. Chem.* **98**, 12968 (1994).

[82] J.A. Berden, R.W. Barker, & G.K. Radda, *Biochim. Biophys. Acta* **375**, 186 (1975).

[83] Yu.E. Shapiro, A.V. Viktorov, L.I. Barsukov, & L.D. Bergelson, *Biofizika* **23**, 727 (1978).

[84] F. Jülicher and R. Lipowsky, *Phys. Rev. E* **53**, 2670 (1996).

[85] A. Gau, *Polymerbedeckte Lipidvesikel*, Doktorarbeit, Universität Potsdam, (1999)

[86] W.A. Goedel, A. Lehmann, *Polymer Preprints* **38**, 630 (1997).

[87] P.L. Hansen, L. Miao, J. Ipsen, *Phys. Rev. E* **58**, 2311 (1998).

[88] E. Sackmann, *FEBS Lett.*, **346**, 3 (1994).

[89] Alberts,B., D.Bray, J.Lewis, M.Raff, K.Roberts, and J.D.Watson. *Molecular Biology of the Cell*, 3rd Ed., Garland Publishing (1994).

[90] Brodsky,F.M. *Science* **242**, 1396 (1988).

[91] Sackmann,E. 1990. *Can.J.Phys.* 68:999.

[92] Siegel,D.P. 1993. Viral fusion mechanisms, J. Bentz, editor. CRC press.

[93] Oster,G.F., L.Y.Cheng, H.H.Moore, and A.S.Perelson. 1989. *J. theor. Biol.* 141:463.

[94] Pfeffer,S.R., and J.E.Rothman. 1987. *Ann.Rev.Biochem.* 56:829.

[95] Pearse,B.M.F., and M.S.Robinson, *Ann.Rev.Cell Biol.* 6:151.

[96] R. Schekman, and L. Orci, *Science* **271**, 1526 (1996).

[97] R.J. Mashl and R.F. Bruinsma, *Biophys. J.*, **74**, 2862 (1998).

[98] H.-G. Döbereiner, Biophys. J. **76**, 1723 (1999).

[99] S. Ghosh, J.C. Strum, and R.M. Bell, *FASEB Journal*, **11** 45 (1997).

[100] U. Seifert, *Phys. Rev. Lett.* **66**, 2404 (1991).

[101] B. Fourcade, M. Mutz & D. Bensimon, *Phys. Rev. Lett.* **68**, 2551 (1992).

[102] F. Jülicher, U. Seifert, & R. Lipowsky, *Phys. Rev. Lett.* **71**, 452 (1993).

[103] X. Michalet & D. Bensimon, *Science* **269**, 666 (1995).

[104] C. K. Haluska, W. T. Góźdź, Hans-Günther Döbereiner, Stephan Förster, Gerhard Gompper, unpublished.

[105] F. S. Bates & G. H. Fredrickson, *Physics Today* **52**, 32 (1999).

[106] N. S. Cameron, M. K. Corbierre & A. Eisenberg, *Can. J. Chem.* **77**, 1311 (1999).

[107] Simkiss, K. & Wilbur K.M. Biomineralization, Academic Press 1989.

[108] S. Mann and G. A. Ozin, *Nature*, **382**, 313 (1996).

B13 Biopolymers: The macromolecules of Life

G. Zaccai
Institut de Biologie Structurale
Grenoble, France

Contents

1 **Introduction** 2

2 **Where has modern biology come from? The discovery of DNA as the support of genetic information** 3

3 **Physics, biology and the discovery of macromolecules** 5

4 **Molecular evolution and the Central Dogma** 6

5 **Proteins are polymers with very special properties** 7

6 **Where is modern biology going? The genome sequencing era** 8

1 Introduction

Modern biology is concerned by a wide range of scales in space and time - from the 0.1Å nm level of atomic distances to the size of the earth as a global eco-system that receives all its energy from the sun – from the femto-second (10^{-15}s) time scale of electronic rearrangements to the billions of years of evolution.

The cell occupies a central place in biology in two senses. It is the basis of all forms of life; each and every living organism is either constituted of cells or has been made up of cells at some stage of its life span. The cell also represents a central point in the organisation of biological structures.

Bacterial cells are about 1 μm (10^{-6}m) long, eukaryotic cells (cells containing a nucleus) about ten times larger (10^{-5}m).

Moving up the length scale, we find progressively larger organisms up to the tens of metres (10m) scale interacting with each other and with their environment in eco-systems that could be on a kilometre scale or even much larger.

To go the other way, towards smaller length scales, we can imagine diving into the interior of a eukaryotic cell. We would observe the membranes that surround the cell and separate its volume into discrete compartments on the 10^{-6}m scale, such as the nucleus, which contains the genetic information, and mitochondria, the power stations of the cell. On the 10^{-8}m scale, we would observe large macromolecular complexes that function as cellular machines, such as ribosomes, which are the protein factories of the cell, chaperones and large proteases, which control protein or multienzyme complexes. At 10^{-9}m, we would observe the biopolymers, proteins and nucleic acids, then small molecules, such as peptides, small sugars and water molecules [1]. Finally on the 10^{-10}m we would observe the organisation of the atoms that make up these molecules.

Structure length scales are static, whereas the time dimension plays an essential role in biological function.

The briefest time of interest also happens to be the smallest measurable time interval, the femtosecond (10^{-15}s). In vision, for example, the first step in the detection of a photon in the eye by the light sensitive molecule retinal is an electronic rearrangement taking place in femto-seconds. Molecular thermal motions are on the pico- to nano-second (10^{-12}m to 10^{-9}m) scale. DNA unfolds in micro-seconds (10^{-6}s); enzymatic catalysis turns over in milli-seconds (10^{-3}m); protein synthesis takes seconds... and so on, until the billions of years of evolution.

An understanding of the importance of evolution is essential if one is to discuss biology [2]. The very existence of a biological macromolecule depends on the fact that it has been selected by evolution – by virtue of its biological function! As physicists or chemists we may claim, for example, that the catalytic properties of zeolites are useful functions. But, contrary to a protein, such materials did not appear in nature because they display these properties. The organising power of nature has been built up in time through evolutionary processes. The very

existence of a biopolymer, its place in a cell, the place of a cell in an organism, can only be understood if their history over billions of years is understood.

Since the discovery that the DNA molecule is the support of genetic information, the biological importance of interactions taking place at the molecular and atomic length and time scales has become increasingly evident. These length and time scales were not easily accessible to study... smaller than the wave-length of light, faster than can be measured by usual clocks. Sophisticated new methodological approaches in physics and chemistry were required and the science of molecular biophysics and biochemistry was born.

2 Where has modern biology come from? The discovery of DNA as the support of genetic information

Jacob [3] quotes Montaigne who in the "Essais" II 37 (16th century) stated the problem of heredity in physical terms. Writing of semen, he asked the question,

". . . this drop of liquid, where does it house this infinite number of forms? . . . so that the grandson will look like the grandfather, the nephew like his uncle "...

Montaigne knew that, physically, the information transmitted during the mating act had to be contained in the few millilitres of sperm that passed between partners. We could take his reasoning further and deduce that since an obviously enormous amount of information was required its support has to be very small – on the level of a molecule. But molecules were not known in Montaigne's time, and it took more than three hundred years for scientists to propose DNA as the answer to his question.

Modern molecular biology arose from a series of essential discoveries, made mainly in the second half of the nineteenth and the first half of the twentieth centuries.

The cell was discovered in the nineteenth century, as were the cell nucleus and chromosomes (coloured bodies seen by staining in microscopy). The chemical substance in chromosomes was named nuclein. It is constituted of protein and nucleic acid. Chromosomes were linked to heredity early in the twentieth century. Until the early nineteen forties, however, it was thought that DNA was a standard polymer of the type $(ACGT)_n$, where A, C, G, T are its component protomers (nucleotides) including the bases, adenine, cytosine, guanine and thymine, respectively. Such a composition obviously cannot encode genetic information. Protein, which was known to be a biopolymer made up of twenty different amino-acids, was a much more promising candidate.

A key experiment towards establishing the genetic role of DNA was performed in 1944 by Avery and co-workers, who showed that pure DNA prepared from one strain of the bacterium pneumococcus could genetically transform another strain. In 1950, Chargaff and co-workers showed that the composition of DNA was much more complicated than $(ACGT)_n$, and that the ratios of A and T were the same as were those of G and C. By using radio-active labelling, Hershey and his co-workers showed that when the *Escherichia coli* bacterium was genetically transformed by T_2 bacteriophage (a bacterial virus), only the viral DNA penetrated into the

cell, the protein remaining outside. A virus is a protein-nucleic acid packet of genetic information. It contains none of the machinery required to reproduce and does so by infecting a compatible cell. Infection consists of a virus introducing its genetic material into the cell and diverting its machinery for its reproductive needs.

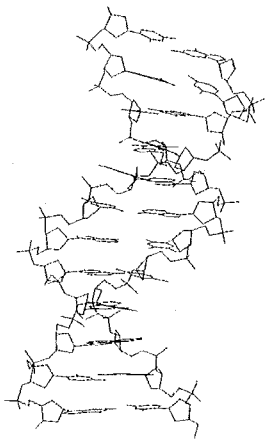


Fig. 1: *A skeleton model of the DNA double helix. The sugar rings can be seen on each strand. The base pairs linking the two strands are almost horizontal in the diagram.*

The structural model proposed for DNA by Watson and Crick, consistent with the X-ray diffraction data of Franklin and Wilkins, was published in 1953. The double helix structure revolutionised biology by illustrating in a simple and elegant way the chemistry of encoding and transmission of genetic information. The DNA biopolymer is constituted of nucleotides. Each nucleotide has a constant part made up of a phosphate group linked to a deoxyribose sugar group, and a variable base, adenine, guanine, cytosine, or thymine also linked to the sugar group. Polymerisation is by the phosphate group of one nucleotide forming a co-valent link with the sugar group of the next. The two strands of the double helix are linked by hydrogen bonding between the bases. The strands of the double helix are complementary. A is across from T and G is across from C. In fact, the hydrogen-bonded A-T pair has the same stereo-chemical dimensions as the G-C pair, which permits the building of a regular double helix structure out of any base sequence. The genetic information is encoded in the base sequence. Its transmission results from the mother double helix strands coming apart, each becoming a template for the synthesis of a complementary strand to form two daughter double helices.

3 Physics, biology and the discovery of macromolecules

Parallel discoveries in physics accompanied and were vital for the development of modern biology. Hydrodynamics and radiation scattering not only played a decisive role in the discovery of macromolecules, but also continue to pre-dominate in current studies.

Hydrodynamics deals with phenomena in which a force acts on a particle in a viscous solution. The discoveries from more than one hundred years ago in this branch of physics are still highly relevant today, and continue to stimulate important new developments in the field. The science of hydrodynamics arose from the classical work of the botanist Robert Brown, who, in 1828, first described the random, thermal motion of small plant particles suspended in water, Brownian motion. Less than thirty years later, A. Fick deduced the fundamental laws governing transport phenomena in solutions, and G. Stokes demonstrated that the coefficient of translational friction of a particle depends on its linear dimensions. The way was cleared for a direct determination of sub-microscopic particle dimensions from hydrodynamic measurements. Brownian motion was explained theoretically by Albert Einstein, in 1905, who, in a series of now classic papers, characterised quantitatively the molecular motions in simple solutions and gasses. Perhaps the decisive demonstration of the existence of proteins as particles of well-defined molecular mass, however, was due to T. Svedberg, who invented the high-speed centrifuge and analytical centrifugation in 1920. He proposed the combined use of sedimentation and diffusion coefficients to obtain a direct estimate of the molecular mass of a particle in solution. In an other Physics experiment that revolutionised biology, A. Tiselius, in 1937, used the difference in the charges on macromolecules to separate them during a fractionation process, thus introducing electrophoresis into extensive biochemical practice. Closer to our epoch, H. Z. Cummings and co-workers, in 1964, following the theory of R. Pekora, published the first experimental paper on dynamic light scattering and demonstrated that the diffusion coefficients of particles in solution can be extracted by this method.

The wave nature of light on which diffraction phenomena are based was first suggested by Huygens, in 1690. About one hundred years later, Haüy wrote his essay on the regularity of crystal forms, which is considered to be the beginning of crystallography. Macromolecules are smaller than the wavelength of light, however, and scientists had to wait for 1895 and the discovery of X-rays by Röntgen in Würzburg, before there was a chance of being able to "see" them. X-ray crystallography [4] was developed in the second decade of the twentieth century following the work of Ewald, Laue, Debye, Darwin and of course the Braggs, father and son, W.H and W.L. In 1924, De Broglie proposed the wave nature of particles, and four years later Thomson the wave nature of the electron was verified by Thomson; the neutron was discovered in 1932 and diffraction of neutrons was observed in 1936. Between 1925 and 1931 appeared the first polymer structure studies, with the analysis of X-ray diffraction from rubber, hair and wool. Small angle scattering (SAS) of X-rays was first observed in 1930 by Krishnamurti, Gray and Zinn on colloids, liquids, charcoal [5]. The theory of SAS including the determination of particle (macromolecule) size was proposed by Guinier in the late 1930s. Also in the nineteen thirties, the first crystals of insulin, proteins and viruses were analysed. In the nineteen forties SAS was applied to characterise biopolymers in solution. After the second World War, neutron beams from pile reactors became available. The structure of DNA was published in 1953 from fibre diffraction and model building. It was followed in the early sixties by the first protein structures from X-ray crystallography.

4 Molecular evolution and the Central Dogma

The central dogma in molecular biology was first proposed by Crick:

$$\text{DNA} \Leftarrow \text{DNA} \Rightarrow \text{RNA} \Rightarrow \text{Protein}$$

DNA $\Leftarrow$ DNA is replication;
DNA $\Rightarrow$ RNA is transcription;
RNA $\Rightarrow$ Protein is translation.

Genetic information is stored in DNA, and when the cell divides, replication results in a faithful copy of this information. A gene codes for a protein. Proteins constitute the machinery of the cell. In order to be acted upon, the genetic information is transcribed into a messenger RNA copy, which is then translated to synthesise the protein. RNA is ribonucleic acid. It is similar in chemical composition to DNA, with ribose replacing deoxyribose and the uracyl base (U) replacing thymine. Complementary base pairs in RNA are AU and GC.

The central dogma had to be adjusted after the discovery of retroviruses, such as HIV, the virus associated with AIDS. Retroviruses are RNA viruses, but contrary to what had been observed with other RNA viruses, retroviral RNA does not enter the cellular machinery as messenger RNA but is copied to DNA and incorporated into the cell's genetic material. The central dogma became:

$$\text{DNA} \Leftarrow \text{DNA} \Leftrightarrow \text{RNA} \Rightarrow \text{Protein}$$

and the back reaction RNA to DNA was named reverse transcription.

Replication, transcription, reverse transcription and translation are extremely complex processes controlled and catalysed by different proteins. For example, DNA polymerases catalyse replication, while DNA-dependent RNA polymerases, as well as various transcription factors (all proteins) are required for transcription. Translation takes place on magnificently complex molecular machines made up of RNA and protein, the ribosomes [6][7] as well as initiation and elongation factors and transfer RNA molecules.

Genetic information flows in the direction DNA to RNA to protein. Protein, however, is required in all steps, showing that the process is an end result of evolution and does not represent a progression or macromolecular hierarchy. This means that all living organisms, even the ones that we consider as most ancient or primitive, are well along the path of evolution and that we know nothing about what preceded them.

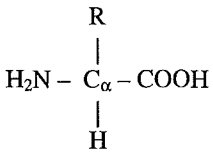
Today, the central dogma appears to be valid for all living organisms, and represents the extraordinary unity of life forms, a unity reflected in genes. As an illustration, we consider the difference in composition between human cytochrome C (a protein involved in respiration) and that from various other organisms: with the ape 1%; with the whale 10%; with the tuna 20%; with the fly 30%; with wheat 40%; with the fungus Candida 50%. But more striking than this similarity in composition is that homologous (*ie* evolved from a common ancestor)

proteins of different organisms have essentially identical three-dimensional structures, related to the biological function they have to fulfil.

5 Proteins are polymers with very special properties

Proteins have evolved to have such special properties related to the way they are biosynthesised that it is useful to be reminded that they are not polymers in the usual sense in physical chemistry [8].

A protein is a linear chain of amino-acid residues. There are twenty main amino acids in proteins. Each is made of a constant part, $H_2N-C_\alpha H-COOH$, which forms the main chain in the protein, and a variable side chain R on the C_α carbon:



Polymerisation is through a bond between CO and NH with the loss of a water molecule.

The protein is encoded in a precise length of DNA. It has a beginning, the N-terminal (the NH end of the chain) and an end, the C-terminal (the C=O end). This means, for example, that in one mL of a 1 μM protein solution there are about 10^{15} macromolecules of strictly identical mass! This is an extraordinary property, unknown in a usual chemical polymer, for which the molecular mass is represented by a statistical distribution around a mean value.

The second difference between a protein and a usual polymer is in the composition. Whereas a usual polymer is a regular repeat of a small number of subunits, a protein chain is constituted of subunits taken from twenty amino acid residues, with no repeat (Fig.2).

The sequence of amino acids in a protein was named its *primary* structure. The amino acid chain has fascinating properties. The NH and CO groups on the main chain form hydrogen bonds that structure it in regular helices or sheets named *secondary* structures, and the variable side chains represent a wide range of chemical properties, charged or neutral, hydrophobic or polar, SH groups, aromatic rings etc. which stabilise the three dimensional conformation of the chain in solution (the *tertiary* structure) and create specific catalytic sites.

A usual polymer in solution takes up a statistical conformation that depends strongly on solvent interactions. The fold of a protein in solution also depends strongly on interactions between its amino-acid residues and solvent. For example, in a water soluble protein, hydrophobic groups will tend to be buried in the protein interior while polar groups and charges will be on the surface; in a membrane protein, hydrophobic groups are on the surface in contact with the apolar lipid environment [9].

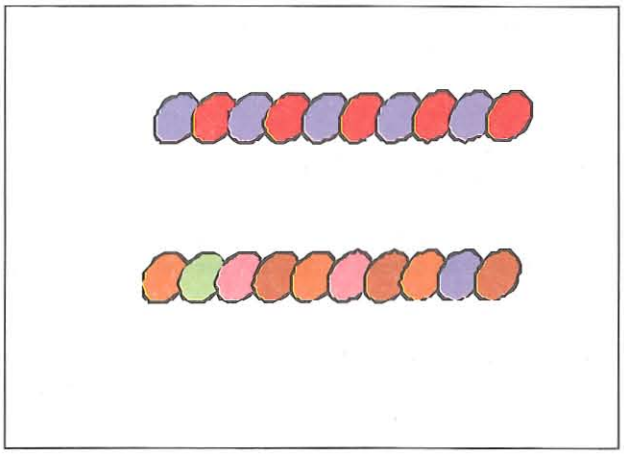


Fig. 2: *Schematic of a polymer (blue-red)$_n$ (top). Schematic of a part of a protein chain, each aminoacid is a different colour (bottom).*

In contrast to the usual polymer, however, the protein tertiary structure is a precise, well-defined conformation, selected by evolution and directly related to its biological activity (Fig.3).

6 Where is modern biology going? The genome sequencing era

There has been an intimate connection between physical methods and progress in biology. Fundamental discoveries in hydrodynamics, crystallography and radiation scattering and spectroscopy led to modern structural molecular biology. These physical methods will be called upon to play an increasingly important role in the post-genome sequencing era that we have now entered.

Two physical methods, X-ray crystallography and NMR, dominate, at present, in determining structures of biological macromolecules to high three-dimensional resolution. These methods will be of utmost importance in structural genomics. It is this science that poses the practical problem of high throughput analysis to biology and physics, in order to approach the tens of thousands of structures predicted in genomes.

The following tasks must be achieved: (1) Choice (by bio-informatics) and cloning of a functional gene region. (2) Choice of a suitable expression system. (3) Expression and purification of the gene-product. (4) Crystallization or isotope labelling for NMR. (5) Structure determination at a synchrotron radiation beam line, or by multidimensional NMR.

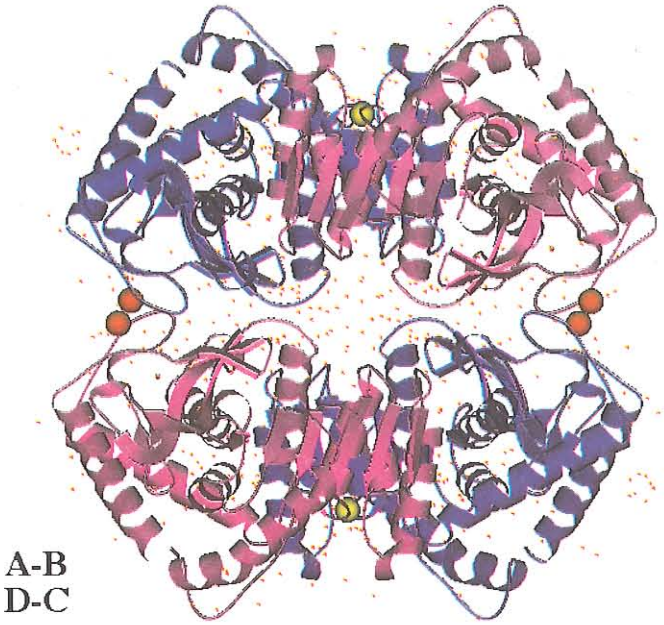


Fig. 3: *Tertiary structure of malate dehydrogenase, an enzyme of intermediate metabolism, from the organism Haloarcula marismortui. The protein is a tetramer (two blue and two violet subunits). The chain fold is drawn to show how the secondary structure helices are organised to form the tertiary structure. The physiological environment of the protein is highly concentrated in salt. The red and yellow balls are solvent chloride and sodium ions, respectively, which are associated in the protein structure and stabilise the tetramer [10].*

If we deal with fundamental structural biology, however, crucial questions still remain to be solved. What is the structure of macromolecules in-situ, within cell? How does macromolecular structure changed during function? How do macromolecules interact in space and time? What is the role of dynamics?

These are questions that can be answered only by combining the results of many methods in biophysics and biochemistry with the results of X-ray, crystallography, NMR, analytical centrifugation, optical methods time-resolved up to femtoseconds, scanning and titration microcalorimetry, electron microscopy, electron crystallography, scanning force microscopy, neutron spectroscopy, small-angle X-ray and neutron scattering.

Developments in physical methods are themselves closely related to advances in computer techniques, electronics, lasers, neutron and synchrotron sources etc.

And finally I should mention single molecule studies. Fluorescence spectroscopy and the atomic force microscope allows the observation and manipulation of single molecules. Up to now, biophysics and biochemistry have dealt with large ensembles for which the laws of thermodynamics are readily applicable. 100 microlitres of a 1mg/ml solution of hemoglobin, for example, are typical protein crystals each containing of the order of 10^{15} macromolecules. Biological molecules in their natural environment, however, act in much fewer copies. The exciting new methods described above allow single molecule behaviour to be probed and pose the challenge of making the link with thermodynamics analysis.

References

[1]T.S. Goodsell, TIBS, **16**, 203 (1991)
[2]M.C. Maurel and G. Zaccai, Bioessays, **23**, 977 (2001)
[3]F. Jacob, La logique du vivant (Editions Gallimard, 1970)
[4]W. L. Bragg (editior), The Crystallic State, Vol.1 (Gr. Bell and Sons, 1939)
[5]A. Guinier and G. Fournet, Small Angle Scattering of X-rays (Wiley, New York, 1955)
[6]A. Yonath and H.G. Wittmann TIBS 14, 329 (1989)
[7]N. Ban, P. Nissen, J. Hansen, P.B. Moore and T.A. Steitz, Science **289**, 905 (2000)
[8]C. Branden and Tooze, Protein Structure (Garland, New York, 1999)
[9]D.M. Engelman and G. Zaccai, Proc. Natl. Acad. Sci. (USA) **77**, 5894 (1980)
[10] S.B. Richard, D. Madern, E. Garcin and G. Zaccai, Biochemistry **39**, 992 (2000)

B 14 Some Aspects of Biomembranes

R. Merkel

Institut für Schichten und Grenzflächen

Forschungszentrum Jülich GmbH

Contents

1 Introduction **2**
- 1.1 General Remarks . . . 2
- 1.2 The Requirement for Biomembranes . . . 2
- 1.3 Principles of Biomembrane Structure . . . 3

2 Compartmentalization of Eukaryotic Cells **4**
- 2.1 The Organelles . . . 4
- 2.2 Membrane Flow . . . 10

3 Molecular Composition of Biomembranes **13**
- 3.1 Some Biologically Important Lipids . . . 14

4 Concluding Remarks **16**

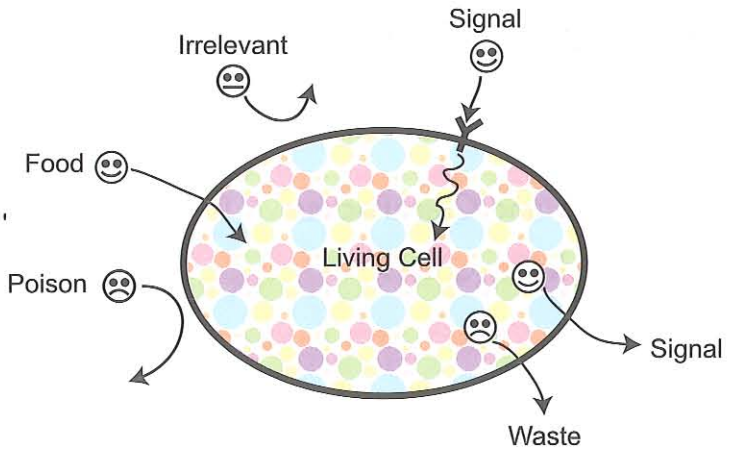


Fig. 1: *The most basic functions of a biomembrane are keeping the molecules of a cell together, blocking the entrance of irrelevant or even harmful substances, and transmitting food as well as signals.*

1 Introduction

1.1 General Remarks

Originally, this contribution was intended to provide a review of function and structure of the membranes of living cells. However, during the collection of material for this talk I realized that this is impossible. Life can take very many different forms, ranging from bacteria to humans. Moreover, life requires that an enormous number of very diverse tasks must be performed at the same time. Examples include making chemical energy available in the form of suitable small chemical components, synthesizing proteins which are the highly specialized nanomachines of a cell, and disposing of waste material via secretion into the environment. Nature often utilizes membranes to perform these tasks. Owing to the diversity of tasks to be performed and the evolutionary pressure to solve these tasks in a highly efficient way, nature developed very many different highly specialized membrane machines. Covering merely the most abundant types of biomembranes would require an entire Summer School. Instead I will present some aspects and ideas. Please note that the selection of topics is highly arbitrary and dictated by my personal interests. If you want or need more balanced and in depth information I can only recommend the study of one of the available excellent text books on cell biology and biochemistry [1, 2, 3].

1.2 The Requirement for Biomembranes

Life is a state far from thermodynamic equilibrium. A division between living entity (the cell) and unanimated environment is vital for the continuous upkeep of such a state. Moreover, a constant conversion of material and energy is a necessary prerequisite for the process of life. These basic functions are illustrated in Figure 1. The advent of biomembranes has provided a means for accommodating these necessities. It serves as a container that keeps together all the diverse biomolecules that constitute a cell and it

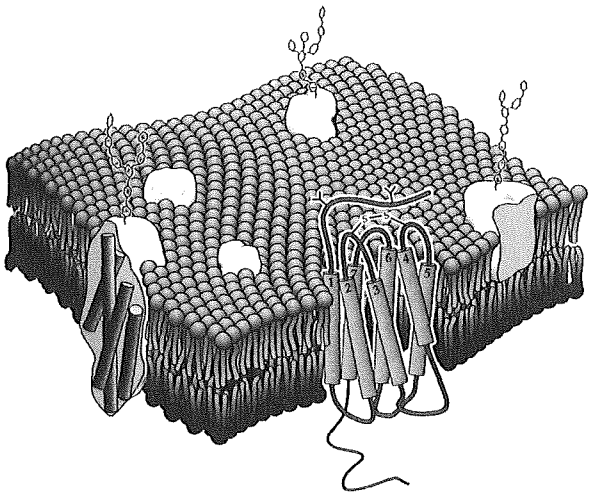


Fig. 2: *The fluid mosaic model. A bilayer of lipids in the fluid phase forms the matrix of the biomembrane. Proteins are embedded in this structure. Taken from [3].*

enables the cell to establish "perfect" conditions in its interior. In view of the paramount importance of the functions of biomembranes it is currently believed that they appeared simultaneously with the first primitive cell.

1.3 Principles of Biomembrane Structure

According to the fluid mosaic model of Singer and Nicholson [4] biomembranes are composed of a lipid bilayer to which membrane proteins are attached in various ways, cf. Figure 2. The lipid bilayer basically serves as two-dimensional solvent for the membrane proteins. *Fluidity* of the lipid layer is necessary for cell survival. The reason for this is that in many chemical reactions within the cell membrane-bound reactants have to meet, e.g. in the electron transfer chain of respiration electrons are transported between various membrane bound enzymes by hydrophobic molecules (the quinones) that are dissolved in the membrane. This process requires sufficient lateral mobility of the reactants which is exclusively given in the fluid phase.[1] Moreover, the permeability of the liquid layer for water is several orders of magnitude higher in the fluid phase.
The various activities (also called functions) a biomembrane has to perform are carried out by the membrane proteins. Examples are binding hormones and transferring a signal into the cell interior, transporting ions or nutrients, and segregating the products of cells like digestive enzymes, cf. Figure 1.

[1]Lipid bilayers exhibit several thermodynamic phases and phase transitions. In the so-called crystalline phase the lipid chains (cf. Figures 2 and 10) are in an all-trans formation and arranged on a crystalline lattice. In the fluid phase the lipid chains exhibit many kinks and no periodicity exists. Translational and rotational diffusion constants of lipids and foreign solutes within lipid membranes are several orders of magnitude higher in the fluid phase. The phase transition temperature depends very strongly on chain length, degree of unsaturation, and branching of the lipid chains. Nature uses this property to control the fluidity of biomembranes. Lipid bilayers exhibit several other phases as well (e.g. tilted versus non-tilted), however no other phase transition has such a profound influence on dynamics.

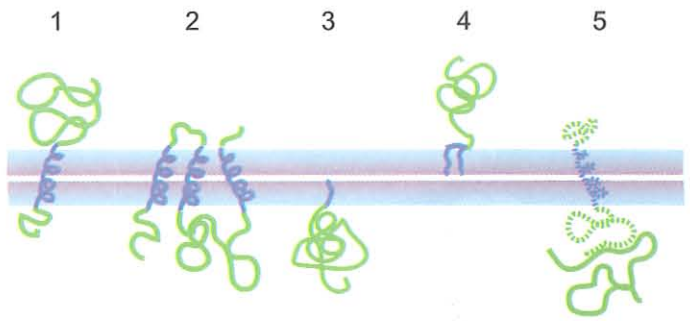


Fig. 3: *shows different ways for the binding of proteins to the membrane. Hydrophobic components are shown in blue color, hydrophilic ones in green. The peptide backbones of the proteins are sketched.* ***1*** *A protein that contains a membrane spanning, hydrophobic α-helix.* ***2*** *A protein that contains several α-helices which form a superstructure, e.g. a pore.* ***3*** *A protein that is anchored by a hydrophobic side group (myristoyl, palmitoyl, or prenyl).* ***4*** *Attachment via a phospholipid anchor (phosphatidyl inositol).* ***5*** *Binding to another membrane anchored protein (depicted as broken line). Proteins 1 and 2 are transmembrane proteins, 1 – 4 integral membrane proteins, and 5 is a peripheral membrane protein.*

Membrane proteins can be attached to the lipid bilayer in different ways, cf. Figure 3. There are three basic strategies for membrane protein interaction: i) hydrophobic stretches in the protein structure, most often a hydrophobic α-helix of suitable length, ii) hydrophobic groups that are attached to the polypeptide. The most important hydrophobic anchor groups are myristic acid, palmitic acid, isoprene, and phosphatidylinositol (a glyco-phospholipid), and iii) binding to other membrane proteins or lipids.
Membrane proteins are classified according to their mode of insertion: peripheral membrane proteins are attached merely by binding to other membrane proteins, whereas integral membrane proteins are embedded with a part of their structure within the hydrophobic core of the membrane. Transmembrane proteins are integral membrane proteins that possess hydrophobic groups on both sides of the membrane. You will learn more on the physics of lipid bilayers in the lectures B8, B9 and B12. The following lecture, B15, will provide a very detailed look on membrane proteins. In the remainder of this lecture I will try to provide some general characteristics of biomembranes.

2 Compartmentalization of Eukaryotic Cells

2.1 The Organelles

Primitive cells (prokaryotes, e.g. bacteria) are lined by a biomembrane that encloses the cytosol, a highly concentrated solution of proteins, DNA, RNA, and other biomolecules (e.g. polysaccharides). These cells were a tremendous achievement of evolution. In fact, their activities changed the earth. Nature exploited the opportunity to use biomembranes in order to form compartments with optimized conditions in the inside for another major step in evolution — the advent of eukaryotic cells. Eukaryotes contain internal organelles that are enclosed by additional membranes within the cell. Figure 4 shows the idealized

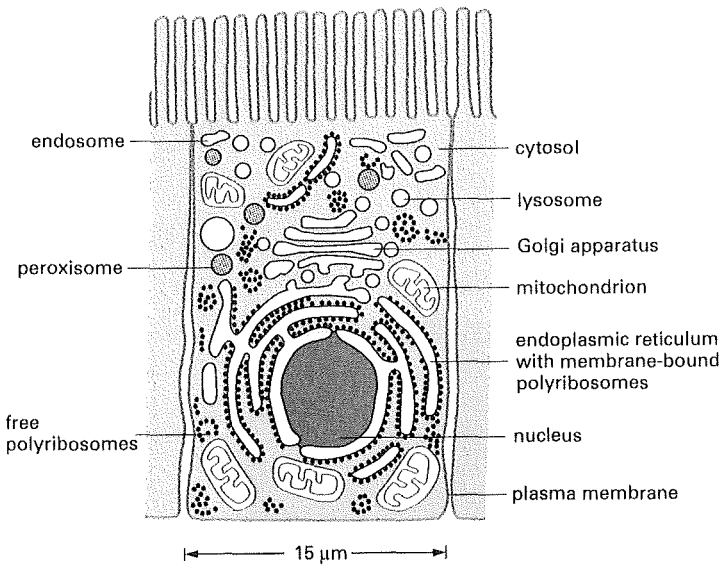


Fig. 4: *Ultrastructure of animal cells. Shown is the idealized architecture of an epithelial cell. While number, size, and shape of the individual organelles may vary widely between different cell types, the underlying architecture is conserved throughout all eukaryotic cells (i.e. higher organisms). Polyribosomes are huge protein aggregates that synthesize proteins, all other structures indicated in the drawing are enclosed by at least one semipermeable membrane. The various organelles are discussed in the text. Taken from [1].*

ultrastructure of an animal cell, while Figure 5 gives a vivid impression of the complexity and density of internal membrane structures.

Each of these organelles serves specific purposes and exhibits a very specific set of biomolecules. Each organelle exhibits an internal medium and a biomembrane that are optimized for the organelle function. Thus each step in a chain of chemical and physical processes can be performed at the optimum conditions. This results in an evolutionary advantage of eukaryotes over prokaryotes which lack this internal organization. In the following we will give a very rough description of the organelles.

The inner medium of the cell is called **cytosol** or **cytoplasm**. Internal cell compartments that are enclosed by separate membranes, i.e. the organelles, are not parts of the cytoplasm. It contains a highly concentrated solution of ions (1%[2]), carbohydrates (3%), proteins (15–20%), and nucleic acid (mostly RNA, 6%). The cytosol is a continuous fluid compartment, that is solutes may disperse throughout the whole cytoplasm. However, it has a very elaborate internal organization. This ultrastructure is based on the *cytoskeleton* which is an extended polymeric network. The cytoskeletal polymer fibers exhibit thicknesses ranging from 9 nm (actin filaments) to about 50 nm (stress fibers which are bundles of actin filaments). Lengths range from short ~20 nm pieces to stress fibers that

[2]All concentrations are given here in weight solute per weight solution.

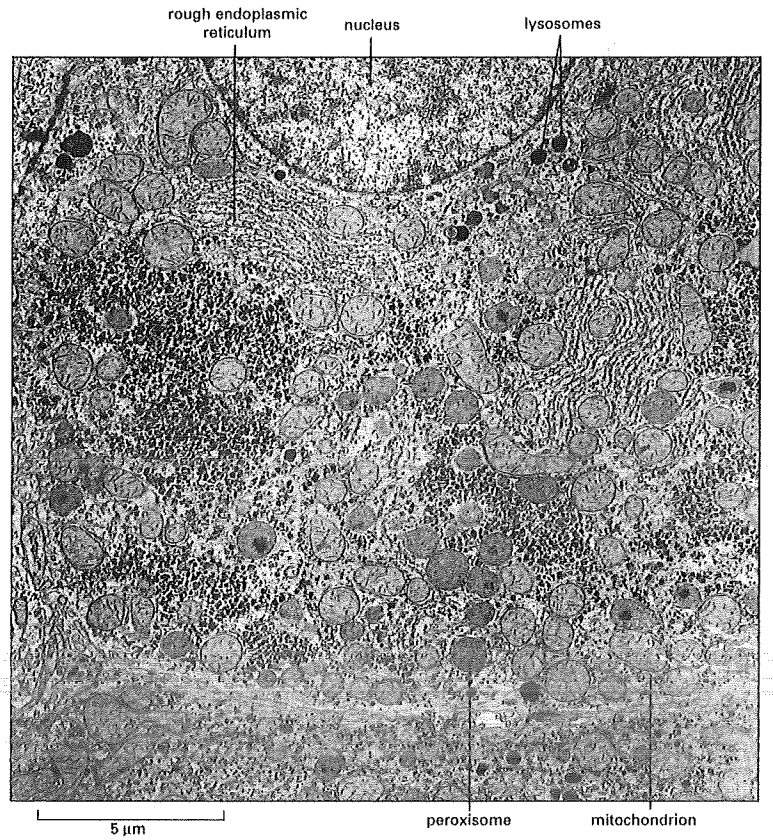


Fig. 5: *Electron micrograph of a liver cell showing a great number of membrane bound organelles. Taken from [1].*

span the whole cell (~50 μm). The cytoskeleton endows the cell with mechanical strength and toughness, the capability to exert mechanical forces[3] and to transport smaller particles like vesicles. Moreover, it serves to organize the cytosol because organelles (e.g. mitochondria) and protein aggregates bind to it and are thus localized in specific regions of the cell. Being the largest compartment of a cell, the cytosol also contains most proteins and is the region of highest biochemical activity.

The **nucleus** contains most of the cellular DNA and serves as "control center" of the cell. It is enclosed by two membranes. Its inner membrane is lined by a polymer network formed by specialized proteins, the lamins. Transport of molecules (messenger RNA and "worn out" proteins leave the nucleus, while many fresh proteins must enter it) is regulated by nuclear pores which are large protein complexes of about 100 nm diameter that span both membranes. Some molecules passively diffuse through this pore while others are actively transported. It has been estimated that ~100 different proteins contribute to this complex, therefore it is not as astonishing that its function is not yet properly understood.

Mitochondria are medium sized (~1 μm) organelles that are abundant throughout the cytoplasm. Like the nucleus they are covered by two membranes. The chemical reactions that convert sugar and oxygen into adenosinetriphosphate (ATP) occur in their interior medium and on their inner membrane which contains many proteins for this purpose. Adenosinetriphosphate contains an energy rich bond and is "the universal source" of free energy throughout cellular metabolism. Figuratively speaking, mitochondria are the "power plants" of the cell. The inner mitochondrial membrane plays a prominent role in this energy conversion process. Within the cell sugars are oxidized in many separate chemical reactions. The electron transport enzymes catalyzing these reactions are embedded and oriented in the inner mitochondrial membrane so that the charge flow due to sugar oxidation results finally in a proton gradient across this membrane. Thus it serves as an electrochemical battery that stores the energy liberated by oxidation of sugar. In a subsequent step these protons flow through a transport protein that spans the inner mitochondrial membrane and uses the free energy release of proton flow to synthesize ATP from its energy poor precursor molecules.

It was shown that mitochondria are not randomly dispersed within the cell. They actively move to locations of highest energy consumption. Pronounced shape changes occur during this process which occurs along cytoskeletal fibers.

Peroxisomes are a second type of oxygen consuming organelles. They contain many oxidative enzymes that serve to oxidize various substances. By this activity they are important for detoxification. Because there are many different molecules to be disposed of, peroxisomes may contain many different enzymes that are produced according to need. Thus peroxisomes are an unusually diverse family of organelles that are very difficult to characterize.

Continuous with the outer nuclear membrane is the membrane of the **endoplasmatic reticulum (ER)**. It is a labyrinth of flattened membrane tubes and sacs and one of the largest organelles of the cell. It is the location where all transmembrane proteins and nearly all secretory proteins are synthesized. Protein are synthesized by polyribosomes which are large (~30 nm) aggregates of proteins and RNA. In the largest part of the ER membrane proteins are synthesized directly at the membrane which therefore carries many

[3]The cytoskeleton can actively condense in a temporally and spatially controlled manner. This condensation is caused by molecular motors, e.g. myosin, that transiently cross-link cytoskeletal fibers and move them with respect to each other. This process requires free energy in form of APT.

polyribosomes. This gives this part of the ER membrane a characteristic appearance in the electron microscope ("rough ER"). Lipids are also synthesized in and at the ER membrane. In some specialized cells (hepatocytes of the liver) hydrophobic toxic substances are chemically processed within some specialized parts of the ER membrane[4]. These parts of the ER membrane exhibit no ribosomes and therefore appear smooth ("smooth ER"). Please note that synthesis of membrane proteins and lipids in the ER is vectorial, that is it occurs exclusively at one side of the membrane. Further transport of these biomolecules from the ER to most other organelles (Golgi apparatus, lysosomes, endosomes, secretory vesicles, and the plasma membrane) occurs via lipid vesicles. This ensures that proteins and lipids maintain their orientation within the membrane during transport. In contrast, transport to mitochondria and peroxisomes occurs through the cytosol via specialized transport proteins. These organelles need specific membrane proteins for protein import and to establish the correct orientation of membrane lipids.

After synthesis in the ER and in some cases a first glycosylation (i.e. the addition of polysaccharides to the proteins) proteins and lipids enter the **Golgi apparatus**. This organelle consists of a series of membrane sacs that are most probably *not* directly connected. Material transport within the Golgi is therefore mediated by vesicles. Within the Golgi apparatus molecules are further processed, especially those bearing oligosaccharides. Moreover, molecules are sorted according to their destination. The different cisternae of the Golgi apparatus contain different enzymes. Therefore the controlled transport of biomolecules through the Golgi apparatus enables the cell to perform series of very complex chemical reactions.

Lysosomes are organelles that are specialized for the breakdown of biomolecules. Their interior contains about 40 different digestive enzymes. The lysosomal membrane contains a proton pump that keeps the interior acidic at a pH of 5, which is the optimum condition for this set of digestive enzymes.

Material that has entered a cell via endocytosis (a process discussed later on) is first brought to **endosomes** via transport vesicles. Within the endosomes incoming biomolecules are sorted. Some are transported back to the cell surface (e.g. receptors or cell surface specific lipids). The rest is subjected to first digestive breakdown processes that end with the entire chemical decomposition of the material after transport to lysosomes.

The last major membrane compartment to be discussed here is the **plasma membrane**. This membrane encloses the entire cell. It thus serves as boundary and interface separating the cell from its environment. Usually the plasma membrane is not considered as a separate organelle, yet it is distinct in several ways from other membranes. The plasma membrane has a pronounced layered structure, cf. Figure 6. From the inside, the plasma membrane is supported by and connected to the cytoskeleton, a highly dynamic and diverse network of specialized proteins that are able to farm huge polymers (up to 100 μm in length). In most cells the cytoskeleton is especially dense close to the membrane and forms a cortical structure for enhanced mechanical strength. The lipid bilayer of the plasma membrane is rich in transmembrane and peripheral proteins. These molecules are important for cell adhesion, cell recognition, and receiving external signals (e.g. hormones or messenger substances). The outside of the plasma membrane is covered by a layer of oligosaccharides, the glycocalix. This polymer layer serves several purposes. On one hand it prevents cell adhesion via steric stabilization and electrostatic repulsion[5]. On

[4]Due to this function hepatocytes possess an extremely large endoplasmatic reticulum.

[5]Many cell surface oligosaccharides are rich in sialic acid which is negatively charged.

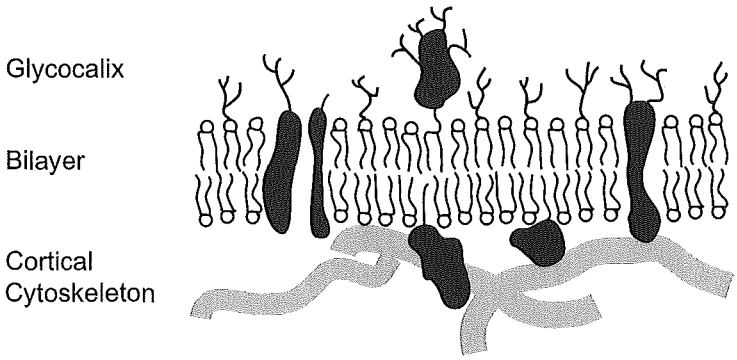


Fig. 6: *The structure of the plasma membrane of an animal cell. The lipid bilayer exhibits a thickness of 6 – 10 nm, the glycocalix is ∼50 nm thick, and the cortical cytoskeleton about 100 – 500 nm. Glycocalix and cortex are highly variable structures that are adapted to the functions of a cell. For example, the cortex may be highly dilute or even absent in very mobile parts of the plasma membrane. The organization of plant or bacterial plasma membranes is very different.*

the other hand, the highly complex chemical structures of these cell-surface saccharides serve as markers for cell type and species and thus may even become target motifs for cell adhesion. Moreover, glycosylation protects the cell surface from attack by exogenous enzymes, e.g. lytic enzymes secreted by bacteria.

Please note that the composition and architecture of the plasma membrane varies widely between different species, different cell types within one organism, and even depends strongly on the location on the surface of one and the same cell.

This discussion of the cellular organelles is summarized by a comparison of their relative sizes and numbers, see Tables 1 and 2. It is apparent from these tables that the relative sizes of the different organelles vary widely between cell types. This reflects the different functions of these cells. Please note that the plasma membrane is only a very minor part of the membraneous system of an eukaryotic cell. This is on a first glance surprising and

Volume of the Various Organelles

Organelle Type	Fraction of Cell Volume (%)	Approximate Number per Cell
Cytosol	54	1
Mitochondria	22	1700
ER	13	1
Golgi	2	several distinct compartments
Nucleus	6	1
Peroxisomes	1	400
Lysosomes	1	300
Endosomes	1	200

Table 1: *Contributions of the organelles to the total cell volume (∼ 5 000 μm^3) in the case of an average hepatocyte (liver cell). Data taken from [1].*

Area of Different Cellular Membranes

Membrane Type	Liver Hepatocyte	Pancreatic Exocrine Cell
Plasma Membrane	2	5
Rough ER	35	60
Smooth ER	16	<1
Golgi Apparatus	7	4
Mitochondria		
— Outer Membrane	7	4
— Inner Membrane	32	17
Nucleus, Inner Membrane	0.2	0.7
Secretory Vesicles	n.d.	3
Lysosome	0.4	n.d.
Peroxisome	0.4	n.d.
Endosome	0.4	n.d.

Table 2: *Distribution of the total membrane area on the various organelles. Values are given in %. The abbreviation n.d. denotes not determined. Membrane area is ~110 000 μm^2 for hepatocytes and ~13 000 μm^2 for pancreatic exocrine cells. The volume of a pancreatic exocrine cell is ~1 000 μm^3. Data taken from [1].*

underlines the importance of inner membranes for cell structure and metabolism.

2.2 Membrane Flow

From the previous sections, it is obvious that the membranes of a cell undergo a permanent and intense turnover. This material flow is accompanied by many highly selective sorting processes. These are necessary because each organelle has its own and distinct lipid and protein composition. Vesicles form from organelle membranes. Thus note only the "cargo" molecules are transported but also other molecules that are destined to remain in the organelle. These materials (mostly lipids and membrane proteins) are sorted out in the target membranes and transported back by a retrograde flow. For the purpose of sorting and correct targeting the vast majority of proteins bear peptides or other chemical groups at their surfaces that serve as signals. These surface markers indicate the final destination of the molecules and thus serve the same purpose as the address label on the mail. Numerous receptors that bind specifically[6] to these chemical marker groups are involved in lipid and protein sorting. Figure 7 depicts the most important pathways of

[6]In molecular recognition specificity and affinity signify very different properties of bonds. Affinity is the strength of a bond as measured by the binding constant or the standard free enthalpy of binding ΔG_0. Specificity is the selectiveness of molecular recognition, in other words the capability of specialized molecules to distinguish between the very many biomolecules within a cell. Specificity of biomolecular recognition is achieved by large contact areas between complementary biomolecules. Dispersed over these contact areas numerous weak ($\sim k_B T$), short-ranged (~0.2 nm), and competitive physical interactions occur. Stable biomolecular complexes exist only if two molecules possess "faces" that match in topography and interactions. This rarely ever happens by pure chance. While biomolecular interactions are usually of low affinity (ΔG_0 is typically on the order of only 10 $k_B T$) their specificity is unsurpassed by any chemistry ever designed by humans. For example, the immune system recognizes some foreign peptides in the blood at levels that correspond to finding 100 rotten apples in the annual world harvest!

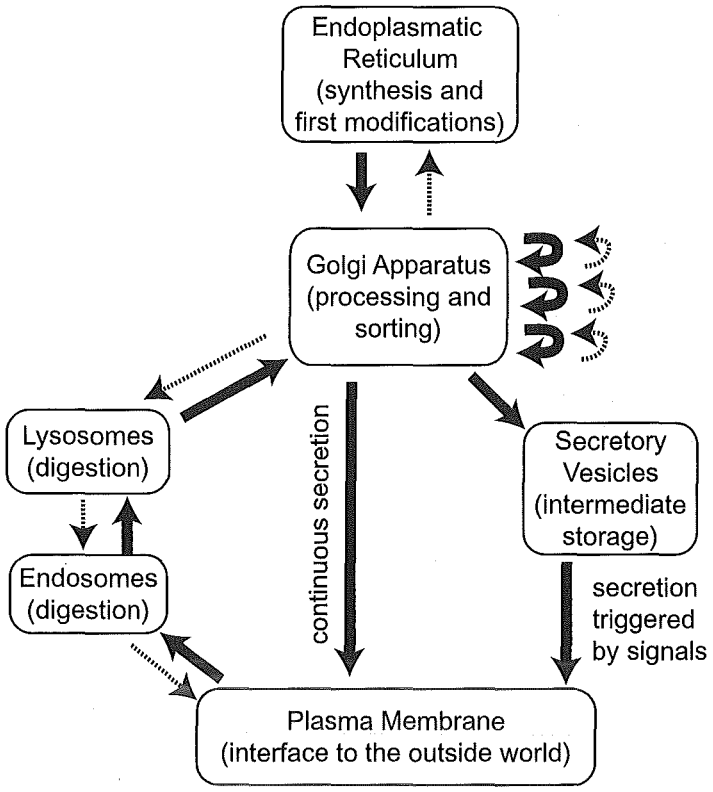


Fig. 7: *Scheme of the material transport within a cell via vesicles (adapted from [1]). Soluble proteins destined for secretion into the extracellular space, membrane proteins, lipids, and smaller biomolecules (e.g. neurotransmitters and hormones) are transported. Primary transport is indicated with thick arrows. A constant back flow of organelle specific molecules (broken arrows) maintains the identity and integrity of the diverse organelles. In the steady state (i.e. stationary cell) all flows must cancel. Most flows occur against concentration gradients and are therefore energy consuming.*

vesicular transport. Obviously metabolic energy is necessary to maintain these permanent sorting and transport processes.

Vesicular transport involves three distinct steps: budding of vesicles from the source membrane, active or passive (i.e. diffusive) motion of the vesicles to their destination, and finally fusion with the target membrane. Figure 5 convincingly shows that each vesicle will hit many different membrane structures on its way. To avoid erroneous deliveries vesicle fusion must be highly specific and tightly regulated. The same holds for vesicle budding. Both processes are difficult to study and in many instances not yet understood.

In this paragraph I will describe the cellular uptake of cholesterol, which includes an intensively studied example of vesicle budding. Cholesterol is transported in the blood bound to a transport protein (low density lipoprotein, LDL). About 2 000 cholesterol molecules and several hundred phospholipids (see below for a discussion of these molecules) are complexed by this protein. Together they form a soluble particle of 22 nm diameter.

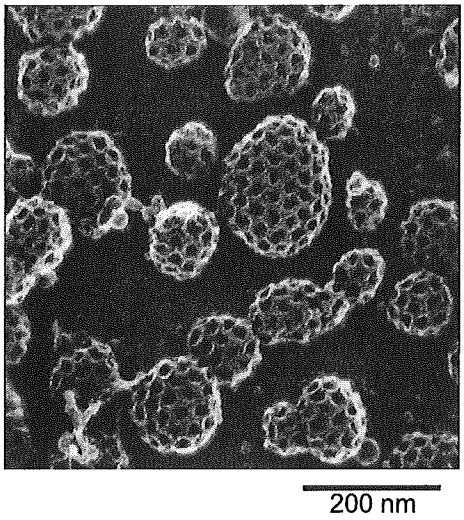


Fig. 8: *An electron micrograph of clathrin coated pits and vesicles at the inner surface of the plasma membrane of a fibroblast. The sample was quick frozen, deep etched, and metal coated. Taken from [1].*

Cells carry surface receptors for these particles[7]. These receptors are transmembrane proteins that bind highly specific to LDL particles. Their cytosolic domain undergoes an, as to now uncharacterized, conformational change. Such conformational charges are a common strategy to transfer signals (here availability of cholesterol) from the outside world into the cell. Loaded receptors are in turn bound to specific adapter proteins at the inside of the membrane. While each cargo (e.g. LDL) has its own specific receptor and each receptor has its own specific adaptor, many different adaptor proteins can bind to clathrin. The latter protein has the shape of a triskelion and self-assembles at the inside of the membrane into a "basket" that closely resembles the seams on a soccer ball, cf. Figure 8. Clathrin assembly results in a strong localized bending of the membrane. Driven by this bending moment, clathrin coated pits form. In the further course of this process these pits bud off the membrane to form clathrin coated vesicles. Following budding the clathrin coat is rapidly disassembled and the vesicles fuse with endosomes (cf. Figure 9). There are as well other ways to form transport vesicles. The uptake of LDL occurs at the plasma membrane. This process, local enrichment of material at the plasma membrane and subsequent uptake by vesicle formation, is termed *endocytosis.*

The reverse process, fusion to the target membrane, is even less understood. It is known that after depolymerization of the vesicle coat a specific marker protein for the vesicle type becomes exposed. This molecule is called V-SNARE. While each biomolecule within the vesicle displays marker groups that signify the destination of these molecules, V-SNARE is an entire molecule that serves the same function for the whole transport vesicle. Strictly speaking there are many different V-SNARE molecules, at least one for each destination of

[7]One human in 500 has defective LDL receptors. Because the cells of those individuals are very ineffective in taking up cholesterol they have very high cholesterol levels in the blood and run a high risk of heart and circulation diseases.

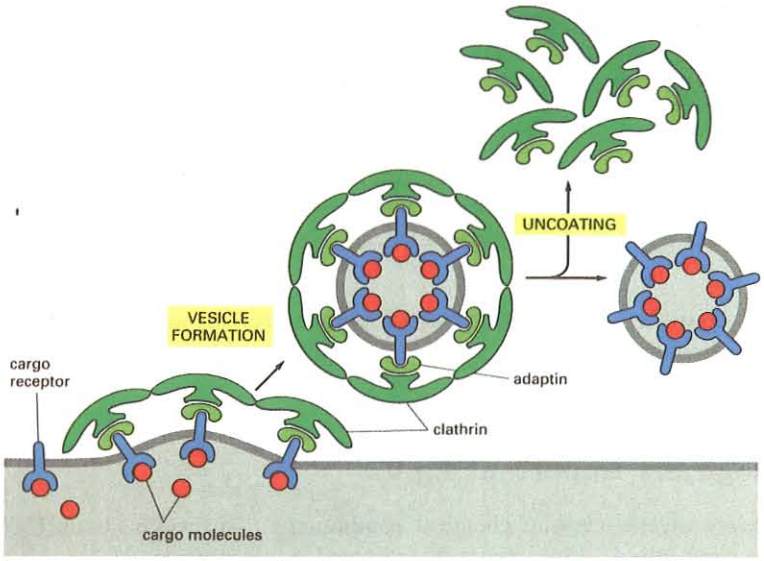


Fig. 9: *Summary of the intermediate steps of material uptake by the cell via clathrin coated vesicles. Please note that the existence of adaptor proteins enables the cell to use the clathrin machinery for different cargoes without impairing specificity of uptake and transport. Taken from [1].*

vesicular transport. The target membranes contain two other proteins, SNAP25 which is ubiquitous in all membranes and T-SNARE which is specific for the target organelle. Upon contact between vesicle and target membrane V-SNARE and T-SNARE bind specifically. This ensures correct targeting. Non-specific fusion of vesicles and other membranes is extremely rare because all biomembranes are negatively charged and most lipids display bulky head groups that keep the hydrophobic moieties apart (see below). The complex of V-SNARE and T-SNARE is further stabilized by binding of SNAP25. In vitro these three proteins are sufficient to induce membrane fusion. In vivo an unknown number of other proteins (at least 5) help to speed up vesicle fusion by at least a factor of 1 000. Moreover, these additional proteins are thought to provide regulatory mechanisms.

3 Molecular Composition of Biomembranes

Biomembranes consist of a mixture of proteins and lipids. Proteins confer function to the membrane whereas lipids are the structure forming elements. The ratio of both molecule types varies widely from cell to cell.

From Table 3 it is obvious that the protein to lipid ratio is correlated to membrane function. The most important function of myelin is serving as electrical insulator. Because lipid membranes are excellent insulators this function requires little protein. Consequently myelin has by far the lowest protein content of all membranes listed in Table 3. Biochemically very active membranes (e.g. mitochondrial and bacterial membrane) are at the other

Protein to lipid ratio (mass per mass) for different membranes			
Myelin	Erythrocyte Plasma Membrane	Mitochondrial Membranes	Bacterial Membrane (E. coli)
28%	150%	320%	300%

Table 3: *Lipid to protein ratio of different membranes. Data taken from [3]. Myelin is a sheath that covers axons of some nerves. It consists of the plasma membranes of specialized cells (Schwann's cells) that are wrapped many times around the axon.*

extreme. According to their very diverse functions, membrane proteins are extremely diverse. Even the most rudimentary discussion of these molecules would require much more time than we have here.

3.1 Some Biologically Important Lipids

Natural lipids are a very diverse class of chemical components. In myelin about 1500 different lipid species were found. From these 30 occurred in sizeable amounts. Most important are phospholipids and cholesterol. The lipid composition varies widely between different membranes as demonstrated in Table 4. Figure 10 depicts the chemical structure of naturally occurring phospholipids, Figure 11 the one of cholesterol.

Phospholipids are composed of an hydrophilic head group and two hydrophobic alkyl chains. This amphiphilic structure results in the formation of large supermolecular aggregates in aqueous environment. Self-assembly of such structures is covered in the contribution B8, therefore I will be very brief here. Please note that lipid bilayers are lamellar phases. In order to be able to form stable lamellar phases an amphiphilic molecule must consist of a hydrophilic and a hydrophobic moiety of equal area. This requirement is met in most natural lipids and explains the bulkiness of the lipid head groups.

Cholesterol exhibits a rigid hydrophobic backbone, see Figure 11. The terminal OH-group is the only polar part of the molecule. Therefore it does not form lamellar phases by itself. Chemically cholesterol is a sterol. Other members of this biologically important class of molecules are hormones and bile acids. Despite its bad reputation cholesterol is an essential constituent of eukaryotic membranes. Cholesterol mostly consists of a rigid hydrophobic structure, whereas the hydrophobic moieties of phospholipids are fluid alkyl chains. Due to this great difference in molecular architecture the phase diagrams of mixtures of cholesterol and lipids are very complex and not yet fully understood. Cholesterol lowers the freezing point of lipid membranes. Moreover, it condenses the lipid chains. This effect results in improved electrical insulation, less permeability to hydrophilic solutes, and much improved mechanical toughness. Nowadays researchers assume that cholesterol was essential to the evolution of eukaryotes which exhibit much larger and more flexible membranes than prokaryotes.

In addition to this remarkable variability in lipid composition, biomembranes also exhibit a pronounced sidedness. Membrane proteins are always embedded in the membrane in a unique orientation. Moreover, the lipid compositions of both leaflets of the bilayer differ. For example, in erythrocyte plasma membranes phosphatidylcholine and sphingomyelin are enriched in the outer leaflet, whereas phosphatidylserine and phosphatidylethanolamine dominate the inner leaflet. In all plasma membranes of animals

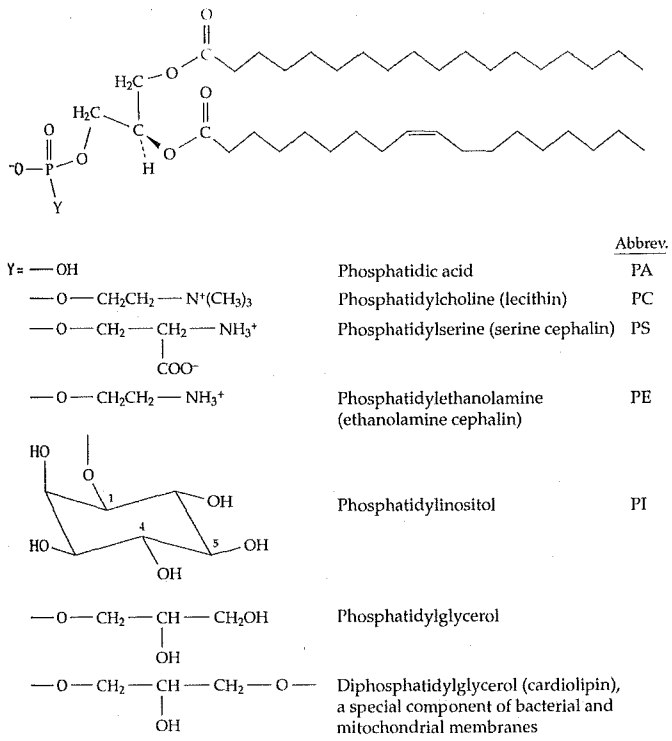


Fig. 10: *Chemical structure of some biologically important phospholipids. Taken from [3]. Natural phospholipids often exhibit a saturated fatty acid in 1-position and an unsaturated one in 2-position as depicted here. Chain length and degree of unsaturation are adapted to the temperature of the environment in order to provide an optimal combination of membrane fluidity and toughness. The charged head group (left from the glycerol moiety) is highly polar, the rest of the molecule apolar. Please note that PC and PE are zwitterionic molecules, whereas the other phospholipids carry one net negative charge under physiological conditions.*

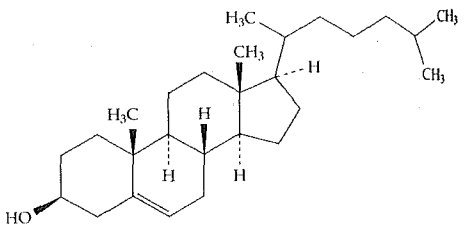


Fig. 11: *Chemical structure of cholesterol. Taken from [3].*

Lipid composition (mass per mass) of different membranes

	Myelin	Plasma Membrane		Mitochondrial	Bacterial	Endoplasmatic
		RBC	Liver Cell	Membrane	Membrane	Reticulum
Chol	22	23	17	3	0	6
PE	15	18	7	35	70	17
PS	9	7	4	2	<1	5
PC	10	17	24	39	0	40
SM	8	18	19	0	0	5
GL	28	3	7	<1	0	<1

Table 4: *All concentrations are given in % of total lipid mass. Abbreviations: RBC red blood cell (erythrocyte), Chol cholesterol, PE phosphatidylethanolamine, PS phosphatidylserine, PC phosphatidylcholine, SM sphingolmyelin, GL glycolipids. Bacterial membrane refers to the membrane of E. coli. Data taken from [1].*

glycolipids are exclusively found at the outer surface. The asymmetry of biomembranes results from the differences between the media on both sides of the membrane, cf. Figure 6. Differences between these media occur in basic physicochemical parameters like pH. For example, the lysosomal membranes separates the cytosol (pH≈7.2) from an acidic medium (pH≈5). Moreover, both sides of a membrane differ greatly in biological function. For example, a hormone must be bound at the outer side of the plasma membrane, whereas this outer signal will result in activation of an enzyme that is attached to the inside of the plasma membrane, cf. Figure 1. Thus both physical and biological effects contribute to membrane asymmetry.

4 Concluding Remarks

Biomembranes are vital parts of cells. They are very dynamic entities that undergo a rapid turnover of lipids and proteins. Because they perform very many different functions that are essential to cell survival they exhibit very complex architectures. Research on biomembranes occurs along two major lines. One is the study of membrane structure and processes of living cells. This is a very exciting, yet extremely complex field of science. In a very different approach scientists try to build "minimal cells" by reconstituting synthetic lipid molecules and a small number of proteins into functional vesicles. Experiments on these vesicles teach us what the minimum requirements for certain biological functions are.

Biomembrane science spans very different areas of science including cell biology, molecular biology, biochemistry, biophysics, soft matter physics, and physical chemistry. At present it is a highly dynamic and expanding field full of surprises. Unfortunately time does not allow to present detailed examples of this research.

References

[1] B. Alberts, D. Bray, J. Lewis, M. Raff, K. Roberts, and J.D. Watson, *Molecular Biology of the Cell* (Garland Publishing, New York, 1994). See especially chapters 10

through 13.

[2] H. Lodish, A. Berk, S.L. Zipursky, P. Matsudaira, D. Baltimore, and J. Darnell, *Molecular Cell Biology* (Freeman and Co., New York, 2001). See especially chapters 1, 5, and 15.

[3] D.E. Metzler *Biochemistry. The Chemical Reactions of Living Cells.* (Harcourt Academic Press, Burlington MA, 2001). See especially chapter 8.

[4] S.J. Singer and G.L Nicolson, Science **175**, 720 (1972)

B15 Biological Nanomachines

G. Büldt and J. Heberle
Institut für Biologische Informationsverarbeitung
IBI-2: Biologische Strukturforschung
Forschungszentrum Jülich GmbH

Contents

1 Biological machines and the proton pump Bacteriorhodopsin (bR)....2

2 The photocycle and proton translocation across bR.....2

3 The ground state structure of bR.....4

3.1 Electron and neutron diffraction on 2D lattices of bR.....4

3.2 The crystal structure of bR.....4

4 Intermediate states of the working cycle of bR 6

4.1 Infrared spectroscopy.....6

4.2 Part of the mechanism evolves 8

4.3 Changes in the tertiary structure of bR 8

4.4 The crystal structure of the M state.....9

5 More details of the mechanism 11

1 Biological machines and the proton pump Bacteriorhodopsin (bR)

One of the most astonishing miracles of molecular biology is that a linear polypeptide chain, composed of 20 different amino acids, can fold to a densely packed protein, which can serve as a nanomachine. Nature has developed a large number of different tools and machines, which cut, tie or modify molecules or synthesize new ones from a template. The knowledge of the mechanisms of these machines allows to improve them or use them under the most optimal conditions or even develop machines for new tasks. The working cycles of many of these tools, called enzmyes, have been elucidated on the basis of the three-dimensional structures of the ground and intermediate states.
There are two classes of proteins, water soluble and membrane integrated proteins. In this lecture the integral membrane protein bacteriorhodopin (bR) is chosen as an example for demonstrating how information is obtained from different biophysical methods to understand the function of this membrane protein on the basis of its structure and dynamics. There are only a few such proteins which have attracted the interest of a large number of research groups.

2 The photocycle and proton translocation across bR

Almost 30 years ago, bacteriorhodopsin (bR) was found in *Haloarchea*. It represents a simple photosynthetic machinery that uses light energy to translocate protons out of the cell interior [1]. Bacteriorhodopsin is densely packed in hexagonal two-dimensional lattices, the so-called purple membranes (PM) in the plasma membrane of the *Halobacterium salinarum*. The characteriziation of the aggregation state of bR in the PM was given by X-ray diffraction [2] on these natural two-dimensional lattices (Fig.1). It was found by Oesterhelt and Stoeckenius [1] that the chromophore, retinal, covalently bound via a Schiff base to Lys 216, enables this protein to pump protons across the cell membrane.
The photocycle of bR (Fig.2) is linked to the active transport of protons by delivering part of the energy of the absorbed photon to this process. In the ground state (BR_{568}) of the photocycle the retinal is in an all-*trans* conformation, the Schiff base being protonated (pK ~ 13) and positively charged. Upon absorption of a photon, the retinal goes via an excited state to a 13-*cis* retinal conformation, which results in a dramatic pK down-shift to 3. Hence in the transition from the L to the M state the proton is released from the Schiff base and after 50 µs a proton appears at the extracellular surface. The first part of the photocycle is quite fast compared to the last part, which occurs in the ms time domain. In this part a proton has to be delivered from the inside of the cell to the Schiff base and the retinal has to reisomerize back to the all-*trans* conformation [3].

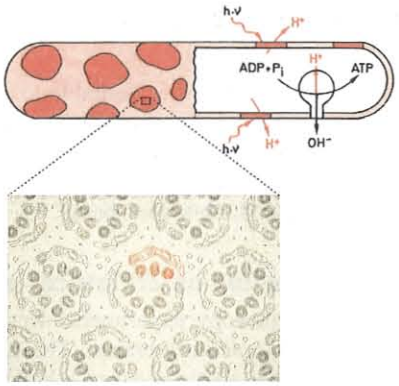


Fig. 1: *Schematic view of the Halobacterium salinarum. bR is aggregated in highly ordered two-dimensional lattices (space group p3). Three bR molecules per elementary cell are surrounded by about 9 lipid molecules. One monomer in a trimer is marked in red. The proton gradient produced by bR drives an ATP-synthase, which synthesizes ATP from ADP and P_i. The energy-rich compound ATP drives numerous cellular processes.*

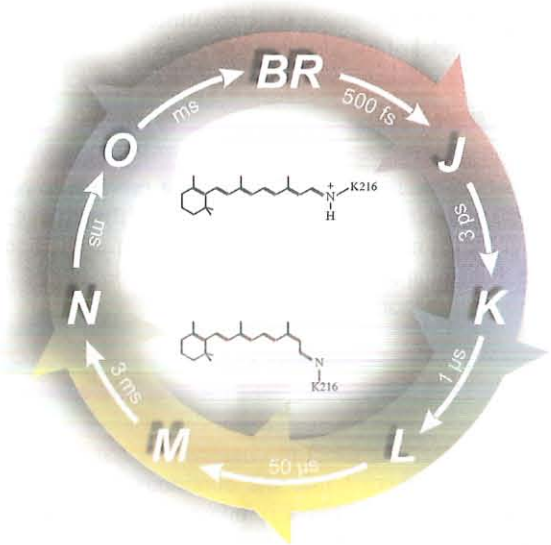


Fig. 2: *The photocycle of bR showing the light-adapted ground state BR_{568} and the intermediates J_{620}, K_{590}, L_{550}, M_{412}, N_{530}, O_{640} (indices: absorption maxima in nm)with their lifetimes. The conformation of all-trans and 13-cis retinals are also depicted. Time-resolved spectroscopy data revealed a splitting of the M intermediate into two substates , an early M_1 and a late M_2 state.*

3 The ground state structure of bR

To elucidate the mechanism of a nanomachine it is desirable to resolve its atomic structure. For water soluble proteins this is achieved by crystallizing the protein and solving the structure using the X-ray diffraction pattern. When structural research on bacteriorhodopsin was started no crystals of an integral membrane protein were ever made. The difficulty arose from the hydrophobic surfaces sticking in the lipid membrane.

3.1 Electron and neutron diffraction on 2D lattices of bR

Therefore electron diffraction and microscopy experiments were performed on the highly ordered two-dimensional lattices, the purple membranes. The basic picture of the tertiary structure, describing the three-dimensional arrangement of α-helices spanning the membrane, was given in several papers on low dose electron microscopy [4]. The knowledge of the amino acid sequence allowed the prediction of a folding model by determining seven α-helical stretches in the polypeptide chain, which were assigned to the seven α-helices seen in the electron microscope structure [5]. In the following years, neutron diffraction was the method of choice to improve this model using bR molecules containing certain perdeuterated amino acids and partially deuterated α-helices [6].
In 1990, cryo-electron microscopy provided an additional breakthrough providing a structure of bR at 3.5 Å resolution in the *X-Y* plane and 7 Å in the *Z*-direction. This picture allowed for the first time, including all the information from other methods mentioned above, the construction of a molecular model of bR [7]

3.2 The crystal structure of bR

Bacteriorhodopsin was one of the first integral membrane proteins to be crystallized in three dimensions [8]. However, these crystals showed only poor diffraction. Considerable progress was made by Schertler et al. [9] using the surfaces of freshly formed benzymidine crystals as nucleation sites. These plate-shaped crystals gave diffraction to 3.6 Å in the *a*- and *b*-directions and 4.2 Å in the *c*-direction.

A novel concept for crystallization of membrane proteins in a lipidic cubic phase was reported by Landau and Rosenbusch [10]. They crystallized bR in a monoolein-water cubic phase and obtained microcrystals of space group $P6_3$ with a unit cell of a = b = 61.76 Å; c = 104.16 Å; $\alpha = \beta = 90°$ and $\gamma = 120°$. Although the exact mechanism of crystallization is still unknown, it seems probable that bR, once inserted into the continous three-dimensional curved lipid bilayer of the cubic phase, diffuses within this bilayer to form a nucleation particle from which well-ordered crystals can grow. They started with microcrystals of up to 30 μm in diameter and 5 μm in thickness. These small crystals already gave diffraction to 2.5 Å resolution on a specially designed beamline, the microfocus beamline ID13 at the ESRF Grenoble [11]. Using a highly focused beam with a diameter of about the same size as the crystal, the signal-to-noise ratio increased significantly.

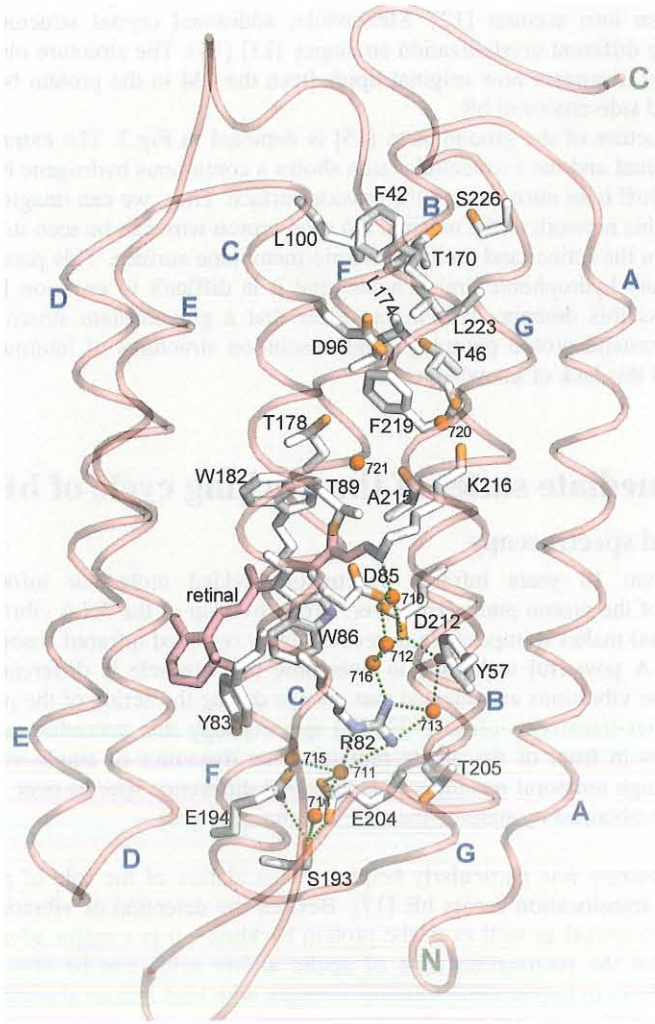


Fig. 3: *Ground-state structure of bR with the cytoplasmic side up and the extracellular side down. The protein backbone is represented by thin ribbons. Several functionally important residues and water molecules are shown. All-trans retinal is in purple colour. Dotted green lines indicate hydrogen bonding distances ranging from 2.3 to 3.4 Å. Structural coordinates have been deposited on the protein data bank (entry: 1cwq).*

The cell constant in the *a*- and *b*-directions of 61.76 Å together with the hexagonal space group gave an indication for an arrangement of bR molecules similar to the PM. The crystal can be described as a stack of PM-like two-dimensional lattices with the stack axis parallel to the screw axis, which is along the c-direction of the crystal. The crystallization conditions in the lipidic cubic phase were continuously improved, so that crystals larger than 400 μm in diameter became available in our group. The crystals showed a merohedral twinning which

had to be taken into account [12]. Meanwhile, additional crystal structures of bR were published using different crystallization strategies [13] [14]. The structure obtained by Essen et al [13] nicely illustrates how original lipids from the PM in the protein boundary interact with amino acid side-chains of bR.
Our crystal structure of the ground state [15] is depicted in Fig.3. The extracellular domain between the retinal and the extracellular side shows a continuous hydrogene bonding network between the Schiff base nitrogen and the outside surface. Thus, we can imagine a proton to be conducted via this network to the outside. No such proton wire can be seen in the cytoplasmic domain between the retinal and the cytoplasmic membrane surface. This part of the structure contains so many hydrophobic amino acids, that it is difficult to envision how a proton is conduced across this domain. This makes clear that a ground state structure alone is not enough to understand proton pumping. High resolution structures of intermediate states are necessary to fill this lack of knowledge.

4 Intermediate states of the working cycle of bR

4.1 Infrared spectroscopy

Since more than 15 years infrared spectrosopy added molecular information to the understanding of the proton pump. However, strong overlap of the 3N-6 vibrations (with N = number of atoms) makes it impossible to record highly resolved infrared absorption spectra of large proteins. A powerful technique to overcome this obstacle is difference spectroscopy where only those vibrations are selected that change during the action of the protein. With the advent of Fourier-transform infrared (FT-IR) spectroscopy this procedure allows to record single vibrations in front of the whole protein. Even dynamics of single vibrations can be followed with high temporal resolution. Nanosecond difference spectra over a broad spectral range have been obtained by state-of-the-art FT-techniques [16].

Infrared spectroscopy was particularly helpful in elucidation of the role of particular amino acids in proton translocation across bR [17]. Besides the detection of vibrational changes of the chromophore retinal as well as of the protein backbone, it is a major advantage of FT-IR spectroscopy that the protonation state of acidic amino acids can be observed. Step-scan spectroscopy allows to follow these transient changes with high temporal resolution [18].
Fig.4 displays difference spectra between ground state bR (negative bands) and the intermediates K, L, M, N, and O (positive bands). The range selected from 1800 to 1000 cm^{-1} is particularly useful because of the richness in band features. Except for the K-bR spectrum, the displaced difference spectra have been obtained with time-resolved attenuated total reflection (ATR) FT-IR spectroscopy. This evanescent wave technique, where the sample is immersed in excess water, allows for the precise control of parameters like pH, temperature and ionic strength [18]. Conditions have been chosen that maximise the transient concentration of the respective intermediate state [19].

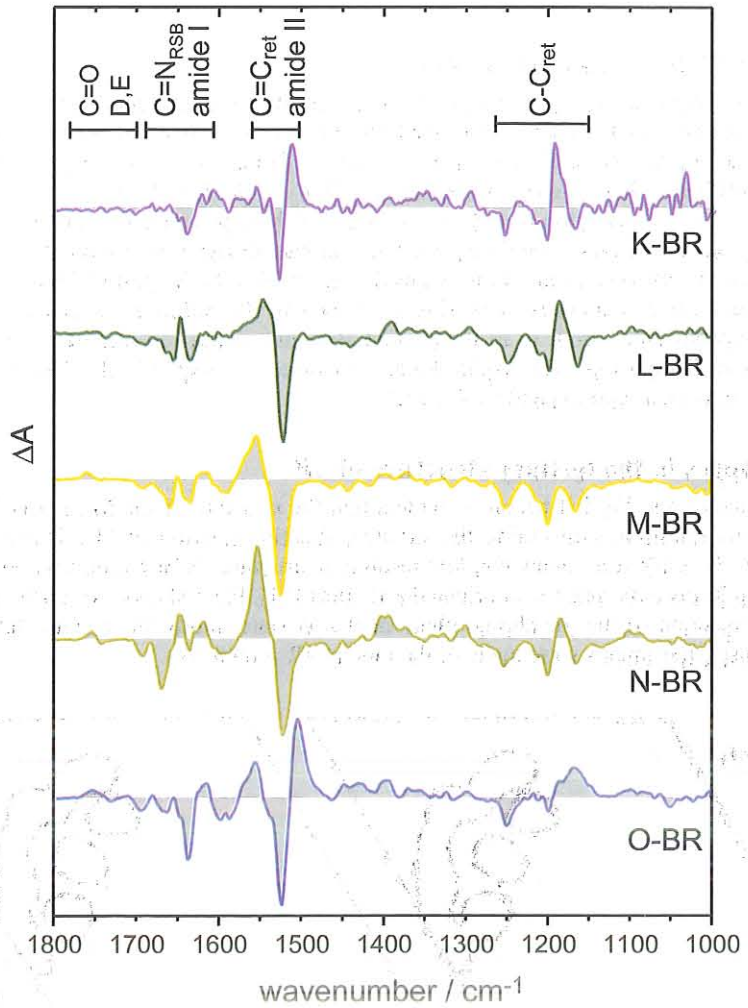


Fig. 4: *Infrared difference spectra of the photocycle intermediates of bR. All but the K-BR spectrum have been extracted from time-resolved ATR/FT-IR experiments under the following conditions: L-BR (10 μs, pH 6.6, 20° C), M-BR (300-400 μs, pH 8.4, 20° C), N-BR (80-100 ms, pH 8.4, 20° C), and O-BR (5-10 ms, pH 4.0, 40° C). The K-BR difference spectrum was obtained under steady-state conditions (continuous illumination of a bR microcrystal with λ = 514 nm from an argon ion laser, sample is kept at 100 K). Spectra are scaled to yield identical negative absorbance at 1252 cm^{-1}. Regions of marker bands are indicated by horizontal bars (D = aspartic acid; E = glutamic acid; RSB = retinal Schiff base; ret = Retinal).*

4.2 Part of the mechanism evolves

The low resolution electron microscopy structure, site-directed mutagenesis and time-resolved FT-IR spectra provided important details of the mechanism. After absorption of a photon an isomerization reaction from all-*trans* to 13-*cis* occurs. Dramatic changes in pK's are observed for the Schiff base (pK 13 → pK 3) and Asp85, (pK 4 → pK 11), the primary proton accepter group, so that in the transition from L → M the Schiff base proton is moving to Asp85. Since Asp85 stays protonated until the O-intermediate, another proton is rejected to the extracellular surface from an unknown group. In the transition from M → N the proton donor group Asp96 in the cytopolasmic domain is delivering its proton to the Schiff base. Between N and O Asp96 is reprotonated. From O to the ground state the retinal reisomerises to the all-*trans* configuration. During this step Asp85 donates ist proton to Asp212 [20]. The initial proton release group is then reprotonated by Asp212.

4.3 Changes in the tertiary structure of bR

From the photocycle Fig.2 it becomes evident that the structure of the M-intermediate would answer many questions concerning the structure-function relation of bR. Therefore already before crystals of bR were available, low resolution structural information was obtained from neutron and X-ray experiments on oriented PM films [21]. Fig.5 shows two difference Fourier maps in projection to the membrane plane of the M state minus the ground state. The PM films in these experiments were made of the mutant bR Asp96 Asn.

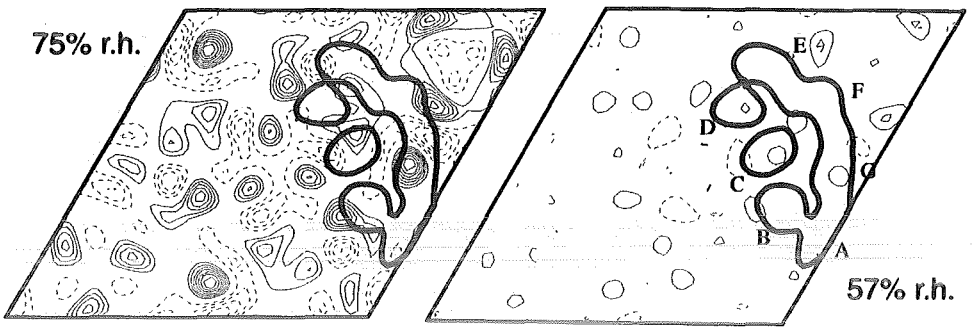


Fig. 5: *Difference density maps (M minus bR ground state) of PM in projection obtained from X-ray diffraction on films of the bR mutant Asp96Asn at different hydration corresponding to 75 % and 57 % relative humidity. The bold contour outlines one of the three bR monomers; individual helices are marked by letters A to G. Continuous lines correspond to five positive, dashed lines to five negative equidistant density levels. The contour levels in both maps are scaled to each other.*

By replacing the protonatable group Asp96 by the neutral amino acid Asn, the reprotonation of the Schiff base becomes difficult resulting in a dramatic increase in the decay time of the M-state by a factor of up to 1000. Thus, it was easy to trap the M state by continuous illumination at room temperature. Unexpectedly large structural changes were observed, especially at helix F and G. The changes at helix F were interpreted as an outward bending in

comparison to the ground state. Interestingly these structural changes are completely vanished at hydration levels of the PM-films corresponding to relative humidities below 60 % (Fig.5). At both hydrations the films are completely yellow indicating up to 90 % M state. Thus, two M states existed with and without structural changes.
If one assumes that both M states would occur in the photocycle also at high hydration but in a sequential order, these changes in the tertiary structure would develop within the M intermediate between two M states M_1 and M_2 and would relax after the N state.
The concept of two M states arose from the evaluation of time-resolved spectroscopy data in the visible wavelength region [22]. An irreversible step was assumed at this position in the photocycle between M_1 and M_2, acting as a switch by changing the proton accessibility of the Schiff base from the extracellular to the cytoplasmic side and thus creating the vectoriality of the proton pump.

4.4 The crystal structure of the M state

When bR crystals diffracting to high resolution became available, immediate efforts to obtain intermediate structures were undertaken. Edman et al. [23] succeeded in solving the crystal structure of the early K intermediate and small structural changes with respect to the ground state bR could be resolved. Luecke et al. [24] trapped the M state in crystals of the mutant Asp96Asn (PDB entries: 1c8r and 1c8s) which has a prolonged decay of the M state. The advantage of this mutant is that a high amount of M can be trapped at room temperature. The disadvantage is that, as indicated by the long decay time of M, the cytoplasmic proton translocation pathway is disturbed. Therefore, Sass et al. [15] trapped the M state in wild-type bR, accumulated approximately 35 % of this intermediate and solved the crystal structure (PDB ID: 1cwq). Both M state structures show quite similar changes on the proton release side of bR and more pronounced changes on the cytoplasmic side. Fig.6 shows the wild-type M_2 structure in comparison to the ground state.

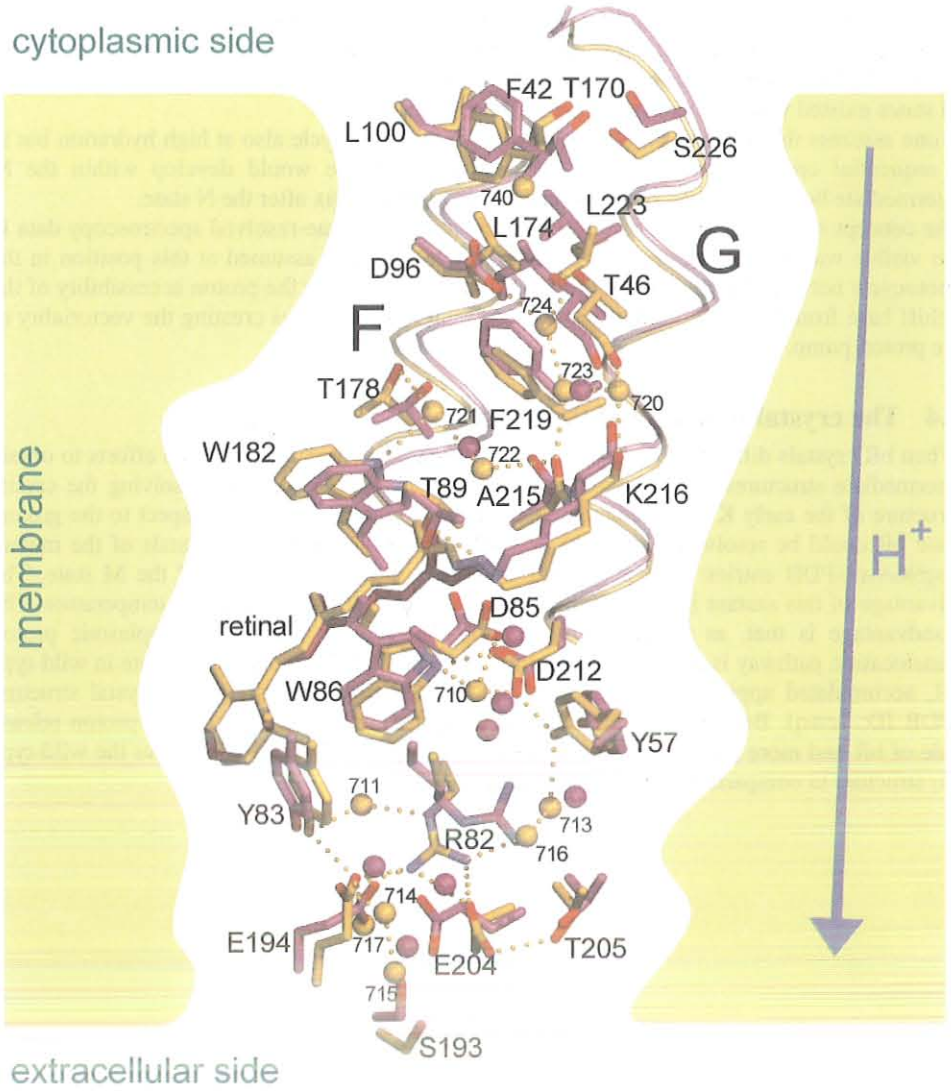


Fig. 6: *Image of the proton pathway of the bR ground state model (purple) and the M_2-state model (yellow). Shown are several functionally important amino acids, the retinal, water molecules and the cytoplasmic parts of helices F and G, showing the most important alterations between these photocycle states. The yellow dotted lines mark distances for possible hydrogen bonds in the M state. The large blue arrow gives the direction of proton pumping.*

5 More details of the mechanism

In the following we shall concentrate on several features of the M state crystal structure which contributes to our understanding of proton transfer steps. The 13-*cis* retinal orients its proton binding site to the cytoplasmic domain. The carboxyl group of Asp85 has changed from negative to neutral and in this way its electrostatic interaction to Arg82 is diminished. Consequently, this group orients downward interacting with negative charges on Glu194 or Glu204. Thus, the affinity of a proton either of these groups or in a cluster of water molecules [25] is decreased and a proton appears on the extracellular surface. In wild-type bR these reactions take place in about 50 μs.

In contrast to this, protonation steps in the cytoplasmic domain occur within several ms, indicating that these reactions are more complicated. The changes in the tertiary structure observed already at low resolution between M_1 and M_2 become now clearly visible in the M_2 crystal structure. Helix F is bending to the outside and helix G is concentrating some density by narrowing in certain parts and changing its loop conformation. These changes give place to at least four water molecules highly important for the proton transfer across these hydrophobic regions. First of all water molecules 740 and 724 help to decrease the pK of Asp96. To reprotonate the Schiff base a proton can follow a hydrogen-bonding network until water molecule 722, which is still 5 Å apart from the Schiff base nitrogen. We assume that his water molecule, only weakly fixed by two hydrogen bonds, can fluctuate and deliver a proton to the Schiff base nitrogen in the transition from M to N. How is Asp 96 reprotonated? According to our M_2-state structure, we can only speculate that water molecule 740 captured in a hydrophobic cavity can fluctuate to Asp96 and deliver a proton to this group. The OH-part of the molecule is escaping to the cytoplasmic surface. We believe that the ms time domain in the last part of the photocycle is caused by the high amplitude of thermal equilibrium fluctuations involved in these protonation reactions, which are coupled to the relaxation of the M_2 conformation, which originated from the altered charge distribution resulting from the protonation reactions between L and M_1.

References

[1] D. Oesterhelt, W. Stoeckenius, Proc. Natl. Acad. Sci USA 70, 2853 (1973)
[2] R. Henderson, Journal of Molecular Biology 93, 123 (1975)
[3] J. Heberle, Biochim. Biophys. Acta 1458, 135 (2000)
[4] R. Henderson, P.N.T. Unwin, Nature 257, 28 (1975)
[5] D.M. Engelman, R. Henderson, A.D. McLachlan, B.A. Wallace, Proceedings of the National Academy of Science USA 77, 2023 (1980)
[6] J.L. Popot, D.M. Engelman, O. Gurel, G. Zaccai, Journal of Molecular Biology 210, 829 (1989)
[7] R. Henderson, J.M. Baldwin, Ceska, T.A., F. Zemlin, E. Beckmann, K.H. Downing, Journal of Molecular Biology 213, 899 (1990)
[8] H. Michel, D. Oesterhelt, Proceedings of the National Academy of Sciences USA 77, 1283 (1980)
[9] G.F.X. Schertler, H.D. Bartunik, H. Michel, D. Oesterhelt, Journal of Molecular Biology 234, 156 (1993)
[10] E.M. Landau, J.P. Rosenbusch, Proceedings of the National Academy of Sciences USA 93, 14532 (1996)
[11] E. Pebay-Peyroula, G. Rummel, J.P. Rosenbusch, E.M. Landau, Science 277, 1676 (1997)
[12] H. Luecke, H. Th. Richter, J.K. Lanyi, Science 280, 1934 (1998)
[13] L. Essen, R. Siegert, W.D. Lehmann, D. Oesterhelt, Proceedings of the National Academy of Sciences USA 95, 11673 (1998)
[14] K. Takeda, H. Sato, T. Hino, M. Kono, K. Fukuda, I. Sakurai, T. Okada, T. Kouyama, Journal of Molecular Biology 283, 463 (1998)
[15] H.J. Sass, G. Büldt, R. Gessenich, D. Hehn, D. Neff, R. Schlesinger, J. Berendzen, P. Ormos, Nature 406, 649 (2000)
[16] W. Uhmann, A. Becker, C. Taran, F. Siebert, App. Spectroscopy 45, 390 (1991)
[17] F. Siebert, Methods Enzymol. 246, 501 (1995)
[18] J. Heberle, C. Zscherp, Appl. Spectroscopy 50, 588 (1996)
[19] C. Zscherp, J. Heberle, J. Phys. Chem. B 101, 10542 (1997)
[20] C. Zscherp, R. Schlesinger, J. Heberle, Biochem. Biophys. Res. Comm. 283, 57 (2001)
[21] M.H.J. Koch, N.A. Dencher, D. Oesterhelt, H.-J. Plöhn, G. Rapp, G. Büldt, EMBO Journal 10, 521 (1991)
[22] G. Varo, J. Lanyi, Biochemstry 29, 2241 (1990)
[23] K. Edmann, P. Nollert, A. Royant, H. Belrhali, E. Pebay-Peyroula, J. Hajdu, R. Neutze, E.M. Landau, Nature 401, 822 (1999)
[24] H. Luecke, B. Schobert, H.T. Richter, J.P. Cartailler, J.K. Lanyi, Science 286, 255 (1999)
[25] R. Rammelsberg, G. Huhn, M. Lübben, K. Gerwert, Biochemistry 37, 5001 (1998)

B 16 Ornstein-Zernike Theories of Fluid Microstructures

G. Nägele

Institut für Festkörperforschung

Forschungszentrum Jülich GmbH

Contents

1 Introduction **2**
1.1 Typical systems and pair potentials 3

2 Radial Distribution Function of Fluids **5**
2.1 General properties 6
2.2 Potential of mean force $w(r)$ 8
2.3 Determination of $g(r)$ by scattering experiments 10
2.4 Thermodynamic properties from $g(r)$ 12

3 Integral Equation Methods of Calculating $g(r)$ **15**
3.1 Ornstein-Zernike equation and direct correlations 15
3.2 Ornstein-Zernike theory of critical opalescence 16
3.3 Closure relations 20
3.4 Percus-Yevick solution for hard spheres 25
3.5 Thermodynamic consistency and Rogers-Young closure 29

4 Generalization to Fluid Mixtures **32**
4.1 Partial correlation functions 32
4.2 Effective interaction between charged colloidal particles 33

5 Summary **38**

1 Introduction

Liquids and dense fluids are distinguished from dilute gases by the importance of short-range correlations and particle collision processes, and from crystalline solids by the lack of long-range order. The distinction between a liquid and a gas is only a quantitative one, since there is no change in symmetry in going from the gas phase to the liquid phase.

The most simple liquid systems are monoatomic liquids consisting of spherically shaped atoms (argon or neon) or quasi-spherical molecules such as methane. The interactions between the atoms can be characterized by simple pair potentials which depend only on the distance between an atomic pair. Colloidal fluids consist of mesoscopically large colloidal particles, typically a few hundred nanometers in size, dispersed in a low-molecular solvent such as water. There are strong local correlations in the positions of these particles ("super atoms") so that they form a colloidal liquid in the liquid (solvent). The omnipresence of colloidal dispersions in chemistry and biology, and the unsurpassed variety and tunability of their particle interactions explains their importance both in industrial applications and fundamental research. Well-studied examples of simple colloidal fluids are suspensions of silica and polymethyl-methacrylate spheres in organic solvents, and aqueous dispersions of globular proteins or polystyrene latex spheres.

While the friction-dominated, diffusive dynamics of colloidal particles is quite different from the ballistic one of atomic liquids, atomic and colloidal liquids are very similar in terms of their equilibrium microstructure, i.e. in terms of the average particle ordering. There are just orders of magnitude differences in their length scales.

In the present lecture, I will discuss a versatile class of liquid state theory methods which allows to calculate microstructural and thermodynamic properties, both of atomic and colloidal liquids, from the knowledge of the particle interactions. These so-called integral equation schemes are based on the Ornstein-Zernike (OZ) equation. Some of the most relevant OZ schemes will be introduced, and we will explore their predictive power in comparison with computer simulations and experiment. The quantity of central importance calculated with integral equation schemes is the radial distribution function, $g(r)$, of an isotropic liquid. The radial distribution function quantifies the probability of finding a particle at some distance from any other one. It can be indirectly measured by radiation scattering experiments and, for very large colloidal particles, also directly using video microscopy.

Typical atomic and colloidal liquids of spherically shaped particles will be briefly characterized in chapter 1 in terms of their interaction potentials. Chapter 2 provides an overview on general properties of $g(r)$, with its relation to scattering experiments and thermodynamic properties. Chapter 3 introduces the fundamental Ornstein-Zernike equation, with a first application to the phenomenon of critical opalescence in near-critical liquids. Various approximate closure relations are discussed which lead to closed integral equations for $g(r)$. Particular focus is given to hard-sphere fluids, since they can serve as a reference system of uncharged liquids, similar to the harmonic solid in solid-state physics. Chapter 4, finally, deals with the generalization of the Ornstein-Zernike integral equation schemes to liquid mixtures. These generalizations will be applied to the important case of a sus-

pension of charge-stabilized colloidal particles. We will calculate the screened electrostatic interaction between the colloidal particles by contracting the neutralizing counter- and salt ions out of the description.

1.1 Typical systems and pair potentials

In the following we exemplify pair potentials suitable for describing the pair forces acting in simple and colloidal fluids of spherical particles. Simple fluids of non-polar atoms or molecules will be considered first, followed by a discussion of pair interactions in suspensions of spherical colloidal particles.

The Lennard-Jones 12-6 potential [1,2]

$$u(r) = 4\epsilon \left[\left(\frac{\sigma}{r}\right)^{12} - \left(\frac{\sigma}{r}\right)^{6} \right] \quad \text{for} \quad r > 0 \tag{1}$$

provides a fair description of the interaction between pairs of rare-gas atoms like in argon, krypton and xenon, and also of quasi-spherical molecules such as CH_4. A sketch of the potential curve is provided in Fig. 1. Two parameters characterize the potential: the collision diameter σ where $u(r) = 0$, and the depth, ϵ, of the potential minimum at $r = 2^{1/6}\sigma$. The values of σ and ϵ have been determined for a large number of atoms using, e.g., atomic scattering techniques. For argon, $\sigma_{Ar} = 0.34$ nm and $\epsilon_{Ar}/k_B = 119.8$ K. The short-range repulsive part of the pair potential proportional to r^{-12} represents approximately the electronic repulsion of two atoms. The longer-range van der Waals attraction between two atoms at a distance r is described by the r^{-6} part.

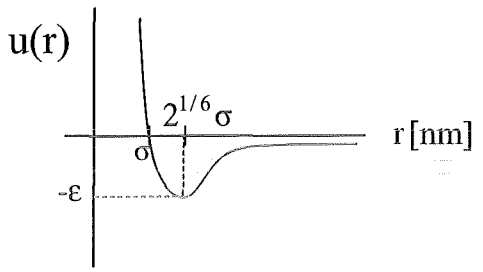


Fig. 1: *Lennard-Jones pair potential for atomic liquids*

The most simple pair potential one can think of is the potential between hard spheres of diameter σ, i.e.

$$u(r) = \begin{cases} \infty & \text{for } r < \sigma \\ 0 & \text{for } r > \sigma \end{cases} . \tag{2}$$

While there exists no atomic fluid of hard atoms, colloidal suspensions of hard spheres are realized within good approximation, by coated polymethyl-methacrylate (PMMA) spheres dispersed in a refractive index-matched non-polar solvent like cyclohexane. The coating consists of a thin layer, as compared to σ, of adsorbed polymer chains (cf. Fig. 2). The polymer brush gives rise to a short-range repulsion between the colloidal spheres

which counterbalances the remnants of the van der Waals attraction. The sizes of the colloidal hard spheres are in the range of several hundred to a few thousand nanometers.

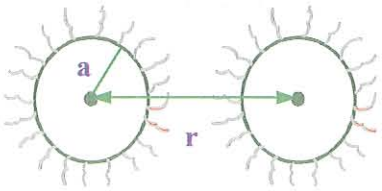


Fig. 2: *Model of colloidal hard spheres: PMMA spheres in non-polar solvent with surface-grafted polymer hairs*

PMMA particles in a non-organic solvent are a paradigm for sterically stabilized dispersions.

A well-studied example of charge-stabilized colloidal dispersions are polystyrene latex spheres dispersed in a polar solvent like water [3]. The latex particles acquire a high surface charge through the dissociation of ionizable surface groups. Each colloidal particle is surrounded by a diffuse layer of oppositely charged counterions, which are monovalent in the simplest case. Overlap of the electric layers of two colloidal macroions leads to an electrostatic repulsion which counteracts the van der Waals attraction and prevents the particles from irreversible aggregation (cf. Fig. 3). As will be shown in section 4.2

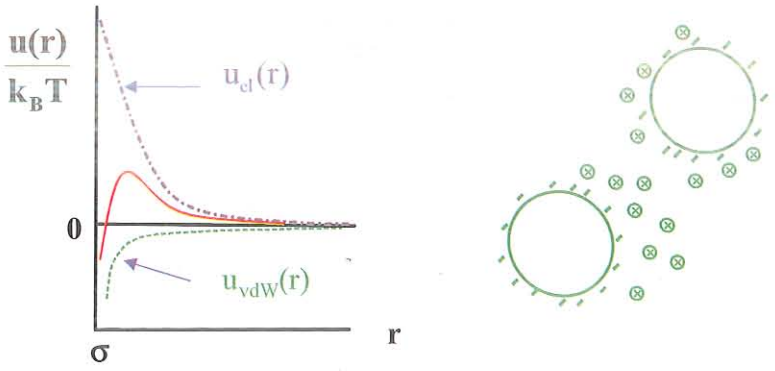


Fig. 3: *Left: Electrostatic and van der Waals potential contributions to the total effective pair potential $u(r)$ (red curve). Right: colloidal macroions and dissociated counterions*

the screened electrostatic repulsion between the charged colloidal spheres in a solvent of

dielectric constant ϵ is approximately described by the effective pair potential

$$\beta u_{el}(r) = L_B Z^2 \left(\frac{e^{\kappa a}}{1+\kappa a}\right)^2 \frac{e^{-\kappa r}}{r}, \quad r > \sigma \tag{3}$$

which is the repulsive electrostatic part of the celebrated Derjaguin-Landau-Verwey-Overbeek (DLVO) potential (cf. lecture A5 by J. Buitenhuis) . Here, Z is the surface charge number of a colloidal particle of radius $a = \sigma/2$, $\beta = 1/(k_B T)$, and $L_B = e^2/(\epsilon k_B T)$ is the so-called Bjerrum length. This length is the characteristic distance, for a pair of elementary charges e, where their Coulomb interaction energy is comparable to the thermal energy $k_B T$. For water at room temperature, $L_B = 0.71$ nm. The Debye-Hückel screening length, κ^{-1}, is defined through

$$\kappa^2 = 4\pi L_B \sum_\alpha \rho_\alpha Z_\alpha^2 \tag{4}$$

where the sum is taken over all types of microions (i.e. counter- and salt ions) of number densities ρ_α and charge numbers Z_α. The range of the potential can thus be controlled by adding or removing small ions. The total effective pair potential, $u(r)$, of charge-stabilized colloidal particles is the sum $u(r) = u_{el}(r) + u_{vdW}$ of $u_{el}(r)$, and of the attractive van der Waals pair potential, $u_{vdW}(r)$. The van der Waals part behaves like r^{-6} for large r and like $(r-\sigma)^{-1}$ near the contact distance $r = \sigma$ (cf. Fig. 3). For dispersions of highly charged colloidal particles, $u_{vdW}(r)$ becomes completely masked by the electrostatic part $u_{el}(r)$. In this case one frequently refers to the colloidal particles (with associated microion layer) as Yukawa spheres, since their microstructural properties are determined only by the Yukawa-like, exponentially screened Coulomb potential $u_{el}(r)$.

It is commonly assumed that the potential energy, $U(\mathbf{r}^N)$, of a N-particle liquid system can be approximated by a sum of pair interactions

$$U(\mathbf{r}^N) \approx \sum_{i<j}^{N} u(|\mathbf{r}_i - \mathbf{r}_j|) = \sum_{i<j}^{N} u(r_{ij}) \tag{5}$$

for any configuration $\mathbf{r}^N = \{\mathbf{r}_1, \cdots, \mathbf{r}_N\}$ of position vectors $\{\mathbf{r}_i\}$ pointing to the particles centres. The quality of this pairwise additivity assumption depends on the choice of $u(r)$, and on how certain many-body aspects (non-additive dispersion forces, influence of solvent molecules, electrostatic screening et cetera) are approximately included in the pair potential. Typically, $u(r)$ is temperature and density dependent. Notice that $U(\mathbf{r}^N)$ is exactly pairwise additive only for systems of ideal hard spheres.

Under the premise of Eq. (5), the thermodynamic and microstructural properties of the fluid are solely expressible in terms of $u(r)$, and of its associated radial distribution function $g(r)$. The latter constitutes the most simple and most relevant reduced distribution function.

2 Radial Distribution Function of Fluids

In this chapter we discuss salient properties of $g(r)$. From a knowledge of $g(r)$, one can calculate macroscopic thermodynamic properties and analyze the local microstructure.

Furthermore, knowledge of static pair correlations is an essential ingredient of most theoretical approaches to the transport and rheology of simple and complex fluids. The aim of the liquid state theory is therefore to calculate $g(r)$ from the particle interactions and to determine from it scattering properties and the thermodynamics.

2.1 General properties

The concept of reduced distribution functions has proven to be most useful in liquid state theory. Consider a system of N identical spherical particles in a volume V at temperature T (canonical NVT ensemble). The function

$$P_N(\mathbf{r}^N) = \frac{e^{-\beta U(\mathbf{r}^N)}}{Z_N(V,T)} \,, \tag{6}$$

with configurational integral

$$Z_N(V,T) = \int d\mathbf{r}_1 \cdots d\mathbf{r}_N \, e^{-\beta U(\mathbf{r}^N)} = \int d\mathbf{r}^N \, e^{-\beta U(\mathbf{r}^N)} \,, \tag{7}$$

is the probability density that the N particles are at the positions $\mathbf{r}_1, \cdots, \mathbf{r}_N$. It provides far more information than is necessary for the calculation of scattering properties and thermodynamic functions. What is really needed for are the reduced distribution functions for a small subset of $n \ll N$ particles irrespective of the positions of the remaining $N - n$ particles.

Hence we introduce the n-particle distribution function [1,4]

$$\rho_N^{(n)}(\mathbf{r}^n) = N(N-1)\cdots(N-n+1) \int d\mathbf{r}_{n+1} \cdots d\mathbf{r}_N \, P_N(\mathbf{r}^N) \tag{8}$$

of finding any set of n particles at a specified configuration $\mathbf{r}^n = \{\mathbf{r}_1, \cdots, \mathbf{r}_n\}$, regardless of how these n identical particles have been labelled. Of major importance are the reduced distribution functions of order $n = 1, 2$. For a homogeneous system

$$\rho_N^{(n)}(\mathbf{r}_1, \cdots, \mathbf{r}_n) = \rho_N^{(n)}(\mathbf{r}_1 + \mathbf{t}, \cdots, \mathbf{r}_n + \mathbf{t}) \tag{9}$$

for an arbitrary displacement vector $\mathbf{t}$. Then $\rho_N^{(1)} = \rho = N/V$ is equal to the average particle number density, ρ, and $\rho_N^{(2)}(\mathbf{r}_1, \mathbf{r}_2) = \rho_N^{(2)}(\mathbf{r}_1 - \mathbf{r}_2)$ depends only on the vector distance $\mathbf{r}_{12} = \mathbf{r}_1 - \mathbf{r}_2$ (to see this choose $\mathbf{t} = -\mathbf{r}_2$).

The correlation length $\xi(T)$ is a characteristic distance over which two particles are correlated. For fluids, ξ is typically of the range of $u(r)$ or larger to some extent, but under certain conditions (i.e., at a critical point) it can become extremely large. For a n-particle cluster of large mutual distances $r_{ij} = |\mathbf{r}_i - \mathbf{r}_j| \gg \xi$ and $N \gg 1$

$$\rho_N^{(n)}(\mathbf{r}_1, \cdots, \mathbf{r}_n) \approx \prod_{i=1}^{n} \rho_N^{(1)}(\mathbf{r}_i) = \rho^n \tag{10}$$

since these particles are then uncorrelated. To describe pair correlations in a fluid relative to a classical ideal gas of uncorrelated particles at the same density and temperature, we introduce the pair distribution function, $g_N(\mathbf{r}_1, \mathbf{r}_2)$, in the NVT-ensemble as

$$g_N(\mathbf{r}_1, \mathbf{r}_2) := \frac{\rho_N^{(2)}(\mathbf{r}_1, \mathbf{r}_2)}{\rho_N^{(1)}(\mathbf{r}_1)\, \rho_N^{(1)}(\mathbf{r}_2)} \,, \tag{11}$$

such that $g_N(\mathbf{r}_1, \mathbf{r}_2) \to 1$ for $r_{12} \to \infty$. If the system is isotropic as well as homogeneous (no spatially varying external force field, no crystals), $\rho_N^{(2)}$ and g_N are functions only of the separation $r = r_{12}$. Then, $g_N(r)$, with

$$g_N(r) = \frac{\rho_n^{(2)}(r)}{\rho^2} = \frac{N(N-1)}{\rho^2} \int d\mathbf{r}_3 \cdots d\mathbf{r}_N \, P_N(\mathbf{r}^N) \tag{12}$$

is usually called the radial distribution function. It plays a central role in one-component fluids, since it is indirectly measurable by radiation scattering experiments. Moreover, thermodynamic quantities can be written as integrals over $g_N(r)$ and $u(r)$, provided that the particles interact by pairwise additive forces (cf. sections 2.3-4).

As an important observation, we note that $\rho g_N(r)$ is the average density of particles a distance r apart from a given one. In fact, integration of $\rho g(r)$ over the system volume leads to

$$\rho \int d\mathbf{r}\, g_N(r) = \frac{N(N-1)}{\rho} \int d\mathbf{r}_{12} \int d\mathbf{r}_3 \cdots d\mathbf{r}_N \, P_N(\mathbf{r}^N) = N - 1 \tag{13}$$

since $\int d\mathbf{r}_{12} = V^{-1} \int d\mathbf{r}_1 d\mathbf{r}_2$. Likewise, Eq. (13) can be rewritten as

$$1 + \rho \int_V d\mathbf{r}\, [g_N(r) - 1] = 0 \quad . \tag{14}$$

Notice in this context for the canonical $g_N(r)$ that $g_N(r \to \infty) = 1 - N^{-1}$ since there are $N - 1$ particles left besides the one at $r = 0$. Eqs. (13) and (14) are only valid for a system of finite and fixed N, where particle number fluctuations are absent. In order to be independent of the specific statistical ensemble used in calculating static properties, it is understood that the thermodynamic limit of very large systems, i.e. $N, V \to \infty$ with $\rho = N/V$ kept fixed, is taken at the end of each calculation. Then

$$g(r) := \lim_{N,V \to \infty} g_N(r) \tag{15}$$

defines the ensemble-independent radial distribution function, $g(r)$, of a macroscopic system.

Let us summarize general properties of $g(r)$ which follow readily from the definition of $g_N(r)$ in Eq. (12):

$$g(r) \geq 0, \quad g(r \to \infty) = 1 \tag{16}$$

$$g(r) \approx 0, \quad \text{for } \beta u(r) \gg 1 \tag{17}$$

$$g(r) = e^{-\beta u(r)} + \mathcal{O}(\rho) \tag{18}$$

$$g(r) \quad \text{continuous for } u(r) \text{ continuous} \tag{19}$$

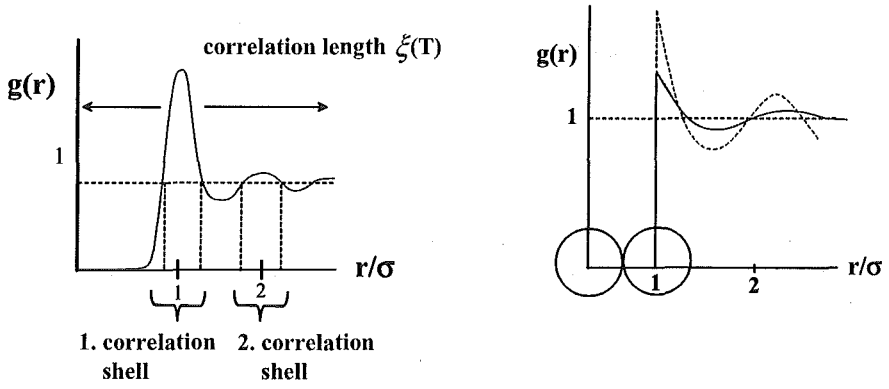


Fig. 4: *The $g(r)$ of a Lennard-Jones liquid (left), and of hard spheres (right)*

The typical behavior of $g(r)$ for an atomic liquid with a soft pair potential of Lennard-Jones type, and for a hard-sphere fluid is sketched in Fig. 4. Regions of r with $g(r) > 1$ ($g(r) < 1$) have a larger (lower) probability of finding a second particle from a given one at $r = 0$, than for an ideal gas at the same T and ρ. The main features are a small-r region where $g(r) = 0$ owing to strong repulsive forces exerted by the particle at the origin, and several peaks representing increasingly diffuse shells, for increasing r, of next neighbors, second next neighbors and so on. This shell layering manifests the granularity (non-continuum nature) of the fluid. The oscillations in $g(r)$ decrease in amplitude with increasing r. Eventually, $g(r)$ approaches its asymptotic value one for $r > \xi(T, \rho)$. The oscillations in $g(r)$ become more pronounced with increasing ρ. Whereas the Lennard-Jones $g(r)$ is continuous at any r, the hard-sphere $g(r)$ jumps from zero to values ≥ 1 at $r = \sigma$, due to the singular nature of the hard-sphere $u(r)$. For hard spheres, $g(r) = \theta(r - \sigma) + \mathcal{O}(\rho)$ according to Eq. (18). Hard-sphere systems are athermal (i.e., T-independent) since the probability for a given particle configuration is either zero or one, independent of β, depending only on whether two or more spheres overlap or not.

2.2 Potential of mean force $w(r)$

There is a remarkable relation between $g(r)$ and the so-called potential of mean force, $w(r)$. For $N \gg 1$, $w(r)$ is defined in terms of $g(r)$ by

$$g(r) =: e^{-\beta w(r)} \tag{20}$$

or

$$w(r_{12}) = -k_B T \ln g(r_{12}) = -k_B T \left[\ln \int d\mathbf{r}_3 \cdots d\mathbf{r}_N \, e^{-\beta U(\mathbf{r}^N)} + \ln \left(\frac{V^2}{Z_N} \right) \right] . \tag{21}$$

To reveal the physical meaning of $w(r)$, we take the derivative of $-w$ with respect to the position vector $\mathbf{r}_1$:

$$-\nabla_1 w(\mathbf{r}_{12}) = \frac{\int d\mathbf{r}_3 \cdots d\mathbf{r}_N \left(-\frac{\partial U}{\partial \mathbf{r}_1} \right) e^{-\beta U}}{\int d\mathbf{r}_3 \cdots d\mathbf{r}_N \, e^{-\beta U}} = \left\langle -\nabla_1 U(\mathbf{r}^N) \right\rangle_{1,2} . \tag{22}$$

The quantity on the right can be interpreted as the force on particle 1 if we hold particle 2 fixed, and average over the positions of all the other particles (as denoted by $\langle \cdots \rangle_{1,2}$). $w(r)$ is the potential for that force and is therefore called the potential of mean force. Likewise, $w(r)$ can be interpreted as the reversible work for a process in which two particles are moved through the system, at constant N, V and T, from infinite separation to a relative separation r. To see this explicitly, recall from statistical mechanics that

$$F(r_{12}) = -k_B T \ln \int d\mathbf{r}_3 \cdots \mathbf{r}_N e^{-\beta U(\mathbf{r}^N)} + F_0(N-2, V, T) \tag{23}$$

is the Helmholtz free energy of a $N-2$-particle system in the presence of two fixed spheres at a distance r_{12}. The spheres 1 and 2 influence the system through their excluded volume and longer-ranged interactions. Moreover, F_0 is the (non-interesting) configuration-independent part of the free energy. Consequently

$$-\frac{\partial w(r_{12})}{\partial \mathbf{r}_{12}} = -\frac{\partial F(r_{12})}{\partial \mathbf{r}_{12}} \tag{24}$$

and

$$w(r_{12}) = F(r_{12}) - F(\infty) \ , \tag{25}$$

with $w(r)$ defined such that $w(r \to \infty) = 0$. The first and second laws of thermodynamics tell us for a reversible displacement that

$$dF = -SdT - pdV + \mu dN + \delta W_{rev} \ . \tag{26}$$

This means that $dF = \delta W_{rev} = -\nabla_{12} w(r_{12}) \cdot d\mathbf{r}_{12}$ is the reversible (maximal) work done by the $N-2$ particle system to achieve an infinitesimal displacement $d\mathbf{r}_{12}$ of the two boundary particles at fixed temperature, system volume and particle number.

The function $w(r)$ is generally a considerably more complicated object than the mere pair potential $u(r)$, since it involves the effects of particles 1 and 2 on the configurations of the other particles. Only in the limit $\rho \to 0$ follows that

$$w(r) \to u(r) \quad \text{i.e.} \quad g(r) \to e^{-\beta u(r)} \ , \tag{27}$$

as will be shown shortly. A sketch of $w(r)$ for hard spheres at finite density is shown in Fig. 5. As seen, two hard spheres effectively attract each other at distances $r \leq 1.5\sigma$. This many-body effect arises from an unbalance of forces on the two spheres when the gap between the two particles is depleted from the other ones. Depletion interactions of this kind may occur in any system with excluded volume interaction contributions. This explains why depletion effects have attracted considerable interest in the past few years. Assuming pairwise additive interactions where

$$-\nabla_1 U(\mathbf{r}^N) = -\sum_{i>1} \nabla_1 u(r_{1i}) \, , \tag{28}$$

the force law for w in Eq. (22) can be rewritten as

$$-\nabla_1 w(r_{12}) = -\nabla_1 u(r_{12}) - \rho \int d\mathbf{r}_3 \frac{g^{(3)}(\mathbf{r}_1, \mathbf{r}_2, \mathbf{r}_3)}{g(r_{12})} \nabla_1 u(r_{13}) \, . \tag{29}$$

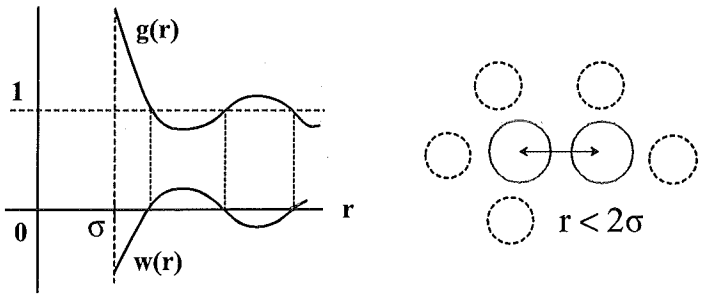


Fig. 5: *Potential of mean force of hard spheres (left) and depletion attraction (right)*

Here,

$$g^{(3)}(\mathbf{r}_1,\mathbf{r}_2,\mathbf{r}_3) := \frac{\rho_N^{(3)}(\mathbf{r}_1,\mathbf{r}_2,\mathbf{r}_3)}{\rho^3} \tag{30}$$

is the triplet distribution function of an isotropic and homogeneous liquid. Actually $g^{(3)}$ depends only on the separations r_{12}, r_{13}, and on the angle between $\mathbf{r}_{13}$ and $\mathbf{r}_{12}$. The mean force on particle 1 in presence of particle 2 at distance r_{12} is thus the sum of a direct interaction between 1 and 2, and the interaction of 1 with a third particle at $\mathbf{r}_3$, weighted by the factor $g^{(3)}(\mathbf{r}_1,\mathbf{r}_2,\mathbf{r}_3)/g(r_{12})$. The latter gives the probability of finding a particle at $\mathbf{r}_3$, given that there are certainly particles at $\mathbf{r}_1$ and $\mathbf{r}_2$. The above equation is the lowest order one of the Yvon-Born-Green hierarchy of equations for the reduced equilibrium probability density functions. Finally, Eqs. (18) and (27) are limiting cases, for $\rho \to 0$, of Eq. (29).

2.3 Determination of $g(r)$ by scattering experiments

Let us shortly recall how pair correlations can be measured by radiation scattering. For more details on scattering experiments consult lecture A1 by T. Brückel. A scattering experiment will have to probe distances of the order of the particle sizes and next neighbor distances, which are Ångstroms in case of atomic liquids, and fractions of microns in case of colloidal dispersions. Therefore, X-rays and neutrons are used for atomic liquids whereas colloids are probed by light scattering and small angle neutron scattering.

A schematic view of a scattering experiment is shown in Fig. 6. Monochromatic radiation of wavelength λ impinges on a fluid sample and is scattered at an angle ϑ into a detector which measures the average intensity, $I(q)$, of scattered neutrons or photons.
For single and quasi-elastic scattering from spherical particles

$$I(q) \propto \langle N \rangle\, P(q)\, S(q) \tag{31}$$

where $q = (4\pi/\lambda)\sin(\vartheta/2)$ is the modulus of the scattering wave vector $\mathbf{q} = \mathbf{k}_f - \mathbf{k}_i$, and $\langle N \rangle$ is the average number of particles in the illuminated volume part of the sample. The so-called (normalized) form factor $P(q)$ contains information on the scattering material distribution inside a particle, i.e. information on the particle size (and form). The most

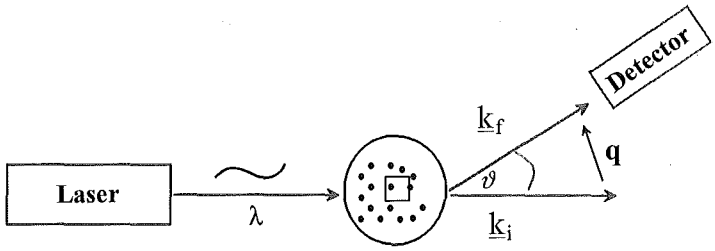


Fig. 6: *Typical scattering experiment setup*

relevant quantity in Eq. (31) including information on inter-particle correlations is called the static structure factor $S(q)$. Its statistical mechanical definition reads

$$S(q) = \left\langle \frac{1}{N} \sum_{l,p=1}^{N} e^{i\mathbf{q}\cdot[\mathbf{r}_l - \mathbf{r}_p]} \right\rangle = \left\langle \left| \frac{1}{\sqrt{N}} \sum_{l=1}^{N} e^{i\mathbf{q}\cdot\mathbf{r}_l} \right|^2 \right\rangle \geq 0 \tag{32}$$

where $\langle \cdots \rangle$ denotes an equilibrium ensemble average. By expanding the double sum into self, $l = p$, and distinct, $l \neq p$, parts, it can be shown that

$$S(q) = 1 + \rho \int d\mathbf{r}\, e^{i\mathbf{q}\cdot\mathbf{r}}\, h(r) = 1 + 4\pi\rho \int_0^\infty dr\; r^2 h(r)\, \frac{\sin(qr)}{qr} \;, \tag{33}$$

where, $h(r)$, with

$$h(r) = g(r) - 1 \tag{34}$$

is called the total correlation function. Notice that $h(r \to \infty) = 0$, and $S(q \to \infty) = 1$. As a result, the static structure factor determines the Fourier transform, $h(q)$, of $h(r)$. Since Fourier transforms are one-to-one mappings, $S(q)$ can be inverted to determine $h(r)$ and thus $g(r)$:

$$g(r) = \mathcal{F}^{-1}\left[\frac{S(q) - 1}{\rho}\right] = 1 + \frac{1}{2\,\pi^2\,\rho\, r} \int_0^\infty dq\, q\, \sin(qr)[S(q) - 1] \;. \tag{35}$$

In principle, this would require to measure $S(q)$ at all wave numbers q where $S(q)$ exhibits significant oscillations. This is often not possible to do since the largest accessible q is limited by $q_{max} = 4\pi/\lambda$, which corresponds to backward scattering.

We have used here the following basic result on Fourier transforms: suppose $h(r)$ is an arbitrary isotropic function, with $h(r) \to 0$ sufficiently fast for $r \to \infty$. The three-dimensional Fourier transform, $h(q)$, of $h(r)$ is defined as

$$h(q) := \mathcal{F}\{h(r)\} = \int d\mathbf{r}\, e^{i\mathbf{q}\cdot\mathbf{r}}\, h(r) = 4\pi \int_0^\infty dr\; r^2 h(r)\, \frac{\sin(qr)}{qr} \tag{36}$$

where the third equality follows from performing two angular integrals in spherical coordinates. The Fourier inversion theorem states then that

$$h(r) = \mathcal{F}^{-1}\{h(q)\} = \frac{1}{(2\pi)^3} \int d\mathbf{q}\, e^{-i\mathbf{q}\cdot\mathbf{r}}\, h(q) = \frac{1}{2\pi^2} \int_0^\infty dq\; q^2\, h(q)\, \frac{\sin(qr)}{qr} \;. \tag{37}$$

For notational simplicity, Fourier transformed functions are distinguished from their real-space counterparts only by their argument q. As an important example we quote the following Fourier transform pair:

$$f(r) = \frac{e^{-\kappa r}}{r} \ , \tag{38}$$

with Fourier transform

$$f(q) = \frac{4\pi}{q^2 + \kappa^2} \tag{39}$$

for $\kappa \geq 0$. This result will be used subsequently.

2.4 Thermodynamic properties from $g(r)$

There exist several routes through which thermodynamic properties of liquids can be related to integrals involving $g(r)$ and $u(r)$. In the following, we review the three most important ones.

The energy equation

$$E = \langle T_{kin} \rangle + \langle U(\mathbf{r}^N) \rangle = \frac{3}{2} N K_B T + \frac{1}{2} \rho N \int_0^\infty dr \, 4\pi r^2 g(r) \, u(r) \tag{40}$$

expresses the internal energy, E, of a one-component N-particle system in terms of $u(r)$ and $g(r)$. The internal energy is the sum of a kinetic part, $(3/2)Nk_BT$, and an interaction part, $\langle U(\mathbf{r}^N) \rangle$. The latter can be understood on physical grounds as follows: for each particle out of N, there are $4\pi r^2 \, \rho \, g(r) \, dr$ neighbors in a spherical shell of radius r and thickness dr, and the interaction energy between the central particles and these neighbors is $u(r)$. Integration from 0 to ∞ gives the interaction energy part of E, with the factor $1/2$ correcting for the double counting of particle pairs.

The pressure equation

$$p = p_{kin} + p_{int} = \rho k_B T - \frac{2\pi}{3} \rho^2 \int_0^\infty dr \, r^3 g(r) \, u'(r) \tag{41}$$

relates the thermodynamic pressure, p, to an integral over $g(r)$ and the derivative, $u'(r)$, of the pair potential. Here, $p_{kin} = \rho k_B T$ is the kinetic pressure of an ideal gas. The pressure contribution, p_{int}, due to particle interactions can be derived along the same lines as the energy equation. For a repulsive pair potential with $u'(r) < 0$, p_{int} is a positive pressure contribution originating from the stronger thermal bombardment of container walls by the mutually repelling particles. A colloidal dispersion consists of colloidal particles *and* of the solvent. For colloids, Eq. (41) gives the osmotic pressure exerted by the particles on a membrane permeable to the solvent.

The compressibility equation ,

$$\frac{\chi_T}{\chi_T^{id}} = \lim_{q \to 0} S(q) = 1 + \rho \int d\mathbf{r} \, [g(r) - 1] \ , \tag{42}$$

links the (osmotic, in case of colloids) isothermal compressibility, χ_T, defined as

$$\chi_T := -\frac{1}{V}\left(\frac{\partial V}{\partial p}\right)_T = \frac{1}{\rho}\left(\frac{\partial \rho}{\partial p}\right)_T \tag{43}$$

to an integral involving only $g(r)$. Here, $\chi_T^{id} = (\rho k_B T)^{-1}$ is the compressibility of an ideal gas. The compressibility equation holds more generally than the energy and pressure equations, since it is valid even when the interparticle forces are not pairwise additive. According to Eqs. (33) and (42), χ_T can be determined experimentally from measuring $S(q)$ in the long-wavelength limit $q \to 0$ (i.e., for $q\xi \ll 1$).

The compressibility equation can be derived only in the grand canonical ensemble representing an open system, at constant V and T, which allows for fluctuations in the particle number. This is perfectly appropriate since $S(q)$ is related to the intensity of quasi-elastically scattered radiation. The radiation beam samples only a fraction of the system volume, and in this subvolume the number of particles, while macroscopically large, fluctuates.
To derive the compressibility equation, we need thus the definition of $g(r)$ in the grand canonical ensemble. For N finite and fixed, we know from Eq. (12) that

$$\begin{aligned}
\rho^2 g_N(r) &= N(N-1)\int d\mathbf{r}_3 \cdots \mathbf{r}_N P_N(\mathbf{r}^N) \\
&= N(N-1)\int d\mathbf{r}_3 \cdots \mathbf{r}_N P_N(\mathbf{r}^N)\frac{1}{V}\int d\mathbf{r}_1 d\mathbf{r}_2\, \delta(\mathbf{r}-\mathbf{r}_{12}) \\
&= \frac{N(N-1)}{V}\langle \delta(\mathbf{r}-\mathbf{r}_{12})\rangle_N = \frac{1}{V}\left\langle \sum_{i\neq j}^{N} \delta(\mathbf{r}-\mathbf{r}_{ij})\right\rangle_N
\end{aligned} \tag{44}$$

where $\langle\cdots\rangle_N$ denotes the canonical (i.e., fixed N) ensemble average. The canonical $g_N(r)$ has been formulated by the most right equality in terms of an ensemble average invoking Dirac δ functions. Next, to obtain the grand-canonical $g(r)$, we merely need to replace the canonical average by the grand canonical one, denoted as $\langle\cdots\rangle_{gc}$:

$$\langle(\cdots)\rangle_N = \int d\mathbf{r}_N P_N(\mathbf{r}^N)(\cdots) \;\to\; \langle(\cdots)\rangle_{gc} := \sum_N P(N)\langle(\cdots)\rangle_N \,. \tag{45}$$

We have introduced here the grand canonical probability, $P(N)$, of finding a system with exactly N particles. The grand-canonical pair distribution function is thus defined as

$$\rho^2 g(r) := \frac{1}{V}\left\langle \sum_{i\neq j}^{N} \delta(\mathbf{r}-\mathbf{r}_{ij})\right\rangle_{gc} \,. \tag{46}$$

For finite and fixed N, it follows from Eq. (13) that

$$\rho^2 \int d\mathbf{r}\, g_N(r) = \frac{N(N-1)}{V} \,. \tag{47}$$

For an open system this leads to

$$\rho^2 \int d\mathbf{r}\, [g(r)-1] = \frac{\langle N(N-1)\rangle_{gc}}{V} - \frac{\langle N\rangle_{gc}^2}{V} = \rho\left[\frac{\langle N^2\rangle_{gc} - \langle N\rangle_{gc}^2}{\langle N\rangle_{gc}} - 1\right] \tag{48}$$

with $\rho = \langle N \rangle_{gc}/V$. The variance of the number fluctuations in an open system is related to the isothermal compressibility through the thermodynamic relation

$$\rho k_B T \chi_T = \frac{\left\langle (N - \langle N \rangle_{gc})^2 \right\rangle_{gc}}{\langle N \rangle_{gc}} \ . \tag{49}$$

This completes our derivation of the compressibility equation. There is no contradiction between the compressibility equation and the canonical ensemble result in Eq. (14). On first sight the latter might suggest that $\lim_{q\to 0} S(q) = 0$ is exactly valid. However, Eq. (14) applies only to a closed system with zero particle number fluctuations. Notice further, for N and V finite and fixed (at given density ρ), that physically allowed wave numbers are restricted to $q > V^{-1/3}$: it makes no sense to consider particle density fluctuations of wave lengths ($\sim q^{-1}$) larger than the system size. The thermodynamic limit of a macroscopic system should be performed first, then the limit $q \to 0$.

The particles of a liquid near the triple point of the gas-liquid-solid coexistence are densely packed such that χ_T is very small. Furthermore, the compressibility is nearly zero for a classical crystal near $T = 0$, since there are hardly any vibrations of the atoms around their equilibrium positions. In contrast, χ_T diverges at the critical point which is the terminal point of the gas-liquid coexistence line. The divergence is due to a long distance tail in $h(r)$ which causes the phenomenon of critical opalescence observed in light scattering studies near critical points. We will study critical opalescence in section 3.2. As a summary, we note

$$\frac{\chi_T}{\chi_T^{id}} \approx \begin{cases} 0, & \text{fluid near triple point} \\ 0, & \text{ideal crystal} \\ \infty, & \text{fluid at critical point} \ . \end{cases} \tag{50}$$

Special care is needed for the case of state-dependent effective pair potentials $u(r) = u(r;\rho,T)$. Potentials of this type occur for liquid mixtures in the process of tracing out the particle degrees of freedom associated with all but a single component. The liquid mixture is hereby mapped onto an equivalent system of pseudo-particles governed by an effective state-dependent pair potential. An example of such a one-component reduction is given in section 4.2, for the case of charged colloidal particles, with a resulting effective pair potential as quoted already in Eq. 3. In case of a state-dependent $u(r)$, the energy and pressure equations must be generalized, in particular, to

$$E = \frac{3}{2} N k_B T + N u_0(\rho) + \frac{1}{2} \rho N \int_0^\infty dr\, 4\pi r^2 g(r) \frac{\partial}{\partial \beta} (\beta u(r)) \ , \tag{51}$$

and

$$p = \rho k_B T + \rho^2 \frac{du_0(\rho)}{d\rho} - \frac{2\pi}{3} \rho^2 \int_0^\infty dr\, r^2 g(r) \left(r \frac{\partial}{\partial r} - 3\rho \frac{\partial}{\partial \rho} \right) u(r) \ . \tag{52}$$

Here, $u_0(\rho)$ is a structure-independent free energy contribution, called volume energy, which depends on the average density of pseudo-particles. The volume energy is a consequence of the one-component reduction. It may significantly influence, e.g., the thermodynamic properties of charge-stabilized dispersions in the limit of low added salt concentrations. For an interesting derivation of the effective pair potential and volume energy of charged colloids based on the analogy between charge-stabilized colloidal dispersions and liquid metals consult [5] and [6].

3 Integral Equation Methods of Calculating $g(r)$

We proceed to discuss theoretical methods which allow to calculate the $g(r)$ and $S(q)$ of dense liquids from a given pair potential. All these methods are based on the so-called Ornstein-Zernike (OZ) equation, initially introduced by Ornstein and Zernike (1917) in their investigations of critical opalescence in near-critical liquids. The OZ equation introduces the direct correlation function, $c(r)$, as a very useful concept. Closed integral equations determining $g(r)$ can be derived from the OZ equation, when $c(r)$ is additionally related in some physically appealing approximation to $g(r)$ and $u(r)$. These additional relations are known as closure relations. We will introduce various closure relations, and discuss their merits and shortcomings.

3.1 Ornstein-Zernike equation and direct correlations

The Ornstein-Zernike equation of a homogeneous and isotropic system is given by

$$h(r_{12}) = c(r_{12}) + \rho \int d\mathbf{r}_3\, c(r_{13})\, h(r_{23}) \ . \tag{53}$$

It introduces the direct correlation function, $c(r)$, as a new function and can be viewed as the definition of $c(r)$ in terms of the total correlation function, $h(r) = g(r) - 1$, of two particles a distance $r = r_{12}$ apart. Eq. (53) can be recursively solved for $h(r_{12})$ to give

$$h(r_{12}) = c(r_{12}) + \rho \int d\mathbf{r}_3\, c(r_{13})c(r_{23}) + \rho^2 \int d\mathbf{r}_3\, d\mathbf{r}_4\, c(r_{13})\, c(r_{24})\, c(r_{34}) + \mathcal{O}(c^4) \ . \tag{54}$$

This leads to the following physical interpretation of the OZ equation: the total correlations between particles 1 and 2, described by $h(r_{12})$, are due in part to the direct correlations, $c(r_{12})$, of these particles but also to an indirect correlation propagated by direct correlations via increasingly large numbers of intermediate particles.

Once information is available about $c(r)$ in form of a closure relation involving $u(r)$, the OZ equation can be viewed also as a closed integral equation for $h(r)$. Some information on $c(r)$ derives from Eq. (53) in the low-density limit $\rho \to 0$ where $c(r) \to h(r)$. With Eq. (18) follows then

$$c(r) \to f(r) \text{ for } \rho \to 0 \ , \tag{55}$$

where

$$f(r) := e^{-\beta u(r)} - 1 \tag{56}$$

is called a Mayer-f function. It follows then that

$$c(r) = -\beta u(r) \tag{57}$$

for $r \to \infty$. Without proof we note that the long-distance asymptotic result (57) holds true for a wide class of pair potentials even at finite densities. The range of $c(r)$ is thus comparable with that of $u(r)$, and the fact that $h(r)$ is generally longer ranged than $u(r)$ can be ascribed to indirect correlation effects. One word of warning: we refer here and in what follows to one-component liquids of electrically neutral particles. Ionic fluids must be distinguished from neutral fluids in that the effect of screening (cf. section 4.2) in such

systems is to cause $h(r)$ to decay exponentially at large r, whereas $c(r)$ still has the range of the infinite Coulomb potential and therefore decays as r^{-1}. In principle, ionic liquids consist of at least two charged components of opposite sign to enforce overall charge neutrality.

To relate $c(r)$ to $S(q)$, we slightly rewrite the OZ equation as

$$h(r) = c(r) + \rho \int d\mathbf{r}'\, c(|\mathbf{r} - \mathbf{r}'|)\, h(r') \tag{58}$$

using $\mathbf{r} = \mathbf{r}_{12}$, $\mathbf{r}' = \mathbf{r}_{23}$ and $|\mathbf{r} - \mathbf{r}'| = \mathbf{r}_{13}$. Fourier transformation of both sides of the OZ equation leads to

$$h(q) = c(q) + \rho\, c(q)\, h(q) \tag{59}$$

or

$$\rho\, h(q) = \frac{\rho\, c(q)}{1 - \rho\, c(q)}\ , \tag{60}$$

where $c(q)$ is the three-dimensional Fourier transform of $c(r)$. From noting that $S(q) = 1 + \rho\, h(q)$, we obtain $S(q)$ in terms of $c(q)$:

$$S(q) = \frac{1}{1 - \rho\, c(q)} \geq 0\ , \tag{61}$$

from which we learn that $\rho\, c(q) \leq 1$.

In the derivation of Eq. (59), we have employed the convolution theorem of Fourier transformation theory. The convolution (german: "Faltung"), $f_1 * f_2$, of two integrable functions $f_1(\mathbf{r})$ and $f_2(\mathbf{r})$ is defined as

$$(f_1 * f_2)(\mathbf{r}) := \int d\mathbf{r}' f_1(\mathbf{r}') f_2(\mathbf{r} - \mathbf{r}') = \int d\mathbf{r}' f_2(\mathbf{r}') f_1(\mathbf{r} - \mathbf{r}')\ . \tag{62}$$

The convolution theorem states that

$$\int d\mathbf{r}\, e^{i\mathbf{q}\cdot\mathbf{r}}\, (f_1 * f_2)(\mathbf{r}) = f_1(\mathbf{q}) f_2(\mathbf{q}) \tag{63}$$

i.e. the Fourier transform of the convolution of two functions is equal to the product of their Fourier transforms.
Using Eq. (61), we finally obtain the compressibility equation in terms of $c(q)$:

$$\frac{1}{\rho\, k_B T \chi_T} = 1 - \rho\, c(q \to 0) = 1 - 4\pi\rho \int_0^\infty dr\, r^2\, c(r)\ . \tag{64}$$

3.2 Ornstein-Zernike theory of critical opalescence

In the following, we explore the behavior of $g(r)$ near a critical point. Consider a one-component system with an attractive part in the pair potential, like a Lennard-Jones-type system (say, argon) or a suspension of sticky colloidal spheres. For a purely repulsive $u(r)$ like the hard-sphere potential, there is only one fluid phase and thus there is no liquid-gas critical point in the one-component case. However, a critical point of a liquid-gas-type

demixing transition may occur in two-component, size-asymmetric dispersions of colloidal hard spheres due to the depletion attraction effect discussed earlier (cf. Fig. 5).

Schematic $p-V$ and $p-T$ phase diagrams of a Lennard-Jones system are displayed in Fig. 7. The gas-liquid coexistence line in the $p-T$ diagram terminates in a critical point

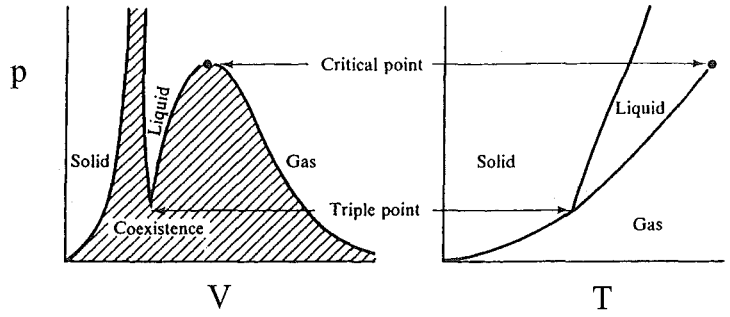


Fig. 7: *Schematic $p-V$ and $p-T$ phase diagrams of a Lennard-Jones system (argon)*

at the critical temperature T_c and pressure p_c. It is the location of a continuous (i.e., 2nd order) phase transition. On approaching the critical point along the coexistence line, the (density-) difference between liquid and gas phases ceases to exist. At the critical point, strong and long-living density fluctuations occur (cf. Eq. (49)) such that χ_T becomes arbitrarily large in the thermodynamic limit (cf. Fig. 7):

$$\left(\frac{\partial p}{\partial V}\right)_T = 0 \quad \text{i.e.} \quad \chi_T = \infty \,. \tag{65}$$

According to Eqs. (42) and (61),

$$\lim_{q\to 0} S(q) = 1 + \rho \int d\mathbf{r}\, h(r) = \frac{1}{1-\rho c(q\to 0)} \to \infty \quad \text{for} \quad T \to T_c \,, \tag{66}$$

which means that $S(q)$ becomes very large for small q as the critical point is approached. Then, regions of larger and smaller densities develop. As the size of these regions approaches the wavelength of visible light, there is in fact so much scattering that the fluid appears cloudy or opalescent. This phenomenon is therefore called critical opalescence. It is due to the occurrence of long-range spatial correlations between particles in the vicinity of a critical point such that the volume integral over $h(r)$ diverges in the limit of an infinite volume. As $T \to T_c$,

$$c(q\to 0) = 4\pi \int_0^\infty dr\, r^2\, c(r) \to \frac{1}{\rho} \tag{67}$$

which means that, contrary to $h(r)$ and $g(r)$, $c(r)$ remains short-ranged with finite second moment.

Since $c(q)$ is well behaved at T_c, we assume that it can be expanded in a truncated Taylor series around $q=0$ up to $\mathcal{O}(q^2)$. Using $\sin(x)/x \approx 1 - x^2/6 + \mathcal{O}(x^4)$, $c(q)$ is thus

approximated, for small q, by

$$\rho c(q) = 4\pi\rho \int_0^\infty dr\, r^2 \frac{\sin(qr)}{qr}\, c(r) = c_0 - c_2 q^2 + \mathcal{O}(q^4) \tag{68}$$

with expansion coefficients

$$c_0 = 4\pi\rho \int_0^\infty dr\, r^2\, c(r) \to 1 \quad \text{for} \quad T \to T_c \tag{69}$$

$$c_2 = \frac{2\pi}{3}\rho \int_0^\infty dr\, r^4\, c(r)\ . \tag{70}$$

We restrict here our attention to small q and thereby to large distances r. Note that $c_0 = \rho\, c(q=0) \leq 1$. Substitution of this truncated expansion into Eq. (61) then gives

$$S(q) \approx \frac{1}{1 - c_0 + c_2\, q^2} = \frac{1}{c_2}\frac{1}{\xi^{-2} + q^2} \tag{71}$$

as an approximation of $S(q)$ for small q, more precisely for $qR_U \ll 1$. This is the small-q approximation for the near-critical structure factor originally proposed by Ornstein and Zernike around 1917. The range of the interaction potential is denoted as R_U, and we have further introduced the correlation length

$$\xi(T) := \left(\frac{c_2}{1-c_0}\right)^{1/2} = [c_2\, S(0)]^{1/2} = \left(c_2 \frac{\chi_T}{\chi_T^{id}}\right)^{1/2}, \tag{72}$$

by assuming the fourth moment, c_2, of $c(r)$ to exist and to be positive. With the compressibility diverging for $T \to T_c$ in a power-law fashion as $\chi_T \propto (T - T_c)^{-\gamma}$, it follows that the correlation length diverges like $\xi \propto (T - T_c)^{-\gamma/2}$. The numerical value of the critical exponent γ is predicted as $\gamma = 1$ in a simple Landau-type mean-field approximation. However, the accepted value of γ for the liquid-gas transition is 1.24, as derived from renormalization group calculations of critical phenomena and verified by high-precision experiments on critical fluids [7,8].

Fourier inversion of the OZ approximation for $S(q)$, using Eqs. (38-39), gives the asymptotic form of $h(r)$ for large pair separation $r \gg R_U$

$$h(r) = \frac{1}{(2\pi)^3\rho}\int d\mathbf{q}\, e^{-i\mathbf{q}\cdot\mathbf{r}}\, [S(q) - 1] \approx \frac{1}{4\pi\rho\, c_2}\frac{e^{-r/\xi}}{r}\ . \tag{73}$$

At the critical temperature, ξ becomes infinite with

$$h(r)|_{T=T_c} \sim \frac{1}{r} \quad \text{for } r \gg R_U \tag{74}$$

which corresponds to

$$S(q)|_{T=T_c} \sim \frac{1}{q^2} \quad \text{for } q \ll {R_U}^{-1}\ . \tag{75}$$

The total correlation function decays thus algebraically, and not exponentially, at the critical point.

If the OZ approximation (Eqs. (71)-(75)) is valid, then

$$\frac{1}{I(q)} \propto \frac{1}{S(q)} = c_2 \left[\xi^{-2} + q^2\right] \tag{76}$$

i.e. a plot of the reduced inverse scattered intensity against q^2 should yield a straight line of practically constant slope, c_2, and an intercept c_2/ξ^2 that approaches zero for $T \to T_c$. Fig. 8 shows such an experimental Ornstein-Zernike plot for argon. It suggests that the mean-field-type OZ approximation is valid to good approximation at least as long as q and $|T - T_c|$ are not very close to zero.

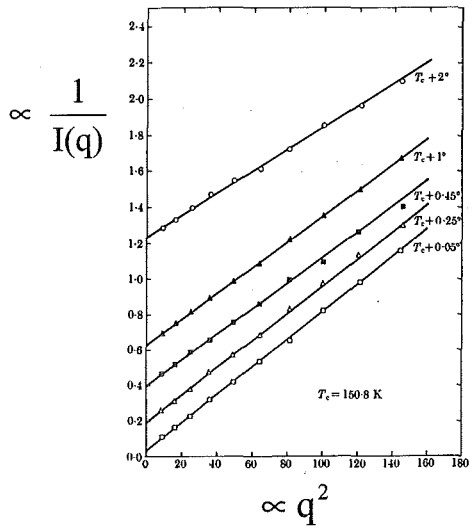


Fig. 8: *Experimental Ornstein-Zernike plot of argon. From Ref. [9]*

Experiments performed very close to T_c reveal in fact deviations at small q from the OZ approximation prediction for $S(q)$. Improved modern renormalization group theory calculations of critical phenomena lead to a corrected asymptotic scaling behavior of $h(r)$ at T_c, given in three dimensions by [7,8]

$$h(r)|_{T=T_c} \sim \frac{1}{r^{1+\eta}} \tag{77}$$

or, equivalently,

$$S(q)|_{T=T_c} \sim \frac{1}{q^{2-\eta}} \,, \tag{78}$$

with a small but nonzero critical exponent η. The accepted theoretical value for η is 0.04. The reason for the failure of the OZ approximation very close to T_c is that, by assuming a truncated small-q expansion of $c(q)$ to hold, one does not account for the full spectrum of correlation fluctuations existing at *all* length scales. We finally remark that the liquid-gas transition at T_c belongs to the same universality class of second-order

phase transitions as the ferromagnetic-paramagnetic transition in uniaxial ferromagnets (cf. the three-dimensional Ising model). All members of the same universality class show the same critical exponents.

3.3 Closure relations

After having explored the long-distance behavior of $g(r)$ in a near-critical liquid, we discuss now various closure relations which express $c(r)$ approximately in terms of $h(r)$ and a given pair potential $u(r)$. These relations, and a deeper understanding of the meaning of $c(r)$, can be obtained by diagrammatic and density functional derivative methods. We take here a pragmatic point of view and establish the closure relations most simply using plausibility arguments. In combination with the OZ equation, the closures lead to closed integral equations for $g(r)$. These integral equations have been found, in comparison with computer simulation results and scattering data, to be most useful in calculating the full r-dependence of $g(r)$ and thermodynamic properties of dense liquids.

For a system with a hard-core excluded volume part in $u(r)$, any closure relation should be consistent with the exact condition

$$h(r<\sigma) = -1\,, \quad \text{i.e.} \quad g(r<\sigma) = 0\,, \tag{79}$$

which states that two spheres of hard-sphere diameter σ can not interpenetrate, and the asymptotic result

$$c(r) = -\beta u(r)\,, \text{ for } r \to \infty \tag{80}$$

valid for a wide class of pair potentials.

Mean-spherical approximation (MSA):

The exact asymptotic form of $c(r)$ forms the basis of the so-called mean-spherical approximation, first introduced into liquid state theory by Lebowitz and Percus (1966). In MSA, $c(r)$ is assumed to be given approximately by the closure relation

$$c(r) \approx -\beta u(r) \tag{81}$$

for all non-overlap distances $r > \sigma$. Together with Eqs. (79) and (81), the OZ equation (58) becomes a *linear* integral equation determining $g(r)$ for $r > \sigma$, and $c(r)$ for $r < \sigma$. The most attractive feature of the MSA closure, as compared to other ones, is that analytic solutions exist, even in the many-component case, for various pair potential models, namely for the hard and sticky hard-sphere potentials, the square well potential, the Coulomb potential, attractive and repulsive Yukawa-type potentials, and for the dipolar hard-sphere potential. These potentials are of particular interest for molten salts, electrolyte solutions and in colloid science. No analytic MSA solution exists for the Lennard-Jones potential.

While the MSA is well suited for short-range attractive and repulsive potentials, it can predict non-physical negative values for $g(r)$ close to contact distance in case of dilute systems of strongly repelling particles. At very low density (more precisely, small volume fractions Φ), the MSA predicts that

$$g(r) = 1 + c(r) + \mathcal{O}(\Phi) \approx 1 - \beta u(r) + \mathcal{O}(\Phi)\,, \quad r > \sigma\,, \tag{82}$$

with a negative $g(r)$ for $\beta u(r) > 1$. This wrong prediction should be contrasted with the exact zero-density form of $g(r)$ given in Eq. (18). The volume fraction $\Phi = (\pi/6)\rho\sigma^3$ is defined as the fraction of the system volume filled by the spherical particles.

Rescaled MSA:

For fluids of (colloidal) particles, where the physical hard core is masked by strong and long-range repulsive forces, there exists an improved variant of the MSA which preserves the positive semi-definiteness of $g(r)$. This variant is called the rescaled MSA (Hansen and Hayter, 1982). It is based on the fact that the $g(r)$ of such systems is continuous at all distances r. Moreover and most importantly, two particles in these systems are virtually never closer to each other than a certain distance $\sigma' > \sigma$, so that $g(r) \approx 0$ for $r < \sigma'$.

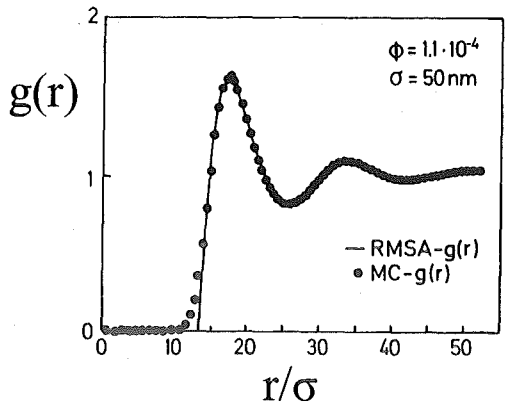


Fig. 9: *Radial distribution function of a charge-stabilized Yukawa-type dispersion. Comparison between RMSA-$g(r)$ and Monte Carlo computer simulation results. From Ref. [3]*

In RMSA, the actual system is replaced by a fictitious system consisting of particles of enlarged diameter $\sigma' > \sigma$, at the same number density ρ and, for $r > \sigma'$, with the same pair potential $u(r)$ than the original one. The (density-dependent) effective diameter, σ', is determined from the continuity of $g(r)$ at $r = \sigma'$, by demanding that

$$g(r = \sigma'; \rho, \Phi') = 0 \ , \tag{83}$$

with $g(r)$ calculated in MSA for a larger rescaled volume fraction $\Phi' = \Phi(\sigma'/\sigma)^3 > \Phi$. The RMSA-$g(r)$ is positive semi-definite since the volume fraction, Φ', of the fictitious system is so much larger than Φ that Eq. (82) does not apply any more.

Fig. 9 includes the RMSA-$g(r)$ for a dilute aqueous suspension of highly charged polystyrene spheres interacting by the Yukawa-type DLVO potential of Eq. (3). The charge number, $Z_{RMSA} = 257$, employed in the RMSA calculation has been selected such that the height of the principal peak of the RMSA $g(r)$ is coincident with that of the "exact" $g(r)$, generated by Monte Carlo (MC) computer simulations using a smaller charge number

$Z_{MC} = 205$. Since $Z_{RMSA} > Z_{MC}$, the RMSA underestimates the structural ordering in systems of strongly correlated particles. However, once Z has been adjusted to fit the actual peak height, the overall shape of $g(r)$ is remarkably well predicted by the semi-analytical RMSA solution. The RMSA has been extended to multi-component systems of Yukawa particles (cf. Ref. [3]).

Percus-Yevick (PY) closure relation:

Aside from the linear MSA, there exist a variety of non-linear integral equation schemes. The Percus-Yevick approximation (Percus and Yevick, 1958) is among the most popular ones. To introduce the PY closure relation, we reformulate the OZ equation as

$$c(r) = g(r) - \left[1 + \rho \int d\mathbf{r}'\, c(r')\, \{g(|\mathbf{r} - \mathbf{r}'|) - 1\}\right] =: g(r) - g_{ind}(r)\ . \tag{84}$$

The term in brackets, $g_{ind}(r)$, describes the indirect part of the pair correlations. Since $g(r) = \exp[-\beta w(r)]$, one can approximate $g_{ind}(r)$ by

$$g_{ind}(r) \approx e^{-\beta[w(r)-u(r)]}\ , \tag{85}$$

or, equivalently, $c(r)$ by

$$c(r) \approx g(r)\left[1 - e^{\beta u(r)}\right] = g(r) - y(r) = f(r)y(r)\ . \tag{86}$$

This is the PY closure relation for $c(r)$. It is an exact relation up to first order in the density, as one can show from a density expansion of $h(r)$ and $c(r)$ based on the iterated OZ Eq. (54). We have introduced here the so-called cavity function, $y(r)$, defined as

$$y(r) := e^{\beta u(r)}\, g(r)\ . \tag{87}$$

Contrary to $g(r)$, which for hard spheres has a jump discontinuity at $r = \sigma$ wholly contained in the factor $\exp[-\beta u(r)]$, $y(r)$ has the useful property of being continuous at all r. It agrees with $g(r)$ for all r where $u(r) = 0$. In PY approximation, $c(r)$ is thus assumed to be zero whenever the pair potential vanishes. The continuity of $y(r)$ is easy to see, using Eq. (12), from noting that

$$y(r_{12}) = \frac{V^2}{Z_N} \int d\mathbf{r}_3 \cdots d\mathbf{r}_N \exp\left[-\beta {\sum_{i<j}}' u(r_{ij})\right] \tag{88}$$

for pairwise additive forces, with the pair $\{i,j\} = \{1,2\}$ omitted from the sum. Hence $y(r)$ is a smooth and non-zero continuation of $g(r)$ into the overlap region ("cavity") $r < \sigma$.

Substitution of Eq. (86) into the OZ equation gives the non-linear PY integral equation

$$y(r) = 1 + \rho \int d\mathbf{r}' \left[e^{-\beta u(|\mathbf{r}-\mathbf{r}'|)}\, y(|\mathbf{r} - \mathbf{r}'|) - 1\right]\left[e^{-\beta u(r')} - 1\right] y(r') \tag{89}$$

for $y(r)$ or, likewise, $g(r)$. This equation can be solved analytically in three dimensions for the important case of hard spheres (cf. section 3.4), and by numerical methods for

arbitrary pair potentials.

Hypernetted-chain (HNC) approximation:

Another frequently used approximate integral equation scheme is the hypernetted-chain approximation (van Leeuwen et al., 1959). The name stems from its diagrammatic derivation. The HNC closure relation in terms of $c(r)$ is

$$c(r) \approx -\beta u(r) + h(r) - \ln[1 + h(r)] = h(r) - \ln y(r) \ . \tag{90}$$

Exponentiation gives

$$g(r) \approx e^{-\beta u(r) + h(r) - c(r)} \ , \tag{91}$$

showing that in HNC approximation the positive definiteness of the exact $g(r)$ is preserved at any density. Since from Eq. (84)

$$c(r) \approx -\beta u(r) \, , \quad r \to \infty \tag{92}$$

the HNC approximation leads further to the correct asymptotic behavior of $c(r)$ for arbitrary ρ. On the other hand the PY-$c(r)$ gives the correct long-distance behavior in general only for small densities.

The HNC closure combined with the OZ equation leads to

$$\ln\left[e^{\beta u(r)} g(r)\right] \approx h(r) - c(r) = \rho \int d\mathbf{r}' \, c(|\mathbf{r} - \mathbf{r}'|) \, h(r') \ . \tag{93}$$

Introducing the cavity function, Eq. (93) can be re-expressed as

$$\ln[y(r)] = \rho \int d\mathbf{r}' \, h(r') \, [-\beta u(|\mathbf{r} - \mathbf{r}'|) + h(|\mathbf{r} - \mathbf{r}'|) - \ln g(|\mathbf{r} - \mathbf{r}'|)] \ . \tag{94}$$

This is the non-linear HNC integral equation for $g(r)$. It can be solved only numerically even for hard spheres. Like in the PY approximation, the HNC approximation predicts $g(r)$ correctly to first order in the density.

The PY is quite successful for hard spheres but, contrary to the MSA, does not work so well for systems with attractive tails. The HNC is complementary to the PY in the sense that it is unsatisfactory for hard spheres but appears to account satisfactorily for the effects of soft cores and, in particular, for long-range repulsive potential tails as given in ionic fluids and dispersions of Yukawa particles. All three integral equation schemes have severe deficiencies near a critical point.

HNC results for a Yukawa system (cf. Eq. (3)) of moderately charged colloidal particles (Z = 107) of diameter $\sigma = 160$ nm and fixed screening parameter $\kappa\sigma$ in an organic solvent ($\epsilon = 10$) are shown in Fig. 10. The charge Z was determined from a fit of the HNC peak height of $S(q)$ to the experimentally given one. There is then rather good agreement between the theoretical and experimental $S(q)$. The deviations at small q and around the minimum can be attributed to polydispersity effects, that is to a spread in the experimental particle sizes. With increasing volume fraction Φ, there is increasing

ordering visible through more pronounced undulations in $g(r)$, and the system becomes less compressible (decreasing $S(0)$). The particles avoid each other as much as possible because of the strong and longer-ranged electrostatic repulsion so that $g(r < 1.5\sigma) = 0$. In monodisperse systems with long-range repulsion, the position, q_m, of the principal peak of $S(q)$ increases with volume fraction approximately as $q_m \sim \Phi^{1/3}$. Away from a critical point, the location, r_m, of the main peak of $g(r)$ is approximately related to q_m by

$$r_m \sim \frac{2\pi}{q_m} \ . \tag{95}$$

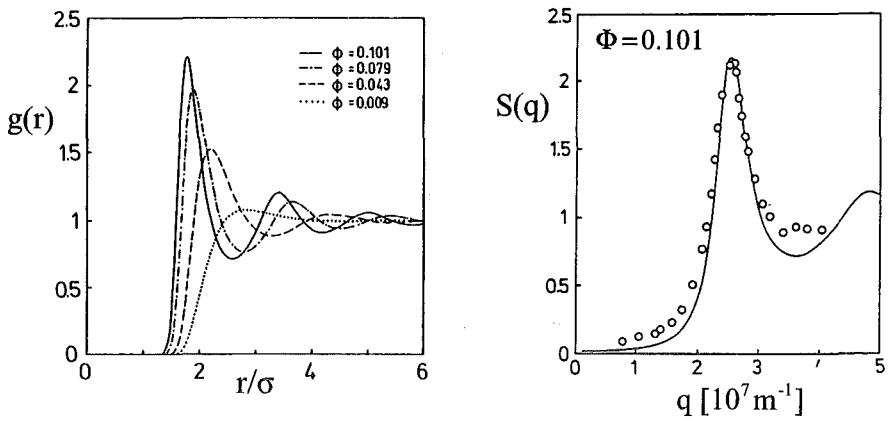


Fig. 10: *HNC radial distribution function $g(r)$ at various volume fractions (left), and static structure factor $S(q)$ (right) of charge-stabilized dispersions of silica spheres. Open circles: light scattering results of $S(q)$. From Ref. [10]*

Random phase approximation (RPA):

Suppose we can separate the pair potential of a liquid system into a short-range reference part, $u_0(r)$, and a long-range perturbational part, $u_l(r)$ (cf. Fig. 11), with

$$u(r) = u_0(r) + u_l(r) \ . \tag{96}$$

Let us further assume that the direct correlation function, $c_0(r)$, of the reference system (where $u = u_0$) is known exactly or to a good approximation. For a reference system of hard spheres, e.g., we could use the analytic PY solution for $c_0(r)$ derived in section 3.4. The true direct correlation function, $c(r)$, of the system can then be approximated by

$$c(r) \approx c_0(r) - \beta u_l(r) \ , \ r > 0 \tag{97}$$

which is asymptotically correct at long pair separations. For historical reasons, this closure relation is referred to as the random phase approximation. In this approximation one obtains

$$S(q) = \frac{1}{1 - \rho c(q)} \approx \frac{1}{1 - \rho c_0(q) + \beta\rho\, u_l(q)} \ . \tag{98}$$

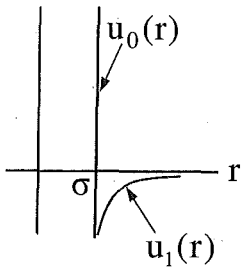


Fig. 11: *Pair potential consisting of hard-sphere reference part, $u_0(r)$, and a longer-ranged, attractive perturbational part $u_l(r)$.*

The static structure factor is thus expressed in terms of the structure factor, $S_0(q)$, of the reference system and the Fourier transform,

$$u_l(q) = \int_0^\infty d\mathbf{r}\, e^{i\mathbf{q}\cdot\mathbf{r}}\, u_l(r) \;, \tag{99}$$

of the perturbational part of $u(r)$. Eq. (98) can be rewritten in the mnemonic form

$$\frac{1}{S(q)} \approx \frac{1}{S_0(q)} + \beta\rho u_l(q) \;. \tag{100}$$

The RPA is the most simple perturbation theory for fluid microstructures, usually suited only for small wave numbers. Its multi-component extension has been successfully used for the calculation of monomer-monomer structure factors of polymer blends [11]. For an ideal gas as reference system, one has $c_0(r) = 0$ and $S_0(q) = 1$. The RPA reduces then to the MSA for point-like particles, referred to in the literature as a version of the Debye-Hückel approximation. One should notice that the perturbation must be sufficiently weak, or the density sufficiently low, to ensure that $\beta\rho u_l(q)S_0(q) > -1$ with $S(q) > 0$. Furthermore, the RPA does not ensure that $g(r < \sigma) = 0$ in case of a hard-sphere reference system. This non-physical feature of the RPA is related to an ambiguity in the choice of the perturbation potential $u_l(r)$ for $r < \sigma$ in Eq. (99). The true $g(r)$ should not depend on this choice.

In the optimized random phase approximation (ORPA), $u_l(r)$ is extended into the hard-core regime $r < \sigma$ such that $g(r < \sigma) = 0$. While the ORPA is a considerable improvement of the RPA, there is a price to pay in form of a much larger numerical effort to calculate $S(q)$.

3.4 Percus-Yevick solution for hard spheres

Hard spheres serve as a reference system in the theory of uncharged liquids, as an ideal gas does in the theory of dilute gases, and a harmonic solid in solid-state physics. The PY approximation leads to an integral equation for the hard-sphere cavity function $y(r)$ which can be solved analytically.

The solution proceeds as follows. For hard spheres,

$$c(r) = g(r)\left[1 - e^{\beta u(r)}\right] = 0, \quad r > \sigma \tag{101}$$

in PY approximation, i.e. the hard-sphere direct correlation is approximately set equal to zero for non-overlap distances. As a matter of fact, the true $c(r)$ has a small but non-vanishing tail for $r > \sigma$. As can be noticed here, the PY closure becomes identical to the MSA closure (cf. Eq. (81)) in case of a hard-sphere fluid.

The hard-sphere cavity function reads

$$y(r) = e^{\beta u(r)} g(r) = \begin{cases} g(r), & r > \sigma \quad \text{exact} \\ -c(r), & r < \sigma \quad \text{PY aproximation} \end{cases} \tag{102}$$

where the lower equality follows from the PY closure in Eq. (86). It follows that $c(r)$ and $g(r)$ have a jump discontinuity at $r = \sigma$, with $g(r = \sigma^+) = -c(r = \sigma^-)$, since $y(r)$ is continuous everywhere.

Upon inserting the hard-sphere potential into Eq. (89), one obtains a quadratic integral equation for $y(r)$ of the form

$$y(r) = 1 + \rho \int_{r'<\sigma} d\mathbf{r}'\, y(r') - \rho \int_{r'<\sigma,\, |\mathbf{r}-\mathbf{r}'|>\sigma} d\mathbf{r}'\, y(r')\, y(|\mathbf{r} - \mathbf{r}'|)\,. \tag{103}$$

It is required to solve this integral equation within $r < \sigma$ for $c(r) = -y(r)$, since $c(r > \sigma) = 0$ is known already. Following Wertheim [12], we use a third-order polynomial

$$c(r) = a_0 + a_1 r + a_2 r^2 + a_3 r^3 \tag{104}$$

as a trial solution of $c(r < \sigma)$, with yet unknown density-dependent expansion coefficients $\{a_i\}$. This ansatz is suggested from the low density form of $c(r)$, which is a third order polynomial in case of hard spheres. For a proof of this statement use Eq. (54) to show that to first order in density (volume fraction Φ), $y(r)$ is given by

$$y(r) = 1 + \rho \int d\mathbf{r}' f(r')\, f(|\mathbf{r} - \mathbf{r}'|) + \mathcal{O}(\rho^2)\,. \tag{105}$$

For hard spheres, the Mayer-f function is $f(r) = -1$ for $r < \sigma$ and zero otherwise. The convolution integral in Eq. (105) is then equal to the volume of overlap of two spheres of equal radii σ with centres separated by r. As a consequence

$$y(r) = 1 + 8\,\Phi \left[1 - \frac{3}{4}x + \frac{1}{16}x^3\right] \theta(2 - x) + \mathcal{O}(\Phi^2)\,, \tag{106}$$

with $x = r/\sigma$. The overlap volume is zero for $x > 2$ as expressed by the unit step function $\theta(2 - x)$. Recall that the PY approximation is correct for $g(r)$ to first order in ρ. In using the polynomial ansatz in Eq. (104), it is assumed that the functional form of $c(r)$ is the same for all volume fractions.

The four expansion coefficients, $\{a_i\}$, are determined by employing the continuity of $y(r)$ and its first two derivatives at $r = \sigma$. Their continuity follows from Eq. (103) and its first two derivatives. A fourth condition follows from the PY integral equation (103) evaluated at $r = 0$:

$$y(0) = 1 + \rho \int_{r'<\sigma} d\mathbf{r}'\, y(r') \; . \tag{107}$$

After inserting Eq. (104) in Eq. (103) and making use of the four boundary conditions to determine the $\{a_i\}$, a lengthy calculation gives the following PY result for the hard-sphere $c(r)$:

$$c(r < \sigma) = -\left[\lambda_1 \left(1 + \frac{1}{2}\Phi\, x^3\right) + \lambda_2\, x\right] \tag{108}$$

with

$$\lambda_1 = \frac{(1+2\Phi)^2}{(1-\Phi)^4} \; , \qquad \lambda_2 = -\frac{6\Phi\,(1+0.5\Phi)^2}{(1-\Phi)^4} \; . \tag{109}$$

The PY result for $-c(r)$ reduces, for small Φ, to the correct first order density form of $y(r)$ given in Eq. (106).

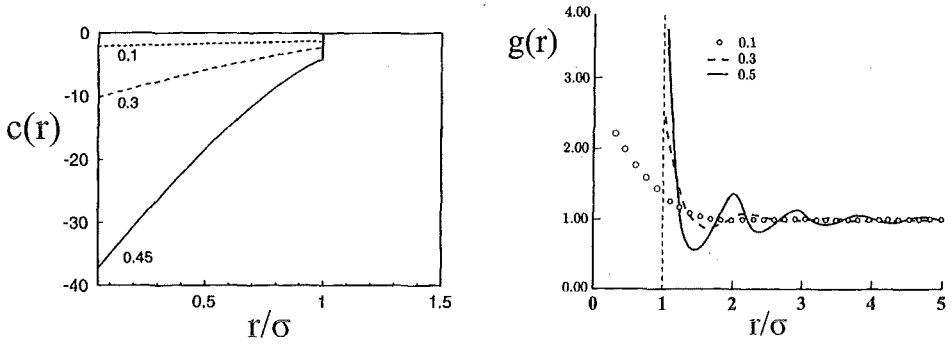


Fig. 12: *Percus-Yevick direct correlation function (left) and radial distribution function (right) of hard spheres*

Fourier transformation of $c(r)$ leads with Eq. (61) to an analytic expression for $S(q)$. This expression reads explicitly [3]

$$S(y) = \frac{1}{X^2(y) + Y^2(y)} \tag{110}$$

with

$$X(y) = 1 - 12\,\Phi\,[A\, f_1(y) + B\, f_2(y)] \tag{111}$$

$$Y(y) = -12\,\Phi\,[A\, f_3(y) + B\, f_4(y)] \; , \tag{112}$$

where

$$A = \frac{1+2\Phi}{(1-\Phi)^2} \; , \qquad B = \frac{1+0.5\Phi}{(1-\Phi)^2} \; , \tag{113}$$

and

$$f_1(y) = \frac{y - \sin(y)}{y^3}, \qquad f_2(y) = \frac{\cos(y) - 1}{y^2} \tag{114}$$

$$f_3(y) = \frac{f_2(y)}{y} + \frac{1}{2y}, \qquad f_4(y) = -y f_1(y) \; . \tag{115}$$

We have introduced here the reduced wave number $y = q\sigma$.

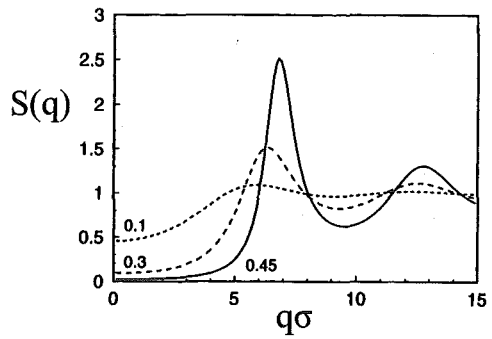


Fig. 13: *Percus-Yevick static structure factor of hard spheres*

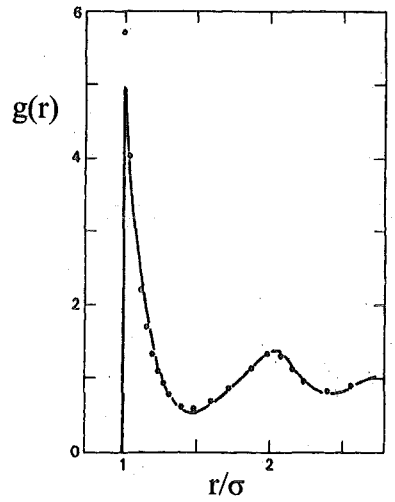


Fig. 14: *Hard-sphere $g(r)$ for a volume fraction $\Phi = 0.49$ close to the freezing transition. Comparison between PY (solid line) and MC computer simulations (filled circles)*

The reduced isothermal compressibility follows as

$$\lim_{q \to 0} S(q) = \frac{(1 - \Phi)^4}{(1 + 2\Phi)^2} \; , \tag{116}$$

which is a monotonically decreasing function in Φ. For given analytical $S(q)$, the hard-sphere $g(r)$ can be determined in principle by numerical Fourier-inversion. However, to avoid problems caused by the jump discontinuity in $g(r)$, it is safer to calculate first the function $\gamma(r) := h(r) - c(r)$ by Fourier-inverting $\gamma(q) = \rho c(q)h(q) = [S(q) - 1]^2 / (\rho S(q))$. The hard-sphere $g(r)$ follows then in PY approximation from $g(r) = y(r) = 1 + \gamma(r)$ for $r > \sigma$. Contrary to $g(r)$, $\gamma(r)$ is continuous also at $r = \sigma$ as one can deduce directly from the OZ equation. Notice here that the identity $y(r) = 1 + \gamma(r)$ holds true only within PY approximation. While the full PY-$g(r)$ of hard spheres can not be represented analytically, one can derive closed expressions for the contact values of $g(r)$ and its first derivative from the continuity of $y(r)$ and its derivative at $r = \sigma$:

$$g(r = \sigma^+) = \frac{1 + 0.5\,\phi}{(1 - \Phi)^2} \,, \tag{117}$$

and

$$\sigma \frac{dg}{dr}(r = \sigma^+) = -\frac{4.5\Phi\,(1 + \Phi)}{(1 - \Phi)^3} \,. \tag{118}$$

PY results for the hard-sphere $c(r)$ and $g(r)$, and for the static structure factor, are shown in Figs. 12 and 13, respectively, for various volume fractions. For $\Phi = 0.1$, we further show the cavity function with $y(r) = -c(r)$ for $r < \sigma$. The PY approximation provides a quite good representation of the true hard-sphere $S(q)$ and $g(r)$ for volume fractions $\phi \leq 0.35$. At larger values of Φ it underestimates the contact value of $g(r)$, as can be seen from Fig. 14 in comparison with Monte Carlo (MC) computer simulation results. The PY approximation further fails to predict the liquid-solid freezing transition which occurs for hard spheres at $\Phi_f = 0.49$. This failure is not restricted to the PY approximation: none of the Ornstein-Zernike integral equations discussed in this lecture can, per se, predict a first-order liquid-crystal phase transition.

3.5 Thermodynamic consistency and Rogers-Young closure

One important reason for the failure of the PY approximation at higher densities is its thermodynamic inconsistency : due to the approximate nature of the PY-$g(r)$, the thermodynamic routes in Eqs. (40-42) give pressure curves, $p(\rho)$, which become increasingly different from each other with increasing density. The results for the thermodynamic properties obtained via the three routes are in general different for all OZ integral equations discussed so far. This lack of thermodynamic consistency is a common feature of approximate theories.

To illustrate the thermodynamic inconsistency of the PY approximation for the case of hard spheres we integrate the compressibility in (116) with respect to Φ. This yields the compressibility equation of state

$$\frac{\beta p^c}{\rho} = \frac{p^c}{p_{id}} = \frac{1 + \Phi + \Phi^2}{(1 - \Phi)^3} \,. \tag{119}$$

Using instead the pressure (or virial) equation of state, Eq. (41), one obtains

$$\frac{\beta p^v}{\rho} = \frac{1 + 2\Phi + 3\Phi^2}{(1 - \Phi)^2} \,, \tag{120}$$

which agrees with the pressure, p^c, derived from the compressibility equation only up to third order in the volume fraction. The pressure Eq. (41) is referred to also as virial equation of state, since it can be derived from the virial theorem of classical mechanics. The energy equation, Eq. (40), can not be used to derive the excess pressure, since the internal energy of hard spheres is of purely kinetic origin.

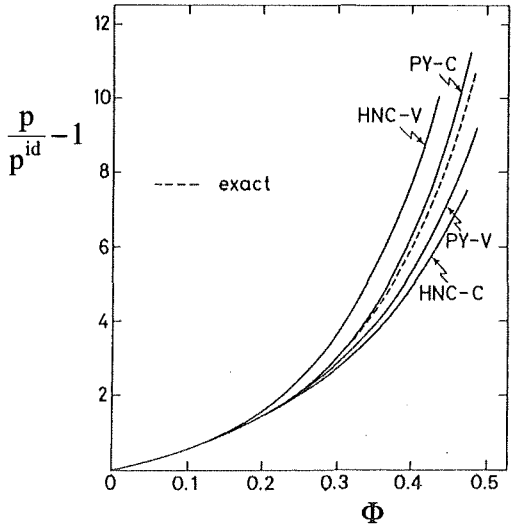


Fig. 15: *Hard-sphere compressibility and pressure (virial) equations of states in PY and HNC approximations. Dashed line: exact pressure curve. From Ref. [1]*

The PY and HNC compressibility and pressure (virial) equation of states for hard spheres are plotted in Fig. 15, in comparison with the "exact" pressure curve obtained from computer simulations. The exact hard-sphere equation of state is very well described in the fluid regime ($\Phi \leq 0.49$) by the Carnahan-Starling formula

$$\frac{\beta p}{\rho} = \frac{1 + \Phi + \Phi^2 - \Phi^3}{(1-\Phi)^3} \ . \tag{121}$$

The exact pressure is bracketed by p^c and p^v, with increasing differences between p^c and p^v for increasing Φ. The PY is obviously a better approximation for hard spheres than the HNC.

Rogers-Young (RY) approximation:

Rogers and Young [13] have combined the PY and HNC approximations in an integral equation scheme which removes part of their thermodynamic inconsistencies. This hybrid scheme was suggested from the observation (cf. Fig. 16) that computer simulation data for the structure factor of systems with purely repulsive pair potentials are bracketed, around q_m, by the PY and HNC structure factors. The RY closure relation is given by

$$g(r) \approx e^{-\beta u(r)} \left\{ 1 + \frac{1}{f(r)} \left[e^{f(r)[h(r)-c(r)]} - 1 \right] \right\} \tag{122}$$

with a mixing function

$$f(r) = 1 - e^{-\alpha r} \tag{123}$$

including a mixing parameter $\alpha \in \{0, \infty\}$. The closure relation is constructed in such a way that for

$$\begin{aligned} r \text{ or } \alpha \to 0: \quad & f(r) \to 0 \quad && \text{RY} \to \text{PY} \\ r \text{ or } \alpha \to \infty: \quad & f(r) \to 1 \quad && \text{RY} \to \text{HNC}\,. \end{aligned} \tag{124}$$

Hence the RY $y(r)$ reduces to its PY value for $r \to 0$ and to its HNC value for $r \to \infty$.

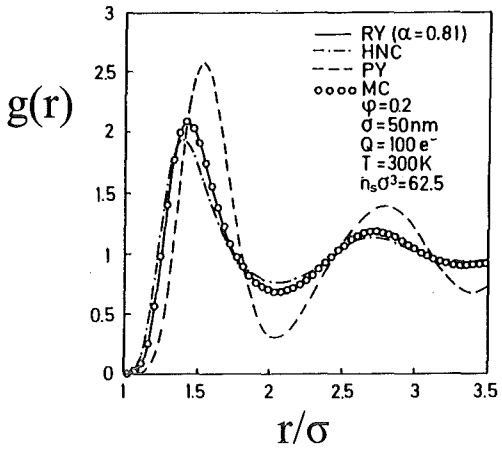


Fig. 16: *Radial distribution functions of a charge-stabilized Yukawa-like suspension at volume fraction $\Phi = 0.2$. Comparison of the RY, HNC, and PY approximations with MC results. From Ref. [14]*

This is consistent with the observation that whereas the HNC closure is correct at large separations, the PY approximation is expected to be more reliable at small r, at least for strongly repulsive potentials. The parameter α determines the proportion in which HNC and PY are mixed at intermediate r. Its numerical value follows from requiring partial thermodynamic consistency by demanding the equality, $\chi_T^p = \chi_T^c$, of the compressibilities obtained from the pressure and compressibility equations od state. Since χ_T is directly related to the long-wavelength limit of the static structure factor, one may expect that the RY approximation will provide reliable results for $S(q)$ at finite q.

The RY mixing scheme has been found to perform very well for three-dimensional liquids with purely repulsive pair potentials. Its predictions of the pair structure are less precise for two-dimensional systems. Monolayers of charged or magnetic colloidal particles at a liquid-gas interface or between two narrowly spaced plates are well-studied examples of such (quasi-) two-dimensional systems. Fig. 16 includes a comparison of RY, HNC and PY results for $g(r)$ with Monte Carlo simulations of a three-dimensional colloidal dispersion of Yukawa spheres. The true (Monte Carlo) $g(r)$ is strongly overestimated by the PY approximation, whereas the fluid microstructure is somewhat underestimated by the HNC approximation, and even more so when the RMSA is used (the $g(r)$ of the latter

is not included in Fig. 16). The RY approximation, on the other hand, reproduces the MC data rather perfectly.

4 Generalization to Fluid Mixtures

The concept of pair and direct correlations, and the Ornstein-Zernike integral equation schemes described in earlier sections, can be generalized without difficulty to multi-component liquids and polydisperse (colloidal) systems. We will discuss these generalizations in the following section. As an interesting application of the many-component liquid state theory we will present a derivation of the effective pair potential in Eq. (3). This potential describes the screened electrostatic interaction of charged colloidal particles.

4.1 Partial correlation functions

Consider an atomic or colloidal liquid consisting of m components of spherical particles of diameters σ_α and partial number densities $\rho_\alpha = N_\alpha/V$. We employ greek symbols, with $\alpha = 1, \ldots, m$, to label the m components which build up the liquid. The particles within each component are identical. We assume that the particle interactions can be described by pairwise additive forces. The following replacements

$$\begin{aligned} u(r) &\rightarrow u_{\alpha\beta}(r) \\ g(r) &\rightarrow g_{\alpha\beta}(r) \\ c(r) &\rightarrow c_{\alpha\beta}(r) \\ h(r) &\rightarrow h_{\alpha\beta}(r) = g_{\alpha\beta}(r) - 1 \end{aligned} \tag{125}$$

are needed for a generalization to a m-component mixture. There are $m(m+1)/2$ partial pair potentials $u_{\alpha\beta}(r)$, radial distribution functions $g_{\alpha\beta}(r)$, total correlation functions $h_{\alpha\beta}(r)$, and direct correlation functions $c_{\alpha\beta}(r)$ (with $\alpha, \beta \in \{1, \ldots, m\}$) necessary to characterize the fluid microstructure. Here, $u_{\alpha\beta}(r)$ is the pair potential of two particles belonging to component α and β, respectively. Furthermore, $g_{\alpha\beta}(r)$ gives the relative conditional probability of finding an β-type particle a distance r apart from a given α-type particle. The partial pair potentials are obviously symmetric in the two component indices, i.e. $u_{\alpha\beta}(r) = u_{\beta\alpha}(r)$. The remaining functions in Eq. (125) are also symmetric.

The one-component OZ equation is replaced in mixtures by a set of $m(m+1)/2$ coupled OZ equations, one for each $h_{\alpha\beta}(r)$. In case of a homogeneous and isotropic liquid mixture, these OZ equations are given by

$$h_{\alpha\beta}(r) = c_{\alpha\beta}(r) + \sum_{\gamma=1}^{m} \rho_\gamma \int d\mathbf{r}'\, c_{\alpha\gamma}(|\mathbf{r} - \mathbf{r}'|)\, h_{\gamma\beta}(r') \; . \tag{126}$$

Fourier-transformation gives the OZ equations in q-space:

$$h_{\alpha\beta}(q) = c_{\alpha\beta}(q) + \sum_{\gamma=1}^{m} \rho_\gamma\, c_{\alpha\gamma}(q)\, h_{\gamma\beta}(q) \; . \tag{127}$$

The total correlation function, $h_{\alpha\beta}$, between two particles of components α and β is thus written as the sum of a direct correlation part, $c_{\alpha\beta}$, and an indirect correlation part mediated through all other particles of components $\gamma = 1, \cdots, m$ with relative weight ρ_γ.

Since there are $m(m+1)/2$ unknown functions, $c_{\alpha\beta}(r)$, in the OZ equations one needs the same number of closure relations to obtain a complete set of integral equations determining the partial radial distribution functions. We quote here only the multi-component generalization of the MSA since it is used subsequently. All other integral equation schemes discussed previously can be generalized accordingly to mixtures. The multi-component MSA closure relations are

$$c_{\alpha\beta}(r) \approx -\beta u_{\alpha\beta}(r)\,, \quad r > \frac{\sigma_\alpha + \sigma_\beta}{2}\,. \tag{128}$$

Together with the exact non-overlap conditions

$$h_{\alpha\beta}(r) = -1\,, \quad r < \frac{\sigma_\alpha + \sigma_\beta}{2}\,, \tag{129}$$

and the OZ equations one obtains a closed set of integral equations for $h_{\alpha\beta}(r)$.

4.2 Effective interaction between charged colloidal particles

Our plan is to calculate the effective electrostatic interaction between two charge-stabilized colloidal particles of radius a and charge Ze immersed in a supporting electrolyte solution (cf. Fig. 17). For this purpose we model the colloidal particles, the counterions of charge $Z_c e$ dissociated from the colloidal particle surfaces, and the salt/electrolyte ions as uniformly charged hard spheres dispersed in a solvent which is described as a structureless, uniform continuum of dielectric constant ϵ. This is the so-called Primitive Model which has been frequently used as a model for electrolytes and charge-stabilized colloidal dispersions. It is "primitive" in the sense that the structure of the solvent and particle surfaces, and polarization effects are completely disregarded.

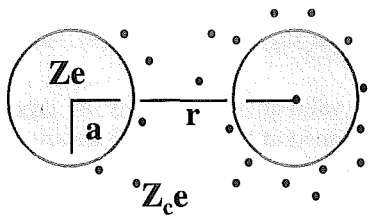


Fig. 17: *Primitive model of charged colloidal hard spheres (macroions) of radius a and charge Ze plus point-like counterions of charge $Z_c e$*

The counterions and salt ions are much smaller than the colloidal particles (macroions). Therefore we assume these microions to be point-like, i.e. of zero diameter. For the sake of simplicity and to minimize the number of particle components to two, only the point-like

counterions will be considered for the time being. Overall charge neutrality requires then that

$$\rho_1 Z + \rho_c Z_c = 0 \; . \tag{130}$$

Typically, $|Z_c| = 1$ and $|Z| \gg |Z_c|$. According to Eq. (127), there are thus three coupled Ornstein-Zernike equations

$$h_{\alpha\beta}(q) = c_{\alpha\beta}(q) + \rho_1 c_{\alpha 1}(q)\, h_{1\beta}(q) + \rho_2 c_{\alpha 2}(q)\, h_{2\beta}(q) \tag{131}$$

for components 1 and 2, i.e. for the colloidal macroions of density ρ_1, and for the point-like counterions of density $\rho_2 = \rho_c$. The subscript c is used here to label the counterions, and not the colloidal particles. The three OZ equations include information on macroion-macroion (11), macroion-counterion (12) and counterion-counterion (22) pair correlations. However, we are only interested here in the macroion-macroion correlations (11). To eliminate explicit reference to the counterions we define an effective one-component Ornstein-Zernike equation for the macroions alone as

$$h_{11}(q) = c_{eff}(q) + \rho_1 c_{eff}(q)\, h_{11}(q) \; . \tag{132}$$

By demanding h_{11} to be the same as in the original OZ equations, the effective direct correlation function, $c_{eff}(q)$, is determined by

$$c_{eff}(q) = c_{11}(q) + \frac{\rho_c c_{12}(q)^2}{1 - \rho_c c_{22}(q)} \; . \tag{133}$$

It is thus related to all three partial direct correlation functions. Eq. (132) is formally identical with the OZ equation of a genuinely one-component system. It describes the microstructure of particles 1 (macroions) immersed in a bath of particles of component 2 (counterions). The counterions do not appear explicitly in Eq. (132). Their effects are hidden in $c_{eff}(q)$.

Suppose $c_{eff}(q)$ and its Fourier-inverse, $c_{eff}(r)$, would be already known from Eq. (133). The effective pair potential, $u_{eff}(r)$, describing the interaction of two ("counterion-dressed") macroions follows then, at least asymptotically, from noting that

$$\lim_{\rho_1 \to 0} h_{11}(r) = \lim_{\rho_1 \to 0} c_{eff}(r) = -\beta u_{eff}(r) \quad \text{for} \quad r \to \text{"}\infty\text{"} \; , \tag{134}$$

where the second equality is valid in general only at large pair distances. The zero-macroion-density limit is performed at the end since we are interested only in the effective interaction of two isolated macroions.

Our task is thus to calculate first the three partial direct correlation functions $c_{\alpha\beta}$ from solving the coupled Ornstein-Zernike equations with appropriate closure relations. Next, $c_{eff}(r)$ can be determined using Eq. (133). We will use here the linear MSA closure for analytical simplicity.

The direct correlation function of the point-like counterions is approximated in MSA by

$$c_{22}(r) = -\beta u_{22}(r) \, , \quad r > 0 \tag{135}$$

where

$$\beta u_{22}(r) = L_B \frac{Z_c^2}{r}, \quad r > 0 . \tag{136}$$

Using Eqs. (38) and (39), Fourier inversion gives

$$c_{22}(q) = -4\pi L_B Z_c^2 \frac{1}{q^2} . \tag{137}$$

Notice in this context that in the limit of point-like ions, or for ionic systems at infinite dilution, the MSA reduces to what is known in electrolyte theory as the Debye-Hückel (DH) approximation. When dealing with direct correlation functions of charged particles, which have short-range (i.e. excluded volume) interaction contributions aside from the long-range Coulomb interactions, it is very helpful to split $c_{\alpha\beta}(r)$ into a short-range part, $c^s_{\alpha\beta}(r)$, and a long-range Coulomb part according to

$$c_{\alpha\beta}(r) = c^s_{\alpha\beta}(r) - L_B \frac{Z_\alpha Z_\beta}{r} , \tag{138}$$

since it holds quite generally that

$$c_{\alpha\beta}(r) \approx -\beta u_{\alpha\beta}(r) = -L_B \frac{Z_\alpha Z_\beta}{r} \quad r \to \infty . \tag{139}$$

In this way, the colloid-counterion direct correlations are expressed as

$$c_{12}(q) = c^s_{12}(q) - 4\pi L_B \frac{Z Z_c}{q^2} . \tag{140}$$

The colloid-colloid direct correlation function is written accordingly as

$$c_{11}(q) = c^s_{11}(q) - 4\pi L_B \frac{Z^2}{q^2} . \tag{141}$$

Substitution of Eqs. (137), (140) and (141) into Eq. (133) results in

$$c_{eff}(q) = c^s_{11}(q) + \rho_c [c^s_{12}(q)]^2 - 4\pi L_B \left[Z + \rho_c Z_c c^s_{12}(q)\right]^2 \frac{1}{\kappa^2 + q^2} \tag{142}$$

where we have introduced the Debye-Hückel screening length, κ^{-1}, with

$$\kappa^2 = 4\pi L_B \rho_c Z_c^2 . \tag{143}$$

Hence the screening parameter is determined by the concentration and charge ("ionic-strength") of dissociated counterions.

The large-r asymptotic behavior of $c_{eff}(r)$ is determined by the factor $[\kappa^2 + q^2]^{-1}$ in Eq. (142), since $c^s_{12}(q)$ and $c^s_{11}(q)$ are Fourier transforms of short-range functions. Fourier inversion leads, with Eqs. (38) and (39), to the intermediate result

$$c_{eff}(r) = \frac{1}{(2\pi)^3} \int d\mathbf{r} e^{-i\mathbf{q}\cdot\mathbf{r}} c_{eff}(q) \sim -\beta g \frac{e^{-\kappa r}}{r} \quad r \to \infty \tag{144}$$

with a yet undetermined interaction strength g. The magnitude of g is determined by the pre-factor of $[\kappa^2+q^2]^{-1}$ which includes $c_{12}^s(q)$. The effective macroion pair potential is asymptotically of the Yukawa-type, with a screening parameter determined by the Debye-Hückel relation Eq. (143). The counterions (and salt ions) distribute themselves around the macroions to screen the colloid-colloid Coulomb repulsion. The only approximation used to obtain the asymptotic result in Eq. (144) is the DH approximation for the counterion correlations $c_{22}(r)$.

To determine g analytically we further apply the MSA to the colloid-colloid and colloid-counterion direct correlation functions:

$$c_{11}(r) = -\beta u_{11}(r) = -L_B\frac{Z^2}{r}, \quad r>\sigma=2a \tag{145}$$

$$c_{12}(r) = -\beta u_{12}(r) = -L_B\frac{ZZ_c}{r}, \quad r>a \tag{146}$$

In MSA the short-range direct correlation parts are thus zero outside the overlap region, i.e. $c_{11}^s(r)=0$ for $r>\sigma=2a$ and $c_{12}^s(r)=0$, for $r>a$. As a consequence, the MSA predicts the counterion-colloid short-range direct correlation part to be a linear function of the colloid charge number. This linearity in Z is exactly valid for the true c_{12}^s only in the limit of weak particle charges. For larger macroion charges, the MSA underestimates the accumulation of counterions close to the surface of a colloidal macroion.

Using these properties of the MSA-$c_{\alpha\beta}^s(r)$, application of the convolution theorem to the second and third term on the right-hand-side of Eq. (142) shows that $g\propto Z^2$ and

$$-c_{eff}(r) = 4\pi L_B\,\mathcal{F}^{-1}\left\{\frac{[Z+\rho_c Z_c c_{12}^s(q)]^2}{\kappa^2+q^2}\right\} \propto Z^2\,\frac{e^{-\kappa r}}{r} \quad r>\sigma\,. \tag{147}$$

That $c_{eff}(r)\propto \exp[-\kappa r]/r$ holds for all $r>\sigma$ and not only at asymptotically large distances is a consequence of the approximation $c_{12}^s(r>a)=0$ used in MSA.

So far, we have accounted only for the counterions whose number density ρ_c, according to Eq. (130), and thus κ become zero when $\rho_l\to 0$. One can rather easily include the effects of point-like added salt ions of number density ρ_s and charge number Z_s (for each additional component s) by increasing accordingly the number of components in Eq. (131). For an overall neutral system

$$\sum_s \rho_s Z_s = 0\,, \tag{148}$$

where the sum runs over all components of salt ions. When the MSA closure is used again for the salt ion - salt ion direct correlation functions, Eq. (142) is easily generalized to

$$c_{eff}(q) = c_{11}^s(q) + \sum_{\alpha=s,c}\rho_\alpha[c_{1\alpha}^s(q)]^2 - 4\pi L_B\left[Z+\sum_{\alpha=s,c}\rho_\alpha Z_\alpha c_{1\alpha}^s(q)\right]^2\frac{1}{\kappa^2+q^2}\,, \tag{149}$$

where $c_{1\alpha}^s(q)$ is the short-range part of the colloid - microion direct correlations functions. The screening parameter is now determined by the ionic strengths of all microions, i.e.

salt- and counterions:

$$\kappa^2 = 4\pi L_B \left[\rho_c Z_c^2 + \sum_s \rho_s Z_s^2\right] . \tag{150}$$

In a final step, we employ the limit $\rho_1 \to 0$ of very small macroion concentrations, where the macroion-microion direct correlation functions, $c_{1\alpha}(r)$ and $h_{1\alpha}(r)$, can be calculated analytically in the MSA (= DH approximation). We omit these rather technical calculations and quote only the results:

$$g_{1\alpha}(r) = \left[1 - L_B Z Z_\alpha \left(\frac{e^{\kappa a}}{1+\kappa a}\right) \frac{e^{-\kappa r}}{r}\right] \theta(r-a) \tag{151}$$

$$c_{1\alpha}(r) = -\left[1 + \frac{L_B}{a} Z Z_\alpha \left(\frac{\kappa a}{1+\kappa a}\right)\right] \theta(a-r) - \left(L_B \frac{Z Z_\alpha}{r}\right) \theta(r-a) \tag{152}$$

and

$$c_{1\alpha}^s(r) = -\left[1 + L_B Z Z_\alpha \left(\frac{\kappa}{1+\kappa a} - \frac{1}{r}\right)\right] \theta(a-r) . \tag{153}$$

The total correlation function, $h_{1\alpha}(r)$, describes the distribution of α-type microions around a colloidal sphere. It decays exponentially at large r due to screening, whereas $c_{1\alpha}(r)$ still has the infinite range of the Coulomb potential. As noted already in section 3.1, this feature distinguishes ionic from neutral liquids. An interesting observation for the DH-$g_{1\alpha}(r)$ in Eq. (137) is that

$$\sum_{\alpha=c,s} \rho_\alpha \int d\mathbf{r}\, g_{1\alpha}(r) Z_\alpha e = -Ze \tag{154}$$

which means that the total charge of the microionic cloud exactly cancels the charge of the colloidal particle in its centre. This is a special case of general local electroneutrality conditions for ionic systems [1]. One can show that the MSA and HNC closure relations are compatible with these exact conditions.

Using finally the DH expression for $c_{1\alpha}^s(r)$ in the Fourier-inverted form of Eq. (149), and noticing that in MSA

$$\left(c_{1\alpha}^s * c_{1\beta}^s\right)(r > 2a) = 0 \tag{155}$$

for the convolution of two colloid - microion short-range direct correlation function parts, we obtain our final result

$$\beta u_{eff}(r) = -\lim_{\rho_1 \to 0} c_{eff}(r) = -\lim_{\rho_1 \to 0} h_{11}(r) = L_B Z^2 \left(\frac{e^{\kappa a}}{1+\kappa a}\right)^2 \frac{e^{-\kappa r}}{r}, \quad r > \sigma \tag{156}$$

for the effective macroion pair potential quoted already in Eq. (3). Within the linearization approximation of weak particle charges,

$$g_{11}(r) = e^{-\beta w_{11}(r)} \approx 1 - \beta w_{11}(r) , \tag{157}$$

which is consistent with the DH-MSA approximation of direct correlations, $u_{eff}(r)$ can be identified with the macroion - macroion potential of mean force $w_{11}(r)$. One might

expect from the mean-spherical-type approximations entering into its derivation that this form of the effective pair potential applies only at long distances r and for weakly charged particles. However, it has been shown that the range of applicability of Eq. (156) can be substantially extended when Z is treated not as the bare macroion charge, but as an effective or dressed colloid charge smaller than the bare one. In this way one accounts approximately for the stronger screening close to strongly charged macroion surfaces.

5 Summary

The purpose of my lecture was to provide an introductionary overview on selected integral equation theories of the liquid state. These theories are based on the Ornstein-Zernike equation and its concept of direct correlations. The OZ based integral equation schemes provide an extremely versatile framework for predicting microstructural and thermodynamic properties of simple and colloidal liquids, from the knowledge of the pair potential. In addition these schemes can be used to obtain effective pair potentials in colloidal systems of various particle species, by contracting the unneeded species out of the description.

Due to the approximate nature and, usually, non-perturbative character of an integral equation scheme, one can not make decisive a priori statements on its accuracy. The accuracy of a scheme depends in general on the range and attractive or repulsive nature of $u(r)$, the system dimensionality, and on the degree of thermodynamic consistency. So-called (partially) self-consistent integral equation theories like the RY approximation, in which different routes to the same thermodynamic properties are enforced, are therefore superior to standard integral equation schemes, for the price of a larger numerical effort.

The importance of OZ integral equation schemes goes well beyond the calculations of $g(r)$ from a given pair potential. In combination with powerful density functional theory methods (cf. lecture B17 by H. Löwen), one can study first-order liquid-solid phase transitions, and calculate structural properties of inhomogeneous fluids near a boundary or at a liquid-gas interface (e.g., layering and wetting phenomena). Incidentally, there exists an interesting empirical criterion, due to Hansen and Verlet, for the onset of freezing in one-component liquids. According to this static criterion, a three-dimensional fluid freezes into a solid when the principal peak height of $S(q)$ exceeds 2.8 to 3.1. The precise height depends somewhat on the range of the pair potential. For dispersions of strongly interacting colloidal particles, this criterion becomes equivalent to certain dynamic freezing criteria [15], as shown recently on the basis of a dynamic mode coupling theory [16].

Integral equation approaches form also the basis of inversion schemes to deduce information on the pair potential from an experimentally determined $g(r)$ or $S(q)$. From the knowledge of $g(r)$, $c(r)$ can be determined using the OZ equation. The pair potential follows then directly (and approximatively) from a closure relation like the HNC closure. HNC based inversion scheme calculations of $u(r)$ for a monolayer of charged colloidal spheres between to closely spaced glass plates suggest, for instance, the possibility of longer-ranged effective attractions between like-charged particles (cf. [17] for such a determination of $u(r)$, and [18] for a consistency check based on computer simulations). Whether such an attraction really occurs and whether existing physical explanations for

its existence do really apply is still a controversial matter of debate.

My lecture has been restricted to fluids of spherical particles with spherically symmetric pair interactions. The integral equation schemes and their closure relations have been broadened in the past to deal also with fluids of non-spherical particles, like molecules, rod-like viruses and polymers. The so-called reference interaction-site model (RISM) method has been used to calculate the site-site distribution function of rigid molecules whose interactions are modelled by an interaction-site potential. The molecule is hereby represented by a discrete set of interaction sites located at the places of the atomic nuclei [1]. The site-site distribution of non-rigid molecules like polymer chains and polyelectrolytes has been successfully determined on the basis of polymer reference interaction-site model (PRISM) calculations. For information on polyelectrolytes and the PRISM, consult lecture B5 by R.G. Winkler and [19]. Finally, the structure of liquids adsorbed in a porous medium, like in a gel or in an arrested particle matrix, can be approximately predicted using the method of replica Ornstein-Zernike (ROZ) equations [20].

References

[1] J.-P. Hansen and I.R. McDonald, *Theory of Simple Liquids* (2nd Edition, Academic Press, London, 1986)

[2] P.A. Egelstaff, *An Introduction to the Liquid State* (2nd Edition, Clarendon Press, Oxford, 1992)

[3] G. Nägele, Phys. Rep. **272**, 215-372 (1996)

[4] V.I. Kalikmanov, *Statistical Theory of Fluids* (Springer, Berlin, 2001)

[5] M.J. Grimson and M. Silbert, Mol. Phys. **74**, 397 (1991)

[6] A.R. Denton, Phys. Rev. E **62**, 3855 (2000)

[7] P.M. Chaikin and T.C. Lubensky, *Principles of Condensed Matter Physics* (Cambrigde University Press, Cambrigde, 1995)

[8] J.J. Binney, N.J. Dowrick, A.J. Fisher and M.E.J. Newman, *The Theory of Critical Phenomena* (Oxford University Press, New York, 1993)

[9] H.E. Stanley, *Introduction to Phase Transitions and Critical Phenomena* (Oxford University Press, New York, 1971)

[10] G. Nägele, O. Kellerbauer, R. Krause and R. Klein, Phys. Rev. E **47**, 2562 (1993)

[11] P.-G. de Gennes, *Scaling Concepts in Polymer Physics* (Cornell University Press, Ithaca, 1979)

[12] M.S. Wertheim, J. Math. Phys. **5**, 643 (1964)

[13] F.J. Rogers and D.A. Young, Phys. Rev. A **30**, 999 (1984)

[14] J.M. Mendéz Alcaraz, Ph.D. thesis, University of Konstanz (1993)

[15] H. Löwen, T. Palberg and R. G. Simon, Phys. Rev. Lett. **70**, 1557 (1993)

[16] R. Pesché, M. Kollmann and G. Nägele, J. Chem. Phys. **114**, 8701 (2001)

[17] H. Acuna-Campa, M.D. Carbajal-Tinoco, J.L. Arauz-Lara and M. Medina-Noyola, Phys. Rev. Lett. **80**, 5802 (1998)

[18] R. Pesché and G. Nägele, Phys. Rev. E **62**, 5432 (2000)

[19] T. Hofmann, R.G. Winkler and P. Reineker, J. Chem. Phys. **114**, 10181 (2001)

[20] J.A. Given and G. Stell, J. Chem. Phys. **97**, 4573 (1992)

B 17 Coarse-Graining Colloids and Polymers

H. Löwen

Institut für Theoretische Physik II

Heinrich-Heine-Universität Düsseldorf

Universitätsstraße 1

D-40225 Düsseldorf

Contents

1 Abstract 2

2 Introduction 2

3 The statistical concept of coarse-graining 3

4 Approximative density functionals 7

5 Charged colloidal dispersions 9

6 Coarse-graining linear polymer solutions 10

7 Star polymers and dendrimers 14

8 Colloids and polymers: depletion interactions 17

9 Binary colloidal "alloys" 19

10 From colloidal to nanoscales 21

11 Conclusions 25

1 Abstract

Solutions of colloidal dispersions and polymers naturally involve widely different length scales. Integrating out parts of the microscopic degrees of freedom leads to the concept of effective interactions and provides a "coarse-grained" picture which can be studied by much simpler means than a full microscopic model. This approach bridges length scales in soft matter systems. This procedure is justified on a Statistical Mechanics level and applied to different systems ranging from charged colloidal dispersions and polymer solutions (including star polymers and dendrimers) to mixtures of colloids and polymers and binary mixtures of sterically-stabilized colloids. Difficulties arising in applying this concept to nano-scales are also discussed.

2 Introduction

By definition, soft matter systems involve different length scales Consider for example dispersions of spherical charge-stabilized colloidal particles (e.g. polystyrene balls) in water. There are at least three different length scales: the microscale of the solvent molecules, the nanoscale of the width of the electric double-layers formed by the co- and counterions (approximately equal to the Debye screening length), and the mesoscale of the colloidal particles (typically hundreds of nanometers). This implies that analytical theories are complicated and that computer simulations are geting time-consuming. For example, even neglecting the molecular nature of water, the practical limit of simulations is a charge asymmetry between colloidal and counterion charge less than 100 [1].

In this lecture I shall discuss systematic coarse-graining procedures which lead to effective interactions between the largest, mesoscopic particles in multicomponent, multiscale fluid mixtures. These effective interactions follow from a rigorous "tracing out" of microscopic degress of freedom. This concept allows for a simple understanding of trends in the phase behaviour, structure and dynamics of colloids and polymers. Moreover, the effective interaction can be used in standard simulations of samples involving only the large particles which now play the role of molecules in atomistic simulations. After a formal Statistical Mechanics justification of the coarse-graining procedure in section 2, we shall briefly propose approximative density functional in section 3 which are necessary to implement calculations within the coarse graining picture. The coarse graining concept will then be successively applied to interacting electric double-layers (section 4), to solutions of polymers (linear polymers, star polymers and dendrimers) (sections 5 and 6), to colloid-polymer (section 7) and binary colloid mixtures (section 8). In section 9 the new challenges of coarse-graining nanoscale rather than mesoscale colloidal systems will be briefly considered, with biomolecular (e.g. protein) solutions in mind. A major part of this lecture (in particular that with an emphasis of computer simulations) is already published elsewhere in a recent review of the author with J. P. Hansen (Cambridge) [2]. Other useful review articles concerning the matter of effective interactions are those from Likos [3] and Belloni [4], Aspects of charged suspensions are reviewed by Hansen and Löwen [5] and a recent review on computer simulations of colloids is provided by Dijkstra [6].

3 The statistical concept of coarse-graining

An efficient statistical description of multi-component systems involving particles of widely different sizes requires a controlled-coarse-graining which may be achieved by integrating ("tracing") out the degrees of freedom of the majority components of "small" particles, which may be solvent molecules, microscopic ions ("micro-ions") or monomers of macromolecules. For the sake of simplicity, consider an asymmetric binary "mixture" of N_1 "large" spherical particles, with centres of positions $\{\vec{R}_i\}$ $(1 \leq i \leq N_1)$, and $N_2 \gg N_1$ "small" particles at positions $\{\vec{r}_j\}$ $(1 \leq j \leq N_2)$. Restriction will be made to thermodynamic equilibrium states. If classical statistics apply, integration over momenta is trivial, and the focus will be on configurational averages. The total potential energy of the mixture may be conveniently split ino three terms:

$$U(\{\vec{R}_i\},\{\vec{r}_j\}) = U_{11}(\{\vec{R}_i\}) + U_{22}(\{\vec{r}_j\}) + U_{12}(\{\vec{R}_i\},\{\vec{r}_j\}) \tag{1}$$

At a fixed inverse temperature $\beta = 1/k_BT$, the configurational part of the Helmholtz free energy F of the two-component system may be formally expressed as:

$$\begin{aligned} \exp(-\beta F) &= Tr_1\, Tr_2\, \exp(-\beta U) \\ &= Tr_1\, \exp(-\beta U_{11})\, Tr_2\, \exp(-\beta(U_{12}+U_{22})) \\ &= Tr_1\, \exp(-\beta U_{11})\, \exp(-\beta F_2(\{\vec{R}_i\})) \\ &= Tr_1\, \exp(-\beta V_{11}(\{\vec{R}_i\})) \end{aligned} \tag{2}$$

where the short-hand trace notation implies integration over the configuration space of species 1 or 2, i.e.

$$Tr_\alpha = \frac{1}{N_\alpha!}\int d^{3N_\alpha}r$$

$V_{11}(\{\vec{R}_i\})$, the effective interaction energy of the large particles, is the sum of their direct (or bare) interaction energy U_{11}, and of the configurational free energy of the fluid of small particles in the "external" field of the large particles F_2; the latter depends parametrically on the configuration $\{\vec{R}_i\}$ of the large particles

$$V_{11}(\{\vec{R}_i\}) = U_{11}(\{\vec{R}_i\}) + F_2(\{\vec{R}_i\}) \tag{3}$$

and can be written as:

$$F_2(\{\vec{R}_i\}) = -k_BT \ln[Tr_2 \exp(-\beta(U_{12}+U_{22})] \tag{4}$$

Up to now, no approximation has been made.
Three key aspects of the effective interaction V_{11} must be underlined. Firstly, *any* physical quantity $\mathcal{A}(\{\vec{R}_i\})$ depending only on the coordinates of the big particles can be formally averaged via the effective interaction

$$Tr_1\, Tr_2 \mathcal{A}(\{\vec{R}_i\}) \exp(-\beta U) = Tr_1 \mathcal{A}(\{\vec{R}_i\}) \exp(-\beta V_{11}(\{\vec{R}_i\})) \tag{5}$$

Hence, once the effective interaction is known, any averages (e.g. pair correlations) of the big particles can be extracted directly.

Secondly, due to the presence of a free energy, F_2, V_{11} is obviously *state-dependent*, and has an entropic contribution of the small particles ($F_2 = U_2 - T\,S_2$).
Finally, although the direct interaction U_{11} may be pair-wise additive, this is no longer true of V_{11}. The free energy $F_2(\{\vec{R}_i\})$ generally has many-body-contributions, so that V_{11} will be of the more general form (with the change of notation $N_1 \to N$ and $V_{11} \to V_N$):

$$V_N(\{\vec{R}_i\}) = V_N^{(0)} + \sum\sum_{i\le j} v_2(\vec{R}_i, \vec{R}_j) + \sum\sum\sum_{i\le j\le k} v_3(\vec{R}_i, \vec{R}_j, \vec{R}_k) + \ldots . \qquad (6)$$

$V_N^{(0)}$ is a state dependent but configuration-independent "volume" term, which has no bearing on the local structure of the large particles, but through its contribution to the thermodynamic properties, it can, in some cases, strongly influence their phase behaviour [7].
Let us now give some important examples of how to apply the concept of coarse-graining to soft matter systems. Obviously one has first of all to specify which statistical degrees of freedom should be considered and which of those should be integrated out ("small particles") and which of them should be left in the effective interaction ("big particles"). Depending on this choice one can cover quite different physical phenomena which are summarized in Table I. These include counterion screening of charged suspensions, depletion interactions in mixtures and polymer modeling by soft spheres. Most of those effects will be described in detail in the next sections.

soft matter system	microscopic degrees which are coarse-grained	resulting physical effect
charged colloids	counterions, salt-ions	screening of Coulomb repulsions
polymers (linear chains, star polymers, dendrimers)	monomers	polymers viewed as soft spheres
colloid-polymer mixtures	polymer coils	depletion attraction between colloids
binary mixtures of big and small colloids	small colloids	depletion attraction and accumulation repulsion
nanoparticles in solvent	solvent particles	discrete solvent effects
polyelectrolyte stars	counterions, salt-ions	entropic interaction between centers

Table I: Type of microscopic degrees of freedom which are integrated out for different kinds of macroparticles.

Expression (3) for the effective interaction , or potential of mean force, was derived in the canonical ensemble, where the total numbers of small and large particles are fixed (closed system). In many practical situations the binary system is in osmotic equilibrium with a pure phase of the small particles (e.g the solvent), and the appropriate ensemble for such an open system is the semi-grand canonical ensemble where N_1 and the chemical potential μ_2 of the small particles (rather than N_2) are fixed. The corresponding thermodynamic

potential is the semi-grand potential $\Omega_2 = \Omega_2(T, N_1, \mu_2; \vec{R}_i)$, and the effective interaction energy of the large particles will then be:

$$V_{11}(\vec{R}_i) = U_{11}(\vec{R}_i) + \Omega_2(\{\vec{R}_i\}) \tag{7}$$

which will again be state-dependent, a function of temperature, volume V and μ_2 (rather than $\rho_2 = N_2/V$).

In summary, the initial two-component system, involving a large number of microscopic degrees of freedom, has been reduced to an effective one-component system involving only the degrees of freedom of the mesoscopic particles. The price to pay is that the effective interaction energy is state-dependent and generally involves many-body terms. Approximations must now be invoked to calculate the highly non-trivial F_2 or Ω_2 term, i.e. the part of the interaction energy between the large particles induced by the small particles. Three different strategies have so far been used in practical implementations:

a) For any given configuration $\{\vec{R}_i\}$ of the large particles, the small particles are subjected to the "external" potential $U_{12}(\{\vec{R}_i\}, \{\vec{r}_j\})$, and hence form an inhomogeneous fluid, characterized by a local density $\rho(\vec{r}; \{\vec{R}_i\})$. The thermodynamic potentials F_2 or Ω_2 are functionals of $\rho(\vec{r})$, and full use can be made of the classical density functional theory (DFT) of non-uniform fluids for the small particles [8, 9]. DFT guarantees the existence of a excess free energy density functional $F_{exc}[\rho(\vec{r}]$ such that the free energies F_2 or Ω_2 can be written exactly as functionals:

$$F_2[\rho(\vec{r}] = F_{id}[\rho(\vec{r}] + F_{exc}[\rho(\vec{r}] + \sum_{j=1}^{N_1} \int \rho(\vec{r}) u_{12}(\vec{r}_i - \vec{R}_j)\, d\vec{r} \tag{8}$$

and

$$\Omega_2[\rho(\vec{r}] = F_2[\rho(\vec{r}] - \mu_2 \int \rho(\vec{r}) d\vec{r} \tag{9}$$

Here, $F_{id}[\rho(\vec{r}]$ is the functional of an ideal gas which is known exactly

$$F_{id}[\rho(\vec{r}] = k_B T \int \rho(\vec{r}) \left[\ln(\Lambda_2^3 \rho(\vec{r})) - 1\right] d\vec{r} \tag{10}$$

with Λ_2 being the thermal wave-length of the small particles. The density functionals given is Eqns. (8) and (9) give the physical free energies F_2 or Ω_2 if the equilibrium density $\rho(\vec{r}; \{\vec{R}_i\})$ of the small particles is inserted into the functional which follows from the variational minimization principle

$$\left.\frac{\delta\Omega_2[\rho^*(\vec{r})]}{\delta\rho^*(\vec{r})}\right|_{\rho^*=\rho} = 0 \tag{11}$$

where $\rho^*(\vec{r})$ is a properly parametrized trial density. The only difficulty is that in general the exact functional $F_{exc}[\rho(\vec{r}]$ is not known. Tractable approximations are known for hard spheres and soft potential fluids which are summarized in the next chapter. The optimization (11) may be implemented by steepest descent or conjugate gradient techniques, and the resulting effective potential energy between

large particles can then be used directly in standard MC or MD simulations [10]. In the latter case, the forces $\vec{F}_i$ acting on the large particles may be directly calculated from a classical version of the Hellmann-Feynman theorem:

$$\begin{aligned} \vec{F}_i &= -\vec{\nabla}_i V_{11}(\{\vec{R}_j\}) \\ &= -\vec{\nabla}_i U_{11}(\{\vec{R}_j\}) - \langle \vec{\nabla}_i U_{12}(\{\vec{R}_j\},\{\vec{r}_l\})\rangle_{\{\vec{R}_j\}} \end{aligned} \tag{12}$$

where the angular bracket denotes an equilibrium average over the degrees of freedom of the small particles, for a forced configuration $\{\vec{R}_i\}$ of the large ones. If the interaction energy U_{12} between the two species is pairwise additive ($U_{12} = \sum_{i=1}^{N_1}\sum_{j=1}^{N_2} u_{12}(|\vec{r}_i - \vec{R}_j|)$), the force $\vec{F}_i$ is directly expressible in terms of the local equilibrium density $\rho(\vec{r})$:

$$\vec{F}_i = -\vec{\nabla}_i U_{11}(\{\vec{R}_j\}) - \int \rho(\vec{r})\, \vec{\nabla}_i u_{12}(\vec{r}_i - \vec{R}_j)\, d\vec{r} \tag{13}$$

The optimization can also be achieved "on the fly", along lines directly inspired by the Car-Parrinello method for ion-electron systems [11]. Successive minimization and large particle updating steps are replaced by a single dynamical evolution, which involves the physical motion of the large particles and fictitious dynamics of the local density of small particles, parametrized by a plane wave expansion [12].

b) The previous DFT optimization method calculates directly the total effective energy of interaction between the large particles, or the resulting forces acting on each of these particles, without dividing V_N up into pair triplet and higher order interactions, as written in eq. (6). Another strategy is to attempt to compute these various contributions separately. At very low concentration of large particles, the effective pairwise interaction v_2 is expected to be dominant. In order to map out v_2 as a function of the distance r between two large particles, one may use standard MC or MD algorithms to simulate a bath of small particles in the field of two fixed large particles. Eq. (12) may then be used to calculate the mean forces acting on the two mesoparticles (which are opposite if the latter are identical) for each distance $r = |\vec{R}_1 - \vec{R}_2|$. The effective pair potential $v_2(r)$ finally follows from an integration of the forces. This procedure must be repeated for each distance r, but there are no time-scale or ergodicity problems, since the two large particles are fixed. The same goal can be achieved by appealing once more to DFT for the inhomogeneous fluid of small particles, subjected to the force field of two fixed large particles. The optimization may be carried out in r-space, using an adequate Eucledian or non-Eucledian [13, 14] grid on which the local density of small particles is defined. For two identical large particles, the local density has obvious cylindrical symmetry, but under favourable conditions, a considerable simplification occurs by fixing one of the large particles and considering an infinitely dilute solution of large particles in a bath of small particles around the fixed large particle. The density profile of the large particles in the zero concentration limit is directly related to the effective pair potential between two large particles in a bath of small particles [15], i.e.,

$$v_2(r) = -k_B T \lim_{\rho_1 \to 0} \ln\left(\frac{\rho_1(r)}{\rho_1(r \to \infty)}\right) \tag{14}$$

The advantage is that the two density profiles $\rho_1(r)$ and $\rho_2(r)$ are now spherically symmetric, but the method requires the prior knowledge of an accurate density functional for an asymmetric binary mixture. This strategy may be generalized to the calculation of three-body and higher order effective interactions, by considering the density profiles of large and small particles around two or more fixed large particles [16]. Applications of this strategy will be discussed in section 5-8.

c) Although the effective interaction energy (3) or (7) is not, in general, pairwise additive at finite concentrations of the large particles, it would be very convenient, for computational purposes, to reduce it, at least approximately, to a pairwise additive form. Contrarily to the two-body potential $v_2(r)$ discussed in the previous paragraph, which is only valid in the low density limit of large particles, the effective pair potential corresponding to finite concentrations is expected to be density-dependent, and will, in some average sense, incorporate the contributions of higher order terms in eq. (6). Such effective density-dependent pair potentials can, in some cases, be derived from approximate functionals or from inversion procedures, examples of which will be described in section 5.

4 Approximative density functionals

In this section we summarize different modern approximations for the excess free energy density functional $F_{exc}[\rho(\vec{r}]$ for different small-small interaction pair potentials $u_{22}(r)$, namely hard spheres and soft particles. The case of Coulomb interactions will be re-discussed in the next chapter.
For *hard spheres* of diameter σ the best current functional approximation is that of Rosenfeld's fundamental measure theory [17]. It can be constructed also for hard sphere mixtures but here we restrict ourselves to a one-component hard sphere fluid. In this approximation one takes

$$\mathcal{F}_{exc}[\rho] = k_B T \int d\vec{r} \Phi[\{n_\alpha(\vec{r})\}] \tag{15}$$

where one introduced a set of weighted densities

$$n_\alpha(\vec{r}) = \int_\Omega d\vec{r'} \rho(\vec{r'}) w_\alpha(\vec{r'} - \vec{r'}) \tag{16}$$

Here, the index $\alpha = 0, 1, 2, 3, V1, V2$ labels six different weighted densities and six different associated weight functions. Explicitly these six weight functions are given by

$$w_0(\vec{r}) = \frac{w_2(\vec{r})}{\pi\sigma^2} \tag{17}$$

$$w_1(\vec{r}) = \frac{w_2(\vec{r})}{2\pi\sigma} \tag{18}$$

$$w_2(\vec{r}) = \delta(\frac{\sigma}{2} - r) \tag{19}$$

$$w_3(\vec{r}) = \Theta(\frac{\sigma}{2} - r) \tag{20}$$

$$w_{V1}(\vec{r}) = \frac{w_{V2}(\vec{r})}{2\pi\sigma} \tag{21}$$

and

$$w_{V2}(\vec{r}) = \frac{\vec{r}}{r}\delta(\frac{\sigma}{2} - r) \tag{22}$$

Note that the index V denotes a vector weight function. We can express this fact by writing $w_{V1} \equiv \vec{w}_{V1}$, $n_{V1} \equiv \vec{n}_{V1}$,... Finally the function Φ is given by

$$\Phi = \Phi_1 + \Phi_2 + \Phi_3 \tag{23}$$

with

$$\Phi_1 = -n_0 \ln(1 - n_3) \tag{24}$$

$$\Phi_2 = \frac{n_1 n_2 - \vec{n}_{V1} \cdot \vec{n}_{V2}}{1 - n_3} \tag{25}$$

and

$$\Phi_3 = \frac{n_3^2(1 - (\vec{n}_{V2}/n_2)^2)^3}{24\pi(1 - n_3)^2} \tag{26}$$

The six weight functions are connected to the geometrical (fundamental) Minkowski measures [18]. There are several arguments in favor of the Rosenfeld approximation: as an example we mention that the freezing transition can be calculated by plugging in a constant density field for the fluid phase and a lattice sum of Gaussian peaks in the solid phase. If the width of the Gaussians and the prefactor are taken as variational parameters one gets a first-order freezing transition with coexisting packing fractions of $\eta_f = 0.491$ and $\eta_s = 0.540$ which are very close to "exact" simulation data $\eta_f = 0.494$, $\eta_s = 0.545$.
In the complementary case of very soft interactions, on the other hand, it has recently been shown that a mean-field approximation for the density functional is a very good approximation [19, 20, 21]. If the pair potential $u_{22}(r)$ is finite at the origin, then it can be shown that a mean-field functional is exact in the limit of very large densities. It works, however, amazingly well also for finite densities. In the mean-field approximation one takes:

$$\mathcal{F}_{exc}[\rho] = \frac{1}{2}\int d\vec{r}\int d\vec{r}'\rho(\vec{r})\rho(\vec{r}')u_{22}(|\vec{r} - \vec{r}'|) \tag{27}$$

All other intermediate cases are more difficult. Some success is to map harsh interaction onto effective hard spheres employing some ideas from the construction of Rosenfeld's functional [22]. Treating attractive tails has mainly been limiting to mean-field-like approaches as well.

5 Charged colloidal dispersions

Electric double-layers around mesoscopic colloidal particles of various shapes (spheres, rods, platelets, ...) or around polyelectrolytes make the generally dominant contribution to the effective interaction between highly-charged particles, which will be referred to as polyions [5, 4]. Most simulations are based on a primitive model, whereby the discrete nature of the aqueous solvent is neglected, and a macroscopic value of the dielectric permittivity ϵ is assumed. At very low polyion concentration, strategy b) of the previous section may be adopted to compute an effective pair interaction between two polyions, which is screened by microscopic counterions of opposite sign, as well as coions in the presence of added salt. The resulting effective pair potential turns out to be invariably repulsive of the screened Coulomb form predicted a long time ago by Derjaguin, Landau Verwey and Overbeek (DLVO) [23] as long as the microions are monovalent. However if divalent counterions are present, they are more strongly correlated, and this may lead to a short-range attraction between equally-charged polyions, due to an overscreening effect [24]. Although most of the work on effective pair interactions has focussed so far on spherical polyions, some recent MC simulations have investigated the case of parallel lamellar colloids [25], and this work has very recently been extended to charged discs of various relative orientations [26]. The triplet interaction between spherical polyions has similarly been calculated by MD simulations of co and counterions in the field of three fixed polyions [27], and turns out to be attractive under most circumstances. In the opposite limit of high concentrations, each polyion is confined to a cage of neighbouring polyions, so that many-body interactions are expected to be important, and pairwise additivity of the effective interaction is expected to break down. It is then reasonable to consider a Wigner-Seiz cell model, where a cell of geometry adapted to the shape of the polyions (e.g. a spherical cell for spherical polyions) contains one polyion at its centre, surrounded by co and counterions, such that overall charge neutrality is ensured, and with appropriate boundary conditions for the electric field on the surface of the cell. A physically reasonable boundary condition is to impose that the normal-component of the electric field vanishes on the surface. The initial problem involving many polyions is thus approximately reduced to the much simpler problem of a single polyion surrounded by its electric double-layer. Although all information on correlations between polyions is lost, the cell model allows a calculation of the thermodynamic properties of concentrated suspension, from MC or MD simulations of the inhomogeneous fluid of microions contained in the cell, as well as an estimate of the effective polyions charge, taking into account the phenomenon of counterion "condensation" [28, 29]. Such simulations provide stringent tests for approximate DFT calculations, including Poisson-Boltzmann (PB) theory.

At moderate polyion concentrations, the two previous strategies break down. Strategy a) of the previous section, based on the step by step or "on the fly" optimization of an appropriate free energy functional of the microion density profiles, is the most appropriate [12]. The free energy functional $F_2[\rho_+(\vec{r}), \rho_-(\vec{r}), \{\vec{R}_i\}]$ of the co- and counterion densities is conveniently split into ideal, Coulomb, external and correlation parts:

$$\begin{aligned} F_2[\rho_+, \rho_-] \;=\; & F_{id}[\rho_+] + F_{id}[\rho_-] + F_{Coul}[\rho_c] \\ & + F_{ext}[\rho_+] + F_{ext}[\rho_-] + F_{corr}[\rho_+, \rho_-] \end{aligned} \tag{28}$$

where:

$$F_{id}[\rho_\alpha] = k_B T \int \rho_\alpha(\vec{r}) \left[\ln(\Lambda_\alpha^3 \rho_\alpha(\vec{r})) - 1\right] d\vec{r} \quad (29)$$

$$F_{Coul}[\rho_\alpha] = \frac{e^2}{2} \int d\vec{r} \int d\vec{r}' \frac{\rho_c(\vec{r})\, \rho_c(\vec{r}')}{|\vec{r} - \vec{r}'|} \quad (30)$$

$$F_{ext}[\rho_\alpha] = \int \varphi_{ext}(\vec{r})\, \rho_\alpha(\vec{r})\, d\vec{r}$$

$$= \sum_{i=1}^{N_1} \int u_{1\alpha}(\vec{r} - \vec{R}_i)\, \rho_\alpha(\vec{r})\, d\vec{r} \quad (31)$$

In (30), $\rho_c(\vec{r}) = z_+\rho_+(\vec{r}) + z_-\rho_-(\vec{r})$ is the charge density of the microions (of valence z_α). The polyion-microion potentials $u_{1\alpha}$ in (31) contain a hard core repulsion and a long-range Coulomb attraction (counterions) or repulsion (coions). Rapid variations of the densities profiles $\rho_\alpha(\vec{r})$ near the surfaces of the polyions, which would pose numerical problems in r-space (grid) or k-space (large $\vec{k}$ Fourier components) may be avoided by the use of appropriate classical polyion-microion pseudopotentials [12]. The correlation term F_{corr} may be expressed within the local density approximation (LDA) [12]. If it is neglected, the functional (28) reduces to the mean-field Poisson-Boltzmann (PB) form. Optimization based on the functional (28-31) has been achieved with the "on the fly" MD strategy for spherical polyions with counterions only (no salt) [12], and the presence if salt (i.e. with co and counterions) [30]. The effective forces between colloids are reasonably well represented by a pair-wise additive screened-Coulomb form provided the (effective) polyion charge and the screening length are treated as adjustable parameters. Other applications include rigid rod-like polyions [31], and flexible polyelectrolytes [10], the latter being investigated by MC simulations coupled with steepest descent optimization, to allow a more efficient exploration of polyelectrolyte configuration space. If F_{corr} is neglected in the functional (28), and the ideal terms are replaced by their quadratic expansion in powers of $\Delta\rho_\alpha(\vec{r}) = \rho_\alpha(\vec{r}) - \rho_\alpha$ (where ρ_α is the bulk concentration of microions), the total functional is quadratic in the $\rho_\alpha(\vec{r})$, and the Euler-Lagrange equations resulting from the extremum conditions (11) can be solved analytically [12]. The resulting total effective energy of the polyions is then strictly pair-wise additive, and the effective pair potentials are of the linearly screened DLVO form. The entire procedure is justified only for relatively weak microion inhomogeneities (i.e. $|\Delta\rho_\alpha(\vec{r})|/\rho_\alpha < 1$), i.e. for low absolute polyion valence $|Z_p|$. If the polyion charge is distributed over a number ν of interaction sites, each carrying a charge $Z_p\, e/\nu$, linear screening may be an adequate approximation for each interaction site. The resulting "Yukawa site" model, where all sites on neighbouring particles interact via a screened Coulomb (or Yukawa) pair potential, has been used to simulate charged rods [31] or charged discs representing clay particles [32].

6 Coarse-graining linear polymer solutions

A solution of linear polymers (e.g. hydrocarbon chains in water) involves many different length scales ranging from microscopic bond length over the persistence length and the radius of gyration (coil size) to the mean-inter coil distance, see Figure 1. Therefore, the direct simulation of on or off-lattice models of polymer solutions or melts are very

computer-intensive [33], because even the simplest linear polymers involve thousands of monomers. Even if the latter are grouped into Kuhn segments, corresponding to one persistence length, the system will involve a very large number of linearly connected, interacting particles. If N is the number of polymer coils, each made up of M segments, the total number of degrees of freedom is $3NM$ which is a factor of ($\gg 1$) larger than for simple fluids or rigid colloidal particles, assuming that the organic or aqueous (for polyelectrolytes) solvent is replaced by a continuum. The question hence naturally arises of how to coarse-grain the initial, full microscopic model involving M monomers or segments per chain. The situation is somewhat different from the previously examined cases, involving large and small particles. The polymer case is more "democratic" in that all monomers play identical roles, at least in the scaling limit $M \to \infty$, where end effects become negligible. An old idea, which goes back at least to Flory [34] is to derive an effective interaction between the centres of mass (CM) of neighbouring polymer coils, by integrating over the individual monomer degrees of freedom of two or more coils, for fixed relative positions of their CM's. Consider first the case of two isolated polymer coils with monomer coordinates $\{\vec{r}_{i\alpha}\}_M$ ($i = 1, 2; 1 \leq \alpha \leq M$) and CM's:

$$\vec{R}_i = \sum_{\alpha=1}^{M} \vec{r}_{i\alpha} \tag{32}$$

If $U(\{\vec{r}_{i\alpha}\})$ is the total potential energy of interaction of all monomers, the probability distribution of the CM's is:

$$P(\vec{R}_1, \vec{R}_2) = \frac{1}{Q_{2M}} \int e^{-\beta U(\{\vec{r}_{i\alpha}\})} \prod_{i=1,2} \delta(\vec{R}_i - \sum_{\alpha} \vec{r}_{i\alpha}) \prod_{\alpha} d\vec{r}_{i\alpha} \tag{33}$$

where Q_{2M} is the corresponding configurational partition function (equal to the $6M$-dimensional integral in eq. (33), without the δ-functions). By analogy with eq. (2), the effective pair interaction between the CM's is then given by:

$$v_2(\vec{R}_1\vec{R}_2) = -k_B T \ln[P(\vec{R}_1\vec{R}_2)] \tag{34}$$

The effective potential will only depend on $r = |\vec{R}_1 - \vec{R}_2|$. $v_2(r)$ is expected to be of the order of the radius of gyration R_g of the polymers, since for $r \geq R_g$, there will be little overlap between two coils. Swollen polymers in good solvent (where $R_g \sim M^\nu$, with $\nu \simeq 0.6$, the Flory exponent) are highly fractal objects, i.e. the mean monomer density inside a coil $\sim M^{1-3\nu}$ goes to zero in the scaling limit. An immediate consequence is that $v_2(r)$ is a "soft" potential, and that $v_2(r = 0)$ is finite [35], i.e. the polymer coils may be modelled as penetrable spheres. On and off-lattice simulations of self-avoiding walk (SAW) polymers [36, 37], as well as renormalization group (RG) calculations for the continuous "thread" model [38], show that the pair potential $v_2(r)$ is well approximated by a single Gaussian:

$$\frac{v_2(r)}{k_B T} = \xi \exp(-J(r/R_g)^2) \tag{35}$$

where $J \simeq 1$, the simulations yield [37] for $M \to \infty$:

$$\xi \simeq 1.80 \pm 0.05 \tag{36}$$

while the RG yields the following $\epsilon = 4 - d$ expansion.

$$\xi = 0.94\epsilon + 0.62\epsilon^2 + O(\epsilon^3) \tag{37}$$

These results are independent of molecular detail, so that the simplest lattice models and most efficient MC sampling (e.g. the pivot algorithm) can be used to determine the effective interactions. Note that for self-avoiding walk (SAW) polymers (which involve only excluded volume interactions between monomers), the effective interaction is purely entropic in nature as signalled by the scaling with k_BT.

When nearest-neighbour attractions between monomers are included to allow for solvent conditions (strong attractions correspond to poor solvent), the effective pair potential between the CM's becomes less repulsive, and develops an attractive part as Θ-conditions are approached [36, 39]. If ϵ_0 denotes the depth of the attraction, ergodicity problems become more and more severe in the simulations, but can be overcome by using Bennett's overlapping distribution method [40, 41]. Returning to the SAW model, appropriate for good solvent-conditions, the method for determining the effective pair potential can be extended to effective three- and more-body interactions, by simulating three or more polymers for various configurations of their CM's [42]. The main qualitative results are that more-than-two body interactions alternate in sign (the three-body potential being mostly attractive), and that the absolute amplitudes of higher order interactions do appear to decrease with increasing order in line with scaling theory [43].

However the strategy of adding higher order effective interactions in simulations of polymer solutions of finite concentration is computationally inefficient. A much more efficient strategy is to determine state-dependent effective pair interactions by a systematic inversion procedure [37]. The pair distribution function $g(r)$ of the CM's of systems of SAW polymers at finite concentration is calculated by direct simulations of a few hundred polymers on a lattice, using efficient MC algorithms [41]. An effective concentration-dependent effective pair potential between the CM's is then determined by Ornstein-Zernike (OZ) inversion, assuming some adequate closure relation, like the HNC closure [44]. In view of the softness of the resulting pair potential, HNC theory becomes asymptotically exact in the high concentration limit, and is extremely accurate at all concentrations [45, 3]. The inversion is a noniterative, one-step procedure, and it has been proven that there is a one-to-one correspondence between any given $g(r)$ and a $v(r)$ (uniqueness theorem [46]). The resulting effective pair potentials turn out to be weakly dependent on concentration [37]. They may be used in large scale simulations of polymer solutions, of polymers at interfaces or of colloid-polymer mixtures [47], to study, in particular, the effect of polymer interactions on the depletion force between colloidal particles [37, 48]. In its original formulation, this coarse-graining strategy has one obvious drawback, namely that simulations of the full monomeric representation of polymer solutions are initially required to determine the CM pair contribution function $g(r)$, for each polymer concentration, a rather formidable task, even if the resulting effective potentials may then be used to explore a range of different large scale phenomena. However even this drawback can be overcome by calculating the monomer-monomer pair distribution function within the accurate PRISM theory [49], and then extracting the CM pair distribution function from its monomeric counterpart, and the form factor (or internal structure factor) of a single polymer coil, using a recently proposed, accurate relation between these three correlation functions [50].

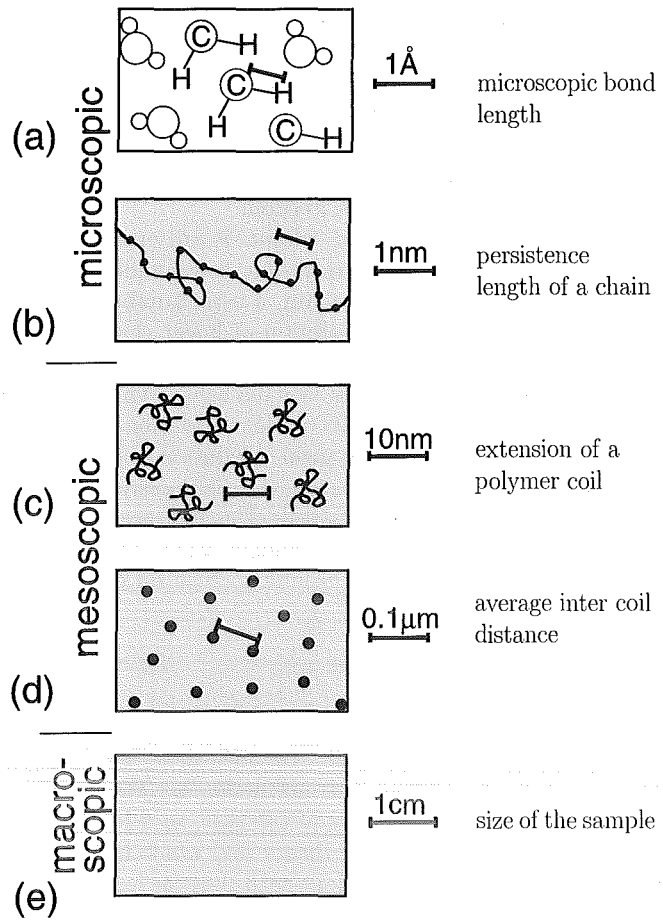


Fig. 1: *Polymer solution on different length scales. (a): microscopic picture, water and hydrocarbon chains are shown, the chemical bonds have a range of typically 1Å. (b): On a larger scale, the persistence length of the chains is relevant. (c): the spatial extension σ of a single polymer coil. (d): all the coils are point particles on this scale governed by the mean intercoil distance (e): size of the macroscopic sample.*

7 Star polymers and dendrimers

The ideas of coarse-graining, as applied to solutions of linear polymer chains in the last chapter, can be generalized to polymers with a more complicated architecture. We shall discuss solutions of star polymers and dendrimers in more detail. Star polymers [51] consist of f linear polymer chains which are chemically anchored to a common centre (f is called functionality or arm number). Obviously, linear polymers are a special case of star polymers when $f = 1, 2$ depending whether the end or middle segment is taken as "centre". Dendrimers, on the other hand, can be viewed as iterated star polymers: periodically, any linear chain branches off into n additional chains (n is called degree of branching) which is repeated g times (g is called generation number). For $f > 3$, in contrast to linear chains, star polymers and dendrimers possess a natural centre which serves as an appropriate statistical degree of freedom.

Let us first focus on *star polymers in a good solvent.* A full monomer-resolved computer simulation is completely out of reach of present-day computers: If N is the number of stars and M the number of monomers per chain, a total number of NfM particles has to be simulated, f times more than for a solution of linear chains and fM times more than for simple fluids. The strategy b) of section 2, however, can be efficiently used to make progress. First consider only two stars at fixed separation r and average the force acting on their centres during an ordinary MC or MD simulation of the monomers. Such a simulation involves $2fM$ particles only. A typical simulation snapshot is shown in Figure 2. This is repeated for different r. By integrating the distance-resolved data for the force, the effective interaction potential $v(r)$ is obtained. This interaction is repulsive, since the presence of another star reduces the number of configurations available to the chains. For small arm numbers $f \leq 10$, the simulation results confirm an effective pair potential of the log-Gauss form:

$$v(r) = \frac{5}{18} k_B T f^{3/2} \begin{cases} -\ln(\frac{r}{\sigma}) + \frac{1}{2\tau^2\sigma^2} & \text{for } r \leq \sigma; \\ \frac{1}{2\tau^2\sigma^2} \exp\left(-\tau^2 \frac{r^2-\sigma^2}{\sigma^2}\right) & \text{for } r > \sigma, \end{cases} \tag{38}$$

where σ is the corona diameter of a single star measuring the spatial extent of the monomeric density. For large distances r, the interaction is Gaussian as for linear chains. It then crosses over, at the corona diameter of the star, to a logarithmic behaviour for overlapping coronae as predicted by scaling theory [52] which implies a very mild divergence as $r \to 0^+$. The matching at $r = \sigma$ is done such that the force $-dv/dr$ is continuous. In Eqn (38) , $\tau(f)$ is known from a fit to computer simulation results; for $f = 2$ we obtain $\tau = 1.03$ in line with the Gaussian potential (35) used for linear chains.

For larger arm numbers, $f > 10$, on the other hand, a geometric blob picture of f cones around the star centre, each containing one linear chain is justified [53]. The effective force for nearly touching coronae decays exponentially with r, the associated decay length is the outermost blob-diameter $2\sigma/\sqrt{f}$. This motivates a log-Yukawa form of $v(r)$ [54]:

$$v(r) = \frac{5}{18} k_B T f^{3/2} \begin{cases} -\ln(\frac{r}{\sigma}) + \frac{1}{1+\sqrt{f}/2} & \text{for } r \leq \sigma \\ \frac{\sigma}{1+\sqrt{f}/2} \frac{\exp(-\sqrt{f}(r-\sigma)/2\sigma)}{r} & \text{for } r > \sigma \end{cases} \tag{39}$$

again matched at the corona diameter $r = \sigma$ such that the force is continuous. This potential was verified in monomer-resolved simulations [55] for a large range of arm numbers.

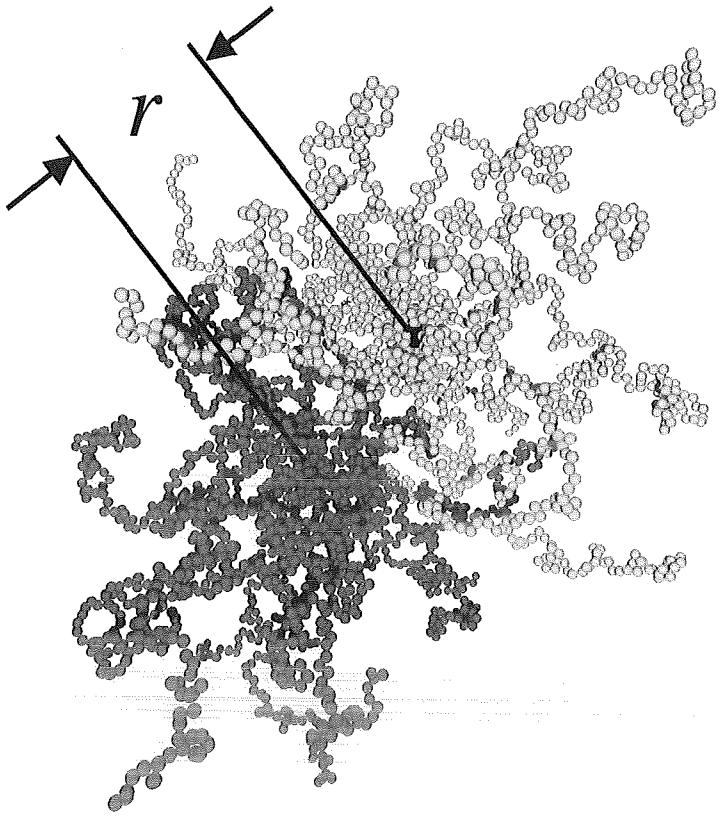


Fig. 2: *Typical configuration for two stars with $f = 18$ and $M = 50$ monomers per chain as obtained from a snapshot during a Molecular Dynamics simulation with r denoting the distance between their centres. By courtesy of A. Jusufi.*

Using scaling theory and monomer-resolved simulations of a triangular configuration of three stars [43], triplet interactions were shown to be negligibly small outside the corona and at most 11 percent of the pairwise forces for penetrating triplets inside the corona; consequently the effective pair-wise description for the many-body system is adequate provided the number density ρ_s of the stars is not much higher than the overlap density $1/\sigma^3$. Large scale simulations involving many stars were performed using the pair potential of Eqn (39) [56, 57]. Due the crossover of $v(r)$ at $r = \sigma$ from a harsh Yukawa to a soft logarithmic behaviour, uncommon structural and thermodynamical properties were obtained. First, the main peak of the liquid structure factor changes non-monotonically with increasing density [57]. Secondly, the bulk phase diagram exhibits [56] a reentrant melting behaviour for $34 < f < 44$ and stable anisotropic crystal lattices. The latter finding has been supported by experiments [58].

Next let us briefly discuss *star polymers in a poor solvent.* The only work in this direction is close to the Θ-point where the chains are weakly interacting. Consequently the resulting effective repulsion is weaker than in good solvent. More quantitatively, an effective potential between two plates is available within a self-consistent field approach for polymers grafted on flat plates where the grafting density is high and the self-avoidance is weak [59]. This was extended to spherical particles by employing the Derjaguin approximation [60, 61] providing an analytical expression for the effective pair potential $v(r)$. In the limit of small core sizes, this expression has been successfully tested against scattering data for $f = 64$ arm stars in a solvent close to Θ conditions [62]. What is still unexplored is a systematic approach for arbitrary solvent quality which continously switches between good solvent quality to the Θ point and beyond.

Much more stretched configurations are achieved for *polyelectrolyte stars* ("porcupines") due to the strong Coulomb repulsion of the charged monomers along the chains. If one brings two polyelectrolyte stars together they hardly interdigitate but retract. A variational analysis [63] for the effective force, which includes Coulomb interactions and entropies of the counterions, reveals that the entropy of the counterions which are inside the coronae of the two polyelectrolyte stars dominates the interaction, confirming an old idea of Pincus [64]. The analytical theory was quantitatively verified by computer simulations with explicit monomers and counterions [63]. Inside the corona, the resulting effective force could be fitted by an inverse-power law $\propto r^{-\gamma}$ where the exponent γ slightly depends on the actual charging conditions but is always around $0.7 - 0.8$. By integration, an effective potential is obtained which stays finite at the origin and behaves inside the corona as $v(r) = v(0) - Cr^{1-\gamma}$ with a positive constant C. However, the actual value $v(0)$ for completely overlapping stars is much larger than k_BT so that significant overlap is rare. Due to the softness of the interaction, similar structural anomalies as obtained for star polymers are expected including a non-monotonic variation of the first peak in the structure factor for increasing density and reentrant melting.

Finally, *dendrimers* in a good solvent have been addressed. For a branching degree $b = 2$ and a generation number $g = 4$ an effective Gaussian potential can be derived theoretically [65], provided the centre-to-centre distance r is larger than the corona diameter σ. In formal analogy to linear polymer chains one obtains:

$$v(r) = B \exp(-r^2/\sigma^2) \tag{40}$$

The important difference from the case of linear polymer chains is that the prefactor

$$\frac{B}{k_BT} = \frac{M^2 v_0}{\pi^{3/2}\sigma^3} \tag{41}$$

is much larger than 1, with M denoting the total number of monomers per dendrimer and v_0 the excluded volume parameter per monomer. The Gaussian interaction (40) was confirmed quantitatively by scattering experiments [65]. A detailed comparison for $b = 2$ dendrimers with higher generation number $g = 5$ reveals that the effective potential $v(r)$ is well described by a sum of two Gaussians [66] comprising the effect of the stiff inner region and the floppy outer region of a dendrimer. The effect of increasing the degree of branching b is much less explored. In principle a Gaussian pair potential (40) (or a superposition of them) is again expected but the prefactor B/k_BT should grow with increasing b. Thereby it should be possible to tune the prefactor B/k_BT to larger values, where freezing is expected [19].
Coarse-graining star polymers and dendrimers thus maps them onto simple liquids with soft interactions (socalled mean-field fluids) which in turn implies peculiar properties. Hence the concept of effective interactions not only allows for efficient simulation, but also provides insight into the physical behaviour.

8 Colloids and polymers: depletion interactions

If a sterically-stabilized colloidal particle is brought into a non-adsorbing polymer solution, the latter are depleted in a zone around the colloidal surfaces due to the colloid-polymer repulsion. The width of this zone is of the order of the radius of gyration $d_p/2$ of the polymers. If one now brings two colloidal particles close to each other, the two depletion zones overlap, which brings about a free energy gain of the polymers relative to a situation of non-overlapping zones, resulting in an effective attraction between the colloids, the so-called depletion attraction. Alternatively one can view the attraction arising from an unbalanced osmotic pressure exerted on the colloidal particles by the surrounding polymers.
The simplest model for colloid-polymer mixtures including the depletion effect is the so-called Asakura-Oosawa (AO) model [67] which assumes hard core interactions between the colloids of diameter d_c, further hard-core interactions between the polymers and the colloids with a range $(d_c+d_p)/2$, but no interaction at all between polymers. The ideality of the polymers is a crucial approximation which is fulfilled only for dilute polymer solutions, but it allows to investigate many of the statistical properties of the AO model analytically. For instance, the effective interaction $v(r)$ between a colloidal pair can be calculated to be the product of the polymer osmotic pressure $P_p = k_BT\rho_p$ and the overlap volume of the two depletion zones consisting of two spherical half-caps. Explicitly it reads

$$\frac{v(r)}{k_BT} = \begin{cases} \infty & \text{for } r \le d_c \\ \rho_p \frac{\pi}{6}(d_c+d_p)^3 \left[1 - \frac{3r}{2(d_c+d_p)} + \frac{1}{2}\frac{r^3}{(d_c+d_p)^3}\right] & \text{for } d_c < r \le d_c + d_p \\ 0 & \text{for } r \ge d_c + d_p \end{cases} \tag{42}$$

Furthermore, by a simple geometric consideration, it can be shown that effective triplet and higher-order many-body forces vanish provided the size ratio between colloids and

polymers $q = d_p/d_c$ is smaller than 0.154. In this case, the AO model is formally equivalent to an effective one-component system with a short ranged attraction, which immediately opens the way for large-scale simulations.
The phase diagram of the AO model was explored by computer simulations on three different levels: first, one-component calculations using the effective pair potential (42) have been performed [68], which are exact for $q < 0.154$. Secondly, more recently, Dijkstra has simulated the full effective Hamiltonian including effective many-body forces to arbitrary order for $q = 1$ [69]. Finally, brute force simulation with explicit ideal-gas polymers have been carried out [70]. The emerging phase diagram involves three phases: gas (i.e. colloidal poor), liquid (i.e. colloidal rich) and an fcc colloidal crystal. A liquid phase is stable if the ratio q is larger than $q_c \approx 0.5$.
On the other hand, theoretical progress was made by constructing a free volume theory for the fluid bulk free energies [71] which provides a reliable estimate for the gas-liquid transition. A free-energy density functional for the AO colloid-polymer mixtures, valid for arbitrary inhomogeneous situations, was constructed [72] in the spirit of Rosenfeld's fundamental measure approach [17], which reproduces the effective interaction (42) for a colloid pair and the free volume theory of Ref. [71]. This density functional was applied to wetting phenomena of planar walls. A novel type of wetting involving growth of only few colloidal liquid layers on top of the wall as liquid-gas coexistence is approached was predicted by density functional theory [73] and confirmed by computer simulations [69, 70]. This wetting scenario only shows up for ratios larger than q_c, so that one can speculate that it is produced by the intrinsic many-body nature of the effective forces.
Obviously, the AO model has the short-coming of idealized interactions. More realistic models involve a non-zero polymer-polymer interaction and a softer polymer-wall interaction [74]. On the other hand, full two-component simulations of colloids and polymers were performed [75, 76] where the polymers are defined on a lattice. Clearly these include any effective many-body interactions. A second computationally less demanding technique is to calculate effective pair interactions between a colloid and a polymer first by a monomer-resolved reference simulation. This strategy was followed in the more general context of mixtures of colloids and star polymers for small size ratios q. Supported by theoretical scaling arguments the following pair interaction between a hard-sphere colloid and a star polymer was obtained [77, 47]:

$$v_{cp}(r) = k_B T \Lambda f^{3/2} \left(\frac{d_c}{2r+d_c}\right) \times \begin{cases} -\ln(\frac{2r-d_c}{\sigma}) + (\frac{(2r-d_c)^2}{\sigma^2} - 1)((1+4\kappa)/(1+2\kappa)) + \zeta & \text{for } r \le (d_c+\sigma)/2; \\ \zeta\, \mathrm{erfc}(\kappa(2r-d_c)/\sigma)/\mathrm{erfc}(\kappa) & \text{else,} \end{cases} \tag{43}$$

Here, Λ and κ are known parameters depending on the functionality f of the star, $\zeta = \sqrt{\pi}\mathrm{erfc}(\kappa)\exp(\kappa^2)/(\kappa(1+2\kappa^2)$, σ denotes the corona diameter of the star and $\mathrm{erfc}(x)$ is the complementary error function. For $r \to d_c/2$ the potential diverges logarithmically as for the star-star interaction (38). Linear polymer chains are obtained as the special case $f = 2$ where $\Lambda = 0.46$ and $\kappa = 0.58$. The two-component system with effective pair interactions was investigated in detail by further simulation and liquid integral equation theory. For different arm numbers f, the fluid-fluid demixing transition was calculated [77] in good agreement with experimental data. Furthermore, the freezing transitions was discussed. Above a critical arm number of $f_c \approx 10$, fluid-fluid demixing was preempted by freezing [78].

In case of polymer size comparable or larger than the colloidal diameter d_c, effective many-body forces play a significant role. Complementary methods such as monomer-resolved liquid intergral equations methods combined with the PRISM approach [79] or field-theoretic calculations [80] have provided valuable insight into the structure of colloid-polymer mixtures. The limit of large q contains completely different physics, since the colloidal spheres represent then small perturbations for the long polymer chains [76].

9 Binary colloidal "alloys"

Binary mixtures of large and small sterically-stabilized colloids exhibit many unexpected phases. Such a binary colloidal "alloy" can be modelled as a two-component hard sphere system involving two colloidal diameters d_1 and d_2 ($d_2 < d_1$). If the size ratio $q = d_2/d_1$ is larger than 0.4, a large variety of stable phases involving different superlattice crystals are predicted by theory [81] and simulation [82] and observed experimentally [83] . We shall focus here more on the case of small q, where a depletion picture, similar to that discussed for colloid and polymer mixtures, should hold. In contrast to the AO-model, however, many-body forces are present for any q in the hard sphere mixture, but these can be shown to be small with respect to the pairwise contribution [14, 16].

The effective depletion potential $v(r)$ between a pair of big spheres in a sea of small spheres has been efficiently calculated and analytically parameterized, based on the procedure of Roth et al. [15] as applied to the two-component hard sphere density functional of Rosenfeld [17]. As a function of r, $v(r)$ involves a short-ranged attraction followed by an oscillatory behaviour decaying exponentially with the bulk correlation length of the small spheres. The density functional predictions were confirmed by computer simulations [84, 85] and by experiments [86].

One key question addressed during the last decade was whether the depletion attraction is strong enough to drive fluid-fluid phase separation (for a recent review see [6]). The problem was finally solved by computer simulation using the effective one-component model with the depletion pair potential [87, 88]: a fluid-fluid demixing is obtained for $q < 0.1$ but this is always metastable with respect to the freezing transition into an fcc solid made up by the big spheres. The simulations of the effective one-component model were confirmed by full simulations of the true binary system [87] showing once more that the influence of triplet forces is negligible [14, 16]. Simulation results for the phase diagram, as presented in terms of the packing fractions $\eta_1 = \pi\rho_1 d_1^3/6$ of the big particles and η_2^r of a reservoir of small particles in coexistence with the whole system, are shown in Figure 3 for $q = 0.2, 0.1, 0.05$. Besides the fluid-fluid demixing which remains metastable, an isostructural solid-solid transition occurs at high η_1 for $q < 0.05$, as familiar for one-component systems with a short-ranged attraction [89, 90]. As q decreases, the fluid-solid coexistence line becomes more and more horizontal until the sticky hard-sphere limit ($q \rightarrow 0^+$) is achieved where a vacuum coexists with a close-packed crystal. This example shows again that the effective interaction picture allows qualitative and quantitative understanding of the topology of phase diagrams.

Further current research is focused on the sensitivity of the depletion potential to polydispersity of the small particles [91], and to small-small and big-small interactions beyond the hard sphere model [92]. Polydispersity smears out the oscillatory behaviour, while keeping the deep attraction near contact unchanged. Different small-small and big-small

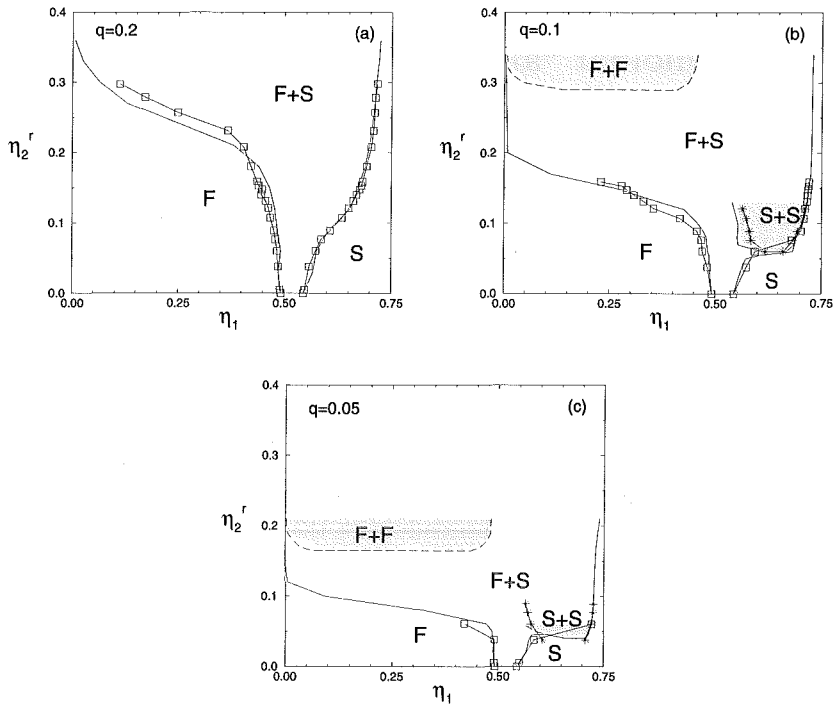


Fig. 3: *Phase diagram of binary hard-sphere mixtures with size ratios (a) $q = 0.2$, (b) $q = 0.1$, and (c) $q = 0.05$ as a function of the large-sphere packing fraction η_1 and the small-sphere reservoir packing fraction η_2^r. F and S denote the stable fluid and solid (fcc) phase. $F + S$, $F + F$, and $S + S$ denote, respectively, the stable fluid-solid, the metastable fluid-fluid, and the (meta)stable solid-solid coexistence regions. The solid and dashed lines are the effective one-component results; the squares and the asterisks (joined by lines to guide the eye) denote, respectively, the fluid-solid and the solid-solid transition obtained from direct simulations of the true binary mixtures. Reproduced from Ref. [87] with permission.*

interaction have a significant impact on the effective big-big interaction: for instance, an attraction between the small particles or the big and small particles leads to repulsive effective interactions due to an accumulation of small particles on the surfaces of the big ones. This "inverse depletion effect" may be called accumulation repulsion. These recent findings imply that the effective interactions can be systematically tuned via the basic interactions and polydispersity.

10 From colloidal to nanoscales

Although the concept of effective interactions as described in chapter II is exact in principle, there are limitations in applying it in practice. These limitations become more and more important if one considers smaller and smaller macroparticles, such that molecular details become more relevant. In fact, on nanoscales, chemical specificity is starting to become crucial, resulting in many different phenomena like solvation effects, hydration, hydrophilicity, hydrophobicity, forces determined by chemical bonding etc. In fact, these effects are essential to explain the structure and function of biological macromolecules in solution, e.g. of proteins. Under these circumstances, it is clear that one cannot get away with relatively simple effective interactions, characterized by few parameters, like those discussed previously in the context of colloidal length scales. The immediate questions arising is when and where does the simple coarse-graining concept break down if one crosses over from the colloidal to the nanoscale. Basically there are *two major caveats*: The first concerns the choice of the microscopic degrees of freedom which are to be integrated out; the second concerns internal degrees of freedom and modelling of the big particles themselves. In the sequel we shall discuss these two points in detail and illustrate them using two examples.

Regarding the first point, even on nanoscales there remains an enormous number of microscopic degrees of freedom. The relevant question is which have to be included explicitly in the starting Hamiltonian or may be ignored or replaced by effective parameters. This is a tricky question when length scales are less clearly separated than in colloidal systems. For long polymer chains, scaling theory implies that molecular details are unimportant for most purposes, such that one can get away with simple lattice models (as discussed for linear polymer chains) or with a simple monomeric description of beads (as discussed for star polymers). For charged colloids, in the primitive approach, the solvent molecules are not considered explicitly but only enter via the dielectric constant. The charged microions, on the other hand, are included explicitly, since their Coulomb interaction is stronger than the dipolar forces acting between the solvent. While this seems to be justified for micron-sized colloidal particles with typical interparticle spacing of microns (provided molecular details on the colloidal surface are encaptured by an effective colloidal charge), it is questionable when the colloidal diameter or the intercolloidal distance is becoming comparable to the correlation lenth or interaction range of the microcopic degrees of freedom, i.e. for nanoparticles.

As an illustration, we consider the effective interaction between two nanosized charged colloidal particles in a *hard sphere solvent* . A systematic comparison between primitive-model calculations where the solvent is neglected and the full system including the hard sphere solvent was performed recently by Allahyarov and one of us [93, 85]. On an intermediate level, one can formally integrate out the solvent, ending up with effective

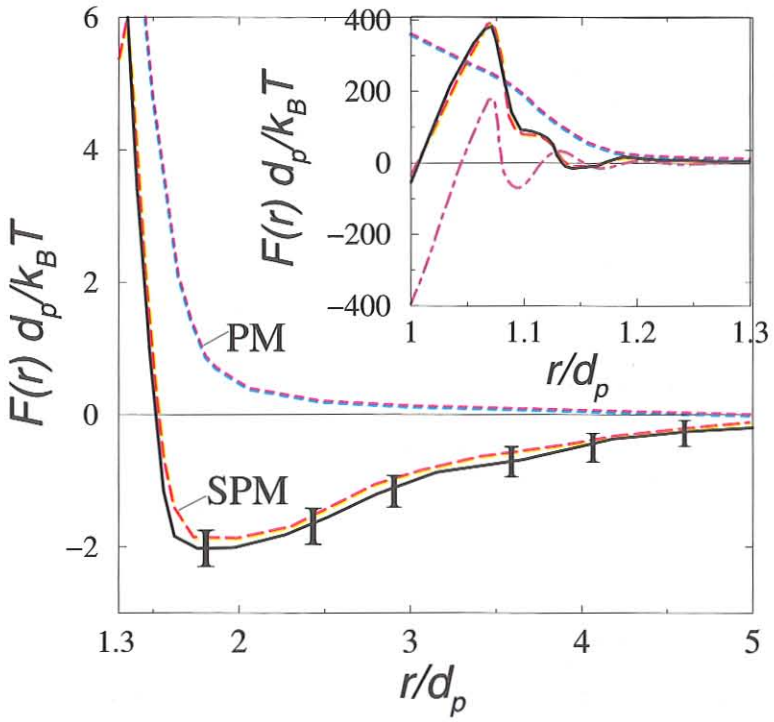


Fig. 4: *Reduced distance-resolved force $F(r)d_p/k_BT$ versus reduced distance r/d_p between two charged colloids as obtained by computer simulations. The inset shows the same for nearly touching polyions of molecular distances. The parameters are: $q_c = 2$, $q_p = -64$, $d_p : d_c : d_s = 14 : 2 : 1$, $\epsilon = 81$, the volume fraction of the polyions in the periodically repeated box is $\eta_p = 5.8 \times 10^{-3}$. Solid line with error bars: full simulation including the hard sphere solvent; long-dashed line: solvent averaged primitive model; short-dashed line: primitive model; dot-dashed line in inset: solvent depletion force alone (for comparison).*

interactions between the charged particles. If these are approximated to be pairwise, one obtains the so-called solvent averaged primitive model [94]. In this model, the interaction between charged species comprises the bare Coulomb interaction and the effective depletion interaction between hard spheres as discussed in section 8. Extensive computer simulations [93, 85] have shown that the total effective force between charged colloidal particles does depend on the presence of the discrete solvent. Even the sign of the effective interaction can be different in the primitive model as compared to the full solvent result. An example for divalent counterions and a charge asymmetry of $q_p : q_c = 64 : 2$ is shown in Figure 4 where the ratio of the three hard-core diameters of colloidal particles, counterions and solvent particles is $d_p : d_c : d_s = 14 : 2 : 1$. In fact, interpreting the solvent size as a microscopic scale, the colloidal diameter is 14 times larger and thus falls into the nano-regime. While the primitive model reference calculations yield a repulsive effective force, the simulations including a hard-sphere solvent result in an attractive force.

The solvent-averaged primitive model, on the other hand, reproduces the data of the full solvent simulation rather well. The simulation time for the solvent-averaged primitive model is similar to that of the primitive model, since the number of particles simulated is the same, while the full simulation requires the inclusion of many solvent particles. Hence the concept of effective interactions as applied to the solvent degrees of freedom alone, makes simulations feasible in the spirit of McMillan-Mayer theory. But even more importantly, the solvent-averaged model also provides insight into the basic physics: the depletion attraction between a colloidal sphere and counterions favours an accumulation of the latter on the colloidal surfaces, thus enhancing the screening. It is this effect which, together with strong Coulomb correlations, leads to the attraction evident in Figure 4 which is completely missing in the primitive model. For large colloidal spheres, on the other hand, it was shown in Ref. [85] that the effect of a discrete hard sphere solvent can completely be accounted for by taking a different (effective) colloidal charge as input in the primitive model calculations. Consequently simple coarse-graining is justified provided an effective colloidal charge is used.

The second caveat for coarse-graining concerns the description of the big colloidal particles. Up to now we have modelled them as homogeneously charged hard spheres in the context of charged suspensions. Coming down to nanoscales, the molecular details and internal degrees of freedom of the large particles themselves, which are neglected in statistical descriptions of colloidal dispersions, are becoming more and more relevant. We shall illustrate this using an example where the *discreteness of the charge pattern* on the colloidal surfaces turns out to be crucial provided the particles are nano-sized. This is of particular importance for proteins which are characterized by nanoscale electrostatic patches.

In a recent computer simulation [95], the effective interaction between two nano-sized colloidal spheres (modelling globular proteins) with a discrete charge pattern was calculated within the primitive model as a function of added salt concentration. A snapshot of a protein pair is shown in Figure 5. Discrete elementary point charges were placed on the protein surface with a finite depth. Consequently the effective interaction not only depends on the centre-to-centre distance r but also on the relative orientations of the two proteins. These represent additional statistical degrees of freedom associated with the macroparticles. The data were compared to the standard description with the charge uniformly smeared over the particle surface. A key quantity controlling protein crystallization [96] is the second osmotic virial coefficient B_2 which can readily be measured by scattering methods in dilute protein solutions. B_2 can be shown [95] to be related to the effective interaction by

$$B_2 = \frac{1}{2}\int d^3r[1 - \exp(-v(r)/k_BT)] \tag{44}$$

in formal analogy to the orientation-independent case of the smeared charged model. Here $v(r)$ is the integral of the canonical orientational average of the distance-resolved effective force projected onto the separation vector between the two proteins [95].

A detailed calculation of B_2 as a function of added salt reveals that it behaves non-monotonically as a function of added salt concentration, in agreement with several experimental studies [97]. This non-monotonicity, however, disappears when the surface charge uniformly smeared out. It can thus be traced back to strong Coulomb correlations induced by the discrete binding centers near the surface. This example shows that

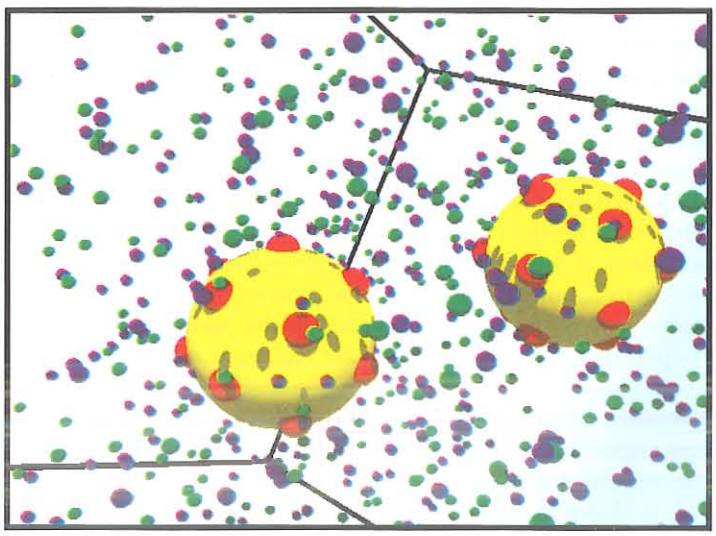


Fig. 5: *Simulation snapshot of a microion configuration around two model proteins separated by $r = 1.7d_p$, d_p denoting the protein hard core diameter. The proteins carry 15 discrete charges e, monovalent salt molarity is $c_s = 0.206 Mol/\ell$. The globular protein molecules are shown as two large grey spheres. The embedded small dark spheres on their surface mimic the discrete protein charges. The small grey spheres are counterions, while the black spheres are coions.*

important effects are lost even qualitatively, when the coarse graining of nanoparticles is pushed too far.

11 Conclusions

In conclusion, we have demonstrated that the concept of effective interactions allows large-scale simulations and provides additional insight into the physical mechanisms governing colloidal dispersions and polymer solutions. We conclude with a discussion about multiple *time* scales in the context of colloidal dispersions.

The dynamics of colloidal particles embedded in a solvent involves many different time scales ranging from the collision time $\tau_s \approx 10^{-14} sec$ of the solvent molecules, over the relaxation time $\tau_B \approx 10^{-9} sec$ of the total colloid momentum and the propagation time $\tau_H \approx 10^{-9} sec$ of hydrodynamic interactions, to the Brownian time $\tau_0 \approx 10^{-6} sec$ on which diffusive motion of the colloidal particles is observed. Consequently there is almost complete time scale separation

$$\tau_s << \tau_B \simeq \tau_H << \tau_0. \tag{45}$$

It is a challenging question whether - in analogy with bridging length scale gaps - one can "integrate out" the fast dynamical processes which happen on the time scale τ_s in order to arrive at an "effective dynamics" on larger time scales. The traditional approach is a stochastic one, as embodied in Langevin and Fokker-Planck formulations [98, 99], but a rigorous derivation of the Fokker-Planck equation from the initial full Liouville equation for dilute colloidal suspensions exposes the intrinsic limitations of the Fokker-Planck equation, due to the similarity of the time scales τ_B and τ_H [100]. Clearly a dynamical counterpart of the effective interaction concept governing the thermodynamics and statics is missing. From a simulation point of view However, relying on an (almost) complete time scale separation between solvent and colloidal dynamics, one typically describes the motion of the colloidal particles by a completely overdamped Langevin equation with stochastic forces exerted onto the colloids modelling the random solvent kicks [101, 102]. Within such a Brownian approach operating on a time scale τ_0, the hydrodynamic interactions act instantaneously. Much of the recent effort was spent to treat these hydrodynamic interactions approximatively [103] by using different computational schemes such as lattice-Boltzmann techniques [104], Stokesian Dynamics [105], dissipative particle dynamics [106], and fluidizing the solid colloidal particles [107]. Although these algorithms are powerful in different applications, it is fair to say that all of these approaches lack a rigorous theoretical justification.

Having established a stochastic Brownian approach for the colloidal particles resulting from the solvent dynamics, a much more modest question concerns the dynamical utility of the effective interaction concept originating from integrating out small particles different from the solvent (counter- and salt ions, polymers, small colloidal particles etc). One may conjecture that it is only in the case of a complete time scale separation between the big and small particle dynamics that the effective interaction has a true dynamical meaning. This is the reason why the effective interaction potential is frequently combined with Brownian dynamics simulations for the colloids. For instance, the effective DLVO-potential has been combined with Brownian dynamics simulations in order to investigate the glass transition [108], long-time self-diffusion [109], linear shear flow [110, 111, 112],

and phase transitions in driven colloidal mixtures [113, 114]. It would be very interesting to test and study systematically how far one can get with the coarse-graining approach as far as dynamical questions are concerned.

Acknowledgements

I thank J. P. Hansen, E. Allahyarov, M. Dijkstra, J. Dzubiella, A. Jusufi, C. N. Likos, A. A. Louis and R. Pierre for help and for valuable comments.

References

[1] V. Lobaskin, A. Lyubartsev, P. Linse, Phys. Rev. E **63**, 020401 (2001).

[2] J.-P. Hansen, H. Löwen, *Effective interactions for large-scale simulations of complex fluids,* Springer Series, 2002.

[3] C. N. Likos, Physics Reports **348**, 267 (2001).

[4] L. Belloni, J. Phys. Condens. Matter **12**, R549 (2000).

[5] J. P. Hansen, H. Löwen, Ann. Rev. Phys. Chem. **51**, 209 (2000).

[6] M. Dijkstra, Current Opinion in Colloid and Interface Science **6**, 372 (2001).

[7] See e.g R. van Roij, M. Dijkstra, J.P. Hansen, Phys. Rev. E **59**, 2010 (1999).

[8] H. Löwen, Phys. Reports **237**, 249 (1994).

[9] For an extensive review of classical DFT see R. Evans in "Fundamentals of Inhomogeneous Fluids", edited by D. Henderson (Marcel Decker, New York, 1992).

[10] J. P. Hansen and E. Smargiassi, in "Monte Carlo and Molecular Dynamics of Condensed Matter Systems", edited by K. Binder and G. Ciccotti (Societa Italiana di Fisica, Bologna, 1996).

[11] See e.g. G. Galli and M. Parrinello, in "Computer Simulations in Materials Science", P. 282, edited by M. Meyer and V. Pontikis (Kluwer, Dordrecht, 1991)

[12] H. Löwen, J. P. Hansen, P. A. Madden, J. Chem. Phys. **98**, 3275 (1993).

[13] F. Gygi, G. Galli, Phys. Rev. B **52**, R 2229 (1995).

[14] S. Melchionna, J. P. Hansen, Phys. Chem. Chem. Phys., to be published

[15] R. Roth, R. Evans, S. Dietrich, Phys. Rev. E **62**, 5360 (2000).

[16] D. Goulding, S. Melchionna, Phys. Rev. E **64**, 011403 (2001).

[17] Y. Rosenfeld, M. Schmidt, H. Löwen, P. Tarazona, Phys. Rev. E **55**, 4245 (1997).

[18] H. Löwen, in: "Spatial Statistics and Statistical Physics", edited by K. Mecke and D. Stoyan, Springer Lecture Notes in Physics, Volume 554, pages 295-331, Berlin, 2000.

[19] A. Lang, C. N. Likos, M. Watzlawek, H. Löwen, J. Phys. Condensed Matter **12**, 5087 (2000).

[20] C. N. Likos, A. Lang, M. Watzlawek, H. Löwen, Phys. Rev. E **63**, 031206 (2001).

[21] A. A. Louis, Philos. Trans. R. Soc. Lond. A **359**, 939 (2001).

[22] M. Schmidt, Phys. Rev. E **60**, R6291 (1999).

[23] B. V. Derjaguin, L. D. Landau, Acta Physicochim. USSR **14**, 633 (1941); E. J. W. Verwey and J. T. G. Overbeek, *Theory of the Stability of Lyophobic Colloids.* (Elsevier, Amsterdam, 1948).

[24] A. Delville, R. J. M. Pellenq, Molecular Simulation **24**, 1 (2000); R. Messina, C. Holm, K. Kremer, Phys. Rev. Lett. **85**, 872 (2000); T. Terao, T. Nakayama, Phys. Rev. E **63**, 041401 (2001); B. Hribar, V. Vlachy, Langmuir **17**, 2043 (2001).

[25] A. Delville, J. Phys. Chem. B **103**, 8296 (1999); A. Delville, P. Levitz, J. Phys. Chem. B **105**, 663 (2001)

[26] S. Meyer, P. Levitz, A. Delville, J. Phys. Chem. B **105**, 10684 (2001).

[27] H. Löwen, E. Allahyarov, J. Phys.: Condensed Matter **10**, 4147 (1998).

[28] R. D. Groot, J. Phys. **95**, 9191 (1991).

[29] M. J. Stevens, M. L. Falk, M. O. Robbins, J. Chem. Phys. **104**, 5209 (1996).

[30] H. Löwen, G. Kramposthuber, Europhys. Lett. **23**, 673 (1993).

[31] H. Löwen, Phys. Rev. Lett. **72**, 424 (1994). J. Chem. Phys. **100**, 6738 (1994).

[32] S. Kutter, J. P. Hansen, M. Sprik, E. Boek, J. Chem. Phys. **112**, 311 (2001).

[33] C. Mischler, J. Baschnagel, K. Binder, Advances in Colloid and Interface Science **94**, 197 (2001).

[34] P. J. Flory, W. R. Krigbaum, J. Chem. Phys **18**, 1086 (1950).

[35] A. Y. Grosberg, P. G. Khalatur, A. R. Khokhlov, Makromol. Chem. Rapid Comm. **3**, 709 (1982).

[36] J. Dautenhahn, C. K. Hall, Macromolecules **27**, 5399 (1994), and references therein.

[37] A. A. Louis, P. G. Bolhuis, J. P. Hansen, E. J. Meijer, Phys. Rev Letters **85**, 2522 (2000) P. G. Bolhuis, A. A. Louis, J. P. Hansen, E. J. Meijer, J. Chem. Phys. **114**, 4296 (2001).

[38] B. Krüger, L. Schäfer, A. Baumgärtner, J. Phys. (Paris) **50**, 319 (1989).

[39] V. Krakoviack, A. A. Louis, J. P. Hansen, to be published.

[40] C. H. Bennett, J. Comp. Phys. **22**, 245 (1976).

[41] D. Frenkel, B. Smit, "Understanding Molecular Simulation", 2^d Edition (Academic Press, San Diego, 2001).

[42] P. G. Bolhuis, A. A. Louis, J. P. Hansen, Phys. Rev. E **64**, 021801 (2001).

[43] C. von Ferber, A. Jusufi, C. N. Likos, H. Löwen, M. Watzlawek, Europhys. Journal E **2**, 311 (2000).

[44] See e.g. J. P. Hansen, I. R. McDonald, "Theory of Simple Liquids" 2^d edition (Academic Press, London, 1986).

[45] A. A. Louis, P. G. Bolhuis, J. P. Hansen, Phys. Rev. E **62**, 7961 (2000).

[46] R. L. Henderson, Phys. Lett. **49A**, 197 (1974).

[47] A. Jusufi, J. Dzubiella, C. N. Likos, C. von Ferber, H. Löwen, J. Phys.: Condensed Matter **13** 6177 (2001).

[48] A. A. Louis, P. G. Bolhuis, E. J. Meyer, J. P. Hansen, cond-mat (011518).

[49] For a review see K. S. Schweizer, J. G. Curro, Adv. Chem. Phys. **98**, 1 (1997).

[50] V. Krakoviack, J. P. Hansen, A. A. Louis, cond-mat / 0110387

[51] For a review see: G. S. Grest, L. J. Fetters, J. S. Huang, D. Richter, Advances in Chemical Physics, Volume XCIV, 67 (1996)).

[52] T. A. Witten, P. A. Pincus, Macromolecules **19**, 2509 (1986).

[53] M. Dauod, J. P. Cotton, J. Phys. (Paris) **38**, 983 (1977).

[54] C. N. Likos, H. Löwen, M. Watzlawek, B. Abbas, O. Jucknischke, J. Allgaier, D. Richter, Phys. Rev. Letters **80**, 4450 (1998).

[55] A. Jusufi, M. Watzlawek, H. Löwen, Macromolecules **32**, 4470 (1999).

[56] M. Watzlawek, C. N. Likos, H. Löwen, Phys. Rev. Letters. **82**, 5289 (1999).

[57] M. Watzlawek, H. Löwen, C. N. Likos, J. Phys. Condensed Matter **10**, 8189 (1998).

[58] G. A. McConnell, A. P. Gast, Macromolecules **30**, 435 (1997).

[59] S. T. Milner, T. A. Witten, M. E. Cates, Macromolecules **21**, 2610 (1988).

[60] J. Mewis, W. J. Frith, T. A. Strivens, W. B. Russel, A. I. Ch. E. J. **35**, 415 (1989).

[61] U. Genz, B. D'Aguanno, J. Mewis, R. Klein, Langmuir **10**, 2206 (1994).

[62] C. N. Likos, H. Löwen, A. Poppe, L. Willner, J. Roovers, B. Cubitt, D. Richter, Phys. Rev. E **58**, 6299 (1998).

[63] A. Jusufi, C. N. Likos, H. Löwen, Phys. Rev. Letters **88**, 018301 (2002).

[64] P. Pincus, Macromolecules **24**, 2912 (1991).

[65] C. N. Likos, M. Schmidt, H. Löwen, M. Ballauff, D. Pötschke, P. Lindner, Macromolecules **34**, 2914 (2001).

[66] C. N. Likos, private communication.

[67] S. Asakura, F. Oosawa, J. Chem. Phys. **22**, 1255 (1954).

[68] M. Dijkstra, J. M. Brader, R. Evans, J. Phys.: Condensed Matter **11**, 10079 (1999).

[69] M. Dijkstra, to be published.

[70] I. Götze, Diploma Thesis, University of Düsseldorf, 2002.

[71] H. N. W. Lekkerkerker, W. C. K. Poon, P. N. Pusey, A. Stroobants, P. B. Warren, Europhys. Lett. **20**, 559 (1992).

[72] M. Schmidt, H. Löwen, J. M. Brader, R. Evans, Phys. Rev. Letters **85**, 1934 (2000).

[73] M. Schmidt, H. Löwen, J. M. Brader, R. Evans, J. Phys.: Condensed Matter **14**, L1 (2002).

[74] A. A. Louis, R. Finken, J. P. Hansen, Phys. Rev. E **61**, R1028 (2000).

[75] E. J. Meijer, D. Frenkel, Physica A **213**, 130 (1995).

[76] A. Johner, J. F. Joanny, S. Diez Orrite, J. Bonet Avalos, Europhys. Letters **56**, 549 (2001).

[77] J. Dzubiella, A. Jusufi, C. N. Likos, C. von Ferber, H. Löwen, J. Stellbrink, J. Allgaier, D. Richter, A. B. Schofield, P. A. Smith, W. C. K. Poon, P. N. Pusey, Phys. Rev. E **64**, 01040 (2001).

[78] J. Dzubiella, C. N. Likos, H. Löwen, to be published.

[79] M. Fuchs, K. S. Schweizer, Phys. Rev. E **64**, 021514 (2001).

[80] A. Hanke, E. Eisenriegler, S. Dietrich, Phys. Rev. E **59**, 6853 (1999).

[81] H. Xu, M. Baus, J. Phys.: Condensed Matter **4**, L663 (1992).

[82] M. D. Eldridge, P. A. Madden, D. Frenkel, Mol. Phys. **79**, 105 (1993).

[83] P. Bartlett, R. H. Ottewill, P. N. Pusey, Phys. Rev. Lett. **68**, 3801 (1992).

[84] R. Dickman, P. Attard, V. Simonian, J. Chem. Phys. **107**, 205 (1997).

[85] E. Allahyarov, H. Löwen, Phys. Rev. E **63**, 041403 (2001).

[86] J. C. Crocker, J. A. Matteo, A. D. Dinsmore, A. G. Yodh, Phys. Rev. Letters **82**, 4352 (1999).

[87] M. Dijkstra, R. van Roij, R. Evans, Phys. Rev. E **59**, 5744 (1999).

[88] N. G. Almarza, E. Enciso, Phys. Rev. E **59**, 4426 (1999).

[89] P. Bolhuis, M. Hagen, D. Frenkel, Phys. Rev. E **50**, 4880 (1994).

[90] C. N. Likos, Z. T. Németh, H. Löwen, J. Phys. Condensed Matter **6**, 10965 (1994).

[91] D. Goulding, J. P. Hansen, Mol. Phys. **99**, 865 (2001).

[92] A. A. Louis, R. Roth, E. Allahyarov, H. Löwen, to be published.

[93] E. Allahyarov, H. Löwen, J. Phys. Condensed Matter **13**, L277 (2001).

[94] H. Löwen, E. Allahyarov, J. Dzubiella, C. von Ferber, A. Jusufi, C. N. Likos, M. Heni, Philos. Trans. R. Soc. Lond. A **359**, 909 (2001).

[95] E. Allahyarov, H. Löwen, A. A. Louis, J. P. Hansen, *Discrete charge patterns, Coulomb correlations and interactions in protein solutions,* Europhys. Letters (in press).

[96] A. George, W. W. Wilson, Acta Cryst. D **50**, 361 (1994); G. A. Vliegenthart, H. N. W. Lekkerkerker, J. Chem. Phys. **112**, 5364 (2000).

[97] B. Guo, S. Kao, H. McDonald, A. Asanov, L. L. Combs, W. W. Wilson, J. Cryst. Growth **196**, 424 (1999); D. N. Petsev, B. R. Thomas, S. T. Yau, P. G. Vekilov, Biophysical Journal **78**, 2060 (2000).

[98] N. G. van Kampen, "Stochastic Processes in Physics and Chemistry (North Holland, Amsterdam, 1990).

[99] W. Hess and R. Klein, Adv. Phys. **32**, 173 (1983).

[100] For a review, see L. Bocquet and J. P. Hansen, in "Dynamics: Models and Kinetic Methods for Non-Equilibrium Many-Body Systems", edited by J. Karkheck (Kluwer Academic, Dordrecht, 2000).

[101] For a review, see P. N. Pusey, in "Liquids, Freezing and the Glass Transition", edited by J. P. Hansen, D. Levesque and J. Zinn-Justin (North Holland, Amsterdam, 1991).

[102] J. K. G. Dhont, "An Introduction to Dynamics of Colloids", Elsevier, Amsterdam, 1996.

[103] G. Nägele, Physics Reports, **272**, 215 (1996).

[104] A. J. C. Ladd, R. Verberg, J. Stat. Phys. **104**, 1191 (2001).

[105] See e.g.: R. Pesché, G. Nägele, Europhys. Lett. **51**, 584 (2000); H. M. Schaink, P. A. Nommensen, R. J. J. Jongschaap, J. Mellema, J. Chem. Phys. **113**, 2484 (2000).

[106] P. B. Warren, Current Opinion in Colloid and Interface Science **3**, 620 (1998).

[107] H. Tanaka, T. Araki, Phys. Rev. Lett. **85**, 1338 (2000).

[108] H. Löwen, J. P. Hansen, J. N. Roux, Phys. Rev. A **44**, 1169 (1991).

[109] H. Löwen, G. Szamel, J. Phys. Condensed Matter **5**, 2295 (1993).

[110] S. Butler, P. Harrowell, J. Chem. Phys. **103**, 4653 (1995); J. Chem. Phys. **105**, 605 (1996).

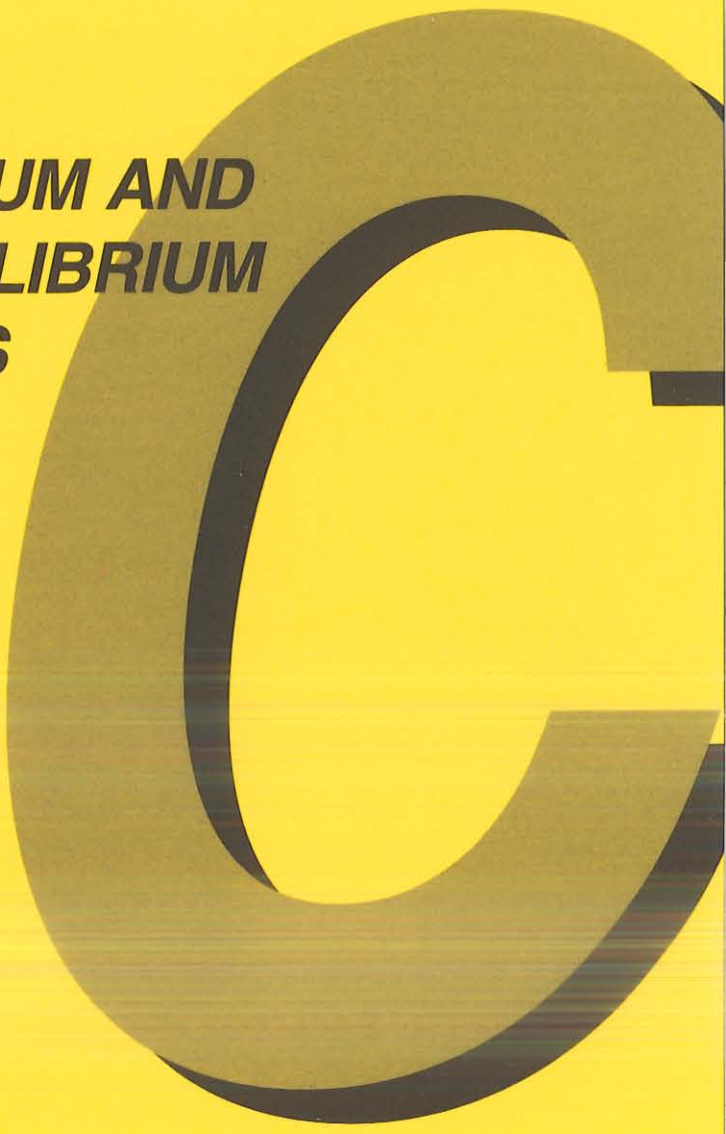
[111] S. R. Rastogi, N. Wagner, S. R. Lustig, J. Chem. Phys. **104**, 9234 (1996).

[112] N. Olivi-Tran, R. Botet, B. Cabane, Phys. Rev. E **57**, 1997 (1998).

[113] H. Löwen, G. Hoffmann, Phys. Rev. E **60**, 3009 (1999).

[114] J. Dzubiella, G. P. Hoffmann, H. Löwen, *Lane formation in binary colloidal mixtures driven by an external field,* Phys. Rev. E (in press).

EQUILIBRIUM AND NON-EQUILIBRIUM DYNAMICS



C 1 Random motion in equilibrium

G. M. Schütz
Institut für Festkörperforschung
Forschungszentrum Jülich GmbH

Contents

1 Brownian motion **2**
1.1 Randomness vs deterministic dynamics 2
1.2 Coarse graining 2
1.3 The Smoluchowski equation 3

2 Langevin, master, and Fokker-Planck equation **7**
2.1 Langevin equation 7
2.2 Master equation and Fokker-Planck equation 9

3 Dynamical correlation functions and linear response theory **12**
3.1 Time correlation functions in equilibrium 12
3.2 Fluctuation dissipation theorem 13

4 Brownian motion in a potential **15**
4.1 Linear potential 16
4.2 Harmonic potential 17

5 Smoluchowski equation for hydrodynamic interaction **18**

1 Brownian motion

1.1 Randomness vs deterministic dynamics

It is known for almost 200 years that small particles such as pollen particles immersed in a fluid perform an irregular type of motion. This discovery by Brown in 1827 of stochastic rather than deterministic dynamical behavior had quickly generated a tremendous amount of research activity and has not ceased until today to fascinate scientists from various branches of physics and beyond. Random motion is very frequently found in many-body systems if observed on intermediate length scales. By this we mean length scales large compared to atomic scales (where quantum mechanics is the relevant framework of description), but small compared to macroscopic scales where objects normally behave deterministically because random fluctuations around the mean quantities (such as velocities or currents) that one measures are too small to be observable in macrocopic objects. On intermediate scales dynamics is governed by effective forces which are usually not easy to derive from microscopic basic laws such as Newtonian mechanics or the Schrödinger equation. The complicated interplay of the many microscopic forces then gives rise to what we observe as randomness.
Therefore the major tasks that physicists have to deal with are (i) the development of suitable tools for describing the various kinds of random motion that occur in many-body systems (What does stochastic motion look like?), (ii) the derivation of random behavior from microscopic laws of nature (Where does it come from?), and (iii) understanding the emergence of collective macroscopic behavior from the stochastic many-body dynamics on intermediate scales. (Where does random motion lead to?) Issue (iii) is the central theme of statistical mechanics and soft matter physics and is treated in various ways in this spring school. Therefore this introductory lecture is devoted to partially answer the first question by reviewing some basic concepts for studying random motion.

1.2 Coarse graining

The random motion of pollen particles in water observed by Brown is now understood as originating in the incessant thermal collisions of the water molecules with the much larger pollen particles. The same mechanism drives the stochastic motion of colloidal particles in a fluid. In the simplest case of just a single particle one may therefore entirely disregard the properties of the fluid and just view it as the source of a random force. If one now takes snapshots of the particle position at regular time intervals τ one sees a picture similar to Fig. 1. After each time step the particle has moved by a random displacement $\vec{\xi}$.
Since the properties of the random forces are in general not easy to derive (question (ii)) we skip this problem here and adopt a phenomenogical point of view as done by Einstein in his famous work on diffusion in 1905 (for original references see [1]). We assume at this point that particle concentrations are very small, such that interactions between particles can be neglected and that there is a linear relation between external forces and the particle flux that may result from such forces. The essential idea for describing the random motion is what in modern physics is referred to as *coarse graining*: Rather than studying microscopic details of the dynamics with a very fast camera and a microscope with an ultra high resolution (neither of which were available when Einstein wrote his paper) we consider

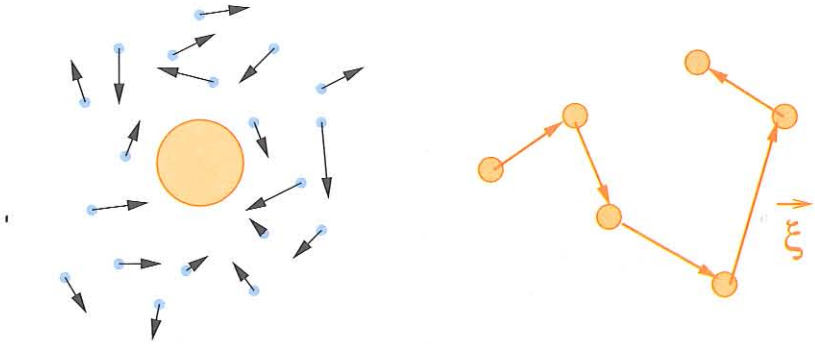


Fig. 1: *Brownian particle immersed in a fluid (left). The thermal motion of the fluid particles (small) causes collisions with the Brownian particle (large). Snapshots of the position of the Brownian particle taken after regular time intervals τ (right).*

time intervals that are large compared to all microscopic times such as collision times between fluid molecules, relaxation times for atomic or molecular excitations, correlation times between subsequent collisions of fluid molecules with the Brownian particle etc. The important insight by Einstein and independently also by Smoluchowski behind this coarse graining of time is that what is observed in experiments is not the perpetual change in the velocity of the Brownian particles due to collisions since between two successive observations of the position of the Brownian particle the velocity has independently grown and decayed many times. Hence what is observed is the net displacement resulting after many variations of the velocity.

We also coarse grain space by restricting our observation of the system to length scales that are large not only compared to the size of the fluid particles but also large compared to the typical diameter of the Brownian particles. This voluntary constraint (which would be easy to overcome by choosing a microscope with sufficiently large magnification) implies that we may replace the individual particle positions $\vec{x}_i(t)$ by a concentration field $c(\vec{x}, t)$: In the observed volume one always assumes to be so many particles that an average concentration is seen rather than the individual particles.

1.3 The Smoluchowski equation

In what follows we restrict ourselves for notational simplicity to a one-dimensional system. We assume the concentration field to be given at some time t_0 and we wish to calculate how locally the concentration changes in time. Clearly, in an equilibrium setting the concentration field would be stationary since the individual Brownian particles (which still perform random motion) are not under observation. The coarse graining imposed by our artificial observation procedure automatically yields the stationary equilibrium average over the particle positions since our observation volume is chosen so large that in contains so many particles that fluctuations cancel out.

In the absence of external forces the stationary equilibrium concentration is uniform. However, after experimentally generating a nonuniform and hence nonequilibrium concentration field the velocity fluctuations of the particles (that we do not observe but that are still there) caused by the thermal motion of the fluid molecules lead to a flux j even

though the mean velocities $\langle v_i \rangle$ of the particles vanish. Therefore the concentration field will change until equilibrium is regained.
Fick's law asserts that locally this current is proportional to the concentration gradient

$$j(x,t) = -D\frac{\partial c}{\partial x} \tag{1}$$

where the constant of proportionality D is a phenomenological quantity called diffusion coefficient. This constant depends on the microscopic details of the system (the properties of the fluid, the size and shape of the particle and so on) and is not under consideration in our treatment. We take it as a quantity measured in an experiment and plugged into our equation, without asking what physical properties determine its value. The origin of Fick's law is not difficult to understand. It arises from the imbalance in the number of particles diffusing from a local region of high density into a region of low density. If all particles are identical and do not interact then the current must indeed be proportional to the density gradient.
Fick's law alone is not sufficient to calculate how a nonuniform concentration field changes in time. However, since there are no sources or sinks for particles the time evolution is governed by the continuity equation

$$\frac{\partial c}{\partial t} = -\frac{\partial j}{\partial x} \tag{2}$$

which holds for any system with particle number conservation. Putting (1) and (2) together yields the famous diffusion equation

$$\frac{\partial c}{\partial t} = D\frac{\partial^2 c}{\partial x^2} \tag{3}$$

also known as heat equation because heat conduction in a solid follows the same law, with D playing the role of the thermal conductivity. The solution of the diffusion equation for a given initial concentration is derived in the appendix. Here we just give the result

$$c(x,t) = \int dx' c_0(x) G(x,x';t) \tag{4}$$

with the propagator

$$G(x,x';t) = \frac{1}{\sqrt{4\pi D t}} \exp\left(-\frac{(x-x')^2}{4Dt}\right) \tag{5}$$

and the initial concentration field $c_0(x)$. The propagator, which for this simple problem is just a Gaussian, is also known as Green function or heat kernel. More complicated, but still linear evolution equations have other propagators. For solving special problems it is useful to notice that the diffusion equation is formally identical not only with the heat equation but also with the Schrödinger equation for a noninteracting particle in imaginary time (see Appendices). Hence essentially all the techniques developed in first-year quantum mechanics can be applied with minor modifications to solving diffusion problems!
For illustration of these basic properties of random motion we first consider as special example the delta-function which describes an nonequilibrium initial state where all particles are located in a very small region of space around the point with coordinate y (Fig.

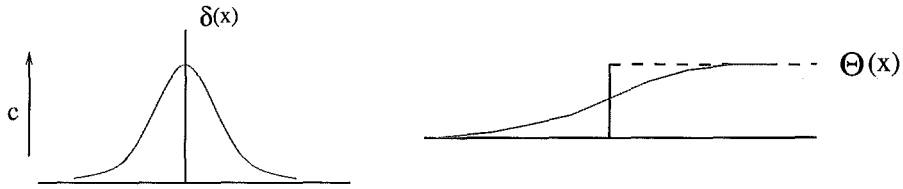


Fig. 2: *Diffusive time evolution of an initially spatially condensed concentration (left). After some time the concentration field is Gaussian. For an initial step function the concentration evolves into an error function (right).*

2). Plugging $c_0(x) = \delta(x-y)$ into (4) yields the Gaussian $G(x,y;t)$ as solution of the diffusion equation. This result also gives insight into the meaning of the propagator. It describes how a point distribution evolves in time. Because of the linearity of the evolution equation all other initial distribution are then obtained by linear superposition. This can be seen in our second example of an initial step function concentration field $c_0(x) = c_0\Theta(x)$. This corresponds to the situation where one half of a very large container is filled with particles at a given uniform concentration c_0 whereas the other half is empty. Such a system would be equilibrium if there were a partition between the two subsystems. Removing this partition creates a nonequilibrium situation with a evolving concentration field

$$c(x,t) = c_0 \int_0^\infty dx' G(x,x';t) = \frac{c_0}{\sqrt{4\pi Dt}} \int_{-\infty}^{x} \exp\left(-\frac{x^2}{4Dt}\right). \tag{6}$$

Up to a constant this is the error function. The width of the transition region between the empty part and the filled part of the subsystem grows in time proportional to $\sqrt{Dt}$, just as the width of the Gaussian describing the evolution of the point concentration.
So far we have assumed that there is no external force $F = -\partial U/\partial x$ acting on the particles. Allowing for a weak force leads to an intrinsic non-zero average velocity

$$v = -\frac{1}{\zeta}\frac{\partial U}{\partial x} \tag{7}$$

Here ζ is the friction coefficient which is determined (like the diffusion coefficient) by microscopic details of the system. Its reciprocal $1/\zeta$ is known as mobility. E.g. for a spherical particle with diameter a in a fluid with viscosity η hydrodynamics gives $\zeta = 6\pi\eta a$. Here η is yet another coefficient determined by microscopic details, albeit of the fluid alone. The relation (7) may be obtained from Newtons equation with friction by neglecting the inertia term $\ddot{x}$. This is justified because following Einstein and Smoluchowski in our basic time interval many independent collisions and hence changes of velocity have taken place so that the (accumulated) net acceleration can be neglected.
This systematic velocity v generates an extra systematic flux $j_{sys} = cv$ which has to be added to Fick's diffusive flux j_{diff} (1) in the continuity equation (2). Hence

$$j = j_{diff} + j_{sys} = -D\frac{\partial c}{\partial x} + cv \tag{8}$$

which gives rise to the so-called Smoluchowski equation

$$\frac{\partial c}{\partial t} = \frac{\partial}{\partial x}\left(D\frac{\partial c}{\partial x} + \frac{c}{\zeta}\frac{\partial U}{\partial x}\right). \tag{9}$$

An important relation between diffusion coefficient and mobility may be obtained by considering a system in equilibrium where the total current j (and hence also $\dot{c}$) vanishes. The modified Fick's law (8) for the equilibrium concentration c^* yields

$$0 = D\frac{\partial c^*}{\partial x} + \frac{c^*}{\zeta}\frac{\partial U}{\partial x}. \tag{10}$$

This ordinary differential equation is straightforward to integrate with the solution

$$c^*(x) \propto \exp\left(-\frac{D}{\zeta}U(x)\right). \tag{11}$$

On the other hand, we know from equilibrium thermodynamics that at temperature T the probability density $\Psi(x,t)$ of finding a particle in the infinitesimal interval between x and $x+dx$ is proportional to the Boltzmann weight $\exp(-E/kT)$ with the local potential energy $E = U(x)$ and the Boltzmann constant k. Since the concentration c is proportional to the probability Ψ we may write $c^*(x) \propto \exp(U(x)/kT)$. Comparing with (11) yields

$$D = \frac{kT}{\zeta} \tag{12}$$

This is the famous Einstein relation which relates two very different quantities, viz. the diffusion coefficient D of thermal motion (describing thermal fluctuations) and the friction coefficient ζ respectively which describes the response to an external force.
The Smoluchowski equation (9) may be directly phrased for the probability density Ψ rather than for the concentration. Moreover, the fluctuation term D is not necessarily a constant since in an inhomogeneous medium the mobility may depend on the local environment. In a more general setting the system is therefore governed by a Smoluchowski equation of the form

$$\frac{\partial \Psi}{\partial t} = \frac{1}{2}\frac{\partial^2}{\partial x^2}B(x)\Psi - \frac{\partial A}{\partial x}\Psi. \tag{13}$$

with a fluctuation term $B(x)$ and a transport term $A(x)$. The only general physical requirements for these quantities are that they are real and differentiable and $B(x)$ be strictly positive for all x. Since probability is a conserved quantity (just as the number of particles) there is a "probability flux"

$$J = A(x)\Psi - \frac{1}{2}\frac{\partial}{\partial x}B(x)\Psi \tag{14}$$

for which (13) is the associated continuity equation.
Finally, we extend the Smoluchowski equation to systems with many degrees of freedom $\{x\} \equiv \{x_1, \ldots, x_N\}$. These may e.g. be coordinates in three-dimensional space, coordinates for internal degrees of freedom, or also the positions of other particles in the presence of particle-particle interactions. Instead of (13) one then has the multivariate Smoluchowski equation

$$\frac{\partial \Psi(\{x\},t)}{\partial t} = \frac{1}{2}\sum_{i,j=1}^{N}\frac{\partial^2}{\partial x_i x_j}B_{ij}\Psi - \sum_{i=1}^{N}\frac{\partial}{\partial x}A_i\Psi. \tag{15}$$

Here B_{ij} and A_i must be real differentiable functions of all the coordinates and B_{ij} must be symmetric and positive definite for all values of the argument.

There is also a generalized Einstein relation between the fluctuation term B_{ij} and the mobility matrix L_{ij} defined by the force-velocity relation

$$v_i = \sum_{j=1}^{N} L_{ij} F_j \tag{16}$$

for weak forces $F_i = -\partial U(\{x\})/\partial x_i$. Since in equilibrium Ψ is proportional to the Boltzmann weight one finds (for constant B_{ij})

$$B_{ij} = 2kTL_{ij}. \tag{17}$$

In this case the functions A_i are given by $A_i = \sum_j L_{ij} F_j$. Plugging this into (15) yields as a final expression

$$\frac{\partial \Psi(\{x\},t)}{\partial t} = \sum_{i,j=1}^{N} \frac{\partial}{\partial x_i} L_{ij} \left(kT \frac{\partial \Psi}{\partial x_j} + \frac{\partial}{\partial x_j} \Psi \right). \tag{18}$$

This equation has no general explicit solution, but serves as the basis for numerical and suitably chosen approximate treatments.

2 Langevin, master, and Fokker-Planck equation

2.1 Langevin equation

In the treatment of Brownian motion developed in the first part of this lecture we adopted a coarse grained point of view in which we did not trace the motion of the individual particles, but rather considered regions of space large enough to contain so many particles that we were permitted to speak of a concentration field. The final result was a deterministic evolution equation for the concentration or probability density respectively. By averaging of over many particles in the spatial coarse graining the randomness in the motion of the individual particles effectively disappeared when we introduced Fick's law. In a different treatment, still coarse grained, one actually studies the motion of a single particle under the influence of a random force. Averaging is done explicitly by making detailed assumptions about the statistical properties of the random force. This is the approach taken by Langevin. Adapted to the problem at hand it works as follows.
We still fix a time interval τ on a coarse grained time scale as discussed above. However, we skip the requirement of having many particles in our test volume. What we observe at discrete times (Fig. 1) $t_{n+1} = t_n + \tau$ is a random series of particle positions

$$x(t+\tau) = x(t) + \xi(t) \tag{19}$$

with the random displacement ξ resulting from many thermal collisions with the fluid particles. Because of our choice of τ correlations between these collisions have already decayed and therefore at each time step $\xi(t)$ is an independent random variable. Assuming that the fluid environment does not change in time, ξ is drawn from the same distribution at each time step, in other words, $\xi(t)$ are independent identically distributed (i.i.d.) random variables. The distribution of ξ must, in principle, be determined experimentally.

However, for sufficiently large τ there have taken place many independent displacement (not only independent collisions!) such that the central limit theorem may be invoked. It asserts that the combined effect of these independent displacements has a Gaussian distribution with zero mean (in the absence of external forces) and some variance which we write as $\sigma^2\tau$, still to be determined experimentally. We remark that for mathematical simplicity such a Gaussion distribution is usually employed as an approximation for theoretical investigations even if it is not clear whether the central limit theorem may be applied. However, as we shall now see, some properties of the random motion are actually independent of the precise nature of the distribution of random displacements.
By iteration it is very easy to solve (19) explicitly. After n time steps $t = n\tau$ one has

$$x(t) = x(0) + \sum_{k=0}^{n-1} \xi(k). \tag{20}$$

It is convenient to choose the origin of the coordinate system as initial position. Averaging over many realizations of the random process (rather than averaging over many particles) one then finds the statistical properties of the random walk $x(t)$ in terms of the statistical properties of the random displacements. In particular, one has

$$\langle\, x(t) \,\rangle \equiv vt = \sum_{k=0}^{n-1} \langle\, \xi(k) \,\rangle \tag{21}$$

This defines the mean velocity v which is zero if the random displacement has mean zero as we assume here. Moreover

$$\langle\, x^2(t) \,\rangle \equiv 2Dt = \sum_{k,l=0}^{n-1} \langle\, \xi(k)\xi(l) \,\rangle. \tag{22}$$

Since the random displacements at different times are independent one has $\langle\, \xi(k)\xi(l) \,\rangle = \sigma^2\tau\delta_{k,l}$. This relates the macroscopic diffusion coefficient to the mesoscopic variance of the displacements,

$$D = \frac{\sigma^2}{2}. \tag{23}$$

The full distribution of ξ enters only in the study of the higher moments of the random walk. E.g. for the probability density $\Psi(y,t)$ envisaged in the treatment by Smoluchowski and Einstein one has to calculate

$$\Psi(y,t) = \langle\, \delta(x(t) - y) \,\rangle \tag{24}$$

which may be calculated using the integral representation

$$\delta(x) = \frac{1}{2\pi} \int d\alpha \mathrm{e}^{i\alpha x} \tag{25}$$

of the δ-function.
Exercise:
Show that

$$\Psi(y,t) = \frac{1}{\sqrt{4\pi Dt}} \exp\left(-\frac{y^2}{4Dt}\right) \tag{26}$$

for a random walk starting at the origin. Hint: Use the factorization of the exponential of a sum into a product of exponentials and the independence of the increments. Notice that (26) is just the solution of the Smoluchowski equation, but in discrete time! For a non-Gaussian distribution of random displacements the distribution of Ψ would be different. Therefore this calculation makes clear the condition under which the two different approaches to random motion are equivalent. For an initial position y_0 off the origin one replaces y by $y - y_0$ in (26).
In the simple case of a free particle one may pass to a continuous-time description by taking the limit $\tau \to 0$. Experimentally this corresponds to a snapshot interval small compared to the full observation time of the system. Using Taylor expansion one may write the stochastic evolution equation (19) in the form

$$\frac{d}{dt}x = \tilde{\xi}(t) \tag{27}$$

with a renormalized displacement $\tilde{\xi}$ with mean zero and δ- correlated variance

$$\langle\, \tilde{\xi}(t)\tilde{\xi}(t') \,\rangle = 2D\delta(t - t'). \tag{28}$$

In the presence of an external force this equation takes the form

$$\zeta\frac{d}{dt}x = -\frac{d}{dx}U + f(t) \tag{29}$$

with the random force $f = \tilde{\xi}/\zeta$ proportional to the random displacement. This is the Langevin equation for a single particle. For many degrees of freedom with a space-dependent mobility matrix one has

$$\frac{d}{dt}x_i = \sum_{j=1}^{N} L_{ij}\left(-\frac{\partial}{\partial x_j}U + f_j(t)\right) + \frac{1}{2}kT\sum_{j=1}^{N}\frac{\partial}{\partial x_j}L_{ij}. \tag{30}$$

The random forces are assumed to have mean zero

$$\langle\, f_j(t) \,\rangle = 0 \tag{31}$$

and a variance

$$\langle\, f_i(t)f_j(t') \,\rangle = 2kT(L^{-1})_{ij}\delta(t - t'). \tag{32}$$

We stress that also for the Langevin equation the Einstein relation is satisfied. This is ensured by the factor of proportionality in the δ-correlated random forces (32). We remark that the passage from discrete time to continous time is in general not a mathematically straightforward procedure because of the definition of random increments in continuous time. For details we refer the reader to the book by van Kampen [2].

2.2 Master equation and Fokker-Planck equation

Notice that according to (19) the probability density $\Psi(y,t)$ (24) satisfies

$$\Psi(y, t+\tau) = \frac{1}{2\pi}\int d\alpha\, \langle\, \mathrm{e}^{i\alpha(x(t)+\xi(t)-y)} \,\rangle \tag{33}$$

where we have again used the integral representation of the δ-function. Since the random displacement $\xi(t)$ is independent of the position $x(t)$ at time t the average may be performed separately, i.e., $\langle\, \mathrm{e}^{i\alpha(x(t)+\xi(t)-y)}\,\rangle = \langle\, \mathrm{e}^{i\alpha x(t)}\,\rangle\langle\, \mathrm{e}^{i\alpha\xi(t)}\,\rangle\langle\, \mathrm{e}^{-i\alpha y}\,\rangle$. On the other hand, for a Gaussian distribution of random forces $\langle\, \mathrm{e}^{i\alpha\xi(t)}\,\rangle = \mathrm{e}^{-\alpha^2\sigma^2/2}$. Finally, we use the Fourier transform of the Gaussian

$$\mathrm{e}^{-\alpha^2\sigma^2/2} = \frac{1}{\sqrt{2\pi}\sigma}\int dz \mathrm{e}^{-i\alpha z}\langle\, \mathrm{e}^{-z^2/2\sigma^2}\,\rangle \tag{34}$$

to obtain the *master equation*

$$\Psi(y,t+\tau) = \int dz\, p(y,z)\Psi(z,t) \tag{35}$$

which is the evolution equation satisfied by the probability density. Here $p(y,z)$ is the transition probability density for moving from point z to point y in the time interval τ. For free Brownian motion we find directly from the derivation of the master equation that

$$p(y,z) = \frac{1}{\sqrt{2\pi}\sigma}\mathrm{e}^{-(y-z)^2/2\sigma^2}. \tag{36}$$

Notice that because of conservation of probability for any process the transition probability density must satisfy

$$\int dy\, p(y,z) = 1. \tag{37}$$

This relation simply states that the particle must move somewhere with probability one. The master equation (35) may be generalized to several coordinates (including momentum variables and other internal degrees of freedom) and represents yet another way of mathematically describing a stochastic process. It is a deterministic equation for the probability density and there is no problem in passing to a continuous-time description by using a Taylor expansion in τ. To this end one introduces transition rates $w = p/\tau$ which are transition probabilities per time unit and writes

$$p(y,z) = \left(1 - \tau\int dx\, w(x,z)\tau\right)\delta(y-z) + w(y,z)\tau. \tag{38}$$

The first term in this decomposition represents the sojourn probability density of the random walker and the second term the probability density of moving from z to y. Inserting this into the master equation (35) yields

$$\Psi(y,t+\tau) = \Psi(y,t) + \left[\int dz\, w(y,z)\Psi(z,t) - \int dz\, w(z,y)\Psi(y,t)\right]\tau \tag{39}$$

The first term in the brackets represents the gain in probability of finding the particle in y by moving there from some point z whereas the second term is a loss term resulting from the motion away from y to z (Fig. 3). Taking the continuous time limit $\tau \to 0$ and using Taylor expansion then gives

$$\frac{d}{dt}\Psi(y,t) = \int dz\, w(y,z)\Psi(z,t) - \int dz\, w(z,y)\Psi(y,t). \tag{40}$$

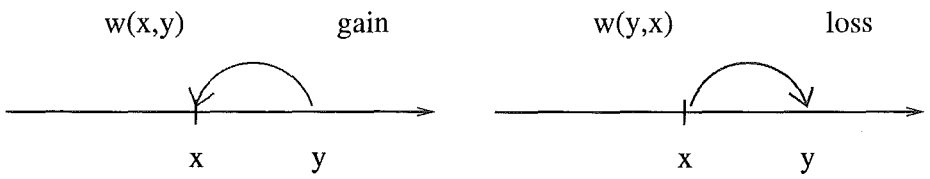


Fig. 3: *Gain in probability of finding the Brownian particle by a jump from an arbitrary point y to point x with rate $w(y,x)$ (left) and loss of probability by moving away to some arbitrary point (right).*

This is the generic form of the master equation for stochastic processes defined in continuous time.

To make contact with the considerations in the first section of this lecture we follow Planck and assume that only small jumps occur, i.e., w is sharply peaked around $r \equiv y - z = 0$. Moreover we assume that both w and Ψ vary only slowly with position. Taylor expansion up to second order in the jump distance r then leads to the Fokker-Planck equation

$$\frac{d}{dt}\Psi(y,t) = \frac{1}{2}\frac{\partial^2}{\partial y^2}a_2(y)\Psi - \frac{\partial}{\partial y}a_1(y)\Psi. \tag{41}$$

with the moments of the jump distribution

$$a_n(y) = \int dz\, z^n w(y,z) \tag{42}$$

By regarding the in principle completely general variable y as space coordinate (as in fact we did all the time) rather than a velocity or some other generalized coordinate (as one could equally well do, depending on the process that one studies) one readily recognizes the Smoluchowski equation (13). The derivation via the master equation provides a relation between the parameters of the Smoluchowski equation with the moments of the transition rate w.

Exercise:

For illustration it is instructive to explicitly study the motion of a free particle in a box of length L in the interval from $-L/2$ up to $L/2$. The Langevin approach would require some specific instruction on how to treat random displacements close to the hard walls of the box. In the Fokker-Planck or Smoluchovski approach one has to solve the diffusion equation (3) for the probability density Ψ with boundary condition $\Psi(\pm L/2, t) = 0$ for all times. This is entirely analogous to the solution of the Schrödinger equation of a free particle confined to a box (appendix A). One immediately finds the equilibrium solution $\Psi^*(x) = 1/L$ inside the box and $\Psi^*(x) = 0$ outside. To solve for the initial value problem with some initial distribution $\Psi_0(x)$ use the cosine transform rather than the Fourier transform. Once the solution is obtained in explicit form show that for times large compared to $\tau^* = L^2/D$ the system is practically in equilibrium. Finally imagine what you would observe for single particle (rather than many identical particles) for times $t \gg \tau^*$.

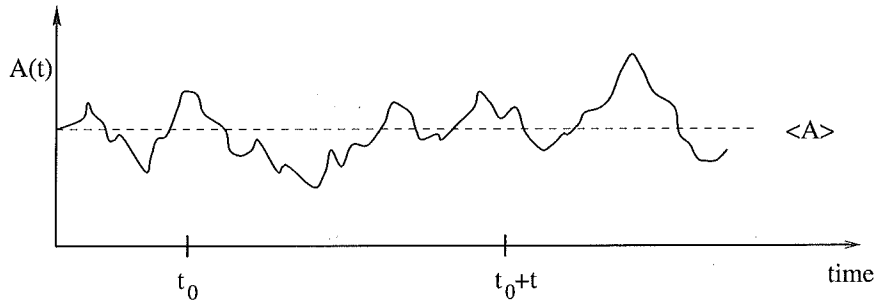


Fig. 4: *Random equilibrium time series for some observable A. Two measurements at times t_0 and $t_0 + t$ yield different results.*

3 Dynamical correlation functions and linear response theory

3.1 Time correlation functions in equilibrium

So far we have used the notion of correlations in an intuitive way when we stressed that the time scale τ should be large enough so that correlations between collisions have decayed. Later we have required also the random displacements to be uncorrelated so that the central limit theorem could be used. These are two of many instances where correlations between random events are important. To give the notion correlation a precise meaning consider the measurement of some quantity A in the equilibrium state of a system at time t. The quantity A could be a position, velocity, energy or any other physical quantity. Because of thermal fluctuations even in equilibrium one would not measure exactly the same value of A at all times but rather a random time series which fluctuates around the equilibrium mean $\langle A \rangle$. Only this mean would not change in time if the system is in equilibrium (Fig. 4).
Let us now make two measurements at times t_0 and $t_0 + t$ and take an average

$$G_{AA}(t) \equiv \langle A(t_0 + t)A(t_0) \rangle \tag{43}$$

of the product of both measurements. This average is understood as an average over many realizations of the experiment, with two measurement taken after the same time interval t. Since the system is in equilibrium this function will not depend on the initial time t_0 which we therefore shall set to 0. For sufficiently small elapsed time t the quantity $G_{AA}(t)$ with not simply be equal to the product $\langle A \rangle^2$ of the two (identical) equilibrium values of A. Instead G_{AA} depends in some nontrivial manner on t and will usually only after some time approach $\langle A \rangle^2$. We therefore define the time-dependent equilibrium correlation function

$$C_{AA}(t) = \langle (A(t) - \langle A \rangle)(A(0) - \langle A \rangle) \rangle = G_{AA}(t) - \langle A \rangle^2. \tag{44}$$

If this function vanishes the two quantities $A(t)$ and $A(0)$ respectively are statistically independent, i.e., uncorrelated. A nonvanishing correlation function provides a well-defined measure how strongly the result of the second measurement depends on the first.

The quantity C_{AA} is sometimes also called autocorrelation if a distinction is to be made to a cross correlation function

$$C_{AB}(t) = \langle\,(A(t) - \langle\,A\,\rangle)(B(0) - \langle\,B\,\rangle)\,\rangle = G_{AB}(t) - \langle\,A\,\rangle\langle\,B\,\rangle \tag{45}$$

between two different observables A and B. These observables may also be local quantities such as local densities. In this case one has a space-time correlation function

$$C_{AB}(\vec{x},t;\vec{y},0) = \langle\,(A(\vec{x},t) - \langle\,A(\vec{x})\,\rangle)(B(\vec{y},0) - \langle\,B(\vec{y})\,\rangle)\,\rangle = G_{AB}(t) - \langle\,A(\vec{x})\,\rangle\langle\,B(\vec{y})\,\rangle \tag{46}$$

In a scattering experiment one usually measures the Fourier transform of space-dependent correlation functions.

There are some generic forms how a correlation function decays at late times which occur very frequently in many different systems. In many cases one observes a decay of the form

$$C(t) \propto \mathrm{e}^{-(t/t^*)^\beta} \tag{47}$$

Here the relaxation time t^* is a crossover time scale far beyond which the correlation may be regarded as having disappeared. The Kohlrausch exponent β can take various values. In glasses exponents between 0.5 and 1 are common. The exponent 1 corresponds to simple exponential. Also sums of exponentials with several relaxation times are observed, but of course at late times only the exponential with the longest relaxation time will make a significant contribution to the correlation function. A special case is an algebraic decay of the form

$$C(t) \propto t^{-\alpha} \tag{48}$$

Here there is no relaxation time beyond which the correlation may considered small. Such behavior is a signature of dynamical scale invariance characterizing systems at a critical point of a second-order phase transition. Therefore α is referred to as critical exponent. Remarkably, many microscopically very different systems may have the same set of critical exponents. This fascinating phenomenon is referred to as universality.

Given the Smoluchowski equation one can compute time correlation functions in terms of the propagator $F(x,x';t)$ of the system. The propagator is the probability of moving from point x' at time 0 to point x at time t. (Of course x could represent a vector or a collection of generalized coordinates $\{x\}$.) Therefore it satisfies the Smoluchowski equation with a delta-function initial condition. Since for the equilibrium correlation function the initial distribution is the equilibrium distribution $\Psi^* \propto \exp(-U/kT)$ one has

$$G_{AB}(t) = \int dx \int dx'\, A(x)B(x')F(x,x';t)\Psi^*(x') \tag{49}$$

The problem of calculating the correlation function is therefore shuffled to the problem of obtaining the propagator for a given Smoluchowski equation. We remark, however, that for some problems the time derivative of G_{AB} or of the correlation function C_{AB} may satisfy a simpler equation that can be treated exactly or by some approximation scheme. An example is given in the next section.

3.2 Fluctuation dissipation theorem

In the discussion of the Einstein relation we made the somewhat vague requirement that external forces be small. We are now in a position to address this issue and clarify the

meaning of small in this context. Consider the response of a system in equilibrium to some change in an external control parameter h. This parameter could e.g. be the temperature or an electric field. To be specific, we measure the time-dependent average $\langle A(t) \rangle_h$ of some quantity A for a given function $h(t)$. By small h we mean that a Taylor expansion of $\langle A(t) \rangle_h$ to first order in h is sufficient to accurately describe our measurement. We are therefore allowed to write

$$\langle A(t) \rangle_h = \langle A(t) \rangle_0 + \int_{-\infty}^{t} dt' \mu(t-t') h(t') \tag{50}$$

for a system that was in equilibrium at time $-\infty$ and then has suffered the influence of the perturbation $h(t)$. The quantity μ is called the response function. Considering only the first order in h is called linear response theory.
The theoretical problem is the calculation of the response function. In many experimental scenarios an external potential $U(x,t)$ is changed in the form $U(x,t) = h(t)B(x)$ where B is the quantity conjugate to the field h. In this case one has

$$\mu(t) = -\frac{1}{kT}\frac{d}{dt} C_{AB}(t) \tag{51}$$

for the response of a quantity A to the change in the field with conjugate quantity B. This central result is known as *fluctuation dissipation theorem* (FDT). It relates the response of a system to a weak external perturbation to the fluctutions of the systems in the absence of the perturbation. A special case is the Einstein relation which relates the mobility (governing the response to a weak force through the velocity) to the diffusion coefficient (describing fluctuations in the absence of the force).
For a derivation of the FDT consider a constant field of small strength h which is switched of at time $t = 0$. Then

$$\langle A(t) \rangle_h - \langle A(t) \rangle_0 = h \int_{-\infty}^{0} dt' \mu(t-t') = h \int_{t}^{\infty} dt' \mu(t') \equiv h\alpha(t). \tag{52}$$

Here $\alpha(t)$ is called the relaxation function because it describes the relaxation of the quantity A from its "old" equilibrium value (with field h) to its "new" equilibrium value (with $h = 0$). On the other hand, by definition,

$$\langle A(t) \rangle_h = \int dx A(x) \Psi(x,t) \tag{53}$$

where $\Psi(x,t)$ is the probability density evolving after switching of the field which is given by

$$\Psi(x,t) = \int dx' F_0(x,x';t) \Psi(x',0) \tag{54}$$

To understand this expression it is crucial to notice that the system evolves *in the absence* of the field to its new equilibrium state. Therefore (54) contains the propagator for vanishing field. On the other hand, this time evolution starts at $t = 0$ when the system still was in its equilibrium state with field. Therefore $\Psi(x',0) = \Psi_h^*(x')$ is the equilibrium distribution in the presence of the field with total potential energy $U(x) = U_0(x) + hB(x)$. Its exact value

$$\Psi_h^*(x') = \frac{\mathrm{e}^{-(U_0(x)+hB(x))/kT}}{\int dx\, \mathrm{e}^{-(U_0(x)+hB(x))/kT}} \tag{55}$$

is not of direct interest since we consider only the first order term in h for the study of the response. Hence we expand (55) to first order in h to obtain

$$\Psi_h^*(x') = \Psi_0^*(x') \left[1 + \frac{h}{kT}(B(x) - \langle B \rangle_0)\right]. \tag{56}$$

Using (49) then leads to

$$\alpha(t) = \frac{1}{kT} C_{AB}(t) \tag{57}$$

and by taking the time derivative to the FDT (51). We stress that the explicit form of the Smoluchowski equation has not been used. Indeed, The FDT applies to any equilibrium system governed by some master equation.
A similar relation may be obtained by considering the situation where some field is switched on at time $t = 0$. This defines a second relaxation function

$$\beta(t) = \int_0^t dt' \mu(t') \tag{58}$$

in terms of the response function. If the observable is identical with the conjugate variable the FDT may be written in the simple form

$$\beta(t) = \frac{1}{2kT} \langle (A(t) - A(0))^2 \rangle. \tag{59}$$

As an application we briefly show how the Einstein relation follows from the FDT. The observable A is the position x of the particle. The field h is a force F, the conjugate quantity of which is x itself (since the change in potential energy is $U - U_0 = Fx$). Using (59) the FDT can be expressed in terms of the mean sqare displacement $\langle (x(t) - x(0))^2 \rangle = 2Dt$ in which the diffusion coefficient enters by definition. Hence

$$\beta(t) = \frac{1}{2kT} \langle (x(t) - x(0))^2 \rangle = \frac{Dt}{kT} \tag{60}$$

On the other hand the response $F\beta(t) = vt$ is the drift of the particle with velocity $v = F/\zeta$. Hence

$$\beta(t) = t/\zeta \tag{61}$$

which together with (60) gives the Einstein relation (12).

4 Brownian motion in a potential

So far our discussion was rather general. The two simplest external potential which are of physical interest are the linear potential corresponding to the gravitational force or to the force on a charged particle in a constant electric field and the harmonic potential not only encountered in a spring, but also as a lowest order approximation to a complicated real system in the neighborhood of a local minimum in the potential energy (Fig. 5).

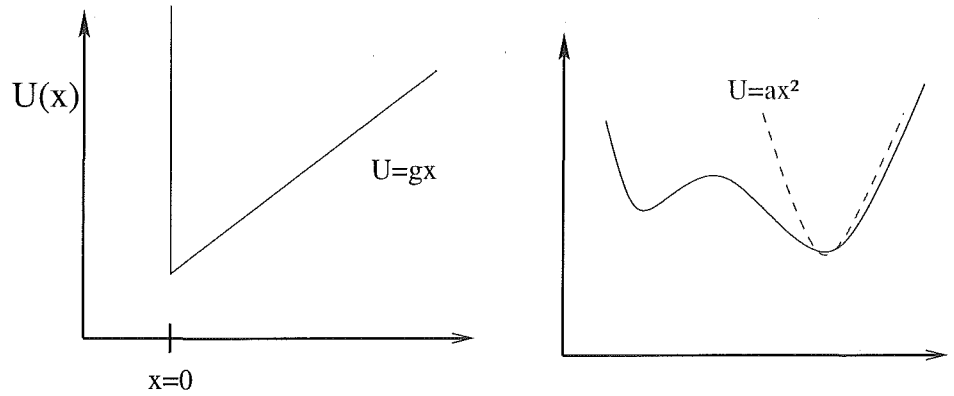


Fig. 5: *Prototypical potentials for a Brownian particle. The linear potential corresponds e.g. to a gravitational force where $x = 0$ (infinite energy) represents the bottom of the container (left). The harmonic potential (right) is shown here as an approximation to a complicated potential in the vicinity of a local minimum.*

4.1 Linear potential

Consider a gravitational force with potential energy $U = gx$. Following the considerations in the first section this gives rise to the Smoluchowski equation

$$\frac{\partial \Psi}{\partial t} = D\frac{\partial^2}{\partial x^2}\Psi + \frac{g}{\zeta}\frac{\partial}{\partial x}\Psi. \tag{62}$$

This corresponds to a probability flux

$$j = D\frac{\partial}{\partial x}\Psi + \frac{g}{\zeta}\Psi. \tag{63}$$

How the particle behaves clearly depends on whether it is far away from the boundaries of the system (e.g. the bottom of a test tube) where the gravitational potential is replaced by the infinite potential barrier of the walls of the container in which the particle moves or whether it is far away from any boundary. Let first consider the second scenario.
We rewrite (62) by using a new coordinate x' obtained from the Galilei transformation $x' = x + vt$. Choosing $v = g/\zeta$ we get

$$\frac{\partial \Psi}{\partial t} = D\frac{\partial^2}{\partial (x')^2}\Psi. \tag{64}$$

The force term is transformed away, implying the intuitively not very surprising result that in a coordinate frame moving with the avarage speed of the particle this particle just performs ordinary Brownian motion.
What happens if the particles reaches the bottom of the container? We cannot perform the Galilei transformation because the presence of the hard wall breaks translational invariance. Let us choose the position of the boundary at $x = 0$. In equilibrium the flux (63) vanishes and hence the equilibrium probability density $\Psi^*(x)$ of finding a particle at position $x > 0$ is given by the solution of the ordinary first-order differential equation

$$0 = D\frac{d}{dx}\Psi^* + \frac{g}{\zeta}\Psi^*. \tag{65}$$

Hence

$$\Psi^*(x) \propto \exp(-x/\xi) \tag{66}$$

with the localization length

$$\xi = g/(D\zeta). \tag{67}$$

The constant of proportionality follows from the condition $\int dx \Psi^*(x) = 1$ of normalization of the probability. The exponential decrease of probability (and hence in particle concentration) is well-known from the atmospheric pressure even though air molecules are not really Brownian particles. Of course, we could have guessed this result straight away since we know from thermodynamics that $\Psi^*(x) \propto \exp(-U/(kT))$ with $U = gx$ which yields (66). With the Einstein relation (12) one recovers (67).
Exercise: The calculation of dynamical properties is only slightly more complicated than for a free particle. Use the techniques of quantum mechanics to calculate the propagator and then the equilibrium correlation function $\langle\, x(t)x(O)\,\rangle$,

4.2 Harmonic potential

Consider now

$$U = \frac{1}{2}ax^2 \tag{68}$$

with the associated Smoluchowski equation

$$\frac{\partial \Psi}{\partial t} = D\frac{\partial^2}{\partial x^2}\Psi + \frac{a}{\zeta}\frac{\partial}{\partial x}x\Psi. \tag{69}$$

and probability flux

$$j = D\frac{\partial}{\partial x}\Psi + \frac{a}{\zeta}x\Psi. \tag{70}$$

The equilibrium distribution, i.e., the solution of (70) with $j = 0$ again follows from thermodynamics, the Einstein relation and the normalization condition for the probability. One has

$$\Psi^*(x) = \sqrt{\frac{a}{2\pi kT}}\exp -\frac{ax^2}{2kT}. \tag{71}$$

This is a Gaussian distribution with mean zero and a variance given by the spring constant a and the temperature T.
In order to calculate the correlation function $\langle\, x(t)x(0)\,\rangle$ one could solve the Smoluchowski equation (again borrowing from quantum mechanics) and use (49). However, it is easier to consider the time derivative of the correlation function and insert the Smoluchowski equation into (49). Instead of solving it one can integrate (49) by parts to find

$$\frac{d}{dt}\langle\, x(t)x(O)\,\rangle = -\frac{1}{\tau}\langle\, x(t)x(O)\,\rangle \tag{72}$$

with $\tau = \zeta/a$. (This is not to be confused with the time step used in the previous section!) This is an ordinary first-order differential equation satisfied by the correlation function, an enormous simplication compared to solving Smoluchowski equation. One immediately finds $\langle\, x(t)x(O)\,\rangle \propto \exp(-t/\tau)$. This shows that τ is a relaxation time, for times large compared to τ the measurements of the position become statistically independent. The

factor of proportionality follows from the initial value of the correlation function at $t = 0$. Since at $t = 0$ the system is in its equilibrium state the value of $\langle x(t)x(O)\rangle$ for $t = 0$ is just the equilibrium variance of (71). Hence we obtain

$$\langle x(t)x(O)\rangle = \frac{kT}{a}\mathrm{e}^{-t/\tau}. \tag{73}$$

It is interesting to note that (72) holds also for initial distributions which are not the equilibrium distribution. Therefore the correlation function decays exponentially with the same relaxation time even if the first measurement at $t = 0$ is averaged over an initial state far from equilibrium. For an arbitrary nonequilibrium initial distribution $\Psi_0(x)$ the moments

$$A_n(t) \equiv \langle x^n(t)\rangle = \int dx \int dx'\, x^n F(x,x';t)\Psi_0(x') \tag{74}$$

of the random walk distribution can be calculated in the same way. Taking the time derivative and integrating by parts yields the set of equations

$$\frac{d}{dt}A_n(t) = -\frac{n}{\tau}A_n + n(n-1)DA_{n-2} \tag{75}$$

which can be solved recursively. Given A_{n-2} this equation can be integrated and one finds

$$A_n(t) = \mathrm{e}^{-nt/\tau}\left(A_n(0) + n(n-1)D\int_0^t dt'\mathrm{e}^{nt'/\tau}A_{n-2}(t')\right). \tag{76}$$

Iterating this expression gives an explicit expression in terms of $A_0 = 1$ (for even moments) or the mean position $A_1(t) = A_1(0)\mathrm{e}^{-t/\tau}$ (for odd moments) respectively. This is an instant of the type mentioned above where the time derivative of an average value or a correlation function satisfies an exactly solvable closed set of equations which is much easier to analyze than to calculate the propagator.

In particular, we find that there is not just a single relaxation time characterizing the relaxation of the process towards equilibrium or characterizing the loss of correlations in equilibrium respectively. Instead there is a whole series of relaxation times

$$\tau_n = \tau/n. \tag{77}$$

It only happens that in the relaxation of mean position A_1 only the longest relaxation time appears. The relaxation of the variance A_2 is governed by the second largest relaxation time τ_2. In the third moment two relaxation times appear, τ_1 and τ_3. We learn from this example that if the measurement of some physical quantity is characterized by a single relaxation time then it does *not* follow that the system as a whole is characterized by only a single relaxation time. A different physical quantity, even if closely related, may have other relaxation times.

5 Smoluchowski equation for hydrodynamic interaction

In the previous section we have considered some paradigmatic types of interaction with external potentials. We now consider interactions between particles. Rather than adding

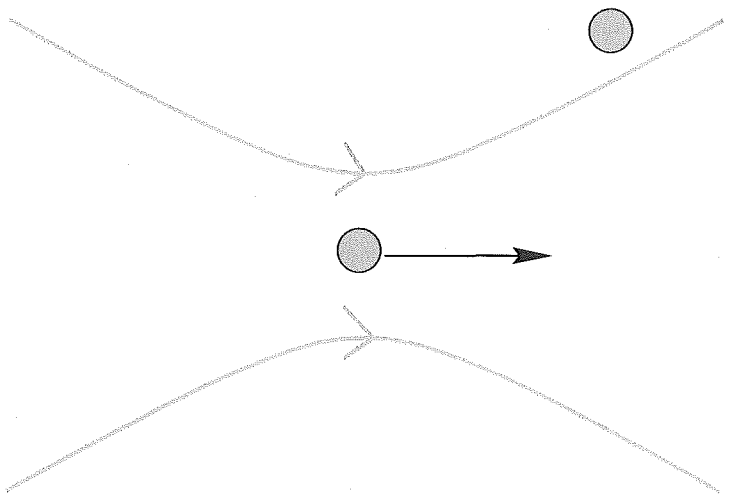


Fig. 6: *Brownian particles in a fluid. The force acting on one particle creates a velocity field in the fluid which drags the other particle and vice versa.*

a force term derived from some external potential to the free Smoluchowski equation this amounts to having to determine the mobility matrix in the general Smoluchowski equation (18) from the interaction between particles.

For simplicity we restrict ourselves to spherical particles with no internal degrees of freedom. However, unlike before, we now consider concentrations sufficiently large to make the suppression of interactions unrealistic. We do not assume any direct interaction e.g. via electrostatic potentials but only the hydrodynamic interaction mediated by the molecules of the fluid. Intuitively this interaction can be understood by the flow field generated by the motion of one particle. This flow field will exert a force on other particles and hence modify their motion. This will generate some new flow which will influence the motion of first and so on (Fig. 6).

For a quantitative analysis one needs some input from hydrodynamics which provides the theoretical foundation for the hydrodynamic interaction between particles immersed in a fluid. We shall restrict ourselves to low Reynolds numbers which one usually encounters in problems involving Brownian motion. Let us denote the force acting on particle n by $\vec{F}_n$ and its velocity by $\vec{v}_n$. It is clear that here it makes no sense to consider a one-dimensional scenario, so we have to work with vectors. Hence the mobility matrix $\mathbf{H}$ defined by the force-velocity relation

$$\vec{v}_n = \sum_m \mathbf{H}_{nm} \vec{F}_m \tag{78}$$

has tensors as matrix elements $\mathbf{H}_{nm}$. For noninteracting particles one would simply have $\mathbf{H}_{nm} = 1/\zeta \mathbb{1} \delta_{nm}$ with the usual friction coefficient $\zeta = 6\pi\eta a$ for particles with diameter a in a fluid with viscosity η and the 3x3 unit matrix $\mathbb{1}$ at position n, m of the mobility matrix.

In order to calculate $\mathbf{H}$ for real, interacting particles one needs to know the velocity field $\vec{v}(\vec{r})$ generated by the motion of all the particles as it is this velocity field which mediates

the interaction. In an incompressible fluid it satisfies the condition

$$\frac{\partial}{\partial r_\alpha} v_\alpha = 0 \tag{79}$$

for the components of the vector $\vec{v}$. Here we have used the summation convention where one takes a sum over equal indices. For an exact calculation one would have to solve the Navier-Stokes equation for fluid dynamics. In practice, however, this is not possible and has to resort to approximations. For low Reynolds number we neglect the inertia force of the fluid and one therefore has the relation

$$\frac{\partial}{\partial r_\beta} \sigma_{\alpha\beta} = -g_\alpha(\vec{r}) \tag{80}$$

between the stress tensor $\sigma_{\alpha\beta}$ and the force g_α acting on a fluid segment. The stress tensor is given by

$$\sigma_{\alpha\beta} = \eta \left(\frac{\partial v_\beta}{\partial r_\alpha} + \frac{\partial v_\alpha}{\partial r_\beta} \right) - P\delta_{\alpha\beta} \tag{81}$$

where P is the pressure. This leads to the Stokes approximation

$$\eta \frac{\partial^2}{\partial r_\beta^2} v_\alpha - \frac{\partial}{\partial r_\alpha} P = -g_\alpha \tag{82}$$

for the flow field.
In order to calculate the flow field one has to specify the force $\vec{g}$. As a further approximation we consider the particles as point particles at positions $\vec{R}_n$. Only the fluid on the "surface" of the "point" particles (which is assumed to move with the same velocity as the particles) experiences a force. Therefore

$$\vec{g}(\vec{r}) = \sum_n \vec{F} \delta(\vec{r} - \vec{R}_n) \tag{83}$$

and (82) becomes

$$\eta \vec{\nabla}^2 \vec{v} - \vec{\nabla} P = -\sum_n \vec{F}_n \delta(\vec{r} - \vec{R}_n). \tag{84}$$

After Fourier transformation one obtains force velocity relation

$$\vec{v}(\vec{r}) = \sum_n \mathbf{H}(\vec{r} - \vec{R}_n) \vec{F}_n \tag{85}$$

with the Oseen tensor

$$\mathbf{H}(\vec{r}) = \frac{1}{8\pi\eta r} \left(\mathbb{1} + \hat{\vec{r}}\hat{\vec{r}} \right]. \tag{86}$$

Here $\hat{\vec{r}}$ is the unit vector parallel to $\vec{r}$. The term in the brackets is a projector arising from the condition of absence of a divergence in the fluid.
Since the particles move with the same velocity as the fluid on their surface we have $\vec{v}_n = \vec{v}(\vec{R}_n)$ and therefore the desired force-velocity relation

$$\vec{v}_n = \sum_m \mathbf{H}(\vec{R}_n - \vec{R}_m) \vec{F}_m \tag{87}$$

with the mobility matrix

$$\mathbf{H}_{nm} = \mathbf{H}(\vec{R}_n - \vec{R}_m) \tag{88}$$

We remark that this is derived for point particles. A treatment for particles with finite diameter is much more difficult and possible only as a perturbative expansion. Notice that for $n = m$ the mobility matrix derived here has an unphysical divergence. However, since the diagonal element represents the mobility of particle n one sets

$$\mathbf{H}_{nn} = \frac{1}{\zeta}\mathbb{1}. \tag{89}$$

With (88) and (89) we have achieved our goal of deriving an approximate mobility matrix and can write down the Smoluchowski equation

$$\frac{\partial}{\partial t}\Psi = \sum_{n,m} \frac{\partial}{\partial \vec{R}_n} \mathbf{H}_{nm} \left(kT \frac{\partial \Psi}{\partial \vec{R}_m} + \frac{\partial U}{\partial \vec{R}_m} \Psi \right) \tag{90}$$

for particles with hydrodynamic interaction and interaction with an external force with potential energy U.

We recall the basic idea of Einstein and Smoluchowski of dropping the process of random velocity changes in favor of random changes in the position of particles occuring after many indepedent collision and changes in the velocity. This is in contrast to the entirely general master equation approach. However, the Smoluchowski equation written in the form (90) is rather general. For particles with e.g. rotational degrees of freedom it is formally essentially identical. The problem to be solved for a specific system is the derivation of the mobility matrix from the interactions and the solution of the equation. For both steps approximation schemes are required which vary from problem to problem. The derivation of the Oseen tensor is one such approximation devised for Brownian motion in an incompressible fluid with low Reynolds number. The solution of (90) is a task that is not the subject of this lecture. Exactly solvable problems involving interacting particles are relatively rare and require advanced solution techniques adapted from related quantum mechanical systems [3].

It is the intention of this lecture to provide an introduction to basic concepts that are not research topics themselves but that have become standard in current statistical mechanics and soft matter research. While not really new these concepts are yet too advanced to appear in a basic physics curriculum. The brief list of references given below therefore points to textbooks rather than research papers. Ref. [1] provides the theoretical framework for the Smoluchowski equation used also here, while Ref. [2] is a standard introduction into the theory and application of stochastic processes. It is recommended for further reading on the relation between the various approaches to random processes and on the assumptions underlying their application. Finally, Ref. [3] describes exactly solvable interacting particle systems using quantum mechanical techniques for treating the master equation and gives an introduction into current research problems in statistical mechanics.

Appendices

Solution of the diffusion equation

The solution of the diffusion equation for a given initial concentration or probability profile is most easily performed by Fourier transformation. One writes the solution $c(x,t)$ to be calculated from $c_0(x) \equiv c(x,0)$ in terms of its Fourier components $\hat{c}(k,t)$

$$c(x,t) = \frac{1}{2\pi} \int dk\, \mathrm{e}^{-ikx} \hat{c}(k,t) \tag{91}$$

Taking the time derivative and comparing with the right hand side of the diffusion equation leaves an ordinary differential equation for the Fourier components

$$\frac{d}{dt}\hat{c}(k,t) = -Dk^2 \hat{c}(k,t) \tag{92}$$

from which we immediately find

$$\hat{c}(k,t) = \hat{c}_0(k)\mathrm{e}^{-Dk^2 t} \tag{93}$$

This solution involves the Fourier transform

$$\hat{c}_0(k) = \int dx\, \mathrm{e}^{ikx} c_0(x) \tag{94}$$

of the initial profile. Putting everything together yields

$$c(x,t) = \frac{1}{2\pi} \int dk \int dy\, c_0(y) \mathrm{e}^{-ik(x-y)} \mathrm{e}^{-Dk^2 t} \tag{95}$$

In particular, for a δ-peaked inital profile $c_0(y) = \delta(y-z)$ one gets the Gaussian propagator

$$c(x,t) = \frac{1}{2\pi} \int dk\, \mathrm{e}^{-ik(x-z)} \mathrm{e}^{-Dk^2 t} \tag{96}$$

$$= \frac{1}{\sqrt{4\pi D t}} \mathrm{e}^{-(x-z)^2/(4Dt)} \tag{97}$$

The second expression - which is the well-known Fourier transform of $\exp(-Dk^2 t)$ - can be used to also write (95) in terms of the Gaussian propagator.
For problems involving a boundary one proceeds as in the solution of the quantum mechanical Schrödinger equation and makes the ansatz

$$c(x,t) = \frac{1}{2\pi} \int dk\, \mathrm{e}^{-Dk^2 t} \left(a_0(k)\mathrm{e}^{-ikx} + b_0(k)\mathrm{e}^{ikx} \right) \tag{98}$$

with the reflected wave $b_0(k)\mathrm{e}^{ikx}$. The exponential $\exp(-Dk^2 t)$ ensures that the diffusion equation is satisfied. The functions a and b resp. are determined by the boundary condition and initial profile. Notice that for $a = b$ one has the cosine transform. If one has two hard walls as boundaries or periodic boundaries not only a and b are fixed, but also the allowed range of Fourier components k will be constrained to discrete values. In this case the integrals have to replaced by sums.

Quantum mechanical formalism for the Smoluchowski equation

The Smoluchowski equation is a linear equation

$$\frac{d}{dt}\Psi = L\Psi \tag{99}$$

with a differential operator L determined by the specific problem to be solved. Formally this is an equation like the Schrödinger equation in imaginary time and as in quantum mechanics the solution may be formally written

$$\Psi(x,t) = \mathrm{e}^{Lt}\Psi(x,0) \tag{100}$$

in terms of the initial distribution $\Psi(x,0) \equiv \Psi_0(x)$. In a Hilbert space notation one introduces vectors

$$|\,\Psi(t)\,\rangle = \int dx\, \Psi(x,t)|\,x\,\rangle \tag{101}$$

where the basis vectors $|\,x\,\rangle$ and their duals $\langle\, x\,|$ satisfy the orthogonality relation

$$\langle\, x\,|\,x'\,\rangle = \delta(x-x') \tag{102}$$

In this notation one may write (2) in the form

$$|\,\Psi(t)\,\rangle = \mathrm{e}^{Lt}|\,\Psi(0)\,\rangle \tag{103}$$

where L is now understood as a matrix and the vector $|\,\Psi(t)\,\rangle$ is a time-dependent solution of the Smoluchowski equation in the "Schrödinger" representation. With the properties of the scalar product one may recover the function $\Psi(x,t)$ through the relation

$$\langle\, x\,|\,\Psi(t)\,\rangle = \int dy\, \Psi(y,t)\langle\, x\,|\,y\,\rangle = \Psi(x,t) \tag{104}$$

The propagator $F(x,x';t)$ for a transition from x' at time $t=0$ to x at time t takes the simple and intuitive form

$$F(x,x';t) = \langle\, x\,|\exp(Lt)|\,x'\,\rangle. \tag{105}$$

Conservation of probability can be expressed by introducing the summation vector

$$\langle\, s\,| = \int dx\langle\, x\,|. \tag{106}$$

It has the property that

$$\langle\, s\,|\,\Psi(t)\,\rangle = \int dx\Psi(x,t) \tag{107}$$

is time-independent. To prove this notice that L can always be written as $L = \partial/(\partial x)J$ with the conserved current J. One then has

$$\begin{aligned}\frac{d}{dt}\langle\, s\,|\,\Psi(t)\,\rangle &= \frac{d}{dt}\langle\, s\,|\mathrm{e}^{Lt}|\,\Psi(0)\,\rangle \\ &= \langle\, s\,|L|\,\Psi(t)\,\rangle \\ &= 0\end{aligned} \tag{108}$$

The last equation follows from applying $L = \partial/(\partial x)J$ to the *left* on the constant summation vector which gives zero because of the space derivative on the left of L. The additional requirement $\langle s \,|\, \Psi(t) \rangle = 1$ (because Ψ is a probability density) is a normalization condition on the vector Ψ which is different from the quantum mechanical requirement $\langle \Psi \,|\, \Psi \rangle = 1$ for the wave function. This is because the quantum mechanical wave function is not a probability by itself, but a complex valued probability amplitude.
This formal approach becomes useful when dealing with correlation functions. E.g. using the properties of the scalar product (49) may be written

$$\langle x(t)x(0) \rangle = \langle s \,|Xe^{Lt}X|\, \Psi^* \rangle \tag{109}$$

where X is the diagonal operator

$$X = \int dx x|\, x \rangle\langle x \,| \tag{110}$$

associated with the observable x. Taking the time derivative immediately suggests acting with L to the left rather than actually calculating the propagtor $\langle x \,|\exp(Lt)|\, x' \rangle$. This immediately yields the "equations of motion" for the average values of observables as e.g. Eqs. (75).

References

[1] M. Doi and S.F. Edwards, *The Theory of Polymer Dynamics* (Oxford University press, Oxford, 1986)

[2] N.G. van Kampen, *Stochastic Processes in Physics and Chemistry* (Elsevier, Amsterdam, 1992)

[3] G.M. Schütz, *Exactly solvable models for many-body systems far from equilibrium*, in: Phase Transitions and Critical Phenomena Vol. **19**, eds. C. Domb and J.L. Lebowitz (Academic Press, London, 2000)

C2 Polymer Dynamics

D. Richter
Institut für Festkörperforschung
Forschungszentrum Jülich GmbH

Contents

1 Introduction 2

2 High Resolution Techniques 3

3 Entropy Driven Dynamics – The Rouse Regime 5
3.1 Entropic forces – the Rouse model 5
3.2 Neutron spin echo results 9
3.3 Computer simulation 12

4 Reptation 15
4.1 Experimental observations of chain confinement 18

5 Intermediate Scale Dynamics 24

6 Local Dynamics 26
6.1 Dynamic structure factors 28
6.2 Experimental results 31

7 Summary and Conclusions 35

1 Introduction

In our every day life plastics or polymers play a very important role. Polymeric materials are used, because they are durable, cheaply to produce, easily to process and because they exhibit very versatile and favorable mechanical properties, e.g. depending on temperature or time the same polymer may be viscose, rubber elastic, very tough with high impact strength or even brittle. In the simplest case polymers are long linear chain molecules, build from one repeating unit, the monomer; such polymers are called linear homopolymers.

Since in general rotational isomers may be easily formed at each bond of the chain backbone, long chain polymers possess a very large number of internal degrees of freedom which contribute importantly to the entropic part of the molecules free energy. At length scales somewhat larger than the size of the monomer, the detailed chemical structure of the chain building blocks ceases to be of importance and very general properties determined by the statistical mechanics of the chains prevail, e.g. the conformational entropy bases on the number of possible arrangements of a chain sequence in space. According to the central limit theorem the most probable arrangement is that of a *Gaussian* coil - the polymer chain performs a random walk in space. If pieces of the chain are now stretched an entropic force arises and acts on these stretched segments endeavouring to restore them to the most probable contorted state. Such forces are the basis of rubber elasticity.

This lecture aims to identify general principles of chain motion on a molecular scale which underlie the macroscopic mechanical properties, and presents concepts and experimental results on these motional mechanisms in space and time. Thereby, we restrict ourselves to melts of homopolymers.

Neutron scattering with its space time sensitivity on a molecular and atomic scale unravels the details of the molecular motions in question. Commencing at the scale of the single bond, where movements take place at a pace as in normal liquids, quasielastic neutron scattering (QENS) provides insight into local relaxation processes. At longer length scales first the entropy driven Rouse motion and at even larger distances the effect of entanglement constraints due to the mutual interpenetration of chains comes into the observation range.

The most powerful technique suitable for these investigations, the neutron spin echo spectroscopy (NSE) operates in the time domain and uncovers a time range from about *2ps* to *200ns* and accesses momentum transfers between 0.01Å^{-1} and 3Å^{-1}. The second important high resolution technique is neutron backscattering providing an energy resolution of about $1\mu eV$ and covering a Q-range $0.1 \le Q \le 2\text{Å}^{-1}$. Both techniques will be briefly described in the second chapter.

Coherent quasi- and inelastic neutron scattering reveals the dynamic structure factor $S(Q,t)$ or its Fourier transformed counterpart $S(Q,\omega)$ [1]

$$S(Q,t) = \frac{1}{N} \sum_{ij} \left\langle \exp\left(-i\underline{Q}\underline{r}_j(t)\right) \exp\left(i\underline{Q}\underline{r}_i(0)\right) \right\rangle \qquad (1)$$

where $\underline{r}_j(t)$ and $\underline{r}_i(0)$ are the position vectors of the scatterers at time t and time $t = 0$ respectively, N is the number of scatterers and $\hbar\underline{Q}$ is the momentum transfer during

scattering. The brackets denote the thermal average. $S(Q,t)$ reflects the pair correlation function and relates to the collective properties of a material. In the neutron cross section it is weighted by the average scattering length $\left|\bar{b}\right|^2$.

Incoherent scattering is related to scattering length disorder which may either origin from spin dependent scattering lengths like in the case of hydrogen or from isotope mixtures with different scattering properties. This disorder prevents constructive interference of partial waves scattered at different atoms and reveals the self correlation function. Eq.[1] provides the self correlation function, if in the double sum only terms with $i=j$ are considered. In the cross section $S_{inc}(Q,t)$ is weighted by the average scattering length fluctuations $\left(\left\langle b^2\right\rangle - \left|\bar{b}^2\right|\right)$.

In Gaussian approximation which is widely used for the calculation of neutron dynamic structure factors for polymer dynamics Eq.[1] is approximated by

$$S(Q,t) = \frac{1}{N}\sum_{ij}\exp\left[-\frac{Q^2}{6}\left\langle\left(r_i(t)-r_j(0)\right)^2\right\rangle\right] \qquad (2)$$

This lecture naturally is not able to review exhaustively the contribution of high resolution neutron scattering to the field of polymer melt dynamics, but rather wants in an exemplary way to display important contributions by example.

2 High Resolution Techniques

For the study of the slow dynamics, which is at the origin of the rheological properties of polymers, high resolution neutron techniques are required which are realized by the backscattering and the neutron spin echo spectrometers [2][3].

In order to achieve high energy resolution, one has to consider carefully the very weak neutron flux of a neutron source. While a typical laser provides 10^{22} monochromatic photons per second in a well collimated beam, the total neutron flux of the most powerful research reactor at the ILL in Grenoble is in the order of 10^{15} neutrons /s cm^2. Thus, a fine energy selection immediately reduces the available neutron flux to a point, where experiments are not possible any more. Therefore, high resolution techniques try to decouple intensity and resolution determining elements.

Neutron backscattering exploits the fact that at a scattering angle of $2\theta=180^\circ$ the selected wavelength in a reflection from a crystal depends only to second order on the divergence of the incoming beam. Choosing backreflection from a perfect crystal in combination with relaxed collimation of the neutron beam leads to acceptable intensities and energy resolutions in the order of 10^{-4}.

Fig.1 displays the general layout of the backscattering spectrometer IN10 at the ILL in Grenoble. The neutrons are monochromatized by a perfect silicon crystal mounted on a Doppler drive which similar as in Moessbauer experiments varies the incident energy of the

neutron by Doppler shifting. These monochromatized neutrons are deflected by a graphite crystal and directed towards the sample. The analyzer crystals are mounted on spherical hollowed plates with a radius of curvature such that they focus the reflected neutrons into detectors which are set up behind the sample. In this way a large solid angle is covered on the analyzer side. The typical resolution achieved with this instrument is in the order of 1μeV corresponding to relaxation times in the order of 1ns. Backscattering measures the dynamic structure factor $S(Q,\omega)$ which obtained by Fourier transformation of Eq.[1].

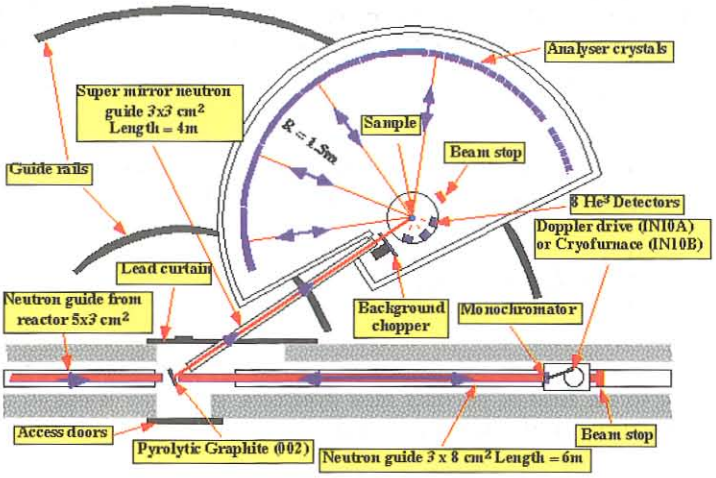


Fig. 1: *Sketch of the backscattering spectrometer IN10 at the ILL reactor.*

While in backscattering the energy transfer at the sample is determined by first measuring the energy of the incident neutron and thereafter that of the scattered neutron and then taking the difference, the unique feature of neutron spin echo (NSE) is its ability to determine energy changes of neutrons during scattering in a direct way. NSE measures the neutron velocities of the incoming and scattered neutrons utilizing the Larmor precession of the neutron spin in an external guide field. Since the neutron spin vector acts like the hand of an internal clock attached to each neutron which stores the result of the velocity measurement on the neutron itself, this measurement is performed for each neutron individually. Therefore, the incoming and outgoing velocities of one and the same neutron can be compared directly and a velocity difference measurement becomes possible. Thus, energy resolution and monochromatization of the primary beam or the proportional neutron intensity are decoupled and an energy resolution of the order of 10^{-5} can be achieved with an incident neutron spectrum of 20% band width.

A basic experimental set up of a NSE spectrometer is shown in Fig.2. A velocity selector together with a polarizer prepares the incoming polarized beam of about 10%-20% bandwidth. The two main magnetic fields before and after the sample are Larmor precession fields, where the neutron spin turns and the neutron time of flight is monitored. The first $\pi/2$-coil starts the Larmor precession, the π-coil after the sample effectively reverses the direction of spin rotation. The final $\pi/2$ coil together with an analyser allows an analysis of the final spin orientation. If the velocity of the neutron does not change upon scattering, then the number of Larmor turns before and after the sample are equal and the final spin state

corresponds to the initial one. If, however, the neutron velocity changes, then the number of turns before and after the sample are different which is detected by the orientation of the final spin state. NSE measures directly the dynamic structure factor $S(Q,t)$ with the time variable being proportional to λ^3HL, where λ is the neutron wavelength, H the guide field and L the length of the field.

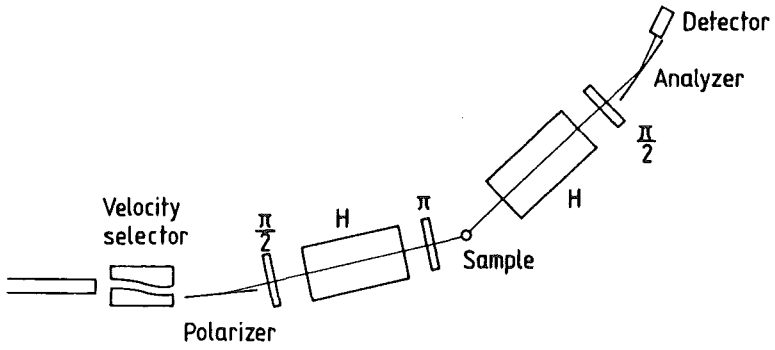


Fig. 2: *Schematic set up of a spin echo spectrometer.*

3 Entropy Driven Dynamics – The Rouse Regime

As outlined in the introduction, the conformational entropy of a chain acts as a resource for restoring forces for chain conformations, deviating from thermal equilibrium. In this Chapter we deal with these entropy driven dynamics in terms of the Rouse model and present NSE results on the space-time evolution of the Rouse relaxation and finally discuss recent molecular dynamic simulations which have been performed in parallel to NSE experiments, in order to explore the limits of the Rouse picture. Here, we like to exemplify the mathematical treatment of chain dynamics problems. Therefore, we detail the description such that it may be followed in all steps. In the discussion of further models later on for details we refer to the relevant literature.

3.1 Entropic forces – the Rouse model

The standard model for chain relaxation, the Rouse model [4][5][6][7]considers a Gaussian chain in a heat bath. The building blocks of such a *Gaussian* chain are segments consisting of several monomers, such that their end to end distance follows a Gaussian distribution. Their conformations are described by vectors $\underline{a}_n = \underline{r}_n - \underline{r}_{n+1}$ along the chain. Thereby $\underline{r}_n$ is the position vector of segment *"n"*. The chain is described by a succession of freely connected segments of length ℓ. We are interested in the motion of these segments on a length scale $\ell < r < R_e$, where $R_e^2 = N\ell^2$ is the end to end distance of the chain and N is the number of segments. The motion is described by a Langevin equation

$$\zeta_0 \frac{d\underline{r}_n}{dt} = \nabla_n F(\{\underline{r}_n\}) + \underline{f}_n(t) \qquad (3)$$

where ζ_0 is the monomeric friction coefficient. For the stochastic force $\underline{f}_n(t)$ we have $\langle \underline{f}_n(t) \rangle = 0$ and $\langle f_{n\alpha}(t) f_{m\beta}(0) \rangle = 2k_B T \ \zeta_0 \delta_{nm} \delta_{\alpha\beta} \delta(t-t')$ α, and β denote the Cartesian components of $\underline{r}$. $F(\{\underline{r}_n\})$ is the free energy of the polymer chain. The force term in Eq.[1] is dominated by the conformational entropy of the chain

$$S = k_B \ell n \ W(\{\underline{r}_n\}) \tag{4}$$

where $W(\{\underline{r}_n\})$ is the probability for a chain conformation $\{\underline{r}_n\}$ of a Gaussian chain of N-segments.

$$W(\{\underline{r}_n\}) = \prod_{i=1}^{N} \left\{ \frac{3}{2\pi \ \ell^2} \right\}^{3/2} \exp \left\{ \frac{-3 \ (\underline{r}_i - \underline{r}_{i-1})^2}{2\ell^2} \right\} \tag{5}$$

Inserting Eq.[3] into Eq.[1] we obtain for the equation of motion

$$\zeta_0 \frac{d\underline{r}_n}{dt} = \frac{3k_B T}{\ell^2} (r_{n+1} - 2\underline{r}_n + r_{n-1}) + \underline{f}_n(t) \tag{6}$$

Regarding the suffix n as a continuous variable Eq.[6] may be rewritten

$$\zeta_0 \frac{\partial \underline{r}_n}{\partial t} = k \frac{\partial^2 \underline{r}_n}{\partial n^2} + \underline{f}_n(t) \tag{7}$$

with the entropy spring constant $k = 3k_B T / \ell^2$. The force free ends require the boundary condition $\left. \frac{\partial \underline{r}_n}{\partial n} \right|_{n=0,N} = 0$. The partial differential equation is solved by cos-Fourier transformation to normal coordinates fulfilling the boundary conditions

$$\underline{x}_p = \frac{1}{N} \int_0^N dn \cos\left(\frac{p\pi n}{N} \right) r_n(t) \tag{8}$$

In normal coordinates the Langevin Eq.[7] becomes

$$\zeta_p \bullet \frac{\partial}{\partial t} \underline{x}_p = -k_p \underline{x}_p + \underline{f}_p \tag{9}$$

where $k_p = \frac{2\pi^2 p^2}{N} k$, $\zeta_p = 2N\zeta_0$. For the stochastic forces we have

$$\langle f_{p\alpha}(t) \ f_{q\beta}(t') \rangle = 2\zeta_p \ k_B T \delta_{pq} \ \delta_{\alpha\beta} \ \delta(t-t') \tag{10}$$

Eq.[9] is readily solved by a single exponential

$$x_p(t) = \frac{1}{\zeta_p} \int_{-\infty}^{t} dt \exp\left((t-t')/\tau_p\right) f(t') \tag{11}$$

where the mode relaxation time τ_p is given by

$$\tau_p = \frac{\zeta_p}{k_p} = \frac{\zeta_0 N^2 \ell^2}{3\pi^2 k_B T p^2} = \frac{\tau_R}{p^2} = \frac{N^2}{W\pi^2 p^2} \tag{12}$$

where τ_R is the Rouse time - the longest time in the relaxations spectrum – and W is the elementary Rouse rate. The correlation function $\langle x_p(t)\, x_p(0)\rangle$ of the normal coordinates is finally obtained by

$$\begin{aligned}\left\langle x_p^\alpha(t)\, x_p^\beta\right\rangle &= \frac{1}{\zeta_p^2} \int_{-\infty}^{t} dt_1 \int_{-\infty}^{0} dt_2 \exp\left[-(t-t_1-t_2)/\tau_p\right] \left\langle f_p^\alpha(t_1)\, f_p^\beta(t_2)\right\rangle \\ &= \frac{1}{\zeta_p^2} \int_{-\infty}^{t} dt_1 \int_{-\infty}^{0} dt_2 \exp\left[-(t-t_1-t_2)/\tau_p\right] 2\zeta_p\, k_B T\, \delta(t_1-t_2)\, \delta_{\alpha\beta} \\ &= \frac{k_B T}{k_p} \exp\left(t/\tau_p\right) \delta_{\alpha\beta} = \frac{N\ell^2}{6\pi^2 p^2} \exp\left(-t/\tau_p\right) \delta_{\alpha\beta}\end{aligned} \tag{13}$$

For the center of mass coordinate one finds

$$\left\langle x_0^\alpha(t)\, x_0^\beta(0)\right\rangle = \delta_{\alpha\beta} \frac{2k_B T}{N\zeta_0} t \tag{14}$$

In order to study Brownian motion, the segment correlation functions in the real space $\Delta r_{nm}^2(t) = \left\langle \left(r_m(t) - r_n(0)\right)^2 \right\rangle$ are required. They are obtained by retransformation of the normal coordinates

$$\underline{r}_n(t) = \underline{x}_0 + 2\sum_p \underline{x}_p \cos\frac{p\pi n}{N} \tag{15}$$

This leads to

$$\begin{aligned}\Delta r_{nm}^2(t) &= 6D_R t + |n-m|\ \ell^2 \\ &+ \frac{4N\ell^2}{\pi^2} \sum_{p=1}^{N} \frac{1}{p^2} \cos\left(\frac{p\pi\ m}{N}\right) \cos\left(\frac{p\pi\ m}{N}\right) \left(1 - \exp\left(-\frac{p^2 t}{\tau_R}\right)\right)\end{aligned} \tag{16}$$

In order to arrive at Eq.[16], we have used $D_R = \frac{1}{6t}\left\langle \left(x_0(t) - x_0(0)\right)^2 \right\rangle$ (D_R: Rouse diffusion coefficient) and $\sum_{p=1}^{\infty} \frac{1}{p^2}\left[\cos\left(\frac{p\pi m}{N}\right) - \cos\left(\frac{p\pi n}{N}\right)\right]^2 = \frac{\pi^2}{2N}|n-m|$. For the special case of the self correlation function ($n = m$) $\Delta r_{nn}(t)$ reveals the mean square displacement of a polymer segment. For large p the $\cos^2$ in Eq.[16] is a rapidly oscillating function which may be replaced by the mean value ½. With this approximation we convert the sum into integral and obtain

$$\begin{aligned} \Delta r_{nn}^2(t) &= \frac{4N\ell^2}{\pi^2}\int_0^{\infty} dp \frac{1}{p^2}\frac{1}{2}\left(1 - \exp\left(-tp^2/\tau_R\right)\right) \\ &= 2N\ell^2\left(\frac{t}{\pi^3\tau_R}\right)^{1/2} = 2\ell^2\left(\frac{3k_BTt}{\pi\zeta_0\ell^2}\right)^{1/2} \end{aligned} \tag{17}$$

In contrast to normal diffusion Δr_{nn}^2 does not grow linearly, but with the square route of time. For the translational diffusion coefficient $D_R = k_BT/N\zeta_0$ is obtained. D_R is inversely proportional to the number of friction performing segments.

According to Eq.[2] the self correlation function relates directly to the mean square displacement of the diffusing segments. Inserting Eq.[17] into Eq.[2] for $t < \tau_R$ we have

$$S_{inc}(Q,t) = \exp\left\{-\frac{2}{\sqrt{\pi}}\left(\frac{k_BT\ell^2}{12\zeta_0}Q^4t\right)^{1/2}\right\} \tag{18}$$

In the case of coherent scattering, which observes the pair correlation function, interferences from scattering waves emanating for various segments complicate the scattering function. Inserting Eq.[16] into Eq.[2] we obtain

$$\begin{aligned} S(Q,t) = \frac{1}{N}\exp\left[-Q^2D_Rt\right]\sum_{nm}\exp\left\{-\frac{1}{6}|n-m|\,Q^2\ell^2\right\} * \\ \exp\left\{-\frac{2}{3}\frac{R_E^2Q^2}{\pi^2}\sum_p\frac{1}{p^2}\left\{\cos\left(\frac{p\pi\ m}{N}\right)\cos\left(\frac{p\ \pi n}{N}\right)\left(1-\exp\left(-\frac{tp^2}{\tau_R}\right)\right)\right\}\right\} \end{aligned} \tag{19}$$

for small Q ($QR_E < 1$) the second and third terms are negligible and $S(Q,t)$ describes the centre of mass diffusion of the chain.

$$S(Q,t) = N\ \exp\left(-D_Rt\right) \tag{20}$$

For $QR_E > 1$ and $t < \tau_R$ the internal relaxations dominate. Converting the sums in Eq.[19] to integrals and after some algebra DeGennes has derived an expression for the dynamic structure factor [7].

$$S(Q,t)=\frac{12}{Q^2\ell^2}\int_0^\infty du\ \exp\left\{-u-(\Omega_R t)^{1/2}\,h\left(u(\Omega_R t)^{-1/2}\right)\right\}$$
$$h(y)=\frac{2}{\pi}\int_0^\infty dx\,\frac{\cos(xy)}{x^2}\left(1-\exp(-x^2)\right) \tag{21}$$

We observe that in spite of the complicated functional form $S(Q,t)$, like the self correlation function, only depends on one variable, the Rouse variable.

$$(\Omega_R t)^{1/2}=\frac{Q^2}{6}\sqrt{\frac{3k_BT\ell^2 t}{\zeta_0}}=\frac{Q^2\ell^2}{6}\sqrt{Wt} \tag{22}$$

Since the Rouse model does not contain an explicit length scale, for different momentum transfers the dynamic structure factors are predicted to collapse to one master curve, if they are represented as a function of the Rouse variable.

3.2 Neutron spin echo results

The self correlation function of a Rouse chain was first observed on polydimethylsiloxane (PDMS) [5]. Since a straight forward study of the incoherent scattering by NSE is very difficult – due to spin flip scattering a severe loss of polarization occurs leading to very weak signals – the measurements of the self correlation function were performed on high molecular weight deuterated PDMS chains which contained short protonated labels at random positions. In such a sample the scattering essentially originates from the contrast between the protonated sequence and a deuterated environment and therefore is coherent. On the other hand the sequences are randomly distributed, so that there is no constructive interference of partial waves arising from different sequences. Under these conditions the scattering experiments measures the self correlation function.

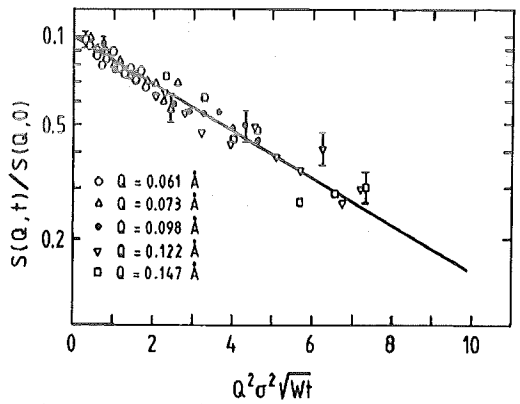


Fig. 3: *Self correlation for a PDMS melt T = 100C. The data at different momentum transfers are plotted vs. the scaling variable of the Rouse model ($\sigma \equiv \ell$).*

In Fig.3 the corresponding NSE spectra are plotted against the scaling variable of the Rouse model. The results for the different momentum transfers follow a common straight line. In Gaussian approximation the incoherent scattering function directly measures the mean square segment displacement, which according to Eq.[18] obeys a square root law in time. This behaviour may be directly read off from Fig.3.

Recently, it become also possible to directly observe the incoherent cross section from a protonated chain.

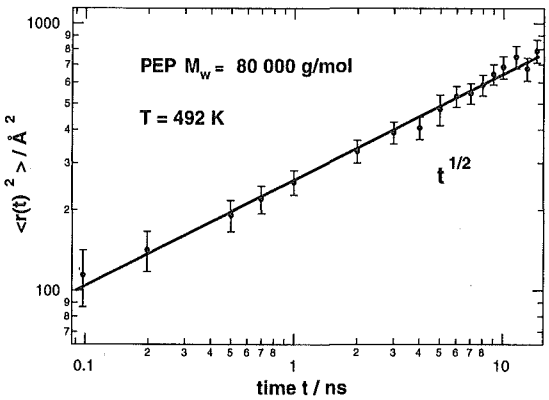


Fig. 4: *Time dependent mean square displacement of a PEP segment. The solid line indicates the prediction of the Rouse model.*

Fig.4 displays the time dependent mean square displacement obtained from a high molecular weight (M_w = 80000) polyethylene-propylene (PEP) melt at 492K. As predicted by Eq.[17] $\left\langle \Delta r^2(t) \right\rangle = -\frac{6}{Q^2} \ln S(Q,t)$ increases with the square root of time. The measurement directly allows to read off the amount of displacement at a given time; e.g. at 10ns the mean square segment displacement amounts to 620Å^2.

The pair correlation function arising from the segment motion within one given chain is observed, if some protonated chains are dissolved in a deuterated matrix. Fig.5 displays the observed spectra from polyethylethylene (90% dPEE, 10% hPEE) with a molecular weight of M_W = 20.000. The solid lines give the prediction of the dynamic structure factor of Eq.[19]. Obviously very good agreement is achieved.

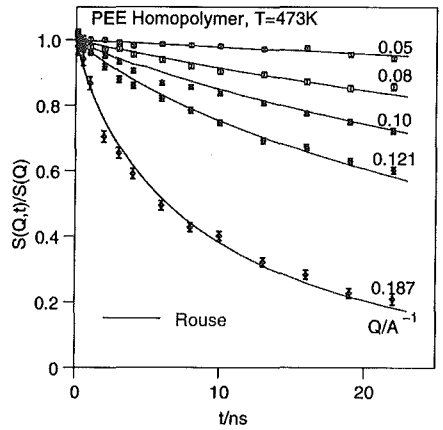


Fig. 5: *Single chain structure factor from a PEE melt at 473K. The solid lines represent a joint fit with the Rouse model.*

We now use these data, in order to investigate the scaling prediction inherent in Eq.[21]. Fig.6 presents a plot of the data of Fig.5, now as a function of the Rouse scaling variable (Eq.[22]).

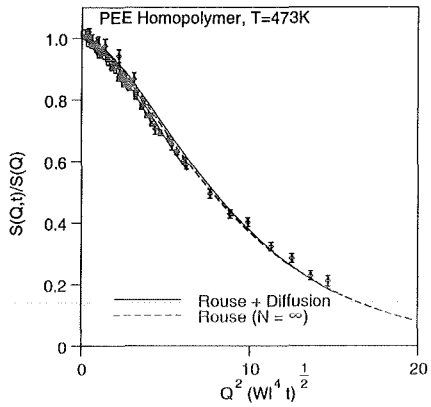


Fig. 6: *Single chain structure factor from PEE melts as a function of the Rouse scaling variable.*

The data follow with satisfying precision the scaling prediction. The small deviations are related to the translational diffusion of the chains. This becomes evident from Fig.7, where the obtained relaxation rates $\Gamma(Q)$ are plotted versus Q in a double logarithmic fashion.

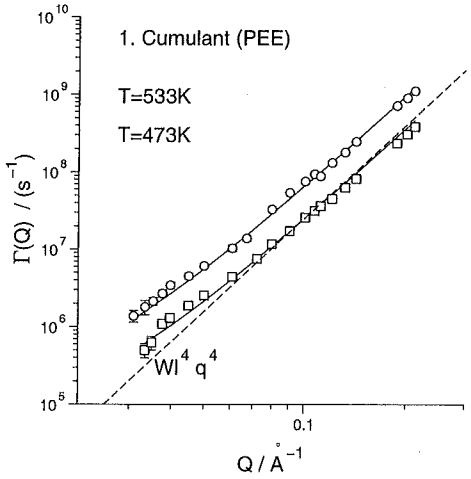


Fig. 7: *Relaxation rates from PEE melts vs. Q for two different temperatures.*

The dashed line gives the Rouse prediction $\Gamma \propto W\ell^4 Q^4$. While at larger momentum transfers the experimental results follow very well this prediction, towards lower Q, a systematic relative increase of the relaxation rate is observed. Including the diffusion, we have

$$\Gamma(Q) = Q^2\left[D + Q^2\frac{W\ell^4}{6}\right] \tag{23}$$

The solid lines in Fig.7 represents the prediction of Eq.[23]. Perfect agreement is obtained.

3.3 Computer simulation

In order to learn about the limits of the Rouse model, recently a detailed quantitative comparison of molecular dynamics (MD) computer simulations on a 100 C-atom polyethylene chain (PE) with NSE experiments on PE chains of similar molecular weight has been performed [6]. Both, the experiment and the simulation were carried out at T = 509K. Simulations were undertaken, both for an explicit *(EA)* as well as for an united *(UA)* atom model. In the latter the *H*-atoms are not explicitly taken into account but reinserted when calculating the dynamic structure factor. The potential parameters for the MD-simulation were either based on quantum chemical calculations or taken from literature. No adjusting parameter was introduced. Fig.8 compares the results from the MD-simulation (solid and broken lines) with the NSE-spectra. In order to correct for the slightly different overall time scales of experiment and simulation, the time axis is scaled with the centre of mass diffusion coefficient. From Fig.8 quantitative agreement between both results is evident.

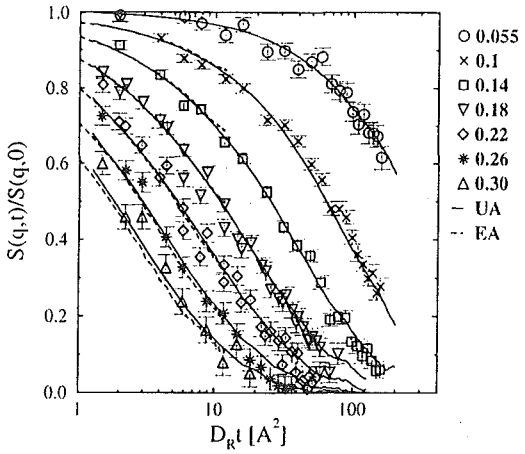


Fig. 8: *NSE data from PE melts vs. computer simulations (see text).*

Fig.9 compares the same experimental data, which agreed quantitatively with the simulations with a best fit to the Rouse model (Eq.[19]). Here a good description is observed for small Q-values ($Q \leq 0.14 Å^{-1}$), while at higher Q important deviations appear. Similarly also the simulations cannot be fit in detail with a Rouse structure factor.

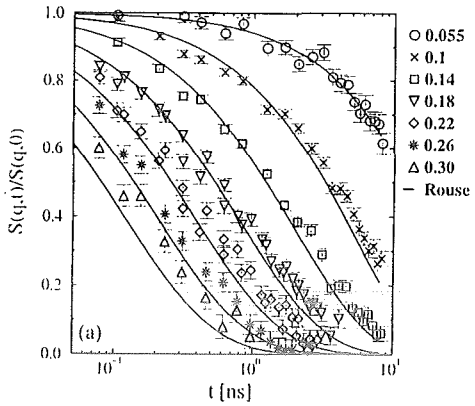


Fig. 9: *NSE data from PE melts in comparison to a best fit with the Rouse model (see text).*

Having obtained very good agreement between experiment and simulation, the simulations which contain complete information about the atomic trajectories may be further exploited, in order to rationalize the origin for the discrepancies with the Rouse model. A number of deviations evolve.

1. According to the Rouse model the mode correlators (Eq.[13]) should decay in a single exponential fashion. A direct evaluation from the atomic trajectories shows that the 3 contributing Rouse modes decay with stretched exponentials displaying stretching exponents β of *(1:β = 0.96 and 2,3:β = 0.86)*

2. A detailed scrutiny of the *Gaussian* assumption (see e.g. (Eq.[19]) reveals that for $t < \tau_R$ deviations occur.

3. While the Rouse model predicts a linear time evolution of the mean squared centre of mass coordinate (Eq.[14]), within the time window of the simulation *($t < 9ns$)* a sublinear diffusion in form of a stretched exponential with a stretching exponent of $\beta = 0.83$ is found. A detailed inspection of the time dependent mean squared amplitudes reveals that the sublinear diffusion mainly originates from motions at short times $t < \tau_R = 2ns$.

The prediction of a time dependent centre of mass diffusion coefficient has recently been corroborated by NSE-experiments on short chain polybutadienes [8]. Fig.10 displays the mean square centre of mass displacement from simulation compared to the same quantity obtained from the dynamic structure factor at various Q-values. Both the simulation as well as the experimental data consistently lead to a weaker than linear time dependence of the centre of mass displacement.

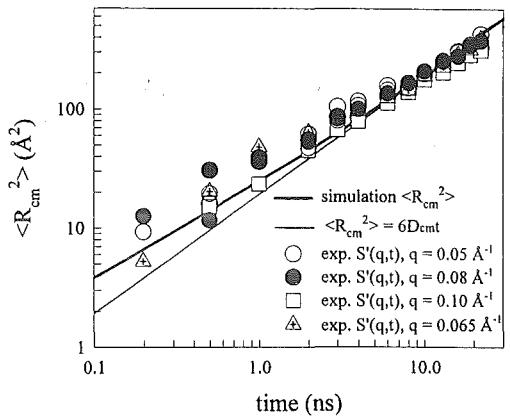


Fig. 10: *Mean square center of mass displacement for PB chains in the melt obtained from* $\left\langle r^2(t)\right\rangle = -\frac{6}{Q^2}\ln S(Q,t)$. *Solid line: simulation result; thin line* $\left\langle r^2(t)\right\rangle = D_R t$.

The overall picture emerging from this combined simulational and experimental effort is, that for chains, which should be ideal Rouse chains, the model is capable of quantitatively describing the behaviour only on time scales of the order of the Rouse time or larger and therefore on length scales of the order of the radius of gyration of the chains or larger and in the regime, where the chains actually show Fickian diffusion. The self diffusion behaviour for times smaller than the Rouse time and the relaxation of the internal modes of the chains show small but systematic deviations from the Rouse prediction. The origin of these discrepancies are traced to interchain interactions. On the other hand, we will see that deviations observed at higher Q relate intrachain potentials.

4 Reptation

In the lecture on viscoelasticity we have seen, that the dynamic modulus of a polymer melt is characterized by a plateau regime, the breath of which increases with increasing molecular weight of the chains [4]. In this plateau regime the polymer melt acts like a rubber, where the elastic properties are derived from the entropy elasticity of the chains between permanent cross links. The modulus of a rubber is inversely proportional to the mesh size and proportional to the temperature. In analogy, it is suggesting to assume that the entanglement or topological interactions between the chains in a melt lead to the formation of a temporary network which then displays rubber elastic properties. Other than in the rubber, for long times the chains may disentangle and the melt flows. Using the analogy to the modulus of a rubber, we may estimate the distances between entanglement points from the plateau modulus G_N^0. For different polymers they come out to be between 30Å and 100Å. On the basis of such assumptions, a number of theories of viscoelasticity have been developed [4]. The most famous among them is the reptation model of DeGennes and Doi and Edwards. In this model, the dominating chain motion is a reptile like creep along the chain profile. The lateral restrictions are modeled by a tube with a diameter d parallel to the chain profile. d relates to the plateau modulus of the melt.

$$d^2 = \frac{4}{5}\frac{R_e^2}{M}\frac{\rho RT}{G_N^0} \tag{24}$$

The restrictions of the motions through other chains are not effective on a monomer scale but rather permit lateral freedom on intermediate length scales. The experimental observations for viscosity and diffusion can be made directly comprehensible in this simple model.

The viscosity relates to the longest relaxation time in a system. If we consider Rouse diffusion along the tube with a Rouse diffusion coefficient $D_R \approx 1/(N\zeta_0)$ then an initial tube configuration is completely forgotten, when the mean square displacement along the tube $\langle r^2(t)\rangle_{tube} = (\textit{contour length } L)^2$. Thus, for the longest relaxation time, we obtain

$$\tau_\eta \approx \frac{L^2}{D_R} \approx N^3\zeta_0 \tag{25}$$

The diffusion coefficient is found by considering that during this time in real space the mean square displacement just amounts to the end to end distance of the chain squared. Thus, we have

$$D_{rep} = \frac{R_e^2}{\tau_\eta} \approx \frac{N}{N^3\zeta_0} \approx \frac{1}{N^2\zeta_0} \tag{26}$$

The reptation model predicts that the viscosity of a melt scales with a chain length to the third power while the diffusion coefficient decreases with the second power of the chain length.

We now would like to consider the consequences of the reptation model with respect to predictions of the mean square displacement of the chain segments.

(i) For short times, when the chain segment has not yet realized the topological constraints ($r < d$), we expect unrestricted Rouse motion $\langle \Delta r^2(t) \rangle \approx t^{1/2}$ (Eq.[17]). If the mean square displacement becomes of the order of the tube diameter, then motional restrictions are expected. More precisely, we consider the Rouse relaxation time $\tau_R = \tau_e$ of an entanglements strand.

$$\tau_e = \frac{1}{3\pi^2} \frac{d^4 \zeta_0}{k_B T \ell^2} \tag{27}$$

(ii) For times $t > \tau_e$ one dimensional curve linear Rouse motion along the tube has to be considered. For displacements $S_n(t)$ along the tube Eq.[16] yields

$$\left\langle \left(S_n(t) - S_n(0)\right)^2 \right\rangle = \left\langle \left(Y_0(t) - Y_0(0)\right)^2 \right\rangle + \frac{4N\ell^2}{3\pi^2} \sum_p \cos^2\left(\frac{p\pi n}{N}\right) \times \left(1 - \exp\left(-tp^2/\tau_R\right)\right) \tag{28}$$

Y_0 is the center of mass coordinate for the curve linear motion. For times $t < \tau_R$ we again get the well known $t^{1/2}$ law, while for $t > \tau_R$ the first term dominates (then $\left\langle \left(S_n(t) - S_n(0)\right)^2 \right\rangle = \frac{k_B T}{N\zeta_0} t$).

If a segment is displaced along the tube by $S_n(t) - S_n(0)$ then the mean square displacement in 3-d real space is $d\left|S_n(t) - S_n(0)\right|$. With that we get

$$\begin{aligned} \left\langle \Delta r_{nn}^2(t) \right\rangle &= d\left\langle \left(S_n(t) - S(0)\right)^2 \right\rangle^{1/2} \\ &= \begin{cases} d\left(\dfrac{k_B T \ell^2 t}{\zeta_0}\right)^{1/4} & \tau_e < t < \tau_R \\ d\left(\dfrac{k_B T l}{N\zeta_0}\right)^{1/2} & \tau_R < t < \tau_d \end{cases} \end{aligned} \tag{29}$$

Thereby, $\tau_d \approx \tau_\eta$ is the time after which a chain has left its original tube.

(i) For times $t > \tau_d$ the dynamics is determined by reptation diffusion. We expect a mean square displacement proportional to time.

$$\left\langle \Delta r_{nn}^2(t) \right\rangle = \frac{k_B T d^2}{N^2 \ell^2 \zeta_0} t \tag{30}$$

With this the reptation model predicts four different dynamic regimes for segmental diffusion. They are displayed schematically in Fig.11.

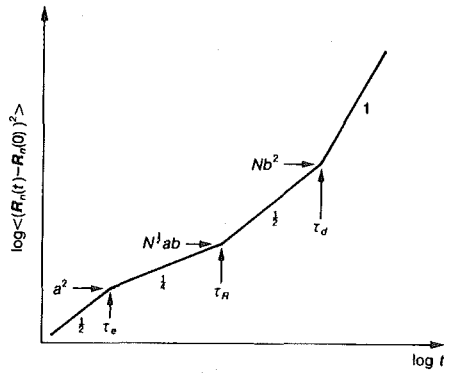


Fig. 11: *Mean square displacement of a chain segment is plotted logarithmically against time.*

The tube constraints also provoke a strong retardation for the single chain relaxations causing a near plateau regime in the time dependent single chain correlation function. Neglecting the initial free Rouse process, DeGennes and Doi and Edwards have formulated a tractable expression for the dynamic structure factor which is valid for $t > \tau_e$, i.e. once confinement effects become important [4][8][9]. In the large Q limit the dynamic structure factor assumes the form

$$\frac{S(Q,t)}{S(Q)} = (1-F(Q))\exp\left(t/\tau_0\right) erfc\sqrt{t/\tau_0} + F(Q)\sum_{p=1}^{N}\frac{\sin^2\alpha_p\, 2N\mu}{\alpha_p^2\left(\mu^2+\alpha_p^2+\mu\right)}\exp\left(-\frac{4\alpha_p^2 t}{\pi^2\tau_d}\right)$$

with $F(Q) = \exp\left(-\frac{d^2Q^2}{36}\right)$ the tube "Debye Waller factor".

$$\tau_0 = \frac{36}{W\ell^4Q^4} \qquad \text{the Rouse time scale}$$

$$\tau_d = \frac{3N^3}{\pi^2}\frac{\ell^2}{Wd^2} \qquad \text{the terminal time} \qquad (31)$$

$$\alpha_p \tan\alpha_p = \mu = \frac{Q^2N\ell^2}{12}$$

For short times $S(Q,t)$ decays mainly due to local reptation (first term), while for longer times (and low Q) the second term resulting from the creep motion dominates. The ratio of two relevant time scales τ_0 and τ_d is proportional to N^3. Therefore, for long chains at intermediate times $\tau_e < t < \tau_d$ a pronounced plateau in $S(Q,t)$ is predicted. Such a plateau is a signature for confined motion and is present also in other models for confined chain motion. Besides the reptation model also other entanglement models have been brought forward. We discuss them briefly by categories.

1. In generalized Rouse models, the effect of topological hindrance is described by a memory function. In the border line case of long chains the dynamic structure factor can be explicitly calculated in the time domain of the NSE experiment. In this class fall entanglement models by Ronca, Hess, Chaterjee and Loring [10] [11] [12].

2. Rubber like models take entanglements literally as temporary cross links. Such an approach has been brought forward recently by des Cloiseaux [13]. He assumes that the entanglement points between chains are fixed as in a rubber and that under the boundary condition of fixed entanglements the chains perform Rouse motion. This rubber like model is conceptually closest to the idea of a temporary network.

3. Recently in a mode coupling approach a microscopic theory describing the polymer motion in entangled melts has been developed. While these theories describe well the different time regimes for segmental motion, unfortunately as a consequence of the necessary approximations a dynamic structure factor could not yet been derived [14][15].

4.1 Experimental observations of chain confinement

Fig.12 compares the dynamic structure factors from polyethylene melts, both taken at 509K for two different molecular weights [16][17][18][19][20]. Fig.12a displays the structure factor for a short chain melt (M_w = 2000g/mol). The solid line display a fit with the Rouse dynamic structure factor according to Eq.[16]. Again very good agreement is achieved. Fig.12b displays similar results from a PE melt with a molecular weight of M_w = 12400g/mol. The solid lines present the predictions of the Rouse model. While for the short chain melts, this model describes sufficiently well the experimental observations for the longer chains the model fails completely. Only in the short time regime the initial decay of the dynamic structure factor is depicted while for longer times the relaxation behaviour is strongly retarded signifying confinement effects. In Fig.13 the data from a M_w = 36000 PE-melt at 509K are plotted as a function of the scaling variable of the Rouse model (Eq.[22]). In contrast to Fig.7 the scaled data do not follow a common curve, but after an initial coming coarse a rather split into Q dependent branches. This splitting is a consequence of the existing of a dynamic length scale which invalidates the Rouse scaling properties. We note, that this length is of purely dynamical character and cannot be observed in static experiments.

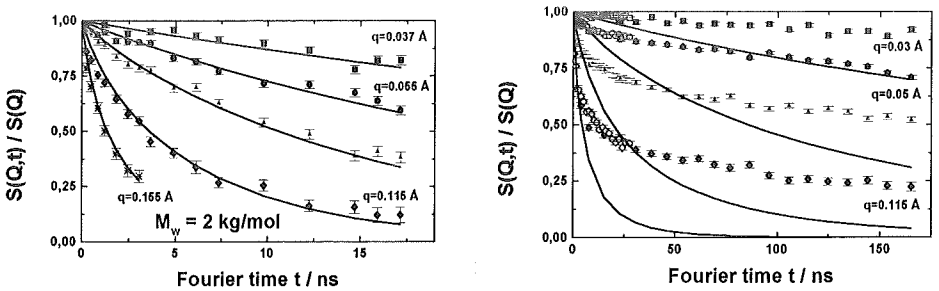


Fig. 12: *Dynamic structure factors from PE-melts at 509K (a) M_w = 2000; (b) M_w = 12400. The solid lines display the predictions of the Rouse model.*

Fig.14 presents recent experimental results on a polyethylene melt (M_w = 190000) which were carried over a time regime of 170ns [19]. The data are compared with the dynamic structure factor of the reptation model (Eq.[31]). It is apparent that these data are very well fit by the dynamic structure factor of the reptation model. We note, that the fits were performed varying only a single parameter, namely the tube diameter d while the Rouse rate was determined from earlier NSE data taken at short times. With this one parameter it is possible to achieve quantitative agreement both with respect to the Q and the time dependence of the dynamic structure factor. We further note, that the dynamic structure factors predicted by the other confinement models discussed above are not able to fit the data.

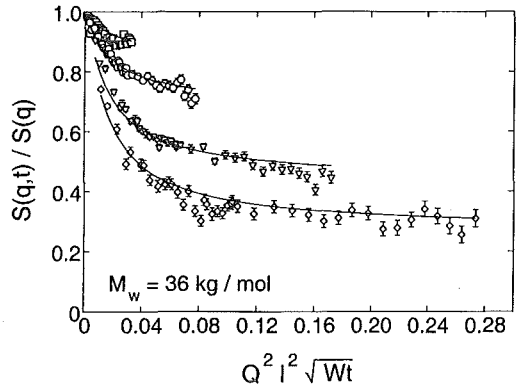


Fig. 13: *Scaling presentation of the dynamic structure factor from a M_w = 36000 PE-melt at 509K as a function of the Rouse scaling variable. The solid lines are a fit with the reptation model (Eq.[31]). The Q-values are from above Q = 0.05, 0.077, 0.115, 0.154Å^{-1}.*

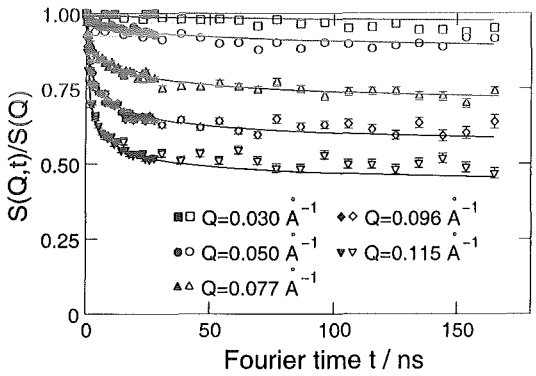


Fig. 14: *Dynamic structure factor from a long chain PE-melt (M_w = 190000) at 509K. The solid lines represent a fit with the reptation model (Eq.[31]).*

It is illustrative to visualize the large spread of the time regimes relevant for the dynamics of the $M_w = 190000$ molecule. The elementary Rouse time amounts to 2.5ps. The cross over time to local reptation $\tau_e = 5$ns. The Rouse time of the chain $\tau_R = 45\mu$s and finally the disentanglement time $\tau_d = 11.7$ms. Thus, the relevant times scales spread over a range of more than nine orders of magnitude. The corresponding length scales are much closer together. The segment length $\ell = \ell_0\sqrt{C_\infty}$, where C_∞ is the characteristic ratio, is 4Å, the tube diameter $d = 46$Å and the chain end-to-end distance $R_e = 418$Å.

We now turn to the mean square displacement of a chain segment, which may be observed by incoherent quasielastic scattering [20]. Here, in the local reptation regime we expect a cross over of the time dependent mean square displacement from a $t^{1/2}$- to a $t^{1/4}$-law (Eq.[29]). Experimentally such incoherent neutron spin echo experiments are extremely difficult. The reason is that (i) incoherent scattering is emitted into the full solid angle 4π, (ii) with the incoherent scattering in two thirds of the scattering events a spin flip of the neutron spin occurs reducing the echo signal from +1 to $-1/3$. This reduced signal sits on a high background caused by the spin flipped neutrons. In order to perform such experiments, very long counting times and a extremely stable instrument are necessary.

Fig.15 presents the mean square displacement obtained from the same $M_w = 190000$ PE sample as studied also in the coherent measurement experiments have been performed at two different Q values and the corresponding mean square displacements are plotted double logarithmically against the time. The two solid lines display the expected asymptotic $t^{1/2}$- and $t^{1/4}$-time laws. As may be seen, the data display a pronounced cross over from a $t^{1/2}$ behavior at short times to a $t^{1/4}$ law at longer times. Surprisingly, a cross over was found at a time $\tau_e = 0.8$ns corresponding to a tube diameter $d = 30$Å in strong disagreement with the value of 46Å from the dynamic structure factor experiment.

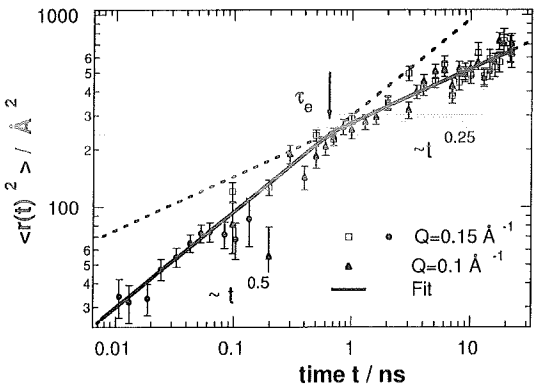


Fig. 15: *Time dependent mean square displacement from a $M_w = 190000$ PE-melt at 509K according to* $\left\langle r^2(t)\right\rangle = -\frac{6}{Q^2}\ell n\, S(Q,t)$. *The solid dashed lines display the $t^{1/2}$- and $t^{1/4}$-laws respectively.*

The origin of this discrepancy is of rather subtle nature [21] and relates to the Gaussian approximation which was taken in order to extract $\langle \Delta r^2(t) \rangle$ from Eq.[2]. For a curve linear motion along a contorted tube this Gaussian assumption is not valid. While the curve linear displacement inside the tube have a Gaussian character, the real space displacements strongly deviate from this behaviour. If this effect is taken into account the discrepancies are removed and both the self as well as the pair correlation function lead to the same tube diameter and cross over times.

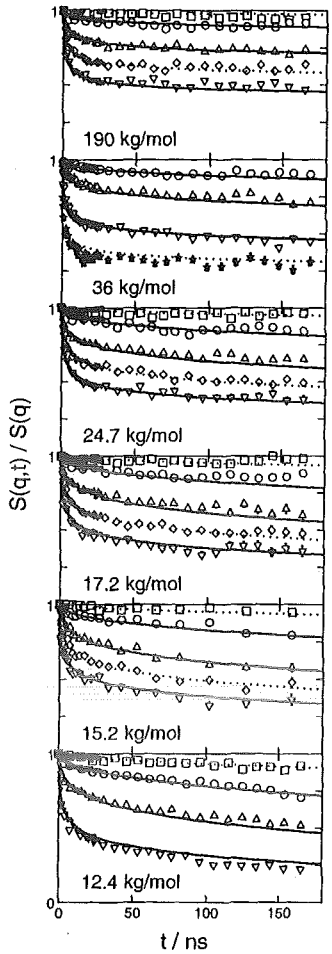


Fig. 16: *Neutron spin echo spectra from the polyethylene melts of various molecular weights. The Q values correspond to squares, $Q = 0.003Å^{-1}$; circles, $Q = 0.005Å^{-1}$, triangles (up), $Q = 0.077Å^{-1}$; diamonds, $Q = 0.096Å^{-1}$; triangles (down), $Q = 0.115Å^{-1}$; crosses, $Q = 0.15Å^{-1}$. Filled symbols refer to a wavelength of the incoming neutrons $\lambda = 8Å$ and open symbols refer to $\lambda = 15Å$. For lines, see explanation in text.*

Now, we ask for the effect of the chain length on chain confinement [19] [22]. For this purpose, NSE experiments were performed on polyethylene melts spanning a molecular

weight range from 12.4kg/mol up to 190kg/mol. Fig.16 displays the result. We first qualitatively discuss the data and compare the spectra at $Q = 0.115\text{Å}^{-1}$. For the highest molecular weight at M_w = 190kg/mol and M_w = 36kg/mol the spectra are characterized by an initial fast decay reflecting the unconstraint dynamics at early times and very pronounced plateaus for $S(Q,t)$ at later times signifying the tube constraints. The plateau values for the two samples are practically identical. Inspecting the results for smaller M_w we realize that (i) the dynamic structure factors decays to lower values (0.5 at M_w = 190kg/mol, 0.4 at M_w = 24.7kg/mol and nearly 0.2 at M_w = 12.4kg/mol); (ii) furthermore, the long time plateaus start to slow more and more the smaller M_w becomes with M_w = 12.4kg/mol nearly loosing the two relaxation step character of $S(Q,t)$. Obviously, the chains are disentangling from the tube and the constraints are successively removed.

If the data are analysed using the pure reptation model of Eq.[31] a tube diameter d, which increases with decreasing molecular weight is obtained. This is displayed in Fig.17, where the tube diameter is plotted as a function of molecular weight. We observe and increase from about 45 to 60Å. Secondly, it is found (not shown here) that the quality of the fit is decreasing with decreasing molecular weight.

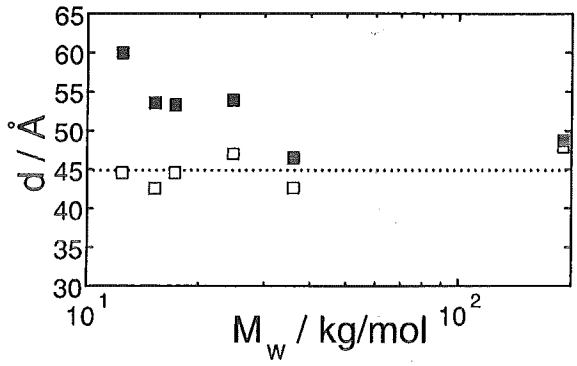


Fig. 17: *Resulting tube diameters from the model fits with pure reptation (filled squares) and reptation and contour-length fluctuations (open squares) as a function of molecular weight. The dotted line is a guide for the eye.*

As it is known from the broad a cross over phenomena observed in the macroscopic chain dynamics such as the molecular weight dependence of the melt viscosity very important limiting mechanism exist which effect the confinement limit of the reptation process. These processes increase in importance as the chain length decreases. In the time regime $t < \tau_R$, theoretically, tube contour length fluctuations removing the tube constraints from the ends have been identified as the most important limiting process. For times $t < \tau_R$ the fraction of monomers released from the tube due to contour length fluctuations has a simple form

$$\Psi(t) = \frac{1.5}{Z}\left(\frac{t}{\tau_e}\right)^{1/4} \tag{32}$$

where $\tau_e = \tau_R/Z^2$ and $Z = N/N_e$ is the number of entanglements per chain.

Following the approach of Clark and McLeish, this result may be incorporated into the structure factor of Eq.[31]. We assume that after time t all monomers between 0 and $s(t)$ and between 1 - $s(t)$ and 1 have escaped from the tube. Here $s(t) = \Psi(t)/2$.

Starting with Eq.[2] and using the fact that the space variable $r(s,t)$ is a Gaussian variable, we may write

$$\left\langle \left[r_\alpha(s,t) - r_\alpha(s',0) \right]^2 \right\rangle = \frac{dL}{3} \begin{cases} |s-s'| & s(t) < s < 1-s(t) \text{ or } s(t) < s' < 1-s(t) \\ |2s(t) - s - s'| & s < s(t) \text{ and } s' < s(t) \\ |2 - s - s' - 2s(t)| & s > 1-s(t) \text{ and } s' > 1-s(t) \end{cases} \tag{33}$$

where $L = Zd$ is the contour length. The summation in Eq.[1] is then replaced by integration as

$$S^{esc}(q,t) = \int_0^1 ds \int_0^1 ds' \exp\left(-2\mu|s-s'|\right) + 2\int_0^{s(t)} ds \int_0^{s(t)} ds' \left(\exp\left\{-2\mu\left[2s(t) - s - s'\right]\right\} - \exp\left(-2\mu|s-s'|\right)\right) \tag{34}$$

with μ as defined in Eq.[31].

The integrals can easily be evaluated and we obtain

$$S^{esc}(q,t) = \frac{N}{2\mu^2}\left[2\mu + e^{-2\mu} + 2 - 4\mu s(t) - 4e^{-2\mu s(t)} + e^{-4\mu s(t)}\right] \tag{35}$$

The lines in Fig.16 display the result of a fit with Eq.[35]. A group of three common Q values for all molecular weights is displayed by thick solid lines to facilitate the easy comparison of the molecular weight dependence of the curves. Additional Q values only available for some M_w's are represented by dotted lines.

The open squares in Fig.17 show the resulting tube diameters. Aside from small fluctuations they now stay constant independent of M_w. We further note, that in particular for smaller M_w the weighted error between fit and data is significantly smaller than for a fit with a pure reptation model. We now consider the tube diameters which result from the two difference approaches (Fig.17). At the highest molecular weight contour lengths fluctuations are insignificant and both lines of fitting yield the same d. At $M_w = 36$kg/mol a slight difference appears which increases strongly with decreasing chain length. At $M_w = 12.4$kg/mol, the difference in the fitted tube diameters between both approaches rises to nearly 50% emphasizing the strong effect of contour length fluctuations in loosening the grip of the entanglements on a given chain. Thus, the comparison between the experimental chain length dependent dynamic structure factor and theoretical predictions clearly show, that for times $t < \tau_R$ contour length fluctuations are the leading mechanisms that limit the chain confinement inherent to the reptation picture. Without any further assumptions or fitting

parameters – the tube diameter d stays constant with M_w - it is possible to describe the full M_w dependence of $S(Q,t)$ in terms of local reptation and the contour length fluctuation mechanism. Even for chain lengths corresponding to only 6-7 entanglements the tube diameter appears to be a well defined quantity assuming the same value as for asymptotically long chains. The confinement is lifted from the chain ends inwards, while the chain center remains confined in the original tube.

Summarizing the chapter on confined motion we may conclude: As it stands NSE spectroscopy accessing quantitatively the dynamic structure factor has by now seen clear and unambiguous signature of reptation in a flexible linear polymer chain. The data cover a region of the time domain where reptation is in principle applicable. Compared with other phenomenological approaches reptation is by now the only approach providing a consistent description of all NSE data. It implies that reptation must emerge from any successful microscopic theory of polymer relaxation.

5 Intermediate Scale Dynamics

A precondition for the validity of the entropy driven Rouse model is the requirement that only chain connectivity enters into the equation of motion and any influence from local stiffness or rotational barriers etc. is negligable. In going to shorter length scales this condition must break down. Measurements of the dynamic structure factor at smaller scales or higher Q-values offer the opportunity to learn about the limitation of the Rouse model towards local scales and to understand the leading processes. Both local chain stiffness as well as rotational potentials may play a role [23][24][25].

Recently, the relevant factors which limit the universal Rouse dynamics towards small scales were studied in comparing the dynamic structure factors $S(Q,t)$ of polyisobutylene (PIB) and polydimethylsiloxane (PDMS) molecules of similar size in the melt and in dilute solution [26][27]. Both polymers show similar static flexibility (the characteristic ratios are very close), but strongly different rotational barriers (PDMS: $E_{rot} \cong 0.1$ kcal/mol; PIB: $E_{rot} = 3$ kcal/mol).

Fig.18a presents the dynamic structure factor from a PIB melt at 470K including a fit with the prediction of the Rouse model. Fig.18b displays comparable data from a PDMS melt at 373K.

While for Q-values above $Q = 0.15\text{Å}^{-1}$ increasing deviations between the experimental results from PIB and the Rouse prediction are evident, the PDMS results are described well over the entire Q-range (up to $Q = 0.4\text{Å}^{-1}$). Since both polymers exhibit the same static flexibility, we may immediately conclude, that chain stiffness is not the leading mechanism limiting the Rouse dynamics for flexible polymers as proposed earlier [25]. A thorough study of the stiffness effects on the dynamics of this polymer was carried out in ref. [26] applying the approaches of the all rotational state model and a bending force model. Stiffness effects were found to be almost neglible.

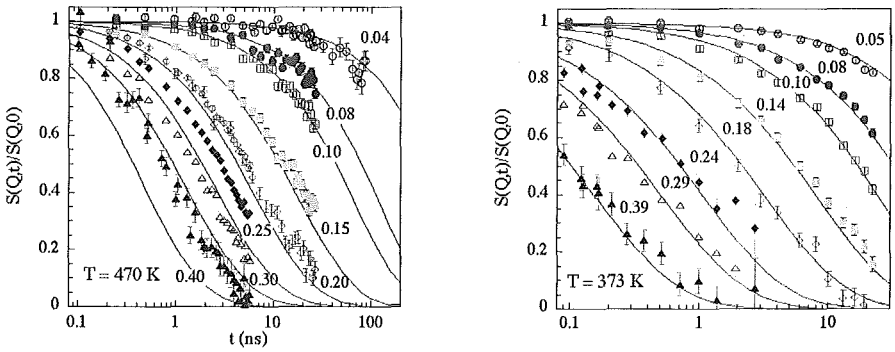


Fig. 18: *Dynamic structure factor of (a) a PIB melt (M_w = 3870, M_w/M_n = 1.06, radius of gyration R_g = 19.2Å) at 470K and (b) of a PDMS melt (M_w = 6460, M_w/M_n = 1.10, R_g = 21.3Å) at 373K (○: Q = 0.04Å^{-1}; ●: Q = 0.08Å^{-1}; □: Q = 0.10Å^{-1}; ▨: Q = 0.15Å^{-1}; ◇: Q = 0.20Å^{-1}; ◆: Q = 0.25Å^{-1}; △: Q = 0.3Å^{-1}; ▲: Q = 0.4Å^{-1}). The solid lines the respective predictions of the Rouse model.*

After the failure of stiffness models, the source for the slowing down of the PIB chain dynamics at intermediate scales must be related to dissipation effect not present in PDMS. Allegra's intrachain viscosity model [23][24] provides a simplified access to such an effect. He describes the intrachain dissipation degrees of freedom - mainly rotational transitions across barriers - by a local relaxation mode characterized by a relaxation time τ_0.

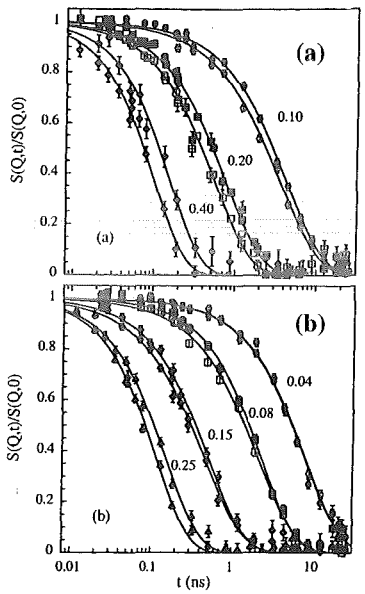


Fig. 19: *Chain dynamic structure factor of PDMS (empty symbols) and PIB (full symbols - in each case the lower curve) in toluene solution at 300K (a) and 378K (b). The corresponding Q values are indicated. Lines through the points are guides to eye.*

In order to access this process without disturbances, experiments on solutions were crucial, where interchain friction effects are weak [27]. Fig.19a,b compare experimental results on PIB and PDMS in toluene at room temperature and 378K. While at low Q both data sets agree – both polymers undergo the same translational diffusion – at larger Q a systematic retardation of the dynamic response of PIB compared to PDMS is visible.

The application of the intrachain viscosity model to the PIB solution data on the basis of the PDMS reference led to a very good description of the NSE results for all Q values and temperatures (Fig.20). The activation energy of 3.1 kcal/mol for the intrachain relaxation time τ_0 agrees very well with the rotational barrier for this hydrocarbon [28].

An application of the model to the melt data allows a quantitative description of the Q-dependent spectra. The activation energy for τ_0 resulted to be about 10 kcal/mol, more than 3 times as high as in solution. Obviously chain relaxation occurs via correlated motions over several barriers or interchain effects come in additionally and the activation energy cannot easily be compared with rotational potentials.

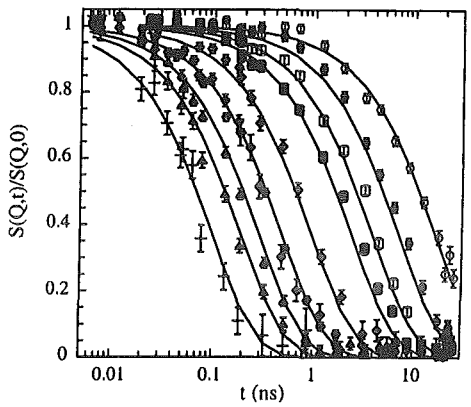


Fig. 20: *Chain dynamic structure factor PIB in toluene solution at 327K at the Q values: 0.04Å^{-1} (○); 0.06Å^{-1} (●); 0.08 Å^{-1} (□); 0.10Å^{-1} (■); 0.15Å^{-1} (◇); 0.20 Å^{-1} (◆); 0.25Å^{-1} (△); 0.30Å^{-1} (▲); 0.40Å^{-1} (+). Solid lines correspond to fitting curves with the Rouse-Zimm model including intrachain viscosity.*

Thus, Allegra's intrachain viscosity model accounts properly for the deviations from universal dynamics. In solution the corresponding relaxation time directly relates to jumps across rotational potentials. Also in the melt intrachain friction effects limit the Rouse dynamics. The relaxation time, however, is not directly related to crossings of single barriers.

6 Local Dynamics

We now turn to the local chain motions involving a few main chain bonds or chain side groups. These motions are behind the classical relaxation processes in polymers, the α- and β-relaxations. They have been studied since more than 50 years by spectroscopic techniques, like dielectric spectroscopy, mechanical spectroscopy and NMR. Fig.21 displays a typical

outcome of such experiments for the case of polybutadiene (PB) $[-C_4\ H_6-]_n$. The dominant relaxation process, the α-relaxation, is related to the macroscopic flow and freezes at a finite temperature, the glass transition temperature T_g. Aside from this process, a secondary relaxation, β_{slow}, departs from the α-relaxation at a temperature about 20% above T_g. This relaxation displays an Arrhenius behaviour and passes unchanged through the glass transition.

As already mentioned, the α-relaxation is behind the viscous flow of polymers. Its relaxation function may be phenomenologically described by a stretched exponential or Kohlrausch-William-Watts function

$$\phi_\alpha(t) = \exp\left\{-\left(\frac{t}{\tau_{KWW}}\right)^\beta\right\} \tag{36}$$

τ_{KWW} is the Kohlrausch-William-Watts relaxation time and $\beta < 1$ the stretching exponent. τ_{KWW} in good approximation follows a Vogel-Fulcher temperature dependence.

$$\tau_{KWW}(T) \approx \exp\left\{\frac{A}{T - T_0}\right\} \tag{37}$$

The temperature offset in the denominator of the exponent leads to a divergence of τ_{KWW} at T_0, a temperature below T_g which, however, may never be reached in equilibrium.

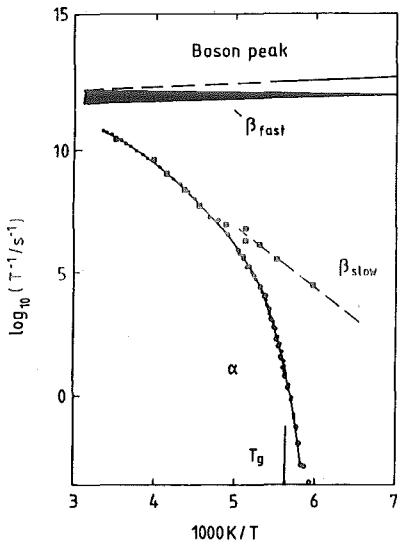


Fig. 21: *Relaxation landscape of PB. α and β_{slow} correspond to the classical relaxation processes and are treated here.*

The dielectric β-relaxation is considered to be a result of a partial reorientation of the molecular dipoles in the substance. It is interpreted as a local activated process, where the dipole hops between two positions separated by an activation energy E. The relaxation time follows an Arrhenius behaviour

$$\tau_\beta(E) = \tau_0^\beta \exp\left[\frac{E}{k_B T}\right] \tag{38}$$

Due to the disorder in the material the activation energies E are distributed around an average value E_0. For the distribution function in general a Gaussian is assumed.

$$g(E) \approx \exp\left\{-\left(\frac{E-E_0}{\sigma}\right)^2\right\} \tag{39}$$

Empirically it is found that the width $\sigma(T)$ decreases with increasing temperature.

Though both the α- and the β-relaxation have been investigated well by spectroscopic techniques, their molecular origin is still unclear. Here QENS with its ability to provide space time resolution on the proper scales contributes to a further exploration of the molecular mechanisms behind these relaxations.

6.1 Dynamic structure factors

We commence with the derivation of the dynamic structure factor for the β-process which we consider as a hopping process between two adjacent sites [29][30]. For such a process the self correlation function is given by a sum of two contributions.

$$S_s(Q,t) = \frac{1}{2}\underbrace{\left[1+\frac{\sin(Qd)}{Qd}\right]}_{S^{el}} + \frac{1}{2}\underbrace{\left[1-\frac{\sin(Qd)}{Qd}\right]}_{S^{inel}} \exp\left(-\frac{2t}{\tau(E)}\right) \tag{40}$$

Here d is the distance between the two sites and $\tau(E)$ is the jump time corresponding to an activation energy E. The elastic contribution S^{el} is also called elastic incoherent structure factor (EISF). It may be interpreted as the Fourier transformed of the asymptotic distribution of the hopping atom for infinite times. The complete scattering function is obtained in averaging Eq.[40] with the barrier distribution function $g(E)$ obtained e.g. by dielectric spectroscopy. The Q-dependence of the two contributions to Eq.[40] is displayed in Fig.22 as a function of Q (d = 1.5Å). From the oscillation of both contributions with Q the jump distance may be obtained. The associated time scale may be found from the time decay of the inelastic part.

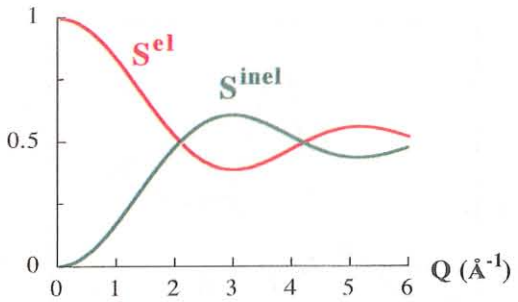


Fig. 22: *Elastic and inelastic contribution to the incoherent scattering function for jump motion between two site. The figure assumes a jump distance of 1.5Å.*

The associated pair correlation function is more difficult to obtain, since now we have to deal with a change of configurations of atoms rather than with single atom jumps. The conceptual difference between the pair and the self correlation function for jump processes may be visualized most easily considering rotational jumps. Let us regard e.g. the 120° rotational jumps of a methyl group around its symmetry axis. An incoherent study would reveal the atomic jumps of the associated hydrogens. The pair correlation function reflects the change of atomic configurations before and after the jump. Since a 120° jump does not change the configuration, a coherent scattering experiment would not reveal any dynamic effect.

Back to the pair correlation function for the β-process, where we will introduce a simple approximation. We know that for $t = 0$ the pair correlation function is reflected by the static structure factor $S(Q)$. Therefore for $t = 0$ the corresponding pair correlation function for the β-process must reveal $S(Q)$. We now assume that the inelastic scattering is related to uncorrelated jumps of the different atoms. Then all interferences for the inelastic process are destructive and the inelastic form factor should be identical to that of the self correlation function. For the normalized dynamic structure factor for the β-process we arrive at

$$\frac{S(Q,t)_\beta}{S(Q)} = \left\langle \frac{S(Q) - S^{inel}(Q)}{S(Q)} + \frac{S^{inel}(Q)}{S(Q)} e^{-2t/\tau(E)} \right\rangle_{g(E)} \tag{41}$$

This incoherent approximation does not reveal e.g. symmetry related cancellations, but displays a major feature of the corresponding dynamic structure factor, namely the relative suppression of the inelastic contributions from local jump processes at the maximum of the structure factor. Fig.23 displays the situation for polybutadiene. There a β-process corresponding to a jump length of $d = 1.5$Å has been found. The corresponding inelastic dynamic structure factor is strongly reduced at the position of the first peak, while it contributes strongly at higher Q. Fig.23 suggests a Q selectivity for the different relaxation processes: at the structure factor maximum local jump processes should not contribute and the relaxation due to flow should dominate. On the other hand at larger Q, in particular in the minimum of the structure factor, the secondary relaxation should reveal itself.

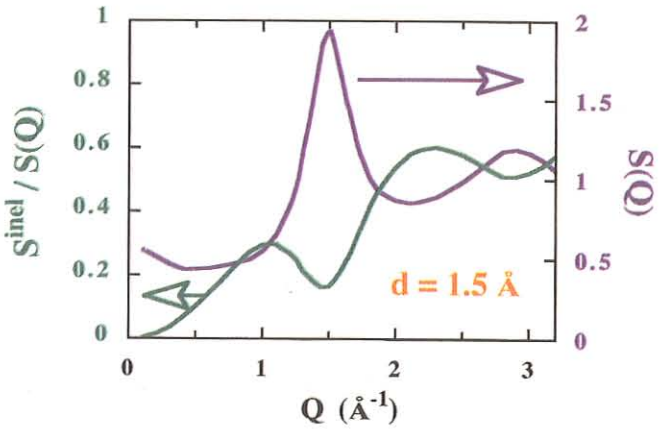


Fig. 23: *Static structure factor S(Q) and normalized inelastic contribution* $\frac{S_{inel}}{S(Q)}$ *to S(Q,t)/S(Q) for PB.*

We now assume that the α- and the β-relaxation are statistically independent. Then, in real space the joint correlation function is given by a convolution of the corresponding functions for both separated processes. In Q-space this convolution becomes a product and we may write the total scattering function as a product of the structure factor due to the α- and β-processes.

$$\frac{S(Q,t)}{S(Q)} = S_\alpha(Q,t) S_\beta(Q,t) / S(Q) \tag{42}$$

The approximation behind Eq.[42] is called Vinyard approximation and approximates the proper pair correlation function by its self counter part. The self correlation function for a diffusive process relates directly to the mean square displacement.

$$S^{self}(Q,t) = \exp\left\{-\frac{Q^2}{6}\left\langle r^2(t)\right\rangle\right\} \tag{43}$$

where $\left\langle r^2(t)\right\rangle$ is the mean square displacement of the flowing particle. According to Eq.[36] this should be described by a stretched exponential with the consequence

$$\left\langle r^2(t)\right\rangle = \tilde{D}\ t^\beta$$
$$\text{and}\quad \tau_{KWW} = Q^{2/\beta}\tilde{D}^{-1/\beta} \tag{44}$$

the combination of Eq.[36] and [43] invokes sublinear diffusion of the polymer segments as the underlying reason for the stretched exponential behaviour. Its signature is a power law dependence of the Kohlrausch-William-Watts relaxation times τ_{KWW} with an exponent $2/\beta$.

We note, that the stretching of Eq.[36] could also origin from a spatially heterogeneous distribution of relaxation process. In such a case Eq.[44] would not hold.

6.2 Experimental results

We commence with the secondary relaxation taking polyisobutylene as an example. Fig.24 presents the relaxation map of PIB [31]. The solid line corresponds to the dielectric β-relaxation, the dashed line named δ represents NMR results interpreted as a methyl group rotation. γ and γ' are theoretically predicted relaxation mechanisms. In the dynamic regime, where the α-relaxation is too slow to contribute, neutron backscattering has been employed, in order to unravel details of the β-process in this polymer [32].

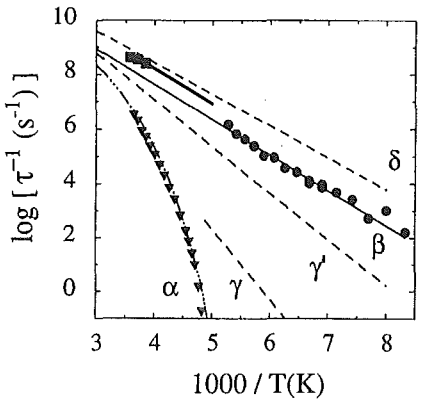


Fig. 24: *Relaxation map for PIB. ▼ marks the α-trace, ● relates to dielectric relaxation experiments on the β-relaxation, ■ results from QENS-experiments.*

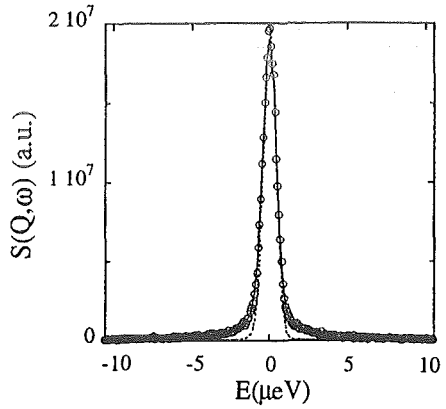


Fig. 25: *Backscattering spectrum from PIB at 270K at a Q-value Q = 1.7Å. The dashed line gives the resolution function, while the solid line displays the fit with the model (see text).*

As an example Fig.25 presents a spectrum taken at T = 270K and Q = 1.7Å^{-1}. The spectrum is characterized by a narrow peak, which nearly coincides with the instrumental resolution function (dashed line) and a broad foot revealing the relaxational behaviour. Such a spectral shape is typical for broad distributions of relaxation times, where only a part of it is resolved in the spectrum.

Fig.26 displays the elastic intensity observed for PIB as a function of Q. The data were corrected for multiple scattering and fitted with Eq.[40]. The elastic incoherent structure factor (EISF) reveals a jump distance d = 2.7Å. For comparison the solid lines display the prediction for methyl group rotation, which was invoked by NMR spectroscopy. Obviously the neutron data point into the direction of a larger motional amplitude.

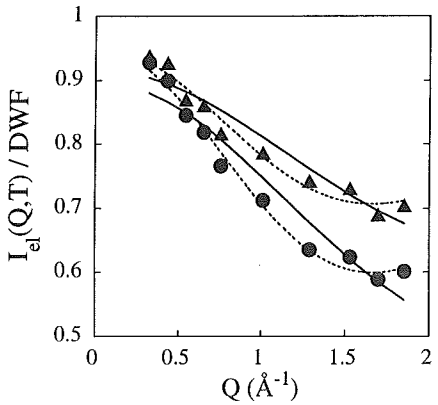


Fig. 26: *EISF for PIB (▲: 250K, ●: 270K). Solid lines: EISF for methylgroup rotation, dashed lines: fit result for a jump distance d = 2.7Å.*

The squares in Fig.23 display the neutron results for the β time scale. Within a factor of 2 they agree with the dielectric spectroscopy results. Since the underlying process has an amplitude of 2.7Å and is also dielectrically active, it cannot be understood as due to a methylgroup rotation alone. A possible interpretation is a combined backbone and methyl motion which is also supported by simulation results.

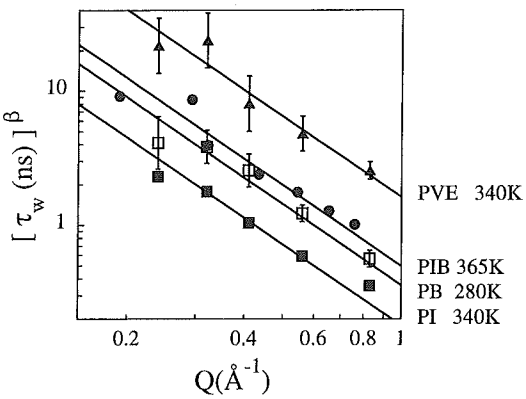


Fig. 27: *$(\tau_{KWW})^\beta$ for 4 different polymers as a function of Q. The solid lines display a Q^2 power law.*

We now turn to the α-relaxation and ask, whether the sub linear diffusion argument is supported by quasielastic neutron scattering. Fig.27 displays Kohlrausch-William-Watts relaxation rates obtained for four different polymers, polyvinylether (PVE) at 340K, polyisobutylene (PIB) at 365K, polybutadiene (PB) at 280K and polyisoprene (PI) at 340K [33].

In order to test Eq.[44] the relaxation rates have been exponentiated with the exponent β, obtained from the stretching of the relaxation functions in these polymers in dielectric spectroscopy. According to Eq.[44], τ^β should be proportional to Q^2. The solid lines in Fig.27 display this power law relation. As may be seen, in all cases within experimental error the experimental relaxation times obtained by backscattering spectroscopy follow the predicted power law behaviour. Thus, the experimental evidence supports a sub linear diffusion process as underlying the α-relaxation. We remark that this result is in disagreement with assertions that the stretched exponential relaxation function of the α-process originates from heterogeneous motional processes, where polymer segments in different parts of the sample would relax at different relaxation rates [34][35].

The dynamic pair correlation function for polymer relaxation has been studied thoroughly on polybutadiene as a function of temperature and momentum transfer [29][30][36][37][38]. Fig.28 gives a synopsis of these results. The dynamic data presented have been taken at the positions of the first and second peaks in the static structure factor of this polymer. As may be seen from the middle part of Fig.28 the first peak of the static structure factor moves strongly with temperature. This peak originates from interchain correlations, where weak v. d. Waals interactions lead to thermal expansion. The second peak relates mainly to intrachain correlations as may be seen from the temperature independence of its position indicative for covalent bonds. The temperature dependent relaxation spectra were rescaled in their time dependence with the characteristic time for viscosity relaxation τ_η (actually the time dependent monomeric friction coefficient was used). By this procedure the time correlation functions at the first peak assemble to a master curve, showing that the dynamics at the interchain distance follows the same relaxational behaviour as the macroscopic flow. On the other hand as evidenced by the lower part of Fig.28 at the second structure peak, such a

scaling does not reassemble the data points to a master curve. Obviously the dynamics at the second peak at higher Q follows different dynamics.

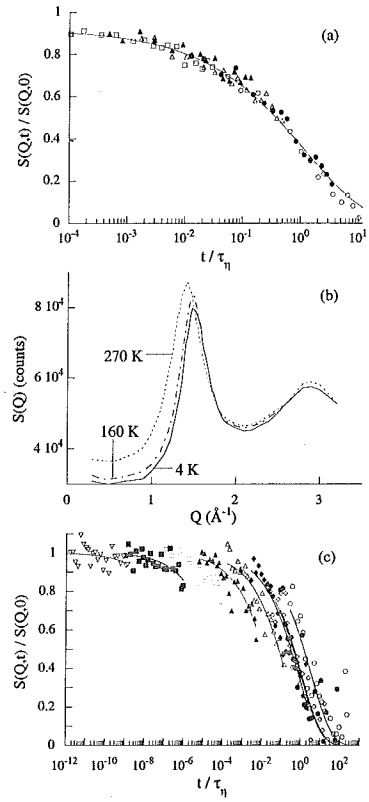


Fig. 28: *NSE spectra from PB taken at the first and second structure factor peak. The time is rescaled with the temperature dependence from flow relaxation. Center: S(Q) for different temperatures.*

Fig.29 displays the temperature dependence of the corresponding relaxation rates. While the data at the first peak nicely agree with the temperature dependence of the α-relaxation, as already evidenced by the scaling, the relaxation rates taken at the second peak follow an Arrhenius temperature dependence with a same activation energy as that of the corresponding dielectric β-process.

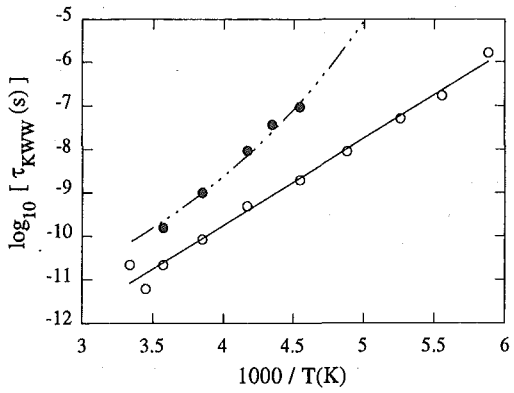


Fig. 29: *Relaxation rates at the first and second structure factor peak of PB in an Arrhenius representation. Solid lines: α- and β traces for this polymers.*

An evaluation of the structure factor following Eq.[41] and [42] reveals a jump distance for the β-process of $d = 1.5$Å. It also shows that the assumption of statistically independent α- and β-relaxations is supported by the temperature and momentum transfer dependent spectra.

7 Summary and Conclusions

In his lecture, we have discussed the dynamics of polymer melts restricting ourself to homopolymers. We have covered the range of molecular motions, commencing at the scale of a single bond to large motions reaching the scale of the entired chains. The lecture attempted to transmit a flavor of what can be achieved with high resolution neutron spectroscopy, which permits to access the molecular motion simultaneously in space and time.

The lecture commenced with a description of the standard model of polymer motion, the entropy driven dynamics, covered by the so called Rouse model. IN the spatial range, where the detailed chemical structure of the monomers ceases to be of importance NSE measurements have by and large confirmed the prediction of the Rouse model both for the self and the pair correlation function. We have briefly discussed an in depth comparison between computer simulation and NSE experiments which pointed out some limits of the Rouse approach.

Towards longer scales topological interactions resulting from the mutually interpenetrating chains gain dominant influence and confine the chain motion to a tube along the chain profile. We have presented measurements of the dynamic structure factor of a reptating chain which unequivocally confirm the picture of local reptation i.e. Rouse relaxation along a contorted tube. A measurement of the self correlation function corroborates with picture – both experiments may be interpreted by the same set parameters. With decreasing chain length, the tube confinement looses its grip and tube length fluctuations free the motions of the chain ends. This picture inherent in the reptation approach was also scorroborated by NSE studies.

Towards shorter length scales in the regime, where the picture of universal chain dynamics governed by entropic forces ceases to be valid, the first order limiting mechanisms were identified by NSE studies. It turned out that intrachain dissipation mechanisms related to rotational jumps between different isomeric states are the leading mechanism limiting the Rouse process towards shorter distances.

In the regime of the classical relaxations of polymers, neutron spectroscopy informs on the geometrical evolution of the motions and question. We have seen that the α-relaxation may be understood as a sublinear diffusion process while the β-relaxation is in good agreement with a local jump process of a few Å distance. Both processes may be considered with good approximation as statistically independent.

Though, this lecture restricted itself to homopolymer melts. We hope to have shown that the investigation of polymer dynamics is a broad and rich field with a great potentials. Neutrons play a key role in such investigations, because they allow to perform observations on the proper length and time scales as well as to exercise hydrogen deuterium contrast variation. Further developments will go in the direction of time dependent phenomena and real time experiments. We will look on nonequilibrium and transient phenomena, on the complexity posed by multicomponent systems, on molecular rheology, in order to understand the functioning of materials, and we will try to find a bridge to biology.

References

[1] G.L. Squires, *Introduction to the theory of thermal neutron scattering*, Cambridge University Press, Cambridge (1978)
[2] Guide to the neutron research facilities at the ILL, www.ill.fr
[3] Neutron Spin Echo, ed. by F. Mezei, Lecture notes in physics 128, Springer Verlag Berlin, Heidelberg, New York (1979)
[4] M. Doi, S.F. Edwards, *The theory of polymer dynamics*, Clarendon, Oxford (1986)
[5] D. Richter, B. Ewen, B. Farago, T. Wagner, Phys. Rev. Lett. **62**, 2640 (1989)
[6] W. Paul, G.D. Smith, D.Y. Yoon, B. Farago, S. Rathgeber, A. Zirkel, L. Willner, D. Richter, Phys. Rev. Lett. **80**, 2346 (1998)
[7] P.G. DeGennes, J. Chem. Phys. **55**, 572 (1971)
[8] G.D. Smith, W. Paul, M. Monkenbusch, D. Richter, J. Chem Phys. **261**, 61 (2000)
[9] P.G. DeGennes, J. Chem. Phys. **55**, 572 (1971)
[10] G. Ronca, J. Chem. Phys. **79**, 1031 (1983)
[11] A. Chatterjee, R. Loring, J. Chem. Phys. **101**, 1595 (1994)
[12] W. Hess, Macromolecules **19**, 1395 (1986); **20**, 2587 (1987); **21**, 2620 (1988)
[13] J. des Cloizeaux, J. Phys. I Fr. **3**, 1523 (1993)
[14] K.S. Schweizer, J. Chem. Phys. **91**, 5802 (1989); **91**, 5822 (1989)
[15] D. Richter, L. Willner, A. Zirkel, B. Farago, L.J. Fetters, J.S. Huang, Phys. Rev. Lett. **71**, 4158 (1993)
[16] D. Richter, B. Farago, L.J. Fetters, J.S. Huang, B. Ewen, C. Lartigue, Phys. Rev. Lett. **64**, 1389 (1990)
[17] R. Butera, L.J. Fetters, J.S. Huang, D. Richter, W. Pyckhout-Hintzen, A. Zirkel, B. Farago, B. Ewen, Phys. Rev. Lett. **66**, 2088 (1991)

[18] P. Schleger, B. Farago, A. Kollmar, C. Lartigue, D. Richter, Phys. Rev. Lett. **81**, 124 (1998)
[19] A. Wischnewski, M. Monkenbusch, L. Willner, D. Richter, A. Likthman, T. McLeish, Phys. Rev. Lett. (in print)
[20] M. Monkenbusch, A. Wischnewski, L. Willner, D. Richter (to be published)
[21] N. Fatkullin, R. Kimmich, Phys. Rev. E **52**, 3273 (1995)
[22] N. Clarke, T.C.B. McLeish, Macromolecules **26**, 5264 (1993)
[23] G. Allegra, F. Ganazzoli, Macromolecules **14**, 1110 (1981)
[24] G. Allegra, F. Ganazzoli, Advances in Chemical Physics **75**, 265 (1989)
[25] L. Harnau, R.G. Winkler, P.J. Reinicker, J. Chem. Phys. **102**, 7750 (1995); **104**, 6355 (1996)
[26] D. Richter, M. Monkenbusch, J. Allgaier, A. Arbe, J. Colmenero, B. Farago, Y. Cheol, R. Faust, J. Chem. Phys. **111** (1999) 6107
[27] A. Arbe, M. Monkenbusch, J. Stellbrink, D. Richter, B. Farago, K. Almdal, R. Faust, Macromolecules **34** (2001) 1281
[28] R. Dejean de la Batie, F. Lauprêtre, and L. Monnerie, Macromolecules **22**, 2617 (1989); A. A. Jones, R. P. Lubianez, M. A. Hanson, and S. L. J. Shostak, Polym. Sci.; Polym. Phys. Ed. **16**, 1685 (1978); Y. Inoue, A. Nishioka, and R. Chûjô, J. Polym. Sci.; Polym. Phys. Ed. **11**, 2237 (1973)
[29] A. Arbe, U. Buchenau, L. Willner, D. Richter, Phys. Rev. Lett. **76**, 1872 (1996)
[30] A. Arbe, D. Richter, J. Colmenero, B. Farago, Phys. Rev. E **54**, 3853 (1996)
[31] D. Richter, A. Arbe, J. Colmenero, M. Monkenbusch, B. Farago, R. Faust, Macromolecules **31**, 1133 (1998)
[32] A. Arbe, J. Colmenero, B. Frick, M. Monkenbusch, D. Richter, Macromolecules **31**, 4926 (1998)
[33] A. Arbe, J. Colmenero, M. Monkenbusch, D. Richter, Phys. Rev. Lett. **81**, (1998) 590
[34] A. Heuer, H.W. Spiess, Phys. Rev. Lett. **82**, 1335 (1999)
[35] A. Arbe, J. Colmenero, M. Monkenbusch, D. Richter, Phys. Rev. Lett **82**, 1336 (1999)
[36] D. Richter, B. Frick, B. Farago, Phys. Rev. Lett. **61**, 2465 (1988)
[37] B. Frick, B. Farago, D. Richter, Phys. Rev. Lett. **64**, 2921 (1990)
[38] B. Frick, D. Richter, Cl. Ritter, Europyhs. Lett. **9**, 557 (1989)

C3 Glassy Polymers

U. Buchenau
Institut für Festkörperforschung
Forschungszentrum Jülich GmbH

Contents

1 **Introduction** 2

2 **Material properties: partially crystalline and amorphous polymers** ... 2

3 **Mechanical properties and glass transition** 6

4 **Mode coupling and energy landscape** 8

5 **Relaxations in the glass phase** 10

6 **Mean field treatment of the glass transition** 12

1 Introduction

This article deals with the mechanical properties of polymers, with particular emphasis on the glass transition. In fact, the glass transition is the borderline between hard and soft matter; if one speaks about soft matter, one implicitly assumes a temperature above the glass temperature of the material in question. Soft matter implies a shear modulus of a few MPa, while hard matter has a shear modulus of the order of GPa, three orders of magnitude higher.

The following section 2 discusses six different polymers, which play an important role in material physics. One distinguishes hard plastics and rubbers, where the former have their glass temperature above room temperature, while the latter have glass temperatures of the order of 200 K. Section 3 focuses on the temperature dependence of the real and imaginary parts of the shear modulus in amorphous polymers. One observes not only the glass transition, but also secondary relaxation at lower temperatures. Section 4 turns to the theoretical concepts, in particular to the energy landscape concept, which becomes essential below the critical temperature of the mode coupling theory [1], still above the glass transition in the undercooled melt. In the glass phase, the energy landscape idea has found a quantitative formulation in terms of the Asymmetric-Double-Well-Potential (ADWP) or Gilroy-Phillips model [2,3], which is the subject of section 5. The ADWP model allows a quantitative description of dynamical mechanical data in terms of the barrier density function f(V). Finally, section 6 will show that the ADWP model does also describe the glass transition itself, if one takes the interaction between secondary relaxations into account.

2 Material properties: partially crystalline and amorphous polymers

From a materials point of view, polyethylene (PE) is the most important polymer, with a wide variety of possible applications. An example is the gasoline container in Fig.1. Chemically, it is the simplest possible polymer, a backbone of carbon atoms, each of which has two bonded hydrogen atoms.



Its structure, however, is not so simple, because it consists of a mixture of about 60 % crystalline and 40 % amorphous domains, with dimensions between 20 and 200 nm. In the crystalline domains, the polyethylene chains are stretched, and lie side by side in a close packing. In the amorphous domains, the chain molecules form an irregular array, like well-cooked spaghetti. Fig.2 gives a schematic view of this kind of mixed structure, Fig.3 shows the crystalline array viewed along the chains.

It is the mixed structure which provides the excellent material properties of polyethylene. A good material is one which does not break under excessive strain, but is able to yield locally without breaking. Polyethylene possesses this property to an unparalleled extent: one can deform a polyethylene foil by more than 200 % without breaking. Naturally, the crystalline part with a melting temperature of 413 K is rigid, but the glass temperature of the amorphous domains is below room temperature. Thus the amorphous part is able to flow. If one stretches

the foil, the crystalline parts turn around to orient the chain direction along the elongation. In this way, one can achieve a high degree of orientation of the chains in the crystalline domains.



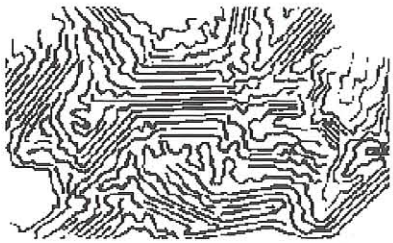


Fig. 1: *Gasoline container out of polyethylene (PE).*
Fig. 2: *Crystalline and amorphous regions in polyethylene at room temperature.*

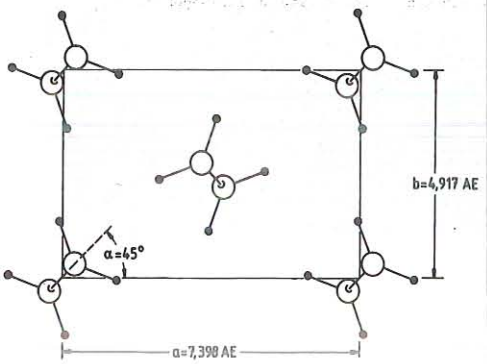
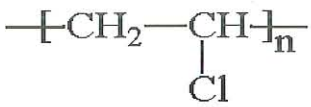




Fig. 3: *Crystalline structure of polyethylene, viewed along the chains.*
Fig. 4: *Pipes made out of PVC.*

Another important and partially crystalline polymer is polyvinylchloride (PVC). It has the monomer unit:



It has only about 11 % crystallinity, and, unlike PE, has the mechanical properties of a fully amorphous polymer. In particular, its glass transition is not smeared out as in PE, probably because the crystalline parts are unconnected islands in an amorphous matrix. Also, its glass temperature is above room temperature, at 357 K, so it is a hard plastic, which does not flow

at room temperature. Again, it has very good mechanical properties; we will see in the next section that these are related to a strong secondary relaxation which is still active at room temperature (any polymer will become brittle when cooled to liquid nitrogen).

From the chloron atom it contains, PVC does not easily burn. That is the reason why it is a preferred material for the tubing (Fig.4).

There are three important hard plastic materials which are fully amorphous: polystyrene (PS) with a glass temperature between 330 and 373 K, depending on the chain length (the longer chains have the higher glass temperature), polymethylmethacrylate (PMMA), better known by the trade name "plexiglass", with a glass temperature of 386 K, and, finally, bisphenol-A-polycarbonate (BPA-PC), with a very high glass temperature of 420 K. Polystyrene is relatively brittle; Fig.5 shows some yaourt cups, which will easily break when squeezed. Again, this brittleness is connected with the weakness of the secondary relaxation active at room temperature. In contrast, PMMA and BPA-PC are again very ductile, with excellent mechanical stability. These two can easily be made fully transparent, so they are good materials for eye glasses and hard contact lens. CD's are made out of BPA-PC (Fig.6).

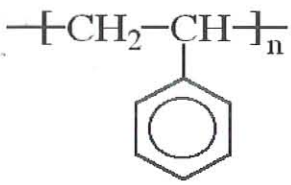




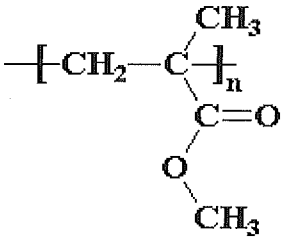
Fig. 5: *Yaourt cups and other food containers made of polystyrene (PS).*
Fig. 6: *CD made out of BPA-PC.*

The formula units are:

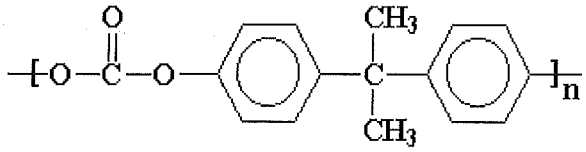
Polystyrene (PS)



Polymethylmethacrylate (PMMA)

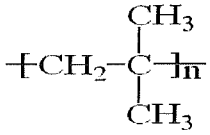


Bisphenol-A-polycarbonate (BPA-PC)



These are polymers with a more complicated structure, polystyrene with the bulky six-membered ring as a side group on the main chain, PMMA with a relatively flexible side group containing two oxygen atoms, and finally BPA-PC, which has two aromatic rings in the main chain.

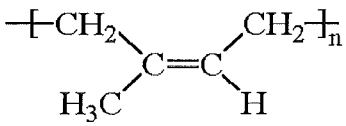
Turning to the rubbers, we present two examples.



The first is polyisobutylene (PIB). It has a glass temperature of 200 K, so it would flow away at room temperature. In order to keep it in shape, one can introduce a chemical cross-link at every twenty to fifty monomers. Then one gets a rubber, which can no longer flow away, but still is no truly rigid solid. Its restoring force does not result from the potential energy, as the elastic restoring force of a sheared solid, but from the entropy of the flexible polymer chain, which tends to form a gaussian coil. Thus rubber is indeed soft matter.

Polyisobutylene has an important additional property: it is airtight, probably because its compact monomers are able to pack so efficiently that small gas molecules do not fit in between. Therefore polyisobutylene is used at the inside of car tyres (Fig.7).

The outside of a car tyre is a complex composite, but the main ingredient is polyisoprene (PI):



This polymer has a double bond in the main chain, very convenient for the introduction of cross links. It is also a polymer which grows in the nature: hevea rubber is polyisoprene. Its glass temperature is at 203 K.



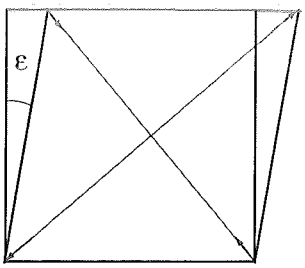
Fig. 7: *A car tyre has a lot of polyisoprene (PI) outside and polyisobutylene(PIB) inside.*

3 Mechanical properties and glass transition

The quantitative treatment of the mechanical properties introduces the shear strain ε (see Fig.8). The shear stress σ is related to the shear strain via the shear modulus G: $\sigma = G\,\varepsilon$.

In a viscoelastic medium, the shear stress after a given initial shear strain at time zero will decay. If one keeps the initial strain ε(0) constant, one can describe the decay of the shear stress with a time-dependent shear modulus G(t)

$$\sigma(t) = G(t)\varepsilon(0) \tag{1}$$



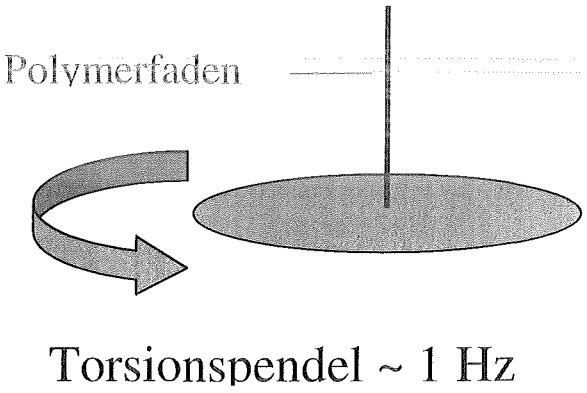


Fig. 8: *Shear distortion ε.*
Fig. 9: *Torsion pendulum (schematic).*

Instead of measuring the decay in time, one can also measure with a periodic strain at the frequency ω. One will find a periodic stress with the same frequency, but with a phase difference. This phase difference is a measure for the loss at the given frequency. One characterizes the response of such a dynamic experiment by a complex shear modulus, with a real part $G'(\omega)$ and an imaginary part $G''(\omega)$. The phase angle δ is given by the relation $\tan \delta = G'/G''$. Thus $G'(\omega)$ measures the restoring force constant at the frequency ω and $G''(\omega)$ the loss. More details are given in the article by Zimmermann [4] in this book.

Here, we focus on torsion pendulum measurements of four polymers, done at a frequency of about 1 Hz, i.e. $\omega = 2\pi = 6.28\ s^{-1}$. A schematic view of a torsion pendulum is given in Fig.9. One measures the resonance frequency and the damping of the pendulum. The filament, on which the disk is hanging, consists of the polymer being studied. One follows the development of the resonance frequency and of the damping as a function of temperature, from very low temperatures up to temperatures above the glass transition. Thus one obtains the curves shown in Fig.10. The data for PMMA, PS and PVC are taken from reference [5], the data of PIB from reference [6].

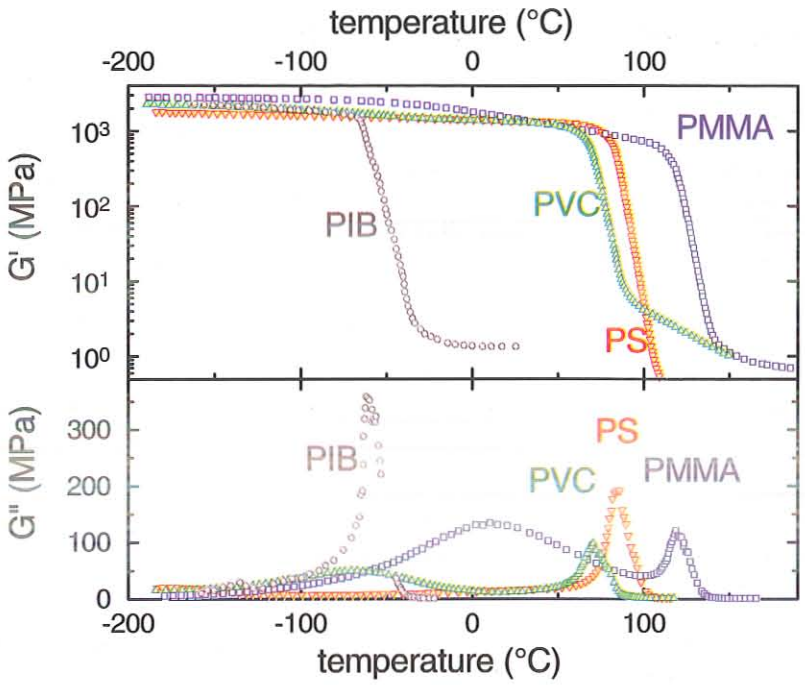


Fig. 10: *Torsion pendulum measurements of $G'(\omega)$ (upper part) and $G''(\omega)$ (lower part) as a function of temperature for three hard plastics and one rubber.*

The most remarkable feature of the G′ measurements is the strong decay by three orders of magnitude at the glass temperature. For the rubber polyisobutylene (PIB), this decay occurs below room temperature, for the other three polymers above. The decay is accompanied by a relatively sharp peak in the loss term G″. However, one sees also losses at lower temperatures, in the glass phase of the polymer. These are particularly pronounced in PVC and PMMA, in both cases markedly stronger than the losses in PS. Obviously, there are physical processes giving rise to dynamical mechanical losses on the time scale of a second even in the glass phase, though the polymer is no longer able to flow. One associates these losses with local structural rearrangements of the polymer, thermally activated jumps between two different minima of its energy landscape. These local thermally activated processes are called *secondary relaxations* to distinguish them from the primary relaxation of the glass transition.

Obviously, the secondary relaxations couple to the shear strain and are thus able to deform the polymer locally. In consequence, a polymer with strong secondary relaxations will not break as easily as a polymer with weak ones. As pointed out above, this explains the brittleness of polystyrene and the ductility of PVC and PMMA.

4 Mode coupling and energy landscape

The article by Richter [7] in this book deals with the influence of the chain connectivity on the mechanical properties of polymers, in particular with the reptation of very long chains. Here we focus on the temperature dependence, which shows no principal difference to the behaviour of other glass formers. An important concept for the mechanical properties of the undercooled liquid phase of glassformers in general is the mode coupling theory [1] of the glass transition (see the article by Zorn [8] in this book), based on the theory of liquids (see Nägele [9] in this book). The mode coupling theory supplies the theoretical basis for the rise of the viscosity with decreasing temperature in the liquid. In its simplest form, it would predict a divergence of the viscosity at a critical temperature T_c where the real liquid still has a low viscosity, about forty to sixty degrees K above the glass temperature T_g . To explain the flow between T_c and T_g, it was postulated [1] that thermally activated hopping processes begin to take over. The viscosity should then be describable in terms of an energy landscape picture, where the system makes thermally activated jumps from one valley to the other.

This postulate has received strong support from recent simulations [10], which showed that the system passes from the saddle points of the energy landscape to the minima at exactly this critical temperature. Thus one does indeed expect thermally activated flow between T_c and the calorimetric glass transition temperature T_g, where the system finally freezes.

Let us see whether this idea describes the breakdown of the shear modulus in Fig.10. We start with the simplest possibility, assuming a single thermally activated process with a relaxation time τ. One can calculate $G'(\omega)$ and $G''(\omega)$ of such a single-exponential decay (usually denoted as Debye process) from the Debye equations

$$G'(\omega) = G\frac{\omega^2\tau^2}{1+\omega^2\tau^2} \qquad (2)$$

$$G''(\omega) = G\frac{\omega\,\tau}{1+\omega^2\tau^2} \tag{3}$$

The equations imply that the height of the peak in the imaginary part at $\omega\tau = 1$ is precisely one half of the high frequency modulus G.

The temperature dependence of a thermally activated process is given by the Arrhenius relation

$$\tau_V = \tau_0 \exp(V / k_B T), \tag{4}$$

where τ_0 is a microscopic vibrational time of the order of 10^{-13} s and V is the barrier height which has to be overcome to get from one valley of the energy landscape to a neighbouring one.

Combining eqs. (2-4), one can calculate the temperature dependence of the real and the imaginary part of the shear modulus. Fig.11 shows an attempt to fit the glass transition of polystyrene in this simplest possible picture. The fit has three parameters, namely the barrier height V, the high frequency shear modulus G and its linear temperature dependence. All three parameters were adapted to the real part of the modulus.

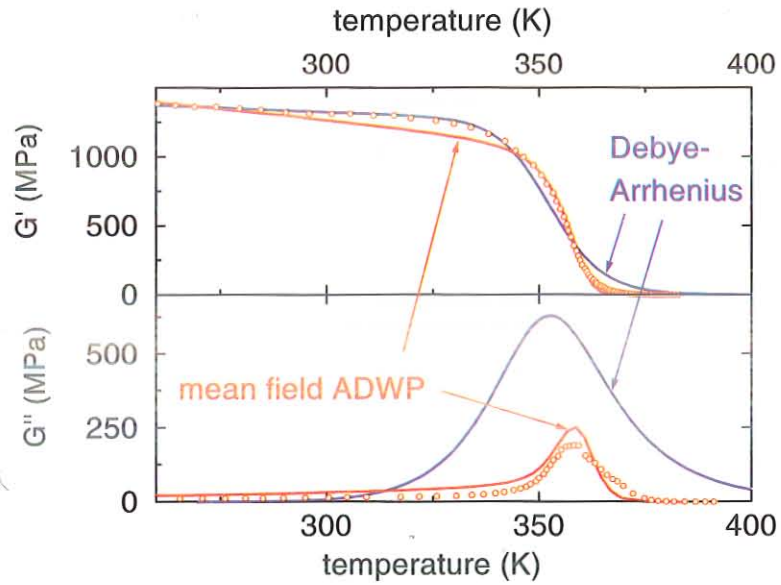


Fig. 11: *Fits of torsion pendulum measurements of $G'(\omega)$ (upper part) and $G''(\omega)$ (lower part) of polystyrene at the glass transition: Debye-Arrhenius and mean field ADWP.*

One learns a lot from the failures of this fit. The main failure is the height of the peak in the imaginary part, which is a factor of three too high. There is an obvious explanation for this

failure: One does not have a single relaxation time. Instead, one should superimpose a large number of processes with different relaxation times. This would indeed bring the peak height down. But: If we do that, we should find a strong broadening of the peak. The measured peak, however, is three to four times narrower than the single Debye peak. This seems to contradict the Kramers-Kronig relation between real and imaginary parts, which states that a step in the real part requires a proportional peak in the imaginary part. Is Kramers-Kronig wrong here?

The answer is naturally that the Kramers-Kronig relation is not wrong, but does indeed hold. The decay cannot be described by a single relaxation time, but must be described by an integral over many relaxation times (this is called the *stretching* of the glass transition process). The reason why the measured peak is so narrow is not its narrow width in frequency, but lies in its temperature dependence: it just runs through the frequency window of the measurement with a much higher speed than the one expected from the Arrhenius relation eq.(4) (this is called the *fragility* of the glass transition process). From the comparison with the Arrhenius-Debye picture in Fig.11, one can immediately quantify the stretching and the fragility: The stretching is a factor of three compared to a single Debye process, the time dependence is about a factor of eight faster than the expected Arrhenius relation. In fact, a compilation [11] of many different measurements at the glass transition of polystyrene supplies precisely these numbers.

How can one then understand the stretching and the fragility of the undercooled polymer melt in terms of thermally activated processes? We will return to this question in the last section. To answer it, one needs first a quantitative description of the secondary relaxation in the glass phase. This is supplied in the next section.

5 Relaxations in the glass phase

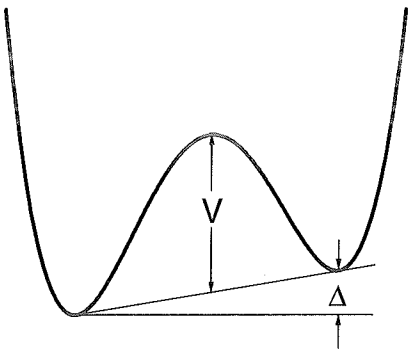


Fig. 12: *Asymmetric double-well potential*

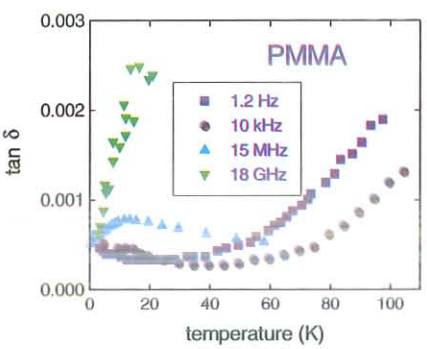
The treatment of the secondary relaxation in the glass phase is based on the energy landscape concept. In the ADWP (Asymmetric Double Well Potential) or Gilroy-Phillips [2] model, a

local structural relaxation is described in terms of three parameters (see Fig.12): the barrier height V, the asymmetry Δ between the two minima and the coupling constant γ to an external shear strain ε, which changes the asymmetry Δ to $\Delta+\gamma\varepsilon$ in the presence of the shear strain ε. The relaxation time τ_V is supposed to be given by the Arrhenius relation, eq.(4), for the given barrier height V.

One assumes a number density function $n(V,\Delta)$ of these local structural relaxing entities, which varies little if V or Δ change by energies of the order k_BT. It is easy to convince oneself that only the Δ-region within a few k_BT around the value $\Delta=0$, the symmetric potential, contributes to the time- and frequency dependence of the shear modulus. Taking $n(V, \Delta)$ to be practically constant in this range, one can integrate over the asymmetry to obtain a net step δG in the shear modulus from all relaxing entities with barrier heights between V and $V+\delta V$

$$\frac{\delta G}{G\delta V} = \frac{\gamma^2 n(V,0)}{G} \equiv f(V) \tag{5}$$

where G is the infinite frequency shear modulus. The relation defines f(V), the barrier density function, which turns out to be the proper tool for the calculation of the mechanical properties. For uncoupled relaxing entities and a frozen energy landscape, one would expect a temperature-independent f(V); as we will see, this approximation holds only at low temperatures in the glass phase. The real and imaginary part of the shear modulus at a given frequency can then be calculated from appropriate integrals of f(V) over all barrier heights [3].



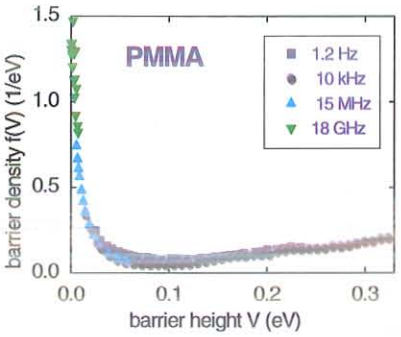


Fig. 13: *tan δ = G″/G′ in PMMA at low temperatures and different frequencies.*
Fig. 14: *f(V) calculated from the data of Fig.13.*

Figs.13 and 14 illustrate the success of the concept. If one looks first at the mechanical loss data of PMMA at low temperature in Fig.13, one wonders whether these measurements stem from the same polymer. However, if one calculates f(V) from these data, using the crude approximation $f(k_BT\ln(1/\omega\tau_0)) \approx 2G''/\pi Gk_BT$, one finds the curves of Fig.14, which agree quite well with each other.

6 Mean field treatment of the glass transition

One can understand the puzzling fragility and stretching of the glass transition in terms of the ADWP- or Gilroy-Phillips model. The treatment requires two basic assumptions, namely a Boltzmann factor for the symmetric double-wells and an interaction between the relaxing entities.

The passage from the glass phase to the undercooled liquid at the glass transition implies a passage from a frozen stress pattern to a time-dependent one, where local stresses build up and decay. For an asymmetric double-well potential as in Fig.12, this implies a time dependence of its parameters, in particular of the asymmetry Δ. In the undercooled liquid, Δ will change with time. The time scale of this change should be approximately the same as that of the change of the stress pattern, because the relaxing entity couples to the local strain with the coupling constant γ.

It is plausible to assume a lowering of the potential energy of the relaxing entity with increasing Δ; sitting in the lower minimum, one gains an energy $\Delta/2$ with respect to the symmetric potential. If this assumption is correct, the symmetric potential is indeed a rare bird. The potential ceases to be a double-well one at $\Delta \approx V$. If one identifies this limit with a potential energy zero, the symmetric double-well is at the energy V/2. In this spirit, one estimates a Boltzmann factor $\exp[-(V-\Delta)/2k_BT]$ for a relaxing entity with barrier height V and asymmetry Δ. As we will see, such a Boltzmann factor is able to explain the fragility, because it greatly reduces the number density of nearly symmetric ADWP's with decreasing temperature, in particular for high barriers.

However, one needs a second important ingredient: the interaction between different relaxing entities. Let us denote the barrier density function *without* interaction by $f_0(V)$ and the effective barrier density function *with* interaction by f(V). Above T_g, $f_0(V)$ is assumed to grow with the Boltzmann factor introduced above

$$f_0(V,T) = f_0(V,T_g)\exp(V/k_BT_g - V/k_BT) \tag{6}$$

In the following, a mean-field relation between f(V) and $f_0(V)$ is derived. Consider a constant shear strain ε_0 applied at time zero. The stress σ after the time t is given by eq.(1) , with the time-dependent shear modulus G(t) given by [3]

$$G(t) = \int_0^\infty \exp(-t/\tau_V) f(V) dV \tag{7}$$

As time proceeds, G(t) goes slowly toward zero. Simultaneously, the zero point of the shear strain shifts slowly from zero to ε_0. A relaxation jump over a barrier of height V will tend to occur at times of the order of the relaxation time τ_V given by the Arrhenius relation eq.(4). At the time τ_V, the stress is diminished by a factor $G/G(\tau_V)$. Consequently, the distance between the actual shear strain ε_0 and its zero point is diminished by the same factor. Nevertheless, the

number of relaxational jumps between V and V+δV needed for the equilibration is not diminished, but corresponds still to the initial strain zero point at zero. This effect enhances f(V) by a factor $G^2/G(\tau_V)^2$ compared to $f_0(V)$, because the square of the distance to the actual zero point of the shear strain enters into the definition of the barrier density function, eq.(5).

This enhancement does not go on forever. For times of the order of the stress relaxation time, the parameters of a given structural relaxation will no longer be time-independent. In particular, the asymmetry Δ will tend to diffuse away from the symmetric value 0, preferably in the direction where the occupied minimum is lowered. As soon as the occupied minimum is lowered by a few times k_BT, this particular relaxation will no longer participate in the stress equilibration. We describe this terminal process by a terminal relaxation time τ_t, which will be close to the stress relaxation time. We incorporate τ_t into the definition of the barrier density function without interaction

$$F_0(V) = f_0(V)\exp(-\tau_V/\tau_t) \tag{8}$$

With this definition and the enhancement described above, the relation between f(V) and $F_0(V)$ is given by

$$f(V) = F_0(V)\frac{G^2}{G(\tau_V)^2} = \frac{F_0(V)}{\left[\int_0^\infty \exp(-\tau_V/\tau_\nu) f(\nu) d\nu\right]^2} \tag{9}$$

In order to solve this integral equation for f(V), one differentiates the integral with respect to V

$$-\int_0^\infty \frac{\tau_V}{\tau_\nu k_B T}\exp(-\tau_V/\tau_\nu) f(\nu) d\nu = \frac{f^{1/2}}{2F_0^{1/2}}\left[\frac{F_0}{f}\right]' \tag{10}$$

Here the prime denotes the differentiation with respect to V, and the functions f and F_0 without argument denote the respective function at V.

In the integral of eq.(10), f(v) is multiplied by a function which strongly peaks at V. Therefore one may use the approximation

$$\int_0^\infty \frac{\tau_V}{\tau_\nu k_B T}\exp(-\tau_V/\tau_\nu) f(\nu) d\nu \approx \frac{f}{F_0}\int_0^\infty \frac{\tau_V}{\tau_\nu k_B T}\exp(-\tau_V/\tau_\nu) F_0(\nu) d\nu \tag{11}$$

Inserting this approximation into eq.(10), one obtains

$$-\int_0^\infty \frac{\tau_V}{\tau_\nu k_B T}\exp(-\tau_V/\tau_\nu) F_0(\nu) d\nu = \frac{F_0^{1/2}}{2f^{1/2}}\left[\frac{F_0}{f}\right]' \tag{12}$$

By integration over V one finds

$$\int_0^\infty \exp(-\tau_V/\tau_\nu)F_0(\nu)d\nu = C + \frac{F_0^{3/2}}{3f^{3/2}} \tag{13}$$

Considering the limit $V \to \infty$, one finds the integration constant C=0. The other limit $V \to 0$ supplies the normalization condition

$$\int_0^\infty F_0(V)dV = \int_0^\infty f_0(V)\exp(-\tau_V/\tau_t)dV = \frac{1}{3} \tag{14}$$

which serves to define the terminal relaxation time τ_t. With this definition, one obtains the final equation

$$f(V) = \frac{F_0(V)}{\left[\int_0^\infty \exp(-\tau_V/\tau_\nu)F_0(\nu)d\nu\right]^{2/3}} \tag{15}$$

This mean field solution has two important properties. The first is that the rigidity vanishes when the integral over the noninteracting relaxation entities is 1/3, i.e. when the noninteracting secondary processes would have reduced the initial shear modulus at time zero to 2/3 of its value. The second is that this vanishing occurs in a rather dramatic way, because the relaxing entities at this critical barrier value receive a strong enhancement by the effect of the collectivity, to such an extent that one is tempted to assume a separate primary process (the so-called α-process) which has nothing to do with the secondary relaxations. In fact, this more or less unconscious assumption underlies most of the present attempts to understand the glass transition [12]. The above mean-field treatment shows such an assumption to be unnecessary; what one sees at the glass transition are simple Arrhenius relaxations of no particularly large number density, blown up to impressive size by the small denominator of eq.(15).

From f(V), one can obtain any shear response using the rheological equations [3]. In particular, one finds the time-dependent shear modulus G(t) using eqs. (9) and (13)

$$G(t) = \left[3\int_0^\infty \exp(-t/\tau_V)F_0(V)dV\right]^{1/3} \tag{16}$$

Similarly, one can calculate the real and imaginary part of the response at the frequency ω

$$G'(\omega) = G\int_0^\infty \frac{\omega^2\tau_V{}^2}{1+\omega^2\tau_V{}^2} f(V)dV \tag{17}$$

$$G''(\omega) = G\int_0^\infty \frac{\omega\,\tau_V}{1+\omega^2\tau_V{}^2} f(V)dV \tag{18}$$

The polystyrene data in Fig.11 were fitted using these equations. The determination of $f_0(V,T_g)$ was done using mechanical loss data in the glass phase. The resulting $f_0(V,T_g)$ and $f(V,T_g)$ are compared to each other in Fig.15. One sees the strong enhancement of $f(V,T_g)$ as compared to $f_0(V,T_g)$, and the decay above 1 eV, where the integral over $f_0(V)$ approaches 1/3.

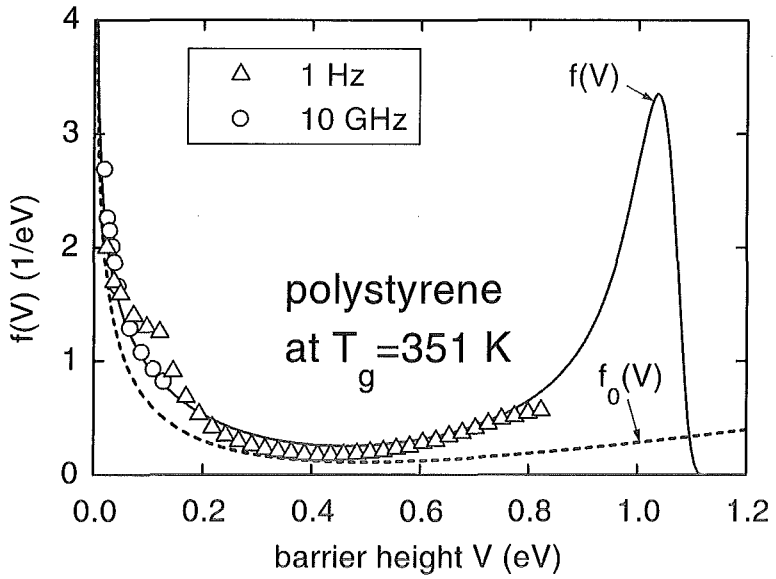


Fig. 15: *f(V) and $f_0(V)$ at T_g=352 K in polystyrene.*

As the temperature increases, $f_0(V,T)$ increases according to the Boltzmann factor of eq.(6). This means that the normalization condition, eq.(14), is already satisfied at a lower cutoff barrier $V_t = k_B T \ln(\tau_t/\tau_0)$. The resulting downward shift of V_t with increasing temperature explains the measured fragility. The curves in Fig.11 denoted by "mean-field ADWP" were calculated in this way.

References

[1] W. Götze and L. Sjögren, Rep. Prog. Phys. 55, 241 (1992)
[2] K. S. Gilroy and W. A. Phillips, Phil. Mag. B 43, 735 (1981)
[3] U. Buchenau, Phys. Rev. B 63, 104203 (2001)
[4] W. Zimmermann, this issue
[5] F. R. Schwarzl, *Polymermechanik,* (Springer, New York 1990), Fig.9.16
[6] K. Schmieder and K. Wolf, Kolloid-Z. 134, 149 (1953)
[7] D. Richter, this issue
[8] R. Zorn, this issue
[9] G. Nägele, this issue
[10] L. Angelani, R. Di Leonardo, G. Ruocco, A. Scala and F. Sciortino, Phys. Rev. Lett. 85, 5356 (2000)
[11] R. Böhmer, K. L. Ngai, C. A. Angell and D. J. Plazek, J. Chem. Phys. 99, 4201 (1993)
[12] M. D. Ediger, C. A. Angell and S. R. Nagel, J. Phys. Chem. 100, 13200 (1996)

C 4 Rotational Brownian Motion of Colloidal Rods

Jan K. G. Dhont
Institut für Festkörperforschung
Forschungszentrum Jülich GmbH

Contents

1 Introduction 2

2 The Smoluchowski Equation for Rigid Rods 4

3 Translational and Rotational Diffusion of non-Interacting Rods 10

4 The Orientational Order Parameter 12

5 The Doi-Edwards Equation of motion and the Maier-Saupe Potential 14

6 An Orientational Closure Relation 17

7 Influence of Shear Flow 18

8 The Isotropic-Nematic Phase Transition 20
8.1 Bifurcation diagrams 21
8.2 The orientational free energy 24

9 Current Research Activities in this Area 25

1 Introduction

Due to thermal collisions of solvent molecules with the surface of a colloidal particle, both the position and orientation of that particle change with time in a chaotic fashion. This thermal motion of colloidal particles is referred to as *Brownian motion* . The chaotic motion of the orientation and position of a colloidal particle are referred to as *rotational-* and *translational* Brownian motion, respectively.

Thermal motion of particles drives macroscopic time changes, like diffusion, relaxation to equilibrium after cessation of an external field, and phase separation. At high concentrations of colloidal particles, interactions between the colloidal particles affect the nature of their Brownian motion. Consider, for example, a suspension of rod like colloidal particles which are oriented by means of an external field. The decay rate of this aligned state after cessation of the external field toward the isotropic state, where all orientations are equally likely, depends on the concentration due to interactions between the rods. At relatively low concentrations, an aligned state will always decay to the isotropic state. At sufficiently high concentration, however, a slightly aligned initial state tends to become even more aligned. The stable equilibrium state is now a so-called nematic state, where the rods are aligned along a preferred direction. The isotropic state is now meta-stable or unstable against the nematic state. Fig.1 shows a photograph [1] of a colloidal system of AlOOH-rods (boehmite) during phase separating, where the isotropic state becomes partly nematic. The photograph is taken with the sample between crossed polarizers, so that isotropic regions appear black. Nematic regions are most likely white, as the result of intrinsic birefringence of the boehmite rods. Since the density of the nematic phase is larger than the isotropic phase, the nematic droplets sediment to the bottom of the container.

This lecture is devoted to rotational Brownian motion of rigid, uniaxial colloidal rods. Relaxation dynamics of such (interacting) rods and the isotropic/nematic phase stability will be treated on a microscopic basis, including the effects of shear flow. The fundamental equation of motion, which is the basis for describing dynamics and kinetics of suspensions, is the Smoluchowski equation. This is the equation of motion for the probability density function of the relevant phase space coordinates of the colloidal particles. The Smoluchowski equation for interacting rigid rods is derived in section 2, which includes both translational and rotational Brownian motion. Translational and rotational diffusion of non-interacting rods is discussed in section 3. To describe orientational order (induced by external means like shear flow, or by rod-rod interactions), the orientational order parameter tensor $\mathbf{S}$ is introduced in section 4. An equation of motion for this tensor (the Doi-Edwards equation) is derived in section 5. This equation of motion contains a higher order orientational average, which will be expressed in terms of $\mathbf{S}$ in section 6. Since shear flow tends to align rod-like particles, one expects that phase transition lines will be shifted by applying shear flow. The additional term to the Smoluchowski equation due to shear flow is considered in section 7. On the basis of the equation of motion derived in sections 5 and 7, and the closure relation constructed in section 6, the concentration dependent orientational dynamics and phase behaviour is then discussed in section 8. Section 9 contains a short overview of the interests in current research related to the present topic.

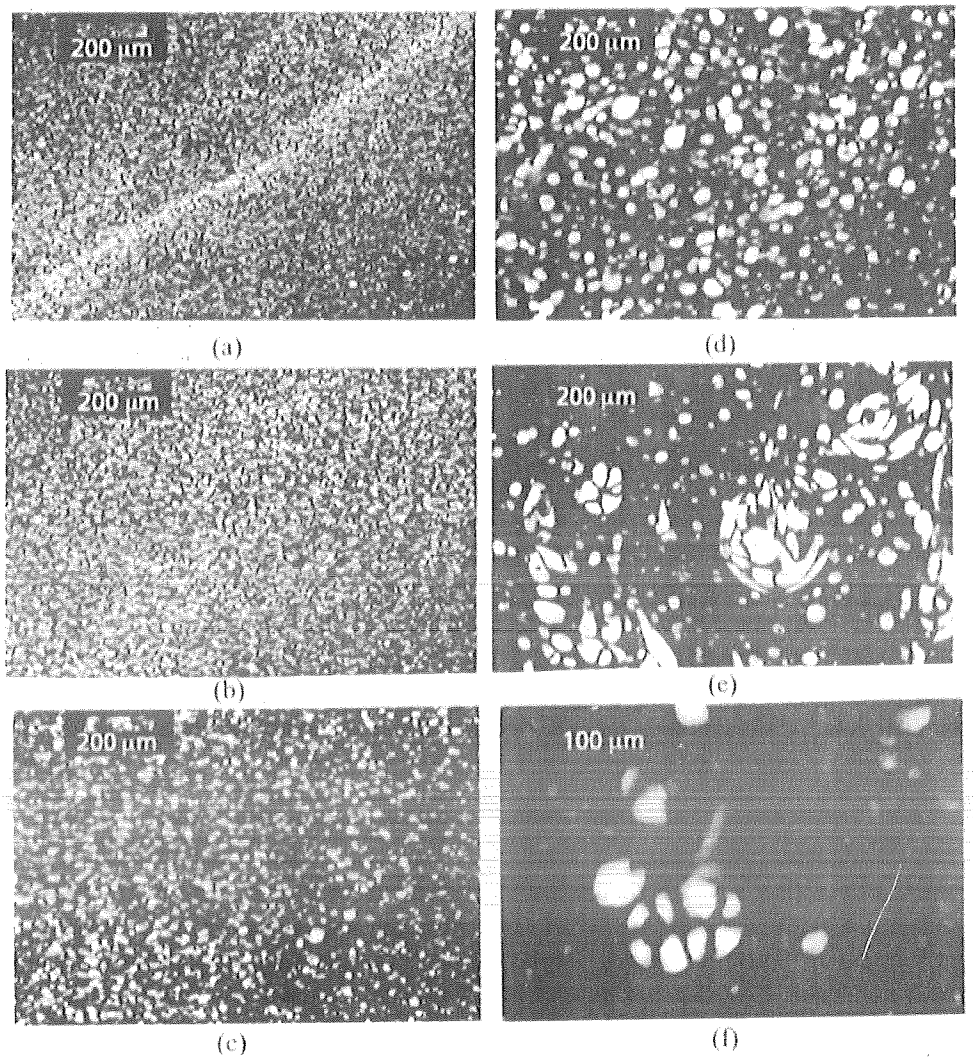


Fig. 1: *A photograph of a suspension of rods during isotropic-nematic phase separation. The sample is in between two crossed polarizers. Time increases from a to f. Nematic regions appear white as the result of birefringence. This photograph is taken from ref.[1].*

2 The Smoluchowski Equation for Rigid Rods

Consider a cylindrically symmetric, rigid rod. The position coordinate of the rod will be denoted by $\mathbf{r}$, while its orientation is characterized by the unit vector $\hat{\mathbf{u}}$ which is directed along the long axis of the rod (see Fig.2a). Here, "unit vector" means that $\hat{\mathbf{u}}$ has length 1, that is, $|\,\hat{\mathbf{u}}\,|=1$. The "microstate" of the rod is thus set by a point in $\Re^3$ (the position vector $\mathbf{r}$) and a point on the unit spherical surface (the tip of the vector $\hat{\mathbf{u}}$), as depicted in Fig.2b. The points in $\Re^3$ and on the unit spherical surface exhibit chaotic motion due to translational- and rotational Brownian motion, respectively. Consider now an ensemble of $\mathcal{N}$ containers filled with solvent and containing just a single Brownian rod (see Fig.3). The "microstate" of this ensemble (as far as the colloidal rod is concerned) is set by $\mathcal{N}$ points in $\Re^3$ (for the positions) and $\mathcal{N}$ points on the unit spherical surface (for the orientations). Let $\mathcal{W}$ denote an arbitrary volume in $\Re^3$, and $\mathcal{A}$ an arbitrary surface area on the unit spherical surface (see Fig.4). The density of points at a certain position and orientation is proportional to the probability of finding a rod in that microstate. To find an equation of motion for that probability, we shall ask for the time rate of change of the number of points inside $\mathcal{W}$ and $\mathcal{A}$. The time dependent "number of points" $N(t)$ is related to the probability density function $P(\mathbf{r},\hat{\mathbf{u}},t)$ for the position $\mathbf{r}$ and orientation $\hat{\mathbf{u}}$, as,

$$N(t) \;=\; \int_{\mathcal{W}} d\mathbf{r} \int_{\mathcal{A}} d\hat{\mathbf{u}}\, P(\mathbf{r},\hat{\mathbf{u}},t)\;, \tag{1}$$

where $d\hat{\mathbf{u}}$ denotes an infinitesimally small surface element on the unit spherical surface (in spherical coordinates this surface element is equal to $\sin\{\Theta\}\, d\Theta\, d\varphi$). The time rate of change of the number of points in $\mathcal{W}$ and $\mathcal{A}$ is thus given by,

$$\frac{d\,N(t)}{dt} \;=\; \int_{\mathcal{W}} d\mathbf{r} \int_{\mathcal{A}} d\hat{\mathbf{u}}\, \frac{\partial}{\partial t} P(\mathbf{r},\hat{\mathbf{u}},t)\;. \tag{2}$$

The rate of change of thee number of points is related to the in- and out-flux of points through the boundaries $\partial\mathcal{W}$ and $\partial\mathcal{A}$ of $\mathcal{W}$ and $\mathcal{A}$, respectively. Consider first the flux through $\partial\mathcal{W}$. Let $\mathbf{v}$ denote the translational velocity of the center of mass of the rod. The only component of $\mathbf{v}$ that contributes to in- or out-flux through $\partial\mathcal{W}$ is the component that is perpendicular to $\mathcal{W}$: when $\mathbf{v}$ is locally parallel to $\partial\mathcal{W}$, there is no local in- nor out-flux contribution. The component of $\mathbf{v}$ that is perpendicular to $\partial\mathcal{W}$ is equal to $\hat{\mathbf{n}}\cdot\mathbf{v}$, where $\hat{\mathbf{n}}$ is the unit normal (which is chosen to be directed outward of $\mathcal{W}$). The local contribution to the rate of change of the number of points in $\mathcal{W}$ is equal to the local density of points $P(\mathbf{r},\hat{\mathbf{u}},t)$, multiplied by the perpendicular component $\hat{\mathbf{n}}\cdot\mathbf{v}$ of $\mathbf{v}$. The total rate of change $dN_{\mathcal{W}}(t)/dt$ of the number of points due to in- and out-flux through $\partial\mathcal{W}$ is thus equal to (with dS an infinitesimally small surface element on $\partial\mathcal{W}$; see Fig.5a),

$$\frac{d\,N_{\mathcal{W}}(t)}{dt} \;=\; -\oint_{\partial\mathcal{W}} dS \int_{\mathcal{A}} d\hat{\mathbf{u}}\; \hat{\mathbf{n}}\cdot[\mathbf{v}\,P(\mathbf{r},\hat{\mathbf{u}},t)]\;. \tag{3}$$

The minus sign here is due to the fact that the direction of $\hat{\mathbf{n}}$ is pointing outward of $\mathcal{W}$: when $\mathbf{v}\sim\hat{\mathbf{n}}$, so that $\hat{\mathbf{n}}\cdot\mathbf{v}>0$, the number points in $\mathcal{W}$ decreases in time. Applying *Gauss's integral theorem* it is found that,

$$\frac{d\,N_{\mathcal{W}}(t)}{dt} \;=\; -\int_{\mathcal{W}} d\mathbf{r} \int_{\mathcal{A}} d\hat{\mathbf{u}}\; \nabla\cdot[\mathbf{v}\,P(\mathbf{r},\hat{\mathbf{u}},t)]\;. \tag{4}$$

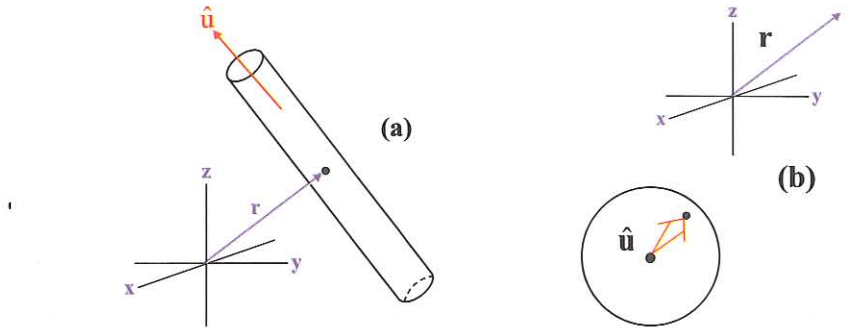


Fig. 2: *(a) Definition of the orientation and position coordinates of a cylindrically symmetric, rigid rod. The orientation* $\hat{\mathbf{u}}$ *is the unit vector pointing along the long axis of the rod and the position coordinate is the position of the center of mass of the rod. (b) The "microstate" of a rod is characterized by a point in* $\Re^3$*, for its position coordinate* $\mathbf{r}$*, and a point on the unit spherical surface, for its orientation* $\hat{\mathbf{u}}$*.*

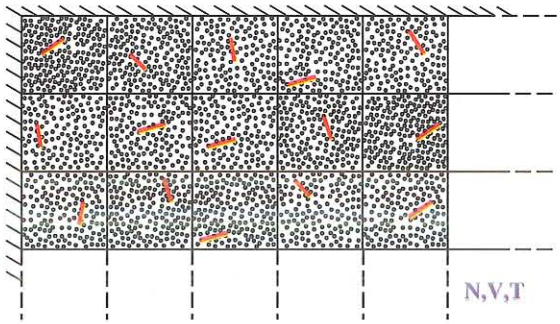


Fig. 3: *An ensemble of many, macroscopically identical systems. Each system contains a fixed number of solvent molecules (depicted by the green points), and just a single rod (in red). The number of particles, the volume and temperature of each system is fixed, that is, we consider the NVT-ensemble.*

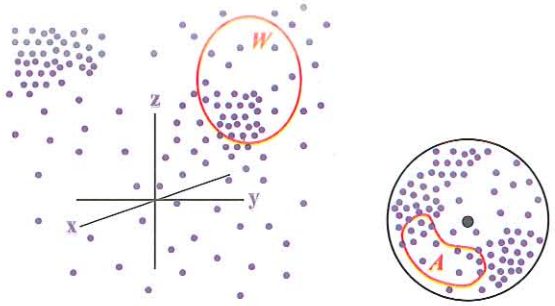


Fig. 4: *The "microstate" of the ensemble is given by a point distribution in* $\Re^3$ *and on the unit spherical surface.* $\mathcal{W}$ *and* $\mathcal{A}$ *are arbitrary subspaces in* $\Re^3$ *and on the unit spherical surface, respectively.*

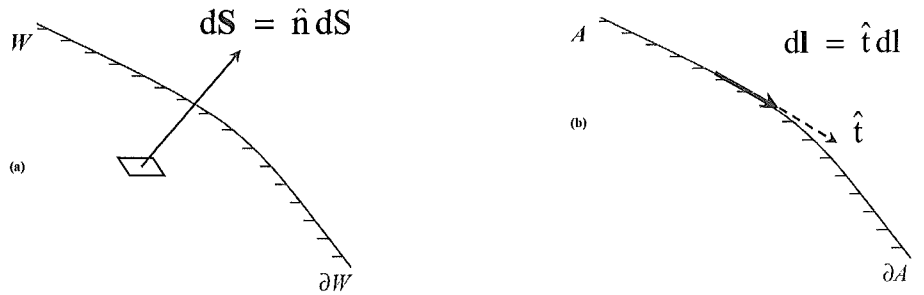


Fig. 5: *(a) Part of the boundary $\partial\mathcal{W}$, and (b) of the boundary $\partial\mathcal{A}$. For an explanation of the symbols in these figures, see the main text.*

Next consider the contribution $dN_{\mathcal{A}}(t)/dt$ of the rate of change due to in- and out-flux through the boundary $\partial\mathcal{A}$ of $\mathcal{A}$. This boundary is a closed curve on the unit spherical surface. Since $\hat{\mathbf{u}}$ is always perpendicular to the unit spherical surface, the vector that is locally perpendicular to $\partial\mathcal{A}$ is equal to $d\mathbf{l}\times\hat{\mathbf{u}}$, where $d\mathbf{l}$ is the infinitesimally small vector that is tangential to the curve $\partial\mathcal{A}$ (see Fig.5b). The component of the velocity $d\hat{\mathbf{u}}/dt$ that is perpendicular to the $\partial\mathcal{A}$ is thus equal to $(d\mathbf{l}\times\hat{\mathbf{u}})\cdot d\hat{\mathbf{u}}/dt$, which is the component that determines the in- and out-flux. Since this is equal to $d\mathbf{l}\cdot(\hat{\mathbf{u}}\times d\hat{\mathbf{u}}/dt)$, the total rate of change $dN_{\mathcal{A}}(t)/dt$ of the number of points in $\mathcal{A}$ is thus equal to,

$$\frac{d\,N_{\mathcal{A}}(t)}{dt} \;=\; -\int_{\mathcal{W}} d\mathbf{r} \oint d\mathbf{l}\cdot\left(\hat{\mathbf{u}}\times\frac{d\hat{\mathbf{u}}}{dt}\right) P(\mathbf{r},\hat{\mathbf{u}},t)\;. \tag{5}$$

Applying *Stokes's integral theorem*, it is found that,

$$\frac{d\,N_{\mathcal{A}}(t)}{dt} \;=\; -\int_{\mathcal{W}} d\mathbf{r}\int_{\mathcal{A}} d\hat{\mathbf{u}}\,\hat{\mathbf{u}}\cdot\left\{\nabla_{\hat{\mathbf{u}}}\times\left(\hat{\mathbf{u}}\times\frac{d\hat{\mathbf{u}}}{dt}\right) P(\mathbf{r},\hat{\mathbf{u}},t)\right\}\;, \tag{6}$$

where $\nabla_{\hat{\mathbf{u}}}$ is the gradient operator with respect to the cartesian components of $\hat{\mathbf{u}}$. For the cylindrical rods under consideration, the component $\boldsymbol{\Omega}$ of the angular velocity that changes the orientation of the rod is equal to,

$$\boldsymbol{\Omega} \;=\; \hat{\mathbf{u}}\times\frac{d\hat{\mathbf{u}}}{dt}\;. \tag{7}$$

This can be seen as follows. By definition we have: $d\hat{\mathbf{u}}/dt = \boldsymbol{\Omega}\times\hat{\mathbf{u}}$. Operating on both sides with $\hat{\mathbf{u}}\times$, using that $\hat{\mathbf{u}}\times(\boldsymbol{\Omega}\times\hat{\mathbf{u}}) = (\hat{\mathbf{u}}\cdot\hat{\mathbf{u}})\boldsymbol{\Omega} - (\hat{\mathbf{u}}\cdot\boldsymbol{\Omega})\hat{\mathbf{u}}$, and noting that $\hat{\mathbf{u}}\cdot\hat{\mathbf{u}} = 1$ and $\hat{\mathbf{u}}\cdot\boldsymbol{\Omega} = 0$, eq.(7) is recovered. Using that $\hat{\mathbf{u}}\cdot\nabla_{\hat{\mathbf{u}}}\times(\cdots) = (\hat{\mathbf{u}}\times\nabla_{\hat{\mathbf{u}}})\cdot(\cdots)$, eq.(6) is thus identical to,

$$\frac{d\,N_{\mathcal{A}}(t)}{dt} \;=\; -\int_{\mathcal{W}}\int_{\mathcal{A}} d\hat{\mathbf{u}}\;(\hat{\mathbf{u}}\times\nabla_{\hat{\mathbf{u}}})\cdot[\boldsymbol{\Omega}\,P(\mathbf{r},\hat{\mathbf{u}},t)]\;. \tag{8}$$

Combining eqs.(4,8) we thus find that,

$$\begin{aligned}\frac{dN(t)}{dt} \;&=\; \frac{d\,N_{\mathcal{A}}(t)}{dt} + \frac{d\,N_{\mathcal{W}}(t)}{dt}\\ &=\; -\int_{\mathcal{W}} d\mathbf{r}\int_{\mathcal{A}} d\hat{\mathbf{u}}\,\Big\{\nabla\cdot[\mathbf{v}\,P(\mathbf{r},\hat{\mathbf{u}},t)] + \hat{\mathcal{R}}\cdot[\boldsymbol{\Omega}\,P(\mathbf{r},\hat{\mathbf{u}},t)]\Big\}\;,\end{aligned} \tag{9}$$

where the *rotation operator* $\hat{\mathcal{R}}$ is defined for convenience as,

$$\hat{\mathcal{R}}\,(\cdots) \;=\; \hat{\mathbf{u}} \times \nabla_{\hat{\mathbf{u}}}\,(\cdots)\;. \tag{10}$$

Note the similarity between the translational and rotational contributions to the rate of change : instead of the translational velocity $\mathbf{v}$, the angular velocity $\boldsymbol{\Omega}$ appears in the rotational contribution, and instead of the gradient operator ∇ the rotation operator $\hat{\mathcal{R}}$ appears. From eqs.(2,9) it is now found that,

$$\int_{\mathcal{W}} d\mathbf{r} \int_{\mathcal{A}} d\hat{\mathbf{u}} \left\{ \frac{\partial}{\partial t} P(\mathbf{r},\hat{\mathbf{u}},t) + \nabla \cdot [\mathbf{v}\, P(\mathbf{r},\hat{\mathbf{u}},t)] + \hat{\mathcal{R}} \cdot [\boldsymbol{\Omega}\, P(\mathbf{r},\hat{\mathbf{u}},t)] \right\} = 0\;. \tag{11}$$

Since this holds for arbitrary volumes $\mathcal{W}$ and surface areas $\mathcal{A}$, the integrand must be equal to 0. Hence,

$$\frac{\partial}{\partial t} P(\mathbf{r},\hat{\mathbf{u}},t) \;=\; -\nabla \cdot [\mathbf{v}\, P(\mathbf{r},\hat{\mathbf{u}},t)] - \hat{\mathcal{R}} \cdot [\boldsymbol{\Omega}\, P(\mathbf{r},\hat{\mathbf{u}},t)]\;. \tag{12}$$

Here, we considered a system that contained just a single rod. For a suspension that contains N rods, the relevant phase space coordinates are,

$$\{\mathbf{r}_1, \mathbf{r}_2, \cdots, \mathbf{r}_N, \hat{\mathbf{u}}_1, \hat{\mathbf{u}}_2, \cdots, \hat{\mathbf{u}}_N\}\;,$$

instead of just $\{\mathbf{r},\hat{\mathbf{u}}\}$, where $\mathbf{r}_j$ is the position of the j^{th} rod, and $\hat{\mathbf{u}}_j$ its orientation. The equation of motion for the probability density function P of these phase space coordinates is found from eq.(12) by simply adding the in- and out-fluxes over all rods,

$$\frac{\partial}{\partial t} P(\mathbf{r}_1, \cdots, \mathbf{r}_N, \hat{\mathbf{u}}_1, \cdots, \hat{\mathbf{u}}_N, t) = -\sum_{j=1}^{N} \left\{ \nabla_j \cdot [\mathbf{v}_j\, P] + \hat{\mathcal{R}}_j \cdot [\boldsymbol{\Omega}_j\, P] \right\}\;. \tag{13}$$

The full phase space coordinate dependence of P is not denoted here on the right hand-side for brevity. Here, $\hat{\mathcal{R}}_j$ is defined as in eq.(10), with $\hat{\mathbf{u}}$ is replaced by $\hat{\mathbf{u}}_j$. This is an exact result, since it merely expresses conservation of the number of particles.

As a last step, the translational- and rotational velocities have to be expressed in terms of functions of the phase space coordinates. In doing so, we shall neglect hydrodynamic interactions between the rods. The reason for this neglect is two-fold. First of all, as will be seen later, the volume fractions of interest here scale as D/L (with D the thickness and L the length of the rods). For very long and thin rods, the volume fractions of interest are very small, implying that on average the two arbitrary surface elements of distinct rods are very far apart. Therefore, hydrodynamic interactions are probably much less important as for suspensions of spherical particles. Secondly, the precise form of hydrodynamic interaction functions for rods is unknown, even on the two-body level.
The key relation to express the velocities in terms of phase functions is the force balance equation. As has been seen in the lecture of G. Schütz, on the Brownian time scale, where the translational (and angular) momentum coordinates relaxed to equilibrium with the heat bath of solvent molecules, the total force (and torque) on each Brownian particle is zero. There are three forces (and torques) working on each rod : the hydrodynamic force $\mathbf{F}_j^h$ (torque $\mathbf{T}_j^h$) that the solvent exerts on the rod, the direct interaction force $\mathbf{F}_j^I$ (torque

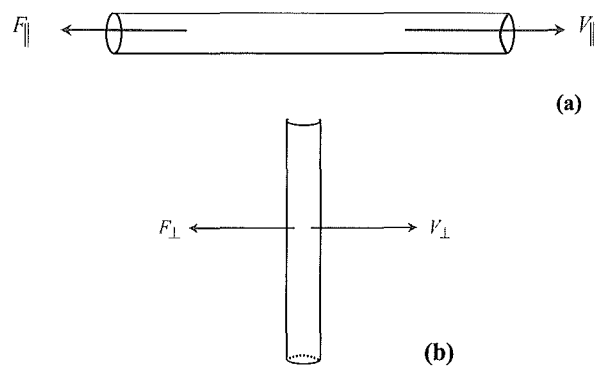


Fig. 6: *Friction of a rod that moves parallel (a) and perpendicular (b) to its long axis.*

$\mathbf{T}_j^I$) and the Brownian force $\mathbf{F}_j^{Br}$ (torque $\mathbf{T}_j^{Br}$), which will be discussed and specified later. Hence,

$$\textit{Total force} \;=\; \mathbf{0} \;=\; \mathbf{F}_j^h + \mathbf{F}_j^I + \mathbf{F}_j^{Br}\,, \tag{14}$$

$$\textit{Total torque} \;=\; \mathbf{0} \;=\; \mathbf{T}_j^h + \mathbf{T}_j^I + \mathbf{T}_j^{Br}\,. \tag{15}$$

The direct force is minus the gradient of the total potential energy Φ of the assembly of Brownian particles,

$$\mathbf{F}_j^I \;=\; -\nabla_j\,\Phi(\mathbf{r}_1,\cdots,\mathbf{r}_N,\hat{\mathbf{u}}_1,\cdots,\hat{\mathbf{u}}_N)\,, \tag{16}$$

while the direct torque is related to Φ as,

$$\mathbf{T}_j^I \;=\; -\hat{\mathcal{R}}_j\Phi\,. \tag{17}$$

With the neglect of hydrodynamic interactions, the hydrodynamic torque and force are just the friction forces of a single rod with the solvent that is otherwise at rest. Contrary to spherical colloidal particles, the friction coefficient for rods depends on the orientation of the rod. When the orientation $\hat{\mathbf{u}}_j$ is parallel to the velocity (see Fig.6a), for not too large velocities, the friction force is equal to,

$$\mathbf{F}_{\parallel,j}^h \;=\; -\gamma_\parallel\,\mathbf{v}_j$$

where $\gamma_\parallel$ is the translational friction coefficient for parallel motion. When the velocity is perpendicular to $\hat{\mathbf{u}}_j$, we have similarly (see Fig.6b),

$$\mathbf{F}_{\perp,j}^h \;=\; -\gamma_\perp\,\mathbf{v}_j$$

where the friction coefficient $\gamma_\perp$ for perpendicular motion is most likely different from $\gamma_\parallel$. Decomposing the velocity in its component $\hat{\mathbf{u}}_j\hat{\mathbf{u}}_j\cdot\mathbf{v}_j$ parallel to $\hat{\mathbf{u}}_j$ and $[\hat{\mathbf{I}}-\hat{\mathbf{u}}_j\hat{\mathbf{u}}_j]\cdot\mathbf{v}_j$ perpendicular to $\hat{\mathbf{u}}_j$, the friction force can thus be written as (appendix 1 discusses the dyadic notation that is used here),

$$\mathbf{F}_j^h \;=\; \gamma_\parallel\,\hat{\mathbf{u}}_j\hat{\mathbf{u}}_j\cdot\mathbf{v}_j \;+\; \gamma_\perp\,[\hat{\mathbf{I}}-\hat{\mathbf{u}}_j\hat{\mathbf{u}}_j]\cdot\mathbf{v}_j \;\equiv\; \boldsymbol{\Gamma}_f\cdot\mathbf{v}_j\,, \tag{18}$$

where the friction tensor $\boldsymbol{\Gamma}_f$ is defined as,

$$\boldsymbol{\Gamma}_f \;\equiv\; \gamma_\parallel\,\hat{\mathbf{u}}_j\hat{\mathbf{u}}_j \;+\; \gamma_\perp\,\left[\hat{\mathbf{I}}-\hat{\mathbf{u}}_j\hat{\mathbf{u}}_j\right]\,. \tag{19}$$

The friction torque is somewhat simpler. A little thought shows that the torque that the solvent exerts on a rotating rod and the rotational velocity have opposite directions. For not too large rotational velocities, the torque is therefore directly proportional to the rotational velocity,

$$\mathbf{T}_j^h \;=\; -\gamma_r\,\mathbf{\Omega}_j\;, \tag{20}$$

where γ_r is the *rotational friction coefficient.* Combining eqs.(14,15) with eqs.(18,20) yields (use that the inverse of $\mathbf{\Gamma}_f$ is equal to $\gamma_{\|}^{-1}\,\hat{\mathbf{u}}_j\hat{\mathbf{u}}_j + \gamma_{\perp}^{-1}\,\left[\hat{\mathbf{I}} - \hat{\mathbf{u}}_j\hat{\mathbf{u}}_j\right]$),

$$\mathbf{\Omega}_j \;=\; D_r\left\{-\beta\hat{\mathcal{R}}_j\Phi + \beta\mathbf{T}_j^{Br}\right\}\;, \tag{21}$$

and,

$$\mathbf{v}_j \;=\; \left(D_{\|}\hat{\mathbf{u}}_j\hat{\mathbf{u}}_j + D_{\perp}\left[\hat{\mathbf{I}} - \hat{\mathbf{u}}_j\hat{\mathbf{u}}_j\right]\right)\cdot\left\{-\beta\nabla_j\Phi + \beta\mathbf{F}_j^{Br}\right\}\;, \tag{22}$$

where $\beta = 1/k_BT$, and *the rotational diffusion coefficient* D_r is defined as,

$$D_t \;=\; k_BT/\gamma_r\;, \tag{23}$$

and the *translational diffusion coefficients* $D_{\|}$ and $D_{\perp}$ for parallel and perpendicular motion, respectively, are defined as,

$$D_{\|} \;=\; k_BT/\gamma_{\|}\;\;,\;\; D_{\perp} \;=\; k_BT/\gamma_{\perp}\;. \tag{24}$$

Hydrodynamic calculations of the friction coefficients for very long and thin rods lead to the following rod length- and thickness dependencies of these diffusion coefficients (L is the length and D the thickness of the cylindrical rods),

$$D_r \;=\; \frac{3k_BT\ln\{L/D\}}{\pi\,\eta_0\,L^3} \tag{25}$$

$$D_{\|} \;=\; \frac{k_BT\ln\{L/D\}}{2\pi\,\eta_0\,L}\;, \tag{26}$$

$$D_{\perp} \;=\; \tfrac{1}{2}\,D_{\|}\;. \tag{27}$$

Note that due to the last two equations here, eq.(22) can be rewritten as,

$$\mathbf{v}_j \;=\; \tfrac{3}{4}\bar{D}\left[\hat{\mathbf{I}} + \hat{\mathbf{u}}_j\hat{\mathbf{u}}_j\right]\cdot\left\{-\beta\nabla_j\Phi + \beta\mathbf{F}_j^{Br}\right\}\;, \tag{28}$$

where *the translational diffusion coefficient* $\bar{D}$ is equal to,

$$\bar{D} \;=\; \tfrac{1}{3}\left[D_{\|} + 2D_{\perp}\right] \;=\; \tfrac{4}{3}\,D_{\perp} \;=\; \tfrac{2}{3}\,D_{\|}\;. \tag{29}$$

The reason for referring to D_r and $\bar{D}$ as "diffusion coefficients" will become clear in the following section, where diffusion of non-interacting rods is considered.
We still have to express the Brownian contributions to the total force and torque in terms of phase functions. This is achieved as follows. Since for infinite time $t \to \infty$, when the

suspension attained equilibrium, the probability density function P is proportional to the Boltzmann exponential $\exp\{-\beta\,\Phi\}$, and $\partial P/\partial t = 0$, it follows from eqs.(13,21,22) that,

$$\begin{aligned} \mathbf{F}_j^{Br} &= -k_B T \nabla_j \ln\{P\}\,, \\ \mathbf{T}_j^{Br} &= -k_B T \hat{\mathcal{R}}_j \ln\{P\}\,. \end{aligned} \tag{30}$$

These Brownian contributions to the total force and torque are the result of the fact that the force balance equations (14,15) are only valid on a coarsened time scale (the Brownian time scale). On such a coarsened time scale, not only the purely microscopic forces $\mathbf{F}_j^h$ and $\mathbf{F}_j^I$ (and the corresponding torques) act on the colloidal particles. The additional Brownian force (and torque) arises from interactions of the colloidal particle with the solvent molecules, averaged with respect to the equilibrium probability density function for the phase space coordinates of the fluid molecules in the external field imposed by the colloidal particles with prescribed positions and orientations. Even in a very dilute system of colloidal particles (an "ideal gas"), where interactions between the colloidal particles can be neglected, the equilibrium state is one where the macroscopic density is constant, independent of position. The forces that drive such an ideal gas to the homogeneous state are the Brownian forces.
In this way the following equation of motion for the probability density function P of the phase space coordinates $\{\mathbf{r}_1, \cdots, \mathbf{r}_N, \hat{\mathbf{u}}_1, \cdots, \hat{\mathbf{u}}_N\}$ is obtained,

$$\frac{\partial}{\partial t} P = \sum_{j=1}^{N} \left[\tfrac{3}{4} \bar{D} \nabla_j \cdot \left[\hat{\mathbf{I}} + \hat{\mathbf{u}}_j \hat{\mathbf{u}}_j \right] \cdot \left\{ \beta\, P \nabla_j \Phi + \nabla_j P \right\} + D_r \hat{\mathcal{R}}_j \cdot \left\{ \beta\, P \hat{\mathcal{R}}_j \Phi + \hat{\mathcal{R}}_j P \right\} \right] . \tag{31}$$

This is the Smoluchowski equation for very long and thin, rigid rods, where hydrodynamic interactions are neglected. The first term on the right hand-side described the rate of change of P due to translational motion, while the second term describes the rate of change due to rotational motion.
An alternative, may be more satisfying derivation of the Smoluchowski equation, is to depart from the Liouville equation (see the lecture of K. Sturm) for a binary mixture : the solvent molecules and the colloidal particles. The Smoluchowski equation is then found after integrating over the fast phase space variables (the phase space coordinates of the solvent molecules and the momentum coordinates of the colloidal particles). Such an approach has been taken, for spherical colloids, in refs.[2], [3]. More about time scales and force balance can be found in refs.[4], [5].

3 Translational and Rotational Diffusion of non-Interacting Rods

Consider the mean squared center of mass displacement of a freely diffusing rod. Its position at time $t = 0$ will be chosen at the origin : $\mathbf{r}(t = 0) = \mathbf{0}$. Free diffusion occurs in suspensions where the concentration of colloidal particles is so small, that on average, rods do not notice each other. In that case, the interaction potential in the Smoluchowski equation (31) may be neglected ($\Phi = 0$), and N can be taken equal to 1, resulting in,

$$\frac{\partial}{\partial t} P(\mathbf{r}, \hat{\mathbf{u}}, t) = \tfrac{3}{4} \bar{D} \nabla \cdot \left[\hat{\mathbf{I}} + \hat{\mathbf{u}}\hat{\mathbf{u}} \right] \cdot \nabla P + D_r \hat{\mathcal{R}}^2 P\,, \tag{32}$$

where $\hat{\mathcal{R}}^2 = \hat{\mathcal{R}} \cdot \hat{\mathcal{R}}$. Integration with respect to $\hat{\mathbf{u}}$ thus leads to,

$$\frac{\partial}{\partial t} P(\mathbf{r},t) \;=\; \tfrac{3}{4}\bar{D}\,\nabla \cdot \oint d\hat{\mathbf{u}}\,\left[\hat{\mathbf{I}} + \hat{\mathbf{u}}\hat{\mathbf{u}}\right] \cdot \nabla P(\mathbf{r},\hat{\mathbf{u}},t)\;.$$

Since, for the very highly diluted systems under consideration,

$$\oint d\hat{\mathbf{u}}\,\hat{\mathbf{u}}\hat{\mathbf{u}}\,P(\mathbf{r},\hat{\mathbf{u}},t) \;=\; \tfrac{1}{3}\,\hat{\mathbf{I}}\,,$$

this is the same as,

$$\frac{\partial}{\partial t} P(\mathbf{r},t) \;=\; \bar{D}\,\nabla^2 P(\mathbf{r},t)\;. \tag{33}$$

The equation of motion for the dyadic product $<\mathbf{r}(t)\mathbf{r}(t)>$ (see appendix 1 for the definition of dyadic products) is obtained by multiplying both sides with $\mathbf{r}\,\mathbf{r}$ and integrating,

$$\begin{aligned}\frac{d}{dt} <\mathbf{r}(t)\mathbf{r}(t)> \;&=\; \bar{D}\int d\mathbf{r}\,\mathbf{r}\mathbf{r}\nabla^2 P(\mathbf{r},t)\\ &=\; \bar{D}\int d\mathbf{r}\,P(\mathbf{r},t)\nabla^2\mathbf{r}\mathbf{r} = 2\bar{D}\,\hat{\mathbf{I}}\,.\end{aligned}$$

Since $<\mathbf{r}(t=0)\mathbf{r}(t=0)>= \mathbf{0}$, time-integration immediately leads to,

$$<\mathbf{r}(t)\mathbf{r}(t)> = \; 2\bar{D}t\,\hat{\mathbf{I}}\,,$$

and hence,

$$<r^2(t)> = \; 6\bar{D}t\,. \tag{34}$$

Note that on taking the Trace of the dyadic product, each spatial dimension (3 in this case) gives rise to a factor 2 on the right hand-side in the mean squared displacement in eq.(34).
For very small times, where the translational velocity of the rod is constant (not yet significantly affected by interactions with solvent molecules), and therefore the displacement is linear in time, one would expect a quadratic time dependence : $< r^2(t) > \sim t^2$. The reason that this is not found in eq.(34) is due to the fact that this result only holds on the Brownian time scale, where the momentum coordinate of the rod long relaxed to equilibrium with the solvent : the force balance equations (14,15) are only valid on this larger time scale. The many chaotic collisions of the rod with solvent molecules leads to a more modest average displacement as a function of time.
Let us now consider the time dependence of the orientation $<\hat{\mathbf{u}}(t)>$, given that $\hat{\mathbf{u}}(t = 0) = \hat{\mathbf{u}}(0)$. For a homogeneous system, $P(\mathbf{r},\hat{\mathbf{u}},t)$ is independent of $\mathbf{r}$, so that eq.(32) reduces to,

$$\frac{\partial}{\partial t} P(\hat{\mathbf{u}},t) \;=\; D_r\,\hat{\mathcal{R}}^2 P(\hat{\mathbf{u}},t)\;. \tag{35}$$

Multiplying both sides with $\hat{\mathbf{u}}$ and integrating over the unit spherical surface gives,

$$\frac{d}{dt} <\hat{\mathbf{u}}(t)> = \; D_r \oint d\hat{\mathbf{u}}\,\hat{\mathbf{u}}\,\hat{\mathcal{R}}^2\,P(\hat{\mathbf{u}},t)\,.$$

Now, from Stokes's integral theorem it follows that for any two (well behaved) functions f and g of $\hat{\mathbf{u}}$ (see appendix 2 for mathematical details) ,

$$\oint d\hat{\mathbf{u}}\, f(\hat{\mathbf{u}})\hat{\mathcal{R}}g(\hat{\mathbf{u}}) \;=\; -\oint d\hat{\mathbf{u}}\, g(\hat{\mathbf{u}})\hat{\mathcal{R}}f(\hat{\mathbf{u}})\,. \tag{36}$$

Applying this result twice, we get,

$$\oint d\hat{\mathbf{u}}\,\hat{\mathbf{u}}\hat{\mathcal{R}}^2\, P(\hat{\mathbf{u}},t) \;=\; \oint d\hat{\mathbf{u}}\, P(\hat{\mathbf{u}},t)\hat{\mathcal{R}}^2\,\hat{\mathbf{u}} = -2 < \hat{\mathbf{u}}(t) >\,,$$

where it is used that $\hat{\mathcal{R}}^2\hat{\mathbf{u}} \;=\; -2\hat{\mathbf{u}}$. The equation of motion we were after thus reads,

$$\frac{d}{dt} < \hat{\mathbf{u}}(t) > \;=\; -2D_r \;< \hat{\mathbf{u}}(t) >\,,$$

the solution of which is,

$$< \hat{\mathbf{u}}(t) > \;=\; \exp\{-2D_r t\}\,\hat{\mathbf{u}}(0)\,. \tag{37}$$

For small times, where $D_r t < 1$, the above exponential can be Taylor expanded as,

$$< \hat{\mathbf{u}}(t) > \;=\; \{1 - 2D_r t\}\;\hat{\mathbf{u}}(0)\,, \tag{38}$$

from which it follows that,

$$<|\,\hat{\mathbf{u}}(t) - \hat{\mathbf{u}}(0)\,|^2> \;=\; 4D_r\, t\,. \tag{39}$$

Notice that for small times $<|\,\hat{\mathbf{u}}(t) - \hat{\mathbf{u}}(0)\,|^2>$ is the displacement of the tip of the unit vector on the plane tangential to the unit spherical surface at $\hat{\mathbf{u}}(0)$. This explains the prefactor 4, which indeed complies with center of mass diffusion in two dimensions (see the remark just below eq.(34)). For later times, the tip of $\hat{\mathbf{u}}(t)$ is confined to the unit spherical surface, for which the mean squared displacement is a much more complicated function of time.

4 The Orientational Order Parameter

In the nematic phase, the rods have a preferred orientation $\hat{\mathbf{n}}$, which is referred to as *the director*. A preferred direction can also be induced in an otherwise isotropic suspension, by means of an external field (like an electric field or shear flow). The question that will be addressed in this section is how the characteristics of orientational order in suspensions of rigid, uniaxial rods can be quantified. The most simple measure for the degree of orientation that comes to mind is $<\cos\{\Theta\}>=<\hat{\mathbf{u}}\cdot\hat{\mathbf{n}}>=<\hat{\mathbf{u}}>\cdot\hat{\mathbf{n}}$, where Θ is the angle of the orientation $\hat{\mathbf{u}}$ of a given rod and the director $\hat{\mathbf{n}}$ (see Fig.7). However, since due to symmetry, an orientation $\hat{\mathbf{u}}$ is equally likely to occur as the orientation $-\hat{\mathbf{u}}$, the average $<\hat{\mathbf{u}}>$ is equal to $\mathbf{0}$. The next most simple measure would then be $<\cos^2\{\Theta\}> \;=\; <(\hat{\mathbf{u}}\cdot\hat{\mathbf{n}})^2>=<\hat{\mathbf{u}}\hat{\mathbf{u}}>:\hat{\mathbf{n}}\hat{\mathbf{n}}$ (see appendix 1 for an explanation of the notation that is used here). Hence, the most simple quantity that characterizes the orientational state is the so-called *orientational order parameter tensor* ,

$$\mathbf{S} \;\equiv\; < \hat{\mathbf{u}}\,\hat{\mathbf{u}} > \;. \tag{40}$$

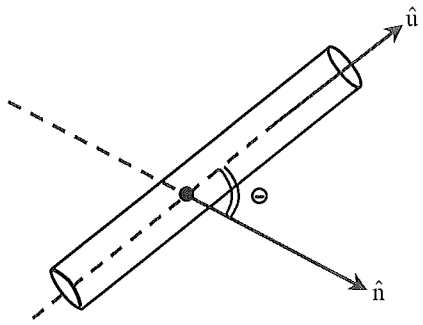


Fig. 7: *The angle* Θ *between the director* $\hat{\mathbf{n}}$ *and* $\hat{\mathbf{u}}$.

The question now is, what information can be distilled from a specified $\mathbf{S}$. To answer this question, let $\hat{\mathbf{e}}$ be a unit vector, and let φ denote the angle between the orientation $\hat{\mathbf{u}}$ of a given rod and $\hat{\mathbf{e}}$. Consider the function,

$$f = <\cos^2\{\varphi\}> = \mathbf{S} : \hat{\mathbf{e}}\hat{\mathbf{e}} = \sum_{m,n} S_{mn}\,\hat{e}_m\,\hat{e}_n \;, \tag{41}$$

where S_{nm} is the nm^{th} component of $\mathbf{S}$, and $\hat{e}_n$ the n^{th} component of $\hat{\mathbf{e}}$. Since the maximum value of $\cos^2\{\varphi\}$ is attained when $\varphi = 0$, and the most likely direction of $\hat{\mathbf{u}}$ is along the director, it is evident that the unit vector $\hat{\mathbf{e}}$ that maximizes f is the director. This maximization of f has to be performed under the constraint that $\hat{\mathbf{e}}$ is a unit vector, that is $\hat{\mathbf{e}} \cdot \hat{\mathbf{e}} = 1$. According to Lagrange's principle, we therefore have to maximize the function,

$$f^* = f - \lambda\,\hat{\mathbf{e}} \cdot \hat{\mathbf{e}} = \sum_{mn} \{S_{mn} - \lambda\,\delta_{mn}\}\;\hat{e}_m\,\hat{e}_n \;, \tag{42}$$

where λ is the Lagrange multiplier, and δ_{nm} is the Kronecker delta ($\delta_{mn} = 0$ when $m \neq n$ and $\delta_{mn} = 1$ when $m = n$). From $\partial f/\partial \hat{e}_m = 0$ it is easily found that,

$$\mathbf{S} \cdot \hat{\mathbf{e}} = \lambda\,\hat{\mathbf{e}} \;, \text{ maximizes or minimizes } f^* \,. \tag{43}$$

By taking the innerproduct on both sides it follows that,

$$\lambda = \mathbf{S} : \hat{\mathbf{e}}\hat{\mathbf{e}} \;, \text{ when } \hat{\mathbf{e}} \text{ maximizes or minimizes } f^* \,. \tag{44}$$

We thus find that,

The eigenvector of $\mathbf{S}$ *with the largest eigenvalue is the director* $\hat{\mathbf{n}}$*, and the largest eigenvalue is equal to* $<\cos\{\Theta\}^2> = \mathbf{S} : \hat{\mathbf{n}}\hat{\mathbf{n}}$.

The largest eigenvalue of $\mathbf{S}$ characterizes the degree of alignment. Note that the largest eigenvalue of $\mathbf{S}$ is equal $1/3$ in the isotropic state (since then $\mathbf{S} = \frac{1}{3}\hat{\mathbf{I}}$), and equal to 1 for a perfectly aligned state (since then $\mathbf{S} = \hat{\mathbf{n}}\hat{\mathbf{n}}$). A commonly used equivalent measure is the so-called P_2-order parameter, which is defined as,

$$P_2 \equiv < P_2(\cos\{\Theta\}) > = \tfrac{1}{2}\left\{3 <\cos^2\{\Theta\}> - 1\right\} = \tfrac{1}{2}\{3\lambda - 1\} \;, \tag{45}$$

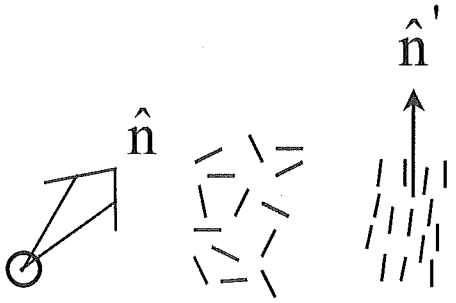


Fig. 8: *A uniaxial nematic (left) and a biaxial nematic (right), where* $\hat{\mathbf{n}}'$ *is the second director. The director* $\hat{\mathbf{n}}$ *points into the paper, and each red line is the projection of a rod onto the plane perpendicular to the director.*

where $P_2(x)$ is the second order Legendre polynomial. The reason for introducing this "rescaled" scalar order parameter P_2 is that it is 0 for an isotropic state and equal to 1 for a perfectly aligned state.
When for a particular nematic suspension the remaining two smaller eigenvalues are equal, the nematic is referred to as "uniaxial" . When they are unequal, the nematic is referred to "biaxial" . For a uniaxial nematic, the projections of the rods onto the plane perpendicular to the director are isotropically distributed, while for a biaxial nematic the orientations of the rods in this projection have a second preferred direction $\hat{\mathbf{n}}'$ (see Fig.8). Biaxial of nematic ordering is found, for example, when a suspension of rigid rods is subjected to simple shear flow. A nematic state of cylindrically shaped rods, in the absence of an external field is always uniaxial.

5 The Doi-Edwards Equation of motion and the Maier-Saupe Potential

In this section we shall derive an equation of motion for the orientational order parameter tensor $\mathbf{S}$ that was introduced in the previous section from the Smoluchowksi equation (31). This equation of motion is known as the Doi-Edwards equation of motion [6].
The orientational order parameter tensor (40) is by definition equal to,

$$\mathbf{S} = \oint d\hat{\mathbf{u}}\, \hat{\mathbf{u}}\, \hat{\mathbf{u}}\; P(\hat{\mathbf{u}}, t) \tag{46}$$

where $P(\hat{\mathbf{u}}, t)$ is the probability density function (pdf) of the orientation $\hat{\mathbf{u}}$ of a given rod. The integral ranges over the unit spherical surface. For an assembly of N interacting rods, this pdf is related to the N-particle pdf as,

$$P(\hat{\mathbf{u}}_1, t) = \int d\mathbf{r}_1 \cdots \int d\mathbf{r}_N \oint d\hat{\mathbf{u}}_2 \cdots \oint d\hat{\mathbf{u}}_N\, P(\mathbf{r}_1, \cdots, \mathbf{r}_N, \hat{\mathbf{u}}_1, \hat{\mathbf{u}}_2, \cdots, \hat{\mathbf{u}}_N, t)\,. \tag{47}$$

Analytical progress can be made by assuming a pair-wise additive total potential, that is,

$$\Phi(\mathbf{r}_1, \cdots, \mathbf{r}_N, \hat{\mathbf{u}}_1, \cdots, \hat{\mathbf{u}}_N) = \sum_{i<j} V(\mathbf{r}_i - \mathbf{r}_j, \hat{\mathbf{u}}_i, \hat{\mathbf{u}}_j)\,, \tag{48}$$

with V the pair-interaction potential. This is exact for rods with hard-core interactions that we shall considered here. According to the integral theorems of Gauss and Stokes, we have, respectively,

$$\int d\mathbf{r}_j \, \nabla_j \cdot (\cdots) \; = \; 0 \;\; , \;\; \text{and} \;\; , \;\; \oint d\hat{\mathbf{u}}_j \, \hat{\mathcal{R}}_j \cdot (\cdots) \; = \; 0 \, . \tag{49}$$

The last equation is a result of Stokes's theorem, as shown in appendix 2. Using the above relations, integration of both sides of the Smoluchowski equation (31) with respect to $\mathbf{r}_1, \cdots, \mathbf{r}_N$ and $\hat{\mathbf{u}}_2, \cdots, \hat{\mathbf{u}}_N$ leads to (with $\hat{\mathbf{u}} = \hat{\mathbf{u}}_1$),

$$\frac{\partial}{\partial t} P(\hat{\mathbf{u}}, t) \; = \; D_r \hat{\mathcal{R}} \cdot \left\{ \hat{\mathcal{R}} P(\hat{\mathbf{u}}, t) - \beta \, P(\hat{\mathbf{u}}, t) \, \bar{\mathbf{T}}(\hat{\mathbf{u}}, t) \right\} \, , \tag{50}$$

where $\hat{\mathcal{R}}$ the rotational operator (10) with respect to $\hat{\mathbf{u}}$. The torque $\bar{\mathbf{T}}$ is equal to (with $\mathbf{R} = \mathbf{r}_1 - \mathbf{r}_2$ and $\hat{\mathbf{u}}' = \hat{\mathbf{u}}_2$),

$$\bar{\mathbf{T}}(\hat{\mathbf{u}}, t) \; = \; -\bar{\rho} \int d\mathbf{R} \oint d\hat{\mathbf{u}}' \, P(\hat{\mathbf{u}}', t) \, g(\mathbf{R}, \hat{\mathbf{u}}, \hat{\mathbf{u}}', t) \hat{\mathcal{R}} V(\mathbf{R}, \hat{\mathbf{u}}, \hat{\mathbf{u}}') \, , \tag{51}$$

where $\bar{\rho} = N/V$ is the number density of rods, where the pair-correlation function g is defined as (with $\mathbf{r} = \mathbf{r}_1$ and $\mathbf{r}' = \mathbf{r}_2$),

$$\begin{aligned} P(\mathbf{r}, \mathbf{r}', \hat{\mathbf{u}}, \hat{\mathbf{u}}', t) \; &\equiv \int d\mathbf{r}_3 \cdots \int d\mathbf{r}_N \oint d\hat{\mathbf{u}}_3 \cdots \oint d\hat{\mathbf{u}}_N P(\mathbf{r}, \mathbf{r}', \mathbf{r}_3, \cdots, \mathbf{r}_N, \hat{\mathbf{u}}, \hat{\mathbf{u}}', \hat{\mathbf{u}}_3, \cdots, \hat{\mathbf{u}}_N, t) \\ &\equiv \; \frac{1}{V^2} P(\hat{\mathbf{u}}, t) \, P(\hat{\mathbf{u}}', t) \, g(\mathbf{r}, \mathbf{r}', \hat{\mathbf{u}}, \hat{\mathbf{u}}', t) \, , \end{aligned} \tag{52}$$

with $P(\mathbf{r}, \mathbf{r}', \hat{\mathbf{u}}, \hat{\mathbf{u}}', t)$ the pdf for the positions and orientations of two rods. Since the product $\frac{1}{V} P(\hat{\mathbf{u}}', t) g(\mathbf{r}, \mathbf{r}', \hat{\mathbf{u}}, \hat{\mathbf{u}}')$ is the conditional pdf for the position $\mathbf{r}'$ and orientation $\hat{\mathbf{u}}'$ of a rod, given the orientation $\hat{\mathbf{u}}$ and position $\mathbf{r}$ of the other rod (see the lectures of K. Sturm and G. Nägele), the torque in eq.(51) is the torque on a rod, with prescribed orientation $\hat{\mathbf{u}}$ and position $\mathbf{r}$, averaged over the orientations and positions of the other rods.

A closed equation of motion for $P(\hat{\mathbf{u}}, t)$ is obtained when g is known. For equilibrium suspensions of very long and thin, rigid and repulsive rods, Onsager [7] showed that,

$$g(\mathbf{r} - \mathbf{r}', \hat{\mathbf{u}}, \hat{\mathbf{u}}', t) \; = \; \exp\{-\beta \, V(\mathbf{r} - \mathbf{r}', \hat{\mathbf{u}}, \hat{\mathbf{u}}')\} \, , \tag{53}$$

where V is the pair-interaction potential. This expression is valid in the isotropic and nematic states (provided the degree of alignment is not too high). In appendix 3 it is shown that in a density expansion of the pair-correlation function, indeed only this leading order term remains, provided that the pair-interaction potential is repulsive and its range along the rods long axis is very much longer than its range perpendicular to the rods long axis. What is neglected in using eq.(53) are dynamic contributions to correlations. So far, nothing is known about such correlation effects, and we shall assume here that these contributions can be neglected.

In case of hard-core interactions we have the identity,

$$\begin{aligned} \exp\left\{-\beta V(\mathbf{r}-\mathbf{r}', \hat{\mathbf{u}}, \hat{\mathbf{u}}')\right\} \hat{\mathcal{R}} V(\mathbf{r}-\mathbf{r}', \hat{\mathbf{u}}, \hat{\mathbf{u}}') \; &= \; -\beta^{-1} \hat{\mathcal{R}} \left[\exp\left\{-\beta V(\mathbf{r}-\mathbf{r}', \hat{\mathbf{u}}, \hat{\mathbf{u}}')\right\} - 1\right] \\ &= \; \beta^{-1} \hat{\mathcal{R}} \, \chi(\mathbf{r} - \mathbf{r}', \hat{\mathbf{u}}, \hat{\mathbf{u}}') \, , \end{aligned} \tag{54}$$

with χ the characteristic function of the excluded volume for two rods : $\chi = 1$ when the cores of the two rods overlap and $\chi = 0$ otherwise. The torque (51) can now be written as,

$$\bar{\mathbf{T}}(\hat{\mathbf{u}},t) \;=\; -\hat{\mathcal{R}}\,V^{eff}(\hat{\mathbf{u}},t)\;, \tag{55}$$

where *the effective potential* V^{eff} is equal to (with $\mathbf{R} = \mathbf{r}' - \mathbf{r}$) ,

$$\begin{aligned} V^{eff}(\hat{\mathbf{u}},t) \;&=\; \beta^{-1}\bar{\rho}\int d\mathbf{R}\oint d\hat{\mathbf{u}}'\,P(\hat{\mathbf{u}}',t)\,\chi(\mathbf{R},\hat{\mathbf{u}},\hat{\mathbf{u}}') \\ &=\; 2DL^2\beta^{-1}\bar{\rho}\oint d\hat{\mathbf{u}}'\,P(\hat{\mathbf{u}}',t)\;|\,\hat{\mathbf{u}}\times\hat{\mathbf{u}}'\,|\,, \end{aligned} \tag{56}$$

where in the last equation it is used that,

$$\int d\mathbf{R}\;\chi(\mathbf{R},\hat{\mathbf{u}},\hat{\mathbf{u}}') \;=\; 2DL^2\;|\,\hat{\mathbf{u}}\times\hat{\mathbf{u}}'\,|\,, \tag{57}$$

for very long and thin rods [6]. The effective potential V^{eff} is the Doi-Edwards potential. We thus find the following closed equation of motion for $P(\hat{\mathbf{u}},t)$,

$$\frac{\partial}{\partial t}P(\hat{\mathbf{u}},t) \;=\; D_r\hat{\mathcal{R}}\cdot\left\{\hat{\mathcal{R}}P(\hat{\mathbf{u}},t) + 2DL^2\bar{\rho}\,P(\hat{\mathbf{u}},t)\,\hat{\mathcal{R}}\oint d\hat{\mathbf{u}}'\,P(\hat{\mathbf{u}}',t)\;|\,\hat{\mathbf{u}}\times\hat{\mathbf{u}}'\,|\right\}. \tag{58}$$

Note that this equation is non-linear in $P(\hat{\mathbf{u}},t)$.
We note here, for those who are familiar with Onsager's work [7], that the stationary solution $P(\hat{\mathbf{u}})$ of the equation of motion (58) satisfies,

$$\ln\{P(\hat{\mathbf{u}})\} + 2DL^2\bar{\rho}\oint d\hat{\mathbf{u}}'\,P(\hat{\mathbf{u}}',t)\;|\,\hat{\mathbf{u}}\times\hat{\mathbf{u}}'\,| = \text{ Constant }, \tag{59}$$

where the Constant is an integration constant. This is precisely the Euler-Lagrange equation that complies with the Onsager free energy functional for very long and thin rods with excluded volume interactions.
Following Doi and Edwards [6], an equation of motion for $\mathbb{S}$ can be obtained by operating on both sides of this equation with $\oint d\hat{\mathbf{u}}\,(\hat{\mathbf{u}}\hat{\mathbf{u}})\,(\cdots)$. The first term on the right hand-side of eq.(58) is easily found to be render,

$$\oint d\hat{\mathbf{u}}\,(\hat{\mathbf{u}}\,\hat{\mathbf{u}})\hat{\mathcal{R}}^2P(\hat{\mathbf{u}},t) \;=\; \oint d\hat{\mathbf{u}}\,P(\hat{\mathbf{u}},t)\hat{\mathcal{R}}^2(\hat{\mathbf{u}}\,\hat{\mathbf{u}}) \;=\; 2\hat{\mathbf{I}} - 6\mathbf{S}\;, \tag{60}$$

where in the first equation two partial integrations have been done (using eq.(36) twice, which is derived in appendix 2), and in the second equation it is used that $\hat{\mathcal{R}}^2(\hat{\mathbf{u}}\,\hat{\mathbf{u}}) = 2\hat{\mathbf{I}} - 6\hat{\mathbf{u}}\,\hat{\mathbf{u}}$. To make further analytical progress, we shall expand the second term in the equation of motion (58) up to third order in the orientational order parameter P_2, as defined in eq.(45). That is, we shall expand with respect to the eigenvalues of tensors like $\mathbf{q} = \hat{\mathbf{u}}\hat{\mathbf{u}} - \frac{1}{3}\hat{\mathbf{I}}$, whose eigenvalues are in between $-1/3$ and $2/3$. Such a third order Ginzburg-Landau expansion complies with a fourth order expansion of the free energy, as will become clear in subsection 8.2. Since the outer product in eq.(56) for the effective potential can be written as (with $\mathbf{q}' = \hat{\mathbf{u}}'\hat{\mathbf{u}}' - \frac{1}{3}\hat{\mathbf{I}}$),

$$|\,\hat{\mathbf{u}}\times\hat{\mathbf{u}}'\,| = \sqrt{1 - \hat{\mathbf{u}}\hat{\mathbf{u}} : \hat{\mathbf{u}}'\hat{\mathbf{u}}'} \;=\; \sqrt{\tfrac{2}{3} - \mathbf{q} : \mathbf{q}'}\;,$$

we can Taylor expand up to leading order with respect to $\mathbf{q}$ and $\mathbf{q}'$,

$$|\,\hat{\mathbf{u}}\times\hat{\mathbf{u}}'\,|\approx\sqrt{\tfrac{2}{3}}\left[1-\tfrac{3}{4}\,\mathbf{q}:\mathbf{q}'\right]\ . \tag{61}$$

Since the next higher order term in this Taylor expansion is of fourth order, this truncation leads to a Ginzburg-Landau expansion up to third order of the equation of motion for $\mathbf{S}$. Since $\sqrt{2/3}$ differs by only 3.8 % from the exact value $\pi/4$ for the isotropic average value of $|\,\hat{\mathbf{u}}\times\hat{\mathbf{u}}'\,|$, we shall replace $\sqrt{2/3}$ in eq.(61) by $\pi/4$. Errors due to truncation of the Taylor expansion in eq.(61) are probably larger. Re-substitution of the definition of the $\mathbf{q}$'s in terms of bilinear products of $\hat{\mathbf{u}}$'s then leads to,

$$|\,\hat{\mathbf{u}}\times\hat{\mathbf{u}}'\,|\approx\tfrac{5\pi}{16}\left[1-\tfrac{3}{5}\,\hat{\mathbf{u}}\hat{\mathbf{u}}:\hat{\mathbf{u}}'\hat{\mathbf{u}}'\right]\ . \tag{62}$$

Note that the effective potential (56) within this Ginzburg-Landau expansion can be written as,

$$V^{eff}(\hat{\mathbf{u}},t)\ =\ \tfrac{5\pi}{8}\,\beta^{-1}DL^2\bar{\rho}\left\{1-\tfrac{3}{5}\,\mathbf{S}:\hat{\mathbf{u}}\hat{\mathbf{u}}\right\}\ . \tag{63}$$

This effective potential is known as the *Maier-Saupe potential* [8]. Using the Ginzburg-Landau expansion (62) in the Smoluchowksi equation (58), and operating on both sides with $\oint d\hat{\mathbf{u}}\,(\hat{\mathbf{u}}\hat{\mathbf{u}})\,(\cdots)$, leads to the Doi-Edwards equation of motion (see appendix 4 for mathematical details),

$$\frac{d}{dt}\mathbf{S}=-6D_r\left\{\mathbf{S}-\tfrac{1}{3}\hat{\mathbf{I}}-\tfrac{L}{D}\,\varphi\,\left(\mathbf{S}\cdot\mathbf{S}-\mathbf{S}^{(4)}:\mathbf{S}\right)\right\}\ , \tag{64}$$

where the concentration is now expressed in terms of the volume fraction $\varphi=\frac{\pi}{4}D^2L\bar{\rho}$, with L the length and D the thickness of the rods. Furthermore, $\mathbf{S}^{(4)}$ is a fourth order tensor, defined as (see appendix 1 for an explanation of the notation used here),

$$\mathbf{S}^{(4)}\ \equiv<\hat{\mathbf{u}}\,\hat{\mathbf{u}}\,\hat{\mathbf{u}}\,\hat{\mathbf{u}}>\ . \tag{65}$$

In order to obtain a closed equation of motion for S, the fourth order tensor $\mathbf{S}^{(4)}$ should be expressed in terms of S. Such a closure relation is discussed in the following subsection.

6 An Orientational Closure Relation

The fourth order average in eq.(65) occurs in the form of a double contraction,

$$\mathbf{A}\ \equiv\ \mathbf{S}^{(4)}:\mathbf{M}\ , \tag{66}$$

where $\mathbf{M}$ is equal to $\mathbf{S}$. As pointed out by Hinch and Leal [9], orientational order increases monotonically with increasing shear-rate, so that interpolation between the known forms for $\mathbf{S}^{(4)}$ in the isotropic state and in the perfectly aligned state will probably lead to quite accurate closures. The four point average $\mathbf{S}^{(4)}$ is known exactly for the two extreme cases of perfect alignment (along the director $\hat{\mathbf{n}}$) and for the isotropic state,

$$<\hat{\mathbf{u}}\,\hat{\mathbf{u}}\,\hat{\mathbf{u}}\,\hat{\mathbf{u}}>_{ijkl}\ =\ \hat{\mathbf{n}}_i\hat{\mathbf{n}}_j\hat{\mathbf{n}}_k\hat{\mathbf{n}}_l\ ,\qquad\text{perfect alignment}\ , \tag{67}$$

$$=\ \tfrac{1}{15}\left[\,\delta_{ij}\delta_{kl}+\delta_{ik}\delta_{jl}+\delta_{ik}\delta_{jl}\,\right]\ ,\ \text{isotropic}\ , \tag{68}$$

with δ_{ij} the Kronecker delta ($\delta_{ij}=1$ when $i=j$, and $\delta_{ij}=0$ when $i\neq j$). Furthermore, we have the following trivial identities,

$$A_{ij} \equiv \sum_{n,m} < \hat{\mathbf{u}}_i \hat{\mathbf{u}}_j \hat{\mathbf{u}}_n \hat{\mathbf{u}}_m > \mathbf{M}_{mn} = A_{ji} , \tag{69}$$

$$\sum_i A_{ii} = \sum_i \sum_{n,m} < \hat{\mathbf{u}}_i \hat{\mathbf{u}}_i \hat{\mathbf{u}}_n \hat{\mathbf{u}}_m > \mathbf{M}_{mn} = \sum_{n,m} \mathbf{S}_{nm}\mathbf{M}_{mn} \equiv \mathbf{S}:\mathbf{M} . \tag{70}$$

The latter identity is especially important in order to ensure that the trace of $\mathbf{S}$ remains equal to 1 on time integration of the equation of motion (64). Using closures which do not satisfy (70) violate the time invariance of the trace of the order parameter. Furthermore,

$$\mathbf{A} = < \hat{\mathbf{u}}\hat{\mathbf{u}}\hat{\mathbf{u}}\hat{\mathbf{u}} > : \overline{\mathbf{M}} , \tag{71}$$

with,

$$\overline{\mathbf{M}} \equiv \tfrac{1}{2}\left[\mathbf{M}+\mathbf{M}^T\right] , \tag{72}$$

the symmetric part of $\mathbf{M}$, where the superscript "T" stands for "the transpose of". This equation implies that the closure relation must be a function of $\overline{\mathbf{M}}$.
Since order parameters tend to increase monotonically with shear rate, an accurate closure relation can be found by constructing an interpolation form between the exact results (67,68) such that the conditions (69-71) are satisfied. Substitution of the most general form of linear combinations of first and second order terms in $\mathbf{S}$,

$$\begin{aligned}\mathbf{A} &= c_1\mathbf{S}\cdot\overline{\mathbf{M}} + c_2\overline{\mathbf{M}}\cdot\mathbf{S} + c_3\hat{\mathbf{I}}\,\mathbf{S}:\overline{\mathbf{M}} + c_4\mathbf{S}\,\hat{\mathbf{I}}:\overline{\mathbf{M}} \\ &+ c_5\mathbf{S}\cdot\mathbf{S}\cdot\overline{\mathbf{M}} + c_6\mathbf{S}\cdot\overline{\mathbf{M}}\cdot\mathbf{S} + c_7\overline{\mathbf{M}}\cdot\mathbf{S}\cdot\mathbf{S} + c_8\mathbf{S}\,\mathbf{S}:\overline{\mathbf{M}} + c_9\overline{\mathbf{M}}\,\mathbf{S}:\mathbf{S} ,\end{aligned}$$

into eqs.(67-71) renders algebraic equations for the coefficients c_j, leading to,

$$< \hat{\mathbf{u}}\hat{\mathbf{u}}\hat{\mathbf{u}}\hat{\mathbf{u}} > : \mathbf{M} = \tfrac{1}{5}\left\{\mathbf{S}\cdot\overline{\mathbf{M}} + \overline{\mathbf{M}}\cdot\mathbf{S} - \mathbf{S}\cdot\mathbf{S}\cdot\overline{\mathbf{M}} - \overline{\mathbf{M}}\cdot\mathbf{S}\cdot\mathbf{S} + 2\mathbf{S}\cdot\overline{\mathbf{M}}\cdot\mathbf{S} + 3\mathbf{S}\,\mathbf{S}:\overline{\mathbf{M}}\right\} . \tag{73}$$

Comparison of exact numerical solutions of the Smoluchowski equation (58) for non-interacting rods, shows that the closure approximation (73) with $\mathbf{M}=\mathbf{S}$ is accurate to within 1%. In ref.[6], Doi and Edwards analyze the equation of motion (64) with a quite inaccurate closure relation. We shall use the much more accurate closure relation (73) in the following.

7 Influence of Shear Flow

Consider a rod in shear flow . The flow in the absence of the rod is taken equal to,

$$\mathbf{u}(\mathbf{r}) = \mathbf{\Gamma}\cdot\mathbf{r} , \tag{74}$$

where $\mathbf{\Gamma}$ is the *velocity gradient tensor*,

$$\mathbf{\Gamma} = \dot{\gamma}\begin{pmatrix} 0 & 1 & 0 \\ 0 & 0 & 0 \\ 0 & 0 & 0 \end{pmatrix} , \tag{75}$$

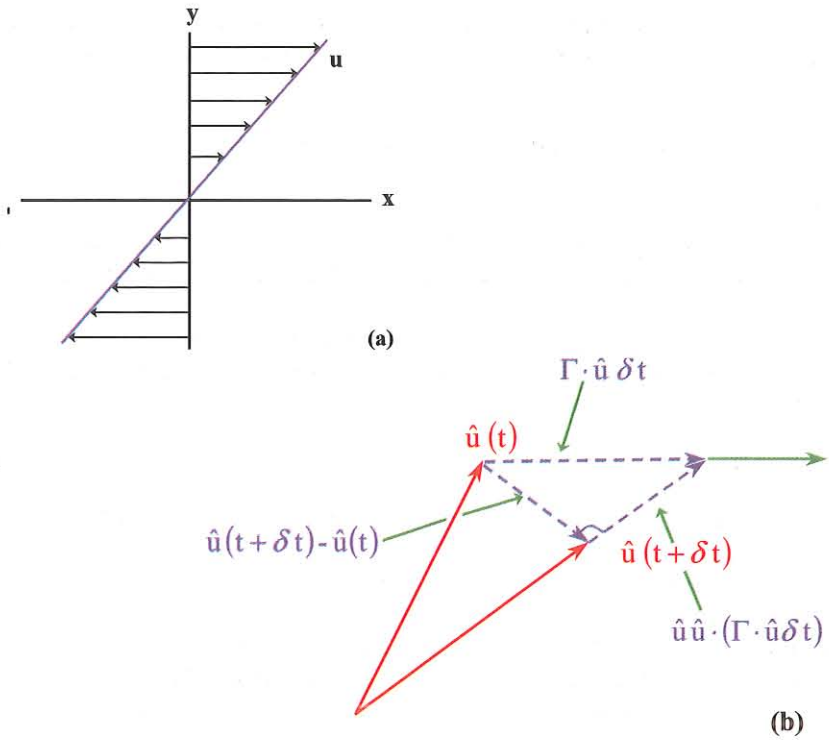


Fig. 9: *(a) The solvent flow velocity as defined in eqs.(74,75). (b) The orientational change of a rod that moves along with the fluid.*

where $\dot{\gamma}$ is referred to as the shear-rate. This velocity field is depicted in Fig.9a : it is a flow in the x-direction (the so-called *flow direction*), linearly increasing in the y-direction (the *gradient direction*, and independent of the z-coordinate (the *vorticity direction*). Clearly, the orientational dynamics of a rod will be influenced by the solvent flow. If the rods "monomers" are simple carried along with the flow, the flow induces a change of the rods orientation by (see Fig.9b) [6],

$$\hat{\mathbf{u}}(t+\delta t) - \hat{\mathbf{u}}(t) \;=\; \boldsymbol{\Gamma}\cdot\hat{\mathbf{u}}\,\delta t \;-\; \hat{\mathbf{u}}\hat{\mathbf{u}}\cdot(\boldsymbol{\Gamma}\cdot\hat{\mathbf{u}})\,\delta t\;,$$

and hence,

$$\frac{d}{dt}\hat{\mathbf{u}} \;=\; \boldsymbol{\Gamma}\cdot\hat{\mathbf{u}} \;-\; \hat{\mathbf{u}}\hat{\mathbf{u}}\cdot(\boldsymbol{\Gamma}\cdot\hat{\mathbf{u}})\;.$$

From eq.(7) we thus find the following additional angular velocity $\boldsymbol{\Omega}_{\dot{\gamma}}$ of the rod due to the flow,

$$\boldsymbol{\Omega}_{\dot{\gamma}} \;=\; \hat{\mathbf{u}}\times(\boldsymbol{\Gamma}\cdot\hat{\mathbf{u}})\;. \tag{76}$$

The corresponding contribution to the equation of motion (13), integrated over all coordinates except for $\hat{\mathbf{u}}_1 = \hat{\mathbf{u}}$, reads,

$$\frac{\partial}{\partial t}P(\hat{\mathbf{u}},t)_{|_{\dot{\gamma}}} \;=\; -\hat{\mathcal{R}}\cdot\{P(\hat{\mathbf{u}},t)\,\hat{\mathbf{u}}\times(\boldsymbol{\Gamma}\cdot\hat{\mathbf{u}})\}\;. \tag{77}$$

Operating on both side with $\oint d\hat{\mathbf{u}}\,\hat{\mathbf{u}}\hat{\mathbf{u}}(\cdots)$ leads to the following additional contribution to the equation of motion for the order parameter tensor (see appendix 4 for mathematical details),

$$\frac{d}{dt}\mathbf{S}(t)_{|\dot\gamma} \;=\; \boldsymbol{\Gamma}\cdot\mathbf{S}+\mathbf{S}\cdot\boldsymbol{\Gamma}^T-2\,\mathbf{S}^{(4)}:\mathbf{E}\,, \tag{78}$$

where $\mathbf{E}=\frac{1}{2}\left[\boldsymbol{\Gamma}+\boldsymbol{\Gamma}^T\right]$ is the symmetric part of the velocity gradient tensor. Furthermore, $\mathbf{S}^{(4)}$ is the fourth order tensor defined in eq.(65), for which the closure relation (73) has been derived in section 6. For non-interacting rods, this closure relation for $\mathbf{M}=\mathbf{E}$ turns out to be accurate to within 10 %.
Adding the contribution (78) to the right hand-side of eq.(64), and using the closure relation (73) for $\mathbf{M}=\mathbf{S}$ and $\mathbf{M}=\mathbf{E}$, leads to a closed equation of motion for the order parameter tensor $\mathbf{S}$,

$$\begin{aligned}\frac{d}{dt}\mathbf{S} \;=\; & -6D_r\left\{\mathbf{S}-\tfrac{1}{3}\hat{\mathbf{I}}-\tfrac{3}{5}\tfrac{L}{D}\varphi\,(\mathbf{S}\cdot\mathbf{S}-\mathbf{S}\,\mathbf{S}:\mathbf{S})\right\} \\ & +\dot\gamma\left\{\hat{\boldsymbol{\Gamma}}\cdot\mathbf{S}+\mathbf{S}\cdot\hat{\boldsymbol{\Gamma}}^T-\tfrac{2}{5}\left[\mathbf{S}\cdot\hat{\mathbf{E}}+\hat{\mathbf{E}}\cdot\mathbf{S}-\mathbf{S}\cdot\mathbf{S}\cdot\hat{\mathbf{E}}-\hat{\mathbf{E}}\cdot\mathbf{S}\cdot\mathbf{S}+2\mathbf{S}\cdot\hat{\mathbf{E}}\cdot\mathbf{S}+3\mathbf{S}\,\mathbf{S}:\hat{\mathbf{E}}\right]\right\}\,,\end{aligned} \tag{79}$$

where $\boldsymbol{\Gamma}=\dot\gamma\hat{\boldsymbol{\Gamma}}$, and similarly for $\hat{\mathbf{E}}$. This is the equation of motion on which our further analysis will be based.
An important thing to notice is, that the outer product $\hat{\mathbf{u}}\times(\boldsymbol{\Gamma}\cdot\hat{\mathbf{u}})$ can not be written in the form $\hat{\mathcal{R}}f$, with f a scalar field. Therefore, the shear contribution (77) to the equation of motion (58) for $P(\hat{\mathbf{u}},t)$ can not be incorporated as a potential. Shear flow, therefore, is a non-conservative external field. Since no potential for shear flow can be defined, one can not define a free energy. Thermodynamic considerations for systems under shear flow are therefore questionable. To describe coexistence under shear flow conditions, one must resort to equations of motion, and time integrate these up to the stationary state.
In the above equation of motion we used the approximation (53) for the pair-correlation function, despite the fact that the system is subjected to shear flow. Note that the pair-correlation function for a homogeneous system is the conditional probability density function (pdf) for the position coordinates of two rods, given their orientations. Positional correlations are probably much less affected by the shear flow, the main effect of which is to align rods. Therefore, the pair-correlation function is expected to be much less affected by shear flow as compared to the single particle pdf's, which justifies the use of the approximation (53) even for systems subjected to shear flow.

8 The Isotropic-Nematic Phase Transition

The equation of motion (79) allows us to calculate the isotropic-to-nematic and the nematic-to-isotropic spinodals. These spinodal concentrations are the concentrations at which the isotropic phase becomes unstable against the nematic phase and where the nematic phase becomes unstable against the isotropic phase, respectively. The location of these spinodal concentrations can thus be obtained from a linear stability analysis of the equation of motion (79). To find the location of binodals, however, equations of motion that include inhomogeneities must be solved, where the stationary solution also describes the interface between the two coexisting bulk phases. A discussion of such equations of motion is beyond the scope of this text.

Let us first calculate the concentration beyond which the isotropic phase becomes unstable. In the isotropic state, $\mathbf{S} = \frac{1}{3}\hat{\mathbf{I}}$. For a linear stability anaysis of the isotropic state, we therefore write,

$$\mathbf{S} = \tfrac{1}{3}\hat{\mathbf{I}} + \delta\mathbf{S} \,, \tag{80}$$

and linearize the equation of motion (79) (with $\dot{\gamma} = 0$) with respect to $\delta\mathbf{S}$. This leads to,

$$\frac{\partial \delta \mathbf{S}}{\partial t} = -6D_r^{eff}(\bar{\rho})\,\delta\,\mathbf{S} \,, \tag{81}$$

where the density dependent, effective rotational diffusion coefficient D_r^{eff} is equal to,

$$D_r^{eff}(\bar{\rho}) = D_r\left(1 - \tfrac{\pi}{20}DL^2\bar{\rho}\right) . \tag{82}$$

The solution of the above equation of motion is simply,

$$\delta\,\mathbf{S} = \exp\left\{-6D_r^{eff}(\bar{\rho})\,t\right\}\delta\,\mathbf{S}(t=0) \,. \tag{83}$$

The orientational order parameter thus becomes unstable when D^{eff} changes from being positive to negative. According to eq.(82) this happens at the density for which $\frac{\pi}{20}DL^2\bar{\rho} = 1$, or equivalently when, $\frac{L}{D}\,\varphi = 5$, where $\varphi = \frac{\pi}{4}D^2L\bar{\rho}$ is the volume fraction of rods. The exact value for this spinodal concentration for very long and thin rods as found by Onsager [7] is $\frac{L}{D}\,\varphi 4$. This value would have been obtained from a linear stability analysis of the equation of motion (58).
The calculation of the nematic-to-isotropic spinodal concentration can not be done analytically, since the stationary solution of eq.(79) around which one should linearize is not known analytically. In the absence of shear flow, there are two ways to find the nematic-to-isotropic spinodal concentration numerically : (i) by construction of the so-called bifurcation diagram or (ii) by considering the free energy that complies with the equation of motion (64) (together with the closure (73)). As was shown in the previous section, no free energy can be defined for system under shear flow, so that the second method only applies in the absence of shear flow. The two methods are discussed in the following two subsections.

8.1 Bifurcation diagrams

A bifurcation diagram is a plot in the shear-rate versus concentration plane of the largest eigenvalue of stationary solutions for $\mathbf{S}$ of its equation of motion (79). There are two possible stationary solutions : stable- and unstable solutions. Let $\mathbf{S}_0$ denote a stationary solution of eq.(79), that is, the right hand-side of eq.(79) vanishes for $\mathbf{S} = \mathbf{S}_0$. Let $\delta\mathbf{S}$ be a small perturbation. The stationary solution $\mathbf{S}_0$ is referred to as a stable solution when an initial state $\mathbf{S}_0 + \delta\mathbf{S}$ relaxes back to $\mathbf{S}_0$ in time, provided $\delta\mathbf{S}$ is small enough. The state $\mathbf{S}_0$ is referred to as unstable, when $\delta\mathbf{S}$ does not relax to $\mathbf{0}$, no matter how small this perturbation is chosen. A linear stability analysis is required to decide whether a stationary solution is either stable or unstable. Such a stability analysis for the stationary isotropic state $\mathbf{S}_0 = \frac{1}{3}\hat{\mathbf{I}}$ has been performed explicitly above. Since eq.(79) is a non-linear equation, other stationary solutions must be found numerically. This is easily done by time integration of eq.(79), starting from some initial state.

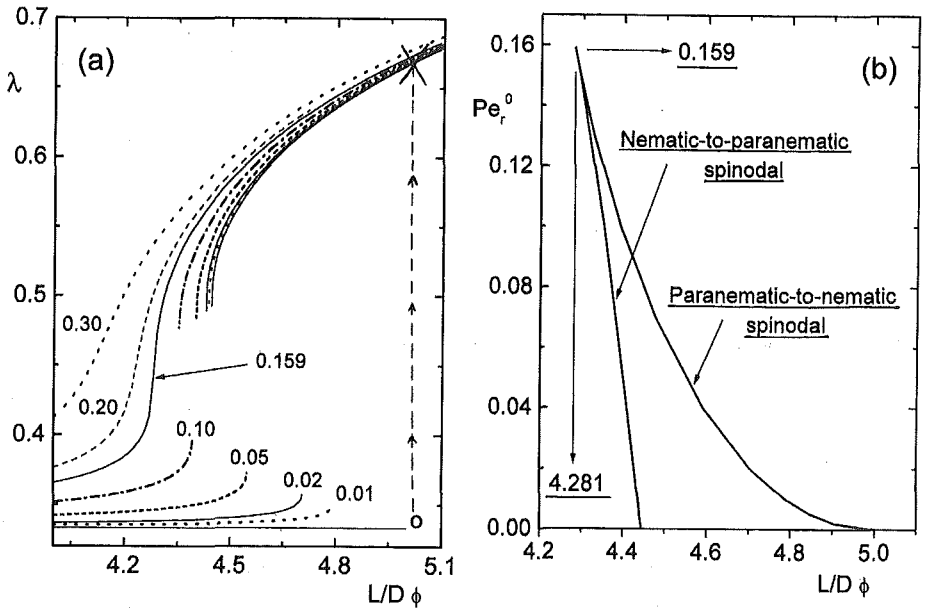


Fig. 10: *(a) Bifurcation diagrams, where only stable stationary solutions* $\mathbf{S}_0$ *of eq.(79) are shown. Here,* λ *is the largest eigenvalue of* $\mathbf{S}_0$ *and* φ *is the volume fraction of rods. The numbers in the plot refer to* Pe_r^0 *; the bare Peclet number as defined in eq.(84). (b) The spinodal points as found from the bifurcation diagrams.*

Bifurcation diagrams are given in Fig.10a, for various shear rates. As can be seen from eq.(79), there are two parameters on which a stationary state depends : the concentration, through the dimensionless parameter $\frac{L}{D}\varphi$, with φ the volume fraction of rods, and the dimensionless shear rate,

$$Pe_r^0 = \dot{\gamma}/D_r \,, \qquad (84)$$

which is referred to as the (bare) *rotational Peclet number* ("bare", because the rotational diffusion coefficient D_r is that of a single non-interacting rod, instead of the "dressed" or "effective" rotational diffusion coefficient, such as in eq.(82)).
The stable isotropic branch ends at $\frac{L}{D}\varphi = 5$, which has been found analytically before. For $\frac{L}{D}\varphi > 5$, the isotropic phase becomes unstable, and the new stable state is the nematic state with a relatively large value for λ, as indicated by the cross in Fig.10a. On subsequently lowering the concentration, the nematic state becomes unstable at $\frac{L}{D}\varphi < 40/9 = 4.4444\cdots$, and the system returns to the isotropic state.
At the spinodal concentration, the effective rotational diffusion coefficient (82) is 0. This is by definition true for the other spinodal concentrations as well. Rotational dynamics is thus extremely slow in the vicinity of a spinodal point. This is reminiscent of what is referred to in case of a gas-liquid phase transition as *critical slowing down* . In the present case, it is not the effective *translational* diffusion coefficient that is zero, as for a gas-liquid transition, but rather the *rotational* effective diffusion coefficient.
We note here that an otherwise isotropic stable state is aligned by shear flow. Such an aligned state is referred to as a *paranematic state* . Similarly, an otherwise stable nematic

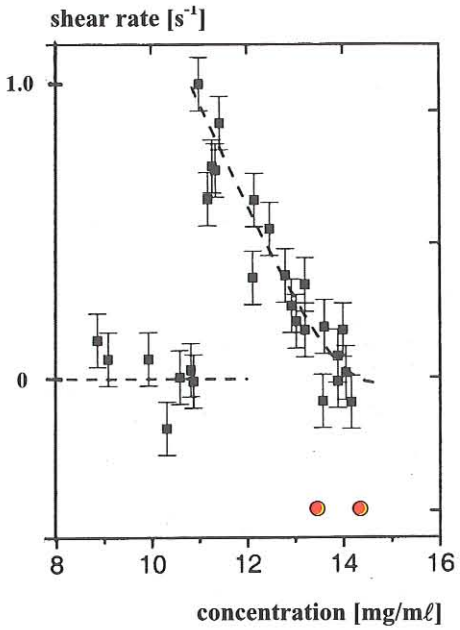


Fig. 11: *The shear-induced shift of spinodal concentrations as probed with time resolved birefringence measurements [10]. The line is located in between the two spinodal concentrations. The red circles below indicate the binodal concentrations in the absence of shear flow.*

state is somewhat more strongly aligned by shear flow.

As can be seen from the bifurcation diagram, shear flow stabilizes the isotropic and nematic phase, since the spinodal concentrations shift to lower concentrations on increasing the shear-rate. This is due to the aligning effect of the flow. At some critical shear rate, the two spinodal points merge. For shear-rates larger than this critical shear-rate, shear aligning forces are so strong, that rod-rod interactions are not able any more to induce a discontinous jump from one state to the other. There is now a continuous and reversible transition from the paranematic state to the nematic state.

The location of the paranematic-to-nematic and nematic-to-paranematic spinodal concentrations as a function of the shear-rate can be read off from the bifurcation diagrams. These spinodal concentrations are plotted in the *non-equilibrium phase diagram* in Fig.10b.

Recent time resolved birefringence experiments by Lenstra [10] confirm a shear induced shift of paranematic-nematic phase boundary lines (see Fig.11). These time resolved birefringence measurements probe a line in the non-equilibrium phase diagram that is in between the two spinodal concentrations. The systems that were used here are fd-virus suspensions. Since fd-virus is a semi-flexible rod rather then a perfectly rigid rod, and the potential between the rods is not a perfect hard-core potential, the actual values for the spinodal (and binodal) concentrations do not agree with those of the above mentioned concentrations. What is seen is that the shear induced shift is much more pronounced as predicted by our simple theory : note that the measured line is displaced to a concentration

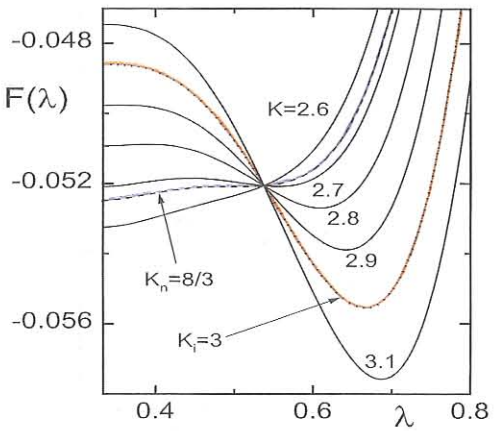


Fig. 12: *The orientational free energy for various concentrations K as a function of λ. The red curve is at the isotropic-to-nematic spinodal concentration, the blue curve at the nematic-to-isotropic spinodal concentration.*

that are far outside the binodal concentrations at zero shear-rate (the points indicated by red circles). The critical shear rate is in reasonable agreement with the one predicted in Fig.10b.

8.2 The orientational free energy

The free energy can be found from eqs.(64,73) as follows. Since in the absence of shear flow the nematic phase is uniaxial, the order parameter tensor will be of the form,

$$\mathbf{S} = \begin{pmatrix} \lambda & 0 & 0 \\ 0 & \frac{1}{2}(1-\lambda) & 0 \\ 0 & 0 & \frac{1}{2}(1-\lambda) \end{pmatrix}, \tag{85}$$

where λ is the largest eigenvalue of $\mathbf{S}$, which takes values in between $1/3$ (for an isotropic state) and 1 (for a perfectly aligned state). Substitution into eqs.(64,73) leads to the following equation of motion for λ,

$$\frac{d\lambda}{dt} = -\tfrac{1}{2} + \left(\tfrac{3}{2} + \tfrac{3}{4}K\right)\lambda - 3\,K\,\lambda^2 + \tfrac{9}{4}\,K\,\lambda^3\,, \tag{86}$$

where K is proportional to the concentration of rods,

$$K = \tfrac{3\pi}{20}\,DL^2\,\bar{\rho} = \tfrac{3}{5}\,\tfrac{L}{D}\,\varphi\,. \tag{87}$$

Since temporal changes are driven by differences in free energy F, provided the system is not too far away from equilibrium, one may infer that $d\lambda/dt \sim dF(\lambda)/d\lambda$. Hence, from integration one finds from eq.(86) that,

$$F(\lambda) = -\tfrac{1}{2}\,\lambda + \left(\tfrac{3}{4} + \tfrac{3}{8}K\right)\lambda^2 - K\,\lambda^3 + \tfrac{9}{16}\,K\,\lambda^4\,. \tag{88}$$

This free energy is plotted as a function of λ in Fig.12, for various values of the concentration K. As can be seen, the energy barrier between the isotropic state and the nematic state disappears for $K = 3$ (the red curve). This is the isotropic-to-nematic spinodal concentration. For larger concentrations there is just one minimum in the free energy at a relatively large value of λ. There is now only one stable (nematic) state. The nematic-to-isotropic spinodal concentration is the concentration where the first maximum and minimum merge and disappear (the blue curve). At this point, $dF(\lambda)/d\lambda = 0 = d^2F(\lambda)/d\lambda^2$. A value of $K = 8/3$ is found. The values 3 and 8/3 of K coincide with the isotropic-to-nematic and the nematic-to-isotropic spinodal concentrations, respectively, as found from the bifurcation diagrams in the previous subsection.

9 Current Research Activities in this Area

The theory discussed in this lecture is limited to spatially homogeneous systems. Phenomena where spatial inhomogeneities play an important role (like phase separation and shear-banding) can not be described by this theory. For an inhomogeneous system, the fluid flow will be spatially varying also. The evolution of the order parameters will be coupled to the flow, and the flow will in turn be coupled to the order parameters. The equation of motion for the suspension flow velocity is the Navier-Stokes equation, which must be specified through the divergence of the stress tensor. Hence, under shear flow conditions, not only the equation of motion (79) must be extended to include spatial inhomogeneities in concentration, shear-rate and orientational order parameter, but in addition, an explicit expression for the stress tensor must be derived, which also includes stresses arising from inhomogeneities. In the present lecture, the fluid flow is simply always equal to the linearly varying field (74). This is no longer true for spatially inhomogeneous systems.

As discussed in section 7, shear flow is a non-conservative external field, so that the usual thermodynamic arguments (equality of chemical potential and pressure in both phases) can not be used to predict the location of phase transition lines in systems under shear flow conditions. Instead, the above mentioned equations of motion should be time-integrated until a stationary state is reached. From these stationary states, the location of binodals can be obtained. For a correct prediction of the location of the binodals, the interfaces between the coexisting bulk phases must be accurately described by the equations of motion. Since spatial gradients in these interfaces may be very large, equations of motion can probably not be based on truncated gradient expansions. Instead, equations of motion must correctly account for very large spatial gradients.

The derivation and analysis of appropriate equations of motion for very inhomogeneous systems in shear flow, that are far away from equilibrium, is a topic of current interest. This interest extends beyond suspensions of rigid rod like colloids, but also involves, for example, polymeric- and surfactant systems. In the latter kind of systems, entirely new structures can be formed by applying shear flow. For example, laminar structures or multi-layer vesicles can be induced by shear flow. Contrary to suspensions of rigid rods, in these systems shear flow can induce entirely new phases that would be meta-stable or unstable in the absence of shear flow.

For many systems (like suspensions of rigid rods, polymeric- and surfactant systems) a so-called shear-banding instability is found . This is a shear induced, hydrodynamic

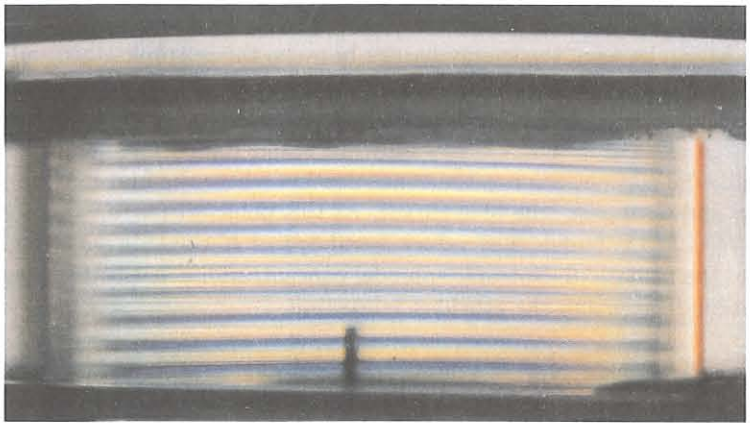


Fig. 13: *A stationary shear-banded structure of a suspension of fd-virus (from Zvonimir Dogic and Pavlik Lettinga, unpublished). This photograph is taken with the shear cell in between two crossed polarizers. This is a side-view of the cylindrical geometry, that is, the shear-bands extend in the vorticity direction.*

instability, where two different kinds of the stationary states are observed in a cylindrical geometry (where the sample is contained in between two concentric cylinders, one of which rotates with a constant speed). The most common banded structure that is found is a structure of alternating regions extending in the vorticity direction. Fig.13 is a photograph of such a banded structure for a fd-virus suspension. This photograph is taken with the shear cell in between two crossed polarizers. The difference in intensity of the two kinds of regions show that the internal orientational states of these regions differ. A second, not so often observed banded structure, is one that extends along the gradient direction : near the rotating cylinder, a region with a relatively high shear-rate is observed, which coexists with a region of low shear-rate near the stationary cylinder. Within these regions (the "bands") the shear-rate is constant, independent of position. The bands are connected by an "interface", where gradients in the shear-rate are very large.

The shear-banding instability giving rise to an alternating banded structure that extends along the vorticity direction is probably driven by normal stress differences. The banded structure of two regions extending in the gradient direction is due to a decrease of the shear-gradient stress component with increasing shear-rate. It is not clear yet, for example, what determines the height of the bands in Fig.13 : is it shear-rate dependent, does it depend on the gap width, etc . ?

The non-equilibrium phase diagram thus contains "phase transition lines" which indicate the lines where shear-banding occurs. It might be that the location of such shear-banding transition lines depends on the geometry of the shear cell. For the calculation of these shear-banding transition lines, it suffices to solve the equations of motion mentioned above. The stationary solution of these equations of motion should now reproduce the shear-banded states. Experimental phase diagrams that include spinodals/binodals and the shear-banding lines have not been determined so far.

Phase separation kinetics can now become quite complicated, also in its initial stages. It can happen that two instabilities are at work simultaneously : the usual "thermodynamic instability" (in the presence of shear flow) and the shear-banding instability. The interplay

between these two instabilities now determines the morphology of the system during phase separation.
For very long and thin rods, the approximation (53) for the pair-correlation function is correct only for repulsive interactions (provided that the degree of alignment is not too high). When attractive pair-interactions between the rods play a role, the approximation (53) is not valid anymore. Taking into account higher order density corrections to the pair-correlation function also fails. Up to now, very little is known about the phase behaviour and microstructural order in systems of attractive rods [11]. Experimentally it is observed that often gels are formed in systems of attractive rods (and spheres) with short ranged attractions. Here, relatively open, quasi-permanent clusters are formed. Like a glass, a gel is a very long lived non-equilibrium state. So far, there is no microscopic understanding of the gel state.

Appendices

Appendix 1 : Dyadic products and projections

Let $\mathbf{a} = (a_1, a_2, a_3)$ and $\mathbf{b} = (b_1, b_2, b_3)$. A tensor can be constructed from these vectors by "dyadic multiplication" . The tensor is denoted as $\mathbf{ab}$ and its nm^{th} component is defined to be equal to $a_n b_m$. In full,

$$\mathbf{ab} = \begin{pmatrix} a_1b_1 & a_1b_2 & a_1b_3 \\ a_2b_1 & a_2b_2 & a_2b_3 \\ a_3b_1 & a_3b_2 & a_3b_3 \end{pmatrix} \tag{89}$$

The action of this tensor on a vector $\mathbf{c} = (c_1, c_2, c_3)$ is,

$$[(\mathbf{ab}) \cdot \mathbf{c}]_i = \sum_j (\mathbf{ab})_{ij} c_j = a_i \sum_j b_j c_j = a_i (\mathbf{b} \cdot \mathbf{c}) . \tag{90}$$

In this equation we used the contraction symbol " $\cdot$ ". This "operator" is defined as : "take the two indices adjacent to $\cdot$ equal, and sum over them". Similarly two dots " : " used, for example, in eqs.(41,64) operate as : "take the next two adjacent indices also equal, and sum over them as well". This is explicitly written in the second line in eq.(41). The "operator " : " is also referred to as a "double contraction".
The dyadic notation can be used to write the component $\mathbf{c}_\parallel$ of the vector $\mathbf{c}$ along a unit vector $\hat{\mathbf{u}}$ as,

$$\mathbf{c}_\parallel = \hat{\mathbf{u}} (\hat{\mathbf{u}} \cdot \mathbf{c}) = [\hat{\mathbf{u}}\hat{\mathbf{u}}] \cdot \mathbf{c} . \tag{91}$$

The component of $\mathbf{c}$ perpendicular to $\hat{\mathbf{u}}$ is simply $\mathbf{c}_\perp = \mathbf{c} - \mathbf{c}_\parallel$, or,

$$\mathbf{c}_\perp = \left[\hat{\mathbf{I}} - \hat{\mathbf{u}}\hat{\mathbf{u}}\right] \cdot \mathbf{c} . \tag{92}$$

The operators $\hat{\mathbf{u}}\hat{\mathbf{u}}$ and $\hat{\mathbf{I}} - \hat{\mathbf{u}}\hat{\mathbf{u}}$ are thus the projection operators parallel and perpendicular to the unit vector $\hat{\mathbf{u}}$, respectively. This notation is used in eqs.(18,19).

The notion of a dyadic product can be extended to define *polyadic products*. For example, the tensor $\mathbf{S}^{(4)}$ in eq.(65) is a polyadic product of order four. It is a fourth order tensor with components,

$$S^{(4)}_{ijmn} = < \hat{u}_i \, \hat{u}_j \, \hat{u}_m \, \hat{u}_n > ,$$

with $\hat{u}_p$ the p^{th} component of $\hat{\mathbf{u}}$. The double contraction in eq.(64), for example, is by definition equal to,

$$\left[\mathbf{S}^{(4)} : \mathbf{S}\right]_{ij} = \sum_{n\,m} S^{(4)}_{ijmn} \, S_{nm} ,$$

and similarly for the double contration appearing in eq.(78).

Appendix 2 : Derivation of eqs.(36,49)

Let us first formulate Stokes's integral theorem. Let $\mathcal{S}$ denote a surface in $\Re^3$ and $\partial\mathcal{S}$ its boundary, which is a closed curve in $\Re^3$. Let $d\mathbf{S}$ denote an infinitesimally small surface element on $\partial\mathcal{S}$: its magnitude is equal to the infinitesimally small surface area dS, while its direction is locally perpendicular to $\partial\mathcal{S}$. Furthermore, let $d\mathbf{l}$ denote an infinitesimally small line element on $\partial\mathcal{S}$: its magnitude is equal to the length of the infinitesimally small line segment dl, while its direction is locally tangential to $\partial\mathbf{S}$. The direction of $d\mathbf{S}$ and $d\mathbf{l}$ are connected through the cork-screw rule. Stokes's integral theorem reads,

$$\int_{\mathcal{S}} d\mathbf{S} \cdot \nabla \times \mathbf{F}(\mathbf{r}) = \oint_{\partial\mathcal{S}} d\mathbf{l} \cdot \mathbf{F}(\mathbf{r}) , \qquad (93)$$

where $\mathbf{F}(\mathbf{r})$ is a (sufficiently differentiable) vector field.
In our application of Stokes's integral theorem, $\mathcal{S}$ is the unit spherical surface with its center at the origin. Therefore, the boundary $\partial\mathcal{S}$ is empty, so that the line-integral on the right hand-side in eq.(93) is zero. Furthermore, the integration variable is now denoted as $\hat{\mathbf{u}}$, instead of $\mathbf{r}$. Since $\hat{\mathbf{u}}$ is always perpendicular to the unit sphere, we shall write $d\mathbf{S} = d\hat{\mathbf{u}}\,\hat{\mathbf{u}}$, where the notation $d\hat{\mathbf{u}}$ is used instead of dS to indicate that the integration is with respect to $\hat{\mathbf{u}}$ (note that in spherical coordinates : $d\hat{\mathbf{u}} = \sin\{\Theta\} d\Theta d\varphi$). Using that $\hat{\mathbf{u}} \cdot (\nabla \times \mathbf{F}) = (\hat{\mathbf{u}} \times \nabla) \cdot \mathbf{F}$, eq.(93) reduces to,

$$\oint d\hat{\mathbf{u}} \; (\hat{\mathbf{u}} \times \nabla_{\hat{u}}) \cdot \mathbf{F}(\hat{\mathbf{u}}) = 0 . \qquad (94)$$

Here, $\nabla_{\hat{u}}$ is the gradient operator with respect to the cartesian components of $\hat{\mathbf{u}}$. Furthermore $\int_{\mathcal{S}}$ is now denoted as $\oint$, to indicate that the integration is over a closed surface (the entire unit spherical surface). This is the last equation in eq.(49).
Now choose $\mathbf{F}(\hat{\mathbf{u}}) = \mathbf{a}\, h(\hat{\mathbf{u}})$ with $\mathbf{a}$ a $\hat{\mathbf{u}}$-independent vector, and $h(\hat{\mathbf{u}})$ a scalar field. Equation (94) implies that,

$$\mathbf{a} \cdot \oint d\hat{\mathbf{u}} \; (\hat{\mathbf{u}} \times \nabla_{\hat{u}}) \, \mathbf{h}(\hat{\mathbf{u}}) = 0 . \qquad (95)$$

Since $\mathbf{a}$ is an arbitrary vector, the integral must vanish. Now taking $h(\hat{\mathbf{u}})$ equal to a product $f(\hat{\mathbf{u}})\, g(\hat{\mathbf{u}})$ of the two scalar fields f and g immediately leads to eq.(36).

Appendix 3 : Density expansion of the pair-correlation function

The first two terms in the density expansion of the equilibrium pair-correlation function of hard particles reads,

$$g(\mathbf{r}_1-\mathbf{r}_2,\hat{\mathbf{u}}_1,\hat{\mathbf{u}}_2) = \exp\{V(\mathbf{r}_1-\mathbf{r}_2,\hat{\mathbf{u}}_1,\hat{\mathbf{u}}_2)\} \times\left\{1+\bar{\rho}\int d\mathbf{r}_3\oint d\hat{\mathbf{u}}_3\,\chi(\mathbf{r}_1-\mathbf{r}_3,\hat{\mathbf{u}}_1,\hat{\mathbf{u}}_3)\chi(\mathbf{r}_3-\mathbf{r}_2,\hat{\mathbf{u}}_3,\hat{\mathbf{u}}_2)\right\}, \quad (96)$$

where χ is the characteristic function for overlap. Since the characteristic functions in the integrand are only non-zero when the core of rod number 3 overlaps with rods 1 *and* 2, the integration with respect to $\hat{\mathbf{u}}_3$ effectively extends over an angular range of the order D/L, and the integration with respect to $\mathbf{r}_3$ is at most of the order DL^2. Hence the second term between the curly brackets in eq.(96) is at most of order $(D/L)\,DL^2\,\bar{\rho}\sim\varphi$. Since the volume fraction of interest scale like D/L, the first order in density contribution to the pair-correlation function is negligibly small for very long and rods. Higher order terms are similarly very small.

Appendix 4 : Mathematical details in the derivation of eqs.(64,78)

Usefull identities for the derivation of eqs.(64,78) are (with $\mathbf{a}$ an arbitrary vector),

$$\hat{\mathcal{R}}\hat{\mathbf{u}}\hat{\mathbf{u}} : \mathbf{S} = 2\hat{\mathbf{u}}\times(\mathbf{S}\cdot\hat{\mathbf{u}}), \quad (97)$$

$$(\hat{\mathbf{u}}\times\mathbf{a})\cdot\hat{\mathcal{R}}\hat{\mathbf{u}}\hat{\mathbf{u}} = \mathbf{a}\hat{\mathbf{u}}+\hat{\mathbf{u}}\mathbf{a}-2\hat{\mathbf{u}}\hat{\mathbf{u}}\hat{\mathbf{u}}\cdot\mathbf{a}. \quad (98)$$

Substitution of the Maier-Saupe potential (63) into eq.(55) for the torque, and subsequently multiplying the corresponding term in eq.(50) by $\hat{\mathbf{u}}\,\hat{\mathbf{u}}$ and integrating, leads to an integral proportional to,

$$\oint d\hat{\mathbf{u}}(\hat{\mathbf{u}}\,\hat{\mathbf{u}})\hat{\mathcal{R}}\cdot\left[P(\hat{\mathbf{u}},t)\hat{\mathcal{R}}\,(\hat{\mathbf{u}}\hat{\mathbf{u}} : \mathrm{S})\right].$$

Performing a partial integration (see eq.(36)) and using eq.(97) leads to,

$$-2\oint d\hat{\mathbf{u}}\,P(\hat{\mathbf{u}},t)\;[\hat{\mathbf{u}}\times(\mathbf{S}\cdot\hat{\mathbf{u}})]\cdot\hat{\mathcal{R}}\,\hat{\mathbf{u}}\hat{\mathbf{u}}\,.$$

Using the identity (98), with $\mathbf{a}=\mathbf{S}\cdot\hat{\mathbf{u}}$, gives,

$$-2\oint d\hat{\mathbf{u}}\,P(\hat{\mathbf{u}},t)\;\{\mathbf{S}\cdot\hat{\mathbf{u}}\,\hat{\mathbf{u}}+\hat{\mathbf{u}}\,\mathbf{S}\cdot\hat{\mathbf{u}}-2\hat{\mathbf{u}}\hat{\mathbf{u}}\hat{\mathbf{u}}\cdot\mathbf{S}\cdot\hat{\mathbf{u}}\}\,.$$

Due to the symmetry of $\mathbf{S}$, this leads immediately to,

$$4\left[\mathbf{S}\cdot\mathbf{S}-\mathbf{S}^{(4)} : \mathbf{S}\right],$$

which is the corresponding term in eq.(64).

Next, multiplying both sides of eq.(77) by $\hat{\mathbf{u}}\hat{\mathbf{u}}$ and integrating leads to the following expression for the additional contribution to the equation of motion for $\mathbf{S}$ as the result of shear flow,

$$\oint d\hat{\mathbf{u}}\,(\hat{\mathbf{u}}\,\hat{\mathbf{u}})\hat{\mathcal{R}}\cdot P(\hat{\mathbf{u}},t)\,\hat{\mathbf{u}}\times(\boldsymbol{\Gamma}\cdot\hat{\mathbf{u}})\;.$$

Performing a partial integration and using eq.(98), with $\mathbf{a}=\boldsymbol{\Gamma}\cdot\hat{\mathbf{u}}$, leads, similarly as above, to eq.(78).

References

[1] M.P.B. van Bruggen, M. Donker, H.N.W. Lekkerkerker, T.L. Hughes, Colloids and Surfaces A; Physicochem. Eng. Aspects **150**, 115 (1999).

[2] J.M. Deutch, I.J. Oppenheim, J. Chem. Phys. **54**, 3547 (1971).

[3] T.J. Murphy and J.L. Aquirre, J. Chem. Phys. **57**, 2098 (1972).

[4] W.B. Russel, D.A. Saville, W.R. Schowalter, Colloidal Dispersions, Cambridge University Press, Cambridge, 1991.

[5] J.K.G. Dhont, An Introduction to Dynamics of Colloids, Elsevier, Amsterdam, 1996.

[6] M. Doi and S.F. Edwards, The Theory of Polymer Dynamics, Oxford University Press, Oxford, 1986.

[7] L. Onsager, Ann. N.Y. Acad. Sci. **51**, 627 (1949).

[8] W. Maier, A. Saupe, Naturforsch. **13A**, 564 (1958), **14A**, 882 (1959), **15A**, 287 (1960).

[9] E.J. Hinch, L.G. Leal, J. Fluid Mech. **76**, 187 (1976).

[10] T.A.J. Lenstra, Z. Dogic, J.K.G. Dhont, J. Chem. Phys. **114**, 10151(2001).

[11] P. van der Schoot, T. Odijk, J. Chem. Phys. **97**, 515 (1992).

C 5 Colloidal Glasses

Reiner Zorn
Institut für Festkörperforschung
Forschungszentrum Jülich GmbH

Contents

1 Motivation **2**

2 Materials **2**

3 Dynamic Light Scattering **3**
3.1 General Principles 3
3.2 Non-Ergodicity 5
3.3 Incoherent Light Scattering 8

4 Experimental Results **9**

5 Mode Coupling Theory **13**
5.1 Outline of the Theory 13
5.2 Comparison to Experiments 15

6 Summary **17**

1 Motivation

In current solid state theory the understanding of the crystalline state of matter is much more developed than that of the amorphous state. Nevertheless, amorphous materials constitute a large part of condensed matter and therefore a theoretical understanding is of immense importance for basic science as well as application purposes.
Amorphous materials comprise a large number of chemically strongly different materials as polymers, silicate glasses, salt melts, metallic glasses, and biopolymers. The study of these materials involves numerous experimental methods as neutron scattering, dielectric spectroscopy, nuclear magnetic resonance, rheology, and computer simulation.
Nevertheless, a kind of universality can be found if results from different materials or different methods are compared. This allows some hope that a simple general model may be developed which can describe the experimental observations.
Besides the scientific interest in such a general theory of glass forming materials there is also a strong interest concerning their technological applications. The oldest and best-known application is that of silicate glasses in windows, bottles etc.. But by now the importance of these materials has been outstripped by glassy polymers, e.g. polymethylmethacrylate (plexiglass), polycarbonates as substrate for compact discs, polystyrene in various forms as styrofoam. Examples of more recent industrial uses of amorphous materials are metallic glasses with their special magnetic properties and glassy sugar solutions as a medium to preserve proteins for medical applications.
In order to study the essentials of the glass transition it is desirable to observe a system which is much simpler than those of technological importance mentioned above. In principle, the basic phenomena should be visible also in systems without internal degrees of freedom (as bond rotations), containing only one sort of particles, and with a simple interparticle potential. On the atomic level, such systems would be noble gases or elemental metals. The problem which completely obstructs the study of the glass transition in these systems is the required speed of cooling. Calculations show that only be quenching at rates of the order 10^{13} K/s they can be transformed into a glass. For realistic cooling rates crystallisation is inevitable.
A way to avoid this problem in experimental studies is to use model glasses where the atoms are replaced by colloidal particles which are more than 1000 times bigger. Also these particles are suspended in a solvent which makes viscous friction forces more important than inertial forces. Altogether, the use of colloids leads to a much slower dynamics enabling experiments on the time scale ranging from hours to months.

2 Materials

The "standard material" for the study of the glass transition in colloids are suspensions of polymer spheres. By using microemulsion polymerisation (explained in another lecture) it is possible to synthesise nearly monodispersely distributed rigid spheres [1]. The size chosen for the spheres is usually about 200 nm with a coating of flexible polymer chains of about 10 nm thickness.
Besides the advantage of extremely slow crystallisation these systems have the advantage that the interparticle potential is close to that of hard spheres (i.e. $U(r) = \infty$ if r becomes smaller than the diameter of a sphere). This makes the application of several theoretical

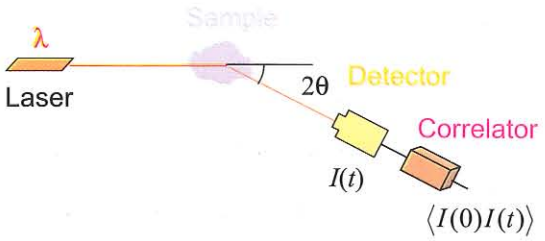


Fig. 1: *Schematic set-up of a dynamic light scattering experiment.*

concepts possible which enable the calculation of the structure factor and dynamical properties. The application of mode coupling theory concepts (see section 5.1) is facilitated by the absence of thermally activated processes ("hopping" over energy barriers) which dominate the dynamics in molecular glass forming liquids at low temperatures.
From the experimental point of view the systems are easy to study because the characteristic dimensions are close the wavelength of light. Therefore, dynamic light scattering can be applied which can observe times ranging from microseconds to hours (10 decades). (To compare, for the same studies on molecular systems the smaller dimensions compel the use of neutron scattering whose dynamical range is $10^{-13} \ldots 10^{-8}$ s, 5 decades.)
As we will see later from the experimental results in section 4 the analogy to atomic or molecular systems is far-reaching. Indeed, dependent on the particle density of the colloids, one finds liquid-like and crystalline order and also a dynamically frozen glass-like structure.
In addition to the classical system of polymer spheres, monodisperse amorphous silica spheres have been used recently [2]. Also star branched polymers with a high number of branches turn out to be effectively hard sphere colloids [3].

3 Dynamic Light Scattering

3.1 General Principles

The most important experimental method to investigate the dynamics of colloidal glasses is *dynamic light scattering* (DLS). In this chapter the basics of this method will be explained. For a detailed derivation of the statements and equations the reader is referred to standard textbooks [5, 6, 7, 8].
Figure 1 shows the schematic experimental set-up of the DLS experiment. Monochromatic laser light of wavelength λ is scattered from the sample. The scattered photons are registered in a detector giving a time dependent intensity signal $I(t)$. From this signal a special purpose computer ("correlator") constructs the correlation function $\langle I(0)I(\tau)\rangle$ as explained later in this section.
The experiment involves two parameters the scattering vector $\mathbf{Q}$ and the correlation time τ. The former is defined as the difference of incident and scattered wave vectors:

$$\mathbf{Q} = \mathbf{k}_1 - \mathbf{k}_0 \,. \tag{1}$$

Because in the experiments considered here the absolute values are approximately the same, $k_1 \approx k_0 = 2\pi n/\lambda$, the scattering vector is determined by the scattering angle, the

wavelength and the index of refraction n:

$$\mathbf{Q} = \frac{4\pi n}{\lambda} \sin\theta \,. \tag{2}$$

The dependence of the scattered intensity on $\mathbf{Q}$ contains the *structural* information obtained by the experiment
The *dynamical* information is contained in the intensity correlation function

$$\langle I(0)I(\tau)\rangle = \lim_{T\to\infty} \frac{1}{T} \int_{t_0}^{t_0+T} I(t)I(t+\tau)\mathrm{d}t \,. \tag{3}$$

(Of course $I(t)$ and also the correlation functions depend on the scattering angle and therefore on $\mathbf{Q}$. To simplify the expressions this dependence will only be shown where necessary.) The practical meaning of this equation is the following: The integral with the factor $1/T$ is the average over the time interval of length T. In order to obtain a stable value independent of the short-time fluctuations one has to take the limit of infinite time interval length T. For comparison the average intensity is defined by

$$\langle I\rangle = \lim_{T\to\infty} \frac{1}{T} \int_{t_0}^{t_0+T} I(t)\mathrm{d}t \,. \tag{4}$$

In contrast to this definition equation (3) contains the product of two intensity measurements which are apart by the time τ. Therefore, $\langle I(0)I(\tau)\rangle$ expresses in how far intensities measured in this temporal distance are correlated. It is easy to see that if there is not temporal correlation (3) reduces to the square of (4), $\langle I\rangle^2$. On the other hand if there is complete correlation (especially for $\tau = 0$) it assumes the value $\langle I^2\rangle$ which is always greater or equal to the former value.
In order to express the degree of correlation independently of the intensity itself a normalised quantity is defined

$$g_2(t) = \frac{\langle I(0)I(t)\rangle}{\langle I^2\rangle} \,. \tag{5}$$

Under certain ideal experimental conditions this function decays from 2 to 1. In order to obtain a connection to the microscopic properties of a colloid one needs the correlation function of the electric field instead of that of the intensities, namely

$$g_1(t) = \frac{\langle E(0)E(t)\rangle}{\langle E^2\rangle} \,. \tag{6}$$

With certain assumptions, the most important being that the electrical field is a Gaussian-distributed quantity, one can derive the *Siegert relation* between the two correlation functions:

$$g_1(t) = \sqrt{g_2(t) - 1} \,. \tag{7}$$

Scattering theory gives a simple relation between the field correlation function (6) and the time dependent particle positions of a liquid-like colloid assuming particles which are identical (monodisperse) with respect to their shape, size, and optical properties:

$$g_1(t) = \frac{S(\mathbf{Q},t)}{S(\mathbf{Q})} \,. \tag{8}$$

Here, $S(\mathbf{Q})$ and $S(\mathbf{Q},t)$ are the static and dynamic structure factor. The former is defined as usual in the theory of diffraction:

$$S(\mathbf{Q}) = \left\langle \sum_{i,j} \exp\left(\mathrm{i}\mathbf{Q}\cdot(\mathbf{r}_i - \mathbf{r}_j)\right) \right\rangle . \tag{9}$$

From this definition it can be seen that it is the spatial Fourier transform of the two-particle correlation function. The particle positions $\mathbf{r}_i$ entering here are those at the same instant. Thus, the static structure factor represents the Fourier transform of a "snapshot picture" of the structure. The dynamic structure factor is a generalisation of (9) involving the correlation of particles *at different times*:

$$S(\mathbf{Q},t) = \left\langle \sum_{i,j} \exp\left(\mathrm{i}\mathbf{Q}\cdot(\mathbf{r}_i(0) - \mathbf{r}_j(t))\right) \right\rangle . \tag{10}$$

The definition implies that the value at $t = 0$ is identical to $S(\mathbf{Q})$ and therefore $g_1(t)$ starts at 1. From this value it decays indicating that the spatial correlation of the particles gets lost due to their motion. If the material is liquid-like, i.e. particles can reach any position in the sample volume after sufficient time, decay is complete: $\lim_{t\to\infty} g_1(t) = 0$. If it is solid like (crystalline or glassy) there is a finite value, called the non-ergodicity parameter f_Q.

3.2 Non-Ergodicity

This naming of f_Q points to a problem arising in the study of the glass-like phases of colloids: If the particle density is so high that the particles block each other they cannot reach any point in the sample within the experimental time of some hours. Then, the system's trajectory in phase space does not reach all its regions any more. In consequence the ergodic hypothesis cannot be employed. But it is clear that the average in the intensity correlation function (3) is a time average while that of the structure factors (9) and (10) are ensemble averages. So the simple relation between dynamic light scattering and microscopic dynamics is invalid in this case.

This is immediately clear already from static light scattering: $S(\mathbf{Q})$ is a smooth function of Q in a disordered sample. It shows a maximum corresponding to a preferred distance of scattering centres, $Q_{\max} = 2\pi/d$ but no Bragg peaks as in a crystalline material. But if one puts a piece of scratched or smoked glass into a laser beam the light is scattered into small patches, so-called speckles. The speckles are more dense close to $Q_{\max}$ but the exact shape of $I(\mathbf{Q})$ is clearly different from that of $S(\mathbf{Q})$. There are several simple ways to obtain the correct $S(\mathbf{Q})$ in this situation[1]: (1) Because a glassy sample is isotropic, only the absolute value $Q = |\mathbf{Q}|$ is relevant. Therefore one can average over detector positions with different azimuthal angle but identical Q. This "radial averaging" involves many speckles and therefore creates a kind of ensemble average. (2) Because the sample is macroscopically homogeneous it can be shifted through the beam during the experiment. Then, different parts of the sample are illuminated creating an ensemble average in an

[1] Actually one will obtain the product of structure factor and form factor of the particle, $S(Q)P(Q)$. Here $P(Q)$ is derived from the shape of a single particle by Fourier transform. But since $P(Q)$ is a smooth function of Q this does not affect the argument.

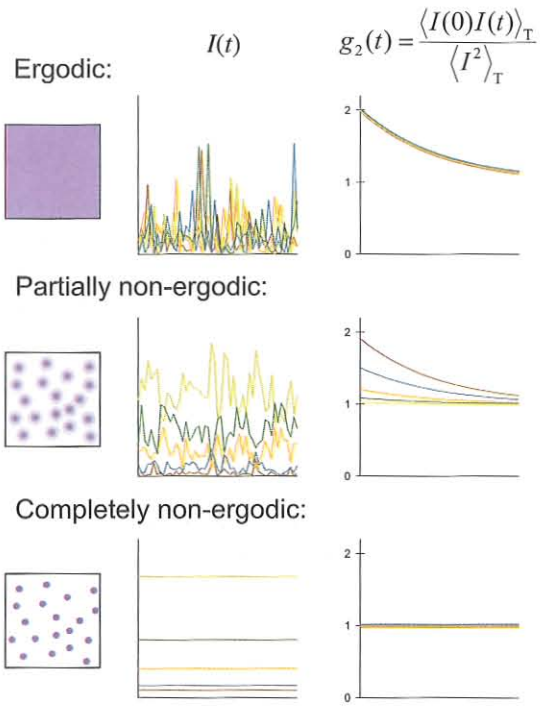


Fig. 2: *Three schematic scenarios of dynamic light scattering on a colloid. Left column: microscopic picture of the sample, averaged over the typical experiment duration. Centre column: intensities $I(t)$ measured for different detector/sample positions corresponding to a single absolute scattering vector Q. Right column: intensity correlation functions at the same positions, the colours correspond to those of the $I(t)$ curves.*

obvious way. (3) Because of the isotropy of the sample the same effect can be achieved by rotating the sample.

The situation for DLS is somewhat more complicated. Figure 2 shows schematically the experimental result for three situations: liquid-like ergodic, completely arrested (non-ergodic), and partially non-ergodic, i.e. the particles can perform a local motion on the experimental time scale but are confined to certain volumes. In the liquid situation all intensities measured by a variation of detector or sample position as described before are different. Nevertheless, the correlation functions are identical, decay from 2 to 1, and can be converted to $g_2(t)$ by the Siegert relation (7). For the completely arrested particles it is clear that the intensities are constant because the scattering centres do not move. They are different because the detector may be placed on a speckle or in between. $g_2(t) = 1$ but from the definition for an arrested sample $S(Q,t)/S(Q) = 1$ so the Siegert relation is clearly inapplicable.

The most interesting case is of course the situation in between. In this partially non-ergodic case the intensity fluctuates and its correlation function depends on the exact position of the detector or sample. If the detector is close to the centre of a speckle the average intensity is high; but since the fluctuations only increase by about the square root

of the average intensity the ratio (5) is smaller, starting from a value $\ll 2$. The situation is "better" for detector positions between speckle centres where this value is closer to 2 but it will be never identical to that value rendering the Siegert relation again useless. Similar experimental solutions as that for static scattering can be employed here. One has to take care that the averaging takes places before the ratio g_2 is calculated:

$$g_2^E(t) = \frac{\langle\langle I(0)I(t)\rangle_T\rangle_E}{\langle\langle I^2\rangle_T\rangle_E}. \tag{11}$$

($g_2^E(t)$ means the ergodic variant of $g_2(t)$ which is the one which can be transformed into $S(Q,t)/S(Q)$ by the Siegert relation.) Here $\langle\ldots\rangle_T$ denotes the time average done in the electronic correlator and $\langle\ldots\rangle_E$ the ensemble average fabricated by repeating the experiment under identical Q conditions. It is clear that repetition of the experiment increases the measuring time which for DLS experiments which are longer anyway is much more an issue than for static scattering.
Therefore, two quasi-continuous experimental methods have been developed [2]. Figure 3 shows a comparison of their results with the "brute force" approach of averaging 4000 experiments of 75 s duration: (1) If the sample is rotated the speckle pattern moves on the detector plane. There is still a correlation within the measured intensity as long as the same speckle falls into the detector. At a rotation rate of $10^{-4}\,\mathrm{s}^{-1}$ this time span is about one second. For times below one second this experiment's result is identical to that of separate experiments. For longer times there is a decay of the correlation function which is not due to the microscopic motion of particles but the macroscopic rotation. Therefore, that part of the data is unusable for further conclusions. (2) On the other hand, correlation is restored when one rotation is completed. Therefore it is possible to rotate the sample at a fast speed, e.g. $1\,\mathrm{s}^{-1}$, and correlate only data which is apart by multiples of the rotation time, here 1 s. This "stroboscopic" method yields $g_2(t)$ only for integer multiples of a relatively large time but can access any long time if the synchronisation between correlator unit and sample rotation is assured precisely. The comparison in figure 3 shows that there is only a slight discrepancy to the "brute force" approach (probably due to imperfections of this synchronisation).
Because also the latter methods are not easy to realise experimentally also a pure mathematical solution has been developed [9]. It basically consists of a suitable renormalisation of the correlation function of a single speckle. It can be shown that under certain conditions (completion of fast motion in the time window of the experiment, small detector area) the Siegert relation changes into

$$\frac{S(Q,t)}{S(Q)} = 1 + \frac{\langle I\rangle_T}{\langle I\rangle_E}\left(\sqrt{g_2^T(t) - g_2^T(0) + 1} - 1\right). \tag{12}$$

In the ergodic case one has $\langle I\rangle_T / \langle I\rangle_E = 1$ and $g_2^T(0) = 2$ and this expression reduces to (7). In the non-ergodic case one has to measure the following additional quantities: $\langle I\rangle_T$ is recorded by the electronic correlator by calculating the integral (4) in addition to those as (3). $\langle I\rangle_E$ is determined by sample/detector movement as explained for static scattering. Because this extra part is only a static experiment this implies not much increase of the measuring time. Finally, $g_2^T(0)$ has to be determined by extrapolation of $g_2^T(t)$ (curves in figure 2) to $t = 0$. This method, although mathematically exact, involves some uncertainty whether the experimental conditions are fulfilled. It is therefore

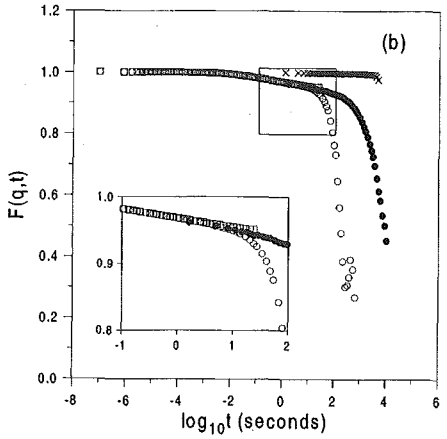


Fig. 3: *Comparison of different experimental methods to obtain the ensemble averaged quantity $F(Q,t) = S(Q,t)/S(Q)$ from DLS experiments on a partially non-ergodic sample. Squares: "brute force" approach, 4000× repetition of the experiment. Open circles: slow rotation with continuous sampling. Filled circles: fast rotation with stroboscopic sampling. The crosses show as a reference the result from a completely non-ergodic sample of quartz glass. From [2].*

necessary to check its validity as shown in figure 4. It can be seen that the results from averaging individual DLS experiments converge to the result obtained by equation (12) from a single experiment.

3.3 Incoherent Light Scattering

A recent extension to the methods of light scattering is that of incoherent DLS [2]. In contrast to the techniques described above which give information about the pair correlation function this methods yields the self-correlation of individual particles.
Incoherent scattering is a standard technique for neutron scattering. There, it is caused by different scattering lengths of chemically identical nuclei (either as different isotopes or by different spin orientation). The analogous technique for light scattering requires the use of particles with identical shape and surface properties but different index of refraction. This has recently been achieved by using polymer spheres and silica spheres of identical size with identical polymer coating grafted on the surface.
As in neutron scattering (see the lecture in this school for details) the total scattering signal can be decomposed into a coherent part and an incoherent part

$$g_1(t) \propto \left(\overline{b^2} - \bar{b}^2\right) S_{\text{inc}}(Q,t) + \bar{b}^2 S_{\text{coh}}(Q,t) \tag{13}$$

where $S_{\text{coh}}(Q,t)$ is the dynamic structure factor as defined in equation (10) called "coherent" her for distinction. $S_{\text{inc}}(Q,t)$ is its incoherent counterpart

$$S_{\text{inc}}(\mathbf{Q},t) = \left\langle \sum_i \exp\left(\mathrm{i}\mathbf{Q}\cdot(\mathbf{r}_i(0) - \mathbf{r}_i(t))\right) \right\rangle . \tag{14}$$

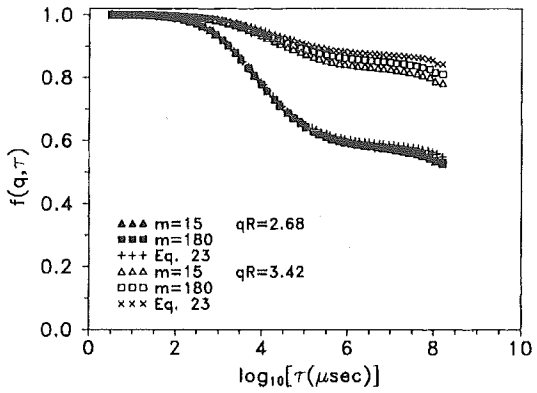


Fig. 4: *Comparison of the mathematical correction formula (12) to obtain quantity* $F(Q,t) = S(Q,t)/S(Q)$ *from DLS experiments on a partially non-ergodic sample with averaged DLS experiments. Crosses and plus signs show the result of the correction formula. Symbols represent averages with different repetition numbers. The filled and open symbols correspond to different* Q *values. From [9].*

Here, only one particle index i occurs. So each particle's position is linked with its own position at a later time but not that of another particle as in (10).
The prefactors in (13) refer to the distribution of scattering lengths of the particles. They depend on size, shape, and refractive index difference with respect to the solvent of a particle. Because of the form factors they are also Q-dependent unless the particles are much smaller than the wavelength of light. It can be seen that if the particles are monodisperse also concerning their optical properties the first prefactor (the variance of scattering lengths) vanishes. In this situation the light scattering is solely coherent. If there is a polydispersity there is in general a mixture of coherent and incoherent scattering. Interestingly, also the situation of pure incoherent scattering can be achieved: Because b may be positive or negative depending on whether the index of refraction of a particle is larger or smaller than that of the solvent the average $\bar{b}$ can be put to zero by a suitable choice of the solvent.

4 Experimental Results

Figure 5 shows cuvettes with suspensions of poly(methyl methacrylate) latex spheres ($\approx$ 200 nm radius) stabilised by a surface coating of poly(12-hydroxy-stearic acid) of about 10 nm thickness. As solvent a mixture of a hydrocarbon (e.g. decalin) with carbon disulfide is used to closely match the refractive index and thus avoid excessive turbidity. The cuvettes are illuminated by white light from behind. One can see different colourful structures in the scattered light. For high as well as low concentrations (right- and leftmost cuvette, respectively) only diffuse scattering is visible. This corresponds to a random distribution of colloid particles in the solvent. For intermediate concentrations multicoloured patches are visible which originate from "crystals", i.e. volumes where the latex spheres assume a regular repetitive structure. Often, these co-exist with amorphous regions.



Fig. 5: *Suspensions of spherical latex particles four hours after randomisation by tumbling. Right to left in the order of increasing concentration:* $\phi_E = 0.48 \ldots 0.64$. *The cuvettes are illuminated by white light from behind. From [10].*

Depending on the concentration the following phenomenology is found:

$\phi_E < 0.49$	liquid-like structure, no tendency of crystallisation
$0.49 < \phi_E < 0.54$	co-existence region liquid-crystal, fast crystallisation, small crystals, homogeneously nucleated
$0.54 < \phi_E < 0.58$	only crystalline phase, fast crystallisation, small crystals, homogeneously nucleated
$0.58 < \phi_E < 0.61$	slow, often only partial crystallisation, large needle-shaped crystals, heterogeneous nucleation
$0.61 < \phi_E$	amorphous structure, only traces of crystals at surface and walls

Up to a concentration $\phi_E \approx 0.58$ this behaviour is what one expects from theoretical considerations and computer simulations on the hard-sphere system[2] [12]. In the concentration range above $0.574 \ldots 0.581$ an obvious change takes place [10]: The crystallisation becomes slower and the crystals have different shape because of the different crystallisation mechanism. This is interpreted as a hindrance of crystallisation due to tight packing of the spheres, a mechanism analogous to the forming of a glass by quenching a molecular liquid to low temperatures.

The same behaviour is visible in the static light scattering patterns, figure 6. Immediately after "randomisation" of the samples, i.e. tumbling the sample cell in order to destroy long-range spatial correlations, all samples show a liquid-like structure factor $S(Q)$ with a broad peak indicating the short-range correlation of the particles. The structure factor agrees reasonably well with that expected from the Percus-Yevick approximation for

[2]Indeed, the effective concentrations ϕ_E given here and in the literature are calculated by assuming that the volume of a latex sphere is such that the crystals start to occur at a volume fraction of 0.494 which is the theoretical hard-sphere value. (This is done because the "volume" of a coated polymer sphere is subject to the definition in how far the coating has to be included.)

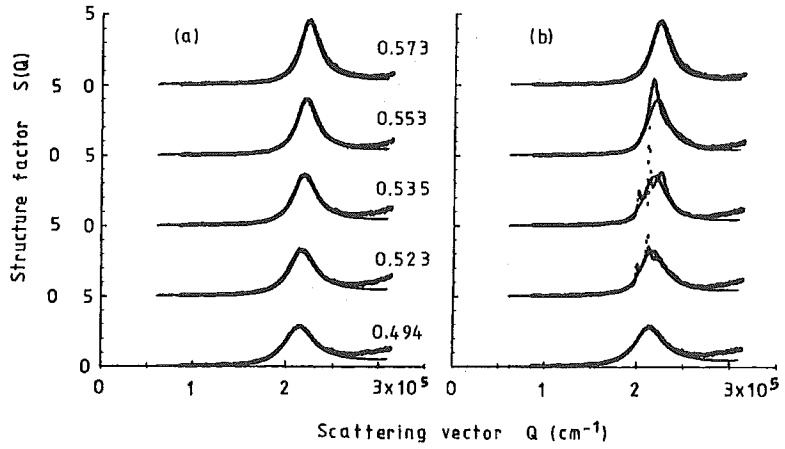


Fig. 6: *Structure factor $S(Q)$ from static light scattering from latex suspensions. The numbers at the curve indicate the effective volume fraction ϕ_E. The continuous curves show the expected $S(Q)$ from the Percus-Yevick theory of hard-sphere liquids. (a) Measurements made immediately after randomisation by tumbling the samples. (b) Measurements made several hours later. From [13].*

hard-spheres [14]. After four hours rest, Bragg peaks arise in the samples of intermediate concentrations while for large and small concentrations the samples remain amorphous. This is the typical behaviour found in molecular glasses, only that the role of temperature is taken by the concentration here. For high temperatures (low concentrations) the liquid phase is thermodynamically stable. For low temperatures (high concentrations) the dynamics are so slow that crystallisation is inhibited and the amorphous phase is kinetically stable, which is called the glassy phase.

In order to explore the dynamics of the colloid particles dynamic light scattering experiments have been done on the same samples. Figure 7 shows some of the results. It can be seen that the curves show an exponential decay in the beginning, as expected from diffusion: $S(Q,t)/S(Q) = \exp(-Q^2Dt)$. Then a slowing down takes places giving rise for a plateau. The plateau becomes longer for higher concentrations and is higher close to the maximum of $S(Q)$. At very high concentration no complete decay of $S(Q,t)$ is visible.

The usual interpretation of these curves is that at short time the particles move freely without hitting their neighbours. This leads to initial decay of correlation obeying the laws of Brownian motion. As soon as the average displacement of the particles reaches the nearest-neighbour distance their motion becomes impeded like they were confined in a cage formed by the neighbour particles. At that stage the correlation does not decay any further (plateau in $S(Q,t)$). The extent of this caging effect increases with concentration. If the concentration is low fluctuations of the particles forming the cage wall create openings from time to time allowing the central particle to escape. In this situation the correlation will decay completely for infinite time. For high concentration this may become impossible so that the plateau in $S(Q,t)$ exceeds to infinite times. This situation would be that of an ideal glass.

The $S(Q,t)/S(Q)$ curves from DLS of figure 7 are very similar to those from neutron

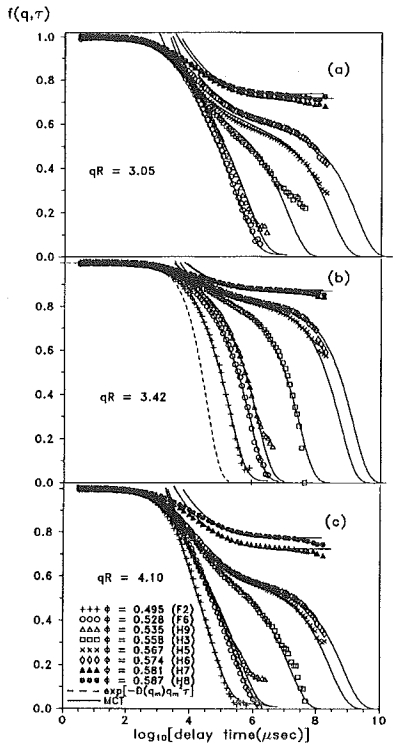


Fig. 7: *Normalised dynamic structure factors $S(Q,t)/S(Q)$ for three scattering vectors Q around the structure factor peak. The solid curves are mode-coupling theory fits to the data. The dashed curve fits the initial exponential decay. From [9].*

scattering on molecular glasses, shown exemplarily in figure 8 for the glass forming salt melt $Ca_{0.6}K_{0.6}(NO_3)_{1.4}$ [15]. Apart from the differences by several orders of magnitude in the length and time scales ($1\,\mathrm{s} \leftrightarrow 1\,\mathrm{ps}$, $200\,\mathrm{nm} \leftrightarrow 0.1\,\mathrm{nm}$) the curves show the same qualitative behaviour with temperature instead of concentration as control parameter.

Qualitatively similar curves are obtained by incoherent light scattering. But for this method the data is more directly interpretable. In the Gaussian approximation the incoherent scattering function is given by

$$S_{\mathrm{inc}}(Q,t) = \exp\left(-Q^2 \left\langle \Delta r^2 \right\rangle /6\right) . \tag{15}$$

This means one can calculate the average mean squared displacement of the colloid particles, see figure 9. Here the three regimes can be seen evidently: For short times $\langle \Delta r^2 \rangle$ increases linearly as expected for Brownian motion. Then there is a plateau at the value corresponding to the distance at which collisions with the neighbour particles take place. Finally, there is an increase of $\langle \Delta r^2 \rangle$ beyond this length which shifts to longer times when the concentration is increased.

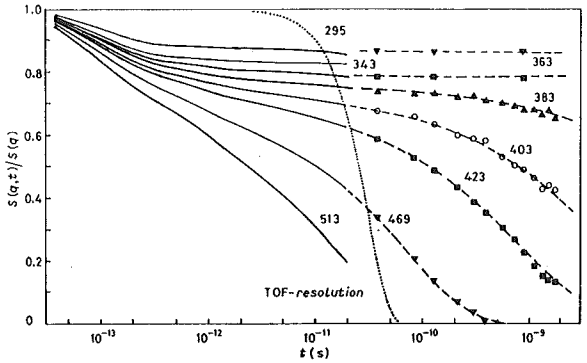


Fig. 8: *Normalised dynamic structure factors* $S(Q,t)/S(Q)$ *of* $Ca_{0.6}K_{0.6}(NO_3)_{1.4}$ *for* $Q = 19\,\mathrm{nm}^{-1}$, *the position of structure factor peak. The solid curves are obtained by Fourier transform from a time-of-flight spectrometer. The individual points at long time are results from neutron spin echo. From [15].*

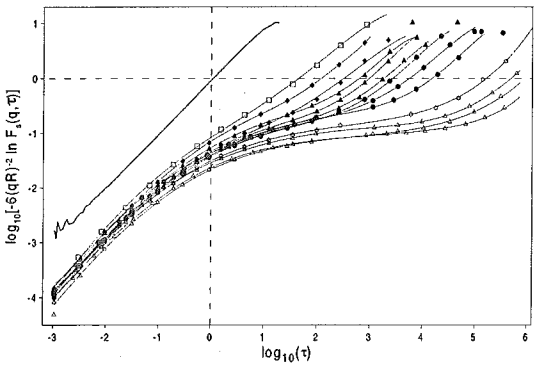


Fig. 9: *Mean squared displacements of latex/silica spheres in the suspensions calculated using the Gaussian approximation (15). The line without symbols corresponds to a very dilute suspension where the particles can diffuse freely. From [2].*

5 Mode Coupling Theory

5.1 Outline of the Theory

The mode coupling theory (MCT) has been developed in the 80s and has since then made a big contribution to the understanding of structural glasses [16]. The central quantity of this theory is the density-density correlation function:

$$\Phi_Q(t) = \frac{\langle \delta\rho_Q^*(t)\delta_Q(0)\rangle}{\langle \delta\rho_Q^*(0)\delta_Q(0)\rangle}. \tag{16}$$

If all particles are identical this quantity is equal to the normalised dynamic structure factor $S(Q,t)/S(Q)$. Therefore, dynamical light scattering experiments should be immediately comparable to the results of the theory.

The main results of MCT are (1) the prediction of a kinetic glass transition, (2) explicit solutions for $\Phi_Q(t)$ for simple systems, e.g. hard spheres, (3) scaling laws, (4) relations between the exponents of scaling laws. It would go beyond the scope of this lecture to derive all results in detail. Only some basic equations and results which are relevant for the interpretation of the data on colloidal glasses will be showed in the following.
The fundamental equations of MCT have a form like

$$\ddot{\Phi} + \gamma\dot{\Phi} + \Omega^2\phi + \Omega^2 \int_0^t M(t-t')\dot{\Phi}(t')\mathrm{d}t' = 0\,. \tag{17}$$

(For a real structural glass forming system the variables Φ and M are also Q dependent and instead of a single equation (17) one has an infinite set. But many fundamental results can already be obtained from this extremely reduced version of the MCT.) The first three terms are those also found in the description of a damped harmonic oscillator. For colloidal systems the second and third term dominate the first, which can be omitted (Brownian motion instead of Newtonian). γ/Ω^2 is a friction coefficient including the viscosity of the solvent and the size of the particles. The additional integral term contains a memory function (passed times $t-t'$ enter through the integration) acting as an additional damping term (time derivative of Φ).
The addition of a memory function in order to describe complex viscoelastic behaviour has already been done before MCT [7]. The crucial step forward by MCT was to relate the memory function itself to the density correlation function. In this simple model this would be done by a polynomial

$$M(t) = \sum_k v_k \Phi^k(t)\,. \tag{18}$$

In the full description of a structural glass also mixed products of $\Phi_Q(t)$ with different Q occur implying that modes of different Q are coupled. The coefficients which then have the form $v_{Q;q_1,q_2...}$ can be calculated from the static structure factor $S(Q)$ alone. For the full as well as the simplified model the equations (17) and (18) form a closed set which can be solved numerically.
The MCT equation systems invariably show two kinds of solutions: (1) For small values of the coupling parameters v_k the solution $\Phi(t)$ decays to zero for long times. As already stated in section 3.1 this corresponds to the liquid state. Therefore, small values of v_k are associated with high temperatures in molecular liquids or small densities in colloids. (2) For high values of v_k a finite value $\Phi(t) = f_Q$ remains, the non-ergodicity parameter. At a certain surface in the space of v_k a discontinuous transition between the two solution types takes place. This is connected with a critical value of the physical control parameter (temperature or density). The distance from the critical value is expressed by a separation parameter $\sigma \propto (T_c - T)/T_c$ or $\sigma \propto (\phi - \phi_c)/\phi_c$, respectively.
Figure 10 shows numerical solutions of (17) with a second order polynomial as (18). The curves show two scaling regimes: The final decay (α relaxation) has always the same shape in the semilogarithmic representation. This implies that by a single scaling time τ_α all curves can be rescaled to a single master curve (time-temperature superposition principle):

$$\Phi_Q(t) = f_Q^c G_Q(t/\tau_\alpha)\,. \tag{19}$$

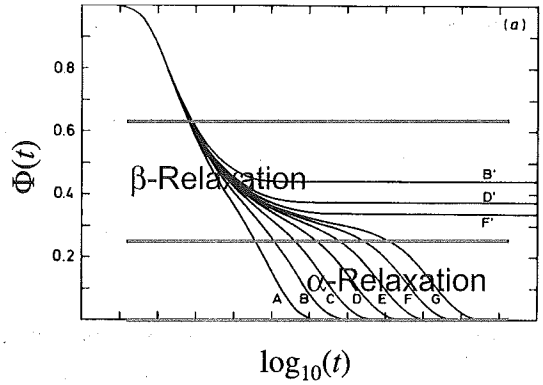


Fig. 10: *Numerical solution of the mode coupling equation (17) with a second order polynomial (18). Curves A... G denote coupling parameters in the liquid range (with decreasing distance to the critical line), B'... F' those in the glass range. For exact parameter values see ref. [17]. The grey lines denote the approximate boundaries of the validity of the scaling laws (19) and (20).*

For shorter times there is another region where scaling is possible using a linear transformation of the ordinate in addition to a scaling time τ_β:

$$\Phi_Q(t) = f_Q^c + |\sigma|^{-1/2} h_Q g_\pm(t/\tau_\beta)\,. \tag{20}$$

It can be seen that the α relaxation expression requires a Q dependent master function G_Q while the β relaxation has only two, g_+ in the glass and g_- in the liquid.
The scaling times depend on the separation from the critical point by power laws

$$\tau_\beta \propto |\sigma|^{-\frac{1}{2a}} \tag{21}$$

$$\tau_\alpha \propto |\sigma|^{-\left(\frac{1}{2a}+\frac{1}{2b}\right)} \tag{22}$$

where a and b can be calculated from the v_k and are universally related by

$$\frac{\Gamma^2(1-a)}{\Gamma(1-2a)} = \frac{\Gamma^2(1+b)}{\Gamma(1+2b)}\,. \tag{23}$$

The exponent parameters a, b and scaling amplitudes f_Q^c, h_Q can be calculated if $S(Q)$ is known. Especially, the Percus-Yevick approximation for hard spheres yields $1/2a = 1.66$ and $1/2a + 1/2b = 2.58$.

5.2 Comparison to Experiments

Figure 11 shows a test of the scaling properties using the DLS data of figure 7. One can see that both scaling laws are reasonably well fulfilled. As predicted by MCT, different curves Q values can be collapsed in the β relaxation region while in α relaxation region each Q needs an individual master function but different concentrations can be scaled together.

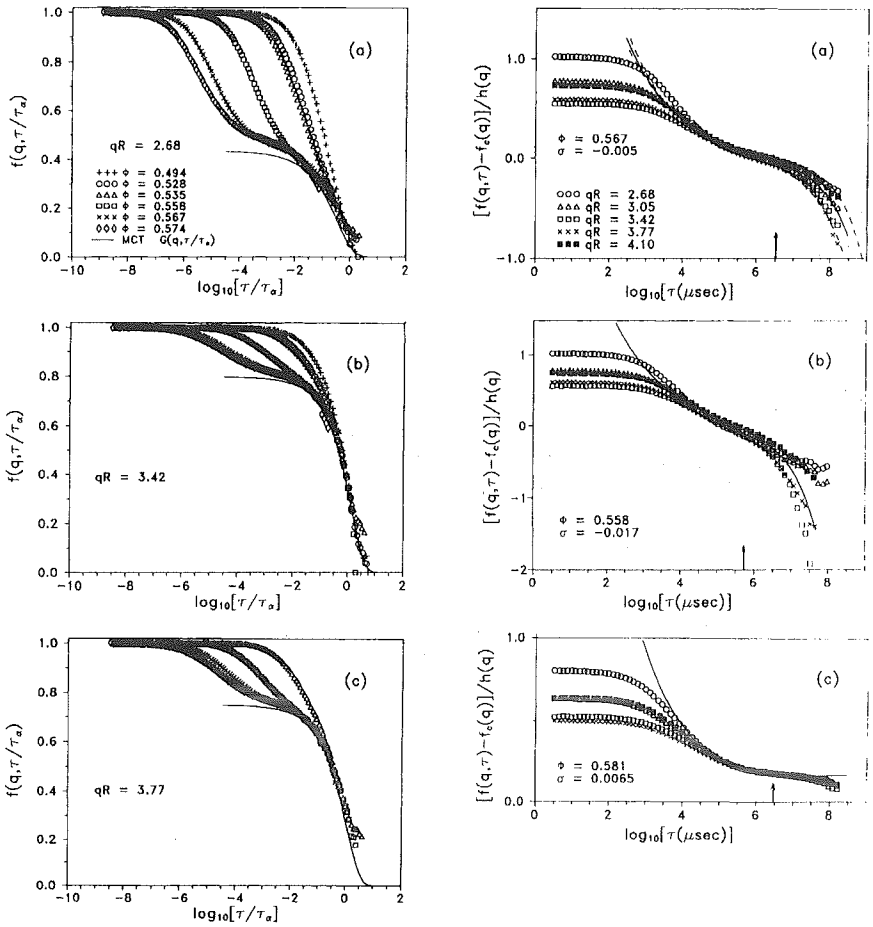


Fig. 11: *Test of the scaling properties of $\Phi_Q(t)$ predicted by MCT. The left column shows the test of the α relaxation scaling 19 of data from different concentrations at identical Q values. The right column shows the β relaxation scaling 20 of curves from different Q. From [9].*

Because there are also other theories predicting e.g. time-temperature superposition it is important that the scaling times used in figure 11 also obey the expected power laws. This is demonstrated in figure 12. The lines in this figure a power laws with the calculated values of the exponents. Thus, they contain no free parameters.

Finally, the scaling of the β relaxation in figure mctt1 yields the parameters f_Q^c and h_Q which, as figure 13 shows, exactly coincide with those calculated from the Percus-Yevick $S(Q)$ for hard spheres.

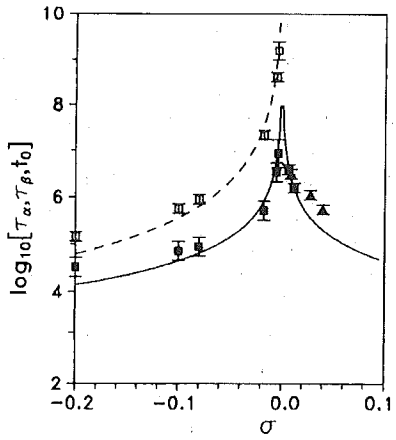


Fig. 12: *Scaling times from DLS data. The empty symbols represent the α relaxation scaling time τ_α, the filled symbols that of the β relaxation τ_β. The dashed and continuous curve show the MCT predictions for α and β relaxation scaling, respectively. From [9].*

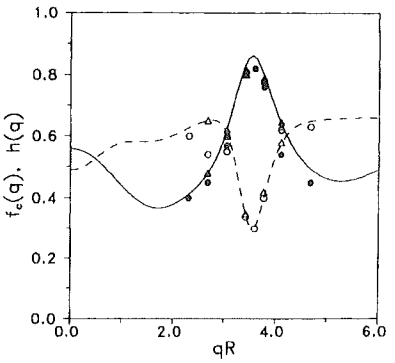


Fig. 13: *β relaxation ordinate scaling parameters of equation (20). The filled and empty symbols represent the values from DLS experiments, the continuous and dashed curves the MCT predictions for f_Q^c and h_Q, respectively. From [9].*

6 Summary

Colloidal Glasses show a transition from a liquid-like phase where particles are able to move freely to a glassy phase where no long-range motion is possible. In this respect, they strongly resemble molecular glasses with the only difference that the temperature is replaced by particle concentration as control parameter. Another difference lies, of course, in the particle dimensions which are of the order 10^{-10} m in molecular glasses but 10^{-7} m for colloidal glasses. This, together with the fact that the dynamics is Brownian and not Newtonian leads to a shift of time scales by many orders of magnitude. This facilitates the study of the microscopic dynamics because length- and time scale for colloidal glasses are appropriate for dynamic light scattering (DLS).
The results from DLS experiments can be straightforwardly interpreted in the framework

of mode coupling theory (MCT). The central predictions of MCT can be confirmed in an impressive way: (1) The α and β relaxation regimes fulfill the required scaling properties. (2) The scaling times obey power laws which contain the exponents calculated from the hard-sphere model. (3) The scaling amplitudes (f_Q^c, h_Q) agree precisely with the prediction from the hard-sphere model in their Q dependence.
This agreement with MCT is much better than what is usually found in the study of molecular glass forming systems by neutron scattering. The main reason is that in colloidal glasses thermally activated "hopping" processes are not important. For molecular glasses, in contrast, these processes often obscure the MCT behaviour close to the critical temperature T_c. This is immediately visible from the fact that the empirical glass temperature is always about 20 % lower than T_c for molecular systems.
In addition to this "ideality", colloidal glasses consist of simple spherical particles with a nearly hard-sphere potential. This makes approximations as Percus-Yevick applicable. From this quantities of the MCT can be calculated. In molecular systems such calculations mostly become impracticable and the same quantities have to be treated as fit parameters.

References

[1] L. Antl, J. W. Goodwin, R. D. Hill, R. H. Ottewill, S. M. Owens, S. Papworth, and J. A. Waters, Coll. Surf. **17**, 67 (1986)

[2] W. van Megen, T. C. Mortensen, S. R. Williams, and J. Müller, Phys. Rev. E **58**, 6073 (1998)

[3] J. Stellbrink, J. Allgaier, and D. Richter, Phys. Rev. E. **56**, R3772 (1997)

[4] E. R. Weeks, J. C. Crocker, A. C. Levitt, A. Schofield, and D. A. Weitz, Science **287**, 627 (2000)

[5] B. Chu, *Laser Light Scattering* (Academic Press, New York, 1974).

[6] H. Z. Cummins, E. R. Pike eds., *Photon Correlation Spectroscopy and Velocimetry* (Plenum Press, New York, 1977).

[7] B. J. Berne, R. Pecora *Dynamic Light Scattering* (Wiley-Interscience, New York, 1976).

[8] R. Pecora, *Dynamic Light Scattering* (Plenum Press, New York, 1985).

[9] W. van Megen, S. M. Underwood, Phys. Rev. E **49**, 4206 (1994).

[10] P. N. Pusey, W. van Megen, Nature **320**, 340 (1986).

[11] W. van Megen, S. M. Underwood, Nature **362**, 616 (1993).

[12] W. G. Hoover, F. H. Ree, J. Chem. Phys. **49**, 3609 (1968).

[13] W. van Megen, P. Pusey, Phys. Rev. A **43**, 5429 (1991).

[14] J. K. Percus, G. J. Yevick, Phys. Rev. **110**, 1 (1958).

[15] W. Knaak, F. Mezei, B. Farago, Europhys. Lett. 7 529 (1988).

[16] W. Götze, *Aspects of Structural Glass Transition* in *Les Houches. Session LI. Liquids, Freezing and the Glass Transition*, eds.: J. P. Hansen, D. Levesque, J. Zinn-Justin (North Holland, Amsterdam, 1991).

[17] W. Götze, L. Sjögren, J. Phys. C: Solid State Phys. **21** 3407 (1988).

C 6 Membrane- and Microemulsion Dynamics

M. Monkenbusch

Institut für Festkörperforschung

Forschungszentrum Jülich GmbH

Contents

1 Introduction 2
- 1.1 Microemulsions . . . 2
- 1.2 Phospholipid bilayers and vesicles . . . 4
- 1.3 Dynamical Fluctuations . . . 4

2 Levels of Modeling 5
- 2.1 Membrane Bending Model . . . 5
- 2.2 Ginzburg-Landau Model . . . 6

3 Membrane Fluctuations 7
- 3.1 Locally planar membrane, Monge gauge . . . 7
- 3.2 Bending Forces and Undulation Amplitudes . . . 8
- 3.3 Membrane Interactions . . . 8
- 3.4 Dynamics of a Free membrane . . . 10
- 3.5 Dynamics on short length scale . . . 12
- 3.6 Scattering Function . . . 14
- 3.7 "Free Membrane" Patch Model: Local Dynamics . . . 15
- 3.8 Experiment on a bicontinuous phase . . . 17

4 Large scale dynamics I 18
- 4.1 Experimental Determination of δ_{st} . . . 21

5 Larger Scale Dynamics II: Ginzburg-Landau Theories 21
- 5.1 Model Properties . . . 22
- 5.2 Scattering Function . . . 23
- 5.3 Time dependent Ginzburg-Landau model . . . 23
- 5.4 Experimental results from NSE and DLS . . . 25

1 Introduction

This chapter is devoted to the dynamical properties of membranes that are formed by self-aggregation of amphiphilic molecules. In particular the relation of interactions and elastic moduli of the membranes to the observable dynamics is considered and discussed in connection with experimental results.

1.1 Microemulsions

Microemulsions consist of two immiscible fluids —usually water and "oil"— and a surfactant consisting of amphiphilic molecules with a hydrophilic and a hydrophobic part [1, 2]. If mixed with the right volume fractions at an appropriate temperature a *microemulsion* forms spontaneously and is in thermodynamical equilibrium. The various microstructures — with typical length scales of the order of 10 nm — exhibit zones of e.g. water separated from "oil" zones by an interface that contains the surfactant molecules . Depending on volume fraction and surfactant properties these zones may be droplets, continuous multiply connected sponge-like, layers etc.. Correspondingly a variety of microemulsion phases will occur (see Fig. 1) depending on composition and external parameters as temperature and pressure [3]. In general the amount of surfactant determines the available interface area. Resulting phases have to accommodate water and "oil" accordingly. In addition the energy needed to bend the interface membranes away from the preferred curvature must stay low and fluctuations must be small enough not to destroy the structure. Preferred, i.e. spontaneous curvatures, may depend on temperature and composition of the surfactant.

The localization of the amphiphilic molecules in the interface such that the hydrophilic parts point into the water domains and the hydrophobic parts into the "oil" domains respectively minimizes the interaction energy. So no enthalpy may be gained by shrinking the interface area. The interface extends until all surfactant is used up [1]. Therefore the membrane has virtually no interface tension and the most important elastic energy contribution is the bending energy (see below). The bending moduli are typically of the order of $1 k_B T$.

As the "oil" in model systems usually a low molecular hydrocarbon $H-(CH_2)_n-H$ with $n \simeq 6 \cdots 12$, i.e. hexane, $\cdots$, dodecane is chosen. As surfactants a wide variety of nonionic and ionic molecules are available. The experimental examples given below are mostly obtained with nonionic surfactants of the type alkyl-polyglycol-ether $H-(CH_2)_n-(CH_2-O-CH_2)_m-H$ in short notation C_nE_m, where the C_n part is hydrophobic and the E_n part is hydrophilic. A prominent member of the ionic variety of surfactants is, e.g. SDS, sodium-dodecyl-sulfate, $Na^- SO_4^- - (CH_2)_{10} - H$ where the Na-ion enters the water domain and SO_4^- is the hydrophilic part. The latter form microemulsions that exhibit additional electrostatic interaction between membranes. Besides pure surfactants also mixtures of surfactants or surfactants plus cosurfactants. e.g. higher alcoholes, or macromolecular analoga of surfactants, e.g. block-copolymers that are analogous to $C_{700}E_{300}$ are used to tune the membrane properties and thereby modify the phase behavior of the microemulsions [4].

With some exceptions most microemulsion systems exhibit structural lengths in the 10 nm regime and need probes with resolution/wavelengths somewhat smaller than visible light.

[1] Here we ignore the small solubility of surfactant molecules in the bulk water or oil phases.

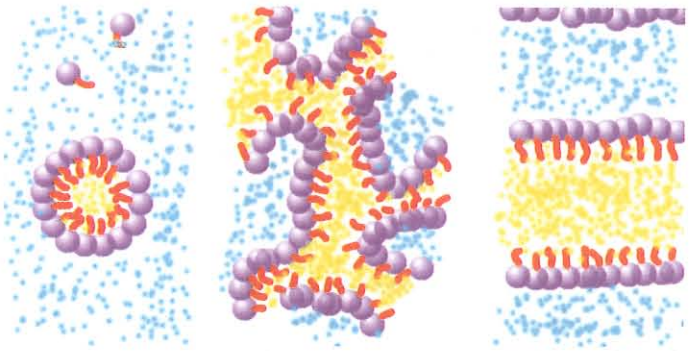


Fig. 1: *Sketch of droplet, bicontinuous and lamellar phases. Blue spheres indicate the hydrophilic and red tails the hydrophobic parts of the surfactant molecules. Note that in addition a large variety of other not shown possible structures exists.*

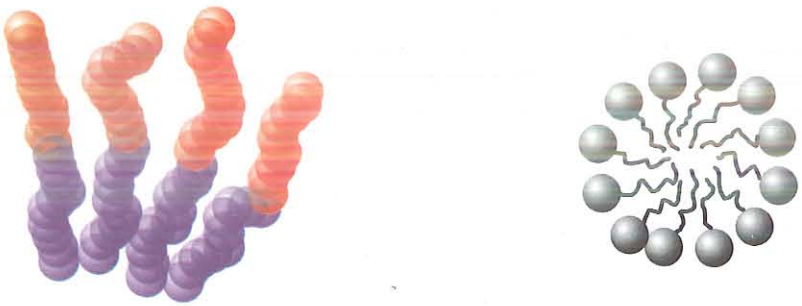


Fig. 2: *Amphiphilic molecules like* C_nE_m *locally in a layer or e.g. SDS as micelle in water.*

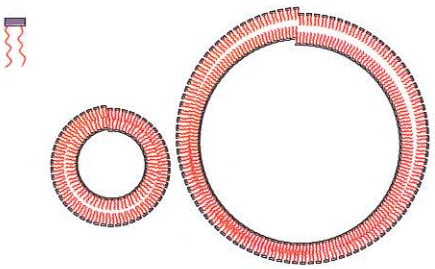


Fig. 3: *Sketch of vesicles composed of a phospholipid with two hydrophobic chains attached to a hydrophilic head. Water is on both sides of the double layered membrane. The size distribution may be broad and depends on preparation.*

Structure may be also investigated with X-rays, however, fluctuation dynamics needs neutron scattering, in particular neutron spin-echo spectroscopy NSE (see Appendix page 25). By use of deuterated water or water and oil the neutron scattering contrast may be set such that only the surfactant layer contributes or that the "oil" versus water contrast dominates. Dynamic properties in the hydrodynamics regime, i.e beyond structural lengths is again accessible by dynamics light scattering, DLS.

1.2 Phospholipid bilayers and vesicles

In biological systems the basic building blocks of membranes are phospholipids which contain a hydrophilic head with two hydrophobic chains attached on one side. In water these molecules aggregate to double layers such that the hydrophobic parts of each single layer are in contact and the both outer sides of the double membrane are hydrophilic. There is no free "oil". In cells the membranes host a large number of membrane proteins that provide specific functionalities like proton pumps, ion channels etc. [5]. In model systems pure phospholipid membranes may be obtained in form of closed *vesicles* with water inside and outside (see Fig. 3). Their size are not controlled by thermodynamics but rather result from the preparation process, e.g. sonification. With typical sizes in the range of several μm and bending moduli $\simeq 10 \cdots 20\, k_B T$ these membranes may be studied by light microscopy [6]. Here dynamics fluctuations may be viewed and analyzed directly using video microscopy and computer image analysis techniques.

1.3 Dynamical Fluctuations

Dynamical fluctuations of membranes are driven in both cases (microemulsions and vesicles) by random fluctuating forces due to the thermal (Brownian) motion of the fluids ("heat bath"). On average any stochastic deviation from equilibrium will relax driven by elastic restoring forces balanced by friction due to viscous flow. Inertial forces are negligible. In the following we will deal with the question of how to describe the resulting relaxations theoretically, connect them to membrane properties, measure them

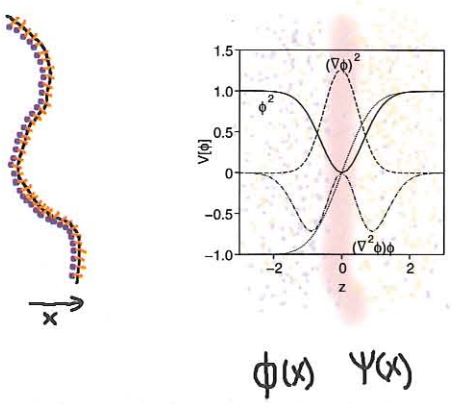


Fig. 4: *Localized membrane with displacement field* $\mathbf{x}$ *versus description in terms of concentration(difference) fields* Φ *and* Ψ.

experimentally and extract physical information from those data.

2 Levels of Modeling

There are two distinct descriptions to model the physics of microemulsions (see Fig. 4):

1. the microemulsion consists of sections containing different fluids (water, "oil") separated by an interface —the membrane— that is described by a curved surface in space. Elastic energy due to the curvature depends on two bending moduli κ and $\overline{\kappa}$.

2. the microemulsion system is described by the difference of concentration of the fluids, $\Phi(\mathbf{r}) = \phi_{water}(\mathbf{r}) - \phi_{oil}(\mathbf{r})$ and eventually a second concentration field $\Psi(\mathbf{r})$ = surfactant density-average. The free energy depends on a functional of these concentration fields.

2.1 Membrane Bending Model

The bending Hamiltonian of a membrane describes the free energy of the microemulsion in terms of an elastic energy that is needed to bend the membrane into the form imposed by the structure of the phase (Helfrich Hamiltonian) [7]

$$E_{el} = \int dS[\frac{\kappa}{2}(C_1 + C_2 - 2C_s)^2 + \overline{\kappa}C_1C_2] \tag{1}$$

where $C_{1,2}$ are the main curvatures. All physical properties of the membrane are lumped into three parameters, C_s the spontaneous curvature, κ the bending modulus and $\overline{\kappa}$ the saddle splay modulus.

$$C_i = \frac{1}{R_i} \tag{2}$$

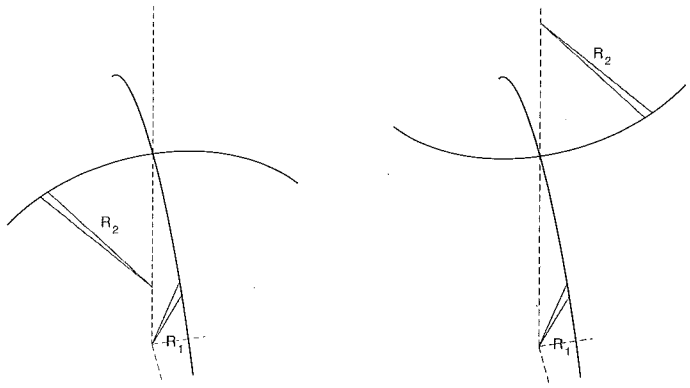


Fig. 5: *Main curvatures during bending (left) and saddle-splay deformation (right). The bending case yields contributions* $\propto \kappa$ *and* $\propto \overline{\kappa}$ *whereas the shown saddle splay provides mainly a contribution* $\propto \overline{\kappa}$ *with negative coefficient and low coefficient for* κ *since* $C_1 \simeq -C_2$.

For a sphere of radius R:

$$E_{el} = 4\pi \frac{\kappa}{2} R^2 (\frac{2}{R} - \frac{2}{R_s})^2 \; + \; 4\pi \, \overline{\kappa} \tag{3}$$

which illustrates the Gauss-Bonnet theorem

$$\begin{aligned} 2\pi\chi_E &= \int dS \; C_1 C_2 \\ \chi_E &= 2 \times (\text{No. of objects} - \text{No. of handles}) \end{aligned} \tag{4}$$

i.e. the energy term proportional to $\overline{\kappa}$ is only relevant if the membrane topology changes. Besides membrane bending the interaction between adjacent membranes contributes to the free energy.

2.2 Ginzburg-Landau Model

Ginzburg-Landau theories are widely used to describe the thermodynamical behavior near critical points including microemulsions [8, 9, 10]. For a complete description in terms of the oil-water **and** the surfactant-surfactant correlation functions, one or two order parameters $\Phi(\mathbf{r})$ and $\Psi(\mathbf{r})$ are introduced. $\Phi(\mathbf{r})$ is the local concentration difference between "oil" and water, $\Psi(\mathbf{r})$ describes the local deviations of the amphiphile concentration from the average concentration $\bar{\Psi}$. The order parameter fields are used to formulate a free-energy functional

$$F\{\phi, \Psi\} = F_0\{\Phi\} + F_1\{\Psi\} + F_{int}\{\Phi, \Psi\} \tag{5}$$

to illustrate the form F_0, the so-called Teubner-Strey free-energy functional is shown here [11, 10]

$$F_0\{\Phi\} = \int d^3r [c(\nabla^2\Phi)^2 + g_0(\nabla\Phi) + \omega_2\Phi^2] \tag{6}$$

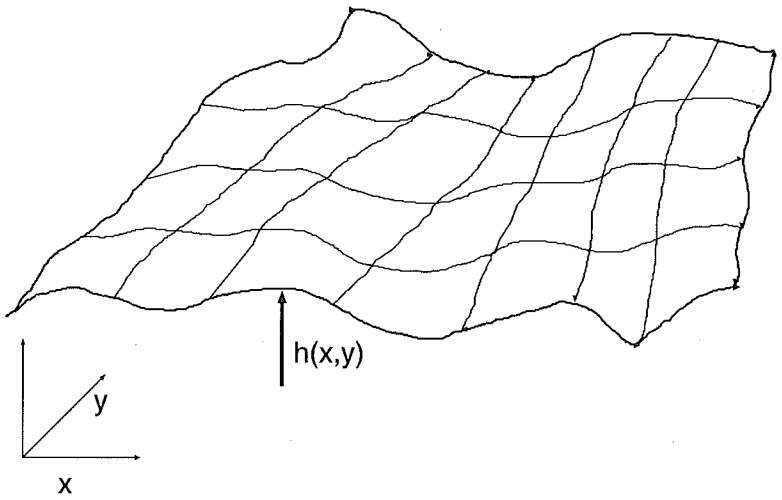


Fig. 6: *Definition of coordinate system for the Monge gauge.*

which is sufficient to describe the form of the scattering intensity of microemulsion —in particular in the bicontinuous phase and at not too large wave vectors— if the contrast water vs. "oil" is employed. We will discuss the form and the resulting scattering in the simplest possible form later. F_1 describes the surfactant molecules, which are solubilized in a homogeneous "oil"- or water-phase and F_{int} the interaction between surfactant and the water-"oil" concentration. Their form is given in Ref [10, 12]. In the following we will only further discuss functionals with one order parameter, Φ.

3 Membrane Fluctuations

3.1 Locally planar membrane, Monge gauge

For a nearly planar membrane the Helfrich-Hamiltonian Eq. (1) may be further simplified. For this purpose a coordinate description as illustrated in Fig. 6 is used. The area of a nearly flat membrane is

$$A = \int dS = \int dx\, dy \sqrt{g(x,y)} \quad > \int dx\, dy \tag{7}$$

which is to lowest order in the displacement amplitude h equal to the projected area $\int dxdy$ since

$$g(x,y) = 1 + [\nabla h(x,u)]^2 = 1 + \mathcal{O}(h^2) \tag{8}$$

To arrive at the bending energy contribution, note that the local bending radius of a function $f(x)$ is given by

$$\frac{1}{R} = \frac{f''(x)}{\sqrt{(1+f'^2)^2}} \tag{9}$$

again to lowest order in f (h) the simple relation $\frac{1}{R} = f''(x)$ holds. For a 2-dimensional plane we may assume that locally the orientation of the coordinate system coincides with the principal axes and $(1/R_x + 1/R_y)^2 = (\partial^2 h/\partial x^2 + \partial^2 h/\partial y^2)^2 = (\nabla^2 h)^2$ which rationalizes the expression for the bending energy contribution to the lowest nonzero order in the undulation amplitude h:

$$\mathcal{H} = \int dx\, dy \left[\frac{\kappa}{2}(\nabla^2 h)^2 + \mathcal{O}(h^4))\right] \tag{10}$$

the spontaneous curvature for a nearly planar membrane without surface tension must be negligible. There is also no contribution $\propto \bar{\kappa}$ because we do not allow for topology changes of the membrane. The simple form of Eq. (10) enables further analytic treatment of the corresponding membrane fluctuations.

3.2 Bending Forces and Undulation Amplitudes

By the thermal stochastic forces the membrane is not flat at equilibrium but fluctuates, i.e exhibits *Brownian motion.* At any time a "random" displacement pattern $h(\mathbf{x})$ is encountered. Assuming the approximations of the Monge representation these undulations may be Fourier transformed to yield a mode representation of $h(\mathbf{x})$.

$$h(\mathbf{x}) = a_k \sin(\mathbf{x} \cdot \mathbf{k}) \tag{11}$$

inserting into the approximate Helfrich Hamiltonian $\mathcal{H}$ yields:

$$\begin{aligned} \mathcal{H}_k &= a_k^2 \int dx\, dy \left[\frac{\kappa}{2}(-k^2 \sin(\mathbf{x} \cdot \mathbf{k}))^2 + \cdots\right] \\ &= a_k^2 \frac{\kappa}{2} k^4 \underbrace{\int dx\, dy \sin^2(\mathbf{x} \cdot \mathbf{q})}_{=A/2} \\ &= a_k^2 (A/2)\ (\kappa/2)\ k^4 \end{aligned} \tag{12}$$

Equipartition attributes $\Delta F = k_B T/2$ per degree of freedom (mode) yields

$$\langle h^2 \rangle = \sum_k \langle a_k^2 \rangle \simeq \int_{k>k_{min}} \frac{d^2k}{(2\pi)^2} \quad \frac{k_b T}{2} \frac{2}{\kappa k^4} \tag{13}$$

conversion of the sum into an integral requires a cutoff at the lower integration limit otherwise the integral would diverge. Physically this corresponds to a finite size of the free membrane which could also be considered as distance between to interaction points (boundaries). As soon as an interaction, e.g. in a lamellar stack of membranes, is considered, the fluctuations are reduced and the "infinite" system becomes stable.

3.3 Membrane Interactions

Here we first insert an argument for the Heflrich membrane interaction which is the dominant repulsive interaction in a stack of non-charged (i.e. nonionic) membranes. It is effected by membrane-membrane collisions due to the fluctuating displacements (undulations). An estimate for the bending elasticity contribution per area is

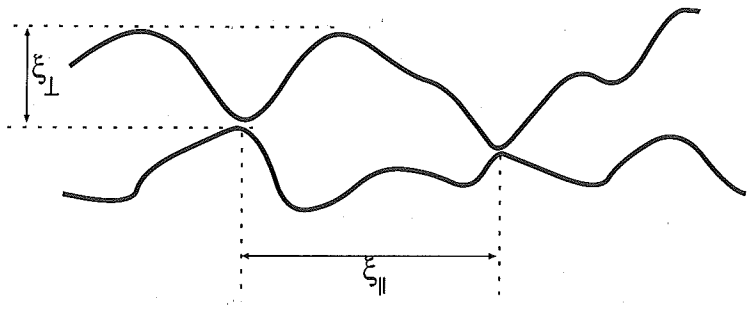


Fig. 7: *Colliding undulating membranes with illustrations of the in plane and out-of-plane correlation lengths $\xi_\parallel$ and $\xi_\perp$.*

$$E_{elast}/A \simeq \kappa(\xi_\perp/\xi_\parallel^2)^2 \tag{14}$$

where $(\xi_\perp/\xi_\parallel^2)^2$ may be considered as coarse grained approximation of $(\nabla^2 h)^2$ in Eq. (10). The entropic contribution results from the reduction of configuration space due to the obstruction at the collision points. In one dimension it is easy to infer that a collision has the effect to map configurations that would cross that point are mapped to their mirror image, i.e. half of the configuration space is lost and $\Delta S = k_B T \ln(2)$. For the membrane an estimated entropy loss of approximately (ignoring factors like the assumed $\ln(2)$) $k_B T$ per collision leads to

$$\Delta S/A \simeq k_B/\xi_\parallel^2 \tag{15}$$

A connection between the layer-layer distance d and the in-plane correlation length $\xi_\parallel$ may be established by the observation that the perpendicular correlation length $\xi_\perp$ must be of the order of d and corresponds to the rms undulation amplitude $\sqrt{\langle h^2 \rangle}$, which depends on $\xi_\parallel$ via the long wavelength cutoff in the summation/integration of contributing bending modes

$$d^2 \simeq \xi_\perp^2 = \langle h^2 \rangle = \int_{q>2\pi/\xi_\parallel} \frac{d^2q}{(2\pi)^2} \frac{k_B T}{\kappa q^4} \simeq \frac{k_B T}{\kappa} \xi_\parallel^2. \tag{16}$$

Combining enthalpic and entropic contributions and equating $\xi_\perp = d$ leads to

$$\frac{\Delta F}{A} = \frac{E_{elast}}{A} - T\frac{\Delta S}{A} \simeq \frac{(k_B T)^2}{\kappa} \xi_\perp^{-2} \simeq \frac{\beta_{\rm st}}{3} \frac{(k_B T)^2}{\kappa} d^{-2} \tag{17}$$

the exact prefactor $\beta_{\rm st}$ requires a more comprehensive and detailed treatment, Helfrich found $\beta_{\rm st} = 0.683$ [7] whereas Monte Carlo [13, 14, 15] and field theoretical calculations yield $\beta_{\rm st} = 0.318$ [16, 17]. Further down we show how the value of $\beta_{\rm st}$ may be inferred from dynamics measurements.

There are other membrane interactions with different range and depended on the electric charges and polarizabilities [18]:

- electrostatic (ionic, no salt) $\Delta F/A \propto \pi(k_B T)^2 \epsilon/4e^2 d$
- electrostatic (screened by salt ions) $\Delta F/A \propto \exp(-d/\lambda_D)$ with λ_D= Debye screening length

- Van der Waals $\Delta F/A \propto -H_{n,m}d^{-4}$ where the Hammacker constants $H_{n,m}$ depend on the difference of the dielectric functions of e.g. membrane (n) and oil (m) [19]
- hydrophobic, short range $\Delta F/A \propto h_0 \exp(-d/\lambda_h)$ with $h_0 \simeq 2 \times 10^{-8}\,\mathrm{J/m^2}$ and $\lambda_h \simeq 0.2\,\mathrm{nm}$ [20]

3.4 Dynamics of a Free membrane

A still simple and solvable model is a patch of a planar free membrane in a viscous fluid. The elastic energy due to bending follows from the mode picture as already explained above

$$\mathcal{H} = \frac{1}{2}\kappa \int d^2r [\nabla_r^2 h(\mathbf{r})]^2 = \frac{1}{2}\kappa \sum_{\mathbf{k}} k^4 h_{\mathbf{k}} h_{-\mathbf{k}} \tag{18}$$

the restoring force per area exerted by the membrane is (see Eq. (26))

$$\kappa\,(\nabla^2)^2 h \tag{19}$$

Equipartition yields the average squared height fluctuation amplitude contributed by each mode

$$\langle h_{\mathbf{k}} h_{-\mathbf{k}} \rangle = \frac{k_\mathrm{B}T}{\kappa k^4} \tag{20}$$

The elastic bending force is balanced by hydrodynamic friction (solvent flow) which may be described by the Navier-Stokes equation for incompressible fluids

$$\begin{aligned} \nabla \cdot \mathbf{u} &= 0 \\ \rho\,\{\partial_t \mathbf{u} + (\mathbf{u}\cdot\nabla)\mathbf{u}\} &= -\nabla p + \eta\nabla^2\mathbf{u} = \nabla\cdot\sigma \end{aligned} \tag{21}$$

with $\mathbf{u}$ = the fluid velocity, η the viscosity and ρ the mass density. For a system with a typical length scale l, the ratio $\rho(\mathbf{u}\cdot\nabla)\mathbf{u}/\eta\nabla^2\mathbf{u}$ is of the order $(\rho u^2/l)/(\eta u/l^2) = \rho u l/\eta = Re$. With typical Reynolds numbers Re in microemulsion systems

$$Re = \frac{\rho u l}{\eta} = \frac{1000\,kg/m^3 \times 0.01\,m/s \times 10^{-8}\,m}{10^{-3}\,Ns/m^2} = 10^{-4} \tag{22}$$

the nonlinear term in $\mathbf{u}$ may be neglected and for observation (and relaxation) times in the nano-second range all inertial forces may be neglected [2]. I.e. the Navier-Stokes equation then become much simpler and linear

$$0 = \nabla \cdot \mathbf{u} \tag{23}$$

$$0 = -\nabla p + \eta\nabla^2\mathbf{u} \tag{24}$$

[2]The typical time for the dissipative loss of kinetic energy of an object may be estimated by considering the time constant of velocity loss of a sphere of density $\rho = 1000\,\mathrm{kg/m^3}$ and radius $R = 5\,\mathrm{nm}$ by flow friction in a medium with the viscosity of water $\eta = 1\,\mathrm{cP} = 0.001\,\mathrm{Nm^{-2}s}$. $m\dot{v} = 6\pi R\eta v$ with $m = 4\pi/3\rho R^3$ yields $v = v_0 \exp(-t/\tau)$ with $\tau = (2/9)\rho R^2/\eta = 5.6 \times 10^{-12}\,s$. This may be compared with the time τ_R the spherical particle needs to diffuse a distance corresponding to its radius. The Einstein-Stokes diffusion coefficient is $D = k_B T/(6\pi\eta R)$ and the time $\tau_R = 570\,\mathrm{ns}$ is given by $R^2 = D\tau_R$ for $T = 300\,\mathrm{K}$.

and by taking the divergence of Eq. (24) and observing Eq. (23)

$$0 = \nabla^2 p. \tag{25}$$

The boundary condition at the surface result from the force (pressure) balance at the membrane. The membrane bending results in a force density f_z by which the membrane acts on the fluid:

$$f_z = \left[\underbrace{\frac{\delta}{\delta h(\mathbf{x})} \int d^2x \frac{\kappa}{2} (\nabla^2 h)^2}_{\kappa(\nabla^2)^2 h} \right] \delta(z - h(\mathbf{x})) \tag{26}$$

for small undulations the force density may be projected onto the surface (nominally at $z = 0$) to balance pressure p and flow friction $\propto \eta \partial_z u_z$ at the surface

$$\sigma_{zz}(z = 0^+) - \sigma_{zz}(z = 0^-) = \kappa(\nabla^2)^2 h \tag{27}$$

where

$$\sigma_{zz} = -p + 2\eta \partial_z u_z \tag{28}$$

is the zz-component of the *fluid stress tensor*. The requirement that the normal velocity of the fluid equals the membrane displacement velocity (impermeable membrane) and the non-slip condition of the parallel component at the membrane yields:

$$\begin{aligned} u_z(z = 0) &= \partial_t h \\ u_\parallel(z = 0) &= 0 \end{aligned} \tag{29}$$

The solution may be obtained by a Fourier Ansatz:

$$\begin{aligned} p(x, z, t) &= f(z)\, e^{ik_\parallel x - \omega t} \\ 0 = \nabla^2 p &= -k_\parallel^2 f(z) + f''(z) \\ \rightarrow \quad f(z) &= A_\pm e^{\mp k_\parallel z} \end{aligned} \tag{30}$$

and with the analogous Ansatz for $u_\perp = u_z$

$$\begin{aligned} u_\perp(x, z, t) &= g(z)\, e^{ik_\parallel x - \omega t} \\ 0 &= [-\nabla p + \eta \nabla^2 \mathbf{u}]_\perp \\ &= -k_\parallel \{\mp A_\mp e^{\mp k_\parallel z}\} - \eta k_\parallel^2 g(z) + \eta g''(z) \\ \rightarrow \quad g(z) &= \frac{1}{4\eta k_\parallel} [(2k_\parallel z \pm 1) A_\pm e^{\mp k_\parallel z} + B_\pm e^{\mp k_\parallel z} \end{aligned} \tag{31}$$

Then $u_\parallel$ follows from $0 = \nabla \mathbf{u}$

$$u_\parallel(x, z, t) = \frac{i}{k_\parallel} \partial_z u_\perp(x, z, t) \tag{32}$$

for both fluid half spaces. Inserting the solutions into the boundary conditions yields the coefficients $A_\pm$ and $B_\pm$:

$$u_\parallel(z = 0) = 0 \rightarrow A_\pm = \pm 4\eta k_\parallel B_\pm \tag{33}$$

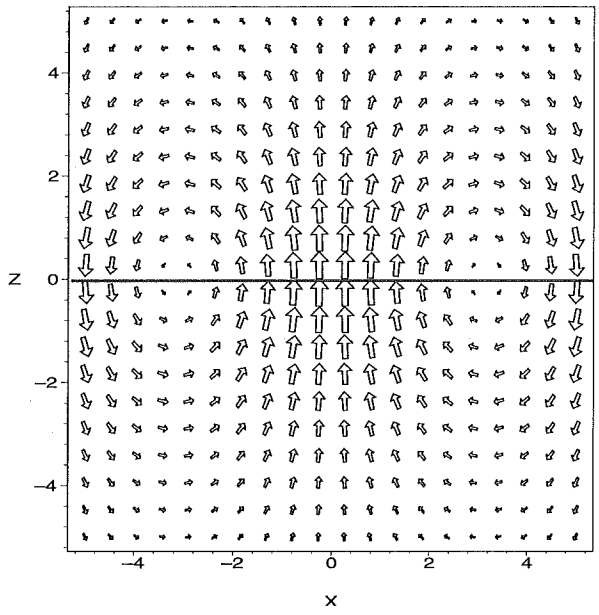


Fig. 8: *Flow pattern as described by the solution Eqn. (30-35).*

$$u_\perp(z=0^+) = u_\perp(z=0^-) \rightarrow A_+ = -A_- \quad , \quad B_+ = B_- \tag{34}$$

$$\begin{aligned} \sigma_{zz}(z=0^+) - \sigma_{zz}(z=0^-) &= 2[-p + 2\eta\partial_z u_z] = \kappa(\nabla^2)^2 h \\ -2\partial_t p + 4\eta\partial_z\partial_t u_z &= \kappa(\nabla^2)^2\partial_t h = \kappa(\nabla^2)^2 u_z(z=0) \end{aligned} \tag{35}$$

Finally inserting of the solutions for p and $\mathbf{u}$ into Eq. (35) results in a condition for the relaxation rate ω:

$$8B\eta k_\parallel \omega = 2B\kappa k_\parallel^4. \tag{36}$$

I.e. the dispersion relation of the relaxations of a free planar membrane with bending elasticity in a viscous fluid is obtained as:

$$\omega = \frac{\kappa k_\parallel^3}{4\eta} \tag{37}$$

The flow pattern computed from the above solution of Eqn. (30-35) is shown in Fig. 8. Observe the fact that its extension is equal to the mode wavelength (as easily read from the factors e^{-k_z} in Eqn. (30 and 31).

3.5 Dynamics on short length scale

The hydrodynamic solution given above allows us to tackle the problem of the dynamics of a membrane (i.e. interface in a microemulsion or vesicle wall) at short length scale. This regime may be found in different phases as long as the specific large scale structures (bicontinuous network, lamellar distance ...) are considerable larger than the spatial

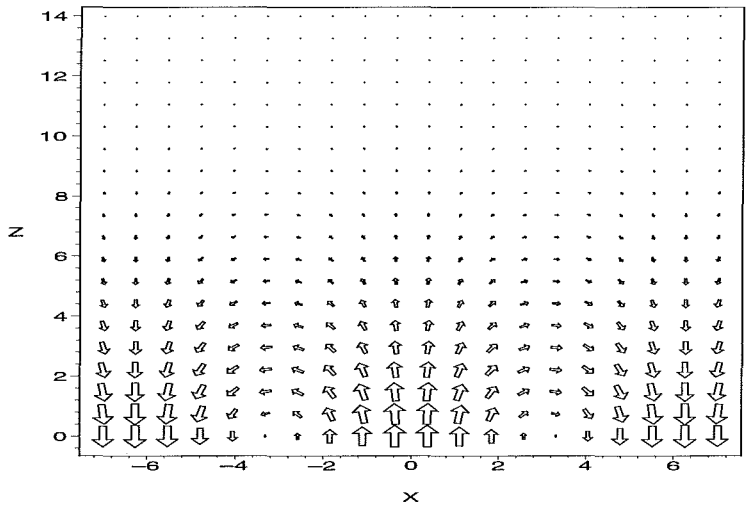


Fig. 9: *The flow pattern decays to negligible strength for distances larger than the undulation mode wavelength.*

resolution at which the membranes are observed. If these details are really negligible the simple approach may even yield "universal" results.
A reason why this may work is contained in the structure of the hydrodynamic solutions: the flow induced by short wavelength undulation extends into the embedding fluids only to a distance corresponding to the mode wavelength as is illustrated in Fig. 9. Consequently the dispersion relation Eq. (37) applies and the the height-height correlation function

$$\langle h_{\mathbf{k}}(t)h_{-\mathbf{k}}(0)\rangle = \frac{k_{\mathrm{B}}T}{\kappa k^4}e^{-\omega(k)t} \tag{38}$$

decays according to that relaxation rate $\omega(k)$. For free membranes with different fluids on both sides the dispersion is

$$\omega(k) = \frac{\kappa k^3}{4\overline{\eta}} = \frac{\kappa k^3}{2(\eta_1+\eta_2)} \tag{39}$$

However, note that the height fluctuation

$$\langle h^2\rangle \simeq \frac{k_B T}{\kappa}\int_{k_{min}} k^{-4}d^2\mathbf{k} \tag{40}$$

would diverge for $k_{min} \to 0$, i.e. for an infinite membrane. In reality the fluctuation stay finite due to the stabilizing effects of the large scale structure in the microemulsion, be it that in a lamellar phase the Helfrich repulsion limits the undulation amplitude or the the structural dimensions of a bicontinuous phase pose a natural limit to the fluctuations etc.. Again the simplest way to account for that is the assumption of a finite size of an undisturbed membrane section and to assume that this sets a limit to the longest undulation mode wavelength. Along these lines Zilman & Granek developed a model of

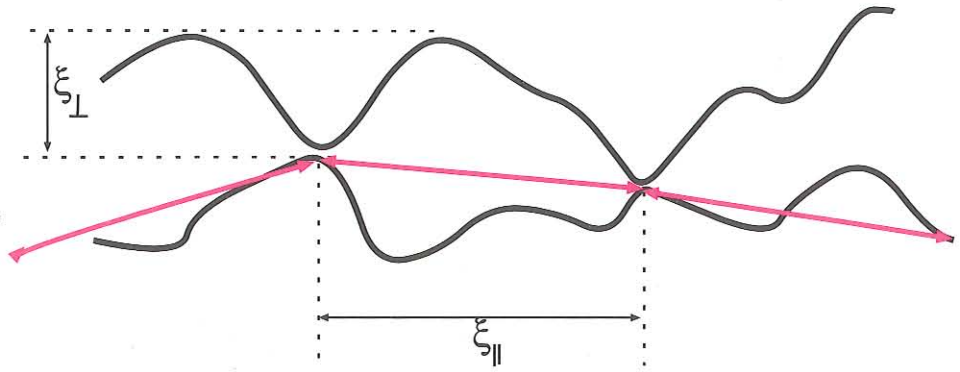


Fig. 10: *The in-plane correlation length determines the average size of independent patches.*

a random ensemble of membrane objects consisting of independent patches which may be applied e.g. to lamellar microemulsions (eventually oriented) or bicontinuous phases (randomly oriented) [21]. The finite patch size translates into a finite lower limit of the k integration in Eq. (40)

$$k_{min} \simeq \frac{\pi}{\xi_\parallel} \tag{41}$$

and is inversely proportional to an in-plane correlation length of the system, see Fig. 10.

3.6 Scattering Function

The method of observation of the membrane fluctuations in the asymptotic "free membrane" regime is scattering of light or neutrons [3]. In general the scattering function is the sum of the amplitudes of the contributions from all scattering centers j, j' (molecules, atoms) with their position-dependent phase

$$S(q, t-t') \propto \left\langle \frac{1}{N} \sum_{j,j'} e^{i\mathbf{q}\cdot(\mathbf{r}_j(t)-\mathbf{r}_{j'}(t'))} \right\rangle \tag{42}$$

the brackets indicate the thermal average. In the case of a planar membrane (in the Monge gauge) the fluctuations consist only of displacements perpendicular to the plane h, we call this direction z. Then

$$S(q,t) = \left\langle \frac{1}{N} \sum_{j,j'} e^{i\mathbf{q}_\parallel\cdot(\mathbf{r}_j-\mathbf{r}'_j)} \; e^{iq_z[h_j(t)-h_{j'}(0)]} \right\rangle \tag{43}$$

and since all fluctuations are described by the $h_j(t)$ the average $\langle \cdots \rangle$ may be restricted to the second exponential factor in Eq. (43). Under the assumption that $h_j(t)$ are Gaussian

[3] Only in the case of vesicles and cell membranes where the object dimensions reach tens of μm direct (video) microscopy in combination with appropriate image analysis is an alternative.

distributed variables the identity $\langle \exp(iu) \rangle = \exp(-\langle u^2 \rangle/2)$ for a Gaussian variable u leads to:

$$S(q,t) = \sum_{j,j'} e^{i\mathbf{q}_\parallel \cdot (\mathbf{r}_j - \mathbf{r}'_j)} \; e^{-q_z^2/2 \langle [h_j(t) - h_{j'}(0)]^2 \rangle} \tag{44}$$

Finally generic membrane dynamics will be observed with a spatial resolution that is better than the structural size but not so high to distinguish individual molecules. Therefore a description of the membrane in terms of a continuous density is adequate. This is achieved by replacing the sums in Eq.(44) by integrals:

$$S(q,t) \propto \langle \int d^2r \int d^2r' e^{i\mathbf{q}_\parallel (\mathbf{r} - \mathbf{r}')} \, e^{-\frac{q_z^2}{2} \langle [h(\mathbf{r},t) - h(\mathbf{r}',0)]^2 \rangle} \rangle_{orientation}. \tag{45}$$

to account for systems with randomly oriented membrane patches an additional angular averaging $\langle \cdots \rangle_{orientation}$ is necessary.

3.7 "Free Membrane" Patch Model: Local Dynamics

The local dynamics of microemulsions which have some large scale structure like bicontinuous or lamellar phases may be approximately treated by considering an ensemble of free membrane patches. A corresponding model has been proposed and worked out first by Zilman & Granek [21]. The model mainly consists in inserting $\langle [h(\mathbf{r},t) - h(\mathbf{r}',0)]^2 \rangle$ appropriate for a free membrane patch into Eq. (45) and perform or approximate the integrations. For that purpose we have to relate $\langle [h(\mathbf{r},t) - h(\mathbf{r}',0)]^2 \rangle$ to the correlation functions:

$$\begin{aligned} \langle [h(\mathbf{r},t) - h(\mathbf{r}',0)]^2 \rangle &= \langle h(\mathbf{r},t) h(\mathbf{r}',t) \rangle - 2\langle h(\mathbf{r},t) h(\mathbf{r}',0) \rangle + \\ &\quad \langle h(\mathbf{r},0) h(\mathbf{r}',0) \rangle \\ &= 2\left[\langle h^2 \rangle - \langle h(\mathbf{r},t) h(\mathbf{r}',0) \rangle \right] \\ &= U(\mathbf{r} - \mathbf{r}', t) \end{aligned} \tag{46}$$

using Eq. (38) in Fourier representation

$$\begin{aligned} U(\mathbf{r} - \mathbf{r}', t) &= \frac{1}{2\pi^2} \frac{k_B T}{\kappa} \int_{k_{\min}} \frac{d^2k}{k^4} [1 - e^{i\mathbf{k}(\mathbf{r} - \mathbf{r}')} \, e^{-\omega(k)t}] \\ &= \frac{1}{2\pi^2} \frac{k_B T}{\kappa} \int_{k_{\min}} \frac{d^2k}{k^4} [1 - e^{i\mathbf{k}(\mathbf{r} - \mathbf{r}')}] \quad + \\ &+ \frac{1}{2\pi^2} \frac{k_B T}{\kappa} \int_{k_{\min}} \frac{d^2k}{k^4} e^{i\mathbf{k}(\mathbf{r} - \mathbf{r}')} [1 - e^{-\omega(k)t}] \\ &= \phi_s(|\, \mathbf{r} - \mathbf{r}' \,|) + \phi_d(|\, \mathbf{r} - \mathbf{r}' \,|, t) \end{aligned} \tag{47}$$

where a separation into a static part $\phi_s(r)$ and a dynamic part $\phi_d(r,t)$ has been achieved With $k_{\min} = \pi/\xi$ the static part $\phi_s(r) \propto r^2 \ln(\xi/r)$, and with $\omega(k) = \kappa k^3/(4\eta)$ and by variable substitution ($u = kr$) it can be seen that the integral for the dynamic part in Eq. (47) has the approximate form:

$$\phi_d(r,t) \simeq \frac{k_B T}{\pi\kappa} r^2 F\left(\frac{\kappa t}{4\eta r^3} \right) \tag{48}$$

with a scaling function $F(x) = x$ for $x \to 0$ and

$$F(x) = \frac{1}{2}\Gamma(\frac{1}{3})\, x^{2/3} - \frac{1}{12}\ln x \; + \cdots \qquad \text{for } x \to \infty \tag{49}$$

then Eq. (48) reads

$$\phi_d(r,t) \simeq \frac{k_B T\,\Gamma(1/3)}{2\pi\kappa}\left(\frac{\kappa}{4\eta}\right)^{2/3} t^{2/3} - \frac{k_B T r^2}{12\pi\kappa}\ln(\frac{\kappa t}{4\eta r^3}) \; + \cdots \tag{50}$$

what implies that

$$U(\mathbf{r}-\mathbf{r}', t \to \infty) \propto t^{2/3} \tag{51}$$

Note also that the leading term of Eq. (50) does not depend on r . Inserting $\phi_s(r)+\phi_d(r,t)$ into Eq. (45) leads after approximate analytical or numerical integration to the desired scattering function. A coarse impression on the general features of the resulting $S(q,t)$ may be gained by combining the features of $\phi_d(r,t)$ as derived above with the structure of Eq. (45). The r-integrations cover the planar patch and as long as $\phi_d(r,t)$ does not depend on r (see Eq. (50)) and ignoring the static part, the dynamic part of $S(q,t)$ is mainly sampled along a "Bragg-rod", e.g. $\mathbf{q}_{\|} \simeq 0$, $q_z \simeq q$ and contributes of $\exp(-q_z^2\phi_d/2) \simeq \exp(-\Gamma q^2 t^{3/2}) = \exp(-[\Gamma q^3 t]^{3/2})$. Of course this is a "hand waving" argument which ,however, explains the general expectation for the type of relaxation function in terms of a stretched exponential. With some more –still approximative– calculation Zilman & Granek arrive for large q and κ at [21]

$$S(q,t) \simeq S(q)\,\exp[-(\Gamma_q t)^{\beta}] \tag{52}$$

i.e. the expected form of a stretched exponential with a stretching exponent $\beta = 2/3$. Note that the k-exponent, 3, in the dispersion relation can be directly related to $2/\beta$. **A direct identification of the experimental wave vector q with the mode wave vector k is not possible** in this high-q regime –even for an oriented sample–. A larger number of different modes contribute to the scattering at any q and consequently a direct measurement of a dispersion relation as Eq. (39) is not possible, only the combined effect on $S(q,t)$ is seen.
The q^3 dependence of the rate factor Γ_q is also as expected by the "hand waving" argument.

$$\Gamma_q = 0.025\gamma_\kappa \left(\frac{k_B T}{\kappa}\right)^{1/2} \frac{k_B T}{\eta}\, q^3 \tag{53}$$

with

$$\gamma_\kappa = 1 - 3\frac{k_B T}{4\pi\kappa}\ln(q\xi) \tag{54}$$

the latter factor results from the approximate treatment and is valid only for large κ it is obvious that it cannot hold for κ-values in the order of $k_B T$.
To get rid of those approximations that are not genuine parts of the model, Eq. (45) may be evaluated numerically, after performing the possible analytic simplifications [22]

$$S(q,t) = \frac{2\pi\xi^2}{a^4}\int_0^1 d\mu \int_0^{r_{\max}=\xi} dr\, r\, \mathrm{J}_0(qr\sqrt{1-\mu^2})\, e^{-k_B T/(2\pi\kappa)q^2\mu^2 \int_{k_{\min}}^{k_{\max}} dk \frac{1-\mathrm{J}_0(\mathrm{kr})\mathrm{e}^{-\omega(\mathrm{k})\mathrm{t}}}{k^3}} \tag{55}$$

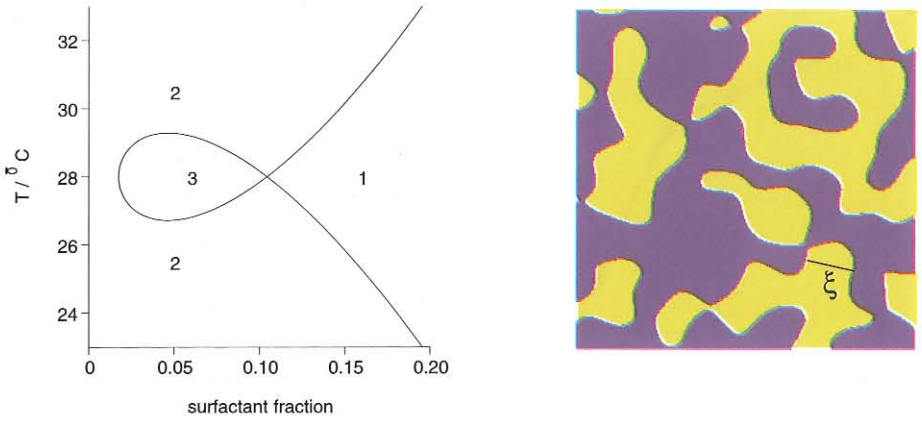


Fig. 11: *Left: Generic phase diagram for the symmetric microemulsion system with a nonionic surfactant ($C_{10}E_4$), the numbers 1,2,3 denote the number of phases present in the corresponding regions. The point where the 3-phase region meets the 1-phase region is called "fish-tail" or optimal point where the minimum amount of surfactant is needed to obtain complete solubilization. Right: sketch of the bicontinuous phase close to "fish-tail" point in the 1-phase region, where the neutron experiments were performed.*

where μ is the cosine of α, the angle between $\mathbf{q}$ and the surface normal, $k_{\max} = \pi/a$ is a physically sound upper integration limit for the membrane mode spectrum, a is the size of a surfactant molecule, $J_0(x)$ denotes the cylindrical Bessel function of order 0.
In the next section we compare experimental results from neutron spin-echo spectroscopy to the above predictions. A short explanation of this important experimental method is given in the Appendix page 25.

3.8 Experiment on a bicontinuous phase

For illustration of a neutron spin echo experiment on a real microemulsion and the applicability of the theoretical concepts, results for a symmetric microemulsion in a bicontinuous phase are presented [22]. Equal amounts of water and oil (decane) were solubilized by the nonionic surfactant $C_{10}E_4$ close to the optimal or "fish-tail" point, see Fig. 11 [23, 4, 12]. The huge difference in scattering length of D and H ($b_H \simeq -b_D/2$) for neutrons allow to apply different contrast situations by selection of the degree of deuteration of the different constituents of the microemulsion. The contrast implied by the coloring of Fig. 11 would be obtained by either using D_2O and normal decane or d-decane and normal water. However, the theoretical $S(q,t)$ as given by Eq. (45) implies visibility of the membrane only. This contrast (film-contrast) is obtained by using D_2O and $d-decane$ with virtually the same scattering length density and a normal (protonated) surfactant $C_{10}E_4$. The latter contrast was used for the NSE experiments that are presented in this section. Figure 12 displays typical results from these NSE experiments. The left picture illustrates the role of NSE as dynamical extension of small angle neutron scattering (SANS) which

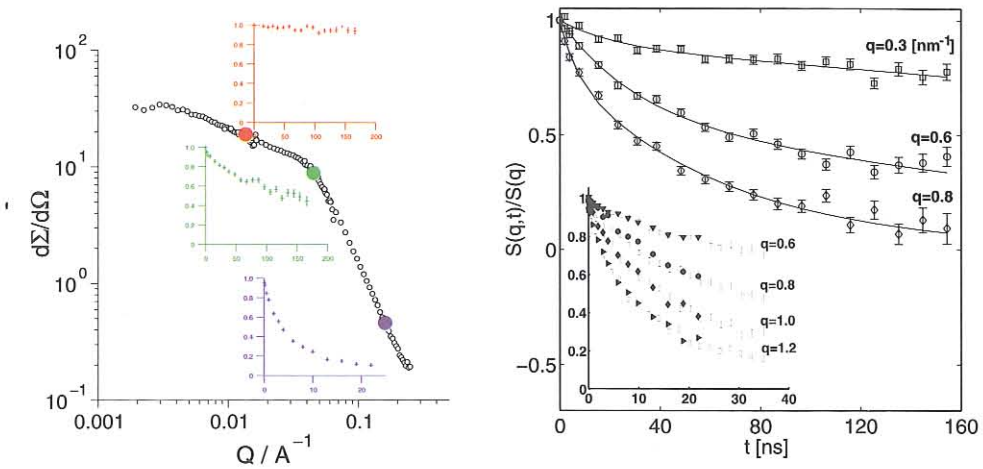


Fig. 12: *SANS and NSE data. Left typical scattering intensity (SANS) from a microemulsion in film-contrast with inserted NSE spectra ($S(q,t)/S(q)$ vs. $t/\,\mathrm{ns}$) at three different q-values. Right: NSE spectra taken at IN15 (long times) [35] and at the FZJ-NSE spectrometer [36, 37] with fitted stretched exponentials[22].*

yields $S(q)$. The right side displays a few typical relaxation curves together with the results from fits to stretched exponentials. Eq. (52) suggests fits with

$$S(q,t)/S(q) = \exp[-(\Gamma(q)t)^{\beta(q)}] \tag{56}$$

where $\beta(q) \simeq 2/3$ and $\Gamma(q) \propto q^3$ is expected. Figure 13 displays the fit results as function of the reduced scattering wave vector $q^* = qd/2\pi$ with d the domain size of the bicontinuous structure which is proportional to ξ. The values for $\Gamma(q)$ are also scaled to yield $\Gamma^*(q) = (\Gamma_q/q^3)\,(\eta_0(T)/k_BT)$ which should be q-independent if the expectation $\Gamma(q) \propto q^3$ is fulfilled. As can be seen the expected value for β is only approached for large q and also Γ^* becomes constant only for $q^* > 4$. Since the theory was made for free membranes this is not unexpected. However, the goal to determine the bending modulus of the surfactant membranes from the obtained values of $\Gamma(q)$ may not be achieved using Eq. (53), which would yield unreasonable values. Better agreement with the expectations for κ from other experiments [12] is achieved by fitting the full expression Eq. (55). The resulting fits are shown in Fig. 14. These fits yield $\kappa \simeq 1.5k_BT$, the results depend on the exact choice of $k_{\min}$ and consistent results are obtained for the canonical choice $k_{\min} = \pi/\xi$.

4 Large scale dynamics I

At larger scale ($q << q^*$) the microemulsions dynamics may be analyzed by dynamical light scattering (DLS). In the thus accessible q-range the typical structure sizes of microemulsions are in most cases not resolvable [4]. In this "hydrodynamic" regime one may

[4] In a few exceptions it is possible to dilute microemulsions such that the structures d are comparable with the wavelength of visible light and interference effects may be observed [24].

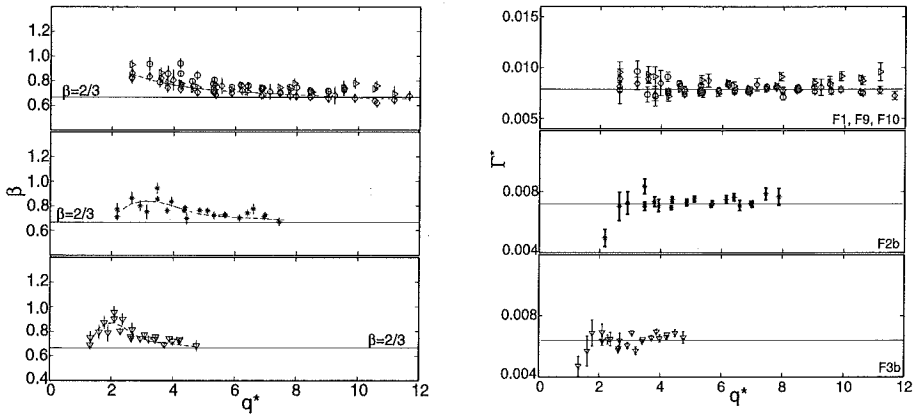


Fig. 13: *Fit results for $\beta(q^*)$ and $\Gamma^*(q^*)$, different symbols indicate presence of a polymeric cosurfactant. The different frames correspond to different surfactant concentrations between 0.075 (top) to 0.17 (bottom)[22].*

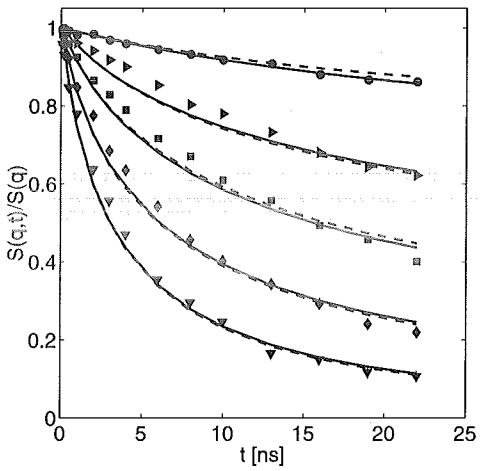


Fig. 14: *Numerical fits to Eq. (55) to NSE data from a symmetric oil-water-$C_{10}E_4$ microemulsion Different curves correspond to different scattering wave numbers $0.5 \leq q/\mathrm{nm}^{-1} \leq 1.6$ Solid lines correspond to individual fits for each scattering vector whereas dashed lines stem from a simultaneous fit [22].*

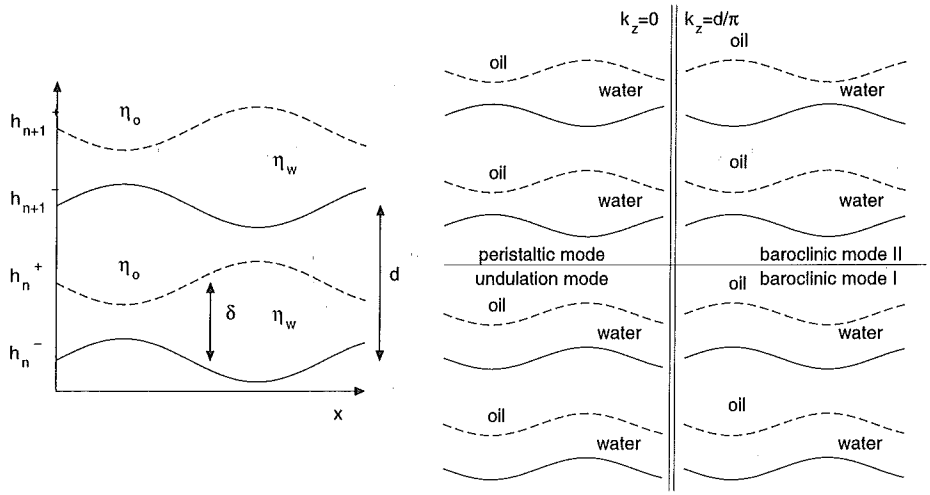


Fig. 15: *Left: Oil-membrane-water-membrane-oil-membrane system, the indices: w=water and o=oil. The repeat distance may be varied by the relative amount of added oil. Right: different modes.*

identify the scattering vector with the mode wave vector $\mathbf{k}$. In the present section the case of an oriented lamellar microemulsion phase will serve as example, in that case

$$\mathbf{q} = [\mathbf{k}_\parallel, k_z] \tag{57}$$

where $\mathbf{k}_\parallel$ is the in-membrane mode vector. Membrane-membrane interactions and hydrodynamic couplings in a membrane stack modify the asymptotic dispersion Eq. (37) at lower values k. The perpendicular component k_z is meaningful only for $k_z < \pi/d$ and describes the relative phase of membrane modes in adjacent layers. Whereas the solution for a stack of membranes is based on the relations given in section 3.5 the expression become lengthy, more details may be found in Refs. [26, 25]. Here we discuss results from [25] that are derived for a system of double layers of surfactant (SDS with pentanol as cosurfactant) containing water that are separated by oil (see Fig. 15). The results are then compared to light scattering (DLS) results on a oil dilution series on this type of microemulsion [27]. Figure 15 (right side) displays the different mode patterns in the long-wavelength limit. At $k_z \simeq 0$ the two membranes in the repeat unit give rise to two modes: the *undulation mode* and the *peristaltic mode*. At $k_z \simeq d/\pi$ analogous to the optical modes in a crystal two further modes: *baroclinic I* and *II* are encountered. The relaxation frequencies of these modes can be extracted from the limiting behavior of the two dispersion branches $\omega_{1,2}(\mathbf{k}_\parallel, k_z)$ for small $k_\parallel$ and either $k_z = 0$ or $k_z = d/\pi$ [25]

- undulation

$$\omega_1(k_\parallel) = \frac{2\kappa}{\eta_w\delta + \eta_o(d-\delta)} k_\parallel^2 \tag{58}$$

- peristaltic

$$\omega_2(k_\parallel) = \frac{1}{12} \frac{\delta^3(d-\delta)^3[V_w(\delta) + V_o(d-\delta)]}{\eta_w(d-\delta)^3 + \eta_o\delta^3} k_\parallel^2 \tag{59}$$

- baroclinic I

$$\omega_1(k_\parallel) = \frac{V_w(\delta)\delta^3}{12\eta_w} k_\parallel^2 \tag{60}$$

- baroclinic II

$$\omega_2(k_\parallel) = \frac{V_o(d-\delta)(d-\delta)^3}{12\eta_o} k_\parallel^2 \tag{61}$$

where $\eta_{w,o}$ are the viscosities of water and oil, d the repeat distance, $V_{w,o}(d)$ the interaction/area force constants ($V(d) = \partial^2[\Delta F_{\text{interaction}}]/A \ /\partial d^2$) through the water or oil layer respectively. Where here the Helfrich interaction $V_{\text{st}} = \beta_{\text{st}}(k_BT)^2/(\kappa d^4)$ and the electrostatic interaction for low salt concentration $V_{\text{el}} = \pi(k_BT)/(4\lambda_B d^3)$ with the Bjerrum length $\lambda_B = e^2/(\epsilon k_BT)$ are relevant. Eqn. (58-61) immediately show that the long-wavelength dispersion is diffusion-like, i.e. $\propto k^2$, the transition to the free membrane dispersion $\propto k^3$ happens around $k_\parallel q \simeq 10$ [25]. The expressions Eqn. (58-61) depend on the layer-layer interactions corresponding to the amount of layer-distance variation effected by the modes. For the undulation all layer distances stay the same, consequently Eq. (58) does neither contain V_o nor V_w. The peristaltic mode changes distances in both fluids so that the sum of both interactions occurs in Eq. (59). Finally it is easy to see that the two baroclinic modes depend on one of the interactions each. Further it may be noted that for $\eta_w \simeq \eta_o$ and $\delta << d$ the undulation relaxation is inversely proportional to d and inserting the expression for the Helfrich interaction the baroclinic II mode relaxes inversely proportional to $d - \delta$. If the water layer is small $\delta << d$ the system may be considered to be a stack of bilayers that perform undulations and baroclinic mode II fluctuations.

4.1 Experimental Determination of δ_{st}

Nallet et al. performed light scattering (DLS) at oriented samples, the oil layer thickness could be varied between $d = 11\,\text{nm}$ and $34\,\text{nm}$ [27]. By different polarization dependence of the scattering from these modes undulation and baroclinic modes can be discriminated. For both modes and all oil-dilutions the q^2-dependence of the mode dispersions $\omega_{u,b}$ (Eqn. (58,61)) are corroborated and effective diffusion coefficients $D_u(d)$ and $D_b(d)$ are obtained. The found dependence of $1/D_{u,b}(d)$ on d is linear starting with some offset ($\simeq 5\,\text{nm}$) due to the influence of a finite δ. From these slopes Eq. (58 and 61) allow to extract κ, since the baroclinic mode relaxation also depends on the value of β_{st} for the steric (Helfrich) interaction a combination of both results will not only yield κ but also β_{st}. Indeed it is not possible to get a consistent description with the original value of $\beta_{\text{st}} = 0.683$ from Helfrich but only the field-theoretical (and Monte-Carlo) value of $\beta_{\text{st}} = 0.318$ yields consistent κ values of 0.38 ± 0.04 and $0.49 \pm 0.03\,k_BT$ respectively.

5 Larger Scale Dynamics II: Ginzburg-Landau Theories

In the low q-regime, covering the gap between light scattering and NSE –somewhat less than one decade– until the low-q region accessible to NSE, Ginzburg-Landau theories and their dynamic extension can be applied (see Ref.[28]).

5.1 Model Properties

The Ginzburg-Landau model describe the configuration of a systems in terms of a field of one (or several) *order parameter(s)*, $\Phi(\mathbf{r})$. For an oil-water mixture this order parameter may be

$$\Phi(\mathbf{r}) = \phi_{\text{oil}}(\mathbf{r}) - \phi_{\text{water}}(\mathbf{r}) \tag{62}$$

the difference between oil and water concentrations $\phi_{\text{oil, water}}$. Then at the interface there must be a plane where $\Phi(\mathbf{r}) = 0$. To determine the configuration of the system a functional $\mathcal{F}[\Phi(\mathbf{r})]$ is needed which yields the probability $\exp(-\mathcal{F}[\Phi(\mathbf{r})])$ of a configuration $\Phi(\mathbf{r})$ in thermal equilibrium. To determine the form of $\mathcal{F}$, symmetry consideration and general conditions on the resulting equilibrium structures can be used. Also a translation of microscopic models into this framework is possible [12]. For a mixture as e.g. oil-water a simple form for $\mathcal{F}$ is used:

$$\mathcal{F} = \int d^3r[g_0(\nabla\Phi)^2 + f(\Phi)] \tag{63}$$

Below the critical point where two fluid phases coexist $f(\Phi)$ must be a function with two (symmetric) minima each of which describes one of the coexisting phases. Since

$$\sigma_{\text{ow}} = 2g_0 \int dz \left(\frac{d\overline{\Phi}(z)}{dz}\right)^2 \tag{64}$$

describes the surface tension of the interface between the coexisting phases, a $g_0 > 0$ suppresses interfaces and yields homogeneous phases. $\overline{\Phi}(z)$ is the concentration profile across the interface that minimizes $\mathcal{F}$. The model Eq. (63) is well established for the description of mixtures close to the critical point [29, 30].

One might attempt to modify this functional such that it describes a microemulsion by only modifying $f(\Phi)$ in a way that it has an additional (3rd) minimum at $\Phi = 0$ which could favor an oil-water interface. The not explicitly occurring amphiphile would concentrate in this interface and cover it homogeneously. However this approach fails because it cannot reproduce the observed scattering intensity with peaks at $q \neq 0$. In Gaussian approximation (see below) $S(q) = 1/(g_0q^2 + f'')$ is a Lorentzian function with only one maximum at $q = 0$. In addition is the surface tension Eq.(64) always positive. A vanishing surface tension required for the formation of a microemulsion would require $g_0 \leq 0$ which is impossible due to stability requirements.

Only the inclusion of further derivations provides a functional that allows a solution with properties that correspond to a microemulsion [31]

$$\mathcal{F} = \int d^3\mathbf{r}[c(\nabla^2\Phi)^2 + g(\Phi)(\nabla\Phi)^2 + f(\Phi)] \tag{65}$$

with $c > 0$ and $g(\Phi)$ a function whose shape depends on the average surfactant concentration (which is not a order-parameter component here). For sufficient surfactant concentration $g(\Phi)$ has a minimum at $\Phi = 0$ with $g(0) < 0$.

5.2 Scattering Function

From Eq. (65) the scattering function is obtained as follows. The scattering function $S(q) = \int d^3r \exp[i\mathbf{q}\cdot\mathbf{r}]G(\mathbf{r})$ is the Fourier transform of

$$G(\mathbf{r}-\mathbf{r}') = \langle\Phi(\mathbf{r})\Phi(\mathbf{r}')\rangle = \frac{1}{Z_0}\frac{\delta^2 Z\{H\}}{\delta H(\mathbf{r})\delta H(\mathbf{r}')}|_{H=0} \tag{66}$$

where the sum of states is written as functional integral of the Boltzmann factor

$$Z\{H\} = \int \mathcal{D}\Phi\; e^{-\mathcal{F}[\Phi]+\int d^3\mathrm{r}H(\mathbf{r})\Phi(\mathbf{r})} \tag{67}$$

where an additional term containing the auxiliary field H has been added to $\mathcal{F}$. A direct and exact evaluation of Eq. (66) is only possible if $\mathcal{F}[\Phi]$ has the quadratic form (in Fourier representation):

$$\mathcal{F} = \int d^3q\; w(q)\; \Phi(\mathbf{q})\Phi(-\mathbf{q}) \tag{68}$$

in that case (see Appendix page 28):

$$S(q) = \frac{1}{2w(q)} \tag{69}$$

Writing Eq. (65) in terms of $\Phi(\mathbf{q})$ leads to $w(q) = 2cq^4 + 2g(0)q^2 + f''(0)$ and consequently

$$S(q) = \frac{1}{2cq^4 + 2g(0)q^2 + f''(0)} \tag{70}$$

which is known as Teubner-Strey scattering function [11]. It successfully describes the low-q scattering intensity of bicontinuous phases, see Fig. 16. The coefficients are related to the characteristic length scales of the microemulsion: $f''(0)/(2c) = [(2\pi/d)^2 + 1/\xi^2]^2$ and $g(0)/c = -2[(2\pi/d)^2 - 1/\xi^2]$. Fourier transform of Eq. (70) yields the real space correlation function, revealing the role of ξ and d:

$$G(r) \propto e^{-r/\xi}\,\frac{\sin(2\pi r/d)}{2\pi r/d} \tag{71}$$

as correlation length (ξ) and domain size (d).

5.3 Time dependent Ginzburg-Landau model

To describe the dynamics in the framework of this Ginzburg-Landau model it is necessary to consider the time-dependence of the order parameter. $\Phi(\mathbf{r},t)$ fluctuates in time around the equilibrium value due to randomly fluctuating forces representing the effect of the heat bath. Since the mass must be conserved, a continuity equation for the order parameter holds:

$$\partial_t\Phi = -\nabla\cdot\mathbf{j} \tag{72}$$

The current $\mathbf{j}$ is driven by gradients of the chemical potential μ:

$$\mathbf{j} = -\Gamma_\Phi\,\nabla\mu_\Phi \tag{73}$$

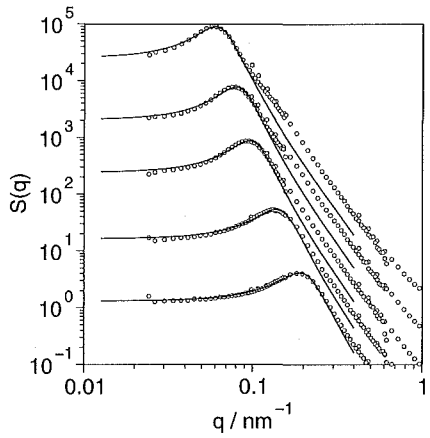


Fig. 16: *Scattering from bicontinuous microemulsions with different amounts of surfactant [12] starting from 0.045 (uppermost curve) and ending at 0.133 (lowest curve). The curves have been shifted by factors of 5 for better visibility. The solid lines are fits to the Teubner-Strey form Eq. (70). As is seen the description is good for low q up to the region just beyond the peak. For larger q deviations occur. Note the shift of the peak at about $2\pi/d$ as a function of surfactant concentration.*

with

$$\mu_\Phi = \frac{\delta \mathcal{F}}{\delta \Phi(\mathbf{r})} \tag{74}$$

In equilibrium dynamics fluctuations are maintained by random forces due to thermal motions in the environment that always create some deviations from the equilibrium density $\Phi(\mathrm{r})$ that relax according to Eqn. (72,74). To introduce this ongoing Brownian motion into the equations of motions a driving stochastic force $\zeta(\mathbf{r}, t)$ has to be added to the effect of $\nabla\mu_\Phi$. For simplicity it is assumed that the stochastic force corresponds to an uncorrelated white noise:

$$\begin{aligned} \langle \zeta(\mathbf{r}, t) \rangle &= 0 \\ \langle \zeta(\mathbf{r}, t)\zeta(\mathbf{r}', t') \rangle &= -2\Gamma_\Phi \nabla^2 \delta(\mathbf{r} - \mathbf{r}')\delta(t - t') \end{aligned} \tag{75}$$

i.e. in Fourier representation

$$\langle \zeta(\mathbf{q}, \omega)\zeta(\mathbf{q}', \omega') \rangle = -2\Gamma_\Phi q^2 \delta(\mathbf{q} + \mathbf{q}')\delta(\omega + \omega') \tag{76}$$

the prefactor and the definition of the latter correlator ensures that the system neither cools down or heats upon continuous action of the stochastic force. Combination of Eqn. (72-74) and adding the stochastic force leads to the *Langevin Equation*

$$\partial_t \Phi = \Gamma_\Phi \nabla^2 \frac{\delta \mathcal{F}}{\delta \Phi} + \zeta. \tag{77}$$

To solve Eq. (77) it is advantageous to transform it to Fourier representation:

$$-i\omega\Phi(\mathbf{q},\omega) = -\Gamma_\Phi\, q^2 \frac{\delta\mathcal{F}}{\delta\Phi(\mathbf{q})}\,\Phi(\mathbf{q},\omega) + \zeta(\mathbf{q},\omega) \tag{78}$$

and using Eq. (68):

$$\frac{\delta\mathcal{F}}{\delta\Phi(\mathbf{q})}\,\Phi(\mathbf{q},\omega) = 2w(q)\Phi(\mathbf{q},\omega) \tag{79}$$

with that and $S(q) = 1/[2w(q)]$ the *Langevin equation* becomes:

$$\zeta(\mathbf{q},\omega) = [-i\omega + \Gamma_\Phi\, q^2\; S(q)^{-1}]\Phi(\mathbf{q},\omega) \tag{80}$$

which may be inserted into Eq. (76) to yield:

$$S(\mathbf{q},\omega) = \langle\Phi(\mathbf{q},\omega)\Phi(-\mathbf{q},-\omega)\rangle = \frac{2\Gamma_\Phi q^2}{\omega^2 + [\Gamma_\Phi q^2/S(q)]^2} \tag{81}$$

back transformation to $S(q,t)$ then results in a simple exponential relaxation with a q-dependent rate Γ_q

$$S(q,t) = S(q)\exp[-\underbrace{\Gamma_\Phi q^2/S(q)}_{=\Gamma_q}\, t] \tag{82}$$

this may be cast into an effective diffusion constant

$$D_{\text{eff}} = \Gamma_q/q^2 = \frac{\Gamma_\Phi}{S(q)} = \frac{D_0}{S(q)}. \tag{83}$$

5.4 Experimental results from NSE and DLS

Eq. (83) indicates that these complex structured fluid exhibit a modulation of the simple diffusive behavior of an unstructured mixture with the inverse structure function $S(q)$. If $S(q)$ has a peak the corresponding slowing down is also called deGennes narrowing. Indeed this effect can be observed by NSE spectroscopy at lower q for the microemulsions discussed above, see Fig. 17. As can be seen there is an gap of a little less than one order of magnitude in q between neutron and light scattering. Nevertheless it is clearly discernible that $D_{\text{eff}}(q)$ nicely interpolates between the dynamic light scattering (DLS) and the neutron spin-echo (NSE) results and has a mimimum where $S(q)$ has its peak. More comprehensive treatments can be found in Ref. [32] and including hydrodynamic coupling in Ref. [33] yield qualitatively similar results.

Appendices

Neutron-spin-echo technique

In a neutron scattering experiment primarily the double differential cross section is measured

$$\frac{d^2\sigma}{d\Omega dE'} = N\frac{k'}{k}b^2 S(\mathbf{q},\omega) \tag{84}$$

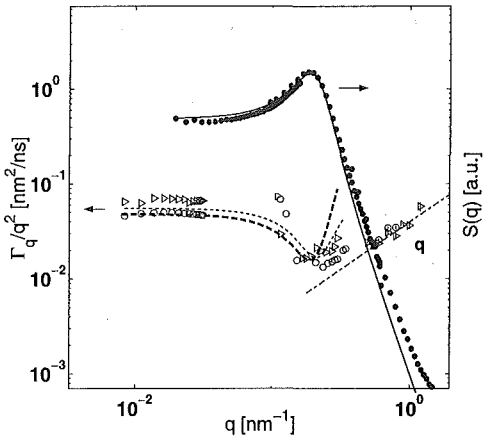


Fig. 17: *Effective diffusion coefficient* $D_{\text{eff}} = \Gamma_q/q^2$ *versus* q *for* $C_{10}E_4$+PEP_{10}-PEO_{10} *microemulsion in bulk contrast: without polymer:* B1 – (○), *and with polymer* B2 – (▷) *[22].*

where k', k are the lengths of the wave vectors of the scattered (k') or of the incoming neutrons respectively. N is the number of atoms (scatterers) in the sample and b is their *scattering length*. The energy transfer during the scattering process is $\hbar\omega = (E - E')$, where E, E' are the energies of the incoming and scattered neutrons. $S(q,\omega)$ is related to $S(q,t)$ by a Fourier transform in the time domain. The momentum transfer (that is a measure for the size of the probe spatial structures) is $\mathbf{q} = \mathbf{k} - \mathbf{k}'$ and the energy transfer is

$$\hbar\omega = (\hbar^2/2m_n)(k^2 - k'^2) \tag{85}$$

where m_n is the mass of the neutron. k, E and the wavelength λ of the neutrons depend on the neutron velocity v and are related by

$$\mathbf{v}m_n = \hbar\mathbf{k} \tag{86}$$

$$\frac{2\pi}{\lambda} = k \tag{87}$$

$$E = \frac{m_n}{2}v^2 \tag{88}$$

therefore the energy transfer may be determined by a measurement of the velocity difference of neutrons before and after scattering.

The comparatively slow relaxation dynamics of floppy membranes –and other relaxations in so-called "soft-matter" problems– requires the ability to detect extremely small neutron velocity differences ($\Delta v/v \simeq 10^{-4\cdots-5}$). A selection of such a narrow velocity band from the Maxwellian type spectrum of a neutron source would lead to extremely low intensities. There is, however, a trick that enables detection of these tiny differences even if a neutron beam with $\Delta v/v \simeq 0.1$ is used, which has sufficient intensity. The neutron spin-echo

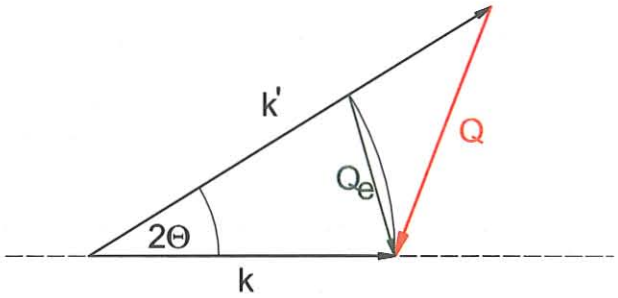


Fig. 18: *Scattering triangle. For high resolution NSE experiments $k \simeq k'$ and $q \simeq Q_e$.*

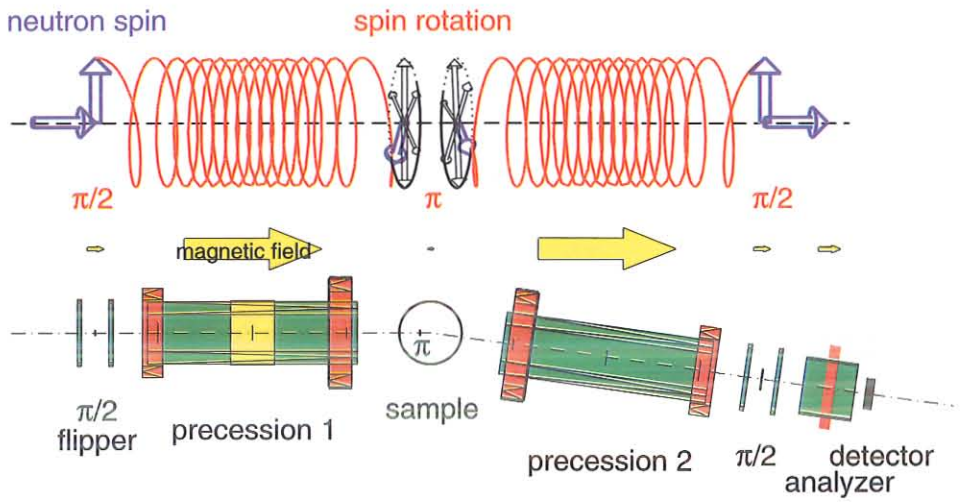


Fig. 19: *Spin history and schematics of an NSE spectrometer [36]*

technique is based on this trick [34, 36]. The point is to use the neutron spins –precessing in a magnetic field – as stop watches that individually keep track on each neutron. Thereby a velocity **difference** is converted into a polarization change. See Fig. 19 for an illustration. Longitudinally polarized neutrons enter the spectrometer from the left, the start of the "racetrack" to measure the initial velocity is give by the first $\pi/2$-flipper where the spin is rotated by 90^0. From there the now transverse spins precess around a longitudinal magnetic field until the first "racetrack" is terminated by the π-flipper close to the sample position. The accumulated precession angle is

$$\Psi = \frac{\gamma}{v}\int_l |B| dl = n2\pi + \alpha \tag{89}$$

where $\gamma = 2\pi \times 2913.06598 \times 10^4 \mathrm{s}^{-1}/\mathrm{Tesla}$ is the gyromagnetic ratio of the neutrons and $|B|$ the modulus of the magnetic induction along the neutron path l. The π-flipper rotates the neutron spins (that all lie in a plane perpendicular to the longitudinal axis)

by 180^0 around a vertical axis. The effect on the apparent precession angle is $\Psi_1 = n2\pi + \alpha \rightarrow n2\pi - \alpha$. Since n and α depend strongly on the neutron velocity (Eq. (89)) at the sample α is uniformly distributed over the full circle. However, the second arm with its symmetric precession field, causes a further rotation $\Psi_2 = n2\pi + \alpha$. If there is no velocity change during scattering the final precession angle is $\Psi_1 + \Psi_2 = (n+n)2\pi - \alpha + \alpha = 2n2\pi = 0 \mod 2\pi$, i.e. the polarization is the same as at the entrance of the spectrometer, independent on the velocity spread of the beam (spin-echo). If small velocity changes occurred, the polarization is only partially recovered. The analyzer transmission $[1 \pm \cos(\Delta\Psi(\Delta v))]/2$ modulates the intensity at the detector. Integrating over the full spectrum $S(q,\omega)$ yields the intensity signal. With

$$J_1 = \int_{l((\pi/2)_1)}^{l(\pi)} |B| dl \qquad J_2 = \int_{l(\pi)}^{l((\pi/2)_2)} |B| dl \tag{90}$$

the detected intensity is

$$I \propto S(q) \int \frac{1}{2}\left[1 \pm \cos(-\frac{\gamma J_1}{v} + \frac{\gamma J_2}{v+\Delta v})\right] w_\omega(\Delta v)\, d\Delta v \tag{91}$$

where w_ω represent the normalized spectrum $S(q,\omega)/S(q)$. Using the relation between k, λ and v and series expansion yields

$$I \propto \int \frac{1}{2}\left[1 \pm \cos(-\frac{\gamma J_1}{(h/m_n)\lambda^{-1}} + \frac{\gamma J_2}{(h/m_n)\lambda^{-1} + \lambda\omega/2\pi})\right] S(q,\omega)\, d\omega \tag{92}$$

For the symmetric setup ($J_1 = J_2 = J$) the λ-dependent terms in Eq. (92) can be combined and approximated for small ω

$$-\frac{1}{\lambda^{-1}} + \frac{1}{\lambda^{-1} + \lambda(m_n/h)\omega/2\pi} \approx -\lambda^3 \frac{m_n \omega}{h 2\pi} \tag{93}$$

then from Eqn. (93 and 92):

$$I = \eta \frac{1}{2}\left[S(q) + \int \cos(\underbrace{\gamma J \frac{m_n^2}{h^2 2\pi}\lambda^3}_{t}\ \omega) S(q,\omega) d\omega\right] \tag{94}$$

The underbraced product corresponds to a time, therefore the integral in Eq. (94) is the (cos-)Fouriertransform of $S(q,\omega)$, i.e. the intermediate scattering function $S(q,t)$. The Fourier-time t can be scanned during an experiment by variation of the magnetic precession field ($J \propto B$) or it may be changed by variation if λ.
Usually NSE data are represented in the form $I(q,t)/I(q,0) = S(q,t)/S(q)$.

Scattering Function from Ginzburg-Landau models

Here a short description is given how the scattering follows from a functional $\mathcal{F}$ that has a quadratic form in Φ, i.e. how to arrive from Eqn. (66,67) at Eq. (69). In Fourier representation the expression for the sum of states including the auxiliary field H is given by

$$Z\{H\} = \int \mathcal{D}\Phi\ e^{\int d^3q[-w(\mathbf{q})\Phi(\mathbf{q})\Phi(-\mathbf{q}) + H(\mathbf{q})\Phi(-\mathbf{q})]} \tag{95}$$

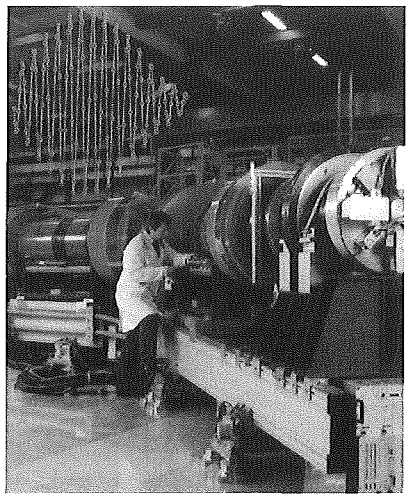


Fig. 20: *NSE spectrometer in Jülich [37].*

because the order parameter $\Phi(\mathbf{r})$ and the auxiliary field $H(\mathbf{r})$ are real $\Phi(-\mathbf{q}) = \Phi(\mathbf{q})^*$ and $H(-\mathbf{q}) = H(\mathbf{q})^*$. Then the argument of the integral in the exponent can be written as

$$\int d^3q[-w(\mathbf{q})\Phi(\mathbf{q})\Phi(-\mathbf{q}) + H(\mathbf{q})\Phi(-\mathbf{q})] =$$
$$\int d^3q \left[-w(q)\left|\Phi(\mathbf{q}) - \frac{H(\mathbf{q})}{2w(q)}\right|^2 - \frac{H(\mathbf{q})H(-\mathbf{q})}{4w(q)}\right] \tag{96}$$

with that and the introduction of $\tilde{\Phi}(\mathbf{q}) = \Phi(\mathbf{q}) - H(\mathbf{q})/2w(q)$

$$Z\{H\} = e^{-\int d^3q \frac{H(\mathbf{q})H(-\mathbf{q})}{4w(q)}} \underbrace{\int \mathcal{D}e^{-\int d^3q w(q)\tilde{\Phi}(\mathbf{q})\tilde{\Phi}(-\mathbf{q})}}_{Z_0} \tag{97}$$

and applying Eq. (66) in Fourier representation

$$G(\mathbf{q}) = \langle\Phi(\mathbf{q})\Phi(-\mathbf{q})\rangle = \frac{1}{Z_0}\frac{\delta^2 Z\{H\}}{\delta H(\mathbf{q})\delta H(-\mathbf{q})}|_{H=0}$$
$$= \frac{\delta^2}{\delta H(\mathbf{q})\delta H(-\mathbf{q})}\left[e^{-\int d^3q \frac{H(\mathbf{q})H(-\mathbf{q})}{4w(q)}}\right]_{H=0} = \frac{1}{2w(q)} \tag{98}$$

References

[1] W.M. Gelbart, A. Ben-Shaul, D.Roux (Eds.), *Micelles, Membranes, Microemulsions and Monolayers*, Springer-Verlag, Berlin (1994)

[2] S.A. Safran, *Statistical Thermodynamics of Surfaces, Interfaces and Membranes*, Addison-Wesley, Reading, MA (1994)

[3] J. Meunier, D. Langevin, N. Boccara (Eds.), *Physics of Amphiphilic Layers*, Springer-Verlag, Berlin (1987)

[4] B. Jakobs *et al.*, Langmuir **15**, 6707 (1999).

[5] R. Lipowsky, E. Sackmann (Eds.), *Structure and dynamics of membranes - from cells to vesicles* Vol 1 of *Handbook of biological physics*, Elsevier, Amsterdam (1995)

[6] F. Nacka *et al.*, Colloids and Surfaces B: Biointefraces **20**, 257 (2001)

[7] W. Helfrich, Z. Naturforsch. **28c**, 693 (1973).

[8] D. Roux *et al.*, Europhys. Lett. **11**, 229 (1990).

[9] D. Roux, C. Coulon, and M. E. Cates, J. Phys. Chem. **96**, 4174 (1992).

[10] G. Gompper and M. Schick, in *Phase Transitions and Critical Phenomena*, edited by C. Domb and J. Lebowitz (Academic Press, London, 1994), Vol. 16, pp. 1–176.

[11] M. Teubner and R. Strey, J. Chem. Phys. **87**, 3195 (1987).

[12] H. Endo *et al.*, J. Chem. Phys.**115**, 580 (2001).

[13] G. Gompper and D. M. Kroll, Phys. Rev. Lett. **81**, 2284 (1998).

[14] W. Janke, H. Kleinert, M. Meinhard, Phys. Lett. B **217**, 525 (1989).

[15] R.R. Netz, R. Lipowsky, Europhys. Lett **29**, 345 (1995).

[16] H. Kleinert, Phys. Lett. A **257**, 269 (1999).

[17] M. Bachmann, H. Kleinert, A. Pelster, Phys. Lett. A **261**, 127 (1999).

[18] D. Roux, C.R. Safinya, J. Phys. (Paris) **49**, 307 (1988).

[19] J. Mahanty, B.W. Ninham, *Dispersion Forces*, Academic Press, London, New York, San Francisco (1976)

[20] R.P. Rand, Ann. Rev. Biophys. Bioeng, **10**, 277 (1981).

[21] A. Zilman, R. Granek, PRL **77**, 4788 (1996).

[22] M. Mihailescu *et al.*, J. Chem. Phys. **115**, 9563 (2001).

[23] T. Sottmann and R. Strey, J. Chem. Phys. **106**, 8606 (1997).

[24] U. Peter *et al.*, Phys. Rev. Lett. **76**, 3869 (1996)

[25] T.Schilling, O.Theissen, G.Gompper, Eur. Phys. J. E **4**, 103 (2001).

[26] S.Ramaswamy, J. Prost, W. Cai, T.C. Lubensky, Europhys Lett. **23**, 271 (1993); S.Ramaswamy, J. Prost, T.C. Lubensky, Europhys Lett. **27**, 285 (1994).

[27] F.Nallet, D.Roux, J.Prost, Phys. rev. Lett. **62**, 276 (1989); F.Nallet, D.Roux, J.Prost, J. Phys. (Paris) **50**, 3147 (1989).

[28] G. Gompper, in *31. Ferienkurs des Istituts für Festkörperforeschung 2000, Dynamik in kondesierter Materie*, Forschungszentrum Jülich, Jülich (2000).

[29] D.J. Amit, *Field Theory, the Renormalization Group and Critical Phenomena* (World Scientific, Singapore, 1984).

[30] J.J. Binney, N.J. Dowrick, A.J. Fisher, M.E.J. Newman, *The Theory of Critical Phenomena* (Claredon Press, Oxford, 1992).

[31] G. Gompper, M. Schick. Phys. Rev. Lett. **65**, 1116 (1990).

[32] M.Hennes, G.Gompper, PRE **54**,3811 (1996)

[33] M. Nomomura, T. Otha, J. Chem. Phys. **100**, 7516 (1999)

[34] F. Mezei, *Proc. Workshop on Neutron Spin Echo*, Berlin: Springer, (1980).

[35] P. Schleger *et al.*, Physica B **241-243**, 164, (1997)

[36] M. Monkenbusch,R. Schaetzler, D. Richter, Nucl. Inst. and Methods in Phys. Research, **A399**, 301 (1997).

[37] M. Monkenbusch, Neutron News **8**, 25 (1997)

C 7 Phase Separation Kinetics

M. P. Lettinga
Institut für Festkörperforschung
Forschungszentrum Jülich GmbH

Contents

1 Introduction **2**

2 Unstable and meta-stable regions **3**
2.1 Unstable region and the spinodal 4
2.2 Meta-stable region and the binodal 7
2.3 Example of experimental phase diagram 8

3 Initial Spinodal Decomposition Kinetics **9**
3.1 The Cahn-Hilliard Theory 10
3.2 Smoluchowski Equation Approach 16
3.3 Some Final Remarks on Initial Decomposition Kinetics 19
3.4 Experiments on spinodal decomposition 21

4 Nucleation and growth **26**
4.1 Classical Nucleation Theory 28
4.2 Simulations on nucleation and growth 29
4.3 Experiments on nucleation and growth 31

A Functional derivatives **33**

B Small Angle Light Scattering by demixing suspensions **35**

1 Introduction

This lecture is concerned with of an initially homogeneous system of colloidal particles into a phase of a high concentration and a phase of a low concentration. Knowledge of the phase separation process of colloidal dispersions and its kinetics is both of practical importance as of fundamental interest. Practical examples are the enhancement of protein nucleation ([1],[2]), phase separation in dairy products ([3]), and the processing of polymers ([4]).
The fundamental interest for the phase separation of colloidal systems originates from the fact that colloids are between 100 and 10^4 times bigger than atoms, but still move randomly through their solvent. Moreover, the interaction potential between the particles can be engineered by grafting the surface of the colloids with polymer brushes, or by addition of polymers that act like depletion agents. Just like molecular systems, colloidal dispersions can be quenched into a meta-stable or unstable region and undergo gas-liquid or gas-solid phase transitions by changing the temperature, the pressure, or the concentration of the particles. The phase with the lower particle concentration is then referred to as the "gas" phase and the phase with the higher concentration is referred to as the "liquid" phase or the solid phase, depending on the structure and dynamics of that phase.
The major advantage of colloidal systems for experimentalists is that, due to the large dimensions of the colloids, the dynamics is much slower and they can be directly imaged. This means that processes in molecular systems that are not accessible for experimentalists can now be followed. The major advantage for theorists is that they can study the influence of the interparticle potential on the phase behavior.
An example of a colloidal system where the pair-interaction potential contains an attractive part are silica cores coated with stearyl alcohol chains dissolved in benzene. Since benzene is a marginal solvent for stearyl alcohol, the alcohol chain brushes on the surfaces of two colloidal particles rather dissolve in each other than in the solvent. This results in a very short ranged attractive interaction super imposed onto the hard-core repulsion (this potential is sketched in Fig.1). The quality of the solvent is diminished as the temperature is lowered, resulting in a stronger attraction, and giving rise to thermodynamic instability. Depending on position in the phase diagram a gas-liquid or a gas solid phase transition can be induced.
An other example of a colloidal system which has a gas-liquid transition is a suspension of hard-sphere colloids with added polymer. There is now an "effective" attraction between the colloidal particles that is induced by the polymers. When two colloidal particles are close together, polymer is expelled from the gap between the two particles, leading to an excess osmotic pressure of the polymer that drives the colloidal particles together. These effective attractions can be so large that they give rise to a gas-liquid phase separation. In addition, there are phase transitions also in monodisperse systems where no attractive component of the pair-interaction potential is present: for example, crystallization can occur in monodisperse hard-sphere colloids. This is a phase transition from a meta-stable state.
When an initially homogeneous system is rendered meta-stable or unstable systems, then macroscopic inhomogeneities in density will develop, eventually leading to a state where two phases with different concentrations or microstructures coexist. Since we are interested in the kinetics of the phase separation, the time dependence of the macroscopic density is the interesting quantity here. It is this quantity that will be calculated, simulated and measured throughout this chapter.

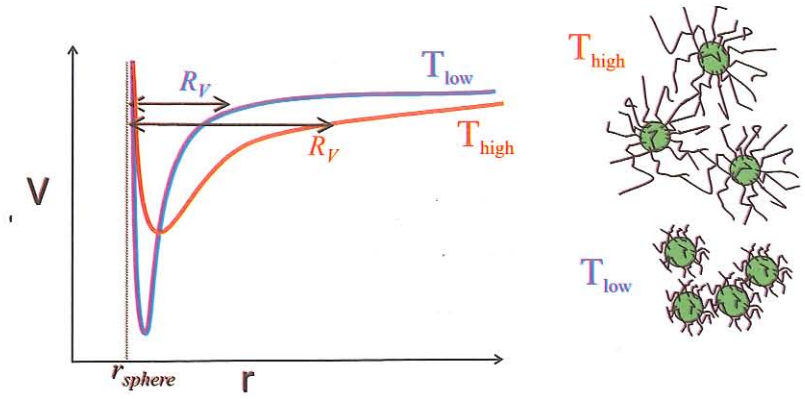


Fig. 1: *A short ranged attractive pair-interaction potential for particles grafted with polymers in a marginal solvent.*

Before entering into quantitative theories, the distinction between phase separation from the meta-stable and unstable state is described in section 2. In section 3, the classic phenomenological theory for decomposition from the unstable state and the equation approach are discussed. These two sections are concerned with the initial stage of phase separation, where inhomogeneities just began to develop. The quantitative analysis of phase separation kinetics during later stages are not considered, since at later stages inhomogeneities are well developed and therefore much more complicated to handle. Experimental techniques to investigate phase separation kinetics are discussed at the end of section 3. The main core of section 2 and 3is taken from chapter 8 and 9 of [5]. The Phase sepeartion from the meta-stable state by nucleation and growth is treated, though less detailed, in section 4.

2 Unstable and meta-stable regions

For a colloidal dispersions with a short-ranged attractive pair-interaction potential, the osmotic pressure of the dispersed colloidal particles plays the same role as the pressure in a molecular gas. For both types of systems similar diagrams can be drawn of the (osmotic) pressure vs. volume, like those depicted in Fig.2. A homogeneous stable system at some temperature T and pressure P can be turned in to an unstable system by suddenly changing the temperature or the pressure the unstable part of the phase diagram. Such a process is commonly referred to as *a quench*. Depending on the type of quench, it will either result in an immediate phase transition or a phase transition that starts up after a certain time. The conditions that determine the pathway of the phase separation will be the subject of this section.

2.1 Unstable region and the spinodal

As with a molecular gas, a colloidal system is unstable when the osmotic pressure Π decreases with increasing number density $\tilde{\rho}(= N/V)$, and (meta-) stable when Π increases.

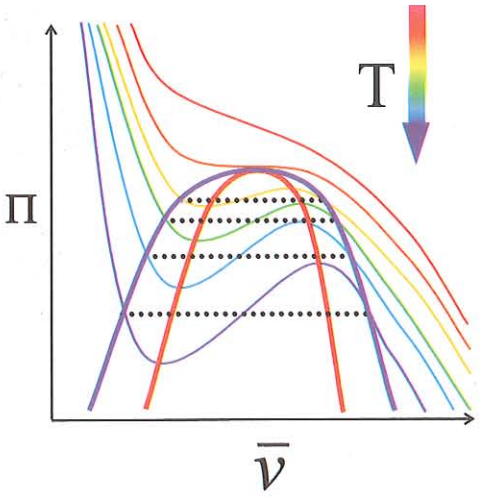


Fig. 2: *A schematic sketch of the reciprocal density dependence of the osmotic pressure* Π *at different temperatures. The thick blue line depicts the . The thick red line depicts the .*

That is,

$$\frac{d\Pi}{d\bar{\rho}} < 0 \iff \textit{thermodynamically unstable}\,. \tag{1}$$

In other words, a system is unstable when an increase in density doesn't result in a higher (osmotic) pressure, which would force the system back to its original lower concentration. So, in the (meta-) stable region of the phase diagram this derivative is positive, while in the unstable region of the phase diagram, it is negative. This stability criterion can be understood thermodynamically as follows. Define $\bar{v} = 1/\bar{\rho}$, the reciprocal concentration. Now using the thermodynamic relation $\Pi = \frac{\partial A}{\partial V}_{|N}$ we find,

$$\frac{d\Pi}{d\bar{\rho}} = -\bar{v}^2\frac{d\Pi}{d\bar{v}} = \bar{v}^2\frac{d^2(A/N)}{d\bar{v}^2} \tag{2}$$

with N the fixed total number of Brownian particles in the system and A the Helmholtz free energy of the system. A negative (positive) value of $d\Pi/d\bar{\rho}$ thus implies a reciprocal density dependence of the Helmholtz free energy (per colloidal particle) as sketched in Fig.3a (b). Consider a system with a concentration $\bar{\rho} = c_0$ in the homogeneous state. Now suppose that an instantaneous realization of the fluctuating density mimics the separation of the system into two parts, each with a different concentration, c_- and c_+ (see Fig.3a,b). The Helmholtz free energy per colloidal particle of this "demixed" system is obtained from the intersection of the straight line connecting the two points $(\bar{v}_- = 1/c_-, A(\bar{v}_-)/N_-)$ and $(\bar{v}_+ = 1/c_+, A(\bar{v}_+)/N_+)$ and the vertical line at the original reciprocal concentration $\bar{v}_0 = 1/c_0$ of the homogeneous system.[1] Since the system tends towards a state where the

[1]This can be understood as follows. From $N_+\bar{v}_+ + N_-\bar{v}_- = N\bar{v}_0$ and $N_+ + N_- = N$ (with $N_\pm$

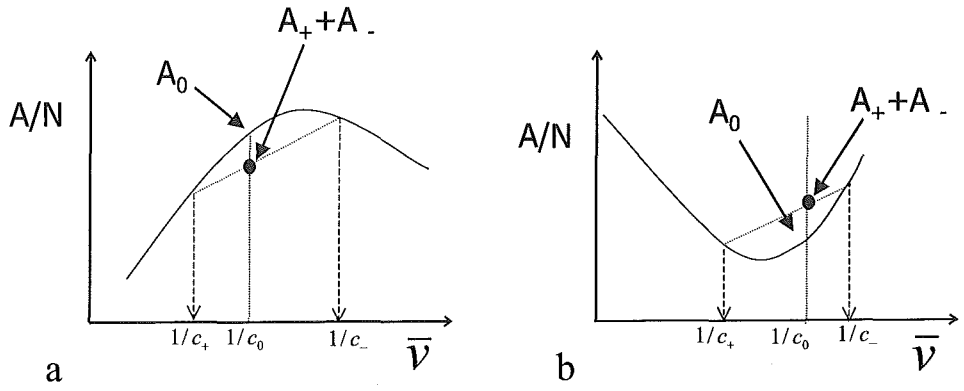


Fig. 3: *The local density dependence of the Helmholtz free energy per particle A/N in case $d\Pi/d\bar{\rho} < 0$, (a), and in case $d\Pi/d\bar{\rho} > 0$, (b). The points • are the free energies of the system when decomposed into two fluids with concentrations c_- and c_+.*

Helmholtz energy attains a minimum value, it is clear from fig.3a that when $d\Pi/d\bar{\rho} < 0$, any demixing fluctuation, no matter how small in amplitude, decreases the Helmholtz free energy, so that the demixed state does not return to the homogeneous state but evolves in time towards more complete demixing. On the other hand, when $d\Pi/d\bar{\rho} > 0$, demixing (with small amplitudes) increases the Helmholtz free energy, so that the system returns to the homogeneous state. The spinodal is the set of number densities and temperatures where the system becomes unstable, that is, where $d\Pi/d\bar{\rho} = 0$. Since the osmotic pressure is a function of the temperature and the concentration, this is an implicit relation between these two quantities, which defines the spinodal.
A typical plot of the osmotic pressure versus the reciprocal concentration $\bar{v} = 1/\bar{\rho}$ at a different temperatures was already given in Fig.2. The *spinodal* (the thick red line in Fig.2) is now obtained by connecting the points in each curve where $d\Pi/d\bar{\rho} = 0$. A homogeneous system in the region under the spinodal is unstable.[2]

2.2 Meta-stable region and the binodal

To understand the mechanism of phase separation of homogeneous systems in the meta-stable region (indicated by the blue line in Fig.4), the reciprocal concentration dependence of the Helmholtz free energy A must be considered over the entire concentration range

the number of colloidal particles in the "phase" with concentration $c_\pm$), it follows that $N_+ = N(\bar{v}_0 - \bar{v}_-)/(\bar{v}_+ - \bar{v}_-)$ and $N_- = N(\bar{v}_0 - \bar{v}_+)/(\bar{v}_- - \bar{v}_+)$. Since the Helmholtz free energy is extensive, the free energy A_{dem} of the demixed system is equal to $A(\bar{v}_-) + A(\bar{v}_+)$. Hence,

$$\frac{A_{dem}}{N} = \frac{\bar{v}_0 - \bar{v}_+}{\bar{v}_- - \bar{v}_+}\frac{A(\bar{v}_-)}{N_-} + \frac{\bar{v}_0 - \bar{v}_-}{\bar{v}_+ - \bar{v}_-}\frac{A(\bar{v}_+)}{N_+}.$$

This is a linear function of $\bar{v}_0$ that connects the points $(\bar{v}_-, A(\bar{v}_-))$ and $(\bar{v}_+, A(\bar{v}_+))$. This proves the above statement concerning the free energy per particle in the demixed system.

[2] A microscopic picture of the mechanism leading to demixing from the unstable state is discussed in subsection 3.2

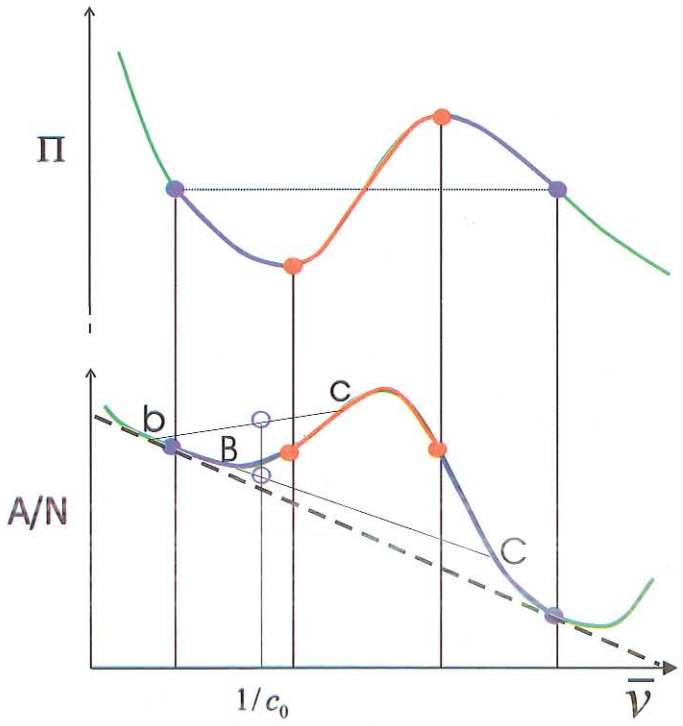


Fig. 4: *A typical reciprocal density dependence of the osmotic pressure Π and of the Helmholtz free energy A. The red line represents concentrations where the system is unstable, the blue line where the system is meta-stable, and the green line where the system is stable. The points mark the spinodal (red) and binodal (blue) points. A demixing fluctuation leading to two phases with reciprocal concentrations b and c leads to an increase of the free energy, while a fluctuation leading to two phases with reciprocal concentrations B and C leads to a lowering of the free energy. The free energies of the demixed state are indicated by a ○.*

(see Fig.4). Although demixing fluctuations of small amplitude lead to an increase of the free energy (such as the demixing in two phases indicated by the points b and c), demixing fluctuations with a large amplitude can lead to a decrease of free energy (such as the demixing in two phases indicated by the points B and C). The free energy of the demixed systems is obtained by the point of intersection of the straight line connecting the reciprocal concentrations of the two phases b and c or B and C, and the vertical line at the reciprocal concentration of the homogeneous system : these points are indicated by a $\circ$. Hence, *phase separation from the meta-stable state is initiated by fluctuations of sufficiently large amplitude, contrary to phase separation from the unstable state, where any fluctuation, no matter how small in amplitude, leads to a lowering of the free energy.* The probability for a large amplitude fluctuation is small, so that phase separation occurs only after some time, the so-called *induction time.* This in contrast to phase separation from the unstable state (spinodal decomposition) where phase separation occurs without any time delay, since density fluctuations of small amplitude are always present. The induction time is roughly inversely proportional to the probability for a demixing fluctuation to occur that leads to a lower free energy. There is a larger probability for a fluctuation resulting in a relatively large change of the concentration in a *small* portion of the system than for such a change in a *large* portion of the system. Phase separation from the meta-stable state is therefore initiated by the fluctuation induced formation of *small entities* of significantly different concentration than the initial concentration. These entities are referred to as *nuclei.* The phase separation mechanism from the meta-stable region is referred to as *nucleation* or *condensation* (see section 4 for theory and experiments on and growth). A little thought shows that the system attains the smallest possible free energy, after phase separation is completed, when the (reciprocal) concentrations of the two coexisting phases are equal to those obtained from a double tangent construction, as depicted in Fig.4. Note that an equal slope of A/N versus $\bar{v}$ implies equal osmotic pressures in the two coexisting phases, which is the definition of equilibrium. The concentrations of the two coexisting phases are two points on the *binodal*, and are marked by a blue $\bullet$ in Fig.4. It is easy to see that there are no demixing fluctuations that lead to a lowering of the free energy of a homogeneous system with concentrations in the range where the free energy is represented by the green line in Fig.4: for such concentrations the system is stable. The line in the phase diagram that separates the stable region from the meta-stable region is *the binodal.* This is depicted as the blue line in Fig.2. There is a special point where the system changes from being stable to unstable, without first becoming meta-stable. This is the point where the binodal and spinodal meet, and is known as *the critical point.*

It should be noted that the Helmholtz free energy plotted in Fig.4 is the free energy without the contribution of gradients in the density. For an inhomogeneous system there are also contributions to the free energy due to concentration gradients. As soon as the system becomes inhomogeneous, for example after a demixing fluctuation occurred, the free energy is larger than calculated on the basis of Fig.4. This is why fluctuations which induce small gradients in the density are preferred fluctuations for initiating phase separation.

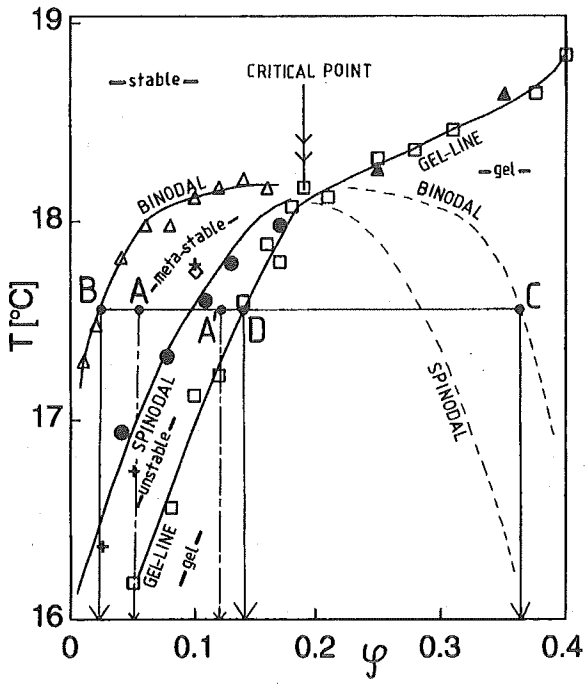


Fig. 5: *Experimental phase diagram of stearyl silica in benzene. The vertical axis is the temperature and the horizontal axis is the concentration in terms of the fraction of the total volume that is occupied by the silica cores of the Brownian particles. The points relate to various experimental techniques to determine the phase lines. Reprinted from [6].*

2.3 Example of Experimental phase diagram

An experimental phase diagram of silica cores coated with stearyl alcohol chains dissolved in benzene is plotted in Fig. 5. At larger temperatures, benzene is a good solvent for stearyl alcohol, resulting in a stable dispersion. At lower temperatures there is a binodal and a spinodal.

Disregarding the gel-line in Fig.5 for the moment, a homogeneous system with a temperature and concentration located between the binodal and spinodal (for example the point A in Fig.5) phase separates into two liquid phases (the points B and C in Fig.5). The phase separation mechanism here is interpreted as *condensation* or *nucleation*. A homogeneous system with a temperature and concentration below the spinodal (for example point A' in Fig.5) will also separate into two liquid phases (again the points B and C in Fig.5). The phase separation mechanism is now quite different from condensation, and is interpreted as *spinodal decomposition*.

Contrary to the phase diagram of simple molecular systems, a gel-line is found for colloidal systems. Below the gel-line the system is mechanically unstable, and a more or less rigid and very long lived, space filling network of mutually connected colloidal particles is

formed. The gel is a solid in the sense that it sustains a finite yield stress : the meniscus of the gel does not flow when tilting the cuvette. The more familiar standard phase diagram is that for simple molecular systems, where the gel-line is absent, and the binodal and spinodal extend to higher concentrations as sketched by the green lines in Fig.4. Since for larger volume fractions the binodal and spinodal are located below the gel-line, the actual phase separation of the silica dispersion is not into two liquid phases with volume fractions B and C, but into a fluid with volume fraction B and a gel with volume fraction D, as depicted in Fig.5. For some not yet understood reason, if there is any, the gel-line intersects the critical point. This point is indicated in Fig.5 by the vertical arrow.

3 Initial Spinodal Decomposition Kinetics

Right after a quench the system starts to develop long ranged correlations. These correlations develop up to a point where they render the system unstable, from which time on the macroscopic density develops inhomogeneities. The evolution of the density is sketched in Fig.6. As will be seen shortly, right after the quench, in the initial stages of the phase separation, one particular sinusoidal density fluctuation is amplified most rapidly.[3] This is due to the fact that the growth rate of sinusoidal density fluctuations with wavelength Λ is proportional to Λ^{-2}, while the driving force for phase separation diminishes with decreasing wavelength. The proportionality of the growth rate with Λ^{-2} merely expresses the fact it takes more time to displace particles over larger distances.[4] The driving force for growth decreases with decreasing wavelength Λ, because the creation of short wavelength density variations corresponds to large gradients of the density, which are not preferred, since these lead to a large increase of the free energy. There is therefore one particular optimum wavelength for which the corresponding density waves grow most rapidly. This is depicted in Fig.6a. In the *initial stage* of the phase separation, both the change $\delta\rho$ of the density and gradients of the density are small. The initial stage is also referred to as the *linear regime*, since equations of motion for the density may be linearized with respect to $\delta\rho$. Then there is the so-called *intermediate stage*, where $\delta\rho$ is not small so that linearization is no longer allowed. Gradients of the density are still small, as in the initial stage, due to the long wavelengths that demix. This stage is depicted in Fig.6b. Subsequently, the decomposition reaches the *transition stage* where the lower and larger binodal concentrations ($\bar{\rho}_-$ and $\bar{\rho}_+$, respectively) are attained in various parts of the system, as sketched in Fig.6c. At this stage, sharp interfaces between the regions with concentrations close to $\bar{\rho}_-$ and $\bar{\rho}_+$ exist. Inhomogeneities are now large, and higher order terms in gradients of the density come into play. In the *late stage* of the phase separation the interfaces develop : concentration gradients sharpen and the interfacial curvatures change to ultimately establish coexistence (see Fig.6d). We thus arrive at the following

[3] Sinusoidally varying density profiles are also referred to as *density waves*.

[4] Sinusoidal density variations relax roughly like $\exp\{-Dk^2t\}$, with D a diffusion coefficient and k the wavevector, which is related to the wavelength Λ as $k = 2\pi/\Lambda$. The factor k^2 in the exponent relates to the Λ^{-2} dependence referred to here.

classification of the different stages during decomposition,

Initial stage : $\delta\rho/\bar{\rho}$ *is small,*
gradients are small ("diffuse interfaces"),

Intermediate stage : $\delta\rho/\bar{\rho}$ *is not small,*
gradients are small ("diffuse interfaces"),

Transition stage : $\delta\rho/\bar{\rho}$ *is large,*
gradients are not small ("sharp interfaces"),

Final stage : $\delta\rho/\bar{\rho}$ *is large,*
gradients are large ("very sharp interfaces").

Equations of motion for the density in the initial and intermediate stage can therefore be expanded to leading order with respect to gradients of the density, while the leading non-linear contribution in $\delta\rho/\bar{\rho}$ must be included in the intermediate stage. The first higher order terms in an expansion with respect to gradients of the density, which must be included in the transition stage, are referred to here as describing the dynamics of *sharp interfaces*, while even higher order terms describe the dynamics of *very sharp interfaces* in the final stage. These very sharp interfaces have a width of the order of a few particle diameters, except in case of quenches very close to the critical point, where the equilibrium interfacial thickness may be large. As density waves grow *independent of their spatial direction*, the morphology of regions with lower and higher concentration is an interconnected labyrinth structure. In an experiment performed under the influence of the earth's gravitational field the regions of high concentration will fall to the bottom of the cell and two bulk phases of high and low concentration will be formed. Experiments in space show that the labyrinth structure is a stable final state.
Let now $\rho(\mathbf{r},t)$ denote the macroscopic number density as a function of the position $\mathbf{r}$ in the system at time t after the system became unstable and started to demix. Define the change of the macroscopic density $\delta\rho(\mathbf{r},t)$ relative to that in the homogeneous state as,

$$\rho(\mathbf{r},t) \;=\; \bar{\rho} + \delta\rho(\mathbf{r},t)\,. \tag{3}$$

In the initial stage of the phase separation we have,

$$\frac{\mid \delta\rho(\mathbf{r},t) \mid}{\bar{\rho}} \;\ll\; 1\,, \tag{4}$$

allowing linearization of equations of motion for the macroscopic density with respect to the change $\delta\rho$ of the density. In the present section we will describe the initial stage of phase separation on the basis of the Cahn-Hilliard theory, which is a phenomenological theory based on thermodynamic arguments, and on the basis of the Smoluchowski equation with the neglect of hydrodynamic interaction.

3.1 The Cahn-Hilliard Theory

In a thermodynamic type of approach, demixing can be described as transport of colloidal particles between volume elements which are internally in equilibrium. These volume elements are supposed to be so small that the wavelengths of density variations which are

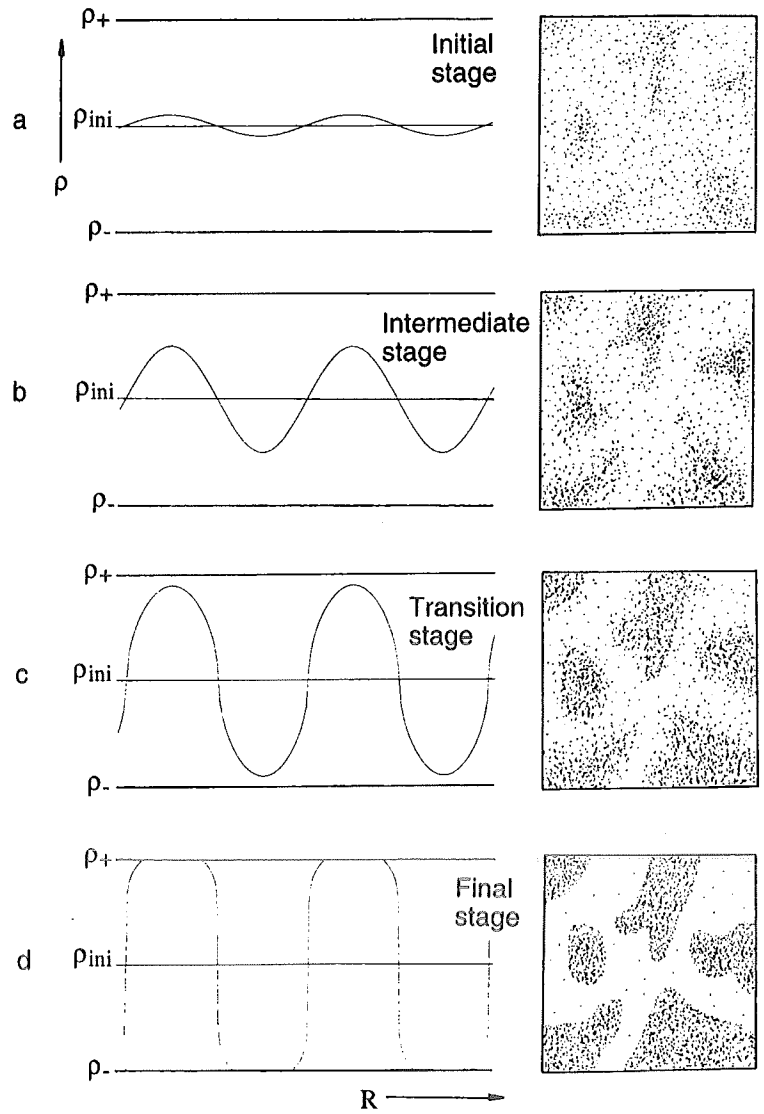


Fig. 6: *A sketch of the time development of the density after a quench in the unstable part of the phase diagram. Time increases from top to bottom. The left column of figures is a sketch of the density versus position, while the right column depicts the corresponding morphology of density variations in the system itself. The concentrations* $\bar{\rho}_+$ *and* $\bar{\rho}_-$ *are the binodal concentrations.*

unstable are very much larger than the linear dimension of the volume elements. This is only possible when *large* wavelength density variations are unstable : this will indeed turn out to be the case, as could have been anticipated on what has been said in the introduction. On the other hand these volume elements are supposed to be so large that they contain many colloidal particles and that the range of correlations between particles is small in comparison to its linear dimensions, in order to make a thermodynamic description of each volume element feasible. Furthermore, each volume element is supposed to be in thermal equilibrium at each instant during the initial stage of the phase separation. This can be achieved only when the rate of demixing is small in comparison to the relaxation time of density variations with a wavelength that fits many times into a volume element. That this is indeed the case is due to (i) the fact that it takes more time to displace colloidal particles over larger distances (for demixing) than over smaller distances (for internal equilibration) and (ii) the fact that the diffusion coefficient which describes the large wavelength demixing is very much smaller than the diffusion coefficient pertaining to relaxation of small wavelength density variations, as will be shown shortly. The latter is reminiscent to critical slowing down, discussed in the previous chapter. The system is thus supposed to be in *local equilibrium*. The idea of fast relaxing small wavelength density fluctuations and slowly growing large wavelength density variations is depicted in Fig.7.

If one is willing to accept the above assumptions, the Helmholtz free energy $A_V(\rho(\mathbf{r},t))$ per unit volume of a volume element at position $\mathbf{r}$, with a homogeneous density $\rho(\mathbf{r},t)$, is well defined and exhibits the double minimum form as a function of the local reciprocal density as sketched in Fig.4. Such a double minimum form can be modeled by a fourth order polynomial in the change $\delta\rho(\mathbf{r},t)$ of the local density relative to $\bar{\rho} = N/V$ as follows,

$$\begin{aligned} A_V(\rho(\mathbf{r},t)) &= A_V(\bar{\rho}) + a_1\delta\rho(\mathbf{r},t) + \frac{1}{2}a_2(\delta\rho(\mathbf{r},t))^2 \\ &\quad + \frac{1}{3}a_3(\delta\rho(\mathbf{r},t))^3 + \frac{1}{4}a_4(\delta\rho(\mathbf{r},t))^4 . \end{aligned} \tag{5}$$

The coefficient a_4 is positive, since for small and large densities the free energy is large and positive. Notice that this free energy is the free energy of a volume element in which fluctuations of the density with wavelengths larger than its own linear dimension are absent, since these simply do not "fit into" the volume. This is the free energy per unit volume of an infinitely large system (with a homogeneous density equal to $\bar{\rho}+\delta\rho$) in which the large wavelength density fluctuations are constrained by means of an external field. In a statistical mechanical calculation of the double minimum form of the free energy, one should thus include an external field to account for the absence of density variations with wavelengths that are very much larger than the range of correlations between the colloidal particles.

The Helmholtz free energy of the total system is not simply equal to the sum of the free energies (eq. 5). There is also a contribution from the diffuse interfaces separating volume elements with different densities, that is, there is also a contribution arising from gradients in the density. Since we are only interested in the dynamics of the long wavelength density variations, leading to small gradients in the density, we may formally expand this contribution with respect to gradients in the density, and keep only the leading term. Since the free energy is invariant against inversion of the coordinate frame, that leading term is proportional to $\int d\mathbf{r}\ |\nabla\delta\rho(\mathbf{r},t)|^2$, where the integral ranges over the volume of the

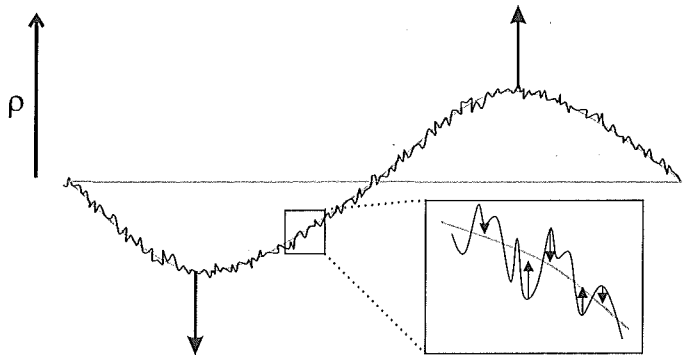


Fig. 7: *Small volume elements are in internal equilibrium due to fast relaxation of small wavelength density fluctuations, while the large wavelength density variations grow slowly.*

entire system under consideration. The proportionality constant is denoted here as $\frac{1}{2}\kappa$, where κ is referred to as *the Cahn-Hilliard square gradient coefficient.* This constant is assumed to be positive : for negative values the formation of gradients would decrease the free energy, leading to a different kind of instability, where the short wavelengths, corresponding to large gradients, are also unstable. The total Helmholtz free energy is therefore the sum (read : integral) of the "bulk contributions" in eq.(5) and the above discussed "diffuse interface contribution",

$$A[\rho(\mathbf{r},t)] = A(\bar{\rho}) + \int d\mathbf{r} \left\{ a_1\delta\rho(\mathbf{r},t) + \frac{1}{2}a_2(\delta\rho(\mathbf{r},t))^2 + \frac{1}{3}a_3(\delta\rho(\mathbf{r},t))^3 + \frac{1}{4}a_4(\delta\rho(\mathbf{r},t))^4 + \frac{1}{2}\kappa \mid \nabla\delta\rho(\mathbf{r},t) \mid^2 \right\} . \quad (6)$$

The square brackets in $A[\rho(\mathbf{r},t)]$) denote *functional dependence* : the numerical value of the free energy now depends on an entire function of position, not just on a single numerical value of the density as for a homogeneous system. An operator that maps functions onto real space is called a *functional.*
Transport of colloidal particles does not occur when the chemical potential $\mu(\mathbf{r},t)$ of the volume elements located at $\mathbf{r}$ is a constant. The number density flux $\mathbf{j}(\mathbf{r},t)$ of colloidal particles is therefore driven by gradients in the chemical potential. When these gradients are not too large, the number density flux is simply proportional to the gradient,

$$\mathbf{j}(\mathbf{r},t) = -D\nabla\mu(\mathbf{r},t) , \quad (7)$$

where D is a phenomenological transport coefficient. The chemical potential is in turn related to the *functional derivative* of the free energy with respect to the density (see appendix A for an introductory discussion on functional differentiation and the derivation of this result),

$$\mu(\mathbf{r},t) = \frac{\delta A[\rho]}{\delta\rho(\mathbf{r},t)} = a_1 + a_2\delta\rho(\mathbf{r},t) + a_3(\delta\rho(\mathbf{r},t))^2 + a_4(\delta\rho(\mathbf{r},t))^3 - \kappa\nabla^2\delta\rho(\mathbf{r},t) . \quad (8)$$

Now, conservation of the number of colloidal particles requires that,

$$\frac{\partial}{\partial t}\rho(\mathbf{r},t) \;=\; -\nabla\cdot\mathbf{j}(\mathbf{r},t)\,. \tag{9}$$

Using eqs.(6-8) in this equation of motion, linearization with respect to $\delta\rho(\mathbf{r},t)$ and Fourier transformation with respect to $\mathbf{r}$ (replacing ∇ by $i\mathbf{k}$) finally yields,

$$\frac{\partial}{\partial t}\delta\rho(\mathbf{k},t) \;=\; -D\,k^2\,\left[a_2+\kappa\,k^2\right]\,\delta\rho(\mathbf{k},t)\,. \tag{10}$$

The solution of this equation is simply,

$$\delta\rho(\mathbf{k},t) \;=\; \delta\rho(\mathbf{k},t=0)\,\exp\{-D^{eff}(k)\,k^2\,t\}\,, \tag{11}$$

where *the effective diffusion coefficient* is defined as,

$$D^{eff}(k) \;=\; D\,\left[a_2+\kappa\,k^2\right]\,. \tag{12}$$

The initial Fourier transform $\delta\rho(\mathbf{k},t=0)$ is the particular realization of the macroscopic density after correlations developed that renders the system unstable, before phase separation occurred.
From eq.(11) it is clear that density waves with a wavelength $\Lambda = 2\pi/k$ are unstable when $D^{eff}(k) < 0$. For these *wavevectors* k, the amplitude $\delta\rho(\mathbf{k},t)$ of the corresponding density wave grows exponentially with time. Since $\kappa > 0$, the effective diffusion coefficient can become negative for certain wavevectors only when $a_2 < 0$. From the definition (5) it follows that (differentiations are at constant N, and μ is the chemical potential of the colloidal particles),

$$a_2 = \frac{d^2(A/V)}{d\bar{\rho}^2} = \frac{d\,(\partial A/\partial N)}{d\bar{\rho}} = \frac{d\mu}{d\bar{\rho}} = \frac{1}{\bar{\rho}}\,\frac{d\Pi}{d\bar{\rho}}\,, \tag{13}$$

so that negative values of the effective diffusion coefficient corresponds, according to eq.(1), to a thermodynamically unstable system, as it should. For density variations with a wavelength $\Lambda = 2\pi/k$ for which
$D^{eff}(k) < 0$, diffusion occurs from regions of low density to larger density. This phenomenon is often referred to as *uphill diffusion*.
The "growth rate" of a sinusoidal density variation is equal to $-D^{eff}(k)\,k^2$, and is sketched in Fig.8 for different values of a_2. As can be seen in this figure all density fluctuations are suppressed when $a_2 < 0$ (Fig. 8a). When $a_2 > 0$ (Fig.8c and d) density fluctuations with wavevectors smaller than the so-called *critical wavevector* k_c will grow exponentially. When the wavevector is bigger than k_c, the fluctuation will again be suppressed. The critical wavevector is easily found to be equal to,

$$k_c \;=\; \sqrt{-\frac{a_2}{\kappa}}\,. \tag{14}$$

Their is also a wavevector k_m of the most rapidly growing density wave, which is easily found by straighforward differentiation,

$$k_m \;=\; \sqrt{-\frac{a_2}{2\kappa}} \;=\; \frac{1}{\sqrt{2}}k_c\,. \tag{15}$$

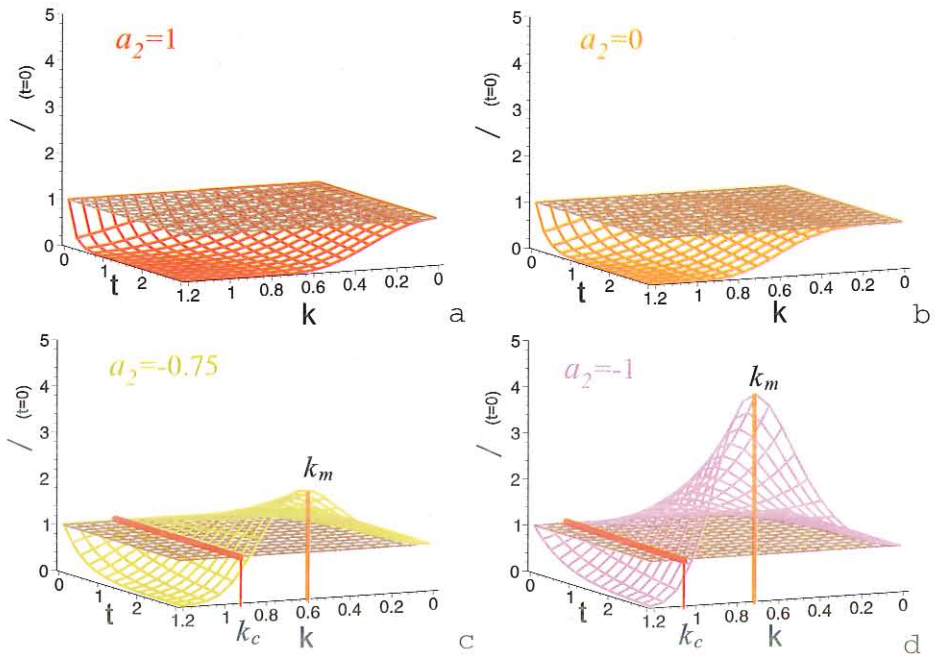


Fig. 8: *A sketch of the growth rate of sinusoidal density variations as a function of their wavevector and of time. In a) the system is stable. Increasing the depth of the quench from b) to d), the system becomes unstable for $k < k_c$ (given by the red line). There is a wavevector k_m of maximum growth rate (orange line).*

The reason for the existence of such a k_m is understood as follows. Density variations with small wavevectors decompose slowly because it takes longer times to transport colloidal particles over large distances. Density variations with larger wavevectors decompose slowly because the driving force for uphill diffusion diminishes, as a result of the fact that less free energy is gained when larger density gradients are created. Note that a deeper quench, where $-a_2$ is relatively large, results in a larger value for the most rapidly decomposing wavevector k_m. See references [8]-[14] for a few of the original papers on the Cahn-Hilliard theory.

3.2 Smoluchowski Equation Approach

The description given in the previous subsection is based on thermodynamic arguments. A microscopic derivation of the Cahn-Hilliard result (11,12) can be given on the basis of the Smoluchowski equation.[15],[16] The Smoluchowski equation is the equation of motion for the probability density function (pdf) $P \equiv P(\mathbf{r}_1, \mathbf{r}_2, \cdots, \mathbf{r}_N, t)$ of the position coordinates $\mathbf{r}_j$, $j = 1, 2, \cdots, N$, of all N colloidal particles in the system, and reads, with the neglect of hydrodynamic interaction,

$$\frac{\partial}{\partial t} P = D_0 \sum_{j=1}^{N} \nabla_{r_j} \cdot \left[\beta [\nabla_{r_j} \Phi] P + \nabla_{r_j} P \right], \tag{16}$$

where D_0 is the Stokes-Einstein diffusion coefficient, $\beta = 1/k_B T$ (with k_B Boltzmann's constant and T the temperature), and $\Phi \equiv \Phi(\mathbf{r}_1, \mathbf{r}_2, \cdots, \mathbf{r}_N)$ the potential energy of the assembly of colloidal particles. Since,

$$\int d\mathbf{r}_2 \cdots \int d\mathbf{r}_N \, P(\mathbf{r}_1, \mathbf{r}_2, \cdots, \mathbf{r}_N, t) \equiv P_1(\mathbf{r}_1, t) = \frac{1}{N} \rho(\mathbf{r}_1, t), \tag{17}$$

with P_1 a reduced pdf, an equation of motion for the macroscopic density can be obtained from the Smoluchowski equation (16) by integration with respect to all the position coordinates, except for $\mathbf{r}_1$. In order to integrate the Smoluchowski equation, a pair-wise additive interaction potential is assumed, that is (with $r_{ij} = |\mathbf{r}_i - \mathbf{r}_j|$),

$$\Phi(\mathbf{r}_1, \mathbf{r}_2, \cdots, \mathbf{r}_N) = \sum_{i,j=1,\, i<j}^{N} V(r_{ij}), \tag{18}$$

with V the pair-interaction potential. Further introducing the pair-correlation function g as,

$$\begin{aligned} P_2(\mathbf{r}_1, \mathbf{r}_2, t) &\equiv \int d\mathbf{r}_3 \cdots \int d\mathbf{r}_4 \, P(\mathbf{r}_1, \mathbf{r}_2, \mathbf{r}_3, \cdots, \mathbf{r}_N, t) \\ &\equiv P_1(\mathbf{r}_1, t) \, P_1(\mathbf{r}_2, t) \, g(\mathbf{r}_1, \mathbf{r}_2, t), \end{aligned} \tag{19}$$

the integrated Smoluchowski equation reads, for identical Brownian particles (with $\mathbf{r}_1$ renamed as $\mathbf{r}$ and $\mathbf{r}_2$ as $\mathbf{r}'$),

$$\begin{aligned} \frac{\partial}{\partial t} \rho(\mathbf{r}, t) &= D_0 \left[\nabla^2 \rho(\mathbf{r}, t) \right. \\ &\quad \left. + \beta \nabla \cdot \rho(\mathbf{r}, t) \int d\mathbf{r}' \left[\nabla V(|\mathbf{r} - \mathbf{r}'|) \right] \rho(\mathbf{r}', t) \, g(\mathbf{r}, \mathbf{r}', t) \right], \end{aligned} \tag{20}$$

where ∇ is the gradient operator with respect to $\mathbf{r}$. There are two terms to be distinguished on the right hand-side : the first term between the square brackets describes the effect of Brownian motion, while the second term represents the effects of direct interactions. The combination,

$$\mathbf{F}^{Int}(\mathbf{r},t) \equiv -\int d\mathbf{r}' \left[\nabla V(|\,\mathbf{r}-\mathbf{r}'\,|)\right] \rho(\mathbf{r}',t)\, g(\mathbf{r},\mathbf{r}',t)\,, \tag{21}$$

is the direct force on a colloidal particle at $\mathbf{r}$ due to particles in a volume element with position $\mathbf{r}'$, averaged with respect to the position of the latter. We will come back to the role of these two contributions in rendering the system unstable in the next subsection. Consider the initial stage of the phase separation, where the change $\delta\rho$ of the macroscopic density, as defined in eq.(3), is small. Let δg denote the accompanied change of the pair-correlation function,

$$g(\mathbf{r},\mathbf{r}',t) \;=\; g_0(|\,\mathbf{r}-\mathbf{r}'\,|) \;+\; \delta g(\mathbf{r},\mathbf{r}',t)\,. \tag{22}$$

Here, g_0 is the pair-correlation function after the quench, before phase separation occurred. Linearization of the Smoluchowski equation (20) with respect to these changes yields,

$$\begin{aligned}\frac{\partial}{\partial t}\delta\rho(\mathbf{r},t) \;&=\; D_0\,[\,\nabla^2\delta\rho(\mathbf{r},t) + \beta\bar{\rho}\nabla\cdot\int d\mathbf{r}'\left[\nabla V(|\,\mathbf{r}-\mathbf{r}'\,|)\right]\\ &\qquad\times\left(\delta\rho(\mathbf{r}',t)\,g_0(|\,\mathbf{r}-\mathbf{r}'\,|) + \bar{\rho}\,\delta g(\mathbf{r},\mathbf{r}',t)\right)\,]\;.\end{aligned} \tag{23}$$

To obtain a closed equation for $\delta\rho$, the change δg of the pair-correlation function must be expressed in terms of $\delta\rho$. Such a *closure relation* may be obtained as follows. The important feature is that the pair-correlation function in the integral in the Smoluchowski equation (23) is multiplied by the pair-force $\nabla V(|\,\mathbf{r}-\mathbf{r}'\,|)$, so that a closure relation is only needed for small distances $|\,\mathbf{r}-\mathbf{r}'\,| \leq R_V$, with R_V the range of the pair-interaction potential. Correlations over such small distances establish much faster than the demixing rates of the very long unstable wavelengths, simply because it takes more time to displace colloidal particles over larger distances. On a coarsened time scale that is much larger than relaxation times of density fluctuations with wavevectors $k \geq 2\pi/R_V$, but which still resolves the phase separation process, the pair-correlation function in the integral in the Smoluchowski equation may therefore be replaced by the equilibrium pair-correlation function. This is the statistical equivalent of the thermodynamic local equilibrium assumption made in the Cahn-Hilliard approach as described in the previous subsection, see therefore also Fig. reflocaleq. The equilibrium pair-correlation function is to be evaluated at the instantaneous macroscopic density in between the positions $\mathbf{r}$ and $\mathbf{r}'$. Hence, to first order in $\delta\rho$, and for $|\,\mathbf{r}-\mathbf{r}'\,| \leq R_V$,

$$\delta g(\mathbf{r},\mathbf{r}',t) = \delta g^{eq}(|\,\mathbf{r}-\mathbf{r}'\,|)\Big|_{density=\rho(\frac{\mathbf{r}+\mathbf{r}'}{2},t)} = \frac{dg^{eq}(|\,\mathbf{r}-\mathbf{r}'\,|)}{d\bar{\rho}}\,\delta\rho(\tfrac{\mathbf{r}+\mathbf{r}'}{2},t)\,, \tag{24}$$

and,

$$g_0(|\,\mathbf{r}-\mathbf{r}'\,|) \;=\; g^{eq}(|\,\mathbf{r}-\mathbf{r}'\,|)\,, \tag{25}$$

where g^{eq} is the equilibrium pair-correlation function for a homogeneous system with density $\bar{\rho}$ and the temperature after the quench. The two relations (24,25) are certainly

wrong for distances $\mid \mathbf{r} - \mathbf{r}' \mid$ comparable to the wavelengths of the unstable density variations. For such distances the system is far out of equilibrium. The validity of the relations (24,25) is limited to small distances, where $\mid \mathbf{r} - \mathbf{r}' \mid \leq R_V$. Substitution of eqs.(24,25) into the Smoluchowski equation (27), renaming $\mathbf{R} = \mathbf{r} - \mathbf{r}'$, yields,

$$\frac{\partial}{\partial t}\delta\rho(\mathbf{r},t) = D_0 \left[\nabla^2\delta\rho(\mathbf{r},t) + \beta\bar{\rho}\nabla \cdot \int d\mathbf{R}\,[\nabla_R V(R)] \times \left(g^{eq}(R)\,\delta\rho(\mathbf{r}-\mathbf{R},t) + \bar{\rho}\frac{dg^{eq}(R)}{d\bar{\rho}}\,\delta\rho(\mathbf{r}-\tfrac{1}{2}\mathbf{R},t)\right)\right], \tag{26}$$

with ∇_R the gradient operator with respect to $\mathbf{R}$. This equation of motion can now be Fourier transformed to yield,

$$\frac{\partial}{\partial t}\delta\rho(\mathbf{k},t) = -D^{eff}(k)\,k^2\,\delta\rho(\mathbf{k},t)\,, \tag{27}$$

where the effective diffusion coefficient is given by,

$$D^{eff}(k) = D_0\left[1 + 2\pi\beta\bar{\rho}\int_0^\infty dR\,R^3\,\frac{dV(R)}{dR} \times \left(2\,g^{eq}(R)\,j(kR) + \bar{\rho}\frac{dg^{eq}(R)}{d\bar{\rho}}\,j(\tfrac{1}{2}kR)\right)\right]. \tag{28}$$

The j-function is equal to,

$$j(x) = \frac{x\,\cos\{x\} - \sin\{x\}}{x^3}\,. \tag{29}$$

The equation of motion (27) is formally identical to the Cahn-Hilliard equation of motion (10), and its solution is given by eq.(11). The effective diffusion coefficient (28) may seem different from the Cahn-Hilliard diffusion coefficient (12) on first sight. However, since in the integrand in eq.(28) the factor $dV(R)/dR$ limits the integration range effectively to values $R \leq R_V$, and the wavevectors of interest are those for which $kR_V \ll 1$, the j-functions may be expanded up to quadratic order of their argument. Taylor expansion of the sine and cosine functions in eq.(29) gives, $j(x) = -1/3 + x^2/30 + O(x^4)$, so that the diffusion coefficient (28) is equal to,

$$D^{eff}(k) = D_0\beta\left[\frac{d\Pi}{d\bar{\rho}} + \Sigma\,k^2\right], \tag{30}$$

up to terms of order $D_0(kR_V)^4$, where,

$$\Pi = \bar{\rho}\,k_BT - \frac{2\pi}{3}\,\bar{\rho}^2\int_0^\infty dR\,R^3\,\frac{dV(R)}{dR}\,g^{eq}(R)\,, \tag{31}$$

and,

$$\Sigma = \frac{2\pi}{15}\,\bar{\rho}\int_0^\infty dR\,R^5\,\frac{dV(R)}{dR}\left(g^{eq}(R) + \frac{1}{8}\,\bar{\rho}\,\frac{dg^{eq}(R)}{d\bar{\rho}}\right). \tag{32}$$

The expression in eq.(31) for Π is precisely the osmotic pressure. Comparison of eq.(30) for the effective diffusion coefficient with the Cahn-Hilliard expression (12) identifies,

$$\left.\begin{array}{rcl} D\,a_2 &=& D_0\,\beta\,\frac{d\Pi}{d\bar{\rho}}\,, \\ D\,\kappa &=& D_0\,\beta\,\Sigma\,. \end{array}\right\} \tag{33}$$

Using that $d\Pi/d\bar{\rho} = \bar{\rho}\,d\mu/d\bar{\rho}$, and $a_2 = d\mu/d\bar{\rho}$ (see eq.(13)), with μ the chemical potential of the colloidal particles, the first of these equation reduces to,

$$D/D_0 \;=\; \beta\,\bar{\rho}\,. \tag{34}$$

This identifies the transport coefficient D in the Cahn-Hilliard theory. The second of the above equations, together with the expression (32) for Σ, identifies the Cahn-Hilliard square gradient coefficient κ in terms of the microscopic quantities $V(R)$ and $g^{eq}(R)$. Needless to say that this identification is approximate, since the closure relation used here is approximate. Note that eq.(15) for the wavevector of the most rapidly growing sinusoidal density component can be written as,

$$k_m \;=\; \sqrt{-\frac{d\Pi}{d\bar{\rho}}\,/\,2\Sigma}\,. \tag{35}$$

A deeper quench, where $-\beta d\Pi/d\bar{\rho}$ is relatively large, results in larger value for k_m.

3.3 Some Final Remarks on Initial Decomposition Kinetics

There are a few subtleties involved in the approximations made in the two approaches. First of all, *when a system is quenched close to the spinodal, the linearized theory fails.* The reason for this is that close to the spinodal, where $\beta d\Pi/d\bar{\rho}$ is small, the linear contribution $D_0\beta\,(d\Pi/d\bar{\rho})\,\delta\rho(\mathbf{r},t)$ is no longer dominant over higher order contributions in $\delta\rho(\mathbf{r},t)$, even in the initial stage of the phase separation. For such shallow quenches, nonlinear terms in the equation of motion for the density are important in the early stage of the phase separation.

A second point is the identification of the pair-correlation function g_0 with the equilibrium pair-correlation function at time $t = 0$ when the system became unstable but before significant phase separation occurred. This can only be done to within errors of the order $\delta\rho(\mathbf{r},t=0)/\bar{\rho}$. *The equations of motion are therefore only appropriate when* $\delta\rho(\mathbf{r},t) \gg \delta\rho(\mathbf{r},t=0)$. It may happen, depending on the kind of system under consideration, that this requirement is already outside the range of density changes where linearization is allowed. The amplitudes of equilibrium fluctuations of the density are then so large that linearization is never allowed. For such systems and quenches there is no linear demixing regime.

It should be noted that eq.(7) for the number density flux of colloidal particles in the Cahn-Hilliard approach assumes that no coupling with other volume elements occurs.[17],[18] To account for *non-local* effects, one might generalize eq.(7) to,

$$\mathbf{j}(\mathbf{r},t) \;=\; -\int d\mathbf{r}'\,D(\mathbf{r}-\mathbf{r}')\nabla'\mu(\mathbf{r}',t)\,. \tag{36}$$

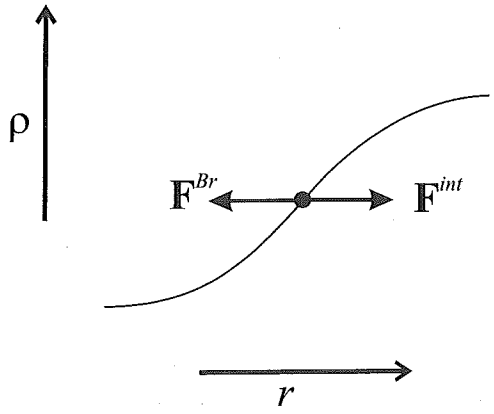


Fig. 9: *The direct and Brownian force on a colloidal particle, indicated by •, in an inhomogeneous system. For an attractive direct force, its direction is towards the region with larger concentration, as sketched here.*

For the special case that $D(\mathbf{r}-\mathbf{r}') = D\,\delta(\mathbf{r}-\mathbf{r}')$, with δ the 3-dimensional delta distribution, the local equation (7) is recovered. The Cahn-Hilliard analysis can be repeated with such a more general non-local diffusion flux, performing a partial integration, omitting the surface integral, and using the convolution theorem, to obtain the equation of motion (11) with,

$$D^{eff}(k) \;=\; D(k)\,\left[a_2 + \kappa\, k^2\right] \;. \tag{37}$$

Little can be said about the wavevector dependence of the effective diffusion coefficient without a microscopic model. The Smoluchowski equation approach shows that with the neglect of hydrodynamic interaction, the local diffusion assumption (7) is correct. For colloidal systems it is therefore expected that the wavevector dependence of the effective diffusion coefficient is simply a linear function of k^2.
It is important to realize that *the Cahn-Hilliard type of approach applies to the initial and intermediate stages only.* Only the leading term in an expansion of the free energy with respect to density gradients is taken into account. In the transition and late stage, where large density gradients exist, higher order terms in such an expansion are certainly important.[19],[20]

The mechanism that renders a system unstable

To understand on a microscopic level why a system can become thermodynamically unstable, let us rewrite the Smoluchowski equation (20) as,

$$\frac{\partial}{\partial t}\,\delta\rho(\mathbf{r},t) \;=\; -M\,\nabla\cdot\rho(\mathbf{r},t)\,\left[\mathbf{F}^{Br}(\mathbf{r},t) + \mathbf{F}^{Int}(\mathbf{r},t)\right] \;, \tag{38}$$

where $\mathbf{F}^{Int}$ is the direct force (21) and,

$$\mathbf{F}^{Br}(\mathbf{r},t) \;=\; -k_B T\,\nabla \ln\{\rho(\mathbf{r},t)\} \,, \tag{39}$$

is the Brownian force on a colloidal particle at the position $\mathbf{r}$. Furthermore,

$M = \beta D_0$ is a "mobility". Now consider a colloidal particle at $\mathbf{r}$ in an inhomogeneous environment, as sketched in Fig.9. The inhomogeneous macroscopic density may be thought of as an instantaneous realization of the fluctuating density. A little thought shows that the Brownian force is always directed towards the region with lower concentration, as depicted in Fig.9. Now suppose that the pair-interaction potential is purely attractive. The direct force $\mathbf{F}^{Int}$ is then directed in the opposite direction, towards the region with a larger density, since in that region there are more neighbouring colloidal particles attracting the particle under consideration : this can also be seen formally from eq.(21) for the direct force, using a purely attractive pair-interaction potential. On lowering the temperature, the Brownian force diminishes, since that force is directly proportional to the temperature. The direct force, however, increases in magnitude, due to the fact that the pair-correlation function becomes more pronounced (to leading order in the density this follows from the expression $g = \exp\{-V/k_BT\}$, where $V < 0$ for an attractive pair-potential). At the temperature where $|\mathbf{F}^{Int}| > |\mathbf{F}^{Br}|$, the net force on the colloidal particle is directed towards the region with a larger density. This is the mechanism that is responsible for *uphill diffusion*, and leads to phase separation. The pair-potential is never purely attractive for real systems since there is always a hard-core repulsion, and there is a competition between the repulsive and attractive components of the direct force. For large densities one can imagine that hard-core repulsion becomes dominant, leading to stabilization. This causes the spinodal to shift to smaller temperatures on increasing the density at sufficiently large concentrations. At smaller concentrations the attractive force can be dominant, leading to an increase of the spinodal temperature on increasing the concentration.
Clearly, the pair-interaction potential must have an attractive component to give rise to a gas-liquid spinodal. For temperature independent pair-potentials the critical point is *an upper critical point*, meaning that the critical temperature is larger than spinodal temperatures. When the pair-potential is temperature dependent, the system may have *a lower critical point*, in which case the standard phase diagram in Fig. 2 is upside-down.

3.4 Experiments on spinodal decomposition

Both theories on the initial stage of the spinodal decomposition we have treated here predict an exponential growth of density fluctuations of sufficiently long wavevectors (eq.(11)). The amplification factor and the wavevector of the most rapidly growing density fluctuation, $k_{m,0}$, are independent of time. Since both theories are linearized to first order in the density fluctuation, they describe only the initial stage of spinodal decomposition. Therefore, $k_{m,0}$ is expected to shift in the intermediate state of the phase separation. From eqs. (11,12) we know that in the linear regime plots of $\ln\{S(\mathbf{k},t)\}/\mathbf{k}^2$ versus k^2 should be straight lines with a slope equal to $D\kappa = D_0\beta\Sigma$ and an intercept $Da_2 = D_0\beta d\Pi/d\bar{\rho}$. As discussed in subsection 3.3, no such linear k^2-dependence of these so-called *Cahn-Hilliard plots* is observed when non-local diffusion occurs (see eq.(37)). Such non-local diffusion, however, is not to be expected for colloidal systems.
Another signature for spinodal decomposition can be found in the morphology of the demixing fluid. Since in the unstable region every density fluctuation with a sufficiently large wavevector will grow, phase separation will occur throughout the sample. As a result one expects to find highly interconnected domains of low and high densities.
The position of the wavevector of the most rapidly growing density wave and the rate

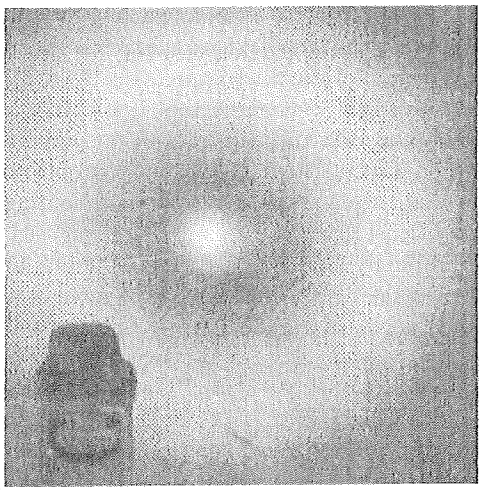


Fig. 10: *A photograph of a typical SALS experiment on a spinodally decomposing sample.*

at which the domains are growing is, in the case of colloidal systems, best measured by using Small Angle Light Scattering (SALS). It can be shown that the intensity of the light scattered by a demixing suspension of identical spheres can be written as

$$I \sim \frac{1}{N} <|\delta\rho(\mathbf{k},t)|^2>_{init} \quad , \quad for \;\; kR_V \ll 1, \tag{40}$$

and thus depends on the wavevector belonging to the density fluctuations. A typical light scattering experiment is shown in Fig.10, where a photograph is taken of the ring-like scattering pattern with on the foreground the cuvette containing the spinodally decomposing sample.
In Fig.11 two experiments on model colloidal systems are shown where the intensity of the scattered light is plotted as a function of the wavevector k (or q, respectively). One system (Fig.11a) contains a mixture of very small silica particles ($r = 10nm$) with Polydimethylsiloxane (PDMS) as a depletion agent. The other system (Fig.11b) is the dispersion of polymer-grafted silica particles in benzene, of which the phase diagram has already been shown in Fig.5.
The expected linear regime, where k_m does not shift in time, is observed for the system with the coated spheres (Fig. 11b), but not for the colloid-polymer mixture (Fig. 11a), where k_m shifts to smaller scattering angles with time. Since the particles used in the latter experiment are much smaller than the coated silica particles, it is reasonable to assume that in the latter case the decomposition is so fast that a first meaningful measurement can be performed only beyond the initial stage.
The linear dependence of $\ln\{S(\mathbf{k},t)\}/kk^2t$ versus k^2 is difficult to test for the system of coated silica spheres, since this system is arrested in a gel state (see Fig. 5). Another problem with this system is that the sample has to be transferred from a bath with a high temperature to a bath with a low temperature in order to quench the system into the spinodal region. Since this process takes sometime the very first stage of the decomposition will be missed.

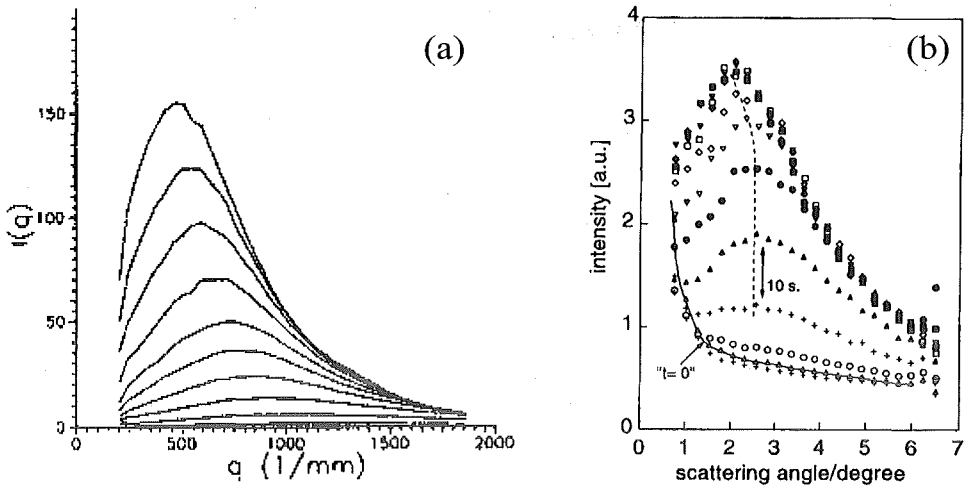


Fig. 11: *Sequences of scattering intensities as a function of the scattering angle for two phase separating colloidal dispersions. (a) a mixture of silica particles ($r = 10nm$) and polymer. The final time here is 18 s after homogenization of the sample (reprinted from [21]). (b) silica spheres ($r = 38nm$) coated with stearyl alcohol dissolved in benzene quenched to a temperature of T=15 °C (reprinted from [6]). Here the time laps between each of these curves is 10 s. The drawn line marks the instant at which long ranged correlations are fully developed. The vertical dashed line marks the intensity peak position.*

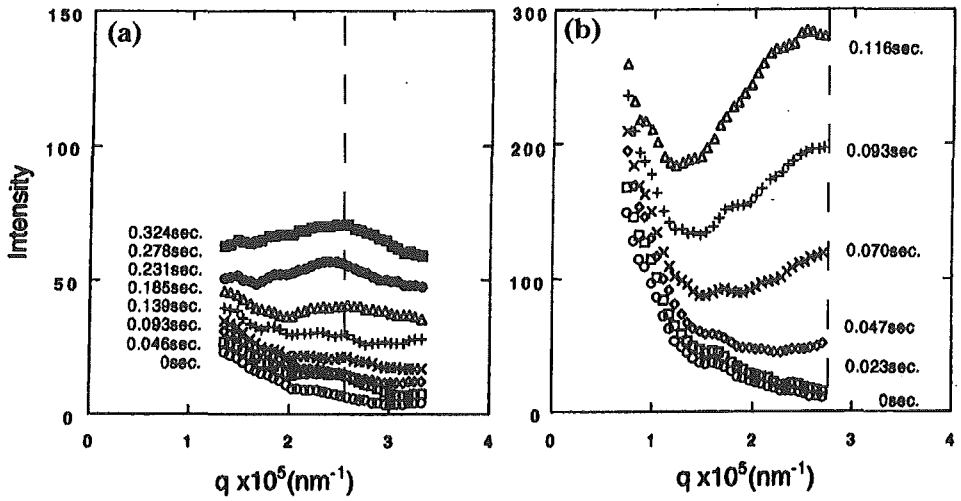


Fig. 12: *Sequences of scattering intensities as a function of the scattering angle during the early stage of a phase separating polymer solution after a pressure drop to* $P = 4.78MPa$ *(a) and* $4.67Mpa$ *(b) at* $T = 453.5K$. *Reprinted from [4].*

Kojima et al (1999) studied the early stage of spinodal decomposition of a polymer solution (polypropylene dissolved in trichlorofluormethane). This solution undergoes a gas-liquid phase transition when pressure jump is made from 4.90 MPa to 4.78 MPa or lower at a temperature of 453 K, depending on how deep the quench should be. The appealing feature of this system is that the quench can be made very fast, since it only involves a change of pressure. Therefore with this system one can excellently study the early stage of spinodal decomposition. In Fig.12 the growth of the structures are shown for a shallow and a deep quench. As predicted by eq.(15) the wavevector of the most rapidly growing density k_m is shifted to bigger wavevectors (so smaller structures) deepening the quench. It can also be seen from this graph that for the deeper quench k_m shifts to small k-vectors with time, indicating that the non-linear regime of spinodal decomposition is entered. With this system it is possible to test the linear dependence of $\ln\{S(\mathbf{k},t)\}/kk^2t$ versus k^2 (see Fig.13, where $R(q)$ corresponds with k^2D_{eff} in eq.(37)). From these plots it is now possible to get the effective diffusion coefficient D_{eff} and $d\Pi/d\bar{\rho}$, depending on the depth of the quench.

The second feature of spinodal decomposition that can be tested experimentally is the morphology of a decomposing sample. Experimental information on the morphology of the fluid can be obtained by (light) microscopy. One expects to find highly interconnected domains of low and high densities. These interconnected regions are indeed observed, as is shown in Fig.14. Here two micrographs are shown of the same colloid-polymer mixture as was used for Fig.11.The pictures are taken during phase separating, by a ordinary light microscope at two time instances after homogenesation.

The same kind of interconnected structures have also been observed for a totally different system namely for a $B_2O_3 - PbO - Al_2O_3$ glass after a quench from the melt into the unstable region. In Fig.15, a transmission electron micrograph is shown for this system.

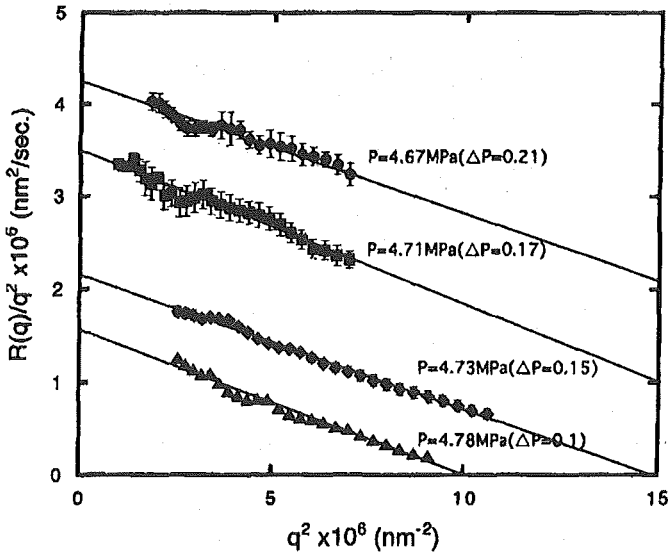


Fig. 13: *Spinodal decomposition of a polymer solution. Reprinted from [4].*

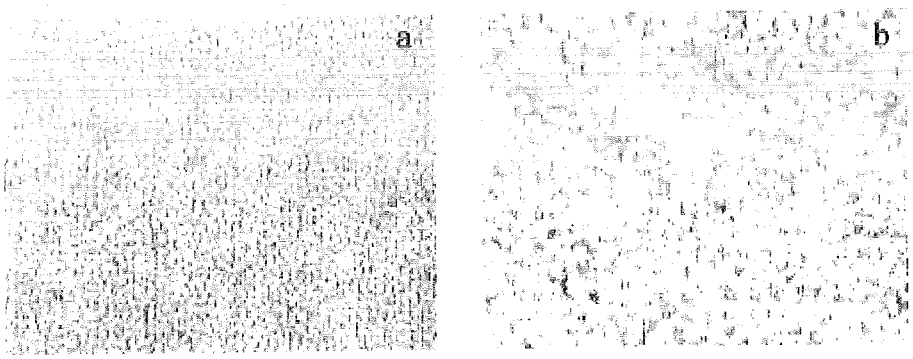


Fig. 14: *Micrographs of a colloid-polymer mixture undergoing spinodal decomposition which displays a typical bicontinuous network of dense and dilute phase. a) has been obtained 14 s after homogenization, b) has been obtained 25 s after homogenization. Reprinted from [21].*

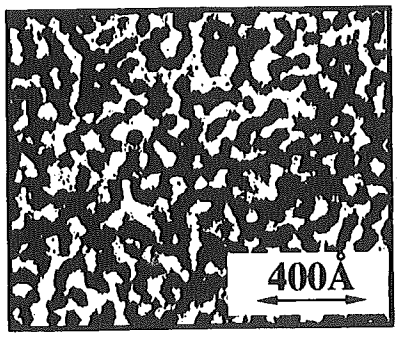


Fig. 15: *Transmission electron micrograph of a* $B_2O_3 - PbO - Al_2O_3$ *glass after a melt into the unstable region. Reprinted from [22].*

Again the interconnected structures are apparent.
One 'experimental' technique which we did not mention up till now is the use of computer simulations. Assuming a known interaction potential between particles, computer simulations can be very useful to study the early stages of spinodal decomposition. Without going into great detail we want to show two illustrative examples. Fig.16 shows the time dependence of the wavelength (1/wavevector) of the fastest growing fluctuation during spinodal decomposition in a three dimensional Lennart-Jones fluid. Note that k_m is time independent in the initial stage of the spinodal decomposition, as we expect from the theory.
The interconnected domains of low and high concentration, which we have discussed above are also observed in the same kind of simulations on spinodal decomposition of a Lennart-Jones fluid, but now in two dimensions (Fig.17). In this example, spinodal decomposition persists up to roughly $40 \times 10^{-12} s$. Thereafter wavegrowth and domain breakup take over. As has been made clear by the examples given in this section, spinodal decomposition is a phenomenon that can be observed throughout a wide range of fields. From atomic systems to polymer solutions. The last three examples have been taken from [7]. This book does not only contain a clear overview of the theory of phase separation kinetics, but also gives a nice survey of al kinds of phase separation processes.

4 Nucleation and growth

In section 2.2 we gave an intuitive picture of how a dispersion in a region will decompose into a phase of very low concentration and a phase of very high concentration (see also Fig.4). It was shown that a large deviation from the (local) equilibrium concentration is required before the stable phase first appears. The probability of such a large density fluctuation is (very) small, since it has to overcome an energy barrier similar to the one depicted in Fig.4. Therefore, these fluctuations are local and occur only after some induction time, typical for a thermally activated process. The small region where a much higher density appears is referred to as a nucleus. This nucleus often has a crystalline ordering and the resulting stable state is a crystalline phase. The nucleus will start to grow only if its size exceeds a critical value r_{crit}, which is connected to the height of the energy

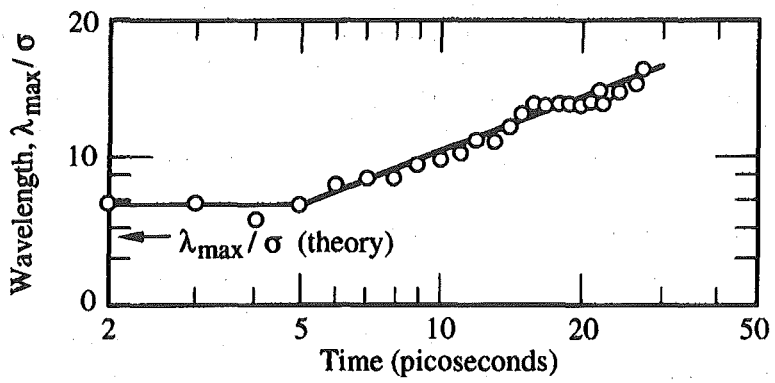


Fig. 16: *Timedependence of the wavelength of the fastest growing density fluctuation (λ_m) during a molecular dynamics simulation of isothermal liquid-vapor spinodal decomposition in the three dimensional Lennard-Jones fluid ($kT/\epsilon = 0.8, \rho(\mathbf{r},t)\sigma^3 = 0.35$). The theoretical value was calculated using Abraham's generalized theory ([14]) of spinodal decomposition. Reprinted from [23].*

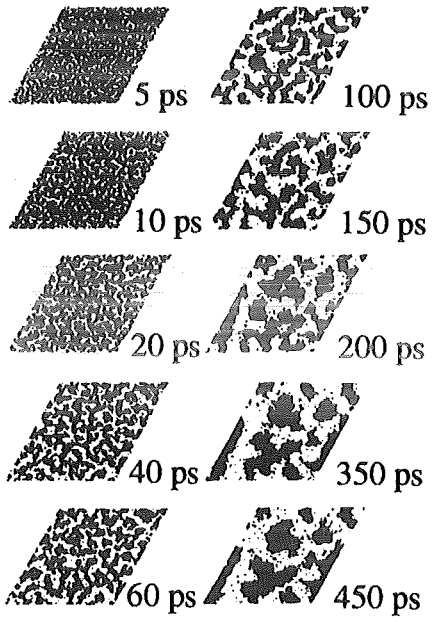


Fig. 17: *A molecular dynamics simulation of isothermal liquid-vapor spinodal decomposition in the two dimensional Lennard-Jones fluid ($kT/\epsilon = 0.45, \rho(\mathbf{r},t)\sigma^3 = 0.325$). Numbers indicate the time elapsed after the initiation of the isothermal simulation, in which atoms were placed on a triangular lattice. Reprinted from [24].*

barrier. If the size of the nucleus is too small it will re-dissolve. The energy barrier can be much lowered when impurities are present in the sample, for example at the surface of the container, which will result in *heterogeneous nucleation*. This section deals, however, with *homogeneous nucleation*, where nuclei appear *ad random* throughout the sample. First the theoretical foundations are discussed. Next, newly reported simulations on the nucleation rate of colloidal hard spheres are reviewed and compared with experiments.

4.1 Classical Nucleation Theory

The nucleation depends on two factors: $P_{\rm crit}$, the very low probability that a critical nucleus is formed, and κ, the very high rate at which the critical nuclei grow. According to the so called *Classical Nucleation Theory* (CNT, see [25] for a review) $P_{\rm crit}$ should depend exponentially on the free energy ΔG that is required to form the nucleus,

$$P_{\rm crit} = \exp\left(-\Delta G/k_B T\right) . \tag{41}$$

This free energy contains two competing parts: a decrease in bulk energy, which favors growth, and an increase in surface energy, which favors shrinking. The free energy of a spherical nucleus can therefore be written as,

$$\Delta G = 4\pi r^2 \gamma - \frac{4\pi}{3} r^3 \rho_s \Delta\mu , \tag{42}$$

where r is the radius, $\Delta\mu$ is the difference between the solid and liquid chemical potentials, and ρ_s is the number-density of the solid. Furthermore, γ is the solid-liquid interfacial free energy density, which is introduced in a similar way as it was for the Cahn-Hilliard theory for spinodal decomposition. It is important to note that the CNT makes the drastic approximation that a free energy can be attributed to a nucleus of just a few particles. In doing so it assigns the equilibrium pressure P_e to the bulk as well as the cluster being formed. We will come back to this later. The free energy is sketched in Fig.18.
The maximum in ΔG defines the size of the critical nucleus,

$$r_{\rm crit} = 2\gamma/(\rho_s \Delta\mu) , \tag{43}$$

and the height of the nucleation barrier,

$$\Delta G_{\rm crit} = \frac{16\pi}{3} \gamma^3/(\rho_s \Delta\mu)^2 . \tag{44}$$

The nucleation rate can now be written as,

$$I = \kappa \exp\left[-\frac{16\pi}{3} \gamma^3/(\rho_s \Delta\mu)^2\right] . \tag{45}$$

Further progress can still be made when a gas-solid transition is considered. In this case the kinetic factor κ can be calculated on the basis of assumption that clusters grow or shrink via the attachment of single particles. This is a reasonable assumption, since particles in the gas phase can diffuse freely until they hit a cluster. For a liquid-solid

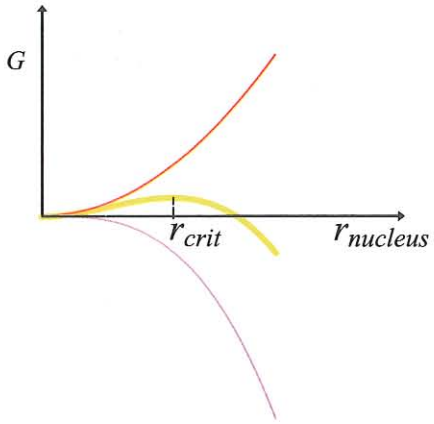


Fig. 18: *Surface (red line) and bulk (blue line) contributions to the free energy barrier for the formation of a nucleus (green line)*

phase transition collective modes of the diffusion may be of more importance for the formation and growth of a nucleus then single particle diffusion. Hence, for the liquid-solid transition, κ can not be elaborated further. More progress can also be made calculating the difference in the chemical potential, but again under the assumption that macroscopic thermodynamic properties may be applied on a cluster of very limited size.
Although eq.(45) contains the functional dependence of the nucleation rate on the relevant physical quantities, *a priori* knowledge of these quantities is needed to make quantitative predictions of the nucleation rate. To date there is no theory that provides 'first principles' predictions of nucleation rates. CNT can therefore only be used to analyze crystal nucleation experiments, with the unconstrained parameters adjusted to fit the observations. In the next subsection we will discuss simulations on the solid-liquid phase transition of hard-sphere colloidal particles. In this case the CNT only gives two fit parameters: κ and P_{crit}.

4.2 Simulations on nucleation and growth

In the last section the CNT was discussed, and its limitations in predicting quantitatively the nucleation rate of gas-solid or liquid-solid transitions. In this section we consider the results of computer simulations on a system of hard colloidal spheres as presented in a recent paper by Auer and Frenkel ([27]). Their simulations are a clear progress in predicting quantitative nucleation rates for various systems. In this case a system of hard colloidal spheres was chosen, since this system has been very well experimentally characterized, and the interaction potential of the particles under consideration is known. Using this potential as the most important input parameter for the simulations, they compute the shape and the height of the nucleation barrier (and therefore also P_{crit}) and the structure of the critical nucleus. In addition they performed kinetic Monte Carlo simulations to compute the kinetic prefactor κ. Thus, they were the first to make quantitative predictions of the nucleation rate.
The main trick of their work is that they used a biased Monte Carlo method. The

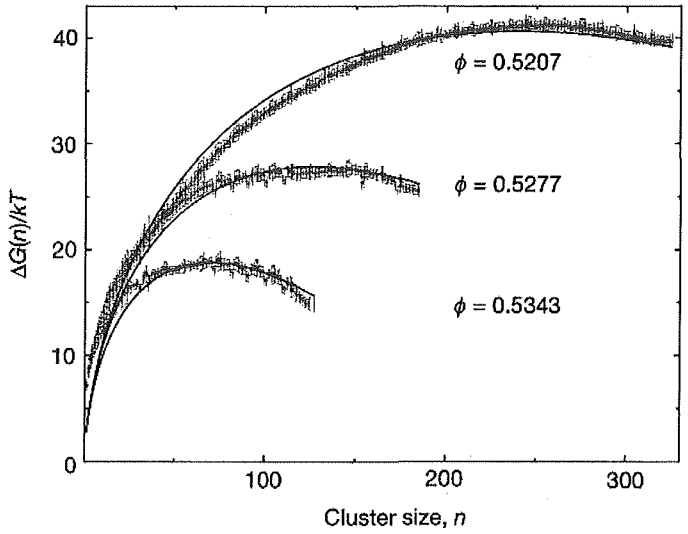


Fig. 19: *The free energy barrier for for homogeneous nucleation of hard-sphere colloids as calculated from bias Monte Carlo simulations. Reprinted from [27].*

nucleation barrier in an experimental system like a hard sphere dispersion, is typically in the order of 75 k_BT. This means that the probability of finding a cluster that has the critical size is extremely small, of the order of 10^{-30}. Hence, the numerical accuracy of any straight forward simulation where spontaneously formed clusters are counted will be very poor. One way to reduce the free energy barrier, which was used by Auer and Frenkel, is to add a well chosen fictitious potential to the real potential, sampling this new potential and correct afterwards for the bias. A non-trivial aspect of the computation is the criterion that identifies which particle is solid-like. In this case particles are counted as belonging to the same cluster when the interparticle distance is less then twice their radius. For gas-solid transitions this identification is easier since there the particle concentration in the surrounding of the nucleus is much lower then the concentration in the nucleus itself.

Fig. 19 shows the computed excess Gibbs free energy associated with the formation of a cluster containing n particles for three different concentrations, and thus also for three different pressures. These concentrations correspond with concentrations used in experiments. As with the Smoluchowski approach for the spinodal decomposition, no assumption of the surface energy γ needs to be made. γ is directly derived from the simulations by fitting the results with the CNT eq.(45). Values were found (in dimensionless parameters) between $\gamma = 0.70$ for $\phi = 0.527 (P = 15)$ to $\gamma = 0.75$ for $\phi = 0.534 (P = 17)$. The equilibrium surface energy equals $\gamma_e = 0.62$ (at ($P_e = 11.67$) see Hoover and Ree), as found by extrapolating γ to the equilibrium pressure. As mentioned earlier, CNT assumes that during nucleation the system is in equilibrium coexistence, with the corresponding pressure P_e *and* surface energy $\gamma = 0.62$. The difference between $\gamma_e = 0.62$, as used by CNT, and the surface energy at concentrations where experiments are performed, $\gamma = 0.75$, seems to be small. However, as $\Delta G \sim \gamma^3$ this difference in γ implies a factor 2 difference in terms of the free energy barrier, which means more than 5 orders of magni-

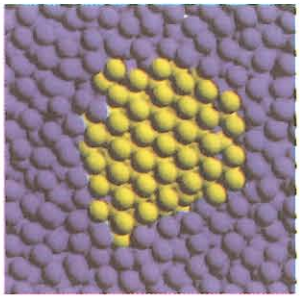


Fig. 20: *Snapshot of a cross-section of a critical nucleus of a hard-sphere crystal at a liquid volume fraction of $\phi = 5207$. Solid-like particles are shown in yellow, and liquid-like are shown in blue. The solid-like particles clearly show a f.c.c.-like stacking. Reprinted from [27].*

tude in the nucleation rate! The first parameter free nucleation rate can now be obtained by computing the kinetic prefactor with kinetic Monte Carlo simulations.
Another feature of the simulations is that the structure of the critical nucleus can be studied. Fig. 20 shows an example of a snapshot of a critical nucleus. The structure of the critical nucleus is of importance since it may influence the bulk crystal that will grow out of it. As mentioned earlier, CNT assumes that the critical nucleus has the same structure as as the resulting stable bulk phase. Ostwald, however, pointed out already in 1897 that the phase that nucleates need not to be the one that is thermodynamically stable.[28] Indeed, this is also observed with the simulations of Auer and Frenkel. The freshly nucleated crystals show a random hexagonal closed packing, which evaluated to a f.c.c.-like structure when the crystal grows. Thus the critical nucleus still has a metastable structure, before it changes to its final stable structure. This corresponds with the old 'step rule' of Ostwald.

4.3 Experiments on nucleation and growth

For molecular systems it is difficult to probe P_{crit}, because when a nucleus has formed it will immediately start growing towards the stable phase very fast. Colloidal systems, however, have the advantage that their dynamics is much slower. Another advantage is that the interaction potentials between the particles can be influenced by the choice of the surface (which can be grafted with polymers), solvent, and the addition of free polymers. They are therefore suited for fundamental research on nucleation and growth.
Nucleation rates have been measured in the past mainly using SALS (see e.g. [29]) and Bragg scattering (see e.g. [30],[31]). Since these techniques give direct ensemble averaged information on the size and amount of particles or clusters of particles in fourier space, it is a useful method for the determination of the nucleation rate. Scattering techniques however, do not give any inside on the morphology of a sample. Hence, the most direct way to experimentally test the results of the simulations as discussed in the last section is by imaging real space hard-sphere colloidal dispersions. The combination of fluorescently labeled particles [34] and Confocal Laser Scanning Microscope (CSLM) [?] has been already very fruitful for the study of random closed packings of particles

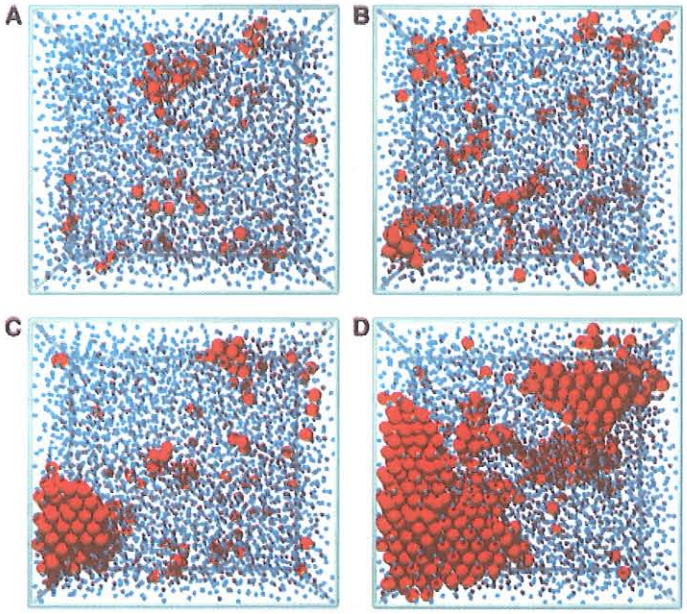


Fig. 21: *Four snapshots during crystallization of a sample with $\phi = 0.45$. The red spheres are drawn to scale and represent particles that were identified as crystal-like. The particles in the metastable liquid state are shown by the blue spheres, reduced in size for clarity. (A) Time $t = 20$ min after shear melting, (B) $t = 43$ min, (C) $t = 66$ min, and (D) $t = 89$ min. Reprinted from [36].*

[33] and stacking disorder in a colloidal crystals.[35] The speed with which the sample can be scanned has improved so much that it is now possible to do real-space imaging of the nucleation and growth in colloidal crystallization. Results of this experiment were presented recently by Gasser et al [36]. In Fig. 21 four snapshots are taken at different time -intervals after the sample was shear melted.

Again, as with the simulations, nuclei are identified, in this case by using an algorithm that finds ordered regions. Since the nuclei can be followed in time it can be observed how they grow and shrink. In accordance with CNT, it is observed that the smallest nuclei shrink far more frequently than they grow. Moreover, the critical nuclei can be identified by observing when the probability to grow exceeds the probability to shrink. Both experiment and simulation find that the critical nuclei are non-spherical, have a rough surface, and contain mainly random hexagonal closed packings. They also agree on the size of the critical nuclei, which contain between 60 and 160 particles.

The main contradiction between the simulation and the experiment is the value for the surface energy γ, which is, as we know from CNT, one of the most relevant parameters for nulceation and growth. They find a value that is about 4 times smaller than found from simulations, and even smaller than the value found from Bragg reflection experiments. Gasser et al calculate γ by examining the statistics of the smallest nuclei. When the nuclei are much smaller than the critical nuclei, the surface term in eq.(42) dominates the free energy of the crystallites. In this region the number of crystallites goes as $N(A) \propto$

$\exp[-A\gamma/(k_BT)]$, where A is the surface area, which is approximated with an ellipsoid, and thus γ can directly be determined. The discripancy may have to do with the roughness of the surfave and the way the surface is defined. Moreover, the particles where weakly charged, which influences the interaction potential.
In this section we have only considered simulations and experiments on liquid-solid transitions. Using dispersions with a low concentration of colloids but with polymers as depletion agents, a gas-solid phase transition can be induced.[37] The problem with that experiment is that the formed clusters start to sediment before nuclei are fully developed. A solution to this problem, which is being worked on to date is to do the experiment in space, as was done for hard sphere systems by Zhu et al.[31]

Appendices

A Functional derivatives

Functional differentiation is used in subsection 3.1 on the Cahn-Hilliard theory to derive an equation of motion for the density on the basis of thermodynamic arguments. The mathematical notion of functional differentiation is introduced in the present appendix, and in addition it is shown that the chemical potential in an inhomogeneous system is related to the functional derivative of the Helmholtz free energy.
A function is a prescription to associate a real (or complex) number to each element in the vector space $\Re^n$. Likewise, a *functional* is a prescription to associate a real (or complex) number to a function which belongs to some linear function space $\mathcal{F}$. In the sequel we shall not specify the function space $\mathcal{F}$ explicitly, but simply assume that the functions have properties, such as continuous differentiability, necessary to justify certain mathematical steps. A simple example of a functional is (with p an integer),

$$F[g(\mathbf{r})] = \int d\mathbf{r}'\, g^p(\mathbf{r}')\,.$$

For each function g defined on $\Re^3$, the integral yields generally a different real number. The functional F thus maps functions onto real numbers. One may ask for the change δF of the functional F as a result of a small change $\delta g(\mathbf{r})$ of the function g. The answer is easy : simply Taylor expand $(g+\delta g)^p = g^p + p\, g^{p-1}\,\delta g + O(\delta g^2)$, yielding, up to $O(\delta g^2)$,

$$\delta F \equiv F[g(\mathbf{r}) + \delta g(\mathbf{r})] - F[g(\mathbf{r})] = \int d\mathbf{r}'\, p\, g^{p-1}(\mathbf{r}')\,\delta g(\mathbf{r}')\,.$$

This is the first term in "the Taylor expansion of the functional" F. The function $p\, g^{p-1}$ is referred to as *the first order functional derivative* of F, which is more generally denoted as $\delta F[g]/\delta g(\mathbf{r})$, and is simply a function of $\mathbf{r}$. The concept of functional differentiation is easily extended to more complicated functionals of the form,

$$F[g(\mathbf{r})] = \int d\mathbf{r}'\, G(g(\mathbf{r}'))\,,$$

with G a differentiable function on $\Re$. Proceeding as above one immediately finds that,

$$\delta F = \int d\mathbf{r}'\, \frac{\delta F[g]}{\delta g(\mathbf{r}')}\delta g(\mathbf{r}')\,,$$

where the first order functional derivative is now equal to,

$$\frac{\delta F[g]}{\delta g(\mathbf{r})} = \frac{dG(g(\mathbf{r}))}{dg(\mathbf{r})} .$$

Things become a little bit more complicated when the functional involves integration over spatial derivatives. Consider for example the functional,

$$F[g(\mathbf{r})] = \int d\mathbf{r}' \, |\nabla g(\mathbf{r}')|^2 .$$

The functional (6) that is encountered in the Cahn-Hilliard theory contains such a contribution. To first order in δg it is found that,

$$\delta F = \int d\mathbf{r}' \, 2 \, [\nabla' g(\mathbf{r}')] \cdot [\nabla' \delta g(\mathbf{r}')] .$$

In order to find the first order functional derivative, the differentiation must be removed from δg. This can be done by applying Gauss's integral theorem, omitting the surface integral at infinity (the function space $\mathcal{F}$ is thus supposed to consist of functions which vanish at infinity fast enough to be able to omit such surface integrals). It is thus found that,

$$\delta F = -\int d\mathbf{r}' \, 2 \, [\nabla'^2 g(\mathbf{r}')] \delta g(\mathbf{r}') .$$

The first order derivative of this functional is thus equal to,

$$\frac{\delta F[g]}{\delta g(\mathbf{r})} = -2 \, \nabla^2 g(\mathbf{r}) .$$

You should now be able to reproduce eq.(8) for the functional derivative of the functional (6).
In eq.(8) we identified the local chemical potential $\mu(\mathbf{r}, t)$ with the first order functional derivative $\delta A[\rho]/\delta\rho(\mathbf{r}, t)$ of the Helmholtz free energy functional A. This can be understood on the basis of the thermodynamic relation,

$$\delta A = -\Pi \delta V - S\delta T + \mu \delta N ,$$

with Π the osmotic pressure and S the entropy. Here we are interested in changes of the free energy due to the change of the number of particles N, with fixed volume V and temperature T. For an inhomogeneous system, the total volume is subdivided into small volume elements, with fixed volumes $V = d\mathbf{r}'$ and fixed temperature, as was done in subsection 3.1 on the Cahn-Hilliard theory. A change δA of the free energy due to changes $\delta N = \delta dN(\mathbf{r}')$ of the number of particles $dN(\mathbf{r}')$ in volume elements with positions $\mathbf{r}'$, corresponding to a change $\delta\rho(\mathbf{r}') = \delta dN(\mathbf{r}')/d\mathbf{r}'$ of the density, is thus equal to,

$$\delta A = \int \mu(\mathbf{r}') \, \delta dN(\mathbf{r}') = \int d\mathbf{r}' \, \mu(\mathbf{r}') \delta\rho(\mathbf{r}') ,$$

where $\mu(\mathbf{r}')$ is not simply the chemical potential of a homogeneous system, but contains additional contributions relating to densities of neighbouring volume elements to account

for inhomogeneity, as discussed in subsection 3.1. From this equation we see that by definition,

$$\mu(\mathbf{r}) = \frac{\delta A[\rho]}{\delta \rho(\mathbf{r})} .$$

This is used in eq.(8) to express the chemical potential in terms of the density and its spatial derivatives.

B Small Angle Light Scattering by demixing suspensions

Here we give a brief explanation of how information on demixing suspension of identical spheres can be obtained from small angle light scattering. For further reading see Dhont (1996). The intensity I scattered by a suspension of identical spherical colloidal particles is equal to,

$$I = C^* P(k) \frac{1}{N} \sum_{i,j=1}^{N} < \exp\{i\mathbf{k} \cdot (\mathbf{r}_i - \mathbf{r}_j)\} > .$$

Here, C^* is a wavevector independent proportionality constant which is not affected by the demixing process. The *form factor* $P(k)$ describes the interference of electric field strengths scattered by volume elements within a single colloidal particle. The form factor is practically equal to 1 for wavevectors $ka < 1$, and may therefore be omitted. The last factor in the equation is the interesting quantity here. This factor describes interference of electric field strengths scattered by distinct colloidal particles. The ensemble averaging $< \cdots >$ is with respect to the position coordinates. The ensemble average will be denoted here by $S(k,t)$, the *static structure factor*, which is time dependent due to the ongoing phase separation. For identical colloidal particles we have,

$$\begin{aligned} S(k,t) &\equiv \frac{1}{N} \sum_{i,j=1}^{N} < \exp\{i\mathbf{k} \cdot (\mathbf{r}_i - \mathbf{r}_j)\} > \\ &= 1 + (N-1) \int d\mathbf{r}_1 \int d\mathbf{r}_2 \, P(\mathbf{r}_1, \mathbf{r}_2, t) \, \exp\{i\mathbf{k} \cdot (\mathbf{r}_1 - \mathbf{r}_2)\} \end{aligned}$$

This equation is connected to the density, using eq.(19) for the probability density function (pdf) $P(\mathbf{r}_1, \mathbf{r}_2, t)$ of the two position coordinates, together with eq.(17) that connects the single particle pdf with the macroscopic density, and introducing the *total-correlation function* $h = g - 1$.
Now, for large distances $|\mathbf{r}_1 - \mathbf{r}_2|$, the total-correlation function is small, since $h \to 0$ as $|\mathbf{r}_1 - \mathbf{r}_2| \to \infty$. The total-correlation function must therefore be retained only for distances equal to a few times the range R_V of the pair-interaction potential.[5] The remaining long ranged correlations give a small contribution and may be neglected. The exponential

[5]This is only true for inhomogeneous systems. For homogeneous systems, the 1 in $1 + h$ gives rise to a delta distribution in $\mathbf{k}$, which does not contribute at finite wavevectors.

function is almost constant on the length scale of a few times R_V for wavevectors with $kR_V \ll 1$, so that we arrive at the following expression for the scattered intensity,

$$\left.\begin{aligned} I &= C^* S(\mathbf{k},t)\,, \\ S(\mathbf{k},t) &= A(t) + \tfrac{1}{N} <|\delta\rho(\mathbf{k},t)|^2>_{init}\ ,\ \textit{for}\ \ kR_V \ll 1\,, \end{aligned}\right\}$$

where $A(t)$ is a wavevector independent "base line". These equations relate the scattered intensity to inhomogeneities of the macroscopic density.
Here it is assumed that the scattering volume is so large, that it contained many independent realizations of the initial macroscopic density before phase separation occurred : the average $< \cdots >_{init}$ is the ensemble average with respect to initial realizations of the density. Furthermore, $\rho(\mathbf{k},t)$ is replaced by $\delta\rho(\mathbf{k},t) = \rho(\mathbf{k},t) - \bar{\rho}$: the difference between $\rho(\mathbf{k},t)$ and $\delta\rho(\mathbf{k},t)$ is proportional to the delta distribution in $\mathbf{k}$, which is zero for non-zero wavevectors. A few approximations are made to arrive at these expressions, and in reality the "base line" $A(t)$ is weakly wavevector dependent. This weak wavevector dependence is insignificant for sufficiently developed inhomogeneities.
In section 3 on initial decomposition kinetics we have seen that small wavevector inhomogeneities develop, and as a result, the intensity of light scattered at the corresponding small scattering angles is enhanced. In the transition and late stage of the demixing process, where sharp interfaces come into play, the relevant scattered intensities extend up to much larger wavevectors, since the spatial variations of inhomogeneities are now no longer smooth on the length scale of a few times R_V.
The above formula for the scattered intensity is only valid at most up to wavevectors $kR_V < 1/2$, say, and does not describe structural changes on length scales comparable to the thickness of interfaces in the transition and final stages (except may be close to the critical point where the interfacial thickness is large). Formation of sharp interfaces and restructering do, however, affect the evolution of large scale structures, and for example do affect the time dependence of the scattered intensity at small scattering angles. The above equations for the scattered intensity can still be used to study interface formation and restructuring, but only in in an indirect way. Scattered intensities at larger wavevectors reflect in a more direct way the dynamics of interface formation and restructuring. For these larger wavevectors, short ranged correlations contribute to the wavevector dependence of the scattered intensity. Short ranged correlations must now be taking into account explicitly. Scattering by interfaces is a complicated problem that will not be considered here.

References

[1] P. R. ten Wolde, D. Frenkel, Nature **277**, (1997) 1975

[2] D. Rosenbaum, P. C. Zamora, C. F. Zukoski, Phys. Rev. Lett. (1996) 150

[3] R. Tuinier and C. G. de Kruif, J. Chem. Phys. **110** (1999) 9296

[4] J. Kojima, M. Takenaka, Y. Nakayama, T. Hashimoto, Macromolecules **32** (1999) 1809

[5] J. K. G. Dhont "An Introduction to Dynamics of Colloids" Elsevier, 1996.

[6] H. Verduin, J. K. G. Dhont, J. Colloid Interf. Sci. **172** (2) (1995) 425

[7] P. G. Debenedetti "Metastable Fluids. Concepts and principles" Princeton University Press, 1996.

[8] J.W. Cahn, J.E. Hilliard, J. Chem. Phys. **28** (1958) 258, **31** (1959) 688.

[9] M. Hillert, Acta Metallica **9** (1961) 525.

[10] J.W. Cahn, Acta Metallica **9** (1961) 795.

[11] J.W. Cahn, J. Chem. Phys. **42** (1965) 93.

[12] J.W. Cahn, Trans. Metall. Soc. Aime **242** (1968) 166.

[13] H.E Cook, Acta Metallica **18** (1970) 297.

[14] F. F. Araham, J. Chem. Phys. **64** (1976) 2660.

[15] J.K.G. Dhont, A.F.H. Duyndam, B.J. Ackerson, Physica A **189** (1992) 503.

[16] J.K.G. Dhont, A.F.H. Duyndam, B.J. Ackerson, Langmuir **8** (1992) 2907.

[17] P. Pincus, J. Chem. Phys. **75** (1981) 1996.

[18] K. Binder, J. Chem. Phys. **79** (1983) 6387.

[19] G. Porod (eds. O. Glatter, O. Kratky), Small Angle X-ray Scattering, Academic Press, London, 1982, page 30.

[20] H. Tomita, Prog. Theor. Phys. **72** (1984) 656, **75** (1986) 482.

[21] N. A. M. Verhaegh, J. S. van Duijneveldt, J. K. G. Dhont, H. N. W. Lekkerkerker, Physica A **230** (1996) 409

[22] J. Zarzycki, F. Nauin, J. Non-Cryst. Sol. **1** (1969) 215

[23] M. R. Mruzik, F. F. Abraham, G. M. Pound, J. Chem. Phys. bf 69 (1978) 3462.

[24] S. W. Koch, R. C. Desai, F. F. Abrahams, Phys. Rev. A **27**, (1983) 2152.

[25] D. W. Oxtoby, J. Phys.: Condens. Matter **4** (1992) 7627

[26] W. G. Hoover and F. H. Ree, J. Chem. Phys. bf 49, (1968), 3609

[27] S. Auer, D. Frenkel, Nature **409**, (2001) 1020

[28] W. Ostwald, Z. Phys. Chem. **22**, (1897), 289

[29] K. Schätzel, B. J. Ackerson, Phys. Rev. E. **48**, (1993) 3766

[30] J. L. Harland, W. van Megen, Phys. Rev. E. **53** (1997) 3054

[31] J. Zhu, M. Li, R. Rogers, W. Meyer, R. H. Ottewill, STS-73 Space Shuttle Crew, W. B. Russel, P. M. Chaikin, Nature **387** (1997) 883

[32] *Confocal Microscopy* (T. Wilson (ed.), Academic press, London (1990))

[33] A. van Blaaderen and P. Wiltzius, Science **270** (1995) 1177

[34] A. van Blaaderen and A. Vrij, Langmuir **8** (1992) 2921

[35] N. A. M. Verhaegh, J. S. van Duijneveldt, A. van Blaaderen, H. N. W. Lekkerkerker, J. Chem. Phys. **102** (1995) 1416

[36] U. Gasser, E. R. Weeks, A. Schofield, P. N. Pusey, D. A. Weitz, Science **292** (2001) 258

[37] E. A. H. de Hoog, W. K. Kegel, A. van Blaaderen,H. N. W. Lekkerkerker, Phys. Rev. E. bf 64, (2001) 021407

C 8 Rheology - Hydrodynamics of Complex Fluids

Walter Zimmermann

Theoretische Physik

Universität des Saarlandes

Contents

1 Introduction 2

2 Rheometry 5

3 Hydrodynamics of simple fluids 7
- 3.1 Equations of motion 7
- 3.2 Low Reynolds-number Hydrodynamics 10
- 3.3 Spherical particles in a Newtonian fluid 11
- 3.4 Pipeflow for a shear thinning fluid 19

4 Nematic liquid crystals 22

5 Polymer liquids 26
- 5.1 Linear Viscoelasticity - Maxwell Model 26
- 5.2 Nonlinear deformations of viscoelastic fluids 27
- 5.3 Single Polymer studies (useful for macroscopic modeling?) 28

A Derivation of the Oseen–Tensor 31

1 Introduction

Flows in the atmosphere, through pipes, around air plane wings, in rivers, etc. exhibit a great variety of fascinating phenomena and the related fluid motion may be rather complex. Motion of gases and fluids is induced by pressure differences, by shear gradients, by stirring or by temperature differences (heating) etc.. With the Navier–Stokes equation since the 19th century there is already a well established theoretical frame work available to describe the motion of simple fluids, such as water and olive oil etc.. Even in the era of powerful computers everybody knows about the limitations of the weather forecast and the predictability of the complexity of fluid motion, such as turbulence. Accordingly research on complex fluid motion attracts much of attention (not only) in the community of nonlinear science [26, 24].

This spring school focuses on physical properties of soft matter and most of the materials considered during all lectures belong to the category of *complex fluids*. Complex fluids exhibit a great variety of fluid phases and ordering phenomena. This complexity of structure and phases has its origin in competing interactions between different components. Examples of complex fluids are liquid crystalline phases, various colloidal orderings, flow induced orderings, membranes, biopolymers etc..

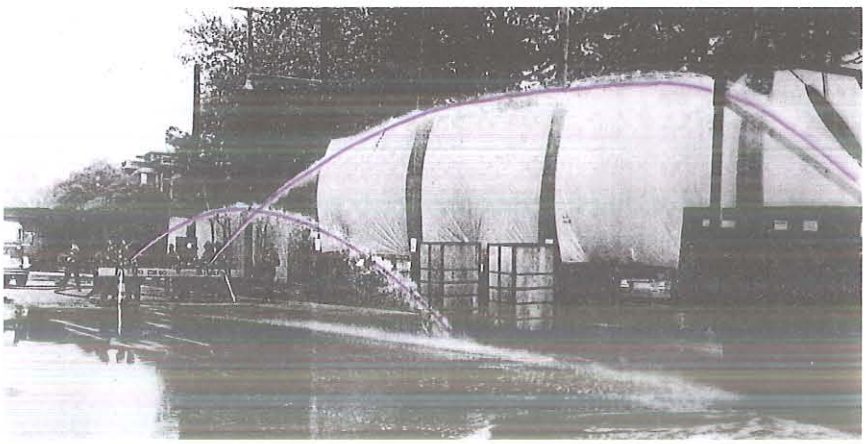


Fig. 1: *Demonstration of turbulent drag reduction with two fire hoses as an example for flow phenomena in viscoelastic fluids. Through fire hose (the left one) pure water is pumped and through the other one water containing* 0.003% *poly ethylene oxide (from Bailey & Koleske: Poly(Ethylene Oxide), Academic Press 1976).*

Complex motion, such as turbulence, occurs already in simple fluids. Fluid motion couples in complex fluids with various ordering phenomena and gives rise to a number of surprising flows. One of the most astonishing one is turbulent drag reduction as indicated in Fig. 1. Only a few ppm of polyethylene oxide added to water reduce the effective viscosity in a fire hose by a huge amount. As a consequence a jet of pure water leaves the fire hose much slower but under the same conditions, such as same pumping power, same fire hoses,

same inclination angle etc. than the jet of water including a few ppm poly-(ethylene) oxide. The mean velocity of turbulent flows through pipes may be enhanced by polymer additives up to a factor of ten. This effect of turbulent drag reduction is also used in the Trans Alaskan oil pipelines in order to save pumping power and in a Bristol sewer pipe. There are suggestions for explanations of this phenomenon, but a number of questions are left open and this problem is still a matter of current research. However, it seems rather obvious that the entropic elasticity of polymers plays a crucial role for this phenomenon. Further examples about viscoelastic flow effects may be found in volume I of Bird et al. [1].

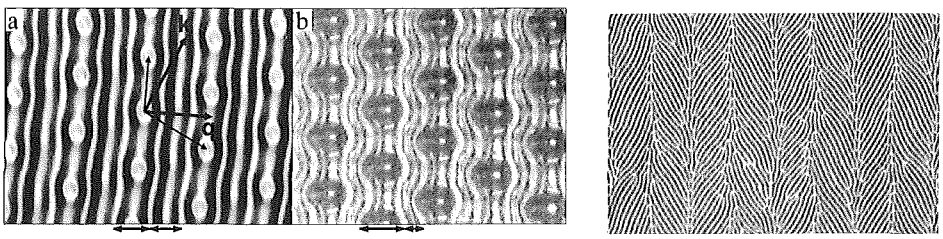


Fig. 2: *These are images of flow patterns occurring in electrically driven nematic liquid crystals. These patterns are observed in an experimental configuration which is rather similar to that of a liquid crystal display (LCD), a device which is used in many applications today. In nematic liquid crystals the viscosity is anisotropic. Nematics have also elastic properties and its interplay with flow leads to the numerous fascinating patterns in these materials, where more of them may be found in Refs. [6, 8, 9, 7, 10]. The pattern as shown in the left part has been understood only recently [11].*

The nonlinear relationship between flow rate and pressure drop for a laminar flow down a pipe (see e.g. Sec. 3.4) is another phenomenon of practical use non–Newtonian fluids. The nonlinear behavior is due to a viscosity which depends on the shear rate. The majority of complex fluids are shear thinning, i.e. their viscosities decrease with shear–rate, see e.g. Fig. 5. A few fluids shear thicken. The thinning is usually because some internal structure is broken down by the flow. Also elastic effects change the time–dependence of flows enormously. Another effect are normal stresses which play a role for instance in rod climbing of viscoelastic fluids, the so–called Weissenberg effect.

Polymers in solution may be considered as deformable suspensions. Undeformable suspensions are less related to elastic and memory effects as suspended polymers. But spherical suspensions change the steady state viscosity as discussed during this lecture. Ferrofluids are a further type of suspension, where the suspended particles carry a magnetic moment. The flow properties may depend on dipole-dipole interaction and viscosity may be varied by the strength of an applied magnetic field. More about ferrofluids may be found in [2, 3, 12]. In a similar manner the viscosity in electrorheological fluid, (where the particles carry a electric dipole) can be varied over a wide range by application of an electrical field [13].

Liquid crystals are examples of fluids with an internal, spontaneously broken symmetry.

Especially nematic liquid crystals are nearly omnipresent nowadays due to their applications in liquid crystal displays (**LCD**). Liquid crystals are switched by an applied voltage. In a quite similar configuration electrohydrodynamic instabilities and bifurcations occur, that lead to a huge variety of flow patterns. Two of them are shown in Fig. 2 and much more images of similar flow patterns, discovered and partially explained quite recently, may be found if Refs. [6, 8, 9, 7, 10, 15, 16]. Polymer melts and polymer solutions exhibit elastic effects which are related to the deformation of polymers and the entropic elasticity. In nematic liquid crystals elastic effects are related to their orientational order and this orientational elasticity is crucial for switching of liquid crystal displays.

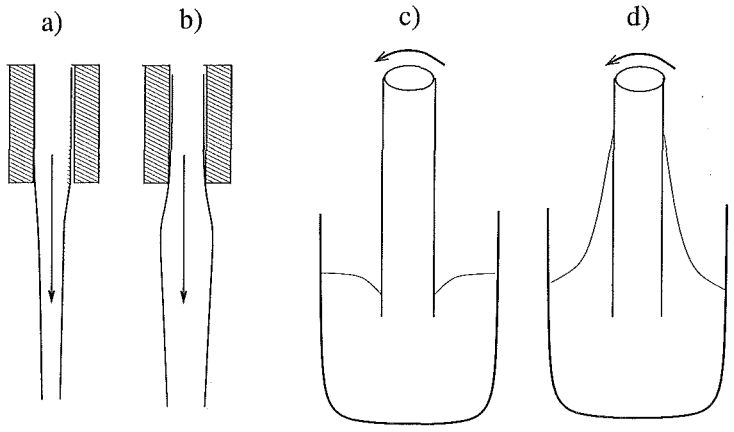


Fig. 3: *A Liquid emerging from a capillary: a) Newtonian liquid and in b) polymeric liquid, showing the die-swell effect. In c) and d) a rod is rotated in a Newtonian liquid in part c) and in a viscoelastic liquid in d). The rod climbing indicated in part d) is the so-called Weissenberg effect. The Weissenberg effect may be observed in a simple household experiment when one prepares pasta during stirring the pastry ("schwäbischer Spätzleteig ")*

Roughly speaking, rheology or hydrodynamics of complex fluids is a branch of research about the relevant laws and equations of motion of all these complex liquids. Are equations of motion at least for some liquids available which are of similar importance as the Navier–Stokes equation for simple (Newtonian) fluids? What are the relevant macroscopic degrees of freedom of each complex fluid which have to be taken into account in equations of motion? How can the relevant constants be measured which arise in the respective equations? Some of these questions are partially discussed, others are only touched in this lecture. The interesting field of rheology of granular materials, an active research area recently, is not considered.

Macroscopic material properties of fluids are described by viscosities and elasticities, but the number of material constants may change from material to material. Simple fluids are characterized by one viscosity, but nematic liquid crystals (having an additional orientational ordering), for instance, are characterized by five independent viscosities and

three elastic constants. On the other hand the viscosity of polymer melts and polymer solutions may also depend on the strength of the applied shear rate (shear thinning, shear thickening ...) or on the excitation frequency. Some techniques for measuring viscosities are described in more detail in lecture C9.

Hydrodynamics is a field theory like electrodynamics or the theory of elasticity (which is a part of hydrodynamics). The state of the system is described by space-time functions and their spatial and temporal variations describe the dynamics of the system. Conservation laws for mass, energy and momentum and the maximal entropy production build the basis for the structure of the equations of motion for simple fluids. For a complex fluid, such as nematic liquid crystals, those fundamental equations have to be supplemented by additional symmetry broken hydrodynamical variables etc.

2 Rheometry

One of the most relevant properties of a fluid is its viscosity. Fluids like honey and many organic fluids are called thick because of the high value of their viscosity. Water and gas are thin because of their low viscosity. Often the notion toughness (in German Zähigkeit) is used instead of viscosity. The viscosity obviously changes from fluid to fluid, but does the viscosity also depend on the flow type?

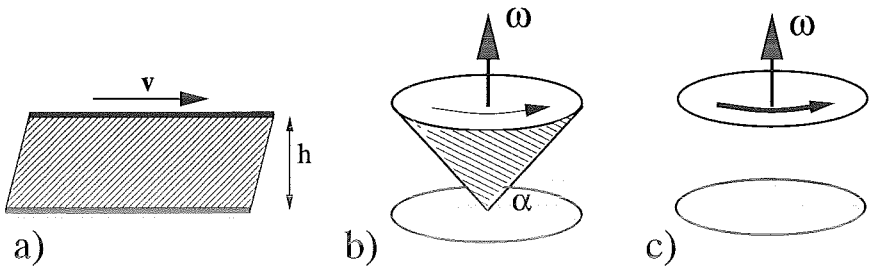


Fig. 4: *Shearing flows: a) sliding plate, b) cone and plate geometry, c) parallel disks (torsional flow)*

If in all three geometries shown in Fig. 4 the gap is filled with a fluid, one needs a force or a torque in order to move the upper plate or cone. For the sliding–plate device, the plane Couette flow, the shear rate $\dot{\gamma} = V/h$ is the ratio of the velocity V of the upper plate and the distance h of the two plates. In order to move the upper plate with V a force $\mathbf{F}$ has to be exerted. The required force F depends on the velocity and on the material. The ratio between this force and the area A of the plates is called *stress* σ

$$\sigma = \frac{F}{A}. \tag{1}$$

Stresses, some of which are defined below, have the dimension force per area ($[N/m^2]$). After applying a steady shear stress for a suitable time the relation between shear rate $\dot{\gamma}$

and shear stress $\sigma(\dot{\gamma})$ reaches a steady state. However, the steady state value may still depend on the shear rate $\dot{\gamma}$, depending on the material between the plates – as discussed below. The ratio between the steady shear stress σ and the shear rate $\dot{\gamma}$ is the *steady state* viscosity $\eta(\dot{\gamma})$

$$\eta = \frac{\sigma}{\dot{\gamma}}. \tag{2}$$

Obviously, the force needed to move the upper plate is higher for honey, than for water: The viscosity for honey is much larger than for a thin fluid such as water.

Oscillatory shear – Storage and Loss Moduli – Another way to explore material properties is to apply a *small–amplitude* oscillatory shearing. This kind of deformation of a fluid can be easily achieved in the cone–and–plate geometry, cf. Fig. 4, by rotating the cone about its axis with an angular velocity that oscillates sinusoidally, $\Omega(t) = \Omega_0 \cos(\omega t)$ (ω is the *frequency* of oscillation). The *shear rate* is then also a sinusoidal function of time $\dot{\gamma}(t) = \Omega/\tan\alpha = \Omega_0 \cos\omega t/\tan\alpha$. The ratio Ω_0/ω is the amplitude of the angular deflection of the cone, and $\gamma_0 = (\Omega_0/\omega)/\tan\alpha$ is the *strain amplitude* imposed on the fluid. In a plane Couette flow (cf. Fig. 4a)), the strain amplitude is the amplitude of the displacement of the sliding plate, divided by the gap.

For small enough strain amplitudes γ_0 (typically $\gamma_0 \ll 1$) the fluid structure is not much disturbed by the shear deformation and the stress measured during the deformation is controlled by rates of spontaneous rearrangements or *relaxations* to the equilibrium state. In a regime of small deformation amplitudes (linear regime) the shear stress $\sigma(t)$ and the applied strain $\gamma(t)$ are proportional to each other. For oscillatory shear both are sinusoidally but not necessary in phase. In general one has

$$\sigma(t) = \gamma_0 \left[G'(\omega)\, \sin(\omega t) + G''(\omega)\, \cos(\omega t)\right] \tag{3}$$

With this notion the contribution to $\sigma(t)$ proportional to $G'(\omega)$ is *in phase with the strain* and hence $G'(\omega)$ is called *storage modulus*. The term containing $G''(\omega)$ is *in phase with the rate of strain* $\dot{\gamma}$ and it is called the *loss modulus*. The storage modulus represents the storage of elastic energy, as it is typical for solids, whereas the loss modulus represents the viscous dissipation of that energy. The ratio G''/G' is high for *liquid-like* materials, but low for *solid-like*. The *complex modulus* $\bar{G}$ is defined by $\bar{G} = G' + iG''$ and the so-called *complex viscosity* is defined by $\eta' - i\eta'' = \bar{\eta} = \bar{G}(\omega)/(i\omega)$ with the magnitude of the viscosity $|\bar{G}(\omega)|/\omega$.
This regime of small amplitude straining (deformations) is called *the linear viscoelastic regime*. Such simple and small amplitude shear experiments with a typical strain amplitude $\gamma_0 = \dot{\gamma}/\omega \sim 0.1$ are possible over a wide range of frequencies $10^{-3}\, s^{-1}$ to $10^5\, s^{-1}$. This is a much wider range than achievable by steady shear rates. The high frequencies probe small scale structures in the fluid.

With modern computer controlled rheometers, other unsteady shear flows can be investigated. It is possible to switch on a stress and to measure the transient *creep*, or to switch off a stress and measure the transient *recoil*. Alternatively one can see the *build up* or *relaxation* of stress when a flow is switched on or off.

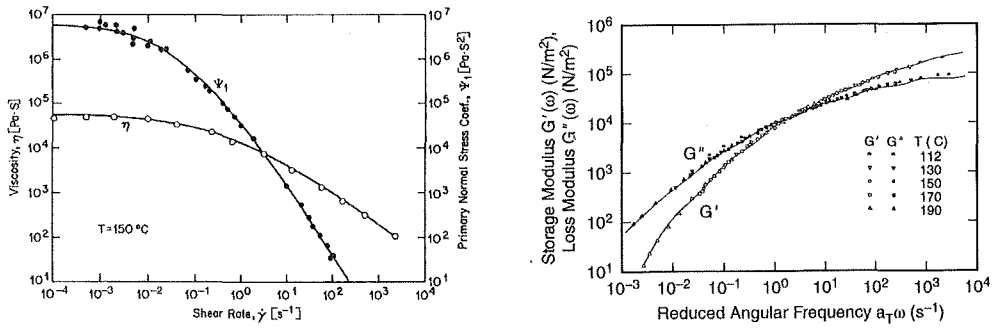


Fig. 5: *a) The steady state shear viscosity η and the first normal stress coefficient ψ_1 as function of the shear rate $\dot{\gamma}$. b) The storage modulus $G''(\omega)$ and the loss modulus $G'(\omega)$ as function of the reduced angular frequency $a_T\omega$ for a low density polyethylene melt.*

3 Hydrodynamics of simple fluids

Hydrodynamics of simple fluids, such as for water or olive oil, is a well established theory since the 19th century. The derivation of the equations of motion for simple fluids is based on conservation laws, such as for mass and momentum, simple linear transport laws for heat and the second law of thermodynamics. A detailed description of the basic equations may be found in many text books. For instance, a rather complete description is given in volume VI of the textbook series of Landau-Lifshitz [17] and from a different perspective in the book of Chaikin/Lubensky [5]. This latter approach may also be generalized to fluids with additional inner degrees of freedom, such as for liquid crystals. For the reader being interested in a qualitative description of classical fluid dynamics the book of Tritton [24] is appropriate.

Hydrodynamics is a field theory like electrodynamics and elasticity (which is part of hydrodynamics) that describes long wave length dynamics of condensed matter (long with respect to atomic or molecular scales) and classical fluid dynamics is a part of it.

3.1 Equations of motion

Hydrodynamics of simple fluids with a velocity field $\mathbf{u}(\mathbf{r},t)$ is described by five partial differential equations. A conservation law for mass density $\rho(\mathbf{r},t)$

$$\frac{\partial \rho}{\partial t} + \nabla \cdot (\rho \mathbf{u}) = 0\,, \tag{4}$$

the so–called continuity equation, and a second one for energy

$$\frac{\partial \varepsilon}{\partial t} + \nabla \cdot (\varepsilon \mathbf{u}) = \nabla \cdot (\kappa \nabla T)\,, \tag{5}$$

with the energy density $\varepsilon(\mathbf{r},t)$, the temperature distribution $T(\mathbf{r},t)$ and the thermal conductivity κ. In Eq. (5) energy is not only redistributed by mass motion but also by thermal conduction. Thermal conduction occurs either as a source or a sink (depending

on the slope of the temperature field) at the right hand side of Eq. (5). Since the entropy production is positive during dissipative processes the thermal conductivity $\kappa > 0$ must be positive.

According to Newton's law there are three equations for the momentum density $\mathbf{g}(\mathbf{r},t) = \rho(\mathbf{r},t)\,\mathbf{u}(\mathbf{r},t)$

$$\frac{\partial g_i}{\partial t} + (\mathbf{u}\nabla\cdot\nabla)\,g_i = -\nabla_i p + \nabla_j \sigma'_{ij} + f'_i\,, \tag{6}$$

and the right hand side includes the external volume forces which are the hydrostatic pressure gradient $\nabla_i p$, the divergence of the viscous stress tensor σ'_{ij} and a force per unit volume f'_i. The external forces f'_i per unit volume may be due to an electric field in charged fluids or due to gravitation.

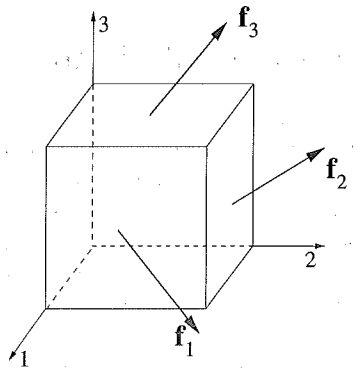


Fig. 6: *The force per area acting onto the plane perpendicular to the i-axis is* $\mathbf{f}_i = (\sigma_{i1}, \sigma_{i2}, \sigma_{i3})$. σ_{ii} *is the normal component and* σ_{ij} $(i \neq j)$ *are the force densities in the planes, similar as in the shear experiment shown in Fig. 4.*

The other forces are due to the interactions of a fluid element with the surrounding fluid elements and those are formally expressed in terms of a stress matrix σ_{ij} such as defined as follows. Consider a small volume element as shown in Fig. 6, with forces per area f_i acting on each surface. These forces form a stress tensor σ_{ij} and integrating the forces over the whole surface gives via Gauss's integral theorem

$$\oint_{\partial V} d\mathbf{f}_j \sigma_{ij} = \int_{\Delta V} dV\, \partial_j \sigma_{ij} = \Delta V\, \partial_j\, \sigma_{ij} \tag{7}$$

The stress σ'_{ij} due to the velocity differences between neighboring fluid elements can be obtained by separating the isotropic stress contribution, $-p\delta_{ij}$ from the total stress σ_{ij}. [1]

[1]The stress tensor of a fluid, σ'_{ij}, is only different from zero, if viscous friction occurs in a fluid. This is the case for non–vanishing velocity gradients, when different parts of the fluid move with different velocities. The leading order expansion of the stress tensor in term of the velocity gradients is

$$\sigma'_{ij} = \eta_{ijkl}\,\nabla_k u_l\,, \tag{8}$$

Eq.(6) is the so–called *Navier–Stokes equation* and the viscous stress–tensor σ'_{ij} is

$$\sigma'_{ij} = \eta\left(\nabla_i u_j + \nabla_j u_i - \frac{2}{3}\delta_{ij}(\nabla\mathbf{u})\right) + \zeta\delta_{ij}\nabla\mathbf{u}\,. \tag{12}$$

η is the shear viscosity and ζ the volume viscosity. The full stress tensor $\sigma_{ij} = -p\delta_{ij} + \sigma'_{ij}$ includes the pressure. For excitation frequencies far below that of sound waves most of the fluids are essentially incompressible

$$\nabla\cdot\mathbf{u}(\mathbf{r},t) = 0\,. \qquad \text{(condition for incompressibility)} \tag{13}$$

In this case the equation for the momentum density simplifies to

$$\rho\left(\frac{\partial u_i}{\partial t} + u_j\partial_j u_i\right) = -\partial_i p + \partial_j\sigma'_{ij} + f_i \tag{14}$$

and the stress tensor is given by

$$\sigma'_{ij} = \eta\dot{\gamma}_{ij}\,, \tag{15}$$

with the rate–of–strain tensor

$$\dot{\gamma}_{ij} = \partial_i u_j + \partial_j u_i\,. \tag{16}$$

Symmetry considerations, the laws of thermodynamics and an expansion of the transport laws up to the leading non–vanishing order lead to this form of the equations of motion for simple fluids with three positive phenomenological parameters: η, ζ and κ. These parameters may be measured for each material respectively. There are three further parameters in the thermodynamic equations of state relating T with p and ρ with ε.

The Operator $d/dt = +\partial/\partial t + \mathbf{u}\cdot\nabla$ is typical in hydrodynamics. This transport derivative (or "traveling equation") describes the phenomenon, that the temporal changes of any field at the location $\mathbf{r}$ do not only depend on the local temporal change of the field but also on the transport of each quantity through a point $\mathbf{r}$. All the equations above have the form of an local conservation law

$$\frac{\partial g_i}{\partial t} + (\mathbf{u}\cdot\nabla)g_i = -\nabla j_i^{(a)}\,. \tag{17}$$

Integrating this equation over a huge volume with the assumption that all current vanish at infinity, the conservation of mass, energy and momentum is recovered.

---

whereby the viscosity tensor η_{ijkl} is of fourth rank and it is the most general transformation between these two tensors σ'_{ij} and $\nabla_k u_l$. One may check that the entropy production due to the viscous dissipation is proportional to $\eta_{ijkl}\nabla_i u_j \nabla_k u_l$ and therefore the viscosity tensor must be invariant against the replacement $kl \to ij$. σ_{ij} must also vanish in the case of rigid rotation of the fluid (there is no viscous friction related). Therefore σ'_{ij} includes only symmetric combinations of the derivatives $\nabla_k u_i + \nabla_i u_k$, (the antisymmetric combinations describe rotations). Since σ'_{ij} must be symmetric the following identities must hold

$$\eta_{ijkl} = \eta_{klij} = \eta_{jikl} = \eta_{ijlk} = \eta_{jilk} \tag{9}$$

There are only two combinations of the Kronecker δ_{ij}

$$\delta_{ij}\delta_{kl} \qquad \text{and} \qquad \delta_{ik}\delta_{jl} + \delta_{il}\delta_{jk} \tag{10}$$

which fulfill this symmetry. Therefore the viscosity tensor includes two independent coefficients

$$\eta_{ijkl} = \eta\delta_{ij}\delta_{kl} + \zeta(\delta_{ik}\delta_{jl} + \delta_{il}\delta_{jk}) \tag{11}$$

Example: Plane Poiseuille flow – Poiseuille flow occurs between two parallel plates or through a pipe. For a fluid between two parallel plates located at $z = \pm d/2$ and parallel to the $x-y$ plane we assume a pressure gradient along the x-direction (linear pressure drop $\partial_x p = const.$) and accordingly, we expect a flow in x–direction $\mathbf{u} = (u_x, 0, 0)$. At the boundaries we assume stick boundary conditions $u_x(z = \pm d/2) = 0$ and therefore the only spatial dependence is along the z-axis. In such a stationary case $\partial_t \mathbf{u} = 0$ and also $(\mathbf{u} \cdot \nabla) = 0$. Hence only the equation $\eta \Delta u_x = \partial_x p = p_c$ is left. This is an ordinary differential equation of second order which may be solved by integration: $u_x(z) = \frac{z^2}{2}(\partial_x p)/\eta + Cz$. The problem is symmetric with respect to reflection $z \to -z$ and therefore $C = 0$. In order to fulfill the boundary conditions we have for the plane

$$u_x(z) = \frac{1}{2}\frac{p_c}{\eta}\left(z^2 - \left(\frac{d}{2}\right)^2\right) \tag{18}$$

induced by the linear pressure drop $p_c = \partial_x p$. This laminar flow is only preferred for small values of the so-called Reynolds number (see below).

3.2 Low Reynolds-number Hydrodynamics

The different terms in the Navier–Stokes equation can be very different in magnitude, depending on the special flow under consideration. The Navier-Stokes equation is nonlinear and may exhibit in many situations turbulence [25, 26]. Analytical solutions of (14) exist only for simple geometries, especially in the limit of small values of the dimensionless *Reynolds number Re*, which we introduce now. Eq. (14) includes essentially three relevant parameters: the *kinematic viscosity* $\nu = \eta/\rho$, a typical length scale l (often the dimension of the container or of an swimming object) and a typical flow velocity u_0.

$$[\nu] = \frac{m^2}{s}, \qquad [l] = m, \qquad \text{and} \qquad [u_0] = \frac{m}{s}. \tag{19}$$

These may be combined to the dimensionless Reynolds number

$$Re = \frac{u_0\, l}{\nu} = \frac{\rho\, u_0\, l}{\eta}, \tag{20}$$

which compares the inertia forces and the viscous ones. With $u = u_0\bar{u}$, $x_i = l x_i'$, $\bar{p} = p\, l/(\eta u_0)$ and a typical time $t_0 = l/u_0$ with $t = t_0\bar{t}$ one obtains after multiplication of (14) by $l^2/(\eta u_0)$

$$Re\left(\frac{\partial \bar{u}_i}{\partial \bar{t}} + \bar{u}_j \bar{\nabla}_j \bar{u}_i\right) = -\bar{\nabla}_i \bar{p} + \bar{\Delta}\bar{u}\,. \tag{21}$$

From this equation it is clear that the Reynolds number Re is the only parameter that indicates the importance of inertia relative to viscous forces. For two different fluids (for example with different viscosities) and two spheres with different radii in the same flow type the velocity $\mathbf{u}/u_0$ depends in both cases on $\mathbf{r}/l$ in the same manner, if the Reynolds number coincides. Flows which may be transformed into each other by such a similarity transformation are called similar fluids.

There are two flow regimes distinguishable: $Re \ll 1$ and $Re \gg 1$. Usually, a flow becomes turbulent beyond a critical value of Re that depends on the flow type. In the

range $Re \ll 1$, the term $Re(\mathbf{u} \cdot \nabla)\mathbf{u}$ can be neglected and equation (14) reduces in the stationary Stokes or *creeping–flow equation*, which is in dimensional form

$$-\nabla p + \eta \nabla^2 \mathbf{u} + \mathbf{f} = 0\,. \tag{22}$$

The creeping–flow equation is particularly useful in describing the flow around colloidal particles because in this case the characteristic length l occurring in the Reynolds number can be identified with the particle size. Even for a colloidal particle as large as 1 μm in water, assuming $\rho = 10^3$ kg m^{-3}, the Reynolds number approaches unity at velocities of about 1 ms^{-1}. Hence for colloidal particles the condition $Re \ll 1$ is almost always satisfied. It must be pointed out that even when the Reynolds number on the size of a colloidal particle is usually less than one, the Reynolds number based on some macroscopic dimension of the flow (e.g. the diameter of a tube) can be much larger than one. Even in turbulent flow, if the particle is smaller than the microscopic scale of turbulence, the local flow in the neighborhood of a colloidal particle is laminar even though the "distant" velocity it experiences is a fluctuating function of time. This is usually the case.

3.3 Spherical particles in a Newtonian fluid

In order to move a particle in a viscous fluid, a force must be applied. Particles with a higher density than the fluid sink for instance due to the gravitational force. The relation between the particle velocity and the applied force as well as the perturbation of the flow and the pressure field are calculated.

Every moving particle perturbs the flow field and this deformation influences the motion of other particles. This effect of hydrodynamic interaction between moving and rather far distant particle (with a next neighbor distance much larger than the diameter of the particles) is described by the so–called Oseen tensor, calculated in this section.

Particles in a local shear field rotate and this rotation perturbs the flow field too. This leads to a higher shear viscosity than for the fluid without particles.

Stokes law for a moving sphere – The force needed to pull a sphere with velocity $\mathbf{v}$ through a quiescent fluid of viscosity η is known as Stokes law (1851). This law and the determination of the induced flow and pressure field around the moving sphere is one of the standard problems in hydrodynamics. It is important for instance for sedimentation processes, Brownian motion and several other problems in colloid science.

At the surface ∂S of a moving sphere the fluid has the same velocity as the sphere (stick boundary conditions) and far away from the sphere the disturbance vanishes:

$$\mathbf{u}(\mathbf{r}) \to 0 \quad \text{for} \quad \mathbf{r} \to \infty \qquad \text{and} \qquad \mathbf{u}(\mathbf{r}) = \mathbf{v}, \quad \mathbf{r}\,\epsilon\,\partial S\,. \tag{23}$$

For incompressible fluids, $div\mathbf{u} = 0$, the flow field $\mathbf{u}(\mathbf{r})$ may be expressed in terms of the curl of a vector field $\mathbf{A}(\mathbf{r})$

$$\mathbf{u} = \nabla \times \mathbf{A}\,, \tag{24}$$

and in addition the identity $\nabla \times (\nabla \times \mathbf{u}) = \nabla(\nabla \cdot \mathbf{u}) - \nabla^2\mathbf{u}$ holds. Therefore equation (22) may be written in the form $-\nabla p - \eta\nabla \times (\nabla \times \mathbf{u}) + \mathbf{f} = 0$.

Since equation (22) is linear the vector field $\mathbf{A}$ must be a linear function of the velocity vector $\mathbf{v}$ of the sphere. Both $\mathbf{u}$ and $\mathbf{v}$ change their sign after inversion $\mathbf{r} \to -\mathbf{r}$. Therefore $\mathbf{A}$ must be invariant with respect to an inversion. This is possible with the representation $\mathbf{A} = (\nabla g(\mathbf{r})) \times \mathbf{v} = g'(\mathbf{n} \times \mathbf{v})$ and a scalar function $g(r)$. Thus we are arriving with $\mathbf{v} = const.$ at the following form of the velocity field of the fluid

$$\mathbf{u}(\mathbf{r}) = \nabla \times ([\nabla g(r)] \times \mathbf{v}) = \mathbf{v}\nabla^2 g(r) + (\mathbf{v} \cdot \nabla)\nabla g(r) . \tag{25}$$

Taking the curl $\nabla\times$ from Eq. (22) with $\mathbf{f} = \mathbf{0}$ for points outside the sphere, yields,

$$\nabla \times \nabla^2\mathbf{u}(\mathbf{r}) = \nabla^2 [\nabla \times (\nabla \times \mathbf{A}(\mathbf{r}))] = \nabla^2 \left[\nabla (\nabla \cdot A) - \nabla^2\mathbf{A}\right] = \mathbf{0} \tag{26}$$

Since

$$\nabla \cdot \mathbf{A}(\mathbf{r}) = \nabla \cdot (\nabla g(r) \times \mathbf{v}) = \mathbf{v} \cdot (\nabla \times \nabla g(r)) = 0 \tag{27}$$

equation (26) reduces to $\Delta^2\mathbf{A} = \mathbf{0}$. With $\mathbf{A} = \nabla g \times \mathbf{v}$ and a constant $\mathbf{v}$ this is equivalent with

$$\nabla\Delta^2 g(r) = \mathbf{0} . \tag{28}$$

A single integration gives $\Delta^2 g(r) = const.$. The flow field $\mathbf{u}$ tends to zero at infinity and $\mathbf{u}$ is related to second order derivatives of g. Therefore fourth order derivatives of g are zero at infinity and one has

$$\nabla^2\nabla^2 g(r) = 0 . \tag{29}$$

In the exterior of the sphere ($r > R$) the solution of the Laplace equation $\Delta\varphi = 0$ is $\varphi \propto 1/r$ and therefore one has with two constants c_0 and c_1

$$\nabla^2 g(r) = \frac{c_0}{r} + c_1 . \tag{30}$$

In order to obtain a vanishing flow velocity $u(\mathbf{r})$ at infinity, the constant $c_1 = 0$ has to vanish. Equation (30) with the inhomogeneity c_0/r is solved by $c_0 r/2$, because of $\nabla r = (\frac{1}{2}d/dr + d^2/dr^2)r = 2/r$. Finally the integration of (30) gives

$$g(r) = \frac{b}{r} + c_3 + ar + \frac{1}{6}c_4 r^2 . \tag{31}$$

c_3 is irrelevant because only derivatives of $g(r)$ contribute to $\mathbf{u}$. $c_4 = 0$ in order to fulfill $\mathbf{u}(r \to \infty) \to 0$. Hence one obtains after a few derivations of $g(\mathbf{r})$

$$\mathbf{u}(\mathbf{r}) = -a\frac{\mathbf{v} + \hat{\mathbf{r}}(\mathbf{v} \cdot \hat{\mathbf{r}})}{r} + b\frac{3\hat{\mathbf{r}}\,(\mathbf{v} \cdot \hat{\mathbf{r}}) - \mathbf{v}}{r^3} . \tag{32}$$

Taking the center of the sphere as the origin of the coordinate system, then the flow velocity at the surface of the sphere, $r = R$, must vanish

$$\mathbf{v}\left(1 - \frac{a}{R} - bR^3\right) + \hat{\mathbf{r}}\,(\mathbf{v} \cdot \hat{\mathbf{r}})\left(-\frac{a}{R} + \frac{3b}{R^3}\right) = 0 . \tag{33}$$

Since this equation holds for arbitrary $\hat{\mathbf{r}}$, each coefficient has to vanish separately. One obtains $a = 3R/4$ and $b = R^3/4$ and therefore [2]

$$g = \frac{3\,R\,r}{4} + \frac{R^3}{4r} \tag{34}$$

$$\mathbf{u}(\mathbf{r}) = -\frac{3R}{4}\,\frac{\mathbf{v} + \hat{\mathbf{r}}(\mathbf{v}\cdot\hat{\mathbf{r}})}{r} + \frac{R^3}{4}\,\frac{3\hat{\mathbf{r}}\,(\mathbf{v}\cdot\hat{\mathbf{r}}) - \mathbf{v}}{r^3} \tag{35}$$

With this expression for the velocity the pressure follows via equations (25) and (22)

$$\nabla p = \eta\Delta v = \eta\Delta\nabla\times\nabla\times(g\mathbf{v}) = \eta\Delta\left[\nabla(\nabla\cdot(g\mathbf{v})) - \mathbf{v}\Delta g\right] . \tag{36}$$

With $\Delta^2 g = 0$ the last term vanishes and integration of the first term gives

$$p = \eta(\mathbf{v}\cdot\nabla)\Delta g + p_0 , \tag{37}$$

where p_0 is the pressure at infinity. Taking the expression for $g(\mathbf{r})$ one obtains finally for the pressure

$$p = p_0 - \frac{3\eta}{2}\,\frac{\mathbf{v}\cdot\hat{\mathbf{r}}}{r^2}\,R . \tag{38}$$

With the expressions from above for the velocity and pressure around the sphere the stress tensor may be calculated at every surface element of the sphere and therefore the whole force $\mathbf{F}$ acting on the moving sphere. Spherical coordinates with the polar axis along $\mathbf{v}$ are again rather useful. According to the symmetry of the problem the stress tensor depends only on the distance r from the center of the sphere and the polar angle θ. The drag force acting on the sphere points obviously in the opposite direction of the velocity $\mathbf{v}$ and we are interested in the magnitude of $\mathbf{F}$

$$F = \oint (p\cos\theta - \sigma'_{rr}\cos\theta + \sigma'_{r\theta}\sin\theta)\,df . \tag{39}$$

With the components of the stress tensor in spherical coordinates

$$\sigma'_{rr} = 2\eta\,\frac{\partial v_r}{\partial r}, \qquad \sigma'_{r\theta} = \eta\left(\frac{1}{r}\frac{\partial v_r}{\partial\theta} + \frac{\partial v_\theta}{\partial r} - \frac{v_\theta}{r}\right) \tag{40}$$

and the velocity and pressure around the sphere one has at the surface of the sphere

$$\sigma'_{rr} = 0, \qquad \sigma'_{r\theta} = -\frac{3\eta}{2R}\,v\sin\theta , \qquad p = p_0 - \frac{3\eta v}{2R}\cos\theta . \tag{41}$$

[2] In spherical coordinates with the polar axis parallel to the direction of the motion of the sphere the components of the fluid velocity are

$$u_r = v\,\cos\Theta\left[1 - \frac{3\,R}{2r} + \frac{R^3}{2r^3}\right] ,$$

$$u_\theta = -v\,\sin\theta\left[1 - \frac{3\,R}{4r} - \frac{R^3}{4r^3}\right] .$$

Only the pressure contributes in the direction of $\mathbf{v}$ and one has

$$F = \frac{3\eta v}{2R} \oint df = 6\pi R\eta v \,. \tag{42}$$

This is the famous *Stokes formula* for the magnitude of a force needed in order to move a sphere of radius R slowly with velocity v in a viscous fluid. The resistance increases linearly with the flow velocity v and the size of the sphere. This dependence on the size and velocity could be expected even without an explicit calculation. Since the density ρ does not occur in the Stokes equation (22) the only combination of the rest of the parameters with the dimension of a force is $\eta v R$. [3]

With the Stokes formula one may also express the induced flow field $\mathbf{u}(\mathbf{r})$ in terms of the applied force $\mathbf{F}$

$$\mathbf{u}(\mathbf{r}) \;=\; -\frac{1}{8\pi\eta\, r}\left(\,\mathbf{1} + \hat{\mathbf{r}}\otimes\hat{\mathbf{r}} + \frac{R^2}{3\,r^2}\;(\mathbf{1} - 3\hat{\mathbf{r}}\otimes\hat{\mathbf{r}})\right)\mathbf{F}\,. \tag{43}$$

For large distances r compared to the radius of the sphere ($R/r << 1$) the second term is negligible. Hence at large distances there is no difference between the flow field $\mathbf{u}(\mathbf{r})$ induced by a sphere and a point force. The first term $\propto 1/r$ in (43) agrees with the so-called Oseen tensor discussed in the next paragraph and in appendix A.

Hydrodynamic interaction between point particles – Sufficiently far from a moving sphere, its effect on the fluid is the same as a point force $\delta(\mathbf{r})\mathbf{f}$ acting on the fluid as indicated by eq.(43) for $R/r << 1$. Assuming in the Stokes equation a point like body force $\delta(\mathbf{r})\mathbf{f}$ at the origin

$$\nabla p = \eta\Delta u + \delta(\mathbf{r})\mathbf{f} \tag{44}$$

the flow field induced by this force is

$$\mathrm{u}(\mathrm{r}) = \Omega(\mathrm{r})\cdot\mathrm{f} = \frac{1}{8\pi\eta r}\left(\mathbb{I} + \frac{\mathrm{r}\otimes\mathrm{r}}{r^2}\right)\cdot\mathrm{f} \tag{45}$$

as shown in appendix A . $\Omega(\mathbf{r})$ is the so-called Oseen tensor.

Equation for point particles – Now we consider N moving point particles located at $\mathbf{R}_i$, $i = 1,\ldots,N$ with a force $\mathbf{F}_i$ acting on each of it. Then the force density is

$$\mathbf{f}(\mathbf{r}') = \sum_{i=1}^{N}\delta(\mathbf{r}' - \mathbf{R}_i)\;\mathbf{F}_i \quad \text{usually} \quad \mathbf{F}_i = const\;. \tag{46}$$

Together with the Oseen-tensor (95) the equation for the perturbed flow field

$$\mathbf{u}'(\mathbf{r}) = \sum_{i=1}^{N}\Omega(\mathbf{r} - \mathbf{R}_i)\cdot\mathbf{F}_i \tag{47}$$

[3] About first order corrections of the Stokes formula with respect to the Reynolds number see for instance the book of Landau-Lifshitz VI and the book of Batchelor.

in terms of many moving point particles follows. The perturbation $\mathbf{u}'(\mathbf{R}_i)$ at the place of the i-th particle is induced by all the other $N-1$ particles

$$\mathbf{u}'(\mathbf{R}_i) = \sum_{j \neq i} \mathbf{\Omega}(\mathbf{R}_i - \mathbf{R}_j) \cdot \mathbf{F}_j \ . \tag{48}$$

For a creeping flow one assumes that a sphere has the same velocity $\dot{\mathbf{R}}_i = \mathbf{v}_i$ than the fluid in the immediate neighborhood $\mathbf{u}(\mathbf{R}_i)$ due to stick boundary conditions. The flow field at the position of the i-th particle may have two contributions. The first contribution is the undisturbed flow field in the absence of particles $\mathbf{u}_0(\mathbf{r})$, such as for example the uniform flow field $\mathbf{u}_0(\mathbf{r}) = const. \cdot \hat{\mathbf{n}}$ along some direction $\hat{\mathbf{n}}$, a linear shear field $(\mathbf{u}_0)_x = sy$ or a parabolic shear profile, e.g. a plane Poiseuille flow with $(\mathbf{u}_0)_x(y) = u_s(d^2 - y^2)$. The second contribution, $\mathbf{u}'(\mathbf{r})$, comes from the flow induced by all the other moving particles. Due to Stokes law the force acting on the i-th particle determines the velocity difference between this flow $\mathbf{u}_0(\mathbf{r}) + \mathbf{u}'(\mathbf{r})$ and the actual velocity $\mathbf{v}_i$

$$\mathbf{v}_i - [\mathbf{u}_0(\mathbf{R}_i) + \mathbf{u}'(\mathbf{R}_i)] = \frac{1}{6\pi\eta a}\mathbf{F}_i \, . \tag{49}$$

Here a is an effective radius of a point particle. For point particles the notion of an effective friction coefficient $\zeta = 6\pi\eta a$ is also common. Hence, the equation of motion for the ith particle is

$$\begin{aligned} \dot{\mathbf{R}}_i \equiv \mathbf{v}_i &= \mathbf{u}_0(\mathbf{R}_i) + \mathbf{u}'(\mathbf{R}_i) + \frac{1}{6\pi\eta a}\mathbf{F}_i \\ &= \mathbf{u}_0(\mathbf{R}_i) + \sum_{j \neq i} \mathbf{\Omega}(\mathbf{R}_i - \mathbf{R}_j) \cdot \mathbf{F}_j + \frac{1}{6\pi\eta a}\mathbf{F}_i \\ &\equiv \mathbf{u}_0(\mathbf{R}_i) + \sum_{k=1}^{N} \mathbf{H}_{ik} \cdot \mathbf{F}_k \ , \end{aligned} \tag{50}$$

where

$$\mathbf{H}_{ik} = \begin{cases} \frac{1}{\zeta}\mathbf{1} & \text{for k = i} \\ \mathbf{\Omega}(\mathbf{R}_i - \mathbf{R}_k) & \text{for k} \neq \text{i} \end{cases} \tag{51}$$

is called the mobility matrix.

The forces acting on the particles may be induced for instance by gravitation or in the case of charged particles by an electric field. In bead spring models for polymers a part of the forces acting on the beads are due to the springs connecting next neighboring beads. Besides the hydrodynamic and spring forces in polymers thermal motion has to be taken into account as well. For more details about bead–spring models for polymers, where the hydrodynamic interaction is taken into account, see for instance Ref.[44] and the references cited therein.

Two simple bead–spring models are the dumbbell and the tetrahedron as shown in Fig. 7. Both are used for modeling certain aspects of polymers. A simple potential for a linear spring with a finite equilibrium length b connecting two neighbor beads is

$$\Phi = \frac{1}{2}k(|\mathbf{R}| - b)^2 \tag{52}$$

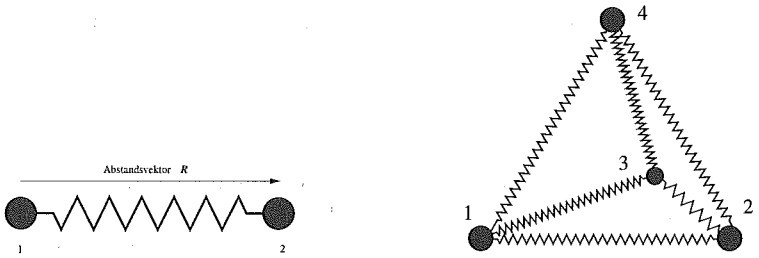


Fig. 7: *Two simple bead–spring models: a) dumbbell and b) tetrahedron.*

with the force law

$$\mathbf{F}(\mathbf{R}) = -\nabla\Phi(R) = -k\left(1 - \frac{b}{|\mathbf{R}|}\right) . \tag{53}$$

For such a spring potential the whole force acting on one bead of a tetrahedron or some complicated connected bead–spring model is

$$\mathbf{F}_j = k\sum_{i(\neq j)}\left(1 - \frac{b}{|\mathbf{r}_i - \mathbf{r}_j|}\right)(\mathbf{r}_i - \mathbf{r}_j) \tag{54}$$

This force together with Eq. (50) builds the equation of motion for the Stokesian dynamics of a bead spring system. More about Stokesian dynamics may be found in Ref. [30]. If the undisturbed flow $\mathbf{u}_0(\mathbf{r})$ is a shear or a Poiseuille flow, a tetrahedron or another three–dimensional object is in permanent motion and rotation. Surprisingly, a tetrahedron migrates during its persistent rotating motion perpendicular to the streamlines [46] and moves to the center of the Poiseuille flow.

A simple consequence of the hydrodynamic interaction may be seen in Fig. 8. Here the force is calculated which is needed in order to keep the two beads fixed in a uniform flow of velocity $\mathbf{u}$. The force can be determined from equation (49) by setting bead velocity $\mathbf{v}_i = 0$. Each bead perturbs the flow an reduces the flow velocity in its neighborhood. Therefore the dragforce on the second bead is reduced compared to that in absence of the first bead. This reduction depends on the distance between the two beads as can be seen from the dependence of the drag force as function of the bead distance d in Fig. 8c). In both cases with the connection vector between the two beads either parallel or perpendicular to the flow, the forces needed to keep both beads fixed point into the opposite direction to the flow velocity. In the case of a finite value of δ_x one has also to apply forces perpendicular to the flow (see Ref. [48] and references cited therein).

Effect of a dilute suspension of particles on the shear viscosity – Mixtures consisting of one material in the form of small particles either solid, liquid, or gaseous, dispersed randomly throughout another fluid material are quite common in nature and industry. The term *suspension* or colloidal suspension usually refers to a system of small solid particles in a liquid, but the nature of the two media is not of particular significance from the dynamical point of view and our use of the word here will include also systems

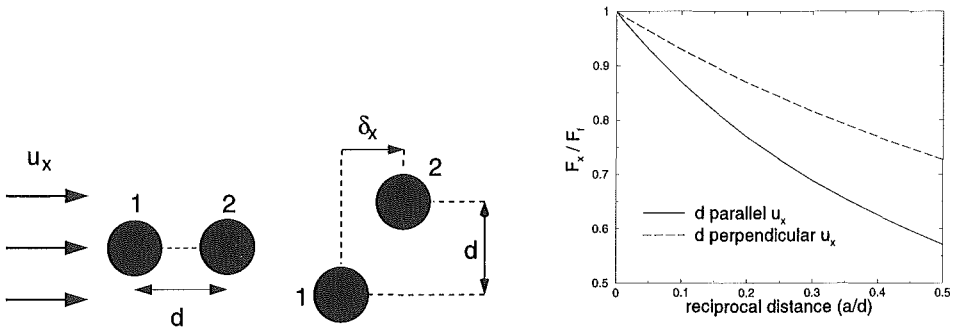


Fig. 8: *Two beads kept fixed in a uniform flow, with the connecting vector either perpendicular or parallel to the flow direction* $\mathbf{u} = (u_x, 0, 0)$. *b) The drag force for each bead of the two bead system normalized to the drag force* $F_f = 6\pi\eta a$ *needed for a single bead* ($F_f = 6\pi\eta a$) . *In the case of a perpendicular orientation we have chosen* $\delta_x = 0$. *a is the effective bead radius and d the distance between the beads (From Ref. [48]).*

of drops of one liquid dispersed either in another liquid (an emulsion) or in a gas. How do such suspensions behave in response to applied forces and moving boundaries like in shear cells? How does a suspension influence the shear viscosity? A. Einstein has shown in 1906 for the first time that suspended particles increase the shear viscosity [27].

Here we want to sketch the calculation of the effective viscosity of an incompressible fluid containing suspended particles of such small linear dimensions that the effects of gravity and inertia on the motion of a particle are negligible. The particle is assumed to move with the ambient fluid locally and the Reynolds number of the disturbance motion resulting from the presence of one particle is small compared with unity. The particles will be assumed to be exactly spherical, for simplicity. In the case of liquid or gaseous particles of small radius, surface tension tends to keep the particles spherical against the deforming effect of the motion, so that an assumption about shape is needed only for solid particles. The suspension will be also assumed to be dilute, with the average distance between particles large compared with their linear dimensions.

Similar as for the derivation of Stokes law, first one has to calculate the flow field around a sphere in a shear flow and the pressure. Near a single particle we assume a linear shear field of the form

$$u_i^{(0)} = \dot{\gamma}_{ij} x_j \,. \tag{55}$$

The fluid is assumed to be incompressible and in this case the trace of the rate of strain tensor $\dot{\gamma}_{ij}$ vanishes

$$\dot{\gamma}_{ii} = 0 \,. \tag{56}$$

We assume that a sphere of radius R in the shear field is located at the origin of the coordinate system. A shear field will set a sphere in rotation producing a perturbation $\mathbf{u}^{(1)}$ with the whole flow field being the sum of the unperturbed flow field $\mathbf{u}^{(0)}$ and its

perturbation: $\mathbf{u} = \mathbf{u}^{(0)} + \mathbf{u}^{(1)}$. One may derive the perturbation of the flow and the pressure field in a similar manner as for the Stokes law

$$\begin{aligned} u_i^{(1)} &= \frac{5}{2}\left(\frac{R^5}{r^7} - \frac{R^3}{r^5}\right)\dot{\gamma}_{kl}x_i x_k x_l - \frac{R^5}{r^5}\dot{\gamma}_{ik}x_k \\ p &= -5\eta_0 \frac{R^3}{r^5}\dot{\gamma}_{ik}x_i x_k \end{aligned} \tag{57}$$

where x_i are the components of the vector $\mathbf{r} = (x_1, x_2, x_3)$. For details of the derivation we refer to one of the books [22, 23, 21, 17].

The central part of this section is the determination of the stress tensor. The stress tensor without the suspended particles is proportional to the viscosity η_0 and with the suspended particles we expect that this viscosity is now replaced by an effective viscosity $\bar{\eta}$ which depends on the concentration of the particles. Here we assume noninteracting particles, therefore the stress tensor in a volume around one sphere is its average

$$\bar{\sigma}_{ik} = \eta_0\left(\frac{\partial \bar{u}_i}{\partial x_k} + \frac{\partial \bar{u}_k}{\partial x_i}\right) - \bar{p}\delta_{ik} + \frac{1}{V_0}\int_{V_0} d^3r \left[\sigma_{ik} - \eta_0\left(\frac{\partial u_i}{\partial x_k} + \frac{\partial u_k}{\partial x_i}\right) + p\delta_{ik}\right] . \tag{58}$$

The integral is only different from zero in the range of a sphere. Since the concentration of the spheres is very low, it is enough to calculate it for a single sphere by disregarding the others. This times the concentration of the spheres gives the result. A detailed calculation of the integrals also needs information about the stress distribution in the sphere but this may be avoided by using Gauss law and integration on a surface far away from the sphere. Due to the identity $\frac{\partial \sigma_{il}}{\partial x_l} = 0$ we also have

$$\sigma_{ik} = \frac{\partial}{\partial x_l}\left(\sigma_{il}x_k\right) . \tag{59}$$

and the stress tensor takes the form

$$\bar{\sigma}_{ik} = \eta_0\left(\frac{\partial \bar{u}_i}{\partial x_k} + \frac{\partial \bar{u}_k}{\partial x_i}\right) - \bar{p}\delta_{ik} + c\oint_{\partial V}\left[\sigma_{il}x_k df_l - \eta_0\left(u_i df_k + u_k df_i\right)\right] . \tag{60}$$

If the surface ∂V is shifted sufficiently far from the sphere only the leading term $\propto 1/r^2$ in the analytical expression for the velocity, cf. (57) is required. During the calculation of the surface integral one has to deal with averages over two combinations of normal vectors, where the components of the normal vector are $n_i = x_i/r$. The surface integral gives

$$c\eta_0\ 20\pi R^3\left(5\dot{\gamma}_{lm} < n_i n_k n_l n_m > - \dot{\gamma}_{il} < n_k n_l > .\right) \tag{61}$$

After performing the averages one obtains with

$$\begin{aligned} < n_i n_k > &= \frac{1}{3}\delta_{ik} \\ < n_i n_k n_l n_m > &= \frac{1}{15}\left(\delta_{ik}\delta_{lm} + \delta_{il}\delta_{km} + \delta_{im}\delta_{kl}\right) \end{aligned} \tag{62}$$

the expression

$$\bar{\sigma}_{ik} = \eta_0 \left(\frac{\partial \bar{u}_i}{\partial x_k} + \frac{\partial \bar{u}_k}{\partial x_i} \right) + 5\eta_0 \dot{\gamma}_{ik} \frac{4\pi}{3} R^3 c \tag{63}$$

With the velocity from (55) the first term gives $2\eta_0 \dot{\gamma}_{ik}$. Therefore the effective viscosity has the form

$$\eta = \eta_0 \left(1 + \frac{5}{2} \varphi \right) \qquad \text{with} \qquad \varphi = \frac{4\pi R^3}{3} c \tag{64}$$

and with φ being part of the volume occupied by the suspended particles.

This law holds for a laminar flow and the suspended particles enhance the effective viscosity. If the suspended particles are not rigid spheres but deformable polymers, the shape may depend on the shear rate. For larger shear rates in the range of $\dot{\gamma}\tau_p > 1$, with τ_p the relaxation time of a polymer in solution, polymers follow to a complex dynamics as observed in Ref. [32] in 1997. Therefore if the flow in a pipe becomes turbulent, such as shown in Fig. 1, flexible and suspended polymers undergo a complex dynamics. In this case the flow not only deforms polymers, but the polymer dynamics affects very much the flow itself and acts similar but in a much more complex way as a reduction of the effective viscosity.

So far sufficiently diluted particle suspensions in shear flow have been considered where the hydrodynamic interaction between particles is sufficiently small and where the particles behave like independent ones. As we have seen above, if two spheres come close enough, say if the ratio between the particle diameter $2R$ and the distance d, R/d, becomes larger, then the drag on one of them is influenced by a second sphere nearby: The spheres experience in this case a *hydrodynamic interaction.* Such interactions between two spheres lead to a contribution to the viscosity $\bar{\eta}$ that is proportional to φ^2, and so on. This effect of two body interactions on $\bar{\eta}$ was computed by Batchelor [29]. Here, in contrast to the hydrodynamic interaction according to the Oseen tensor, which describes the interaction of point particles, also the particle rotations have to be taken into account when the particle interactions are calculated. When combined with Einstein's result the calculation in Ref.[29] gives

$$\bar{\eta} = \eta_0 \left(1 + \frac{5}{2} \varphi + 6.2 \varphi^2 \right) . \tag{65}$$

For polystyrene spheres this formula holds good up to a concentration $\varphi \leq 0.10$.

3.4 Pipeflow for a shear thinning fluid

In a number of complex fluids one observes shear thinning behavior as shown in Fig. 5. A shear–rate–dependence of the viscosity occurs when the shear rate is high enough to disturb the equilibrium distribution of the inter particle spacing and the particles cannot relax fast enough. The rate at which the particle equilibrium is regained is controlled by the particle diffusivity, given in dilute solution by

$$D_0 = \frac{k_B T}{6\pi\eta R} . \tag{66}$$

The time t_D for a particle to diffuse a distance equal to its Radius R is therefore

$$t_D \sim \frac{R^2}{D_0} = \frac{6\pi\eta R^3}{k_B} \tag{67}$$

The shear rate has the dimension 1/time, therefore one can define a dimensionless shear rate, or *Peclet number*, as

$$\mathrm{Pe} = \frac{\eta\dot{\gamma}R^3}{k_B T} \propto \dot{\gamma} t_D \tag{68}$$

With τ_R the relaxation time of polymers in solution, a polymer in a shear field large enough with

$$\dot{\gamma}\tau_R > 1 \tag{69}$$

cannot adjust to its equilibrium coiled shape as well. Hence shear thinning may also occur in polymer solutions.

In the range of large shear rate, this shear rate dependent viscosity may be described by an approximate "power-law" expression

$$\eta(\dot{\gamma}) = m\dot{\gamma}^{n-1} \tag{70}$$

with n from the interval $n = 0.15 \ldots 0.8$. Obviously, this shear rate dependent viscosity may change the flow, e.g. as through a pipe.

Stationary flows of shear rate dependent complex fluids, such as a stationary pipe flow, may be described by the Navier-Stokes equation with a shear rate dependent viscosity. The stationary form of equation (14) for a shear rate dependent viscosity and incompressibility is

$$0 = -\partial_{x_i} p + \left(\partial_{x_k}\eta\right)\left(\partial_{x_k} u_i + \partial_{x_i} u_k\right) + \eta\partial^2_{x_k} u_i \ . \tag{71}$$

With the axis of the pipe along the z-axis the velocity in the pipe is $\mathbf{u}(r) = (0, 0, u_z(r))$. With the Laplacian and the gradient in cylindrical coordinates (only the r dependent part is shown) $\Delta u_z = \frac{1}{r}\partial_r(r\partial_r u_z)$ and $\nabla f(r) = \hat{e}_r\, \partial_r f(r)$ one obtains

$$\frac{p_0 - p_L}{L} = \frac{1}{r}\frac{d}{dr}\left(r\eta\frac{du_z}{dr}\right) \tag{72}$$

with the pressure drop $(p_0 - p_L)$ along the pipe of length L. With $\dot{\gamma} = \partial_r u_z$ and η from (70) an integration with respect to r gives

$$m\left(\frac{du_z}{dr}\right)^n = \frac{(p_0 - p_L)r}{2L} + \frac{C_1}{r} \ . \tag{73}$$

Since the shear rate on the axis of the pipe at $r = 0$ is finite or zero (symmetry) the constant C_1 must vanish. With $\tau_R = \frac{(p_0 - p_L)R}{2L}$ one has

$$m\left(\frac{du_z}{dr}\right)^n = \tau_R\frac{r}{R} \ . \tag{74}$$

Integration of this equation gives the velocity-profile

$$u_z = -\left(\frac{\tau_R}{mR}\right)^{1/n} \frac{r^{1+\frac{1}{n}}}{1+\frac{1}{n}} + C_2 \ . \tag{75}$$

Since the flow velocity vanishes at the pipe wall $u_z(r = R) = 0$ (stick boundary condition) it follows with the constant C_2 from this condition

$$u_z = \left(\frac{\tau_R}{mR}\right)^{1/n} \frac{R}{1+\frac{1}{n}} \left[1 - \left(\frac{r}{R}\right)^{\frac{1}{n}+1}\right] \ . \tag{76}$$

One should remember that the power-law behavior of the viscosity is an approximation that holds only for large enough shear rates (therefore close to the pipe boundary).

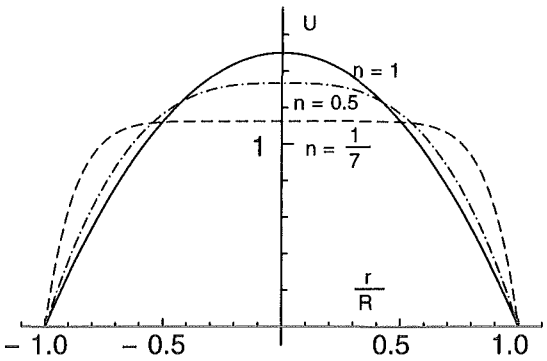


Fig. 9: *The velocity* $U = u_z(r)/ < u_z(r) >$ *normalized to the average velocity* $< u_z(r) >$ *is shown for the Newtonian fluid* $n = 1$, *for* $n = 1/2$ *and* $n = 1/7$.

In the limit $n \to 0$ the flow velocity $U(r) = u_z(r)/ < u_z(r) >$ becomes a constant besides a small range close to the wall, where the shear rate diverges $\frac{d}{dr}u_z(r \sim R) = -(\tau_R/m)^{1/n}$.

In addition of high practical relevance is the volume rate Q going through the pipe

$$\begin{aligned} Q &= \int_0^{2\pi} d\varphi \int_0^R u_z(r)\, r dr\, d\varphi \\ &= 2\pi R^2 \int_0^1 u_z \frac{r}{R}\, d\left(\frac{r}{R}\right) = \frac{\pi R^3}{\frac{1}{n}+3} \left(\frac{\tau_R}{m}\right)^{1/n} \\ &= \frac{\pi R^3}{\frac{1}{n}+3} \left(\frac{(p_0 - p_L)R}{2mL}\right)^{1/n} \end{aligned} \tag{77}$$

For $n = 1$ and $m = \eta$ this reduces to the Hagen-Poiseuille equation for laminar flow of Newtonian fluids through a pipe. Rather interesting is now Qm/τ_R, which is independent of the pressure drop for Newtonian fluids whereas for non-Newtonian fluids one has

$$\frac{Qm}{\tau_R} \sim (p_0 - p_L)^{(1-n)/n} \ . \tag{78}$$

For large pressure drops the volume rate for non-Newtonian fluids may be much higher than for Newtonian fluids. However, this conclusion holds only as long the fluid is laminar and not turbulent.

4 Nematic liquid crystals

Complex fluids are deformable materials which have, compared with simple fluids, further inner degrees of freedom. In order to describe these additional degrees of freedom the equations of motion for simple fluids (4,5,6) must be generalized and coupled with further equations. For a two component fluid mixture, such as water–alcohol, one needs for each component a conservation law for mass. However, instead of two conservation laws for mass one may use a conservation law for the whole mass and an equation for the concentration of one fraction. In charged systems one has in addition a conservation law for the charge

$$\dot{\rho}_e + \nabla \cdot \mathbf{j}^{(e)} = 0 \tag{79}$$

with the electrical current density $\mathbf{j}^{(e)}$.

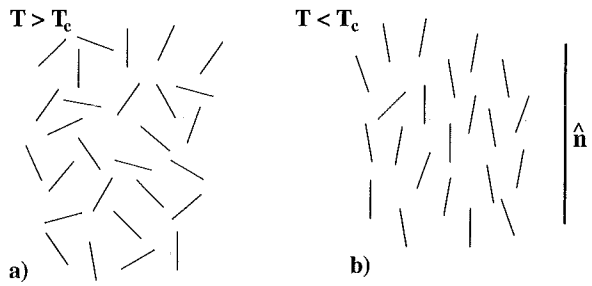


Fig. 10: *a) Disordered (isotropic) phase beyond the isotropic–nematic transition ($T > T_c$) and the phase with orientational order (nematic phase) below the nematic–isotropic phase transition ($T < T_c$). $\hat{\mathbf{n}}$ is the director.*

In many component and charged systems conservation laws completely determine the set of hydrodynamical variables. For liquid crystals or superfluids there are one or more broken–symmetry hydrodynamic variables. In a nematic liquid crystalline phase one has an additional spontaneously broken rotational symmetry. Organic liquids with a nematic phase in some temperature range become anisotropic due to an orientational ordering of non spherical molecules. The angle distribution of the anisotropic molecules is uniform in the isotropic phase, cf. Fig. 10 a), but in the anisotropic nematic phase the angle distribution exhibits a local maximum and this preferred direction is described by the director field $\mathbf{n}(\mathbf{r}, t)$. The director field has a $\pm$–symmetry ($\mathbf{n}$ = - $\mathbf{n}$) and hence in the nematic phase the rotational symmetry is broken. Since this symmetry is spontaneously broken (broken during a phase transition) without application of external fields, it is called a *spontaneously broken* symmetry. Similar as in simple fluids there is no positional order

of the molecules in nematic liquid crystals. In the absence of boundaries every spontaneously formed direction has the same energy, as long as the orientation of the director $\mathbf{n}$ is everywhere the same. Therefore, pure rotations of the whole fluid volume don't cost energy in the absence of boundaries.

Related to the orientational ordering of the molecules is the anisotropy of material properties. The dielectric constant is different for a light wave with the wave vector $\mathbf{k}$ parallel to $\mathbf{n}$ ($\varepsilon = \varepsilon_\parallel$) and perpendicular to $\mathbf{n}$ ($\varepsilon = \varepsilon_\perp$). The same holds for the index of refraction, which is also different parallel to $\mathbf{n}$ ($n = n_\parallel$) and perpendicular to $\mathbf{n}$ ($n = n_\perp$). Due to the anisotropy, $\Delta n = n_\parallel - n_\perp$, nematic materials are birefringent.

Only spatially varying deformations of the director field $\mathbf{n}(\mathbf{r})$ lead to a change (increase) of the free energy. Therefore spatially deformations tend to relax to the homogeneous director orientation and if the wavelength of the deformations becomes larger and larger, the relaxation time increases too. Therefore, the deformation of the director field is an additional hydrodynamic mode in nematic liquid crystals and the equations must be generalized accordingly: To any spontaneously broken continuous symmetry, there is a symmetry variable behaving hydrodynamically $\omega(k \to 0) \to 0$.

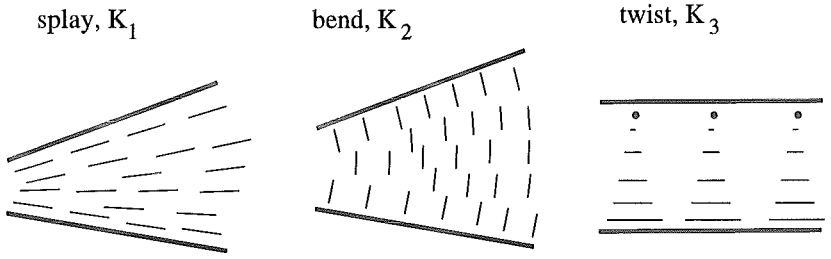


Fig. 11: *The three fundamental distortions of the nematic director field* $\mathbf{n}(\mathbf{r}, t)$*: a) splay, b) bend and c) twist deformation.*

Changes of the director field δn_i are not conserved. The deformations of the director field are elastic and any deformation can be decomposed in three fundamental deformations, the splay, the bend and the twist deformation, cf. Fig. 11. The energy stored in each deformation is proportional to an elastic constant: K_1 the splay elastic constant, K_2 the twist elastic constant and the bend elastic constant K_3. The Frank free energy of the director deformations is

$$\mathcal{F} = \frac{1}{2}\int d^3r \left(K_1 \left(\nabla \cdot \mathbf{n}\right)^2 + K_2 \left[\mathbf{n} \cdot (\nabla \times \mathbf{n})\right]^2 + K_3 \left[\mathbf{n} \times (\nabla \times \mathbf{n})\right]^2 - \varepsilon_0 \varepsilon_a (\mathbf{n} \cdot \mathbf{E})^2 \right) \quad (80)$$

with $\varepsilon_a = \varepsilon_\parallel - \varepsilon_\perp > 0$. The last contribution describes the coupling to an applied electric field. For $\varepsilon_a > 0$ a parallel alignment between the director field and the electric field reduces the free energy. If a magnetic field is applied, the free energy contribution $-\varepsilon_0 \varepsilon_a (\mathbf{n} \cdot \mathbf{E})^2$ has to be replaced by $-\chi_a (\mathbf{n} \cdot \mathbf{H})^2$. A detailed derivation of this free energy for the distortions of the director field and the respective equation of motion for $\mathbf{n}(\mathbf{r}, t)$ may be found in the books [18, 5, 4].

The orientation of the director close to a container boundary depends on the surface preparation. There are several surface preparation techniques which induce close to the boundary an orientation of **n** either parallel or perpendicular or with some oblique angle with respect to the container boundary. Due to the elastic energy of orientational deformations of the director field the orientation of **n** at the boundaries is transmitted to the bulk. An example is shown for a sandwich geometry in Fig. 12a) with the orientation of the director parallel to the wall and with the same orientation at both walls. The result is a homogeneous orientation of **n** in the bulk. If an electric field is applied, as indicated in Fig. 12b), and if the material has a positive dielectric anisotropy, $\varepsilon_a > 0$, the energy is decreased when **n** and **E** become parallel. This orientation effect of the applied electric field competes with the boundary induced director orientation. As long as the effect is weaker as the boundary orientation effect, **n** stay parallel to the wall. However, the electric field can distort the director in the bulk. Since in this configuration the electric field is perpendicular to the initial orientation, a critical electrical field is required. This field driven orientation transition in the bulk is the so-called Fredericks transition. If the electric field is switched off, the director relaxes back to the initial configuration. Since the nematic liquid crystal is birefringent its optical properties can be changed by switching on and off by an electric field or a voltage between the two bounding plates. The initial configuration in an LCD is a twisted state, but the LCD is switched by the same mechanism.

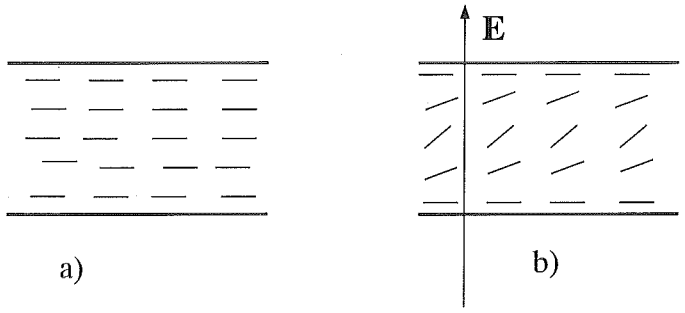


Fig. 12: *a) Homogeneous director orientation induced by the boundary orientation. b) The director is distorted in the bulk by application of an electric field (Fredericks transition).*

Viscosity in a uniaxial liquid - anisotropic viscosity – Due to the orientational order the viscosity depends on the orientation of the director **n** with respect to the shear plane. As we have seen that the orientation of the director can be enforced by application of a magnetic or electric field. Hence we will assume that the director is strongly aligned along the $x_3 = z$–direction, cf. Fig. 13. In this case the expression for the linear shear stress are

$$\sigma'_{12} = \sigma'_{21} = \eta_3 \left(\frac{\partial u_1}{\partial x_2} + \frac{\partial u_2}{\partial x_1} \right) ,$$
$$\sigma'_{23} = \eta_4 \frac{\partial u_2}{\partial x_3} + \eta_1 \frac{\partial u_3}{\partial x_2} , \qquad \sigma'_{32} = \eta_2 \frac{\partial u_2}{\partial x_3} + \eta_4 \frac{\partial u_3}{\partial x_2} , \tag{81}$$

$$\sigma'_{31} = \eta_4 \frac{\partial u_3}{\partial x_1} + \eta_2 \frac{\partial u_1}{\partial x_3}, \qquad \sigma'_{13} = \eta_1 \frac{\partial u_3}{\partial x_1} + \eta_4 \frac{\partial u_1}{\partial x_3}, \tag{82}$$

The four viscosities η_1, η_2, ,η_3 and η_4 constitute four of five independent viscosities in an uniaxial system. Note that the coefficient of $\partial u_2/\partial x_3$ in the equation of σ'_{23} and the coefficient of $\partial u_3/\partial x_2$ in the equation of σ'_{32} are (like the corresponding coefficients in the last equation) identical. Their identity, which constitutes the only surprise of the three equations above, is an example of an *Onsager relation*, and readers who are unfamiliar with Onsager relations, and with the subject of irreversible thermodynamics in which they arise, should take it on trust or should read the books of deGennes/Prost [4], of Landau [18], of Chaikin/Lubensky [5] or the original literature about nematic liquid crystals. These five viscosities have been measured at least for two substances.

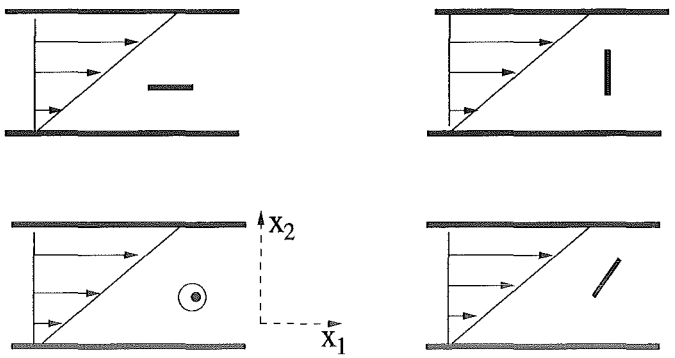


Fig. 13: *Measuring different shear viscosities for different orientations of the nematic director with respect to the shear plane.*

If there are deformations of the director field, their relaxations excite a flow and any flow influences the orientation of the director field. Therefore in the equation for the momentum conservation there are contributions due to the director deformation and in the dynamic equation for the director $\dot{\mathbf{n}}$ the shear fields $\partial_i u_j$ occur. Due to the many material parameters in nematics the equations look much more complicated than the Navier–Stokes equation, but they are solvable and all the material parameters may be measured. The systematic derivation of the equations for nematodynamics is described in [4, 8, 18]. Since the director field is a local unit vector ($\mathbf{n}^2 = 1$), the dynamics of the director field is restricted to rotations $\dot{n}_i\, n_i = 0$.

The mean orientation of the molecules close to container boundaries depends on the preparation of the surface. The surface of the shear cell are coated in that way that the molecules align parallel to the container boundaries If the upper plate is moved with some velocity $\mathbf{v}$ the director is still undistorted close to the upper and the lower plate, but in the center of the shear cell the director field becomes distorted and non-parallel to the bounding walls as indicated in Fig. 14. Vesicles show a similar inclined flow alignment in shear flow [31]. Suspended non spherical objects may be oriented in shear fields by similar mechanisms. About flow effects in further liquid crystal phases see [4, 8].

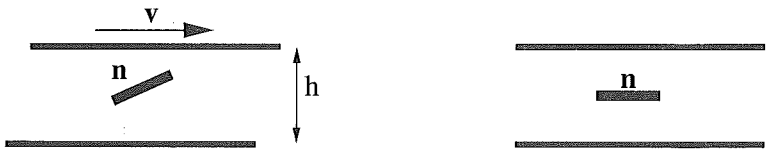


Fig. 14: *Flow alignment of the director field in the center of the plane shear cell.*

5 Polymer liquids

The viscosities of polymer liquids as shown in Fig. 5 indicate both elastic and viscous behavior. Nematic liquid crystals are also elastic but with respect to the orientational order. The elasticity of polymer solutions is due to the entropic elasticity of the polymers which resembles in some respects more the elasticity of a solids with respect to positional deformations. On a short time scale (high frequencies) the elastic behavior is pronounced and on a long time scale (small frequencies) the viscous behavior. The notion high and low frequency depends on the material and its internal relaxations. With increasing excitation frequencies any material exhibits elastic behavior beyond some critical frequency or below a certain time scale. Especially polymer liquids, where the relaxation of polymers may be rather slow, show elastic behavior already at rather low frequencies that often belong to the frequency range of hydrodynamic modes. Therefore slow relaxation may not only be due to slow hydrodynamic relaxations but also due to "microscopic" relaxation processes. A hydrodynamic theory disregarding such slow microscopic processes is restricted to unreasonable long time scales.

A hydrodynamic theory of simple or multicomponent fluids relays on conservations laws. Systems with spontaneously broken symmetries take into account the dynamical equations for broken–symmetry hydrodynamic variables. In both cases the fast dynamics at molecular level adjusts immediately to the far slower hydrodynamic motion. For viscoelastic fluids one has to couple the slow hydrodynamic modes (slow in terms of the dynamics at the molecular level) to appropriate slow modes of the microscopic dynamics. This field of rheology is less mature than hydrodynamic theories for simple fluids and for liquids with spontaneously broken symmetries.

Only for small deformations of the fluids there is with the linear Maxwell model a reasonable description of the viscoelastic behavior available.

5.1 Linear Viscoelasticity - Maxwell Model

Lets consider the symmetric deformation field

$$E_{ij} = \frac{1}{2}\left(\nabla_i w_j + \nabla_j w_i\right) \tag{83}$$

with $w_i = r_i - r_i'$ with r_i the final and r_i' the initial position of a fluid element. This symmetric deformation tensor does not include simple rotations. For small deformations, which we only consider in this section, the field E_{ij} is related to the stress tensor via

Hooke's law. However, after a certain time polymers or some particle arrangements relax to a new equilibrium configuration and the elastic stress contribution relaxes too. This is different to a solid where the stress only relaxes when all the atoms or molecules relax to their fixed equilibrium positions.

Therefore in a viscoelastic liquid one has the shear stress and a relaxing elastic stress. This suggests the following equation of motion for the stress tensor in the case of small fluid deformations

$$\sigma_{ij} + \lambda_1 \frac{\partial}{\partial t}\sigma_{ij} = \eta\dot{\gamma}_{ij} \,. \tag{84}$$

It is the so–called Maxwell model for linear viscoelastic fluids. For simplicity we have only one relaxation constant λ_1. This is a first order inhomogeneous and linear differential equation for the stress tensor, which may be easily integrated

$$\sigma_{ij} = e^{-t/\lambda_1}\left[\int\left(-\frac{\eta}{\lambda_1}\dot{\gamma}(t')e^{t'/\lambda_1}dt'\right) + C_{ij}\right] . \tag{85}$$

This solution of the Maxwell model shows a memory behavior of a viscoelastic fluid. Especially this memory contributions due to elastic effects make a continuum formulation of the viscoelastic fluids intricate.

With the ansatz $\dot{\gamma} = \omega\gamma_0\cos(\omega t)$ as in section 2 where the same ansatz for $G(t)$ used was used one obtains from eq. (84) the expressions for the loss and storage modulus

$$G'(\omega) = \frac{\eta\lambda_1\omega^2}{1+\lambda_1^2\omega^2} \qquad \text{and} \qquad G''(\omega) = \frac{\eta\omega}{1+\lambda_1^2\omega^2} \,. \tag{86}$$

From measurements with oscillatory shear one can determine the two unknown parameters, the shear viscosity η and the relaxation λ_1 in the Maxwell-model.

5.2 Nonlinear deformations of viscoelastic fluids

Most of the flow problems of viscoelastic fluids cannot be described by the linear Maxwell model, as in Eq. (84). In a flow of a Newtonian fluid the temporal change of a field has two contributions described by the substantial derivative: $d/dt = \partial/\partial t + (\mathbf{u}\cdot\nabla)$. We assume at some initial time the distance $|\delta\mathbf{r}| = |\mathbf{r}_1 - \mathbf{r}_2|$ between two fluid elements. At some time later the positions of the fluid elements might have changed to $\delta\mathbf{r}' = \mathbf{r}_1' - \mathbf{r}_2'$ and the distance is very likely not the same anymore $|\delta\mathbf{r}'| \neq |\delta\mathbf{r}|$. This does not have any consequence for Newtonian fluid, only energy has been dissipated during the motion relative to each other. In a viscoelastic fluid such a change of the distance between neighboring fluid elements means an elastic deformation that contributes to the stress tensor. The time derivative of the stress tensor in viscoelastic fluids must be changed accordingly.

It is known from classical mechanics that time derivatives of vector or tensor components in an moving frame of reference obey special transformation rules. In continuum mechanics there are two common formulations of the time derivative for the stress tensor (see e.g. [1])

$$\dot{\sigma}' \to \frac{D}{Dt}\sigma' = \partial_t\sigma' + (\mathbf{u}\cdot\nabla)\,\sigma'_{ij} - \sigma'_{ij}\cdot\nabla\mathbf{u} - (\nabla\mathbf{u})^\dagger\cdot\sigma' \tag{87}$$

with $(\nabla \mathbf{u})_{ij} = \partial_i u_j$. Here $\dot{\sigma}'$ denotes the time derivative in the local frame of reference of a fluid element, where the partial derivatives on the right hand side refer to space and time coordinates in a fixed frame of reference. This is known as the *(upper) convected derivative.* Alternatively one has with

$$\dot{\sigma}' \to \frac{\hat{D}}{\hat{D}t}\sigma' = \partial_t \sigma' + (\mathbf{u}\cdot\nabla)\,\sigma'_{ij} - \sigma'_{ij}\cdot(\nabla\mathbf{u})^{\dagger} - (\nabla\mathbf{u})\cdot\sigma' \tag{88}$$

also the *(lower) convected derivative.* In the traditional literature the upper convected derivative is preferred and this is justified by the so–called *material frame independence.* Recently, however it was argued that the lower convected is the appropriate one, because it provides the appropriate limit of an elastic solid [40].

With this definition one obtains with (84) either the upper or lower convected Maxwell model

$$\sigma' + \lambda\frac{D}{Dt}\sigma' = \eta\dot{\gamma} \tag{89}$$

This model has been applied to various situations, but with the continuum formulation of the equations of motion of viscoelastic fluids there is besides the appropriate choice of the time derivative the question about the appropriate macroscopic description of the polymer deformations. Or in other words, what are appropriate additional contributions on the right hand side of Eq.(89) in order to describe for instance the viscoelasticity of flow polymer solutions? There are a number of models used in the literature, but a heuristic approach with a similar fundamental importance than the Navier–Stokes equation for Newtonian fluids, is not available yet.

5.3 Single Polymer studies (useful for macroscopic modeling?)

The macroscopic description of viscoelastic fluids, such as polymer solutions, is still incomplete. For instance there is still no systematic approach for a mapping between the single polymer behavior on a microscopic scale in solution and the macroscopic dynamics of diluted polymer solutions. Which kind of additional terms, for example, have to be introduced on the right hand of Eq. (89) to describe theoretically turbulent drag reduction for diluted polymer solutions or similar phenomena?

The linear Maxwell model may be sufficient to predict for instance instabilities in hydrodynamic systems, such as the Faraday instability, when only small deformations of the fluid are involved [39]. A description of the *nonlinear* behavior of non-Newtonian fluids is much less advanced and it requires for instance in diluted polymer solutions a thorough analysis of the interplay between flows and polymers. Accordingly two basic questions have been addressed in a number of recent experimental [32] and theoretical works (for references see e.g. [44]). How does the flow field deform a tethered polymer and how is the flow field modified by the presence of the polymer?

In classical experiments on the dynamics of polymers in solution such as light scattering, birefringence, rheometry and small angle neutron scattering one measures only volume–averaged quantities. A huge step forward in the analysis of the crucial interplay between

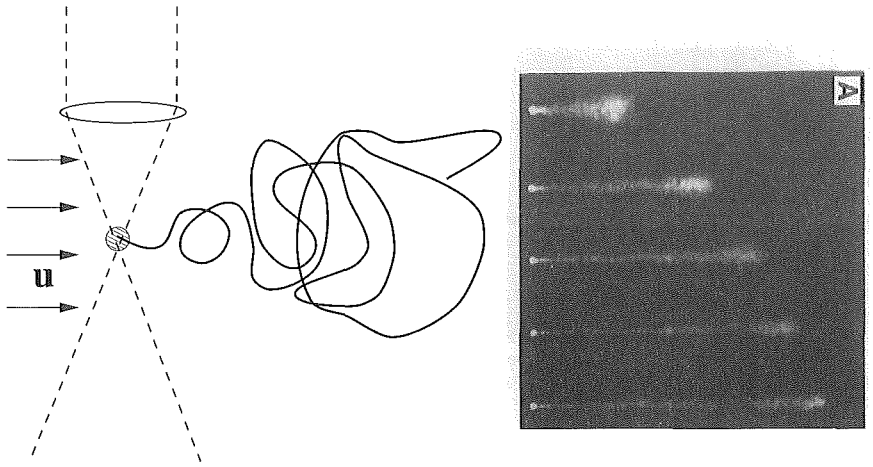


Fig. 15: *A sketch of a tethered DNA molecule, which is attached with one end at a latex sphere that is fixed in a uniform flow with velocity* **u** *by a laser beam (tweezer). The polymer shape is determined by the balance of the drag forces exerted by the flow and the entropic elasticity of the polymer. In the experiment reported by S. Chu et al. [33] the polymer is tethered at the bright points at the left boundary in part b). The velocity of the uniform flow increases from top to bottom and the polymer is elongated accordingly.*

the flow field and the deformations of the polymers has been achieved by studying single DNA molecules. DNA is much larger than synthetic polymers like polyethylene(-oxide) and can be manipulated with optical tweezers. DNA molecules with a length of about $10 \ldots 100$ μm have been used. When decorated by fluorescent dyes, the action of flows on the polymer can be followed under an optical microscope [32, 33, 34, 35] .

The elongation of a tethered polymer in a uniform flow is a very simple form of interaction between the polymer and a flow, which has been investigated successfully. Studies about the temporal evolution of single polymers in elongational flow and in shear flow provide important insight about the polymer dynamics [34, 35]. In shear flow polymers are at some moments elongated but it rotates and contracts later. The polymer extension as function of behaves rather erratically. In elongational flow the polymer distortions show a great variety, what deGennes called *Molecular individualism* [37]. Insight from such single polymers may provide important guidance to improve the present versions of a macroscopic description of polymer solutions. However, in all these experimental examples and also in a number of numerical and analytical investigations [41, 36, 45] only the (complex) reaction of a single polymer on special flows has been investigated, but not the action of the polymer on the flow in its neighborhood.

The elongation of a single polymer in a uniform flow field has been calculated too, either by analytical calculations in terms of the so–called blob model [41, 42] or by simulations of bead–spring models for polymers [36, 45, 43, 44]. On the scale of a polymer the Reynolds number is very small. Therefore in numerical simulations of bead spring

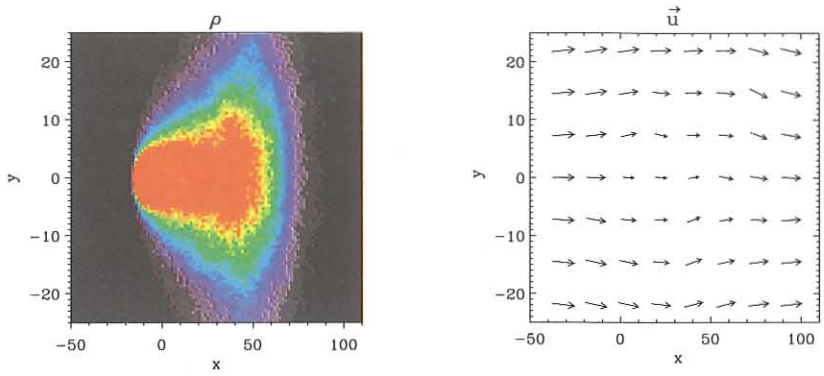


Fig. 16: *The results from simulations of a bead–spring model for polymers fixed at one end in a uniform flow. Part b) shows the flow field. It indicates partial penetration of the flow into the polymer [43].*

models creeping flow can be assumed and the hydrodynamic interaction between different parts of a polymer model is described by the Oseen tensor as introduced above. Polymers undergo a Brownian motion in a flow and this Brownian dynamics is indeed simulated [36, 45, 43, 44]. More details of that may be found in Ref. [44] and references cited therein.

Since the hydrodynamic interaction is of the long range type the interaction between all segments of the polymer have to taken into account in such simulations. Having bead spring models for a polymer with N beads the number of operations increases like N^3 for a straight forward algorithm. Accordingly in some of the simulations the time consuming part of the hydrodynamic interactions have been neglected. However, if something should be learned about the back–action of the deformed polymer on the flow the hydrodynamic interaction is crucial. [4] One major result of the hydrodynamic interaction effects is for instance that a flow penetrates only partially into a polymer [43, 44], cf. Fig. 16, in contrast to previous assumptions used for blob models [41].

It is well known from Stokes's law that the force on a fixed sphere in a flow increases linearly with the flow velocity. Taking the hydrodynamic interaction into account, it can be shown that the force needed in order to keep a tethered DNA molecule fixed, grows *nonlinearly* with the flow velocity [47]. Such a nonlinear behavior of a generalized Stokes law is due to the interplay of the hydrodynamic interaction between different parts of the polymer and the deformability of the polymer. For polymer brushes (polymers fixed at spheres) similar nonlinear effects might be important for their behavior in a flow [48].

Flows of diluted polymer solutions offer even further surprises. In Sec. 3.2 we have mentioned that turbulence occurs due to the inertial effects in the Navier Stokes equation. Turbulence is absent for creeping flow in the limit of low Reynolds number. However, for

[4] With appropriate approximations the number of required operations grows with the number of beads only like $\sim N^{\sim 2.2}$.

polymer solutions in small shear fields, corresponding to a very small Reynolds number, turbulent flow behavior might occur too [38]. In simple fluids the advective term $(\mathbf{u}\cdot\nabla)\mathbf{u}$ causes turbulence. For polymer solutions in shear flow at low Reynolds number the nonlinearity causing turbulent types flow is caused by the nonlinear interaction between the flow and the polymer dynamics.

Appendix

A Derivation of the Oseen–Tensor

In this section we derive in the limit of a the Reynolds–number $Re \ll 1$ from Stokes equation (22)

$$\eta\Delta\mathbf{u}' - \nabla p' + \mathbf{f} = 0\ . \tag{90}$$

the Oseen–Tensor, describing the hydrodynamic interaction of moving particles. This is a linear partial differential equation and may be solved by Fourier-transformation of $\mathbf{u}'(\mathbf{r},t)$, $p'(\mathbf{r},t)$ and $\mathbf{f}(\mathbf{r},t)$:

$$\begin{aligned}
\mathbf{u}'(\mathbf{r}) &= \int \frac{d^3\mathbf{k}}{(2\pi)^3}\,\mathbf{u}'(\mathbf{k})e^{i\mathbf{k}\cdot\mathbf{r}}\ ,\\
p'(\mathbf{r}) &= \int \frac{d^3\mathbf{k}}{(2\pi)^3}\,p'(\mathbf{k})e^{i\mathbf{k}\cdot\mathbf{r}}\ ,\\
\mathbf{f}(\mathbf{r}) &= \int \frac{d^3\mathbf{k}}{(2\pi)^3}\,\mathbf{f}(\mathbf{k})e^{i\mathbf{k}\cdot\mathbf{r}}\ .
\end{aligned} \tag{91}$$

With this ansatz the linear Stokes equation (90) and the incompressibility condition take the form

$$\begin{aligned}
\eta\mathbf{k}^2\,\mathbf{u}'(\mathbf{k}) + i\mathbf{k}\,p'(\mathbf{k}) &= \mathrm{f}(\mathbf{k}),\\
\mathbf{k}\cdot\mathbf{u}'(\mathbf{k}) &= 0\ .
\end{aligned} \tag{92}$$

Multiplication of equation (90) with wave number $\mathbf{k}$ leads to

$$\begin{aligned}
\underbrace{-i\eta\mathbf{k}^2\,\mathbf{k}\cdot\mathbf{u}'(\mathbf{k})}_{\equiv 0} + \mathbf{k}\cdot\mathbf{k}\,p'(\mathbf{k}) &= -i\mathbf{k}\cdot\mathbf{f}(\mathbf{k})\\
\rightarrow p'(\mathbf{k}) &= -i\frac{\mathbf{k}\cdot\mathbf{f}}{\mathbf{k}^2}\ .
\end{aligned} \tag{93}$$

and this together with (92) gives

$$\mathbf{u}'(\mathbf{k}) = \frac{1}{\eta\mathbf{k}^2}\left(\mathbf{1} - \hat{\mathbf{k}}\hat{\mathbf{k}}\right)\cdot\mathbf{f}(\mathbf{k})\ , \tag{94}$$

for the perturbed velocity field $\mathbf{u}'$ as function of the force field $\mathbf{f}$ ($\hat{\mathbf{k}}\hat{\mathbf{k}}$ describes a dyadic product). In real space one has a *nonlocal* relation between the flow perturbation and the

force field

$$\begin{aligned}\mathbf{u}'(\mathbf{r}) &= \int \frac{d^3\mathbf{k}}{(2\pi)^3}\frac{1}{\eta\mathbf{k}^2}\left(1-\hat{\mathbf{k}}\hat{\mathbf{k}}\right)\cdot\mathbf{f}(\mathbf{k}) \\ &= \int d^3\mathbf{r}\left\{\int \frac{d^3\mathbf{k}}{(2\pi)^3}\frac{1}{\eta\mathbf{k}^2}\left(1-\hat{\mathbf{k}}\hat{\mathbf{k}}\right)e^{i\mathbf{k}\cdot(\mathbf{r}-\mathbf{r})}\right\}\cdot\mathbf{f}(\mathbf{r}) \\ &= \int d^3\mathbf{r}\,\boldsymbol{\Omega}(\mathbf{r}-\mathbf{r})\cdot\mathbf{f}(\mathbf{r})\ , \end{aligned} \tag{95}$$

with unit matrix $\mathbf{1}$ and the explicit from of the integral kernel

$$\boldsymbol{\Omega}(\mathbf{r}) = \int \frac{d^3\mathbf{k}}{(2\pi)^3}\frac{1}{\eta\mathbf{k}^2}\left(1-\hat{\mathbf{k}}\hat{\mathbf{k}}\right)e^{i\mathbf{k}\cdot\mathbf{r}}\ . \tag{96}$$

The relation between $\mathbf{u}'$ and $\mathbf{f}$ is nonlocal but linear. For the evaluation of the integral we use the isotropy of space and therefore the ansatz

$$\Omega_{\alpha\beta} = A\delta_{\alpha\beta} + B\hat{r}_\alpha\hat{r}_\beta\ . \tag{97}$$

The trace of the matrix $\boldsymbol{\Omega}$ is

$$\begin{aligned} Tr(\boldsymbol{\Omega}) &\equiv \Omega_{\alpha\alpha} = 3A + B = \frac{1}{(2\pi)^3}\int d^3\mathbf{k}\,\frac{1}{\eta\mathbf{k}^2}(3-1)e^{i\mathbf{k}\cdot\mathbf{r}} \\ &= \frac{1}{(2\pi)^3}\frac{8\pi}{\eta r}\underbrace{\int_0^\infty dk\,\frac{\sin(kr)}{k}}_{\pi/2} = \frac{1}{2\pi\eta r}\ . \end{aligned} \tag{98}$$

With tensor contraction of $\boldsymbol{\Omega}$

$$\begin{aligned} \hat{\mathbf{r}}\cdot\boldsymbol{\Omega}\cdot\hat{\mathbf{r}} &= \hat{r}_\alpha\Omega_{\alpha\beta}\hat{r}_\beta \\ &= A\hat{r}_\alpha\delta_{\alpha\beta}\hat{r}_\beta + B\hat{r}_\alpha\left(\hat{r}_\alpha\hat{r}_\beta\right)\hat{r}_\beta \\ &= A + B = \int \frac{d^3\mathbf{k}}{(2\pi)^3}\frac{1}{\eta k^2}\left[1-\left(\hat{\mathbf{k}}\cdot\hat{\mathbf{r}}\right)^2\right]e^{i\mathbf{k}\cdot\mathbf{r}} \\ &= \frac{1}{(2\pi)^2\eta}\int_0^\infty\int_0^\pi dk\,d\cos\theta\left(1-\cos^2\theta\right)e^{ikr\cos\theta} \\ &= \frac{1}{(2\pi)^2\eta}\left\{\int_0^\infty dk\,\frac{2}{r}\frac{\sin kr}{k}\right. \\ &\quad \left. -\int_0^\infty dk\,d\cos\theta\,\frac{1}{(ir)^2}\,\partial_k^2\,e^{ikr\cos\theta}\right\} \\ &= \frac{1}{(2\pi)^2\eta}\left\{\frac{\pi}{r}+\frac{2i}{r^3}\partial_k\left(\frac{\sin kr}{k}\right)_0^\infty\right\} \\ &\overset{\text{l'Hospital}}{=} \frac{1}{4\pi\eta r}+\frac{2i}{(2\pi)^2\eta r}\underbrace{\left(\frac{-kr^2\sin kr}{2k}\right)}_{\substack{k\to 0\\ \longrightarrow 0}} \\ &= \frac{1}{4\pi\eta r}\ . \end{aligned} \tag{99}$$

one obtains a second equation for the determination of the two constants A and B.:

$$\left.\begin{aligned} 3A + B &= \tfrac{1}{2\pi\eta r} \\ A + B &= \tfrac{1}{4\pi\eta r} \end{aligned}\right\} \Longrightarrow A = B = \frac{1}{8\pi\eta r} ,$$

The final form of the matrix

$$\mathbf{\Omega}(\mathbf{r}) = \frac{1}{8\pi\eta r}\left(\mathbf{1} + \hat{\mathbf{r}}\hat{\mathbf{r}}\right) . \tag{100}$$

is the so-called Oseen–Tensor.

References

[1] R. B. Bird, R. C. Armstrong, and O. Hassager, *Dynamics of Polymeric Liquids, Vols.* I, II, 2nd ed. (John Wiley & Sons, New York, 1987).

[2] R. G. Larson, *The Structure and Rheology of Complex Fluids*,(Oxford Press, Oxford, 1999).

[3] R. E. Rosenzweig, *Ferrohydrodynamics* (Cambridge University Press, Cambridge, 1985).

[4] P. G. deGennes and J. Prost, *The Physics of Liquid Crystals* (Clarendon Press, Oxford, 1995).

[5] P. M. Chaikin and R. C. Lubensky, *Principles of Condensed Matter Physics* (Cambridge University Press, Cambridge England, 1995) Chap. 6

[6] W. Zimmermann, *Pattern Formation in Electrohydrodynamic convection*, Mat. Res. Bull. **16**, 46 (1991).

[7] S. Kai und W. Zimmermann, *Pattern Dynamics in Electrohydrodynamics of Nematic Liquid Crystals*, Prog. Theor. Phys. Suppl., **99**, 458 (1989)

[8] A. Buka and L. Kramer Eds., *Pattern Formation in Liquid Crystals*, (Springer, New York, 1996)

[9] L. Kramer and W. Pesch, *Convection Instabilities in Nematic Liquid Crystals*, Annual Review of Fluids Mechanics **27**, 515 (1995)

[10] S. Nasuno, O. Sasaki, S. Kai und W. Zimmermann, *Secondary Instabilities in Electrohydrodynamic Convection of Nematics* Phys. Rev. **A 46**, 4954 (1992)

[11] B. Dressel, A. Joets, L. Pastur, W. Pesch, E. Plaut and R. Ribotta, Phys. Rev. Lett. **88**, 024503-1 (2002).

[12] S. Odenbach, *Ferrofluide - ihre Grundlagen und Anwendungen: Magnetische Flssigkeiten kontrollieren*, in Physik in unserer Zeit, **32**, 122 (2001)

[13] T. C. Halsey, Science **258**, 761 (1992); T. C. Halsey and J. E. Martin, Scientific American **58** Oct. 1993.

[14] H. Pleiner, *Hydrodynamik komplexer Fluide* in *Komplexe Systeme zwischen Atom und Festkörper*, 25. IFF Ferienkurs, Eds. W. Zimmermann, K. Sturm, K. Kremer und G. Eilenberger (Forschungszentrum Jülich, 1994)

[15] F. H. Busse and S. C. Müller Eds., *Evolution of Spontaneous Structures in Dissipative Continuous Systems*, (Springer, Berlin, 1998).

[16] M. C. Cross and P. C. Hohenberg, *Pattern formation outside of equilibrium*, Reviews of Modern Phys. **65** , 851 (1993).

[17] L. D. Landau and E. M. Lifshitz, *LEHRBUCH DER THEORETISCHEN PHYSIK VI: Hydrodynamik* (Akademie-Verlag, Berlin, 1990)

[18] L. D. Landau and E. M. Lifshitz, *LEHRBUCH DER THEORETISCHEN PHYSIK VII: Elastizitätstheorie* (Akademie-Verlag, Berlin, 1990)

[19] E. J. Hinch, Three lectures given at the school *Multiscale dynamics in complex fluids and biology* in July 2000 in Cargese (Corsica).

[20] H. Lamb, *Hydrodynamics* (Cambridge Univ. Press, Cambridge, 1932)

[21] G. K. Batchelor, *An Introduction to fluid dynamics*, (Cambridge Univ. Press, Cambridge, 1967).

[22] J. K. G. Dhont *An introduction to dynamics of colloids* (Elsevier, Amsterdam, 1996)

[23] J. Happel and H. Brenner, *Low Reynolds Number Hydrodynamics* (Prentice Hall, 1965).

[24] D. J. Tritton, *Physical Fluid Dynamics* (Clarendon Press, Oxford,1987).

[25] H. Tennekes and J. L. Lumely *A First Course in Turbulence*, (MIT Press, Cambridge Mass, 1972).

[26] S. B. Pope, *Turbulent Flows* (Cambridge Univ. Press, Cambridge, 2000).

[27] A. Einstein, *Eine neue Bestimmung der Moleküldimension*, Ann. Phys. **19**, 289 (1906) und **34**, 591 (1911).

[28] J. L. Lumley, Annu. Rev. Fluid Mech. **1**, 367 (1969); P. S. Virk, AIChE J. **21**, 625 (1975); N. S. Berman, Annu. Rev. Fluid Mech. **10**, 47 (1978); P.-G. deGennes, Physica A **140**, 9 (1986).

[29] G. K. Batchelor and J. T. Green, *The determination of the bulk stress in a suspension of spherical particles to order* c^2, J. Fluid Mech. **56**, 401-427 (1972).

[30] J. F. Brady and G. Bossis, *Stoksian Dynamics*, Ann. Rev. Fluid Mech. **20**, 111 (1988); D.R. Foss and J. F. Brady, *Structure, diffusion and rheology of Brownian suspensions by Stokesian Dynamics simulation*, J. Fluid. Mech. **407**, 167 (2000);

[31] M. Kraus, W. Wintz, U. Seifert and R. Lipowsky, Phys. Rev. Lett. **77**, 3685 (1996); M. Abkarian, C. Lartigue and A. Viallat, Phys. Rev. Lett **88**, 068103 (2002) and references therein.

[32] T. T. Perkins, S. R. Quake, D. E. Smith, and S. Chu, Science **264**, 822 (1994); S. Manneville *et al.*, Europhys. Lett. **36**, 413 (1996); T. T. Perkins, D. E. Smith, and S. Chu, Science **276**, 2016 (1997); S. R. Quake, H. Babcock, and S. Chu, Nature **388**, 151 (1997).

[33] T. T. Perkins, D. E. Smith, R. G. Larson, and S. Chu, Science **268**, 83 (1995)

[34] D. E. Douglas and S. Chu, *Response of Flexible Polymers to a Sudden Elongational Flow*, Science **281**, 1335 (1998)

[35] D. E. Douglas, H. P. Babcock and S. Chu, *Single Polymer Dynamics in Steady Shear Flow*, Science **283**, 1724 (1999).

[36] R. G. Larson, T. T. Perkins, D. E. Smith, and S. Chu, Phys. Rev. E **55**, 1794 (1997).

[37] P. G. deGennes, *POLYMER PHYSICS: Molecular Individualism*, Science **276**, 1999 (1997).

[38] A. Groisman and S. Steinberg, *Elastic turbulence in a polymer solution flow*, Nature **405**, 53 (2000); *Efficient mixing at low Reynolds numbers using polymer additives*, Nature **410**, 905 (2001).

[39] H. W. Müller and W. Zimmermann, *Farady instability in a linear viscoelastic fluid*, Europhys. Lett. **45**, 169 (1999); C. Wagner, H. W. Müller and K. Knorr, *Faraday Waves on a Viscoelastic Liquid*, Phys. Rev. Lett. **83**, 308 (1999); S. Kumar, *Vibration–induced interfacial instabilities in viscoelastic fluids*, Phys. Rev. **E 65**, 026305 (2002)

[40] H. Temmen, H. Pleiner, M. Liu and H. R. Brand, *Convective Nonlinearity in Non-Newtonian Fluids*, Phys. Rev. Lett. **84**, 3228 (2000); Phys. Rev. Lett. **86**, 745 (2001);

[41] F. Brochard-Wyart, Europhys. Lett. **23**, 105 (1993); **30**, 387 (1995).

[42] D. Kienle and W. Zimmermann, *F-shell Blob Model for a Tethered Polymer in Strong Flows*, Macromolecules **34**, 9173 (2001).

[43] R. Rzehak, D. Kienle, T. Kawakatsu, and W. Zimmermann, *Partial draining of a tethered polymer in flow*, Europhys. Lett. **26**, 821 (1999).

[44] R. Rzehak, W. Kromen, T. Kawakatsu and W. Zimmermann, *Deformations of tethered polymers in uniform flow*, Euro. Phys. J. **E 2**, 3(2000).

[45] P. S. Doyle, E. S. G. Shaqfeh and A. P. Gast, Phys. Rev. Lett. **78**, 1182 (1997); B. Ladoux and P. S. Gast, Europhys. Lett. **52**, 511 (2000); P. S. Doyle, B. Ladoux and J. L. Viovy, Phys. Rev. Lett. **84**, 4769 (2000).

[46] A. Arendt, J. Leonhard, D. Kienle, G. Ristow, R. Rzehak and W. Zimmermann, *Cross-Streamline migration of deformable objects in Poiseuille flow* (to be published).

[47] D. Kienle, R. Rzehak and W. Zimmermann, *Nonlinear Stokes law and strong fluctuations of polymers in flow* (to be published).

[48] D. Kienle and W. Zimmermann, *Viscous Drag on single polymers, star polymers and polymer coated particles* (to be published).

C 9 Practical Rheology

Silke Rathgeber
Institut für Festkörperforschung - Weiche Materie
Forschungszentrum Jülich GmbH

Contents

1 Introduction 2

2 Definitions and basic models for material response 3
2.1 Definitions: stress, deformation, deformation rate 3
2.2 Constitutive relation: Hookean solid and Newton Fluid 4
2.3 Spring-dashpot models: Voigt-Kelvin solid and Maxwell fluid 6
2.4 Linear viscoelasticity and relaxation time spectrum 8
2.5 Summary of rheological test modes 9
2.6 Oscillatory shear 11

3 Concepts and realizations of shear rheometry 12
3.1 Pressure-driven and drag-flow rheometers 12
3.2 Rotational rheometer: Shear flow geometries 13
3.3 Flow instabilities: Reynolds- and Taylor-instability 15
3.4 Stress-controlled and strain-controlled measurements 16

4 Applications in polymers, colloids and complex fluids 18
4.1 Effect of entanglements on the rheological response of polymers 18
4.2 Shear-thinning and thickening in highly concentrated colloidal suspensions 23
4.3 Shear-band formation in self-assembled surfactant solutions 26

1 Introduction

Rheology can be defined as the science of deformation and flow of matter in response to the application of mechanical force. The term comes from the Greek word "rheos" meaning "to flow". The science of rheology can be said to have been founded with the meeting of an international scientific committee in 1929 to draw up a constitution for the society of rheology. Though the word "rheology" was coined in 1929 by M. Reiner and E. Bingham substantial scientific contributions certainly date back to much earlier times, when for example R. Hooke in 1660 discovered the law governing linear elastic deformation of solids or when Sir I. Newton in 1687 proposed his law relating stress to velocity gradients in fluids.

Although rheology spans classical, solid mechanics at one end and fluid mechanics at the other, generally materials show both deformation and flow under the influence of mechanical force. These so called viscoelastic materials undergo irreversible, viscous changes through energy dissipative processes as well as reversible, elastic changes through energy storage processes. Energy is dissipated mainly in form of heat or sound, and stored as potential energy by conversion from kinetic energy. The exact balance between energy dissipation and storage, elastic and viscous response of the same material depends on many parameters, such as temperature but also on the magnitude of the deformation or force. So for example the viscosity of some materials strongly depends on the applied stress or rate of deformation. This behavior is called shear-thickening or shear-thinning, depending whether the viscosity increases or decreases with shear rate or stress. One remarkable example for a shear thinning material is quicksand. The viscosity rapidly drops by thrashing about in it (high shear rate), whereas slow and deliberate movements reduce the shear rate. In the latter case the viscosity is maintained and consequently a person would sink more slowly. Whether a material appears as a fluid or solid also depends on the time scale of the laboratory experiment relative to the characteristic times of the internal material processes. Thus the Himalayas rose and are still rising up from the Indian Plains as a result of the sub-continent of India colliding with Asia in a manner similar to the piling of butter in front of a spreading knife; both are analogous rheological phenomena only separated by viscosity and time.

The value of the understanding of the rheological response of materials to industrial applications is obvious. Flow is used in industrial processing to convey, to mix materials, and to extrude them into useful shapes. So for example in crude-oil industry the pumping of huge volumes of oil through pipelines over rather long distances is only possible, if the viscosity first can be lowered by appropriate additives. Even in medicine rheological techniques are now accepted for the diagnosis of blood disorders and for characterizing other biological fluids. Because of the broad range of materials and physical concepts involved, rheology is truly interdisciplinary science spanning the gap between chemistry, physics, mathematics, engineering and life science.

With this lecture we would like to give a short introduction into these rather complex field of science. After starting with basic definitions of rheological variables and simple models for material response, we then will give some practical inside in the different rheometer types, shear configuration and rheological test modes. Finally we will try to apply our knowledge to some examples taken from the field of soft matter physics: polymers, colloids and complex fluids.

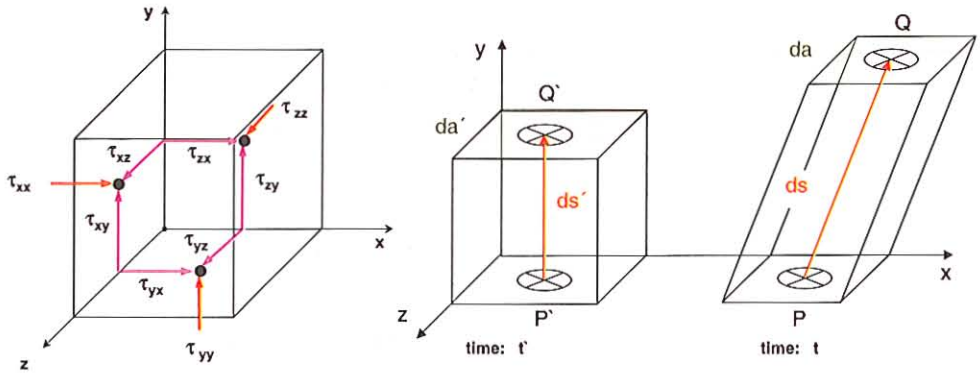


Fig. 1: *Stresses acting on a cubic test volume (left) and deformation of a test volume with time (right) under shear.*

2 Definitions and basic models for material response

2.1 Definitions: stress, deformation, deformation rate

In rheology we generally have to answer the question, how a material deforms when an external mechanical force or stress (force per unit area) is applied or vice versa how the stresses in a material relax or built up under deformation. The stress on any plane through an arbitrary point P in a sheared substance can be expressed in terms of the three-dimensional *stress tensor* $\underline{\underline{\sigma}}$, which describes the stresses acting on three perpendicular planes through P as sketched in fig.(1). In Cartesian coordinates $\underline{\underline{\sigma}}$ reads:

$$\underline{\underline{\sigma}} = \begin{bmatrix} -p+\tau_{xx} & \tau_{xy} & \tau_{xz} \\ \tau_{yx} & -p+\tau_{yy} & \tau_{yz} \\ \tau_{zx} & \tau_{zy} & -p+\tau_{zz} \end{bmatrix}. \tag{1}$$

The diagonal elements τ_{ij} (i=j) are normal forces directed perpendicular and the off-diagonal elements τ_{ij} (i≠j) denote shear stresses directed parallel to one of the three planes. Since we are only interested in the effect of shear on the stress without the contribution of the isotropic pressure p, we define the shear stress tensor for our considerations as $\underline{\underline{\tau}} = p\underline{\underline{I}} + \underline{\underline{\sigma}}$, where $\underline{\underline{I}}$ is the unit tensor. For the definition of the deformation (or strain) and the deformation rate (or strain rate) we consider the deformation of a small test volume as shown in fig.(1). Q' and P' denote two arbitrary, neighboring points separated by the vector ds' within this test volume at earlier time t'. The quantities Q, P and ds denote the same variables at present time t, but moved by shear. The *deformation gradient tensor* $\underline{\underline{\delta}}$ relates the actual distances in the sample to those at previous times: $ds = \underline{\underline{\delta}} ds'$ with $\underline{\underline{\delta}}$ in Cartesian coordinates:

$$\underline{\underline{\delta}} = \begin{bmatrix} \partial x/\partial x' & \partial x/\partial y' & \partial x/\partial z' \\ \partial y/\partial x' & \partial y/\partial y' & \partial y/\partial z' \\ \partial z/\partial x' & \partial z/\partial y' & \partial z/\partial z' \end{bmatrix}. \tag{2}$$

For us the *deformation- or strain tensor* $\underline{\underline{\gamma}} = \underline{\underline{\delta}}\underline{\underline{\delta}}^T - \underline{\underline{I}}$ is important. The strain tensor describes the relative local area change of an area with normal vector $\underline{n}$ in respect to the undeformed state: $da'^2/da^2 - 1 = \underline{n}\underline{\underline{\gamma}}\underline{n}$. When there is no deformation, all strains are zero.
The *velocity gradient tensor* $\dot{\underline{\underline{\delta}}}$ is given by the time derivate of the deformation gradient tensor $\underline{\underline{\delta}}$ for the limit $(ds' - ds) \rightarrow 0$:

$$\dot{\underline{\underline{\delta}}} = \begin{bmatrix} \partial v_x/\partial x & \partial v_x/\partial y & \partial v_x/\partial z \\ \partial v_y/\partial x & \partial v_y/\partial y & \partial v_y/\partial z \\ \partial v_z/\partial x & \partial v_z/\partial y & \partial v_z/\partial z \end{bmatrix}. \tag{3}$$

The *deformation- or strain rate tensor* is simply the time derivate of $\underline{\underline{\gamma}}$ also for the limit $(ds' - ds) \rightarrow 0$ and can be expressed in terms of the velocity gradient tensor by: $\dot{\underline{\underline{\gamma}}} = \dot{\underline{\underline{\delta}}} + \dot{\underline{\underline{\delta}}}^T$.

2.2 Constitutive relation: Hookean solid and Newton Fluid

Hookean solid The relation between applied force and the resulting deformation or vice versa is called, *constitutive relation*. In 1678 Hooke proposed that the force in a "springy body" is proportional to its extension. But it took more than 150 years until Cauchy in the 1820s completed the three-dimensional formulation of Hooke's law for small deformations of solid materials. It took another 130 years before Rivlin in 1948 wrote down the stress-deformation relation using the tensor description introduced above. If the stress at any point is linearly proportional to deformation for an isotropic material, then the extra stress due to deformation should be determined by a constant multiplied by the deformation:

$$\underline{\underline{\tau}} = G\underline{\underline{\gamma}}, \tag{4}$$

where the constant of proportionality G, called *elastic modulus* is an intrinsic property of the solid. If the deformation is expressed in terms of an applied stress $\underline{\underline{\gamma}} = J\underline{\underline{\tau}}$, the constant of proportionality is called *compliance*.
For simple shear as depicted in fig.(2) a tangential one-dimensional force is applied, for example in x direction. Material planes slide over each other in x-direction but the other directions (y,z) remain unchanged. The displacement of the x-coordinate is simply $\gamma = dx/dy = tan(\alpha)$ so that the deformation gradient tensor and the deformation tensor can be written as:

$$\underline{\underline{\delta}} = \begin{bmatrix} 1 & \gamma & 0 \\ 0 & 1 & 0 \\ 0 & 0 & 1 \end{bmatrix} \quad \text{and} \quad \underline{\underline{\gamma}} = \begin{bmatrix} \gamma^2 & \gamma & 0 \\ \gamma & 0 & 0 \\ 0 & 0 & 0 \end{bmatrix}. \tag{5}$$

The shear stress $\tau_{xy} = \tau_{yx} = G\gamma$ is proportional to the deformation and the normal force $\tau_{xx} = G\gamma^2$ increases quadratically with the strain. Obviously, a three-dimensional approach is existential to describe rheological response of materials even if only an one-dimensional deformation is applied.
For example normal forces lead to the so called *Weissenberg effect* ("rod climbing"). In fig.(3) the behavior of a purely viscous oil and a viscoelastic polymer solution with high elastic contribution to the rheological response are shown under rotational shear

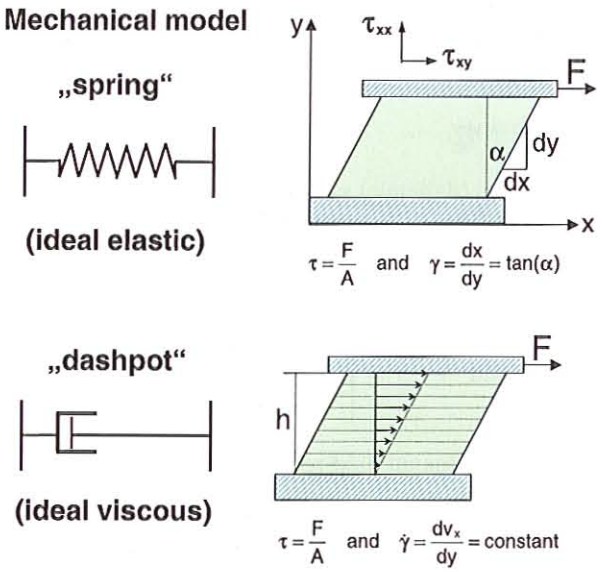


Fig. 2: *Deformation of a Hookean solid and a Newtonian fluid under simple shear conditions shown with their mechanical counterparts.*

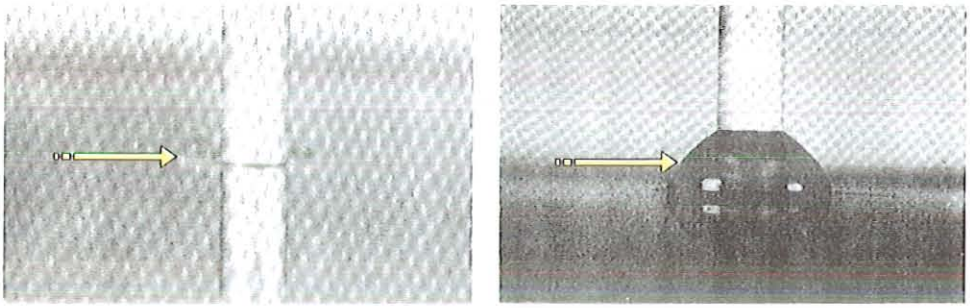


Fig. 3: *Rod climbing (Weissenberg effect): (left) Rod rotating in a Newtonian oil and (right) in a viscoelastic fluid (polyisobutylene solution), respectively [5, 2].*

conditions. The inner rod is rotating. The partly elastic response of the polymer solution has its origin in a temporary entanglement network, which is discussed in more detail in sec.(4.1). For the Newtonian oil the centrifugal force only generates a small negative pressure resulting in a small depression of the surface close to the rotating rod. In a viscoelastic fluid normal forces create a large pressure in the direction of the inner cylinder, causing the fluid to rise up the rod. In analogy to Hookean solid under simple shear the force is directed in the direction of the moving surface. We would like to point out that the observed "rod climbing" is a non-linear effect (see also sec.(2.4) and sec.(2.6)).

Newtonian fluid In 1687 Newton formulated his fundamental idea that the local stress arising from a "lack of slipperiness" between fluid layers is proportional to the velocity gradient. The "lack of slipperiness" has its origin in the exchange of material between

fluid layers with different velocity due to the Brownian motion of the molecules. In 1845 Stokes was finally able to write out the three-dimensional form of the constitutive equation of a Newtonian fluid:

$$\underline{\underline{\tau}} = \eta \underline{\underline{\dot{\gamma}}}, \tag{6}$$

where the constant of proportionality η is the (dynamic) viscosity of the fluid. For simple shear flow the friction between the layers results in a constant velocity profile as depicted in fig.(2) with $v_y = v_z = 0$ and $\dot{\delta} = dv_x/dy = constant$. The velocity gradient tensor and the deformation rate tensor simply read:

$$\underline{\underline{\dot{\delta}}} = \begin{bmatrix} 0 & \dot{\gamma} & 0 \\ 0 & 0 & 0 \\ 0 & 0 & 0 \end{bmatrix} \quad \text{and} \quad \underline{\underline{\dot{\gamma}}} = \begin{bmatrix} 0 & \dot{\gamma} & 0 \\ \dot{\gamma} & 0 & 0 \\ 0 & 0 & 0 \end{bmatrix}. \tag{7}$$

The shear stress for simple shear flow of a Newtonian fluid reduces to $\tau_{xy} = \tau_{yx} = \eta\dot{\gamma}$ and all normal forces are equal to zero.
In general, the deformation of a material is not only governed by the constitutive relation between stress and deformation, it also has to obey the principles of *conservation of mass* and *conservation of momentum*. From the condition that the change of mass in any volume must equal the net flux of mass though its surface the *continuity equation*

$$\frac{\partial \rho}{\partial t} = -\rho \nabla \cdot \underline{v} \tag{8}$$

can be derived, which reduces for an incompressible fluid (ρ= constant) to $\nabla \cdot \underline{v} = 0$. The momentum balance reads:

$$\frac{\partial \rho \underline{v}}{\partial t} = -\nabla \cdot \rho \underline{v}\,\underline{v} + \nabla \cdot \underline{\underline{\sigma}} + \rho \underline{g}, \tag{9}$$

taking into account the momentum transfer to a body due to convection through its surface, due to contact forces acting on its surface and body forces like gravity acting on the volume. Insertion of the continuity equation reduces the momentum balance to

$$\rho \frac{\partial \underline{v}}{\partial t} = \nabla \cdot \underline{\underline{\sigma}} + \rho \underline{g}, \tag{10}$$

which can be further simplified to a stress balance ($\nabla \cdot \underline{\underline{\sigma}} = 0$), if the body is in static equilibrium and gravity can be neglected. This condition is automatically satisfied for the special cases of a Hookean solid and a Newtonian fluid under simple shear since under these special conditions the stress is homogeneous, so all its derivates are equal to zero.

2.3 Spring-dashpot models: Voigt-Kelvin solid and Maxwell fluid

If a force (deformation) is applied to a Hookean solid, also called ideal elastic solid, the deformation (stress) follows instantaneously without any delay. After unloading the sample no stresses or deformation remain since no energy has been dissipated in the system. The same behavior is known from an ideal spring, which would be the mechanical

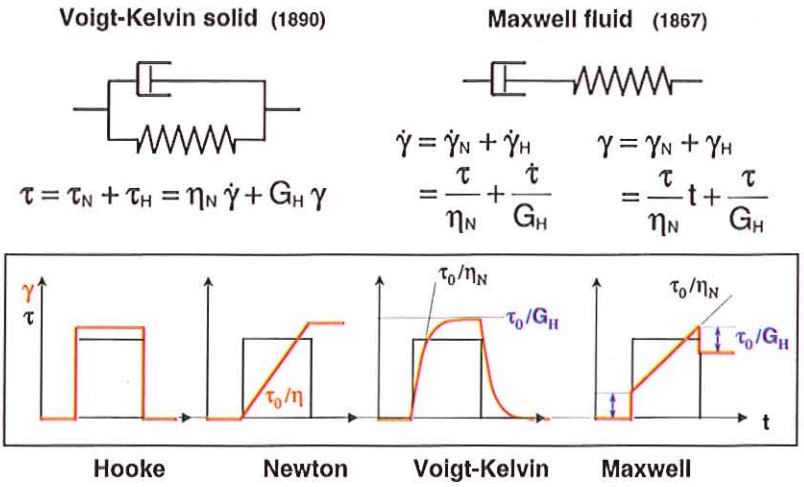


Fig. 4: *Viscoelastic properties: Voigt-Kelvin solid and Maxwell fluid and their stress response to a box-shaped deformation in comparison to responses of a Hookean solid and a Maxwell fluid.*

analog. In fig.(4) the applied stress and the material response (deformation) are shown for a box-shaped time dependence of the stress. If the same box-shaped stress is applied to an Newtonian fluid, also called ideal viscous fluid, the deformation increases linearly with time. After stress relief the sample remains deformed since the energy has been fully dissipated. An analogy to a dashpot can be drawn as the mechanical counterpart. From combinations of spring and dashpot in serial and parallel connection a descriptive presentation of the viscoelastic characteristics of solids and fluids can be obtained. It is important to mention that these models do not lead to a microscopic understanding of the rheological response but give some informative inside into the basic rheological properties of viscoelastic materials.

Voigt-Kelvin solid The parallel connection of a spring with elastic modulus G_H and a dashpot with viscosity η_N leads to the Voigt-Kelvin element. Spring and dashpot undergo the same deformation and the overall stress is the sum of the single stresses for each element.

$$\tau = \tau_N + \tau_H = \eta_N \dot{\gamma} + G_H \gamma. \tag{11}$$

For a stepwise increase and decrease of the applied stress to (from) a plateau value τ_0 the solution of this inhomogeneous differential equation reads

$$\gamma_{up} = \frac{\tau_0}{G_H}[1 - exp(-t/\lambda)] \qquad \text{and} \qquad \gamma_{down} = \frac{\tau_0}{G_H} exp(-t/\lambda) \tag{12}$$

with the relaxation time $\lambda = \eta_N / G_H$. Since the restoring force of the spring leads to a finite deformation τ_0/G_H and the deformation goes back to zero after stress relief the Voigt-Kelvin element represents a solid (see fig.(4)).

Maxwell fluid The serial connection of a spring with elastic modulus G_H and a dashpot with viscosity η_N leads to the Maxwell element. The overall deformation as well as the overall deformation rate is the sum of the single contributions of each element.

$$\gamma = \gamma_N + \gamma_H \qquad \text{and} \qquad \dot{\gamma} = \dot{\gamma}_N + \dot{\gamma}_H. \tag{13}$$

For a stepwise increase and decrease of the applied stress to (from) a plateau value τ_0 the deformation can be directly given by

$$\gamma = \frac{\tau_0}{\eta_N} t + \frac{\tau_0}{G_H} \tag{14}$$

Applying a stress the spring deforms instantaneously $\gamma_H = \tau_0/G_H$ followed by a linear deformation of the dashpot with slope $\gamma = \tau_0/\eta_N$. After stress relief only the elastic spring contribution relaxes spontaneously but the maximal deformation of the dashpot $\tau_0 t/\eta_n$ remains. From the differential equation in eq.(13) the stress relaxation for a step-wise shear deformation ($\gamma = 0$ for $t < 0$ and $\gamma = \gamma_0$ for $t \geq 0$) can be calculated. With $\dot{\gamma} = 0$ and the initial condition $\tau(0) = \gamma_0 G_H$ follows

$$\tau = \gamma_0 \, G_H \, exp(-t/\lambda). \tag{15}$$

The relaxation time $\lambda = \eta_N/G_H$ is the same as obtained for the Voigt-Kelvin element. Since arbitrary large deformations can be achieved if the stress is just applied long enough and the stress relaxes to zero if a constant deformation is imposed the Maxwell element describes a fluid.

2.4 Linear viscoelasticity and relaxation time spectrum

The major conclusion, which can be drawn from the mechanical analogs is that for a viscoelastic material the rheological response functions become time-dependent. For example for a Maxwell fluid, from eq.(14) and eq.(15) the time-dependence of the shear modulus and the compliance can be derived:

$$G(t) = G_H \, exp(-t/\lambda) \qquad \text{and} \qquad J(t) = \frac{1}{G_H} + \frac{t}{\eta_N}. \tag{16}$$

Linear viscoelasticity In case of linear (viscoelastic) behavior, the response functions are time-dependent but independent of the applied deformation or stress. The deformation or stress can be expressed as the linear superposition of the response on a series of single stress or deformation steps: $\Delta\tau(t) = G(t - t')\Delta\gamma(t')$ and $\Delta\gamma(t) = J(t - t')\Delta\tau(t')$ as sketched in fig.(5). For infinite small time steps this leads to the integral equations:

$$\tau = \int_{t'=0}^{t} G(t - t')\dot{\gamma}(t')dt' \qquad \text{and} \qquad \gamma = \int_{t'=0}^{t} J(t - t')\dot{\tau}(t')dt'. \tag{17}$$

The *relaxation function* $G(t - t')$ and the *compliance* $J(t - t')$ are so called *memory functions* since the rheological response of the material depends not only on the present shear conditions, but also on its shear history at previous times.

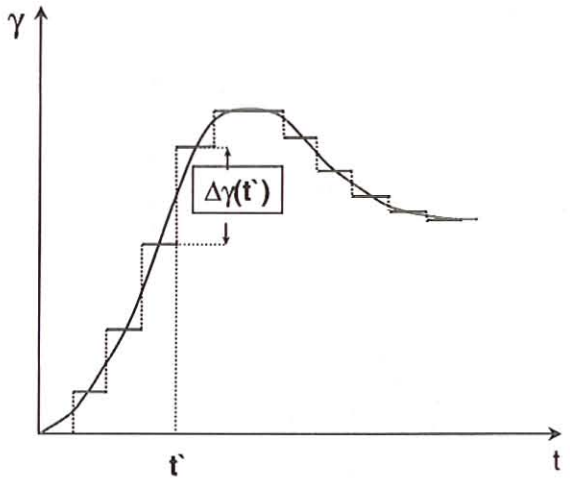


Fig. 5: *Superposition principle for linear response.*

Relaxation spectrum We have seen that for the Maxwell element one relaxation time is sufficient to describe the temporal development of the relaxation function $G(t)$. The stress relaxation, i.e. $G(t)$ shows a single exponential decay. In general, different microscopic relaxation processes with different characteristic times λ_i contribute to the relaxation of $G(t)$. The mechanical analog would be an extended Maxwell-model, where N serial connections of spring G_{Hi} and dashpot η_{Ni} with relaxation times $\lambda_i = \eta_{Ni}/G_{Hi}$ are put together in parallel connection. The generalized relaxation function then reads

$$G(t) = \sum_{i=1}^{N} G_{Hi}\, exp(-t/\lambda_i). \tag{18}$$

Polymer molecular theories predict an infinite series form for the relaxation modulus. For example the Rouse model, formulated for non interacting polymer chains [10, 9] (see also the contribution D. Richter (C2)),

$$G_{Hi} = G_{H0}\frac{\lambda_i}{\sum\limits_i \lambda_i} \qquad \text{and} \qquad \lambda_i = \frac{\lambda_0}{i^2} \tag{19}$$

is obtained, leaving only two adjustable parameters for the data fit; the form of $G(t)$ is predetermined. Analogous equations can be found for the compliance J and the viscosity η. For details see [6, 2]. Using a continuous relaxation time spectrum $H(\lambda)$ rather than a discrete set leads to the integral equation:

$$G(t) = \int_0^\infty \frac{H(\lambda)}{\lambda} exp(-t/\lambda)\, d\lambda. \tag{20}$$

2.5 Summary of rheological test modes

Fig.(6) summarizes the most important test modes, from which different rheological response function can be obtained:

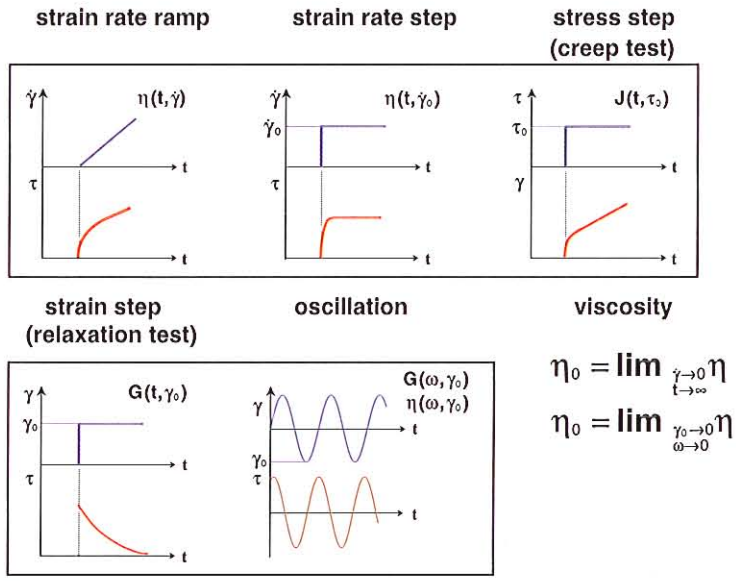


Fig. 6: *Summary of rheological test modes: Input, output and obtained response function.*

- Strain rate ramp $\dot{\gamma}(t) = (t - t_0)/(t_{max} - t_0)\,\dot{\gamma}_{max}$: Linear increase of the shear rate up to a given maximal value in a predetermined time interval. Detection of the stress leads to the viscosity as a function of the shear rate.
- Strain rate step $\dot{\gamma}(t) = \dot{\gamma}_0(t \geq t_0)$: Stepwise increase of the shear rate to a plateau value. Through detection of the stress after sufficient long times the stationary value of the viscosity is obtained for a particular $\dot{\gamma}_0$.
- Stress step or creep test $\tau(t) = \tau_0(t \geq t_0)$: Stepwise increase of the shear stress to a plateau value. From the measured deformation the time dependent compliance can be determined for $\tau = \tau_0$.
- Strain step or relaxation test $\gamma(t) = \gamma_0(t \geq t_0)$: Stepwise increase of the deformation to a plateau value. Detection of the stress allows the determination of the time dependent relaxation function for a certain deformation γ_0.
- Oscillatory shear $\gamma(t) = \gamma_0\, sin(\omega t)$: Imposing an oscillatory deformation and detection of the oscillatory stress. The dissipative G'' and elastic contribution G' to the shear modulus as well as viscosity can be determined for a particular deformation amplitude and frequency (see sec.(2.6)).

Since the viscosity is generally a function of the frequency and time and might also depend on the deformation in the non-linear regime its value for slow deformation rates and long times $\eta(\dot{\gamma} \to 0, t \to \infty)$ or equivalent for small frequencies and small deformations $\eta(\gamma_0 \to 0, \omega \to 0)$ is used to characterize a particular material.

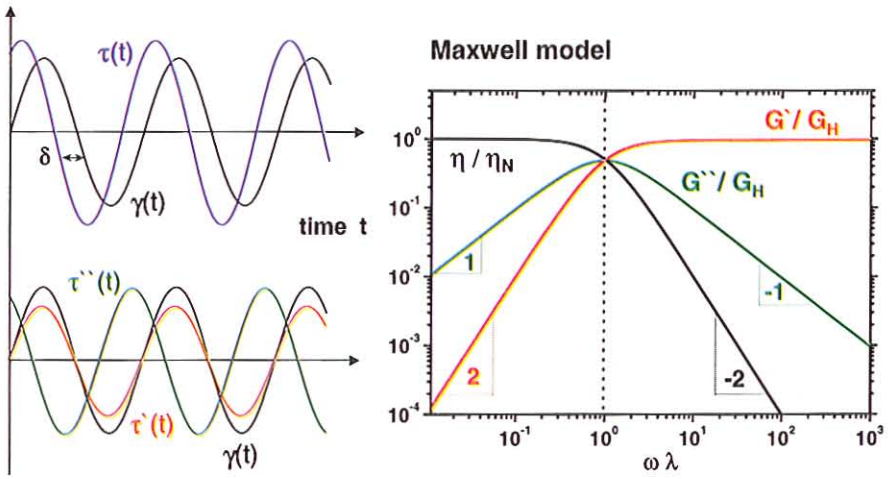


Fig. 7: *Oscillatory shear: time-dependence of the applied deformation and the stress τ including its real τ' and imaginary part τ'' (left) and the frequency-dependence of the viscosity, the storage G' and loss modulus G'' as obtained for the Maxwell element (right).*

2.6 Oscillatory shear

Since high frequencies correspond to short times and vice versa the oscillatory shear mode offers the possibility to probe the rheological response of a material over a large time range by simply changing the frequency of the applied deformation. In combination with the time-temperature superposition principle as described in sec.(4.1) it is possible to cover easily several decades in frequency. Small sample quantities and the fact that periodic signals can be measured with high accuracy make this method so successful.
An oscillatory deformation $\gamma(t) = \gamma_0 sin(\omega t)$ leads to a deformation rate $\dot{\gamma}(t) = \gamma_0 \omega cos(\omega t)$, which can be written in complex notation as $\dot{\gamma}(t) = \gamma_0\, \omega\, [sin(\omega t) - i\, cos(\omega t)]$. Insertion into eq.(17) leads to a complex expression for the stress:

$$\begin{aligned} \tau(t) &= \gamma_0 \left[G' sin(\omega t) - iG'' cos(\omega t)\right] \quad \text{with} = \tau'(t) + i\,\tau''(t) \\ G'' &= \omega \int_0^\infty G(t-t') cos(\omega t') dt' \quad \text{and} \\ G' &= \omega \int_0^\infty G(t-t') sin(\omega t') dt', \end{aligned} \tag{21}$$

where the so called *loss modulus* G'' in the imaginary part is a measure of the energy, dissipated per deformation cycle and per unit volume. The so called *elastic* or *storage modulus* G' in the real part is a measure of the energy stored in the sample per cycle of deformation and unit volume. As shown in fig.(7) the elastic contribution is in-phase with the applied deformation signal, whereas the dissipative contribution is shifted by a phase angle of $\pi/2$. Generally the stress can be written in the following form:

$$\tau(t) = |G^\star| \, sin(\omega t + \delta), \tag{22}$$

with the amplitude $|G^\star| = \gamma_0 \sqrt{G'^2 + G''^2}$ and the phase shift $tan(\delta) = G''/G'$. The stress signal has the same frequency but is shifted by a phase angle δ relative to the deformation as can be seen in fig.(7). In case of non-linear viscoelastic behavior, when the material response is also deformation dependent, higher harmonics would show up in the stress signal.
For the viscosity we obtain

$$\eta^\star = \tau/\dot{\gamma} = \eta' + i\eta'' = \frac{G''}{\omega} + i\frac{G'}{\omega} \qquad \text{and} \qquad |\eta^\star| = \frac{|G^\star|}{\omega}. \tag{23}$$

Note, that the imaginary part of the complex viscosity describes the elastic part, whereas the real part contains the dissipative part.
For a Maxwell fluid G', G'' and η can be easily determined by use of eq.(13):

$$G' = G_H \frac{\omega^2\lambda^2}{1+\omega^2\lambda^2}; \quad G'' = G_H \frac{\omega\lambda}{1+\omega^2\lambda^2}; \quad \eta = \eta_N \frac{1}{1+\omega^2\lambda^2}. \tag{24}$$

In fig.(7) G'/G_H, G'/G_H and η/η_N are plotted in a double-logarithmic presentation as a function of the non dimensional variable $(\omega\lambda)$. The limiting frequency dependencies are also marked in the figure.

3 Concepts and realizations of shear rheometry

3.1 Pressure-driven and drag-flow rheometers

Depending on how the flow is generated, shear rheometers can be divided into two groups. First *drag-flow rheometer*, in which shear is generated between a moving and a fixed solid surface and second *pressure-driven flow rheometers*, in which shear is generated by a pressure difference over a closed channel.
Pressure-driven rheometers includes the capillary rheometers and the flow cups shown in fig.(8). The latter are only used in industry for quality control measurements since the measured viscosity depends strongly on the die geometry. In the capillary rheometers the flow is much more well defined. The capillary is rather long so that edge effects can be neglected. However the measuring principle is the same for both of them: The kinematic viscosity η_k can be calculated from the capillary geometry (diameter, length), the applied pressure difference and the time a certain sample volume needs to flow through the capillary or die. η_k is related to the dynamic viscosity η by the sample density ρ: $\eta_k = \eta/\rho$. The pressure difference can be created by gravitational forces, by gas pressure or mechanically with cocks. With high-pressure capillary rheometers shear rates up to $10^6/s$ can be reached.
Drag-flow rheometers include the falling or rolling ball rheometer and drag-flow indexer shown in fig.(8). With the falling ball rheometer the time required for a ball to fall a given distance in a fluid is measured. The shear rate can be varied by tilting the tube and allowing the ball to roll down one side. Drag-flow indexers are widely used in industry since they are easy to load and they ensure adequate sample mixing. The construction principle is quite simple: a body of complex shape rotates in a large quantity

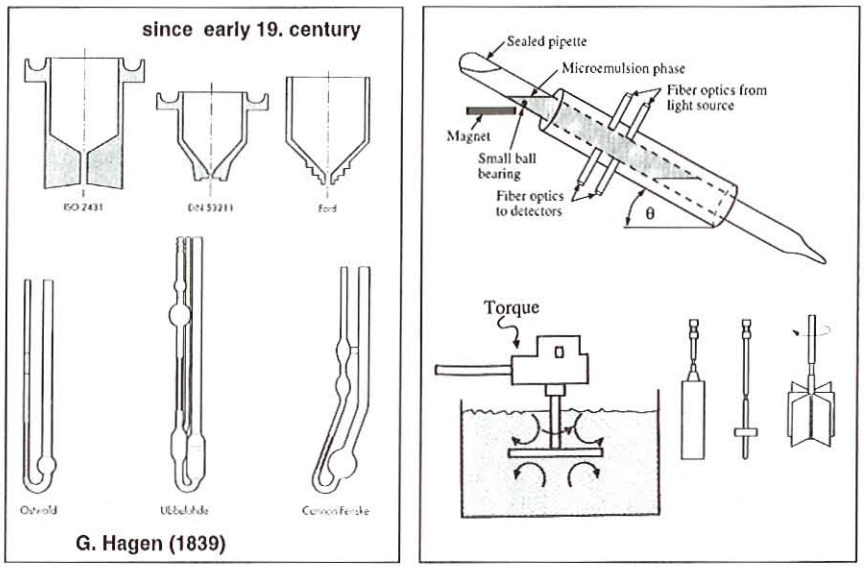


Fig. 8: *Pressure-driven flow: Flow cups (top) and capillary rheometers (bottom) and drag-driven flow: rolling ball (top) and drag-flow indexer (bottom).*

of sample. The angular velocity (shear rate) and the torque exerted on the motor axis are monitored, from which the dynamic viscosity can be determined. Again, not well defined flow conditions reduce the application of these rheometers to quality control measurement monitoring relative changes in viscosity.

3.2 Rotational rheometer: Shear flow geometries

Only if the rheometer deformation is homogeneous, i.e. stress and strain are independent of the position throughout the sample, as for example for the sliding plates, the true material response function can be directly obtained also for the non-linear regime. However the realization of translational deformations is difficult, especially if large deformation are needed. The solution to this problem are rotational rheometers, where the translation is transformed into a rotation. Most common shear geometries with quite well defined flow conditions are (1) the cone-plate, (2) the plate-plate and (c) the concentric cylinder configuration. Fig.(9) shows a schematic picture of the different shear geometries including the most important geometry parameters. The deformation profile and the velocity profile as a function of the radial distance from the rotating axis are also shown.
For the *cone-plate configuration* the deformation is homogeneous within the sample and for small opening angles α, this also holds for the shear rate and the stress:

$$\gamma = \frac{\phi}{\alpha} \quad \dot{\gamma} = \frac{\Omega}{\alpha} \quad \tau = \frac{3M}{2\pi R^3}, \tag{25}$$

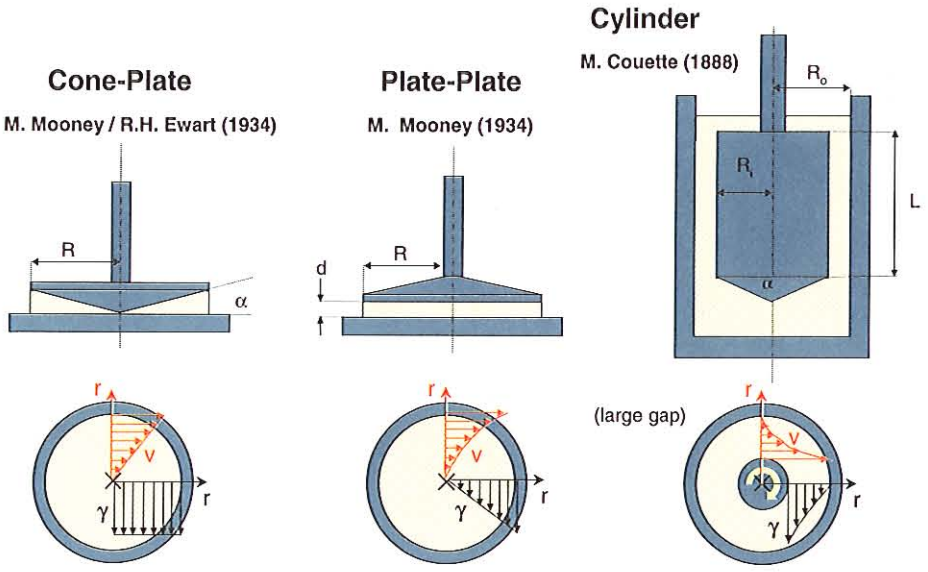


Fig. 9: *Shear geometries for a rotational rheometer.*

where ϕ denotes the rotation angle and Ω the angular velocity and M the momentum on the plate or cone. Through the measurement of the angular velocity, the rotation angle and the momentum on the plate or cone the material response can be correctly measured also in the non-linear regime.
For the *plate-plate configuration* the deformation and the shear rate increases linearly with increasing distance from the center

$$\gamma(r) = \frac{\phi r}{d} \quad \dot{\gamma}(r) = \frac{\Omega r}{d}. \tag{26}$$

For the shear stress as a function of the measured momentum the following relation can be derived:

$$\tau = \frac{M}{2\pi R^3}[3 + \frac{dln(M)}{dln[\dot{\gamma}(R)]}]. \tag{27}$$

Thus to evaluate the shear stress for an unknown fluid the dependency of $ln(M)$ versus $ln[\dot{\gamma}(R)]$ has to be determined with sufficient accuracy. The advantage of the plate-plate configuration is that the shear rate and the shear strain can be varied independently by either changing the angular velocity or the gap height.
For *concentric cylinders* the relation between the measured torque M and the stress is given by

$$\tau(R_i) = \frac{M_i}{2\pi R_i^2 L} \quad \text{or} \quad \tau(R_o) = \frac{M_o}{2\pi R_o^2 L} \tag{28}$$

whether M is measured on the outer M_o or inner cylinder M_i. For very narrow gaps $\kappa = R_i/R_o > 0.99$, the curvature can be neglected and the shear strain will be the same

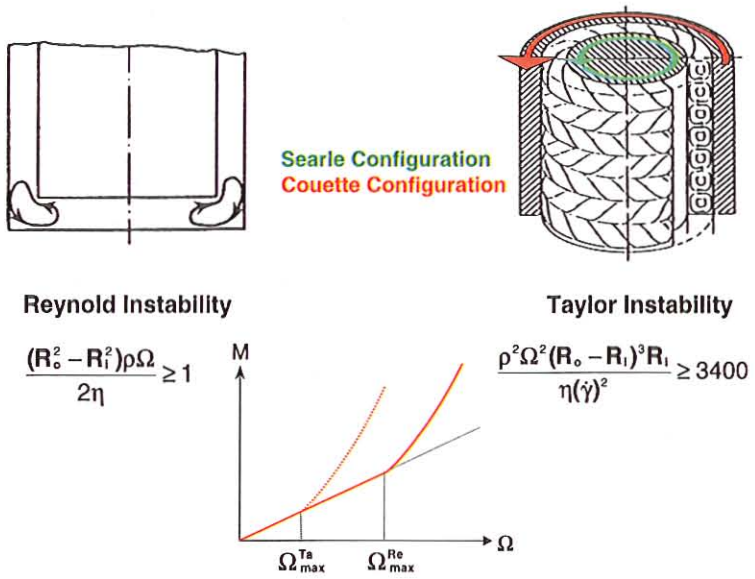


Fig. 10: *Flow instabilities: Reynolds- and Taylor-instability [1].*

as between parallel plates:

$$\gamma = \frac{\Delta x}{\Delta r} = \frac{\phi \bar{R}}{R_o - R_i}, \tag{29}$$

with the average radius $\bar{R} = (R_o + R_i)/2$. As for parallel plates the velocity gradient is constant and the shear rate is the average in the gap:

$$\dot{\gamma} = \frac{\Delta v}{\Delta r} = \frac{\Omega \bar{R}}{R_o - R_i}, \tag{30}$$

Through the measurement of the angular velocity, the rotation angle and the momentum on the inner or outer cylinder the material response can be measured also in the non-linear regime. For broader gaps similar corrections as for the plate-plate configuration can be found. For a more detailed description see [2].

3.3 Flow instabilities: Reynolds- and Taylor-instability

Laminar flow conditions were the major requirement for all our considerations so far. Flow instabilities can reduce the working range of the shear geometries drastically. In the following we will discuss two examples by means of the concentric cylinders configuration. The flow fields in the gap between outer and inner cylinder and between inner cylinder and baseplate are different. We can think of these as a combination of a plate-plate and cylinder configuration. This leads to turbulence's at the cylinder edges, as shown in fig.(10), which expand with increasing angular velocity into the cylinder gap. This turbulence, called *Reynolds-instability* give rise to an additional friction and as a consequence

the measured momentum increases drastically if a certain critical angular velocity Ω_{max}^{Re} is exceeded. The onset for Reynolds-instabilities is predicted for

$$\frac{(R_o^2 - R_i^2)\rho\Omega}{2\eta} \geq 1, \tag{31}$$

where ρ is the sample density. With increasing gap width and with decreasing samples viscosity the onset of the Reynolds-instability shifts to smaller angular velocities.
The *Taylor-instability* occurs especially for low viscosity samples at much lower critical angular velocities Ω_{max}^{Ta} than the Reynolds-instability. The instability has its origin in the destabilizing effect of the centrifugal force $F = mv^2/r$, which is in competition with the stabilizing effect of the viscous drag force. In case the centrifugal force is superior the fluid continues to be ejected outward until it encounters the outer cylinder, here the fluid is forced to overturn and, hence, travels in a helical path that constitutes the inversely arranged Taylor-vortices shown in fig.(10). The condition for the onset of the Taylor-instability is given by:

$$\frac{\rho^2\Omega^2(R_o - R_i)^3\, R_i}{\eta(\dot{\gamma})^2} \geq 3400. \tag{32}$$

The Taylor-instability onset shifts to lower angular velocities with increasing gap width and decreasing sample viscosity as it has been found for the Reynolds-instability. The configuration, where the inner cylinder is rotating and the outer cylinder is fixed is called *Searle configuration*. In the *Couette configuration* the outer rotating cylinder is rotating, whereas the inner cylinder is static. Taylor-instabilities are suppressed in the Couette configuration since the velocity gradient is reversed and the layers close to the inner cylinder, which experienced the largest radial acceleration before have now the slowest velocity. However, since tempering the moving outer cylinder is more difficult and consequently more expensive, the Searle type configuration is quite often preferred.

3.4 Stress-controlled and strain-controlled measurements

We will see that for the examples given in sec.(4.2) and sec.(4.3) the material response can strongly depend on whether a strain or stress is imposed. In principle with the same rheometer both can be implemented, but note that a rheometer is either, intrinsically stress or intrinsically strain controlled; the alternative measuring mode is conducted electronically. This can lead to quite long regulation times until the target value for the stress or strain is reached. In fig.(11) the schematic diagrams for a stress- and a strain controlled rheometer are shown.
For a *stress controlled rheometer* a given stress or momentum, is converted into a current, which drives a motor (drag cup motor) exerting a certain momentum on the sample. The actual rotational speed Ω or rotation angle Φ can be measured for example by an optical encoder. If we now want to perform with the same instrument a strain controlled measurement, for a given speed Ω or rotation angle Φ the initial start value for the current is converted into a momentum. The actual rotation angle or speed is compared to the target value. Adjustment to the target value is done iteratively. Even though a single regulation step might take only milliseconds regulation to the target value might take seconds.

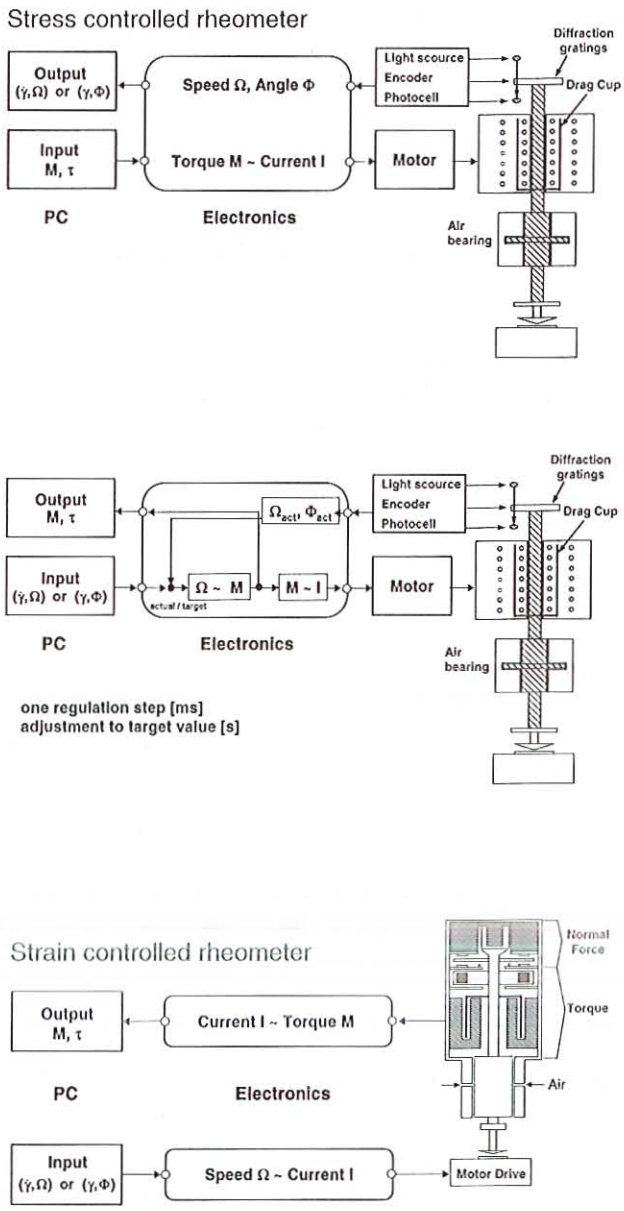


Fig. 11: *Schematic diagrams for an intrinsic stress controlled rheometer in stress- (top) and strain control mode (middle) and an intrinsic strain controlled rheometer in strain control mode (bottom).*

For the *strain controlled rheometer* a given rotational speed Ω or rotation angle Φ, is converted into a current to drive the motor. The torque exerted via the sample on the upper axis will lead to a twist, which can be measured optically, capacitively or through slip rings etc.. In fact, for a forced rebalanced transducers, torsion of the upper axis is prevented by a rotary motor. The current necessary to prevent torsion is a measure for the torque or stress, which is given as output. In an analogous way normal forces can be measured.

4 Applications in polymers, colloids and complex fluids

The aim of this section is to impart basic knowledge about the rheological response of some representative systems taken from the large field of soft matter physics. In addition some fundamental rheological phenomena and methods like

- Deborah number
- time-temperature superposition principle
- shear thinning- and shear thickening
- and shear-banding

will be discussed by means of examples taken from the main domains of soft matter physics: polymers, colloids and complex fluids.

4.1 Effect of entanglements on the rheological response of polymers

First we would like to give a short introduction into the peculiarities of the rheological behavior of polymers. In fig.(12) the relaxation modulus is plotted as a function of the shear frequency for polystyrene melts at a reference temperature of 433K. The molecular weight is increasing from right to the left. With increasing molecular weight the relaxation modulus exhibits a plateau region, where the shear modulus follows the Hookean law - the deformation of the polymeric material is purely elastic. This phenomenon is characteristic for polymeric liquids and is due to entanglements between different macromolecules. On intermediate times ($t \propto \omega^{-1}$) these entanglement cannot be resolved, flow is suppressed and the polymeric material behaves like a rubber, in which the permanent cross-links are of chemical nature. De Gennes (1971) described the restrictions exerted by the surrounding chains by an effective tube-like potential that forces the chains to execute reptative motions along their own contour lines (see schematic picture in fig.(12)) [11, 9]. This creep motion allows disentanglement with a characteristic time, which is given by the time the chain needs to leave its original tube. It is intuitively clear that this process will take longer with increasing polymer length, resulting in a broadening of the plateau region with increasing molecular weight of the macromolecules. Vanishing of the plateau for low molecular weights indicates the absence of an entanglement network for these systems. For each specific polymer a critical molecular weight M_c can be found, below which entanglements have no impact on the rheological response. This can be also seen in fig.(12), where the dependence of the viscosity on the molecular weight is plotted

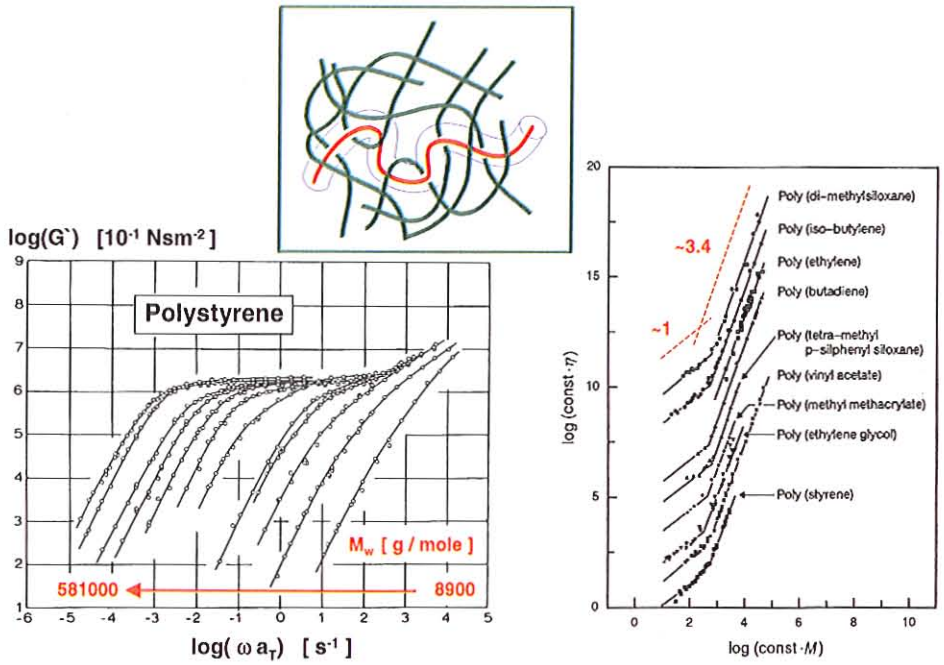


Fig. 12: *Storage modulus versus frequency of a polystyrene melt for various molecular weights reduced to $T = 433K$ by temperature-frequency superposition (left) and molecular weight dependence of the viscosity for various polymers (right) [6, 7].*

in a double-logarithmic presentation for various polymers. Two power-law regions can be distinguished: $\eta_0(M)/\eta_0(M_c) = (M/M_c)^x$ with $x = 1$ for molecular weights M below the critical molecular M_c. This behavior is predicted by the Rouse model describing non interacting chains [10, 9]. For $M > M_c$ an exponent of $x = 3.4$ is obtained, which is in disagreement with the prediction $x = 3$ of the Reptation model. Graessley [6, 9] was the first who attributed these deviation to additional constraint release processes due to the finite mobility of the surrounding chains. Pure reptation should only be found in the limit of very high (infinite) molecular weights. Contour length fluctuation should also reduce the disentanglement time. For more details see also the contribution of D. Richter (C2).

The Deborah number In 1964 R.I.M. Reiner cited the prophetess Deborah "The mountains flow before God" to define the nondimensional Deborah number [3]

$$D = \frac{\text{time of relaxation}}{\text{time of observation}}. \tag{33}$$

With his citation he wanted to motivate the basic idea that in case the observation time, which is infinite for God, is just long enough everything, even rocks flow. This might become more obvious to us if we have a closer look at the faults and kinks seen for example in the mountain range of the Rockies close to Alberta, Canada (see fig.(13)). With his

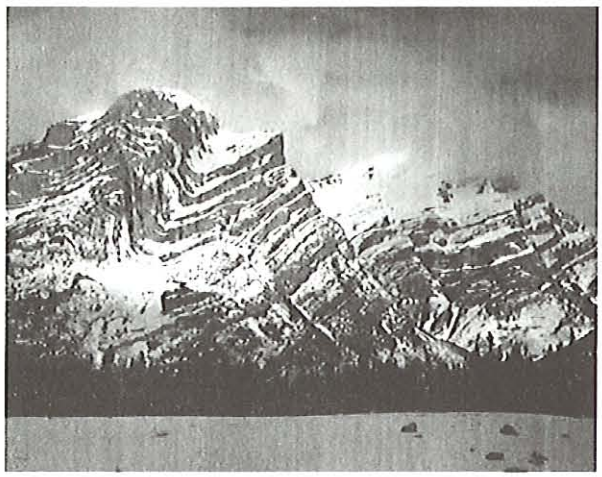


Fig. 13: *"Everything flows": Faults and kinks seen in the mountain range of the Rockies, Alberta, Canada.*

definition, he brought solids and fluids under a common concept: If the observation time is very large, or, vice versa the relaxation time of the material very small, the material has the appearance of a fluid. On the other hand, if the observation time is very short or the relaxation time of the material is longer than the observation time, the material can be considered as a solid for all practical purposes. For the rheological definition of a solid, fluid and viscoelastic material we can therefore conclude the following conditions:

$$\begin{aligned} D &\ll 1 \quad \text{fluid} \\ D &\approx 1 \quad \text{viscoelastic} \\ D &\gg 1 \quad \text{solid.} \end{aligned} \tag{34}$$

We should have these general consideration in mind when we discus the rheological response of a polymeric material over a broad time- or frequency range. In fig.(14) the tensile elastic modulus E of polyisobutylene [1] at a reference temperature of 298K (see below) is shown over a time range of about 19 decades ranging from 10^{-15}h up to 10^{3}h. The curve is representative for all amorphous, i.e. non-crystalline polymers. Crystallization of polymers is often repressed since growth of crystallites would presuppose disentanglement of the coiled, mutually interpenetrating polymers. Therefore polymers have a strong tendency to form glasses, a state, in which the amorphous fluid like structure is frozen in. At very short times, shorter than the characteristic time of the β relaxation process, which includes local conformational rearrangements, the polymeric material should behave like an elastic solid. The elastic modulus is smaller than for other materials since the intermolecular bonding forces between different macromolecules are much weaker. With increasing observation time, first the β relaxation processes should come into play and, later on, the α relaxation processes. These include relaxations of larger portions of the chain up to a certain length, which is restricted by the distance between two entanglements. The characteristic times of the α relaxation processes are therefore much longer than those of the β relaxation processes. The latter lead to the strong decay of $E(t)$ in

[1] The tensile elastic modulus is defined as the force needed to elongate a material: $\tau = E\,\Delta l/l_0$, where Δl is the length change due to the applied force and l_0 the original length.

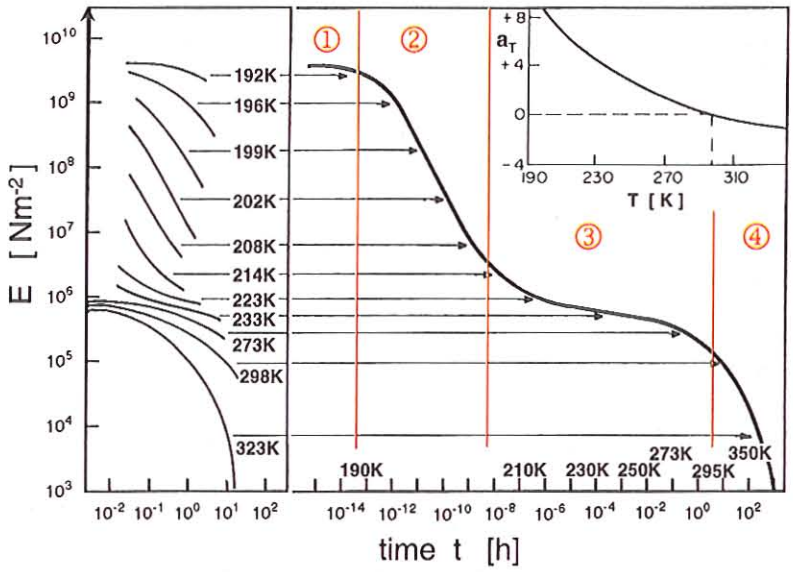


Fig. 14: *Tensile elastic modulus versus time for polyisobutylene reduced to $T = 298K$ by time-temperature superposition. The insert shows the temperature dependence of the shift factor [8, 7].*

section (2) of fig.(14). In agreement with the observation for the frequency dependence of the shear modulus, shown in fig(12), $E(t)$ reaches a plateau value in section (3) - the material exhibits elastic behavior. The macromolecules feel the topological restrictions imposed by the surrounding chains. The entanglements between the chains are fixed on the time scale of the experiment and as a consequence the material behaves like a rubber, where the cross-links are due to permanent chemical bonds. The final decay of $E(t)$ confirms the temporary character of the entanglement network. Entanglements can be resolved via a reptative motion of the polymers along their own chain contour. On time scales much larger than the typical live time of an entanglement the polymeric material behaves like a fluid.

Time-Temperature superposition principle The broad time- and frequency range of about 10-20 decades in fig.(12) and fig.(14) cannot be covered with a single rheological experiment. The typical working range of a single probe geometry of a rotational rheometer covers about three decades. Under the assumption that a change in temperature only results in an acceleration of the underlying relaxation processes, curves taken at different temperatures can be superimposed to a single master curve. This is shown in fig.(14). The master curve for $T = 298$K is obtained by shifting the data taken at different temperatures horizontally along the logarithmic time axis by a temperature dependent shift factor. The temperature dependence of the shift factor is shown in the insert in the same figure. The fact that a change in time or frequency can be replaced by a change in temperature is called time-temperature superposition principle.

For thermally activated processes, which have to overcome an energy barrier E a simple, more quantitative derivation can be performed. The probability P per unit time to overcome the energy barrier is given by the Arrhenius-law to

$$P = exp\left(\frac{E}{k_B T}\right), \tag{35}$$

where k_B is the Boltzmann constant. The product $(P\,t)$ gives the probability for the occurrence of a relaxation process during time t. If we now change the temperature or the time in such a way that the product $(P\,t)$ stays constant, there should be no change in the macroscopic response of the material. The response is determined by the number of microscopic relaxation processes during the observation time t. From $P\,t$ =constant directly follows

$$ln(t) = \frac{E}{k_B T} + constant \quad \text{and} \quad \delta[ln(t)] = -\delta T \frac{E}{k_B T^2}. \tag{36}$$

A variation in $ln(T)$ is proportional to a variation in $-T$ but with a temperature dependent shift factor. Since the zero shear viscosity is determined by a single relaxation time, the relaxation time of the slowest process in the system, the viscosity at any temperature T can be calculated from the viscosity at any reference temperature T_0 by

$$\frac{\eta_0(T)}{\eta_0(T_0)} = \frac{exp\left(\frac{E}{k_B T}\right)}{exp\left(\frac{E}{k_B T_0}\right)} = a_T. \tag{37}$$

In case the relaxation times of all processes contributing to the relaxation modulus G or the compliance J are changed by the same temperature shift factor a_T, it can be easily shown by use of eq.(18) that the following equations hold:

$$\begin{aligned} G(t;T) &= G(\frac{t}{a_T};T_0) \quad \text{and} \quad G(t;T) = G(\omega a_T;T_0) \\ J(t;T) &= J(\frac{t}{a_T};T_0) \quad \text{and} \quad J(t;T) = J(\omega a_T;T_0). \end{aligned} \tag{38}$$

Plotting of the relaxation modulus G or the compliance J versus the generalized variable $a_T\omega$ or t/a_T should lead to a single master curve for data taken at different temperatures. This is shown in fig.(12) and fig.(14) for the amorphous polymer systems discussed above. From the fact that we find a simple shift factor for the time-temperature superposition, a major conclusion about the nature of the glass transition can be drawn: The glass transition is of purely kinetic nature rather than a structural transition like the melting process or a solid-solid phase change, which would involve slow nucleation processes. All relaxation times are scaled by the same shift factor a_T.
For melts of glassy polymers in the region between the glass temperature T_g up to T_g+100 a Williams-Landel-Ferry (WLF) law is usually more appropriate to describe the temperature dependence of a_T

$$a_T = exp\left[\frac{-c_1(T-T_0)}{c_2 + (T-T_0)}\right], \tag{39}$$

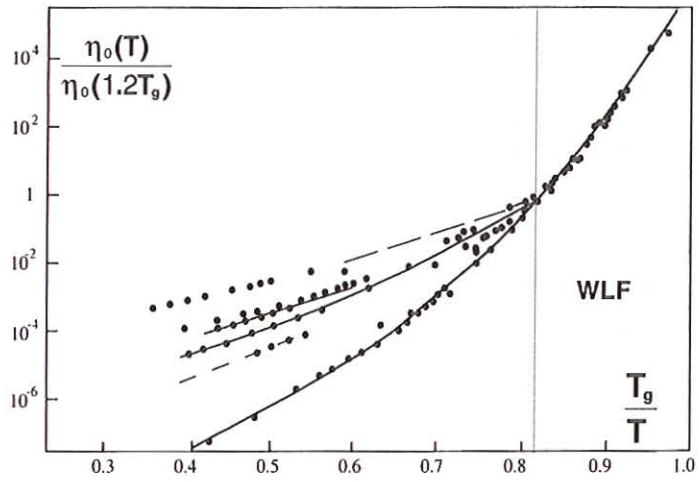


Fig. 15: *Normalized viscosity for various polymers as a function of T_g/T [4].*

where $c_1 = c_1(T_0)$ and $c_2 = c_2(T_0)$ are material specific constants, which also depend on the reference temperature T_0. This equation is a direct result of the dependence of the viscosity on the free volume for glass-forming materials. If the glass temperature is chosen as reference temperature, it was found that the values for c_1 and c_2 do not significantly vary for different polymers. In fig.(15) the viscosity normalized to its value at $1.2\,T_g$ is plotted versus the nondimensional variable T/T_g for various polymers. Even though the authors have chosen a superposition relation different to that given in eq.(39), they obtain an superposition of the viscosity in the temperature region, where the WLF-relation is valid for all polymers. For temperatures $T \geq 1.2\,T_g$, where the viscosity should rather follow the Arrhenius-relation than the WLF-relation the curves start to split - the value of the activation energy is correlated to the specific polymer structure. For more details see [4].
For the so called Vogel-temperature $T_V = T_0 - c_2$ the a_T defined by eq.(39) diverges and with T_V as reference temperature we obtain the Vogel-relation

$$a_T = \frac{exp\left(\frac{c_1 c_2}{T - T_V}\right)}{exp\,(c_1)}, \tag{40}$$

which has a formal similarity to the Arrhenius-equation if we replace in eq.(37) the temperature by the temperature difference measured relative to the Vogel-temperature.

4.2 Shear-thinning and thickening in highly concentrated colloidal suspensions

On the basis of two colloidal systems we would like to introduce the terms shear-thinning and shear-thickening, which denote the phenomena that the viscosity decreases or increases with the applied shear rate or frequency. We would like to focus on the rather

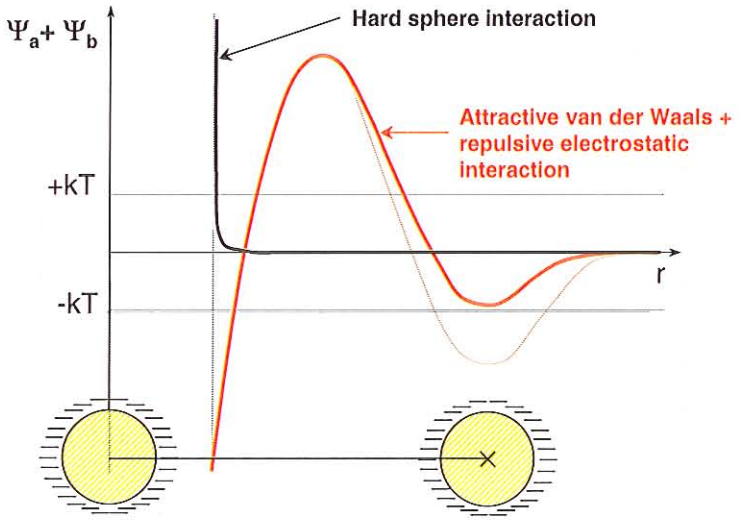


Fig. 16: *Interaction potential for colloids with (a) hard-sphere interaction and (b) attractive van der Waals plus repulsive electrostatic interaction.*

simple systems of charge stabilized spheres and those with pure hard-sphere interaction. The pair potential of two charged spheres can be described by a superposition of an attractive potential rising from the van der Waals forces and a repulsive contribution due to electrostatic interactions. Possible results for the overall interaction potential are shown in fig.(16) as a function of the interparticle distance. Due to their Brownian motion the particle are able to overcome the second minimum, if the depth is of the order of k_BT. In case the depth is much larger than the thermal energy of the colloids, stable associates can be formed. As a consequence, body-centered cubic or hexagonal close packed lattice-like structures can be found for these systems even at low colloid volume fractions. The hard-sphere potential is purely repulsive and diverges when the interparticle distance equals the particle diameter $2R$. Compared to the charged stabilized systems, longer-ranged lattice-like structures are observed at higher concentration and are due to steric crowding.

In fig.(17) the viscosity is plotted for both systems as a function of the stress with the colloid volume fraction Φ_V as parameter. The results for colloids with hard-sphere interaction are shown on the left [13]. For a different system, a comparison between hard-sphere interaction and charged stabilized colloids is plotted on the right [12]. For low stresses the authors observed an decrease in the viscosity, which becomes rapidly stronger with increasing Φ_V. The hard-sphere as well as the charged stabilized system show a strong shear thinning behavior for high volume fraction of colloids. Further increase of the applied stress generates the opposite effect. The viscosity increases with increasing stress - the samples exhibits shear thickening behavior.

From scattering and rheo-optical experiments on-line information about the structural changes during shear can be obtained. Both, experiments [17, 18, 19, 20] as well as computer simulations [15, 16] draw the picture, described below, about the origin of the

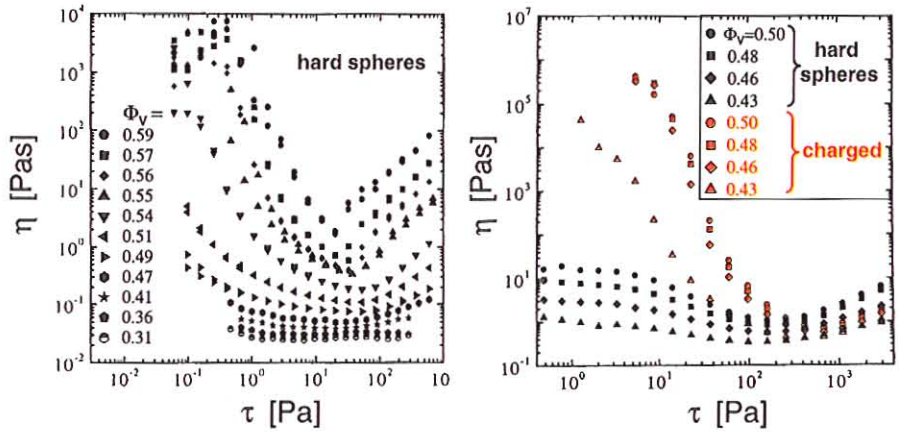


Fig. 17: *Viscosity of concentrated colloidal systems (charged stabilized and hard-sphere interaction) as a function of the stress [12, 13]*

shear thinning and thickening behavior of these systems. The pictures shown in fig.(18) are taken from a two-dimensional simulation [15] but are consistent with experimental results obtained for bulk systems [16] (and references therein). The flow direction is marked by the arrow. With increasing stress the highly concentrated systems undergo microstructural changes from a lattice-like structure with longer-ranged ordering (a) to parallel layers oriented along the flow direction (b). Collisions between the colloids are drastically reduced due to the layered structure and lubrification forces (see below) that enable slipping of the layers on top of each other. As a consequence the overall viscosity will be reduced. Perfectioning of the layers with increasing stress leads to the observed shear-thinning behavior. The shear thinning effect for the charged stabilized colloids is enhanced in comparison to the system with hard-sphere interaction at the same concentration. This can be explained by the higher initial viscosity due to the longer-ranged order in the charged stabilized system.
With further increase of the stress increasing hydrodynamic forces cause the layers to become imperfect (c), followed by a regime of a more random structure, in which the colloids form curved strings with, in respect to the flow, random orientation (d). Finally a smooth transition to clusters without internal order is observed (e). The clusters are rather persistent but occasionally break up and form new clusters. In the presence of hydrodynamic interaction energy has to be spend to bring two colloids in contact to each other since the fluid has to be expelled from the intersection, as sketched in fig.(19).

In case of the sliding layers this leads to the described "lubrification" effect. Particles moving in gradient direction because of their Brownian motion can bring up sufficient high kinetic energy to overcome this barrier in case of sufficient high shear gradients. Since the fluid has to flow back into the intersection, separation of the particles again costs energy (see fig.(19)). The particle stick together and at high colloid concentration,

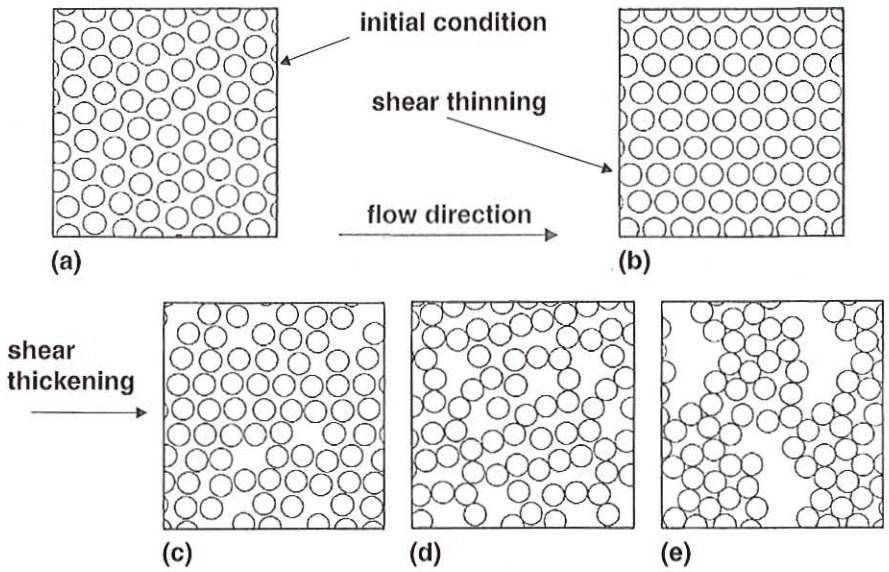


Fig. 18: *Structural changes as explanation for the observed shear thinning and shear thickening behavior in highly concentrated colloidal suspensions (pictures taken from a two dimensional computer simulation) [15].*

when the probability for collisions is high enough, clusters are formed. For the onset of shear thickening a critical threshold of the shear rate has to be exceeded as can be seen from fig.(19). This threshold is lower for the system with hard-sphere interactions than for the charged stabilized colloids since for the latter system the kinetic energy must be high enough to overcome the additional repulsive electrostatic forces. Computer simulation by D.R. Foss and J.F. Brady [16], demonstrating that in the absence of hydrodynamic forces no clustering is observed, support this explanations.
The shear thickening process is fully reversible. As a proof fig.(20) shows the response of a sample to a stress and a rate jump into the shear thickening regime taken under controlled stress and controlled rate conditions, respectively. In the controlled stress experiment a spontaneous response of the sample to a stepwise change in the applied stress is observed and, after stress relief, the sample instantaneously recovers its initial viscosity. Under controlled strain conditions the response becomes erratic. After longer shearing times, fracture and failure of the sample is observed supporting "jamming" effects predicted by the theory of Farr et al. [14] for controlled strain conditions.

4.3 Shear-band formation in self-assembled surfactant solutions

Surfactants are amphiphilic molecules consisting of polar head groups and nonpolar chains. To minimize unfavorable interactions between either the polar head groups or the nonpolar chains and the solvent, they spontaneously aggregate in a variety of microstructures. Typical characteristic domain dimensions are of the order of several 10

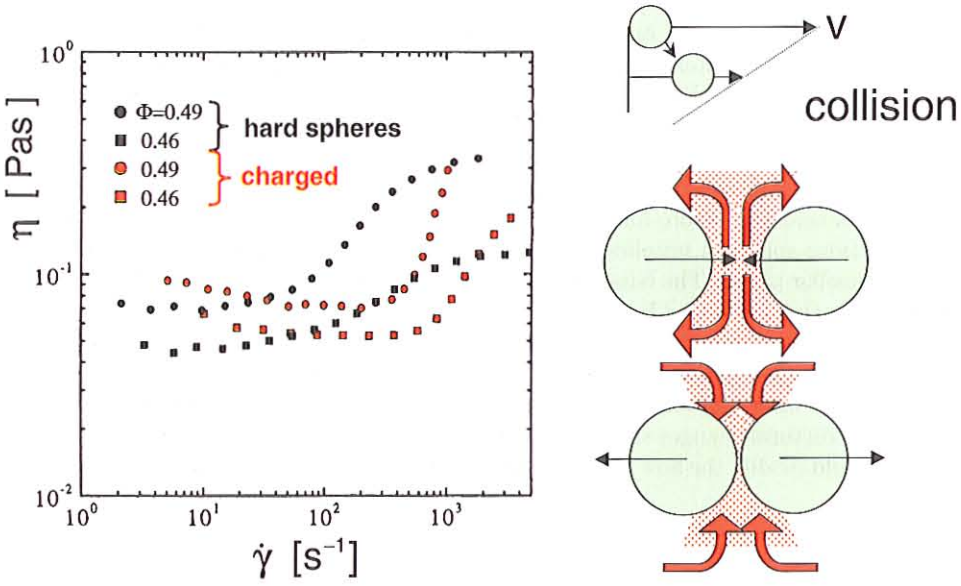


Fig. 19: *Left: Shift in the onset of shear thickening between charged colloids and those with hard-sphere interaction [12]. Right: Schematic picture to explain the effect of hydrodynamic forces.*

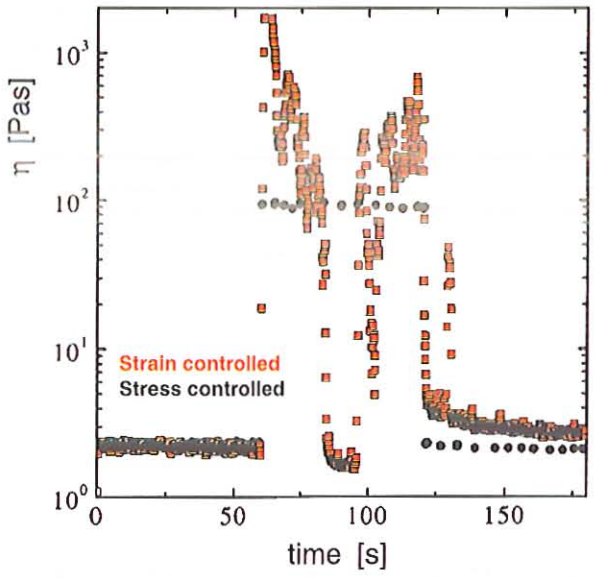


Fig. 20: *Time dependent response of the viscosity to a box-shaped stress and rate jump into the shear thickening regime measured under stress- and strain control condition, respectively [13].*

nanometers. To promote self-assembling the solvent must be either very nonpolar (like oil) or very polar (like water). For more details on self-assembling surfactant solutions and microemulsions see [24] and the contribution of W.F.C Sager (A6).
We are in particular interested in the system of AOT (sodium 1,4-dialkyl-3-sulfonate-succinate) in water. Addition of NaCl changes the polarity of the head groups resulting in a screening of the electrostatic repulsion between them. As a consequence the head groups can come closer together allowing the formation of structures with higher local curvature. The equilibrium phase diagram of the AOT/H_2O/NaCl system is shown in fig.(21), a schematic picture for each microstructure is also presented. At low surfactant concentrations spherical micelles are formed. With increasing AOT content the system forms a lamellar phase. The lamellae consist of bilayers of surfactant molecules stacked on top of each other separated by water. For the formation of a bicontinuous sponge phase more salt has to be added to reduce the electrostatic repulsion between the head groups. If the shear rate is high enough to be of the same order as the characteristic frequencies of the surfactant layer undulations, one would expect that shear flow can induce structural changes. Structural changes should have an influence on the viscosity of the liquid, which in turn should modify the flow field. Therefore we expect the equilibrium phase transitions

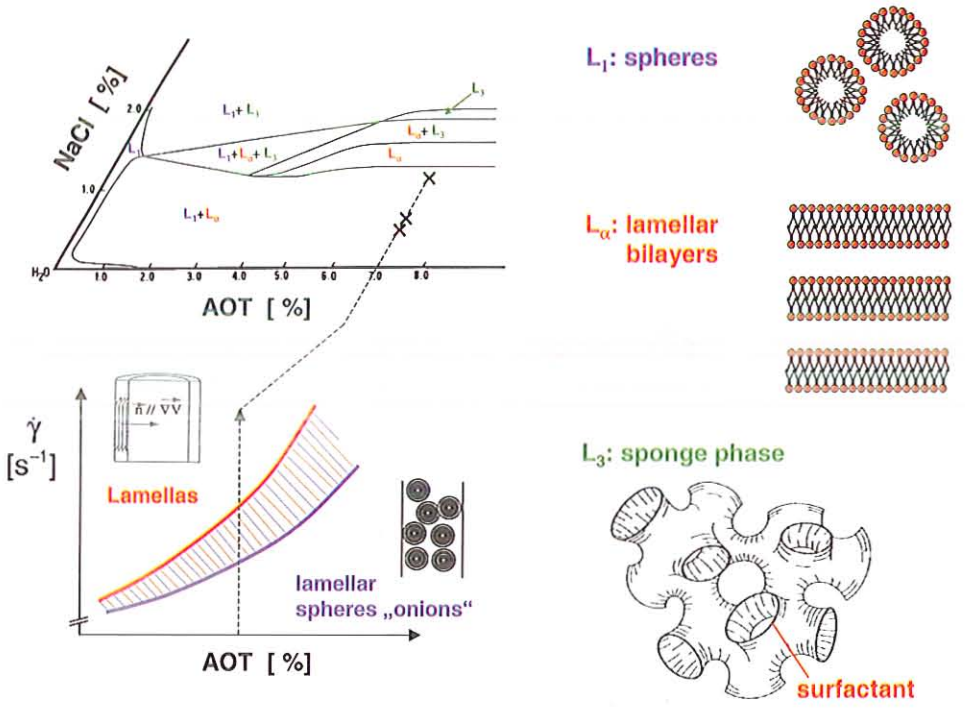


Fig. 21: *Equilibrium phase diagram of AOT in ($NaCl/H_2O$) solutions (T=303K) [25] with a sketch for the microscopic structure found in each phase. A schematic presentation of the shear induced phase transitions is also shown.*

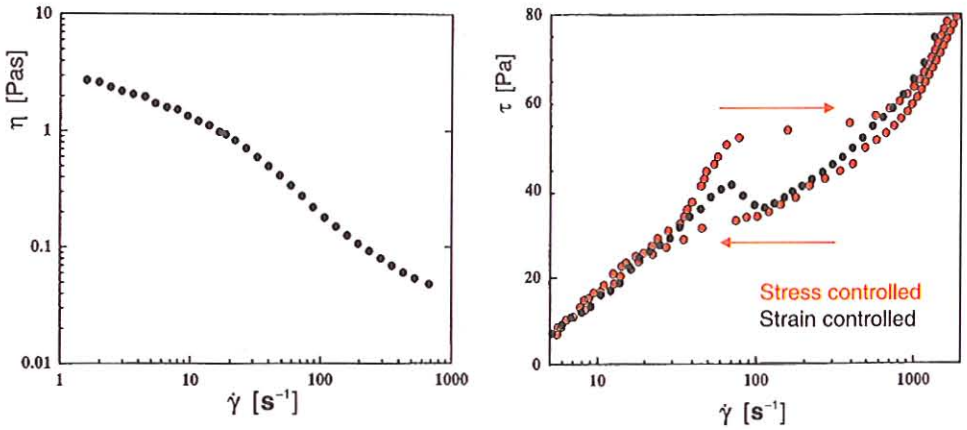


Fig. 22: *Shear-thinning behavior found for AOT in ($NaCl/H_2O$) solution (left). On the right the stress as a function of the shear rate is shown for a stress- and a strain controlled measurement. In the stress controlled measurement hysteresis is found for an up- and down loop [21].*

occurring in these systems to be strongly influenced by shear.

The rheological measurements described below are all performed on systems with 7% AOT and NaCl contents between 0.5% and 1.2% marked in phase diagram of fig.(21) by crosses. Without applied shear the system is in the twophase region, where spherical micelles and lamellae coexist. The influence of shear on the phase diagram is schematically shown in fig.(21). At low shear rates a new phase is observed, where the bilayers role up to form lamellar spheres, called "onions". The onions form a turbid gel-like phase with high viscosity. With increasing shear rate a lamellar phase is found, where the lamellae are oriented along the shear flow with the normal vector in the gradient direction. The lamellar phase has a much lower viscosity compared to the onion phase. The sample exhibits strong shear thinning as shown in fig.(22). Under controlled strain conditions the one phase regions are separated by a region, where the two states coexist. The rheological response of the sample strongly depends on whether the experiment is performed under controlled stress- or strain conditions. This can be seen from fig.(22), where the shear stress is shown as a function of the shear rate. For imposed stress a large hysteresis is found between data taken starting from low shear rates with increasing $\dot{\gamma}$ and those taken starting in the high shear rate regime with decreasing $\dot{\gamma}$. Upon increasing the shear rate the sample tends to remain at a higher viscosity, whereas for decreasing shear rates lower viscosities are found. In the same shear rate region, where the hysteresis was found under imposed stress, the stress as a function of the shear rate shows a van der Waals like loop under controlled strain conditions. The shear rate is a multi-valued function of the stress. Thus the reason for the observed hysteresis might be a bistability of the surfactant solution, with an energy barrier between the two states. If this hypothesis is correct, imposing a certain stress in the bistable region should yield more than one value for the shear rate or analogously for the viscosity. In fig.(23) the viscosity as a function of time for imposed stress is shown: (1) for a sample presheared at low shear rates in the high viscosity

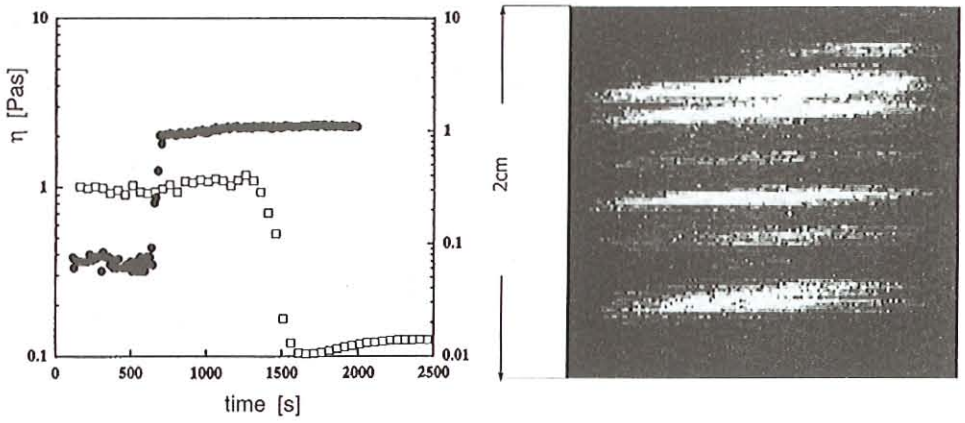


Fig. 23: *Left: Time dependence of the viscosity in the bistable-shear region after preshearing the sample in the high viscosity "onion"-like one phase region (yellow) and after preshear in the low viscosity lamellar one phase region (black). Right: Flow visualization experiment with "Kalliroscope" particles. Different brightness corresponds to different flow strength. Shear bands are clearly visible [21].*

"onion"-like phase region (yellow) and (2) for a sample presheared at high shear rates in the stable low-viscosity lamellar state (black). For both a spontaneous transition to a lower (1) and higher (2) viscosity is found. The transition times, as a measure of the life time of the initial state show a broad distribution but are of typical 1000s. The answer to what happens in the sample under controlled strain conditions is still missing. Fig.(23) presents the results of a flow visualization experiment in a transparent Couette cell with imposed strain in the unstable region and with view direction along the gradient direction. The dimensions of the picture are 2cm×2cm. The flow field is visualized through the addition of "Kalliroscope" particles to the surfactant solution. These particles reflect light when viewed under the right angle. Thus alignment in the regions with stronger flow or lower viscosity appears more luminous, whereas regions with slower flow or higher viscosity are dark. In fig.(23) separation into regions with higher and lower shear rates, called shear bands, is obvious. The bands are aligned in flow direction (interface directors pointing in the neutral direction). However, from theoretical consideration [26] for a van der Waals like loop in the stress-shear rate curve separation into phases with interface directors in the gradient direction are expected as shown in fig.(24a). In this case the phases have a common stress τ_c but different shear rates $\dot{\gamma}_{1/2}$ and the actually measured common stress would stay constant if the applied $\dot{\gamma}$ is varied in the phase separation region. The van der Waals like loop is only seen if phase separation is suppressed as it might be the case when the shear rate is changed too rapidly and the sample does not reach the stationary state. Separation into phases with interface directors pointing in the neutral direction are only expected if the stress is a multi-valued function of the shear rate. Under controlled stress condition the sample then can separate into phases with common shear rate $\dot{\gamma}_c$ but different stresses $\tau_{1/2}$ (see fig.(24b)).

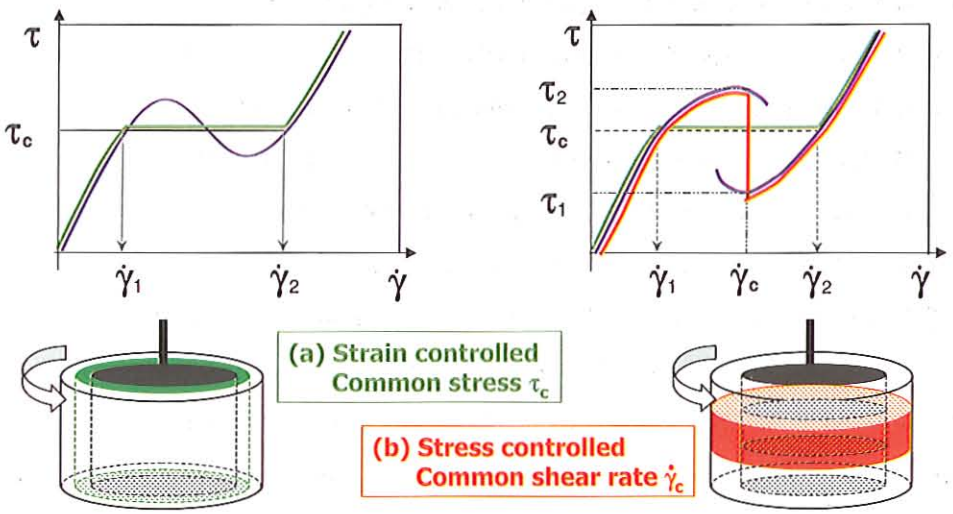


Fig. 24: *Van der Waals like loop and multi-valued stress as a function of the shear rate and possible shear band formation in cylinder geometry for stress- and strain controlled measurements.*

References

[1] M. Pahl, W. Gleißle, H.M. Laun, *Praktische Rheologie der Kunststoffe und Elastomere*, VDI Verlag, Düsseldorf, 1995.

[2] C.W. Macosko, *Rheology: Principles, Measurements, and Applications*, Wiley-VCH, New York, 1994.

[3] R.I.M. Reiner, Physics Today **17**, 62 (1964).

[4] D.W. van Krevelen, *Properties of Polymers*, Elsevier, Amsterdam, 1993.

[5] G.S. Beavers and D.D. Joseph, J. Fluid Mech. **69**, 475 (1975).

[6] W.W. Graessley, *The Entanglement Concept in Polymer Rheology* in *Advances in Polymer Science*, Springer-Verlag, Berlin, 1974.

[7] G. Strobl, *The Physics of Polymers*, Springer-Verlag, Berlin, 1996.

[8] E. Castiff and T.S. Tobolsky, J. Colloid Sci. **10**, 375 (1955).

[9] M. Doi and S.F. Edwards, *The Theory of Polymer Dynamics*, Clarendon Press, Oxford, 1988.

[10] P.E. Rouse, J. Chem. Phys. **21**, 1272 (1953).

[11] P.G. de Gennes, J. Chem. Phys. **55**, 572 (1971).

[12] B.J. Maranzano and N.J. Wagner, J. Rheology **45**, 1205 (2001).

[13] B.J. Maranzano and N.J. Wagner, J. Chem. Phys. **114**, 10514 (2001).

[14] R.S. Farr, J.R. Melrose and C. Ball, Phys. Rev. E **55**, 7203 (1997).

[15] W.H. Boersma, J. Laven and H.N. Stein, J. Rheology **39**, 841 (1995).

[16] D.R. Foss and J.F. Brady, J. Fluid Mech. **407**, 167 (2000).

[17] J.W. Bender and N.J. Wagner, J. Colloid Interf. Sci. **172**, 171 (1995).

[18] L.B. Chen, B.J. Ackerson and C.F. Zukoski, J. Rheology **38**, 193 (1994).

[19] P. D'Haene, J. Mewis and G.G. Fuller, J. Colloid Interf. Sci. **156**, 350 (1993).

[20] J.-H. So, S.-M. Yang and J.C. Hyun, Chem. Eng. Sci. **56**, 2967 (2001).

[21] D. Bonn, J. Meunier, O. Greffier, A. Al-Kahwaji and H. Kellay, Phys. Rev. E **58**, 2115 (1998).

[22] D. Roux, F. Nallet and O. Diat, Europhys. Lett. **24**, 53 (1993).

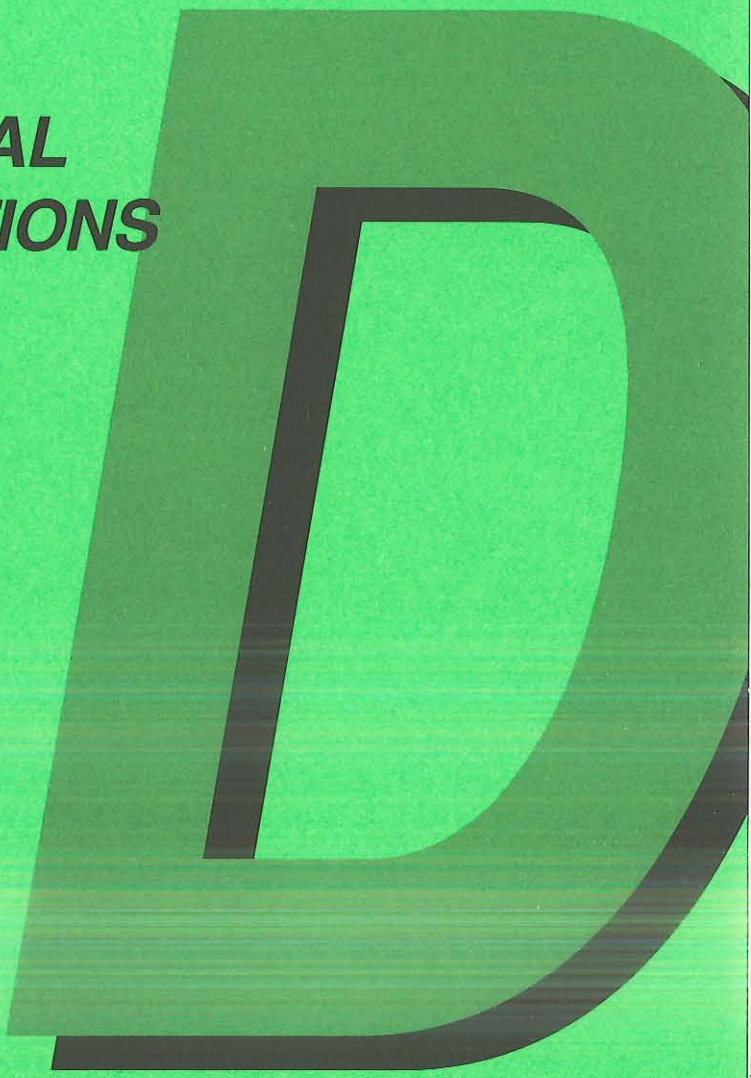
[23] O. Diat, D. Roux and F. Nallet, J. Phys. II **3**, 1427 (1993).

[24] D.F. Evans and H. Wennerström, *The Colloidal Domain: Where Physics, Chemistry, Biology, and Technology Meet*, Wiley-VCH, New York, 1999.

[25] O. Ghosh, C. A. Miller, J. Phys. Chem **91**, 4528 (1987).

[26] J.K.G. Dhont, Phys. Rev. E **60**, 4534 (1999).

INDUSTRIAL APPLICATIONS



D 1 Birth and Fate of Nanoparticles in Water

J. Rieger
Polymer Physics
BASF Aktiengesellschaft, Ludwigshafen

Contents

1 Introduction 2

2 Classical Nucleation Theory 5

3 More Recent Knowledge 7

3.1 Precursors 7

3.2 The Structure of Clusters and Nuclei 7

3.3 Computer Simulation of the Early Stages of Particle Formation 8

3.4 Particle Growth 8

4 Particle Formation by Mixing Two Components 9

5 Experimental Aspects 11

6 Precipitation of $CaCO_3$ as a generic example 13

1 Introduction

The importance of nanoparticles, i.e. particles with dimensions in the range of about 10 nm to a few hundred nanometers is obvious [1] [2] [3]. They determine our life in the form of protein complexes, as viruses, as colloidal particles in drinking water, surface water and sea water, and as aerosols. They find use as dispersion colors and as adhesives. In industry they play an important role in the formulation of pigments and in the production of catalysts. Numerous attempts are being made to deliver nanoparticulate forms of pharmaceutically active compounds specifically to the desired site of the action in the body. Nanoparticles occur as intermediates in crystallization processes as nuclei; in seawater desalination plants as well as in the washing machine these nuclei must be stabilized by suitable additives in order to prevent encrustation [4]. Finally, the use of nanoparticles as quantum dots with special properties for electronic components is also mentioned. Beyond these practical aspects there is active scientific interest in nanoparticles owing to their special properties, which lie between the properties of molecules and those of bulk material. Figure 1 shows some examples of nanoparticles and applications thereof. There are many reasons why nanoparticulate systems are often preferred to bulk material: apparent homogeneity, e.g. in paints and lotions, increase in solubility in pharmaceutical formulations, the improvement in biological resorption, and the modification of optical, electrooptical, and other physical properties which are achievable only with particle sizes in the middle or lower nanometer range (10 - 500 nm).

There is a clear gap between that which is reported in many textbooks on particle formation and the current state of knowledge. This unsatisfactory situation was the motivation for a recent review on modern aspects of particle formation on which this article is based [1]. In most cases particle formation from a supersaturated liquid is described as sketched in Figure 2: nuclei of the solid particles appear which grow to the final particles (crystallization). The corresponding classical theory of particle formation is outlined in the next chapter, as well as some of its shortcomings.

In many cases the particle formation process is far more complicated; Figure 3 gives an initial view of the complexity of particle formation which will be discussed below. Special experimental techniques that are needed to study the process of particle formation will be outlined. The precipitation of $CaCO_3$ as an example for nanoparticle formation will be considered in more detail.

The synthetic preparation of polymer dispersions [5] as a special class of organic nanoparticles of considerable economic significance will not be discussed here - as well as other procedures which have also found extensive use in the preparation of inorganic nanoparticles [6], such as sol-gel processes [7], synthesis in microemulsion templates [8], and aerosol procedures [9]. Any discussion of nanoparticles by aggregation of block polymers [10] or by the targeted synthesis of extended molecules such as dendrimers [11] and other branched systems [12] will also be omitted.

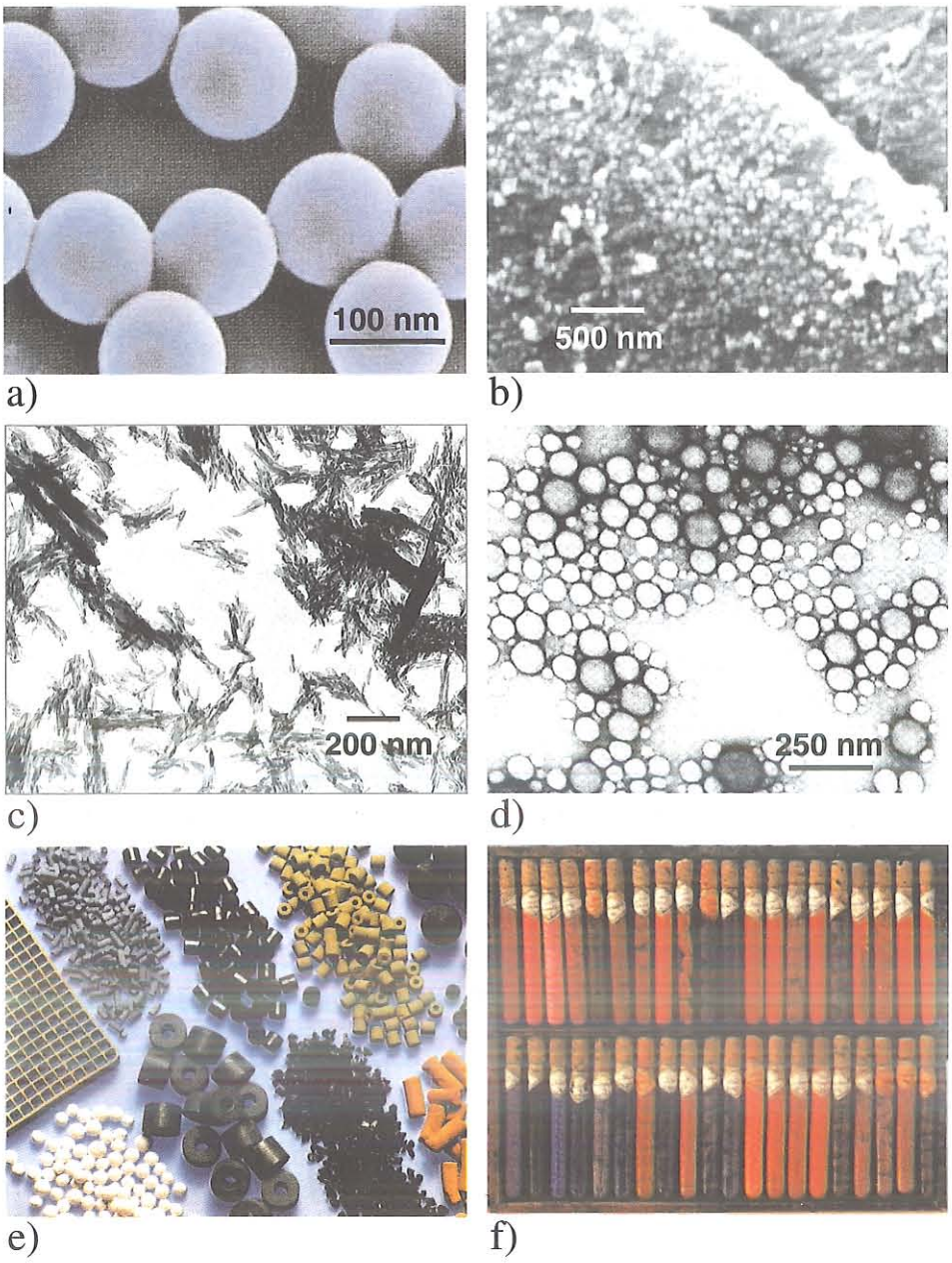


Fig. 1: *Examples for systems that originate from the nanoparticulate state or that are made of nanoparticles: a) compact spheres in a polymer dispersion, b) $CaCO_3$-particles on cotton (encrustation), c) red pigment quinacridone, d) nanodispersed β-carotene (provitamin A) hydrosol, e) macroscopic catalyst particles and f) pigments prepared by precipitation or crystallization*

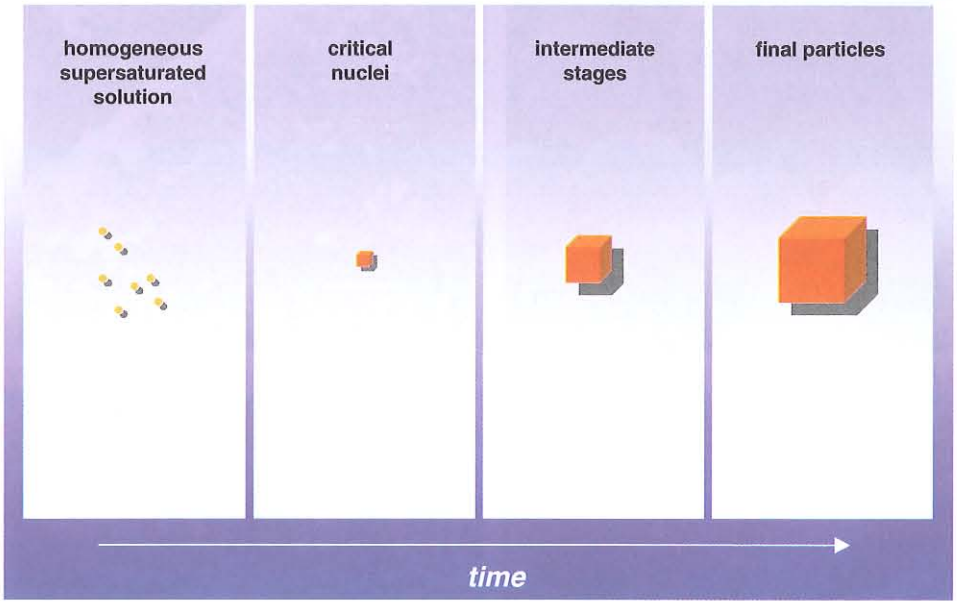


Fig. 2: *"Textbook" picture of particle formation from a supersaturated state via nucleation and growth*

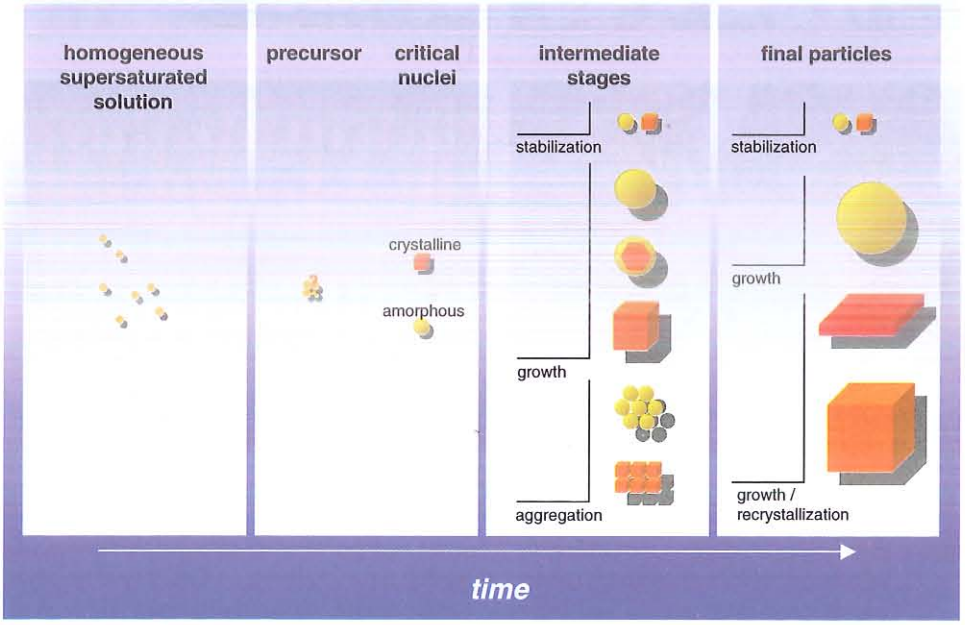


Fig. 3: *Stages of particle formation as realized in many real systems*

The preparation of nanoparticles from homogeneous supersaturated solutions has occupied scientists for a long time. But several points arise from a perusal of the literature on this topic: a strongly phenomenological approach is frequently encountered, i.e. attempts are made to deduce a mechanism of formation from the structure of the product; often a purely descriptive treatment is considered satisfactory. If one looks beyond text book knowledge on the topic "supersaturation, nucleation, growth" a "zoo" of theories and interpretations is encountered which must be taken into account if there is a desire to understand at a basic, i.e. molecular, level how a nanoparticulate system is formed. This knowledge is of prime importance in as much as only with a knowledge of the mechanistic aspects of particle formation can the process be manipulated specifically in the sense of control - whether it be by variation of the process parameters or by the use of suitable additive molecules. This area of research is truly interdisciplinary since chemists, physicists, and engineers, each with their specialist knowledge are in demand.

2 Classical Nucleation Theory

Textbook knowledge may be summarized in the following way [13] [14]. A multicomponent system exists initially as a single phase. By modification of boundary conditions such as temperature and pressure or by homogenous mixing with a further component the free energy changes in such a way that phase separation is energetically more favorable. It is assumed that particles (atoms, ions, molecules) of the one component coalesce and form nuclei of the separating phase. At this level of consideration it is immaterial whether it is, for example the separation of a solid phase in the liquid medium (the subject matter of this article), condensation from the gaseous phase, or bubble formation in a liquid (foaming). The free energy of a spherical nucleus with radius r can be described in respect of the single-phase state to a first approximation as follows

$$\Delta G = \Delta G_S + \Delta G_V = 4\pi r^2\gamma + 4/3\pi r^3 \Delta g_V \qquad (1)$$

where ΔG_S is a positive contribution from the formation of an interface between the nucleus and the bulk solution and ΔG_V is a negative contribution from the formation of the thermodynamically more favorable nucleus; γ stands for the surface tension between the two phases and Δg_v for he difference in free energy per unit volume between the two phases. The two terms on the right of the equation have opposite signs so that ΔG as a function of r passes through a maximum (Figure 4). The critical nucleus radius r* is defined by the position of the maximum of the free energy and equates to

$$r^* = -2\gamma / \Delta g_V. \qquad (2)$$

Particles with a radius smaller than r* redissolve, whilst particles which by reason of statistical fluctuations exceed this size are stable and grow further.

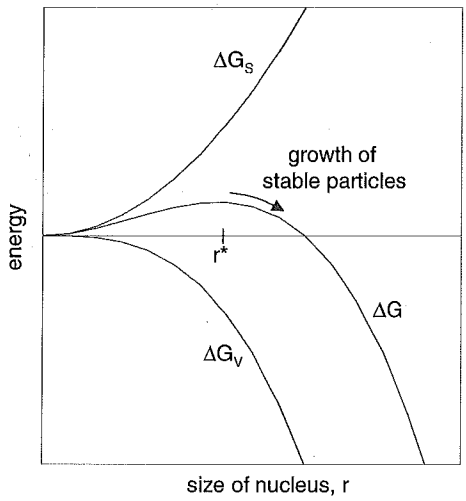


Fig. 4: *Energy diagram to explain the nucleation process; ΔG: free energy of a particle with radius r, ΔG_S: surface energy, ΔG_V: bulk energy, r*: radius of the critical nucleus. The particle sizes fluctuate because of statistical processes. Particles with a radius r<r* redissolve, those with r>r* grow further.*

Within the scope of a quasi-equilibrium approach (Arrhenius) the rate of nucleation, i.e. the number of nuclei which form per unit time and volume, is described as

$$J=A \exp\left(-\Delta G^*/kT\right), \tag{3}$$

in which A is determined by the frequency of the molecular processes, k is the Boltzmann constant and T the temperature. The rate of nucleation thus becomes

$$J=A \exp\left(-\left(16\pi\gamma^3 v^2\right)/\left(3k^3T^3\left[\ln S\right]^2\right)\right), \tag{4}$$

where in accordance with the term $kT\ln(S)=2\sigma v/r$ [13] the supersaturation $S = c(r)/c^*$ is coupled with the particle radius; v is the molar volume, c(r) denotes the solubility of a particle with radius r, and c* the equilibrium solubility.

In classical colloid chemistry a further model concept is used especially to explain monodispersity in certain systems [15], cf. Figure 5: the concentration of a dissolved substance continues to rise, for example by release in a reaction, until the critical nucleation concentration is reached. At this point in time a shower of nuclei are formed which begin to grow. In this way the concentration falls momentarily below the critical threshold so that no new nuclei can form. The nuclei already formed grow until the concentration of the still dissolved material has fallen to the equilibrium concentration.

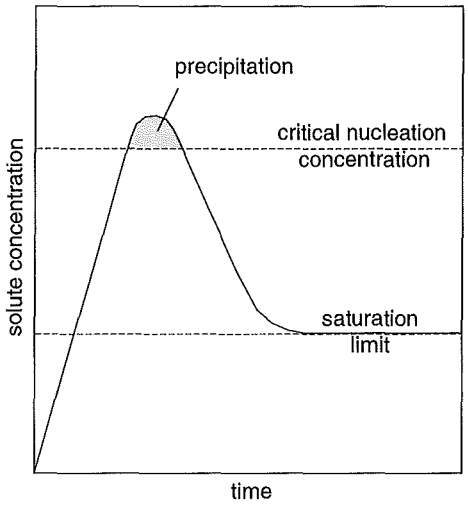


Fig. 5: *Schematic representation of the concentration relationships in controlled particle formation according to the model representation of LaMer.*

3 More Recent Knowledge

In the following new ideas on particle formation from supersaturated systems will be presented in chronological order from the stage of the homogeneous starting state to that of the colloidal particle. An assessment has been intentionally omitted, as there is rapid development in this area. For reasons of space a complete citation has to be omitted; the reader is referred to Ref. [1] for more information.

3.1 Precursors

A fundamental assumption of classical nucleation theory is that prior to production of the supersaturation, which initiates particle formation, the system can be treated as homogeneous, i.e. it is assumed that the components are present in a molecularly dispersed state. Numerous experiments suggest, however, the existence of precursors, i.e. species that form from the reacting components, the size of which is still below that of a critical nucleus. This is not meant to suggest transient clusters arising from fluctuations in nucleation, but long-living species, which are not considered as part of classical nucleation theory [13] [16].

3.2 The Structure of Clusters and Nuclei

In classical nucleation theory it is assumed that the critical nuclei are spherical and that the structure of the nuclei and their surface can be described by that of the corresponding macroscopic phase, i.e. that γ and Δg_v are defined by the corresponding values of the bulk phase. In many cases this assumption in respect of Δg_v does not apply, most clearly when the nuclei are comprised of only a small number of molecules, as has been observed with, for example proteins [17]. In turn this point has consequences for the assumptions which are

made for the surface tension. Some theories have been proposed for the structure of particle surfaces in order to take into account that, for example a density gradient can exist in the transition from particle interiors to the dispersed medium [18]. Moreover, that γ is dependent upon the curvature of the particle surface is not considered in classical nucleation theory. This deficiency was recognized early and has been redressed in a number of theories [19].

3.3 Computer Simulation of the Early Stages of Particle Formation

With the aid of computer simulation it has in the meanwhile become possible to obtain an insight into structure formation during the early stages - even if initially only with the most idealized systems. For fundamental investigations of the behavior of many-body systems the so-called Lennard-Jones α-β potential (LJ α-β) for the description of the interaction of two particles $V(r) = - a/r^{\alpha} + b/r^{\beta}$ is widely used. With the help of this potential (with α=6 and β=12) the homogeneous nucleation of particles from the liquid phase has been studied [20]. With use of the LJ 6-12 potential at moderate cooling, i.e. low supersaturation, it has been possible to establish how in the pre-critical phase aggregates with liquid-like structure are formed initially which on exceeding the critical size are present mainly in face-centered cubic (fcc) form. A more precise investigation of the critical nuclei showed that the core exhibits an fcc structure, whereas the shell is liquid-like. In a layer between these two structures a body-centere cubic structure is realized. Simulations of this type give an insight into the causes for the so-called Ostwald rule which states that the phase which forms by nucleation is not necessarily that with the thermodynamically most stable (crystal) structure but that which in respect to its free energy is closest to the melt.

3.4 Particle Growth

Particle growth may occur via crystallization or via aggregation. The investigation of the growth of crystals (crystallization) is a well-established area of research with a countless amount of published work. For this reason reference will be made at this juncture to only one still current book [13]. Aggregation phenomena play a critical role in the preparation of many colloidal systems so that for application in general explanations are needed for conditions under which colloids are stable, or how colloidal particles themselves can be targetedly aggregated or flocculated. Less frequently discussed is the question as to how far the colloidal particles are formed by the aggregation of precursors. There is extensive literature on the "classical" aggregation of colloidal particles, of which just a few, more recent references are cited here [21] [22] [23]. In most of this work it is assumed that the kinetics of formation of aggregate populations are determined by the interaction potential between the particles, the particle size, and the flow conditions within the system. It is intuitively obvious that the latter point is complex. However, there are also still unresolved questions of a fundamental nature regarding the interaction between colloidal particles - in contrast to the impression occasionally given in introductory contributions on the stability of colloidal systems. The question as to how far classical theories, for example the frequently used Derjaguin-Landau-Verwey-Overbeek (DLVO) theory, correctly describe interaction effects is under intense discussion [24].

4 Particle Formation by Mixing Two Components

The supersaturation necessary for the induction of a precipitation/crystallization reaction may be produced by a variety of methods: 1. change in temperature or pressure, 2. change in the solvent quality of the fluid phase in which the material to be precipitated is initially present by mixing with a second fluid phase which is miscible with the solvent and in which the substance is poorly soluble or insoluble, and 3. by mixing two solvents whose dissolved components are insoluble in the reacted state. The theoretical approaches described previously do not differentiate between these three cases since homogeneous supersaturation is always assumed at the start of the experiment. Within the context discussed here only cases 2 and 3 are primarily of interest. During precipitation by mixing two liquid flows it is often implicitly assumed that the mixing is so intensive and so rapid down to small length scales that the system is homogeneously mixed before particle formation commences. That assumption is clearly only justified when the corresponding time constants are sufficiently different, see below. In practice attempts are made to achieve homogeneity as rapidly as possible by turbulent mixing with high-energy input. The following will describe why an understanding of the mixing behavior is critical for an understanding of the particle formation process, especially when the reaction for phase separation begins during mixing.

According to Baldyga the mixing of two liquid flows can be divided into macro-, meso-, and micromixing [25]. The term macromixing includes flow phenomena on length scales of decimeters such as are relevant in stirred vessels. By mesomixing is meant mixing effects on a length scale of millimeters; they are founded upon the breakdown of turbulent vortices into increasingly smaller vortices until viscous processes predominate over inertial forces. The term micromixing encompasses processes in the region of micrometers. In Figure 6 the processes taking place during turbulent mixing on the scale of micromixing are outlined. Two approaching liquid compartments envelop each other when the layers become increasingly thinner. Locally the two educt flows exist as lamellae. Respective simulations illustrate clearly this effect as well as the inhomogeneity of the turbulence, cf. Figure 7 [26]. In each case a boundary layer initially exists between the two flows. This boundary layer is initially the site of maximum supersaturation. Whether the rate of particle formation is slower or faster than the time to complete homogeneous mixing, which on small length scales is defined by the rate of diffusion of the molecules, is critical for consideration of the particle formation process. In the first case the previously described theories may be used with the named limitations. It is otherwise in the second case: which supersaturation processes and structures form at the boundary surface between the two mixing educt flows must be explicitly considered. Relatively little is still known experimentally on this point.

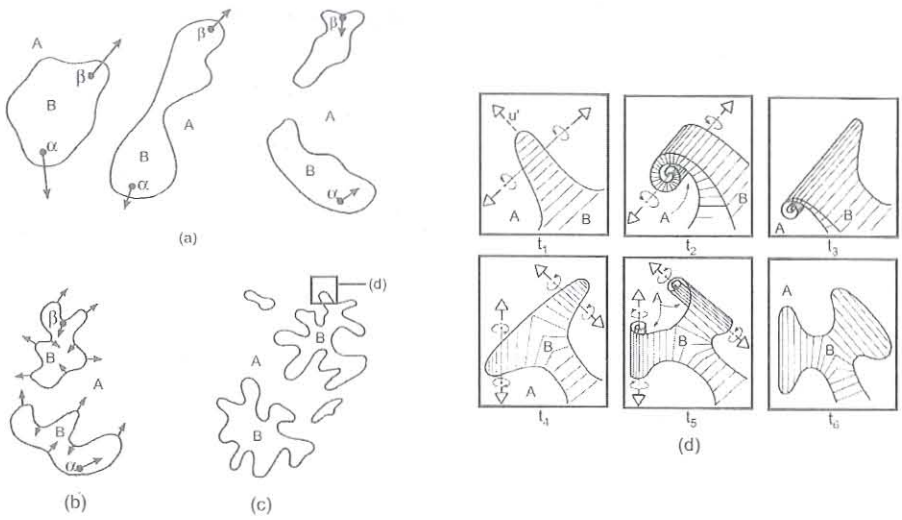


Fig. 6: *Schematic representation of the mixing processes of two educt flows during turbulent mixing (J. Baldyga and J.R. Bourne [25]).*

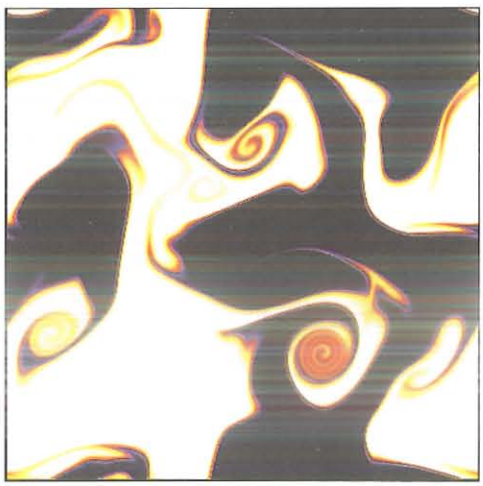


Fig. 7: *Two-dimensional simulation of the mixing of two educt flows under turbulent conditions (W. Gerlinger, K. Schneider, and H. Bockhorn [26])*

In the use of additives for control of the particle formation process the points mentioned gain further in importance: if an additive is added to one of the two educt flows a number of interactions of additive molecules with the particle formation process is conceivable. 1. The additive molecules act as nucleation initiators. 2. The additive molecules form a complex with some of the educt molecules and thus lower the level of supersaturation, which can lead to an

increase in the induction time or to a change in the reaction mechanism. 3. The additive molecules are incorporated during particle formation. On the one hand this incorporation can possibly be used targetedly to induce a certain crystal modification during the early stage of particle formation. On the other hand such incorporation is undesirable when for example particles for pharmaceutical purposes need to be prepared in a pure state. 4. The additive molecules coat the surface of the nanoparticles being formed and by efficient dispersing fix a certain particle size distribution.

5 Experimental Aspects

In order to understand the stages through which the formation of colloidal particles pass it is necessary to record experimentally the particle formation process by time resolution from the moment when supersaturation is realized. That the time-resolved description of processes is in no way trivial is recognized from the limited number of publications in this area. In most cases a description of the mechanism of particle formation is still limited to a retrospective derivation from the structure of the particle formed. That the amount of work published in this problem area is quite limited is because - unlike crystallization - particle formation in precipitation reactions occurs on a clearly shorter time scale, down to the region of milliseconds.

Where time resolution of the chosen measurement method is sufficient the stop-flow method has proved effective: two educt volumes are lead through a mixing cell into a measurement cell (Figure 8). At a predetermined moment the flow is interrupted and the particle formation process is measured by a suitable method, for example light scattering or the scattering of intense X-rays (synchrotron radiation). If the measurement method requires longer measurement times the flow reactor or precipitation jet may be used [27] [28]. Here, both educt flows are passed through a mixing cell and then through a reactor tube or, after a defined distance, directed as a free beam into a defined atmosphere, see Figure 9. Assuming that the system is quasistationary, i.e. that over an extended period of time the precipitating system is in the same state at definite positions of the precipitation tube, at a known flow rate v in the tube the detection point x (measured from the mixing cell) at which, for example spectroscopic or diffractive characterization methods are attached, may be converted into reaction time $\tau = x/v$. Alternatively the tube length may be varied and samples for off-line methods (especially microscopic methods) obtained, for example by quenching liquid samples at the beam outlet. It is assumed when using these systems that the time scale of the reaction process is longer than the time to homogeneous mixing of the educts in and after the mixing cell; typical mixing times lie in the range of milliseconds for the stop-flow technique and in the range of microseconds with special flow cells. Hitherto there have been but few investigations of processes *during* mixing. More recent experiments show, however, that precursor structures which break down to nanoparticles are already forming at the boundary interfaces of the two turbulently mixing educt flows.

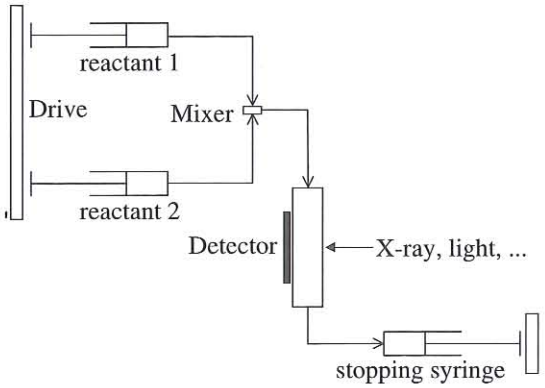


Fig. 8: *Principle of the stop-flow technique*

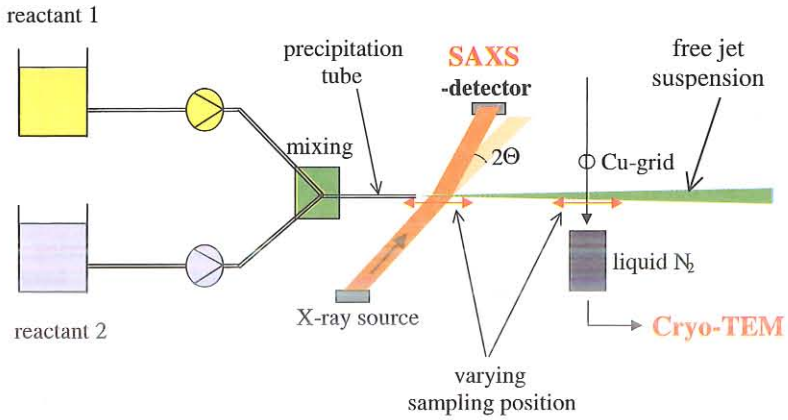


Fig. 9: *Principle of the reaction tube for the time-resolved investigation of particle formation processes that are initiated by the mixing of two educt solutions.*

In the following a number of experimental methods will be described briefly with which particle formation processes may be investigated on length scales of nanometers. Static and dynamic light scattering are established techniques for the investigation of colloidal systems [29]. More recently correlation spectroscopic methods such as fluorescence correlation spectroscopy (FCS) and Raman correlation spectroscopy (RCS) have been developed for the characterization of nanodispersed systems [30]. Concentrated dispersions can also be characterized reliably by filer optic quasielastic light scattering (FOQELS) [31]. Small-angle X-ray and neutron scattering (SAXS, SANS) are also classical methods for the characterization of colloidal systems and have been used in many investigations for the determination of primary particle size and aggregate structures [32]. Investigations on the following systems are cited as examples: lysozyme clusters as precursor for critical nuclei (SANS) [33], precursor formation in zeolite crystallization (SAXS) [34], aggregation and compaction in the formation of SiO2 and TiO2 particles (SAXS) [35] [36], and hydrolysis and condensation of metal alkoxides [28].

6 Precipitation of $CaCO_3$ as a generic example

The precipitation of $CaCO_3$ was studied with a combination of characterization methods: scanning and transmission electron microscopy (including cryo-TEM), X-ray microscopy, small and wide angle X-ray scattering, light scattering, analytical ultracentrifuge, and ion-sensitive electrodes - in all cases with emphasis on time-resolved data. Our approach for studying particle formation phenomena was guided by the principle that a fundamental understanding requires knowledge about the processes going on in supersaturated systems on all length scales from interatomic distances to millimeters and on all time scales from milliseconds to hours.

The experiments disclosed that the process of precipitation is by far more complicated than usually described in textbooks on crystallization. It was found that upon mixing 0.01 M $CaCl_2$ and 0.01 M Na_2CO_3 solutions initially amorphous particles of $CaCO_3$ with a size below 100 nm develop, see Figure 10. These nanoparticles either deposit onto surfaces or they aggregate (Fig. 10b) or dissolve again. In any case the material recrystallizes finally to a crystalline form that corresponds to a thermodynamically more stable state (calcite), cf. Fig. 10b. It is to be noted that the occurrence of nanoparticles did not find appropriate consideration so far in many experiments reported in the literature. These particles simply passed through the filters for preparation of the samples to analyze.

In order to gain detailed knowledge about the mode of action of polymers upon precipitation, experiments in supersaturated systems have been performed in the presence of polycarboxylates, i.e. charged macromolecules, with concentrations in the ppm-range. Such polymers are used, e.g., as additives in laundry detergents and in seawater desalination plants in order to prevent encrustation (scaling) on the surfaces. The investigations showed that the reduction / prevention of scaling is achieved by several mechanisms. The polycarboxylate molecules stabilize the intermediate nanoparticles, prevent recrystallization due to the effective wrapping in of the nanoparticles, and impede crystal growth by blocking the respective growing crystal surfaces. The first mechanism is exemplified in Fig. 11, where the $CaCO_3$ nanoparticles are seen, which are embedded in a polycarboxylate floc. The second point is discussed in more detail in Ref. [37]. The third mechanism is treated in Ref. [38].

The efficiency with which these mechanisms work depends on the detailed chemical structure of the respective polycarboxylate used, i.e. which monomeric units like acrylic acid, maleic acid, aspartic acid, etc. are copolymerized.

By knowledge of the molecular processes leading to scaling and understanding the interference of polycarboxylates with these processes, it is thus possible to present important aspects of a rational approach for the control, i.e. minimization or prevention of scaling in seawater desalination plants by the use of suitable polymeric additives.

This aspect is closely related to the points discussed in the foregoing chapters: controlling the birth and the fate of nanoparticles.

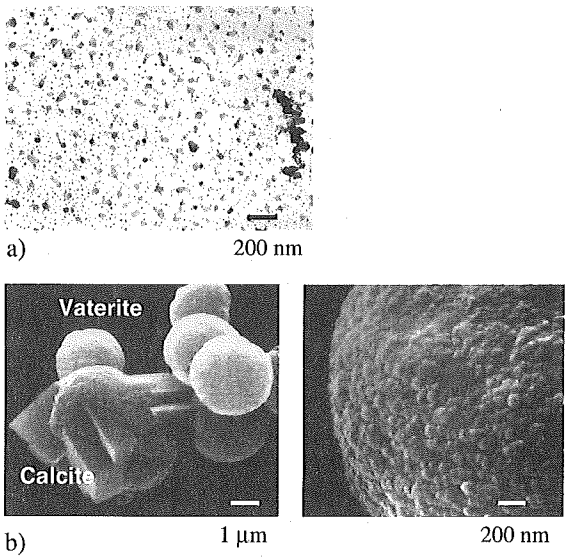


Fig. 10: *a) State of the $CaCO_3$ precipitation 20 msec after starting the reaction. The micrograph was taken by quenching the system in liquid nitrogen and transferring the frozen sample to a cryo-transmission electron microscope. $CaCO_3$ nanoparticles are to be seen. b) State of the system after 5 min as seen by scanning electron microscopy. The spheres supposedly form by aggregation of the nanoparticles seen in (a). They transform to calcite rhombohedra, which is the stable modification of $CaCO_3$.*

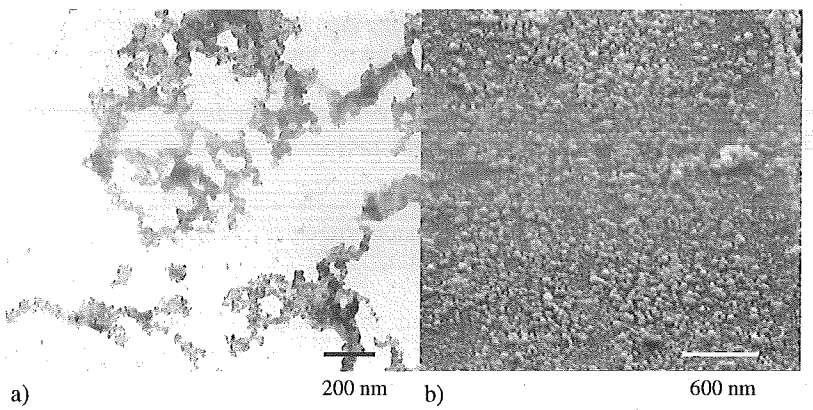


Fig. 11: *a) State of the $CaCO_3$ precipitation 5 min after starting the reaction in the presence of 600 ppm polycarboxylates. The micrograph was taken by quenching the system in liquid nitrogen and transferring the frozen sample to a cryo-transmission electron microscope. $CaCO_3$ nanoparticles embedded in a floc consisting of polycarboxylate molecules are to be seen. b) Same as (a) but seen by means of scanning electron microscopy on a substrate (cotton).*

Acknowledgements

I thank my colleagues Dr. André, Dr. Auweter, H. Debus, Dr. Franke, Dr. Frechen and Dr. Heckmann for the kind supply of information.

References

[1] D. Horn and J. Rieger, Angew. Chem. Int. Ed. 40, 4330 (2001)
[2] P.C. Hiemenz, R. Rajagopalan, Principles of Colloid and Surface Chemistry, 3rd Ed. (Marcel Dekker, New York, 1997)
[3] Fine Particles Science and Technology, Ed.: E. Pelizzetti (Kluwer Academic Publishers, Dordrecht, 1996)
[4] J. Rieger, E. Hädicke and K.-H. Büchner, in: Scaling in Seawater Desalination, Eds.: H. Glade and J. Ulrich (Shaker Verlag, Aachen, 2001), pp. 181
[5] D. Distler, Wäßrige Polymerdispersionen (Wiley-VCH, Weinheim, 1999)
[6] Fine Particles: Synthesis, Characterization, and Mechanisms of Growth, Ed.: T. Sugimoto (Marcel Dekker, New York, 2000)
[7] J. Brinker and G.W. Scherer, Sol-Gel Science (Academic Press, New York, 1990)
[8] F.C. Sager, Curr. Opin. Colloid. Interface Sci. 3, 276 (1998)
[9] T.T. Kodas and M.J. Hampden-Smith, Aerosol Processing of Materials (Wiley-VCH, New York, 1999)
[10] O. Rheingans, N. Hugenberg, J.R. Harris, K. Fischer and M. Maskos, Macromolecules 33, 4780 (2000)
[11] G.R. Newkome, C.N. Moorefield and F. Vögtle, Dendritic Molecules - Concepts, Syntheses, Perspectives (Wiley-VCH, Weinheim, 1996)
[12] A. Sunder, J. Heinemann and H. Frey, Chem. Eur. J. 6, 2499 (2000)
[13] J.W. Mullin, Crystallization (Butterworth-Heinemann, Boston, 1992)
[14] P.G. Debenedetti, Metastable Liquids (Princeton University Press, Princeton, 1996)
[15] J.D.F. Ramsay, in: Controlled Particle, Droplet and Bubble Formation, Ed.: D.J. Wedlock (Butterworth-Heinemann, Oxford, 1994)
[16] J. Stávek and J. Ulrich, Cryst. Res. Technol. 29, 465 (1994)
[17] O. Galkin and P.G. Vekilov, J. Am. Chem. Soc. 122, 156 (2000)
[18] L. Gránásy and D.W. Oxtoby, J. Chem. Phys. 112, 2399 (2000)
[19] J. Barrett, J. Chem. Phys. 111, 5938 (1999)
[20] P.R. tenWolde and D. Frenkel, Phys. Chem. Chem. Phys. 1, 2191 (1999)
[21] J. Schmelzer, G. Ropke and R. Mahnke, Aggregation Phenomena in Complex Systems (Wiley-VCH, Weinheim, 1999)
[22] M. Elimelech, J. Gregory, X. Jia and R.A. Williams, Particle Deposition and. Aggregation (Butterworth-Heinemann, 1995)
[23] M. Vanni, J. Colloid Interface Sci. 221, 143 (2000)
[24] B.W. Ninham, Adv. Colloid Interface Sci. 83, 1 (1999)
[25] J. Baldyga and J.R. Bourne, Turbulent Mixing and Chemical Reactions (Wiley, Chichester, 1999)
[26] W. Gerlinger, K. Schneider and H. Bockhorn, Chem. Ing. Tech. 72, 618 (2000)
[27] J. Rieger, E. Hadicke, I.U. Rau and D. Boeckh, Tenside Surfactants Detergents 34,
[28] M.Z.-C. Hu, J.T. Zielke, C. Byers, J.S. Lin and M.T. Harris, J. Mat. Sci. 35, 1957 (2000)

[29] B. Chu, Laser Light Scattering, 2nd ed. (Academic Press, Boston, 1991)
[30] D. Horn, J. Klingler, W. Schrof and K. Graf, Prog. Colloid Polym. Sci. 112, 27 (1998)
[31] H. Wiese and D. Horn, Ber. Bunsenges. Ber. Bunsenges. Phys. Chem. 97, 1589 (1993)
[32] Neutron, X-Ray and Light Scattering, Eds.: P. Lindner and T. Zemb (North-Holland, Amsterdam, 1991)
[33] O. Vidal, M.C. Robert and F. Boué, J. Cryst. Growth 192, 257 (1998)
[34] P.-P.E.A. deMoor, T.P.M. Beelen and R.A. vanSanten, J. Phys. Chem. B 103, 1639 (1999)
[35] H. Boukari, J.S. Lin and M.T. Harris, J. Colloid Interface Sci. 194, 311 (1997)
[36] J.-P. Jalava, E. Hiltunen, H. Kähkönen, H. Erkkilä, H. Härmä and V.-M. Taavitsainen, Ind. Eng. Chem. Res. 39, 349 (2000)
[37] J. Rieger, J. Thieme and C. Schmidt, Langmuir 16, 8300 (2000)
[38] E. Hädicke, J. Rieger, I.U. Rau and D. Boeckh, Phys. Chem. Chem. Phys. 1, 3891 (1999)

D2 Dynamic Light Scattering by Nonergodic Media

Jacques G.H. Joosten
DSM Research, P.O. Box 18
6160 MD Geleen, The Netherlands

1 Summary

Dynamic light scattering (DLS) measures the time-averaged time correlation function (ICF) of the intensity $I(q,t)$ of light scattered by a sample in the direction described by the scattering vector $\underline{\mathbf{q}}$. In recent years, the effect of nonergodicity of solid-like materials like colloidal glasses or polymeric gels on DLS has attracted a great deal of attention. In these systems the scattering elements are restricted to certain spatial regions within the sample. This implies that these units (colloidal particles or polymer segments) are only able to perform limited Brownian motion about fixed average positions. As a result, one particular sample of the system is trapped in a restricted region of phase space defined by its average configuration and the extent of the fluctuations about this configuration. A colloidal glass or a (chemically) cross-linked gel may thus be regarded as a nonergodic medium since a time-averaged measurement on a particular sample will not, in general, be equivalent to an ensemble-averaged measurement, i.e., one averaged over a representative number of all possible spatial configurations. A theory of DLS by nonergodic media, developed by Pusey and van Megen, provides a method to extract from time-averaged intensity correlation function measurements the normalized dynamic structure factor $f(q,t)$ associated with the concentration fluctuations. More specifically, from $f(q,t)$ one can determine the fraction of frozen-in fluctuations resulting from the constrained motion of the scattering elements.

In the lecture the basic notions of DLS from nonergodic media will be presented. Next to this examples from experiments on real systems and computer simulations will be used to illustrate the phenomenon.

D 3 Colloidal stability of casein micelles in milk

C.G. de Kruif and R. Tuinier*
NIZO food research, Ede, The Netherlands and
Van 't Hoff Laboratory for Physical and Collloid Chemistry,
Debye Research Institute, University of Utrecht,
The Netherlands

*present affiliation:
Institut für Festkörperforschung
Forschungszentrum Jülich GmbH

Contents

1 **Introduction** 2

2 **Casein Micelles: Composition and Structure** 3

3 **Stability of Casein Micelles** 4

4 **Interaction Potential Between Two Casein Micelles** 7

5 **Cheese-making** 11

6 **Yoghurt making** 13

7 **General Discussion and Conclusions** 14

1 Introduction

Milk is produced in the mammalian gland of mammals; production starts when the young is born and can continue for more than a year until the young is weaned. Neonates depend entirely on the mother's milk for their energy and growth. At least for the neonate, milk is a 'complete' nutrition. It contains all necessary components for the suckling.
In the past, man has domesticated several animals and *milked* them for his own nutrition, and made products, which could be preserved for some time. These are products like butter, cheese and yoghurt. The variety in these products is huge and represents an interesting case of natural selection in product development. The production of milk by buffalo and cow is, worldwide about 10^{12} litres per annum, of which approximately 10^{11} litres is produced in Europe, including about 10^{10} litres in The Netherlands. To put this in perspective: 10^{12} litres is the equivalent of about 10 super tankers of 250 000 tons every day. So milk is a real industrial commodity. The year-average composition of bovine milk in The Netherlands is given in Tab.1.

Table 1. *Composition of cow's milk as a mixed particle dispersion, size and volume fraction.*

	cont. phase	whey proteins	casein micelles (incl $CaPO_4$)	milk fat
radius nm	<0.5	5	100	3000
mass perc. %	92	0.7	3.0	4.4
vol. fract. %	83	1	11	5

Cow's milk is a mixed colloidal dispersion. All the properties of milk and its behaviour during production of dairy products can be understood from a colloid physics point of view. The aim of this chapter is to illustrate the colloidal nature of milk and milk products. A simple example is the following.
Milk contains fat globules as an emulsion for the energy intake of the young. On standing, the emulsion droplets (in fresh milk) rise to the surface, i.e. the milk *creams*. Skimming of this cream layer gives the product whipping cream. Destabilizing the emulsion and phase inversion leads to an oil phase (butter) and a water phase (buttermilk).
The next largest particles in milk are the casein micelles, the main subject of this chapter. The casein micelles are a factor of 10 smaller than the emulsion droplets. Another factor of 10 smaller are the whey proteins, which are a mixture of a large number of proteins and enzymes with different physiological functions, such as the immunoglobulins that contribute to the immune system of the neonate. The main whey proteins are β-lactoglobulin and α-lactalbumin.
Another factor of 10 smaller still we mainly find lactose (milk sugar 4.4 %w/w), salt ions and water. Milk is isotonic with blood and the ionic strength in milk is 0.08 molar, a value much too high for electrostatic repulsion between the colloidal particles to be effective. Nevertheless milk is an amazingly stable mixed colloidal dispersion. One can add salt and limited amounts of alcohol. Milk may be frozen, thawed, and boiled without any apparent loss in stability. Try this with ink, paint or mayonnaise!

The main topic of this chapter is the casein micelle. Casein micelles are association colloids and are about 100 nm in radius. Milk contains about 2.7 % w/w of casein and 0.35 %w/w of calcium phosphate. Together they form the so-called casein micelles, which have a voluminosity of 4.4 ml/g casein at room temperature. Therefore the volume fraction of the casein micelles in milk is between 0.10 and 0.13. The casein micelles are responsible for the white appearance of milk. The main physiological function of casein micelles appears to be the transport of calcium for the skeleton of the neonate. The calcium and casein contents in milk are linearly related although the level varies greatly between species. In Fig.1 we plot the casein content ($\propto$ calcium) in milk as a function of the estimated growth rate, defined as 1/(# months required to double the weight of the neonate). Clearly man grows very slowly compared to rat and sheep and therefore the calcium and casein content is low in human milk. So much for an introduction to milk and casein micelles. In the following sections we will discuss the properties of casein micelles and treat them as real colloidal particles.

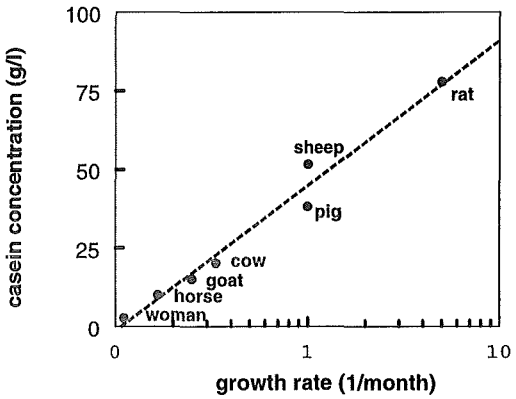


Fig. 1: *Amount of casein in milk as a function of growth rate for various species.*

2 Casein Micelles: Composition and Structure

Phenomenologically, casein micelles are polydisperse colloidal particles of about 100 nm radius. Their composition is known [1]. They contain four different types of caseins: α_{s1}-casein , α_{s2}-casein. β-casein and κ-casein in a ratio of 4:1:4:1. Furthermore about 6% of the particle is amorphous calcium phosphate. In the mammary gland calcium phosphate is supersaturated and nucleates into so-called nanoclusters. If the growth of the nuclei is not prevented that would lead to calcification of the mammary gland and probably the death of the mother, a phenomenon observed in animals that are deficient in casein production. The growth is stopped through the adsorption of the phospho-caseins, i.e. α_s-caseins and β-casein. So, a layer of protein polymers covers the nanoclusters. It should be noted here that the pure

caseins have no clear secondary structure; they cannot be 'denatured'. However, pure caseins have a very distinct amphiphilic nature as follows from their amino acid sequence and their spontaneous micellisation (like soap micelles). Interestingly, the 'hydrophobic, core of β-casein is at the outside of the nanocluster. In other words the nanoclusters are decorated with a protein coat that is in a poor solvent. Consequently, the nanoclusters will have a tendency to associate/flocculate/gel into larger structures. This growth is prevented by the protein κ-casein, which is strongly amphiphilic but is not calcium sensitive. Therefore the κ-casein will associate with the hydrophobic coat of the nanoclusters. The κ-casein is driven to the outside of the casein micelle and thus provides a steric stabilization layer. The size of the casein micelle scales inversely with the amount of κ-casein present. So, the more κ-casein, the smaller the casein micelle, which contains typically 1000 nanoclusters per casein micelle. An artist's impression of the casein micelle [2]) is shown in Fig.2.

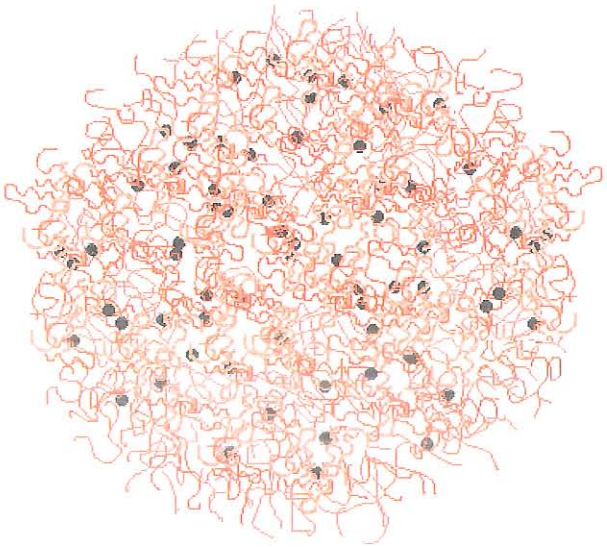


Fig. 2: *Model structure of the casein micelle showing a more-or-less homogeneous protein matrix containing calcium phosphate nanocluster-like particles distributed with a mean spacing of 18 nm.*

The model described above thus predicts that a whole casein micelle contains 1000 nanoclusters and is stabilized by a coat or brush of κ-casein molecules. Especially this last property is referred to as the "hairy" casein micelle. Small-angle neutron-scattering contrast-variation measurements indeed revealed the predicted correlation length of 18 nm in the internal structure of the casein micelles [2][3].

3 Stability of Casein Micelles

From a colloid physics point of view, casein micelles can be regarded as colloidal particles stabilized by a coat or brush of κ-casein (and probably some β-casein) on the outside. From

this point of view they thus resemble latex particles, and experiments done by physicists and colloid chemists on latex particles can also be done on casein micelles.

Recently we calculated the colloidal stability of casein micelles in a DLVO-like approach, i.e. we summed the various contributions to the interaction potential between two micelles. We distinguished the following contributions:

a) Steric interactions

We consider the κ-casein hairs on the outside as a polyelectrolyte brush whose interaction with a similar brush must be calculated. For the interaction potential between hard parallel plates at a distance h carrying brushes we use the Alexander-de Gennes theory [4][5], which leads to the following expression for the *force* between two parallel flat plates:

$$\frac{K_{brush}(h)}{kT} = \sigma^{\frac{3}{2}}\left[\left(\frac{2H}{h}\right)^{9/4} - \left(\frac{h}{2H}\right)^{3/4}\right] \quad \text{for } h < 2H$$
$$= 0 \quad \text{for } h > 2H \qquad (1)$$

where the first term between the square brackets represents the increase in the osmotic pressure (leading to repulsion) due to the increase of the brush concentration between the plates and the second term represents the change in elastic free energy of the brush upon compression. The parameter H is the brush height and h is the distance between the bristles. The grafting density is given by σ and will be defined below (equation 3).

By subsequently applying the Derjaguin approximation to the potential between two flat surfaces, the following expression for the interaction potential between two spheres, with radius a, is obtained [6][7]:

$$\frac{W_{brush}(h)}{kT} = \infty \quad \text{for } h < 0$$
$$= \frac{16\pi a H^2 \sigma^{\frac{3}{2}}}{35}\left[\left(28\left(\frac{2H}{h}\right)^{1/4} - 1\right) + \frac{20}{11}\left(1 - \left(\frac{h}{2H}\right)^{\frac{11}{4}}\right) + 12\left(\frac{h}{2H} - 1\right)\right] \quad \text{for } 0 < h < 2H \qquad (2)$$
$$= 0 \quad \text{for } h > 2\ H$$

which is supposed to be valid as long as a>>H. In order to calculate this potential we need to calculate the brush height H as a function of pH and chain density σ. As discussed by De Kruif and Zhulina [8], κ-caseins can be described as charged brushes in the 'salted brush' regime. In this regime the ionic strength is such that it penetrates the brush and screens the electrostatic interactions between the charged polyacid groups and the Debye length κ^{-1}<<H. Then the polyacid brush is quasi-neutral; its characteristics are identical to those of neutral brushes. Consequently, in the strong stretching approximation, the brush height then reads [9]:

$$H = Nb\left(\frac{8v^{eff}\theta}{\pi^2}\right)^{\frac{1}{3}}, \qquad (3)$$

where N is the number of segments of the brush, each having a length b. Here N = 15 segments (coinciding with the number of charged groups) and b = 0.6 nm. The quantity θ is the grafting density: the fraction of 'sites' occupied by the brushes at the surface. The parameter σ (in m^{-2}) is the grafting density θ divided by the surface area occupied by a brush. It is calculated from the known composition of milk and casein micelles and their size distribution. The molar mass of κ-casein is 19032 g/mol, and the brush density thus corresponds to approximately 7500 chains per casein micelle, and the average distance between the chains is 4 nm. The area occupied by one chain at the surface is at least the squared length of an amino acid group in the κ-casein brush, where the length equals about 0.32 nm. We therefore estimate σ as 0.006. The above data gives a brush height of 7.0 nm, which is consistent with dynamic light-scattering experiments [10]. The effective excluded volume is denoted by v^{eff} and is defined as [9]:

$$v^{eff} = v + \frac{\alpha^2}{\phi_s}, \qquad (4)$$

where v is the (dimensionless) excluded volume per segment (normalized with the segment volume), $v = 1 - 2\chi$ (with χ the Flory-Huggins interaction parameter taken as $\chi = 0.5$ making it a theta-solvent), and ϕ_s ($\cong 0.01$ in milk) is the salt volume fraction. We take a very simple model for the dissociation of the polyacid brush in which we assume that the various dissociating groups do not affect one another, which leads to the following relation between the pH and the degree of dissociation α:

$$\alpha = \frac{K_a}{K_a + [H^+]}, \qquad (5)$$

where $[H^+]$ is the proton concentration ($\equiv 10^{-pH}$) and K_a the mean value of the dissociation constant of the carboxylic groups along the chain: $pK_a = 4.9$, a value given by Swainsgood [11]. The above offers us a simplified model for the brush height as a function of pH. It is realized that equation 3 loses its applicability at low pH (where there is no longer a strong-stretching regime).

b) Electrostatic repulsion

Casein micelles have a clear electrophoretic mobility, which becomes very small, however, near pH = 5. At physiological (pH = 6.7) a zeta potential of 8 mV has been reported by Schmidt [12]. The expression for the interaction potential between two spheres due to electrostatic repulsion $W_{er}(h)$ can be derived from a linear approximation to the Boltzmann charge distribution around two colloids [13]:

$$\frac{W_{er}(h)}{kT} = -2\pi a\varepsilon_0\varepsilon_r\Psi^2\ln(1+\exp(\kappa h)), \qquad (6)$$

where Ψ is the surface potential, taken to be equal to 20mV at pH = 7 and to fall linearly to zero at pH = 4.9; the permittivity in vacuum ε_0= 8.854 10^{-12} C^2 /(Nm^2); ε_r = 80; e = 1.60210·10^{-19} C; k = 1.38054·10^{-23} J/K; a=100 nm. The Debye length, given by the parameter κ^{-1} is found from:

$$\kappa^{-1} = \sqrt{\frac{\varepsilon_r\varepsilon_0 RT}{F^2 I}} \rightarrow \kappa \cong 3\sqrt{I}\,(nm^{-1}), \qquad (7)$$

The ionic strength I is about 0.08 M in milk [1], corresponding to a Debye length of the order of 1 nm. The electrostatic repulsion between casein micelles in milk is therefore short-ranged.

c) Van der Waals attraction

For the Van der Waals attraction, $W_{vdW}(h)$, between two spheres separated by a distance h, where h= r – 2a, a is the sphere radius and r is the sphere centre- to- centre distance, one finds [14]:

$$\frac{W_{VdW}(h)}{kT} = -\frac{A}{6}\left(\frac{2a^2}{(h+2a)^2-4a^2} + \frac{2a^2}{(h+2a)^2} + \ln\left\{\frac{(h+2a)^2-4a^2}{(h+2a)^2}\right\}\right), \qquad (8)$$

where A is the Hamaker constant. We may use results of the Hamaker constant as found for proteins. For β-lactoglobulin and lysozyme, values of respectively 5 [15] and 7 kT [16] are reported. The protein density of casein micelles is about 6 times less than that of globular proteins and therefore we estimated A as 1.0 kT.

4 Interaction Potential Between Two Casein Micelles

We are now in a position to calculate the total of the interaction potential between two casein micelles by adding the various contributions:

$$\frac{W_{tot}(h)}{kT} = \frac{W_{VdW}(h)}{kT} + \frac{W_{er}(h)}{kT} + \frac{W_{brush}(h)}{kT}. \qquad (9)$$

In Fig.3 (a) and (b) we calculated the contributions of the various terms to $W_{tot}(h)/kT$ at two different pH values. Clearly the contribution of the electrostatic repulsion is small if not negligible, which is consistent with the insensitivity of the system to salt. As illustrated in Fig.3 the contribution of the electrostatic interaction term is very small at both pH values. Also we calculated $W_{tot}(h)/kT$ for three values of the brush density. Renneting means that the brush is enzymically removed as in the cheesemaking process. So the potential barrier

remains repulsive up to removal of half of the brush but becomes effectively attractive when two-third of the brush is removed; see Fig.4.

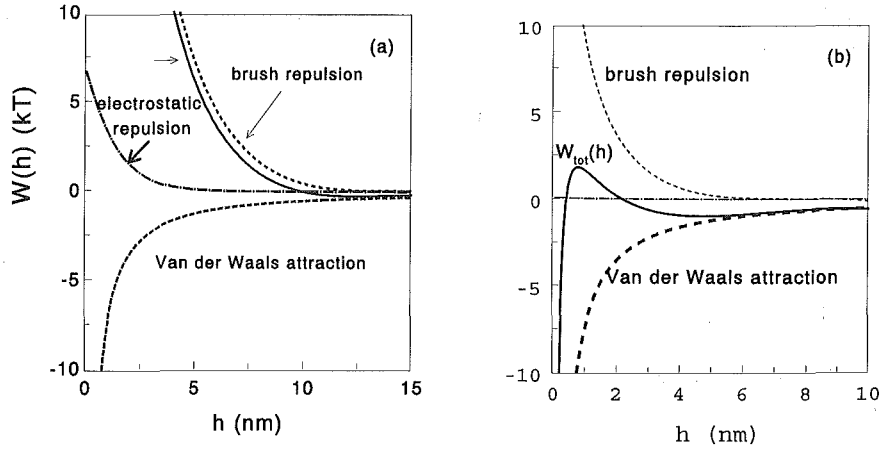


Fig. 3: *Total interaction potential and its various contributions as a function of the distance between two casein micelles at pH 6.7 (Fig. 3(a); fresh skim milk) and pH 4.7 (Fig. 3(b); acidified skim milk).*

From statistical mechanics [17] we can calculate the second osmotic virial coefficient B_2 from $W_{tot}(r)$, with r = h+2a:

$$B_2 = \frac{2\pi}{V_c}\int_0^\infty r^2\left[1-\exp\left(-\frac{W_{tot}(r)}{kT}\right)\right]\,dr, \qquad (10)$$

where V_c is the volume of the casein micelle. The second osmotic virial coefficient is a parameter that monitors the stability of a colloidal dispersion. Since the potential is short-ranged it is justifiable to simplify the interaction potential.

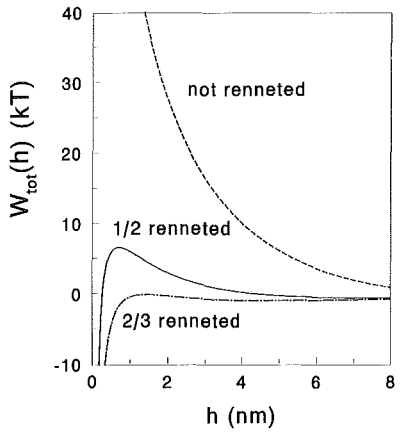


Fig. 4: *Total interaction potential between two casein micelles at pH 6.7 for various degrees of renneting.*

Attractive interactions in colloid and interface science can be simplified considerably by modelling the interaction as a square-well potential, which is illustrated in Fig.5. This potential has the main features of the $W_{tot}(h)/kT$ between casein micelles in that its attractive well is very short ranged (a few nm) compared to the particle size (100nm). Actually the square-well potential is probably more realistic in that its depth is finite, at incomplete renneting and pH values slightly above clotting. There we observe a reversible attractive interaction rather than a probability to get stuck in the primary minimum. The square-well potential is defined by:

$$\frac{V(r)}{kT} \begin{cases} = \infty & \text{for } r < 2a \\ = -\varepsilon & \text{for } 2a < r < 2a + \delta \\ = 0 & \text{for } h > 2a + \delta \end{cases} , \qquad (11)$$

and is schematically depicted in Fig.5:

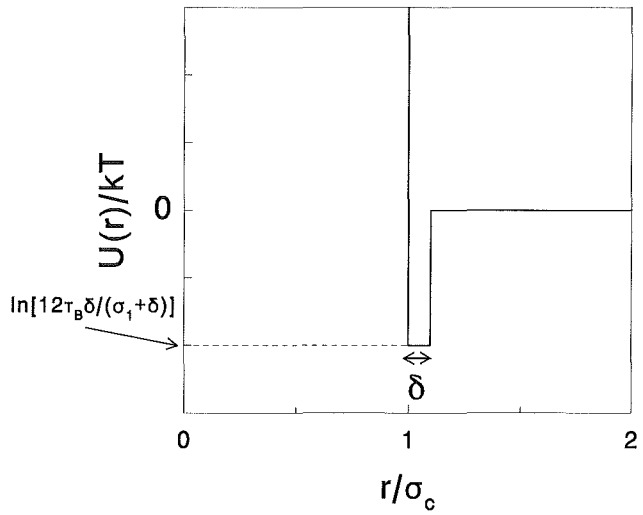


Fig. 5: *Schematic representation of the square-well potential.*

The second osmotic virial coefficent for this potential is:

$$B_2 = 4 - \frac{\delta}{2a}[\exp(\varepsilon) - 1]. \tag{12}$$

Even simpler is the adhesive hard sphere theory of Baxter [18], which can be used to describe both equilibrium and transport properties of colloidal dispersions. In Baxter's approach $\delta \rightarrow 0$. The effective attraction in this model is expressed by the Baxter parameter τ_B. For the Baxter potential the second osmotic virial coefficient becomes:

$$B_2 = 4 - \frac{1}{\tau_B}. \tag{13}$$

Since the square-well potential is easily mapped on the Baxter potential we also used this potential by relating the well depth to an observable parameter directly. For the relative viscosity Cichocki and Felderhof [19] derived the following equation for adhesive hard spheres:

$$\eta_r = 1+\frac{5}{2}\phi+\left(5.9+\frac{1.9}{\tau_B}\right)\phi^2, \qquad (14)$$

where ϕ is the volume fraction of the spheres, about 0.11 for casein micelles in skim milk. In Fig.6 we give an illustration of the predicted viscosity behaviour of acidified milk. Although not fully quantitatively correct, the theoretical prediction is in good agreement with the experimentally observed behaviour.

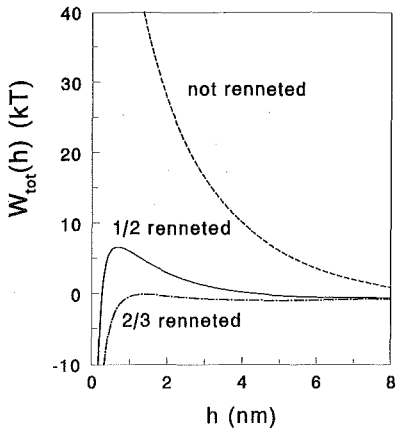


Fig. 6: *pH-dependence of the relative viscosity as a function of the degree of renneting.*

In the following sections we use the above concepts to describe two industrially important processes, i.e. cheese making and yoghurt making, in a (semi-) quantitative way.

The full description of the interaction potential serves to identify the important contributions and to "get the physics right". On the other hand it contains a large variety of parameters that are not exactly known parameters. Therefore we used the square well potential, which contains only one adjustable parameter, i.e. the well depth, and can be related to an observable quantity.

5 Cheese-making

In cheese-making an enzyme preparation called rennet (extracted from the stomach of calves/cows) is added to the milk. The enzyme chymosin present in rennet cleaves off very specifically the κ-casein brush on the surface of the casein micelles. Actually, chymosin cuts off 64 amino acids of the C-terminal part. Pictorially speaking the κ-casein fur is cut off. We did not use the word 'shave' because the enzymatic reaction occurs at random. As the enzymatic

reaction obeys simple first-order reaction kinetics the brush density as a function of time is given by:

$$\frac{P_\infty - P(t)}{P_\infty} = e^{-\frac{k[E]t}{[E_0]}} = \frac{\sigma}{\sigma(t)}, \tag{15}$$

where k is a reaction constant, and has a value $k = 8 \cdot 10^{-4}$ s^{-1} and $[E] = [E_0]$ corresponds to an enzyme concentration used as standard addition in practice.
The well depth is simply equated to the enzyme kinetics [10]:

$$\frac{P_\infty - P(t)}{P_\infty} = e^{-\frac{k[E]t}{[E_0]}} = \frac{\sigma}{\sigma(t)}, \tag{16}$$

where h is a proportionality constant with a value h = 1.63. Thus in this model the interaction potential and therewith the static and dynamic properties are simple functions of enzyme kinetics in a given experiment. We checked this and found that turbidity, viscosity and diffusivity can be described with a single set of parameters using the adhesive hard sphere model.

In Fig.7(a) we plotted the apparent Stokes radius of casein micelles as a function of time. In Fig.7(a) we plot the apparent Stokes radius as measured and calculated using the adhesive hard sphere model. The data in Fig.7 (a) were measured in the small-angle scattering wave vector limit and were thus interpreted using expressions for the collective self-diffusion of the adhesive hard spheres. In Fig.7 (b) we give an example of the viscosity as a function of the amount of κ-casein split off from the surface of the micelles. The dashed line in Fig.7(b) represents the result obtained using W_{tot} (h) at pH = 6.7. Again the result is qualitatively correct. According to the calculations, the casein micelles lose their stability already if 60% of the steric layer of κ-casein is cut off. In practice this is as high as 90%.

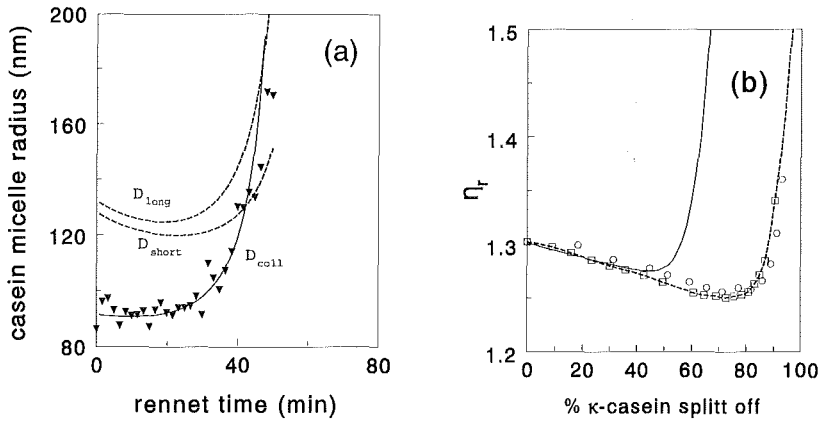


Fig. 7: *Casein micelle radius as a function of renneting time (a) and viscosity of a skim milk dispersion (b) as a function of the percentage of κ-casein cleaved off during renneting. The experimental data are given as the data points from refs. [10] and [20] and the full curve is calculated using equations 9, 10, 13 and 14.*

The discrepancy may arise from several effects not accounted for in the calculations. The two most important are probably the following. First, the outside layer will contain also an amount of β-casein. It is known that β-casein can leave the micelle on lowering the temperature to a few degrees C. This extra polymer is not renneted but does contribute to the steric stabilization. Secondly it is known that the strength of the steric stabilization at low coverage may be underestimated leading to an increased stability as well.

6 Yoghurt making

In yoghurt making the pH of the milk is gradually lowered by the activity of lactic acid bacteria, which convert the milk sugar (lactose) into lactic acid. Depending on conditions and the type of bacteria used the pH may reach values as low as pH = 4.

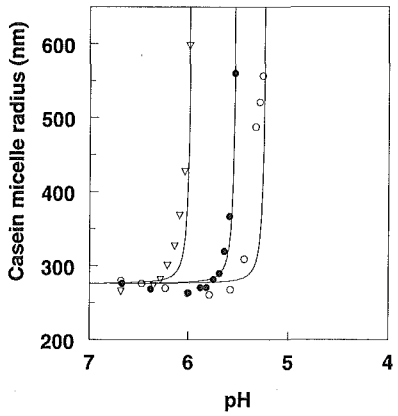


Fig. 8: *Stokes radius as a function of pH for various degrees of renneting.*

The experimental results in Fig.8 were obtained by partially renneting the casein micelles. The partial renneting lowers the pH stability as was shown by De Kruif and Zhulina [8]. The results in Fig.8 were fitted to the adhesive hard sphere model by setting the well depth equal to 1/(pH-pCrit) where pCrit is a critical value of the pH where the brush collapses [21]. Fig.8 is consistent with the results in Fig.6 if we assume that the increase in apparent particle radius is comparable to the viscosity increase.

7 General Discussion and Conclusions

Casein micelles in milk are sterically stabilized association colloids. The steric stabilization derives from a short brush of κ-casein 'hairs' on the surface of the casein micelles. The physical behaviour of casein micelles in fresh skimmed milk can be described with the hard sphere model. During the production of dairy products the stabilizing brush is changed in either of two ways. In cheese-making the brush is cut off by an enzymatic reaction. As a result the casein micelles lose their steric coat and an attractive interaction between the micelles eventually leads to flocculation and gelation (the cheese curd.). The behaviour of the micelles can be understood quantitatively using the adhesive hard sphere model.

In yoghurt making, lowering the pH diminishes the brush stability. The brush hairs can be considered as polyelectrolyte chains. Their solvency depends on the charge density along the chain. On lowering the pH the carboxylic acid groups become less dissociated and the κ-casein hairs lose their stability. As a result the brushes collapse and the casein micelles flocculate at a lowered pH.

Some further useful references on casein micelles are given as references [22][23][24][25].

References

[1] Walstra, P., Jenness, R., *Dairy Chemistry and Physics*, Wiley, 1984

[2] De Kruif, C.G., Holt, C., *Casein Micelle Structure, Functions and Interactions*; to be published as Chapter 3 in 2001 in *'Advances in Dairy Chemistry,'* Vol. Q, ed. P.F. Fox, P.L.H. McSweeney

[3] Holt, C., *et al.*, unpublished results

[4] Alexander, S., *J. Phys. (France)* 38 (1977) 983

[5] de Gennes, P.G., *Adv. Colloid and Interface Sci.* 27 (1987) 189

[6] Braithwaite, G.J.C., Luckham, P.F., Howe, A.M., *J. Colloid Interface Sci.* 213 (1999) 525

[7] Likos, C.N., Vaynberg, K.A., Löwen, H., Wagner, N.J., *Langmuir* 16 (2000) 4100

[8] De Kruif, C.G., Zhulina, E.B., *Coll. Surf. A* 117 (1996) 151

[9] Israels, R., Leermakers, F.A.M., Fleer, G.J., *Macromolecules* 27 (1994) 3087

[10] De Kruif, C.G., *Langmuir* 8 (1992) 2932

[11] Swainsgood, H.E., In: *'Advances in Dairy Chemistry,'* Vol. 1: Proteins, ed. P.F. Fox, Elsevier Applied Science, London, 1992

[12] Schmidt, D.G., Poll, J.K., *Neth. Milk Dairy J.* 40 (1986) 269

[13] Hogg, R., Healy, T.W., Fuerstenau, D.W., *Trans. Faraday Soc.* 62 (1966) 1638

[14] Verwey, E.J.W., Overbeek, J.Th.G., *'Theory of the Stability of Lyophobic Colloids,'* Elsevier, Amsterdam, 1948

[15] Schaink, H.M., Smit, J.A.M., *Phys. Chem. Chem. Phys.* 2 (2000) 1537

[16] Gripon, C., Legrand, L., Rosenman, I., Vidal, O., Robert, M.C., Boué, F., *J. Cryst. Growth* 178 (1997) 575

[17] McQuarrie, D.A., *Statistical Mechanics*, Harper & Row, New York, 1976

[18] Baxter, R.J., *J. Chem. Phys.* 49 (1968) 2770

[19] Cichocki, B., Felderhof, B.U., *J. Chem. Phys.* 89 (1988) 3705

[20] De Kruif, C.G., Jeurnink, Th.J.M., Zoon, P., *Neth. Milk Dairy J.* 46 (1992) 123

[21] De Kruif, C.G., *J. Dairy Sci.*, 81 (1998) 3019

[22] Holt, C., In: *'Advances in Protein Chemistry,'* vol. 43, Eds. C.B. Anfinsen, J.D. Edsall, F.R. Richards, and D.S. Eisenberg, Academic Press, San Diego, p.63-151, 1992

[23] Holt, C., Horne, D.S., *Neth. Milk Dairy J.* 50 (1996) 85

[24] Horne, D.S., *Int. Dairy J.* 8 (1998) 171

[25] Holt, C., *'The Stability of bovine casein micelles,'* In: *'Proceedings International Conference on Colloid and Interface Science, vol. 1'*, Akadémiai Kiadó, E. Wolfram, Ed. 1975, p. 641-644

D 4 From the Fundamentals to Balanced Properties of Polymer Products by Means of Structure-Property-Relationships

Dr. Péter Krüger, Dr. Klaus Sommer
Zentrale Forschung, Physics Department
Bayer AG, Leverkusen

Contents

1. Introduction 2

2. Basic Aspects on Structure-Property-Relationships of filled Elastomers 3

3. Thermoplastics and their Properties 9

3.1 Rubber Toughening of Amorphous Thermoplastics 12

3.2 Reinforcement and Barrier Properties in Semicrystalline Thermoplastics 16

3.3 Optimized Thermoplastics as Substrate Polymers for Optical Data Storage Applications 19

4. Polymer Processing of Polyurethanes 21

5. Final Remarks 23

1. Introduction

Synthetic macromolecular materials have become an irreplaceable class of materials used in our modern society. There is a long history of scientific research and commercial development of various kinds of polymers in the past century. The most important milestones of the polymer research conducted at Bayer, one of the large commercial producers of polymeric materials, can be briefly listed as follows [1]:

- The invention of synthetic rubber in 1909 and the beginning of its production one year later
- The discovery of polyurethane chemistry by Otto Bayer in 1937
- The first patent for polycarbonate issued in 1953

The great progress in chemical research has accelerated the commercial use of macromolecular materials, accompanied by the fast development of engineering production techniques.
In the very early stages of polymer research the urgent need for the fundamental understanding of generated chemical structures and their correlations with the resulting physical properties has become clear. Initially the creation of adequate techniques and equipments was required. Following this, structure-property-relationships for special types of polymeric materials had to be generated.

In contrast to the scientific work on fundamental understanding of polymers carried out in academic research facilities such as universities, the efforts in industrial research and development for polymers are focused on the optimization of products to satisfy customer demands. This means that the techniques, methods, theories, and models used in academic research are also used in industrial research, and new developments will only be performed if the solution to a given problem is not available in the scientific community elsewhere. This holds especially true for the preferred application of commercially available characterization methods and techniques and software solutions. This general philosophy of doing scientific research only when needed and focusing on application concerns as much as possible is very common for most of the polymer producing companies [2].
However, in the case of industrial research and development of new materials and for optimization of existing products a broad range of very different parameters of structure and properties has to be balanced. In the non-industrial scientific community there is mostly only a limited knowledge of complex structure-property-relationships for commercially important products and existing problems. This is because in academic research, generally, idealized special model systems are used to get detailed quantitative information on a rather limited number of parameters for structure and property.
Based on this reality there is still – after several decades of physical research on polymers – a strong need for the generation of strictly product- and application-oriented structure-property-relationships (including detailed experimental knowledge) within a polymer producing company such as Bayer, BASF [2] or others.

It should be emphasized that in several product classes, such as polyurethanes, coatings and even for rubber based materials, the final product properties are generated by chemical reactions of different combinations of raw materials and other ingredients (e.g. polymerization of polyols and isocyanates; blending, reinforcement and curing of rubber; polymerization and crosslinking of coating ingredients) outside of the raw material producing companies.

D 4 From the Fundamentals to Balanced Properties of Polymer Products by Means of Structure-Property-Relationships

Dr. Péter Krüger, Dr. Klaus Sommer
Zentrale Forschung, Physics Department
Bayer AG, Leverkusen

Contents

1. Introduction 2

2. Basic Aspects on Structure-Property-Relationships of filled Elastomers 3

3. Thermoplastics and their Properties 9

3.1 Rubber Toughening of Amorphous Thermoplastics 12

3.2 Reinforcement and Barrier Properties in Semicrystalline Thermoplastics 16

3.3 Optimized Thermoplastics as Substrate Polymers for Optical Data Storage Applications 19

4. Polymer Processing of Polyurethanes 21

5. Final Remarks 23

1. Introduction

Synthetic macromolecular materials have become an irreplaceable class of materials used in our modern society. There is a long history of scientific research and commercial development of various kinds of polymers in the past century. The most important milestones of the polymer research conducted at Bayer, one of the large commercial producers of polymeric materials, can be briefly listed as follows [1]:

- The invention of synthetic rubber in 1909 and the beginning of its production one year later
- The discovery of polyurethane chemistry by Otto Bayer in 1937
- The first patent for polycarbonate issued in 1953

The great progress in chemical research has accelerated the commercial use of macromolecular materials, accompanied by the fast development of engineering production techniques.
In the very early stages of polymer research the urgent need for the fundamental understanding of generated chemical structures and their correlations with the resulting physical properties has become clear. Initially the creation of adequate techniques and equipments was required. Following this, structure-property-relationships for special types of polymeric materials had to be generated.

In contrast to the scientific work on fundamental understanding of polymers carried out in academic research facilities such as universities, the efforts in industrial research and development for polymers are focused on the optimization of products to satisfy customer demands. This means that the techniques, methods, theories, and models used in academic research are also used in industrial research, and new developments will only be performed if the solution to a given problem is not available in the scientific community elsewhere. This holds especially true for the preferred application of commercially available characterization methods and techniques and software solutions. This general philosophy of doing scientific research only when needed and focusing on application concerns as much as possible is very common for most of the polymer producing companies [2].
However, in the case of industrial research and development of new materials and for optimization of existing products a broad range of very different parameters of structure and properties has to be balanced. In the non-industrial scientific community there is mostly only a limited knowledge of complex structure-property-relationships for commercially important products and existing problems. This is because in academic research, generally, idealized special model systems are used to get detailed quantitative information on a rather limited number of parameters for structure and property.
Based on this reality there is still – after several decades of physical research on polymers – a strong need for the generation of strictly product- and application-oriented structure-property-relationships (including detailed experimental knowledge) within a polymer producing company such as Bayer, BASF [2] or others.

It should be emphasized that in several product classes, such as polyurethanes, coatings and even for rubber based materials, the final product properties are generated by chemical reactions of different combinations of raw materials and other ingredients (e.g. polymerization of polyols and isocyanates; blending, reinforcement and curing of rubber; polymerization and crosslinking of coating ingredients) outside of the raw material producing companies.

As a consequence, structure-property-relationships have to include all intended and even not intended influences of every production and processing step inside and outside of the raw material producing companies. In addition to this, even possible changes (e.g. due to physical and chemical aging) of properties during the lifetime at the consumer's place have to be taken into account. Based on these broad requirements it becomes clear that, in contrast to the more rigorous and more time consuming nature of results on a restricted area of interest in university research, the also fundamental but rather qualitative understanding of correlations has to be accepted in industrial polymer research. This is especially true if the usual short period of time available for development is taken into account. However, results generated in industrial research are not evaluated based on strictly academic criteria, their justification is mainly given by the success of resulting products and services at the customer.

Based on these diverse requirements for the generation of powerful structure-property-relationships it should also be clear that industrial research takes place in a very complex environment, at the interface of different disciplines such as physics, chemistry, biology, engineering science, etc. In addition to collaborations within the interdisciplinary scientific environment of the company, an intensive cooperation with customers and suppliers is also often necessary.
Hence, in addition to an excellent education in physics (broad fundamental knowledge in general physics as well as in experiments and theories and detailed understanding of polymer physics) the willingness to learn important scientific contents and facts in several other disciplines and well developed soft skills are urgently needed in industrial research environments.

In the following sections, important aspects of structure-property-relationships for polymers will be discussed. The given examples should point out the broad range of topics investigated in industrial research at Bayer, starting with fundamental and quantitative considerations for filled elastomers continuing with more qualitative but very interdisciplinary subjects dealing with modified thermoplastics up to the phenomenological treatment of polyurethane processing.

2. Basic Aspects on Structure-Property-Relationships of filled Elastomers

Research, development and production of rubber has a long and successful history. Beginning with natural rubber, the "weeping wood" of the Amazonian Indians, it has given us the abundance of synthetic general purpose rubbers and special polymers now available in the market (for a detailed overview on rubber technology compare [3]).
Formerly the term "rubber" referred only to natural rubber (poly-cis-isoprene) and "vulcanization" only to crosslinking of raw rubber using sulfur as vulcanizing agent. The development of many synthetic rubbers as well as new crosslinking systems has changed todays terminology.
Raw rubbers as non crosslinked, high molecular weight polymers, with a glass transition temperature T_g (transition from the high modulus, energy elastic solid state to the low modulus entropy elastic state, compare Fig. 1) well below ambient temperature, can be

changed into elastomers by vulcanization (elastomers are often synonymously labeled as vulcanizates), i.e. by the creation of chemical crosslinks. Elastomers show a predominantly but not completely reversible elastic deformation behavior and are not able to undergo an extensive viscous flow below their degradation temperatures. It should be noted that rubber can also undergo other transitions, such as crystallization and melting induced by temperature or mechanical deformation.
Beside the crosslinking of the raw rubber, the addition of reinforcing fillers is needed during the rubber processing in order to fulfil i.e. strength requirements in several applications. Carbon black or silica are widely used as reinforcing filler, affecting also other properties such as abrasion behavior, rolling resistance (mechanical damping, loss factor under periodic deformation conditions) of tires, stability against oxidation and UV induced degradation of the macromolecules.
Elastomers which are amorphous in the undeformed state can exhibit crystallization when stretched (due to a certain parallel orientation of the chains). This strain induced crystallization, observed in natural rubber (NR), polyisoprene (IR) and polychloroprene (CR), though not in styrene-butadiene rubber (SBR) or acrylonitrile-butadiene rubber (NBR), acts as a self-reinforcement, manifesting itself, for example, in an increase in the strength of raw rubber and also in the tensile strength of the elastomer. This should be distinguished from low temperature crystallization as mentioned above.

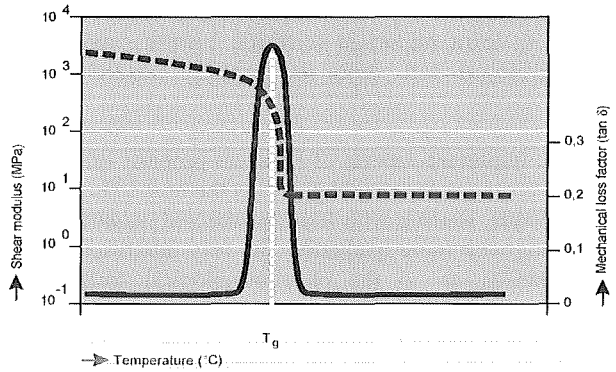


Fig. 1: *The shear modulus and the mechanical loss factor tan δ of elastomers as a function of temperature (schematic).*

Due to more market driven thinking, three different categories of rubbers can be distinguished in commercial applications:
General purpose rubbers are for instance used for vehicle tires and mass-produced articles of all types. This group consists of NR and the synthetic rubbers such as IR, polybutadiene (BR) and SBR. The market share of this group based on the total market volume is approximately 82 wt.-% and only 60 % based on turnover.
Special purpose rubbers are synthesized for high performance applications. This category contains butyl rubber (IIR), ethylene-propylene-diene rubber (EPDM), NBR. The market share of this group based on the total market volume is approximately 17 wt.-% and 30 % based on turnover.
Specialities in the rubber market are materials of outstanding performance, such as silicon and fluorine rubber. Their market volume based on the total market is approximately 1 wt.-% and 10 % based on turnover. The distinction of above categories is of course somewhat arbitrary.

An overview of the most important elastomers and their properties and main applications is given in Tab. 1.

For reasons based on availability and cost, the list of monomers used to produce essentially different types of raw rubber is not very extensive. Nevertheless an enormous number of polymers arises from the use of 2 or 3 monomers: co-polymerization, in contrast to homo-polymerization, leads to copolymers and terpolymers. Furthermore, variations can result from different sequences of the monomers in the chain. Variations of the catalyst and/or process parameters lead to a variety of further combinations. This has become relevant in large-scale polymer synthesis, especially through the work of Ziegler and Natta.

The elastomer-specific applications of rubber (i.e. those in which other materials either cannot be used or are poor substitutes) are based on:

- Easy going deformation behavior: Flexible coatings of all types (conveyor belting, cables, fabric coatings, footwear), sleeves, hoses, air balloons, rubber gloves.
- Reversibility of deformation (i.e. on the accompanying restoring forces): Gaskets, profiles, diaphragms, rubber rings.
- High elasticity (energy transmission): Tires, flexible joints, rollers, soles, balls.
- Damping properties (energy conversion): Bearing pads, buffers and springs.

The deformation of an elastomer is largely but not completely reversible. The remaining residual deformation (compression set, tension set) depending on stress mode (pressure/tension, temperature, surrounding medium) is an important parameter for the technologist. The highly elastic state has the general disadvantage that the mechanical strength is modest, compared to that of construction materials, such as thermoplastics or metals for example. This disadvantage can be compensated to some extent by the combination of rubber with reinforcing materials (monofilaments, cord, fabric, metal or plastic components), similar to reinforced thermoplastics (see below in the next chapter). The resulting composite materials (also in composite articles) are limited in extensibility in one well defined direction (because of the orientation of reinforcing elements). Hence mechanical properties (modulus and strength) are improved in the desired direction and in the perpendicular direction they remain unchanged. The importance of reinforcement is demonstrated by the fact that the majority of the world's rubber consumption - in the range of 15 million tons (8 million tons synthetic rubber) in the year 2000 - goes into composite articles such as: tires, conveyor belts, V-belts, reinforced hoses, cables, rubber to metal bonded parts etc..

Elastomers contain at least 5-6 additives, but often as many as 10 or 20. The effect of an additive may be crucial (without reinforcing carbon black, SBR tires would not exist) or it may lead only to slight modifications. However, the chemistry of the raw rubber determines a definite range in which the properties of resulting crosslinked and reinforced elastomer can be varied by the use of appropriate additives. However, improvements induced by additives are limited. For instance, the low temperature flexibility of vulcanized NBR can be improved by means of plasticizers, but the desired low values of T_g can not be achieved in all cases. Antioxidants improve the heat resistance of certain elastomers by avoiding degradation, i.e. chain scission, but only to a limited extent depending on the raw rubber material. The oil resistance of NR remains unaffected by additives.

Additives can not only enhance the properties of elastomers but also improve the processability of compounds and/or reduce the compounding cost, e.g. by shortening the vulcanization time.

The facts mentioned above raise the important question of structure-property-relationships. How can we improve desired properties by the addition of oils, reinforcing and other fillers and processing additives without damaging useful ones?

The physical properties (for instance the resistance to chemical agents) of the elastomer can often be predicted by using rough approximations, if the chemical structure is taken into consideration.
However, as a general rule, such relationships between chemical and morphological structures and physical properties of polymers cannot be established for the deformation and mechanical properties of any specific elastomer. Therefore intensive research is necessary to gain a deep understanding of corresponding structure-property relationships of reinforced elastomers in order to extend the product range of available elastomers.

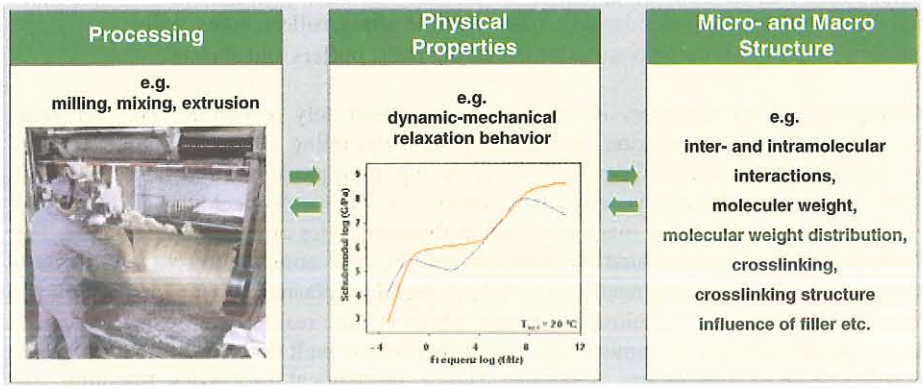


Fig. 2: *Elastomer physics research at Bayer.*

One of the main interests of Bayer's elastomer physics research is to establish fundamental correlations between the microstructure of polymer network chains, network structures, rubber-filler interactions and the properties of elastomeric products (for tires e.g. rolling resistance, wet grip behavior, wear), particularly with regard to tire manufacturing applications (since this application consumes nearly 70 % of the world wide rubber production).

Since the introduction of Michelin' s "Green Tire", the outstanding rolling resistance and wet grip behavior of which result from the use of bonding agents between the polymer matrix and the silica fillers, the development of improved tire treads has become focused on these rubber-filler and filler-filler interactions [5]. This example has demonstrated that it is possible to escape from the well known target conflicts in the "magic triangle" of tire properties (optimization of the three properties, rolling resistance, wet grip, and abrasion resistance simultaneously, Fig. 3) by deep understanding of the role of the interactions. The optimization of the rolling resistance [4] could be achieved by a reduction of the dissipating deformation

processes in a certain frequency range through a better coupling of the polymer matrix and the filler, without increasing the abrasion of tires and decreasing wet grip.
Hence, coupling mechanisms between the filler and the elastomeric matrix have to be investigated intensively for further reduction of rolling resistance while maintaining the good wet grip and low wear level in tire applications. This can be done by the detailed analysis of the dynamic mechanical damping behavior of the tread compound in the relevant deformation and frequency regime. Selecting the right analysis procedure provides deep insights to relevant physical processes, providing also a clear guideline for further optimized chemical structures.

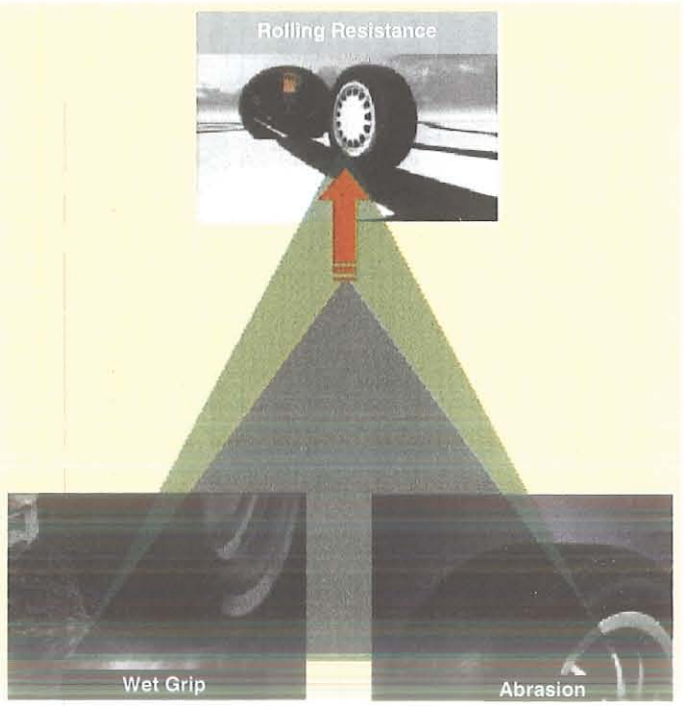


Fig. 3: *The magic triangle of tire properties: optimization of rolling resistance, wet grip, and abrasion resistance simultaneously.*

Name	Abbreviation	Properties	Temperature of use	Main application areas
Natural rubber	NR	High tensile strength, high elasticity, good tear resistance	-50 to + 80°C	Tires, conveyor belts, highly elastic articles
Polyisoprene	IR	Approx. Like NR, more homogeneous, transparent	-50 to + 80°C	Food packaging, alternative to NR
Polybutadiene	BR	High elasticity, wear resistant low temperature flexibility	-80 to + 90°C	Tires, conveyor belts, dynamically highly stressed articles
Styrene-butadiene rubber	SBR	Aging resistant, all-round rubber, high variety of different types	-40 to + 90°C	Tires conveyor belts, technical rubber articles
Butyl rubber	IIR, CIIR, BIIR	Extremely low gas permeability, high mechanical damping	-50 to + 130°C	Inner tubes, inner liner, bumpers, chewing gum
Polychloroprene	CR	Low oil swelling dynamically similar to NR, high flame resistance	-40 to + 110°C	Conveyor belts, driving belts, cables, wires
acrylonitrile-butadiene rubber	NBR	Low oil and fuel swelling, low gas diffusion	-60 to + 110°C	Motor parts, fuel and oil hoses, sealing, food
hydrogenated NBR	HNBR	Low oil and fuel swelling, low gas diffusion	-30 to + 150°C	High performance V-belts, sealing

Table 1: Overview of the most important elastomers, their properties and possible applications (not complete)

3. Thermoplastics and their Properties

Thermoplastic polymeric materials are mainly characterized by their glass transition and crystallization (and melt) temperatures, which are both located well above room temperature [6]. They are also characterized by their melt processing, made possible because of the lack of chemical crosslinks between single molecular chains. This melt processing technique is shortly detailed below.

The first step consists of heating up the material (usually consisting of pellets after polymerization) well above its glass transition temperature and/or its melt temperature where it is in a more or less low viscous liquid state.

A sufficiently low viscous polymer melt can then be injected into a particular mold, and the system can be cooled below the crystallization and/or the glass transition temperatures. Such a process is known as injection molding. Once the solid state has been reached, the finished good can be demolded and additional processing steps can be performed if needed (e.g. additional coating).

If the viscosity of the thermoplastic material is too high (and it cannot be lowered by increasing the melt temperature without damaging the material itself) then technically available injection pressures are not sufficient to fill a detailed or a very large and thin mold. In this case the high viscous polymer melt will be pressed through a narrow and boad slit resulting in large extended thin sheets. These sheets are cooled down to the solid state for further handling. The final product is produced by a second heating slightly above the glass transition or melt temperatures of the material. Then the sheets of high viscous material will be pressed by a stamp or pulled by a vacuum into the desired form. This method of thermoforming is preferentially used for the production of very large final parts, especially if the property balance requires a high molecular weight material (i.e. a material possessing a high viscosity in the melt) for high toughness, high stress cracking resistance against solvents and others.

The processing of thermoplastics has been detailed above, to outline their limitations (viscosity, temperature, degradation). One has to keep in mind that it makes no sense to develop products with a well balanced final property profile which cannot be processed commercially (due to intrinsic flow properties of the base material) without damaging one or more important properties.

Thermoplastics (as well as polymers in general) can be divided into two classes of materials depending on their state: they are either amorphous or semi-crystalline.

Single phase amorphous thermoplastics are usually transparent (because of the lack of inclusions in the size of the wavelength of the visible light responsible for scattering phenomena and turbidity) and more or less colorless depending on the polymerization technique. The thermo-mechanical behavior of amorphous thermoplastics [10] is determined by the glass transition temperature T_g.

Nearly all amorphous thermoplastics except polycarbonate (PC, $T_g \approx$ of 150 °C) exhibit a brittle fracture behavior under mechanical deformation at room temperature in combination with a relatively high elastic modulus almost up to T_g. Polycarbonate shows ductile deformation behavior at least under plain stress (shear stresses) conditions at ambient temperature in combination with a somewhat lower elastic modulus compared to that of other amorphous thermoplastics. Important amorphous thermoplastics are polystyrene: (PS, $T_g \approx$

100 °C), polymethylmethacrylate (PMMA, $T_g \approx 100$ °C), polyphenyleneoxide (PPO, $T_g >$ 200 °C!) and polystyrene-acrylonitrile (SAN, $T_g \approx$ of 110 °C).
The main applications of amorphous thermoplastics are toys, small appliances, automobile interior, the housing of electronic equipments, pipings and others.

Semi-crystalline polymers consist of at least two phases: the amorphous phase characterized by its T_g and the crystalline phase characterized by its melt and crystallization temperature. Semi-crystalline polymers may have a ductile or brittle deformation behavior depending on temperature, stress conditions (plain strain or plain stress) and deformation rate.
The maximum service temperature (the maximum temperature for long term applications) of semi-crystalline materials is usually desired to be near the melt temperature T_m. Hence, for applications up to T_m it has to be taken into account that the level of modulus substantially decreases by going through the glass transition (compare Fig. 1).

The most important semi-crystalline thermoplastics are:

		T_g	T_m
polyethylene	(PE)	below –60 °C	110 to 140 °C depending on microstructure
polypropylene	(PP)	in the range of 0 °C	in the range of 160°C
polyethyleneteraphtalate	(PET)	in the range of 80°C	in the range of 250 °C
polybuthyleneteraphtalate	(PBT)	in the range of 50°C	in the range of 220 °C
polyamide 6	(PA 6)	in the range of 20-50 °C depending on the water content	in the range of 220 °C
polyamide 66	(PA 66)	in the range of 20-60 °C as a function of water content,	in the range of 250 °C

Main applications of semi-crystalline thermoplastics are small appliances, the housing of electronic equipments which require high strength, vehicle exterior parts, automotive applications under the engine hood and fuel tanks (resistance against heat and aggressive chemicals).

In addition to the above classification of thermoplastics based on physical criteria there is a more property-price-sales volume driven categorization:
Low price, low (but reasonable) performance and high sales-volume products are very often labeled as "standard" or "commodity thermoplastics". The important representatives of this class are: PS, PE, PP, polyvinylenchloride PVC. The market volumes of these thermoplastics are in the order of 130 million tons per year.
The category of intermediate price, performance and sales-volume thermoplastics is called "engineering thermoplastics". The best known polymers in this category are: SAN, PC, PBT and PA 6. PET is on the borderline to commodities and PA 66 is on the borderline to specialities (definition given below). The market volume of this class is in the range of 11 million tons per year, i.e. one order of magnitude lower than that of commodities.
Thermoplastics in the high price segment in combination with high performance (high service temperature, high resistance against aggressive chemical environments, etc) and low market

volume are called "specialities" or "high performance thermoplastics". The main representants of this class are: liquid-crystalline polymers LCP, polyetheretherketones PEEK, polyphenylensulfides PPS, fluorinated polymers and modified polyestercarbonates. The market volume of this class is approximately one order of magnitude lower than that of specialities, therefore in the range of 1 million tons per year. All market numbers are based on market data published for the year 2000.

Coming back to structure-property-relationships, it has to be emphasized that there are in general several options for optimizing and improving product property profiles.

First of all, molecular structure (controlling molecular weights and weight distributions) and chemical composition (including other monomers, e.g. polymerization in presence of co-monomers, i.e. co-polymerization) can be varied. The best known example might be the co-polymerization of acrylonitrile and styrene monomers to SAN in order to get a slightly higher elastic modulus, a slightly better fracture behavior and a higher stress cracking resistance in the presence of aggressive chemical agents compared to PS.
This route is very often restricted by chemically driven difficulties in co-polymerization. Even if the chemical modification can be performed at the laboratory scale, the transfer to commercial production scale is not always possible.
Instead of co-polymerization, it is a much easier to mix different polymers and other ingredients and additives (in case of thermoplastics by means of melt mixing, similar to the processing procedure described above) to achieve an optimized property profile of the resulting composite materials of high structural complexity [10]. The basic philosophy behind the blending strategy is to improve an important deficient property without reducing desired good properties to a large extent.
Since most polymers are not miscible on a molecular level, the resulting structure will consist of a complex phase structure. The mixture will exhibit different glass transitions, dependent on the partial miscibility of the components, being more or less shifted in temperature compared to the initial polymers, as well as melting and crystallization transitions. The resulting phase structure in the solid state is basically controlled by a thermodynamically driven phase separation, by the tendency to minimize interfaces on one side and by the kinetics of phase separation (molecular mobility vs. thermal history, e.g. cooling rate and applied thermal treatment for instance during additional processing steps) and shear rates during melt mixing on the other side.
It should be noted that one prominent example for molecular miscibility of two components is represented by the mixture of PS and PPO. PPO itself cannot be melt processed without degradation because of its low thermal stability in combination with its high viscosity in the temperature range of thermal stability (T_g > 200 °C!). Through the addition of PS the T_g of the resulting one phase material can be decreased as a function of the composition of the mixture. This example demonstrates that the consideration of processability on a commercial scale is an important part of generating structure-property-relationships, as discussed above.

Since amorphous thermoplastics are characterized by a more or less insufficient, i.e. brittle fracture behavior, the optimization of mechanics (relation of fracture resistance and elastic modulus) in combination with rheological behavior is essential for the creation of balanced property profiles. One way to enhance the properties of the brittle thermoplastic material is for instance to add a small amount of modifier, mainly consisting of rubber particles by means of melt blending.

In the case of semi-crystalline thermoplastics the general stiffness of the material and especially the modulus decrease above T_g are subjects of main concern. One way to overcome this problem is to add several types of organic or inorganic fillers to the semi-crystalline material.
Prevention and control of the permeation of gases and vapors through plastic films, membranes or other parts are strongly required in industrial and packaging applications. The solution of this problem can be based on the incorporation of intercalated nano-clays into a semicrystalline matrix.

The digital storage technology based on optical data discs has become of significant importance in the past few years. New hardware solutions (such as disc player) are creating increased requirements on the properties of disc substrate materials. Critical disc requirements can be deduced by means of modeling future optical disc drives. These disc requirements have to be can be transformed into polymer properties. Then new substrate materials such as polycarbonate can be developed in a more straight forward manner if the relationships between molecular structures and polymer properties are well understood.

In the following sections several aspects of these topics will be discussed in terms of structure-property-relationships in more detail.

3.1 Rubber Toughening of Amorphous Thermoplastics

One basic requirement for engineering thermoplastics is to achieve good toughness, i.e. the ability of the material to resist fracture by absorbing energy during a mechanical deformation under given conditions such as temperature, deformation rate and geometry of the affected surface region, which influences the local stress state.
In materials science toughness is usually expressed as an energy needed (measured by registration of applied stress and corresponding displacement during a deformation experiment) for the generation of a unit area of fractured surface. For an overview on fracture behavior of thermoplastics see ref. [7].
As mentioned above, most engineering thermoplastics (especially PS, SAN and PMMA) exhibit a brittle fracture behavior. This means that they show a linear force-deflection curve in fracture tests. Within the local deformation zone near the fracture surface the energy absorbed per unit volume of material is considerably high (100 MJ/m^3), more details can be found in ref. [9]. However, the amount of polymer involved in the energy absorption is very limited, and the fracture is therefore essentially brittle. This problem becomes even more pronounced if the surface of the test specimens or final parts contains an initial crack or a sharp notch.
Fracture initiation and unstable instantaneous crack propagation is fundamentally caused by a local concentration of triaxial, i.e. hydrostatic tensile stresses in the immediate surrounding of single defects such as cracks, notches or scratches on the surface or discontinuities, inhomogeneities within the polymeric matrix. In order to avoid highly localized critical hydrostatic stresses followed by unstable crack propagation a basic mechanism is needed to remove the sharp stress peak and generate a homogeneous stress distribution below the critical level within a wide range of the matrix followed by all kinds of local deformation processes (crazing, shear yielding) in a large volume fraction of the material [9].
This concept is realized by the technology of rubber toughening, which involves the modification of the brittle thermoplastic material by melt blending it with small amounts (10-30 %) of rubber particles sized in the range between 0.1 µm and several µm.

In the first stage of this technology in the late 1940s and early 1950s virgin non-crosslinked rubber was melt mixed with the brittle thermoplastic. Because of the missing compatibility between both components, the resulting structure showed only a poorly dispersed, coarse and unstable (during processing) rubber phase within the thermoplastic matrix.
In the next stage, the compatibility of the rubber surface was improved by polymerizing an outer shell to the surface of rubber particles. The chemical nature of the shell could be adjusted to get an optimized compatibility and interaction to the desired matrix material. By choosing an appropriate chemical design for the shell, the degree of dispersion of the particle in the matrix (tendency to form well dispersed systems or to agglomerate and to form network like structures) and the coupling of particles to the surrounding matrix could be controlled.

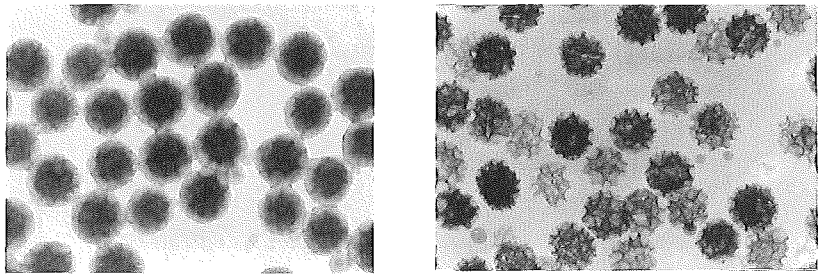


Fig. 4: *Left: The morphology of SAN grafted rubber particles. Dark regions show the rubber core, the more bright shell represents the thin SAN layer. Right: The morphology of the continuous SAN matrix and dispersed rubber particles in the final melt mixed ABS material. Note that the graft shell is not visible anymore in the mixture. The size of rubber particles is of the order of 300 nm.*

Today the main technology for rubber modification consists of the following processing steps: polymerization of rubber particles in emulsion (important parameters are: particle size and distribution, crosslinking level, chemical structure and T_g), subsequent graft-co-polymerization of the outer shell (important parameters are: chemical composition, homogeneity, thickness, core-shell volume ratio, process induced hard occlusions of the grafted material within the rubbery core), precipitation and drying of the grafted-rubber latex. This grafted rubber material with a rubber content in the range between 40 % and 80 % (the so called rubber modifier) can be subsequently diluted by melt mixing with an independently polymerized matrix material.
The advantage of this technology lies in the broad range of adjustable rubber level in the finished product (between 12 % and 30 % depending on the desired application). The thecnology allowes to find a well balanced compromise between sufficiently improved toughness, reduced elastic modulus and increased viscosity.
The commercially most important rubber modified thermoplastics is acrylonitrile-butadiene-styrene ABS. It is produced by melt mixing of SAN with SAN-grafted polybutadiene rubber particles as toughness modifier. Main applications are toys (e.g. Lego bricks), housings of small appliances, electronic devices, automobile interior and so on.
Besides the high maximum service temperature the combination of ABS with PC (the T_g of PC being at 150 °C and that of SAN at 110 °C) provides the improvement of the low temperature toughness of the blend compared to that of each components. Main applications are those where high heat resistance in combination with excellent fracture behavior is needed down to –40 °C, such as for cover parts of guarded air bags in automobile interior.

In addition to matrix parameters (chemical composition, microstructure, molecular weight and molecular weight distribution) the appropriate physical and chemical structure of the grafted rubber modifier is the key issue for the optimization of rubber toughened thermoplastics. Therefore the recipe and the polymerization procedure is the best guarded confidential intellectual property of any company producing toughened thermoplastics.

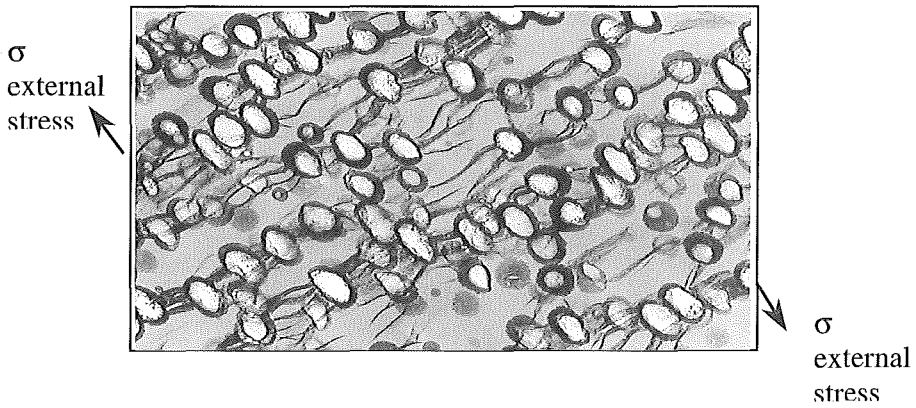


Fig. 5: *The well pronounced craze structure (dark lines between particles) in ABS after deformation. The cavitations in the particles are clearly visible as bright areas. The rather elongated form of particles indicates the high level of coincident local yielding. The size of rubber particles is of the order of 300 nm.*

Even though basic phenomenological aspects of rubber toughening of brittle thermoplastics were well understood long ago, the exact role of rubber particles has been a subject of controversy (compare [8] and references therein) since the commercialization of such materials in the middle of the last century.

Initially a strong interaction of the rubber particles with the surrounding rigid thermoplastic matrix by means of the outer graft shell was assumed to be essential for optimizing toughness [11]. Through the entanglement of grafted chains with the macromolecules of the matrix a strong coupling should be achieved to avoid debonding of particles from the matrix. Moreover the appropriately grafted shell should adjust the particle-particle interaction within the matrix, in order to get the right morphology of the resulting network like structure in the matrix. Large agglomerates should be avoided, since they generate localized sharp stress peaks in the matrix by mechanical deformation, leading finally to brittle fracture behavior.
Therefore the control of the rubber-matrix interaction by optimizing the graft shell structure was the most important target (besides other parameters such as crosslinking, average particle size and particle size distribution, chemical composition of rubber connected to T_g, etc) of industrial research efforts.

For a long time it was assumed that the interaction strength of rubber particles with the surrounding matrix (i.e. the "quality" of grafting) could be measured by the T_g shift of the rubber phase in the blend (rubber T_g in the blend compared to that of the virgin rubber

material) for instance by means of dynamic-mechanical measurement (DMA) of the shear modulus [17] [18].
Such T_g shifts were observed in the early stages of polymer research on rubber modified thermoplastics, and they were explained by the following mechanism: in order to perform a DMA measurement the sample must be cooled down to temperatures below the rubber T_g. The thermal expansion coefficient of the rubber phase is higher than that of the matrix in the temperature range between the rubber T_g and the matrix T_g. Therefore the rubber particles shrink more strongly then the surrounding matrix during cooling. Because of the coupling of the particles to the matrix by through the grafted shell, hydrostatic stresses are generated within the rubber particles during cooling. Such hydrostatic stresses produce a significant decrease of rubber T_g [17] [18].
Hence, a missing T_g-shift in DMA-measurements of rubber modified thermoplastics has been explained by the lack of hydrostatic stresses within the rubber particles caused by the debonding of particles from their surrounding matrix. Consequently the optimization of the grafted shell had to be carried out in order to adjust its load bearing capability.
Already in the late 1970s some doubts came up regarding this mechanism [12] [19]. However, a serious scientific discussion of the alternative mechanism based on the internal rupture (cavitation) of particles started only approximately ten years ago, compare ref. [13] [14] and references therein.

By means of the measurement of thermal expansion coefficients of different kinds of rubber modified thermoplastics under several experimental conditions it could be proven in the Physics Department at Bayer [15], that not debonding but rather cavitation (i.e. internal rupture of particles) occurs during cooling. The experiment is based on the idea that the stress release in particles caused by cavitations should be detected by the deviation from the linear shrinkage behavior during cooling [16]. Since this effect was found to be reversible in a second cooling step after an appropriate previous thermal treatment of the sample, it become clear that stress release effects are caused by internal rupture processes in the particle and not by debonding from the matrix [20].

Based on this result it became clear that the adjustment of cavitation behavior, i.e. of the internal structure of rubber particles may have at least the same or even a greater importance for the toughness optimization than the graft shell does.
The cavitation phenomenon is currently further investigated to generate new types of modifiers for optimized rubber toughened thermoplastics.

3.2 Reinforcement and Barrier Properties in Semicrystalline Thermoplastics

For many applications (e.g. housings of power drills) the combination of high modulus, high bending strength and high environmental stress cracking resistance is needed. For applications under the engine hood of cars a high resistance against thermal loading and aggressive chemical agent is of high importance as well. For a detailed discussion of reinforced thermoplastics compare [21].

The addition of several types of fillers (such as fibers, talc, mica, etc.) to a semi-crystalline thermoplastic matrix is a well established concept to meet these property requirements. The role of the polymeric matrix, reinforcing filler and the interface between them can be briefly summarized as follows: The matrix is responsible for transfering the load to the reinforcement, for the distribution of stress among filler particles and to protect the reinforcing elements from aggressive chemical agents. The main task of filler elements consists of bearing the load due to their higher modulus and strength compared to that of the surrounding matrix. The interface between matrix and filler is responsible for the transfer of load and stresses from the matrix to the reinforcement. In addition, the chemical composition of the interface in combination with that of the matrix controls the distribution of filler elements in the matrix. Both tasks are similar to those of the graft shell in rubber modified thermoplastics as discussed above. Furthermore, the interface also influences the crystallization within the matrix, providing an internal surface to enhance crystallization rates and refine the crystallite morphology.

Plate-like (e.g. talc, mica, glass flake, etc) and fibrous (wollastonite, textile-, glass-, carbon-, aramid-fibres) materials (typical size in the range of several µms to several hundreds of µms) of natural and artificial origins are often used as reinforcing elements. If the aspect ratio (ratio of length and thickness) of filler particles exceeds 5 then the tendency to create anisotropy has to be taken into account. In addition to that, possible inhomogenities in filler distribution may occur, causing an inferior fracture behavior under mechanical loading (because of stress concentration around agglomerated filler particles) in the composites compared to that of the neat thermoplastic.

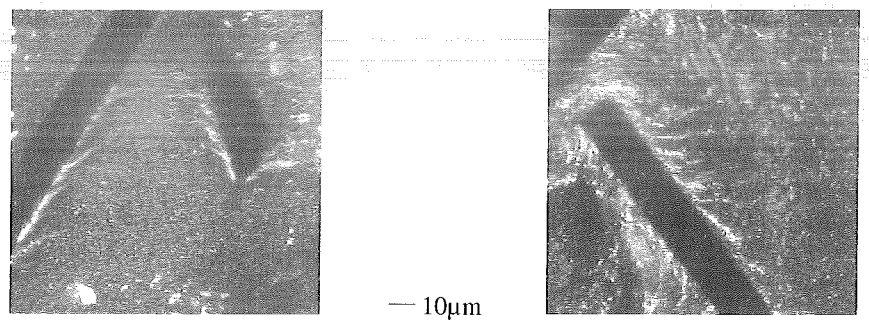


Fig. 6: *Confocal laser scanning micrographs of glass fiber reinforced PA 6 (with rubber modification on the right and without rubber modification on the left) after impact fatigue loading [22]. The traces of cavitated particles (the bright structures in a wide range surrounding the fiber on the right figure) and of the debonding of the fiber from the matrix on the right figure are clearly visible.*

Very often a rubber modifier is added to the reinforced material, in order to compensate drawbacks in the fracture behavior of the composites. The local shear yielding in the surrounding of cavitated rubber particles helps to release sharp stress peaks caused by agglomerated reinforcing elements and avoids brittle fracture at low external stress level.

Long term periodic low energy impact loading and unloading of glass-fiber reinforced semicrystalline thermoplastics is very common in many dynamic applications, such as in automotive applications or housings of power drills. Therefore the detailed understanding of fracture behavior (crack initiation and growth) is needed under such conditions. The influence of reinforcing elements and rubber particle on the impact fatigue behavior of rubber modified and glass fiber reinforced PA 6 has been studied in the Physics Department at Bayer [22]. The goal was to predict and optimize the lifetime of such composite materials under a large number of impact loading and unloading cycles at low energy levels of several J per period per sample volume.

It could be shown by means of the combination of several microscopic techniques (light microscopy, confocal laser scanning microscopy and scanning electron microscopy), that large shear yielding initiated by particle cavitation occurs under impact fatigue experiments. This reduces the debonding of the fiber ends from the matrix and the fiber pull out, due to the release of stress peaks.
Therefore we can conclude that due to the pronounced effect of rubber modification, the crack initiation and propagation in rubber modified glass fiber reinforced PA 6 is strongly inhibited under low energy impact fatigue conditions.

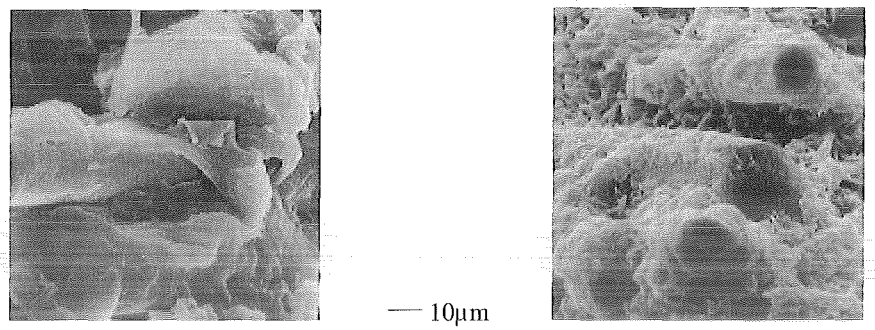


Fig. 7: *Scanning electron micrographs of glass fiber reinforced PA 6 (with rubber modification on the right and without rubber modification on the left) after impact fatigue loading [22]. The debonding of the fiber from the matrix on the right figure is clearly visible.*

As mentioned above, prevention and control of the permeation of gases and liquids through plastic films, membranes or other parts are strongly required in industrial and packaging applications. Outstanding barrier properties are especially critical in food packaging and in fuel tanks for instance.
In order to optimize the permeation behavior of thermoplastics several blending concepts can be used. Very often co-continuous interpenetrating networks or co-extruded layers with appropriate components (e.g. Polyvinylalcohol, PE, etc.) provide a sufficient improvement of the barrier properties [23].

To obtain transparent PA 6 films with sufficient barrier properties, clay-polymer-nanocomposites were considered in a collaboration of the Physics Department with the Plastics Division at Bayer (see also ref. [29]). Nano-clays consist of stacks of platelets (e.g. Montmorillonite with an aspect ratio of 10^3, Vermicullite with an aspect ratio of 10^4), each having a thickness of the order of 1 nm.
Several surface modified nano-clays have been initially melt mixed with PA 6 and the resulting clay-nanocomposites have been tested regarding their permeation properties. The preliminary results were less promising than expected, since all clay stacks tended to cluster for all types of surface modifications. Due to that clustering of stacks no enhancement in barrier properties and a strongly reduced fracture behavior (generation of localized stress peaks in the thermoplastic matrix) could be detected.

In the following step the condensation of PA 6 was performed in the presence of surface modified nano-clays [24]. In this case the highly mobile small monomer molecules could penetrate into the stacks and the polymerization of PA 6 macromolecules could occur inside the stacks (in-situ-polymerization). Due to this procedure a delamination and a homogenous dispersion of the thin platelets could be achieved. In addition to that, a high level of surface interaction between the modified platelets and the surrounding polymer has been reached.

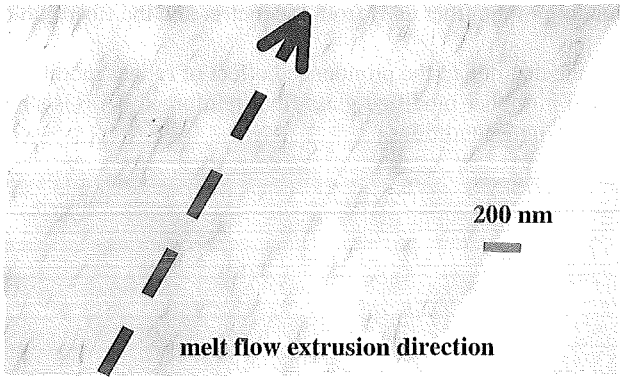


Fig. 8: *Homogenous dispersion of the delaminated thin platelets in the PA 6 matrix originated by in situ polymerization in the presence of surface modified nano-clay stacks [24].*

Because of the increased length of the diffusion path within the matrix the gas permeation could be reduced by 50 % compared to that of the non-modified PA 6 film. The strong interaction of the reinforcing clays with the matrix polymer and the optimized crystalline structure (the delaminated platelets are acting very effectively as nucleating agents due to their large specific surface area, refining the crystallite morphology) improved the elastic modulus by a factor of 2, without negatively influencing the fracture behavior (no localized high stress peaks). The nano-sized thickness of the mineral-plates and the refined crystallite morphology protected the sufficient transparency of the material. Moreover the flame resistance of nanocomposite materials could be improved due to the high specific surface area of the reinforcing mineral component (reduction of drop formation during burning).

3.3 Optimized Thermoplastics as Substrate Polymers for Optical Data Storage Applications

The electronic data processing technology has shown a very dynamic development in the last few decades worldwide. Computers and other electronic devices using enormous amounts of digital information have become an important part of our life today.
Besides transfer and processing of digital data the increase of data storage density has become more and more crucial (see ref. [25] and references therein for additional information). It turned out that the optical disc has become a data storage medium of high importance. In the optical disc storage technology the laser beam coming from the optical pick up head has to pass through a polymer, in order to read out the digital information stored in embossed pits (as carriers of single information bits in prerecorded formats such as CD and DVD) on the opposite surface side of the transparent substrate. This type of optical disc construction makes this medium very resistant against mechanically damaging the stored information such as by finger prints and scratches. On the other hand, the polymeric substrate becomes a part of the optical read out system and therefore has to fulfil the same high optical and mechanical alignment requirements as all other parts of the optical pick-up head to reach high optical resolution among single digital carriers of information.

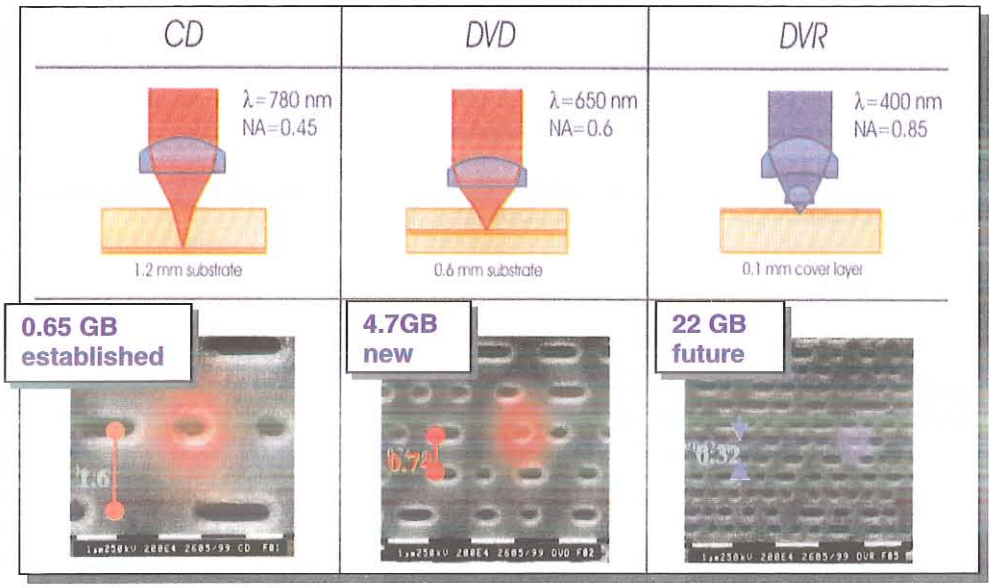


Fig. 9: *Increased optical data storage density in read-only formats [25].*

For the use as optical data storage medium various material properties are crucial: First of all the high accuracy replication (the dimensions of structural deviations have to be much smaller than the wavelength λ of the used laser beam) of the sub-micron pit structures by injection molding (desired cycle time in the range of seconds) of optical discs is strictly required. The good adhesion to metals and sputtered layers is needed to achieve a stable reflection layer. Apart from the optical properties such as high transparency, low birefringence and low number of scattering particle contaminations (dust), thermal and mechanical properties such

as sufficient heat resistance and toughness, high dimensional stability under varying environmental conditions (low water absorption) are also required.

Polycarbonate (PC) as an amorphous thermoplastic polymer with excellent optical and mechanical properties has turned out to be especially suitable for optical data disc applications. The sale-volume of PC for this application has increased from approximately 26 kilotons in the year 1990 to approximately 390 kilotons in the year 2000, worldwide. The major part (230 kilotons) of this world wide amount of PC for this application was consumed in the Far East.

The current rapid development of digital electronic data processing technology is accompanied by the strong need for substantially increased optical digital data storage densities. In order to achieve a maximum storage density the dimensions of the embossed pits are diffraction limited, i.e. they are of the order of the laser wavelength λ. Hence, for a required further improvement of the maximum optical data storage capacity the wavelength λ of the laser beam has to be reduced and the numerical aperture (NA) of the optical pick up head system has to be increased (keepinng in mind that the needed the minimum laser spot size is proportional to λ/NA). To increase the storage density, permanently new optical disc players are in development based on the use of blue laser technology.

Since the new hardware is not available before the introduction of the new optical data storage format a direct comparison of different substrate polymeric materials cannot be performed. Nevertheless it is essential for a polymer producer to be able to provide a suitably optimized high performance substrate material in the needed amount as early as possible.

To develop new materials and to optimize existing substrate polymers the following three step strategy has been chosen by the Physics department at Bayer [25]:

In the first stage the fundamental physical understanding of optical disc technology in combination with computer simulations enables the estimation of critical disc requirements, even for future devices. The simulation of the read out signal by scalar diffraction theory reveals the importance of high accuracy pit replication, birefringence and tilt of the disc normal versus the optical axis.

Then the future disc requirements have to be carefully translated into quantitative polymer properties by means of a physical model. For instance the pit replication can be related to flow and demolding properties of the substrate material. Birefringence is influenced by the combination of the rheo-optical constant and of internal stresses in the disc due to cooling induced orientations, related to the elasticity of the melt. A significant radial tilt in the disc may occur by changing environmental conditions such as humidity. A rigorous physical model of the transient bending of the single side metallized disc due to non-homogenous swelling through the free surface by water before full saturation reveals the importance of the equilibrium water content and that of the swelling constant.

Finally molecular modeling supported by fundamental structure-property-relationships has to be used to propose promising monomer and comonomer structures leading to desired polymer properties. It means that the complex viscosity, rheo-optical constant, swelling behavior by

different media (such as water, chemical solvents), adhesion to metals and other physical properties have to be predicted by using appropriate models and simulations.

The success of the above strategy has been demonstrated by the development of suitable modified co-polycarbonates with lower rheo-optical constants and lower water absorption as substrate materials for optical data storage disc applications.

4. Polymer Processing of Polyurethanes

Polyurethane chemistry is based on the reaction of isocyanate (NCO) and alcohol (OH) endgroups to form urethane bonds as schematically shown in Fig. 10. Generally bifunctional or trifunctional isocyanates and alcohols are used for the poly-addition. For general informations on polyurethanes see ref. [26].

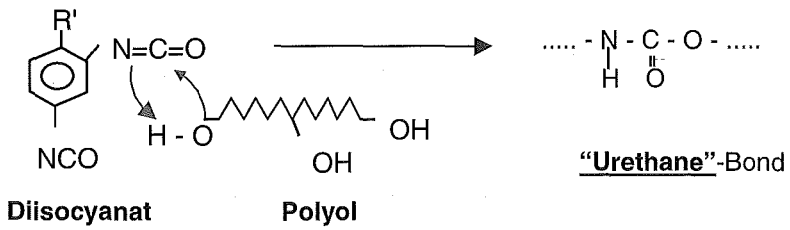


Fig. 10: *The addition of isocyanate and alcohol endgroups leading to a covalent urethane bond (schematic).*

Organic chemistry provides a tremendous variety of multifunctional isocyanates (e.g. hexane-diisocyanates HDI, toluylene-diisocyanates TDI, methane-diphenyl-diisocyanates MDI, and many others) and alcohols (alcanediols, polyesterpolyols, polyetherpolyols, polycarbonatpolyols, etc..) used as comonomers in polyurethane reactions.
In addition to of the primary chemical and molecular structure (tacticity, molecular weight, branching) non-covalent interactions among the molecular chains (hydrogen bridges between CO and NH) are mainly responsible for the final morphology of the polyurethanes due to the supra-molecular arrangement of the chains.
Based on the specific chemical structure of the components and on the selected reaction process an enormous wide range of very different product properties can be obtained in polyurethanes.

Linear, chemically uncrosslinked molecular structures can be obtained by the combination of bifunctional isocyanate and alcohol comonomers.
The resulting phase structure may be semi-crystalline (HDI, butanediol) similar to that seen in polyamides, providing high hardness, tensile-strength and high resistance against aggressive chemical agents.
An amorphous phase structure can also be obtained for instance by combining TDI and ethyleneglycol, having high transparency and hardness but low heat resistance.

Combining diisocyanates, long chain bifunctional polyols and low molecular weight chain extenders (glycol, diamine, water, low molecular weight polyols) provides a segmented (block-copolymer type) chain structure. The highly mobile coiled soft-segments of the chain consist of long chain polyols. The rigid oligourethane sequences are labeled as hard segments consisting of isocyanates and chain extender molecules.
Soft and hard segments are not miscible thermodynamically and therefore phase separation occurs. In general each of the separated phases (soft and hard segment domains) may have amorphous and crystalline parts. Especially the crystallites of the hard segment domains are stable up to high temperatures, based on the stabilized crystalline structure due to hydrogen bonds, as mentioned above.
These segmented linear polyurethanes show similar mechanical properties to chemically crosslinked elastomers (low modulus, high elasticity, high deformability), since segregated hard segment domains can act as physical crosslinks. However, such segmented polyurethanes can be processed at high temperatures, since the crystallites in the hard segment domains are not stable above the melting point.
Because of these particularities, segmented linear polyurethanes are labeled as thermoplastic elastomers (TPEs). The main applications are similar to those of classical rubber (see Section 2) in combination with thermoplastic processing such skiboots, cable encapsulation, toys, fibers, foils etc..

The combination of multifunctional comonomers (polyols) leads to chemically crosslinked (segmented or non-segmented) structures. Depending on the crosslink density (based on the chemistry of comonomers and composition) elastomeric or duromeric (analogous to elastomers but possessing T_g well above ambient temperature) structures may result.
Polyurethane foams can be produced by using non reacting foaming agents during the reaction in addition. This process leads to soft or hard foams depending on crosslink density.

Polyurethanes with a worldwide market of 8.4 million tons for the year 1999 are mainly used for automotive applications, for insulation in construction and appliances, for furniture and mattresses, as well as for coatings and adhesives.

In contrast to the polymeric materials such as thermoplastics and raw rubber the polymerization of polyurethanes takes place at the manufacturer site. It means that the material producer (such as Bayer) provides basically the components (mainly TDI, MDI, polyesterpolyols, polyetherpolyols and prepolymers such as pre-extended isocyanates and polyols) and the desired physical properties of the polymer in final products are created by the customers himself.

Besides the research for new isocyanates, polyols, catalysts and detailed structure-property-relationships for polyurethanes a deep insight and a detailed understanding of processing procedures at the manufacturer site becomes more and more essential in order to ensure the further quality improvements of resulting products [27].

The technology of reinforced reaction injection molding (comonomers, reinforcing elements such as glass or mineral fibers are injected in the mold and the polymerization takes place in a few seconds) has been developed among others for special high performance exterior automotive applications long ego. The quality of final parts has been optimized (balancing

high heat resistance, low thermal expansion coefficient, excellent surface appearance, good adhesion of coatings) based on detailed structure-property-relationships.

To get further optimization, especially with respect to lower production costs, and to keep a constant quality on a high level an automated process control of the final parts at the manufacturer site is required. The development of the desired process control requires several components. Initially all important process parameters have to be recorded by means of appropriate (existing or newly developed) equipments. The relationships between materials, process parameters and physical properties of the final parts have to be generated using various statistical techniques such as regression analysis, neural networks, etc. By using these data an online quality control system can be installed directly for each reaction injection molding equipment at the manufacturer facility.
Based on this computer aided technology the physical properties of each reaction injection molded part will be predicted, results will be compared with specifications and finally in case of significant deviations suggestions for corrections of process parameters will be given to the operator [28].

This computer aided processing technology for the reaction injection molding of polyurethane parts for automotive applications has been successfully introduced at several manufacturing facilities. This new tool has become an important part of the well accepted zero-fault strategy of suppliers for the automotive industry

5. Final Remarks

In conclusion, we have pointed out that structure-property-relationships based on a detailed interdisciplinary understanding of material properties are a powerful tool for the development of improved new materials and processes. This fundamental understanding has to be supported by advanced experimental, theoretical and computational methods. The overall goal is to obtain optimized products for our customers.
The interdisciplinary research for further improved and completely new materials still remains an exciting challenge for scientists at universities and in industry.

This lecture is based on the scientific work of a large number of our colleagues from different disciplines (physicists, chemists, engineers, mathematicians etc.) at Bayer. Their dedication and expertise is the foundation for many decades of progress in research and development. The individual contributions can be studied in more detail using the references given in the appendix.
We would like to express our gratitude and appreciation for the help and support by our colleagues and acknowledge their important contributions.

References

[1] E. Verg, G. Plumpe, H. Schultheis, Meilensteine, Herausgeber: Bayer AG, Intermedia Verlags-GmbH, Köln, (1988)

[2] J. Rieger, R. Iden, *Polymer- und Kolloidphysik in der BASF*, Physikalische Blätter (2001), **57**, 55

[3] Manual for the rubber industry, Th Kempermann, S.Koch, J. Sumner, eds, Bayer AG Rubber Business Goup, Leverkusen, (1993)

[4] C. Wrana, U. Eisele, S. Kelbch, *Vorhersage und molekulare Beschreibung des Rollwiderstands von Reifenlaufflächen*, Kautschuk, Gummi, Kunststoffe (2000) **3**, 126

[5] C. Wrana, W. Pechhold, *Dynamic – mechanical analysis of filled elastomers* ACS – Meeting Dallas, (2000), Paper No. 54

[6] B. Wunderlich, *Macromolecular Physics 1-3*, Academic Press, New York and London (1973)

[7] C. B. Bucknall, *Characterizing Toughness using Standard Empirical Tests*, in Polymer Blends, Volume 2: Performance, D. R. Paul and C. B. Bucknall, eds, John Wiley & Sons, New York/Chichester/Weinheim/Brisbane/Singapore/Toronto (1999)

[8] P. I. Vincent, F. M. Willmouth, A. J. Cobbold, *Stress-Whitening in Thermoplastics,* 2nd Int. Conf. Yield, Deformation and Fracture of Polymers, Cambridge (1973)

[9] C. B. Bucknall, *Deformation Mechanisms in Rubber Toughened Polymers*, in Polymer Blends, Volume 2: Performance, D. R. Paul and C. B. Bucknall, eds, John Wiley & Sons, New York/Chichester/Weinheim/Brisbane/Singapore/Toronto (1999)

[10] J. J. Scobbo, Jr., *Thermomechanical Performance in Polymer Blends*, in Polymer Blends, Volume 2: Performance, D. R. Paul and C. B. Bucknall, eds, John Wiley & Sons, New York/Chichester/Weinheim/Brisbane/Singapore/Toronto (1999)

[11] J. Stabenow, F. Haaf, Die Angew. Makromol. Chem. (1973), **29/30,** 1-23

[12] H. Breuer, F. Haaf, J. Stabenow, *J. Macromol. Sci.* (1977), **B14**, 387

[13] R. A. Bubeck, D. J. Buckley, E. J. Kramer, H.R. Brown, *J. Mat. Sci.* (1991), **26**, 6249

[14] C. B. Bucknall, in *"The Physics of Glassy Polymers"*, R. N. Haward and R. J. Young, eds, Chapman & Hall, London (1997)

[15] D. J. Dijkstra, F. Bruder, A. Karbach, K.-H. Busch, *Internal report Bayer AG*, DDJ 019 (1995)

[16] C. B. Bucknall, D. S. Ayre, D. J. Dijkstra, *Detection of Rubber Particle Cavitation in Toughened Plastics using Thermal Contraction*, Polymer (2000), **41**, 5937

[17] L. Morbitzer, K. H. Ott, H. Schuster, D. Kranz, Die Angew. Makromol. Chem. (1972), **7**, 57

[18] L. Morbitzer, D. Kranz, G. Humme, K. H. Ott, J Appl. Polymer Sci. (1976), **20**, 2691

[19] H. C. Booij, Brit. Polymer. J. (1977), 47

[20] P. Krüger, *On the Reversible Nature of Rubber Particle Cavitation*, Macromol. Mat. Eng. (2001), **286**, 675-681

[21] J. Kárger-Kocsis, *Reinforced Polymer Blends*, in Polymer Blends, Volume 2: Performance, D. R. Paul and C. B. Bucknall, eds, John Wiley & Sons, New York/ Chichester/ Weinheim/Brisbane/Singapore/Toronto (1999)

[22] D.J. Dijkstra, V. Altstaedt, N. Mitra, *Impact Fatigue Behavior of Rubber Modified Glass Fiber Reinforced Polyamide 6*, Macromol. Mat. Eng. (2001), **286**, 669-674

[23] P. M. Subramanian and I. G. Plotzker, *Barrier Materials by Blending*, in Polymer Blends, Volume 2: Performance, D. R. Paul and C. B. Bucknall, eds, John Wiley &

Sons, New York/Chichester/Weinheim/Brisbane/Singapore/Toronto (1999)
[24] J. Gonzáles-Blanco, S. Gestermann, C. Scherer, A. Karbach, *Nanotechnology for Polymer Films: Organoclay-Polyamide 6 Films for Food Packaging Applications*, Intern. Conf. on Nanocomposites, 2000, Brüssel
[25] F. Bruder, *On an Integrated Approach for Optimizing Substarte Polymers for Future Optical Disk Requirements*, Macromol. Mat. Eng. (2001), **286**, 685-690
[26] Polyurthane, G. Oertel, ed, Hanser Verlag, München Wien (1993)
[27] K.-H. Dörner, H.J. Meiners, H.J. Ludwig, *PUR-Teile kostengünstig fertigen*, Kunststoffe, (2001) **91**
[28] F. Schnabel, K.-H. Dörner, H.J. Meiners, H.J. Ludwig, *Experten mit System*, Kunststoffe, (1998) **88**
[29] German Patent DE3632865 (04.1987) Toyota; European Patent EP0358415 (03.1990) Toyota; US Patent US5164440 (11.1992) Toyota, Ube

INDEX

Index

A

AB-copolymer, A7.14, A7.26
acrylonitrile-butadiene rubber, D4.4
acrylonitrile-butadiene-styrene, D4.13
activity, B1.13
additives, I1.15
ADE model, B12.13
ADE phase diagram, B12.15
adsorption, B11.5
ADWP model, C3.14
aggregation, D1.8
alcanediols, D4.21
alcohol, D4.20
amorphous material, C5.2
amorphous thermoplastics, D4.9
amphiphilic block copolymers, B9.35
amphiphilic molecules, B9.8, C9.26, I1.7
anchored polymers, B9.36
anionic polymerization, A4.3
anisotropic viscosity, C8.25
area difference, B12.15
area difference elasticity, B12.13
Arrhenius-diagram, A3.15
Arrhenius-law, C2.27, C3.10, C9.22
Asakura-Oosawa model, B10.8
ATP-synthase, B15.3
autocorrelation function, A1.34

B

backscattering, C2.3
bacteriorhodopsin, B15.2
balanced microemulsions, B9.34
Bancroft rule, A6.9
baroclinic mode, C6.21
barrier properties, D4.17
Baxter potential, D3.10
BBGKY hierarchy, B1.5
bead-spring model, A7.9, C8.15, C8.32
bending elasticity, B12.6, B12.13
bending energy, B8.17
bending modulus, B12.6, C6.5
bending rigidity, B9.8, B10.2, B10.9, B10.11, B10.13
benzoin isobutylether, A3.17
biaxial nematic, C4.14
bicontinuous microemulsion, A6.8
bicontinuous phase, dynamics, C6.17
bicontinuous sponge phase, C9.28
bicontinuous structure, B9.17, B9.18
bifurcation diagram, C4.21
bilayer, B8.12, B12.2, B12.13
binary colloidal "alloys", B17.19
binary polymer mixtures, A7.26
binodal, B6.10, C7.4
biomembrane, B14.1
biomimetic approach, A6.4
biomineralisation, A6.4
birefringence, D4.20
bisphenol-a-polycarbonate (BPA-PC), C3.6
bistability, B12.22
Bjerrum length, B5.3
blob, B3.5
blob model, C8.32
Bloch equation, A2.8
block copolymer, A4.10, A4.14
boehmite, A5.9
Boltzmann equation, B1.6
bond-fluctuation algorithm, A7.18
Born approximation, A1.5, A1.14
Born-Green equation, B1.21
Bragg reflection, A1.9
Bragg–rods, B11.12
branched polymer, A4.8
Brillouin spectroscopy, A1.25
broken symmetry, C8.4, C8.24, C8.28
Brownian dynamics, A7.8, A7.16
Brownian motion, C1.2, C1.7, C1.10, C1.15, C1.19, C4.2, C5.14, C6.4, C9.25
brush, D3.14
budding transition, B12.18
butanediol, D4.21
butyl rubber, D4.4

C

$CaCO_3$, D1.13
Cahn-Hilliard, C7.3
canonical ensemble, B1.9
canonical partition function, B1.9

capillary rheometers, C9.12
capillary waves, B7.4, B7.6–B7.8, B7.13, B7.14
carbon black, D4.4
casein micelles, D3.3
catenoid, B9.11, B9.42
cavitation, D4.15
cellular morphology, B12.32
central limit theorem, I1.10
chain entropy, B3.3, I1.10
chain extenders, D4.21
characteristic ratio, B2.9
characterization of colloidal particles, A5.13
charge stabilization, A5.3, B16.4
charge stabilized spheres, C9.24
charged colloidal dispersion, B17.9
cheese, D3.8
chemical potential, B1.12
chemical shift, A2.19
cholesterol, B14.14
chymosin, D3.11
clay-polymer nanocomposites, D4.17
cleaning process, I1.9
closure relations, B5.13, B16.20
cloud point, B8.11
cluster, D1.7
co-polymerization, D4.11
coarse graining, A7.31, B17.3, C1.2
coherent scattering, A1.15, A1.21
coiled-chain conformation, I1.10
colloid, A5.2, B10.2, B12.25, C5.2, C9.23, D3.2
colloidal crystal, I1.2
colloidal particles, I1.3
colloidal suspensions, I1.4
colloidal system, I1.2
colloids and polymers, B17.17
complex fluids, I1.2
complex viscosity, C9.12
complexity, I1.13
compliance, A3.5, C9.4, C9.8
compressibility equation, B16.12
concentrated polymer solutions, A7.13
cone-plate configuration, C9.13
configuration, B2.2
configuration integral, B1.11
conformation, B2.2, B3.2
conservation of mass, C9.6
conservation of momentum, C9.6
constitutive relation, C9.4
constraint release processes, C9.19
continuity equation, C9.6
continuous wave spectroscopy (CW), A2.12
contrast factor, B6.8
convected derivative, C8.30
copolymer, A4.8, A7.26, B10.2, B10.10
correlation function, A3.6, A3.11, B3.10, B7.3, B7.14, C1.12, C1.17, C5.4
correlation length, B3.9, B9.27
cosurfactant, B8.7, C6.2
Couette configuration, C9.16
counterion condensation, B5.15, B5.18
coupling constant, A2.22
crazing, shear yielding, D4.12
creep test, C9.10
creeping flow, C8.15, C8.32, C8.33
critical exponent, B16.19
critical micelle concentration (cmc), A6.6, B8.3
critical molecular weight, C9.18
critical opalescence, B16.16
critical phenomena, I1.4
critical slowing down, C4.22
cross section, A1.4
crystal structure, B15.4
crystallization, C5.10, D1.8
curvature energy, A6.9, B9.8
curvature tensor, B9.6, B9.42
cut–off, B7.3, B7.9, B7.13, B7.14
cylinder configuration, C9.13
cytoplasm, B14.5
cytoskeleton, B14.5
cytosol, B14.5

D

de Broglie thermal wavelength, B1.11
de Gennes narrowing, C6.25
debonding, D4.15
Deborah number, C9.19
Debye function, B4.11
Debye-Hückel potential, B5.4, B5.6
deformability, I1.2
deformation, C9.3
deformation gradient tensor, C9.3

deformation rate, C9.3
deformation rate tensor, C9.4
deformation tensor, C9.4
dendrimers, B17.14
density
  n-particle, B1.15
density correlation function, C5.13
density functional, B17.7
density-pressure relation, B10.13–B10.15
depletion force, A6.21
depletion interaction, I1.15
depletion zone, B10.5, B10.6
detailed balance, A7.6
detergent composition, I1.9
diblock copolymer, B6.14, B12.3
dielectric function (permittivity), A3.8, A3.11, A3.15
dielectric spectroscopy, A3.2, A3.12
differential geometry, B9.4
dimerization algorithm, A7.11
dimyristoyl-phosphatidylcholine, B12.30
dipole fluctuations, A3.16
dipole-dipole interaction, A2.21
direct correlation function, B5.11, B16.15
director, C8.22
director field, C8.24, C8.25
dispersion colloids, I1.4
dispersion of relaxations, C6.12
dispersion relation, B7.6–B7.8
dispersions, A5.2
displacement amplitudes, C6.8
distribution function
  n-particle, B1.15
distribution of end-to-end vectors, B2.8
dividing interface, B11.4
DLVO potential, B16.5
DNA, B2.16, I1.5
double-jet, A5.12
drag-flow indexers, C9.12
drag-flow rheometers, C9.12
droplet phases exchange kinetics, A6.18
droplet phases stability, A6.20
dyadic products, C4.27
dynamic light scattering (DLS), A1.29, C5.3, C6.4
dynamic structure factor, C5.5, C5.13
dynamic susceptibility, B7.6, B7.7
dynamic viscosity, C9.6
dynamically triangulated surfaces, B9.29

E

Edwards-Singh approximation, B5.7
effective bond length, B2.9
effective diffusion, C6.25
effective Hamaker constant, B7.6, B7.7, B7.10, B7.14
effective interaction, B16.33, B17.4, C4.16, I1.14
efficiency boosting by amphiphilic block copolymers, B9.35
eicosan, B11.9
elastic modulus, C9.4, C9.11
elastic solid, C9.6
elasticity of the melt, D4.20
elastomers, D4.4
electrolyte, B12.24
electron diffraction, B15.4
electron microscopy, A5.13
electronic data processing, D4.18
electrophoresis, A5.14
electrostatic repulsion, D3.7
emulsification failure, B9.22
emulsion brake down, A6.21
emulsion polymerisation, A6.28
emulsion stabilisation, A6.20
end density, B10.4, B10.5
end-to-end distance, B3.2, I1.10
end-to-end vector, B2.4
endocytosis, B14.12
endoplasmatic reticulum, B14.7
endosome, B14.8
energy landscape, C3.10
entanglement, A4.14, A7.22, A7.28, C2.15, C9.18, C9.21
enthalpy, B7.2, B7.4
enthalpy of mixing, B4.4
entropy, B7.2, B7.4
entropy of mixing, B4.2
enzyme, D3.11
equilibrium ensemble average, B1.8
equipartition theorem, B9.14
ergodicity hypothesis, C5.5
ethylene-propylene-diene rubber, D4.4
ethyleneglycol, D4.21

eukaryotic cell, B14.4
Euler characteristic, B9.8
European Spallation Source (ESS), A1.2, A1.20
evanescent wave, B11.11
excess free energy, B1.11
excluded volume interaction, A7.4, A7.30, B2.17, B5.6, B10.13

F

falling ball rheometer, C9.12
fd-virus, I1.5, I1.6, I1.14
Fermi-Pasta-Ulam problem, A7.10
Fermi-Pseudo potential, A1.15
ferrofluids, C8.3
field inhomogeneity, A2.9
filler-filler interactions, D4.6
film thickness, B7.7, B7.9, B7.10, B7.12, B7.13
finite size effects, B7.6
fission, B12.31
flip-flop, B12.24
Flory approximation, B3.4
Flory exponent, B6.6, B10.14
Flory free energy, B5.5
Flory lattice, B6.3
Flory radius, B3.5
Flory theorem, B3.10, B4.3
Flory theory, B2.19
Flory-Huggins parameter, B6.6
Flory-Huggins theory, B4.2
flow cups, C9.12
flow instabilities, C9.15
flow visualization experiment, C9.30
fluctuation dissipation theorem, A3.7, C1.13
fluctuations, A3.6, C1.2, C1.3, C1.6, C1.12, C1.14
fluid mixtures, B16.32
fluid mosaic model, B14.3
fluid-gel transition, B12.4
Fokker-Planck equation, C1.11
form factor, A1.7
form factor of Gaussian chain, B2.11
Fourier-transform infrared (FT-IR), B15.6
fracture behavior, D4.11
fragility, C3.14
Fraunhofer approximation, A1.4
free electron lasers, A1.2
free energy, B3.7, B5.23
free energy of micellisation, B8.9
free induction decay (FID), A2.12
free membrane dynamics, C6.10
free polymer, B10.2, B10.7, B10.12
freely jointed chain, B2.7
freely rotating chain, B2.6
Fresnel's law, B11.10
friction coefficient, C8.15
frozen capillary waves, B7.9
FT-NMR, A2.12

G

Gauss-Bonnet theorem, B9.8, C6.6
Gaussian chain, B2.10, B3.3
Gaussian coil, A7.9, A7.16
Gaussian random fields, B9.22
gel line, I1.5, I1.6
gels, A7.23
genus, B12.36
geometrical constraints, B12.8
giant vesicles, B12.2
Gibbs adsorption equation, B11.6
Gibbs adsorption isotherm, A6.6
Gibbs phase rule, A6.8
Gibbs triangle, A6.15
Gibbs-Bogoliubov approximation, B5.7
Gibbs-Bogoliubov-Feynman inequality, B9.26
Gilroy-Phillips model, C3.14
Ginzburg-Landau expansion, C4.17
Ginzburg-Landau model, C6.6, C6.22
glass, C5.2, C5.17
glass transition, A7.31, C3.10, C5.2, C5.14, C9.22
glass transition temperature, A4.12, B7.3, B7.11, B7.14
glassy polymers, C9.20, C9.22
globular proteins, B17.23
Golgi apparatus, B14.8
grafted polymer, B10.2, B10.6, B10.9
grand canonical ensemble, B1.12
grand canonical partition function, B1.13
gravitation, B7.6, B7.7, B7.9
grazing incidence x–ray diffraction, B11.10
Green Tire, D4.6
growth, A5.7, D1.8

H
halobacterium salinarum, B15.2
Hamilton's equation, B1.3
Hamiltonian, A2.17
hard segments, D4.21
hard spheres, C5.11
hard-core potential, I1.5
hard-sphere fluid, A7.4
hard-sphere interaction, C9.24
hard-sphere solvent, B17.21
Helfrich expansion, B10.2, B10.9, B10.10, B10.13
Helfrich free energy, A6.17
Helfrich Hamiltonian, C6.5
Helfrich interaction, C6.9
hexagonal phase, B8.13
hexane-diisocyanates, D4.21
history, I1.16
homopolymers, I1.10
Hooke's law, C9.4
Hookean solid, C9.4
hydration shell, A7.15
hydrodynamic interaction, C1.19, C8.11, C8.14, C8.15, C8.19, C8.32, C8.33, C9.25
hydrophilic, I1.7
hydrophobic, I1.7
hydrophobic effect, A6.6, B8.5, B9.8, I1.8
hydrophobic interaction, A7.15
hydrophobic-hydrophilic-balance temperature, B9.18
hypernetted-chain approximation (HNC), B16.23

I
impact fatigue, D4.16
incoherent scattering, A1.15, A1.21, C5.8
industrial polymer production, I1.12
injection molding, D4.9
integral scattering, A1.22
interaction, A5.3
interconnected cylinders, A6.17
interface excess quantities, B11.4
intermediate scattering function, C5.5
intermicellar exchange, A6.25
internal stresses, D4.20
intra-chain potentials, A7.29
inversion recovery experiment, A2.14
Ising model
  3D-Ising model, B6.13
iso-electrical point, A5.3
isocyanate, D4.20
isotropic-nematic phase transition, C4.20

J
jamming effect, C9.26

K
kinematic scattering, A1.5
kinematic viscosity, C9.12
kinetics, C7.2
Kohlrausch-William-Watts, C2.27
Krafft point, B8.11
Kramers-Kronig relation, A3.6
Kratky-Porod model, B2.15

L
L_3-phase, B8.12, B9.16, B9.17
lamellar phase, B8.13, B9.16, C6.18
Lamor frequency, A2.3
Langevin equation, B5.19, C1.7
Laue function, A1.9
law of large numbers, I1.10
Lennard-Jones potential, A7.4, B16.3
level surfaces, B9.22
linear polymers, B2.2
linear response, A3.4, A3.12, B4.9
linear viscoelasticity, C9.8
Liouville equation, B1.4
lipid bilayer, I1.7, I1.8
lipidic cubic phase, B15.4
liquid crystal display (LCD), C8.3, C8.4, C8.25
liquid crystals, B8.13
liquid-crystalline polymers, D4.11
living cell, B14.1
living polymers, I1.13
local dynamics, C6.15
longitudinal and transversal magnetization, A2.6
longitudinal relaxation time, A2.8
Lorentz curve, A2.10
loss modulus, C8.6, C8.29, C9.11
lubrification effect, C9.25
lyotropic phases, I1.8

lysis tension, B12.6
lysosome, B14.8

M

macroemulsion, A6.20
magic triangle of tire properties, D4.6
Maier-Saupe potential, C4.17
Markov process, B4.9
master equation, A7.8, C1.10, C1.15
material properties, C3.3
Maxwell fluid, C9.8, C9.12
Maxwell model, C8.28
mean square end-to-end distance, B5.7, B10.3, B10.10, B10.14
mean square radius of gyration, B10.3
mean-spherical approximation(MSA), B16.20
mechanical properties, C3.7
membrane, B10.2, B10.10, B15.2
membrane asymmetry, B12.24
membrane dynamics, B12.34, C6.12
membrane fluctuations, B9.13, B9.20, C6.7
membrane fusion, B14.12
membrane interactions, C6.8
membrane lipid, I1.7
membrane model, C6.5
membrane proteins, B14.4
membranes, B12.2
memory functions, C9.8
mesoporous, A6.31
mesoscopic simulations, A7.33
metallocene polymerization, A4.8
metastable, B4.6, C7.26
methane-diphenyl-diisocyanates, D4.21
metric tensor, B9.4
Metropolis algorithm, A7.7, A7.15
micellar aggregate, A6.3
micellar kinetics, B8.10
micelle, A6.25, I1.8
micelle formation, C9.26
micelle shape, B8.12
micellisation, B8.8
microcanonical ensemble, B1.8
microemulsion, A6.3, B8.20, B9.18, B10.11, C6.2, I1.8
microemulsion phase evolution, A6.13
microemulsion structural evolution, A6.13
microgravity, A7.4
microphase separation, A4.11
mineral skeleton, B12.38
minimal surfaces, B9.9
mitochondrion, B14.7
mixed micelles, B8.21
mixing, D1.9
mobility matrix, C8.15
mode coupling theory, C5.13
modulus, A3.5
molecular dynamics simulations, A7.4, A7.30, B5.19
molecular individualism, C8.31
molecular modeling, D4.20
molecular weight, A4.11, B7.3
molecular weight distribution, A4.12
Monge representation, B9.11, C6.7
monodisperse colloidal particles, A5.7
monolayer, B11.12
monomer, I1.10
monomer density, B10.13
Monte Carlo simulations (MC), A7.6
morphosynthesis, B12.38
multi-component Ornstein-Zernike equations, B16.32
multiscale modelling, A7.27
mushroom regime, B9.38

N

n-butanol, A3.11
nanoclays, D4.17
nanomachine, B15.2
nanoparticle, A6.4, D1.1
nanoreactor, A6.2
nanorods, A6.24
nanostructured materials, A6.3
natural rubber, D4.3
Navier-Stokes equation, B7.5, C6.10, C8.2, C8.9, C8.10, C8.20, C8.26, C8.30
necklace globule, B5.23
nematic, C4.2
nematic liquid crystal, C8.3, C8.4, C8.22
networks, A4.8, A4.14
neutron diffraction, B15.4
neutron scattering, A1.20, A7.32, C2.2
neutron spin echo (NSE), A1.27, C2.2, C6.4, C6.18, C6.25
Newtonian dynamics, A7.5

Newtonian fluid, C9.5
NMR spectrometer, A2.10
non-adsorbing polymer, B10.2
non-equilibrium molecular dynamics simulations, A7.6
non-equilibrium phase diagram, C4.23
non-ergodicity, C5.5
non-linear effects, C9.5, C9.12
non-reversing random walk, A7.18
normal force, C9.3
nucleating agents, D4.18
nucleation, A5.7, C7.7, D1.5
nucleus, B14.7

O

oliourethane, D4.21
onion-like phase, C9.29
optical disc, D4.18
organelles, B14.4
orientational closure relation, C4.18
orientational free energy, C4.24
orientational order, C8.4, C8.22
orientational order parameter, C4.12
Ornstein-Zernike equation, B5.2, B5.11, B16.15
oscillatory shear, C9.10, C9.11
Oseen tensor, C1.20, C8.14, C8.19, C8.32, C8.35
osmotic pressure of sponge phases, B9.31
Ostwald ripening, A5.12, A6.5
overdamped modes, B7.8
overlap concentration, B9.38

P

packing parameter, A6.7, B8.15
paint, I1.5
pair correlation function, B5.11
pair distribution function, B16.7
Pake spectrum, A2.22
paranematic state, C4.22
partial dewetting, B7.13
partial structure factor, B6.8
particle formation, D1.8
particle-to-polymer size ratio, B10.6–B10.8
particles, A5.2
partition function, B5.6
Patterson function, A1.6
pearl necklace model, A7.9
penetration depth, B11.11
Percus-Yevick approximation, B16.22, C5.10
perfluoralkylalkanes, B11.14
peristaltic mode, C6.21
permeability, B12.8
peroxisome, B14.7
persistence length, B2.5, B5.8, B5.9, B9.14
phase contrast microscopy, B12.9
phase inversion, A6.12
phase inversion temperature, A6.21
phase separation, B4.5, C7.2
phase space probability density function, B1.3
phase transitions, I1.4
phosphatidyl-choline (PC), I1.7
phospholipid, B12.2, B14.14
photo aquation, B12.27
photo chemistry, B12.27
pit replication, D4.20
plasma membrane, B9.4, B14.8
plate-plate configuration, C9.13
Poiseuille flow, C8.10, C8.15, C8.16
Poisson-Boltzmann equation, B5.4
polarizability, A3.11
polarization, A3.3
polyadic products, C4.28
polyampholyte chain, A7.14, B5.25
polybutadiene, B12.3
polycarbonat-polyols, D4.21
polycarbonate, D4.9
polycarboxylate, D1.13
polychloroprene, D4.4
polycondensation, A4.6
polydimethylsiloxane (PDMS), C2.9
polyelectrolyte, A7.25, B5.2, D1.2
polyestercarbonates, D4.11
polyesterpolyols, D4.21
polyetheretherketones, D4.11
polyethylene (PE), C3.2
polyethyleneoxide (PEO), B9.36
polyethylenepropylene (PEP), B9.36
polyethylenoxide (PEO), B12.3
polyisobutylene (PIB), C2.24, C3.6
polyisoprene (PI), C3.5, D4.4
polymer architecture, I1.10
polymer coated, B12.30
polymer dynamics simulations, A7.15

polymer form factor, B6.4
polymer glasses, A7.27
polymer melt
  simulations, A7.19
  two dimensional, A7.19
polymer membranes, B12.6
polymer miscibility, A4.10
polymer mixture, B4.12
polymer networks, A7.23
polymer simulations, A7.8
polymer solution, B17.10
polymer synthesis, A4.2
polymer-induced bending rigidity, B9.38
polymer-mediated interaction, I1.15
polymeric additives, I1.12
polymerized membranes, B9.29
polymers, C2.2, C9.18
polymersomes, B12.34
polymethylmethacrylate (PMMA), C3.6, D4.10
polyphenyleneoxide, D4.10
polyphenylenesulfides, D4.11
polystyrene (PS), C3.4
polystyrene-acrylonitrile, D4.10
polyvinylacetate, A3.15
polyvinylchloride (PVC), C3.4
poor solvent, B5.23
potential of mean force, B5.4, B16.8
power spectral density, B7.3, B7.7, B7.9–B7.11, B7.13, B7.14
precession, A2.4
precipitation, A5.2, D1.9
pressure-driven rheometers, C9.12
primitive model, B16.33
PRISM, B5.2, B5.11
process control, D4.22
prolate-oblate transition, B12.22
protein, B12.32
proton gradient, B15.3
proton translocation, B15.2
pseudo-potential for a Gaussian chain, B2.14
pulse
  180^0–pulse, A2.12
  90^0–pulse, A2.12
PY solution for hard-sphere fluid, B16.25

Q

quadrupolar interaction, A2.22
quantum chemistry, A7.29

R

radial distribution function, B1.15, B16.7
radical polymerization, A4.3
radius of gyration, B2.5
Raman spectroscopy, A1.25
random copolymer, A7.14
random phase approximation, B4.9, B6.6, B6.11
rate of strain, C8.6, C8.17
Rayleigh light scattering, A1.13
Rayleigh modes, B7.8
Rayleigh-Gans-Debye scattering theory, A1.13
real time image analysis, B12.11
recrystallization, A5.10
red blood cell, I1.3
reduced phase space distribution function, B1.4
reduced volume, B12.14
reflectivity, B11.10
reinforced reaction injection molding, D4.22
reinforcing filler, D4.4
relaxation
  α relaxation, A3.9, C2.27, C5.14, C9.20
  β process, C2.28
  β relaxation, A3.15, C2.28, C5.15, C9.20
relaxation function, C9.8
relaxation spectrum, C9.9
relaxation test, C9.10
relaxation time, B7.8, B7.9, B7.11–B7.13, B8.10, C9.7, C9.8
renormalized rigidity, B9.20
reptation, A7.22, C9.18
reptation algorithm, generalised, A7.13
reptation model, C2.15
retinal, B15.2
reverse micelles, B8.5
Reynolds instability, C9.15
Reynolds number, C8.10, C8.14, C8.17, C8.32, C8.33
rheo-optical constant, D4.20
rheological behavior, D4.11
rigidity constant, A6.5
rod climbing, C8.3, C9.4

rods, A5.9
Rogers-Young (RY) approximation, B16.30
rolling ball rheometer, C9.12
rotating frame, A2.5
rotational Brownian motion, C4.2
rotational diffusion coefficient, C4.9
rotational Peclet number, C4.22
rotational rheometers, C9.13
Rouse model, A7.10, A7.16, C2.5, C9.9, C9.19
rubber, A4.10, C2.15
rubber elasticity, I1.10
rubber modifier, D4.13
rubber toughening, D4.12
rubber-filler, D4.6

S

saddle-shaped membrane geometry, B9.17, B9.24
saddle-splay modulus, B9.8
SAN, D4.11
saturated monolayer, I1.8
scaling, B3.4
scaling laws, C5.15
scattering, A5.14
scattering experiments, B16.10
scattering function, A1.21, A1.24, C6.14, C6.23
scattering intensity of microemulsions, B9.27, B9.35, B9.40
Scherk's minimal surface, B9.11
sea urchins, B12.38
Searle configuration, C9.16
second osmotic virial coefficient, D3.10
second rank tensor, A2.19
secondary relaxation, C3.9
sedimentation, A5.15
self-assembling, B9.8, C9.26
self-assembly, A6.6
self-avoiding polymers, B2.17
self-avoiding surfaces, B9.29
self-avoiding walk (SAW), A7.9
semi-crystalline thermoplastics, D4.10
semi-dilute, B3.8
semiflexible chain, B5.6
shape representation, B12.12
shape transitions, B12.15
shear flow, C4.18
shear flow geometries, C9.13
shear history, C9.8
shear modulus, I1.3
shear-banding, C4.25, C9.30
shear-thickening, C9.23
shear-thinning, C8.3, C8.19, C9.23
Siegert relation, A1.30, C5.4, C5.6
signaling, B12.32
silica, A5.8, D4.4
silver halides, A5.3
simple shear, C9.4, C9.6
small angle neutron scattering (SANS), B6.2, D1.12
small angle x-ray scattering (SAXS), D1.12
Smoluchowski equation, C1.5, C1.9, C1.11, C1.13, C1.16, C1.19, C7.3
Smoluchowski equation for rods, C4.4
sodium dodecyl sulfonate (SDS), I1.7
soft matter, I1.2, I1.12, I1.15
soft segments, D4.21
solubilisation, B8.20
solubilisation limit, A6.17
specificity, B14.10
speckles, B7.10–B7.12
spectral density, A2.17, A3.7, A3.9
sphere-cylinder transition, A6.19
spherical globule, B5.23
sphingomyelin, B12.32
spin-echo, A2.15
spin-spin coupling, A2.19
spinodal, B4.6, B6.10, B12.16, C4.23, C7.4
spinodal fluctuations, B12.18
sponge phase, B9.16, B9.17
spontaneous curvature, A6.5, B8.15, B9.8, B12.14, B12.15, B12.24
spontaneous emulsification, A6.9
spring-dashpot models, C9.6
square well, D3.11
stability, D3.2
stabilization, A5.3
star polymer, B17.14
starfish vesicles, B12.22
static structure factor, B16.11
statistical copolymer, A4.10
statistical mechanics, B2.14
stearoyl-oleoyl-phosphatidylcholin, B12.2,

B12.30
steric, D3.12
steric membrane interaction, B9.17, C6.9
steric stabilization, A5.3
Stokes law, C8.11, C8.15, C8.17, C8.33
stop-flow technique, D1.11
storage modulus, C8.6, C8.29, C9.11
strain, C9.3
strain control, C9.16, C9.26, C9.29
strain rate, C9.3
strain rate ramp, C9.10
strain rate step, C9.10
strain rate tensor, C9.4
strain step, C9.10
strain tensor, C9.4
stress, C9.3
stress control, C9.16, C9.26, C9.29
stress step, C9.10
stress tensor, B7.5, C8.8, C8.13, C8.18, C8.29, C9.3
stretched exponential, C6.16
stretching, C3.14
stretching elastic modulus, B12.6
stretching elasticity, B12.6
structural changes, B15.9
structure factor, A1.24, B4.11, B5.12, B5.14, C5.5
structure of linear polymers, B2.2
styrene-butadiene rubber, D4.4
sublinear diffusion, C2.30
superstructures, B12.37
surface curvature, B10.10
surface modes, B7.7, B7.8, B7.10
surface roughness, B7.3, B7.14
surface tension, B5.23, B7.6, B7.7, B7.14, B8.3, B9.2, B9.8, B11.3
surface viscosity, B12.8
surfactant, C6.2, C9.26, I1.7
surfactant consumption, I1.9
susceptibilities, A3.8
suspension, C5.2, I1.4
swollen coil, A7.9
synchrotron radiation sources, A1.19
synthesis, A5.2

T

Taylor instability, C9.16
temperature shift factor, C9.22
template, A6.31
tensile elastic modulus, C9.20
test modes, C9.9
tethered polymer, C8.31
tethered polymer chains, A7.25
Teubner-Strey, B9.27, C6.23
thermal expansion, B12.7
thermal expansivity, B12.7
thermal neutrons, A1.14
thermodynamic consistency, B16.29
thermoforming, D4.9
thermoplastic elastomers, D4.22
theta temperature, A7.13
Thomson scattering, A1.11
tilt angles, B11.12
time average, B1.6
time dependent Ginzburg-Landau model, C6.23
time-of-flight (TOF), A1.26
time-temperature superposition principle, C9.21
tobacco mosaic virus (TMV), I1.5
toluylene-diisocyanates, D4.21
topological constraints, C2.16
topological invariant, B9.8
topology, B9.24, B12.36
topology fluctuations, B9.19
torsion pendulum, C3.8
total correlation function, B5.11, B16.11
total external reflection, B11.11
transversal relaxation time, A2.8
triply-periodic minimal surfaces, B9.11
turbulences, C9.15
turbulent drag reduction, C8.2, C8.30

U

undulation mode, B9.14, C6.21
uniaxial nematic, C4.14
universality, A7.9, I1.10, I1.13

V

Van der Waals, A5.4
Van der Waals attraction, D3.7
Van Hove theory, A1.21
variational approach, B9.26
velocity gradient tensor, C9.4
vesicle, B8.12, B12.2, B14.10, C6.4

vesicle classification, B12.4
vesicle shapes, B12.13
vesicular transport, B14.11
virial function, B1.7
viscoelasticity, A4.14, C8.2, C8.6, C8.28, C9.7, C9.8
viscosity, B7.5, B7.9, B7.12, C9.6, C9.10
viscous fluid, C9.7
Vlasov equation, B1.5
Vogel temperature, C9.23
Vogel-Fulcher law, A7.31, C2.27
Voigt-Kelvin solid, C9.7
vulcanization, D4.4

W

water-surfactant mixtures, B9.15
Weissenberg effect, C8.3, C9.4
white noise, B5.19
Williams-Landel-Ferry law, C9.22
Winsor phase equilibria, A6.22
worm-like chain, B2.15

X

X–ray diffraction, B15.2
X–ray scattering, B7.10, B7.14

Y

YBG hierarchy, B1.21
yoghurt, D3.2

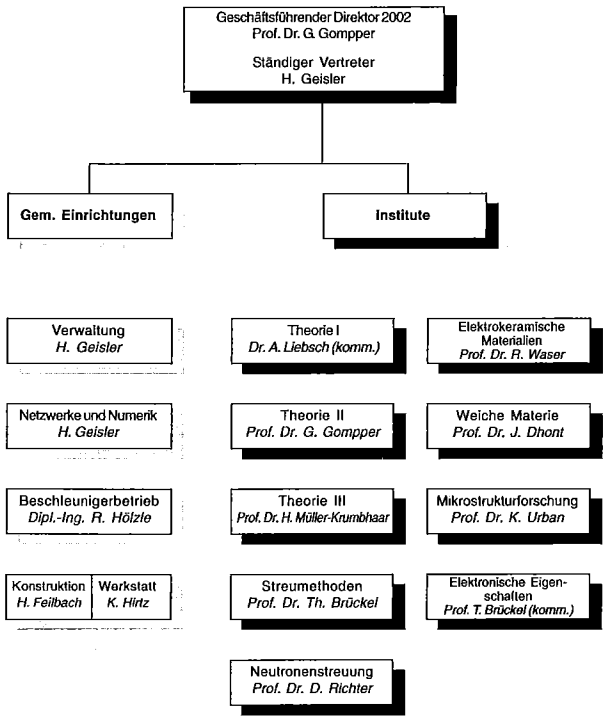
Z

Zeeman splitting, A2.17
Zilman-Granek model, C6.14

DAS INSTITUT FÜR FESTKÖRPER-FORSCHUNG (IFF) IM FORSCHUNGSZENTRUM JÜLICH

D-52425 Jülich
Tel. (0 24 61) 61 - 44 65, Telefax (0 24 61) 61 - 24 10
http://www.kfa-juelich.de/iff

Organisation des IFF



Das Institut für Festkörperforschung (IFF) betreibt Forschung zur Physik der kondensierten Materie im festen wie im flüssigen Zustand. Aufbauend auf seinen Untersuchungen von Volumeneigenschaften der kondensierten Materie widmet sich das IFF auch inhomogenen Systemen und mit dimensionaler Begrenzung verbundenen Phänomenen. Dies betrifft insbesondere die Physik der Cluster, Grenzflächen, dünnen Filme und Membranen. Dabei kann man in den experimentellen wie theoretischen Arbeitsgruppen drei strategische Ausrichtungen unterscheiden:

- **Die phänomenorientierte Forschung:** Suche, Entdeckung, Erforschung und Erklärung allgemeiner Phänomene und Verhaltensweisen in kondensierter Materie sowie der zugrundeliegenden mathematisch-physikalischen Konzepte und Strukturen.

- **Die materialorientierte Forschung:** Untersuchung spezifischer Materialien oder Materialklassen mit dem Ziel, ihre besonderen Eigenschaften zu verstehen und gegebenenfalls bis zu einem Anwendungshorizont zu entwickeln. Herstellung neuartiger Materialien und Präparation sowie Charakterisierung wohldefinierter Proben.

- **Die methodenorientierte Forschung:** Entwicklung neuartiger und Optimierung bestehender Methoden auf experimentellem oder theoretisch-mathematischem/numerischem Gebiet.

Die allgemeinen physikalischen Grundlagen für diese Arbeitsrichtungen sind die statistische Physik und die Quantenmechanik. Sie bestimmen im mikroskopisch Kleinen das Verhalten und die Reaktion auf äußere Einflüsse von Elektronen und atomaren Bausteinen, deren Aggregation und Kooperation schließlich kondensierte Materie hervorbringt. Diese Zusammenhänge sind in ihren aktuellen Fragestellungen Gegenstand der Anstrengungen der *theoretischen* und *experimentellen* Arbeitsgruppen.

Zugleich haben in den letzten Jahren, ausgehend von der Entwicklung von Präparations- und Charakterisierungsverfahren auf der mikroskopischen atomaren Skala, in den *experimentellen* Gruppen die Arbeiten zur Entwicklung von Bauelementen und Systemen weiter zugenommen, in denen diese Verfahren

und Prozesse neuartige Materialeigenschaften erschliessen. Dies hat wiederum zu einem Engagement der *theoretischen* Arbeitsgruppen geführt, mit modernen Methoden das zum Teil außerordentlich komplexe Verhalten solcher neuen Systeme zu beschreiben und zu verstehen.

In Verfolgung einer zukunftsorientierten Forschungsstrategie hat das IFF seine Arbeitsthemen mit der Gründung des Instituts für Elektrokeramische Materialien und des Instituts für Streumethoden wesentlich erweitert. Hierdurch werden im Department gleichzeitig neue zukunftsträchtige Arbeitsrichtungen definiert uns erschlossen und die Kernkompetenzen erweitert. In die gleiche Richtung zielen die Aktivitäten auf dem Gebiet der Weichen Materie durch das neue Teilinstitut und die der Theorie II. Diese unterstreichen die strategische Entscheidung zugunsten dieses Themenbereiches, welche auch ausgedehnte und attraktive Kooperationsmöglichkeiten innerhalb des Forschungszentrums eröffnet.

Die folgenden speziellen Arbeitsschwerpunkte des IFF werden durch die besonderen Möglichkeiten und Aufgaben eines Helmholtz-Forschungszentrums bestimmt:

- Mitarbeit am Aufbau und Nutzung neuer Experimentiereinrichtungen und Messplätze an internationalen Quellen für Neutronen- und Synchrotronstrahlung. Neben dem Jülicher Forschungsreaktor DIDO werden hierfür die folgenden Neutronenquellen in Argonne, Berlin, Brookhaven, Gathersburg, Grenoble, München, Risø, Saclay und Appleton genutzt. Das Forschungszentrum Jülich beteiligt sich im Rahmen des FE-Programms für die Europäische Spallationsquelle (ESS), an deren Entwurf 11 europäische Länder zusammenarbeiten.

Bei den Tätigkeiten am IFF handelt es sich um die Erforschung der Schockwelleneffekte am flüssigen Quecksilbertarget, der Optimierung des Targets und der Moderatoren sowie der Entwicklung der Instrumentierung.

Experimente mit Synchrotronstrahlung werden bei BESSY, DELTA, HASYLAB in Deutschland sowie international in Argonne (APS), Berkeley (ALS), Brookhaven (NSLS), ESRF (Grenoble) und ELETTRA (Trieste) durchgeführt.

- Nutzung der Grossrechenanlagen des Forschungszentrums Jülich, vorwiegend für theoretische Untersuchungen und numerische Simulationen besonderen Umfangs.

- Themen deren Bearbeitung (in den meisten Fällen im Rahmen nationaler und internationaler Kooperationsobjekte und Serviceleistungen) besonders grosser Investitionen oder der Kontinuität eines festen qualifizierten Mitarbeiterstammes bedürfen. Beispiele sind: Zentrum für hochauflösende Elektronenmikroskopie, Betrieb von Beschleunigern, Elektrokeramisches Laboratorium, Supraleitertechnologie, Entwicklung aufwendiger numerischer Verfahren und Programme.

Das IFF hat in seiner langjährigen Forschungstätigkeit ein breites und international anerkanntes wissenschaftliches Profil erlangt. Ganz besondere technische Kompetenz wurde auf folgenden Feldern entwickelt: Anwendung von Synchrotron- und Neutronenstrahlung, Elektronenmikroskopie, Elektronenspektroskopie, Hochtemperatursupraleitung, Magnetoelektronik, Clusterphysik, Elektronentheorie, dynamische Phänomene bei Phasenübergängen, Quasikristalle sowie Polymerphysik. Voraussetzung für die genannten Arbeitsschwerpunkte ebenso wie für Eignung und Akzeptanz in internationalen Kooperationen ist eine hohe Grundlagenkompetenz. Das IFF betreibt daher Grundlagenforschung dort, wo sich interessante und zukunftsträchtige Entwicklungen in der Festkörperphysik abzeichnen, auch als Nährboden der anwendungsorientierten Forschung.

Bei echten Innovationen (im Gegensatz zu blossen Weiterentwicklungen) ist es sogar typisch, dass sie sich oft ungeplant als frappierendes Resultat rein neugierorientierter Grundlagenforschung ergeben. Dies zeigt besonders schön der entdeckte Riesenmagnetowiderstandseffekt, der in den letzten Jahren zu einem sehr aktiven Gebiet der Festkörperforschung wurde. Er hat höchst attraktive Anwendungen in der Magnetosensorik, z.B. zum Auslesen von Datenträgern oder zur Kontrolle beweglicher Teile. Die Lizenzeinnahmen für die auf dieser Arbeit beruhenden Patente machen den grössten Einzelposten unter den Lizenzeinnahmen des Forschungszentrums aus!

Das IFF beteiligt sich im engen Verbund mit dem ISI und dem IGV am Jülicher Schwerpunktprogramm „Grundlagenforschung zur Informationstechnik" (PGI). Hier hat das IFF in den letzten Jahren ausgehend von festkörperphysikalischen Grundlagenarbeiten seine Möglichkeiten zur Technik- bzw. Bauelemententwicklung kontinuierlich ausgebaut. Unter anderem hat dies dazu geführt, dass das Vorhaben des IFF im Rahmen des HGF-Strategiefondsprojektes „Mikrotechnische Hochleistungsbauteile - Mikroinduktoren" bewilligt wurde. Im Jahre 1999 wurde ein weiteres Strategiefondsprojekt zur Entwicklung und Charakterisierung von Schichtsystemen für die Magnetoelektronik bewilligt. Das über Jahre im IFF aufgebaute Arbeitsgebiet Hochtemperatursupraleiter für die Kommunikationstechnik wurde grössenteils in die Supraleitungsforschung im ISI eingegliedert. Die Arbeitsgebiete SQUID-Mikroskopie und Hilbert-Transformationsspektroskopie werden im IFF verstärkt fortgeführt.
Von den 308 Vorträgen waren 183 Eingeladene Vorträge; 125 Sonstige Wissenschaftliche Vorträge. Dazu kamen 65 Poster. Ausserdem wurden von den Mitarbeitern Lehrveranstaltungen an Universitäten durchgeführt. 27 Mitarbeiter sind durch ihre Lehrverpflichtungen im Vorlesungsplan der Hochschulen eingebunden.

Die traditionelle IFF-Ferienschule stand 1999 unter dem Thema: „Magnetische Schichtsysteme" und wurde von etwa 250 Teilnehmern besucht.
12 Diplomanden und 17 Doktoranden haben 1999 ihre Arbeit abgeschlossen. Im Berichtsjahr 1999 waren 17 Diplomanden und 52 Doktoranden im IFF beschäftigt.

2. Wissenschaftlich-Technische Infrastruktur

Das IFF hat in den letzten Jahren seine Infrastruktur gestrafft und dabei versucht, durch organisatorische und strategische Massnahmen im Rahmen der auf ein Minimum reduzierten personellen Möglichkeiten eine optimale Leistungsfähigkeit der departmentsinternen Dienstleistungen zu erhalten. Einrichtungen mussten geschlossen und der Verlust von technischer Kompetenz in Kauf genommen werden, wenn Mitarbeiter im technischen Bereich nach ihrem Ausscheiden nicht mehr besetzt werden konnten. Diese Massnahmen haben die kritische Grenze erreicht.
Forschung in „Frontbereichen" setzt allerdings voraus, dass Experimentiereinrichtungen in Hochtechnologie konstruiert und gebaut werden können. Dies trifft in gleicher Weise für die Grundlagenforschung des IFF an den nationalen und internationalen Strahlungsquellen wie für seine angewandte Forschung zu, deren Geräteausstattung gerade dann, wenn sie industrienah sein soll, den ausserordentlich hohen Standards genügen muss. Kompetenz und Effektivität der vom Forschungszentrum insgesamt, insbesondere aber vom IFF selbst vorgehaltenen technischen Infrastruktur ist daher eine der Grundvoraussetzungen der Arbeit des Departments.

Das Elektroniklabor des Instituts betreibt und wartet die Workstation-Cluster und Netze. Es unterstützt die Wissenschaftler beim Aufbau und beim Betrieb ihrer Experimente sowie bei der Vernetzung und Nutzung ihrer PCs und Workstations. Im Rahmen seiner personellen Möglichkeiten erbringt es Hilfeleistungen durch fachliche Beratung in Hard- und Software und die Beschaffung und Reparatur von Komponenten. Es werden Hardware- und Softwareeinheiten entwickelt und autorisierte Experimentiersysteme aufgebaut.

Die Gruppe Numerische Methoden und Datenverarbeitung ist zuständig für Fragen der Numerik und der Datenauswertung. Sie betreut gemeinsam mit dem Elektroniklabor die Systemsoftware der IFF-Workstation-Cluster, bietet Programmberatung an und beteiligt sich regelmässig an der Ausbildung von Mathematisch-Technischen Assistenten.

Die Beschleunigergruppe ist für den Betrieb des Kompaktzyklotrons und des Tandetrons zuständig.

Konstruktion und Werkstatt entwerfen und bauen Geräte für das IFF, wobei die Spannweite von einfacher Mechanik bis zu anspruchsvoller, moderner Technik reicht. Hierbei arbeitet diese Einrichtung eng mit den Wissenschaftlern und Ingenieuren der Institute zusammen, um die hohen Anforderungen der Experimentatoren an Qualitäten und Toleranzen zu erreichen.

3. Sonstige Wissenschaftliche Aktivitäten, Zusammenarbeit mit Hochschulen, anderen Forschungseinrichtungen und mit der Industrie

Die Leistungsfähigkeit eines Forschungsinstituts wird entscheidend mitbestimmt durch seine Fähigkeit zum wissenschaftlichen Austausch und zur wissenschaftlichen und technischen Zusammenarbeit. Hierfür bietet das Forschungszentrum hervorragende Möglichkeiten. Intern steht eine vorbildliche Infrastruktur zur Verfügung und hilft effizient bei der Organisation von Arbeitsaufenthalten und Vortragsbesuchen. Infrastruktur und Mittelgrossgeräte konnten von vielen Gasforschern genutzt werden. Moderne Neutroneninstrumente stehen im Gebäude des Reaktors DIDO und im Messhaus ELLA (Externes Neutronenleiterlabor) einer Vielzahl von Gästen des IFF für aktuelle Untersuchungen zur Verfügung. Die vielfältigen Kollaborationen der Neutroneninstitute mit externen Gruppen führen zu einer optimalen Nutzung des Gerätepotentials. Im Gegenzug sind für das IFF Arbeitsmöglichkeiten an anderen Instituten und Forschungseinrichtungen wichtig, insbesondere trug das IFF durch Bau- und Entwicklung von Messeinrichtungen zum Ausbau und zur besseren Nutzung externer Grossgeräte bei (ILL und CEN Grenoble, DELTA Dortmund, HASYLAB Hamburg, BESSY Berlin, NSLS Brookhaven, NIST Washington).

Es bestehen bilaterale Absprachen über die Nutzung des Jülicher Zentrums für hochauflösende Elektronenmikroskopie für spezielle Arbeiten auf dem Gebiet der quantitativen und hochauflösenden Elektronenmikroskopie und zur Nutzung des Jülicher Mikroskops mit Korrektur der sphärischen Aberration durch Paul-Drude-Institut Berlin, RWTH Aachen, IBM Rüschlikon sowie die Universitäten Bonn, Göttingen und Kiel.

Die Leistungen des IFF als Unterauftragnehmer grosser Firmen (z.B. Bosch, Siemens, Daimler-Benz, Thompson, Philips) haben in den letzten Jahren stark zugenommen. In einigen Arbeitsgruppen sind sie zu einem bestimmten Faktor der wissenschaftlichen Arbeit geworden. Dies gilt insbesondere für Leistungen im Rahmen grosser nationaler und internationaler Drittmittelprojekte. Das IFF ist hier insbesonders an dem BMBF-Leitprojekt „Magnetoelektronik" beteiligt. Das IFF vermietet, betreut durch das Technologietransferbüro des Forschungszentrums Anlagen an Firmen des Jülicher Technologiezentrums. Darüber hinaus hat das IFF den Auftrag von Industrieunternehmen Pilotanlagen entwickelt und aufgebaut.

Zu den wichtigen Aufgaben eines Grossforschungszentrums gehört es, die dort gebauten und betriebenen Grossgeräte Hochschulen und anderen Forschungseinrichtungen zugänglich zu machen, auch für Forschungsvorhaben, die nicht notwendig einen wissenschaftlichen Zusammenhang mit eigenen Vorhaben aufweisen. Dazu bietet das FZJ mit seiner vorbildlichen Infrastruktur in Verbindung mit gastgebenden Instituten aus dem IFF folgende, viel genutzte Möglichkeiten; diese werden realisiert im Vorhaben 23.06.0 Sonder- und Gästeprogramm zur Festkörperforschung.

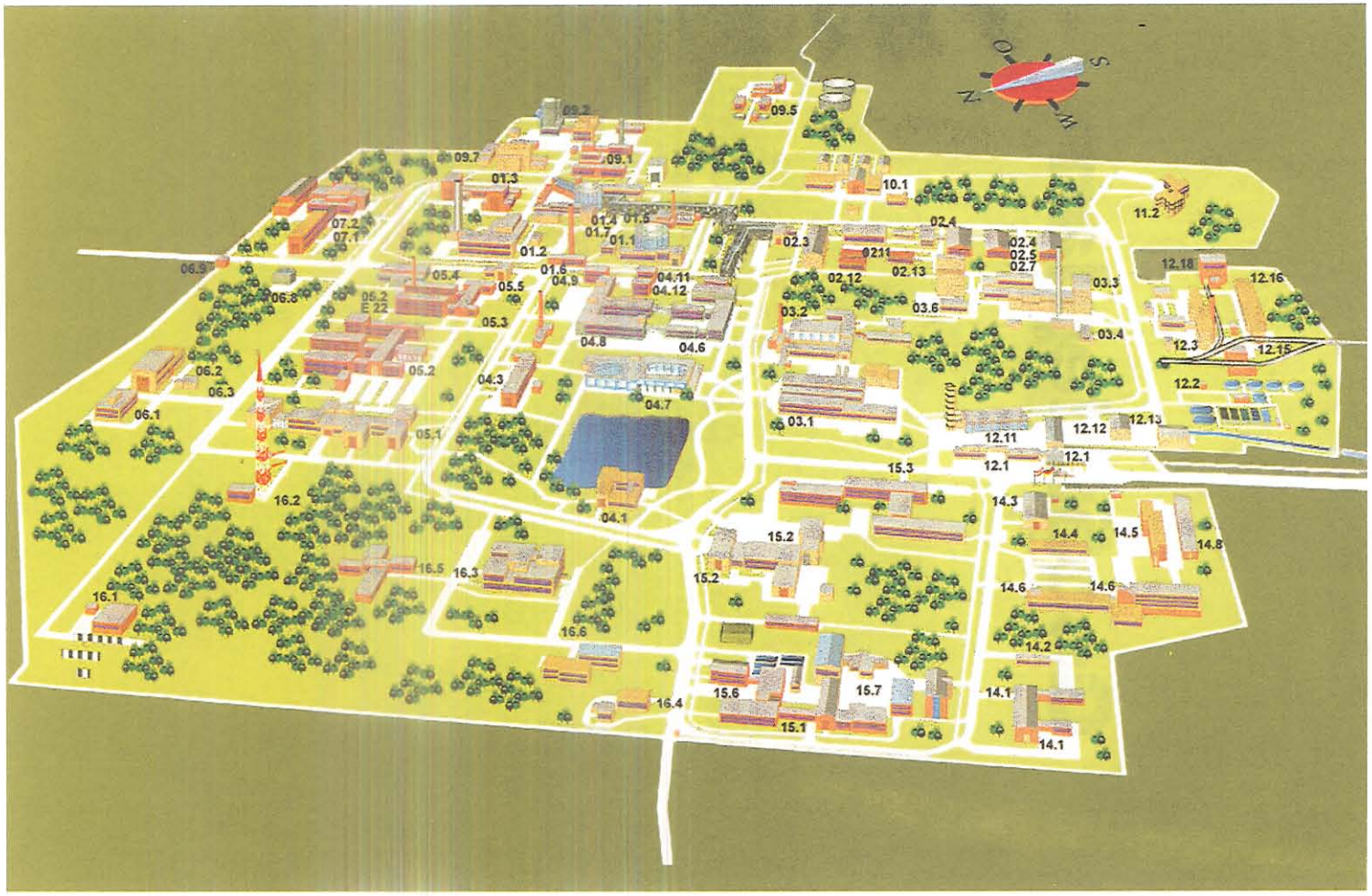
Zahlreiche Mitarbeiter des IFF wirken in wissenschaftlichen Gremien mit (Beiräte, Programmkomitees für internationale Tagungen, Herausgeber von Proceedings, Zeitschriften und Datensammlungen, Mitarbeit, teilweise Vorsitz in den Vorständen wissenschaftlicher Gesellschaften sowie als Gutachter, z.B. für die Forschungsgemeinschaft, Sonderforschungsbereiche und in Preiskomitees). Besonders erfreulich war wieder die Zusammenarbeit mit anderen Instituten innerhalb des Forschungszentrums. Die gemeinsame Nutzung von Geräten und Einrichtungen führte wie üblich zu regelmässigen Abstimmungen bei gemeinsamen Interessengebieten.

Herrn Prof. Dr. K. Urban, Institut Mikrostrukturforschung wurde am 25. Juni 1999 die Heyn-Denkmünze der Deutschen Gesellschaft für Materialkunde verliehen. Herrn Dr. Günter Schütz wurde am 22. März 2000 von der Deutschen Physikalischen Gesellschaft e.V. der Gustav-Hertz-Preis 2000 in Dresden verliehen.

Sonder- und Gästeprogramm zur Festkörperforschung

- Der FRJ-2 steht mit seinen Experimentiereinrichtungen der deutschen und internationalen Forschergemeinde zur Durchführung von Neutronenstreuexperimenten offen.
- Nutzung des Jülicher Zentrums für hochauflösende Elektronenmikroskopie.
- Kurzfristige Bereitstellung von Strahlzeit am Zyklotron und Tandetron für Gäste im Rahmen der Verbundforschung.
- Weiterentwicklung und Betrieb der Apparatur JUSIFA am HASYLAB, Betreuung von Gästeexperimenten.

Gebäudeplan


O
S
N
W
09.2
09.5
09.7
09.1
01.3
10.1
11.2
07.2
07.1
01.4
01.5
01.7
01.1
02.4
02.3
02.11
02.4
02.5
02.7
12.18
12.16
06.3
06.8
05.4
05.5
01.2
01.6
04.9
04.11
04.12
02.12
02.13
03.3
06.2
E 22
05.3
03.2
03.6
03.4
04.8
04.6
12.3
12.15
06.2
06.3
05.2
04.3
12.2
04.7
06.1
05.1
03.1
12.11
12.12
12.13
12.1
12.1
15.3
16.2
14.3
04.1
15.2
14.4
14.5
14.8
16.5
16.3
15.2
14.6
14.6
16.1
16.6
14.2
15.6
15.7
14.1
16.4
15.1
14.1

Forschungszentrum Jülich GmbH

12.15	Abfallager (ZFK-DE)
15.3	TIA, Technische Infrastruktur und Anlagenplanung
04.3	ASS, Abteilung Sicherheit und Strahlenschutz
04.3	ASS-AS, Arbeitsschutz
04.3	ASS-BS, Betrieblicher Strahlenschutz
04.3	ASS-GE, Genehmigungen
05.5	ASS-OS, Objektsicherung
04.3	ASS-ST, Sicherheitstechnik
04.3	ASS-UW, Umweltschutz
09.2	AVR, Arbeitsgemeinschaft Versuchs-Reaktor GmbH
14.1	Bauaufsicht
14.6	BEO, Projektträgerschaft Biologie, Energie, Ökologie
15.2	Betriebsärztlicher Dienst (PVA-MED)
14.5	Bildstelle (TIA-G)
14.4	BR, Betriebsrat
01.5	Brennstoffzellenlabor (IWE-BZ)
04.1	Casino I (See) (PVA-SAV)
11.2	Casino II (Wald) (PVA-SAV)
05.4	Chemiezellen (ISR-CZ)
07.1	COSY Jülich (IKP)
09.7	COSY-Bürogebäude
09.6	COSY-Testhalle
12.3	Dekontamination (ZFK-DE)
01.4	DIDO (ZFK-FRJ-2)
09.1	DLR, Deutsche Forschungsanstalt für Luft- und Raumfahrt (MAVIS)
14.5	Druckerei (TIA-G)
15.3	DSB, Datenschutzbeauftragter
15.3	EM, Einkauf und Materialwirtschaft
01.7	ELLA (IFF)
15.3	FA, Finanzabteilung
14.1	FBA, Finanzbauamt
12.11	Feuerwehr (TIA-F)
14.3	Fernmeldezentrale (TIA-N)
01.1	FRJ-1 (MERLIN ZFK)
01.4	FRJ-2 (DIDO ZFK)
06.9	Hambacher Tor (ASS-OS)
12.1	Hauptwache (ASS-OS)
03.3	Heizwerk (TIA-V)
04.11	HLRZ, Höchstleistungsrechenzentrum
01.2	HZ, Heiße Zellen (IWE-HZ)
01.3	IWE-2, Institut für Werkstoffe der Energietechnik
15.1	IBI, Institut für Biologische Informationsverarbeitung
15.7	IBT, Institut für Biotechnologie (IBT-1 und -2)
16.6	IBT, Institut für Biotechnologie (IBT-3)
05.2	ICG 1, Institut für Stratosphärische Chemie
05.2	ICG 2, Institut für Chemie der belasteten Atmosphäre
05.2	ICG 3, Institut für Atmosphärische Chemie
06.1	ICG 4, Institut für Erdöl- und organische Geochemie
06.2	IPC, Institut für Angewandte Physikalische Chemie
05.3	INC, Institut für Nuklearchemie
05.2	IET, Institut für Enzymtechnologie (Univ. Düsseldorf)
03.2	IEV, Institut für Energieverfahrenstechnik
04.6	IFF, Institut für Festkörperforschung
04.8	IFF, Institut für Festkörperforschung
05.2	IFF, Institut für Festkörperforschung
02.4	IGV, Institut für Grenzflächenforschung und Vakuumphysik
07.1	IKP, Institut für Kernphysik
15.2	IME, Institut für Medizin
14.6	INT, Internationales Büro
10.1	IPP, Institut für Plasmaphysik
09.1	IPP, Institut für Plasmaphysik
16.4	IRA, Institut für Radioagronomie
15.6	IRA, Institut für Radioagronomie
05.1	IWE-1, Institut für Werkstoffe der Energietechnik
02.11	ISI, Institut für Schicht- und Ionentechnik
02.13	ISI, Institut für Schicht- und Ionentechnik
04.9	ISI, Institut für Schicht- und Ionentechnik
16.5	ISR, Institut für Sicherheitsforschung und Reaktortechnik
09.1	ISR, Institut für Sicherheitsforschung und Reaktortechnik
06.8	Kaltwasserversorgung (TIA-V) Kälteanlage (TIA-V)
10.1	KFS, Projekt Kernfusion
12.13	Kfz-Halle (TIA-K)
12.12	Kfz-Werkstatt (TIA-K)
12.2	Kläranlage (ZFK-DE)
01.1	MERLIN (ZFK, FRJ-1)
16.2	Meteorologischer Turm (ASS-UW)
14.6	MUT, Programmgruppe Mensch, Umwelt, Technik
04.7	ÖA, Stabsstelle Öffentlichkeitsarbeit
14.2	OIV, Organisation und Informationsverarbeitung
16.5	OIV, Organisation und Informationsverarbeitung
04.12	PFR, Projektträgerschaft für Erforschung kondensierter Materie und Neue Technologien in den Geisteswissenschaften
14.6	PLR, Projektträgerschaft Material- und Rohstofforschung
15.3	PVA, Personal- und Verwaltungsabteilung
15.3	RPA, Rechts- und Patentabteilung
14.2	REV, Revision
14.3	Sicherheitszentrale
14.6	STE, Programmgruppe Systemforschung und Technologische Entwicklung
12.1	Tankstelle (KV)
01.4	Technikumshalle DIDO (ZFK)
10.1	TEXTOR (IPP)
14.5	TIA-E, Elektrotechnik
14.3	TIA-N, Nachrichtentechnik
14.5	TIA-G, Graphische Betriebe
02.7	TIA-H, Haustechnik und Instandhaltung TIA-V, Versorgungswerke TIA-A, Allgemeine Dienste
14.6	TFF, Programmgruppe Technologiefolgenforschung
14.1	TTB, Technologie-Transfer-Büro
04.5	Umspannstation Mitte (TIA-E)
16.1	Umspannstation Nord (TIA-E)
15.5	Umspannstation West (TIA-E)
06.3	Umweltprobenbank (IPC)
15.3	VS, Vorstand
01.6	Wache 01 (ASS-OS)
03.4	Wäscherei (TIA-A)
09.5	Wasserversorgung (TIA-V)
15.3	WTA, Wissenschaftlich-Technische Abteilung
14.6	WTR, Wissenschaftlich-Technischer Rat
16.3	ZAM, Zentralinstitut für Angewandte Mathematik
02.3	ZAT, Zentralabteilung Technologie
03.1	ZAT-MF, Mechanische Fertigung
02.12	ZAT-NPT, Neue Physikalische Technologien
04.7	ZB, Zentralbibliothek
04.8	ZCH, Zentralabteilung Chemische Analysen
02.5	ZEL, Zentrallabor für Elektronik
01.4	ZFK, Zentralabteilung Forschungsreaktoren und Kerntechnische Betriebe
12.3	ZFK-DE, Dekontamination
12.18	ZFK-DE, Abfallager-Halle IV
07.2	Zyklotron (IKP)

Vorlesungsmanuskripte des
17. IFF-Ferienkurses 1986

Dünne Schichten und Schichtsysteme

Einführung in die modernen Methoden der Herstellung, Modifikation, Mikroanalytik und technische Anwendungen dünner Schichten und Schichtsysteme.

Hauptthemen: Präparation · Haftung und innere Spannungen · Grenzflächen · Kohärente Vielfachschichten · Mikroanalytik · Schichten für Informationstechnik

744 Seiten

nicht mehr verfügbar

Vorlesungsmanuskripte des
18. IFF-Ferienkurses 1987

Synchrotronstrahlung in der Festkörperforschung

Einführung in die Anwendung der Synchrotronstrahlung zu Strukturuntersuchungen in der Festkörperforschung.

Hauptthemen: Quanten · Elektronentheorie · Strukturuntersuchungen · Absorptionsspektroskopie · Photoelektronenspektroskopie · Lithographie · Mikroanalytik

812 Seiten

nicht mehr verfügbar

Vorlesungsmanuskripte des
19. IFF-Ferienkurses 1988

Supraleitung und verwandte Quantenphänomene

Einführung in die Supraleitung und verwandte Quantenphänomene.

Hauptthemen: Supraleitung und Anwendungen · Supraflüssigkeit · Stark korrelierte Elektronen · Lokalisierung

786 Seiten

nicht mehr verfügbar

Vorlesungsmanuskripte des
20. IFF-Ferienkurses 1989

Computersimulation in der Physik

Einführung in numerische Methoden zur Simulation komplexer Systeme in der Physik.

Hauptthemen: Molekular-Dynamik-Methoden · Monte-Carlo-Methoden · Partielle Differentialgleichungen

1011 Seiten, EUR 17,90

ISBN 3-89336-013-1

Vorlesungsmanuskripte des
21. IFF-Ferienkurses 1990

Festkörperforschung für die Informationstechnik

Einführung in die materialphysikalischen Grundlagen der modernen Informationstechnik.

Schwerpunkte: Physik der Halbleiter · Physik der Magnetspeichermaterialien · Funktion typischer Bauelemente · Industrielle Fertigung aktueller Bauelemente · Physikalische Aspekte zukünftiger Technik

1028 Seiten, EUR 17,90

ISBN 3-89336-033-6

Vorlesungsmanuskripte des
22. IFF-Ferienkurses 1991

Physik der Polymere

Einführung in die physikalischen Stoffeigenschaften von Polymeren und Kunststoffen.

Schwerpunkte: Struktur, Dynamik und Thermodynamik · Konformation · Kristallisation und Glasumwandlung · Gummi- und Viskoelastizität · Molekulare Dynamik · Computersimulation · Polymermischungen · Werkstoffe

900 Seiten, EUR 23,00

ISBN 3-89336-055-7

Obtaining address:
Forschungszentrum Jülich GmbH · ZENTRALBIBLIOTHEK · 52425 Jülich
Tel. 02461/61-5368 · Fax 02461/61-6103 · e-mail: zb-publikation@fz-juelich.de

Vorlesungsmanuskripte des
23. IFF-Ferienkurses 1992

Synchrotronstrahlung zur Erforschung kondensierter Materie

Einführung in die Anwendung von Synchrotronstrahlung zur Bestimmung der geometrischen und elektronischen Struktur von Festkörpern und Grenzflächen.

Schwerpunkte: Erzeugung und Charakteristika der Synchrotronstrahlung · Instrumentierung · Wechselwirkung von Licht und Materie · Elektronische Struktur von Festkörpern, Oberflächen und Grenzflächen; Theorie und Experiment · Spinauflösende Messungen und Magnetismus · Halbleiter-Oberflächen und Schichtsysteme · Adsorbate auf Oberflächen · Streuung und Beugung von Röntgenstrahlung · Strukturanalyse mit EXAFS · Mikroskopie und Lithographie

ca. 900 Seiten, EUR 28,00

ISBN 3-89336-088-3

Vorlesungsmanuskripte des
24. IFF-Ferienkurses 1993

Magnetismus von Festkörpern und Grenzflächen

Einführung in den Magnetismus von metallischen Festkörpern und Grenzflächen.

Schwerpunkte: Konventionelle und moderne Meßmethoden · Theorie und Experimente zum Bandmagnetismus · Magnetische Domänen und Abbildungsverfahren · Volumen- und Grenzflächenanisotropie · Spinwellen · Phasenübergänge und kritische Exponenten · RKKY-Wechselwirkung · Kopplungsphänomene und elektrischer Transport in Schichtsystemen · Werkstoffe

ca. 900 Seiten, EUR 28,00

ISBN 3-89336-110-3

Vorlesungsmanuskripte des
25. IFF-Ferienkurses 1994

Komplexe Systeme
zwischen Atom und Festkörper

Einführung in die bei komplexen Systemen auftretende Phänomene und die zur Beschreibung verwendeten Konzepte und Theoretischen Methoden.

Schwerpunkte: Moleküle, Cluster, Fullerene (Dichtefunktional, Molekulardynamik, komplexe Energieflächen, Clusterspektroskopie) · Defekte in Quasikristallen, Fluiden, Mustern (Topologische Methoden, Energiefunktional) · Grenzflächen, Schichtsysteme (Adsorption, Benetzung, Aufrauhung, Reibung, STM, Kraftmikroskop, Heterostrukturen) · Komplexe Fluide (Hydrodynamik, Polymere, Polyelektrolyte, Kolloide, Membranen, Gläser) · Musterbildung, Chaos und Turbulenz (in Flüssigkeiten, chemischen Reaktionen und Biologie) · Poröse und granulare Medien (Transport, Nichtmischbare Flüssigkeiten)

1022 Seiten, EUR 30,70

ISBN 3-89336-128-6

Vorlesungsmanuskripte des
26. IFF-Ferienkurses 1995

Elektrokeramische Materialien
Grundlagen und Anwendungen

Einführung in die physikalischen und physikalisch-chemischen Grundlagen elektrochemischer Materialien, vor allem mit Perowskit- oder Perowskitähnlicher Struktur, die sich durch außergewöhnliche elektrische und dielektrische Eigenschaften auszeichnen.

Schwerpunkte: Kristallstruktur · Elektronenstruktur · Defekt-Physik und Chemie · Elektronische und ionische Transporteigenschaften · Mechanische Eigenschaften

Untersuchungs- und Präparationsmethoden: Impedanz-, dielektrische und mechanische Relaxationsspektroskopie · Neutronenstreuung · Dünne Schichten · Sintern · Kristallzüchtung

Anwendungen: Dielektrische Schichten · Varistoren · PTC · Piezo- und pyroelektrische Keramik · Ferroelektrika · Optische Bauelemente · Ionenleiter und Brennstoffzellen · Oxidische Supraleiter

ca. 900 Seiten, EUR 33,20

ISBN 3-89336-146-4

Obtaining address:
Forschungszentrum Jülich GmbH · ZENTRALBIBLIOTHEK · 52425 Jülich
Tel. 02461/61-5368 · Fax 02461/61-6103 · e-mail: zb-publikation@fz-juelich.de

Vorlesungsmanuskripte des
27. IFF-Ferienkurses 1996

Streumethoden zur Untersuchung kondensierter Materie

Einführung in die Wechselwirkung und Streuung von Strahlung zur Untersuchung der atomaren Eigenschaften von kondensierter Materie, insbesondere in die Streutheorie zur Interpretation der Meßdaten; Experimentelle Methoden der Diffraktometrie zur Strukturanalyse, der Kleinwinkelstreuung, der Reflektometrie und der Spektroskopie von Neutronen und Röntgenstrahlen. Strahlungsquellen und Instrumentierung. Relaxationsspektrometrie mit Licht.

Die Untersuchungsmethoden werden an den wichtigsten Stoffklassen demonstriert, beispielsweise Metalle, Legierungen, magnetische Verbindungen, Oxide, Gläser, Kunststoffe, Membranen und Proteine sowie Schichtsysteme von Polymeren und Halbleitern.

ca. 850 Seiten, EUR 35,80

ISBN 3-89336-180-4

Vorlesungsmanuskripte des
28. IFF-Ferienkurses 1997

Dynamik und Strukturbildung in kondensierter Materie

Einführung in dynamische Vorgänge und Strukturbildung in verschiedenen Formen der kondensierten Materie auf atomaren bis hin zu makroskopischen Längen- und Zeitskalen.

ca. 900 Seiten, EUR 38,40

ISBN 3-89336-204-5

Vorlesungsmanuskripte des
29. IFF-Ferienkurses 1998

Physik der Nanostrukturen

Vorstellung der Methoden, die es erlauben, die Nanostrukturen mit höchster Präzision herzustellen und zu charakterisieren. Vorstellung von Beispielen nanostrukturierter Festkörper und Oberflächen aus der aktuellen Forschung, in denen es gelungen ist, neue Materialeigenschaften zu beobachten und auch teilweise schon technologisch nutzbar zu machen. Erforschung von Clustern, die entweder isoliert im Molekularstrahl oder als Cluster-Materialien vorgestellt und diskutiert werden.

ca. 1000 Seiten, EUR 40,90

ISBN 3-89336-217-7

Vorlesungsmanuskripte des
30. IFF-Ferienkurses 1999

Magnetische Schichtsysteme

Einführung in die Grundlagen der Wechselwirkungen, die zu kollektivem Magnetismus führen. Dazu gehört eine Einführung in die Dichtefunktionaltheorie und den Bandmagnetismus. Weiterhin wird eine Übersicht über verschiedene magnetische Materialklassen sowie relevante Messmethoden gegeben. Die Behandlung des Dünnfilmmagnetismus beginnt mit der Einführung der wichtigsten Präparationsmethoden und strukturellen Charakterisierungsmöglichkeiten. Daran schließt sich die Beschreibung der Eigenschaften des Magnetismus in Einzelschichten an, sowie deren Kopplungsphänomene in Multischichten. Besondere Beachtung erhalten Transportphänomene, die durch spinabhängige Elektronenstreuung und Reflektivität an den Grenzflächen oder einen spinabhängigen Tunneleffekt über isolierende Zwischenschichten verursacht werden. Auch die bereits in Einzelschichten auftretenden Anisotropien, sowie die Magnetostriktion werden theoretisch und experimentell behandelt, ebenso die Magnetooptik und der Röntgendichroismus.

Die wichtigsten Themen sind: · Grundlagen von Magnetismus und magnetischen Materialien
· Präparation magnetischer Schichtsysteme
· Spinstrukturen in Schichtsystemen
· Zwischenschichtaustauschkopplung
· Magnetische Anisotropie und Magnetooptik
· Spinabhängiger Transport

ca. 1300 Seiten, zahlreiche z.T. farb. Abb., EUR 56,24

ISBN 3-89336-235-5

Obtaining address:
Forschungszentrum Jülich GmbH · ZENTRALBIBLIOTHEK · 52425 Jülich
Tel. 02461/61-5368 · Fax 02461/61-6103 · e-mail: zb-publikation@fz-juelich.de

Vorlesungsmanuskripte des
31. IFF-Ferienkurses 2000

Femtosekunden und Nano-eV

Dynamik in kondensierter Materie

Die charakteristischen Längen- und Zeitskalen der Dynamik kondensierter Materie erstrecken sich über viele Größenordnungen: von ultraschnellen elektronischen Prozessen im Subfemtosekundenbereich über die Bewegung von Makromolekülen im Nano- bis Mikrosekundenbereich bis hin zu langsamen kollektiven Relaxationsprozessen im Stundenbereich, wie sie etwa bei Spingläsern auftreten.

Diese extreme Bandbreite, die in anderen Disziplinen ihresgleichen sucht, erfordert einen ganzen Zoo von experimentellen Untersuchungsmethoden, die auf der Wechselwirkung von elektromagnetischer Strahlung und von Teilchenstrahlung mit Materie beruhen. Durch revolutionäre Entwicklungen bei den Strahlungsquellen und neue raffinierte experimentelle Verfahren wurden in den letzten Jahren die Grenzen der Festkörperspektroskopie zu extremen Werten der Orts-, Zeit- und Energieauflösung verschoben. So können heute Nanopartikel mit einer Zeitauflösung im fs-Bereich bzw. Energieauflösungen im neV-Bereich untersucht werden.

In dem IFF-Ferienkurs 2000 werden diese modernen experimentellen Verfahren vorgestellt, wobei als Sonden elektromagnetische Strahlung (von Infrarot- bis harter Röntgenstrahlung), Neutronen und Elektronen diskutiert werden. Viele Experimente wurden erst durch neue Strahlungsquellen realisierbar, wie Synchrotronstrahlungsquellen der dritten Generation oder Spallationsneutronenquellen.

Es werden die Eigenschaften dieser Quellen diskutiert, wobei Begriffe wie Kohärenz und Zeitstruktur eine zentrale Rolle spielen, und ein Ausblick auf Großprojekte im neuen Jahrtausend gegeben. Moderne experimentelle Verfahren wie fsec-Laserspektroskopie, neV-Neutronenspinechospektroskopie, Röntgenkorellationsspektroskopie oder mehrdimensionale Kernspinresonanz werden zusammen mit den wissenschaftlichen Anwendungsfeldern vorgestellt.

Die Dynamik der kondensierten Materie wird in ihrer ganzen Breite behandelt: von elektronischen Anregungen und Transport über die klassische Elementaranregungen wie Phononen und Magnonen hin zu diffusiven Bewegungen oder die wesentlich entropisch getriebene Dynamik weicher Materie z.B. von Polymeren, Membranen und komplexen Flüssigkeiten. Weitere Schwerpunkte bilden ultraschnelle Prozesse in Molekülen, der zeitliche Ablauf chemischer Reaktionen, metallische und magnetische Systeme und schließlich die dynamischen Prozesse an Oberflächen. Anwendungsnahe Themen wie etwa die Magnetoelektronik werden ebenfalls angesprochen.

Die wichtigsten Themen sind:

- fsec-Spektroskopie
- inelastische Steuung von elektromagnetischer Strahlung, Neutronen
- Elektronenelektronische Anregungen und Transport
- Magnetisierungsdynamik und Magnetoelektronik
- Oberflächendynamik
- chemische Reaktionen und transiente Zustände
- Diffusion, Relaxationsprozesse, Elementaranregungen.

ca. 1000 Seiten, zahlreiche z.T. farb. Abb.,
EUR 48,57 (Hardcover)

Vorlesungsmanuskripte des
32. IFF-Ferienkurses 2001

Neue Materialien für die Informationstechnik

Die Möglichkeiten der heutigen Informations- und Kommunikationstechnik werden zunehmend bestimmt durch den Einsatz neuer elektronischer Materialien – jenseits der klassischen Siliziumtechnik. Dies betrifft sowohl die Erweiterung der konventionellen Mikroelektronik durch neuartige Funktionen als auch den Einsatz in integrierten Hybridsystemen. Der IFF-Ferienkurs 2001 behandelt alle Materialklassen, die in modernen

Obtaining address:
Forschungszentrum Jülich GmbH · ZENTRALBIBLIOTHEK · 52425 Jülich
Tel. 02461/61-5368 · Fax 02461/61-6103 · e-mail: zb-publikation@fz-juelich.de

Systemen der Informationstechnik heute bereits eingesetzt werden oder ein hinreichend großes Marktpotential für zukünftige Anwendungen aufweisen.

Der Ferienkurs hat einen betont interdisziplinären Charakter. Er verbindet Aspekte der Festkörperphysik, der Kristall- und Molekülchemie sowie der Biologie mit der Mikroelektronik. Der Schwerpunkt wird auf der Verknüpfung des mikroskopischen Verständnisses der Materialien und der Nutzung ihrer Eigenschaften in Bauelementefunktionen liegen.

Es werden materialübergreifende Konzepte der Informationstechnik diskutiert und aufgezeigt, in wie großer Breite neue Materialien in Bauelemente und Systeme vordringen. Das Spektrum der Vorlesungen umfasst u. a. folgende Themen:

- **dielektrische und ferroelektrische Oxide** für künftige Generationen schneller, nichtflüchtiger Arbeitsspeicher und hochintegrierter Logik-ICs,
- **ultradünne Metallschichten** mit spin-abhängiger Leitfähigkeit für magnetische Speicher und Leseköpfe heutiger Festplattengenerationen
- **Phasenwechsel-Materialien** für wiederbeschreibbare DVDs,
- **photoadressierbare Polymere** für holographische 3D-Speicher,
- **akusto-optische und elektro-optische Oxide** für die optische Datenübertragung,
- abstimmbare **keramische Dielektrika** für die Mikrowelentechnik, komplexe organische Verbindungen für hochauflösende **Flüssigkristall-Displays** und die künftige **Molekularelektronik**,
- Komponenten für **Plasma- und Feldemissionsdisplays**,
- Materialien für die Verknüpfung der **biologischen** und der **mikroelektronischen** Informationsverarbeitung.

ca. 800 Seiten, zahlreiche z.T. farb. Abb.,
EUR 61,36 (Hardcover)

Obtaining address:
Forschungszentrum Jülich GmbH · ZENTRALBIBLIOTHEK · 52425 Jülich
Tel. 02461/61-5368 · Fax 02461/61-6103 · e-mail: zb-publikation@fz-juelich.de

Forschungszentrum Jülich



Band / Volume 10
ISBN 3-89336-297-5

Materie und Material
Matter and Materials